Helmholtz Alliance Linear Collider Forum

Proceedings of the Workshops
Hamburg, Munich, Hamburg 2010-2012
Germany

edited by:
G. Moortgat-Pick

Verlag Deutsches Elektronen-Synchrotron

Impressum[1]

Proceedings of the Helmholtz Alliance Linear Collider Forum 2010–2012, Hamburg, München, Hamburg, Germany

Conference homepage
`https://lcforum.desy.de/e137560/`

Workshop Sessions

- 14-15 June 2010, DESY, Hamburg
- 1 December 2010, Internationales Congress Center, Dresden
  (at the 4th Annual Workshop of the Helmholtz Alliance 'Physics at the Terascale')
- 14-15 July 2011, Max-Planck-Institut für Physik, Munich
- 7 December 2012, Beethovenhalle, Bonn
  (at the 5th Annual Workshop of the Helmholtz Alliance 'Physics at the Terascale')
- 7-9 February 2012, DESY, Hamburg
- 3 December 2012, DESY, Hamburg
  (at the 6th Annual Workshop of the Helmholtz Alliance 'Physics at the Terascale')

Slides at
`http://indico.desy.de/conferenceDisplay.py?confId=3040`
`http://indico.desy.de/conferenceDisplay.py?confId=3094`
`http://indico.desy.de/conferenceDisplay.py?confId=4375`
`http://indico.desy.de/conferenceDisplay.py?confId=4421`
`http://indico.desy.de/conferenceDisplay.py?confId=4980`
`http://indico.desy.de/conferenceDisplay.py?confId=5679`

Online proceedings at
`https://lcforum.desy.de/`

[1] Plot on the title page by courtesy of K. Fujii and J. Tian

Organizer of the Linear Collider Forum: I. Fleck, G. Moortgat-Pick, S. Riemann, F. Simon
April 2013
DESY 12-123H
DESY-PROC-2013-02
ISBN 978-3-935702-73-7
ISSN 1435-8077

Published by
Verlag Deutsches Elektronen-Synchrotron
Printed by
Kopierstelle Deutsches Elektronen-Synchrotron
Notkestraße 85
22607 Hamburg
Germany

Preface

The Linear Collider Forum is an initiative born within the Helmholtz-Alliance "Physics at the Terascale", a network of German Universities and Research Centers working in high-energy particle physics. Yearly dedicated meetings focus on the physics case and the technologies at a future linear collider, covering both the ILC and CLIC concepts.
In February 2012 an extended meeting with significant international participation was dedicated to the discussion of physics scenarios to strengthen and update the case for a linear e+e- collider in light of new developments and the latest LHC results.
Contributions to LC Forum sessions were collected on the DESY LC-note server with a dedicated mark 'LC-REP-year-number'.
These Proceedings comprise all contributions that have been submitted with the dedicated mark in 2012 and 2013. Therefore also contributions are included that actually have not been presented on a LC Forum meeting but are strongly related to the subject.

G. Moortgat-Pick[2]

[2]indebted to all authors and participants for their lovely contributions and with special thanks to the great organization team of the LC Forum.

Contents

Chapter 1

Setting the Scene

The following three articles comprise the framework of the physics potential of the Linear Collider.

The first article was also a contribution to the European Strategy 2012 and was written by the Linear Collider Report Committee, attached is also their charge. This article summarizes the physics landscape in 2012 and gives predictions for the expected physics outcome of ILC and CLIC from $\sqrt{s} = 250$ GeV up to 3 TeV.
The second contribution was presented at the Linear Collider Forum in February 2012 and summarizes the Higgs physics potential of the ILC on basis of the physics landscape at that time, i.e. the Higgs discovery at the LHC was not yet confirmed but was already at the horizon.

More details to the studies, updates as well as further new studies of LC physics are presented in the Chapters 2–7.

Currently the topic of a 'staged approach' for the Linear Collider is under discussion and the third article in this chapter gives an overview about technical issues with such a staged approach, in particular addressing questions on the corresponding drive beam energies of the positron source and the estimated amount of integrated luminosity in terms of physics performance.

Further technical detector and machine related aspects and new simulations are presented in Chapter 8.

ILC ESD-2012/4, CLIC-Note-949 (July 30, 2012)

The Physics Case for an e^+e^- Linear Collider

James E. Brau[a], Rohini M. Godbole[b], Francois R. Le Diberder[c], M.A. Thomson[d], Harry Weerts[e], Georg Weiglein[f], James D. Wells[g], Hitoshi Yamamoto[h]

A Report Commissioned by the Linear Collider Community[†]

[(a)]Center for High Energy Physics, University of Oregon, USA; [(b)]Centre for High Energy Physics, Indian Institute of Science, Bangalore, India; [(c)]Laboratoire de l'Accélérateur Linéaire, IN2P3/CNRS et Université Paris-Sud, France; [(d)]Cavendish Laboratory, University of Cambridge, UK; [(e)]Argonne National Laboratory, Argonne, USA; [(f)]DESY, Hamburg, Germany; [(g)]CERN, Geneva, Switzerland; [(h)]Tohoku University, Japan

1 Introduction

The physics motivation for an e^+e^- linear collider (LC) has been studied in detail for more than 20 years [1]-[10]. These studies have provided a compelling case for a LC as the next collider at the energy frontier. The unique strengths of a LC stem from the clean experimental environment arising from e^+e^- collisions. In particular, the centre-of-mass energy and initial-state polarisations [11] are precisely known and can be adjusted, and backgrounds are many orders of magnitude lower than the QCD backgrounds that challenge hadron collider environments. The low backgrounds permit trigger-free readout, and the measurements and searches for new phenomena are unbiased and comprehensive. Full event reconstruction is possible. These favourable experimental conditions will enable the LC to measure the properties of physics at the TeV scale with unprecedented precision and complementarity to the LHC.

Thanks to the extraordinary achievements of the LHC machine and of the ATLAS and CMS experiments, our field witnessed a deep revolution in the middle of 2012: the discovery of a new boson. The observation at the LHC of this new particle compatible with a light Higgs boson strengthens the physics case for a LC even more.

The main goals of the LC physics programme are:

- precise measurements of the properties of the Higgs sector;
- precise measurements of the interactions of top quarks, gauge bosons, and new particles;
- searches for physics beyond the Standard Model (SM), where, in particular, the discovery reach of the LC can significantly exceed that of the LHC for the pair-production of colour-neutral states; and
- sensitivity to new physics through tree-level or quantum effects in high-precision observables.

The complementarity of the LC and LHC has been established over many years by a dedicated worldwide collaborative effort [9]. It has been shown in many contexts that for new particles found at the LHC, the LC will be essential in determining the properties of these new particles and unraveling the underlying structure of the new physics.

The development of the SM was a triumph for modern science. The experimental confirmation of the $SU(3)_C \times SU(2)_L \times U(1)_Y$ gauge structure of the SM and the precise measurement of its parameters were achieved through a combination of analyses of data from e^+e^- and hadron colliders and from deep-inelastic lepton-nucleon scattering. These precision measurements are compatible with the minimal Brout-Englert-Higgs mechanism of Electroweak Symmetry Breaking (EWSB), through which the masses of all the known

[†]See Addendum for this committee's origin and charge. The committee also wishes to express thanks to the many reviewers of earlier drafts of this report whose input has been very helpful.

fundamental particles are generated. Within the SM the measurements of electroweak precision observables show a pronounced preference for a light Higgs boson, below about 150 GeV.

The observation of a new particle compatible with a Higgs boson of mass $\sim 125\,\text{GeV}$ is a major breakthrough in particle physics. It represents one of the most significant discoveries of modern science. Given the far-reaching consequences for our understanding of the fundamental structure of matter and the basic laws of nature, it is of the highest priority to probe the properties of this particle with a comprehensive set of high-precision measurements to address such questions as:

- What are the couplings of this particle to other known elementary particles? Is its coupling to each particle proportional to that particle's mass, as required in the SM by the Higgs mechanism?
- What are the mass, width, spin and CP properties of this particle?
- What is the value of the particle's self-coupling? Is this consistent with the expectation from the symmetry-breaking potential?
- Is this particle a single, fundamental scalar as in the SM, or is it part of a larger structure? Is it part of a model with additional scalar doublets? Or, could it be a composite state, bound by new interactions?
- Does this particle couple to new particles with no other couplings to the SM? Is the particle mixed with new scalars of exotic origin, for example, the radion of extra-dimensional models?

The LC provides a unique opportunity to study Higgs properties with sufficient precision to answer these fundamental questions. The large numbers of Higgs bosons that would be produced at a LC, between 10^5 and 10^6 depending on centre-of-mass energy and integrated luminosity, and the clean final states mean that a LC can be considered as a Higgs factory where the properties of the Higgs boson can be studied in great detail. In particular, a LC provides the possibility of model-independent measurements of the Higgs couplings to the gauge bosons and fermions at the few percent level.

Whilst the discovery of a signal compatible with a Higgs boson at the LHC represents a breakthrough in particle physics, it should be kept in mind that the minimal EWSB theory of the SM without other dynamical mechanisms has theoretical shortcomings, and a richer and more complex structure is generally favoured. Most of the ideas for physics beyond the SM (BSM) are driven by the need to achieve a deeper understanding of the EWSB mechanism. Furthermore, the presence of non-baryonic dark matter in the cosmos is an experimentally established fact that implies BSM physics. To date, no clear sign of BSM physics has emerged from LHC data. For new states that are colour-neutral, a LC provides excellent sensitivity for direct discovery via pair production. This complements the search reach of the LHC, where the highest sensitivity is achieved for BSM coloured states. Should the two machines be operating concurrently, the LC results could even provide feed-back to the LHC experiments and vice versa.

The flexibility of the LC will give rise to a rich physics programme which could consist of i) a low-energy phase with $\sqrt{s}$ in the range of $250 - 500\,\text{GeV}$, enabling the study of ZH, $t\bar{t}$, HHZ and $t\bar{t}H$ thresholds, and ii) a high-energy phase with $\sqrt{s} > 500\,\text{GeV}$ allowing a high statistics study of the Higgs boson through the WW fusion process and allowing access to rarer Higgs production processes such as $e^+e^- \to HH\nu_e\bar{\nu}_e$. The choice of the centre-of-mass energy range for the higher energy operation would be determined by the BSM physics scale, where the flexibility in energy of a LC would allow the threshold behaviour for any new physics process to be mapped out in detail. While this document focuses on the minimal LC programme, there are a number of optional phases of LC operation, like GigaZ, which is a high-luminosity Z-factory, and ee, $e\gamma$ and $\gamma\gamma$ configurations.

Two options for a future e^+e^- LC have been developed, with different main linac acceleration schemes. The International Linear Collider (ILC) uses superconducting RF, whereas the Compact Linear Collider (CLIC) uses a separate drive beam to provide the accelerating power. The ILC technology is mature and provides an option for a Higgs and top factory to be constructed on a relatively short timescale. The CLIC technology provides the potential to reach higher centre-of-mass energies, but it requires further development. In recent years there has been extensive collaboration between ILC and CLIC physicists with the

goal of realising a LC as the next major new facility. Furthermore, the ILC and CLIC are being organised under the same formal worldwide body, the Linear Collider Board (LCB), reporting directly to ICFA. The strong accelerator development programme is complemented by an active theory and experimental community working on the physics and detectors for a future LC. These studies have resulted in detailed designs for the detectors at a LC, and, based on detailed simulation studies, have provided a clear demonstration that the LC physics goals can be achieved.

A comprehensive review of LC physics has been given in the Physics volume of the ILC RDR report [3], with extensions to higher energies in the CLIC CDR [4]. More recently, many important measurements at the ILC and CLIC have been simulated with fully realised model detectors [4–7]. Finally, new reports on LC physics have attempted to bring the discussion of the LC capabilities [4, 7] up to date in relation to recent results from the LHC. The main results from these physics studies are summarised below within the context of the results that have been obtained at the LHC up to now and with a view also to the possible progress from the running of the LHC during the next years. Unless otherwise stated, the discussion refers generically to a Linear Collider (LC) rather than to the specific realisations ILC or CLIC.

2 Higgs Physics and Electroweak Symmetry Breaking

In the SM, the Higgs boson plays a special role. The Higgs mechanism is responsible for electroweak symmetry breaking and accounts for the generation of the masses of all the other elementary particles. In order to distinguish a SM Higgs from possible alternative scenarios, it is necessary to measure precisely its couplings to the gauge bosons, to the fermions, and to itself. Furthermore, the spin and the CP-properties of the new state need to be determined, and it must be clarified whether there is more than one physical Higgs boson. At the LHC ratios of the Higgs couplings to different particles can be measured for a subset of the possible decays. Earlier LHC studies [12] suggest that even with 3000 fb^{-1} of data the precision achievable on these ratios remains somewhat limited, $\Gamma_W/\Gamma_Z \sim 10\%$, $\Gamma_W/\Gamma_b \sim 25\%$ and $\Gamma_W/\Gamma_\tau \sim 30\%$. It should be anticipated that with real data in hand LHC experiments likely will perform better than initially projected. At a LC, the precisions achievable are of the order of a few percent, and a wider range of decay channels can be studied.

A LC is the only place where model-independent measurements of the Higgs boson couplings can be made, including to invisible final states. A number of these measurements are unique to a LC, and the precision achievable for extracting parameters significantly surpasses that anticipated at the LHC. The LC measurements would establish whether the Higgs boson has the properties predicted by the SM, or is part of an extended Higgs sector such as in SUSY models, or whether it has a completely different physical origin which would be the case for a composite Higgs.

2.1 Higgs Production at a Linear Collider

At a LC, the main Higgs production channels are through the Higgs-strahlung and vector boson fusion processes (see Figure 1). At relatively low centre-of-mass energies the Higgs-strahlung process, $e^+e^- \to ZH$, dominates, with a peak cross section at approximately 30 GeV above the ZH production threshold. At higher centre-of-mass energies, the WW fusion process $e^+e^- \to H\nu_e\bar{\nu}_e$ becomes increasingly important. For a Higgs boson mass of ~ 125 GeV the fusion process dominates above $\sqrt{s} \sim 500$ GeV. The WW fusion cross section increases with $\sqrt{s}$, allowing large samples of Higgs bosons to be studied at a TeV-scale LC. The ZZ fusion process $e^+e^- \to He^+e^-$ has a cross section that is approximately an order of magnitude smaller than the WW fusion process. Table 1 compares the expected number of ZH and $H\nu_e\bar{\nu}_e$ events at the main centre-of-mass energies considered in the ILC and CLIC studies. Even at the lowest LC energies considered, large samples of Higgs bosons can be accumulated. In addition to the main Higgs production processes, rarer processes such as $e^+e^- \to t\bar{t}H$, $e^+e^- \to ZHH$ and $e^+e^- \to HH\nu_e\bar{\nu}_e$ provide access to the top quark Yukawa coupling and the Higgs trilinear self-coupling.

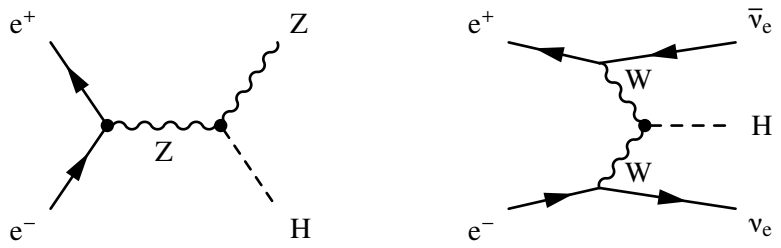

Figure 1: The two main Higgs production processes at a LC.

	250 GeV	350 GeV	500 GeV	1 TeV	1.5 TeV	3 TeV
$\sigma(e^+e^- \to ZH)$	240 fb	129 fb	57 fb	13 fb	6 fb	1 fb
$\sigma(e^+e^- \to H\nu_e\bar{\nu}_e)$	8 fb	30 fb	75 fb	210 fb	309 fb	484 fb
Int. $\mathcal{L}$	250 fb^{-1}	350 fb^{-1}	500 fb^{-1}	1000 fb^{-1}	1500 fb^{-1}	2000 fb^{-1}
# ZH events	60,000	45,500	28,500	13,000	7,500	2,000
# $H\nu_e\bar{\nu}_e$ events	2,000	10,500	37,500	210,000	460,000	970,000

Table 1: The leading-order Higgs unpolarised cross sections for the Higgs-strahlung and WW-fusion processes at various centre-of-mass energies for $m_H = 125$ GeV. Also listed is the expected number of events accounting for the anticipated luminosities obtainable within 5 years of initial operation at each energy.

2.2 Higgs Coupling Measurements at $\sqrt{s} < 500$ GeV

The Higgs-strahlung process provides the opportunity to study the couplings of the Higgs boson in a *model-independent* manner. This is unique to a LC. The clean experimental environment, and the relatively low SM cross sections for background processes, allow $e^+e^- \to ZH$ events to be selected based on the identification of two opposite charged leptons with invariant mass consistent with m_Z. The remainder of the event, i.e. the Higgs decay, is not considered in the event selection. For example, Figure 2 shows the simulated invariant mass distribution of the system recoiling against identified $Z \to \mu^+\mu^-$ decays at a LC for $\sqrt{s} = 250$ GeV. A clear peak at the generated Higgs mass of $m_H = 120$ GeV is observed. Because only the properties of the di-lepton system are used in the selection, this method provides an absolute measurement of the Higgs-strahlung cross section, regardless of the Higgs boson decay modes; it would be equally valid if the Higgs boson decayed to invisible final states. Hence a model-independent measurement of the coupling g_{HZZ} can be made. With a dedicated analysis using also the hadronic decays of the Z the sensitivity to invisible decay modes can be improved very significantly as compared to the fully model-independent analysis. The LC provides in fact a unique sensitivity to invisible decay modes of the Higgs boson, extending down to a branching ratio into invisible states as low as 1%. The precisions achievable on the Higgs-strahlung cross section and the coupling g_{HZZ} are shown in Table 2 for $m_H = 120$ GeV.

The recoil mass study provides an absolute measurement of the total ZH production cross section and therefore the total number of Higgs bosons produced would be known with a statistical precision of 3 – 4 %. The systematic uncertainties from the knowledge of the integrated luminosity and event selection are expected to be significantly smaller. Subsequently, by identifying the individual final states for different Higgs and Z decay modes, absolute measurements of the Higgs boson branching fractions can be made. High flavour-tagging efficiencies are achievable and the $H \to b\bar{b}$ and $H \to c\bar{c}$ decays can be separated. Neglecting the Higgs decays into light quarks, one can also infer the branching ratio of $H \to gg$. Table 3 summarises the branching fraction precisions achievable at a LC operating at either 250 GeV or 350 GeV where model-independent measurements of the Higgs boson couplings to the b-quark, c-quark, τ-lepton, W-boson and Z-boson can be made to better than 5 %.

Preliminary results of ongoing studies confirm that a precision of $\Delta g_{ttH}/g_{ttH} \sim 10\%$ can be achieved,

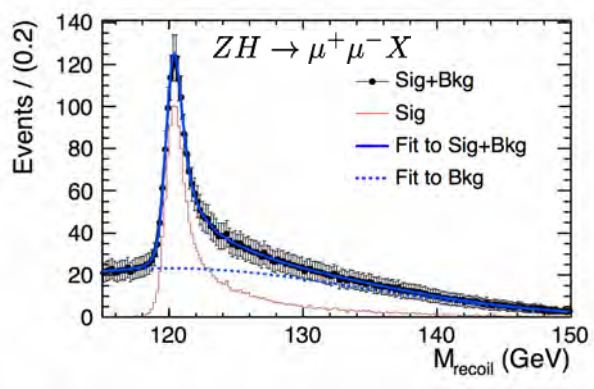

Figure 2: The recoil mass distribution for $e^+e^- \to ZH \to \mu^+\mu^- H$ events with $m_H = 120\,\text{GeV}$ in the ILD detector concept at the ILC [6]. The numbers of events correspond to $250\,\text{fb}^{-1}$ at $\sqrt{s} = 250\,\text{GeV}$, and the error bars show the expected statistical uncertainties on the individual points.

$\sqrt{s}$	250 GeV	350 GeV
Int. $\mathcal{L}$	$250\,\text{fb}^{-1}$	$350\,\text{fb}^{-1}$
$\Delta(\sigma)/\sigma$	3 %	4 %
$\Delta(g_{HZZ})/g_{HZZ}$	1.5 %	2 %

Table 2: Precision measurements of the Higgs coupling to the Z at $\sqrt{s} = 250\,\text{GeV}$and $\sqrt{s} = 350\,\text{GeV}$ based on full simulation studies with $m_H = 120\,\text{GeV}$. Results from [6] and follow-up studies.

even near threshold at 500 GeV with 1 ab^{-1}, thanks to the factor of two enhancement of the QCD-induced bound-state effect. The measurement, which is made difficult by a very large $t\bar{t}$ background, relies on the foreseen performances of the LC detectors. Furthermore, $\Delta g_{H\gamma\gamma}/g_{H\gamma\gamma}$ can be measured at $\sim 5\%$ precision at a 500 GeV LC with 500 fb^{-1} of integrated luminosity.

2.3 Higgs Coupling Measurements at $\sqrt{s} \geq 500$ GeV

The large samples of events from both WW and ZZ fusion processes would lead to a measurement of the relative couplings of the Higgs boson to the W and Z at the 1 % level. This would provide a strong test of the SM prediction $g_{HWW}/g_{HZZ} = \cos^2\theta_W$.

The ability for clean flavour tagging combined with the large samples of WW fusion events allows the production rate of $e^+e^- \to H\nu_e\bar{\nu}_e \to b\bar{b}\nu_e\bar{\nu}_e$ to be determined with a precision of better than 1 %. Furthermore, the couplings to the fermions can be measured more precisely at high energies, even when accounting for the uncertainties on the production process. For example, Table 3 shows the precision on the branching ratio obtained from full simulation studies as presented in [4]. The uncertainties of the Higgs couplings can be obtained by combining the high-energy results with those from the Higgs-strahlung process. The high statistics Higgs samples would allow for very precise measurements of relative branching ratios. For example, a LC operating at 3 TeV would give a statistical precision of 1.5 % on g_{Hcc}/g_{Hbb}.

2.4 Higgs Self-Coupling

In the SM, the Higgs boson originates from a doublet of complex scalar fields described by the potential

$$V(\phi) = \mu^2\phi^\dagger\phi + \lambda(\phi^\dagger\phi)^2\,.$$

	250/350 GeV	500 GeV†	3 TeV
$\sigma \times Br(\mathrm{H} \to \mathrm{bb})$	1.0/1.0 %	0.6 %	0.2 %
$\sigma \times Br(\mathrm{H} \to \mathrm{cc})$	7/6 %	4 %	3 %
$\sigma \times Br(\mathrm{H} \to \tau\tau)$	6*/6 %	5 %	?
$\sigma \times Br(\mathrm{H} \to \mathrm{WW})$	8/6 %	3 %	?
$\sigma \times Br(\mathrm{H} \to \mu\mu)$	−/−	?	15 %
$\sigma \times Br(\mathrm{H} \to \mathrm{gg})$	9/7 %	5 %	?

	250/350 GeV	500 GeV†	3 TeV
g_{Hbb}	1.6/1.4 %	?	2 %
g_{Hcc}	4/3 %	2 %	2 %
$g_{\mathrm{H}\tau\tau}$	3*/3 %	2.5 %	?
g_{HWW}	4/3 %	1.4 %	< 2 %
$g_{\mathrm{H}\mu\mu}$	−/−	−	7.5 %
$\frac{g_{\mathrm{HWW}}}{g_{\mathrm{HZZ}}}$	?/?	?	< 1 %*
g_{Htt}	−/−	15 %	?

Table 3: The precision on the Higgs branching ratios and couplings obtainable from studies of the Higgs-strahlung process at a LC operating at either $\sqrt{s} = 250\,\mathrm{GeV}$, $\sqrt{s} = 350\,\mathrm{GeV}$ and $\sqrt{s} = 500\,\mathrm{GeV}$. The dagger on the 500 GeV columns indicates that the quoted numbers are based on projections to be updated in [7]. The uncertainties on the couplings include the uncertainties on g_{HZZ} obtained from the absolute measurement of the ZH cross section. Also shown are the precisions achievable from the WW fusion process at a LC operating at 3 TeV. The numbers marked with asterisk are estimates, all other numbers come from full simulation studies with $m_{\mathrm{H}} = 120\,\mathrm{GeV}$. The question marks indicate that the results of ongoing studies are not yet available. In all cases the luminosities assumed are those given in Table 1.

After spontaneous symmetry breaking, this form of the potential gives rise to a triple Higgs coupling of strength proportional to λv, where v is the vacuum expectation value of the Higgs potential. The measurement of the strength of the Higgs trilinear self-coupling therefore provides direct access to the quartic potential coupling λ assumed in the Higgs mechanism. This measurement is therefore crucial for experimentally establishing the Higgs mechanism. For a low-mass Higgs boson, the measurement of the Higgs boson self-coupling at the LHC will be extremely challenging even with $3000\,\mathrm{fb}^{-1}$ of data. At a LC, the Higgs self-coupling can be measured through the $\mathrm{e^+e^-} \to \mathrm{ZHH}$ and $\mathrm{e^+e^-} \to \mathrm{HH}\nu_\mathrm{e}\bar{\nu}_\mathrm{e}$ processes [8]. The precision achievable is currently being studied for the $\mathrm{e^+e^-} \to \mathrm{ZHH}$ process at $\sqrt{s} = 500\,\mathrm{GeV}$ and for the $\mathrm{e^+e^-} \to \mathrm{HH}\nu_\mathrm{e}\bar{\nu}_\mathrm{e}$ process at $\sqrt{s} > 1\,\mathrm{TeV}$. Given the complexity of the final state and the smallness of the cross sections, these studies are being performed with a full simulation of the LC detector concepts. The preliminary results indicate that a precision of about 20 % on λ could be achieved, with the greatest sensitivity coming from $\mathrm{e^+e^-} \to \mathrm{HH}\nu_\mathrm{e}\bar{\nu}_\mathrm{e}$.

2.5 Total Higgs Width

For Higgs boson masses below 125 GeV, the total Higgs decay width in the SM (Γ_{H}) is less than 5 MeV and cannot be measured directly. Nevertheless, at a LC it can be determined from the relationship between the total and partial decay widths, for example

$$\Gamma_H = \Gamma(\mathrm{H} \to \mathrm{WW}^*)/Br(\mathrm{H} \to \mathrm{WW}^*)\,.$$

Here $\Gamma(\mathrm{H} \to \mathrm{WW}^*)$ can be determined from the measurement of the HWW coupling obtained from the fusion process $\mathrm{e^+e^-} \to \mathrm{H}\nu_\mathrm{e}\bar{\nu}_\mathrm{e}$. When combined with the direct measurement of $Br(\mathrm{H} \to \mathrm{WW}^*)$, this allows the Higgs width to be inferred. A precision on the total decay width of the Higgs boson of about 5% at $\sqrt{s} = 500\,\mathrm{GeV}$ can be reached. This improves to better than 4 % at 1 TeV.

2.6 Impact of the Precision Measurements of the Higgs Couplings

Whilst the precise measurements at a LC of the Higgs couplings to gauge bosons, fermions and to itself are of interest in their own right, they will be crucial for testing the fundamental prediction of the Higgs mechanism that the Higgs coupling to different particles is proportional to masses, as summarised in Figure 3.

The precise measurements at a LC will provide a powerful probe of the structure of the Higgs sector. The SM with a single Higgs doublet is only one of many possibilities. The model-independent measurements at

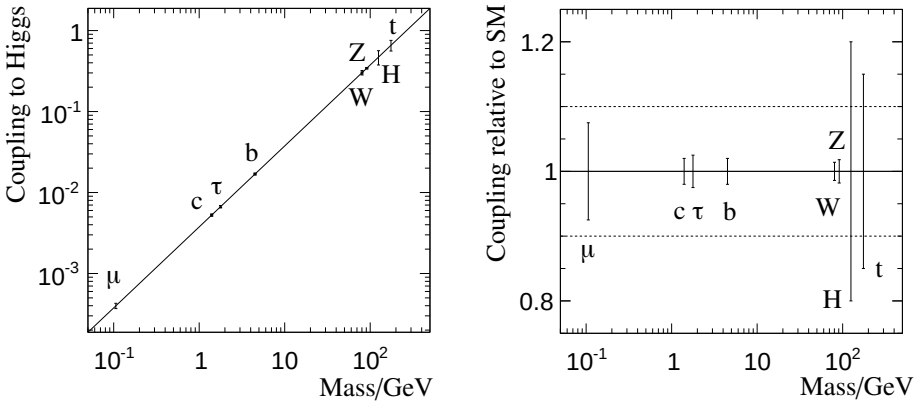

Figure 3: An illustration of the typical precisions to which the relation between the Higgs couplings to the masses of the particles can be tested at a linear collider, assuming operation at one energy point below and one above $\sqrt{s} = 500\,\text{GeV}$ with the integrated luminosities of Table 1. The ultimate sensitivity will depend on the precise integrated luminosity recorded and the centre-of-mass energies at which the LC is operated. The two plots show the absolute and relative precision that can be reached. The values shown assume SM couplings.

a LC will be crucial to distinguish between the different possible manifestations of the underlying physics. It is a general property of many extended Higgs theories that the lightest Higgs scalar can have nearly identical properties to the SM Higgs boson. In this so-called decoupling limit, additional states of the Higgs sector are heavy and may be difficult to detect both at the LHC and LC. Thus, precision measurements are crucial in order to distinguish the simple Higgs sector of the SM from a more complicated scalar sector. Deviations from the SM can arise from an extended structure of the Higgs sector, for instance if there is more than one Higgs doublet. Another source of possible deviations from the SM Higgs properties are loop effects from BSM particles. The potential for deciphering the physics of EWSB is directly related to the sensitivity for verifying deviations from the SM. For example, in Figure 4 (left) the typical deviations from the SM predictions for a Two-Higgs-Doublet model are compared to the precision on the couplings achievable at a LC. In this example, the high-precision measurements at the LC would clearly indicate the non-SM nature of the EWSB sector.

Furthermore, small deviations from SM-like behaviour can arise as a consequence of fundamentally different physics of EWSB. For example, if an additional fundamental scalar such as the radion mixes slightly with the Higgs boson, the subtle shifts compared to the SM Higgs boson in the branching ratios and overall decay width may only be discernible through the high-precision and model-independent measurements of couplings available at a LC.

2.7 Higgs Boson Mass, Spin and CP Properties

A LC is the ideal place to measure the properties of the Higgs boson. For example, the mass of the Higgs boson can be determined at a LC with a precision of better than 50 MeV, either from the recoil mass distribution at $\sqrt{s} = 250\,\text{GeV}$ or from the direct reconstruction of its decay products. This would improve on the precise measurement obtained from the $\gamma\gamma$ decay mode at the LHC.

The spin of the Higgs boson can be obtained through the Higgs-strahlung process from the threshold dependence of the cross section as well as angular distributions of the Z and its decay products. For example, a threshold scan with an integrated luminosity of just $20\,\text{fb}^{-1}$ at each point is sufficient to establish the spin of the Higgs boson. Although the determination of the Higgs boson spin will be achieved early at the LHC, a LC provides a unique window into the possibility of detecting CP violation in the Higgs and top sector.

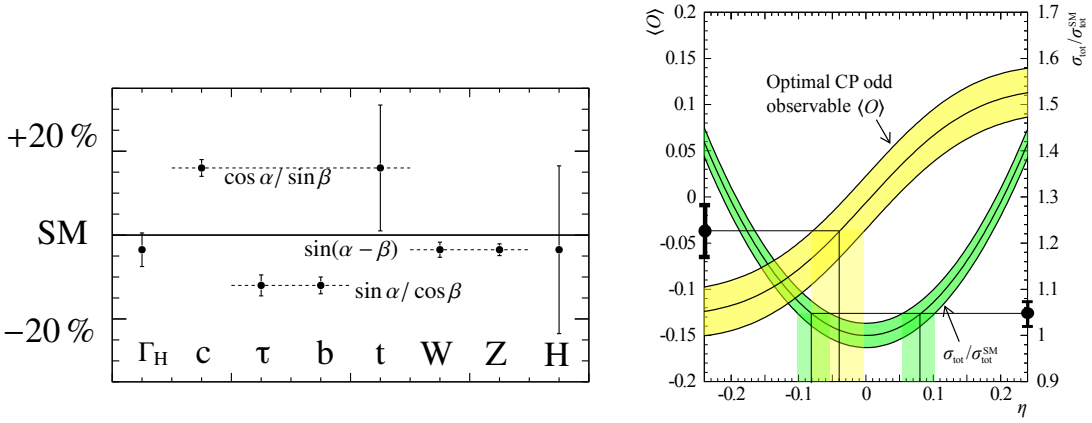

Figure 4: Left: Typical deviations of the Higgs couplings to different particles from the SM predictions in a Two-Higgs-Doublet model. The LC precisions for the various couplings are the same as in Figure 3. Right: Determination of the admixture η of a CP-odd state in $e^+e^- \to ZH$ at $\sqrt{s} = 350$ GeV with 500 fb^{-1}, using the measurement of the cross section together with an 'optimally chosen' CP-odd observable.

Furthermore, the energy dependence of the Higgs-strahlung cross section in the SM contains a factor β, whereas for a CP-odd Higgs boson with $J^{PC} = 0^{+-}$, the corresponding factor would be β^3. Again the threshold behaviour of the cross section can differentiate between the two spin-0 cases.

Angular correlations in $e^+e^- \to HZ \to 4f$ as well as $H \to \tau^+\tau^-$ decays are also sensitive to the CP nature of the Higgs state. Since *a priori* the observed Higgs state can be an admixture of CP even and CP odd states, the determination of the CP properties is experimentally more challenging than the measurement of the spin of the Higgs boson. For a Higgs boson, H, the most general model independent expression for the HVV vertex can be written as

$$g_{HVV} = -gM_V \left[\alpha g^{\mu\nu} + \beta\left(p \cdot q\, g_{\mu\nu}/M_V^2 - p_\nu q_\mu\right) + i\,\gamma/M_V^2 \epsilon_{\mu\nu\rho\sigma} p^\rho q^\sigma\right],$$

where V represents either a W or Z boson and p, q are the four momenta of the two vector bosons. For a SM Higgs $\alpha = 1$ and $\beta = \gamma = 0$. In contrast, for a pure CP odd Higgs boson, $\alpha = \beta = 0$, and γ is expected to be small. A LC provides a unique laboratory to determine α, β and γ and probe the complete tensor structure of the HVV coupling and the CP properties of the Higgs boson. For example, it has been shown that angular observables can be used to measure the mixing between a CP-even and a CP-odd Higgs state to an accuracy of 3 − 4% [8]; see Figure 4 (right). The measurements of the CP properties of the Higgs based on the HVV coupling, both at the LHC and a LC, project out the CP-even component of the Higgs and therefore require very large luminosities. A LC is unique in that the measurement of the threshold behaviour of the process $e^+e^- \to t\bar{t}H$, which depends on the H$f\bar{f}$ coupling, provides an unambiguous determination of the CP of the Higgs boson and provides the potential for a precision measurement of CP-mixing, even when it is small.

3 Top and the Gauge Sector

In addition to the precision studies in the Higgs sector, a further important part of the programme is establishing the detailed profile of the top quark and studying the gauge sector with high precision, to probe the dynamics of EWSB and BSM physics.

3.1 Top Physics

The top quark plays a very special role in the SM. Being the heaviest of the fundamental fermions it is the most strongly coupled to the EWSB sector and hence intimately related to the dynamics behind the symmetry breaking mechanism. Its large mass affects the prediction for many SM parameters, including the Higgs mass and the W and Z couplings, through radiative corrections. High-precision measurements of the properties and interactions of the top quark can have sensitivity to physics at mass scales much above the EWSB scale. These studies are therefore a very important laboratory for explorations of SM and BSM physics. A LC will have broad capabilities to establish the top-quark profile in a precise and model-independent way.

Top Quark Observables

The top mass measurement at the Tevatron has reached an accuracy of about 1 GeV. While the statistics at the LHC will be huge, because of (theoretical) systematic effects, it appears nevertheless questionable whether a further significant improvement of this measurement can be reached. In particular, an important systematic uncertainty is associated with the problem of how to relate the mass parameter that is actually measured at the Tevatron and the LHC to a parameter that is well-defined so that it can be used as an input for theoretical predictions in the SM (or its extensions), such as the $\overline{\text{MS}}$ mass. The relation between those parameters is affected by non-perturbative contributions, which can be the limiting factor in further improving the accuracy of the top-quark mass from measurements at hadron colliders. At the LC the measurement of the top-quark mass from the $\mathrm{t\bar{t}}$ threshold will be unique since it will enable a high-precision measurement of a "threshold mass", for which the relation to a well-defined top-quark mass is precisely known and theoretically well under control.

The statistical precision from a threshold scan (see left panel of Figure 6 for an example) at the LC with approximately $30\,\mathrm{fb}^{-1}$ will be about 20 MeV for the top-quark mass and 30 MeV for the top width. Including the systematic uncertainty from relating the "threshold mass" to the suitable mass parameter of the SM yields an overall precision on m_{t} of better than 100 MeV, which corresponds to an order of magnitude improvement compared to the measurement at hadron colliders.

Top-antitop asymmetries

Besides the measurements of the top-quark mass and width, the top physics programme at the LC offers a variety of further observables that have a high sensitivity to potential effects of new physics. Some interesting examples are the forward-backward asymmetry in top-antitop production, A_{FB} , the beam polarisation asymmetry A_{LR} and the polarisation of the top. The first of these, A_{FB}, has received a lot of attention lately. Both CDF and D0 experiments have reported a possible deviation of this asymmetry from the SM prediction in $\mathrm{p\bar{p}}$ collisions whereas the measurements of a related asymmetry for the pp initial state at the LHC currently show no significant deviation from the SM prediction. Due to the clean LC environment, one expects a significant improvement with respect to Tevatron and LHC measurements. Accuracies of about 5% can be achieved, which can probe, for example, Kaluza-Klein excitations of the gluons up to 10-20 TeV.

Couplings to Gauge Bosons

Precise and model-independent measurements at the LC of the top couplings to weak gauge bosons will be sensitive to BSM sources [3]. The production of $\mathrm{t\bar{t}}$ pairs in $\mathrm{e^+e^-}$ collisions and the subsequent decay of the top provide a sensitive probe of the $\mathrm{t\bar{t}\gamma}$ and $\mathrm{t\bar{t}Z}$ vertices. Since the top quark decays before it hadronises, not just the cross-sections and angular distribution of the produced top, but also various angular distributions of the decay products of the top, which retain the memory of its polarisation, can be used effectively towards this end.

A study of $\mathrm{e^+e^-} \to \mathrm{t\bar{t}} \to \ell^{\pm}$ + jets can lead to sensitivity below the percent level for BSM correction terms to $\mathrm{t\bar{t}Z}$ and $\mathrm{t\bar{t}\gamma}$ vertices at $\sqrt{s} = 500\,\mathrm{GeV}$ and $\sim 100\ \mathrm{fb}^{-1}$ [8]. Use of polarised beams and polarisation asymmetries can improve matters by providing observables that can disentangle different couplings and also increase the accuracy at a given luminosity.

Measurement of the $\mathrm{t\bar{t}}$ production below threshold, assuming that the top width is measured to the

above-mentioned accuracy, will allow a measurement of g_{tbW} at the few percent level. With such precision, a variety of new physics models such as Little Higgs Model or models of top flavour [3] can be probed, for example, with simultaneous measurements of the $t\bar{t}Z$ axial coupling and left-handed tbW vertex. Use of beam polarisation can even allow probing anomalous effects in the $t\bar{t}g$ system, particularly by testing symmetries with construction of observables that have specific CP,T transformation properties and are, e.g., T–odd, CP–even or T–odd and CP–odd. It should be noted that the LHC can give an indication of an anomalous $t\bar{t}g$ coupling through a study of top-quark polarisation in top-pair production, but only the LC can probe the structure in an unambiguous way. Thus the LC can map out the t couplings to all the gauge bosons in a precise manner to probe new physics.

3.2 WW, ZZ Scattering and the Dynamics of Strong Electroweak Symmetry Breaking

Despite the likely perturbative nature of EWSB indicated by the value of the Higgs mass, from both indirect electroweak precision constraints and direct observation at the LHC, one point is worth remembering. Even with a light Higgs, there exist formulations of EWSB, such as composite Higgs models, where the light Higgs boson is part of a larger spectrum of strongly interacting particles, and discernible effects of the strong dynamics are possible, affecting gauge boson couplings with each other. A study of WW/ZZ scattering and WW final state processes can reveal these effects.

The close connection between the WWγ and WWZ vertices and restoration of unitarity at high energies in W pair production in e^+e^- collision means that this process is highly sensitive to the triple-gauge-boson vertices and to heavy resonances with mass far exceeding the LC energy. Further, the same connection underlines the importance of this measurement to look for footprints of any new physics. The most general WWV interactions consistent with Lorentz symmetry involve twelve (six each for the γ and the Z) independent couplings, out of which only four have nonzero values in the SM. Terms involving different couplings are characterised by different tensor structures and different momentum dependencies. Specific models of the strong dynamics have specific predictions for some of the anomalous couplings.

These different kinds of couplings can be disentangled from each other using production angle distributions and decay product angular distributions, the latter being decided by the polarisation of the produced W. High beam polarisations (both e^- and e^+) can be used effectively to probe these. An analysis using a fast simulation performed at the two energies $\sqrt{s}$ = 500 GeV and 800 GeV [3, 9] shows that deviations of all these couplings from their SM values can be measured to better than one per mil level with luminosities up to 1 ab^{-1}. In many cases the measurements are up to an order of magnitude better than the capabilities of a 14 TeV LHC that have been projected [3, 9].

A chiral Lagrangian for EWSB has numerous operators that govern the interactions of the vector boson degrees of freedom. For example in the Minimal Strong Coupling Theory a small correction term, absent in the SM, yields a measurable contribution to the anomalous magnetic moment of the W boson. While it is marginally measurable at the LHC, it is readily observable at a 500 GeV LC [10].

The above is an example of deviations in the triple-gauge-boson vertices due to strong dynamics in the EWSB sector. There are also deviations in quartic boson interactions, which directly affect pure gauge boson scattering through local contact interactions, such as WW $\rightarrow$ WW. The processes $e^+e^- \rightarrow \nu_e\bar{\nu}_e W^+W^- \rightarrow \nu_e\bar{\nu}_e jjjj$ and $e^+e^- \rightarrow \nu_e\bar{\nu}_e ZZ \rightarrow \nu_e\bar{\nu}_e jjjj$ have been studied for LC at $\sqrt{s}$ = 1 TeV with 1 ab^{-1} of integrated luminosity [6], with a view to study these anomalous quartic vertices. The LC sensitivity is comparable to the values predicted in models of strong dynamics in the EW sector, where the non-SM operators are constrained to be consistent with the EW precision tests. These measurements require study of angular correlations among the decay products of the W/Z and further needs separation of the W and Z final states decaying to quarks. This indeed has been a benchmark requirement, which has driven the need for excellent jet-energy resolution, which in turn has driven the design of LC detector concepts and has been shown to be achievable.

As mentioned above, one could have strong dynamics at the origin of EWSB, even for a light Higgs boson, and it could be a composite particle remnant. In the case of these composite Higgs models, the

Lagrangian of the Higgs boson interactions with the vector bosons receives correction terms proportional to $v^2/\Lambda^2_{\text{comp}}$, where Λ_{comp} is the compositeness scale. Precision measurements of production cross-sections $VV \to VV$, $VV \to \text{HH}$, and $\text{e}^+\text{e}^- \to \text{HZ}$ provide sensitivity to the composite scale. The results show that 14 TeV LHC with 100 fb^{-1} of integrated luminosity should have sensitivity of Λ_{comp} up to 7 TeV, 500 GeV LC with 1 ab^{-1} up to 45 TeV, and 3 TeV LC with 1 ab^{-1} up to 60 TeV [4].

4 New Physics

The physics programme of the LC for exploring Terascale physics consists of three broad categories, all of which will be crucial for revealing the possible structure of new physics and for discriminating between different possible manifestations of physics beyond the SM:

- *Refining LHC discoveries:* Phenomena of new physics discovered at the LHC will be probed at the LC in a clean experimental environment and with high precision. This is expected to be decisive for revealing the physics mechanisms behind the observed phenomena.
- *New direct discoveries:* The LC will have a potential for direct discoveries that is complementary to the LHC. In particular, the searches for colour-neutral states of new physics, including the full structure of the Higgs sector, will have a discovery potential that far surpasses that of the LHC.
- *Discoveries through precision:* Measurements of observables involving known particles at the LC with the highest possible precision will have a high sensitivity to resolving the fingerprints of new physics, which in many scenarios only manifest themselves in tiny deviations from the SM prediction. Examples for the achievable precisions can be found on page 230 of [4] and Table 5.2 of [3].

In the following subsections we give examples of new physics where one or more of the above categories of the LC physics programme is on display, some examples of the last having been presented in the earlier discussions of the precision studies in the Higgs, top and the gauge sector.

4.1 New Electroweak Matter States

In the BSM context, there are many electroweak states that are well known to be difficult to find directly at the LHC. The event rates at the LHC are small in comparison to strongly interacting particle creation that makes for a challenging background environment.

Of the many ideas that one can use to demonstrate how well new electroweak matter states can be found at a LC, perhaps the most well known is supersymmetry. Supersymmetry provides a good study ground not only because it is a highly motivated scenario for physics beyond the SM, but also because it provides a rather complete and calculable framework beyond the SM with multiple new scalars and fermions of different gauge charges.

The LHC has very good prospects for discovering pair-produced coloured particles up to masses of 2–3 TeV. On the other hand, non-coloured particles, charginos, neutralinos and sleptons are not copiously produced by the LHC. Although these electroweak particles may be found in cascade decays of strongly interacting squarks and gluinos, their prospects for discovery rely on the details of the model. Their accessibility through the decay chains is unlikely to be complete. On the other hand, an e^+e^- collider running at sufficiently high centre-of-mass energy potentially can produce each of these states directly with manageable backgrounds leading to discovery. The discovery reach for these particles produced in pairs at the LC is usually close to $\sqrt{s}/2$, and in some cases even higher if $m_A \neq m_B$ in $\text{e}^+\text{e}^- \to AB$ searches.

The precision studies that are possible at a LC can test many of the properties of the discovered particles, such as per mil precise values of their masses and their couplings to SM particles, and assignment of spins. This can be accomplished through several means, including collecting high integrated luminosity at high energies and also through threshold scans, which are particular good at measuring the spin due to the shape

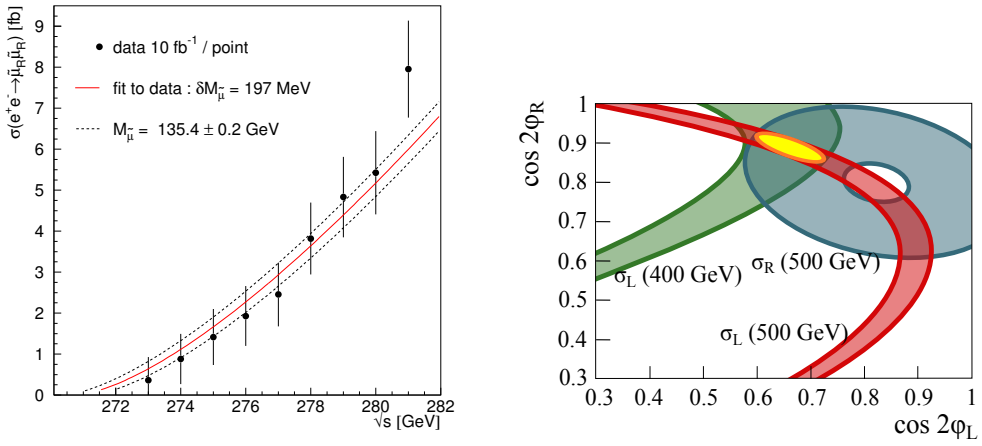

Figure 5: Left: Cross section at threshold for the production of the superpartners of the right-handed muons at the LC, $e^+e^- \to \tilde{\mu}_R\tilde{\mu}_R$, from which the spin of the produced particles can be determined and their mass can be precisely measured (limited by statistics; the plot shows a 'difficult' scenario with backgrounds from other light SUSY particles). Right: Determination of the chargino mixing angles $\cos 2\phi_{L,R}$ from LC measurements with polarised beams and at different centre-of-mass energies.

of the cross-section versus near-threshold energy. The precise measurement of the couplings then enables tests and resolutions of the underlying structure. Detailed measurements of this kind will be crucial for discriminating different sources of new physics. For example, the predictions for the spins, quantum numbers, couplings and certain mass relations are characteristic features of supersymmetry that need to be experimentally tested. Furthermore, the precision measurements of the electroweak superpartner masses at the LC, combined with the measurements of the masses of the strongly interacting superpartner masses at the LHC, enable us to test many ideas of the underlying organisational principle for supersymmetry breaking. Through renormalisation group scaling of well-measured parameters one gets access to the high-scale (e.g., scale of Grand Unification $\sim 10^{16}$ GeV) structure of the theory, enabling a test of properties like coupling and mass unification.

4.2 Dark Matter

It is well established now that the Universe must contain a sizable fraction of cold dark matter. An ideal candidate for this dark matter is a chargeless massive state χ that interacts with approximately weak gauge force strength (weakly interacting massive particle, "WIMP").

There are several model-dependent prospects for finding dark matter at the LHC and LC. These include cascade decays of parent particles that terminate in a stable dark matter particle candidate that carries off missing energy. These missing energy signature rates depend crucially on many different parameters of the overarching theory and generally have little to do with the couplings directly relevant to the dark matter particle itself.

On the other hand, a more direct and less model-dependent search for dark matter focusses on the (effective) $f\bar{f}\chi\chi$ interaction. If the annihilation cross-section is in accordance with the observed relic density, there are good prospects for the production of dark matter directly at colliders through $f\bar{f} \to \chi\chi\gamma$, where the initial-state radiated photon (or gluon) is needed to tag the event. The sensitivity of this process at the LHC is limited because of significant backgrounds. While at the LHC and in direct detection searches the WIMP interaction with quarks is probed, the LC provides complementary information on the WIMP interaction with electrons. Within the clean LC environment, making use of polarised beams, the WIMP

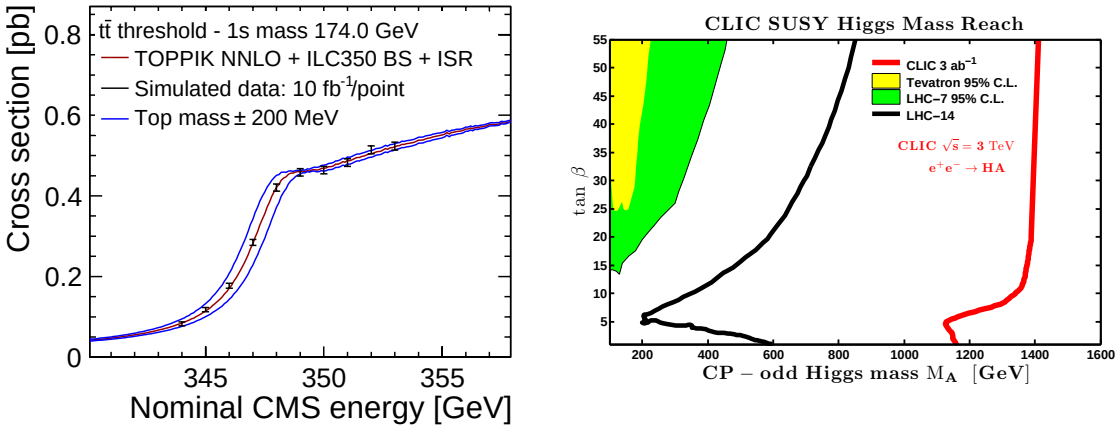

Figure 6: Left: The $t\bar{t}$ production cross-section scan near the threshold, leading to 30 MeV determination of the top mass. The study is based on full simulation of the ILD detector and includes initial state radiation, beamstrahlung and other machine-induced effects [7]. Right: Search reach in the $m_A - \tan\beta$ plane for LHC and for 3 TeV LC. The yellow and green regions are limits already in place from Tevatron and LHC (7 TeV run) analyses. The black line is a 5σ discovery projection for the LHC at 14 TeV with 300 fb^{-1} [12] (limits are roughly 150 GeV uniformly higher with 3000 fb^{-1}), and the red line is a projection for 3 TeV e^+e^- with 3 ab^{-1} of integrated luminosity [4].

mass, the strength and the chiral structure of the $e^+e^-\chi\chi$ interaction, as well as the dominant partial wave of the production process can be determined.

LC measurements can also provide a comprehensive set of high-precision experimental information on the properties of the dark matter particle and the other states affecting annihilation and co-annihilation of the dark matter particle. This can then be used to predict the dark matter relic density in our Universe. The comparison of the prediction based on the measurements of new physics states at the LHC and the LC with the precise measurement of the relic density from cosmological data would constitute an excellent test of the dark matter hypothesis.

4.3 Additional Higgs Bosons

After the confirmation of the existence of a state compatible with the SM Higgs boson, there is still the prospect of additional Higgs bosons in the spectrum. These additional Higgs bosons include extra singlet Higgs bosons that mix with the SM-type Higgs boson. Or, there may be an extra $SU(2)_L$ doublet that fills out the full Higgs sector of the theory.

Again, supersymmetry provides a calculable framework through which to analyze the discovery prospects of an extra Higgs boson. Over a large part of the parameter space the Higgs sector consists of one light state ($m_h \lesssim 135$ GeV) whose couplings are very similar to the SM Higgs boson, and four extra states (A^0, H^0 and $H^\pm$) of nearly equal mass. Figure 6 shows the direct discovery reach of the heavy Higgs bosons at the LHC and a 3 TeV LC as a function of m_A. The result is impressive, with a search capacity for the heavy Higgs near $\sqrt{s}/2$ for the LC. If the dark matter particle has less than half the mass of a Higgs boson, invisible Higgs decays could be another good way to identify it. This possibility can be studied in detail at the LC for all Higgs bosons within its kinematic reach.

An extended Higgs sector could also contain a light Higgs, possibly in addition to a SM-like Higgs at about 125 GeV, with a mass below the LEP limit of about 114 GeV and with suppressed couplings to gauge bosons. While at the LHC the search for such a light Higgs state will be very challenging in the standard search channels, at the LC there will be a high sensitivity for probing scenarios of this kind.

4.4 New Gauge Boson Interactions

The quintessential example of a new gauge boson is a Z′ boson. The mass reach for direct discovery at the LHC of an "ordinary" Z′ boson, whose couplings to the SM fermions are $O(1)$, is generally about 5 TeV. However, it is well documented that through non-resonance observables an e^+e^- collider with energy above a few hundred GeV has an even higher reach for detecting BSM signals. This is accomplished by studying precisely the observables of the $e^+e^- \to f\bar{f}$ processes. Small deviations in $\sigma_{\rm tot}^{f\bar{f}}$, $A_{\rm FB}^{\rm f}$ and $A_{\rm LR}^{\rm f}$ can be found for Z′ masses well above the centre-of-mass energy of the machine. For example, at a 500 GeV LC with 1 ab^{-1} of integrated luminosity, a BSM signal is detectable in the left-right model (i.e., theory with $SU(2)_R \times U(1)_{B-L} \to U(1)_Y$) if the corresponding Z′ has a mass below 9 TeV, which is more than one order of magnitude beyond the centre-of-mass energy of the collider. This search reach increases to about 16 TeV at a 1 TeV LC (see sec. 5.2.1 of [8]) and to well beyond 30 TeV for a 3 TeV LC (see sec. 1.5 of [4]).

4.5 Model-Independent Searches

Some of the discussion above has revolved around specific model scenarios. However, it must be emphasised that the LC is an excellent machine to do model-independent analyses in the context of the uniquely clean e^+e^- collision environment. Searches can be made to test whether the event rates in different channels are anomalous, and thus indicate the presence of new physics. A minimum number of theoretical assumptions are necessary to determine the spin, mass and couplings of new particles, which can then be used in a second step to obtain theoretical interpretations in different models. Thus, instead of referring to a particular class of models, like the discussion above of Z′ effects suppressed by $M_{Z'}$, one can also interpret the LC results in terms of general effective operators, such as non-renormalizable contact operators suppressed by a scale Λ. These more general interpretations of the LC sensitivities may not always be stated explicitly since many studies have been carried out within a well-defined BSM model, but it is an advantageous feature of the LC that such model-independent interpretations are possible.

With the so-called GigaZ option of the LC, i.e. a run at the Z peak with polarised e^- and e^+ beams collecting about 10^9 events, the LC can provide high-precision measurements that have a very high sensitivity to effects of new physics, which are probed in a model-independent way. In particular, the GigaZ run would reduce the present experimental uncertainties on the effective weak mixing angle, $\sin^2\theta_W^{\rm eff}$, by more than an order of magnitude, and resolve or confirm the significant (3σ) disagreement between the two most precise determinations of $\sin^2\theta_W^{\rm eff}$ from $A_{\rm FB}^{\rm b}$ at LEP and $A_{\rm LR}$ at SLC. As an example, the precision achievable for $\sin^2\theta_W^{\rm eff}$ at GigaZ has the potential to reveal the impact of new physics even in a scenario where no states of physics beyond the SM would be observed at the LHC and the first phase of a LC.

Executive Summary

The observation at the LHC of a SM-like Higgs particle provides the first direct test of the minimal SM EWSB scenario of a single scalar doublet Higgs field producing the vacuum expectation value. This discovery makes the physics case for a LC extraordinarily strong. The LC provides the capability to study the details of this new form of matter, establishing agreement with the SM predictions to new levels of sensitivity, or revealing a break from the patterns expected in the SM. The precision of the LC opens sensitivity to new physics well beyond the LC's direct reach, enabling detection before discovery, such as past indirect evidence for the Higgs boson, the top quark, the charm quark, and the weak gauge bosons.

The most powerful and unique property of the LC is its flexibility. It can be tuned to well-defined initial states, including polarisation, allowing numerous model-independent measurements, from the Higgs threshold to multi-TeV operation, as well as the possibility of unprecedented precision at the Z-pole (GigaZ). Furthermore, the relative simplicity of the production processes and final-state configurations makes complete and extremely accurate reconstruction and measurement possible. The envisioned physics programme includes precision measurements of many Higgs decay widths, some of which are uniquely accessible at the

LC ($c\bar{c}$, gg, the invisible mode and the full width), decisive tests of the CP properties of the Higgs candidate, and determinations of the top-Higgs and trilinear Higgs self couplings, also uniquely accessible at the LC. Using a LC, the complete SM, including Higgs, top quark and VV interactions, can be studied, both at tree level and through quantum corrections. The LC reaches well into new physics territory. Well-motivated BSM physics ideas such as dark matter, supersymmetry, composite Higgs bosons, contact interactions, and extra space dimensions could be discovered and explored. The physics reach of the LC is essentially limited by statistics, not systematics. Its discovery reach exceeds that of the LHC at any integrated luminosity in many cases, and discoveries of new particles or interactions at either machine can be subjected to further precision analysis at the LC to reveal deeper structures of nature.

References

[1] K. Abe *et al.* [ACFA Linear Collider Working Group Collaboration], *Particle physics experiments at JLC*, hep-ph/0109166.

[2] E. Accomando *et al.* [CLIC Physics Working Group Collaboration], *Physics at the CLIC multi-TeV linear collider,* hep-ph/0412251.

[3] G. Aarons *et al.* [ILC Global Design Effort and World Wide Study], *International Linear Collider Reference Design Report Volume 2: Physics at the ILC,* arXiv:0709.1893 [hep-ph].

[4] L. Linssen *et al.* [CLIC Working Groups], *Physics and Detectors at CLIC: CLIC Conceptual Design Report,* arXiv:1202.5940 [physics.ins-det].

[5] H. Aihara *et al.* [SiD Concept Group], *SiD Letter of Intent,* arXiv:0911.0006 [physics.ins-det].

[6] T. Abe *et al.* [ILD Concept Group], *The International Large Detector: Letter of Intent,* arXiv:1006.3396 [hep-ex].

[7] H. Baer *et al.*, *Physics at the International Linear Collider*, to be published in the *ILC Detailed Baseline Design Report* (2012). A preliminary version is available at http://lcsim.org/papers/DBDPhysics.pdf.

[8] J. A. Aguilar-Saavedra *et al.* [ECFA/DESY LC Physics Working Group Collaboration], *TESLA: Technical design report. Part 3. Physics at an e^+e^- linear collider,* hep-ph/0106315.

[9] G. Weiglein *et al.* [LHC/LC Study Group Collaboration], *Physics interplay of the LHC and the ILC*, Phys. Rept. **426** (2006) 47 [hep-ph/0410364].

[10] T. Abe *et al.* [American Linear Collider Working Group Collaboration], *Linear collider physics resource book for Snowmass 2001*, hep-ex/0106055, SLAC-R-570.

[11] G. Moortgat-Pick *et al.*, *The Role of polarized positrons and electrons in revealing fundamental interactions at the linear collider*, Phys. Rept. **460** (2008) 131 [hep-ph/0507011].

[12] F. Gianotti *et al.*, *Physics potential and experimental challenges of the LHC luminosity upgrade,* Eur. Phys. J. C39 (2005) 293.

Addendum: Charge for the Linear Collider Report Committee

During the international Linear Collider Workshop in Granada October 2011 it was proposed and agreed to charge a small expert group with drafting a common Linear Collider Physics report to be submitted as input to the European Strategy process. The initiative was presented in Granada by the GDE European Regional Director (Brian Foster), the CERN Linear Collider Studies Leader (Steinar Stapnes) and the Chair of the ECFA Study for the Linear Collider (Juan Fuster), and was a result of discussions and consensus in several ILC and CLIC steering committee meetings earlier in 2011. These three subsequently suggested a composition of the expert committee based on input from the community, and proposed the mandate of the committee. The draft report has been through internal reviews, and has been made openly available to the full international LC community for further comments and suggestions before submission by end of July 2012.

Mandate of the committee:

The committee is requested to review the physics case for a linear electron-positron collider in the centre-of-mass energy range from around 250 GeV − 3 TeV in the light of LHC results up to mid-2012 and building on previous studies. The committee should consider the case for a linear collider in terms of the physics reach beyond that of the LHC under the assumptions in the current CERN planning; a) 300 fb^{-1} and b) 3000 fb^{-1}.

It should assume linear collider performance based on the details contained in current documents from ILC and CLIC but without a detailed comparison of the relative performance of the machines. The aim is to make the strongest possible case for a generic linear collider for submission to the European Strategy process.

The committee is requested to submit its draft report to the GDE European Regional Director, the CERN Linear Collider Studies Leader and the Chair of the ECFA Study for the Linear Collider by June 18th 2012. The final version of the report should be delivered by end of July 2012.

Physics at the ILC

Kiyotomo Kawagoe

Kyushu University, 6-10-1 Hakozaki, Higashi, Fukuoka, 812-8581 Japan

DOI: will be assigned

This year (2012) would be recorded as a memorial one in high-energy physics, as some decisive results on the long-awaited Higgs boson are to be obtained at the LHC. The LHC results have strong impacts on the possible physics scenario at the International Linear Collider (ILC). In this talk possible physics studies at the ILC are presented with a focus on the Higgs factory in the case where a light Higgs-like particle be found at the LHC.

1 Introduction

To explore the energy frontier in particle physics, it is desired to have a hadron collider, which has an enormous discovery potential for heavy particles, and a lepton collider, which is very good at precise measurements of new particles and phenomena, at the same time. Since the Large Hadron Collider (LHC) started its physics run in March 2009, the LHC has been very successfully operated, delivering an integrated luminosity of about 5 fb^{-1} to each experiment by the end of 2011. On the other hand, we have had no electron-positron collider since the end of the LEP operation in 2000. The LEP collider, with the maximum center of mass energy of 209 GeV, is assumed to be the last circular e^+e^- collider because of the beam energy loss due to synchrotron radiation.The concept of of a linear electron-positron collider was first proposed to overcome this limit well before 1980 [1]. Extensive R&D studies for the linear collider started in 1980's in Asia, Europe, and North America, and each region proposed a project: GLC [2] from Asia, TESLA [3] from Europe, and NLC [4] from North America, respectively. However, any project could not be funded. Probably the linear collider is financially too large as a regional project.

In 2003 a worldwide consensus was made that the next energy frontier machine after the LHC should be an electron-positron linear collider with an initial center-of-mass energy reach of 500 GeV, upgradable to 1 TeV. In 2004 the International Technology Review Panel recommended that the superconducting radio-frequency technology should form the design of the linear collider. This is the International Linear Collider (ILC). The layout of the ILC given in the Reference Design Report (RDR) [5] is shown in Fig. 1.

In this document the physics strategy at the ILC is discussed, taking account of the current status of new particle searches at the LHC.

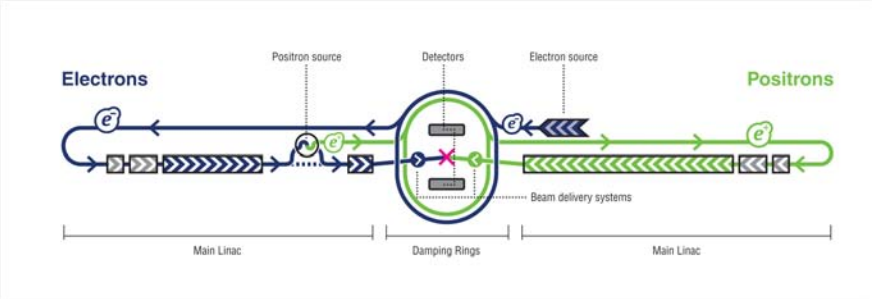

Figure 1: The layout of the ILC taken from the RDR [5] .

2 Hints for the light Higgs boson ?

The Standard Model (SM) of particles physics has been so far extremely successful, without any significant deviation between theoretical expectations and experimental measurements. The model consists of three sectors: the gauge boson sector, the fermion sector, and the Higgs sector. While the former two sectors were experimentally tested with good precision at lepton and hadron colliders in the past, the last sector is, at least experimentally, totally-unknown. The Higgs field plays a key role in the SM, and assumed to be the origin of the electroweak symmetry breaking and to produce the masses of all elementary particles. Until the LHC era, the Higgs boson still escapes detection in spite of all the efforts devoted at the LEP and Tevatron experiments. However, the precise electroweak measurements at LEP, SLC, and Tevatron can constrain the SM Higgs boson mass to be less than 161 GeV [6] (one-sided 95 % confidence level upper limit). The direct Higgs search at LEP set an lower limit of the SM Higgs mass to be 114 GeV [7], while Tevatron excluded a mass range from 156 GeV to 177 GeV [8]. The situation without the LHC results is summarized in Fig. 2 .

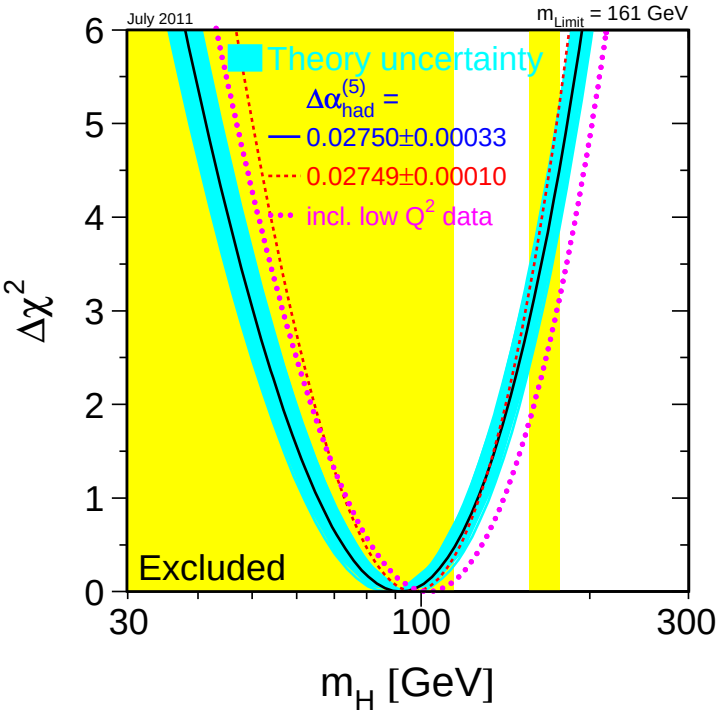

Figure 2: The $\Delta\chi^2$ curve derived from high-Q^2 precision electroweak measurements, performed at LEP, SLC, and Tevatron as a function of the SM Higgs boson mass. The mass regions excluded by LEP and Tevatron are alson shown.

The physics run of the LHC started in March 2010. In 2011, the LHC very successfully delivered an integrated luminosity of about 5 fb^{-1} at a center-of-mass energy of 7 TeV to each of the general purpose proton-proton collision experiments, ATLAS and CMS. The LHC is a very powerful machine for discovery of new heavy particles. Although any evidence for the Higgs boson has not been obtained yet, the LHC already set a very stringent limit on the SM Higgs boson mass [9, 10]. The heavy SM Higgs boson ($m_H >\sim 160$ GeV), which is inconsistent with the electroweak measurements, is excluded in the mass region up to ~ 600 GeV. If a heavier Higs-like particle is found, it should not be the "SM" Higgs boson. On the other hand, the light SM Higgs boson ($m_H <\sim 160$ GeV), if it exists, should be in the mass region $115.5 < M_H < 127$ GeV. In addition, interestingly, bumps are observed at $M_H \sim 125$ GeV by each of the ATLAS and CMS experiments

as shown in Figs 3 and 4 (the peak positions are slightly different). Because of low statistics of the 2011 data, any decisive conclusion cannot be obtained for the Higgs "discovery" yet. In 2012, the LHC is supposed to deliver an integrated luminosity of about 15 fb^{-1} at a center-of-mass energy of 8 TeV to each experiment. Using the 2012 data, the ATLAS and CMS experiments are expected to discover a light Higgs-like particle, or exclude the existence of the SM Higgs boson. In either case, the result will be memorized a great discovery in particle physics, and must have a great impact on the physics scenario at the ILC.

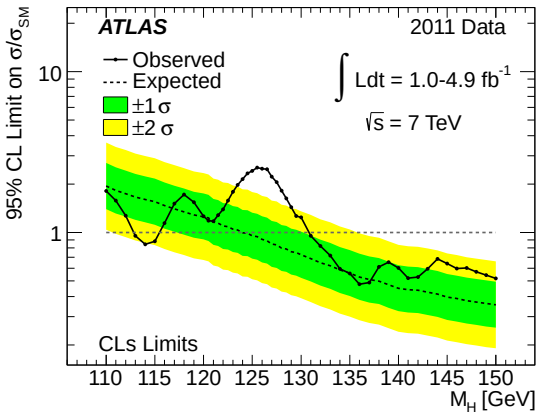

Figure 3: The combined 95% CL upper limit of the signal strength as a function of m_H obtained by the ATLAS experiment [9]; the solid curve indicates the observed limit and the dotted curve illustrates the median expected limit in the absence of a signal together with the $\pm 1\sigma$ (green) and $\pm 2\sigma$ (yellow) bands.

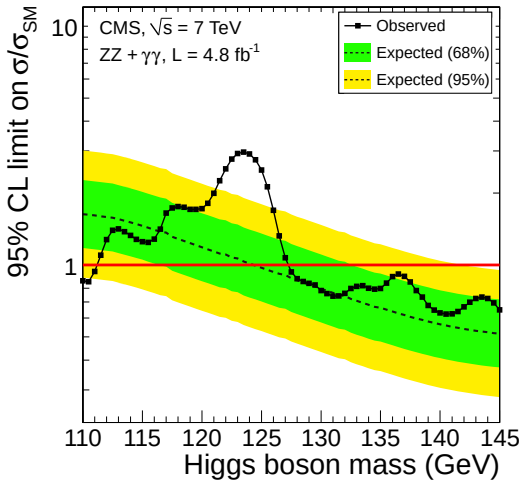

Figure 4: The ZZ and $\gamma\gamma$ combined 95% CL upper limit of the signal strength as a function of m_H obtained by the CMS experiment [10]; the solid curve indicates the observed limit and the dotted curve illustrates the median expected limit in the absence of a signal together with the $\pm 1\sigma$ (green) and $\pm 2\sigma$ (yellow) bands.

No indication for other new particles, predicted by "Beyond the Standard Model" physics such as supersymmetry (SUSY) and extra-dimensions, has been found at the LHC yet. The light Higgs boson with its mass $m_H \sim 125$ GeV can be still consistent with the SUSY expectation. We still have a good chance to discover new particles beyond the Standard Model at the LHC, at higher center-of-mass energies and with more luminosity. Discovery of such new particles would have another great impact on the physics scenario at the ILC.

3 Physics at the ILC

Hereafter in this document it is assumed that a light Higgs boson (or a light Higgs-like particle) will be discovered at the LHC in near future, probably by the end of year 2012. In this case, regardless whether other new particles will be found or not, the ILC should be planned naturally as the Higgs factory, first of all. The reason why the Higgs factory is necessary is clear: The Higgs boson belongs to a completely new category of particles that we have never encountered. We don't know any other spin-0 elementary particle. The properties of the Higgs boson, to be discovered at the LHC, are experimentally unknown, and should be thoroughly investigated at the ILC, where we can observe interactions of elementary particles, with well-known initial states and relatively simple final states in a clean experimental environment. Polarization of electrons as well as positrons at the ILC can be used as a powerful tool.

At the ILC with an initial center-of-mass energy reach of about 500 GeV (the first phase), we will have three important energy steps:

1. We start the physics run at the ILC at a center-of-mass energy of about 250 GeV ($\sim m_H + 120$ GeV), where the production cross section of the Higgsstrahlung process ($e^+e^- \to HZ$) is at maximum (Fig. 5a). At this energy we can measure the following properties very precisely:

   - Measurement of the mass and production cross section: The measurement can be performed independent from the Higgs branching ratios, by reconstructing the recoil mass of the $Z \to \ell^+\ell^-$ decay ($\ell = e, \mu$). The total production cross section, including the invisible decay modes of the Higgs boson, can be measured.
   - The spin of the Higgs-like particle can be unambiguously determined by the cross section scan around the production threshold and the measurement of the production angle distribution. The CP characteristic of the particle can also be determined.
   - The branching ratios of the SM Higgs boson are shown in Fig. 5b as a function of its mass. The light Higgs boson with its mass $110 < m_H < 150$ GeV is an ideal physics target at the ILC, as most of the decay branching ratios can be measured very precisely. Figure 6 shows the expected precision of the measurements as a function of m_H [11] , where a center-of-mass energy of 250 GeV, an integrated luminosity of 250 fb^{-1}, and a beam polarization of 80% for electrons and 30% for positrons are assumed, respectively. If the light Higgs indeed exists, we will have many decay channels to be measured with good precision. The accuracy is typically a few percent. The measurement of the Higgs boson properties is limited at the LHC: only a few decay modes can be measured with much more degraded accuracy, typically 30% or worse. In order to tell the physics behind the Higgs-like particle, we definitely need the accuracy to be achieved at the ILC.

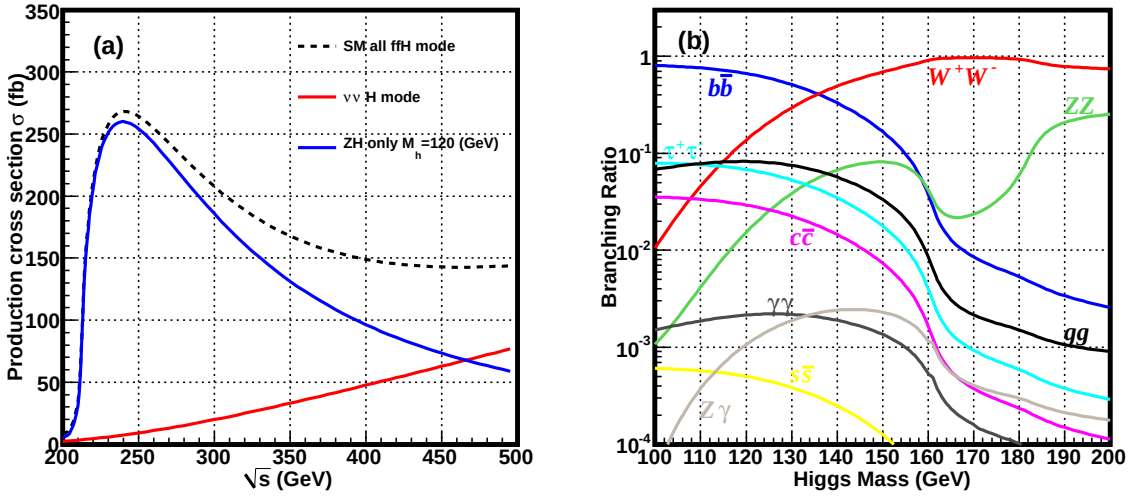

Figure 5: (a) The production cross section of the Standard Model Higgs boson as a function of the center-of-mass energy and (b) the Higgs branching ratios predicted by the Standard Model as a function of the Higgs boson mass.

2. The next center-of-mass energy for the ILC operation will be around 350 GeV, where the top-quark pair-production becomes for the first time possible at an e^+e^- collider. We can precisely measure a variety of top-quark properties such as the top mass, the production cross section, and the momentum distribution at the threshold center-of-mass energy. At this energy the vector-boson fusion process ($e^+e^- \to \nu\bar{\nu}H$) becomes more important for the Higgs production. The di-boson productions ($e^+e^- \to WW,\ ZZ$) may also be interesting processes to be studies at the energy region.

3. At the center-of-mass energy of 500 GeV (or higher) two more essential measurements of the Higgs boson can be performed at the ILC:

- Measurement of the Higgs self-coupling constant λ_{hhh} using the processes $e^+e^- \to ZHH$ and $e^+e^- \to \nu\bar{\nu}H$: This measurement will determine the Higgs potential which causes the electroweak symmetry breaking.
- Measurement of the top quark Yukawa coupling by measuring the $t\bar{t}H$ cross section: This measurement is important as the top-quark is the heaviest fermion and the Yukawa interaction between the top-quark and the Higgs boson is assumed to generate the mass term which breaks the electroweak gauge symmetry in the SM.

The two measurements are extremely difficult at the LHC. Previous fast-simulation studies showed that the measurements are possible at the ILC with the center-of-mass energy of 500 GeV, however, recent full-simulation studies have not reproduced the fast-simulation results yet. We have to develop more advanced simulation studies to convince the feasibility of the measurements at the ILC.

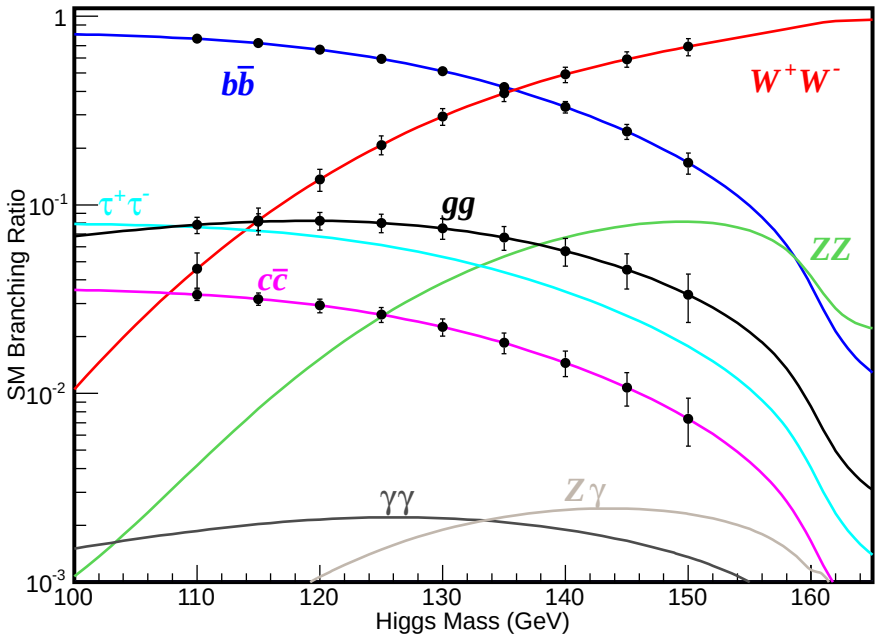

Figure 6: Measurement accuracies of the Higgs branching ratios extrapolated from the result at $m_H = 120$ GeV.

As for the Higgs sector, the ILC can determine the coupling constants of the Higgs boson to the fermions, gauge bosons, and the Higgs boson itself, with much better precision than at the LHC. With the precisions we can test if the coupling is proportional to the mass of the particles. Any deviation from the SM expectations directly leads to new physics beyond the Standard Model, e.g., Supersymmetry, extra-Dimensions, and Little Higgs models. The model parameters of the new physics may also be determined. The Higgs boson is a powerful tool to explore new physics at Terascale.

The strategy of the ILC up to about 500 GeV is summarized in Fig. 7, where the center-of-mass energy and the integrated luminosity required to complete various physics studies is shown. We will start the ILC with center-of-mass energy at 250 GeV to study the Higgs boson properties in detail. At 350 GeV, we can study the top-pair production in detail. At center of mass energy of 500 GeV or higher, we can measure the Higgs self-coupling and top-quark Yukawa-coupling. Rich physics programme are guaranteed at the ILC, once a light Higgs-like particle is discovered at the LHC.

Although the LHC has so far shown no indication of other new particles, it is still possible that heavy colored particles will be discovered with higher energies and more integrated luminosities at the LHC. Once

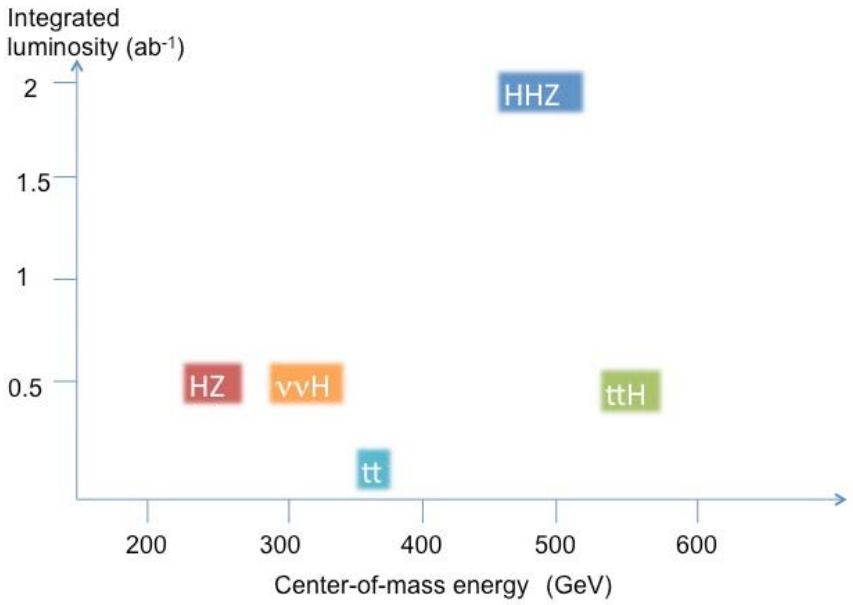

Figure 7: The center-of-mass energy and the integrated luminosity required for various studies at the ILC.

heavy particles are discovered, the masses of lighter new particles may be estimated through their decay chains. The LHC is very powerful to produce colored particles, but not for colorless particles. Therefore light colorless particles may easily escape detection at the LHC. It is thus possible that light new colorless particles will be discovered at the ILC, even if the LHC fails to discover no new particles. If a new particle is discovered at the LHC or at the ILC, it may not be alone. A series of new particles must exist, and we will enter an era of "New Particle Discoveries". This can be originated from supersymmetry, extra-dimensions, or whatever else. In any model, the lightest new particle, which is stable due to some conservation law, may be the dark matter candidate.

In the case of supersymmetry, the masses and couplings of superpartners can be precisely measured, if they are within the reach of the ILC. Then we can test directly the SUSY relations and GUT relations. It is possible to get some information of the neutrino seesaw mechanism. Measurements of SUSY particles at the LHC and the ILC would enable us to precisely calculate the dark matte density in the universe, which will be compared with the future precise measurement by the Planck satellite.

Even if no new particles were found at the ILC, precise measurements at the ILC can explore physics at much higher energies. A god example is the Z' boson. For example, from precise measurements of fermion pair production at the ILC, the model of the new gauge boson may be determined.

Precise measurements of the new particles will determine the next energy required for the collider beyond the first phase of the ILC. If it is less than 1 TeV, the ILC should be subsequently upgraded to its second phase, up to ~ 1 TeV. Otherwise we will have to consider to build the CLIC or Muon Collider more seriously.

4 Summary and outlook

By the end of this year it is very likely that a light Higgs-like particle will be discovered at the LHC. The discovery will be the start of a new revolution in particle physics, as the Higgs boson is a completely newcomer in particle physics. As the next step we need the linear collider for precise measurements of the

new particles. The ILC will reveal the principle of new physics with much better sensitivity. First of all, the properties of the new particle must be thoroughly measured and investigated at the ILC. In this case the physics scenario at the ILC (the first phase) will have the following three steps: (1) study of Higgs properties at $\sqrt{s} \sim$ 250 GeV where ZH production cross section is at maximum, (2) studies of the Higgs boson, the top-quark, and di-boson production at $\sqrt{s} \sim 350$ GeV (the $t\bar{t}$ threshold), and (3) studies ZHH and $t\bar{t}H$ productions at $\sqrt{s} \sim 500$ GeV to measure the Higgs self-coupling and the top-quark Yukawa-coupling. These are guaranteed physics targets at the first phase of the ILC. In addition, the ILC has many possibilities to explore the physics beyond the Standard Model. The new physics can be supersymmetry, extra-dimensions, or anything else. Any surprise may happen at the high-energy frontier.

The LHC results will determine the direction of ILC. We have to be ready for construction of the ILC as soon as possible, so that we can respond any possible result at the LHC.

References

[1] M. Tigner, Nuovo Cimento **37**, 1228 (1965), U. Amaldi, Phys. Lett. **61B**, 313 (1976).

[2] GLC Project: Linear Collider for TeV Physics, KEK-REPORT-2003-7.

[3] TESTR TDR: http://lcdev.kek.jp/TESLA-TDR/

[4] NLC: Zeroth-Order-Design Report, http://www-project.slac.stanford.edu/lc/ZDR/Zeroth.html

[5] RDR: http://www.linearcollider.org/about/Publications/Reference-Design-Report

[6] The LEP Electroweak Working Group: http://lepewwg.web.cern.ch/LEPEWWG/

[7] The ALEPH, DELPHI, L3 ans OPAL Collaborations, Phys. Lett. **B565** 61-75 (2003).

[8] The CDF and D0 Collaborations, "Combined CDF and D0 Upper Limits on Standard Model Higgs Boson Production with up to 8.6 fb^{-1} of Data", arXiv:1107.5518 [hep-ex].

[9] The ATLAS Collaboration, Phys. Rev. Lett. **108**, 111803 (2012).

[10] The CMS Collaboration, Phys. Lett. **B710** 26-48 (2012).

[11] H. Ono and A. Miyamoto, "Higgs Branching Fraction Study in ILC", arXiv:1202.4955 [hep-ex].

Possible Staging Scenarios for the ILC

Benno List[1]

[1]DESY, 22603 Hamburg, Germany

The ILC baseline design describes an accelerator with 500 GeV centre-of-mass energy. In view of the recent discovery of a Higgs particle, possible scenarios for a staging of the centre-of-mass energy and luminosity are presented, including the possibility to run the electron and positron beams at different energies in order avoid the need of a dedicated electron pulse for positron production at centre-of-mass energies below 250 GeV. Dedicated studies to determine the most efficient beam energies for the ILC physics program will help to optimize the machine layout, and are thus needed now, before a decision on the energy reach and possible intermediate stages will be met. A figure of merit is proposed that quantifies the value of an amount of integrated luminosity in terms of physics performance.

1 Introduction

The recent discovery [1, 2] and first characterization [3, 4] of "a" Higgs boson with a mass of 126 GeV at LHC has worldwide renewed the interest to build the ILC [5]. Measurements of the Higgs properties, such as couplings, width, and quantum numbers, can be performed under the ILC's clean experimental conditions with very good accuracy [6]; some crucial measurements, such as the absolute coupling to the Z^0 that sets the scale for all partial decay widths, are only possible at the ILC.

Precision measurements of the Higgs and top quark properties provide a rich physics program for the ILC [7], spanning the energies between 230-270 and 500-600 GeV. Recently, discussions have started about a scenario in which the ILC would be built in two or more stages, with rising beam energies, in the hope to reduce the initial investment, and possibly the construction time.

The ILC baseline design is a blueprint for an accelerator with a 500 GeV centre-of-mass energy, which could easily be adapted to yield a machine with 550 or 600 GeV CME. The baseline design foresees a possible later extension to 1 TeV centre-of-mass energy, and the central part, in particular the beam delivery system (BDS) is designed to accommodate the increased beam energy. However, no detailed design for this extension is yet available, and it is assumed that an energy upgrade would be designed at a time when further progress in superconducting cavity technology will make it possible to produce and operate cavities at larger gradients than currently possible. The TeV upgrade of the ILC is beyond the scope of this report; more information can be found in the Technical Design Report (TDR) [8].

In the following, some issues from the accelerator point of view will be presented first that may shed some light on the possible advantages and disadvantages of the scenarios under discussion. Then the problems of running at low energies (at 230-270 GeV, slightly above the threshold for Z^0h production) are discussed, with asymmetric running as a possible solution. Section 3 presents prospects to increase the luminosity, then some staging scenarios that have been investigated in somewhat more detail are presented. Section 5 is concerned with the need to define a figure of merit that would allow a more quantitative comparison of different running options, and thus help to optimize the machine design.

2 Accelerator Issues

2.1 Positron Source

The production of positrons in sufficient quantities is a key issue for the ILC operation. The baseline solution is a source where gamma ray photons are produced off the main electron beam in a superconducting helical undulator section. These photons impinge on a rotating target, where positrons are produced and subsequently collected by a flux concentrator. Photon production by a helical rather than a more common

planar undulator offers two advantages: the photon intensity is twice as large, and the photons are longitudinally polarized, which results in a longitudinal polarization of the positrons of up to 60 %. All three parts, the undulator, target, and flux concentrator, pose significant engineering challenges. Therefore the baseline design includes a 50 % overproduction margin, i.e. if everything works according to plan, 50 % more positrons can be delivered to the damping rings than needed.

The energy spectrum and overall intensity of the photons produced in the helical undulator, and thus the resulting positron yield at the target, depends strongly on the beam energy. The baseline design foresees 42 undulators of 3.5 m length, for a total active length of 147 m. However, 24 additional undulators could be installed, bringing the total length to 231 m. In the baseline configuration the photon intensity is sufficient for the nominal yield[1] of 1.5 for electron beam energies above 150 GeV. Below that energy, the positron yield drops rapidly, such that at 125 GeV, the positron intensity is half that at 150 GeV. Part of that loss could be compensated, if necessary, by the installation of more undulator modules, but the fact remains that below 125 GeV electron beam energy positron production with the helical undulator source becomes rapidly unpractical.

The solution to this problem is the so-called "10 Hz" scheme (see Tab. 1), in which alternating electron pulses of 150 GeV for positron production and at lower energies for collisions are produced. This scheme essentially allows to provide electron beams for physics down to energies as low as 45 GeV needed for Z^0 running[2], albeit at the price of producing (and thereafter wasting) an additional 150 GeV beam. More implications of the 10 Hz scheme are discussed below.

2.2 Damping Rings

One main challenge for the damping rings is to reduce the vertical emittance of the beams, in particular the positron beam, in a very short time: the initial emittance of the positrons is approximately $\epsilon_y \approx 0.8\,\mu$m, while the final vertical emittance is 10 pm rad, almost six orders of magnitude smaller. This reduction has to be achieved within $t = 200$ or even 100 ms, which means that the vertical damping time τ_y has to of the order of $\tau_y \leq 2t/\ln(\epsilon_{y,ini}/\epsilon_{y,final}) = 15.5$ ms for 10 Hz operation [11]. The large energy loss per turn that is necessary for the required synchrotron radiation damping is achieved by the insertion of 54 wigglers in each ring, which lead to an energy loss of up to 7.7 MV per turn and a vertical damping time of $\tau_y = 13$ ms. This results in up to 3.3 MW RF power necessary to store the a positron beam at the design current of 390 mA, which can be compared to the average beam power of the accelerated positron beam, which is 2.6 MW for a 250 GeV positron beam.

When the number of bunches per pulse was halved in the SB2009 process in order to save costs, the circumference of the damping rings was also halved, so that the bunch spacing and average current did not change. Doubling the number of bunches again would increase the current in each damping ring to 780 mA, which is feasible for the electron ring, but difficult for the positron rings, which would suffer from electron cloud formation and resulting beam instabilities. Therefore, the damping ring tunnel design leaves space for the installation of a second positron damping ring above the electron ring (the first positron damping ring lies below the electron ring), so that each ring would carry the same number of bunches as in the baseline configuration.

2.3 Main Linac

The performance of the Main Linac is limited in several places, some of which we will discuss in the following.

The most notorious performance limit is the accelerating gradient g, which determines how much energy per unit length can be transferred to the beam[3]. The ILC baseline assumes a gradient, averaged over all cavities, of $g = 31.5$ MV/m, with a spread of the gradients of individual cavities within ±20 %. The gradient of a cavity is measured during fabrication in a vertical test stand. There, the cavities have to achieve a gradient of 35 MV/m on average; the 10 % reduction accounts for the expected performance loss between the performance in the vertical test stand and within a cryomodule that houses eight or nine cavities.

[1] The positron yield is defined as the ratio of positron bunch intensity at the damping ring entrance divided by the electron bunch intensity at the undulator.

[2] Note that 45 GeV running for physics production is not included in the official baseline design.

[3] The maximal electric field in the cavities is larger by a factor $\pi/2$.

Increasing the accelerating gradient has been the goal—and the result—of more than twenty years of successful R&D [13]. Increasing the gradient means that the same beam energy can be achieved with fewer cavities, fewer cryomodules, and a shorter tunnel, in short, at reduced cost.

However, not everything gets cheaper with higher gradient; two quantities scale quadratically with gradient, and thus rise linearly with gradient for a linac with a given total beam energy: the stored energy in the cavity, and its dynamic heat load.

It is well known that the energy density of any electric field, and thus the energy stored within a resonating cavity, grows quadratically with the field strength. Because the ILC operates in a pulsed mode, at each pulse this energy has to be transferred into the cavity, and after the pulse it has to be dumped to a load[4] at room temperature.

At the ILC in the baseline configuration, a full RF pulse lasts 1.65 ms, of which 0.93 ms (56 %) are spent to fill the cavities, and only 0.73 ms (44 %) to accelerate the beam. The corresponding numbers for a luminosity upgrade with twice the number of bunches is 0.61 ms (39 %) for filling and 0.96 ms (61 %) for acceleration.

Thus, from an efficiency point of view it is desirable to accelerate more bunches per pulse, in order to make optimal use of the stored energy in the cavity, which is lost at the end of each pulse. The limits to that are posed by the maximum pulse length of the klystrons of about 1.6 ms, and the number of bunches that can be stored in the damping rings. In addition, the total electrical energy that is needed for one beam pulse has to be stored in the modulators, so a larger pulse energy means more modulators.

The second quantity that grows quadratically with gradient is the dynamical heat load. Although superconducting materials transport DC current losslessly, alternating fields penetrate the superconducting material within a finite skin depth, and there they accelerate the unpaired electrons which generate resistance and thus heat. The power P dissipated within one cavity of length L_{cav} ($L_{\mathrm{cav}} = 1.038\,\mathrm{m}$ for the ILC) is given by [14]

$$P = \frac{g^2 L_{\mathrm{cav}}}{(r/Q)Q_0},$$

where $r/Q = 1036\,\Omega$ is the shunt impedance per unit length, which depends only on the shape of the cavity, and Q_0 is the cavity's quality, which depends on the surface resistance of the cavity material. Therefore, the dynamic heat load from cavity heating (which accounts for 76 % of the cryomodule heat load at 2 K and 45 % of the overall heat load [15]) grows linearly with the cavity gradient, if the overall beam energy (and hence the product of the number of cavities times the gradient) is kept constant.

In summary, higher gradients reduce costs for tunnels, cavity material, cavities, couplers, and cryomodules, but increase costs for RF and cryogenic equipment and power consumption. Hence, there must exist a gradient that optimizes the overall cost, which has been estimated for the ILC to be beyond 60 MV/m [16]

2.4 Beam Delivery System

The main tasks of the beam delivery system are the measurement of beam properties, the collimation of the beams, and the final focussing. Measurement of the beam properties include energy, polarization and emittance; these measurements are used to tune the machine and correct effects such as coupling of vertical and horizon betatron oscillations, but also to dump beams to protect the detector, e.g. after a klystron trip. The collimation section removes halo particles with large amplitudes of the transverse (betatron) oscillations or large deviations from the nominal energy. The energy collimation section consists of two consecutive bends with zero net angle (a so-called dogleg) that displace the beam laterally. In the middle of the dogleg, off-momentum particles are displaced laterally from the main beam (this energy-dependent displacement is called the dispersion) and can be collimated. However, strong bending fields in regions of large dispersions cause emittance growth and thus have to be avoided; this effect grows fast with energy. Thus the allowed emittance increase limits the bending angles of the magnets employed in the dogleg and determine its length. The ILC design foresees a 1100 m long dogleg that is long enough to accommodate a 500 GeV beam (for 1 TeV centre-of-mass energy) with acceptable emittance growth. In the baseline configuration with 250 GeV beams, only every fifth magnet will be installed, which is sufficient at this energy.

[4] When the klystron is switched off, and there is no beam in the cavity, the RF field leaves the cavity via the waveguide system and is absorbed in a special, water-cooled load.

A basic property of longitudinal acceleration of beams is that it leaves the normalized emittance $\gamma\epsilon$ constant[5], where γ is the Lorentz boost of the accelerated particle, so that the emittance ϵ decreases with energy E as $1/\gamma$, or $1/E$. Consequently, for a given value β^* at the interaction point, the RMS beam size $\sigma = \sqrt{\beta^*\epsilon}$ also decreases, and the luminosity, which is proportional to $1/(\sigma_x\sigma_y)$, rises proportional to E. However, β^* is not only limited by the achievable strength of the final focus quadrupoles, which makes focussing harder at large beam energies, but also by the beam size within these quadrupoles, which has to fit into the magnet's aperture. This beam size limits the vertical beam size at lower energies, which means that the luminosity drops somewhat faster the with E if the beam energy is reduced, as can be seen in Tab. 1.

3 Running at Low Energies

3.1 The 10 Hz Scheme

As discussed above, the 10 Hz scheme is based on decoupling the two functions of the electron beam, namely to collide with the positrons for physics measurements, and to produce photons for the positron source. Originally this scheme was proposed for a machine capable of running at 250 GeV beam energy or more, to allow such a machine to operate below 125 GeV beam energy. Under that circumstances, the Main Linac would run at approximately half its nominal gradient, and therefore need about half of the maximum power for RF production, and even less for cryogenic cooling: the cryogenic power needed for the Main Linac is dominated by dynamic losses, i.e. by the heat deposited in the superconducting cavities by the accelerating fields, an those grow quadratically with the gradient. Therefore, an electron Main Linac capable of delivering electron pulses of 250 GeV at a repetition rate of 5 Hz is able to deliver alternating pulses of 150 GeV and $\leq$ 125 GeV at 5 + 5 Hz without the same cryogenic cooling power and the same overall electrical power consumption. However, although no additional investments (such as larger cryo plants or larger transformer stations) in the Main Linac are needed to enable the operation under the 10 Hz scheme, the total efficiency (electrical energy, or dollars, per unit of integrated luminosity) is significantly reduced by the necessity to accelerate a second high energy electron beam solely for positron production. In the case of Z^0 running, the electron beam energy used for positron production would be a factor 1.6 larger than the total beam energy used for collisions.

For a staged machine, the situation becomes more complex, and even less attractive: While a symmetric machine (where electrons and positron beams have the same energies) operating at 250 GeV centre-of-mass energy needs a 125 GeV electron beam, efficient positron production requires a machine capable of delivering a 150 GeV electron beam. Even worse, now the electron linac has to run at full gradient for the positron production beam and the "physics" beam, so that it requires almost twice the electrical power and cryogenic cooling capacity to allow running with the 10 Hz scheme, compared to nominal 5 Hz operation. While this may make running with alternating beams for the purpose of calibration runs at the Z^0 possible, it appears highly undesirable for real physics operation.

For the damping rings, the 10 Hz operation also poses significant challenges, because the lingering time of the beams in the damping rings is halved from 200 ms to 100 ms. Therefore, the already challenging task to reduce the positron vertical emittance by more than five orders of magnitude within 200 ms now becomes twice as hard. To achieve this goal, the vertical damping time has to be reduced from 24 ms to 13 ms, which is achieved by adding more wigglers (for more synchrotron radiation damping) and more RF power to replenish the synchrotron radiation loss. It should be noted that this means that the damping rings in the new configuration are capable of delivering fully damped beams at twice the rate that is needed for nominal physics operation, which opens up the possibility to increase the luminosity of the machine by an increased repetition rate.

In summary, any staging scenario should avoid physics data taking for any extended time in the 10 Hz scheme at full gradient, because the cost to luminosity ratio becomes unfavorable. Running at sufficiently large electron beam energies (above 125 GeV) and possibly an extended helical undulator will help to avoid 10 Hz running. However, running at higher pulse rates to increase overall luminosity may be possible.

[5] A slight rise of $\gamma\epsilon$ along the main linac is caused by imperfections and the need to follow the earth's curvature.

3.2 Asymmetric Running

An alternative way to run at lower centre-of-mass energies is the operation with beams of different energies. For instance, a centre-of-mass energy $E_{\mathrm{CM}} = 235\,\mathrm{GeV}$ could be achieved by colliding 150 GeV electrons with 92 GeV positrons, with a moderate boost of $\beta = 0.25$.

Detailed studies about the ramifications of such a scheme are still outstanding. Obvious questions to be answered from the detector and analysis point of view are how the resulting boost would affect the acceptance and resolution of tracks and jets. Since the Higgs strahlung process $e^+e^- \to Z^0h$ that provides the motivation to run at energies around $230-270\,\mathrm{GeV}$ is asymmetric in itself, a moderate longitudinal boost should not be too problematic, in contrast to measurements at the Z^0 pole that involve forward-backward asymmetries. On the accelerator physics side, studies would be needed to figure out which luminosity would be the achievable in such a scenario, and what the resulting beam disruption parameters and backgrounds (e.g. from pair production) would be.

4 Increasing the Luminosity

An important change in the baseline parameters that occurred between the ILC Reference Design Report (RDR) of 2007 and the Technical Design Report (TDR) of 2013 was the reduction of the number of bunches per pulse from $N_{\mathrm{bunch}} = 2625$ to 1312 in oder to reduce the necessary RF power and thus save costs. During the beam pulse, the total RF power that has to be provided by the klystrons is simply given by $P = E_{\mathrm{beam}}/eI_{\mathrm{beam}}$, where E_{beam} is the total beam energy, $I_{\mathrm{pulse}} = Q_{\mathrm{b}}/\Delta t_{\mathrm{b}}$ the beam current during the pulse (with the bunch charge $Q_{\mathrm{b}} = en_{\mathrm{b}}$ and time between bunches Δt_{b}), and e is the elementary charge (see Tab.1 for the actual values).

Naively one would expect that halving the number of bunches but keeping the total pulse length $t_{\mathrm{pulse}} = n_{\mathrm{b}}\Delta t_{\mathrm{b}}$ constant, which halves also the bunch current, would allow a reduction of the number of klystrons by a factor of two as well. However, this neglects the fact the fill time t_{fill}, which is the time needed to ramp up the cavity gradient from zero to the nominal 31.5 MV/m, also increases, so that the maximum pulse time of 1.6 ms that can be provided by the klystrons is exceeded. Thus, while the number of bunches was halved, the current was reduced only by 36 % from 9 to 5.8 mA, and the number of the klystrons was reduced by one third.

Turning that calculation around shows that to double the luminosity by a doubling of the number of bunches per pulse requires only 50 % more klystrons, and improves the luminosity-to-power ratio significantly[6]. The damping rings are designed to accommodate this increased number of bunches. For the electron damping ring, it is expected that it can store the full number of bunches. In the case of the positron damping ring, a doubling of the number of bunches in the ring will necessitate to build a second positron damping ring, which is foreseen in the tunnel design.

A further increase of the number of bunches per pulse is limited by capacity of the damping rings due to the onset of instabilities, and by the maximal pulse length that the klystrons can provide. However, the damping rings are designed to achieve the necessary damping within 100 ms, which would allow a doubling of the luminosity by doubling the pulse rate to 10 Hz, provided that the cryogenic plants are upgraded to provide more cooling capacity. Whether the positron source, in particular the target, is capable to run at 10 Hz needs, however, to be checked. What makes a doubling of the pulse frequency attractive is the fact that no additional klystrons and modulators are needed; the modulators (which accumulate the energy needed to provide the high power pulses for the klystrons) would simply charge at twice the rate. Such a luminosity upgrade could be realized relatively fast, provided that the cryogenic plants are can designed for easy upgradeability. The downside of this upgrade path is that the luminosity-to-cost ratio hardly improves.

Another advantage of a luminosity increase through an increased repetition rate is that it can be continuously adjusted: any repetition rate up to the maximal rate of 10 Hz is feasible, whereas the number of klystrons can only be increased in fixed steps. In a staged scenario it is conceivable that one would install the full cryogenic capacity early on, and run the accelerator at each energy at the maximum repetition rate allowed by the available cooling capacity.

[6] Even more so as many other contributors to the power consumption are independent of the beam current.

			baseline				upg.
Centre-of-mass energy	E_{CM}	GeV	200	250	350	500	500
Luminosity pulse repetition rate		Hz	5	5	5	5	5
Positron production mode			10 Hz	10 Hz	nom.	nom.	nom.
Site AC power consumption	P_{AC}	MW	114	122	121	163	206
Average beam power	$P_{\rm ave}$	MW	4.2	5.3	7.4	10.5	21.0
Bunch population	N	$\times 10^{10}$	2	2	2	2	2
Number of bunches	n_b		1312	1312	1312	1312	2625
Linac bunch interval	Δt_b	ns	554	554	554	554	366
Beam current in pulse	$I_{\rm pulse}$	mA	5.8	5.8	5.8	5.8	8.8
Beam pulse duration	$t_{\rm pulse}$	µs	727	727	727	727	961
Average gradient	g	MV/m	12.6	15.8	22.1	31.5	31.5
RF pulse length	$t_{\rm RF}$	ms	1.10	1.19	1.37	1.65	1.57
RMS bunch length	σ_z	µm	300	300	300	300	300
Normalized horizontal emittance at IP	$\gamma\epsilon_x$	µm	10	10	10	10	10
Normalized vertical emittance at IP	$\gamma\epsilon_y$	nm	35	35	35	35	35
Horizontal beta function at IP	β_x^*	mm	16	13	16	11	11
Vertical beta function at IP	β_y^*	mm	0.34	0.41	0.34	0.48	0.48
RMS horizontal beam size at IP	σ_x^*	nm	904	729	684	474	474
RMS vertical beam size at IP	σ_y^*	nm	7.8	7.7	5.9	5.9	5.9
Vertical disruption parameter	D_y		24.3	24.5	24.3	24.6	24.6
Fract. RMS energy loss to beamstrahlung	δ_{BS}	%	0.65	0.97	1.9	4.5	4.5
Luminosity	L	10^{34} cm^{-2} s^{-1}	0.56	0.75	1.0	1.8	3.6
Fraction of L in top 1% E_{CM}	$L_{0.01}$	%	91	87	77	58	58
Electron polarisation	P_-	%	80	80	80	80	80
Positron polarisation	P_+	%	30	30	30	30	30
Electron relative energy spread at IP	$\Delta p/p$	%	0.20	0.19	0.16	0.13	0.13
Positron relative energy spread at IP	$\Delta p/p$	%	0.19	0.15	0.10	0.07	0.07
Beamstrahlung parameter (av.)	$\Upsilon_{\rm ave}$		0.013	0.020	0.030	0.062	0.062
Beamstrahlung parameter (max.)	$\Upsilon_{\rm max}$		0.031	0.048	0.072	0.146	0.146
Energy loss from BS	$\delta E_{\rm BS}$	%	0.65	0.97	1.9	4.5	4.5
e^+e^- pairs per bunch crossing	$n_{\rm pairs}$	10^3	45	62	94	139	139
Pair energy per B.C.	$E_{\rm pairs}$	TeV	25	47	115	344	344

Table 1: Summary table of the 200–500 GeV baseline parameters for the ILC [8, 9, 10], including parameters for a possible luminosity upgrade. The numbers for energies between 200 and 350 GeV correspond to a situation where the full 500 GeV accelerator is being operated at a reduced energy.

			Minimal	Scenario 1	Scenario 2	Baseline
Centre-of-mass energy	$E_{\rm CM}$	GeV	250	250	250	500
... extensible in tunnel to	$E_{\rm CM}$	GeV	250	500	500	500[a]
Site AC power consumption	$P_{\rm AC}$	MW	120[b]	120[b]	125[b]	163
Relative cost (estimated)		%	67[b]	73[b]	75[b]	100

Table 2: Overview over possible staging scenarios [17].
[a] The baseline design includes an option to extend the energy to 1 TeV, but not within the initial tunnel.
[b] If the 10 Hz scheme is avoided, an estimated 25 MW of AC power and 3 % of costs can be saved.

5 Staging Scenarios being Discussed

Fig. 1 illustrates several possible scenarios for an ILC with an (initial) energy of 250 GeV, in comparison with the nominal 500 GeV baseline design [17].

A minimal Higgs factory, limited to about 250 GeV centre-of-mass energy, is one possible option. In such a scenario, the central region could be reduced, because the BDS would not have to accommodate a high-energy beam, which would save some cost. Altogether, such a machine is estimated [17] to cost approximately 67 % of the machine in the full TDR baseline design configuration.

A truly staged machine, with a central region that makes future upgrades possible, could come in two forms:

In scenario 1, the initial stage would include a main tunnel long enough to accommodate the full accelerator, but have the bunch compressor immediately adjacent to the shortened main linac, so that an energy upgrade necessitates a relocation of the RTML turn-around and bunch compressor, which corresponds to about 2200 m of beamline on either side. This scenario is estimated to cost about 73 % of the full machine. The moderate price difference compared to the minimal Higgs factory illustrates that the tunnel itself is not the biggest cost driver at the ILC. A possible advantage of this scenario might be that not the full tunnel has to be ready from the beginning on; however, in the Japanese site, the tunnel sections would be excavated by several teams working in parallel, so that a shorter tunnel would not be finished much faster than the full tunnel.

In scenario 2, the turn-around and the bunch compressor are built at their final positions from the beginning on, and the space reserved for the installation of further cryomodules is bridged by a transfer line in the first stage. This option is estimated to cost about 75 % of the full machine. This scenario would make upgrading much faster and cheaper (no relocation of the turnaround, no re-commissioning of the bunch compressor), and conceivably allow to upgrade the energy with an intermediate step around the top threshold at 350 GeV. If such a scenario is envisioned, the cryomodule production schedule could be stretched, which may actually save costs because less infrastructure for cavity and coupler production, cryomodule assembly, and testing would be needed.

6 Optimizing the Energy: An Experimental Figure of Merit

Defining the (initial) energy reach of the ILC will depend heavily on factors outside the control of the physics community, such as constraints from accelerator physics, constraints from the chosen site, available funding, and politics. One constraints from accelerator physics comes from the fact that the round trip that a positron takes from (roughly) the middle of the Damping Ring injection line to the IP must be an integer multiple of the DR circumference of 3.2 km, which results in a quantization of the (positron) beam energy in steps of roughly 34 GeV, assuming that the available tunnel space will be fully equipped with cryomodules. The site may have an influence because some places may be more or less suitable for access shafts. Financial considerations always play a role, obviously, because a larger linac costs more, but also because initial investments can be partially traded against running costs: a longer machine costs more initially, but may deliver more events per unit running cost.

However, the physics and detector community can certainly make an important input to these considerations, if a quantitative figure of merit can be given that indicates how much luminosity at a given centre-of-mass energy (and other conditions, such as beamstrahlung or disruption parameter) is needed to obtain a certain physical result.

For example: Consider the measurement of the Higgs production cross section with the recoil mass technique in $e^+e^- \to Z^0h \to \mu^+\mu^- X$, where the Higgs mass peak is reconstructed from the $\mu^+\mu^-$ recoil mass spectrum. We can expect the relative statistical uncertainty $\delta\sigma/\sigma$ of the cross section σ to be given by $\delta\sigma/\sigma = q/\sqrt{\sigma L}$, where L is the integrated luminosity, and q is a quality factor that depends on the performance of the detector and analysis code, but also on the centre-of-mass energy and the beam parameters, in this particular case on the beam energy spread (or, equivalently, the disruption parameter).

Thus, the integrated luminosity L that is needed to achieve a certain statistical precision $\delta\sigma$ is given by $L = q^2/\sigma/(\delta\sigma/\sigma)^2$, so that q^2/σ serves as a figure of merit for different beam energies and running conditions.

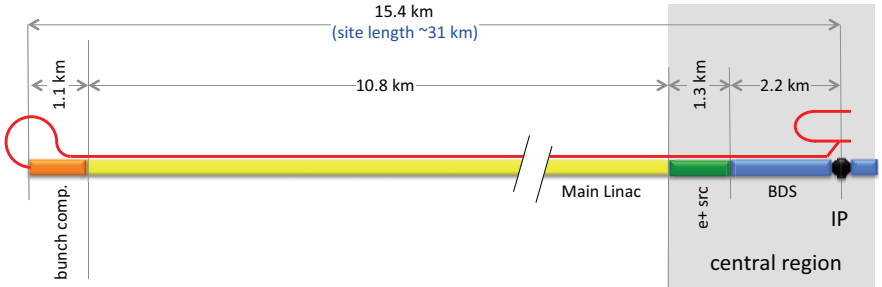

TDR 500 GeV Baseline

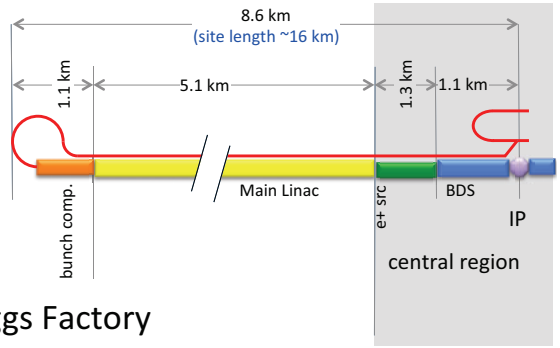

250 GeV Minimal Higgs Factory

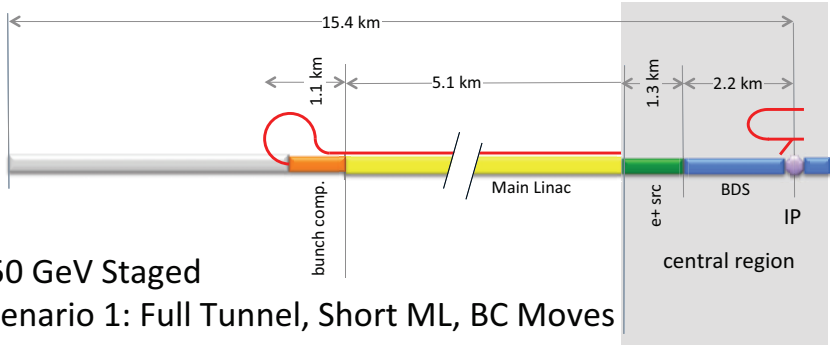

250 GeV Staged
Scenario 1: Full Tunnel, Short ML, BC Moves

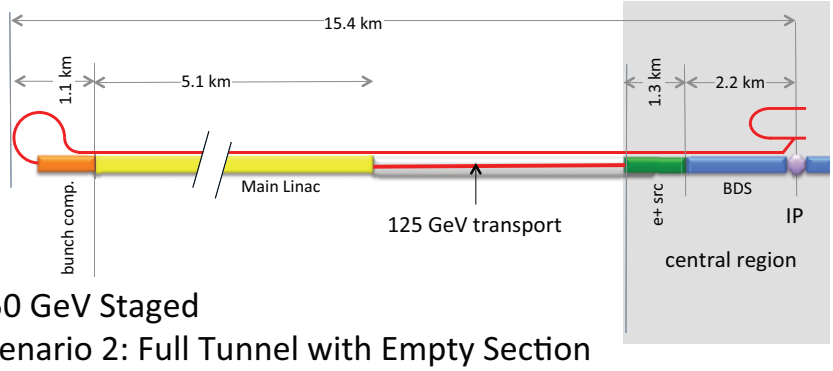

250 GeV Staged
Scenario 2: Full Tunnel with Empty Section

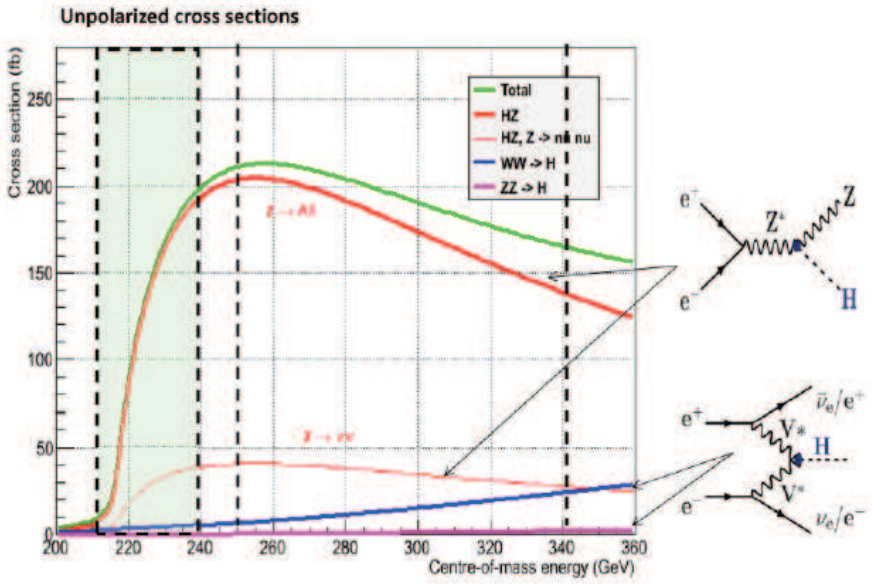

Figure 2: Higgs boson production cross section [19].

For the recoil mass measurement, the mass resolution is best around 20 GeV above the threshold for Z^0h production [18], i.e. around 235 GeV (see Fig. 2). However, below 250 GeV or so, the helical undulatory becomes so inefficient that it may be necessary to resort to the 10 Hz running scheme, where between two beam pulses with colliding e^+e^- beams (that occur at 5 Hz) an intermediate e^- beam pulse is accelerated to 150 GeV just for positron production. Thus, one 150 GeV beam alternates with two beams of 235 GeV total beam energy, therefore only $235/(150 + 235) = 61\,\%$ of the beam energy are used for physics, with a corresponding (though not necessarily proportional) increase in costs per inverse femtobarn of produced integrated luminosity. In addition, the instantaneous luminosity (at constant beam disruption) of a linear collider rises at least linearly with the beam energy, because the beams get smaller at larger energies. In essence, the operation cost per inverse femtobarn falls with energy. Therefore, from an accelerator physics point of view the conditions to produce luminosity become more favorable as the centre-of-mass energy is increased to, say, 260 or 270 GeV. This effect is further enhanced by the fact that the Z^0h cross section has its maximum around 260 GeV.

Experimentally, on the other hand, conditions become less favorable with increasing energy because the boost of the Z^0 in the laboratory frame rises, which leads to a deterioration of the recoil mass resolution, and thus to more background under the broadening peak and a reduced quality factor q. However, existing studies indicate [18] that the measurement of the Z^0h coupling, which is probably the more relevant measurement to be performed with the recoil mass method, works well at 250 GeV and is much less affected by an increase of the centre-of-mass energy than the mass measurement.

A quantitative investigation of the pros and cons of running at higher or lower centre-of-mass energies is of interest now, before the layout of the detectors and the accelerator has been finalized, because it may have an impact on this design: If it turned out that indeed energies significantly below 250 GeV are necessary to achieve the physics goals, then an optimization of the helical undulatory positron source should be considered, for instance with a longer undulatory or an undulatory with different parameters. If, on the other hand, running at higher energies such as 250 or 270 GeV turned out to be viable, then further parameter changes might result: The reduced resolution in the recoil mass spectrum would result in a smaller impact of the beam energy spread, allowing running at larger disruption parameters, which increases the luminosity. Since the recoil mass resolution is the driving force for the tracking resolution of the detectors, even that might be influenced.

Similar considerations should be applied in the determination of the maximum beam energy of the

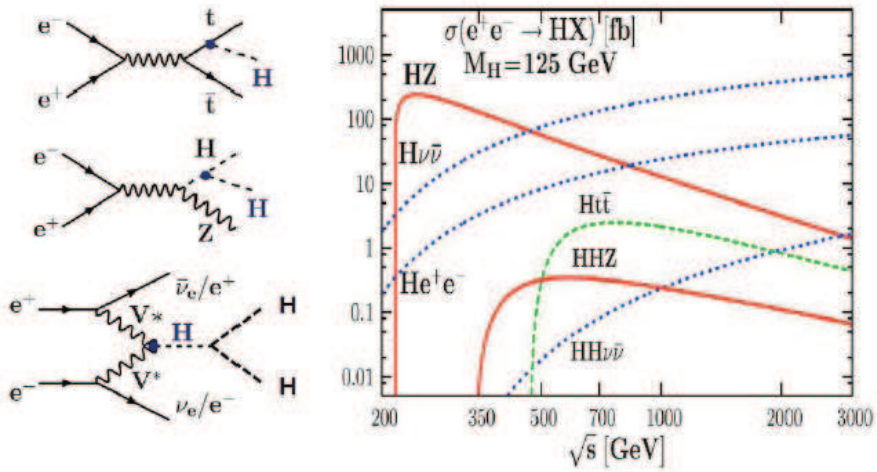

Figure 3: Higgs boson production cross section at larger energies [19].

accelerator (not of the possible TeV upgrade, but of the half-TeV-ish machine): From the point of view of Higgs physics, two measurements stick out that require energies around or above half a TeV: The top-Higgs-coupling, and the Higgs self coupling. The top-Higgs-coupling is based on the process $e^+e^- \to t\bar{t}h$ with a threshold of 475 GeV, with a cross section that rises rapidly between threshold and 600 GeV, as shown in Fig. 3. For this process, more energy is clearly better, so the trade-off is clearly between initial costs and operating costs. But again, to quantify the cost advantage that a rise of the centre-of-mass energy from 500 to, say, 550 or 600 GeV would have, experimental studies of the corresponding quality factor q (or $q^2\sigma$) are needed. In fact it may turn out that a measurement of the $t\bar{t}h$ coupling is unviable (meaning that it produces no noticeable improvement over the expected LHC performance) at 500 GeV, but viable at a slightly larger energy. For instance, the $t\bar{t}h$ cross section rises by a factor of 3.7 between 500 and 550 GeV [20]. From the machine point side, a quantitative evaluation of the relative size of running costs and investment costs might be interesting. One can guess that one year of machine operation costs would be comparable to the cost increase needed to raise the machine's energy by anywhere between 25 and 100 GeV.

Another process that profits a lot from increased centre-of-mass energy is the measurement of the Higgs self coupling. This measurement is based on the detection of double Higgs production events from a $h \to hh$ branching. As in single Higgs production, the intermediate Higgs can be produced by Higgs-strahlung off a Z^0, or by the fusion process $W^+W^- \to h$. However, other diagrams that do not involve a tri-Higgs coupling can also produce Higgs pairs, in particular repeated Higgs-strahlung off a Z^0 or a t-channel W. As Fig. 3 shows, the relevant cross sections are quite small, but in particular the $hh\nu\bar{\nu}$ cross section rises significantly with the centre-of-mass energy. Studies performed for the TDR [21] assume an integrated luminosity of the order of $2\,\mathrm{ab}^{-1}$ at 550 GeV, corresponding to many years of running, and predict just a $5\,\sigma$ effect for that amount of data. If one estimates that one year of ILC operation might cost about as much as 50 GeV worth of Main Linac, it is well possible that at 600 GeV the prospects for this extremely important measurement might be better.

7 Conclusions

With the discovery of a Higgs boson at LHC, an exiting physics program for the ILC lies ahead of us. This program needs the ILC's capabilities at comparatively low energies around 230-270 GeV as well as at high energies around 500–600 GeV. Physics studies and deliberations among the physics communities which amounts of data at which energies and in which sequence would produce the most interesting and relevant physics results are needed now, in order to define the optimal final and intermediate configuration of the ILC. In several places one may trade initial investments for running costs to achieve an optimal physics

performance at a given budget, within a reasonable time.

8 Acknowledgments

I thank Nick Walker, Jenny List, Eckhard Elsen, Karsten Büßer, Brian Foster, Georg Weiglein, Gudrid Moortgat-Pick and Sven Heinemeyer for many helpful discussions and explanations.

References

[1] G. Aad *et al.* [ATLAS Collaboration], Phys. Lett. B **716** (2012) 1-29 [arXiv:1207.7214 [hep-ex]].

[2] S. Chatrchyan *et al.* [CMS Collaboration], Phys. Lett. B **716** (2012) 30-61 [arXiv:1207.7235 [hep-ex]].

[3] The ATLAS Collaboration, *Combined coupling measurements of the Higgs-like boson with the ATLAS detector using up to* $25\,\mathrm{fb}^{-1}$ *of proton-proton collision data,* ATLAS-CONF-2013-034 (2013).

[4] S. Chatrchyan *et al.* [CMS Collaboration], *Observation of a new boson with mass near* $125\,GeV$ *in pp collisions at* $\sqrt{s} = 7$ *and* $8\,\mathrm{TeV}$*,* arXiv:1303.4571 [hep-ex] (2013).

[5] S. Heinemeyer *et al.* (eds), *Implications of LHC results for TeV-scale physics: signals of electroweak symmetry breaking,* Submitted to the Open Symposium of the European Strategy Preparatory Group, 2012, `https://indico.cern.ch/contributionDisplay.py?contribId=131&confId=175067`.

[6] M. E. Peskin, *Comparison of LHC and ILC capabilities for Higgs boson coupling measurements,* arXiv:1207.2516 [hep-ph] (2012).

[7] J. E. Brau *et al.*, *The physics case for an* e^+e^- *linear collider,* arXiv:1210.0202 [hep-ex] (2012).

[8] P. Burrows *et al.* (eds.), *International Linear Collider Technical Design Report, Volume 3: Accelerator, Part II: Baseline Design,* DESY 13-062, 2013.

[9] N. Walker, *ILC parameters,* 2012, `http://ilc-edmsdirect.desy.de/ilc-edmsdirect/item.jsp?edmsid=D00000000925325`.

[10] *ILC Technical Design Documentation,* `http://www.linearcollider.org/ILC/GDE/technical-design-documentation`.

[11] A. Wolski, *Damping ring design and physics issues,* lectures given at the Fourth International Accelerator School for Linear Colliders, Beijing, 2009, `http://ilcagenda.linearcollider.org/conferenceOtherViews.py?view=standard&confId=3475`.

[12] M. A. Palmer and S. Guiducci, *ILC Damping Ring parameters,* 2012, `http://ilc-edmsdirect.desy.de/ilc-edmsdirect/item.jsp?edmsid=D00000000960955`.

[13] P. Burrows *et al.* (eds.), *International Linear Collider Technical Design Report, Volume 3: Accelerator, Part I: R&D in the Technical Design Phase,* DESY 13-062, 2013.

[14] H. Padamsee, *Designing superconducting cavities for accelerators,* Proc. CERN Accelerator School 2002, Erice, Italy, CERN-2004-008 (2004) 233-252.

[15] T. Peterson, *ILC cryogenic heat loads and cryoplant parameters,* 2012, `http://ilc-edmsdirect.desy.de/ilc-edmsdirect/item.jsp?edmsid=D00000000994395`.

[16] C. Adolphsen, *Review of machine parameter / cost relationships,* presented at ILCWS'11, Granada, Spain, `http://ilcagenda.linearcollider.org/conferenceOtherViews.py?view=standard&confId=5134`.

[17] N. Walker, *ILC as a Higgs factory,* talk at Accelerators for a Higgs Factory: Linear vs. Circular (HF2012), Fermilab, 2012, `https://indico.fnal.gov/conferenceOtherViews.py?view=standard&confId=5775`.

[18] H. Li *et al.* [ILD Design Study Group Collaboration], *HZ recoil mass and cross section analysis in ILD,* arXiv:1202.1439 [hep-ex] (2012).

[19] A. Blondel *et al.*, *Report of the ICFA Beam Dynamics Workshop 'Accelerators for a Higgs Factory: Linear vs. Circular' (HF2012),* arXiv:1302.3318 [physics.acc-ph] (2013).

[20] C. Farrell and A. H. Hoang, Phys. Rev. D **72** (2005) 014007 [arXiv:hep-ph/0504220].

[21] J. Brau *et al.* (eds.), *International Linear Collider Technical Design Report, Volume 2: Physics,* DESY 13-062, 2013.

Chapter 2

Top Physics

Top-Quark Physics Results From LHC

Luca Fiorini[1]
on behalf of the ATLAS and CMS collaborations.

1- Instituto de Física Corpuscular (IFIC), Universitat de València and CSIC.
Edificio Institutos de Investigación Apartado de Correos 22085
46071 Valencia - Spain
E-mail: Luca.Fiorini@cern.ch

The top-quark is a fundamental element of the physics program at the Large Hadron Collider (LHC). We review the current status of the top-quark measurements performed by ATLAS and CMS experiments in pp collisions at $\sqrt{s}$=7 TeV by presenting the recent results of the top-quark production rates, top mass measurements and additional top quark properties.
We will also describe the recent searches for physics beyond the Standard Model in the top-quark sector.

1 Introduction

The top-quark is the heaviest known elementary particle, with a mass measured by TeVatron experiments to be about 173 GeV [1]. Due to its high mass, the top-quark is believed to play a special role in the electro-weak symmetry breaking mechanism and possibly in models of new physics beyond the Standard Model (SM).

The Large Hadron Collider (LHC) [2] operated in 2010 and 2011 with an energy in the centre of mass ($\sqrt{s}$) of 7 TeV. The delivered integrated luminosity ($\int Ldt$) to ATLAS [3] and CMS [4] experiments was of about 5 fb^{-1} per experiment in 2011 and the peak luminosity was of $3.7 \cdot 10^{33}$ cm^{-2}s^{-1}. Measurements presented in this proceeding are based on the statistics collected up to summer 2011 and use at most 2.1 fb^{-1} . The $t\bar{t}$ production rate at LHC $\sqrt{s} = 7$ TeV is a factor of 20 larger than at the TeVatron, allowing the production of top-quarks with unprecedented abundance.

2 Top-quark production measurements

2.1 $t\bar{t}$ production measurements

Figure 1 shows the leading order diagrams of the $t\bar{t}$ production process. The $t\bar{t}$ production is dominated by the gluon-fusion process at LHC energies. The $t\bar{t}$ production cross-section, $\sigma_{t\bar{t}}$, is predicted to be at the approximate next to next to leading order $\sigma_{t\bar{t}}{}^{approx\ NNLO} = 165^{+11}_{-16}$ pb [5]. The top-quark decays to a W and a b-quark almost 100% of the times. The W decays hadronically in about 68% of the times. The $t\bar{t}$ final states are categorised by the number of leptons from the W decays in the final state: di-lepton, single lepton and full hadronic channels. Both ATLAS and CMS measured $\sigma_{t\bar{t}}$ in several final states: di-lepton ($\ell = e, \mu, \tau$), single-lepton and full hadronic. The results are shown in Figures 3 and 4.

- The $t\bar{t}$ cross-section has been measured by ATLAS [6, 7] and CMS [8] in the single-lepton channel with either an electron or a muon in the final state. The events are required to have a high-p_{T} lepton and at least three jets. The $\sigma_{t\bar{t}}$ has been measured with and without the requirement of a b-tagged jet. Results are obtained for $\int Ldt =$

35 pb^{-1} and 0.7 fb^{-1} for ATLAS and (0.8-1.1) fb^{-1} for CMS. Figure 3 show the ATLAS single-lepton results obtained with $\int Ldt = 35$ pb^{-1}, while result for 0.7 fb^{-1} is $\sigma_{t\bar{t}} = 179 \pm 9.8$ (stat.) $\pm$ 9.7 (syst.) $\pm$ 6.6 (lumi.) pb. Figure 4 shows the CMS results with 2011 data. Uncertainties with 2011 data are at the level of 9% for ATLAS and CMS which is comparable to the NNLO theoretical uncertainty.

- The event selection for di-lepton final states require the presence of 2 high-p_{T} leptons of opposite charge, two central jets (from b-quarks) and large $E_{\mathrm{T}}^{\mathrm{miss}}$ or large transverse activity (H_T). The $E_{\mathrm{T}}^{\mathrm{miss}}$ is the missing energy in the transverse plane, calculated taking into account the transverse momentum of the muons and transverse energy of the electrons and jets in the events. H_T is the scalar sum of the transverse momentum of the muons, transverse energy of the electrons, $E_{\mathrm{T}}^{\mathrm{miss}}$ and transverse energy of the jets in the event. In the case that the leptons in the final state are e or μ, ATLAS results are obtained with and without the requirement of a b-tagged jet [11,12]; CMS results are obtained with b-tagging requirement [13]. ATLAS produced results with 0.7 fb^{-1} of data, while CMS used 1.1 fb^{-1} of data for the result with b-tagging requirement. Their uncertainties are about 11% dominated by systematics. The $\sigma_{t\bar{t}}$ has been measured also in the $\tau\mu$ final state by ATLAS [14] and CMS [15], where a calorimeter-seeded τ is reconstructed in the event together with a high-p_{T} muon. The resulting $\sigma_{t\bar{t}}$ measurements are obtained for $\int Ldt$ =1.1 fb^{-1} and have similar uncertainties: 24% CMS and 21% ATLAS[a].

- The $\sigma_{t\bar{t}}$ has been measured by ATLAS [16] and CMS [17] also in the full hadronic final state. Events are required to have at least six high-p_{T} jets of which at least two b-tagged jets. The results are obtained for $\int Ldt$ = 1.1 (1.0) fb^{-1} for CMS (ATLAS)[b].

CMS combined the cross-section measurements obtaining $\sigma_{t\bar{t}}$ = 166 $\pm$ 2 (stat.) $\pm$ 11 (syst.) $\pm$ 8 (lumi.) pb. The measurements of the $t\bar{t}$ cross-section at LHC are in agreement with the theoretical predictions. Their accuracy is similar to the uncertainty of the NNLO prediction and the most sensitive results in the single-lepton channel are limited by systematic uncertainties.

2.2 Single-top production measurements

Figure 2 shows the leading order diagrams of the electro-weak single-top-quark production, that is characterised by the W-mediated t-channel ($\sigma_t^{approx\ NNLO}$ =64 $\pm$ 3 pb) [18], s-channel ($\sigma_s^{approx\ NNLO}$ =4.6$\pm$0.3 pb) [19] and the associated Wt production ($\sigma_{Wt}^{approx\ NNLO}$ =15.7$^{+1.3}_{-1.4}$ pb) [20]. Compared to TeVatron experiments, the single-top production in t-channel and Wt mode is much larger than the s-channel.

The single-top-quark production in the t-channel has been measured by ATLAS [21] with 0.7 fb^{-1} of data and by CMS [22] with 36 pb^{-1} of data. ATLAS measurement is σ_t = 90 $\pm$9 (stat.) $^{+31}_{-20}$ (syst.) pb and CMS measurement is σ_t = 84 $\pm$30 (stat.+syst.) $\pm$3 (lumi.) pb. Searches of the Wt channel have been performed by CMS [23] and ATLAS [24] with 2.1 fb^{-1} and 0.7 fb^{-1} of data respectively. This mode has escaped so far direct observation. ATLAS rejects the background-only hypothesis at the 1.2 σ level and

[a] ATLAS: $\sigma_{t\bar{t}}$ = 142 $\pm$ 21 (stat.) $^{+20}_{-16}$ (syst.) $\pm$ 5 (lumi.) pb ; CMS results are in Figure 4.

[b] CMS results are in Figure 4 and ATLAS obtains $\sigma_{t\bar{t}}$ = 167 $\pm$ 18 (stat.) $\pm$ 78 (syst.) $\pm$ 6 (lumi.) pb.

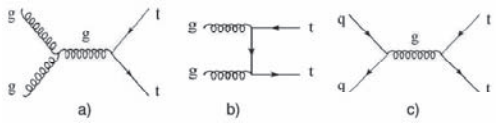

Figure 1: Lowest level diagrams of the $t\bar{t}$ production. Gluon scattering processes, `a)` and `b)`, are the dominant processes at LHC energies, while quark scattering, process `c)`, is the dominant one at TeVatron energies.

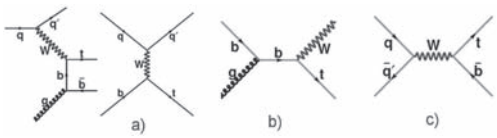

Figure 2: Diagrams of single-top production at the lowest level: `a)` t-channel, `b)` Wt associated production, `c)` s-channel.

CMS obtains a signal significance of 2.7 σ. Searches of single-top-quark production in the s-channel have been performed by ATLAS with $\int Ldt = 0.7$ fb^{-1} [25]. An upper limit at 95% C.L. on the production cross section of $\sigma_s < 26.5$ pb has been obtained.

3 Top-quark properties

3.1 Top-quark mass

Among the various top-quark properties, ATLAS and CMS measured the top-quark mass (m_t) in several final states.
In the SM the mass of the top-quark is a free parameter that, together with the W mass, can constrain the mass value of an eventual Higgs boson [26]. Figure 5 summarises the measurement of m_t by ATLAS experiment [27]. A measurement in the single-lepton final state has been obtained with 0.7 fb^{-1} of data with an uncertainty that is at the level of 1.6%: $m_t = 175.9 \pm 0.9$ (stat.) $\pm$ 2.7 (syst.) GeV. CMS measured m_t with $\int Ldt = 36$ pb^{-1} in the single-lepton [28] and di-lepton [29] final states, obtaining $m_t = 173.1 \pm 2.1$ (stat.) $^{+2.8}_{-2.1}$ (syst.) GeV (single-lepton) and $m_t = 175.5 \pm 4.6$ (stat.) $\pm$ 4.6 (syst.) GeV (di-lepton). Both experiments have also measured the top-quark pole mass, m_{pole}, from the $\sigma_{t\bar{t}}$ measurement [30], [31]. This is a complementary measurement of a different observable with respect to the measurement of the top-quark invariant mass from the top-quark decay products. Results are shown in Figure 6.

3.2 Top-anti-top quark mass difference

The SM assumes that top and anti-top-quarks have the same mass. An eventual CPT violation can manifest itself as a mass difference between the top and anti-top-quark. CMS measured the mass difference in the μ+jets final state [32]: Δm_t = -1.2 $\pm$ 1.2 (stat.) $\pm$ 0.5 (syst.) GeV. These measurements are threfore consistent with the SM.

3.3 Top-quark charge asymmetry

Recently TeVatron experiments reported forward-backward asymmetry in $t\bar{t}$ events that is larger then theoretical predictions by about 3σ [33, 34]. At the Next-to-Leading-Order (NLO), a small difference of about 1% in the top and anti-top rapidity distribution is expected at LHC [35]. Results are obtained for CMS [36] and ATLAS [37] in the single-lepton final state for $\int Ldt = 1.1$ (0.7) fb^{-1} for CMS (ATLAS) experiment. CMS measured the

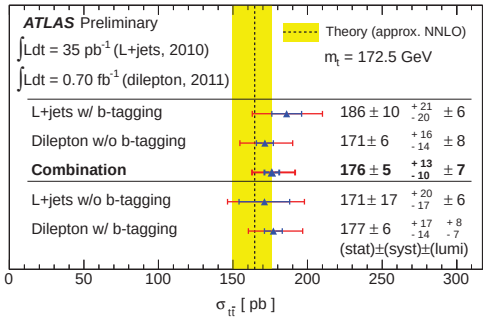

Figure 3: Summary of the $t\bar{t}$ cross-section measurements from ATLAS Collaboration [9].

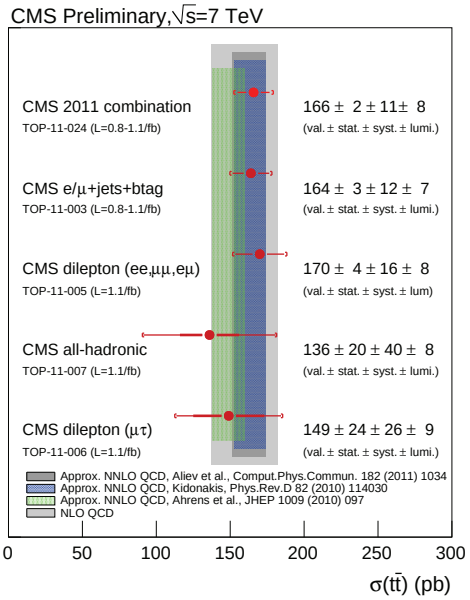

Figure 4: Summary of the $t\bar{t}$ cross-section measurements from CMS Collaboration [10].

asymmetry from the top-anti-top pseudo-rapidity distribution, while ATLAS measured it from the rapidity distribution. The asymmetry measured is A_C = -1.6 ± 3.0 $^{+1.0}_{-1.9}$% (CMS) for a theoretical prediction of 1.3% and A_C = -2.4 ± 1.6 ± 2.3 % (ATLAS) for a theoretical prediction of 0.6%.

3.4 Other top-quark properties

ATLAS measured the W helicity in $t\bar{t}$ single-lepton and di-lepton decays [38]. No significant deviations from NNLO QCD predictions were observed. A combination of the measurements in the single-lepton and di-lepton channels with the right-handed helicity fraction set to zero leads to: $F_0 = 0.75 \pm 0.08\,(stat. + syst.)$ and $F_L = 0.25 \pm 0.08\,(stat. + syst.)$[c]. ATLAS also measured the top-quark charge [39] and the $t\bar{t}$ spin correlation in di-lepton decays [40].

4 New physics searches in the top-quark sector

Several New Physics (NP) scenarios can produce deviations from the SM in $t\bar{t}$ and single-top-quark production. Examples of NP in the top sector are: Flavour Changing Neutral Current (FCNC) decays of the top-quark to a quark with same charge and different flavour: $t \to (Z, \gamma, g)\, q$; heavy neutral particles decaying to $t\bar{t}$, like heavy vector-bosons or Kaluza-Klein resonances: $(Z', g_{KK}) \to t\bar{t}$; heavy top-like partners decaying to a top-quark and a

[c]The W bosons are produced as real particles in top decays and their polarisation can be longitudinal, left-handed or right-handed. The fractions of events with a particular polarisation, F_0, F_L and F_R, respectively, are referred to as helicity fractions

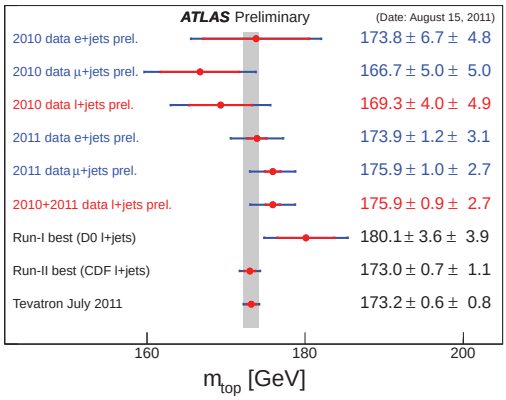

Figure 5: Summary of the top-quark mass measurements from ATLAS Collaboration [27].

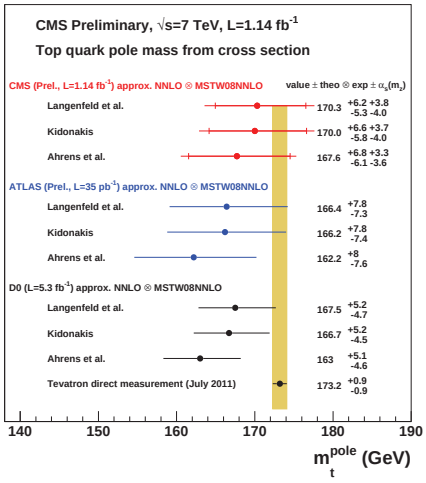

Figure 6: Summary of the top-quark pole mass measurements from CMS, ATLAS and D0 Collaborations [31].

stable or unstable neutral particles: $T \rightarrow t\,(A^0, Z)$.

4.1 FCNC

Searches of FCNC were performed by CMS with 35 pb^{-1} and by ATLAS with 0.7 fb^{-1} and 35 pb^{-1} of data. CMS searched for same-sign tt pairs [41], that can be induced by t-channel exchange of a massive neutral vector boson (Z'). CMS placed a 95% confidence level limit on the four-fermions contact interaction term for a Z' mass of 2 TeV: $\frac{C_{RR}}{\Lambda} < 2.7$ TeV^{-2}[d]. ATLAS placed 95% confidence level limits on BR($t \rightarrow qZ$) $< 1.1\%$ [42] and $\sigma_{qg\rightarrow t} \times$ BR($t \rightarrow Wb$) < 17.3 pb [43].

4.2 Heavy reasonances

Searches for heavy neutral particles decaying to $t\bar{t}$ have been performed by ATLAS in the single-lepton final state with 0.2 fb^{-1} of data [44] and in the di-lepton final state with 1.0 fb^{-1} of data [45]. 95% confidence level limits on g_{KK} mass have been placed at 0.65 TeV and 0.84 TeV respectively. CMS searched for heavy neutral particles decaying to $t\bar{t}$ in the μ+jets and full hadronic final state with 1.1 fb^{-1} and 0.9 fb^{-1} of data respectively [46, 47]. 1 pb limits on the cross-section were put with 95% confidence level for $m_{Z'} < 1.3$ TeV in the μ+jets channel and for $m_{Z'} < 1.1$ TeV in the full hadronic channel.

[d] $\frac{C_{RR}}{\Lambda} <$ defines the coupling strength of the four-fermions contact interaction as a function of the NP energy scale (Λ).

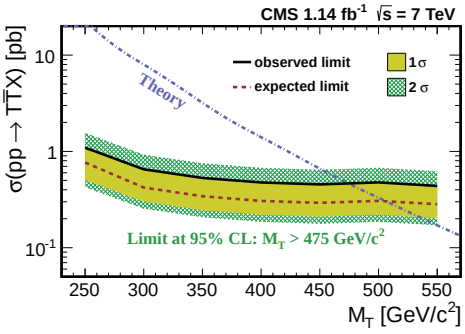

Figure 7: Limits on the cross-section production rates of $T \to tZ$ in events with three leptons, jets and $E_{\mathrm{T}}^{\mathrm{miss}}$ by the CMS Collaboration [48].

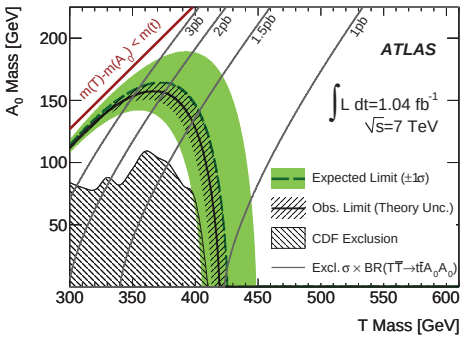

Figure 8: Limits on the cross-section production rates of $T \to tA^0$ in events with one lepton, jets and large $E_{\mathrm{T}}^{\mathrm{miss}}$ by the ATLAS Collaboration [49].

4.3 Top partners

Searches for top-like partners decaying as $T \to t\,Z$ were performed by CMS in the final state with 3 leptons [48] with 1.1 fb^{-1} of data. A 95% confidence level limit on the T mass has been set: $m_T > 475$ GeV, as shown in Figure 7. ATLAS searched for top-like partners decaying as $T \to t\,A^0$ in $t\bar{t}$+large $E_{\mathrm{T}}^{\mathrm{miss}}$ events in the single lepton channel with 1.0 fb^{-1} of data [49]. A limit at 95% confidence level for a production rate of 1.1 pb was set for $(m_T, m_{A^0}) = (420$ GeV, 10 GeV) as shown in Figure 8.

5 Conclusions

The top-quark physics program at LHC is extremely vast and complete.
The $\sigma_{t\bar{t}}$ has been measured in almost all the final states predicted by SM with an accuracy, limited by systematics, that is similar to the NNLO theoretical predictions, entering in a phase of precise measurements just one year after the first top-quark observations at the LHC. The single-top-quark production mechanism has been clearly established by LHC experiments in the t-channel, while it needs more data to be observed in Wt channel and s-channel.
A large number of the top-quark properties has been measured by the ATLAS and CMS experiments. The top mass, top-anti-top mass difference, W helicity, $t\bar{t}$ charge asymmetry, top charge and $t\bar{t}$ spin correlation have been successfully measured.
The unprecedented energy in the centre of mass of the LHC and its rapidly increasing luminosity is delivering new stringent limits in the search for new physics related to the top-quark sector. These searches will benefit from higher collected statistics.

References

[1] CDF and D0 collaborations, [arXiv:1107.5255]

[2] Lyndon Evans and Philip Bryant Eds. "The LHC Machine" *JINST* **3** (2008), S08001.

[3] ATLAS Collaboration, "The ATLAS Experiment at the CERN Large Hadron Collider" *JINST* **3** (2008), S08003.

[4] CMS Collaboration, "The CMS experiment at the CERN LHC" *JINST* **3** (2008), S08004.

[5] S. Moch, P. Uwer, "Theoretical status and prospects for top-quark pair production at hadron colliders" *Phys. Rev.* **D78** (2008), 034003 [arXiv:0804.1476].

[6] ATLAS Collaboration, submitted to *Phys. Lett. B*, [arxiv:1201.1889]

[7] ATLAS Collaboration, ATLAS-CONF-2011-121, [https://atlas.web.cern.ch/Atlas/GROUPS/PHYSICS/CONFNOTES/ATLAS-CONF-2011-121/]

[8] CMS Collaboration, TOP-11-003, [http://cdsweb.cern.ch/record/1386709?ln=en]

[9] ATLAS Collaboration, ATLAS-CONF-2011-108, [https://atlas.web.cern.ch/Atlas/GROUPS/PHYSICS/CONFNOTES/ATLAS-CONF-2011-108/]

[10] CMS Collaboration, TOP-11-024, [https://cdsweb.cern.ch/record/1401250?ln=en]

[11] ATLAS Collaboration, accepted by *Phys.Lett.* **B 707** (2012) 459-477, [arxiv:1108.3699]

[12] ATLAS Collaboration, ATLAS-CONF-2011-100, [https://atlas.web.cern.ch/Atlas/GROUPS/PHYSICS/CONFNOTES/ATLAS-CONF-2011-100/]

[13] CMS Collaboration, TOP-11-005, [http://cdsweb.cern.ch/record/1377323?ln=en]

[14] ATLAS Collaboration, ATLAS-CONF-2011-119, [https://atlas.web.cern.ch/Atlas/GROUPS/PHYSICS/CONFNOTES/ATLAS-CONF-2011-119/]

[15] CMS Collaboration, TOP-11-006, [http://cdsweb.cern.ch/record/1371010?ln=en]

[16] ATLAS Collaboration, ATLAS-CONF-2011-140, [https://atlas.web.cern.ch/Atlas/GROUPS/PHYSICS/CONFNOTES/ATLAS-CONF-2011-140/]

[17] CMS Collaboration, TOP-11-007, [http://cdsweb.cern.ch/record/1371755?ln=en]

[18] N. Kidonakis, *Phys. Rev.* **D83** (2011), [arxiv:1103.2792]

[19] N. Kidonakis, *Phys. Rev.* **D81** (2010), [arxiv:1101.5034]

[20] N. Kidonakis, *Phys. Rev.* **D82** (2010), [arxiv:1105.4451]

[21] ATLAS Collaboration, ATLAS-CONF-2011-101, [https://atlas.web.cern.ch/Atlas/GROUPS/PHYSICS/CONFNOTES/ATLAS-CONF-2011-101/]

[22] CMS Collaboration, *Phys. Rev. Lett.* **107** (2011) [arXiv:1106.3052]

[23] CMS Collaboration, TOP-11-022, [http://cdsweb.cern.ch/record/1385552?ln=en]

[24] ATLAS Collaboration, ATLAS-CONF-2011-104, [https://atlas.web.cern.ch/Atlas/GROUPS/PHYSICS/CONFNOTES/ATLAS-CONF-2011-104/]

[25] ATLAS Collaboration, ATLAS-CONF-2011-118, [https://atlas.web.cern.ch/Atlas/GROUPS/PHYSICS/CONFNOTES/ATLAS-CONF-2011-118/]

[26] GFitter group, Proceedings of the 45th Rencontres de Moriond, La Thuile, Italy, March 2010, [arXiv:1109.4985]

[27] ATLAS Collaboration, ATLAS-CONF-2011-120, [https://atlas.web.cern.ch/Atlas/GROUPS/PHYSICS/CONFNOTES/ATLAS-CONF-2011-120/]

[28] CMS Collaboration, TOP-10-009, [http://cdsweb.cern.ch/record/1356578?ln=en]

[29] CMS Collaboration, *JHEP* **07** (2011) [arXiv:1105.5661]

[30] ATLAS Collaboration, ATLAS-CONF-2011-054, [https://atlas.web.cern.ch/Atlas/GROUPS/PHYSICS/CONFNOTES/ATLAS-CONF-2011-054/]

[31] CMS Collaboration, TOP-11-008, [http://cdsweb.cern.ch/record/1387001?ln=en]

[32] CMS Collaboration, TOP-11-019, [http://cdsweb.cern.ch/record/1376668?ln=en]

[33] D0 Collaboration, D0 Note 6062-CONF, [http://www-d0.fnal.gov/Run2Physics/WWW/results/prelim/TOP/T90/T90.pdf]

[34] CDF Collaboration, Conf. Note 10584, [http://www-cdf.fnal.gov/physics/new/top/2011/AfbComb/Afb_combo_5invfb.pdf]

[35] J. A. Aguilar-Saavedra, M. Perez-Victoria, [arXiv:1105.4606]

[36] CMS Collaboration, TOP-11-014, [http://cdsweb.cern.ch/record/1369205?ln=en]

[37] ATLAS Collaboration, ATLAS-CONF-2011-106, [https://atlas.web.cern.ch/Atlas/GROUPS/PHYSICS/CONFNOTES/ATLAS-CONF-2011-106/]

[38] ATLAS Collaboration, ATLAS-CONF-2011-122, [https://atlas.web.cern.ch/Atlas/GROUPS/PHYSICS/CONFNOTES/ATLAS-CONF-2011-122/]

[39] ATLAS Collaboration, ATLAS-CONF-2011-141, [https://atlas.web.cern.ch/Atlas/GROUPS/PHYSICS/CONFNOTES/ATLAS-CONF-2011-141/]

[40] ATLAS Collaboration, ATLAS-CONF-2011-117, [https://atlas.web.cern.ch/Atlas/GROUPS/PHYSICS/CONFNOTES/ATLAS-CONF-2011-117/]

[41] CMS Collaboration, *JHEP* 08 **005** (2011) [arXiv:1106.2142]

[42] ATLAS Collaboration, ATLAS-CONF-2011-154, [https://atlas.web.cern.ch/Atlas/GROUPS/PHYSICS/CONFNOTES/ATLAS-CONF-2011-154/]

[43] ATLAS Collaboration, ATLAS-CONF-2011-061, [https://atlas.web.cern.ch/Atlas/GROUPS/PHYSICS/CONFNOTES/ATLAS-CONF-2011-061/]

[44] ATLAS Collaboration, ATLAS-CONF-2011-087, [https://atlas.web.cern.ch/Atlas/GROUPS/PHYSICS/CONFNOTES/ATLAS-CONF-2011-087/]

[45] ATLAS Collaboration, ATLAS-CONF-2011-123, [https://atlas.web.cern.ch/Atlas/GROUPS/PHYSICS/CONFNOTES/ATLAS-CONF-2011-123/]

[46] CMS Collaboration, EXO-11-055, [http://cdsweb.cern.ch/record/1376673/files/EXO-11-055-pas.pdf]

[47] CMS Collaboration, EXO-11-006, [http://cdsweb.cern.ch/record/1370237/files/EXO-11-006-pas.pdf]

[48] CMS Collaboration, accepted by *Phys. Rev. Lett.*, [arXiv:1109.4985]

[49] ATLAS Collaboration, accepted by *Phys Rev. Lett.*, [arxiv:1109.4725]

Electroweak non-resonant corrections to top pair production close to threshold

Martin Beneke[1], *Bernd Jantzen*[*1] *and Pedro Ruiz-Femenía*[1,2] [†]

[1]Institut für Theoretische Teilchenphysik und Kosmologie, RWTH Aachen University, 52056 Aachen, Germany

[2]Fakultät für Physik, Universität Wien, 1090 Wien, Austria

LC-REP-2012-064

The production of $W^+W^-b\bar{b}$ from e^+e^- collisions at energies close to the $t\bar{t}$ threshold is dominated by the resonant process with a nearly on-shell $t\bar{t}$ intermediate state. The Wb pairs in the final state can also be reached through the decay of off-shell tops or through background processes containing no or only single top quarks. This non-resonant production starts to contribute at NLO to the $W^+W^-b\bar{b}$ total cross section in the non-relativistic power-counting $v \sim \alpha_s \sim \sqrt{\alpha_{EW}}$. The NLO non-resonant corrections presented in this talk represent the non-trivial NLO electroweak corrections to the $e^+e^- \to W^+W^-b\bar{b}$ cross section in the top anti-top resonance region. In contrast to the QCD corrections which have been calculated (almost) up to NNNLO, the parametrically larger NLO electroweak contributions have not been completely known so far, but are mandatory for the required accuracy at a future linear collider. We consider the total cross section of the $e^+e^- \to W^+W^-b\bar{b}$ process and additionally implement cuts on the invariant masses of the W^+b and $W^-\bar{b}$ pairs.

1 Introduction

The top-quark mass is currently known from direct production at the Fermilab Tevatron (and soon at the Large Hadron Collider) with a precision $\gtrsim 1$ GeV. From a threshold scan of the $e^+e^- \to t\bar{t}$ cross section at the planned International Linear Collider (ILC), however, an order of magnitude improvement in the precision can be achieved experimentally [2]. Aside from determining a fundamental parameter of the Standard Model, accurate top-mass measurements constrain the quantum fluctuations from non-standard interactions in electroweak precision measurements. Other characteristics of the top quark such as its width and Yukawa coupling provide information about its coupling to other particles and the mechanism of electroweak symmetry breaking. For these reasons top-quark pair production near threshold in e^+e^- annihilation has been thoroughly investigated following the non-relativistic QCD (NRQCD) approach, which treats the leading colour-Coulomb force exactly to all orders in perturbation theory. In this framework, where the strong coupling α_s is of the same order as v, the small relative velocity of the top and anti-top, most QCD corrections to the total cross section have been calculated up to NNNLO (see the summary [3]), and next-to-next-to-leading logarithms of v have been partially summed [4].

Here we focus on the subleading electroweak corrections, which have received much less attention. The top quark is unstable with a significant width Γ_t of about 1.5 GeV due to the electroweak interaction. The width is essential in threshold production, since it prevents the top and anti-top from forming a bound state and causes a broad resonance structure in the energy dependence of the cross section on top of the increase due to the opening-up of the two-particle phase space. Once the top width is included, due to top decay, the physical final state is $W^+W^-b\bar{b}$ – at least if we neglect the decay of top into strange and down quarks, as justified by $V_{tb} \approx 1$, and consider W bosons as stable. The $W^+W^-b\bar{b}$ final state can also be produced non-resonantly, i.e. through processes which do not involve a nearly on-shell $t\bar{t}$ pair. The latter effects are

*Speaker.

†This contribution to the 1st Linear Collider Forum Meeting 2010 is also part of the ICHEP2010 proceedings [1].

not included in the standard non-relativistic treatment. Adopting a counting scheme where $\alpha_{\rm EW} \sim \alpha_s^2$, we find that the leading non-resonant and off-shell effects are NLO for the total cross section, since there is an additional power of $\alpha_{\rm EW}$ but no phase-space suppression, hence the relative correction is $\alpha_{\rm EW}/v \sim \alpha_s$. Purely resonant electroweak effects, on the other hand, yield NNLO corrections [5].

In this talk we present the calculation of the non-resonant NLO electroweak contributions to the $e^+e^- \to W^+W^-b\bar{b}$ process in the $t\bar{t}$ resonance region, for the total cross section as well as including invariant-mass cuts on the Wb pairs. The calculation is performed with unstable-particle effective field theory [6], which provides the framework for consistently including resonant and non-resonant effects while maintaining an expansion in the small parameters of the problem.

2 Unstable-particle effective theory for pair production near threshold

The cross section for the $e^+e^- \to W^+W^-b\bar{b}$ process is obtained from the $W^+bW^-\bar{b}$ cuts of the e^+e^- forward-scattering amplitude. In the energy region $\sqrt{s} \approx 2m_t$ the amplitude is dominated by the production of resonant top quarks with small virtuality. This allows us to integrate out hard modes ($\sim m_t$) and represent the forward-scattering amplitude as the sum of two terms [6],

$$i\mathcal{A} \;=\; \sum_{k,l} C_p^{(k)} C_p^{(l)} \int d^4x \, \langle e^-e^+|\mathrm{T}[i\mathcal{O}_p^{(k)\dagger}(0)\, i\mathcal{O}_p^{(l)}(x)]|e^-e^+\rangle + \sum_k C_{4e}^{(k)} \langle e^-e^+|i\mathcal{O}_{4e}^{(k)}(0)|e^-e^+\rangle \,. \quad (1)$$

The matrix elements in (1) are evaluated in the "low-energy" effective theory, which includes elements of soft-collinear and non-relativistic effective theory. The first term on the right-hand side of (1) describes the production of a resonant $t\bar{t}$ pair in terms of production (decay) operators $\mathcal{O}_p^{(l)}(x)$ ($\mathcal{O}_p^{(k)\dagger}(x)$) with short-distance coefficients $C_p^{(k,l)}$. The second term accounts for the remaining non-resonant contributions, which in the effective theory are described by four-electron production-decay operators $\mathcal{O}_{4e}^{(k)}$. The calculation of the short-distance coefficients $C_{4e}^{(k)}$ is performed in standard fixed-order perturbation theory in the full electroweak theory. In particular, the top propagator is the free one not including the top width, which ensures that the amplitude depends only on the short-distance scales. The leading imaginary parts of $C_{4e}^{(k)}$ arise from the cut two-loop diagrams of order $\alpha_{\rm EW}^3$ shown in Fig. 1. The corresponding contribution to the cross section is

$$\sigma_{\rm non-res} = \frac{1}{s} \sum_k \mathrm{Im}\left[C_{4e}^{(k)}\right] \langle e^-e^+|i\mathcal{O}_{4e}^{(k)}(0)|e^-e^+\rangle \,. \quad (2)$$

Technically, this simply amounts to the calculation of the spin-averaged tree-level processes $e^+e^- \to tW^-\bar{b}$ and $e^+e^- \to \bar{t}W^+b$ with no width supplied to the intermediate top-quark propagators. Instead, the divergence from the top-quark propagators going on-shell is regularized dimensionally. Details on the computation and integral representations of the result for (2) can be found in [7].

Through the computation of the four-electron matching coefficients loose cuts ($\sim m_t$) on the bW^+ and $\bar{b}W^-$ invariant masses can be incorporated easily, as it has been discussed in the context of W-pair production near threshold [8]. The result obtained in [7] covers the case of symmetric cuts on the invariant mass of the bW subsystems (p_{bW}^2) of the form $m_t - \Delta M_t \le \sqrt{p_{bW}^2} \le m_t + \Delta M_t$, for $\Delta M_t \gg \Gamma_t$, up to the total cross section ($\Delta M_{t,\rm max} = m_t - M_W$). An alternative approach has been developed in parallel [9, 10] that includes the effects of invariant-mass cuts on the Wb pairs entirely through calculations in NRQCD. This works if the invariant-mass cuts around m_t are neither very loose nor very tight, and provided that the non-resonant background processes are small (which at NLO was checked [10] by computing the full $e^+e^- \to W^+W^-b\bar{b}$ cross section at tree-level with MadGraph). Under these assumptions, part of the α_s-corrections to the non-resonant contributions has already been analyzed in [10], which in our approach correspond to NNLO contributions.

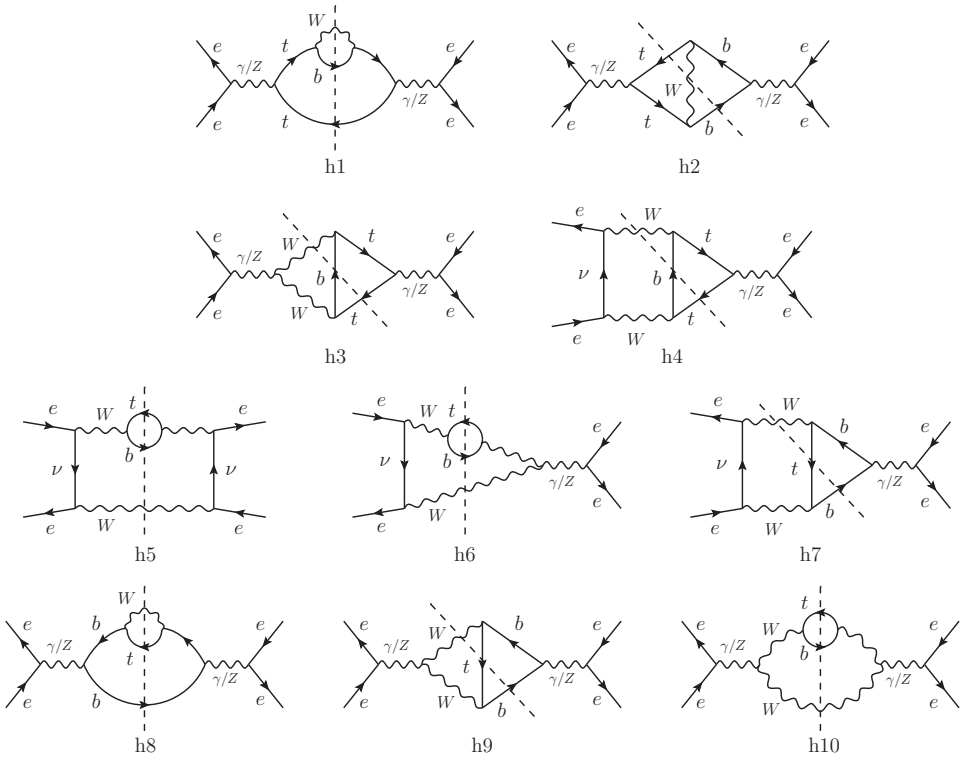

Figure 1: Two-loop forward-scattering amplitude diagrams with $\bar{t}bW^+$ cuts. $t\bar{b}W^-$ cuts and symmetric diagrams are not shown. The contribution to the $W^+W^-b\bar{b}$ cross section from diagrams h_1–h_{10} can be interpreted as the $\bar{b}W^-$ pair originating from a nearly on-shell anti-top decay, while the bW^+ pair is produced non-resonantly, either from a highly virtual top (diagrams h_1–h_4), or without an intermediate top (h_5–h_{10}).

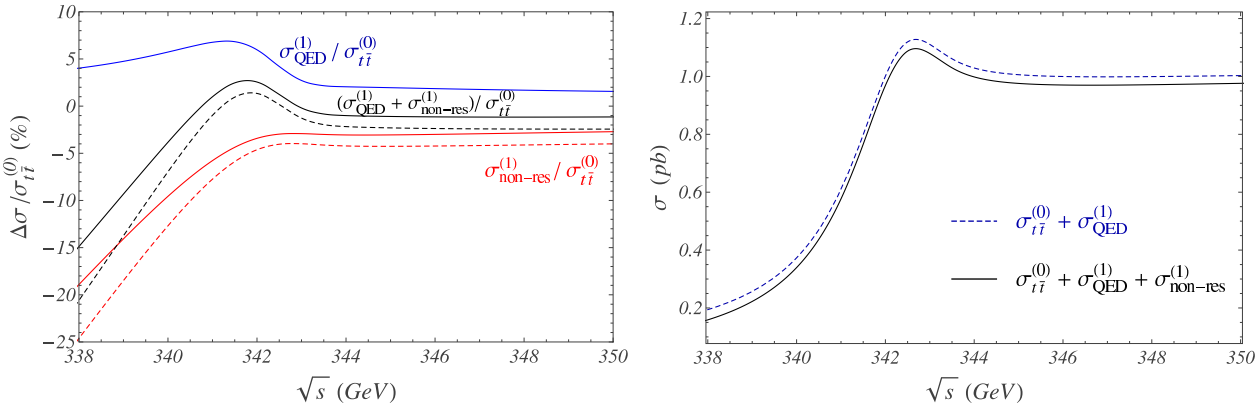

Figure 2: Left: Relative sizes of the QED, $\sigma^{(1)}_{\rm QED}$, and non-resonant, $\sigma^{(1)}_{\rm non-res}$, corrections with respect to the LO cross section, $\sigma^{(0)}_{t\bar{t}}$, in percent, for $\Delta M_{t,\rm max}$ (solid) and $\Delta M_t = 15$ GeV (dashed). Right: Total cross section with LO QCD effects (dashed) and including NLO electroweak corrections (solid) at energies close to threshold. Input parameters: $m_t = 172$ GeV, $\Gamma_t = 1.47$ GeV and $\alpha_s(30\ \text{GeV}) = 0.142$.

3 Results

The left plot in Fig. 2 displays the relative sizes of the NLO electroweak corrections with respect to the LO result for the $e^+e^- \to W^+W^-b\bar{b}$ cross section, which includes the summation of Coulomb corrections. The QED contribution represents a correction of about 2% above threshold and rises to a maximum of 7% just below the peak, while the non-resonant contributions give a constant negative shift of about 3% above threshold. Below threshold the relative size of the non-resonant corrections is very large, since the LO result rapidly vanishes, reaching up to 19%. Hence below threshold they represent the leading electroweak correction to the total $t\bar{t}$ cross section. We observe a partial cancellation of the QED and non-resonant corrections in the peak region and at energies above. A sensitivity to the invariant-mass cut ΔM_t in the bW^+ and $\bar{b}W^-$ subsystem enters first at NLO through the non-resonant contributions. Restricting the available phase-space for the final-state particles by tightening the invariant-mass cuts ΔM_t makes the non-resonant contributions even more important. This is shown by the dashed lines in Fig. 2, corresponding to $\Delta M_t = 15$ GeV.

Aside from the pure QCD corrections, the NLO prediction for the $e^+e^- \to W^+W^-b\bar{b}$ total cross section is displayed by the solid line in the right plot of Fig. 2. The absolute size of the non-resonant correction is given by the difference between the dashed line, which only includes the QED NLO correction, and the solid one. This negative shift amounts to 27–35 fb for $\sqrt{s}$ in the interval $(338, 350)$ GeV.

Acknowledgements

This work is supported by the DFG Sonderforschungsbereich/Transregio 9 “Computergestützte Theoretische Teilchenphysik”.

References

[1] M. Beneke, B. Jantzen and P. Ruiz-Femenía, PoS ICHEP2010 076 (2010), arXiv:1012.0824 [hep-ph], TTK-10-53, SFB/CPP-10-124.

[2] M. Martinez and R. Miquel, Eur. Phys. J. **C27** 49 (2003).

[3] M. Beneke, Y. Kiyo and K. Schuller, PoS RADCOR2007 051 (2007).

[4] A. H. Hoang, A. V. Manohar, I. W. Stewart and T. Teubner, Phys. Rev. **D65** 014014 (2002);
A. Pineda and A. Signer, Nucl. Phys. **B762** 67 (2007).

[5] A. H. Hoang and C. J. Reisser, Phys. Rev. **D71** 074022 (2005).

[6] M. Beneke, A. P. Chapovsky, A. Signer and G. Zanderighi, Phys. Rev. Lett. **93** 011602 (2004);
M. Beneke, A. P. Chapovsky, A. Signer and G. Zanderighi, Nucl. Phys. **B686** 205 (2004);
M. Beneke, P. Falgari, C. Schwinn, A. Signer and G. Zanderighi, Nucl. Phys. **B792** 89 (2008).

[7] M. Beneke, B. Jantzen and P. Ruiz-Femenía, Nucl. Phys. **B840** 186 (2010).

[8] S. Actis, M. Beneke, P. Falgari and C. Schwinn, Nucl. Phys. **B807** 1 (2009).

[9] A. H. Hoang, C. J. Reisser and P. Ruiz-Femenia, Nucl. Phys. Proc. Suppl. **186** 403 (2009).

[10] A. H. Hoang, C. J. Reisser and P. Ruiz-Femenia, Phys. Rev. **D82** 014005 (2010).

CERN - European Organization for Nuclear Research

LCD-Note-2012-013

Prospects for the Measurement of the Top Mass in a Threshold Scan at CLIC and ILC

Katja Seidel[*†], Frank Simon[*†], Michal Tesař[*]

[*] *Max-Planck-Institut für Physik, Munich, Germany,*
[†] *Excellence Cluster 'Universe', TU München, Garching, Germany*

November 3, 2012

Abstract

We present a study of the capability of CLIC to measure the top quark mass and the strong coupling constant in a scan of the top threshold. The analysis is based on full detector simulations of the CLIC_ILD detector concept using Geant4, including realistic beam-induced background contributions from two photon processes. Event reconstruction is performed using a particle flow algorithm with stringent cuts to control the influence of background. With these simulations the signal and background selection efficiencies are determined. Signal event yields as a function of energy are obtained using these efficiencies together with NNLO top pair cross-sections corrected for ISR and the CLIC beam energy spectrum. For comparison, the analysis is also performed with the ILC beam energy spectrum. In addition to the statistical errors for m_t and α_s, systematic uncertainties from theory and from the precision of the strong coupling constants as well as the influence of the precision of the background description and of the understanding of the luminosity spectrum have been studied.

Contents

1 Introduction

As the heaviest Standard Model particle, the top quark is of particular interest since it most strongly couples to the Higgs field and may provide sensitivity to Beyond the Standard Model physics. Experiments at e^+e^- colliders offer the possibility for a wide variety of studies involving top quarks, ranging from the precise measurement of top quark properties to the investigation of asymmetries providing large sensitivity to various New Physics models. Among those is the precise determination of the top quark mass, which is possible with two different techniques: through the direct reconstruction of top quarks from their decay products at energies above the production threshold, and through a scan of the top-pair production threshold. The latter technique has the advantage of providing the mass measurement in a theoretically well-defined scheme, while the former measurement can be performed essentially at arbitrary energies above threshold, however with potentially significant uncertainties due to non-perturbative contributions when transferring the measured invariant mass to a theoretically meaningful value. Progress has been made recently in establishing connections between the top mass parameters used in theory and the experimentally observable invariant mass of the decay products [1, 2], but theoretical uncertainties remain substantial.

In this note, we investigate the potential for the determination of the top quark mass from a measurement of the top-pair production cross-section at several energies around the threshold near 350 GeV at the Compact Linear Collider CLIC, with a total integrated luminosity of up to 100 fb^{-1}. This study complements a previous CLIC study of top mass measurements at 500 GeV by means of a direct reconstruction of the invariant mass of the decay products. This study has shown that the invariant mass of the top quark can be determined with a precision of better than 100 MeV with 100 fb^{-1} in fully hadronic and semi-leptonic decays of the top pairs [3].

2 Experimental Conditions at CLIC at the Top Threshold

CLIC is a collider concept based on normal conducting accelerating cavities and two-beam acceleration, which is designed to provide up to 3 TeV collision energy. In a staged approach, a shorter, lower energy version would be operated initially, while construction is under way for the full energy phase.

In the present note, we study the case of a 500 GeV CLIC machine operated at energies close to the top pair production threshold by a reduction of the acceleration gradient through reduced drive-beam currents. At 350 GeV, the rate of $\gamma\gamma \to$ hadrons events [4] is relatively small, with only 0.05 events per bunch crossing, down by almost an order of magnitude compared to 500 GeV collisions. The effect from pile-up of this background, in particular after the application of the particle flow object selection cuts [5, 3], is thus very minor. The impact of backgrounds is further marginalized by the fact that the measurement at the top threshold is a measurement of the cross section. It requires the separation of signal and background events, but not the precise reconstruction of the invariant mass which might be affected by the presence of background.

The detector model used in the present study is a variant of CLIC_ILD [6], a detector concept based on Particle Flow event reconstruction. It consists of a low-mass, high-precision vertex detector and an inner silicon tracker, surrounded by a large-volume time projection chamber,

followed by highly granular electromagnetic and hadronic calorimeters contained inside a 4 T solenoidal magnet with instrumented flux return for muon identification. The detector design is based on the ILD detector concept for the ILC, adapted to account for the higher energy (3 TeV) and more severe background conditions at CLIC. This leads to an increased radius of the innermost layer of the vertex detector, which sits at 31 mm compared to 16 mm in ILD at the ILC. Here, the case of a 500 GeV CLIC machine operated at 350 GeV is studied. The detector model is thus one optimized for 500 GeV with slight modifications with respect to the 3 TeV design. While the large systems of the detector such as the calorimeters and the main tracker are expected to stay unchanged for different energy stages, the interaction region and the innermost vertex detector are adapted to the significantly reduced background levels at 500 GeV compared to 3 TeV. In particular the innermost vertex detector layer for CLIC_ILD can move in by 6 mm to a radius of 25 mm, improving flavor tagging at low momentum. To distinguish the modified detector design from the 3 TeV design, the detector model is referred to as CLIC_ILD_CDR500.

3 Simulation Strategy

For the correct description of the cross-section near threshold, the inclusion of high-order QCD contributions is necessary. Since no appropriate event generator is publicly available at present, the study follows the strategy of earlier studies performed for the TESLA collider [7] by factorising the simulation study into the determination of event selection efficiency and background contamination and the calculation of the top-pair production threshold. In this approach, the signal selection and background rejection is determined using fully simulated top-pair signal events as well as relevant background channels at a nominal center of mass energy of 352 GeV, slightly above the production threshold for the selected top mass of 174 GeV. This energy is chosen to be able to generate the events with PYTHIA, which requires a center-of-mass energy in excess of twice the generator top mass. Data points along the threshold curve are then generated by taking the signal cross section determined using NNLO calculations combined with the selection efficiency, adding background events assuming a constant level over the considered energy range of 10 GeV as determined from the full simulations. In the following, more details are given on the individual steps.

In the present analysis, we assume a threshold scan with 10 data points with an integrated luminosity of 10 fb^{-1} each. The measurement points are spaced by 1 GeV, spanning the threshold region. In some of the analyses below, only the first six out of these ten point are used to illustrate the sensitivity of different regions of the threshold to systematic effects.

3.1 Top Pair Production Cross Section

The top-pair signal cross-section is determined using full NNLO calculations provided by the code TOPPIK [8, 9]. The top mass input is set to 174 GeV in the 1S mass scheme [8]. The strong coupling constant α_s is taken to be 0.118. Since TOPPIK provides the cross section in units of R, the ratio of $\sigma(e^+e^- \to X)$ to $\sigma(e^+e^- \to \mu^+\mu^-)$, the appropriate conversion factor of the energy-dependent cross section $e^+e^- \to \mu^+\mu^-$ is applied in addition.

Since this cross section is calculated for the energy at the e^+e^- vertex, additional corrections

for initial state radiation (ISR) and for the beam energy spectrum of the accelerator have to be applied, as discussed in the following.

3.1.1 Initial State Radiation

ISR reduces the available collision energy E' due to the radiation of photons off the incoming electron and positron prior to the collision. This effect in general lowers the signal cross-section, since events are shifted to lower energies with typically a lower top-pair cross-section. The electron and positron "structure functions" are taken from the approximate YFS (Yennie-Frautschi-Suura) solution as given in [10], which provides the normalized probability density for a given fraction of the lepton momentum x (ranging from 0 to 1) in the final collision.

The folding of the ISR distribution with the theoretically calculated cross section is performed numerically. For this, a histogram of the structure function with 0.175 MeV wide bins is built, with the value in each bin taken by evaluating the approximate YFS solution at the bin center. The highest-energy bin is topped off to ensure correct normalization, accounting for the extreme increase in the structure function near 1. The folding is performed by evaluating 100 000 randomly generated energy points with the individual beam energies distributed according to this histogram. The mean value of the cross-section of these 100 000 trials is taken as the ISR-corrected cross section at a given center-of-mass energy.

3.1.2 Luminosity Spectrum

The centre-of-mass energy distribution also influences the cross section as a function of nominal collider energy. The luminosity spectrum is roughly characterized by the width of the main peak and by a longer tail to lower energies from beamstrahlung. To be able to compare the impact of the different luminosity spectra of CLIC and ILC, spectra from both colliders, operated at 350 GeV, are used to calculate the final signal cross-section.

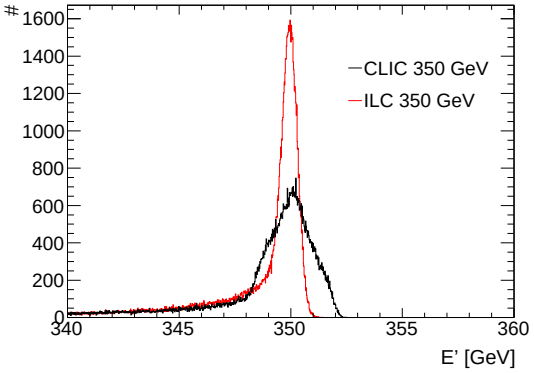

Figure 1: Luminosity spectrum for CLIC and ILC at 350 GeV.

Figure 1 shows the high-energy part of the luminosity spectrum of CLIC and ILC operated at 350 GeV. As for the case of ISR, the folding of the signal cross-section with the luminosity spectrum is performed numerically using 100 000 beam events at each energy point.

3.1.3 Combined Cross-Section

The final signal cross-section is obtained by combining the effects of ISR and of the luminosity spectrum. Here, 100 000 trials per energy point are performed, where the collision energy is determined from the luminosity spectrum with a subsequent addition of ISR. Based on this sample of collision energies, the top pair cross section at both CLIC and ILC is determined using the TOPPIK calculations.

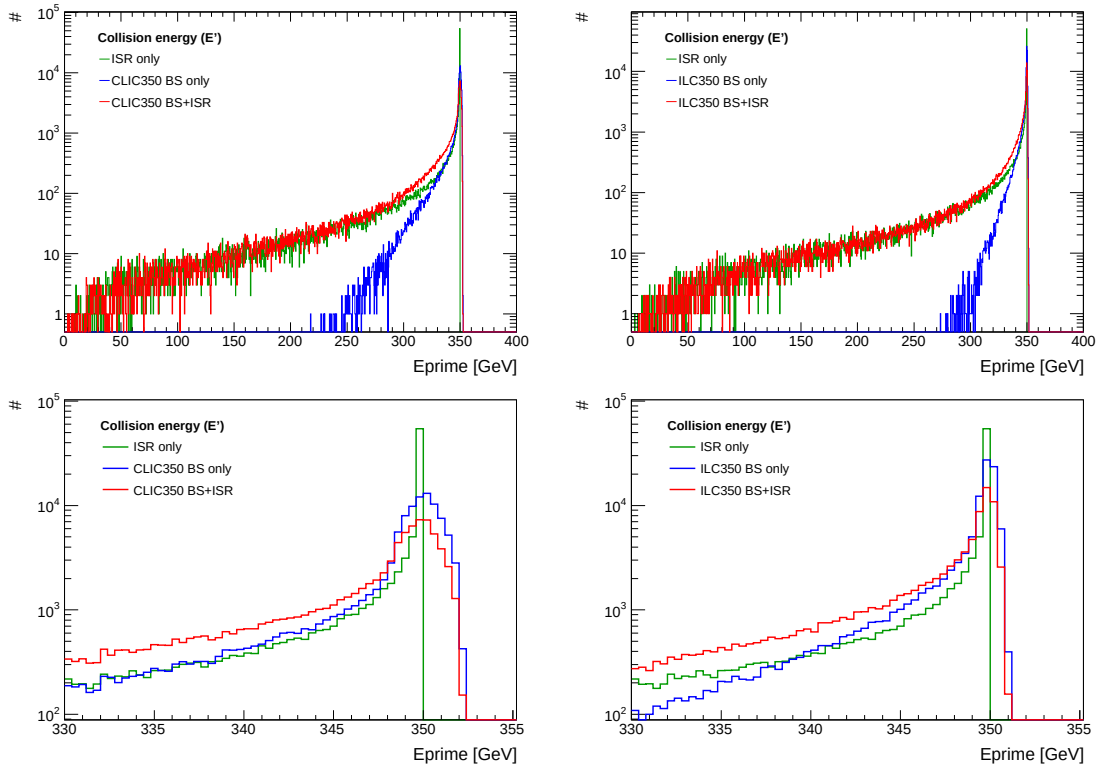

Figure 2: E' distribution taking ISR and the luminosity spectrum (CLIC (left) and ILC (right)) into account. The lower row of figures shows a blow-up of the peak region of the distributions.

Figure 2 shows the distribution of the real collision energy E' for CLIC and ILC for beam energy spectrum and ISR separately as well as the resulting combined spectrum. The effect on the top pair production cross-section is shown in Figure 3. The cross-section with all effects included is used to determine the signal yield as a function of nominal collision energy in the subsequent analysis steps.

3.2 Signal Selection Efficiency and Background Contamination

The event selection efficiency and the background contributions, mainly from di- and tri-boson production, are determined using events generated with PYTHIA at a collision energy of 352 GeV

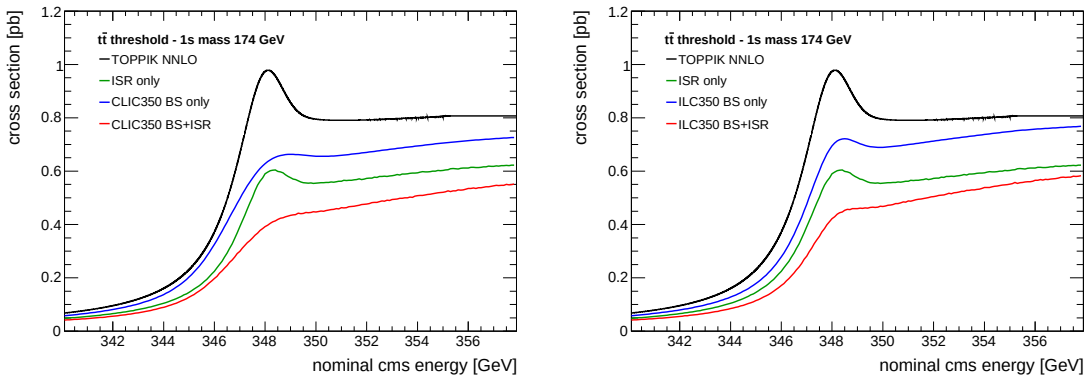

Figure 3: Top pair production cross-section from theory calculations, with the luminosity spectrum and ISR as well as for all effects combined for both CLIC (left) and ILC (right).

with a top mass of 174 GeV. These events are fully simulated in GEANT4, including the addition of pile-up from $\gamma\gamma \to$ hadrons background. For signal identification and background rejection the same technique as for the 500 GeV top mass study [3] is used. The top pair events are identified in the fully hadronic decay mode $t\bar{t} \to W^+bW^-\bar{b} \to q\bar{q}q\bar{q}b\bar{b}$ and in the semi-leptonic mode $t\bar{t} \to W^+bW^-\bar{b} \to q\bar{q}\ell^\pm\nu_\ell b\bar{b}$, $(l = e, \mu)$. The events are clustered into six or four jets depending on the number of identified isolated leptons. A kinematic fit with constraints on overall energy, on the difference of the two top masses and on the mass of the intermediate W bosons is used to form the top candidates. The fit also provides powerful background rejection, since most background events fail the kinematic fit. Additional background reduction is obtained with a binned likelihood using flavor tagging, the reconstructed W masses and the differences of the two reconstructed top masses without kinematic fit, the number of particles in the event, the sphericity and jet number information to discriminate signal from background.

In addition to these background rejection steps, no further selection based on the reconstructed top quark mass is performed, since this does not provide a substantial additional benefit, while it would add potential systematic uncertainties from the additional cut. Figure 4 shows the reconstructed invariant mass distribution for top quark candidates after all selections for accepted signal and background events, as well as the signal significance as a function of a possible invariant mass cut assuming a top pair production cross-section of 450 fb^{-1}, which corresponds to the cross section reached a few GeV above the production threshold. Overall, a signal selection efficiency of 70.2% is achieved, with an efficiency in excess of 90% for the selected fully-hadronic and semi-leptonic decay modes. For the major background channels, the cross-section is reduced by two to three orders of magnitude. Table 1 summarizes the signal and background cross-sections before and after selection.

Even though the study is performed using the CLIC_ILD detector model and CLIC background conditions, the conclusions drawn about the signal selection efficiency and background contamination also apply to ILC and the ILD detector. In terms of detector model, the most relevant difference is the radius of the innermost vertex detector layer, which is larger at CLIC

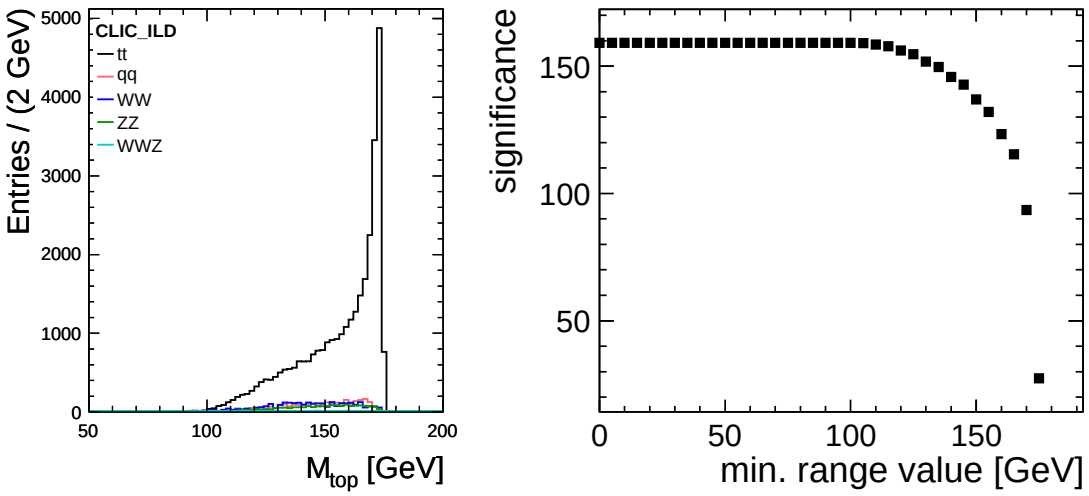

Figure 4: Reconstructed top quark mass for accepted events. Signal as well as each of the backgrounds are shown separately (left). Signal significance as a function of the value of the minimum invariant mass required for the reconstructed top candidates assuming a top pair production cross-section of 450 fb^{-1} (right).

Table 1: Signal and considered physics background processes, with their cross section calculated for CLIC at 352 GeV before and after event selection. The combined background cross-section after selection is 78 fb.

type	$e^+e^- \to$	σ at 352 GeV	selected σ
Signal (m_{top} =174 GeV)	$t\bar{t}$	450 fb	316 fb
Background	$q\bar{q}$	25.2 pb	28 fb
Background	WW	11.5 pb	28 fb
Background	ZZ	865 fb	19 fb
Background	WWZ	10 fb	3 fb

due to the higher background level of incoherent e^+e^- pairs. For the identification of $t\bar{t}$ events, b-tagging is crucial, but not the separation of charm and bottom. Thus, the differences in performance of the two detector models are expected to be negligible for this analysis. The same also applies for the background rejection. Thus, the selection efficiencies and background levels determined for CLIC are also used for a study of a threshold scan at ILC.

3.3 Generation of Data Points

Simulated data points are generated by taking the ISR and beam spectrum corrected top pair cross-section at the desired energy to calculate the nominal number of events expected. The simulated number of signal events is determined on a random basis following a gaussian distri-

bution with the mean set to the nominal number of events and the standard deviation given by the square root of that number. With the same method, background events are added, using a constant cross-section of 78 fb as discussed above. It is assumed that the nominal background contribution is well known both from theory and from measurements below threshold, so the nominal number of background events is subtracted from the signal, leaving just the statistical variations on top of the signal data with its own statistical uncertainty.

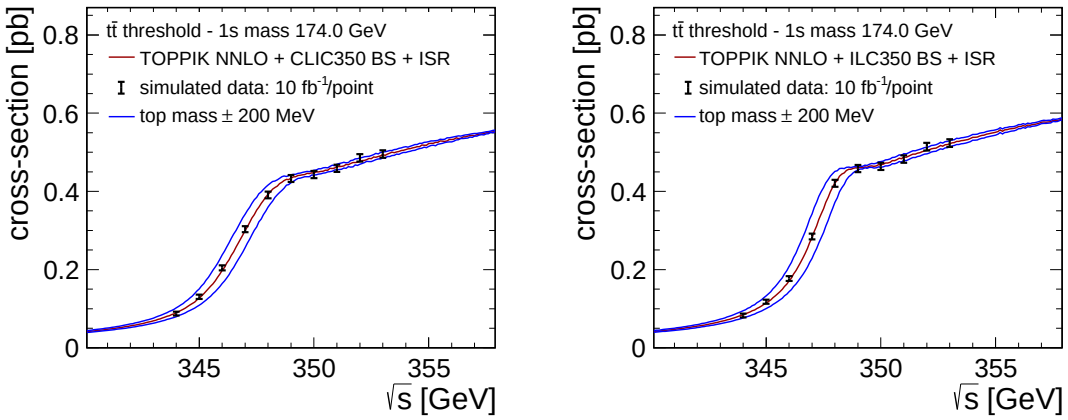

Figure 5: Background-subtracted simulated cross-section measurements for 10 fb^{-1} per data point, together with the cross-section for the generator mass of 174 GeV as well as for a shift in mass of $\pm$200 MeV for both CLIC (left) and ILC (right)).

Figure 5 shows the ten simulated data points for CLIC and for ILC with an integrated luminosity of 10 fb^{-1} at each point.

4 Results

Two extractions of the top mass are being considered here:

- A one-dimensional template fit performed by comparing the simulated data with theory curves calculated in 50 MeV steps in top mass assuming α_s is known, subsequently labelled "1D"
- A two-dimensional template fit in top mass and α_s for a simultaneous determination of the top mass and the strong coupling constant, labelled "2D"

The measured top mass, and α_s in the case of the 2D fit, is given by the minimum of a parabolic fit to the χ^2 distribution of the different templates. The statistical uncertainty is taken from the standard deviation of the measured mass in 5000 trials with different simulated data points.

In the 1D fit, two main sources of systematic uncertainties are considered: A theory uncertainty taken as an overall normalization uncertainty of the calculated cross section, and an uncertainty from the knowledge of α_s. For the theory uncertainty, two levels are considered:

A normalization uncertainty of 3%, assumed as a reasonably conservative estimate of current theory uncertainties [11], and an uncertainty of 1% optimistically assumed to be achievable with additional theoretical work in time for experiments at linear colliders. To determine the systematic error due to α_s, the current uncertainty of the world average of 0.0007 is assumed. The interpretation of the data points above threshold is particularly sensitive to the overall theory normalization uncertainty and to the strong coupling constant. In the 1D fit, uncertainties can thus be somewhat reduced by just considering the first six data points from 344 GeV to 349 GeV, without a reduction of the statistical sensitivity to the top mass. Table 2 summarizes the results.

Table 2: Summary of the results for the 1D top mass determination with a threshold scan at CLIC. For the systematic uncertainty originating from α_s, the current error on the world average of 0.0007 is assumed.

1S top mass 1D fit

measurement	stat. error	theory syst. (1%/3%)	α_s syst.
six point scan	21 MeV	15 MeV / 47 MeV	20 MeV
ten point scan	21 MeV	18 MeV / 56 MeV	21 MeV

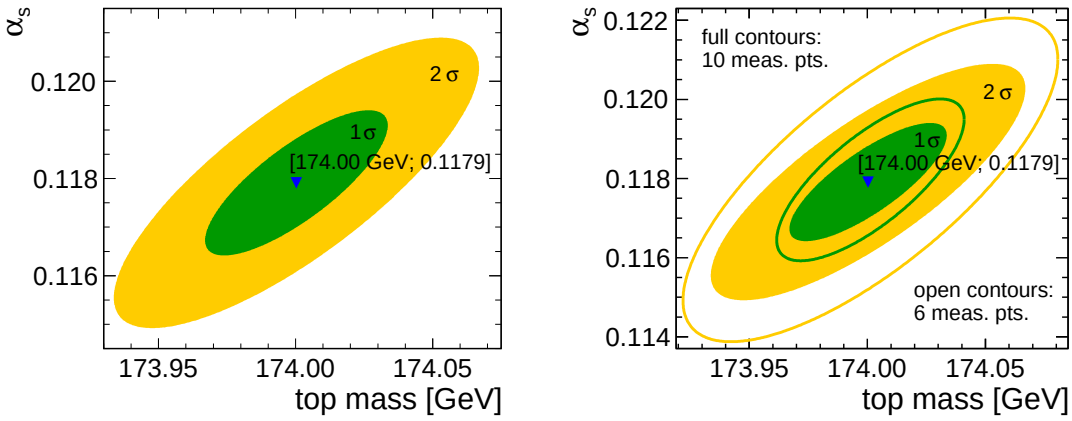

Figure 6: Simultaneous fit of the top mass and the strong coupling constant, showing the correlation of the two variables and the achieved precision (left). Difference in precision of top mass and α_s fit using just the first 6 points in the threshold scan or all 10 points (right).

Figure 6 shows the resulting precision of the top mass and the strong coupling constants obtained with the 2D fit, demonstrating the clear correlation of the two variables. Since the high-energy points in the scan provide the highest sensitivity to α_s, a reduced scan with six points along the strongly rising region of the cross-section leads to significantly increased uncertainties. In the case of the 2D fit, only the theory uncertainty is considered as a source for systematic uncertainties in the fit. The results are summarized in Table 3.

Table 3: Results summary for the 2D simultaneous top mass and α_s determination with a threshold scan at CLIC.

1S top mass and α_s combined 2D fit

measurement	m_t stat. error	m_t th. syst. (1%/3%)	α_s stat. error	α_s th. syst. (1%/3%)
six point scan	40 MeV	1 MeV / 3 MeV	0.0013	0.0007 / 0.0020
ten point scan	34 MeV	5 MeV / 8 MeV	0.0009	0.0008 / 0.0022

5 Results for ILC beam conditions

The influence of the beam energy spectrum of the accelerator is studied by repeating the analysis using the ILC beam energy spectrum, as discussed in Section 3.1.2. The faster rise of the cross section due to the sharper main luminosity peak is expected to lead to somewhat reduced statistical uncertainties on the top mass for a given integrated luminosity due to increased differences between different mass hypotheses in the threshold region. As for the CLIC analysis, an integrated luminosity of 10 fb^{-1} per point is assumed. The same one- and two-dimensional fits of m_t and m_t and α_s combined are also performed for data points generated with the ILC beam spectrum.

Table 4: Summary of results for the 1D top mass fit and the 2D simultaneous top mass and α_s determination with a threshold at ILC.

ILC 1D 1S top mass fit

measurement	m_t stat. error	m_t th. syst. (1%/3%)	α_s syst.
six point scan 1D fit	18 MeV	15 MeV / 47 MeV	18 MeV
ten point scan 1D fit	18 MeV	13 MeV / 39 MeV	17 MeV

ILC 2D 1S top mass and α_s combined fit

measurement	m_t stat. error	m_t th. syst. (1%/3%)	α_s stat. error	α_s th. syst. (1%/3%)
six point 2D	31 MeV	2 MeV / 1 MeV	0.0011	0.0006 / 0.0018
ten point 2D	27 MeV	5 MeV / 9 MeV	0.0008	0.0007 / 0.0022

Table 4 summarizes the results of both 1D and 2D fits, while Figure 7 shows the results of the combined extraction of the top mass and the strong coupling constant, illustrating the statistical uncertainty and the correlation of the two variables. In comparison to the statistical precision achieved assuming the CLIC beam energy spectrum, in the ILC case a 15% smaller uncertainty is observed in the 1D top mass fit, and a 20% smaller uncertainty on the top mass and a 10% smaller uncertainty on α_s is obtained in the combined extraction. The CLIC-ILC differences are negligible compared to the systematic uncertainties originating from theory and from the precision of the strong coupling constant.

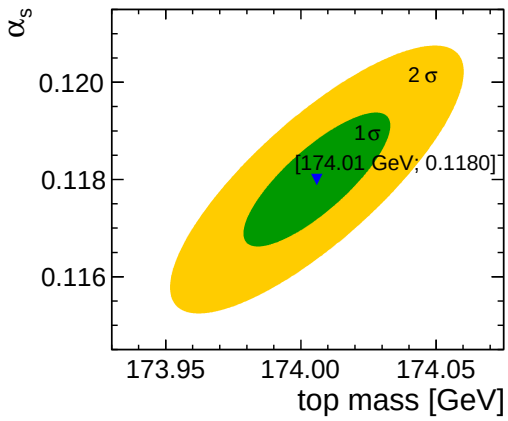

Figure 7: Simultaneous fit of the top mass and the strong coupling constant for data points simulated with the ILC beam energy spectrum, showing the correlation of the two variables and the achieved precision.

6 Additional Systematic Studies

In addition to the theory uncertainties and the uncertainty of α_s in the case of the 1D fit, additional potential sources for systematic errors were studied.

A potential dependence of the result on the choice of energy values for the scan in relation to the top mass was excluded by shifting the measurement points to higher energies by 0.5 GeV without a change in the determined mass and α_s values.

The precise knowledge of the non-top background after event selection is crucial for the measurement of the signal cross section. The effect of an imperfect non-top physics background description is studied by subtracting 5% and 10% too little or too much background before the fit. The 5% variation results in a 18 MeV shift in the top mass and 0.0007 in α_s, corresponding to approximately two thirds of the statistical uncertainty on the top mass and close to the statistical uncertainty on α_s. Subtracting only 90% of the background leads to a shift of twice the size for both values, but also significantly reduces the stability of the template fit. Subtracting 110% of the background leads to a 30 MeV shift of the top mass and a shift of 0.0014 in α_s. This shows that an understanding of the background contamination at the level of 5% or better is important to keep systematic effects substantially below the statistical uncertainties.

In addition to these analysis-related uncertainties, also machine-related uncertainties, such as the knowledge of the center-of-mass energy of the collider and the shape of the luminosity spectrum are highly relevant for this study. Previous experience at LEP [12] and studies in the context of the ILC [13] suggests that a precision of 10^{-4} on the center-of-mass energy is readily achievable given the high available integrated luminosity at each data point, resulting in systematics below the statistical errors of the top mass. The knowledge of the luminosity spectrum is very important for the correct description of the signal cross section, and thus also for the precision of the template fit. A full study has not yet been performed, but a very preliminary

first study indicates that already a 20% uncertainty of the RMS width of the main luminosity peak results in top mass uncertainties of approximately 75 MeV, far in excess of the statistical uncertainties. Further studies to quantify the effects of realistic uncertainties of the beam energy spectrum are needed.

7 Conclusions

In this study, we have investigated the achievable precision of the top quark mass measurement with a threshold scan at CLIC. Compared to the direct measurement of the invariant mass of the top quark decay products the threshold scan has the advantage that the mass is directly determined in a theoretically well-defined mass definition. The study uses event selection efficiencies and background contaminations from fully simulated events including the effects of the CLIC beam spectrum and $\gamma\gamma \to$ hadrons backgrounds and top pair signal cross-sections from NNLO calculations corrected for ISR and the luminosity spectrum. With an integrated luminosity of 100 fb^{-1} divided across ten data points spaced by 1 GeV, a statistical precision of the top quark mass in the 1S scheme of 33 MeV is obtained in a combined fit together with the strong coupling constant, which is determined with a precision of 0.0009. A one-dimensional fit with fixed α_s yields a precision of 21 MeV. Using the ILC luminosity spectrum results in 15% to 20% smaller uncertainties on the mass and in a 10% smaller uncertainty of the strong coupling constant. Combined systematic uncertainties from theory and background understanding are expected to be of similar order as the statistical errors. Together with a previous study of top quark mass measurements from direct reconstruction of the decay products this study demonstrates that precision top measurements are possible at CLIC both at and above threshold.

References

[1] S. Fleming, A. H. Hoang, S. Mantry, and I. W. Stewart. Jets from massive unstable particles: Top-mass determination. *Phys.Rev.*, vol. D77 p. 074010, 2008.

[2] S. Fleming, A. H. Hoang, S. Mantry, and I. W. Stewart. Top Jets in the Peak Region: Factorization Analysis with NLL Resummation. *Phys.Rev.*, vol. D77 p. 114003, 2008.

[3] K. Seidel, S. Poss, and F. Simon. Top quark pair production at a 500 GeV CLIC collider. *LCD-Note-2011-026*, 2011.

[4] T. Barklow, D. Dannheim, O. Sahin, and D. Schulte. Simulation of $\gamma\gamma \to$ hadrons background at CLIC. *LCD-Note-2011-021*, 2011.

[5] J. Marshall, A. Münnich, and M. A. Thomson. PFA: Particle Flow Performance at CLIC. *LCD-Note-2011-028*, 2011.

[6] A. Münnich and A. Sailer. The CLIC ILD CDR Geometry for the CDR Monte Carlo Mass Production. *LCD-Note-2011-002*, 2011.

[7] M. Martinez and R. Miquel. Multiparameter fits to the $t\bar{t}$ threshold observables at a future e^+e^- linear collider. *Eur. J. Phys.*, vol. C27 pp. 49–55, 2003. hep-ph/0207315.

[8] A. H. Hoang and T. Teubner. Top quark pair production close to threshold: Top mass, width and momentum distribution. *Phys. Rev.*, vol. D60 p. 114027, 1999. CERN-TH-99-59, DESY-99-047, hep-ph/9904468.

[9] A. H. Hoang and T. Teubner. Top quark pair production at threshold: Complete next-to-next-to-leading order relativistic corrections. *Phys. Rev.*, vol. D58 p. 114023, 1998. UCSD-PTH-98-01, DESY-98-008, hep-ph/9801397.

[10] M. Skrzypek and S. Jadach. Exact and approximate solutions for the electron nonsinglet structure function in QED. *Z.Phys.*, vol. C49 pp. 577–584, 1991.

[11] A. Hoang and M. Stahlhofen. NNLL Top-Antitop Production at Threshold. 2011. arXiv:1111.4486 [hep-ph].

[12] R. Assmann et al. Calibration of centre-of-mass energies at LEP 2 for a precise measurement of the W boson mass. *Eur.Phys.J.*, vol. C39 pp. 253–292, 2005.

[13] A. Hinze and K. Mönig. Measuring the beam energy with radiative return events. *eConf*, vol. C050318 p. 1109, 2005.

LC-REP-2013-007
IFIC/13-06

A precise determination of top quark electroweak couplings at the ILC operating at $\sqrt{s} = 500\,\mathbf{GeV}$

M.S. Amjad[1], M. Boronat[2], T. Frisson[1], I. Garcìa Garcìa[2], R. Pöschl*[1], E. Ros[2], F. Richard[1,2], J. Rouëné[1] and M. Vos[2]

[1]LAL, CNRS/IN2P3, Université Paris Sud, F-91898 Orsay CEDEX, FRANCE
[2]IFIC, Universitat de Valencia CSIC, c/ Catedràtico José Beltràn, 2 46980 Paterna, SPAIN

Abstract

Top quark production in the process $e^+e^- \to t\bar{t}$ at a future linear electron positron collider with polarised beams is a powerful tool to determine the scale of new physics. The presented study assumes a centre-of-mass energy of $\sqrt{s} = 500\,\text{GeV}$ and a luminosity of $\mathcal{L} = 500\,\text{fb}^{-1}$ equality shared between the incoming beam polarisations of $P_{e^-,+} = \pm 0.8, \mp 0.3$. Events are selected in which the top pair decays semi-leptonically. The study comprises the cross sections, the forward-backward asymmetry and the slope of the helicity angle asymmetry. The vector, axial vector and tensorial CP conserving couplings are separately determined for the photon and the Z^0 component. The sensitivity to new physics would be dramatically improved w.r.t. to what expected from LHC for electroweak couplings.

1 Introduction

The top quark, or t quark, is by far the heaviest elementary particle of the Standard Model. Its large mass implies that this is the Standard Model particle that is most strongly coupled to the mechanism of electroweak symmetry breaking. For this

*Corresponding author: poeschl@lal.in2p3.fr

and other reasons, the t quark is expected to be a window to any new physics at the TeV energy scale. New physics will modify the electro-weak $t\bar{t}X$ vertex described in the Standard Model by *V*ector and *A*xial vector couplings V and A to the vector bosons $X = \gamma, Z^0$,

Generally speaking, an e^+e^- linear collider (LC) can measure t quark electroweak couplings at the % level. In contrast to the situation at hadron colliders, the leading-order pair production process $e^+e^- \to t\bar{t}$ goes directly through the $t\bar{t}Z^0$ and $t\bar{t}\gamma$ vertices. There is no concurrent QCD production of t quark pairs, which increases greatly the potential for a clean measurement. In the literature there a various ways to describe the current at the $t\bar{t}X$ vertex. The Ref. [1] uses

$$\Gamma_\mu^{ttX}(k^2,\, q,\, \overline{q}) = ie\left\{\gamma_\mu\,\left(\widetilde{F}_{1V}^X(k^2) + \gamma_5\widetilde{F}_{1A}^X(k^2)\right) + \frac{(q-\overline{q})_\mu}{2m_t}\left(\widetilde{F}_{2V}^X(k^2) + \gamma_5\widetilde{F}_{2A}^X(k^2)\right)\right\}. \tag{1}$$

with k^2 being the four momentum of the exchanged boson and q and $\overline{q}$ the four vectors of the t and $\bar{t}$ quark. Further γ_μ with $\mu = 0, .., 3$ are the Dirac matrices describing vector currents and $\gamma_5 = i\gamma_0\gamma_1\gamma_2\gamma_3$ is the Dirac matrix allowing to introduce an axial vector current into the theory

The Gordon composition of the current reads

$$\Gamma_\mu^{ttX}(k^2, q, \overline{q}) = -ie\left\{\gamma_\mu\left(F_{1V}^X(k^2) + \gamma_5 F_{1A}^X(k^2)\right) + \frac{\sigma_{\mu\nu}}{2m_t}(q+\overline{q})^\mu\left(iF_{2V}^X(k^2) + \gamma_5 F_{2A}^X(k^2)\right)\right\}, \tag{2}$$

with $\sigma_{\mu\nu} = \frac{i}{2}\left(\gamma_\mu\gamma_\nu - \gamma_\nu\gamma_\mu\right)$. The couplings or form factors $\widetilde{F}_i^X$ and F_i^X appearing in Eqs. 1 and 2 are related via

$$\widetilde{F}_{1V}^X = -\left(F_{1V}^X + F_{2V}^X\right), \qquad \widetilde{F}_{2V}^X = F_{2V}^X, \qquad \widetilde{F}_{1A}^X = -F_{1A}^X, \qquad \widetilde{F}_{2A}^X = -iF_{2A}^X. \tag{3}$$

Within the Standard Model the F_i have the following values:

$$F_{1V}^{\gamma,SM} = -\frac{2}{3},\; F_{1A}^{\gamma,SM} = 0,\; F_{1V}^{Z,SM} = -\frac{1}{4s_w c_w}\left(1 - \frac{8}{3}s_w^2\right),\; F_{1A}^{Z,SM} = \frac{1}{4s_w c_w}, \tag{4}$$

with s_w and c_w being the sine and the cosine of the Weinberg angle θ_W. The coupling F_{2V}^γ is related via $F_{2V}^\gamma = Q_t(g-2)/2$ to the anomalous magnetic moment $(g-2)$ with Q_t being the electrical charge of the t quark. The coupling F_{2A} is related to the dipole moment $d = (e/2mt)F_{2A}(0)$ that violates the combined *C*harge and *P*arity symmetry CP. Note, that all the expressions above are given at Born level. Throughout the article no attempt will be made to go beyond that level.

Today, the most advanced proposal for a linear collider is the *I*nternational *L*inear *C*ollider, ILC [2,3], which can operate at centre-of-mass energies between about

0.1 TeV to 1 TeV. The ILC provides an ideal environment to measure these couplings. The $t\bar{t}$ pairs would be copiously produced, several 100,000 events at $\sqrt{s} = 500\,\mathrm{GeV}$ for an integrated luminosity of $500\,\mathrm{fb}^{-1}$. It is possible to almost entirely eliminate the background from other Standard Model processes. The ILC will allow for polarised electron and positron beams. With the use of polarised beams, t and $\bar{t}$ quarks oriented toward different angular regions in the detector are enriched in left-handed or right-handed t quark helicity [4]. This means that the experiments can independently access the couplings of left- and right-handed chiral parts of the t quark wavefunction to the Z^0 boson and the photon. In principle, the measurement of the cross section and forward-backward asymmetry A_{FB}^t for two different polarisation settings allows extracting both, the photon and Z^0 couplings of the t quark for each helicity state. This study introduces the angle of the decay lepton in semi-leptonic decays of the $t\bar{t}$ in the rest frame of the t quark. This angle will be called the *helicity angle*. The slope of the resulting angular distribution is a measure for the fraction of t quarks in left-handed helicity state, t_L and right-handed helicity state, t_R, in a given sample. There are therefore six independent observables

- The cross section;
- The forward backward asymmetry A_{FB}^t;
- The slope of the distribution of the helicity angle;

for two beam polarisations. This allows for a separate extraction of the six CP conserving form factors defined for the Z^0 and the photon: F_{1V}, F_{1A} and F_{2V}.

This article is organised as follows. After this introduction the experimental environment and the used data samples will be introduced. After that the selection of semi-leptonic decays of the $t\bar{t}$ pair will be presented and the selection efficiencies will be given. The determination of A_{FB}^t will be followed by the extraction of the slope of the distribution of the helicity angle.. This leads finally to the independent extraction of up to six form factors as explained above. This study goes therefore beyond earlier studies published in [5,6].

2 Observables and Form Factors

According to [7], the cross section for any process in e^+e^- collisions in case of polarised beams can be written as

$$\sigma_{\mathcal{P},\mathcal{P}'} = \frac{1}{A}\left[(1-\mathcal{P}\mathcal{P}')(\sigma_{-,+}+\sigma_{+,-}) + (\mathcal{P}-\mathcal{P}')(\sigma_{+,-}-\sigma_{-,+})\right] \tag{5}$$

In this equation the symbols $-$ and $+$ indicate full polarisation of the incoming beams with electrons and positrons of left-handed, L, or right-handed, R, helicity, respectively. The configurations $\sigma_{-,-}$ and $\sigma_{+,+}$ have been neglected due to helicity conservation at the electron vertex in the high energy limit. The degree of polarisation of the incoming beams is expressed by $\mathcal{P}$, for electrons, and $\mathcal{P}'$, for positrons.

In case of polarised beams Ref. [8] suggests to express the form factors introduced in Sec. 1 in terms of the helicity of the incoming electrons,

$$\begin{aligned} \mathcal{F}_{ij}^{L} &= -F_{ij}^{\gamma} + \Big(\frac{-\frac{1}{2} + s_w^2}{s_w c_w}\Big)\Big(\frac{s}{s - m_Z^2}\Big) F_{ij}^{Z} \\ \mathcal{F}_{ij}^{R} &= -F_{ij}^{\gamma} + \Big(\frac{s_w^2}{s_w c_w}\Big)\Big(\frac{s}{s - m_Z^2}\Big) F_{ij}^{Z} \ , \end{aligned} \tag{6}$$

with $i = 1, 2$ and $j = V, A$ and m_Z being the mass of the Z^0 boson. The cross section for $t\bar{t}$ quark production for electron beam polarisation $I = L, R$ reads

$$\sigma_I = 2\mathcal{A} N_c \beta \left[(1 + 0.5\gamma^{-2})(\mathcal{F}_{1V}^{I})^2 + (\mathcal{F}_{1A}^{I'})^2 + 3\mathcal{F}_{1V}^{I}\mathcal{F}_{2V}^{I} \right], \tag{7}$$

where $\mathcal{A} = \frac{4\pi\alpha^2}{3s}$ with the running electromagnetic coupling α and N_c is the number of quark colours. Furthermore γ and β are the Lorentz factor and the velocity, respectively. The term $\mathcal{F}_{1A}^{I'} = \beta \mathcal{F}_{1A}^{I}$ describes the reduced sensitivity to axial vector couplings near the $t\bar{t}$ production threshold. The cross sections at the Born level of the signal process $e^+e^- \to t\bar{t}$ and the main Standard Model background processes at a centre-of-mass energy of 500 GeV are summarised in Table 1.

Channel	$\sigma_{unpol.}$ [fb]	$\sigma_{-,+}$ [fb]	$\sigma_{+,-}$ [fb]	A_{LR}^{SM}%
$t\bar{t}$	572	1564	724	36.7
$\mu\mu$	456	969	854	6.3
$\sum_{q=u,d,s,c} q\bar{q}$	2208	6032	2793	36.7
$b\bar{b}$	372	1212	276	62.9
γZ^0	11185	25500	19126	14.2
WW	6603	26000	150	98.8
Z^0Z^0	422	1106	582	31.0
Z^0WW	40	151	8.7	89
$Z^0Z^0Z^0$	1.1	3.2	1.22	45

Table 1: *Unpolarised cross-sections and cross-sections at the Born level for 100% beam polarisation for signal and background processes. The last column gives the left right asymmetry as expected from the Standard Model.*

The forward-backward asymmetry A^t_{FB} can be expressed as

$$(A^t_{FB})_I = \frac{-3\mathcal{F}^{I'}_{1A}(\mathcal{F}^I_{1V} + \mathcal{F}^I_{2V})}{2\left[(1+0.5\gamma^{-2})(\mathcal{F}^I_{1V})^2 + (\mathcal{F}^{I'}_{1A})^2 + 3\mathcal{F}^I_{1V}\mathcal{F}^I_{2V}\right]}, \tag{8}$$

which in the Standard Model takes the values $(A^t_{FB})_L = 0.38$ and $(A^t_{FB})_R = 0.47$.

The fraction of right-handed tops is given by the following expression:

$$(F_R)_I = \frac{(\mathcal{F}^I_{1V})^2(1+0.5\gamma^{-2}) + (\mathcal{F}^{I'}_{1A})^2 + 2\mathcal{F}^I_{1V}\mathcal{F}^{I'}_{1A} + 2\mathcal{F}^I_{2V}(3\mathcal{F}^I_{1V} + 2\mathcal{F}^{I'}_{1A}) - \beta\mathcal{F}^I_{1V}\mathfrak{Re}(\mathcal{F}^I_{2A})}{2\left[(1+0.5\gamma^{-2})(\mathcal{F}^I_{1V})^2 + (\mathcal{F}^{I'}_{1A})^2 + 3\mathcal{F}^I_{1V}\mathcal{F}^I_{2V}\right]}. \tag{9}$$

The values expected in the Standard Model are $(F_R)_L = 0.25$ and $(F_R)_R = 0.76$. The Eq. 9 contains a CP violating term proportional to $\mathfrak{Re}(\mathcal{F}^I_{2A})$. This term will not be determined in ths present study but can also be precisely estimated using CP violating observables, see later in Tab. 5. This implies that CP conserving form factors can be fully disentangled without the assumption of CP conservation.

3 Experimental environment and data samples

The International Linear Collider is a proposal for a linear electron-positron accelerator at the TeV scale. For a detailed description of the machine the reader is referred to [2,3]. For the studies presented in this article it is important to emphasise that the machine can deliver polarised electron and positron beams. At a centre-of-mass energy of $\sqrt{s} = 500\,\text{GeV}$ the envisaged degree of polarisation is 80% in case of electrons and 30% in case of positrons.

The ILD detector is designed as a detector for Particle Flow. This means that the jet energy measurement is based on the measurement of individual particles [9]. A detailed description of the current model of the ILD detector can be found elsewhere [10]. The z-axis of the right handed co-ordinate system is given by the direction of the incoming electron beam. Polar angles given in this note are defined with respect to this axis. The most important sub-detectors for this study are described in the following.

- The vertex detector consists of three double layers of silicon extending between 16 mm and 60 mm in radius and between 62.5 mm and 125 mm in z direction. It is designed for an impact parameter resolution of $\sigma_{r\phi} = \sigma_{rz} = 5 \oplus 10/(p\sin^{\frac{3}{2}}\theta)\,\mu$m.
- The measurement of charged tracks is supported by an inner Silicon Tracker (SIT) in the central region and by a set of silicon disks in forward direction, i.e. towards large absolute values of $cos\theta$.

- The ILD detector contains a large Time Projection Chamber (TPC) with an inner sensitive radius of 395 mm and an outer sensitive radius of 1743 mm. The half length in z is 2250 mm. Recent simulation studies confirm that the momentum of charged particle tracks can be measured to a precision of $\delta(1/P_T) \sim 2 \times 10^{-5}\,\mathrm{GeV}^{-1}$. Here P_T denotes the transverse component of the three momentum P of the particles.

- The electromagnetic calorimeter is a SiW sampling calorimeter. Its longitudinal depths of $24\,\mathrm{X}_0$ allows for the complete absorption of photons with energies of up to 50 GeV as relevant for the studies here. The simulated energy resolution of the electromagnetic calorimeter is $\frac{\Delta E}{E} = 15\%/\sqrt{E\,[\mathrm{GeV}]}$

- The hadronic calorimeter surrounds the electromagnetic calorimeter and comprises 4.5 interaction length λ_I.

  Two proposals exist for the hadronic calorimeter. A semi-digital variant consisting of steel absorbers and gas RPC chambers with a pixel size of $1 \times 1\,\mathrm{cm}^2$ as active material. The second one features scintillating tiles with size of $3 \times 3\,\mathrm{cm}^2$ as active material. The latter option is employed in the present work.

3.1 Event generation and technical remarks

The events are generated with version 1.95 of the `WHIZARD` event generator [11,12] in the form of six fermion final states of which $t\bar{t}$ events form a subsample.

The generated events are then passed to the PYTHIA simulation program to generate parton shower and subsequent hadronisation. Events are selected for which the difference between the invariant masses of the three fermion systems forming a top from WHIZARD and the input t mass to WHIZARD of 174 GeV is smaller than $5\Gamma_t$. Here Γ_t is the total decay width of the t quark. By this only about 70% of the events generated by WHIZARD are recognised as $t\bar{t}$ events and treated accordingly. The following analysis is based on the described sub-selection of events.

The study has been carried out on a fully polarised sample. Realistic values of the beam polarisations at the ILC at $\sqrt{s} = 500\,\mathrm{GeV}$ are however $\mathcal{P}, \mathcal{P}' = \pm 0.8, \mp 0.3$. The cross section and therefore its uncertainty scales with the polarisation according to Eq. 5. The observables A_{FB}^t and λ_t vary only very mildly with the beam polarisation. Again, the reduced cross section leads to a higher statistical error for non-fully polarised beams. This will be correctly taken into account in the uncertainty of the results.

Events corresponding to a luminosity of $250\,\mathrm{fb}^{-1}$ for each of the polarisation configurations were subject to a full simulation of the ILD detector and subsequent event

reconstruction using the version `ILD_o1_v05` of the ILC software. In Ref. [13] it was shown that the background can be nearly eliminated for the semi-leptonic final state (95% purity). Therefore at this stage none of the listed background processes are included in the analysis.

4 Event selection

The analysis starts out from the studies presented in detail in [13]. The samples analysed here contain background generated by beam beam interactions, so-called $\gamma\gamma$ background. No cut to remove this background is applied in this analysis. Such a study is left for future work. The produced $t(\bar{t})$-quark decays almost exclusively in to a bW pair. The b quark hadronises giving rise to a jet. The W boson can decay *hadronically* into light quarks, which turn into jets, or *leptonically* into a pair composed by a charged lepton and a neutrino. The *semi-leptonic process* is defined by events in which one W decays hadronically while the other one decays leptonically, i.e.

$$t\bar{t} \to (bW)(bW) \to (bqq')(b\ell\nu) \tag{10}$$

In the Standard Model the fraction of semi-leptonic final states in $e^+e^- \to t\bar{t}$ is about 43%. The charged lepton allows for the determination of the t quark charge. The t quark mass is reconstructed from the hadronically decaying W which is combined with one of the b-quark jets. In general leptons are identified using typical selection criteria. The lepton from the W boson decay is either the most energetic particle in a jet or has a sizeable transverse momentum w.r.t. neighboured jets. More specific the following criteria are applied

$$x_T = p_{T,lepton}/M_{jet} > 0.25 \quad \text{and} \quad z = E_{lepton}/E_{jet} > 0.6, \tag{11}$$

where E_{lepton} is the energy and $p_{T,lepton}$ the transverse momentum of the lepton within a jet with energy E_{jet} and mass M_{jet}. The decay lepton in case of e and μ can be identified with an efficiency of about 85%, where the selection has a tendency to reject low momentum leptons. The τ leptons can decay themselves into e or μ, which are collinear with the produced τ but have lower momentum than primary decay leptons. Taking into account the τ leptons, the efficiency to identify the decay lepton is about 70%.

The identified lepton is removed from the list of reconstructed particles and the remaining final state is again clustered into four jets. Two of these must be identified as being produced by the b-quarks of the t quark decay. The b-likeness or *b-tag* is determined with the `LCFIPlus` package, which uses information of the tracking system as input. Secondary vertices in the event are analysed by means of the jet mass, the

decay length and the particle multiplicity. The jets with the highest b-tag values are selected. As shown in Fig. 1 the higher b-tag value is typically 0.92 while the smaller one is still around 0.65.

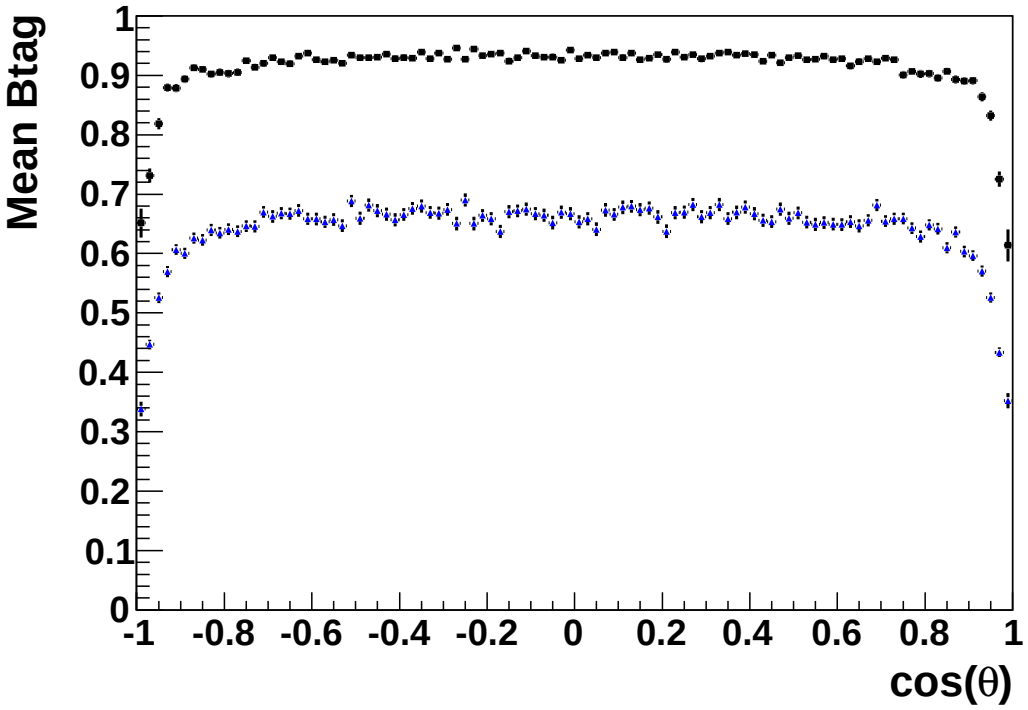

Figure 1: *The b-tag values as a function of the polar angle of the jets with the highest b-tag value (black dots) and of that with the second highest b-tag value (blue dots).*

These values are nearly independent of the polar angle of the b quark jet but drop towards the acceptance limits of the detector. Finally, the two remaining jets are associated with the decay products of the W boson. The signal is reconstructed by choosing that combination of b quark jet and W boson that minimises the following equation:

$$d^2 = \left(\frac{m_{cand.} - m_t}{\sigma_{m_t}}\right)^2 + \left(\frac{E_{cand.} - E_{beam}}{\sigma_{E_{cand.}}}\right)^2 + \left(\frac{p_b^* - 68}{\sigma_{p_b^*}}\right)^2 + \left(\frac{cos\theta_{bW} - 0.23}{\sigma_{cos\theta_{bW}}}\right)^2 \quad (12)$$

In this equation $m_{cand.}$ and $E_{cand.}$ are invariant mass and energy of the t quark candidate decaying hadronically, respectively, and m_t and E_{beam} are input t mass and the beam energy of 250 GeV. Beyond that it introduces the momentum of the b quark jet in the centre-of-mass frame of the t quark, p_b^* and the angle between the b quark

and the W boson. The measured values are compared with the expected ones and the denominator is the width of the measured distributions. Distribution of latter two observables are shown in Fig. 2. Note, that the figure shows separately good and badly reconstructed events. This is explained in Sec. 5. Further cuts on jet thrust $T < 0.9$ and on the hadronic mass of the final state $180 < m_{had.} < 420\,\text{GeV}$ are applied. In addition the mass windows for the reconstructed W-boson and t-quark are chosen to $50 < m_W < 250\,\text{GeV}$ and $120 < m_t < 270\,\text{GeV}$.

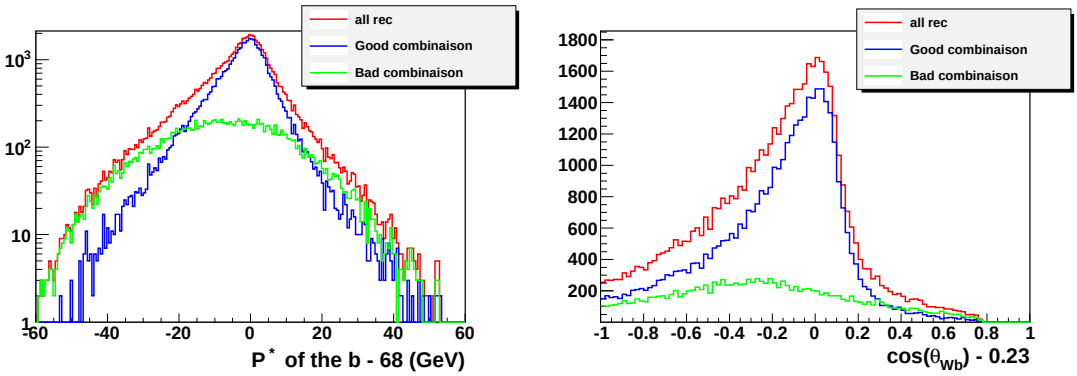

(a) Momentum of b jet at top rest frame.

(b) Angle between b-jet and W.

Figure 2: *Distributions of the momentum of the b quark jet in the centre-of-mass frame of the t quark, p_b^* and the cosine of the angle θ_{bW} between the b quark and the W boson.*

The entire selection retains 53.5% signal events for the configuration $\mathcal{P}, \mathcal{P}' = -1, +1$ and 56.5% for the configuration $\mathcal{P}, \mathcal{P}' = +1, -1$.

5 Measurement of the forward backward asymmetry

Garcìa For the determination of the forward-backward asymmetry A_{FB}^t, the number of events in the hemispheres of the detector w.r.t. the polar angle θ of the t quark is counted, i.e.

$$A_{FB}^t = \frac{N(\cos\theta > 0) - N(\cos\theta < 0)}{N(\cos\theta > 0) + N(\cos\theta < 0)}. \tag{13}$$

Here, the polar angle of the t quark is calculated from the decay products in the hadronic decay branch. The direction measurement depends on the correct association of the b quarks to the jets of the hadronic b quark decays. The analysis is carried out separately for a left-handed polarised electron beam and for a right handed polarised beam. Therefore, two different situations have to be distinguished, see also Fig. 3:

- In case of a *right*-handed electron beam the sample is expected to be enriched with t-quarks with *right*-handed helicity [4]. Due to the $V-A$ structure of the standard model an energetic W boson is emitted into the flight direction of the t-quark. The W boson decays into two energetic jets. The b quark from the decay of the t quark are comparatively soft. Therefore, the direction of the t quark is essentially reconstructed from the direction of the energetic jets from the W boson decay. This scenario is thus insensitive towards a wrong association of the jet from the b quark decay to the jets from the W boson decay

- In case of a *left*-handed electron beam the sample is enriched with t quarks with *left*-handed helicity. In this case the W boson is emitted opposite to the flight-direction of the t quark and gains therefore only little kinetic energy. In fact for a centre-of-mass energy of 500 GeV the W boson is nearly at rest. On the other hand the b quarks are very energetic and will therefore dominate the reconstruction of the polar angle of the t quark. In this case a wrong association of the jets with that from the b quark can flip the reconstructed polar angle by π giving rise to migrations in the polar angle distribution of the t quark.

The explanations above apply correspondingly to polarised positron beams and $\bar{t}$-quarks.

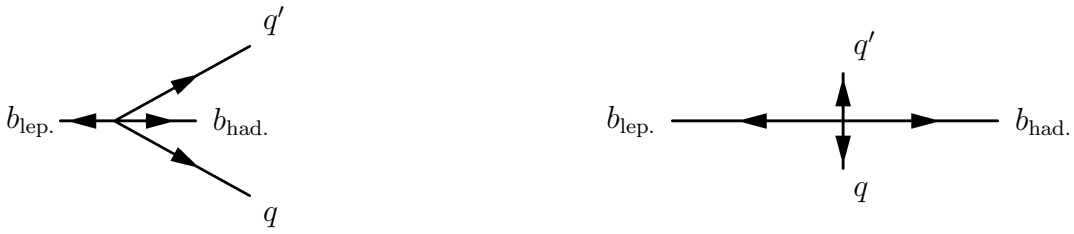

Figure 3: *In case of a t_R decay, the jets from the W dominate the reconstruction of the polar angle of the t quark. In case of a t_L the W is practically at rest and jets from the b quark dominate the and reconstruction of the polar angle of the t quark.*

The described scenarios are encountered as shown in Figure 4. First, the reconstructed spectrum of polar angles of the t quark in the case of right handed electron beams is in resonable agreement with the generated one. On the other hand the reconstruction of $\cos\theta_{\text{t}}$ in case of left-handed t quarks suffers from considerable migrations. As discussed, the migrations are caused by a wrong association of jets stemming from b quarks to jets stemming from W decays. This implies that the reconstruction of observables will get deteriorated. This implication motivates to restrict the determination of A_{FB}^{t} in case of $\mathcal{P},\mathcal{P}' = -1,+1$ to cleanly reconstructed events as already studied previously in [14,15].

The quality of the reconstructed events is estimated by the following quantity

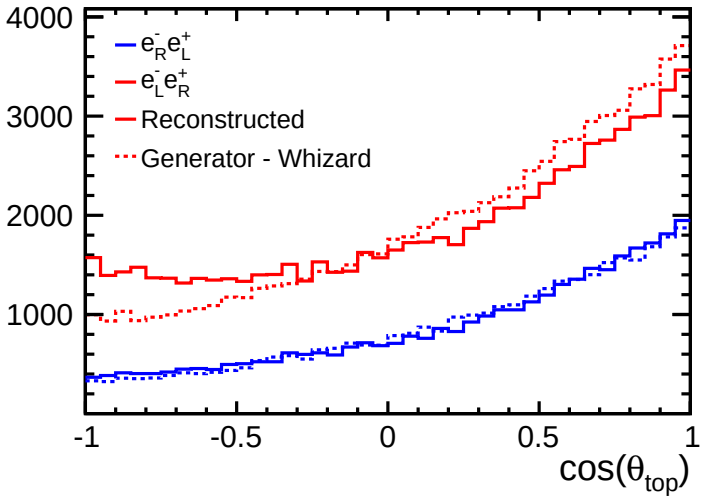

Figure 4: *Reconstructed forward backward asymmetry compared with the prediction by the event generator WHIZARD for two configurations of the beam polarisations.*

$$\chi^2 = \left(\frac{\gamma_t - 1.435}{\sigma_{\gamma_t}}\right)^2 + \left(\frac{E_b^* - 68}{\sigma_{E_b^*}}\right)^2 + \left(\frac{cos\theta_{bW} - 0.26}{\sigma_{cos\theta_{bW}}}\right)^2 \tag{14}$$

The observables p_b^* and $\cos\theta_{bW}$ have already been introduced in Sec. 4. The defined χ^2 comprises in addition the Lorentz factor $\gamma_t = E_t/M_t$ of the final state t quark, which is shown in Figure 5. The correct association of the of jets from b quarks to that from W bosons is checked with the MC truth information Events in which this association went wrong, labelled as *bad combination* in Figs. 2 and 5, lead to a distorted distribution in these observables.

For $\chi^2 < 15$ the reconstructed spectrum agrees very well with the generated one. For this cut on χ^2, the reconstruction efficiency is 27.6%. The Fig. 6 demonstrates the improved agreement between the reconstructed and generated direction of the t quark direction in case $\mathcal{P}, \mathcal{P}' = -1, +1$. The forward-backward asymmetry A_{FB}^t can be derived from these angular distributions. For completeness it has to be noted that effects of beam related $\gamma\gamma$ background on the angular distribution have been studied. The reconstruction of the angular distribution works better without these effects. The detailed treatment and quantification of these effects is left for further studies.

The numerical results are given in Tab. 2 and compared with the generated value. The statistical error is corrected for the realistic beam polarisations $\mathcal{P}, \mathcal{P}' =$

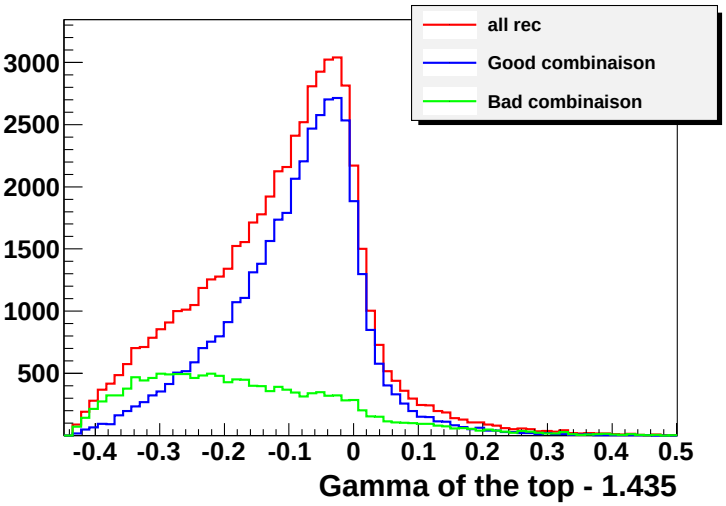

Figure 5: *Lorentz factor of the top to define the quantity χ^2, see Eq. 14, for the selection of well reconstructed events in case of $\mathcal{P}, \mathcal{P}' = -1, +1$ beam polarisation.*

$\pm 0.8, \mp 0.3$. It shows that for the standard luminosity statistical precisions of better than 2% can be expected. When selecting well reconstructed events the systematic error due to the ambiguities is expected to be significantly smaller than the statistical error.

$\mathcal{P}, \mathcal{P}'$	$(A^t_{FB})_{gen.}$	A^t_{FB}	$(\delta_{A_{FB}}/A_{FB})_{stat.}$ [%]
$-1, +1$	0.360	0.359	1.7 (for $\mathcal{P}, \mathcal{P}' = -0.8, +0.3$)
$+1, -1$	0.433	0.410	1.3 (for $\mathcal{P}, \mathcal{P}' = +0.8, -0.3$)

Table 2: *Statistical precisions expected for A^t_{FB} for different beam polarisations.*

6 Determination of the slope of the helicity angle distribution

The helicity approach has been suggested for top studies at Tevatron [16]. In the rest system of the t quark, the angle of the lepton from the W boson is distributed like:

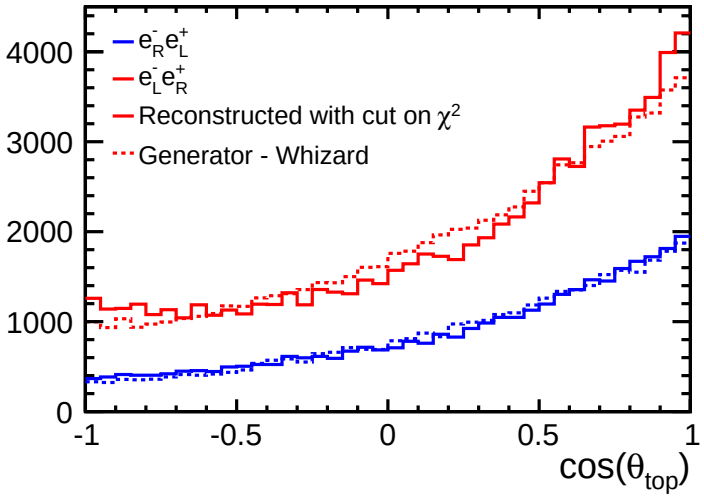

Figure 6: *Reconstructed forward backward asymmetry compared with the prediction by the event generator WHIZARD after the application of a on* $\chi^2 < 15$ *for the beam polarisations* $P, P' = -1, +1$ *as explained in the text. Note that no correction is applied for the beam polarisations* $\mathcal{P}, \mathcal{P}' = +1, -1$

$$\frac{1}{\Gamma}\frac{d\Gamma}{dcos\theta_{hel}} = \frac{1+\lambda_t cos\theta_{hel}}{2} = \frac{1}{2} + (2F_R - 1)\frac{cos\theta_{hel}}{2}$$

$$\lambda_t = 1 \text{ for } t_R \quad \lambda_t = -1 \text{ for } t_L \tag{15}$$

This angular distribution is therefore linear and very contrasted between t_L and t_R. In practice there will be a mixture of t_R and t_L (beware that here L and R mean left and right handed helicities) and λ_t will have a value between -1 and +1 depending on the composition of the t quark sample.

According to [16], the angle θ_{hel} is measured in the rest frame of the t quark with the z-axis defined by the direction of motion of the t quark in the laboratory. As discussed in [4] this definition of θ_{hel} is not unique but some detailed investigations not reproduced in this note have shown that the choice of [16] seems optimal. The observable $cos\theta_{hel}$ is computed from the momentum of the t quark decaying semi-leptonically into a lepton, a b quark and a neutrino. If ISR effects (with the photon lost in the beam pipe) are neglected, one can simply assume energy momentum conservation. This, by means of the energy-momentum of the t quark decaying hadronically, allows for deducing the energy-momentum of the t quark decaying semi-leptonically. A

Lorentz transformation boosts the lepton into the rest system of the t quark. This should give a very precise knowledge of $\cos\theta_{hel}$. To determine the helicity angle only the angle of the lepton needs to be known. For the leptonic decays of the τ lepton, which significantly contribute to this analysis (10-15%), the charged lepton and the τ lepton are approximately collinear and therefore the method remains valid.

6.1 Analysis of the helicity angle distribution

Based on the selection introduced in Sec. 4 the angular distribution of the decay lepton in the rest frame of the t quark is shown in Fig. 7 for fully polarised beams.

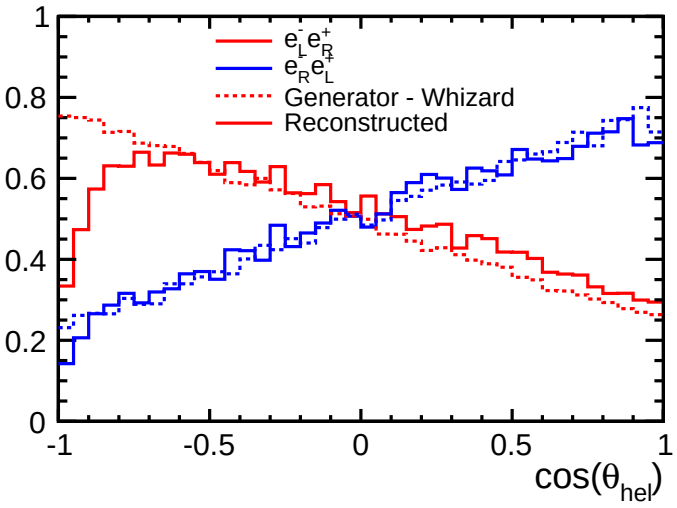

Figure 7: *Polar angle of the decay lepton in the rest frame of the t quark.*

The distribution exhibits a drop in reconstructed events towards $\cos\theta_{hel} = -1$. This drop can be explained by the event selection which suppresses leptons with small energies. Outside this region and in contrast to e.g. the forward-backward asymmetry the reconstructed angular distribution agrees very well with the generated one. This means that this observable suffers much less from the migration effect described in Sec. 5. It is therefore not necessary to tighten the selection in the same way as for A^t_{FB}. The reason for the bigger robustness of the angular distribution can be explained by kinematics.

As outlined in Sec. 5 the migrations described there are provoked mainly by longitudinally polarised, *soft* W bosons from the decay of left handed t quarks. The W_L boson decay proportional to $\sin^2\theta$. Therefore any boost into the rest frame of the top leads predominantly to leptons with $\cos\theta_{hel} < 0$.

The parameter λ_t can be derived from the slope of the helcity angle distribution that is obtained by a fit to the linear part of the angular distribution in the range $\cos\theta_{hel} = [-0.6, 0.9]$. The results are summarised in Table 3 for the two initial beam polarisations $\mathcal{P} = \pm 1$ and $\mathcal{P}' = \mp 1$, where the statistical error is given for $\mathcal{P}, \mathcal{P}' = \mp 0.8, \pm 0.3$. The results are compared with the values of λ_t as obtained for the generated sample. A quarter of shift between the generated and the reconstructed value is taken into account for the systematic error of the measurement. The result changes by about 1% when changing the fit range to $\cos\theta_{hel} = [(-0.4, 0.5), 0.9]$. The errors on the slope from the variation of the fit range and that from the difference between generated and reconstructed slope are added in quadrature.

$\mathcal{P}, \mathcal{P}'$	$(\lambda_t)_{gen.}$	$(\lambda_t)_{rec.}$	$(\delta\lambda_t)_{stat.}$ for $\mathcal{P}, \mathcal{P}' = \mp 0.8, \pm 0.3$	$(\delta\lambda_t)_{syst.}$
$-1, +1$	-0.514	-0.476	0.011	0.011
$+1, -1$	0.546	0.510	0.016	0.010

Table 3: *Results on λ_t derived from the slope of the helicity angle distribution with errors for different beam polarisations at the ILC.*

7 Discussion of systematic uncertainties

In the previous sections measurements of either cross sections or asymmetries have been presented. This section makes an attempt to identify and quantify systematic uncertainties, which may influence the precision measurements.

- Luminosity: The luminosity is a critical parameter for cross section measurements only. The luminosity can be controlled to 0.1% [17].
- Polarisation: The polarisation is a critical parameter for all analyses. It enters directly the cross section measurements. The studies for the DBD using W pair production [18] lead to an uncertainty of 0.1% for the polarisation of the electron beam and to an uncertainty of 0.35% for the polarisation of the positron beam. This translates into an uncertainty of 0.25% on the cross section for $\mathcal{P}, \mathcal{P}' = -0.8, +0.3$ and 0.18% on the cross section for $\mathcal{P}, \mathcal{P}' = +0.8, -0.3$ The uncertainty on the polarisation can be neglected with respect to the statistical uncertainty for A_{FB}^t and λ_t.
- Migrations: It has been shown in Sec. 5 that migrations have to be taken into account for the measurement of A_{FB}^t, in particular for the polarisations $\mathcal{P}, \mathcal{P}' =$

$-1, +1$. These migrations are reduced by stringent requirements on the event selection using a χ^2 analysis. This in turn leads to a penalty in the efficiency. The success of the method depends in addition on a very sharp measurement of the variables used for the χ^2 analysis. A review of the procedure to handle the ambiguities will however be made in future studies. In the ideal case the ambiguities can be eliminated by a proper measurement of the charge of the b quark from the t decay.

- Other experimental effects: There is a number of other experimental effects imaginable like acceptance, uncertainties of the b tagging or the influence passive material. These effects depend on the experimental conditions that will really be encountered. The LEP experiments quote a systematic uncertainty on R_b of 0.2% a value which may serve as a guiding line for values to be expected at the ILC.

- Theory: The analysis performed here considers only the Born-level $t\bar{t}$ production diagrams. The electroweak corrections have been estimated in Ref. [19] and QCD corrections in [20]. Even if the corrections themselves are sizeable, the theoretical uncertainty on the total and differential production rate is not expected to dominate over the experimental uncertainties. A further complication arises from several other processes that yield the same final state. Single top production at the LC in association with a W boson and bottom quark (through WW^* production) leads to the same final state as t quark pair production. The interference between single t and t quark pair production processes is sizeable and must be taken into account in a realistic experimental strategy. This is left for a future study.

As a summary it can be concluded that the total systematic uncertainties will not exceed the statistical uncertainties. This, however, requires an excellent control of a number of experimental quantities on which the results depend.

8 Interpretation of results

The results on the reconstruction efficiency, A^t_{FB} and λ_t presented in the previous sections are transformed into precisions on the form factors $\widetilde{F}_i$. The results are summarised in Table 4 and Figure 8 and are compared with results of earlier studies for a linear e^+e^- collider as published in the TESLA TDR [6] as well as with precisions expected for the LHC. For completeness, Tab. 5 compares sensitivites expected at the LHC with the results from the TESLA TDR [6] for CP violating form factors not

Coupling	SM value	LHC [1] $\mathcal{L} = 300$ fb^{-1}	e^+e^- [6] $\mathcal{L} = 300$ fb^{-1} $\mathcal{P}, \mathcal{P}' = -0.8, 0$	e^+e^-[*ILC DBD*] $\mathcal{L} = 500$ fb^{-1} $\mathcal{P}, \mathcal{P}' = \pm 0.8, \mp 0.3$
$\Delta\widetilde{F}^{\gamma}_{1V}$	0.66	$^{+0.043}_{-0.041}$	– –	$^{+0.002}_{-0.002}$
$\Delta\widetilde{F}^{Z}_{1V}$	0.23	$^{+0.240}_{-0.620}$	$^{+0.004}_{-0.004}$	$^{+0.003}_{-0.003}$
$\Delta\widetilde{F}^{Z}_{1A}$	-0.59	$^{+0.052}_{-0.060}$	$^{+0.009}_{-0.013}$	$^{+0.005}_{-0.005}$
$\Delta\widetilde{F}^{\gamma}_{2V}$	0.015	$^{+0.038}_{-0.035}$	$^{+0.004}_{-0.004}$	$^{+0.003}_{-0.003}$
$\Delta\widetilde{F}^{Z}_{2V}$	0.018	$^{+0.270}_{-0.190}$	$^{+0.004}_{-0.004}$	$^{+0.006}_{-0.006}$

Table 4: *Sensitivities achievable at 68.3% CL for CP conserving form factors $\widetilde{F}^{X}_{1V,A}$ and $\widetilde{F}^{X}_{2V}$ defined in Eq. 1 at the LHC and at linear e^+e^- colliders. The assumed luminosity samples and, for e^+e^- colliders, the beam polarisation, are indicated. In the LHC studies and in earlier studies for a linear e^+e^- collider as published in the TESLA TDR [6] study, only one coupling at a time is allowed to deviate from its Standard Model value. In the present study, denoted as* ILC DBD*, the form factors are allowed to vary independently. The sensitivities are based on statistical errors only.*

calculated in the present study. Note, that in the LHC and TESLA studies only one form factor was varied at a time while here all six form factors are varied simultaneously. It is obvious that the measurements at an electron positron collider leads to a spectacular improvement and thus allow for a profound discussion of effects of new physics. Two examples are given in the following.

8.1 An example: The Randall-Sundrum scenario

The sensitivity new physics can be parameterised by general dimension six operators contributing to the $t\bar{t}\gamma$ and $t\bar{t}Z^0$ vertex [21]. However, the potential of the ILC might be demonstrated more clearly by presenting a concrete example with one particular model. In the original model of Randall and Sundrum [22] there are additional massive gauge bosons in an assumed extra dimension. The modelpredicts increased couplings of the t quark, and perhaps also the b quark, to these Kaluza-Klein particles. Following the analysis in [23,24,25], one can fix the parameters of the model so that these enhancements fit the two anomalies observed in the forward-backward asymmetry for b quarks A^b_{FB} at LEP1 and for t quarks A^t_{FB} at the Tevatron. This gives a viable model of t quark interactions associated with top and Higgs compositeness. Figure 9 shows the expected modifications of the helicity angle distributions within this scenario for a Kaluza-Klein mass of $M_{KK} = 2\,\text{TeV}$. Staying within the framework of the Randall-Sundrum model, the ILC at $\sqrt{s} = 500\,\text{GeV}$ can observe

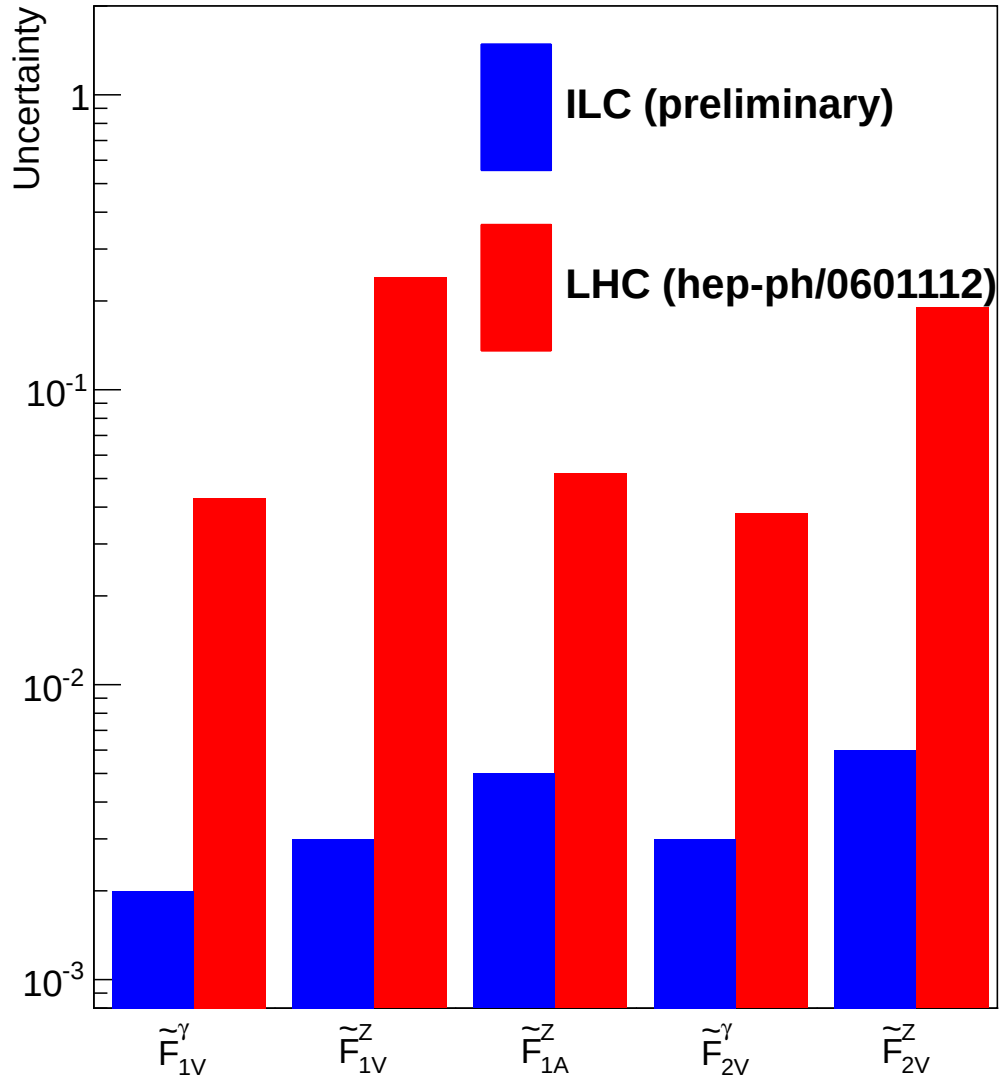

Figure 8: *Comparison of statistical precisions on CP conserving form factors expected at the LHC, taken from [1] and at the ILC. The LHC results assume an integrated luminosity of $\mathcal{L} = 300\ fb^{-1}$. The results for ILC assume an integrated luminosity of $\mathcal{L} = 500\ fb^{-1}$ at $\sqrt{s} = 500\,GeV$ and a beam polarisation $\mathcal{P} = \pm 0.8, \mathcal{P}' = \mp 0.3$.*

Coupling	LHC [1] $\mathcal{L} = 300$ fb^{-1}	e^+e^- [6] $\mathcal{L} = 300$ fb^{-1} $\mathcal{P}, \mathcal{P}' = -0.8, 0$
$\Delta\mathrm{R}e\,\widetilde{F}^{\gamma}_{2A}$	$+0.17$ -0.17	$+0.007$ -0.007
$\Delta\mathrm{R}e\,\widetilde{F}^{Z}_{2A}$	$+0.35$ -0.35	$+0.008$ -0.008
$\Delta\mathrm{I}m\,\widetilde{F}^{\gamma}_{2A}$	$+0.17$ -0.17	$+0.008$ -0.008
$\Delta\mathrm{I}m\,\widetilde{F}^{Z}_{2A}$	$+0.035$ -0.035	$+0.015$ -0.015

Table 5: *Sensitivities achievable at 68.3% CL for the top quark magnetic and electric dipole form factors $\widetilde{F}^{V}_{2A}$ defined in Eq. 1, at the LHC and at for a linear e^+e^- collider as published in the TESLA TDR [6]. The assumed luminosity samples and, for TESLA, beam polarisation, are indicated. In the LHC study and in the TESLA study only one coupling at a time is allowed to deviate from its Standard Model value. The sensitivities are based on statistical errors only*

more than three standard deviations on t quark couplings for masses of Kaluza-Klein particles of up to 50 TeV.

8.2 The anomalous magnetic moment $(g-2)_t$

The determination of $\widetilde{F}^{\gamma}_{2V}$ gives access to anomalous magnetic moment $(g-2)_t$ in a rather simple way. For instance $\widetilde{F}^{\gamma}_{2V} = Q_t(g-2)_t/2$. $(g-2)_t$ receives Standard Model contributions from QED, QCD and electroweak interactions [26]. One sees that this quantity will be measured to about 10% accuracy.

What is known about $(g-2)_t$? In Ref. [27] it said that the limits on g_t come from the reaction $b \to s\gamma$ giving a very crude constraint :

$$-3.5 < g_t < 3.6 \tag{16}$$

The expected precision on $(g-2)_t/2$ of 0.1% is proportional to m_t/M where M is the scale of compositeness. It follows hence that with the accuracy expected at the ILC the compositeness of the t quark can be tested up to about 100 TeV.

9 Summary and outlook

This article presents a comprehensive analysis of $t\bar{t}$ quark production using the semi-leptonic decay channel. Results are given for a centre-of-mass energy of $\sqrt{s} =$

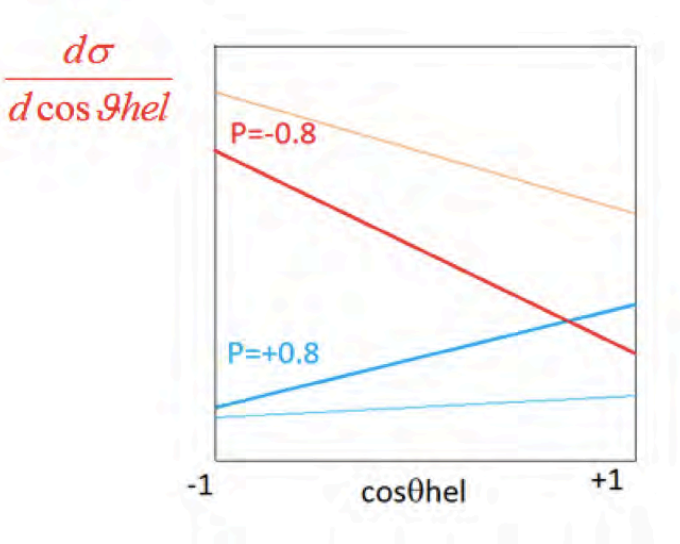

Figure 9: *Distributions of the helicity angle* $\cos\theta_{hel}$ *expected from the Standard Model (thick lines) and their modifications by the Randall-Sundrum framework (thin lines) described in the text. The results are shown for beam polarisations of* $\mathcal{P}, \mathcal{P}' = \pm 0.8, \mp 0.3$.

500 GeV and an integrated luminosity of $\mathcal{L} = 500\,\mathrm{fb}^{-1}$ shared equally between the beam polarisations. $P = \pm 0.8$ and $P' = \mp 0.3$.

Semi-leptonic events, including those with τ leptons in the final state can be selected with an efficiency of about 55%. The cross section of the semi-leptonic channel of $t\bar{t}$ quark production can therefore be measured to a statistical precision of about 0.5%. The second observable is the forward-backward asymmetry A^t_{FB}. It was shown that in particular for predominantly left handed polarisation of the initial electron beam the $V - A$ structure leads to migrations, which distort the theoretical expected A^t_{FB}. These migrations can be remedied by tightening the selection criteria of the events. Taking into account this correction the forward-backward asymmetry can be determined to a precision of better than 2% for both beam polarisations. Finally, the study introduced the slope of the helicity angle distribution, which is a new observable for ILC studies. This observable measures the fraction of t quarks of a given helicity in the event sample. This variable is very robust against e.g. the migration effects and can be measured to a precision of about 4%.

The observables together with the unique feature of the ILC to provide polarised beams allow for a disentangling of the individual couplings of the t quark to the Z^0 boson and the photon. These couplings can be measured with high precision at the ILC and always more than one order of magnitude better than it will be possible at the LHC with $\mathcal{L} = 300\,\mathrm{fb}^{-1}$. This precision would allow for the verification of a great number of models for physics beyond the Standard Model. Examples for these

models are extra dimensions and compositeness. The current analysis allows in the future to define observables to e.g. measure CP violation or to test other theoretical models. They constitute therefore a perfect basis for discussions with theoretical groups.

It has to be noted that the results contain only partially experimental systematical errors. These will have to be estimated in future studies. From the achieved precision it is mandatory that systematics are controlled to the 1% level or better in particular for the measurement of the cross section.

References

[1] A. Juste *et al.*, "Report of the 2005 Snowmass top/QCD working group" *ECONFC0508141:PLEN0043* (2005) , arXiv:hep-ph/0601112.

[2] **ILC Global Design Effort and World Wide Study**, N. Phinney, N. Toge, and N. Walker, eds., *ILC Reference Design Report Volume 3 - Accelerator*. 2007. arXiv:0712.2361 [physics.acc-ph]. ILC-REPORT-2007-001.

[3] "ILC TDR". https://forge.linearcollider.org/tdr.

[4] S. J. Parke and Y. Shadmi, "Spin correlations in top quark pair production at e^+e^- colliders" *Phys.Lett.* **B387** (1996) 199, arXiv:9606419 [hep-ph].

[5] **American Linear Collider Working Group Collaboration**, T. Abe *et al.*, "Linear Collider Physics Resource Book for Snowmass 2001 - Part 3" arXiv:hep-ex/0106057.

[6] R. D. Heuer, D. J. Miller, F. Richard and P. M. Zerwas (eds.), "Tesla technical design report part iii: Physics at an e^+e^- linear collider" arXiv:hep-ph/0106315.

[7] G. Moortgat-Pick *et al.*, "The role of polarized positrons and electrons in revealing fundamental interactions at the linear collider" *Phys.Rept.* **460** (2008) 131, arXiv:hep-ph/0507011.

[8] C. Schmidt, "Top quark production and decay at next-to-leading order in e^+e^- annihilation" *Phys.Rev.* **D54** (1996) 3250, arXiv:hep-ph/9504434.

[9] J. C. Brient and H. Videau, "The calorimetry at the future e^+e^- linear collider" *eConf* (2001) no. C010630, E3047, arxiv:hep-ex/0202004v1.

[10] "The International Large Detector - DBD". http://ific.uv.es/~fuster/DBD-Chapters/Chapter%204%20ILD.pdf.

[11] W. Kilian, T. Ohl, and J. Reuter, "WHIZARD: Simulating multi-particle processes at LHC and ILC" *Eur.Phys.J.* **C21** (2011) 1742, arXiv:0708.4233 [hep-ph].

[12] M. Moretti, T. Ohl, and J. Reuter, "O'mega: An optimizing matrix element generator" arXiv:hep-ph/0102195-rev.

[13] P. Doublet, *Hadrons in a highly granular SiW ECAL - Top quark production at the ILC*. PhD thesis, Laboratoire de l'Accélérateur Linéaire and Université Paris Sud - Paris XI, 2011. http://tel.archives-ouvertes.fr/tel-00657967.

[14] P. Doublet, F. Richard, T. Frisson, R. Pöschl, and J. Rouëné, "Determination of Top-quark Asymmetries at the ILC".

[15] I. Garcìa Garcìa, "Top quark studies at a Linear Collider" Master's thesis, Universitat de Valencia, 2012. http://digital.csic.es/handle/10261/64306.

[16] E. Barger *et al.*, "The Top Quark Production Asymmetries A^t_{FB} and A^ℓ_{FB}" *Phys.Rev.Lett.* **108** (2012) , arxiv:1201.1790 [hep-ph].

[17] C. Rimbault, P. Bambade, K. Mönig, and D. Schulte, "Impact of beam-beam effects on precision luminosity measurements at the ILC" *LAL 07-157, EUROTEV-Report-2007-017* (2007) . http://publication.lal.in2p3.fr/2007/lal07157.pdf.

[18] A. Rosca, "Measurement of the beam polarisation at the ILC using the WW annihilation data" *LC-REP-2013-009* . http://www-flc.desy.de/lcnotes/notes/LC-REP-2013-009.pdf.

[19] J. Fleischer, A. Leike, T. Riemann, and A. Werthenbach, "Elektroweak one-loop corrections for e^+e^- annihilation into $t\bar{t}$ including hard bremsstrahlung" *Eur.Phys.J.* **C31** (2003) 37, arXiv:hep-ph/0302259.

[20] E. Glover *et al.*, "Top quark physics at colliders" *ActaPhys.Polon.* **B35** (2004) 2671, arXiv:hep-ph/0410110.

[21] J. A. Aguilar-Saavedra, M. C. N. Fiolhais, and A. Onofre, "Top effective operators at the ILC" arXiv:1206.1033 [hep-ph].

[22] L. Randall and R. Sundrum, "A large mass hierarchy from a small extra dimension" *Phys.Rev.Lett.* **83** (1999) 3370, arXiv:9905221 [hep-ph].

[23] A. Djouadi, G. Moreau, and F. Richard, "Resolving the A^b_{FB} puzzle in an extra dimensional model with an extended gauge structure" *Nucl.Phys.* **B773** (2007) 43, arXiv:hep-ph/0610173.

[24] A. Djouadi, J. Moreau, F. Richard, and R. K. Singh, "The forward-backward asymmetry of top quark production at the Tevatron in warped extra dimensional models" *Phys.Rev.* **D82** (2010) 071702, arXiv:0906.0604 [hep-ph].

[25] A. Djouadi, J. Moreau, F. Richard, and R. Singh, "Forward-backward asymmetries of the bottom and top quarks in warped extra-dimensional models: LHC predictions from the LEP and Tevatron anomalies" *Phys.Lett.* **B701** (2011) 458, arXiv:1105.3158 [hep-ph].

[26] A. G. Grozin, P. Marquard, J. H. Piclum, and M. Steinhauser, "Three-Loop Chromomagnetic Interaction in HQET" *Nucl.Phys.* **B789** (2008) 277, arXiv:0707.1388 [hep-ph].

[27] L. Labun and J. Rafelski, "Top anomalous magnetic moment and the two photon decay of Higgs" arXiv:arXiv:1209.1046 [hep-ph].

Forward backward asymmetry in $e^+e^- \to t\bar{t}$ at $\sqrt{s} = 500\,\text{GeV}$ for fully hadronic decays of the $t\bar{t}$ pair

M.S. Amjad, T. Frisson, R.Pöschl, F. Richard, J Rouëné

Abstract

We determine the statistical precision for the forward back asymmetry A^t_{FB} in $e^+e^- \to t\bar{t}$ for the fully hadronic decay mode $t\bar{t} \to (bq\bar{q})(\bar{b}q\bar{q})$ at $\sqrt{s} = 500\,\text{GeV}$. Results are given for the beam polarisations $P(e^-, e^+) = (-80\%, +30\%)$ and $P(e^-, e^+) = (+80\%, -30\%)$ for an integrated luminosity of $250\,\text{fb}^{-1}$ for each polarisation. Only signal events are used for the analysis, with $\gamma\gamma$ overlay. The expected precisions are 2.9% in case of $P(e^-, e^+) = (-80\%, +30\%)$ and 3.2% in case of $P(e^-, e^+) = (+80\%, -30\%)$.

1 Introduction

Top quark physics is one of the most important channels at ILC. The forward backward asymmetry A^t_{FB} for fully hadronic decays of the top or t quarks was determined in the Letter of Intent of the ILD concept [1] for the beam polarisations $P, P' = -0.8, +0.3$ of the incoming electron and positron beams, respectively. The charge was to repeat this analysis for the detector DBD. Therefore, the analysis presented in this short note follows closely the procedure described in [2]. It is also a test for the updated software packages mainly `ILCSoft` and `LCFIPlus`.

2 Event selection

The present study assumes a centre-of-mass energy of $\sqrt{s} = 500\,\text{GeV}$ and a luminosity of $\mathcal{L} = 500\,\text{fb}^{-1}$ equality shared between the beam polarisations $P, P' = \pm 0.8, \mp 0.3$ of the incoming electron and positron beams.

We use the data generated with `WHIZARD 1.95`. The analysis is carried out on samples with fully polarised beams and then corrected for the realistic case of non-full beam polarisation. *We select the signal events for analysis, for which a $t\bar{t}$ pair is required to be present in the generated event record. For more details about the input samples, please read the Technical Remarks at the end of this note.* The software version `ILCSoft 01-16` is used for event

reconstruction. The package `LCFIPlus v00-05-02` is used for flavor tagging and vertex charge reconstruction.

The t quark decays nearly exclusively into a pair of b quarks and W bosons. The b quarks hadronise into a jet, called b jet hereafter, which contains a B meson. The six jet final state is reconstructed using the Durham jet finder. Subsequently the jets are analysed with the `LCFIPlus` package, which assigns a b likeness called b -tag to the jet. The two jets with the highest b-tag values are considered to be the jets from the b quarks. Events for which one of the b-tag values is smaller than 0.3 are rejected. The two W bosons are reconstructed from the remaining four jets. A combination of two jets, which are closest to the W mass, m_W, is defined to be W_1 while the remaining two are combined into W_2.

After having reconstructed the jets from W bosons and b quark jets, the jets are combined to form t quarks. Out of four possible combinations of two b jets with these Ws, $Top = W_i + b_k$ with $i, k = (1, 2)$, two tops are reconstructed with the minimal χ^2.

$$\chi^2 = \left(\frac{m_t - 174}{\sigma_{m_t}}\right)^2 + \left(\frac{E_t - 250}{\sigma_{E_t}}\right)^2 + \left(\frac{p_b^* - 69}{\sigma_{p_b^*}}\right)^2,$$

with

$$p_b^* = \gamma p_b (1 - \beta_t \cdot \cos(\theta_{tb}))$$

being the momentum of the b quark in the rest frame of the t quark, E_t the energy of the t quark candidate and m_t the mass of the t quark.

The defined χ^2 is a quality criterium for the events and only events that satisfy $\chi_1^2 < 20$ and $\chi_2^2 < 40$ are retained. Finally, events are selected for which both t quarks and both W bosons are in the range $50 < m_t < 200\,\mathrm{GeV}$ and $60 < m_W < 100\,\mathrm{GeV}$

After having selected the t quarks, the b quark charge Q_b at the vertex is determined to identify whether it came from a t or $\bar{t}$ quark. The charge at the vertex is reconstructed as the sum of the charge of all particles related to this vertex. For both jets $|Q_b| < 5$ is required, otherwise the event is rejected.

In order to verify the charge reconstruction it is compared with b quark and $\bar{b}$ quark in the Monte Carlo record. Additionally, a cross check is performed using B mesons, which are formed from the b quark. The Fig. 1 shows in its left part the measured jet charges originating from b or $\bar{b}$ quarks. The right hand part is the same but now the reference charge is given by a B meson in the jet. For the majority of the events the charge of the original particle is reconstructed correctly. The distributions are compatible with those shown in Ref. [2]. It should at this point be emphasised that the `LCFIPlus` package is so far not optimised for the charge measurement. This means that further improvement can be expected in the future.

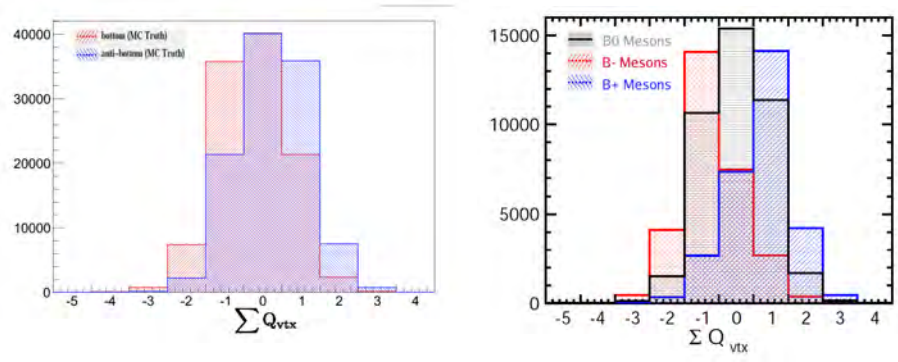

Figure 1: *Left: Reconstructed charge for jets originating from b or $\bar{b}$ quarks. Right: The charge of the B meson is taken as a reference for the verification of the vertex charge measurement.*

For the association of the b jets b_1 and b_2 having charge Q_{b_1} and Q_{b_2} to t or $\bar{t}$ the event charge $C = Q_{b_1} - Q_{b_2}$ is defined. The Fig. 2 shows the distribution of the event charge. As expected, most of the events have a non-zero C value, which in turn implies that we can distinguish between a t quark and a $\bar{t}$ quark. The following criteria are applied

- In case $C = 0$ an event is discarded;
- If $C < 0$ the b_1 is assumed to be produced in the decay of a t quark;
- If $C > 0$ the b_1 is assumed to be produced in the decay of a $\bar{t}$ quark.

All introduced event selection criteria are summarised in Table 1.

Cut number	*Type*
1	$\mathrm{b\,tag}_{1,2} > 0.3$
2	$\chi^2_1 < 20$ and $\chi^2_2 < 40$
3	$50 < m_t < 200\,\mathrm{GeV}$
4	$60 < m_W < 100\,\mathrm{GeV}$
5	$Q_b < 5$
6	$C \neq 0$

Table 1: *Cuts as applied in this analysis in the sequence as they appear in the text.*

The final selection efficiency is about 13% independent for both beam polarisations. This is about 8% smaller than reported in [2]. The main reason for this is the relatively hard cut on the W boson mass, see Sec. 4 for further discussion.

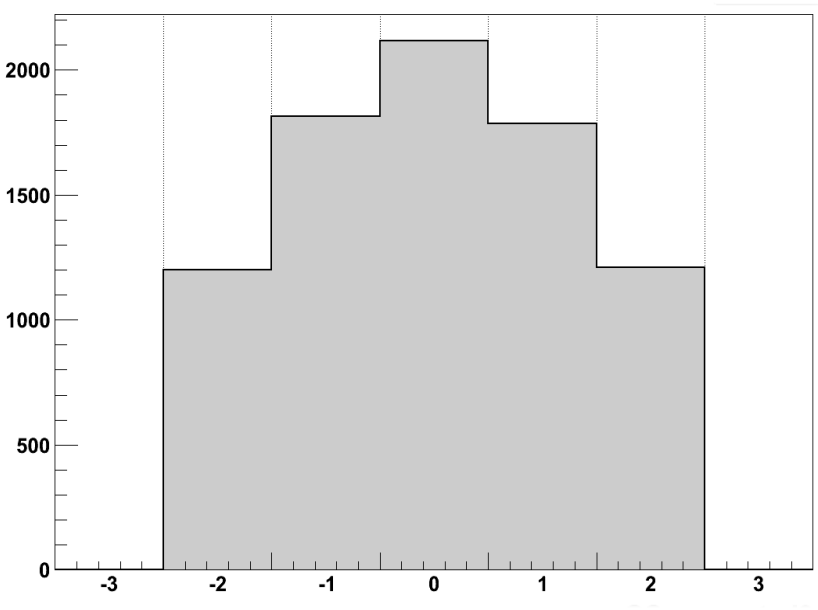

Figure 2: *Event Charge* $C = Q_{b_1} - Q_{b_2}$*, the variable used to identify the charge of top quark.*

3 Determination of the forward backward asymmetry $\mathbf{A_{FB}^t}$

The forward backward asymmetry is defined as follows

$$A_{FB}^t = \frac{N(0 < \theta_{top} \leq \frac{\pi}{2}) - N(\frac{\pi}{2} < \theta_{top} \leq \pi)}{N(0 < \theta_{top} \leq \frac{\pi}{2}) + N(\frac{\pi}{2} < \theta_{top} \leq \pi)}$$

The polar angle θ_{top} is defined w.r.t. to the incoming electron beam. The quantity N is the number of events in the different detector hemispheres.

For convenience the asymmetry is given for t quarks only and the angle of $\bar{t}$ is inverted by π to add it to t.

$$\cos\theta_t = -1 * \cos\theta_{\bar{t}}$$

The Fig. 3 shows the forward backward asymmetry for the polarisation $P, P' = -1, +1$ after the selection described in the previous section. A clear asymmetry is visible. The measured charge of the b quark is compared with the MC truth and remaining events with a wrong charge assignment are identified. These events are also indicated in Fig. 3.

For about 65% of the t quarks selected according to Sec. 2 the charge is measured correctly. For the final result events with wrong charge assignment are subtracted from the number of observed events. The resulting

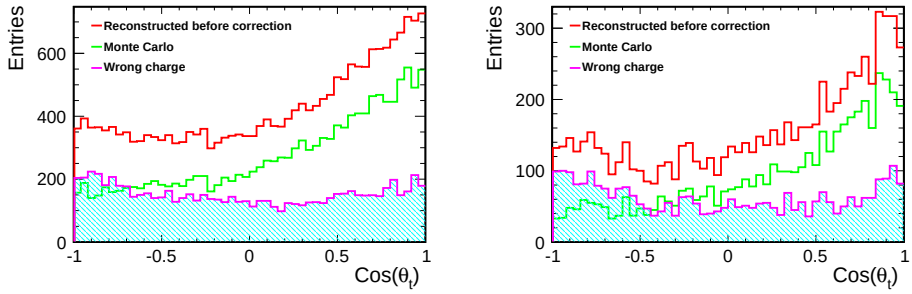

Figure 3: *Left: Asymmetry for $P, P' = -1, +1$ after application of cuts in Tab. 1. The figure shows in addition the generated distribution and the events for which the b quark charge is incorrectly reconstructed. Right: The same as left but for $P, P' = +1, -1$*

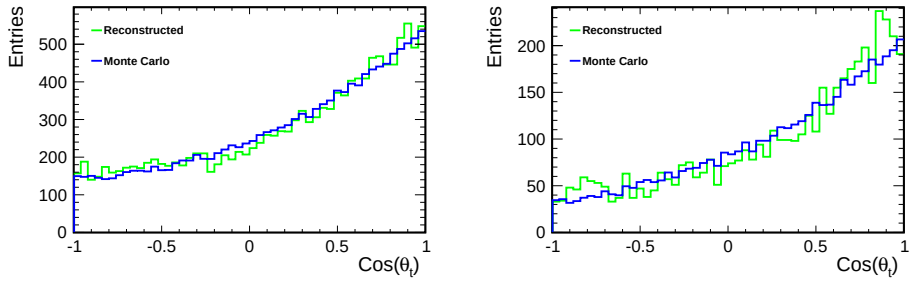

Figure 4: *Left: Asymmetry for $P, P' = -1, +1$ after application of cuts in Tab. 1 and correction for events in which the b quark charge was incorrectly reconstructed. The corrected result is compared with the generated distribution. Right: The same as left but for $P, P' = +1, -1$*

asymmetries for both beam polarisations are shown in Fig. 4 and the results are summarised in Tab. 2. Note, that 1/4 of the difference between generated and reconstructed A^t_{FB} is taken as the systematic error. The statistical error is given for the number of events expected for $250\,\mathrm{fb}^{-1}$ and $P, P' = \pm 0.8, \mp 0.3$

P, P'	$(A^t_{FB})_{gen.}$	A^t_{FB}	$(\delta_{A_{FB}}/A_{FB})_{stat.}$ [%]	$(\delta_{A_{FB}}/A_{FB})_{syst.}$ [%]
$-1, +1$	0.355	0.344	2.9 (corrected to $P, P' = -0.8, +0.3$)	0.8
$+1, -1$	0.438	0.443	3.2 (corrected to $P, P' = +0.8, -0.3$)	0.3

Table 2: *Precisions expected for A^t_{FB} for different beam polarisations.*

4 Discussion of results

The selection efficiency in the present analysis is about 8% smaller than this was case for the LOI study. The reason is mainly the tighter selection cuts on the W boson mass. The analysis cuts have been varied within reasonable limits. The efficiency can be increased to about 20% and better while the absolute result of A_{FB}^t changes by less than 6%. It might also be required to define different selection cuts for the two configurations of the beam polarisation. Clearly, the definition of an optimal cut scenario is a task for further studies. A major source of systematic error is that the final correction for wrongly measured b quark charges is based on Monte Carlo truth information. This is turn would require a perfect modeling of the final state. The error of the charge measurement may however be controlled in situ with semi-leptonic events. More studies on the optimisation of the measurement b or charge are needed in the future.

5 Summary and outlook

A repetition of the LOI analysis of the asymmetry A_{FB}^t in fully hadronic decays of the t quark is presented. The asymmetry A_{FB}^t can be measured with a precision of about 3%. The obtained result is within statistical limits compatible with what ILD has presented in the LOI. The analysis may be improved by means of an optimisation of the analysis cuts. The new `LCFIPlus` package is not yet optimised for the measurement of the b quark charge. Yet it gives already results, which are at least similar to those of the LOI. This promises future improvement of the study. In order to control systematic effects due to a non-perfect modeling of the final state, the charge measurement can be studied using semi-leptonic events. In general it is clearly attractive to investigate how the fully hadronic and semi-leptonic analysis can be combined in the future. In addition the full SM background will have to be included. Due to reasons of limited time this was not possible up to now. In the LOI analysis it was however shown that this is no major concern.

Technical remarks

The events are generated with version 1.95 of the `WHIZARD` event generator [3, 4] in form of six fermion final states. The generated events are then passed to the PYTHIA simulation program to generate parton shower and subsequent hadronisation. For this events are selected for which the difference between the invariant masses of the three fermion systems forming a t quark from WHIZARD and the input t quark mass to WHIZARD of 174 GeV is smaller than $5\Gamma_t$. Here Γ_t is the total decay width of the t quark. By this only about

70% of the events generated by WHIZARD are recognised as $t\bar{t}$ events and treated accordingly. The analysis is based on the described sub-selection of events. In reality only the six fermion final state is available. The relation between the measurement of the six fermion final state and e.g the couplings of the t quark to the photon and the Z^0 boson remains to be established.

References

[1] The ILD Concept Group.
The International Large Detector - Letter of Intent.
DESY 2009-87, Fermilab-Pub-09-682-E, KEK Report 2009-6, arXiv:1006.3396v1 [hep-ex].

[2] Katsumasa Ikematsu, Akiya Miyamoto and Keisuke Fujii. arXiv:1005.4635v1 [hep-ex] 25 May 2010.

[3] W. Kilian, T. Ohl, and J. Reuter, "Whizard: Simulating multi-particle processes at lhc and ilc" *Eur.Phys.J.* **C21** (2011) 1742, arXiv:0708.4233 [hep-ph].

[4] M. Moretti, T. Ohl, and J. Reuter, "O'mega: An optimizing matrix element generator" arXiv:hep-ph/0102195-rev.

The potential of the $t\bar{t}$ charge asymmetry measurement at a Linear Collider with $\sqrt{s}$ in the range 500 GeV − 1 TeV

I. Garcia[1], E.Ros[1], J.Trenado[2], M.Vos[1]

[1] IFIC (Univ. Valencia - CSIC), Spain
[2] Univ. Barcelona, Spain

DOI: will be assigned

Precision measurements of electroweak parameters are a sensitive probe for BSM physics. In this lecture it is shown how to extract experimentally the top forward-backward charge asymmetry at a Linear Collider with $\sqrt{s}$ in the range 500 GeV − 1 TeV (even without beam polarizations). We show that ambiguities in the top reconstruction, present at $\sqrt{s} = 500$ GeV, are removed for $\sqrt{s} = 1$ TeV and beyond.

1 The FB charge asymmetry for top quarks

The FB charge asymmetry for top quarks is defined as

$$A_{FB}(t) = \frac{N_F - N_B}{N_F + N_B}$$

where $N_F(N_B)$ are defined as the number of events with forward (backward) outgoing top quark. The direction of the top is defined relative to the incoming electron direction. Therefore, if θ is the angle between the incoming electron and the outgoing top, N_F is the number of events with $\cos\theta > 0$ and N_B the number of events with $\cos\theta < 0$. The same holds for the incoming positron and the outgoing antitop.

The FB charge asymmetry has been extensively studied at LEP ($\sqrt{s} = M_Z$) for all fermions except top, that could not be procuced since the center-of-mass energy of LEP is below top production threshold. Table 1 shows the FB asymetries measured by LEP experiments [1]. One can notice some tension between the SM value and the measurement for b-quarks. The measurement of the left-right symmetry by SLD [] offers a complementary constraint on the $Z/\gamma^* q\bar{q}$ vertex. These two sets of measurements provide the most precise measurements of the Weinberg angle, that differ at the 3 σ level.

Table 1: FB asymmetries measured by LEP experiments at $\sqrt{s} = M_Z$.

A_{FB}	measured value	deviation (in sigmas)
e	0.0145(25)	−0.7
μ	0.0169(13)	+0.6
τ	0.0188(17)	+1.6
s	0.0976(114)	−1.4
c	0.0707(35)	+0.8
b	0.0992(16)	−2.3

The FB asymmetry can be shown to be sensitive for example to warped Extra Dimension models [3] and in general to a large variety of BSM models.

A top charge asymmetry can also be defined for hadron colliders [4]. Evidence for a deviation from the value predicted by the Standard Model is claimed by the CDF collaboration for events with large invariant mass ($m_{tt} > 450$ GeV [5]). The D0 collaboration finds no statistically significant enhancements of A_{FB}, neither for high $m_{t\bar{t}}$ nor for top quark pairs with a large rapidity difference.

A top charge asymmetry can be also defined at the LHC, where gluon-gluon collisions form the main source of top production. In this case one defines the asymmetry as

$$A_c = \frac{N_+ - N_-}{N_+ + N_-}$$

where $N_+(N_-)$ is the number of events with $|y_t| - |y_{\overline{t}}| > 0 (< 0)$, where y_t and $y_{\overline{t}}$ are the rapidity of the top quark and anti-top quark, respectively. This quantity should vanish in the SM, except for % level higher order corrections in QCD. The first analyses of the CMS and ATLAS experiments have not observed any anomaly in this quantity:

$$A_c = -0.013 \pm 0.028^{+0.026}_{-0.031} \qquad \text{[CMS, 1.09 } fb^{-1} \text{ [7]]}$$

$$A_c = -0.024 \pm 0.016 \pm 0.023 \qquad \text{[ATLAS, 0.7 } fb^{-1} \text{ [8]]}$$

The analysis of this asymmetry, together with other observables like the total cross-section and the invariant mass spectrum, can be used to constrain a large variety of BSM models.

Concerning $A_{FB}(t)$ for a Linear Collider, it can be used as a benchnark for the sensitivity to detect a seuential Z' well beyond the $\sqrt{s}$ of the collider. This resonance will interfere with the γ/Z to produce a deviation in $A_{FB}(t)$. If we assume a precision for this asymmetry of 1.5%, the sensitivity at $\sqrt{s} = 500$ GeV is up to a mass of 3 TeV. For a Collider with $\sqrt{s} = 1$ TeV, the sensitivity goes beyond 5 TeV. In certain warped ED models [9], the sensitivity is considerably enhanced for top quarks. Technically, $A_{FB}(t)$ is more easy to measure at $\sqrt{s} = 500$ GeV due to an increased cross-section (0.6 pb, compared to 0.2 pb at 1 TeV), resulting in a statistical error of $\Delta A_{FB} = 0.4\%$ (compared to 0.7% at 1 TeV), if we assume a total integrated luminosity of 1 ab^{-1} and event acceptance od 12% for semileptonic top decays. In practice the situation is more complicated due to problems in the top reconstruction at the low energy (see next section) and to an increased sensitivity of the asymmetry to the top mass uncertainty resulting in $\Delta A_{FB} = 0.4\%$ at $\sqrt{s} = 500$ GeV, to be compared to $\Delta A_{FB} = 0.1\%$ at 1 TeV. In both cases we assume a precision of 1.6 GeV for the top mass.

We note here that the use of polarized electron and/or positron beams allows for a more precise determination of the top quark couplings than that possible with A_{FB}. This study will be extended to include a study of the left-right asymmetry, but in this note these results are not yet included.

2 Top quark reconstruction

The top quark decays to a W boson and a bottom quark with a branching fraction close to 100 %. Depending on whether the W bosons decays to a charged lepton and a neutrino or to quark anti-quark, the final state formed in $t\bar{t}$ pair production is categorized as:

- fully hadronic: both W-bosons decay to quark anti-quark, resulting in a final state with at least six jets and no isolated leptons
- one lepton + jets (or semi-leptonic): one W boson decays to a charged lepton and a neutrino, yielding a distinctive signature of an isolated lepton and missing (transverse) energy and at least four jets
- di-lepton: both W-bosons decay to a charged lepton and a neutrino, leading to a final state with two isolated leptons, missing energy with contributions from two neutrinos and two b-jets

In many analyses (at hadron colliders) final states with τ-leptons form a separate category to deal with the difficulties inherent in the isolation of hadronic τ-lepton decays and the ambiguities due to the additional neutrinos in leptonic τ-lepton decays.

Reconstruction algorithms have been developed for these different final states. In final states with at most one leptonically decaying W-boson the measurement of the missing energy can be used to reconstruct the neutrino momentum. In hadron colliders, the missing transverse energy is identified with the neutrino p_T, while the longitudinal component of the neutrino momentum is inferred (with a two-fold ambiguity) from the measured lepton momentum and the W-mass constraint. Jets are assigned to top quark candidates using a combination of b-tagging information and mass constraints. The ambiguities that inevitably arise in this procedure are studies in detail in the next section.

In the years leading up to the start-up of the LHC many authors have pointed to the experimental challenge posed by the reconstruction of highly boosted top quarks [10, 11]. Since then, new techniques have been developed that are geared particularly towards the highly collimated topologies that form in the N-body decay of highly boosted objects [12, 13]. The LHC experiments have evaluated the potential of these methods in detailed MC simulations [14] and have tested some of the crucial assumptions in analyses of the first LHC data [15, 16, 17]. We expect that these techniques will reach maturity to provide a new window on BSM physics at the LHC and future high-energy e^+e^- colliders.

3 Results for a future linear collider

In the following we present a study of top reconstruction using the PYTHIA generator, including ISR, and a fast simulation of the detector response, for both center-of-mass energies of 500 GeV and 1 TeV. Our 500 GeV simulation study gives an overall result compatible to another result presented in this workshop, using this time a full simulation based on the ILD detector [18]. We claim therefore that the reconstruction problems that we observe at the low energy (500 GeV) are intrinsic of the event configuration and cannot be removed by an improved detector resolution.

Semi-leptonic quark decays are selected by demanding a highly energetic electron ($E_l > 20$ GeV, $|\cos\theta_l| < 0.996$), missing energy ($p_{miss} > 20$ GeV) and at least 4 jets in the event. Note that the missing energy is obtained from the momentum imbalance in the 3 directions x, y, z, ignoring therefore ISR, that for $t\bar{t}$ is very small, since radiative return to the Z^0 is forbidden. It is possible in this way to obtain the full momentum imbalance (i.e. the neutrino energy) and not just its transverse component as for hadron colliders. The next step in the selection is the reconstruction of the W from the leptonically decaying top-quark. This is achieved by demanding

$$|M_{inv}(l - miss) - M_W| < 25(35) \quad \text{GeV}$$

for 500 GeV and 1 TeV, respectively, $M_W = 80.4$ GeV being the W mass. The leptonic top reconstruction is achieved by demanding

$$|M_{inv}(W - j) - M_t| < 35(60) \quad \text{GeV}$$

for 500 GeV and 1 TeV, respectively, $M_t = 175$ GeV being the top mass, and j a jet with $E_j > 20$ GeV and $|\cos\theta_j| < 0.996$. The jet j producing the best fit is selected as the 'b-jet' from the top semi-leptonic decay. No b-tagging requirement is imposed besides this fitting condition. The final requirement is that the total beam energy can be reconstructed from the energy of the various particles produced in the decay of the top quark, i.e.

$$|E_W + E_j - E_{beam}| < 75(200) \quad \text{GeV}$$

for 500 GeV and 1 TeV, respectively, E_{beam} being the beam energy of 250 (500) GeV.

Only the leptonic side of the reconstructed top is used in the analysis. The charge of the lepton can be related to the charge of the top (l^+ for top, l^- for antitop) and allows therefore the reconstruction of the scattering angle θ between the incoming e^- and the outgoing top (or between e^- and the antitop). This scattering angle (that provides the A_{FB} asymmetry) is displayed in Fig. 1a and Fig. 1b, for 500 GeV and 1 TeV, respectively.

We can see that at $\sqrt{s} = 500$ GeV a very large migration in the reconstructed $\cos\theta$ distribution, leading to a reduced asymmetry of 0.22, to be compared to the partonic value of 0.40. Similar problems in mapping the reconstructed top quark direction back onto the true direction are reported by the LHC collaborations. Repeating our study for the LHC environment, we find our response matrices are in qualitative agreement with those found by ATLAS in Reference [8].

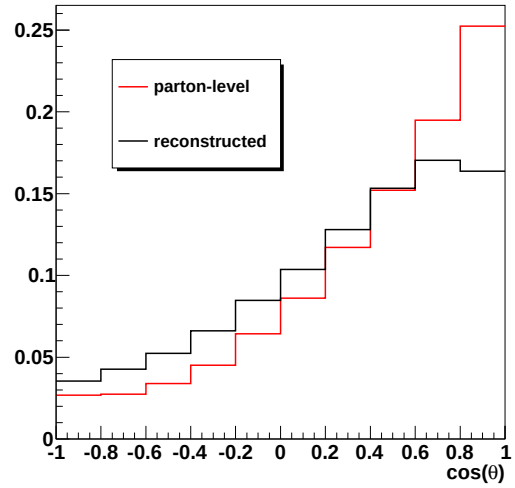

(a) 500 GeV

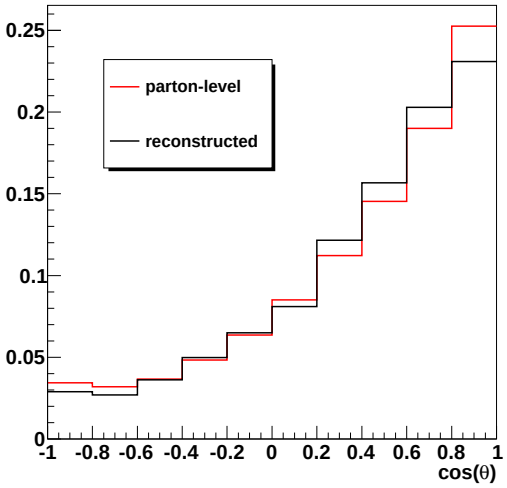

(b) 1 TeV

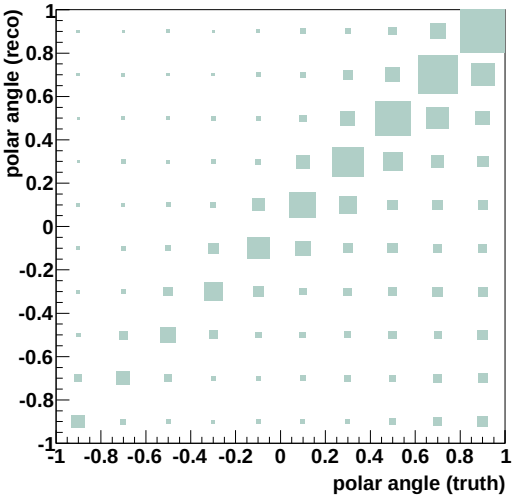

(c) 500 GeV

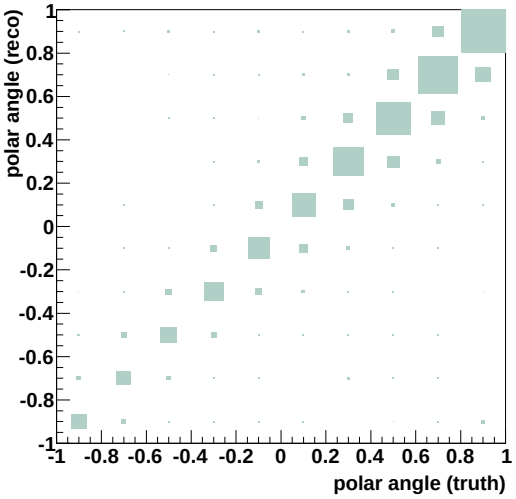

(d) 1 TeV

Figure 1: $\cos\theta$ distribution for top quark scattering at center-of-mass energies of (a) 500 GeV and (b) 1 TeV. The reconstructed distribution using a fast detector simulation is compared to the distribution obtained at the partonic level. The 2D response matrices are shown in (c) for 500 GeV and (d) for 1 TeV.

This migration effect has almost vanished at 1 TeV, where the reconstructed and partonic asymmetries are 0.52 and 0.56, respectively. In the following, we discuss the origin of this migration effect. This origin is the impossibility to select the correct b-quark from the leptonic top decay for any detector with finite resolution, as illustrated in Fig. 2a. This figure shows at parton level, and for the 500 GeV case, the reconstructed top mass using the correct b-quark and also the wrong combination. Fig. 2b shows the same result after including detector simulation. This figure shows a very large overlap between both distributions, implying a very large probability for confusing the correct and the wrong b-quarks. This probability is in fact of the order of 40%. When the wrong b-quark is selected, the direction of the reconstructed top is erratic, leading to the migration effect discussed before.

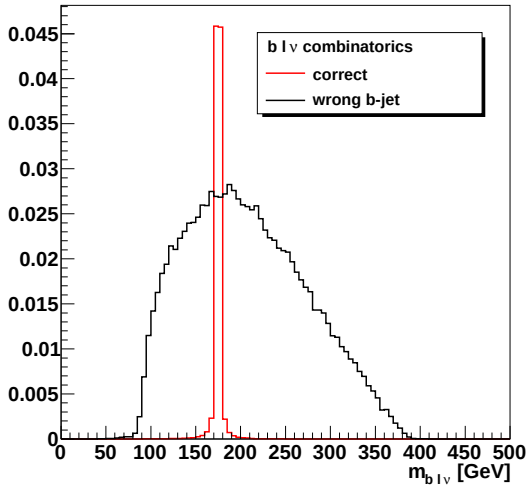

(a) 500 GeV

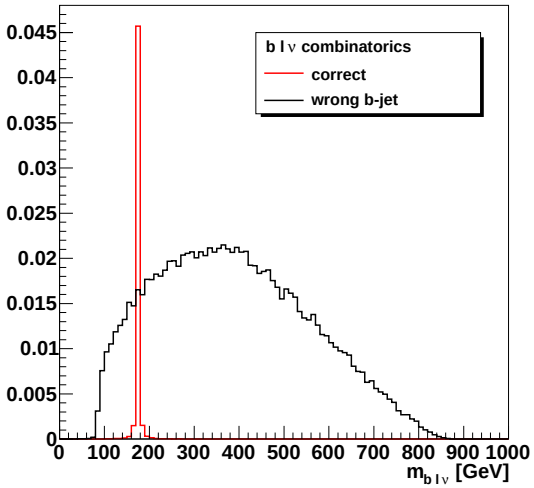

(b) 1 TeV

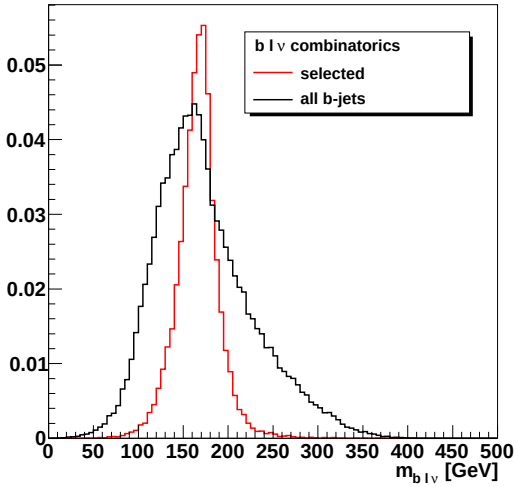

(c) 500 GeV

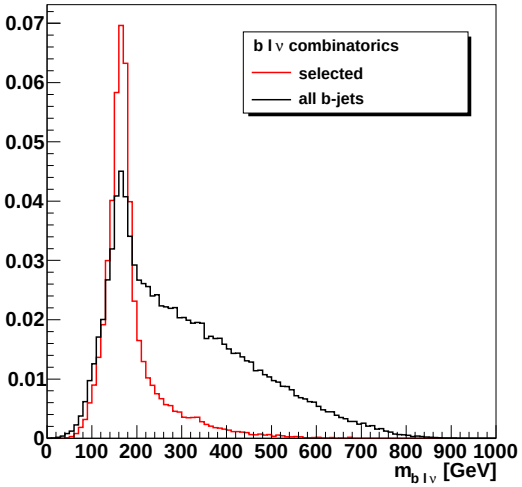

(d) 1 TeV

Figure 2: Reconstructed top (a,b) at parton level and (c,d) after detector simulation. In both cases the comination using the correct b-quark (red) and wrong combinatuons (black) are presented. The center-of-mass energy is 500 GeV. The same quantities, (c) and (d), are also displayed at 1 TeV.

The power of the top quark mass constraint to resolve the ambiguities increase slightly at 1 TeV, as seen in Fig. 2c and Fig. 2d. A drastic improvement is achieved using the boost of the top quarks (at 500 GeV they are nearly at rest). As a result the lepton and the correct b-quark are close together, as illustrated by Fig. 3 that shows the quantity $cos(\theta_b - \theta_l)$ at 500 GeV (a) and 1 TeV (b). A simple cut of the type $cos(\theta_b - \theta_l) > 0$ is sufficient to select the correct b-quark and therefore remove the migration effect discussed before. An improved detector resolution may have some impact in the migration effect observed at 500 GeV, as discussed in [18], where the full capabilities of the ILD detector are used. It is noted however that the migration effect is still present with this improved resolution, and is even present at the parton level.

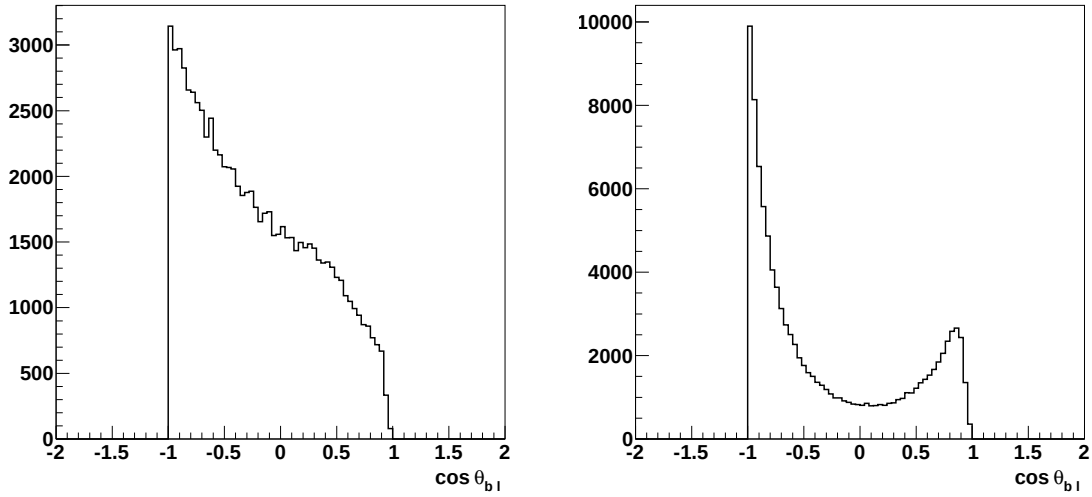

(a) 500 GeV (b) 1 TeV

Figure 3: $|cos(\theta_b - \theta_l)$ at 500 GeV (a) and 1 TeV (b).

4 Summary and conclusions

1) A measurement of the FB top asymmetry at ILC-1000 (or CLIC-3 TeV) is complementary in several ways to a measurement at CLIC-500, since statistical and systematic errors differ substantially, but add finally to a total value with similar uncertainty.
2) The relatively modest boost at 1 TeV is sufficient to circumvent the potentially large systematic due to ambiguities in the assignement of b-jets to top-quarks candidates.
3) These conclusions will be reinforced by repeating the analysis with full simulation and extending the number od observables to quantities like, for example, LR asymmetries.

Acknowledgements

The authors would like to thank the organizers of the LC forum for the opportunity to share these results and Franois Richard for his very helpful suggestions.

References

[1] PDG2010, K.Nakamura et al., Journal of Physics G37 (2010) 075021.
The LEP Collaborations, the LEP Electroweak Working Group, The SLD Heavy Flavour and Electroweak Working Groups, CERN-EP/2000-016, January 2000.

[2] SLD collaboration, Phys.Rev.Lett.84:5945-5949,2000.

[3] A.Djouadi, G.Moreau, F.Richard, Nucl.Phys. B773 (2007) 43.

[4] J.H.Kuhn, G.Rodrigo, Phys.Rev. D59 (1999) 054017.

[5] CDF Collaboration, Phys.Rev. D83(2011)112003.

[6] D0 Collaboration, Phys.Rev. D84(2011)112005.

[7] The CMS Collaboration CMS-TOP-11-014 [arXiv:1112.5100 [hep-ex]]

[8] The ATLAS Collaboration ATLAS-CONF-2011-106

[9] F. Coradeschi, LCWS10 workshop, Beijing (China), 2010.
M. Battaglia, LCWS11 workshop, Granada (Spain), 2011.

[10] B. Lillie, L. Randall and L. T. Wang, JHEP **0709** (2007) 074 [arXiv:hep-ph/0701166].

[11] K. Agashe, A. Belyaev, T. Krupovnickas, G. Perez and J. Virzi, Phys. Rev. D **77** (2008) 015003 [arXiv:hep-ph/0612015].

[12] A. Abdesselam *et al.*, Eur. Phys. J. C **71** (2011) 1661 [arXiv:1012.5412 [hep-ph]].

[13] A. Altheimer *et al.*, arXiv:1201.0008 [hep-ph].

[14] The ATLAS collaboration ATL-PHYS-PUB-2010-008

[15] The ATLAS collaboration ATLAS-CONF-2011-073

[16] The CMS collaboration CMS-PAS-JME-10-013

[17] The CMS collaboration CMS-PAS-EXO-11-006

[18] R.Poeschl, 'Top quark studies at 500 GeV', this workshop.

Measurement of the top Yukawa coupling at $\sqrt{s} = 1$ TeV using the ILD detector

Tony Price[a], Tomohiko Tanabe[b], Keisuke Fujii[c], Victoria Martin[d], Nigel Watson[a]

[(a)]University of Birmingham, United Kingdom; [(b)]ICEPP, The University of Tokyo, Japan; [(c)]High Energy Accelerator Research Organization, Tsukuba, Japan; [(d)]University of Edinburgh, United Kingdom

Abstract

We evaluate the potential of the International Large Detector (ILD) to measure the top Yukawa coupling of a 125 GeV Higgs boson at the International Linear Collider (ILC) operating at $\sqrt{s}$=1 TeV. The hadronic and semileptonic decay modes of the process, $e^+e^- \to t\bar{t}H$, are considered with the Higgs boson decaying via the dominant $b\bar{b}$ channel. Two methods are used to perform the analysis, a cut based approach and a multivariate approach using the TMVA package. When combining the hadronic and semileptonic decay modes a statistical uncertainty on the top Yukawa coupling of 4.3% can be achieved using the multivariate approach.

1 Introduction

The International Linear Collider (ILC) is a proposed e^+e^- linear collider which will operate at centre-of-mass energies up to 1 TeV. Due to the nature of e^+e^- colliders the state of the initial interaction can be controlled and calculated with a high degree of certainty and thus high precision measurements can be achieved. This will allow a rich physics program to be completed including accurate measurements of the couplings of the Higgs boson to matter. According to the Standard Model (SM) of particle physics, the strength of the Yukawa coupling of the Higgs boson to matter fermions scales with the mass of these particles by

$$g_{ffH} = \frac{M_f}{v} \tag{1}$$

where M_f is the mass of fermion and $v = 246\,\text{GeV}$ is the vacuum expectation value.

Figure 1 demonstrates the expected experimental precision of the Yukawa couplings of the Higgs boson after running several years at each center-of-mass energies at 250 GeV, 500 GeV, and 1 TeV. As the top quark is the heaviest

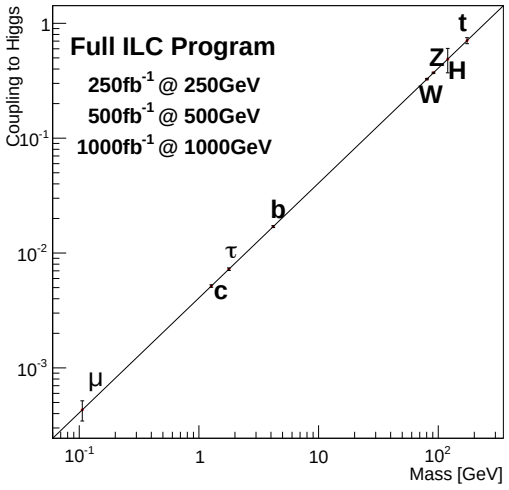

Figure 1: Expected experimental precision of the Yukawa couplings of the Higgs boson following a full ILC program running at 250 GeV, 500 GeV, and 1 TeV [1].

known particle in the SM, its Yukawa coupling is expected to be the largest. Any deviations away from the SM in the

couplings would be an indication of new physics. It is thus essential to evaluate the capability of the ILC to measure the top Yukawa coupling. It is also worthwhile to note that the measurement of the top quark polarization combined with the beam polarization information offers the possibility of determining structure of the $t\bar{t}H$ coupling, although this is beyond the scope of this analysis.

In principle, the top Yukawa coupling could be measured indirectly. This could be achieved either through top pair production near threshold provided that the theoretical uncertainties are reduced to $O(1)\%$ level, or via the $H\to gg$ decay channel where the top quark contribution dominates in the loop. However, whilst the top quark, due to it having the largest mass, is favoured in the loop there are other interfering processes which are reliant on Higgs couplings which lead to increased theoretical uncertainties. Direct measurements of the top Yukawa coupling is thus desired.

At the ILC, the direct measurement of the top Yukawa coupling becomes possible starting at around $\sqrt{s} = 500\,\text{GeV}$ via the $e^+e^- \to t\bar{t}H$ reaction. The optimal centre-of-mass energies to measure the top Yukawa coupling are $\sqrt{s} = 700$–$800\,\text{GeV}$, around which the $e^+e^- \to t\bar{t}H$ production cross section attains its maximum. However, one must also keep in mind the concurrency of various measurements at the ILC. By far the most demanding in terms of integrated luminosity is the Higgs self-coupling measurement. At around $\sqrt{s} = 500\,\text{GeV}$ the $e^+e^- \to ZHH$ reaction reaches its maximum cross section, making 500 GeV the first important energy for this measurement. The $e^+e^- \to \nu\bar{\nu}HH$ reaction via WW fusion rises at higher energies, which demands a centre-of-mass energy as high as possible. At the ILC, $\sqrt{s} = 1\,\text{TeV}$ is the highest centre-of-mass energy that is considered to be technologically feasible. It also remains to show that the ILC detectors are capable of performing physics measurements at $\sqrt{s} = 1\,\text{TeV}$. Several reactions were chosen as detector benchmarks including the top Yukawa coupling measurement.

The final state consists of eight fermions with at least four jets, potential leptons, and missing energy and this study will also demonstrate the ability of the ILD detector to reconstruct complicated topologies.

In this note, the precision of the top Yukawa coupling is estimated using the International Large Detector (ILD) concept.

2 Signal and Backgrounds

Figure 2 summarizes the cross sections for signal and typical background processes as a function of the center-of-mass energy. Figure 3 illustrates the lowest order Feynman diagrams for the process $e^+e^- \to t\bar{t}H$. The diagram $e^+e^- \to ZH$

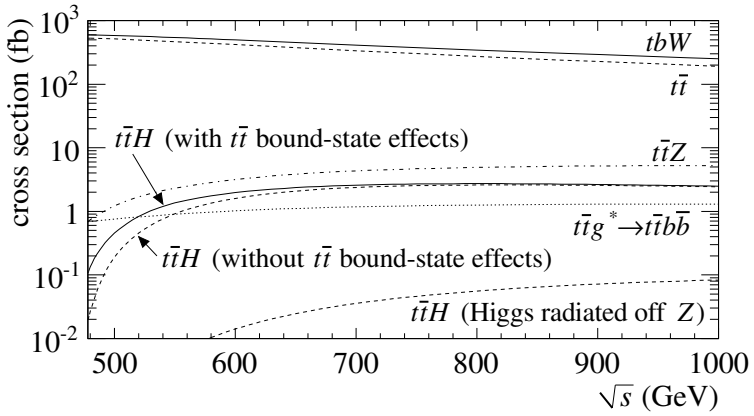

Figure 2: Summary of cross sections for signal and background processes for unpolarized initial beams [2].

(Higgs-strahlung) with $Z\to t\bar{t}$ which does not contain the top Yukawa coupling has small yet non-negligible contribution to the total cross section. The size of this effect is studied by looking at how the $e^+e^- \to t\bar{t}H$ cross section varies when modifying the top Yukawa coupling from the SM value using the cross section calculation of the event generator. The result is shown in Fig. 4 for $e_L^- e_R^+$ initial state (left) and $e_R^- e_L^+$ initial state (right). It is found that a quadratic curve models the behavior of the cross section dependence on the top Yukawa coupling quite well. The slope $d\sigma/dy_t$ is extracted at the SM value of the top Yukawa coupling to compute the factor needed to convert the precision in the cross

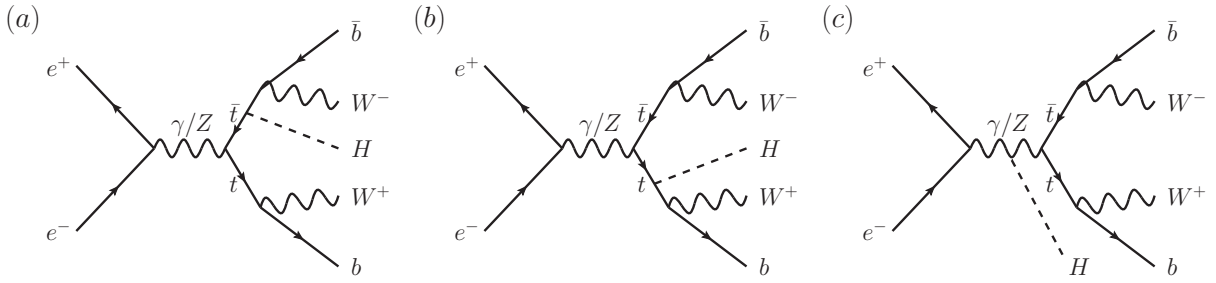

Figure 3: The lowest order Feynman diagrams for the process $e^+e^- \to t\bar{t}H$. In (a) and (b) the Higgs boson is radiated from a top quark and (c) is the background Higgs-strahlung process where the Higgs boson is radiated from the Z boson.

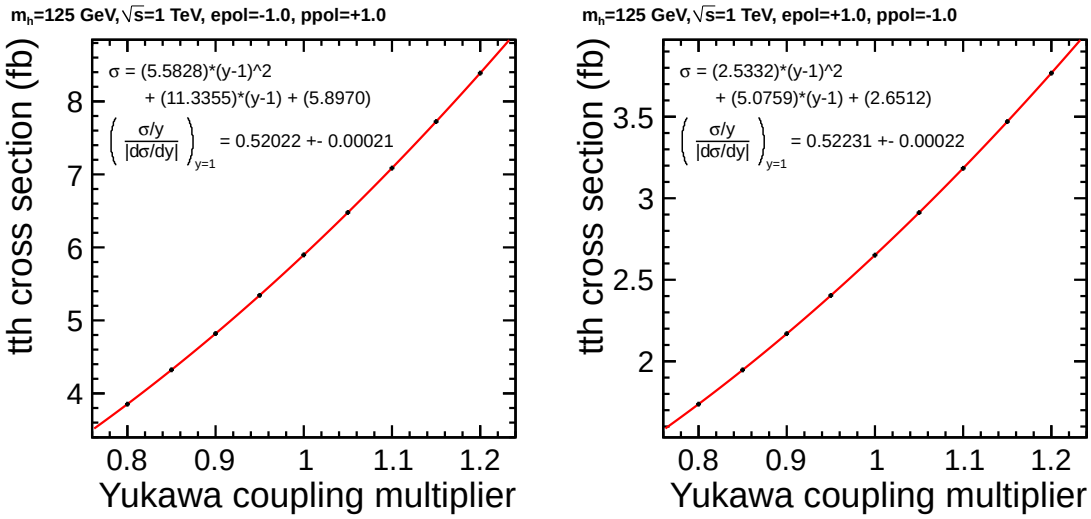

Figure 4: Sensitivity of the cross section to the top Yukawa coupling for $e_L^- e_R^+$ initial state (left) and $e_R^- e_L^+$ initial state (right).

section into the precision of the top Yukawa coupling, using the following equation:

$$\frac{\Delta y_t}{y_t} = \left(\frac{\sigma/y_t}{|d\sigma/dy_t|} \right)_{y_t = y_t(SM)} \frac{\Delta\sigma}{\sigma}. \tag{2}$$

The pre-factor in the r.h.s. is exactly equal to 1/2 if there is no contribution of the Higgs-strahlung diagram. In actuality, we find that $\left(\frac{\sigma/y_t}{|d\sigma/dy_t|} \right)_{y_t = y_t(SM)} = 0.52$. which indicates that the Higgs-strahlung contribution is about 4% of the total cross section. This factor will be used in the final extraction of the top Yukawa coupling precision.

For this study the semileptonic and hadronic decays of the $t\bar{t}$ system were studied with the Higgs decaying via the dominant decay mode into a $b\bar{b}$ pair. For the fully hadronic decay channel this leads to a signal of 8 jets, 4 of which should be tagged as b-jets. In the semileptonic mode the final signal in the detector consists of 6 jets, 4 of which should be tagged as b-jets, an isolated lepton, and missing energy and momentum from a neutrino. These two competing modes act not only as a signal process but also as a background to each other.

Irreducible backgrounds to these processes arise from the 8 fermion final states of $t\bar{t}Z$ where the Z decays into a $b\bar{b}$ pair and $t\bar{t}b\bar{b}$ where the $t\bar{t}$ system radiates a hard gluon which forms a $b\bar{b}$ pair. A large background contribution arises from $t\bar{t}$ due to the huge relative cross section compared to the signal. There is also a contribution from the other decay modes of the $t\bar{t}H$ system such as the Higgs not decaying to a $b\bar{b}$ pair and the fully leptonic decays of the top quarks.

The signal is selected using the variables described in Section 6 via the methods described in Sections 7 and 8.

3 Sample Generation

The samples for this study were generated using two event generators, WHIZARD v1.95 [3], and PHYSSIM [4]. The $t\bar{t}$ samples were generated using WHIZARD whereas the $t\bar{t}H$, $t\bar{t}b\bar{b}$, and $t\bar{t}Z$ samples used PHYSSIM due to its improved phase space integration time for the eight fermion final states compared to WHIZARD. We include as background all six fermion final states generated with WHIZARD which are compatible with the final states of the $t\bar{t}$ process; these processes will be called "$t\bar{t}$" processes despite their containing contributions which are non-resonant in $t\bar{t}$.

The detector simulations were conducted using the Mokka/GEANT4 software with the **ildconfig-v01-14-01-p00** configuration and the **ILD_o1_v5** detector geometry model. The "o1" model indicates the choice of silicon-tungsten electromagnetic calorimeter with 5×5 mm^2 cell sizes, and scintillator-steel hadronic calorimeter with 3×3 cm^2. The simulation detector model is validated by software experts for correctness of the material and geometry, such as gaps and/or overlaps. The $\gamma\gamma \to$ hadrons pile-up backgrounds are overlayed at the level of simulated hits, with an average of 4.1 interactions per bunch crossing. The reconstruction used software packages consistent with the versions in iLCSoft v01-16 [5, 6] (ildconfig-v01-16-p03) including; MarlinTrk, a new Kalman-filter based track finder; PandoraPFA [7] particle flow algorithm, and LCFIPlus [8] for jet clustering and flavour tagging. The analysis was carried out using the Data Summary Tables (DSTs) which were centrally produced at DESY [9] and reweighted to give an integrated luminosity of 1000 fb^{-1} split equally between two polarisation states, (e^+, e^-) = (±0.2, ∓0.8).

4 Event Reconstruction

The final state of the $t\bar{t}H$ decays contain eight fermions, eight jets for the hadronic and 6 jets, a lepton and a neutrino in the case of the semileptonic mode. This leads to a large number of possible combinations to reconstruct the final state of two W bosons, two top quarks and a Higgs boson. The optimal combination of jets was found by minimising

$$\chi^2 = \frac{(M_{t_1} - M_t)^2}{\sigma_{t_1}^2} + \frac{(M_{t_2} - M_t)^2}{\sigma_{t_2}^2} + \frac{(M_{b\bar{b}} - M_H)^2}{\sigma_H^2} \tag{3}$$

where the top quarks are formed by combining a b-jet with a W boson, and the Higgs boson from the remaining two b-jets. The W bosons are formed using the four least b-like jets in the hadronic mode, and the two least b-like jets form one W in the semileptonic mode with the other formed from the isolated lepton and neutrino. The resolutions σ_i are taken to be all roughly equal and are found to be insensitive to small variation for the final mass resolutions.

The neutrino was reconstructed assuming that all of the missing momenta is attributed to a neutrino with zero mass. Figure 5 shows that this assumption is valid for events with small amounts of ISR but as the amount of ISR increases

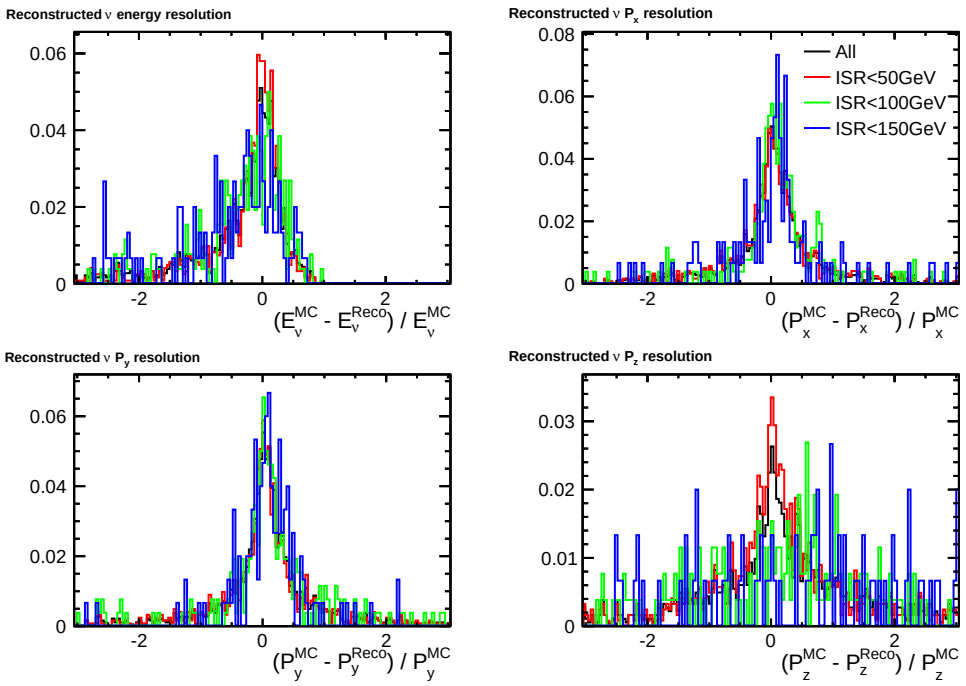

Figure 5: The neutrino reconstruction for varying amounts of ISR and its effect on the energy reconstruction (top left), p_x (top right), p_y (bottom left), and p_z (bottom right).

the neutrino reconstruction suffers. This is primarily observed in the z-direction as the ISR photons have small p_t but large p_z.

The effect of the neutrino reconstruction can be seen in Figure 6 where the leptonic W and top reconstruction has a much broader width than the equivalent hadronic particles. However, this behaviour is expected and as the masses peak in the correct places with the correct shapes this is not an issue. It can also be seen that the reconstructed Higgs mass peaks at 125 GeV as expected and the total mass of the final system has a maximum at the expected 470 GeV. These properties demonstrate that the semileptonic decay mode can be reconstructed well.

As with the semileptonic case, the hadronic events can be successfully reconstructed as demonstrated by Figure 7. The expected behaviour is observed for the W boson, top quarks, Higgs boson, and total masses. The W boson and top quark histograms have twice the statistics of the Higgs boson due to there being two of these particles in each event.

5 $\gamma\gamma \rightarrow$hadrons Overlay Removal

In addition to the underlying event, there is an extra component to the event from unrelated $\gamma\gamma \rightarrow$hadrons "pile-up" events. On average there are 4.1 pile-up events per bunch-crossing leading to an additional 50 GeV in the reconstructed event. Figure 9 demonstrates that without the removal of the pile-up the reconstructed energy in the event is overestimated. This is due to the Durham algorithm forcing all of the particles in an event into the jets. In order to use the Durham algorithm implemented within LCFIPlus these pile-up events must be removed.

The particles in the pile-up events are generally low p_T and happen at angles close to the beam axis as shown in Figure 8. As the pile-up events are, in general, separate from the underlying event they were removed using the kt algorithm with optimised values of R. The optimal values of R was found to be 1.2. The isolated leptons were removed first followed by the $\gamma\gamma \rightarrow$hadrons removal to ensure that none were discarded with the pile-up events.

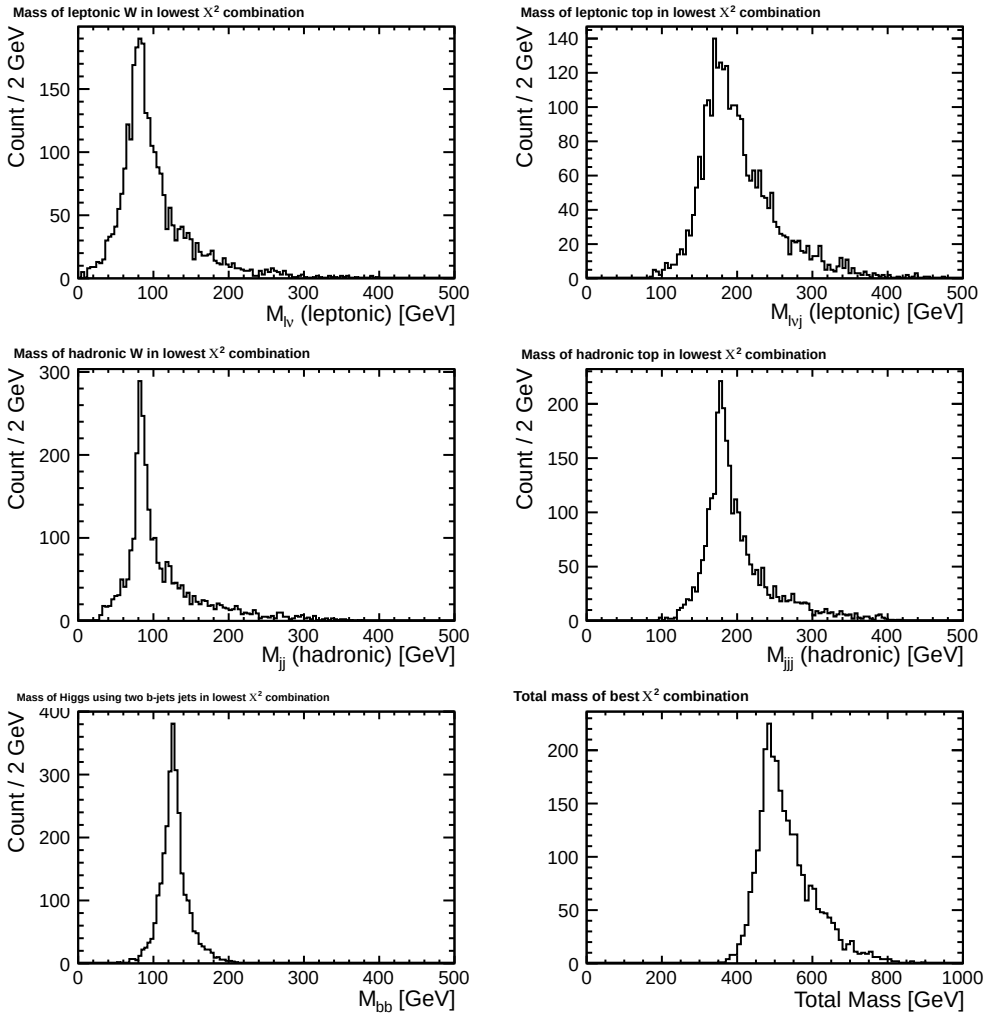

Figure 6: Reconstructed masses for the semileptonic decay mode for the leptonic W boson (top left), leptonic top quark (top right), hadronic W boson (middle left), hadronic top quark (middle right), Higgs boson mass (bottom left), and the total mass of the system (bottom right).

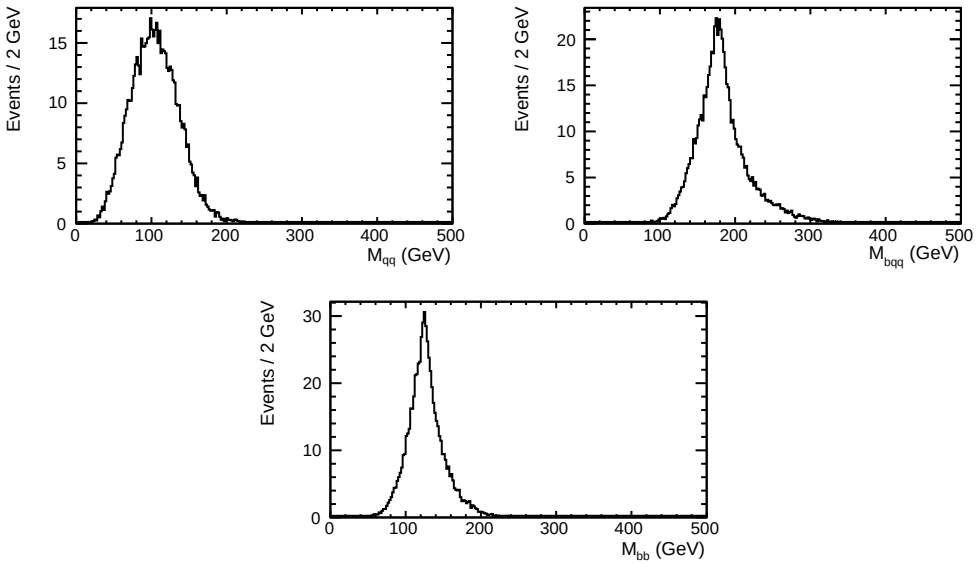

Figure 7: Reconstructed masses for the hadronic decay mode for the W boson (top left), top quark (top right), Higgs boson mass (bottom).

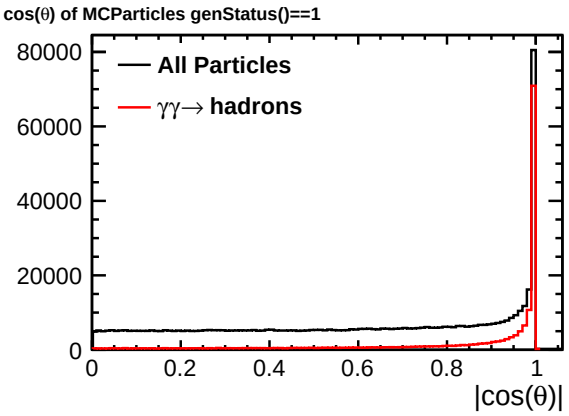

Figure 8: The angle relative to the beam axis of all MCParticles in the events (black), and the $\gamma\gamma \rightarrow$hadrons pile-up only (red).

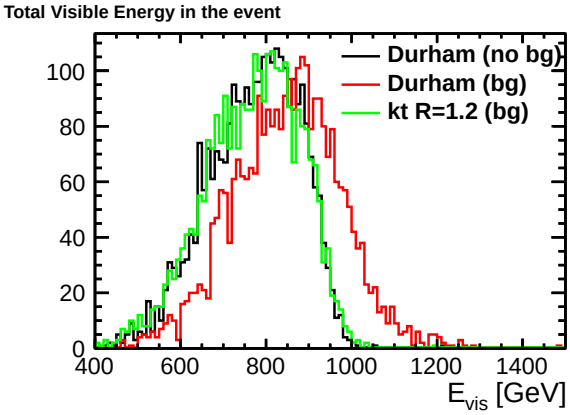

Figure 9: The total visible energy for events with and without $\gamma\gamma \rightarrow$hadrons clustered using the Durham algorithm, and the kt algorithm for the semileptonic mode.

6 Selection Variables

The signal is selected and the background reduced using a series of selection variables. These include the number of isolated leptons in the event, the total visible energy and number of Particle Flow Objects (PFOs) in the final state, the thrust of the event and jet clustering variables from the Durham algorithm (y_{ij}), the number of jets tagged as good b-jets in LCFIPlus, the consistency of the final reconstructed masses with the expected values, and the helicity of the $b\bar{b}$ pair associated with the Higgs boson. Figures 11–15 illustrate the normalised distributions for the cuts used for the semileptonic and hadronic modes and the $t\bar{t}Z$, $t\bar{t}b\bar{b}$, $t\bar{t}H \rightarrow$other, and the $t\bar{t}$ backgrounds.

6.1 Lepton Isolation

To ensure that the samples used for the semileptonic and hadronic modes were completely independent the samples were first split using the number of isolated leptons found utilising the LAL Lepton Finder isolation method as presented here [10]. The PFOs in the events were forced into 8 jets and the isolation of constituent particles within these jets checked using

$$z = \frac{E_{lep}}{E_{jet}} \tag{4}$$

where E_{lep} and E_{jet} are the energies of the lepton and the jet within which the lepton resides, and

$$x_T = \frac{p_T}{M_{jet}} \tag{5}$$

where p_T is the transverse momentum of the lepton and M_{jet} is the mass of the jet. The values of z and p_T were optimised to yield the best performance at values of $x_T > 0.25$, and $z > 0.6$ as shown in Figure 10. Table 1 shows the efficiency of this method for locating isolated leptons, coupled with the purity of the selection and the source of the isolated leptons. An efficiency of 82% (89%) and purity of 95% (97%) for electrons (muons) from W decays is observed.

Lepton	Efficiency	Composition			
		$W \rightarrow e, \mu$	$W \rightarrow \tau \rightarrow e, \mu$	Other e, μ	Fake e, μ
Electrons	84.0%	94.2%	2.9%	1.6%	2.3%
Muons	90.5%	96.3%	2.4%	1.2%	0.7%

Table 1: The performance of the isolated lepton finder including the efficiency of selecting a genuine lepton from a W decay, and the composition of the selected samples including fake leptons.

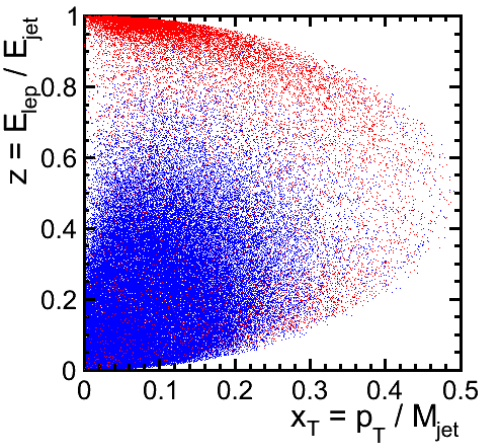

Figure 10: A scatter plot showing the variables used in the lepton isolation for leptons originating from a W boson (red) and all other leptons (blue).

6.2 Total Visible Energy

Events were selected within a window of the total visible energy, E_{vis}^{tot}, in an event in order to remove events with a large number of particles removed alongside the $\gamma\gamma \rightarrow$hadrons due to very forward jets, events with a large amount of ISR, and events which contained multiple neutrinos in the final state.

6.3 Number of Particle Flow Objects

Events with a small number of PFOs were rejected to further protect against backgrounds with multiple neutrinos especially those containing two leptons, two neutrinos, and just four jets. This is of particular relevance for the $t\bar{t}$ background which contains two lepton processes with high cross sections in the final state.

6.4 Thrust

The thrust of an event is given by

$$T = \max \frac{\sum_i |\hat{n} \cdot \vec{p}_i|}{\sum_i |\vec{p}_i|} \tag{6}$$

where p_i is the momentum of the jet. The thrust of an event with two back to back jets is one whereas for an event where the jets are spherically symmetric in the detector is 0.5. As the $t\bar{t}$ system is effectively a two fermion system the thrust of the event is larger than the $t\bar{t}H$, $t\bar{t}Z$, and $t\bar{t}b\bar{b}$.

6.5 Jet Clustering

The signal and backgrounds were clustered using the Durham algorithm into 6 and 8 jet final states. The distance parameter between n and (n+1) jets in the final state is given by

$$Y_{ij} = \frac{\min(E_i^2, E_j^2)(1 - \cos\theta_{ij})}{E_{CM}^2} \tag{7}$$

where i=n and j=(n+1) jets, and $\cos\theta_{ij}$ is the angle between the jets. If the event is forced into more jets than necessary, Y_{ij} becomes small. As the values of i and j are signal dependent the two signals used different values of Y_{ij}. For the semileptonic decay mode the values of Y_{45} and Y_{56} were interesting to study the change between 6 and 7 jets, and the hadronic mode used Y_{67} and Y_{78}.

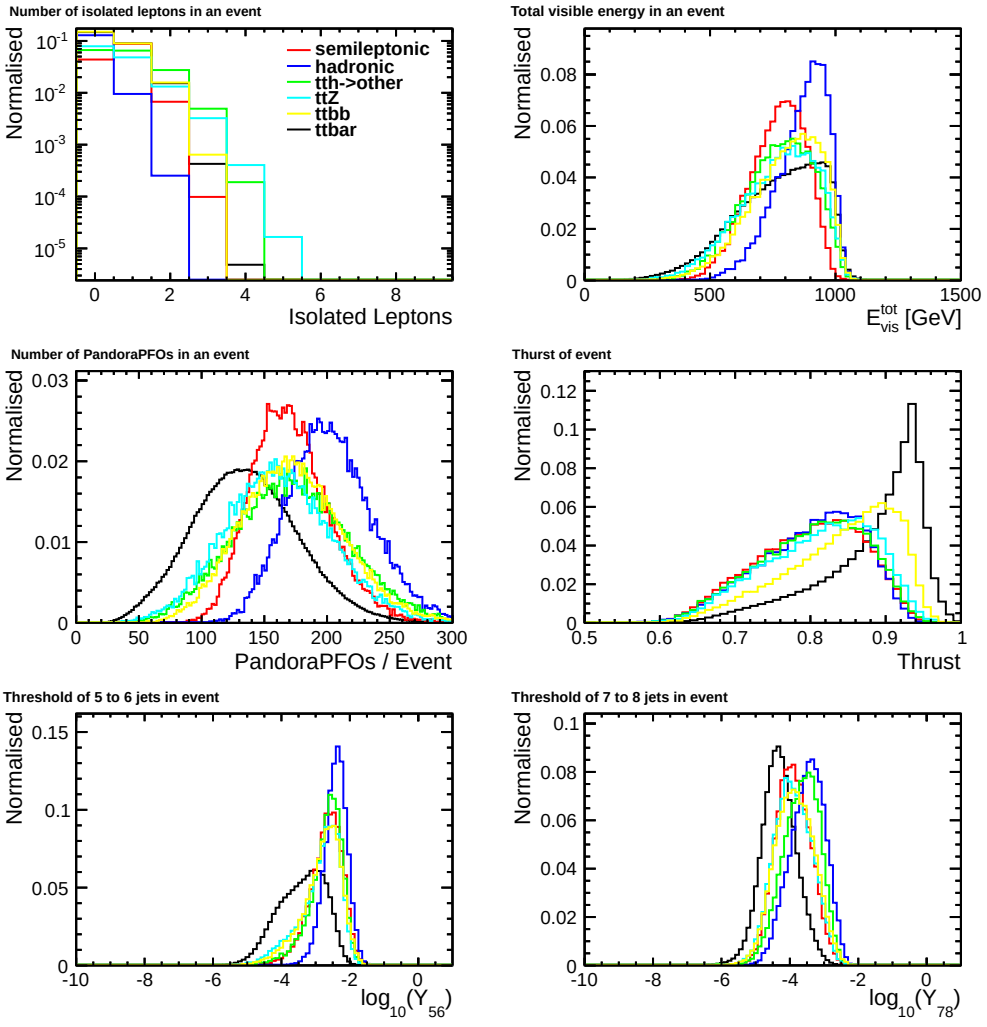

Figure 11: Normalised histograms of the number of identified isolated leptons (top left), total visible energy (top right), number of PandoraPFOs (middle left), thrust (middle right), and the jet parameters (bottom right and bottom left) within the events for the semileptonic (red) and hadronic (blue) modes alongside the backgrounds.

6.6 Flavour Tags

Both the semileptonic and the hadronic signals have four b-jets in the final state, two from the top decays and two from the Higgs decay. The $t\bar{t}$ background will only contain two b-jets from the top decays as will ∼80 % of $t\bar{t}Z$. The flavour tagging is thus a very good discriminant between the signal and backgrounds. The b-tag values from LCFIPlus were ordered from largest to smallest and cuts were made on the third and fourth values to remove the events containing just two b-jets.

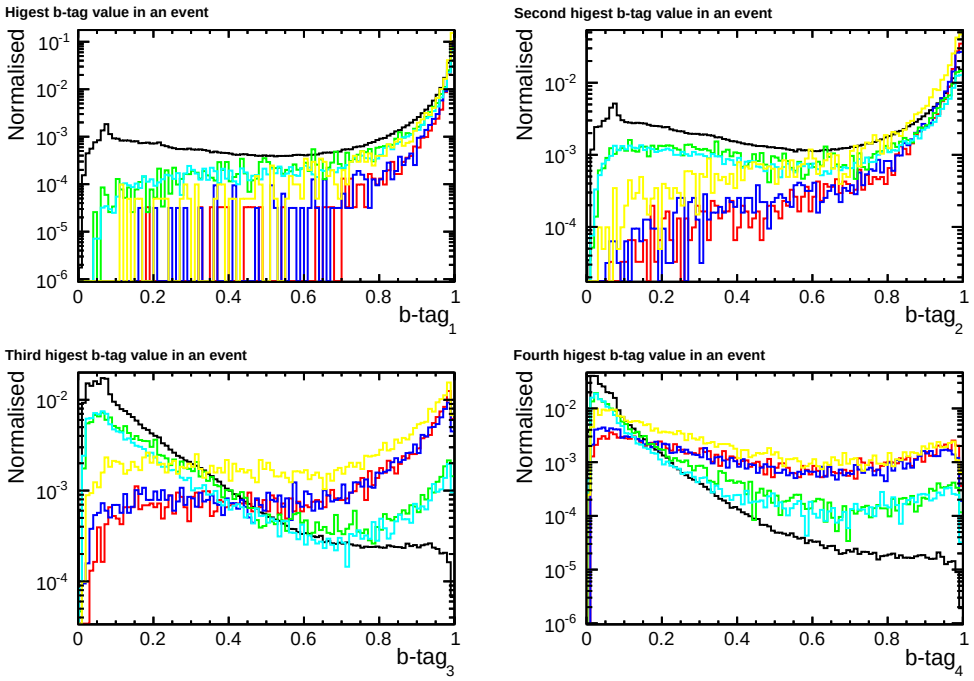

Figure 12: Normalised histograms for the response of the b-tagging from LCFIPlus for the highest ranked jet in an event (top left), second highest (top right), third highest (bottom left), and fourth highest (bottom right) for the semileptonic (red) and hadronic (blue) signal modes and all backgrounds.

Figure 12 shows the differences in the expected profiles of the third and fourth largest b-tags. For the background, there are small peaks at higher values of the b-tag due to the small contributions from genuine backgrounds with four b-jets, but the shape, especially $t\bar{t}$, is dominated by the peak at 0.1.

6.7 Event Reconstruction and Masses

After finding the optimal combination of jets from Equation 3 and reconstructing the event, cuts were made on the resulting masses of the top quarks, Higgs boson and total masses to ensure that the final event is consistent with $t\bar{t}H$.

Figure 13 demonstrates the final masses for all events which have exactly one isolated lepton. This requirement was essential for the reconstruction of the leptonically decaying top quark in the semileptonic mode. The statistics in the hadronic plots of Figure 13 are poor due to the excellent rejection of events which do not contain any isolated leptons. This is also reflected by the lack of a peak in the reconstructed mass of the leptonic W for the hadronic sample as there are no genuine isolated leptons for the reconstruction. A peak is observed in all of the backgrounds due to the finite fraction of expected leptonic top decays in the samples. There is a large fraction of events within the $t\bar{t}$ background which do not reconstruct a good W boson and in turn a good hadronic top due to the low multiplicity in the events containing multiple neutrinos.

Figure 14 shows the equivalent plots when there are no identified isolated leptons. In general, the reconstruction of the events for the hadronic mode is improved across all of the signal and background channels. This is a consequence of the events which have been selected by the isolation criteria. The events which pass this cut have hadronically decaying W bosons leading to higher particle multiplicities which removes the reconstruction issues of the semileptonic samples.

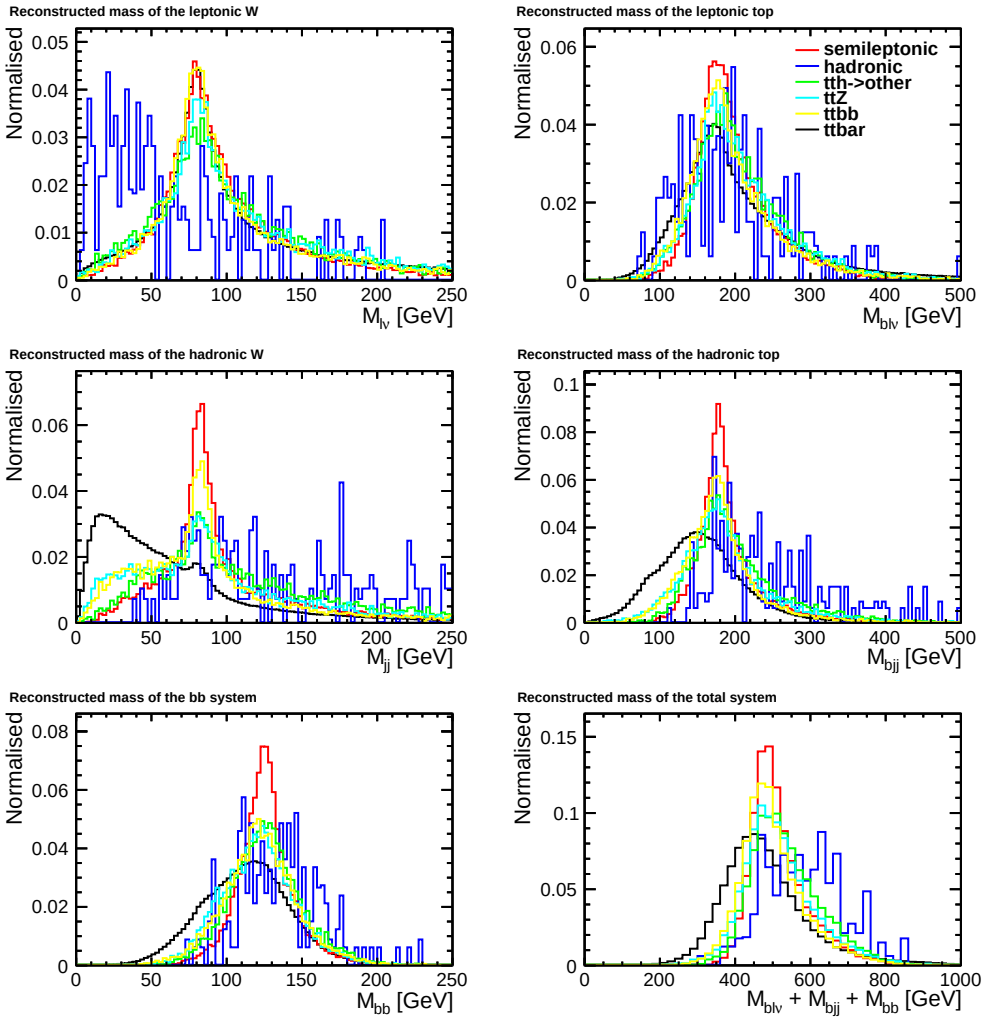

Figure 13: The reconstructed masses of the leptonic W boson (top left), leptonic top quark (top right), hadronic W boson (middle left), hadronic top quark (middle right), Higgs boson (bottom left) and total mass (bottom right) when there is exactly one identified isolated lepton in the event.

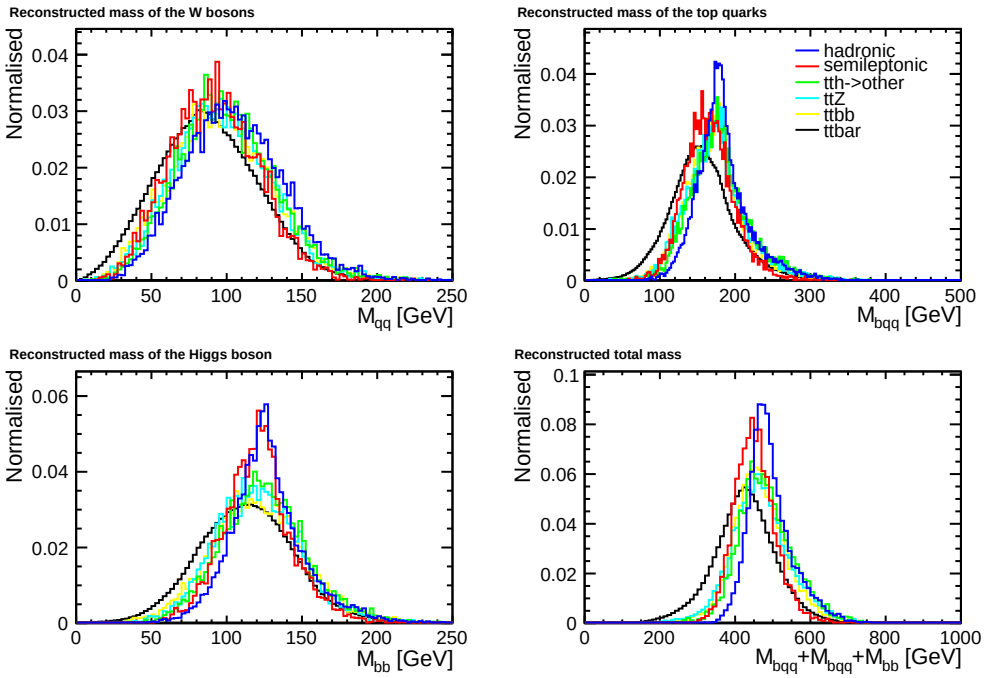

Figure 14: The reconstructed masses of the W boson (top left), top quark (top right), Higgs boson (bottom left) and total mass (bottom right) when there are no identified isolated leptons.

6.8 Helicity of Higgs Decay

The nature of the Higgs boson, especially its spin, is expected to be well-established by the time this analysis will commence. We make use of the fact that in the SM the Higgs boson is a scalar particle, whose decay products are distributed isotropically (and back-to-back) in the rest frame of the Higgs boson. We calculate the helicity angle of the Higgs decay as defined by the angle of the two b jets, in the rest frame of the Higgs boson, with respect to the direction of the Higgs momentum. This can be used to discriminate the $t\bar{t}Z$ process in which the Z boson is vector particle and results in non-uniform helicity angle distribution. From Figure 15 it is also found that this variable is also useful in discriminating $t\bar{t}b\bar{b}$ and $t\bar{t}$ backgrounds.

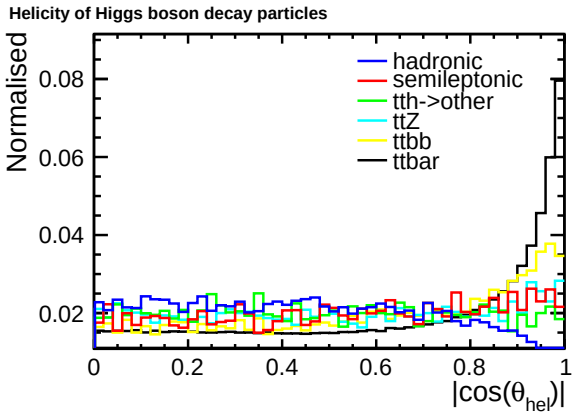

Figure 15: The helicity of the decay products associated with the Higgs boson for the semileptonic (red) and hadronic (blue) decay modes relative to the Higgs direction.

Cut	leptonic	semileptonic	hadronic	$t\bar{t}H \rightarrow$other	$t\bar{t}Z$	$t\bar{t}b\bar{b}$	$t\bar{t}$	$\frac{S}{\sqrt{S+B}}$
Total Events	151.4	628.7	652.7	1046.1	5332.4	1434.5	308800.9	1.11
N_{isolep}=1	74.6	363.5	5.0	371.8	1581.5	439.9	101295.2	1.13
610< E_{vis} <1000	49.6	338.5	4.7	312.7	1228.9	373.8	75507.1	1.21
nPFOs>154	15.0	235.0	4.1	195.0	589.0	194.5	12605.9	2.00
Thrust<0.88	12.5	205.6	3.7	168.9	492.6	140.0	6092.3	2.44
$\log_{10}(Y_{45})$ >-2.25	7.7	151.3	3.2	108.5	295.2	91.0	2067.2	2.90
$\log_{10}(Y_{56})$ >-3.35	6.9	145.1	3.2	106.2	277.6	86.0	1836.1	2.92
b-tag$_1$ >0.96	6.7	135.1	2.8	79.8	216.9	78.3	1367.8	3.11
b-tag$_2$ >0.91	6.1	118.2	2.3	41.2	135.1	66.9	715.2	3.59
b-tag$_3$ >0.67	5.5	102.1	1.6	5.7	59.4	56.0	137.2	5.33
b-tag$_4$ >0.04	5.5	100.5	1.5	5.4	58.3	54.8	128.7	5.34
χ^2 <450	5.3	100.0	1.4	5.2	56.8	53.7	126.0	5.36
364< M_{Total} <808	5.2	99.7	1.4	5.2	56.5	53.5	124.7	5.36
98< M_H <234	4.6	95.1	1.2	4.7	46.1	48.6	109.9	5.40

Table 2: The number of events passed each cut when the cut values are optimised to select the semileptonic signal with maximum significance. The $t\bar{t}H \rightarrow$other is the background where the Higgs boson does not decay to a $b\bar{b}$ pair.

7 Cut Based Analysis

The variables described in Section 6 were applied to the data sets to select the signal and reject the background events. The variables were optimised to maximise the significance $\mathscr{S} = S/\sqrt{S+B}$, of selecting the signal where S and B are the number of signal and background events passed the cut. Each cut was applied and optimised to the subset of events which passed all of the previous cuts.

Table 2 shows the optimised cut values for the semileptonic analysis and the number of events expected passed each cut for 1000 fb^{-1} split between the two polarisation states. The $t\bar{t}H$ events where the Higgs does not decay to a $b\bar{b}$ are incorporated into the tth$\rightarrow$other events. Whilst the cuts before the b-tags demonstrate excellent background reduction, the main discriminant in this analysis is the b-tag$_3$ cut as this yields the largest increases in the signal significance of the sample. The small increases observed when applying the mass cuts is a result of the excellent background suppression from the previous cuts leading to only events which are consistent with $t\bar{t}H$.

The expected number of events for the hadronic selection are shown in Table 3. As observed in the semileptonic channel the main discriminant is the b-tagging. The final hadronic sample has a much larger significance than the semileptonic channel due to the cut on the number of isolated leptons removing less than one percent of the events compared with 42% for the semileptonic study. The large number of semileptonic events in the final hadronic sample is believed to be a result of the lepton isolation criteria which rejects the events which contain taus.

Cut	leptonic	semileptonic	hadronic	tth$\rightarrow$other	$t\bar{t}Z$	$t\bar{t}b\bar{b}$	$t\bar{t}$	$\frac{S}{\sqrt{S+B}}$
Total Events	151.4	628.7	652.7	1046.1	5332.4	1434.5	308800.9	1.11
N_{isolep}=0	20.9	261.2	647.9	556.7	3226.1	932.5	188911.4	1.47
E_{vis}> 650	9.8	221.0	636.2	497.5	2743.5	849.3	157389.6	1.58
Thrust<0.87	8.1	187.8	577.6	440.1	2219.7	540.9	46916.1	2.56
$\log_{10}(Y_{78})$ >-4	3.7	143.6	549.5	415.5	1926.6	474.6	27472.1	3.12
b-tag$_4$ >0.38	1.9	81.0	275.0	17.6	230.0	209.6	680.6	7.11
$\cos(\theta_{hel})$ <0.9	1.6	73.8	263.7	16.5	215.9	189.2	584.9	7.19
M_t >120	1.5	68.9	255.4	15.6	207.8	178.5	530.93	7.20

Table 3: The number of events passed each cut when the cut values are optimised to select the hadronic signal with maximum significance. The $t\bar{t}H \rightarrow$other is the background where the Higgs boson does not decay to a $b\bar{b}$ pair.

Figure 16 demonstrates the power of the background suppression. Before any cuts have been applied the reconstructed Higgs mass peak in the signal is completely swamped by background events. Following the cuts the number of signal and background events remaining are comparable with each other and the Higgs mass peak is clearly visibly above the signal.

After the cuts have been applied the efficiency of signal selection, ε_{sig}, is 39.1% (15.1%) with a selected sample purity, $\rho^{\text{sel}}_{\text{sample}}$, of 20.3% (30.6%) for the hadronic (semileptonic) mode. This yields a signal significance of 7.20 (5.40) and a statistical uncertainty of 7.2% (9.6%) on the value of $g_{t\bar{t}H}$. The uncertainty is reduced in the hadronic channel

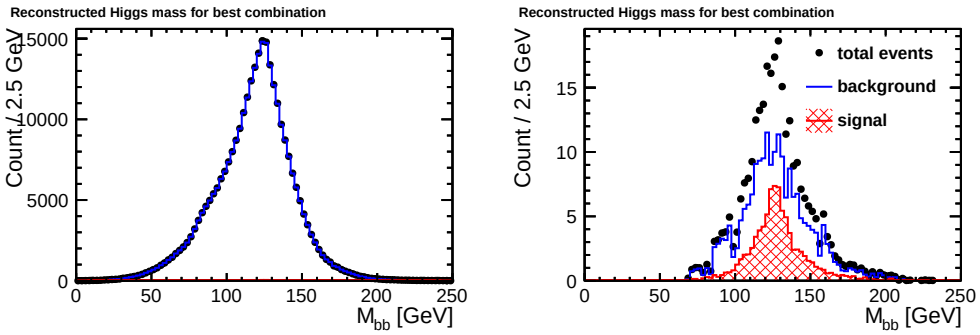

Figure 16: The reconstructed Higgs boson mass for the optimal combination of jets in the semileptonic decay mode for all events (left) and only the events which pass all of the cuts (right).

due to a higher relative cross section as the tau decays are rejected from the semileptonic channel. As the samples were split by the number of isolated leptons and minimal amounts of the signals remain as backgrounds in the final selections the final numbers can be combined to yield an overall significance of 9.01 and statistical uncertainty of 5.8% on the value of $g_{t\bar{t}H}$.

8 TMVA Analysis

A multivariate analysis using the TMVA toolkit [11] was implemented using boosted decision trees (BDT) to improve the signal and background separation. It was found that BDT with gradient boosting (BDTG) offers superior performance over BDT with adaptive boosting. The variables used as an input to the analysis are the same as those defined in Section 6 after the lepton isolation leading to input variables of the; visible energy; number of PandoraPFOs; thrust; jet clustering parameters; b-tags for the four highest jets; total mass of the final system; masses of the W bosons, top quarks, and Higgs boson, and the helicity of the decay products of the Higgs.

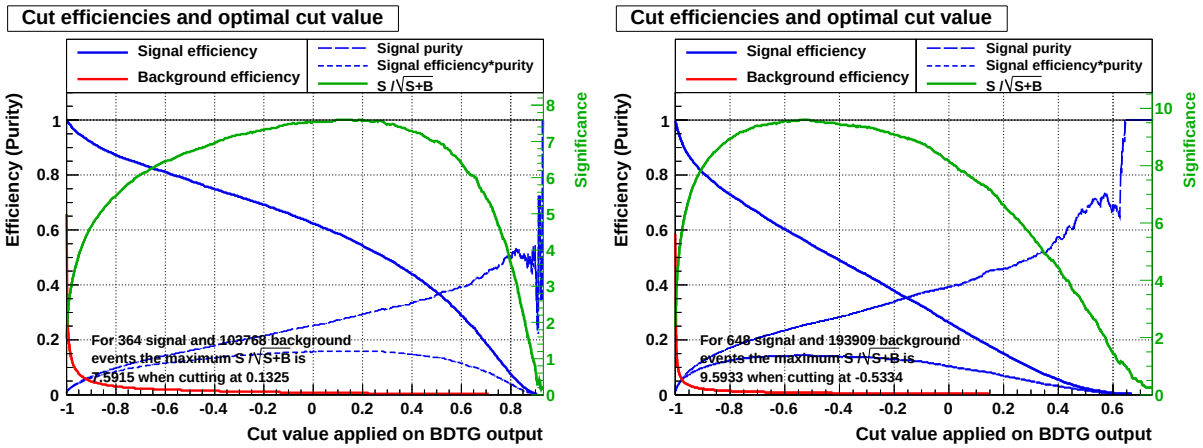

Figure 17: The response of the multivariate analysis for the semileptonic (left) and hadronic (right) decay modes.

Figure 17 shows the cut efficiencies, purities, and significance for the BDTG output value for both modes. The optimal cut values of -0.5334 (0.1325) yield a maximal significance of 9.59 (7.59) leading to a statistical uncertainty on $g_{t\bar{t}H}$ of 5.4% (6.9%) for the hadronic (semileptonic) modes. The performance for each mode is significantly improved with the use of a TMVA over the cut based method. As with the cut based method the performance in the hadronic channel is observed to be better than the semileptonic channel as expected. When the results are combined an uncertainty on $g_{t\bar{t}H}$ of 4.3% is obsevered. The efficiencies and purities of the final results are summarized in Tabs. 4-6.

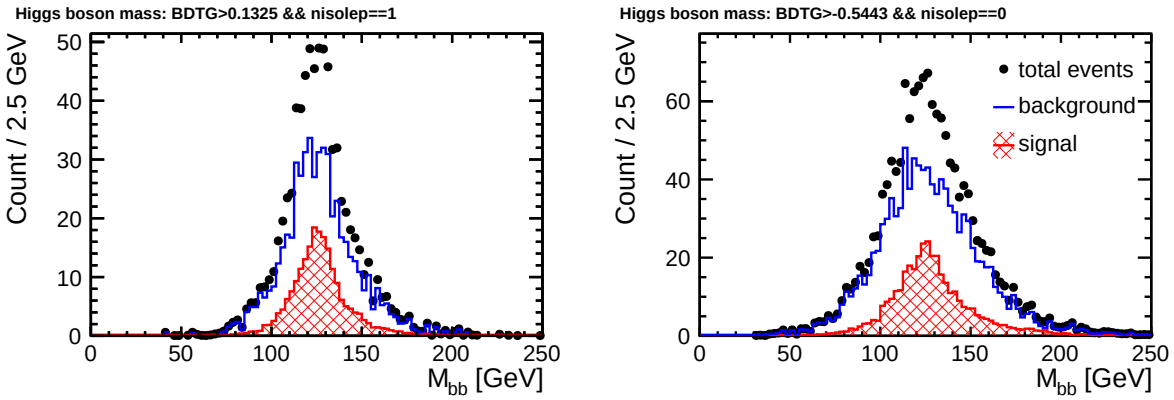

Figure 18: Reconstructed masses for the Higgs boson candidate after applying a cut on the multivariate classifier for the semileptonic (left) and hadronic (right) decay modes.

Cut	leptonic	semileptonic	hadronic	tth→other	$t\bar{t}Z$	$t\bar{t}b\bar{b}$	$t\bar{t}$	$\frac{S}{\sqrt{S+B}}$
Total Events	151.4	628.7	652.7	1046.1	5332.4	1434.5	308800.9	1.11
$\mathrm{BDTG}_{\mathrm{semil}} > 0.1325$	18.7	208.0	2.1	10.1	126.1	125.4	261.2	7.59

Table 4: The number of events passed each cut in the TMVA analysis for the semileptonic channel.

Cut	leptonic	semileptonic	hadronic	tth→other	$t\bar{t}Z$	$t\bar{t}b\bar{b}$	$t\bar{t}$	$\frac{S}{\sqrt{S+B}}$
Total Events	151.4	628.7	652.7	1046.1	5332.4	1434.5	308800.9	1.11
$\mathrm{BDTG}_{\mathrm{had}} > -0.5334$	0.3	65.5	365.6	25.0	260.5	222.6	513.6	9.59

Table 5: The number of events passed each cut in the TMVA analysis for the hadronic channel.

	Efficiency	Purity	Significance
Semileptonic (Cut)	15.1%	30.6%	5.40
Hadronic (Cut)	39.1%	20.3%	7.20
Semileptonic (TMVA)	33.3%	28.0%	7.59
Hadronic (TMVA)	56.0%	25.2%	9.59

Table 6: Summary of efficiencies, purities, and significances.

9 Consideration of systematic uncertainties

Given that the final sample used in the extraction of the top Yukawa coupling contains signal and background events in comparable proportion, it is expected that the estimation of the background will be a dominant source of systematic uncertainties. The total cross section is expected to be calculable from theory to very good precision for $t\bar{t}Z$ and $t\bar{t}$ processes. The $t\bar{t}b\bar{b}$ cross section may present an issue; in principle the measurement of the gluon splitting rate at relevant energies will provide a handle to estimate its size. The most crucial aspect is expected to be the estimation of the efficiencies. For this, one needs to know how well the event selection variables are modeled. Here we illustrate how one might arrive at control samples for different background sources in order to control the efficiency of each background component.

It is foreseen that the $t\bar{t}Z$ final state can be reconstructed in a similar fashion to the $t\bar{t}H$ final state. For hadronically decaying Z, the number of jets in the final state will be the same as in the $t\bar{t}H$ analysis. For our nominal integrated luminosities, 1400 events are expected for $t\bar{t}H(\rightarrow b\bar{b})$ whereas 800 events are expected for $t\bar{t}Z(\rightarrow b\bar{b})$, taking into account the $Z \rightarrow b\bar{b}$ branching ratio. The other hadronic decays of the Z will have large $t\bar{t}$ background due to the absence of the two b jets. The Z leptonic decays may help increase the sensitivity. Overall, one can naively expect that the statistical uncertainty for $t\bar{t}Z$ will be similar to that of $t\bar{t}H$, i.e. at the few percent level.

In the case of $t\bar{t}$, although its cross section is large, it should be checked on data whether the events passing the $t\bar{t}H$ event selection come from the core or the tail of the $t\bar{t}$ system. Once it is found that the core of $t\bar{t}$ is responsible for most of the $t\bar{t}$ background, the systematic uncertainty can be evaluated in the same way as in $t\bar{t}Z$.

For $t\bar{t}b\bar{b}$, the gluon splitting rate is expected to be measured for $t\bar{t}$ processes at various energies.

Other sources of systematic uncertainties such as the luminosity measurement, jet energy scale, and flavor tagging are typically at the 1% level or better for e^+e^- colliders.

10 Conclusions

The uncertainty on the measurement of the top Higgs Yukawa coupling has been studied at 1 TeV for the hadronic and semileptonic decay modes using a conventional cut-based approach and a multivariate analysis. The semileptonic analysis leads to an uncertainty of 6.9% (9.6%) for the multivariate (cut based) methods and the hadronic analysis yields improved values of 5.4% (7.2%). When the samples were combined an uncertainty on $g_{t\bar{t}H}$ of 4.3% is achieved via the multivariate method. This demonstrates the robustness of the physics reconstruction of high jet multiplicity final states at $\sqrt{s} = 1$ TeV under realistic simulation conditions.

11 Acknowledgments

The authors of the study would like to thank their colleagues in the Linear Collider community for various support and discussions at numerous occasions; in particular, T. Barklow, M. Berggren, and A. Miyamoto for the event generation; J. Engels for the mass production of samples; P. Roloff and J. Strube for the cross-checking of the results with the SiD analysis; R. Poeschl and A. Ishikawa for the review of the results in this study. This work was supported in part by the Grant-in-Aid for Specially Promoted Research No. 23000002 by the Japan Society for Promotion of Science.

References

[1] H. Baer *et al.*, "Physics at the International Linear Collider". `http://lcsim.org/papers/DBDPhysics.pdf`. to be published in the ILC Detailed Baseline Design Report.

[2] R. Yonamine, K. Ikematsu, T. Tanabe, K. Fujii, Y. Kiyo, *et al.*, "Measuring the top Yukawa coupling at the ILC at $\sqrt{s} = 500$ GeV" *Phys.Rev.* **D84** (2011) 014033, `arXiv:1104.5132 [hep-ph]`.

[3] W. Kilian, T. Ohl, and J. Reuter, "WHIZARD: Simulating Multi-Particle Processes at LHC and ILC" *Eur.Phys.J.* **C71** (2011) 1742, `arXiv:0708.4233 [hep-ph]`.

[4] "Physics Study Libraries". `http://www-jlc.kek.jp/subg/offl/physsim/`.

[5] F. Gaede, "Marlin and LCCD: Software tools for the ILC" *Nucl.Instrum.Meth.* **A559** (2006) 177–180.

[6] F. Gaede, T. Behnke, N. Graf, and T. Johnson, "LCIO: A Persistency framework for linear collider simulation studies" *eConf* **C0303241** (2003) TUKT001, `arXiv:physics/0306114 [physics]`. SLAC-PUB-9992, CHEP-2003-TUKT001.

[7] M. Thomson, "Particle Flow Calorimetry and the PandoraPFA Algorithm" *Nucl.Instrum.Meth.* **A611** (2009) 25–40, arXiv:0907.3577 [physics.ins-det]. CU-HEP-09-11.

[8] T. Tanabe *et al.*, "LCFIPlus". http://ilcagenda.linearcollider.org/getFile.py/access?contribId=16&sessionId=1&resId=0&materialId=slides&confId=5496. ILD Workshop, Kyushu, May, 2012.

[9] "DBD Samples". http://ilcsoft.desy.de/dbd/generated/.

[10] J. Rouene, "Measurement of $t\bar{t}$ asymmetries with the ILD at the ILC". http://ilcagenda.linearcollider.org/getFile.py/access?contribId=50&sessionId=10&resId=0&materialId=slides&confId=5468, 2012.

[11] A. Hocker, J. Stelzer, F. Tegenfeldt, H. Voss, K. Voss, *et al.*, "TMVA - Toolkit for Multivariate Data Analysis" *PoS* **ACAT** (2007) 040, arXiv:physics/0703039 [PHYSICS].

MZ-TH/12-41
August 2012

Single top quark polarization at $O(\alpha_s)$ in $t\bar{t}$ production at a polarized linear e^+e^- collider

S. Groote[1], *J.G. Körner*[2], *B. Melić*[3], *S. Prelovsek*[4]

[1]Loodus- ja Tehnoloogiateaduskond, Füüsika Instituut, Tartu Ülikool, Riia 142, EE–51014 Tartu, Estonia
[2]Institut für Physik der Johannes-Gutenberg-Universität, Staudinger Weg 7, D–55099 Mainz, Germany
[3] Rudjer Bošković Institute, Theoretical Physics Division, Bijenička c. 54, HR–10000 Zagreb, Croatia
[4] Physics Department at University of Ljubljana and Jozef Stefan Institute, SI–1000 Ljubljana, Slovenia

DOI: will be assigned

We present a detailed investigation of the NLO polarization of the top quark in $t\bar{t}$ production at a polarized linear e^+e^- collider with longitudinally polarized beams. By appropiately tuning the polarization of the beams one can achieve close to maximal values for the top quark polarization over most of the forward hemisphere for a large range of energies. This is quite welcome since the rate is largest in the forward hemisphere. One can also tune the beam polarization to obtain close to zero polarization over most of the forward hemisphere.

1 Introductory remarks

The top quark is so heavy that it keeps its polarization at production when it decays since $\tau_{\text{hadronization}} \gg \tau_{\text{decay}}$. One can test the Standard Model (SM) and/or non-SM couplings through polarization measurements involving top quark decays (mostly $t \to b + W^+$). New observables involving top quark polarization can be defined such as $\langle \vec{P}_t \cdot \vec{p} \rangle$ (see e.g. Refs. [1, 2, 3, 4, 5, 6]). It is clear that the analyzing power of such observables is largest for large values of the polarization of the top quark. This calls for large top quark polarization values. One also wants a control sample with small or zero top quark polarization. Near maximal and minimal values of top quark polarization at a linear e^+e^- collider can be achieved in $t\bar{t}$ production by appropiately tuning the longitudinal polarization of the beam polarization [8]. At the same time one wants to keep the top quark pair production cross section large. It is a fortunate circumstance that all these goals can be realized at the same time. A polarized linear e^+e^- collider may thus be viewed as a rich source of close to zero and close to 100% polarized top quarks.

Let us remind the reader that the top quark is polarized even for zero beam polarization through vector–axial vector interference effects $\sim v_e a_e$, $v_e a_f$, $v_f a_e$, $v_f a_f$, where

$$\begin{aligned} v_e, a_e \quad &: \quad \text{electron current coupling} \\ v_f, a_f \quad &: \quad \text{top quark current coupling} \end{aligned} \tag{1}$$

In Fig. 1 we present a NLO plot of the $\cos\theta$ dependence of the zero beam polarization top quark polarization for different characteristic energies at $\sqrt{s} = 360\,\text{GeV}$ (close to threshold), $\sqrt{s} = 500\,\text{GeV}$ (ILC phase 1), $\sqrt{s} = 1000\,\text{GeV}$ (ILC phase 2) and $\sqrt{s} = 3000\,\text{GeV}$ (CLIC).

2 Top quark polarization at threshold and in the high energy limit

The polarization of the top quark depends on the c.m. energy $\sqrt{s}$, the scattering angle $\cos\theta$, the electroweak coupling coefficients g_{ij} and the effective beam polarization P_{eff}, i.e. one has

$$\vec{P} = \vec{P}\,(\sqrt{s}, \cos\theta, g_{ij}, P_{\text{eff}})\,, \tag{2}$$

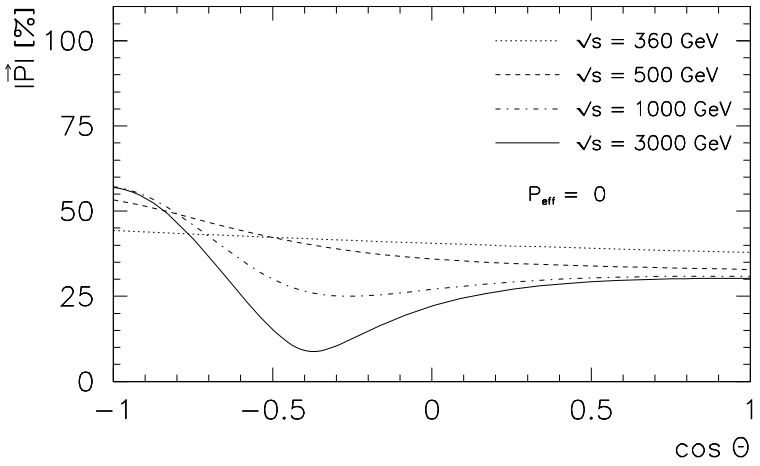

Figure 1: Magnitude of NLO top quark polarization for zero beam polarization

where the effective beam polarization appearing in Eq. (2) is given by [9]

$$P_{\rm eff} = \frac{h_- - h_+}{1 - h_- h_+}\,. \tag{3}$$

and where h_- and h_+ are the longitudinal polarization of the electron and positron beams ($-1 < h_\pm < +1$), respectively. Instead of the nonchiral electroweak couplings g_{ij} one can alternatively use the chiral electroweak couplings $f_{mm'}$ ($m, m' = L, R$) introduced in Refs. [11, 12]. The relations between the two sets of electroweak coupling coefficients can be found in Ref. [8]. In this report we shall make use of both sets of coupling parameters.

For general energies the functional dependence in Eq. (2) is not simple. Even if the electroweak couplings g_{ij} are fixed, one remains with a three-dimensional parameter space $(\sqrt{s}, \cos\theta, P_{\rm eff})$. Our strategy is to discuss various limiting cases for the Born term polarization and then to investigate how the limiting values extrapolate away from these limits. In particular, we exploit the fact that, in the Born term case, angular momentum conservation (or m-quantum number conservation) implies 100% top quark polarization at the forward and backward points for the $(e^-_L e^+_R)$ and $(e^-_R e^+_L)$ beam configurations.

In this section we discuss the behaviour of $\vec{P}$ at nominal threshold $\sqrt{s} = 2m_t$ ($v = 0$) and in the high energy limit $\sqrt{s} \to \infty$ ($v \to 1$). At threshold and at the Born term level one has

$$\vec{P}_{\rm thresh} = \frac{P_{\rm eff} - A_{LR}}{1 - P_{\rm eff} A_{LR}}\ \hat{n}_{e^-}\,, \tag{4}$$

where A_{LR} is the left–right beam polarization asymmetry $(\sigma_{LR} - \sigma_{RL})/(\sigma_{LR} + \sigma_{RL})$ and $\hat{n}_{e^-}$ is a unit vector pointing into the direction of the electron momentum. We use a notation where $\sigma(LR/RL) = \sigma(h_- = \mp 1; h_+ = \pm 1)$. In terms of the electroweak coupling parameters g_{ij}, the nominal polarization asymmetry at threshold $\sqrt{s} = 2m_t$ is given by $A_{LR} = -(g_{41} + g_{42})/(g_{11} + g_{12}) = 0.409$. Eq. (4) shows that, at threshold and at the Born term level, the polarization $\vec{P}$ is parallel to the beam axis irrespective of the scattering angle and has maximal values $|\vec{P}| = 1$ for both $P_{\rm eff} = \pm 1$ as dictated by angular momentum conservation. Zero polarization is achieved for $P_{\rm eff} = A_{LR} = 0.409$.

In the high energy limit the polarization of the top quark is purely longitudinal, i.e. the polarization points into the direction of the top quark. At the Born term level one finds $\vec{P}(\cos\theta) = P^{(\ell)}(\cos\theta) \cdot \hat{p}_t$ with

$$P^{(\ell)}(\cos\theta) = \frac{(g_{14} + g_{41} + P_{\rm eff}(g_{11} + g_{44}))(1 + \cos\theta)^2 + (g_{14} - g_{41} - P_{\rm eff}(g_{11} - g_{44})(1 - \cos\theta)^2}{(g_{11} + g_{44} + P_{\rm eff}(g_{14} + g_{41}))(1 + \cos\theta)^2 + (g_{11} - g_{44} - P_{\rm eff}(g_{14} - g_{41}))(1 - \cos\theta)^2}\,. \tag{5}$$

In the same limit, the electroweak coupling coefficients appearing in Eq. (5) take the numerical values $g_{11} = 0.601$, $g_{14} = -0.131$, $g_{41} = -0.201$ and $g_{44} = 0.483$. For $\cos\theta = \pm 1$ and $P_{\rm eff} = \pm 1$ the top quark is

100% polarized as again dictated by angular momentum conservation. The lesson from the threshold and high energy limits is that large values of the polarization of the top quark close to $|\vec{P}| = 1$ are engendered for large values of the effective beam polarization parameter close to $P_{\rm eff} = \pm 1$.

Take, for example, the forward–backward asymmetry which is zero at threshold, and large and positive in the high energy limit. In fact, from the numerator of the high energy formula Eq. (5) one calculates

$$A_{FB} = \frac{3}{4}\,\frac{g_{44} + P_{\rm eff} g_{14}}{g_{11} + P_{\rm eff} g_{41}} \;=\; 0.61\,\frac{1 - 0.27 P_{\rm eff}}{1 - 0.33 P_{\rm eff}}\,. \tag{6}$$

The forward-backward asymmetry is large and only mildly dependent on $P_{\rm eff}$. More detailed calculations show that the strong forward dominance of the rate sets in rather fast above threshold [8]. This is quite welcome since the forward region is also favoured from the polarization point of view.

As another example take the vanishing of the polarization which, at threshold, occurs at $P_{\rm eff} = 0.409$. In the high energy limit, and in the forward region where the numerator part of Eq. (5) proportional to $(1 + \cos\theta)^2$ dominates, one finds a polarization zero at $P_{\rm eff} = (g_{14} + g_{41})/(g_{11} + g_{44}) = 0.306$. The two values of $P_{\rm eff}$ do not differ much from another.

3 Overall rate and left-right (LR) and right-left (RL) rates

The overall rate σ for partially longitudinal polarized beam production can be composed from the LR rate σ_{LR} and the RL rate σ_{RL} valid for 100% longitudinally polarized beams. The notation is such that LR and RL refer to the $(e^-_L e^+_R)$ and $(e^-_R e^+_L)$ longitudinal polarization configurations, respectively. The relation reads [10]

$$\begin{aligned}
\frac{d\sigma}{d\cos\theta} &= \frac{1-h_-}{2}\frac{1+h_+}{2}\frac{d\sigma_{LR}}{d\cos\theta} + \frac{1+h_-}{2}\frac{1-h_+}{2}\frac{d\sigma_{RL}}{d\cos\theta} \\
&= \frac{1}{4}(1 - h_- h_+)\Big(\frac{d\sigma_{LR} + d\sigma_{RL}}{d\cos\theta} - P_{\rm eff}\frac{d\sigma_{LR} - d\sigma_{RL}}{d\cos\theta}\Big)\,.
\end{aligned} \tag{7}$$

Using the left–right polarization asymmetry

$$A_{LR} = \frac{d\sigma_{LR} - d\sigma_{RL}}{d\sigma_{LR} + d\sigma_{RL}} \tag{8}$$

one can rewrite the rate (7) in the form

$$\frac{d\sigma}{d\cos\theta} = \frac{1}{4}(1 - h_- h_+)\frac{d\sigma_{LR} + d\sigma_{RL}}{d\cos\theta}\Big(1 - P_{\rm eff} A_{LR}\Big)\,. \tag{9}$$

The differential rate $d\sigma/d\cos\theta$ carries an overall helicity alignment factor $(1 - h_- h_+)$ which enhances the rate for negative values of $h_- h_+$. Also, Fig. 2 shows that A_{LR} varies in the range between 0.30 and 0.60 which leads to a further rate enhancement from the last factor in Eq. (9) for negative values of $P_{\rm eff}$.

Let us define reduced LR and RL rate functions $D_{LR/RL}$ by writing

$$\frac{d\sigma_{LR/RL}}{d\cos\theta} = \frac{\pi\alpha^2 v}{3s^2} D_{LR/RL}(\cos\theta) \tag{10}$$

such that, in analogy to Eq. (7),

$$D = \frac{1}{4}(1 - h_- h_+)\left(D_{LR} + D_{RL} - P_{\rm eff}(D_{LR} - D_{RL})\right)\,. \tag{11}$$

In the next step we express the reduced rate functions through a set of independent hadronic helicity structure functions. For the LR reduced rate function one has

$$\begin{aligned}
2D_{LR}(\cos\theta) &= \frac{3}{8}(1 + \cos^2\theta)\left((f^2_{LL} + f^2_{LR})H^1_U + 2 f_{LL} f_{LR} H^2_U\right) \\
&\quad + \frac{3}{4}\sin^2\theta\left((f^2_{LL} + f^2_{LR})H^1_L + 2 f_{LL} f_{LR} H^2_L\right) \\
&\quad + \frac{3}{4}\cos\theta (f^2_{LL} - f^2_{LR}) H^4_F
\end{aligned} \tag{12}$$

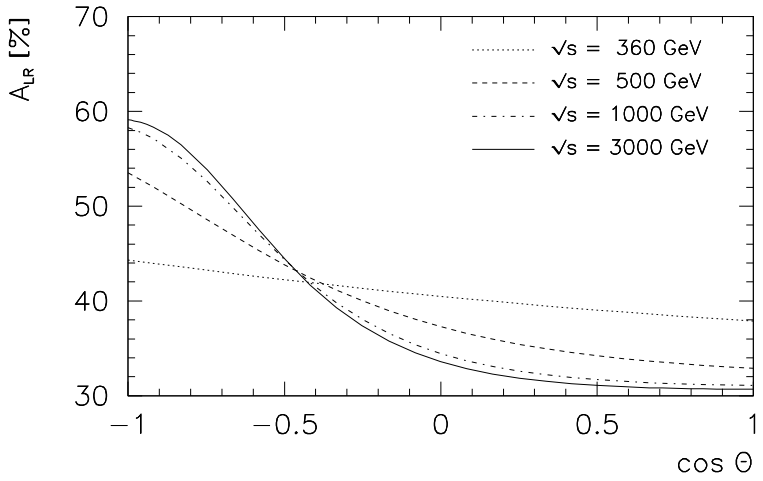

Figure 2: NLO left–right polarization asymmetry A_{LR} for $\sqrt{s} = 360$, 500, 1000, and 3000 GeV

and accordingly for D_{RL} with $f_{LL} \to f_{RR}$ and $f_{LR} \to f_{RL}$.

At NLO one has $H_a^j = H_a^j(Born) + H_a^j(\alpha_s)$. The radiatively corrected structure functions $H_a^j(\alpha_s)$ are listed in Ref. [8]. If needed they can be obtained from S.G. or B.M. in Mathematica format. For the non-vanishing unpolarized Born term contributions $H_a^j(Born)$ one obtains (see e.g. Ref. [7, 8])

$$\begin{aligned} H_U^1(Born) &= 2N_c s(1+v^2), \qquad H_L^1(Born) = \; H_L^2(Born) = N_c s(1-v^2), \\ H_U^2(Born) &= 2N_c s(1-v^2), \qquad H_F^4(Born) = 4N_c sv. \end{aligned} \tag{13}$$

Following Refs. [11, 12], $D_{LR}(\cos\theta)$ (and $D_{RL}(\cos\theta)$) can be cast into a very compact Born term form

$$D_{LR}(Born) = \frac{3}{8}\left(C_{LR}^2 - 2f_{LL}f_{LR}v^2\sin^2\theta\right) 2N_c s, \tag{14}$$

where

$$C_{LR}(\cos\theta) = f_{LL}(1 + v\cos\theta) + f_{LR}(1 - v\cos\theta)\,. \tag{15}$$

The corresponding RL form D_{RL} is obtained again by the substitution $(L \leftrightarrow R)$ in Eqs. (14) and (15).

With the help of the compact expression in Eq. (14) and the translation table $2(g_{11} - g_{41}) = (f_{LL}^2 + f_{LR}^2)$, $2(g_{14} - g_{44}) = -f_{LL}^2 + f_{LR}^2$, $2(g_{11} + g_{41}) = f_{RR}^2 + f_{RL}^2$, $2(g_{14} + g_{44}) = f_{RR}^2 - f_{RL}^2$ one can easily verify the threshold value for A_{LR} and the high energy limits for A_{FB} discussed in Sec. 2.

4 Single top polarization in $e^+e^- \to t\bar{t}$

The polarization components $P^{(m)}$ ($m = \ell$: longitudinal; $m = tr$: transverse) of the top quark in $e^+e^- \to t\bar{t}$ are obtained from (the antitop quark spin is summed over)

$$P^{(m)}(P_{\rm eff}) = \frac{N^{(m)}(P_{\rm eff})}{D(P_{\rm eff})}\,, \tag{16}$$

where the dependence on $P_{\rm eff}$ is given by

$$N^{(m)}(P_{\rm eff}) = \frac{1}{4}(1 - h_- h_+)\left(N_{LR}^{(m)} + N_{RL}^{(m)} - P_{\rm eff}(N_{LR}^{(m)} - N_{RL}^{(m)})\right)\,. \tag{17}$$

$P^{(tr)}$ is the transverse polarization component perpendicular to the momentum of the top quark in the scattering plane. The overall helicity alignment factor $(1 - h_- h_+)$ drops out when one calculates the normalized polarization components according to Eq. (16). This explains why the polarization depends only on $P_{\rm eff}$ and not separately on h_- and h_+ (see Eq. (2)).

The numerator factors $N_{LR}^{(m)}$ and $N_{RL}^{(m)}$ in Eq. (16) are given by

$$\begin{aligned} -2N_{LR}^{(\ell)}(\cos\theta) &= \frac{3}{8}(1+\cos^2\theta)\,(f_{LL}^2-f_{LR}^2)H_U^{4(\ell)}+\frac{3}{4}\sin^2\theta\,(f_{LL}^2-f_{LR}^2)H_L^{4(\ell)} \\ &\quad +\frac{3}{4}\cos\theta\left((f_{LL}^2+f_{LR}^2)H_F^{1(\ell)}+2f_{LL}f_{LR}H_F^{2(\ell)}\right), \end{aligned} \tag{18}$$

$$\begin{aligned} -2N^{(tr)}(\cos\theta) &= -\frac{3}{\sqrt{2}}\sin\theta\cos\theta\;(f_{LL}^2-f_{LR}^2)\,H_I^{4(tr)} \\ &\quad -\frac{3}{\sqrt{2}}\sin\theta\left((f_{LL}^2+f_{LR}^2)H_A^{1(tr)}+2f_{LL}f_{LR}H_A^{2(tr)}\right), \end{aligned} \tag{19}$$

and $N_{RL}^{(m)}=-N_{LR}^{(m)}(L\leftrightarrow R)$. Note the extra minus sign when relating $N_{LR}^{(m)}$ and $N_{RL}^{(m)}$.

The LO longitudinal and transverse polarization components read (see e.g. Ref. [7, 8])

$$\begin{aligned} H_U^{4(\ell)}(Born)&=4N_c s v, \qquad H_F^{1(\ell)}(Born)=2N_c s(1+v^2), \\ H_L^{4(\ell)}(Born)&=0, \qquad H_F^{2(\ell)}(Born)=2N_c s(1-v^2), \end{aligned} \tag{20}$$

and

$$H_I^{4(tr)}(Born)=2N_c s\frac{1}{2\sqrt{2}}v\sqrt{1-v^2}, \quad H_A^{1(tr)}(Born)=H_A^{2(tr)}(Born)=2N_c s\frac{1}{2\sqrt{2}}\sqrt{1-v^2}\,. \tag{21}$$

The LO numerators (18) and (19) can be seen to take a factorized form [11, 12]

$$\begin{aligned} N_{LR}^{(\ell)}(\cos\theta) &= -\frac{3}{8}\Big(f_{LL}(\cos\theta+v)+f_{LR}(\cos\theta-v)\Big)\,C_{LR}(\cos\theta)\;2N_c s\,, \\ N_{LR}^{(tr)}(\cos\theta) &= \frac{3}{8}\sin\theta\sqrt{1-v^2}\,(f_{LL}+f_{LR})\,C_{LR}(\cos\theta)\;2N_c s\,, \end{aligned} \tag{22}$$

where the common factor $C_{LR}(\cos\theta)$ has been defined in Eq. (15).

One can then determine the angle α enclosing the direction of the top quark and its polarization vector by taking the ratio $N_{LR}^{(tr)}/N_{LR}^{(\ell)}$. One has

$$\tan\alpha_{LR}=\frac{N_{LR}^{(tr)}(\cos\theta)}{N_{LR}^{(\ell)}(\cos\theta)}=-\frac{\sin\theta\sqrt{1-v^2}\,(f_{LL}+f_{LR})}{f_{LL}(\cos\theta+v)+f_{LR}(\cos\theta-v)}\,. \tag{23}$$

For $v=1$ one finds $\alpha_{LR}=0$, i.e. the polarization vector is aligned with the momentum of the top quark, in agreement with what has been said before. In Ref. [8] we have shown that radiative corrections to the value of α_{LR} are small in the forward region but can become as large as $\Delta\alpha_{LR}=10^\circ$ in the backward region for large energies.

Eqs. (22) and (22) can be used to find a very compact LO form for $|\vec{P}_{LR}|$. One obtains [8]

$$|\vec{P}_{LR}|=\frac{\sqrt{N_{LR}^{(\ell)2}+N_{LR}^{(tr)2}}}{D_{LR}}=\frac{\sqrt{1-4a_{LR}}}{1-2a_{LR}}=1-2a_{LR}^2-8a_{LR}^3-18a_{LR}^3\ldots, \tag{24}$$

where the coefficient a_{LR} depends on $\cos\theta$ through

$$a_{LR}(\cos\theta)=\frac{f_{LL}f_{LR}}{C_{LR}^2(\cos\theta)}v^2\sin^2\theta\,. \tag{25}$$

Again, the corresponding expressions for $|\vec{P}_{LR}|$ and a_{LR} can be found by the substitution $(L\leftrightarrow R)$.

For the fun of it we also list a compact LO form for $|\vec{P}(P_{\rm eff}=0)|$. One has

$$|\vec{P}(P_{\rm eff}=0)|=\frac{\sqrt{(C_{LR}^2-C_{RL}^2)^2-4v^2\sin^2\theta(C_{LR}f_{LL}-C_{RL}f_{RR})(C_{LR}f_{LR}-C_{RL}f_{RL})}}{C_{LR}^2+C_{RL}^2-2v^2\sin^2\theta(f_{LL}f_{LR}+f_{RR}f_{RL})}\,. \tag{26}$$

Eq. (26) would produce a LO version of Fig 1.

5 Effective beam polarization

As described in Sec. 2, large values of the effective beam polarization $P_{\rm eff}$ are needed to produce large polarization values of $\vec{P}$. It is a fortunate circumstance that nearly maximal values of $P_{\rm eff}$ can be achieved with non-maximal values of (h_-, h_+). This is shown in Fig. 3 where we drawn contour plots $P_{\rm eff} = const$ in the (h_-, h_+) plane. The two examples shown in Fig. 3 refer to

$$\begin{aligned} &(h_- = -0.80,\, h_+ = +0.625) \qquad \text{leads to} \quad P_{\rm eff} = -0.95, \\ &(h_- = +0.80,\, h_+ = -0.625) \qquad \text{leads to} \quad P_{\rm eff} = +0.95. \end{aligned} \tag{27}$$

These two options are at the technical limits that can be achieved [13]. In the next section we shall see that the choice $P_{\rm eff} \sim -0.95$ is to be preferred since the polarization is more stable against small variations of $P_{\rm eff}$. Furthermore, negative values of $P_{\rm eff}$ gives yet another rate enhancement as discussed after Eq. (9).

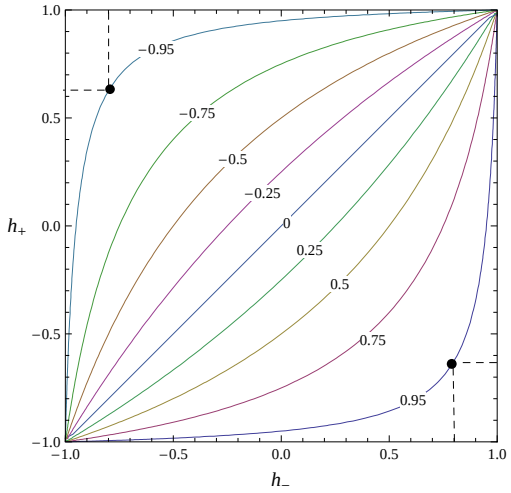

Figure 3: Contour plots of $P_{\rm eff} = const$ in the (h_+, h_-) plane

6 Stability of polarization against variations of $P_{\rm eff}$

Extrapolations of $|\vec{P}|$ away from $P_{\rm eff} = \pm 1$ are more stable for $P_{\rm eff} = -1$ than for $P_{\rm eff} = +1$. Because the derivative of the magnitude of $|\vec{P}|$ leads to rather unwieldy expressions, we demonstrate this separately for the two polarization components $P^{(\ell)}$ and $P^{(tr)}$. The polarization components are given by $(m = \ell, tr)$

$$P^{(m)} = \frac{N_0^{(m)} - P_{\rm eff} N_P^{(m)}}{D_0 - P_{\rm eff} D_P}\,, \tag{28}$$

where $N_0^{(m)} = N_{LR}^{(m)} + N_{RL}^{(m)}$ and $N_P^{(m)} = N_{LR}^{(m)} - N_{RL}^{(m)}$ and similarly for D_0 and D_P. Upon differentiation w.r.t. $P_{\rm eff}$ one obtains

$$\frac{dP^{(m)}}{dP_{\rm eff}} = \frac{-N_0^{(m)} D_P + N_P^{(m)} D_0}{(D_0 - P_{\rm eff} D_P)^2}\,. \tag{29}$$

For the ratios of the slopes for $P_{\rm eff} = -1$ and $P_{\rm eff} = +1$ one finds

$$\frac{dP^{(m)}}{dP_{\rm eff}}\Big|_{P_{\rm eff}=-1} \Big/ \frac{dP^{(m)}}{dP_{\rm eff}}\Big|_{P_{\rm eff}=+1} = \left(\frac{D_0 - D_P}{D_0 + D_P}\right)^2 = \left(\frac{D_{RL}}{D_{LR}}\right)^2 = \left(\frac{1 - A_{LR}}{1 + A_{LR}}\right)^2\,. \tag{30}$$

Depending on the energy and the scattering angle, Fig. 2 shows that A_{LR} varies between 0.3 and 0.7 which implies that $(D_{RL}/D_{LR})^2$ varies between 0.29 and 0.06, i.e. for $P_{\rm eff} = -1$ the polarization components are

much more stable against variations of $P_{\rm eff}$ than for $P_{\rm eff} = +1$. At threshold the ratio of slopes of $|\vec{P}_{\rm thresh}|$ for $P_{\rm eff} = -1$ and $P_{\rm eff} = +1$ is given by $-(D_{RL}/D_{LR})^2 = -0.18$ where the minus sign results from having taken the derivative of the magnitude $|\vec{P}|$ (see Eq. (4)).

7 Longitudinal and transverse polarization $P^{(\ell)}$ vs. $P^{(tr)}$ for general angles and energies

In Fig. 4 we plot the longitudinal component $P^{(\ell)}$ and the transverse component $P^{(tr)}$ of the top quark polarization for different scattering angles θ and energies $\sqrt{s}$ starting from threshold up to the high energy limit. The left and right panels of Fig. 4 are drawn for $P_{\rm eff} = (-1, -0.95)$ and for $P_{\rm eff} = (+1, +0.95)$, respectively. The apex of the polarization vector $\vec{P}$ follows a trajectory that starts at $\vec{P} = P_{\rm thresh}(-\cos\theta, \sin\theta)$ and $\vec{P} = P_{\rm thresh}(\cos\theta, -\sin\theta)$ for negative and positive values of $P_{\rm eff}$, respectively, and ends on the line $P^{(tr)} = 0$ in the high energy limit. The two 60° trajectories show that large values of the size of $|\vec{P}|$ close to the maximal value of 1 can be achieved in the forward region for both $P_{\rm eff} \sim \mp 1$ at all energies. However, the two figures also show that the option $P_{\rm eff} \sim -1$ has to be preferred since the $P_{\rm eff} \sim -1$ polarization is more stable against variations of $P_{\rm eff}$.

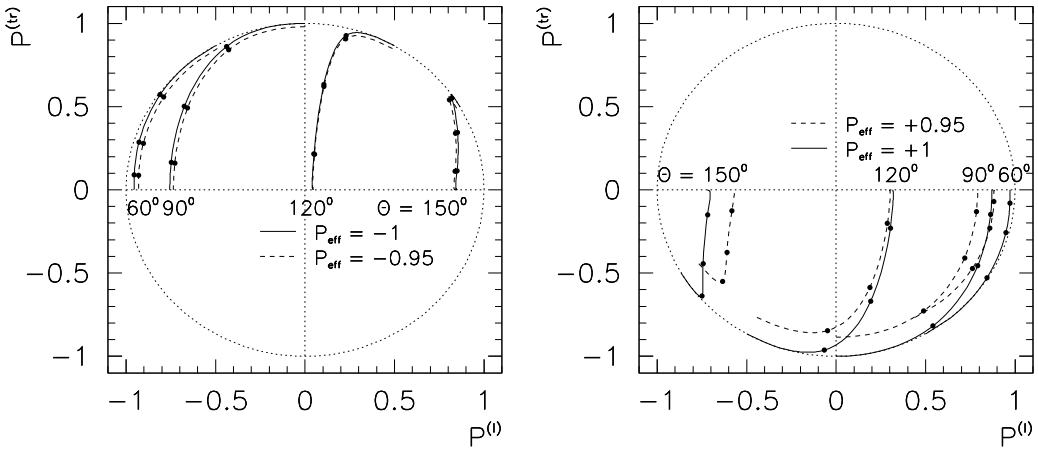

Figure 4: Parametric plot of the orientation and the length of the polarization vector in dependence on the c.m. energy $\sqrt{s}$ for values $\theta = 60°$, 90°, 120°, and 150° for i) (left panel) $P_{\rm eff} = -1$ (solid lines) and $P_{\rm eff} = -0.95$ (dashed lines) and ii) (right panel) $P_{\rm eff} = +1$ (solid lines) and $P_{\rm eff} = +0.95$ (dashed lines). The three ticks on the trajectories stand for $\sqrt{s} = 500\,GeV$, $1000\,GeV$, and $3000\,GeV$.

It is noteworthy that the magnitude of the polarization vector remains closer to $|\vec{P}| = 1$ in the forward region than in the backward region when $\cos\theta$ is varied. Let us investigate this effect for $P_{\rm eff} = -1$ by expanding the high energy formula (5) in $\Delta\cos\theta$ around $\cos\theta = +1$ and $\cos\theta = -1$. Since the first derivative vanishes, one has to expand to the second order in $\Delta\cos\theta$. The result is

$$\begin{aligned} \text{Forward} \qquad |\vec{P}_{LR}| &= 1 - \frac{1}{2}\left(\frac{f_{LR}}{f_{LL}}\right)^2 (\Delta\cos\theta)^2 + \ldots \\ \text{Backward} \qquad |\vec{P}_{LR}| &= 1 - \frac{1}{2}\left(\frac{f_{LL}}{f_{RL}}\right)^2 (\Delta\cos\theta)^2 + \ldots . \end{aligned} \tag{31}$$

Numerically, one has $f_{LR}^2/f_{LL}^2 = 0.13$ and $f_{LL}^2/f_{LR}^2 = 7.53$. The second derivative is very much smaller in the forward direction than in the backward direction. This tendency can be clearly discerned in Fig. 4. A similar but even stronger conclusion is reached for the second derivative of $|\vec{P}_{RL}|$ where the corresponding second order coefficients are given by $f_{RL}^2/f_{RR}^2 = 0.064$ for $\cos\theta = +1$, and by $f_{RR}^2/f_{RL}^2 = 15.67$ for $\cos\theta = -1$. Corresponding v-dependent expansions can be obtained from Eq. (24).

We mention that at NLO there is also a normal component of the top quark polarization $P^{(n)}$ generated by the one–loop contribution which, however, is quite small (of $O(3\%)$) [8].

8 Summary

The aim of our investigation was to maximize and to minimize the polarization vector of the top quark $\vec{P}\,(\sqrt{s}, \cos\theta, g_{ij}, P_{\rm eff})$ by tuning the beam polarization. Let us summarize our findings which have been found in NLO QCD in the context of the SM.

A. Maximal polarization: Large values of $\vec{P}$ can be realized for $P_{\rm eff} \sim \pm 1$ at all intermediate energies. This is particularly true in the forward hemisphere where the rate is highest. Negative large values for $P_{\rm eff}$ with aligned beam helicities ($h_- h_+$ neg.) are preferred for two reasons. First there is a further gain in rate apart from the helicity alignment factor $(1 - h_- h_+)$ due to the fact that generally $\sigma_{LR} > \sigma_{RL}$ as explained after Eq. (7). Second, the polarization is more stable against variations of $P_{\rm eff}$ away from $P_{\rm eff} = -1$. The forward region is also favoured since the 100% LO polarization valid at $\cos\theta = 1$ extrapolates smoothly into the forward hemisphere with small radiative corrections.

B. Minimal polarization: Close to zero values of the polarization vector $\vec{P}$ can be achieved for $P_{\rm eff} \sim 0.4$. Again the forward region is favoured. In order to maximize the rate for the small polarization choice take quadrant IV in the (h_-, h_+) plane.

Acknowledgements

J.G.K. would like to thank X. Artru and E. Christova for discussions and G. Moortgat-Pick for encouragement. The work of S.G. is supported by the Estonian target financed project No. 0180056s09, by the Estonian Science Foundation under grant No. 8769 and by the Deutsche Forschungsgemeinschaft (DFG) under grant 436 EST 17/1/06. B.M. acknowledges support of the Ministry of Science and Technology of the Republic of Croatia under contract No. 098-0982930-2864. S.P. is supported by the Slovenian Research Agency.

References

[1] E. Christova and D. Draganov, Phys. Lett. **B434** (1998) 373

[2] M. Fischer, S. Groote, J.G. Körner, M.C. Mauser and B. Lampe, Phys. Lett. **B451** (1999) 406

[3] M. Fischer, S. Groote, J.G. Körner and M.C. Mauser, Phys. Rev. **D65** (2002) 054036

[4] S. Groote, W.S. Huo, A. Kadeer and J.G. Körner, Phys. Rev. **D76** (2007) 014012

[5] J.A. Aguilar-Saavedra and J. Bernabeu, Nucl. Phys. **B840** (2010) 349;
J.A. Aguilar-Saavedra and R.V. Herrero-Hahn, arXiv:1208.6006

[6] J. Drobnak, S. Fajfer and J.F. Kamenik, Phys. Rev. **D82** (2010) 114008

[7] S. Groote and J. G. Körner, Phys. Rev. D **80** (2009) 034001

[8] S. Groote, J.G. Körner, B. Melic and S. Prelovsek, Phys. Rev. **D83** (2011) 054018

[9] G.A. Moortgat-Pick *et al.*, Phys. Rept. **460** (2008) 131

[10] X. Artru, M. Elchikh, J.M. Richard, J. Soffer and O.V. Teryaev, Phys. Rept. **470** (2009) 1

[11] S. Parke and Y. Shadmi, Phys. Lett. **B387** (1996) 199

[12] J. Kodaira, T. Nasuno and S.J. Parke, Phys. Rev. **D59** (1998) 014023

[13] G. Alexander, J. Barley, Y. Batygin, S. Berridge, V. Bharadwaj, G. Bower, W. Bugg and F.J. Decker *et al.*, Nucl. Instrum. Meth. **A610** (2009) 451

Chapter 3

Electroweak Precision Physics

The muon magnetic moment and new physics

Dominik Stöckinger
Institute for Nuclear and Particle Physics
TU Dresden, Germany

September 12, 2012

1 Introduction

The LHC era has had its first spectacular success with the discovery of a new particle compatible with a Standard Model (SM) Higgs boson. The LHC promises great progress in understanding the nature of electroweak symmetry breaking (EWSB). Additional, non-LHC observables are nevertheless important, for they can provide complementary information on EWSB, and they can unravel the existence of physics beyond the SM invisible at the LHC and possibly unrelated to EWSB.

The muon magnetic moment a_μ has a special role because it is sensitive to a large class of models related and unrelated to EWSB and because it combines several properties in a unique way: it is a flavour- and CP-conserving, chirality-flipping and loop-induced quantity. In contrast, many high-energy collider observables at the LHC and a future linear collider are chirality-conserving, and many other low-energy precision observables such as electric dipole moments or processes such as $\mu \to e\gamma$ are CP- or flavour-violating. These properties might be the reason why there is a significant deviation between the experimental and the SM value of a_μ,

$$a_\mu^{\rm exp} - a_\mu^{rmSM} = (28.7 \pm 8.0)10^{10}, \tag{1}$$

while there is no significant deviation in electroweak precision observables and searches for electric dipole moments and lepton-flavour violation have been unsuccesful.

In these proceedings we will first briefly review the current status and future prospects of $a_\mu^{\rm exp}$ and $a_\mu^{\rm SM}$ and we will explain the general structure and model-dependence of contributions from new physics. Then we will discuss concrete examples of contributions from and constraints on new physics models, with particular emphasis on the complementarity to recent LHC results.

2 Current status and future prospects

The uncertainty quoted in Eq. (1) is the quadratic sum of various experimental and theoretical errors. The experimental value of the muon magnetic moment has been determined by a series of measurements at BNL [1] with a final statistical and systematic uncertainty of $(\pm 5.4_{\rm stat} \pm 3.3_{\rm syst}) \times 10^{-10}$, which is dominated by statistics. The importance of this result has motivated two new experiments. One is already under construction at Fermilab, using the same technique as used at BNL, where high-energy muons at the "magic relativistic γ" are used, for which electric focusing fields in the ring do not perturb the muon precession. The second is planned at J-PARC, using ultra-cold muons with smaller γ but no electric focusing field. Both of these complementary experiments aim to reduce the statistical uncertainty by more than a factor 4.

The precision of the SM theory prediction is currently even higher than the experimental one. The remaining theory error is dominated by the hadronic vacuum polarization (HVP) contributions. These can be related to the cross section for $e^+e^- \to$ hadrons, and the increasingly precise experimental data for this cross section lead to consistent recent evaluations by several groups [2, 3, 4] (for recent overviews see [4, 5]). The error used in Eq. (1) is taken from Ref. [2] and is $\pm 4.2 \times 10^{-10}$. Earlier discrepancies between these e^+e^--based results and alternative ones using data from τ-decays have been dramatically reduced [2, 6, 7].

A subdominant part of the SM theory error is due to the hadronic light-by-light scattering (HLbL) contributions. Here progress is very difficult since hadronic dynamics is relevant in kinematical regimes where neither perturbation theory nor established low-energy effective theories are valid. In spite of using different approaches, the results of various groups agree within the quoted errors, see in particular Refs. [4, 8]. The result quoted in Eq. (1) is based on the evaluations of Refs. [2, 8], and has the theory error $\pm 2.6 \times 10^{-10}$.

3 New physics contributions in general

General contributions from new physics to a_μ are best understood by using a relation between a_μ and m_μ, the muon mass. Both a_μ and m_μ correspond to quantum field operators which flip chirality, i.e. convert a left-handed into a right-handed muon. For this reason, contributions of new physics at some scale Λ to both quantities, a_μ(N.P.) and δm_μ(N.P.), are linked as

$$a_\mu(\text{N.P.}) = \mathcal{O}(1) \times \left(\frac{m_\mu}{\Lambda}\right)^2 \times \left(\frac{\delta m_\mu(\text{N.P.})}{m_\mu}\right). \tag{2}$$

As discussed in [9], this relation is model-independent, but the *value* of the constant $C = \delta m_\mu(\text{N.P.})/m_\mu$ is highly model-dependent. It is important that the $\mathcal{O}(1)$ factors do not contain any coupling constants of $1/16\pi^2$ factors — those are contained in the constant C. A first consequence of this relation is

that new physics can explain the currently observed deviation (1) only if Λ is at the TeV scale or smaller (assuming no fine-tuning in the muon mass, $|C| < 1$).

Second, the relation illustrates how widely different contributions to a_μ are possible.

- For models with new weakly interacting particles (e.g. Z', W', little Higgs or universal extra dimension models [10, 11]) one typically obtains perturbative contributions to the muon mass $C = \mathcal{O}(\alpha/4\pi)$. Hence for weak-scale masses these models predict very small contributions to a_μ and might be challenged by the future more precise a_μ measurement. Models of this kind can only explain a significant contribution to a_μ if the new particles interact with muons but are otherwise hidden from searches. An example is the model with a new gauge boson associated to a gauged lepton number $L_\mu - L_\tau$ [12], where a gauge boson mass of $\mathcal{O}(100\ \text{GeV})$ is viable.

- For supersymmetric (SUSY) models one obtains an additional factor $\tan\beta$, the ratio of the two Higgs vacuum expectation values [13]. A numerical approximation for the SUSY contributions is given by

$$a_\mu^{\text{SUSY}} \approx 13 \times 10^{-10} \left(\frac{100\,\text{GeV}}{M_{\text{SUSY}}}\right)^2 \tan\beta\ \text{sign}(\mu), \tag{3}$$

  where M_{SUSY} denotes the common superpartner mass scale and μ the Higgsino mass parameter. It agrees with the generic result (2) for $C = \mathcal{O}(\tan\beta \times \alpha/4\pi)$ and is exactly valid if all SUSY masses are equal to M_{SUSY}. The formula shows that the observed deviation could be explained e.g. for relevant SUSY masses of roughly 200 GeV and $\tan\beta \sim 10$ or SUSY masses of 500 GeV and $\tan\beta \sim 50$. However, the SUSY prediction for a_μ depends strongly on the detailed scenario, and if SUSY exists a_μ will help to measure the SUSY parameters.

- Models with large $C \simeq 1$ are of interest since there the muon mass is essentially given by new physics loop effects. Some examples of such radiative muon mass generation models are given in [9]. For examples within SUSY see e.g. [14, 15]. In such models a_μ can be large even for particle masses at the TeV scale.

4 Supersymmetry and a_μ

As discussed above, supersymmetry with moderate to large $\tan\beta$ and masses in the 200–500 GeV range can easily explain the currently observed deviation (1). We now discuss the supersymmetry contributions in more detail. At the one-loop level, the diagrams involve either charginos and sneutrinos, or neutralinos and smuons. The relevant parameters are thus the soft mass parameters for the 2nd generation sleptons, the gaugino masses M_2, M_1, and the Higgsino mass parameter μ. Strongly interacting particles, squarks and gluinos, and their masses are irrelevant.

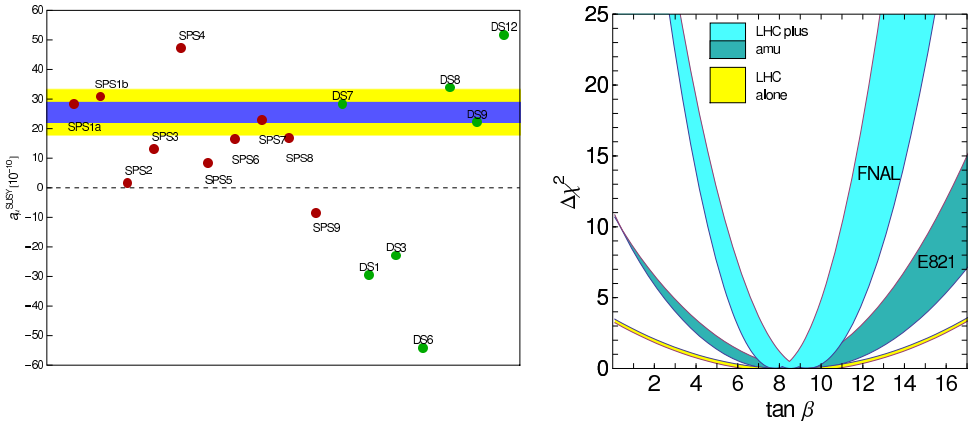

(a) (b)

Figure 1: (a) SUSY contributions to a_μ for the SPS benchmark points (red), and for the "degenerate solutions" from Ref. [22]. (b) Possible future $\tan\beta$ determination assuming that a slightly modified MSSM point SPS1a (see text) is realized. The bands show the $\Delta\chi^2$ parabolas from LHC-data alone (yellow) [24], including the a_μ with current precision (dark blue) and with prospective precision (light blue). The width of the blue curves results from the expected LHC-uncertainty of the parameters (mainly smuon and chargino masses) [24].

If all the relevant mass parameters are equal, the approximation (3) is valid, and the dominant contribution is from the chargino–sneutrino diagrams. If μ is very large, the bino-like neutralino contribution is approximately linear in μ and can dominate. If there is a large mass splitting between the left- and right-handed smuon, even the sign can be opposite to Eq. (3), see the discussions in [16, 13].

At the two-loop level various contributions are possible with potentially relevant impact. Photonic two-loop corrections always decrease the one-loop result slightly [19], and two-loop diagrams with either a sfermion (stop, sbottom, ...) loop or a chargino loop can be large even if the one-loop contributions are suppressed [17, 18]. For large $\tan\beta$, two-loop $(\tan\beta)^2$-enhanced effects become important [20].

Within supersymmetry the contributions to a_μ are therefore very model-dependent, and a_μ places important constraints on how supersymmetry can be realized. Fig. 1 illustrates this. The left plot shows the values for the so-called SPS benchmark points [21]. These span a wide range and can be positive or negative, due to the factor sign(μ) in Eq. 3. The discriminating power of the current (yellow band) and an improved (blue band) measurement is evident from Fig. 1(a). One might think that if SUSY exists, the LHC-experiments will find it and measure its parameters. The green points illustrate that this is not the case. They correspond to "degenerate solutions" of Ref. [22] — different SUSY parameter points which cannot be distinguished at the LHC alone (see also Ref.

[23] for the LHC inverse problem). They have very different a_μ predictions, in particular different signs for μ, and hence a_μ can resolve such LHC degeneracies.

The right plot of Fig. 1 illustrates that the SUSY parameter $\tan\beta$ can be measured more precisely by combining LHC-data with a_μ. It is based on the assumption that SUSY is realized, found at the LHC and the origin of the observed a_μ deviation (1). To fix an example, we use a slightly modified SPS1a benchmark point with $\tan\beta$ scaled down to $\tan\beta = 8.5$ such that $a_\mu^{\rm SUSY}$ is equal to an assumed deviation $\Delta a_\mu = 255\times10^{-11}$.[1] Ref. [24] has shown that then mass measurements at the LHC alone are sufficient to determine $\tan\beta$ to a precision of ±4.5 only. The corresponding $\Delta\chi^2$ parabola is shown in yellow in the plot. In such a situation one can study the SUSY prediction for a_μ as a function of $\tan\beta$ (all other parameters are known from the global fit to LHC data) and compare it to the measured value, in particular after an improved measurement. The plot compares the LHC $\Delta\chi^2$ parabola with the ones obtained from including a_μ, $\Delta\chi^2 = [(a_\mu^{\rm SUSY}(\tan\beta) - \Delta a_\mu)/\delta a_\mu]^2$ with the errors $\delta a_\mu = 80\times10^{-11}$ (dark blue) and 34×10^{-11} (light blue). As can be seen from the Figure, using today's precision for a_μ would already improve the determination of $\tan\beta$, but the improvement will be even more impressive after a future more precise a_μ measurement.

To date, the LHC has not found indications for supersymmetric particles, so a tension is rising between four pieces of experimental information and theoretical prejudice:

- If supersymmetry is the origin of the deviation in a_μ, the supersymmetric particles cannot be too heavy, in particular the smuons and charginos/neutralinos.
- The negative results of the LHC searches for supersymmetric particles imply lower limits, in particular on squark and gluino masses.
- The constraint that a SM-like Higgs boson mass is around 126 GeV requires either very large loop corrections from large logarithms or non-minimal tree-level contributions from additional non-minimal particle content.
- The requirement of small fine-tuning between supersymmetry-breaking parameters and the Z-boson mass prefers certain particles, in particular stops, gluinos and Higgsinos to be rather light.

Apart from fine-tuning, it is of course possible to accommodate all experimental data in the minimal supersymmetric standard model, which has enough free parameters [25]. However, the Constrained MSSM (CMSSM) cannot simultaneously describe all data [26], while slight extensions such as the Non-universal Higgs mass model (NUHM) or a model with gauge-mediated supersymmetry

[1] The actual SPS1a point is ruled out by LHC, however for our purposes only the weakly interacting particles are relevant, and these are not excluded. The following conclusions are neither very sensitive to the actual $\tan\beta$ value nor to the actual value of the deviation Δa_μ.

breaking and extra vector-like matter [27] are marginally consistent with all data.

Models inspired by naturalness, where the spectrum is such that fine-tuning is minimized while squarks and gluinos evade LHC bounds, can explain the observed Higgs boson mass but completely fail to explain a_μ [28].

An interesting possibility is provided by supersymmetric scenarios that realize radiative generation of the muon mass. Since the muon mass at tree level is given by the product of a Yukawa coupling and the vacuum expectation value of the Higgs doublet H_d, there are two kinds of such scenarios. First, one can postulate that the muon Yukawa coupling is zero but chiral invariance is broken by soft supersymmetry-breaking A-terms. Then, the moun mass, and $a_\mu^{\rm SUSY}$, arises at the one-loop level and $a_\mu^{\rm SUSY}$ can be large even for TeV-scale smuon masses [14, 15]. Second, one can postulate that the vacuum expectation value $\langle H_d \rangle$ is very small or zero [29, 30]. Then, the muon mass and $a_\mu^{\rm SUSY}$ arise at the one-loop level from loop-induced couplings to the other Higgs doublet.

5 Conclusions

In spite of tremendous progress at the LHC, a_μ is still a very important constraint on physics beyond the SM. The increasing difficulty to explain the a_μ deviation and satisfy LHC bounds and Higgs mass constraints highlights this. It is conceivable that the observed deviation (1) is real but not due to new physics at the electroweak scale, but e.g. due to new very light particles, as suggested e.g. in [31]. In such a case, the resolution of the EWSB puzzle would be the task of the LHC and a possible future linear collider, while the new light particles could be probed by dedicated low-energy precision experiments such as the next generation a_μ measurements.

References

[1] G.W. Bennett, et al., (Muon ($g-2$) Collaboration), Phys. Rev. D **73**, 072003 (2006).

[2] M. Davier, A. Hoecker, B. Malaescu and Z. Zhang, Eur. Phys. J. C **71** (2011) 1515 [Erratum-ibid. C **72** (2012) 1874] [arXiv:1010.4180 [hep-ph]].

[3] K. Hagiwara, R. Liao, A. D. Martin, D. Nomura and T. Teubner, J. Phys. G G **38** (2011) 085003 [arXiv:1105.3149 [hep-ph]].

[4] F. Jegerlehner and A. Nyffeler, Phys. Rept. **477** (2009) 1.

[5] J. Miller, E. de Rafael, B.L. Roberts, D. Stöckinger, Ann.Rev.Nucl.Part. (2012) 62.

[6] F. Jegerlehner and R. Szafron, Eur. Phys. J. C **71** (2011) 1632 [arXiv:1101.2872 [hep-ph]].

[7] M. Benayoun, P. David, L. DelBuono and F. Jegerlehner, Eur. Phys. J. C **72** (2012) 1848 [arXiv:1106.1315 [hep-ph]].

[8] J. Prades, E. de Rafael and A. Vainshtein, arXiv:0901.0306 [hep-ph].

[9] A. Czarnecki and W. J. Marciano, Phys. Rev. D **64** (2001) 013014.

[10] M. Blanke, A. J. Buras, B. Duling, A. Poschenrieder and C. Tarantino, JHEP **0705** (2007) 013 [arXiv:hep-ph/0702136].

[11] T. Appelquist and B. A. Dobrescu, "Universal extra dimensions and the muon magnetic moment," Phys. Lett. B **516** (2001) 85 [arXiv:hep-ph/0106140].

[12] E. Ma, D. P. Roy and S. Roy, Phys. Lett. B **525** (2002) 101 [hep-ph/0110146]. J. Heeck and W. Rodejohann, Phys. Rev. D **84** (2011) 075007 [arXiv:1107.5238 [hep-ph]].

[13] D. Stöckinger, J. Phys. G G **34** (2007) R45.

[14] F. Borzumati, G. R. Farrar, N. Polonsky and S. D. Thomas, Nucl. Phys. B **555** (1999) 53 [hep-ph/9902443].

[15] A. Crivellin, J. Girrbach and U. Nierste, Phys. Rev. D **83** (2011) 055009 [arXiv:1010.4485 [hep-ph]].

[16] T. Moroi, Phys. Rev. D **53** (1996) 6565 [Erratum-ibid. **56** (1997) 4424].

[17] S. Heinemeyer, D. Stöckinger and G. Weiglein, Nucl. Phys. B **690** (2004) 62.

[18] S. Heinemeyer, D. Stöckinger and G. Weiglein, Nucl. Phys. B **699** (2004) 103.

[19] G. Degrassi and G. F. Giudice, Phys. Rev. D **58** (1998) 053007, P. von Weitershausen, M. Schafer, H. Stockinger-Kim and D. Stockinger, Phys. Rev. D **81** (2010) 093004 [arXiv:1003.5820 [hep-ph]].

[20] S. Marchetti, S. Mertens, U. Nierste and D. Stöckinger, Phys. Rev. D **79**, 013010 (2009).

[21] B. C. Allanach *et al.*, in *Proc. of the APS/DPF/DPB Summer Study on the Future of Particle Physics (Snowmass 2001)* ed. N. Graf, Eur. Phys. J. C **25** (2002) 113.

[22] C. Adam, J. -L. Kneur, R. Lafaye, T. Plehn, M. Rauch and D. Zerwas, Eur. Phys. J. C **71** (2011) 1520 [arXiv:1007.2190 [hep-ph]].

[23] N. Arkani-Hamed, G. L. Kane, J. Thaler and L. T. Wang, JHEP **0608**, 070 (2006) [arXiv:hep-ph/0512190].

[24] M. Alexander, S. Kreiss, R. Lafaye, T. Plehn, M. Rauch, and D. Zerwas, Chapter 9 in M. M. Nojiri *et al.*, arXiv:0802.3672 [hep-ph].

[25] R. Benbrik, M. G. Bock, S. Heinemeyer, O. Stal, G. Weiglein and L. Zeune, arXiv:1207.1096 [hep-ph].

[26] P. Bechtle, T. Bringmann, K. Desch, H. Dreiner, M. Hamer, C. Hensel, M. Kramer and N. Nguyen *et al.*, JHEP **1206** (2012) 098 [arXiv:1204.4199 [hep-ph]].

[27] M. Endo, K. Hamaguchi, S. Iwamoto, K. Nakayama and N. Yokozaki, Phys. Rev. D **85** (2012) 095006 [arXiv:1112.6412 [hep-ph]].

[28] H. Baer, V. Barger, P. Huang and X. Tata, JHEP **1205** (2012) 109 [arXiv:1203.5539 [hep-ph]].

[29] B. A. Dobrescu and P. J. Fox, Eur. Phys. J. C **70** (2010) 263 [arXiv:1001.3147 [hep-ph]].

[30] W. Altmannshofer and D. M. Straub, JHEP **1009** (2010) 078 [arXiv:1004.1993 [hep-ph]].

[31] M. Pospelov, Phys. Rev. D **80** (2009) 095002 [arXiv:0811.1030 [hep-ph]].

Physics Applications of Polarized Positrons

S. Riemann
DESY Zeuthen, Platanenallee 6, D-15738 Zeuthen, Germany

Abstract

With the LHC a new era of measurements at the energy frontier has started, and exciting new discoveries are expected. However, also measurements at the precision frontier will be necessary to fully understand the underlying physics model. The programme for the e^+e^- collider projects ILC and CLIC is focused on precision tests of the Standard Model and new physics beyond it at the TeV scale. Polarized positron beams play a crucial role in these analyses. Here, the advantages as well as the requirements using also polarized positron beams for measurements at e^+e^- colliders are discussed.

1 Introduction

So far, the particle physics experiments have confirmed the Standard Model (SM) with excellent precision. Neither significant deviations from the SM predictions nor new physics phenomena have been obtained. Based on the global analysis of the measurements it is expected that the SM Higgs boson has a mass of $\mathcal{O}(100)\,\mathrm{GeV}$. The fundamental question whether the Higgs boson exists will be answered soon by the measurements at the LHC, and the experiments are well prepared to discover and probe new physics beyond the SM. But the full understanding of phenomena obtained at the LHC is only possible if complementary measurements from lepton colliders are available. The precise knowledge of type, energy and helicity of the interacting particles allows to test theoretical models at the level of quantum corrections up to higher orders. The microscopic world of electroweak interactions is not left-right symmetric and so are new phenomena suggested by various extensions of the SM. The chiral structure of interactions can be analyzed best using high-energy lepton colliders with polarized beams. However, the production of an intense, highly polarized electron beam with high energy is simple in comparison to the generation of the corresponding polarized positron beam.

But the flexibility and the substantial advantages justify the effort necessary to create the polarized positron beam.

In this paper important features of measurements at e^+e^- colliders with polarized beams are discussed. Section 2 presents few selected examples for precision physics with polarized beams. In subsections 2.1–2.3 the basics of measurements with polarized beams are introduced. The experimental requirements to utilize polarized positron beams are described in section 3. Section 4 summarizes.

2 Physics with Polarized Positrons

The era of precision electroweak measurements [2] at high energies was based on experiments at the Large Electron Positron Collider (LEP) at CERN and at the SLAC Linear Collider (SLC). The Standard Model has been confirmed with extremely high precision, up to loop corrections. Its parameters have been determined and the mass of the SM Higgs boson has been predicted. One of the important SM parameters that describe the electroweak symmetry breaking is the weak mixing angle, $\sin^2\theta_{\mathrm{W}}$. The measurement of this observable was performed by the four LEP collaborations, ALEPH, DELPHI, L3 and OPAL, and by the SLD collaboration; the results and details can be found in reference [2] . It was impressive to see that the SLD collaboration achieved a slightly more precise measurement of this parameter than the four LEP collaborations combined although the latter obtained a more than 30 times higher number of Z bosons created in e^+e^- collisions. The crucial point was the polarized electron beam which increased the sensitivity to the left-right asymmetry of the Z boson coupling to fermions. If SLD would have used also polarized positrons a further reduction of the uncertainty by a factor of about two would have been possible.

This simple Gedankenexperiment demonstrates the potential of polarized beams in high energy particle physics experiments. The precise test of the SM at high energies as well as the understanding of new phenomena benefit substantially if electron and positron beams are polarized. A comprehensive overview of physics with both beams – electrons and positrons – polarized is given in reference [1] . Here, some of the basics are emphasized.

First, few remarks about the requirements for measurements at the precision frontier. Future lepton colliders have to complement and to attend the physics goals achieved with the LHC. This implies physics at center-of-mass energies between 200 GeV and 1 (3) TeV. Two projects are under development: the International Linear Collider (ILC) [3] with energies between 200 GeV and 1 TeV and the possibility to run also at the Z boson resonance,

$\sqrt{s} = 91.2\,\text{GeV}$, and the Compact Linear Collider (CLIC) [4] foreseen for energies up to 3 TeV. To interprete the results and to examine the SM and possible extensions, the precision of measurements must be better than the size of higher order corrections to the observables. With other words: Only high intensities (combined with a highly sophisticated detector) allow to detect the huge number of events for all interesting processes which is necessary to perform measurements with uncertainties at and below the percent-level. However, it is not at all easy to produce a beam with the required high luminosity. Since the cross sections in lepton colliders fall as $\sigma \sim 1/E^2$, the increase of energy by a factor f has to be compensated by a factor f^2 for the luminosity to keep the number of events almost constant. Further, the stability of energy and luminosity must be very high – below 0.1% for the ILC – and the precise measurements of energy and luminosity must be possible. Similar requirements exist for the beam polarization. As shown in the SLD experiment at SLC, electron beam polarization of 80% is possible and measurable with a precision of 0.5% [2]. Further improvements are possible at the ILC [5]. In the following features of precision measurements using polarized beams are discussed.

2.1 Fermion-Pair Production in the s-Channel

Some important advantages of physics with colliding polarized beams can be explained best for the fermion-pair production process. Photon and Z boson are spin-1 particles, and in the SM they are exchanged in this process, $e^+e^- \to Z, \gamma \to f\bar{f}$. The Feynman diagram in lowest order is shown in figure 1. For longitudinally polarized beams, the cross section can be written as

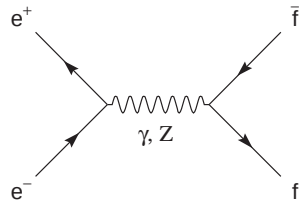

Figure 1: The Feynman diagram in lowest order for the fermion-pair production; in the SM, photon and Z boson are exchanged (J=1).

$$\begin{aligned}\sigma_{\mathcal{P}_{e^-}\mathcal{P}_{e^+}} &= \frac{1}{4}\left[(1-\mathcal{P}_{e^-})\,(1+\mathcal{P}_{e^+})\,\sigma_{\mathrm{LR}} + (1+\mathcal{P}_{e^-})\,(1-\mathcal{P}_{e^+})\,\sigma_{\mathrm{RL}}\right.\\ &\quad \left. + (1-\mathcal{P}_{e^-})\,(1-\mathcal{P}_{e^+})\,\sigma_{\mathrm{LL}} + (1+\mathcal{P}_{e^-})\,(1+\mathcal{P}_{e^+})\,\sigma_{\mathrm{RR}}\right]\,, \quad (1)\end{aligned}$$

with the electron beam polarization $\mathcal{P}_{e^-}$ and the positron beam polarization $\mathcal{P}_{e^+}$. σ_{LR} denotes the cross section if the electron beam is 100% left-handed polarized ($\mathcal{P}_{e^-} = -1$), and the positron beam 100% right-handed polarized ($\mathcal{P}_{e^+} = +1$). The other cross sections, σ_{RL}, σ_{LL} and σ_{RR}, are defined correspondingly. Since the exchange of the spin-1 particles, photon and Z boson, in the fermion-pair production is only possible for $J = 1$, the cross sections σ_{RR} and σ_{LL} are zero in the SM[1]. Figure 2 shows the possible combinations of electrons and positrons with helicities ± 1. It is not excluded that further – yet unknown – particles contribute either to processes with $J = 1$ or $J = 0$. If these particles are not too heavy they can be studied by precise measurements of the process $\mathrm{e^+e^-} \to \mathrm{f\bar{f}}$.

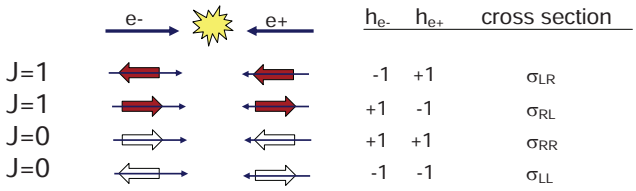

Figure 2: Helicity combinations in collisions of electrons and positrons and the corresponding contributions to the cross section.

The cross section (1) can be expressed with

$$\sigma_{i,j} = \frac{1}{4}\sigma_u \left[1 - \mathcal{P}_{\mathrm{e^+}}\mathcal{P}_{\mathrm{e^-}} + A_{\mathrm{LR}}\left(-\mathcal{P}_{\mathrm{e^+}} + \mathcal{P}_{\mathrm{e^-}}\right)\right], \tag{2}$$

where A_{LR} is the left-right asymmetry caused by the different coupling strength of Z bosons to left- an right-handed fermions, and the indices i, j describe the sign of the polarization: σ_{-+}, σ_{+-}, σ_{++}, σ_{--}. Taking into account beams with realistic polarization, $|\mathcal{P}| < 1$, the measured cross sections for the different helicity combinations are

$$\sigma_{-+} = \frac{1}{4}\sigma_u \left[1 + |P_{e^+}P_{e^-}| + A_{LR}\left(+|P_{e^+}| + |P_{e^-}|\right)\right] \tag{3}$$

$$\sigma_{+-} = \frac{1}{4}\sigma_u \left[1 + |P_{e^+}P_{e^-}| + A_{LR}\left(-|P_{e^+}| - |P_{e^-}|\right)\right]$$

$$\sigma_{++} = \frac{1}{4}\sigma_u \left[1 - |P_{e^+}P_{e^-}| + A_{LR}\left(-|P_{e^+}| + |P_{e^-}|\right)\right] \tag{4}$$

$$\sigma_{--} = \frac{1}{4}\sigma_u \left[1 - |P_{e^+}P_{e^-}| + A_{LR}\left(+|P_{e^+}| - |P_{e^-}|\right)\right]$$

[1]The cross section for the exchange of Higgs bosons ($J = 0$) yields only tiny contributions and is neglected.

where σ_u denotes the cross section with unpolarized beams. The cross sections σ_{++} and σ_{--} ($J = 0$) are zero for $\mathcal{P}_{e^-} = \mathcal{P}_{e^+} = \pm 1$, in contrast to $\sigma_{+-} \neq 0$ and $\sigma_{-+} \neq 0$ for $\mathcal{P}_{e^-} = -\mathcal{P}_{e^+} = \pm 1$ ($J = 1$). It is easy to see that in case of unpolarized electron and positron beams half of the collisions is spent for helicity combinations that yield $\sigma = 0$. Figure 2 illustrates the combinations and resulting cross section contributions.

If the electron beam is 100% longitudinally polarized, but the positron beam is unpolarized, one half of the measurements is performed with the orientation $\mathcal{P}_{e^-} = +1$, the other half with $\mathcal{P}_{e^-} = -1$. Also in this case initial state helicity combinations occur that do not contribute to the cross section. Hence, only half of the possible helicity combinations yields $\sigma \neq 0$.

However, if both beams are 100% polarized and $\mathcal{P}_{e^-} = -\mathcal{P}_{e^+}$, all possible combinations of initial state helicity amplitudes contribute to the cross section measurement and the luminosity is enhanced compared to the case of unpolarized beams. Figure 3 demonstrates these options.

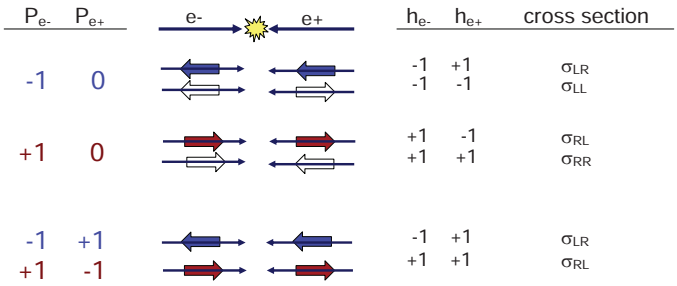

Figure 3: Helicity combinations in collisions of a longitudinally polarized electron and unpolarized positron beam (upper part) and in collisions with both beams polarized. The corresponding helicities of the initial state particles as well as the contributions to the cross section are shown.

2.2 Cross Sections

It is an important result, that the effective luminosity can be substantially enhanced if both beams are polarized. The unpolarized cross section, σ_u, is given by the sum

$$\sigma_u = \frac{1}{4}\left(\sigma_{+-} + \sigma_{-+} + \sigma_{--} + \sigma_{++}\right) . \tag{5}$$

Using unpolarized beams, σ_u is measured obtaining the number N_u of events for the integrated luminosity $\mathcal{L}$,

$$\sigma_u = \frac{N_u}{\mathcal{L}}\,. \tag{6}$$

If the electron beam is 100% polarized but the positron beam unpolarized, and the luminosity is equally distributed to collisions with $\mathcal{P}_{e^-} = -1$ and $\mathcal{P}_{e^-} = +1$, one finds

$$\sigma_u = \frac{\sigma_{+0} + \sigma_{-0}}{2} = \frac{N_{+0} + N_{-0}}{\mathcal{L}/2} = \frac{N_u}{\mathcal{L}}\,. \tag{7}$$

If also the positron beam is polarized, the unpolarized cross section is

$$\sigma_u = \frac{\sigma_{-+} + \sigma_{+-}}{2} = \frac{N_{+-} + N_{-+}}{\mathcal{L}/2} = \frac{N_u}{(1 - \mathcal{P}_{e^+}\mathcal{P}_{e^-})\,\mathcal{L}}\,. \tag{8}$$

The luminosity is effectively enhanced,

$$\mathcal{L}_{\text{eff}} = (1 - \mathcal{P}_{e^+}\mathcal{P}_{e^-})\,\mathcal{L}\,, \tag{9}$$

resulting in a smaller statistical error of the measurement. With positron beam polarization of $|\mathcal{P}_{e^+}| = 0.4$ (0.6), the effective luminosity can be increased by about 30% (50%) having an electron beam polarization of $|\mathcal{P}_{e^-}| = 0.8$. In the same way, also processes beyond the SM, e.g. due to the exchange of spin-0 particles, can be enhanced. However, in that case also runs with combinations of the initial state helicities are necessary that are 'inefficient' with respect to the SM cross sections. But the flexibility to chose the desired initial state helicities improves the precision of SM measurements as well as the sensitivity to new phenomena beyond the SM.

It must be mentioned that the uncertainties for the left-handed and right-handed cross section measurements, $\delta\sigma_{+-}$, $\delta\sigma_{-+}$, include also the error of the polarization measurement. For $\delta\mathcal{P}_{e^+}/\mathcal{P}_{e^+} = \delta\mathcal{P}_{e^-}/\mathcal{P}_{e^-} = \delta\mathcal{P}/\mathcal{P}$ the additional error contribution due to the beam polarization measurement is

$$\frac{\delta\sigma_{ij}}{\sigma_{ij}} \;=\; \frac{\delta\mathcal{P}}{\mathcal{P}}\sqrt{2\mathcal{P}_{e^+}^2\mathcal{P}_{e^-}^2 + A_{\text{LR}}^2\left(\mathcal{P}_{e^+}^2 + \mathcal{P}_{e^-}^2\right)}\,, \tag{10}$$

which is unimportant for small relative polarization errors and small A_{LR}. However, for high luminosities larger $1\,\text{ab}^{-1}$ and $\delta\mathcal{P}/\mathcal{P} = 0.25\%$, this contribution can approach the magnitude of the statistical error of the cross section measurement. The corresponding contribution to the uncertainty of the unpolarized cross section is

$$\frac{\delta\sigma_u}{\sigma_u} \;=\; \frac{\mathcal{P}_{e^+}\mathcal{P}_{e^-}}{1 - \mathcal{P}_{e^+}\mathcal{P}_{e^-}}\sqrt{\left(\frac{\delta\mathcal{P}_{e^+}}{\mathcal{P}_{e^+}}\right)^2 + \left(\frac{\delta\mathcal{P}_{e^-}}{\mathcal{P}_{e^-}}\right)^2}\,. \tag{11}$$

and increases slightly the uncertainty of the measurement. The knowledge of the contributions (10) and (11) is important for precision measurements with high luminosities and high beam polarizations. Large errors on the polarization measurement could limit the precision to measure unpolarized quantities, or the right-handed and left-handed cross-sections, σ_{LR} and σ_{RL}, correspondingly.

2.3 Left-Right Asymmetry

The left-right asymmetry A_{LR} is an important observable to measure the left- and right-handed coupling of bosons to fermions. It is defined as

$$A_{\mathrm{LR}} = \frac{\sigma_{\mathrm{LR}} - \sigma_{\mathrm{LR}}}{\sigma_{\mathrm{LR}} + \sigma_{\mathrm{LR}}} \,. \tag{12}$$

Since in realistic beams $|\mathcal{P}| < 1$, A_{LR} is derived from measurements by

$$A_{\mathrm{LR}} = \frac{\sigma_{-+} - \sigma_{+-}}{\sigma_{-+} + \sigma_{+-}} = \frac{A_{\mathrm{LR}}^{\mathrm{meas}}}{\langle \mathcal{P}_{\mathrm{eff}} \rangle} \tag{13}$$

with the effective polarization, $\mathcal{P}_{\mathrm{eff}}$:

$$\mathcal{P}_{\mathrm{eff}} = \frac{-\mathcal{P}_{\mathrm{e}^-} + \mathcal{P}_{\mathrm{e}^-}}{1 - \mathcal{P}_{\mathrm{e}^-}\mathcal{P}_{\mathrm{e}^+}} \tag{14}$$

The effective polarization is larger than the individual $\mathrm{e}^{\pm}$ beam polarizations; 80% polarization of the electron beam are increased to an effective polarization of almost 95% using a 60% polarized positron beam. Because of error propagation the uncertainty of the effective polarization is substantially decreased. Assuming that the relative error for polarization measurement of the electron and positron beam is $\delta\mathcal{P}_{\mathrm{e}^+}/\mathcal{P}_{\mathrm{e}^+} = \delta\mathcal{P}_{\mathrm{e}^-}/\mathcal{P}_{\mathrm{e}^-} = \delta\mathcal{P}/\mathcal{P}$, the uncertainty of the effective polarization yields

$$\frac{\delta\mathcal{P}_{\mathrm{eff}}}{\mathcal{P}_{\mathrm{eff}}} = \frac{\delta\mathcal{P}}{\mathcal{P}} \frac{\sqrt{\left(1 - \mathcal{P}_{\mathrm{e}^+}^2\right)^2 \mathcal{P}_{\mathrm{e}^-}^2 + \left(1 - \mathcal{P}_{\mathrm{e}^-}^2\right)^2 \mathcal{P}_{\mathrm{e}^+}^2}}{\left(\mathcal{P}_{\mathrm{e}^+} + \mathcal{P}_{\mathrm{e}^-}\right)\left(1 + \mathcal{P}_{\mathrm{e}^+}\mathcal{P}_{\mathrm{e}^-}\right)} \,. \tag{15}$$

Assuming 80% (90%) electron polarization, and an uncertainty of the polarization measurement of $\delta\mathcal{P}/\mathcal{P} = 0.25\%$[5], the error of the effective polarization is reduced by a factor 3.7 if the positron beam is 60% polarized. This fact is important for precise A_{LR} measurements with large integrated luminosity. In this case the error contribution due to the polarization uncertainty could dominate the total error, δA_{LR}, given by

$$\delta A_{\mathrm{LR}} = \sqrt{\frac{1 - \mathcal{P}_{\mathrm{eff}}^2 A_{\mathrm{LR}}}{\mathcal{P}_{\mathrm{eff}} N} + A_{\mathrm{LR}}^2 \left(\frac{\delta\mathcal{P}_{\mathrm{eff}}}{\mathcal{P}_{\mathrm{eff}}}\right)^2} \,. \tag{16}$$

2.4 u,t-Channel Processes

In sections 2.1–2.3 some basic advantages are discussed for s-channel processes. Without going into detail it should be mentioned that the search for new phenomena benefits from polarized positrons also if u- and t-channel processes are considered. In u- and t-channel processes the helicity of the particle's final state is directly coupled to the helicity of the initial state fermion, it does not depend on the helicity of the second incoming beam particle. This gives a direct access to the helicity of the exchanged particle and allows an enhancement or suppression of specific processes. An example is the production of single W bosons, $e^+e^- \to W\,e\,\nu$, which is one basic process to study CP violation. For more details and examples, in particular the sensitivity to supersymmetric phenomena, the interested reader is strongly encouraged to consult reference [1] .

2.5 W^+W^- Pair Processes

The precise measurement of the Three-Gauge-Boson-Coupling (TGC) in the process $e^+e^- \to Z, \gamma \to W^+W^-$ allows a test of the weak gauge structure as described by the SM, and it is very sensitive to new physics scenarios. Since the SM defines the TGC, deviations of precision measurements from the SM prediction are hints to new phenomena. To select this process with high efficiency, the contribution of the neutrino exchange in the t-channel, $e^+e^- \to \nu \to W^+W^-$ (see figure 4), is suppressed using a polarized electron beam. A further improvement is possible with polarized positrons in addition to polarized electrons.

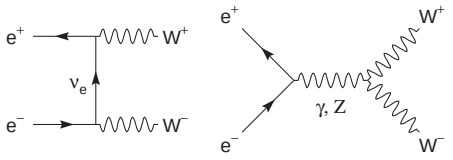

Figure 4: Feynman diagrams for the process $^+e^- \to W^+W^-$. Only the right diagram is important to measure TGC.

2.6 Higgs Factory

The Higgs boson is a scalar particle which can be produced in e^+e^- annihilation by the Higgsstrahlung or boson fusion (see figure 5). The dominating

process is determined by the Higgs mass which is not yet known. In case of a light Higgs boson as suggested by the electroweak precision measurements at LEP and SLD [2], the Higgsstrahlung is dominating. With polarized positrons the Higgs production can be enhanced by a factor $(1 - \mathcal{P}_{e^+}\mathcal{P}_{e^-})$. If the Higgs boson is heavy, it is produced via WW fusion, $e^+e^- \to \nu_e\bar{\nu}_e H$. This process can be enhanced (or suppressed) by the factor $(1 + \mathcal{P}_{e^+})(1 - \mathcal{P}_{e^-})$ choosing the proper sign of the $e^\pm$ polarizations. For $(\mathcal{P}_{e^-}, \mathcal{P}_{e^+}) = (-80\%, +60\%)$, the WW fusion process is enhanced by a factor of 2.88 in comparison to unpolarized beams.

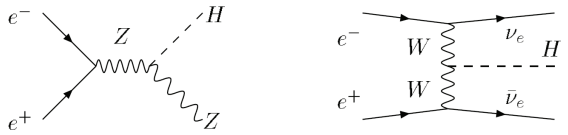

Figure 5: Feynman diagrams for Higgs production processes: Higgsstrahlung process (left) and WW boson fusion (right).

2.7 GigaZ Option

Electroweak precision measurements at the Z resonance were performed by the experiments ALEPH, DELPHI, L3 and OPAL at LEP and SLD at SLC. Taking into account the results for the top quark mass and the W boson mass, the SM has been confirmed at the one-loop level of quantum corrections. The results of LEP and SLD are in good agreement, however, the A_{LR} measurement at SLD results in values for the weak mixing angle or correspondingly for the Z boson couplings to fermions that are slightly different from that determined by the LEP experiments. Running at the Z resonance again by utilizing polarized $e^\pm$ beams and a much higher luminosity would substantially improve the accuracy of electroweak measurements. This option is called GigaZ since the luminosity available at the ILC allows to produce and record about 10^9 Z bosons within few months of running. High-luminosity measurements at the Z resonance combined with updated precise results for the W boson mass, the top-quark mass, and hopefully the Higgs boson mass allow excellent consistency tests of the SM and provide a high sensitivity to models beyond the SM. This would also to test whether the slightly differing values for observables measured at LEP and SLD is a fluctuation as assumed so far, or whether it is due to a certain yet unknown phenomenon. At GigaZ a relative precision of less than 5×10^{-5} can be achieved for the

effective weak mixing angle – more than 10 times better than the values achieved with LEP/SLD measurements. This allows precise conclusions on new physics models, e.g. supersymmetry. The GigaZ option requires very precise measurements of energy, luminosity and beam polarization. If both beams are polarized, the Blondel scheme [6] can be applied to determine the beam polarization and A_{LR} simultaneously with highest precision [7].

2.8 Transversely Polarized Beams

Finally it must be mentioned that also collision of transversely polarized beams are interesting. They allow access to helicity correlations, CP violating effects and new phenomena like extra dimension [8]. The contribution to the differential cross section due to transverse polarization is

$$\frac{\mathrm{d}\sigma}{\mathrm{d}\Omega} \sim \mathcal{P}_{\perp}^{\mathrm{e}^+}\mathcal{P}_{\perp}^{\mathrm{e}^-}\,\sin\theta\cos 2\phi\,, \tag{17}$$

which is zero if one of the colliding beams is unpolarized. New physics phenomena yield additional terms resulting in substantially modified differential cross sections. For example, extra dimensions differential cross sections measured for transversely as well as longitudinally polarized beams with angular distributions typical for special classes of models. Hence, physics runs with transversely polarized beams will help to distinguish between models and to resolve ambiguities.

3 Requirements for Physics

Polarized positron and polarized electron beams offer the best flexibility and an improved sensitivity to fulfill the physics programme for future high energy lepton colliders. Unfortunately, it is quite difficult to produce an intense polarized positron beam for a high energy linear collider. The ILC baseline design proposes to generate the positrons using photons created in an undulator passed by a high energy electron beam [9]. Since the photon yield in a helical undulator is higher up to a factor 2 than in a planar undulator, the ILC positron source design is based on a helical undulator. The photons generated in a helical undulator are circularly polarized. If they hit the positron production target, longitudinally polarized electron-positron pairs are created. The scheme has been tested successfully in the proof-of-principle experiment E-166 at SLAC [10].

Using a helical undulator, the ILC will provide a polarized positron beam. The degree of polarization is determined by the parameters of the undulator

and the source design. The opening angle of the photon beam decreases with the electron energy, $\propto 1/\gamma$. The polarization of the photons is distributed such that a collimation of the photon beam increases its average polarization. The loss of intensity has to be compensated using a longer undulator. For more details see the references [11, 12] .

In order to exploit the positron and electron beam polarization for physics measurements, the degree of polarization must be kept up to the interaction point. Therefore spin rotation systems upstream the damping ring rotate the particle spins from the longitudinal to the vertical direction, parallel (or anti-parallel) to the magnetic field in the damping ring. Downstream the turnaround the spins are rotated back to the longitudinal direction so that the beams have the desired polarization at the IP.

The electron and positron beam polarization is measured at the IP using Compton polarimeters. To meet the high precision requirements, the relative uncertainty of the polarization measurement must be at the level of (few) per-mille.

One important issue must be mentioned: The direction of the helical undulator winding determines the orientation of the photon polarization and therefore the sign of the positron polarization. Switching to the opposite orientation of positron beam polarization requires an additional spin-flip equipment. This point is discussed in the subsection 3.3. It should be remarked that in a polarized positron source based on Compton back-scattering the helicity reversal can be easily realized by switching the polarization of the laser light.

3.1 Polarimetry at the Interaction Point

The beam polarization at the interaction point is measured using Compton polarimeters. In order to determine the luminosity-weighted longitudinal polarization at the interaction point (IP) at the ILC, one polarimeter is located at the beginning of the Beam Delivery System upstream the IP, the other in the extraction line downstream the IP. The two polarimeters are highly complementary. The upstream polarimeter has a clean environment and a much higher counting rate; the fast polarization measurement is important to detect correlations. The downstream polarimeter measures the polarization of the outgoing beam. Since the background in the downstream polarimeter is high and the beam is disrupting after the IP, the counting rate is substantially smaller than in the upstream polarimeter. But the downstream polarimeter has access to depolarization effects: Due to the small bunch sizes high electromagnetic fields act between the particles in the crossing bunches and induce the radiation of hard photons. The resulting depolar-

ization has to be taken into account to attain the required precision of the polarization measurement. The combination of both polarimeters allows the determination of the luminosity-weighted polarization; cross checks between both polarimeters are possible. Measurements without collisions can be used to control the spin transport through the Beam Delivery System. However, due to the large beam disruption at CLIC the downstream polarimeter will not work with the required precision.

Present studies and test measurements show that at the ILC a precision of $\delta\mathcal{P}/\mathcal{P} \approx 0.25\%$ can be achieved [5] for the longitudinal polarization. For comparison: the precision for the polarization measurement reached with the Compton polarimeter at the SLD experiment was $\delta\mathcal{P}/\mathcal{P} = 0.5\%$. The measurement of the transverse polarization at the IP is under study.

3.2 Positron Polarimetry at the Source

Since the production of an intense positron beam needs some effort the degree of polarization should also be measurable at the positron source. At the electron source a Mott polarimeter is used. Due to the design and the parameters of a polarized positron source it is not recommended to apply a Mott polarimeter. Instead, a Bhabha polarimeter located at beam energies of few hundred MeV is a promising option [13].

3.3 Frequency of Helicity Reversal

As discussed in section 2, a substantial enhancement of the effective luminosity is possible with polarized beams. But the increase by the factor $(1 - \mathcal{P}_{e^-}\mathcal{P}_{e^+})$ is only possible in case of an efficient pairing of initial states $(+-)$, $(-+)$. This requires the same helicity reversal frequencies for the electron and the positron beam. The polarization of the electron beam can be flipped easily by reversing the polarity of the laser beam which hits the photocathode. A fast and random flipping between the beam polarization orientations reduces systematic uncertainties substantially (see also reference [2]). The orientation of the positron beam polarization can be reversed using a spin rotator. However, it is impossible to switch the high magnetic field in the spin rotator within very short time, e.g. from train to train as possible for the electron beam. There is no gain for the effective luminosity if the helicity of the positrons is reversed from run to run (or even less often) and the the helicity of the electrons train-by-train. Further, to control systematic effects, a very high long-term stability is necessary. A possible solution of this problem would be to kick the positron beam to parallel spin rotation lines with opposite magnetic fields, similar as suggested in reference [14] .

The precision measurements require almost identical intensities and polarizations for the left- and right-handed oriented beams. The measured left-right asymmetry is related to the left-right asymmetry by

$$A_{\mathrm{LR}} = \frac{A_{\mathrm{LR}}^{\mathrm{meas}}}{\langle \mathcal{P}_{\mathrm{eff}} \rangle} \,. \tag{18}$$

If the luminosities and degrees of polarization are identical for σ_{-+} and σ_{+-}, one gets

$$A_{\mathrm{LR}} = \frac{N_{-+} - N_{+-}}{N_{-+} - N_{+-}} \frac{1}{\langle \mathcal{P}_{\mathrm{eff}} \rangle} \,. \tag{19}$$

Also for fast helicity reversal small differences in luminosity and polarization occur between the running modes $(+-)$ and $(-+)$. They have to be taken into account,

$$A_{\mathrm{LR}} = \frac{A_{\mathrm{LR}}^{\mathrm{meas}}}{\langle \mathcal{P}_{\mathrm{eff}} \rangle} + \frac{1}{\langle \mathcal{P}_{\mathrm{eff}} \rangle} \left[(A_{\mathrm{LR}}^{\mathrm{meas}})^2 A_{\mathcal{P}} + \langle \mathcal{P}_{\mathrm{eff}} \rangle \Delta_{\mathcal{P}} + A_{\mathcal{L}} + \dots \right] , \tag{20}$$

where $A_{\mathcal{L}}$ and $A_{\mathcal{P}}$ are the left-right asymmetries of the integrated luminosity and of the beam polarization; the asymmetries of residual background, the center-of-mass energy, detector acceptance and efficiency are not shown in equation (20). The contribution $\Delta_{\mathcal{P}}$ depends on $\Delta\mathcal{P}_{\mathrm{e}^+}\mathcal{P}_{e^-} + \Delta\mathcal{P}_{\mathrm{e}^-}\mathcal{P}_{e^+}$ with $\Delta\mathcal{P}_{\mathrm{e}}$ as difference between + and − sign of the beam polarization. A slower helicity reversal for the positron than for the electron beam yields different luminosities for the running modes $(+-)$ and $(-+)$, and also the degree of polarization could vary. The resulting corrections in equation (20) could be large. The corrections to A_{LR}, i.e. $A_{\mathcal{L}}$, $A_{\mathcal{P}}$ and $\Delta_{\mathcal{P}}$, must be determined and should be as small as possible. In particular, the uncertainty of $A_{\mathcal{L}}$ and $\Delta_{\mathcal{P}}$ should be at the per-mille level to achieve the desired high precision for A_{LR}.

Detailed studies are ongoing to evaluate the influence of parallel spin rotation lines on the final physics performance with polarized beams, and to find alternative solutions with fast and flexible helicity reversal at the undulator-based positron source.

4 Summary

Precision measurements of SM physics and phenomena beyond the SM can be performed at future linear $\mathrm{e}^+\mathrm{e}^-$ colliders. They will extend and complement the achievements of the LHC. The best conditions are provided if high luminosity, a wide energy range and polarized beams are available. In particular, the flexible choice of initial state helicities is desired to reveal unexpected phenomena and their nature.

The polarization of both beams, electrons and positrons, affords substantial advantages: The occurrence of desired processes can be enhanced. The effective luminosity for s-channel processes with exchange of spin-1 particles can be increased by the factor $(1 - \mathcal{P}_{e^-}\mathcal{P}_{e^+})$ if the luminosity is equally distributed to running modes with the initial state helicities $(+-)$ and $(-+)$. The uncertainty of the effective polarization is reduced which is important for precision measurements of left-right asymmetries. Among many arguments to have polarized positrons it should be emphasized: If signals from physics beyond the SM are found, a much better distinction between models is possible than with only one polarized beam. For the GigaZ option the electron and the positron beam must be polarized to achieve the required precision for the $A_{\rm LR}$ and polarization measurement. In order to benefit from these advantages, it must be possible to reverse the helicity of positrons as frequent as the helicity of electrons. Hence, for a positron source based on a helical undulator an additional facility is necessary to realize the fast spin flip for the positrons.

Finally, it should be emphasized that a positron source based on a helical undulator will provide a polarized positron beam; the degree of polarization depends strongly on the undulator parameters and the energy of the electrons passing through. One may ask what minimum degree of positron polarization is necessary. Recent ILC studies [1, 15] show that for $\mathcal{P}_{e^+} > 30\%$ the physics analyses clearly benefit from polarized electron and positron beams. Of course, a high degree of positron polarization is desired and can be realized by photon beam collimation for the undulator-based source (see also reference [16]). Thus, an excellent feasibility is provided to perform the high energy linear collider physics programme at the precision frontier.

Acknowledgments

I would like to thank my collaborators, in particular Gudrid Moortgat-Pick and Jenny List for discussions about physics with polarized positron beams. I am grateful to Prof. Jie Gao and his local team for organizing this successful POSIPOL 2011 Workshop. I enjoyed the interesting sessions, the fruitful discussions, the social program and the stay in Beijing.

References

[1] G. Moortgat-Pick, *et al.*, Phys. Rept. **460**, 131 (2008) [hep-ph/0507011].

[2] ALEPH, DELPHI, L3 and OPAL and SLD and LEP Electroweak Working Group and SLD Electroweak Group and SLD Heavy Flavour Group Collaborations, Phys. Rept. **427**, 257 (2006) [hep-ex/0509008].

[3] J. Brau, (Ed.) *et al.* [ILC Collaboration], arXiv:0712.1950 [physics.acc-ph];
G. Aarons *et al.* [ILC Collaboration], arXiv:0709.1893 [hep-ph];
T. Behnke, (Ed.) *et al.* [ILC Collaboration], arXiv:0712.2356 [physics.ins-det].

[4] R.W. Assmann *et al.*, CERN-2000-008; E. Accomando *et al.*, hep-ph/0412251;
http://project-clic-cdr.web.cern.ch/project-CLIC-CDR/

[5] S. Boogert, M. Hildreth, D. Käfer, J. List, K. Mönig, K. C. Moffeit, G. Moortgat-Pick and S. Riemann *et al.*, JINST **4**, P10015 (2009) [arXiv:0904.0122 [physics.ins-det]].

[6] A. Blondel, Phys. Lett. B **202**, 145 (1988) [Erratum-ibid. **208**, 531 (1988)].

[7] J. Erler J *et al.*, Phys. Lett. B **486**, 125 (2000).

[8] T. G. Rizzo, [arXiv:1011.2185 [hep-ph]];
T. G. Rizzo, JHEP **0308**, 051 (2003) [hep-ph/0306283];
T. G. Rizzo, JHEP **0302**, 008 (2003) [hep-ph/0211374].

[9] V.E. Balakin and A.A. Mikhailichenko, Budker Institute of Nuclear Physics Report No. BINP 79-85, 1979; R.C. Wingerson, Phys. Rev. Lett. **6**, 446 (1961).

[10] G. Alexander *et al.*, Nucl. Instrum. Meth. A **610**, 451 (2009) [arXiv:0905.3066 [physics.ins-det]]; G. Alexander *et al.*, Phys. Rev. Lett. **100**, 210801 (2008).

[11] A. Ushakov *et al.*, these proceedings, arXiv:1202.0752 [physics.acc-ph].

[12] W. Gai, these proceedings.

[13] G. Alexander *et al.*, EUROTeV-Report-2008-091.

[14] K. Moffeit *et al.*, SLAC-TN-05-045.

[15] M. Berggren, arXiv:1007.3019 [hep-ex].

[16] F. Staufenbiel *et al.*, these proceedings, arXiv:1202.5987 [physics.acc-ph].

Impact of polarized beams for a staged approach at the LC

G. Moortgat-Pick[1,2], *A. Ushakov*[1]

[1]II. Inst. f. Theo. Physics, University of Hamburg, Hamburg, Germany
[2]DESY, Hamburg, Germany

In this note we provide the achievable polarization degrees for the undulator-based e^+ source at the different energy stages of the International Linear Collider (ILC). In particular we discuss the physics potential for the different energy stages.

1 Introduction

1.1 Beam polarization basics

Both Higgs physics as well as precision top quark physics strongly benefits from the use of polarized beams. New physics will manifest itself with new fermionic and bosonic particles carrying unknown spins. Disentangling and studying the underlying physics benefits from the polarization of both beams because of several facts:

- a higher effective degree of polarization causing higher cross sections and better sensitivity to the chirality of the couplings;
- an efficient suppression of background processes;
- exploitation of couplings only accessible via transversely-polarized beams;
- a reduced uncertainty of the effective polarisation and of the left-right asymmetry.

Concerning physics examples for all these cases, including quantitative and qualitative gain factors, please see also Table 2.1 in [1].

Physics processes occur through e^-e^+ annihilation ('s'-channel diagrams) and scattering ('t, u'-channel diagrams). In annihilation diagrams the helicities of the incoming beams are coupled to each other, whereas in scattering processes, they are coupled to those of the final particles and therefore are directly sensitive to their chiral properties. In such processes only simultaneously-polarized e^+ and e^- beams can uniquely test the couplings of the final 'new' particles. Prominent applications are given, for instance, in Supersymmetry models.

To exploit the effects of transversely polarized beams the polarization of both beams is required, otherwise all effects at leading order from transverse polarization vanish for $m_e \to 0$ (suppression by $m_e/\sqrt{s}$). This option has substantial applications in determining CP–violating effects, distinctions of models with large extra dimensions and high-precision tests of the Standard Model.

For details, please, see also S. Riemann, LC-REP-2013-017 [2].

1.2 Staged energy approach and achievable polarization degrees

a) 'Higgs frontier':
With the discovery of the Higgs boson with about $m_H \sim 125$ GeV, the dominant production process at lower energy is Higgsstrahlung $e^+e^- \to ZH$ and the first energy stage to measure Higgs couplings is at about $m_H + m_Z + 30$ GeV~ 240 GeV.

With a drive beam energy of $E(e^-) = 120$ GeV a yield of $\#e^+/\#e^- = 1.5$, which is crucial to match the luminosity requirements, can also be fulfilled with the helical undulator-based e^+ source. Applying a collimator with a radius of $R_{\rm col} \sim 3.5$ mm a positron polarization $P(e^+) = 40\%$ is achievable for 231 m active length of the undulator with 11.5 mm period and K value of 0.92, details see the note

LC-REP-2013-019, contribution by A. Ushakov et al. The effective polarization P_{eff} and corresponding uncertainty $\Delta P_{\text{eff}}/P_{\text{eff}}$ are listed in Tab.1.

b) 'Top frontier':
The next important energy stage is at about the top quark threshold, i.e. $\sqrt{s} \sim 350$ GeV. Performing a threshold scan is mandatory to achieve a measurement of the top mass with $\Delta m_t = 100$ MeV. In addition the measurement of the left-right asymmetry in $e^+e^- \to t\bar{t}$ is crucial for the measurement of the electroweak top couplings.

With a corresponding e^- drive beam energy of 175 GeV a yield requirement of $\#e^+/\#e^- = 1.5$ does not cause any problems for the undulator-based e^+ source. Applying the collimator as before with $R_{\text{col}} = 1.2$ mm yields a positron polarization of $P(e^+) = 56\%$ (Fig. 1).

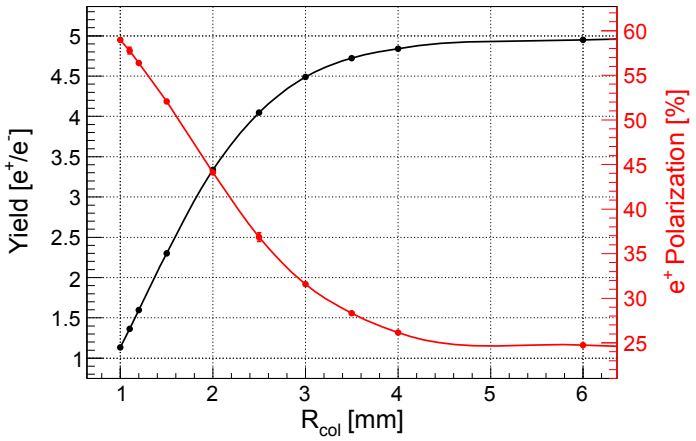

Figure 1: Positron yield (black curve) and polarization (red curve) versus the aperture radius of photon collimator of e^+ source with 175 GeV electron drive beam and 231 m helical undulator (11.5 mm period and $K = 0.92$).

c) 'Design energy frontier':
The currently foreseen design energy is $\sqrt{s} = 500$ GeV. The undulator-based positron source with 143.5 m undulator and an applied collimator of 0.7 mm aperture radius will deliver $P(e^+) = 59\%$. Detailed material tests concerning the collimator are still under work.

This stage allows a first measurement of the top Yukawa coupling g_{ttH} and e^+ polarization decisive for a partial compensation of the severe statistical limitations of this process.

d) 'Energy upgrade':
A discussed upgrade energy up to $\sqrt{s} = 1$ TeV will, for instance, provide reasonable precision for the trilinear Higgs couplings. Using a modified undulator-based e^+ source with a 176 m undulator (period of 4.3 cm, $K = 2.5$), and a collimator with $R_{\text{col}} = 0.9$ mm at such a high e^- drive beam energy of $E(e^-) = 500$ GeV would still deliver $P(e^+) = 54\%$, details see the note LC-REP-2013-012, contribution by A. Ushakov et al. Detailed studies on the effects of misalignments are still under work.

For reasons of simplicity, we assume for all energy stages $\sqrt{s} = 350$, 500 and 1000 GeV an e^+ beam polarization of $P(e^+) = 55\%$. The corresponding $P_{\text{eff}} = (P(e^-) - P(e^+))/(1 - P(e^-)P(e^+))$, $\mathcal{L}_{\text{eff}} = (1 - P(e^-)P(e^+))\mathcal{L}$ and $\Delta P_{\text{eff}}/P_{\text{eff}}$ are listed in Tab.1.

2 Polarization issues at $\sqrt{s} = 240$ GeV

Up to this energy stage the main physics questions to be addressed are the measurement of Higgs mass and its couplings to light quarks, τ's and the gauge bosons. The advantage of polarized beams is mainly given

$\sqrt{s}$	$P(e^-)$	$P(e^+)$	$P_{\rm eff}$	$\mathcal{L}_{\rm eff}$	$\frac{1}{x}\Delta P_{\rm eff}/P_{\rm eff}$
total range	$\mp 80\%$	0%	$\mp 80\%$	1	1
250 GeV	$\mp 80\%$	$\pm 40\%$	$\mp 91\%$	1.3	0.43
$\geq$350 GeV	$\mp 80\%$	$\pm 55\%$	$\mp 94\%$	1.4	0.30
total range	$\mp 90\%$	0%	$\mp 90\%$	1	1
250 GeV	$\mp 90\%$	$\pm 40\%$	$\mp 96\%$	1.4	0.43
$\geq$350 GeV	$\mp 90\%$	$\pm 55\%$	$\mp 97\%$	1.5	0.29

Table 1: The effective polarization $P_{\rm eff}$, luminosity $\mathcal{L}_{\rm eff}$ and $\Delta P_{\rm eff}/P_{\rm eff}$ in dependence of the achievable e^+ polarization for the different energies. Concerning the polarization measurement, x is defined via $x = \Delta P(e^-)/P(e^-) = \Delta P(e^+)/P(e^+)$.

by the enhancement of the cross section compared to the run with unpolarized beams, assuming that the polarization uncertainty is sufficiently small.

Providing only polarized e^- with $P(e^-) = -80\%$ ($P(e^-) = -90\%$) will enhance $\sigma(e^+e^- \to HZ$ by about a factor of 1.12 (1.14) but $P(e^-) = +80\%$ ($P(e^-) = +90\%$) will decrease the process by about a factor of 0.88(0.86). Simultaneously polarized beams with $P(e^-) = -80\%$ ($P(e^-) = -90\%$) and $P(e^+) = +40\%$, however, would enhance $\sigma(e^+e^- \to HZ)$ by about a factor of 1.50 (1.56) corresponding to an increase of 35% (37%) compared to the case with only polarized electron beams. With the opposite polarization configuration the cross section would also be enhanced, but only slightly: with $P(e^-) = +80\%$ ($P(e^-) = +90\%$) and $P(e^+) = -40\%$ the enhancement factor is of about 1.14 (1.16). The enhancement factor for $e^+e^- \to HZ$ is practically given by:

$$\frac{\sigma^{\rm pol}(HZ)}{\sigma^{\rm unpol}(HZ)} = \frac{L^2[1-P(e^-))(1+P(e^+)] + R^2[1+P(e^-)][1-P(e^+)]}{L^2+R^2},$$

where the couplings are approximately given by $L = -0.269$ and $R = 0.231$.

The availability of polarized beams at this stage ensures that already an ultimate precision in the determination of the Higgs couplings can be achieved at this low energy stage. Such a high precision may be crucial to detect any hints whether one has a pure SM-like Higgs or not.

An important property of the Higgs is the CP property. In the SM the Higgs should be a pure CP-even state. In BSM models, however, the observed boson state *a priori* can be any admixture of CP-even and CP-odd states. Therefore it is crucial to determine not only whether it has CP-even state components or not but in particular whether it is a mixed CP-state. The HVV coupling projects out only the CP-even components, therefore the degree of CP admixture cannot be tackled via analyzing these couplings. Therefore the precise measurement of the Higgs couplings to fermions is decisive. For instance, analyzing the decays of the new boson into 3rd generation fermions *tau*'s provides the possibility to construct CP–odd observables via the polarization vector of the τ's[5]. The polarization states of the Higgs decay product τ's are suitable to determine uniquely the degree of the CP-admixture in the parent Higgs state. Keeping in mind, however, that in the SUSY parameter space even in CP-max scenarios only admixtures of CP–odd Higgs couplings of 0.1% can be obtained, shows which crucial role precision aspects may play and any improvement via, for instance, beam polarization should be exploited[1].

3 Polarization issues at $\sqrt{s} \geq 350$ GeV, 500 GeV and beyond

At $\sqrt{s} = 350$ GeV further physics challenges open up as, for instance, the measurement of the top quark mass and the measurement of the total width of the Higgs. Also the polarization of the top quark gives important information whether one has SM-like couplings or new physics contributions involved. In order to maximize the top quark polarization beam polarization is very crucial[6].

But also new physics scenarios not observable at the LHC may directly be accessible at this energy stage at the LC. For instance, higgsino-like SUSY scenarios that lead often to mass degenerated light states with radiative soft photon decays are practically in a hidden sector concerning the physics potential of the LHC.

The polarization of both beams is definitely needed to enhance the signal, to provide enough observables and to unravel the mixing character of the neutralinos/charginos[1, 7].

In general, determining the fundamental SUSY parameters, one is —due to the expected high precision at the LC— even sensitive to effects from virtual, heavy particles via loop effects and can predict their mass, as for instance, $m_{\tilde{t}}$[8].

Raising the energy to $\sqrt{s} = 500$ GeV allows to determine the top-Yukawa coupling g_{ttH}. It is expected to achieve an accuracy of $\Delta g_{ttH}/g_{ttH} \sim 10\%$[9], although it is close to the threshold. But thanks to QCD-induced enhanced threshold effects such an accuracy should be achievable with 1 ab^{-1}. The polarization of both beams is again crucial to enhance the small cross section and the sensitivity of this study. For instance, if only polarized electrons with $P(e^-) = -80\%$ are available, the improvement in Δg_{ttH} is expected to be only of about 19% with respect to unpolarized beams. However, using simultaneously $P(e^+) = +60\%$ as well, the improvement in Δg_{ttH} is expected to be 45% (see [1] and references therein).

It is of great importance to measure this Yukawa coupling with high precision in order to test the Higgs mechanism and verify the measured top mass $m_t = y_{ttH} v/\sqrt{s}$. Also admixtures of non-SM contributions are expected to become visible in this coupling. For instance, in general Two-Higgs-Doublet model the deviations to the SM value can here achieve typically 20%.

Concerning the Higgs sector, this energy stage also provides first access to the trilinear Higgs coupling λ, that is important for the establishment of the electroweak symmetry breaking mechanism and the determination of the Higgs potential:

$$V = \frac{1}{2} m_H^2 \Phi_H^2 + \lambda v \Phi_H^3 + \frac{1}{4} \kappa \Phi_H^4,$$

where $v = 246$ GeV. The cross section for double Higgsstrahlung is small but has a maximum of about 0.2 fb for a Higgs with $m_H \sim= 125$ GeV at this energy stage. The uncertainty scales with $\Delta\lambda/\lambda = 1.8 \Delta\sigma/\sigma$. Beam polarization of both beams is crucial to enhance the tiny cross section and it is expected to get a precision on the Higgs self coupling $< 40\%$ already at this energy stage[10].

As soon as non-SM physics shows up the polarization of both beams gets mandatory to have the best sensitivity to the chirality of the couplings of the new particles and to determine the underlying structure of the model as precise as possible. Many physics examples have been studied[9, 1, 2].

One is also sensitive to new physics models via indirect searches. For instance, effects from heavy Z'[11] become observable in $e^+e^- \to W^+W^-$. Having both beams polarized allows to distinguish the variety of different Z'-models already at this energy $\sqrt{s} = 500$ GeV, exceeding the limits given by the LHC.

Contributions from CP–violating coupling or scalar- and tensor-like interactions can become observable as well at $\sqrt{s} = 500$ GeV if transversely-polarized beams are used[12, 13, 1]. To exploit this option, both beams have to be polarized as explained above and in [2]. Transversely-polarized beams are also mandatory to test specific CP-violating triple gauge boson couplings in $e^+e^- \to W^+W^-$ ([1] and references therein). Concerning technical issues of how accurate one can measure the polarization degree of transversely-polarized beams at the ILC, see [14].

4 Polarization issues at $\sqrt{s} \sim 92$ GeV

In case the LHC has only discovered the SM-like Higgs but no hints for physics beyond the SM show up another LC option may become a superior choice to clarify whether inconsistencies within the SM point to the underlying structure of a more general physics model.

There exists, for instance, a strong relation between the measured Higgs mass and the electroweak mixing angle $\sin^2\theta_{\rm eff}^{\rm lept}$. The currently still most accurate experimental measurements still offer a more than 2σ-discrepancy between the derived $\sin^2\theta_{\rm eff}^{\rm lept} = 0.23221 \pm 0.00029$ at LEP and 0.23098 ± 0.00026 at SLC. The world average is given by $\sin^2\theta_{\rm eff}^{\rm lept} = 0.23153 \pm 0.00016$. Such a deviation between the two measurements may look just as a small experimental fact. However, since there exists the strong relation between the electroweak precision observables that are theoretically calculated at the quantum level, clarifying the 'true' value would have a big impact. For instance, studying the two values separately, see Fig.2a,b, shows that the current value from the LEP measurement would rule out immediately the SM as well as the MSSM (Fig2a).

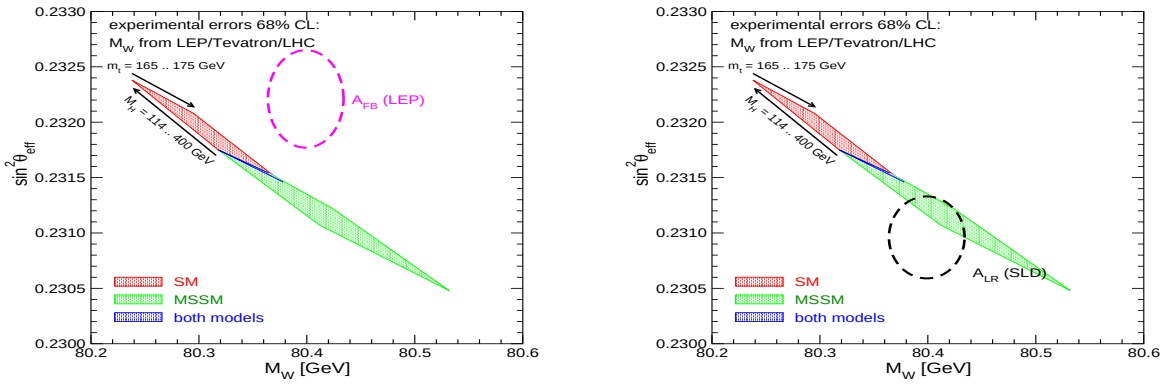

Figure 2: Left panel: The 1σ uncertainty area of $\sin^2\theta_{\rm eff}$ depicted at the measured value at $A_{\rm FB}$ at LEP in dependence of m_W for the SM and the MSSM. Both models would be excluded. Right panel: The 1σ uncertainty area of $\sin^2\theta_{\rm eff}$ depicted at the measured value at $A_{\rm LR}$ at SLC in dependence of m_W for the SM and the MSSM. The MSSM would be favoured [16, 17, 18].

Contrary the measured value at SLC would more favour the MSSM, see Fig2b and would immediately rule out the SM.

At GigaZ, the high luminosity option for running at the Z-pole, offers to determine the mixing angle up to a precision of 1.3^{-5}[1]. Simultaneously polarized $e^{\pm}$ beams are mandatory to achieve such ultimate high precision goals (see also [2]). However, one should note that the achievable precision is still driven by parametric uncertainties from Δm_Z, $\Delta\alpha_{\rm had}$ and $\Delta m_{\rm top}$. A top precision of $m_{\rm top} = 0.1$ GeV is expected to be achievable only at the LC via threshold scan measurements, but such a precision will be mandatory to fully exploit the GigaZ precision[15].

In case no further new physics appears in LHC results in the near future, it may be a natural step for the ILC after the first energy stages to go back to the GigaZ option. On basis of such a precision of $\Delta m_{\rm top} = 0.1$ GeV one could fully interprete the ultimate precisions tests at GigaZ at the ILC. In Fig.3 the expected achievable precision at GigaZ around the current central value of the world average for $\sin^2\theta_{\rm eff}$ is given. This figure also demonstrates how important it is both to shrink the uncertainty as well as to clarify the actual central value.

Due to the high sensitivity of such electroweak precision observables to loop effects, they are also sensitive to effects from heavy virtual new particles as, for instance, heavy SUSY particles, that are even beyond the discovery range of the LHC. The chosen example scenario in Fig. 4 shows that the measurements with GigaZ precision would even still be sensitive to SUSY scenarios that have a multi-TeV coloured sector beyond the kinematic range of the LHC[16]. Therefore such ultimate precisions measurements at GigaZ can give even hints to outline the underlying new physics scale.

5 Summary

Polarization plays an important role in the full physics programme of the Linear Collider. In order to be competitive to the LHC results and estimates, the physics potential of the ILC has to be maximized. Therefore simultaneously polarized e^- and e^+ beams are needed in the full energy range. The polarization may play a crucial part in particular in the first energy stages in order to optimize the results in Higgs and top physics and to widen the accessible physics potential for beyond Standard Model physics. Furthermore, polarized beams will play the substantial role when analyzing the structure of the underlying new physics models.

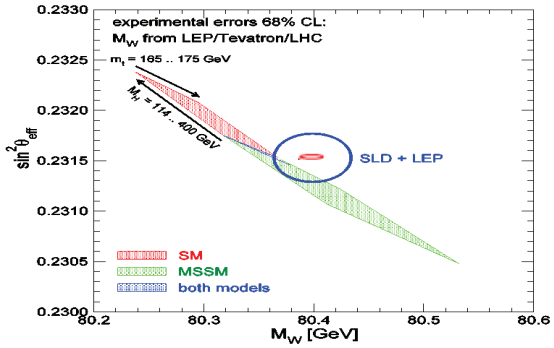

Figure 3: Evaluation of $\sin^2\theta_{\rm eff}$ in dependence of m_W for the SM and the MSSM. The blue circle denotes the 1σ uncertainty around the current central value of the world average, the red circle denotes the 1σ uncertainty expected at GigaZ[16, 17, 18].

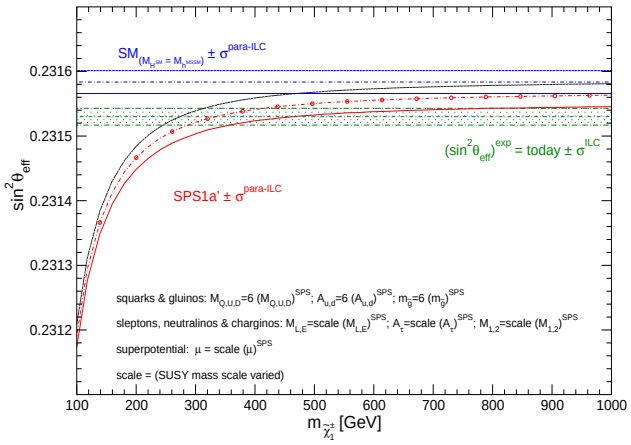

Figure 4: Theoretical prediction for $\sin^2\theta_{\rm eff}$ in the SM and the MSSM (including prospective parametric theoretical uncertainties) compared to the experimental precision at the ILC with GigaZ option. An SPS 1a' inspired scenario is used, where the squark and gluino mass parameters are fixed to 6 $\times$ their SPS 1a' values. As can be seen from the figure, one is still sensitive to the mass differences between both models, even if the on-shell particles are beyond the kinematic range. [16, 17, 18].

References

[1] G. Moortgat-Pick, T. Abe, G. Alexander, B. Ananthanarayan, A. A. Babich, V. Bharadwaj, D. Barber and A. Bartl *et al.*, Phys. Rept. **460** (2008) 131 [hep-ph/0507011].

[2] S. Riemann, *Physics Applications of Polarized Positrons*, LC-REP-2013-017, these proceedings.

[3] A. Ushakov, V. Kovalenko, G. Moortgat-Pick, S. Riemann, F. Staufenbiel, *Simulations of the ILC positron source with 120 GeV electron drive beam*, LC-REP-2013-019, these proceedings.

[4] A. Ushakov, G. Moortgat-Pick, S. Riemann, W. Gai, W. Liu, *Positron Source Simulations for ILC 1 TeV Upgrade*, LC-REP-2013-012, these proceedings.

[5] S. Berge, W. Bernreuther, H. Spiesberger, *Determination of the CP parity of Higgs bosons in their tau decay channels at the ILC*, LC-REP-2012-068, these proceedings.

[6] S. Groote, J.G. Körner, B. Melic, S. Prelovsek, *Single top quark polarization at $O(\alpha_s)$ in $t\bar{t}$ production at a polarized linear e^+e^- collider*, LC-REP-2012-076, these proceedings.

[7] C.M. Berggren, F. Brümmer, J. List, G. Moortgat-Pick, T. Robens, K. Rolbiecki, H. Sert,*Higgsinos at the ILC*, in preparation.

[8] A. Bharucha, J. Kalinowski, G. Moortgat-Pick, K. Rolbiecki, G. Weiglein, *One-loop effects on MSSM parameter determination via chargino production at the LC*, LC-REP-2013-020, these proceedings.

[9] International Linear Collider, Technical Design Report, *Physics at the ILC*, ed. H. Baer *et al.*.

[10] J. Tian, *Study of Higgs self-coupling at the ILC based on the full detector simulation at $\sqrt{s} = 500$ GeV and $\sqrt{s} = 1$ TeV*, LC-REP-2013-003, these proceedings.

[11] V. V. Andreev, G. Moortgat-Pick, P. Osland, A.A. Pankov, N. Paver, *Discriminating Z' from anomalous trilinear gauge coupling signatures in $e^+e^- \to W^+W^-$ at ILC with polarized beams*, LC-REP-2012-008, these proceedings.

[12] B. Ananthanarayan, S. K. Garg, M. Patra and S. D. Rindani, Phys. Rev. D **85** (2012) 034006 [arXiv:1104.3645 [hep-ph]].

[13] B. Ananthanarayan, J. Lahiri, M. Patra and S. D. Rindani, Phys. Rev. D **86** (2012) 114019 [arXiv:1210.1385 [hep-ph]].

[14] I.B. Mordechai, G. Alexander, *A Transverse Polarimeter for a Linear Collider of 250 GeV $e^{\pm}$ Beam Energy*, LC-M-2012-001, these proceedings.

[15] S. Heinemeyer, S. Kraml, W. Porod and G. Weiglein, hep-ph/0409063.

[16] S. Heinemeyer, W. Hollik, A. M. Weber and G. Weiglein, JHEP **0804** (2008) 039 [arXiv:0710.2972 [hep-ph]].

[17] S. Heinemeyer and G. Weiglein, arXiv:1007.5232 [hep-ph].

[18] S. Heinemeyer, G. Weiglein, L. Zeune, private communication; update from [16].

Measurement of the beam polarization at the ILC using $e^+e^- \to W^+W^- \to qq\ell\nu$ data

A. Rosca[1]

[1] DESY, Hamburg, D 22607, Germany

Abstract

An assessment of the achievable precision on the measurement of the longitudinal polarization of high energy electron and positron beams in collision at the International Linear Collider operated at 1 TeV is presented. Two methods to extract the beam polarization using the $e^+e^- \to W^+W^- \to qq\ell\nu$ process are investigated: a modified Blondel scheme with both beams polarized and an angular fit method based on the W-boson production angle.

1 Introduction

The measurement of the beam polarization at the ILC will be performed by Compton polarimeters. They will measure the average beam polarization at their location with high statistics. Due to effects such as polarization spread, spin transport between the polarimeter and interaction point, and disruptions due to beam-beam effects, the result of the polarimeter measurement will differ from the luminosity-weighted beam polarization. Using a physics process that is sensitive to the beam polarization, the average luminosity-weighted polarization at the interaction point can be directly extracted. The process $e^+e^- \to W^+W^-$ can be used to achieve this goal.

We compare two techniques to measure the polarization: a modified Blondel scheme that relies on the dependence of the total cross sections of semileptonic W-pair production for different incoming beam polarizations, and an angular fit method that uses the distribution of the production angle $\cos\theta_W$ of the W^- with respect to the electron beam axis.

This study investigates the capability of the ILD detector to measure the longitudinal polarization of high energy electron and positron beams at the ILC operated at $\sqrt{s} = 1$ TeV. The simulation of the signal and background processes is described in Section 2. Event selection is described in Section 3. The methods to extract the polarization are presented in Section 4 and conclusions are summarized in Section 5. The achievable accuracy of this measurement for the ILC at $\sqrt{s} = 500$ GeV has been reported by [7].

2 Simulation of the signal and background processes

Signal and background events are generated using the WHIZARD [1] event generator. The effects of initial state radiation and beamstrahlung are included. The four- momenta of the final-state quarks and leptons are passed as input to PYTHIA 6.422 [2] for parton showering and hadronization. The detector response is simulated using the MOKKA [3] full Monte Carlo detector simulation.

The detector model used in this analysis is ILD_o1_v05 and it is described in Reference [4].

Events were generated at a centre-of-mass energy of 1 TeV assuming 100% polarized beams. Events corresponding to different polarization configurations were obtained by properly mixing the samples in order to obtain realistic cases of partial polarizations. The final results are reported for an integrated luminosity of 1000 fb^{-1}, but propagation of the uncertainties at different luminosities are also shown.

The hadronic cross-section for $\gamma\gamma \to$ hadrons events, with mass exceeding 2 GeV, is several hundred nb [5], so that about 4.1 events of this type are produced per bunch crossing. These events (pile-up) are overlaid to the physics events. Since the pile-up events are produced in the t-channel q-exchange most of the resulting final state particles are distributed at low angles.

3 Event selection

W bosons decay into hadrons, mostly through $W^- \to \bar{u}d$ or $\bar{c}s$, or leptons, $W^- \to \ell^-\bar{\nu}_\ell$, where ℓ denotes an electron, muon or tau lepton. W-boson pair production yields three classes of events: the fully- leptonic, $\ell\nu\ell\nu$, the semi-leptonic, $qq\ell\nu$, and the fully-hadronic, $qqqq$, final states. Due to the presence of more than one neutrino in the $\ell\nu\ell\nu$ final state, the masses of the W bosons cannot be directly reconstructed from their decay products and this decay channel is not further considered here. The $qqqq$ final state has been excluded as well due to the fact that the charge of the W-boson cannot be reconstructed with sufficient precision from the jets of the hadronic decay.

In order to measure the charge of the W-boson with high purity we only considered here the semi-leptonic final state $qq\ell\nu$ where ℓ denotes an electron or a muon. The channel $qq\tau\nu$ is considered as a background as well.

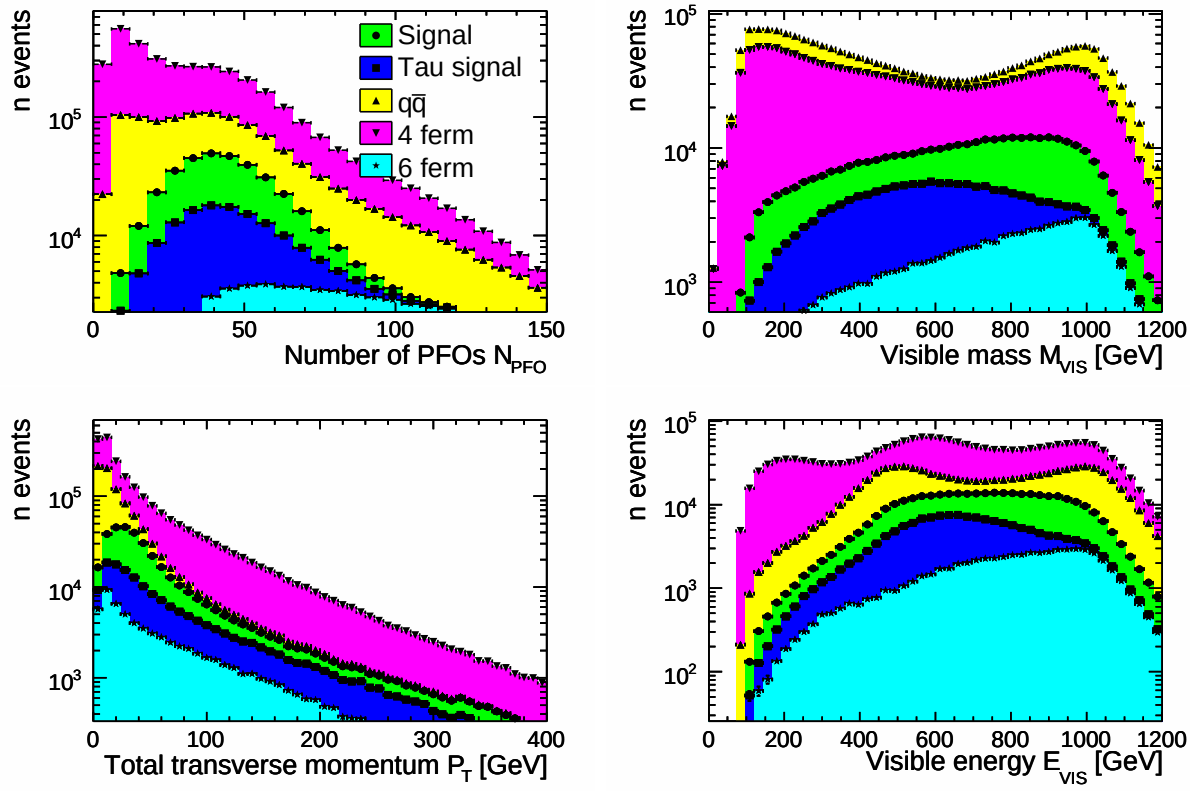

Figure 1: Distributions of the number of PFO N_{PFO} (top left), visible mass M_{VIS} (top right), total transverse momentum P_T (bottom left) and visible energy E_{VIS} (bottom right). Events with pile-up.

Visible final-state fermions are reconstructed in each event. Electrons and muons from W-boson decays are measured in the calorimeters and in the tracking system. Lepton candidates are defined by the following ratios: E_{ECAL}/E_{tot} and E_{tot}/p_{track}, where E_{ECAL} is the energy measured in the electromagnetic calorimeter, E_{tot} is the total measured energy in the calorimeters, and p_{track} is the measured track momentum in the tracking detectors. We require that E_{ECAL}/E_{tot} is greater than 0.9 for electrons and less than 0.5 for muons and E_{tot}/p_{track} be greater than 0.8 for electrons and below 0.4 for muons. Jets originating from quarks are reconstructed by combining information from calorimetric clusters and associated tracks into jets using the kt algorithm [6], see section 3.2.

The event selection for the process $qq\ell\nu$ requires high particle-multiplicity, an identified lepton, and missing momentum.

Events are selected requiring the number of reconstructed particle flow objects N_{PFO} be greater than 15, the total transverse momentum P_T larger than 5 GeV, a total visible energy below 1200 GeV and a visible mass greater than 100 GeV. The distributions of the variables used for the preselection of the $qq\ell\nu$ events are shown in Figure 1.

3.1 Identification of isolated leptons

In the $qq\ell\nu$ final state, the lepton from the $W \to \ell\nu$ tends to be energetic and isolated from the rest of the event. To identify an isolated lepton, a cone with a half-opening angle θ_{cone} is constructed around each lepton candidate. The cone energy E_{cone} is defined to be the sum of the energy of all the tracks inside the cone, excluding the lepton candidate. We require the value of the $\cos\theta_{cone}$ to be 0.98.

For illustration purposes we show in Figure 2 the distribution of the cone energy versus the lepton candidate energy for the processes $W^+W^- \to qqqq$ (in blue) and $ZZ \to \ell^+\ell^-\ell^+\ell^-$ (in red). The energetic isolated leptons have high energy and a low cone energy, thus populating the lower right

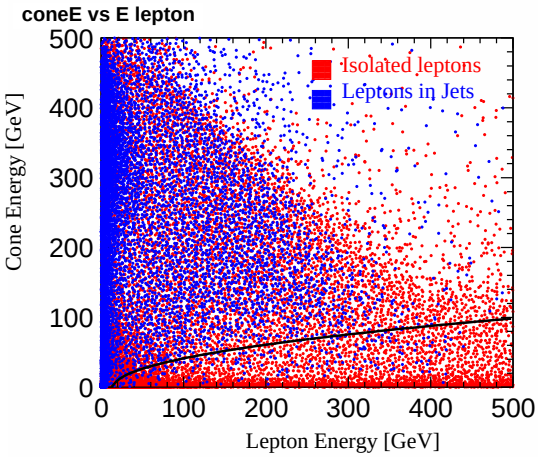

Figure 2: Distribution of the cone energy and the lepton energy. Leptons below the curve are identified as isolated leptons.

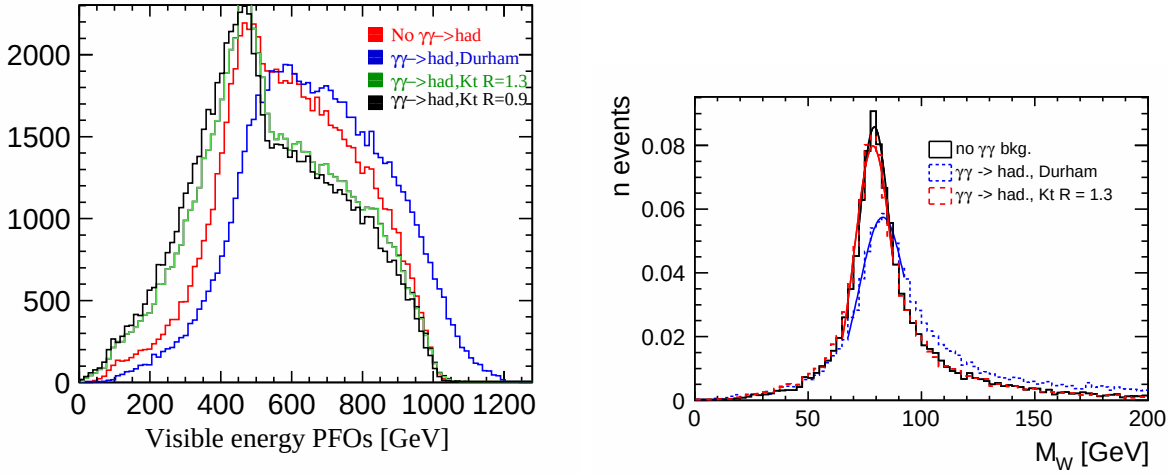

Figure 3: Left: Distribution of the visible energy of the PFOs after applying a jet clustering algorithm in events with pileup, compared to the visible energy of the PFOs in events without $\gamma\gamma$ overlay (red curve). Right: Reconstructed invariant mass of the W-boson using different jet clustering algorithms. The black curve is obtained for events without $\gamma\gamma$ overlay.

region, shown as red points in Figure 2. Leptons from heavy flavour jets are likely to be less energetic and have a higher cone energy, shown as blue dots in Figure 2. The selection of isolated leptons is performed by applying a cut on the cone energy which varies as the lepton energy and is given by the equation $E_{cone} < \sqrt{20E_\ell - 300}$. We require one and only one isolated lepton.

3.2 Jet clustering and suppression of $\gamma\gamma$ overlay events

We employ a jet clustering algorithm to separate the event into 2 jets, after taking out the isolated lepton. At the ILC, the physics event is accompanied by significant additional energy from $\gamma\gamma \rightarrow$ hadrons background. For this reason it is not possible to use the jet clustering algorithms developed for LEP which combine all particles into jets. We found that the kt algorithms [6] developed for hadron collisions are more suitable since they reduce the inclusion of background particles into the jets from the e^+e^- interaction. Figure 3 (left) compares the reconstructed visible energy observed with the Durham algorithm to that from the kt algorithm for different values of the jet radius parameter

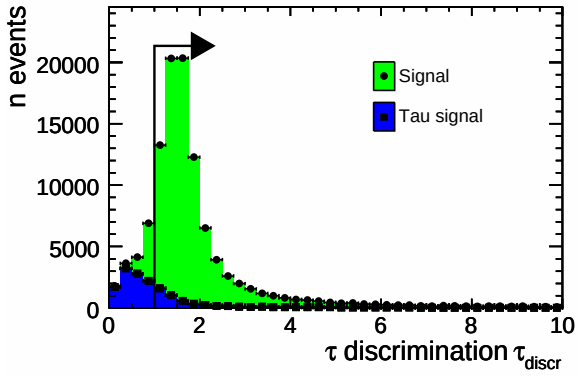

Figure 4: Distribution of the discriminating variable used to suppress tau decays of the W-boson in $qq\ell\nu$ events. The discrimination is performed requiring $\tau_{discr} > 1$.

Cut	$qq\ell\nu$	$qq\tau\nu$	2 ferm.	4 ferm.	6 ferm.
Initial events	210841.0	104698.0	776759.0	2369330.0	69277.0
Preselection	192576.7	95783.3	427708.3	1130853.3	63785.0
Single isolated lepton	117451.7	20010.0	19167.5	234110	22696.7
Fit probability	100232.0	17606.7	12490.7	68277.0	17983.3
$\tau_{discr} < 1$	91281.7	5651.0	10294.7	52409.3	16445.0
Mass cuts	76415.0	4120.0	2550.2	14051.9	3010.0
$\cos\theta_W >$ -0.95	76101.7	4100.0	2369.5	12442.5	2886.7

Table 1: Summary of the cuts to select $qq\ell\nu$ events. Estimated yields are given assuming an integrated luminosity of 100 fb^{-1} with beam polarizations (P_{e^-}, P_{e^+}) = (-0.8,+0.2).

R. The Durham algorithm adds about 100 GeV energy from the background to the reconstructed jets, while this effect is reduced using the kt algorithm.

Jets are reconstructed from PFOs using the kt algorithm in its exclusive mode with R=1.3 and using the E recombination scheme. The clustering is stopped when two jets are found.

As an example, the reconstruction of W bosons is illustrated in Figure 3 (right). The distributions obtained with and without the overlay of $\gamma\gamma$ events are compared.

3.3 Kinematic fit

A kinematic fit, assuming four-momentum conservation and other constraints, is used to improve energy and angle resolutions. The four-momentum conservation requirement determines in the case of our final state the momentum and the direction of the neutrino. The mass resolution of the two W bosons is improved by the additional constraint of requiring these masses to be equal. This procedure results in a two-constraint (2C) fit of $qq\ell\nu$ events. The reconstructed mass obtained in the 2C fit, M_{2C} fit is required to be $40 < M_{2C} < 120$ GeV.

The suppression of the $qq\tau\nu$ is performed using the same discriminating variable τ_{disc} as defined in ref. [7]. Candidates with $\tau_{disc} < 1$ are considered $qq\tau\nu$ events and rejected. Figure 4 shows the distribution of this discriminating variable.

We summarize the yields after applying each cut for the case of polarized beams (P_{e^-}, P_{e^+}) =(-0.8,+0.2) in Table 1, where the yields are normalized assuming an integrated luminosity of 100 fb^{-1}.

The total signal efficiency is estimated to be 36% in the presence of the pile-up events. The purity of the selection is 82% at 1 TeV. The residual background, not originating from W-boson pair

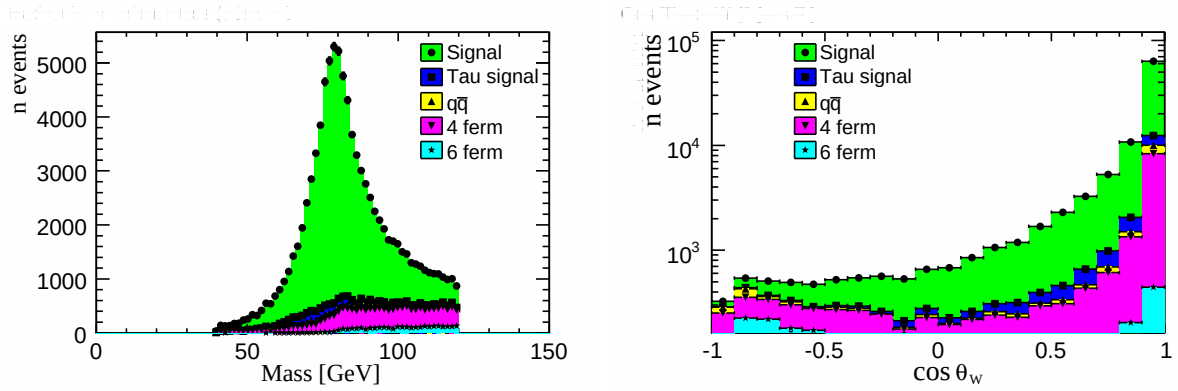

Figure 5: Left: Distribution of reconstructed W-boson mass after applying the kinematic fit using the equal-mass constraint and all selection cuts. Right: Distribution of the cosine of the polar angle of the W^-.

production, is dominated by $qqe\nu$ events (70.3%), followed by $q\bar{q}$ events (13.4%) and 6 fermion events (16.3%). The $qq\tau\nu$ events amount to 5%. The $qqe\nu$ events considered here as a background originate from single-W production and fail the signal definition:

$$M_{qq/e\nu} = M_{W^+W^-} \pm 50\ GeV.$$

The distributions of M_{2C} and $\cos\theta_W$, after applying all the cuts, are shown in Figure 5.

4 Methods to extract the beam polarization

The first method considered to measure the beam polarization is a modified Blondel scheme. This technique requires to spend some luminosity with all four possible combinations of the beam polarizations: $++$, $+-$, $-+$ and $--$, where the signs are for the positron, and respectively electron polarizations. The absolute polarization values of the left- and right-handed degrees of polarization are required to be equal. The beam polarization is obtained by measuring the total cross section for each helicity combination [8]:

$$|P_{e^\pm}| = \sqrt{\frac{(\sigma_{-+} + \sigma_{+-} - \sigma_{--} - \sigma_{++})(\pm\sigma_{-+} \mp \sigma_{+-} + \sigma_{--} - \sigma_{++})}{(\sigma_{-+} + \sigma_{+-} + \sigma_{--} + \sigma_{++})(\pm\sigma_{-+} \mp \sigma_{+-} - \sigma_{--} + \sigma_{++})}},$$

where σ_{+-} is the total cross section measured for right-handed positron beam and left-handed electron beam (σ_{--} and σ_{++} are defined analogously) and P_{e^+} (P_{e^-}) is the resulting positron (electron) beam polarization.

The four cross sections σ_{++}, σ_{+-}, σ_{-+} and σ_{--} have been measured using Monte Carlo samples for an integrated luminosity of 100 fb^{-1}. The equation above has been applied and the statistical uncertainty on the measured polarizations has been calculated. The error has been propagated towards higher luminosities, as shown in Figure 6 (left). The total luminosity is assumed to be shared equally between the four polarization sets. For a total integrated luminosity of 1000 fb^{-1} the precision obtained on the electron and positron polarizations is $\Delta P_{e^-}/P_{e^-} = 0.44\%$ and $\Delta P_{e^+}/P_{e^+} = 1.19\%$, respectively.

The Blondel scheme requires high integrated luminosities in order to obtain small uncertainties on the polarization. This motivates the use of alternative techniques, for instance an angular fit to the $\cos\theta_W$-distribution. This method uses the additional information contained in the distribution of the W-pair production angle.

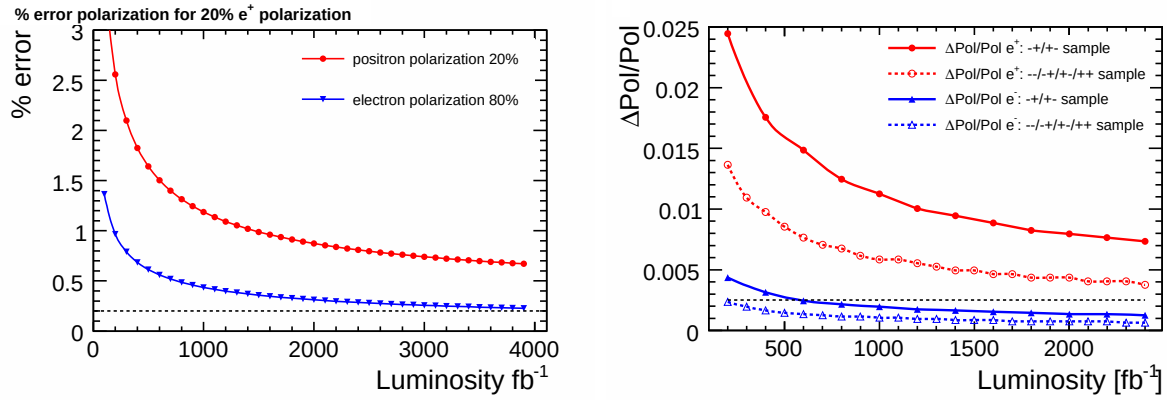

Figure 6: Statistical precision on the polarization obtained with the Blondel technique (left). The integrated luminosity is shared equally between the four polarization sets. Results for the angular fit method are also shown (right). Here the integrated luminosity is divided equally between $\mathcal{P}_{-80,+20}$ and $\mathcal{P}_{+80,-20}$ (solid lines) or it is divided among $\mathcal{P}_{-80,-20}$, $\mathcal{P}_{-80,+20}$, $\mathcal{P}_{+80,-20}$ and $\mathcal{P}_{+80,+20}$ in the proportions 1:4:4:1 (dotted lines). The horizontal dashed line indicates the optimum precision of 0.2%.

The angular fit method is based on the creation of Monte Carlo templates of the $\cos\theta_W$ distribution for several sets of beam polarizations. The electron (positron) polarization was scanned in the interval [-90%,+90%] ([-70%,+70%]). Each distribution is divided into 20 bins, which cover the full range of variability of $\cos\theta_W$ [-0.95,+1]. The $\cos\theta_W$ distribution of the data are fitted to the templates in order to measure the polarization using MINUIT [9]. The fit has been performed with two free parameters for P_{e^-} and P_{e^+}, with a linear least squares minimization:

$$\chi^2 = \sum_{j=1}^{4}\sum_{i=1}^{20} \frac{(N_{i,j}^{DATA} - f_i(\pm P_{e^+}, \pm P_{e^-}))^2}{N_{i,j}^{DATA}},$$

where $N_{i,j}^{DATA}$ is the content of the i-th bin of the $\cos\theta_W$ distribution for the j-th data sample of the four samples for different helicity sets. The Monte Carlo template f_i for the same bin of $\cos\theta_W$ and the polarizations P_{e^-} and P_{e^+} depend on the sample j. For each considered integrated luminosity the fit is repeated several times. The resulting fit parameters are Gaussian distributed around the expected value, as shown in Figure 7. The fit statistical errors are obtained from the widths of the Gaussian fitted to the parameter distributions.

The precision achieved with the angular fit method is summarized in Figure 6 (right).

The angular fit is more powerful than the Blondel technique, yielding the same precisions at much lower luminosities. For an integrated luminosity of 1000 fb^{-1} divided among the four polarization sets $\mathcal{P}_{-80,-20}$, $\mathcal{P}_{-80,+20}$, $\mathcal{P}_{+80,-20}$ and $\mathcal{P}_{+80,+20}$ in the proportion 1:4:4:1 the precision obtained on the electron and positron polarizations is $\Delta P_{e^-}/P_{e^-} = 0.11\%$ and $\Delta P_{e^+}/P_{e^+} = 0.6\%$, respectively.

We also assessed the achievable error on the polarizations when reducing to zero the integrated luminosity spent on the $++$ and $--$ polarization sets. Such configurations of the helicities are of low interest for most of the physics studies, since they suppress the s-channel production. The results obtained are shown in Figure 6 (right, solid lines). For an integrated luminosity of 1000 fb^{-1} the precision obtained on the electron and positron polarizations is $\Delta P_{e^-}/P_{e^-} = 0.19\%$ and $\Delta P_{e^+}/P_{e^+} = 1.13\%$, respectively.

5 Conclusions

Using W-pair production it will be possible to measure the average luminosity-weighted beam polarization at the ILC with high sensitivity. Assuming an integrated luminosity of 1000 fb^{-1} at $\sqrt{s}$=1

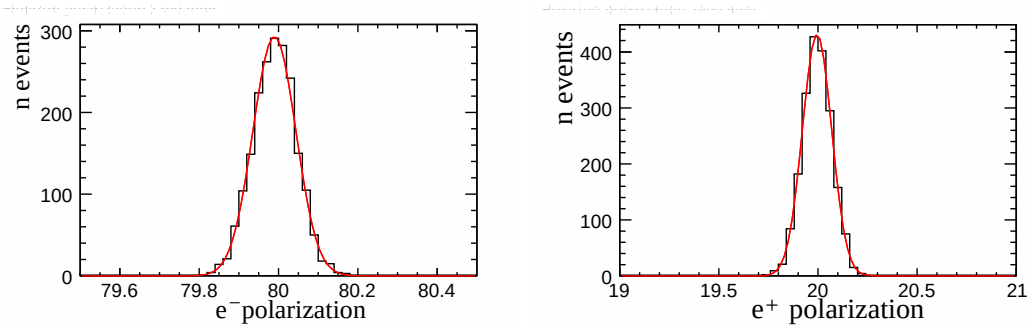

Figure 7: Distributions of the fitted parameters for the electron (left) and positron (right) polarizations.

	ΔP_{e^-}	$\Delta P_{e^-}/P_{e^-}$	ΔP_{e^+}	$\Delta P_{e^+}/P_{e^+}$
Blondel technique (25% ++/+−/−+/−−)	0.0035	0.44%	0.0024	1.19%
Fit method (10% ++/−−) (40% +−/−+)	0.00084	0.11%	0.0012	0.6%
Fit method (50% +−/−+)	0.0016	0.19%	0.0023	1.13%

Table 2: Achievable errors for the two beam polarizations using $qq\ell\nu$ events and 1000 fb^{-1} at $\sqrt{s}$ = 1 TeV.

TeV, Table 2 summarizes the obtainable errors on the electron and positron polarizations.

The study has not yet evaluated all backgrounds, particularly $\gamma\gamma$ and $e\gamma$ processes need to be looked at in more detailed. If the impact of these backgrounds becomes important, the selection cuts can be tightened with an expected degradation of the efficiency by a factor about 1.8.

Also it should be mentioned that the precision of the angular fit method does not depend on assuming that the TGCs are consistent with the SM expectations. A simultaneous fit of the polarization and TGCs is possible [7] without loosing sensitivity on the polarization.

References

[1] W. Kilian, T. Ohl, and J. Reuter, "WHIZARD: Simulating multi-particle processes at LHC and ILC", Eur.Phys.J. **C71** (2011) 1742, arXiv:0708.4233 [hep-ph].

[2] T. Sjoestrand, S. Mrenna, and P. Skands, J. High Energy Phys. 05 (2006) 026.

[3] P. Mora de Freitas and H. Videau, "Detector simulation with MOKKA/Geant4: Present and future", LC-TOOL-2003-010;
http://polzope.in2p3.fr:8081/MOKKA.

[4] T. Abe et al. [ILD Concept Group - Linear Collider Collaboration], "The International Large Detector: Letter of Intent", KEK Report 2009-06

[5] The Particle Data Group, K. Hagiwara et al., Phys. Rev. **D66** (2002) 010001.

[6] M. Cacciari, G.P. Salam, *Dispelling the N3 myth for the kt jet-finder* Phys. Lett.B 641 (2006) 57

[7] I. Marchesini, "Triple gauge couplings and polarization at the ILC and leakage in a highly granular calorimeter", DESY-THESIS-2011-044.
P. Bechtle, W. Ehrenfeld and I. Marchesini, "Triple gauge couplings and polarization at the ILC", LC-DET-2009-003.

[8] K. Moenig, "The use of positron polarization for precision measurements", LC-PHSM-2000-059.

[9] F. James and M. Roos, "Minuit: A system for function minimization and analysis of the parameter errors and correlations", Comput. Phys. Commun., 10:343-367, 1975.

Acknowledgments

The author would like to thank I. Marchesini and the members of the ILD physics working group for many helpful discussions, as well as the generation and production teams.

Chapter 4

Higgs mechanism

$H \to \tau^+\tau^-$ branching ratio study at $\sqrt{s} = 250$ GeV at the ILC with the ILD detector

Shin-ichi Kawada[1,†], Keisuke Fujii[2], Taikan Suehara[3],
Tohru Takahashi[1], Tomohiko Tanabe[3]

February 2, 2013 (revised at March 22, 2013)

1: Advanced Sciences of Matter (AdSM), Hiroshima University, 1-3-1, Kagamiyama, Higashi-Hiroshima, Hiroshima, 739-8530, Japan
2: High Energy Accelerator Research Organization (KEK), 1-1, Oho, Tsukuba, Ibaraki, 305-0801, Japan
3: International Center for Elementary Particle Physics (ICEPP), The University of Tokyo, 7-3-1, Hongo, Bunkyo-ku, Tokyo, 113-0033, Japan

† : s-kawada@huhep.org

Abstract

We evaluated the measurement accuracy of the branching ratio of $H \to \tau^+\tau^-$ mode at $\sqrt{s} = 250$ GeV at the ILC with the ILD detector. We assumed the Higgs mass $M_H = 120$ GeV, branching ratio $\mathrm{Br}(H \to \tau^+\tau^-) = 8.0$ %, beam polarization $P(e^-, e^+) = (-0.8, +0.3)$, and integrated luminosity $\int L\, dt = 250$ fb^{-1}. We used the LOI samples as the Monte-Carlo samples. The evaluation was performed by the ILD full detector simulation. All Standard Model backgrounds were included in this study. We obtained the accuracy $\Delta(\sigma\cdot\mathrm{Br})/(\sigma\cdot\mathrm{Br}) = 3.5$ %. The scaled result to $M_H = 125$ GeV is calculated to be 4.2 %.

1 Introduction

A new Higgs-like particle was discovered by the ATLAS and the CMS experiments [1, 2]. One of the next important themes for particle physics is the investigation of that new particle, especially the mass generation mechanism.

One of the important properties of Higgs boson is its branching ratio. In the Standard Model (SM) of particle physics, the Yukawa coupling constant of matter fermions with the Higgs boson is proportional to the fermion mass. Besides, if there is new physics, the coupling constant may deviate from the SM prediction. Therefore, the branching ratio is a probe for new physics.

In this note, we focus on the branching ratio of $H \to \tau^+\tau^-$ mode. We estimate the measurement accuracy of the $H \to \tau^+\tau^-$ branching ratio at $\sqrt{s} = 250$ GeV with the ILD full detector simulation.

2 Signal and Background

The main Higgs production process at $\sqrt{s} = 250$ GeV is the Higgs-strahlung process ($e^+e^- \to ZH$). There are three types of signal depending on the decay of the Z boson, as shown in Figure 1. In this note, we concentrate on (A) $Z \to l^+l^-$ mode and (B) $Z \to q\bar{q}$ mode.

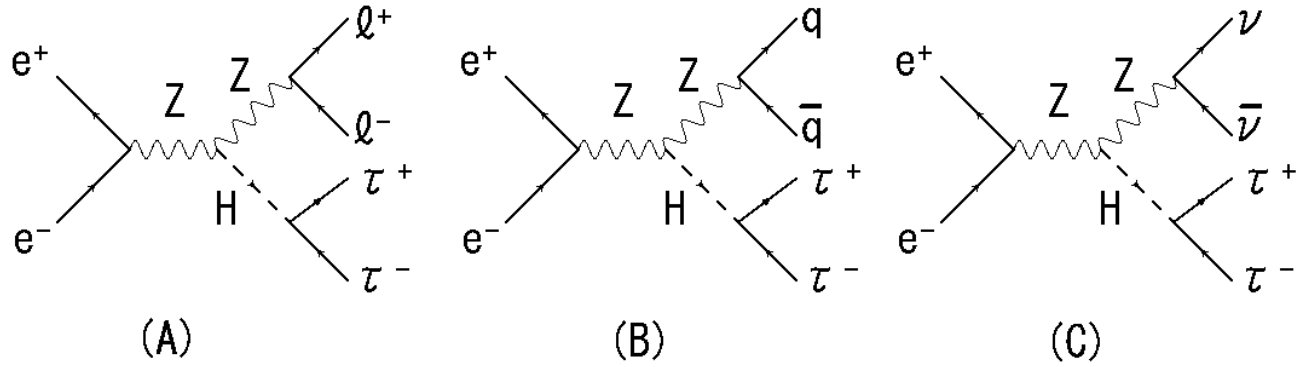

Figure 1: The diagrams of signal processes. (A): $Z \to l^+l^-$ mode, (B): $Z \to q\bar{q}$ mode, (C): $Z \to \nu\bar{\nu}$ mode.

The $Z \to \nu\bar{\nu}$ mode has been found to contribute negligibly to the overall precision which is dominated by the $Z \to q\bar{q}$ mode. However, at higher center-of-mass energies, the $e^+e^- \to \nu\bar{\nu}H$ mode is expected to contribute substantially due to the increase in the cross section of WW fusion process.

2.1 $Z \to l^+l^-$ mode

In this mode, we only considered $Z \to e^+e^-$ mode and $Z \to \mu^+\mu^-$ mode as the signal process. The signal cross section of this mode is 1.9 fb. The dominant background processes are the four leptons processes ($e^+e^- \to eeee$, $ee\mu\mu$, $ee\tau\tau$, $\mu\mu\mu\mu$, $\mu\mu\tau\tau$, and $\tau\tau\tau\tau$). An example diagram is shown in Figure 2-(A). Other background processes are $e^+e^- \to ZH$ reactions where the Higgs boson does not decay to tau pairs.

2.2 $Z \to q\bar{q}$ mode

The signal cross section of this mode is 19.8 fb. The possible background processes for this mode are $qqqq$, $qqll$, and $qql\nu$, which come from $e^+e^- \to W^+W^-$ or $e^+e^- \to ZZ$ reactions. An example diagram is shown in Figure 2-(B). Other possible backgrounds are $e^+e^- \to ZH$ with $Z \to \tau^+\tau^-$ and $H \to q\bar{q}$. These processes have the same final state to the signal.

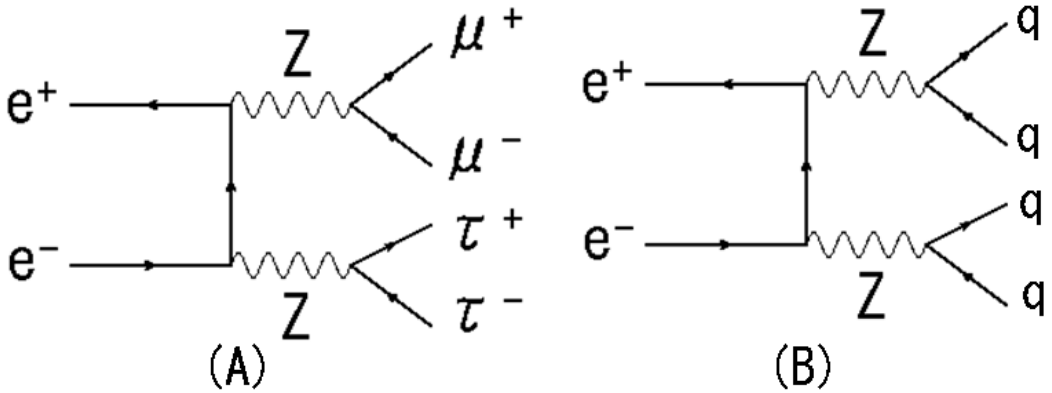

Figure 2: Example diagrams of possible background. (A): $\mu\mu\tau\tau$ background for $Z \to l^+l^-$ mode, (B): $qqqq$ background for $Z \to q\bar{q}$ mode.

3 Simulation Conditions

We performed the detector simulation with Mokka [3], a Geant4-based [4] full simulation, with the ILD_00 detector model. TAUOLA [5] was used for the tau decay simulation. The ILD_00 detector model is consists of vertex detector, time projection chamber, electromagnetic calorimeter (ECAL), hadronic calorimeter (HCAL), and yoke.

We used the signal and background samples which were generated in the context of the Letter of Intent [6]. The assumed center-of-mass energy is 250 GeV. The effects of beamstrahlung and initial state radiation are included. All Monte-Carlo sample information (process ID, process, polarization, cross section, number of events, and luminosity) are summarized in Tables 6 (page 9) and 7 (page 10). We assumed the Higgs mass $M_H = 120$ GeV, branching ratio $\mathrm{Br}(H \to \tau^+\tau^-) = 8.0$ % as assumed by PYTHIA [8], integrated luminosity $\int L\, dt = 250$ fb^{-1}, and beam polarization $P(e^+, e^-) = (+0.3, -0.8)$. We also rescale the final result to the case of $M_H = 125$ GeV and the $H \to \tau^+\tau^-$ branching ratio which includes the NNLO corrections [9].

4 Event Reconstruction and Event Selection

4.1 $Z \to l^+l^-$ mode

In this mode, we take the strategy of reconstructing the Z boson first, followed by the reconstruction of the tau pairs from the Higgs decay.

We applied lepton identification at first for dividing $Z \to e^+e^-$ events and $Z \to \mu^+\mu^-$ events by using the information of energy deposit in the calorimeter (E_{ECAL} and E_{HCAL}, where E_{ECAL} is the energy deposit in ECAL, E_{HCAL} is the energy deposit in HCAL, respectively) and track momentum (P_{track}). Figures 3 - 6 are the plots of $E_{\mathrm{ECAL}}/(E_{\mathrm{ECAL}} + E_{\mathrm{HCAL}})$ and $(E_{\mathrm{ECAL}} + E_{\mathrm{HCAL}})/P_{\mathrm{track}}$.

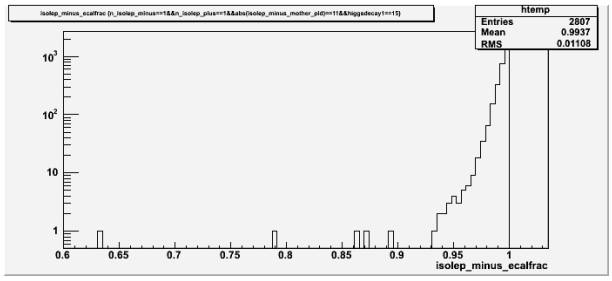

Figure 3: The plot of $E_{\mathrm{ECAL}}/(E_{\mathrm{ECAL}} + E_{\mathrm{HCAL}})$ for the e in eeH samples.

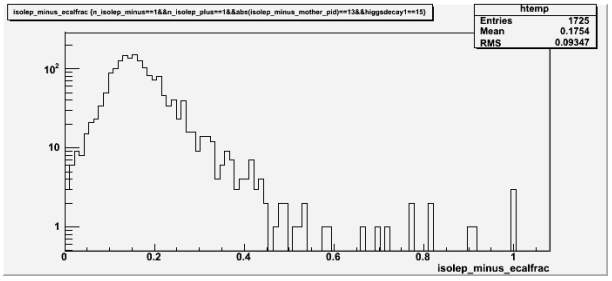

Figure 4: The plot of $E_{\mathrm{ECAL}}/(E_{\mathrm{ECAL}} + E_{\mathrm{HCAL}})$ for the μ in $\mu\mu H$ samples.

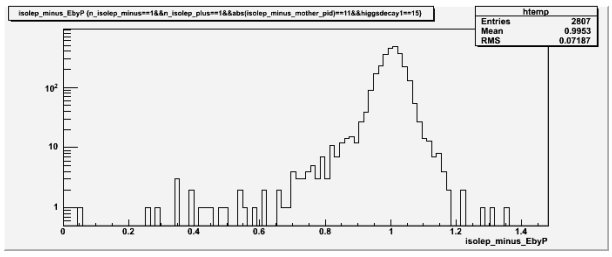

Figure 5: The plot of $(E_{\mathrm{ECAL}} + E_{\mathrm{HCAL}})/P_{\mathrm{track}}$ for the e in eeH samples.

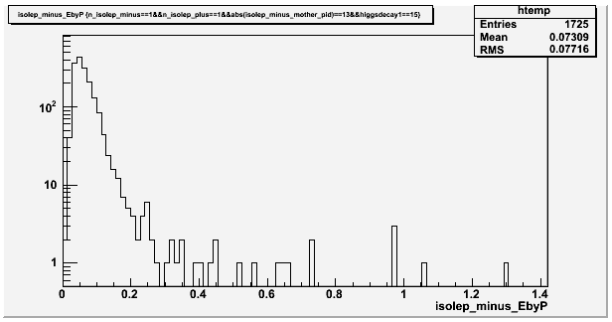

Figure 6: The plot of $(E_{\mathrm{ECAL}} + E_{\mathrm{HCAL}})/P_{\mathrm{track}}$ for the μ in $\mu\mu H$ samples.

From these plots, we define the criteria for lepton identification. The criteria for electron identification (e-ID) are: $E_{\mathrm{ECAL}}/(E_{\mathrm{ECAL}} + E_{\mathrm{HCAL}}) > 0.92$ and $(E_{\mathrm{ECAL}} + E_{\mathrm{HCAL}})/P_{\mathrm{track}} > 0.5$. The criteria for muon identification (μ-ID) are: $E_{\mathrm{ECAL}}/(E_{\mathrm{ECAL}} + E_{\mathrm{HCAL}}) < 0.6$ and $(E_{\mathrm{ECAL}} + E_{\mathrm{HCAL}})/P_{\mathrm{track}} < 0.5$.

After the lepton identification, we applied selections to remove secondary leptons from tau decays. The strategy of this selection is to remove tracks which do not come from the interaction point (IP) by using the track energy E_{track} and impact parameter in the transverse direction d_0 and longitudinal direction z_0 with respect to the beam axis. Figures 7 - 12 show the $|d_0/\sigma(d_0)|$, $|z_0/\sigma(z_0)|$, and E_{track} plots which through the lepton identification. We defined the tau rejection cut for the objects through the e-ID: $|d_0/\sigma(d_0)| < 50$, $|z_0/\sigma(z_0)| < 5$, and $E_{\mathrm{track}} > 10$ GeV, and for the objects through the μ-ID: $|d_0/\sigma(d_0)| < 3$, $|z_0/\sigma(z_0)| < 7$, and $E_{\mathrm{track}} > 20$ GeV.

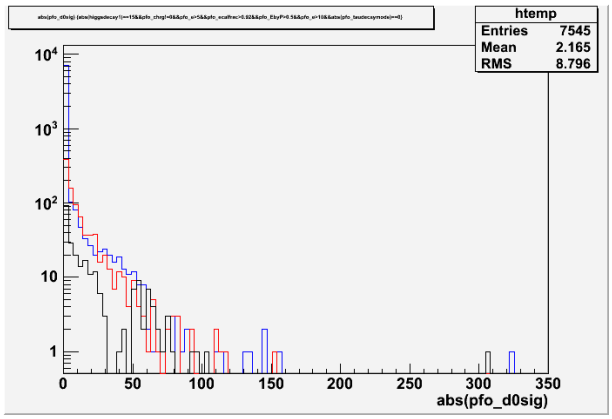

Figure 7: The plot of $|d_0/\sigma(d_0)|$ of e of eeH process. Blue, red, and black histograms show the e from $Z \to e^+e^-$, the e from $\tau \to e\nu\nu$, and the hadrons from τ decay, respectively.

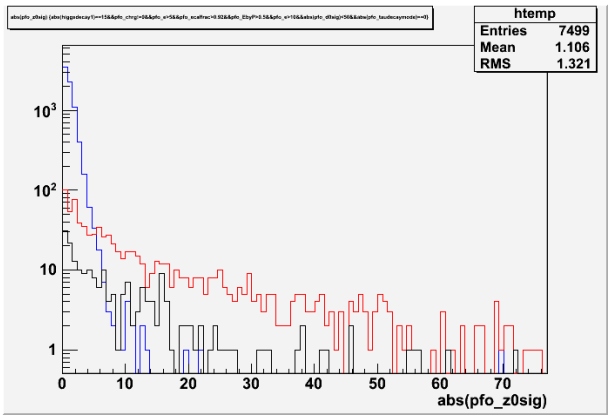

Figure 8: The plot of $|z_0/\sigma(z_0)|$ of e of eeH process. Blue, red, and black histograms show the e from $Z \to e^+e^-$, the e from $\tau \to e\nu\nu$, and the hadrons from τ decay, respectively.

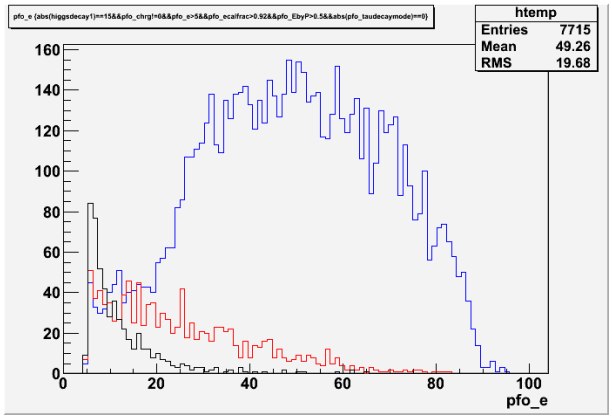

Figure 9: The plot of E_{track} of e of eeH process. Blue, red, and black histograms show the e from $Z \to e^+e^-$, the e from $\tau \to e\nu\nu$, and the hadrons from τ decay, respectively.

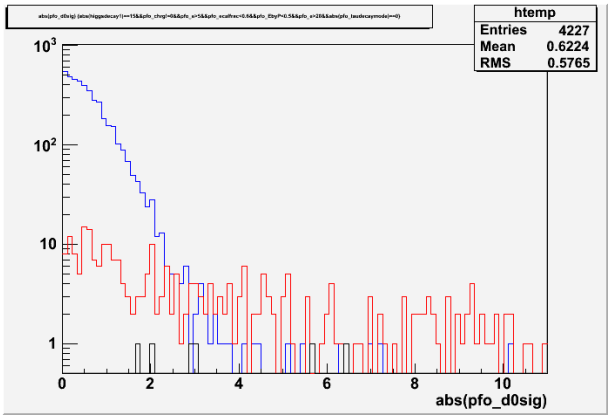

Figure 10: The plot of $|d_0/\sigma(d_0)|$ of μ of $\mu\mu H$ process. Blue, red, and black histograms show the μ from $Z \to \mu^+\mu^-$, the μ from $\tau \to \mu\nu\nu$, and the hadrons from τ decay, respectively.

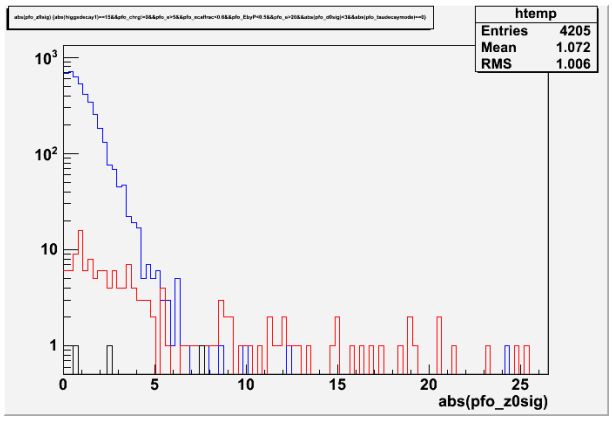

Figure 11: The plot of $|z_0/\sigma(z_0)|$ of μ of $\mu\mu H$ process. Blue, red, and black histograms show the μ from $Z \to \mu^+\mu^-$, the μ from $\tau \to \mu\nu\nu$, and the hadrons from τ decay, respectively.

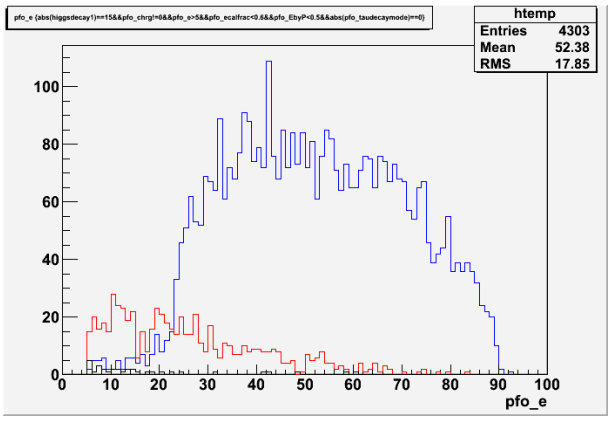

Figure 12: The plot of E_{track} of μ of $\mu\mu H$ process. Blue, red, and black histograms show the μ from $Z \to \mu^+\mu^-$, the μ from $\tau \to \mu\nu\nu$, and the hadrons from τ decay, respectively.

We applied the energy recovery procedure to correct for bremsstrahlung and final state radiation. In order to reconstruct the original Z boson, we have to use both the charged particles and the radiated photons. To achieve this, we defined the cone as shown in Figure 13. The four-momenta of the neutral particles in the cone were combined with that of the lepton candidate. We defined the half-opening angle of the cone with $\cos\theta_{\text{cone}} = 0.999$ and applied the recovery procedure to the lepton candidates. The results are shown in Figures 14 and 15.

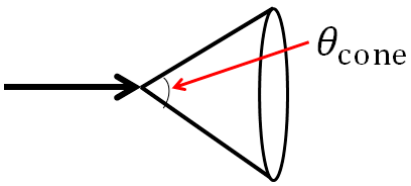

Figure 13: The definition of the cone. Black arrow shows the lepton candidate. θ_{cone} is the angle of the cone.

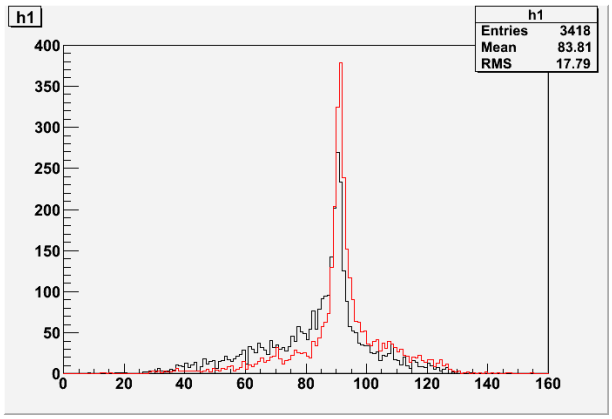

Figure 14: The results of recovery for $Z \to e^+e^-$ mode. The horizontal axis shows the M_Z. Black and red histograms show the results of without recovery and with recovery ($\cos\theta_{\text{cone}} = 0.999$), respectively.

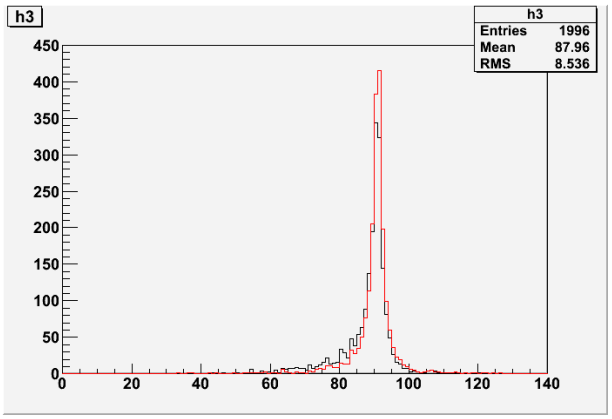

Figure 15: The results of recovery for $Z \to \mu^+\mu^-$ mode. The horizontal axis shows the M_Z. Black and red histograms show the results of without recovery and with recovery ($\cos\theta_{\text{cone}} = 0.999$), respectively.

After that, we applied the tau finder to the remaining objects to reconstruct tau leptons. First of all, the objects which already used at Z boson reconstruction were rejected from tau reconstruction analysis. Then we search the highest energy track from the remaining objects, and combine the neighboring particles (which satisfies the angle with respect to the highest energy track less than 1.0 radian) with the combined mass less than 2 GeV. We regarded the combined object as a tau candidate. Then repeat these processes until there are no charged particles.

After finishing the event reconstruction, we applied the cuts for selecting signal, rejecting background. Before optimizing the cuts, we applied the preselection as follows for $Z \to e^+e^-$ mode: number of e^+ and $e^- = 1$, number of τ^+ and $\tau^- = 1$, and for $Z \to \mu^+\mu^-$ mode: number of μ^+ and $\mu^- = 1$, number of τ^+ and $\tau^- = 1$.

We applied the following cuts for $Z \to e^+e^-$ mode: number of tracks ≤ 8, 115 GeV $< E_{\rm vis} <$ 230 GeV, $|\cos\theta_{\rm miss}| < 0.99$, 81 GeV $< M_Z <$ 113 GeV, $\cos\theta_{e^-} < 0.92$, $\cos\theta_{e^+} > -0.92$, $E_{e^-} <$ 90 GeV, $E_{e^+} <$ 90 GeV, $\cos\theta_{\tau^+\tau^-} < -0.45$, $\cos\theta_{\tau^-} < 0.92$, $\cos\theta_{\tau^+} > -0.92$, and 116 GeV $< M_{\rm recoil} <$ 142 GeV, where $E_{\rm vis}$ is the visible energy, $\theta_{\rm miss}$ is the missing momentum angle with respect to beam axis, $\theta_{e^-(e^+)}$ is the $e^-(e^+)$ angle with respect to beam axis, $E_{e^-(e^+)}$ is the $e^-(e^+)$ energy, $\theta_{\tau^+\tau^-}$ is the angle between τ^+ and τ^-, $\theta_{\tau^-(\tau^+)}$ is the $\tau^-(\tau^+)$ angle with respect to beam axis, and $M_{\rm recoil}$ is the recoil mass, respectively. The histograms of all cut variables are shown in Figures 17 - 28 (page 11 - 12). Table 1 shows the cut statistics of this mode. After the cuts, the $Z \to e^+e^-$ signal events of 108.9 and background events of 76.0 remained. The statistical significance was calculated to be $S/\sqrt{S+B} = 108.9/\sqrt{108.9+76.0} = 8.0\sigma$.

We applied the following cuts for $Z \to \mu^+\mu^-$ mode: number of tracks ≤ 8, 115 GeV $< E_{\rm vis} <$ 235 GeV, $|\cos\theta_{\rm miss}| < 0.98$, 72 GeV $< M_Z <$ 107 GeV, $E_{e^-} <$ 90 GeV, $E_{e^+} <$ 90 GeV, $\cos\theta_{\tau^+\tau^-} < -0.5$, and 118 GeV $< M_{\rm recoil} <$ 143 GeV. The histograms of all cut variables are shown in Figures 29 - 36 (page 13 - 14). Table 2 shows the cut statistics of this mode. For the $Z \to \mu^+\mu^-$ mode case, 131.2 signal events and 91.2 background events were remained. The significance was $S/\sqrt{S+B} = 131.2/\sqrt{131.2+91.2} = 8.8\sigma$.

Table 1: The cut statistics of $Z \to e^+e^-$ mode.

	eeH $H \to \tau\tau$	$\mu\mu H$ $H \to \tau\tau$	$\tau\tau H$ $H \to \tau\tau$	ZH with no τ	$ee\tau\tau$	other 4 leptons	other SM bkg	signi.
No cut	228.3	211.1	214.6	7325	2.388×10^5	5.238×10^5	1.492×10^{10}	0.0019
preselection	171.3	0.155	1.532	47.05	1.338×10^4	3.215×10^4	1.023×10^7	0.053
# of tracks	169.4	0.155	1.532	41.56	1.316×10^4	3.205×10^4	1.009×10^7	0.053
$E_{\rm vis}$	162.3	0.155	0.912	38.36	1.068×10^4	1.039×10^4	4.761×10^6	0.074
$\cos\theta_{\rm miss}$	160.6	0.155	0.912	38.03	8719	1906	5.155×10^5	0.22
M_Z	148.0	0	0.017	29.09	2408	501.2	1.299×10^4	1.2
$\cos\theta_{e^-(e^+)}$	133.9	0	0.009	25.40	1067	101.5	729.7	3.0
$E_{e^-(e^+)}$	133.0	0	0.009	24.93	690.3	78.70	629.7	3.4
$\cos\theta_{\tau^+\tau^-}$	130.8	0	0	3.536	254.9	30.70	155.4	5.5
$\cos\theta_{\tau^-(\tau^+)}$	123.4	0	0	3.074	212.1	9.161	3.817	6.6
$M_{\rm recoil}$	108.9	0	0	2.474	72.35	1.134	0.034	8.0

Table 2: The cut statistics of $Z \to \mu^+\mu^-$ mode.

	$\mu\mu H$ $H \to \tau\tau$	eeH $H \to \tau\tau$	$\tau\tau H$ $H \to \tau\tau$	ZH with no τ	$\mu\mu\tau\tau$	other 4 leptons	other SM bkg	signi.
No cut	211.1	228.3	214.6	7325	3513	7.591×10^6	1.492×10^{10}	0.0017
preselection	168.5	0	0.155	43.01	1698	7546	7732	1.3
# of tracks	167.4	0	0.155	39.65	1684	7537	7400	1.3
$E_{\rm vis}$	162.9	0	0.155	37.40	1586	2285	3713	1.9
$\cos\theta_{\rm miss}$	158.6	0	0.155	36.51	1386	227.5	55.48	3.7
M_Z	153.2	0	0	32.84	1038	55.28	42.54	4.2
$E_{e^-(e^+)}$	153.2	0	0	32.70	738.6	42.41	36.72	4.8
$\cos\theta_{\tau^+\tau^-}$	146.3	0	0	3.638	259.4	20.19	0.756	7.1
$M_{\rm recoil}$	131.2	0	0	2.875	82.36	5.311	0.301	8.8

4.2 $Z \to q\bar{q}$ mode

In this mode, the tau pairs are reconstructed first, followed by the di-jet reconstruction of the Z decay.

At first in this mode, we applied the tau finder to all objects to reconstruct tau leptons. In this analysis, we search the highest energy track and combine the neighboring particles, which satisfy $\cos\theta_{\text{cone}} > 0.98$, with the combined mass less than 2 GeV. We regarded the combined object as a tau candidate. Then we applied the selection cuts as following: $E_{\text{tau candidate}} > 3$ GeV, $E_{\text{cone}} < 0.1E_{\text{tau candidate}}$ with $\cos\theta_{\text{cone}} = 0.9$, and rejecting 3-prong with neutral particles events. These selection cuts were tuned for minimizing misidentification of part of quark jets as tau jets. The survived tau candidate regarded as a tau jet. After the selection cuts, we applied the charge recovery to obtain better efficiency. The charged particles in tau jet which have the energy less than 2 GeV are detached one by one from smallest energy from the tau jet until satisfying the conditions as following: the charge of tau jet is $+1$ or -1, and the number of track(s) in tau jet is 1 or 3. The tau jet after detaching is rejected if it does not satisfy the above conditions. After the selection cuts and detaching, we repeat the above processes until there are no charged particles which have the energy greater than 2 GeV.

After the tau reconstruction, we applied the collinear approximation [10] to reconstruct $M_{\tau^+\tau^-}$. In this approximation, we assumed that the visible decay products of tau and the neutrino(s) from tau is collinear, and the contribution of missing transverse momentum is only comes from the neutrino(s) of tau decay. The invariant mass of the tau pair with the collinear approximation shown in Figure 16.

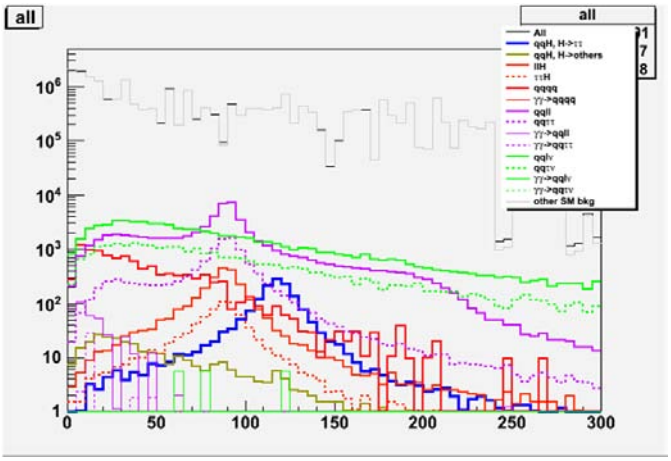

Figure 16: The plot of M_{colapp} in the unit of GeV, the invariant mass of di-tau with collinear approximation. Blue histogram shows the signal process $ZH \to qq\tau\tau$.

After that, we applied the Durham jet clustering method [11] with two jets for the remaining objects for the reconstruction of the Z boson.

After the tau and Z reconstruction, we applied the cuts to select signal process. Before optimizing cuts, we applied the preselection as follows: number of quark jets = 2, number of τ^+ and $\tau^- = 1$, number of tracks in $\tau \leq 3$, and the events which have the tracks in both $\tau = 3$ were rejected (double 3-prong cut). We applied the following cuts to reject the background: $9 \leq$ number of tracks < 50, 110 GeV $< E_{\text{vis}} < 235$ GeV, $|\cos\theta_{\text{miss}}| < 0.98$, 77 GeV $< M_Z < 135$ GeV, 80 GeV $< E_Z < 135$ GeV, $\cos\theta_{\tau^+\tau^-} < -0.5$, $\log_{10}|d_0/\sigma(d_0)|(\tau^+) + \log_{10}|d_0/\sigma(d_0)|(\tau^-) > -0.7$, $\log_{10}|z_0/\sigma(z_0)|(\tau^+) + \log_{10}|z_0/\sigma(z_0)|(\tau^-) > -0.1$, $M_{\tau^+\tau^-} < 115$ GeV, $E_{\tau^+\tau^-} < 125$ GeV, 100 GeV $< M_{\text{colapp}} < 170$ GeV, 100 GeV $< E_{\text{colapp}} < 280$ GeV, and 112 GeV $< M_{\text{recoil}} < 160$ GeV, where $M_{\tau^+\tau^-}$ and $E_{\tau^+\tau^-}$ is the invariant mass and energy without using collinear approximation, M_{colapp} and E_{colapp} is the invariant mass and energy with collinear approximation, respec-

tively. The histograms of all cut variables are shown in Figures 37 - 49 (page 14 - 16). Table 3 shows the cut statistics of this mode. After the cuts, the signal events and background events were remained 1026 and 554.4. The statistical significance of $Z \to q\bar{q}$ mode is calculated to be $S/\sqrt{S+B} = 1026/\sqrt{1026+554.4} = 25.8\sigma$.

Table 3: The cut statistics of $Z \to q\bar{q}$ mode.

	qqH $H \to \tau\tau$	ZH with no τ	llH	$\tau\tau H$	$qqqq$	$qqll$	$qq\tau\tau$	$qql\nu$	$qq\tau\nu$	other SM bkg	signi.
No cut	4233	4.829×10^4	5377	2596	4.038×10^6	3.563×10^5	4.169×10^4	2.788×10^6	1.326×10^6	1.494×10^{10}	0.035
preselection	1647	578.8	2761	765.4	1.230×10^4	6.378×10^4	1.161×10^4	1.249×10^5	4.948×10^4	2.570×10^7	0.32
# of tracks	1644	549.8	2680	765.4	1.230×10^4	6.059×10^4	1.146×10^4	1.214×10^5	4.806×10^4	5.190×10^5	1.9
$E_{\rm vis}$	1607	492.3	1015	744.2	4443	2.106×10^4	1.107×10^4	1.192×10^5	4.693×10^4	2.383×10^5	2.4
$\cos\theta_{\rm miss}$	1572	474.7	860.5	725.1	2127	8315	1.021×10^4	1.171×10^5	4.415×10^4	5939	3.6
M_Z	1440	376.1	791.3	682.8	778.6	4987	8674	8189	3288	997.3	8.3
E_Z	1429	352.0	782.7	528.7	505.0	4797	7857	7703	3061	609.9	8.6
$\cos\theta_{\tau^+\tau^-}$	1386	46.28	442.2	255.6	191.4	1468	2001	2831	1154	475.6	13.7
$d_0$sig	1338	30.29	235.1	244.3	131.4	854.9	1928	1786	1044	248.1	15.1
$z_0$sig	1287	19.54	105.0	234.7	81.77	408.2	1845	909.9	883.4	244.6	16.6
$M_{\tau^+\tau^-}$	1286	19.39	103.2	234.7	72.05	349.1	1837	883.5	883.4	243.9	16.7
$E_{\tau^+\tau^-}$	1282	19.39	103.0	234.7	72.05	324.7	1836	873.2	883.4	243.9	16.7
$M_{\rm colapp}$	1065	3.074	18.76	47.94	10.28	72.83	616.9	150.8	137.0	0.746	23.1
$E_{\rm colapp}$	1062	2.454	18.01	46.72	10.28	71.27	612.1	93.05	93.52	0.454	23.7
$M_{\rm recoil}$	1026	2.144	14.54	21.24	9.938	57.07	366.3	39.64	43.31	0.161	25.8

5 Summary

We evaluated the measurement accuracy of the branching ratio of the $H \to \tau^+\tau^-$ mode at $\sqrt{s} =$ 250 GeV at the ILC with ILD_00 detector model. We assumed $M_H = 120$ GeV, $\mathrm{Br}(H \to \tau^+\tau^-) =$ 8.0 %, $\int L\ dt = 250$ fb^{-1}, and the polarization $P(e^+, e^-) = (+0.3, -0.8)$. The obtained values were summarized in Table 4.

Table 4: The analysis results of $\sqrt{s} = 250$ GeV.

mode	$Z \to e^+e^-$	$Z \to \mu^+\mu^-$	$Z \to q\bar{q}$
significance	8.0σ	8.8σ	25.8σ

From these results, the combined significance was calculated to be $\sqrt{8.0^2 + 8.8^2 + 25.8^2} = 28.4\sigma$. Therefore, the measurement accuracy $\Delta(\sigma \cdot \mathrm{Br})/(\sigma \cdot \mathrm{Br})$ was calculated to be $\Delta(\sigma \cdot \mathrm{Br})/(\sigma \cdot \mathrm{Br}) = 1/28.4 = 3.5$ %.

The results are extrapolated to the case of $M_H = 125$ GeV by scaling the signal yields by the $e^+e^- \to ZH$ cross section and the branching ratio $\mathrm{Br}(H \to \tau^+\tau^-) \to 6.32$ % [9]. We assumed that the selection efficiencies the same. The results are summarized in Table 5.

Table 5: The results of the extrapolation to $M_H = 125$ GeV.

$Z \to e^+e^-$	$Z \to \mu^+\mu^-$	$Z \to q\bar{q}$	Combined	$\frac{\Delta(\sigma \cdot \mathrm{Br})}{\sigma \cdot \mathrm{Br}}$
6.8σ	7.4σ	21.9σ	24.1σ	4.2 %

A Monte-Carlo Samples

Table 6: Monte-Carlo information which used in this analysis. From the left line, the process ID, process, beam polarization (ep for positrons, em for electrons), cross section in the unit of fb, number of Monte-Carlo events, integrated luminosity in the unit of fb^{-1}, are shown. This list continues to Table 7.

21564 aa_bb ep+0.0em+0.0 960.971 96 0.099899
21565 aa_bb ep+0.0em+0.0 5218.47 521 0.0998377
21566 aa_bb ep+0.0em+0.0 5205.84 520 0.0998878
21567 aa_bb ep+0.0em+0.0 4768.41 476 0.0998236
21560 aa_cc ep+0.0em+0.0 25826.9 2582 0.0999733
21561 aa_cc ep+0.0em+0.0 158487 15848 0.0999956
21562 aa_cc ep+0.0em+0.0 158287 15828 0.0999956
21563 aa_cc ep+0.0em+0.0 208135 20813 0.0999976
23532 aa_ccbb ep+0.0em+0.0 0.010556 10 947.329
23533 aa_ccbb ep+0.0em+0.0 0.004464 10 2240.14
23534 aa_ccbb ep+0.0em+0.0 0.004538 10 2203.61
23432 aa_cccc ep+0.0em+0.0 0.038923 10 256.918
23433 aa_cccc ep+0.0em+0.0 0.012718 10 786.287
23434 aa_cccc ep+0.0em+0.0 0.01308 10 764.526
23528 aa_ccdd ep+0.0em+0.0 0.008955 10 1116.69
23529 aa_ccdd ep+0.0em+0.0 0.002019 10 4952.95
23530 aa_ccdd ep+0.0em+0.0 0.002071 10 4828.59
23516 aa_cce1e1 ep+0.0em+0.0 0.475002 10 21.0525
23517 aa_cce1e1 ep+0.0em+0.0 0.574236 10 17.4144
23518 aa_cce1e1 ep+0.0em+0.0 0.578067 10 17.299
23519 aa_cce1e1 ep+0.0em+0.0 0.095982 10 104.186
23520 aa_cce2e2 ep+0.0em+0.0 0.473937 10 21.0999
23521 aa_cce2e2 ep+0.0em+0.0 0.578748 10 17.2787
23522 aa_cce2e2 ep+0.0em+0.0 0.581645 10 17.1926
23523 aa_cce2e2 ep+0.0em+0.0 0.095404 10 104.817
23524 aa_cce3e3 ep+0.0em+0.0 0.809322 10 12.356
23525 aa_cce3e3 ep+0.0em+0.0 1.07006 10 9.34527
23526 aa_cce3e3 ep+0.0em+0.0 1.07435 10 9.30795
23527 aa_cce3e3 ep+0.0em+0.0 0.198611 10 50.3497
23392 aa_csdu ep+0.0em+0.0 0.644164 10 15.524
23393 aa_csdu ep+0.0em+0.0 0.001171 10 8539.71
23394 aa_csdu ep+0.0em+0.0 0.001482 10 6747.64
23380 aa_cse1n1 ep+0.0em+0.0 0.225189 10 44.4071
23384 aa_cse2n2 ep+0.0em+0.0 0.225196 10 44.4058
23388 aa_cse3n3 ep+0.0em+0.0 0.225468 10 44.3522
23396 aa_cssc ep+0.0em+0.0 0.650312 10 15.3772
23397 aa_cssc ep+0.0em+0.0 0.002852 10 3506.31
23398 aa_cssc ep+0.0em+0.0 0.003221 10 3104.63
21552 aa_dd ep+0.0em+0.0 1611.35 161 0.0999162
21553 aa_dd ep+0.0em+0.0 9902.35 990 0.0999763
21554 aa_dd ep+0.0em+0.0 9913.25 991 0.0999672
21555 aa_dd ep+0.0em+0.0 12993.6 1299 0.0999723
21536 aa_e1e1 ep+0.0em+0.0 75475.4 7547 0.0999928
21537 aa_e1e1 ep+0.0em+0.0 551033 107786 0.195607
21539 aa_e1e1 ep+0.0em+0.0 1.42431e+06 137431 0.0964895
23556 aa_e1e1bb ep+0.0em+0.0 0.031025 10 322.321
23557 aa_e1e1bb ep+0.0em+0.0 0.028705 10 348.371
23558 aa_e1e1bb ep+0.0em+0.0 0.02884 10 346.741
23559 aa_e1e1bb ep+0.0em+0.0 0.004257 10 2349.07
23549 aa_e1e1dd ep+0.0em+0.0 0.050209 10 199.167
23550 aa_e1e1dd ep+0.0em+0.0 0.050399 10 198.417
23551 aa_e1e1dd ep+0.0em+0.0 0.008768 10 1140.51
23536 aa_e1e1e1e1 ep+0.0em+0.0 0.662331 10 15.0982
23537 aa_e1e1e1e1 ep+0.0em+0.0 0.971629 10 10.292
23538 aa_e1e1e1e1 ep+0.0em+0.0 0.97552 10 10.2509
23539 aa_e1e1e1e1 ep+0.0em+0.0 0.236858 10 42.2194
23540 aa_e1e1e2e2 ep+0.0em+0.0 1.68665 10 5.92891
23541 aa_e1e1e2e2 ep+0.0em+0.0 3.07145 20 6.51158
23543 aa_e1e1e2e2 ep+0.0em+0.0 0.971522 10 10.2931
23544 aa_e1e1e3e3 ep+0.0em+0.0 3.14724 10 3.17739
23545 aa_e1e1e3e3 ep+0.0em+0.0 6.49529 10 1.53958
23546 aa_e1e1e3e3 ep+0.0em+0.0 6.52147 10 1.5334
23547 aa_e1e1e3e3 ep+0.0em+0.0 2.55979 10 3.90657
23552 aa_e1e1ss ep+0.0em+0.0 0.044906 10 222.687
23553 aa_e1e1ss ep+0.0em+0.0 0.050028 10 199.888
23554 aa_e1e1ss ep+0.0em+0.0 0.050343 10 198.637
23555 aa_e1e1ss ep+0.0em+0.0 0.008754 10 1142.33
21540 aa_e2e2 ep+0.0em+0.0 75532.1 7553 0.0999972
21541 aa_e2e2 ep+0.0em+0.0 550664 55066 0.0999993
21542 aa_e2e2 ep+0.0em+0.0 551685 55168 0.0999991
21543 aa_e2e2 ep+0.0em+0.0 1.42387e+06 141987 0.0997191
23576 aa_e2e2bb ep+0.0em+0.0 0.031069 10 321.864
23577 aa_e2e2bb ep+0.0em+0.0 0.028705 10 348.371
23578 aa_e2e2bb ep+0.0em+0.0 0.028893 10 346.105
23579 aa_e2e2bb ep+0.0em+0.0 0.004264 10 2345.22
23568 aa_e2e2dd ep+0.0em+0.0 0.044878 10 222.826
23569 aa_e2e2dd ep+0.0em+0.0 0.050182 10 199.275
23570 aa_e2e2dd ep+0.0em+0.0 0.050545 10 197.844
23571 aa_e2e2dd ep+0.0em+0.0 0.008769 10 1140.38
23560 aa_e2e2e2e2 ep+0.0em+0.0 0.663421 10 15.0734
23561 aa_e2e2e2e2 ep+0.0em+0.0 0.97309 10 10.2765
23562 aa_e2e2e2e2 ep+0.0em+0.0 0.975528 10 10.2509
23563 aa_e2e2e2e2 ep+0.0em+0.0 0.236644 10 42.2576
23564 aa_e2e2e3e3 ep+0.0em+0.0 3.15328 10 3.1713
23565 aa_e2e2e3e3 ep+0.0em+0.0 6.51091 20 3.07177
23567 aa_e2e2e3e3 ep+0.0em+0.0 2.56862 10 3.89314
23572 aa_e2e2ss ep+0.0em+0.0 0.044865 10 222.891
23573 aa_e2e2ss ep+0.0em+0.0 0.049876 10 200.497
23574 aa_e2e2ss ep+0.0em+0.0 0.050324 10 198.712
23575 aa_e2e2ss ep+0.0em+0.0 0.008735 10 1144.82
21544 aa_e3e3 ep+0.0em+0.0 447301 4473 0.00999998
21545 aa_e3e3 ep+0.0em+0.0 4.00527e+06 10000 0.00249671
21546 aa_e3e3 ep+0.0em+0.0 3.99604e+06 10000 0.00250248
21547 aa_e3e3 ep+0.0em+0.0 2.06478e+07 10000 0.000484313
23592 aa_e3e3bb ep+0.0em+0.0 0.048481 10 206.266
23593 aa_e3e3bb ep+0.0em+0.0 0.055322 10 180.76
23594 aa_e3e3bb ep+0.0em+0.0 0.05558 10 179.921
23595 aa_e3e3bb ep+0.0em+0.0 0.009567 10 1045.26
23584 aa_e3e3dd ep+0.0em+0.0 0.073276 10 136.47
23585 aa_e3e3dd ep+0.0em+0.0 0.096953 10 103.143
23586 aa_e3e3dd ep+0.0em+0.0 0.097375 10 102.696
23587 aa_e3e3dd ep+0.0em+0.0 0.019565 10 511.117
23580 aa_e3e3e3e3 ep+0.0em+0.0 2.98239 10 3.35302
23581 aa_e3e3e3e3 ep+0.0em+0.0 5.81718 10 1.71905
23582 aa_e3e3e3e3 ep+0.0em+0.0 5.83263 10 1.71449
23583 aa_e3e3e3e3 ep+0.0em+0.0 2.0741 10 4.82137
23588 aa_e3e3ss ep+0.0em+0.0 0.073357 10 136.32
23589 aa_e3e3ss ep+0.0em+0.0 0.09712 10 102.965
23590 aa_e3e3ss ep+0.0em+0.0 0.097381 10 102.689
23591 aa_e3e3ss ep+0.0em+0.0 0.019638 10 509.217
23312 aa_n1e1du ep+0.0em+0.0 0.225273 10 44.3906
23300 aa_n1e1e1n1 ep+0.0em+0.0 0.076337 10 130.998
23304 aa_n1e1e2n2 ep+0.0em+0.0 0.073443 10 136.16
23308 aa_n1e1e3n3 ep+0.0em+0.0 0.073757 10 135.58
23316 aa_n1e1sc ep+0.0em+0.0 0.225277 10 44.3898
23436 aa_n1n1e2e2 ep+0.0em+0.0 0.003527 10 2835.27
23440 aa_n1n1e3e3 ep+0.0em+0.0 0.003793 10 2636.44
23400 aa_n1n1uu ep+0.0em+0.0 0.002035 10 4914
23332 aa_n2e2du ep+0.0em+0.0 0.225253 10 44.3945
23320 aa_n2e2e1n1 ep+0.0em+0.0 0.073442 10 136.162
23324 aa_n2e2e2n2 ep+0.0em+0.0 0.076285 10 131.087
23328 aa_n2e2e3n3 ep+0.0em+0.0 0.073621 10 135.831
23412 aa_n2n2cc ep+0.0em+0.0 0.002028 10 4930.97
23456 aa_n2n2e1e1 ep+0.0em+0.0 0.003538 10 2826.46
23460 aa_n2n2e3e3 ep+0.0em+0.0 0.003797 10 2633.66
23352 aa_n3e3du ep+0.0em+0.0 0.22566 10 44.3145
23340 aa_n3e3e1n1 ep+0.0em+0.0 0.073677 10 135.728
23344 aa_n3e3e2n2 ep+0.0em+0.0 0.073519 10 136.019
23348 aa_n3e3e3n3 ep+0.0em+0.0 0.077072 10 129.749
23356 aa_n3e3sc ep+0.0em+0.0 0.225636 10 44.3192
23420 aa_n3n3cc ep+0.0em+0.0 0.002032 10 4921.26
23476 aa_n3n3e1e1 ep+0.0em+0.0 0.003529 10 2833.66
23480 aa_n3n3e2e2 ep+0.0em+0.0 0.003535 10 2828.85
23416 aa_n3n3uu ep+0.0em+0.0 0.002035 10 4914
21556 aa_ss ep+0.0em+0.0 1612.02 161 0.0998747
21557 aa_ss ep+0.0em+0.0 9919.95 992 0.100001
21558 aa_ss ep+0.0em+0.0 9874.29 987 0.0999566
21559 aa_ss ep+0.0em+0.0 13010.8 1301 0.0999939
23372 aa_uddu ep+0.0em+0.0 0.650353 10 15.3763
23373 aa_uddu ep+0.0em+0.0 0.002865 10 3490.4
23374 aa_uddu ep+0.0em+0.0 0.003197 10 3127.93
23360 aa_ude1n1 ep+0.0em+0.0 0.225336 10 44.3782
23364 aa_ude2n2 ep+0.0em+0.0 0.225701 10 44.3064
23368 aa_ude3n3 ep+0.0em+0.0 0.225594 10 44.3274
23376 aa_udsc ep+0.0em+0.0 0.643852 10 15.5315
23377 aa_udsc ep+0.0em+0.0 0.001171 10 8539.71
23378 aa_udsc ep+0.0em+0.0 0.001484 10 6738.54
21548 aa_uu ep+0.0em+0.0 25709.9 2570 0.0999615
21549 aa_uu ep+0.0em+0.0 158254 31658 0.200045
21551 aa_uu ep+0.0em+0.0 208230 20823 0.1
23512 aa_uubb ep+0.0em+0.0 0.010578 10 945.358
23513 aa_uubb ep+0.0em+0.0 0.004456 10 2244.17
23514 aa_uubb ep+0.0em+0.0 0.004531 10 2207.02
23428 aa_uucc ep+0.0em+0.0 0.078277 10 127.751
23429 aa_uucc ep+0.0em+0.0 0.027362 10 365.47
23430 aa_uucc ep+0.0em+0.0 0.027931 10 358.025
23496 aa_uue1e1 ep+0.0em+0.0 0.476112 10 21.0035
23498 aa_uue1e1 ep+0.0em+0.0 0.58118 10 17.2064
23499 aa_uue1e1 ep+0.0em+0.0 0.095015 10 105.247
23500 aa_uue2e2 ep+0.0em+0.0 0.474597 10 21.0705
23502 aa_uue2e2 ep+0.0em+0.0 0.576787 10 17.3374
23503 aa_uue2e2 ep+0.0em+0.0 0.095267 10 104.968
23504 aa_uue3e3 ep+0.0em+0.0 0.808463 10 12.3691
23505 aa_uue3e3 ep+0.0em+0.0 1.07061 10 9.34047
23506 aa_uue3e3 ep+0.0em+0.0 1.07551 10 9.29791
23507 aa_uue3e3 ep+0.0em+0.0 0.19932 10 50.1706
23508 aa_uuss ep+0.0em+0.0 0.008966 10 1115.32
23509 aa_uuss ep+0.0em+0.0 0.001999 10 5002.5
23510 aa_uuss ep+0.0em+0.0 0.002084 10 4798.46
23424 aa_uuuu ep+0.0em+0.0 0.03894 10 256.805
23425 aa_uuuu ep+0.0em+0.0 0.012785 10 782.167
23426 aa_uuuu ep+0.0em+0.0 0.013116 10 762.428
21101 aa ep+1.0em-1.0 49250.8 241254 4.89848
21102 aa ep-1.0em+1.0 49267.2 237936 4.8295
21105 aaa ep+1.0em-1.0 5300.06 26500 4.99994
21106 aaa ep-1.0em+1.0 5298.17 26091 4.92453
21109 aaaa ep+1.0em-1.0 324.752 1624 5.00074
21110 aaaa ep-1.0em+1.0 323.783 1619 5.00026
21120 ae1_e1a ep-1.0em+0.0 371863 18393 0.0494618
21121 ae1_e1a ep-1.0em+0.0 5.36047e+06 266224 0.0496643
21122 ae1_e1a ep+1.0em+0.0 372274 18614 0.0500008
21123 ae1_e1a ep+1.0em+0.0 5.36372e+06 266186 0.0496271
21684 ae1_e1bb ep-1.0em+0.0 196.883 196 0.995515
21685 ae1_e1bb ep-1.0em+0.0 741.99 742 1.00001
21686 ae1_e1bb ep+1.0em+0.0 235.7 235 0.99703
21687 ae1_e1bb ep+1.0em+0.0 729.393 729 0.999461
21660 ae1_e1cc ep-1.0em+0.0 2633.94 2633 0.999643
21661 ae1_e1cc ep-1.0em+0.0 14122.4 14122 0.999972
21662 ae1_e1cc ep+1.0em+0.0 2683.16 2683 0.99994
21663 ae1_e1cc ep+1.0em+0.0 14237 14037 0.985952
21676 ae1_e1dd ep-1.0em+0.0 262.926 262 0.996478
21677 ae1_e1dd ep-1.0em+0.0 1209.36 1209 0.999702
21678 ae1_e1dd ep+1.0em+0.0 305.707 305 0.997687
21679 ae1_e1dd ep+1.0em+0.0 1204.94 1204 0.99922
21664 ae1_e1e1e1 ep-1.0em+0.0 7275.46 7275 0.999937
21665 ae1_e1e1e1 ep-1.0em+0.0 44860.5 44060 0.982156
21666 ae1_e1e1e1 ep+1.0em+0.0 7327.35 7327 0.999952
21667 ae1_e1e1e1 ep+1.0em+0.0 44910.9 44910 0.99998
21668 ae1_e1e2e2 ep-1.0em+0.0 7859.36 7859 0.999954
21669 ae1_e1e2e2 ep-1.0em+0.0 53497.7 52297 0.977556
21670 ae1_e1e2e2 ep+1.0em+0.0 7874.12 6874 0.872986
21671 ae1_e1e2e2 ep+1.0em+0.0 53695.4 52695 0.981369
21672 ae1_e1e3e3 ep-1.0em+0.0 13442.9 13442 0.999933
21673 ae1_e1e3e3 ep-1.0em+0.0 96101.5 94701 0.985427
21674 ae1_e1e3e3 ep+1.0em+0.0 13483 13283 0.985167
21675 ae1_e1e3e3 ep+1.0em+0.0 96257.6 94057 0.977138
21648 ae1_e1n2n2 ep-1.0em+0.0 33.3463 33 0.989615
21649 ae1_e1n2n2 ep-1.0em+0.0 14.4871 14 0.966377
21650 ae1_e1n2n2 ep+1.0em+0.0 52.0695 52 0.998665
21651 ae1_e1n2n2 ep+1.0em+0.0 22.6358 22 0.971912
21652 ae1_e1n3n3 ep-1.0em+0.0 33.3836 33 0.988509
21653 ae1_e1n3n3 ep-1.0em+0.0 14.5035 14 0.965284
21654 ae1_e1n3n3 ep+1.0em+0.0 52.1148 52 0.997797
21655 ae1_e1n3n3 ep+1.0em+0.0 22.6013 22 0.973395
21680 ae1_e1ss ep-1.0em+0.0 263.497 263 0.998114
21681 ae1_e1ss ep-1.0em+0.0 1205.28 1205 0.999768
21682 ae1_e1ss ep+1.0em+0.0 304.802 304 0.997369
21683 ae1_e1ss ep+1.0em+0.0 1203.83 1203 0.999311
21656 ae1_e1uu ep-1.0em+0.0 2630.42 2630 0.99984
21657 ae1_e1uu ep-1.0em+0.0 14117.2 14117 0.999986
21658 ae1_e1uu ep+1.0em+0.0 2696.52 2696 0.999807
21659 ae1_e1uu ep+1.0em+0.0 14189.1 14189 0.999993
21189 bb ep+1.0em-1.0 47506.1 99600 2.09657
21190 bb ep-1.0em+1.0 27566 99800 3.6204
21533 bbbb ep+1.0em-1.0 67.0078 67008 1000
21534 bbbb ep-1.0em+1.0 28.7721 28772 999.997
22281 bbcsdu ep+1.0em-1.0 0.029907 10000 334370
22285 bbcssc ep+1.0em-1.0 0.034435 10000 290402
22286 bbcssc ep-1.0em+1.0 0.002779 10000 3.59842e+06
20633 bbh ep+1.0em-1.0 75.602 75602 1000
20634 bbh ep-1.0em+1.0 48.4438 48444 1000
22261 bbuddu ep+1.0em-1.0 0.033986 10000 294239
22262 bbuddu ep-1.0em+1.0 0.002776 10000 3.60231e+06
22265 bbudsc ep+1.0em-1.0 0.030041 10000 332878
21165 cc ep+1.0em-1.0 44745.7 99600 2.22591
21166 cc ep-1.0em+1.0 27317.2 88600 3.24338
21449 ccbb ep+1.0em-1.0 123.789 99000 799.748
21450 ccbb ep-1.0em+1.0 56.6712 55671 982.351
21349 cccc ep+1.0em-1.0 54.3735 53774 988.974
21350 cccc ep-1.0em+1.0 26.3297 26330 1000.01
24477 ccccbb ep+1.0em-1.0 0.003422 10000 2.92227e+06
24478 ccccbb ep-1.0em+1.0 0.001756 10000 5.69476e+06
21445 ccdd ep+1.0em-1.0 120.779 100000 827.959
21446 ccdd ep-1.0em+1.0 55.1663 54566 989.118
24773 ccddbb ep+1.0em-1.0 0.004519 10000 2.21288e+06
24774 ccddbb ep-1.0em+1.0 0.002267 10000 4.41112e+06
21432 cce1e1 ep-1.0em-1.0 448.721 96400 214.833
21433 cce1e1 ep+1.0em-1.0 506.805 98000 193.368
21434 cce1e1 ep-1.0em+1.0 464.383 96800 208.449
21435 cce1e1 ep+1.0em+1.0 448.339 99200 221.261
21437 cce2e2 ep+1.0em-1.0 53.1354 52935 996.229
21438 cce2e2 ep-1.0em+1.0 29.3345 29335 1000.02
21441 cce3e3 ep+1.0em-1.0 52.7484 52548 996.201
21442 cce3e3 ep-1.0em+1.0 29.1511 29151 999.997
20609 cch ep+1.0em-1.0 59.231 59231 1000
20610 cch ep-1.0em+1.0 37.8798 37880 1000.01
21309 csdu ep+1.0em-1.0 6513.67 99600 15.2909
21310 csdu ep-1.0em+1.0 59.9344 59534 993.319
21297 cse1n1 ep+1.0em-1.0 2466.05 92400 37.4688
21298 cse1n1 ep-1.0em+1.0 20.9278 11528 550.846
21299 cse1n1 ep+1.0em+1.0 86.2613 80061 928.122
21301 cse2n2 ep+1.0em-1.0 2268.39 100000 44.0841
21302 cse2n2 ep-1.0em+1.0 20.8866 20887 1000.02
21305 cse3n3 ep+1.0em-1.0 2266.29 100000 44.125
21306 cse3n3 ep-1.0em+1.0 20.8669 20867 1000
21313 cssc ep+1.0em-1.0 6638.5 99800 15.0335
21314 cssc ep-1.0em+1.0 112.648 79200 703.075
21181 dd ep+1.0em-1.0 48065.6 100000 2.08049
21182 dd ep-1.0em+1.0 28036.9 99200 3.53819
21521 ddbb ep+1.0em-1.0 137.124 90200 657.799
21522 ddbb ep-1.0em+1.0 58.9095 58909 999.992
21513 dddd ep+1.0em-1.0 67.066 66666 994.036
21514 dddd ep-1.0em+1.0 28.8606 24661 854.487
24973 ddddbb ep+1.0em-1.0 0.001092 10000 3.15751e+06
20625 ddh ep+1.0em-1.0 75.8898 75890 1000
20626 ddh ep-1.0em+1.0 48.5522 48552 999.996
21517 ddss ep+1.0em-1.0 134.545 65800 489.056
21518 ddss ep-1.0em+1.0 57.7479 51748 896.102
24981 ddssbb ep+1.0em-1.0 0.002197 10000 4.55166e+06
24982 ddssbb ep-1.0em+1.0 0.001108 10000 9.02527e+06
21116 e1a_e1a ep+0.0em-1.0 372192 18610 0.0500011
21117 e1a_e1a ep+0.0em-1.0 5.39497e+06 269148 0.0498887
21118 e1a_e1a ep+0.0em+1.0 372426 18621 0.0499992
21119 e1a_e1a ep+0.0em+1.0 5.39207e+06 267003 0.0495177
21624 e1a_e1bb ep+0.0em-1.0 235.778 235 0.9967
21625 e1a_e1bb ep+0.0em-1.0 729.568 729 0.999221
21626 e1a_e1bb ep+0.0em+1.0 196.862 196 0.995621
21627 e1a_e1bb ep+0.0em+1.0 742.713 742 0.99904

Table 7: Monte-Carlo information which used in this analysis. From the left line, the process ID, process, beam polarization (ep for positrons, em for electrons), cross section in the unit of fb, number of Monte-Carlo events, integrated luminosity in the unit of fb^{-1}, are shown. This list is series of Table 6.

21600	e1a_e1cc	ep+0.0em-1.0	2692.03	2000 0.742934
21601	e1a_e1cc	ep+0.0em-1.0	14238.4	14238 0.999972
21602	e1a_e1cc	ep+0.0em+1.0	2630.76	2630 0.999711
21603	e1a_e1cc	ep+0.0em+1.0	14172	14172 1
21616	e1a_e1dd	ep+0.0em-1.0	305.228	305 0.999253
21617	e1a_e1dd	ep+0.0em-1.0	1207.73	1207 0.999396
21618	e1a_e1dd	ep+0.0em+1.0	263.602	263 0.997716
21619	e1a_e1dd	ep+0.0em+1.0	1210.08	1210 0.999934
21604	e1a_e1e1e1	ep+0.0em-1.0	7311.26	7311 0.999964
21605	e1a_e1e1e1	ep+0.0em-1.0	45047.7	43047 0.955587
21606	e1a_e1e1e1	ep+0.0em+1.0	7282.56	7282 0.999923
21607	e1a_e1e1e1	ep+0.0em+1.0	44999.4	43999 0.977769
21608	e1a_e1e2e2	ep+0.0em-1.0	7880.39	7880 0.99995
21609	e1a_e1e2e2	ep+0.0em-1.0	53812.4	53412 0.992559
21610	e1a_e1e2e2	ep+0.0em+1.0	7869.66	7869 0.999916
21611	e1a_e1e2e2	ep+0.0em+1.0	53765.8	50565 0.940468
21612	e1a_e1e3e3	ep+0.0em-1.0	13471.9	13471 0.999933
21613	e1a_e1e3e3	ep+0.0em-1.0	96603.4	94803 0.981363
21614	e1a_e1e3e3	ep+0.0em+1.0	13459.7	13459 0.999948
21615	e1a_e1e3e3	ep+0.0em+1.0	96607	95607 0.989649
21588	e1a_e1n2n2	ep+0.0em-1.0	52.0727	52 0.998604
21589	e1a_e1n2n2	ep+0.0em-1.0	21.8282	21 0.962058
21590	e1a_e1n2n2	ep+0.0em+1.0	33.307	33 0.990783
21591	e1a_e1n2n2	ep+0.0em+1.0	13.982	14 1.00129
21592	e1a_e1n3n3	ep+0.0em-1.0	52.0479	52 0.99908
21593	e1a_e1n3n3	ep+0.0em-1.0	21.8319	21 0.961895
21594	e1a_e1n3n3	ep+0.0em+1.0	33.3573	33 0.989289
21595	e1a_e1n3n3	ep+0.0em+1.0	13.9806	14 1.00139
21620	e1a_e1ss	ep+0.0em-1.0	305.28	305 0.999083
21621	e1a_e1ss	ep+0.0em-1.0	1203.61	1203 0.999493
21622	e1a_e1ss	ep+0.0em+1.0	263.322	263 0.998777
21623	e1a_e1ss	ep+0.0em+1.0	1210.02	1210 0.999983
21596	e1a_e1uu	ep+0.0em-1.0	2697.07	2697 0.999974
21597	e1a_e1uu	ep+0.0em-1.0	14270.7	14270 0.999951
21598	e1a_e1uu	ep+0.0em+1.0	2631.22	2631 0.999916
21599	e1a_e1uu	ep+0.0em+1.0	14186.3	14186 0.999979
21168	e1e1	ep-1.0em-1.0	1.72542e+07	25000 0.00144892
21169	e1e1	ep+1.0em-1.0	1.73374e+07	22500 0.00129777
21170	e1e1	ep-1.0em+1.0	1.72946e+07	24500 0.00141663
21171	e1e1	ep+1.0em+1.0	1.72517e+07	25000 0.00144913
21472	e1e1bb	ep-1.0em-1.0	57.2207	57221 1000.01
21473	e1e1bb	ep+1.0em-1.0	106.063	100000 942.836
21474	e1e1bb	ep-1.0em+1.0	68.9777	68978 1000
21475	e1e1bb	ep+1.0em+1.0	57.3099	57310 1000
21464	e1e1dd	ep-1.0em-1.0	73.3921	72592 989.098
21465	e1e1dd	ep+1.0em-1.0	123.983	100000 806.562
21466	e1e1dd	ep-1.0em+1.0	85.3261	84126 985.935
21467	e1e1dd	ep+1.0em+1.0	73.442	73442 1000
21452	e1e1e1e1	ep-1.0em-1.0	942.464	92200 97.8287
21453	e1e1e1e1	ep+1.0em-1.0	995.595	91400 91.8044
21454	e1e1e1e1	ep-1.0em+1.0	982.404	97400 99.1445
21455	e1e1e1e1	ep+1.0em+1.0	943.694	97800 103.635
21456	e1e1e2e2	ep-1.0em-1.0	1073.64	100000 93.1411
21457	e1e1e2e2	ep+1.0em-1.0	1106.71	99800 90.1772
21458	e1e1e2e2	ep-1.0em+1.0	1088.6	100000 91.8611
21459	e1e1e2e2	ep+1.0em+1.0	1068.97	99000 92.6125
21460	e1e1e3e3	ep-1.0em-1.0	941.685	98800 104.918
21461	e1e1e3e3	ep+1.0em-1.0	965.145	97800 101.332
21462	e1e1e3e3	ep-1.0em+1.0	948.774	99000 104.345
21463	e1e1e3e3	ep+1.0em+1.0	942.984	98200 104.138
20612	e1e1h	ep-1.0em-1.0	0.644995	10000 15504
20613	e1e1h	ep+1.0em-1.0	17.8919	17892 1000.01
20614	e1e1h	ep-1.0em+1.0	11.2894	11289 999.965
20615	e1e1h	ep+1.0em+1.0	0.645477	10000 15492.4
21468	e1e1ss	ep-1.0em-1.0	73.2531	73253 999.999
21469	e1e1ss	ep+1.0em-1.0	123.972	100000 806.634
21470	e1e1ss	ep-1.0em+1.0	85.4529	65600 767.674
21471	e1e1ss	ep+1.0em+1.0	73.152	71752 980.862
21173	e2e2	ep+1.0em-1.0	17077.6	99000 5.79707
21174	e2e2	ep-1.0em+1.0	12859.5	99400 7.72969
21493	e2e2bb	ep+1.0em-1.0	56.5071	56307 996.459
21494	e2e2bb	ep-1.0em+1.0	29.5793	28779 972.944
21485	e2e2dd	ep+1.0em-1.0	57.5377	57538 1000.01
21486	e2e2dd	ep-1.0em+1.0	30.2016	30202 1000.01
21477	e2e2e2e2	ep+1.0em-1.0	11.4311	11431 999.991
21478	e2e2e2e2	ep-1.0em+1.0	7.23464	10000 1382.24
21481	e2e2e3e3	ep+1.0em-1.0	23.1405	23140 999.978
21482	e2e2e3e3	ep-1.0em+1.0	14.6585	14658 999.966
20617	e2e2h	ep+1.0em-1.0	17.126	17126 1000
20618	e2e2h	ep-1.0em+1.0	10.9671	10967 999.991
21489	e2e2ss	ep+1.0em-1.0	57.6073	57607 999.995
21490	e2e2ss	ep-1.0em+1.0	30.1803	29980 993.363
21177	e3e3	ep+1.0em-1.0	17102.4	98800 5.77697
21178	e3e3	ep-1.0em+1.0	12852.9	99800 7.76478
21509	e3e3bb	ep+1.0em-1.0	56.1355	55535 989.303
21510	e3e3bb	ep-1.0em+1.0	29.4194	29219 993.188
21501	e3e3dd	ep+1.0em-1.0	57.2295	56830 993.019
21502	e3e3dd	ep-1.0em+1.0	30.0379	29838 993.345
21497	e3e3e3e3	ep+1.0em-1.0	11.4274	11427 999.965
21498	e3e3e3e3	ep-1.0em+1.0	7.21497	9800 1358.29
20621	e3e3h	ep+1.0em-1.0	17.0988	17099 1000.01
20622	e3e3h	ep-1.0em+1.0	10.9435	10944 1000.05
21505	e3e3ss	ep+1.0em-1.0	57.3548	57155 996.516
21506	e3e3ss	ep-1.0em+1.0	30.0502	30050 999.993
21228	n1e1du	ep-1.0em-1.0	86.3492	86349 999.998
21229	n1e1du	ep+1.0em-1.0	2467.16	100000 40.5324
21230	n1e1du	ep-1.0em+1.0	20.8701	20870 999.995
21216	n1e1e1n1	ep-1.0em-1.0	43.5841	43384 995.409
21217	n1e1e1n1	ep+1.0em-1.0	939.099	98800 105.207
21218	n1e1e1n1	ep-1.0em+1.0	27.4575	26858 978.166
21219	n1e1e1n1	ep+1.0em+1.0	43.6248	43625 1000
21220	n1e1e2n2	ep-1.0em-1.0	28.824	28424 986.123
21221	n1e1e2n2	ep+1.0em-1.0	822.5	98000 119.149
21222	n1e1e2n2	ep-1.0em+1.0	7.09688	10000 1409.07
21224	n1e1e3n3	ep-1.0em-1.0	28.6769	28477 993.029
21225	n1e1e3n3	ep+1.0em-1.0	823.729	97800 118.728
21226	n1e1e3n3	ep-1.0em+1.0	7.10283	10000 1407.89
21232	n1e1sc	ep-1.0em-1.0	86.1229	86123 1000
21233	n1e1sc	ep+1.0em-1.0	2470.34	100000 40.4803
21234	n1e1sc	ep-1.0em+1.0	20.9005	20701 990.455
21125	n1n1a	ep+1.0em-1.0	23969.4	238694 9.95828
21126	n1n1a	ep-1.0em+1.0	2878.85	27788 9.65247
21137	n1n1aa	ep+1.0em-1.0	1582.94	15829 9.99975
21138	n1n1aa	ep-1.0em+1.0	281.145	2811 9.9984
21149	n1n1aaa	ep+1.0em-1.0	69.1909	692 10.0013
21150	n1n1aaa	ep-1.0em+1.0	16.0647	161 10.022
21369	n1n1bb	ep+1.0em-1.0	85.7148	85715 1000
21370	n1n1bb	ep-1.0em+1.0	25.0179	25018 1000
21321	n1n1cc	ep+1.0em-1.0	81.3195	81319 999.994
21322	n1n1cc	ep-1.0em+1.0	24.5259	24526 1000
21361	n1n1dd	ep+1.0em-1.0	87.9093	87909 999.997
21362	n1n1dd	ep-1.0em+1.0	25.5486	25549 1000.02
21353	n1n1e2e2	ep+1.0em-1.0	44.7068	42707 955.269
21354	n1n1e2e2	ep-1.0em+1.0	12.8466	12847 1000.03
21357	n1n1e3e3	ep+1.0em-1.0	44.4167	43417 977.493
21358	n1n1e3e3	ep-1.0em+1.0	12.7892	12789 999.984
20593	n1n1h	ep+1.0em-1.0	60.8309	60831 1000
20594	n1n1h	ep-1.0em+1.0	21.6813	21681 999.986
21365	n1n1ss	ep+1.0em-1.0	87.6368	87637 1000
21366	n1n1ss	ep-1.0em+1.0	25.4646	25465 1000.02
21317	n1n1uu	ep+1.0em-1.0	81.2845	81084 997.533
21318	n1n1uu	ep-1.0em+1.0	24.5303	24330 991.835
21249	n2e2du	ep+1.0em-1.0	2268.24	98600 43.4698
21250	n2e2du	ep-1.0em+1.0	20.8833	19883 952.1
21237	n2e2e1n1	ep+1.0em-1.0	822.267	95800 116.507
21238	n2e2e1n1	ep-1.0em+1.0	7.11354	10000 1405.77
21239	n2e2e1n1	ep+1.0em+1.0	28.8352	28835 999.993
21241	n2e2e2n2	ep+1.0em-1.0	779.633	98800 126.726
21242	n2e2e2n2	ep-1.0em+1.0	19.3972	18197 938.125
21245	n2e2e3n3	ep+1.0em-1.0	755.228	97400 128.968
21246	n2e2e3n3	ep-1.0em+1.0	7.11024	9400 1322.04
21253	n2e2sc	ep+1.0em-1.0	2265.78	97000 42.8109
21254	n2e2sc	ep-1.0em+1.0	20.8933	20493 980.841
21129	n2n2a	ep+1.0em-1.0	4486.97	42870 9.55433
21130	n2n2a	ep-1.0em+1.0	2875.61	28756 9.99996
21141	n2n2aa	ep+1.0em-1.0	439.022	4390 9.9995
21142	n2n2aa	ep-1.0em+1.0	280.164	2802 10.0013
21153	n2n2aaa	ep+1.0em-1.0	25.1552	252 10.0178
21154	n2n2aaa	ep-1.0em+1.0	16.0995	161 10.0003
21389	n2n2bb	ep+1.0em-1.0	59.3921	47792 804.686
21390	n2n2bb	ep-1.0em+1.0	24.9283	24928 999.988
21329	n2n2cc	ep+1.0em-1.0	54.498	54498 1000
21330	n2n2cc	ep-1.0em+1.0	24.5273	24327 991.834
21381	n2n2dd	ep+1.0em-1.0	60.6737	60474 996.709
21382	n2n2dd	ep-1.0em+1.0	25.509	25509 1000
21372	n2n2e1e1	ep+1.0em-1.0	16.1179	15718 975.189
21373	n2n2e1e1	ep+1.0em-1.0	38.3067	37307 973.903
21374	n2n2e1e1	ep-1.0em+1.0	21.4025	21403 1000.02
21375	n2n2e1e1	ep+1.0em+1.0	16.124	16124 1000
21377	n2n2e3e3	ep+1.0em-1.0	24.5789	24579 1000
21378	n2n2e3e3	ep-1.0em+1.0	12.7721	11772 921.697
20597	n2n2h	ep+1.0em-1.0	33.8385	33839 1000.01
20598	n2n2h	ep-1.0em+1.0	21.6474	21647 999.982
21385	n2n2ss	ep+1.0em-1.0	60.5318	56932 940.53
21386	n2n2ss	ep-1.0em+1.0	25.5038	24304 952.956
21325	n2n2uu	ep+1.0em-1.0	54.5125	52513 963.32
21326	n2n2uu	ep-1.0em+1.0	24.5195	24519 999.98
21269	n3e3du	ep+1.0em-1.0	2264.41	99000 43.72
21270	n3e3du	ep-1.0em+1.0	20.8481	20248 971.216
21257	n3e3e1n1	ep+1.0em-1.0	821.691	98000 119.266
21258	n3e3e1n1	ep-1.0em+1.0	7.10352	9600 1351.44
21259	n3e3e1n1	ep+1.0em+1.0	28.6767	28677 1000.01
21261	n3e3e2n2	ep+1.0em-1.0	755.344	99800 132.125
21262	n3e3e2n2	ep-1.0em+1.0	7.10407	10000 1407.64
21265	n3e3e3n3	ep+1.0em-1.0	777.523	99800 128.356
21266	n3e3e3n3	ep-1.0em+1.0	19.3359	19136 989.662
21273	n3e3sc	ep+1.0em-1.0	2267.88	97600 43.0358
21274	n3e3sc	ep-1.0em+1.0	20.906	20906 1000
21133	n3n3a	ep+1.0em-1.0	4488.88	44889 10
21134	n3n3a	ep-1.0em+1.0	2885	28850 10
21145	n3n3aa	ep+1.0em-1.0	440.452	4405 10.0011
21146	n3n3aa	ep-1.0em+1.0	280.722	2807 9.99922
21157	n3n3aaa	ep+1.0em-1.0	25.0412	250 9.98355
21158	n3n3aaa	ep-1.0em+1.0	16.0991	161 10.0006
21409	n3n3bb	ep+1.0em-1.0	59.3812	59381 999.997
21410	n3n3bb	ep-1.0em+1.0	24.936	24936 1000
21337	n3n3cc	ep+1.0em-1.0	54.5355	54335 996.323
21338	n3n3cc	ep-1.0em+1.0	24.532	24132 983.695
21401	n3n3dd	ep+1.0em-1.0	60.5857	60586 1000
21402	n3n3dd	ep-1.0em+1.0	25.5446	25545 1000.02
21392	n3n3e1e1	ep-1.0em-1.0	16.1083	16108 999.981
21393	n3n3e1e1	ep+1.0em-1.0	38.2851	37732 985.553
21394	n3n3e1e1	ep-1.0em+1.0	21.4031	20403 953.273
21395	n3n3e1e1	ep+1.0em+1.0	16.1459	16146 1000.01
21397	n3n3e2e2	ep+1.0em-1.0	24.7238	24324 983.829
21398	n3n3e2e2	ep-1.0em+1.0	12.8475	12847 999.961
20601	n3n3h	ep+1.0em-1.0	33.8138	33814 1000.01
20602	n3n3h	ep-1.0em+1.0	21.6936	21694 1000.02
21405	n3n3ss	ep+1.0em-1.0	60.567	60567 1000
21406	n3n3ss	ep-1.0em+1.0	25.5558	25556 1000.01
21333	n3n3uu	ep+1.0em-1.0	54.5087	54109 992.667
21334	n3n3uu	ep-1.0em+1.0	24.5484	24348 991.836
21185	ss	ep+1.0em-1.0	48249.2	98200 2.03527
21186	ss	ep-1.0em+1.0	28018.8	99400 3.54762
21529	ssbb	ep+1.0em-1.0	137.055	100000 729.634
21530	ssbb	ep-1.0em+1.0	58.9474	58947 999.993
20629	ssh	ep+1.0em-1.0	75.8803	75880 999.996
20630	ssh	ep-1.0em+1.0	48.5657	48566 1000.01
21525	ssss	ep+1.0em-1.0	67.1388	66739 994.045
21526	ssss	ep-1.0em+1.0	28.8318	28832 1000.01
24993	ssssbb	ep+1.0em-1.0	0.001091	10000 9.1659e+06
21289	uddu	ep+1.0em-1.0	6633.45	100000 15.0751
21290	uddu	ep-1.0em+1.0	112.876	99400 880.612
21277	ude1n1	ep+1.0em-1.0	2467.75	98200 39.7933
21278	ude1n1	ep-1.0em+1.0	20.8973	20897 999.986
21279	ude1n1	ep+1.0em+1.0	86.4364	86036 995.368
21281	ude2n2	ep+1.0em-1.0	2268.37	89800 39.5879
21282	ude2n2	ep-1.0em+1.0	20.9171	19717 942.626
21285	ude3n3	ep+1.0em-1.0	2263.51	100000 44.1792
21286	ude3n3	ep-1.0em+1.0	20.8931	20893 999.995
21293	udsc	ep+1.0em-1.0	6522.1	98600 15.1178
21294	udsc	ep-1.0em+1.0	59.9897	59190 986.669
21161	uu	ep+1.0em-1.0	44890.2	89800 2.00044
21162	uu	ep-1.0em+1.0	27372	95400 3.48531
21429	uubb	ep+1.0em-1.0	123.961	99400 801.865
21430	uubb	ep-1.0em+1.0	56.7304	56330 992.942
21345	uucc	ep+1.0em-1.0	109.296	99200 907.627
21346	uucc	ep-1.0em+1.0	52.8917	52892 1000.01
24457	uuccbb	ep+1.0em-1.0	0.006837	10000 1.46263e+06
24458	uuccbb	ep-1.0em+1.0	0.003574	10000 2.79799e+06
21412	uue1e1	ep-1.0em-1.0	448.519	99800 222.51
21413	uue1e1	ep+1.0em-1.0	505.705	100000 197.744
21414	uue1e1	ep-1.0em+1.0	464.733	100000 215.177
21415	uue1e1	ep+1.0em+1.0	449.636	99200 220.623
21417	uue2e2	ep+1.0em-1.0	53.0187	53019 1000.01
21418	uue2e2	ep-1.0em+1.0	29.2736	29274 1000.01
21421	uue3e3	ep+1.0em-1.0	52.7824	52582 996.203
21422	uue3e3	ep-1.0em+1.0	29.0929	27893 958.756
20605	uuh	ep+1.0em-1.0	59.1744	59174 999.993
20606	uuh	ep-1.0em+1.0	37.9259	37926 1000
21425	uuss	ep+1.0em-1.0	120.989	98800 816.603
21426	uuss	ep-1.0em+1.0	55.1501	53950 978.239
24713	uussbb	ep+1.0em-1.0	0.004512	10000 2.21631e+06
24714	uussbb	ep-1.0em+1.0	0.002273	10000 4.39947e+06
21341	uuuu	ep+1.0em-1.0	54.3813	50981 937.473
21342	uuuu	ep-1.0em+1.0	26.3337	26134 992.417
24441	uuuubb	ep+1.0em-1.0	0.003435	10000 2.91121e+06
24442	uuuubb	ep-1.0em+1.0	0.001759	10000 5.68505e+06

B Histograms of cut variables

B.1 $Z \to e^+e^-$ mode

Figures 17 - 28 show the histograms of cut variables. The blue lines in all histograms show the signal process $ZH \to e^+e^-\tau^+\tau^-$.

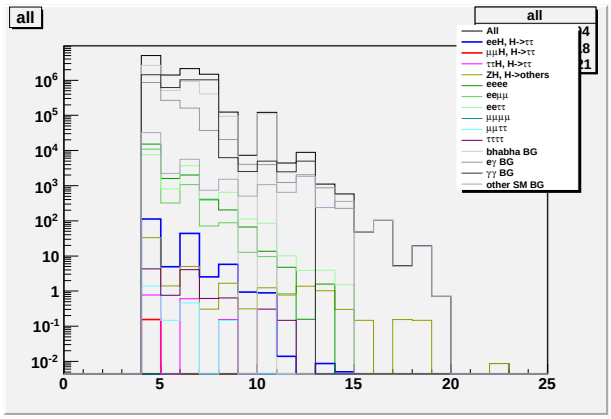

Figure 17: Number of tracks ≤ 8.

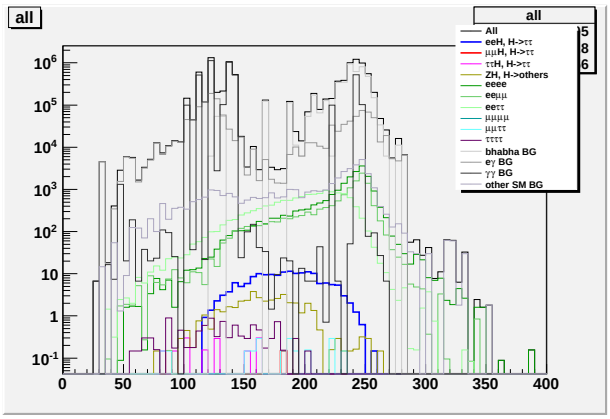

Figure 18: 115 GeV $< E_{\text{vis}} <$ 230 GeV.

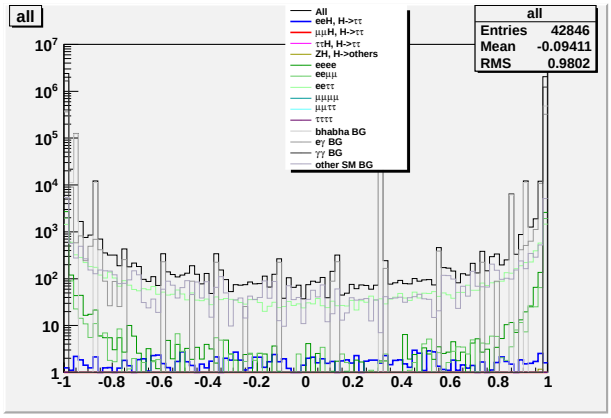

Figure 19: $|\cos\theta_{\text{miss}}| < 0.99$.

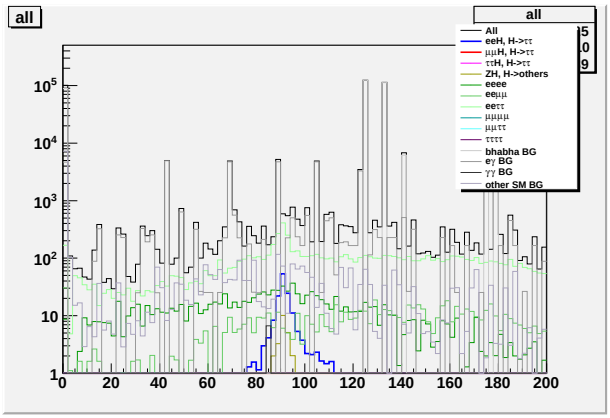

Figure 20: 81 GeV $< M_Z <$ 113 GeV.

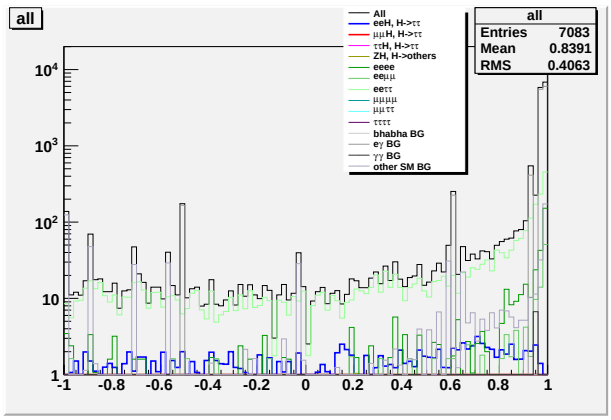

Figure 21: $\cos\theta_{e^-} < 0.92$.

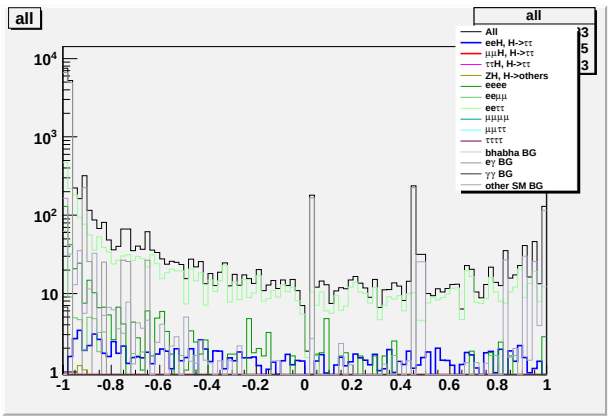

Figure 22: $\cos\theta_{e^+} > -0.92$.

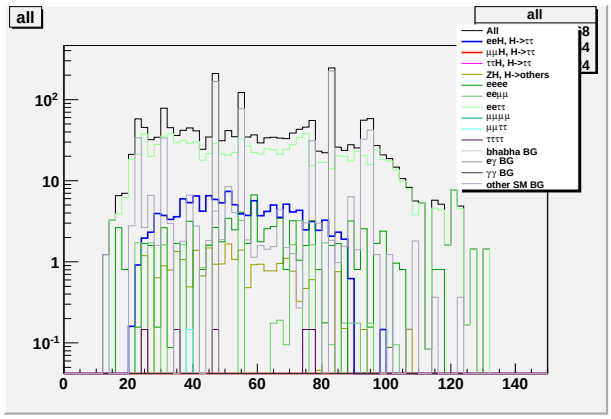

Figure 23: $E_{e^-} < 90$ GeV.

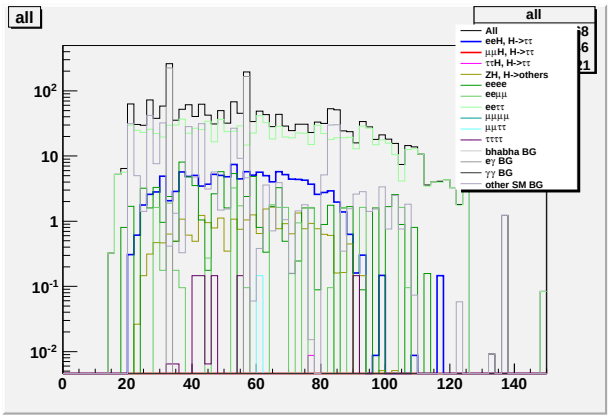

Figure 24: $E_{e^+} < 90$ GeV.

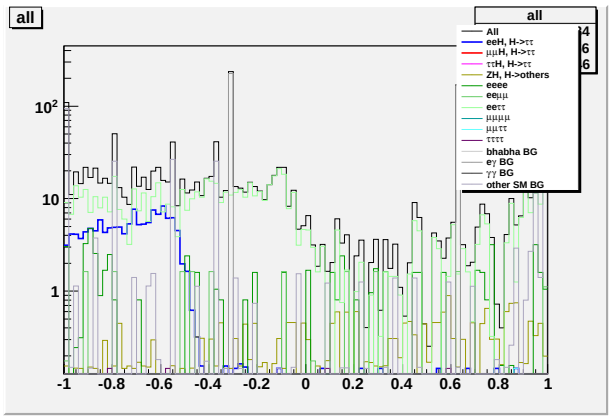

Figure 25: $\cos\theta_{\tau^+\tau^-} < -0.45$.

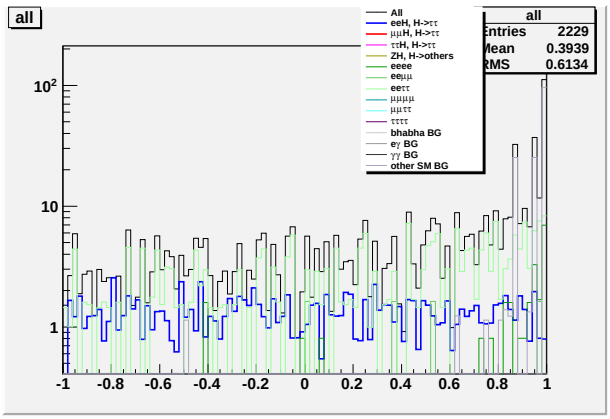

Figure 26: $\cos\theta_{\tau^-} < 0.92$.

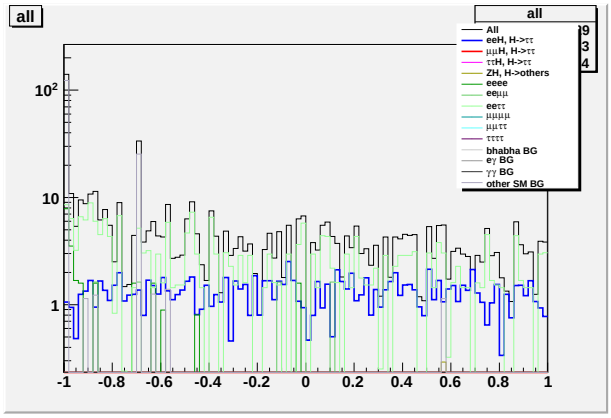

Figure 27: $\cos\theta_{\tau^+} > -0.92$.

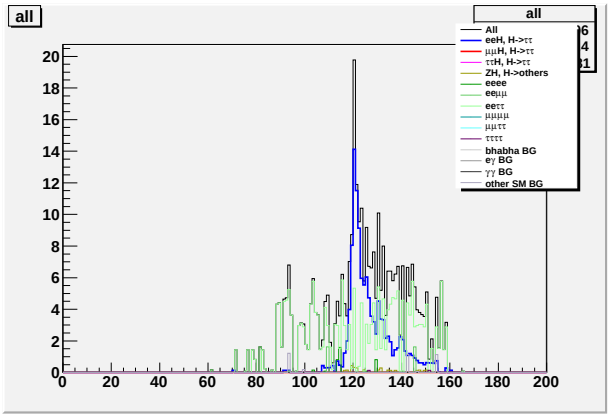

Figure 28: 116 GeV $< M_{\text{recoil}} <$ 142 GeV.

B.2 $Z \to \mu^+\mu^-$ mode

Figures 29 - 36 show the histograms of cut variables. The red lines in all histograms show the signal process $ZH \to \mu^+\mu^-\tau^+\tau^-$.

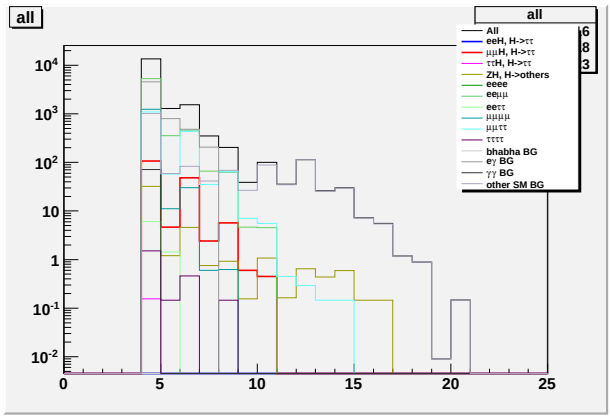

Figure 29: Number of tracks ≤ 8.

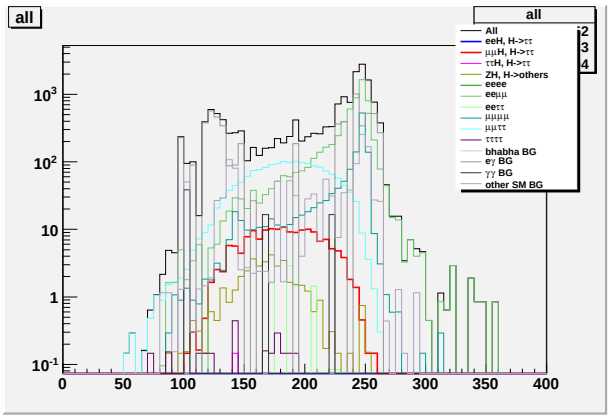

Figure 30: 115 GeV $< E_{\text{vis}} <$ 235 GeV.

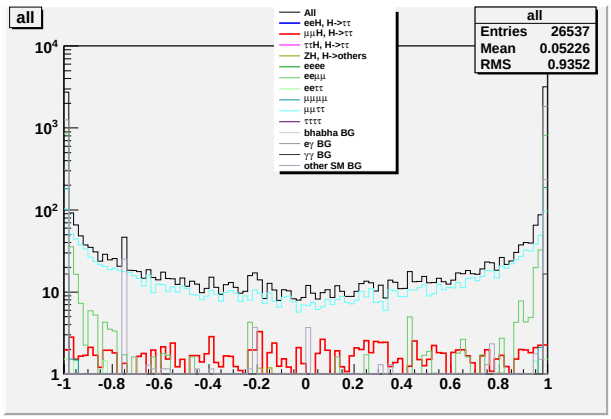

Figure 31: $|\cos\theta_{\text{miss}}| < 0.98$.

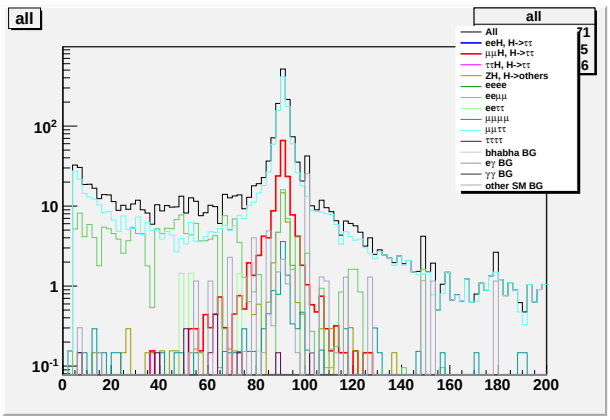

Figure 32: 72 GeV $< M_Z <$ 107 GeV.

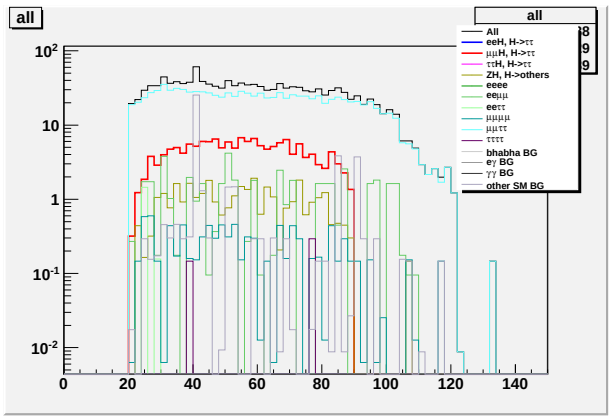

Figure 33: $E_{e^-} < 90$ GeV.

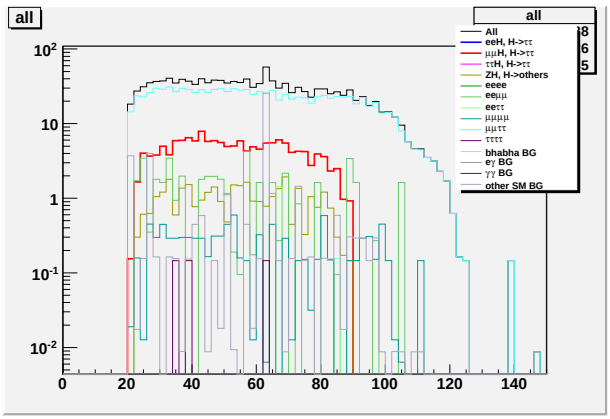

Figure 34: $E_{e^+} < 90$ GeV.

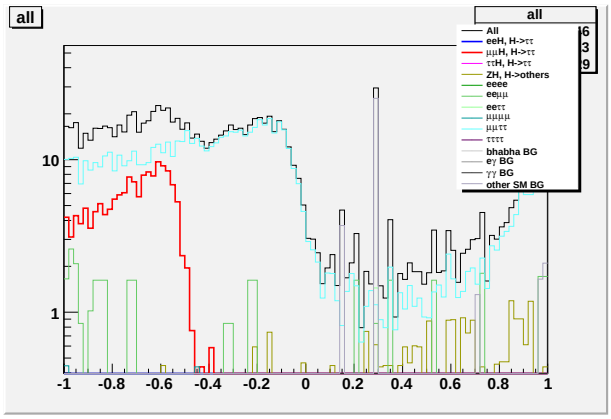

Figure 35: $\cos\theta_{\tau^+\tau^-} < -0.5$.

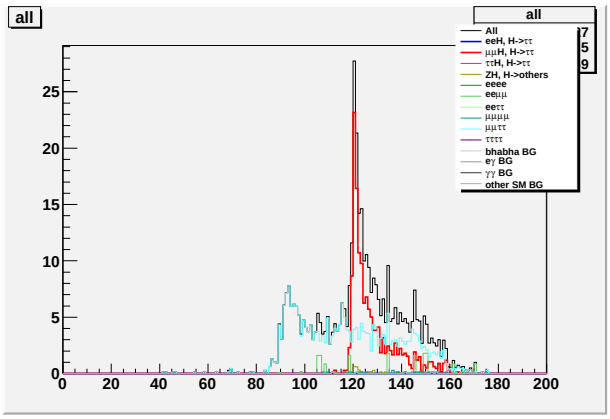

Figure 36: 118 GeV $< M_{\text{recoil}} <$ 143 GeV.

B.3 $Z \to q\bar{q}$ mode

Figures 37 - 49 show the histograms of cut variables. The blue lines in all histograms show the signal process $ZH \to q\bar{q}\tau^+\tau^-$.

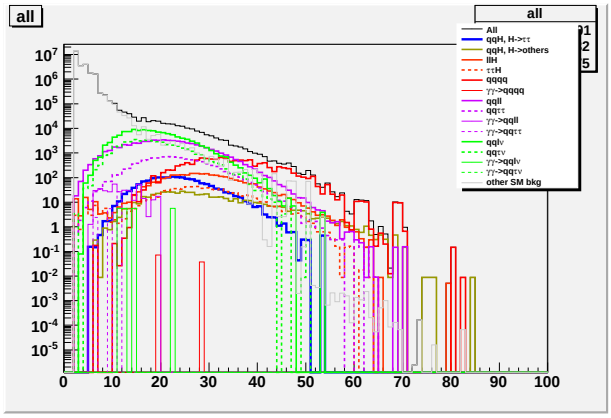

Figure 37: $9 \leq$ number of tracks < 50.

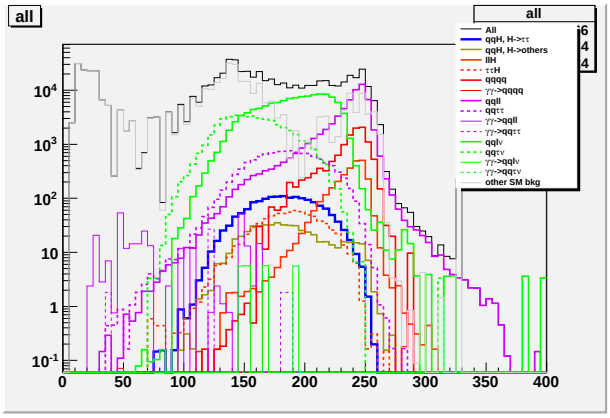

Figure 38: 110 GeV $< E_{\text{vis}} <$ 235 GeV.

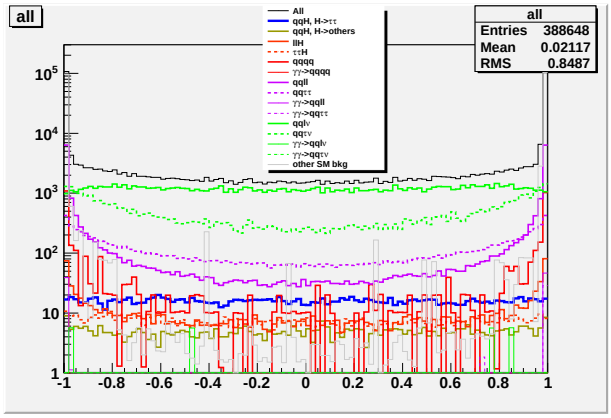

Figure 39: $|\cos\theta_{\text{miss}}| < 0.98$.

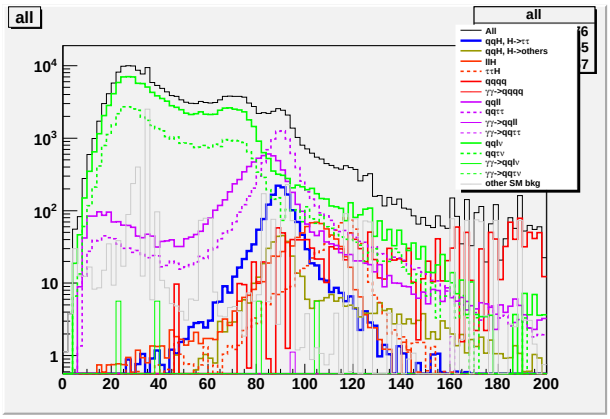

Figure 40: 77 GeV $< M_Z <$ 135 GeV.

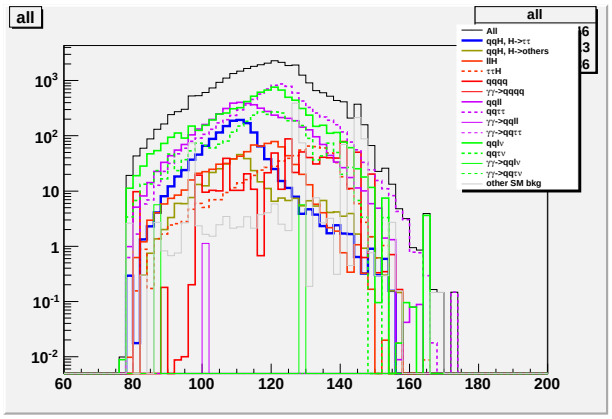

Figure 41: 80 GeV $< E_Z <$ 135 GeV.

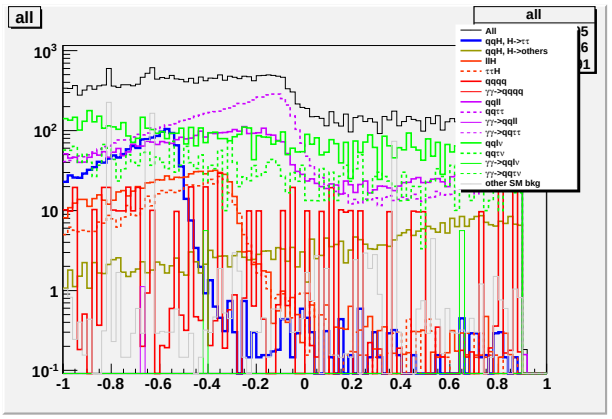

Figure 42: $\cos\theta_{\tau^+\tau^-} < -0.5$.

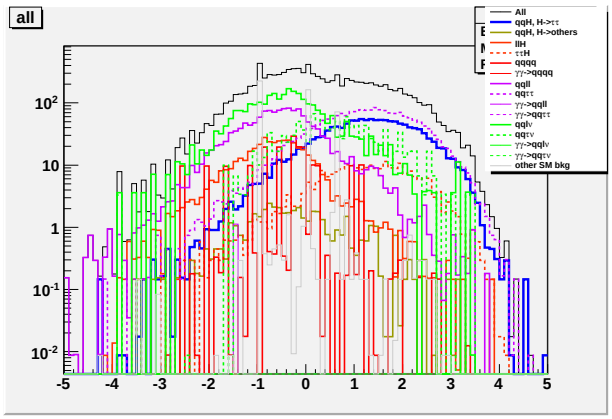

Figure 43: $\log_{10}(|d_0/\sigma(d_0)|)(\tau^-) + \log_{10}(|d_0/\sigma(d_0)|)(\tau^+) > -0.7$.

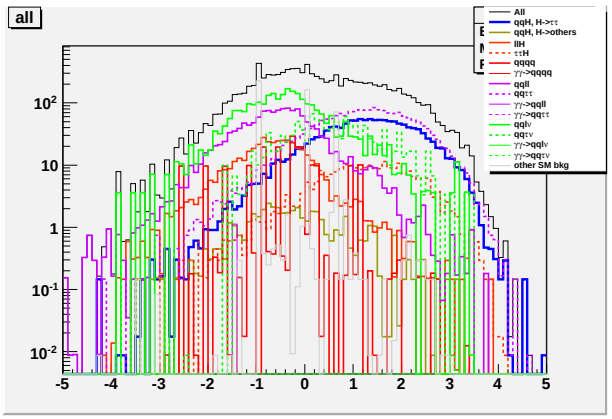

Figure 44: $\log_{10}(|z_0/\sigma(z_0)|)(\tau^-) + \log_{10}(|z_0/\sigma(z_0)|)(\tau^+) > -0.1$.

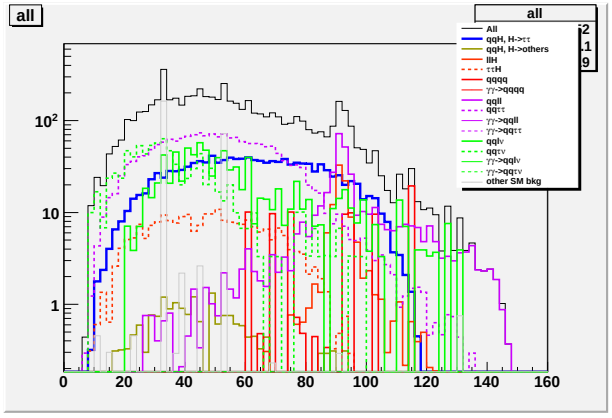

Figure 45: $M_{\tau^+\tau^-} <$ 115 GeV.

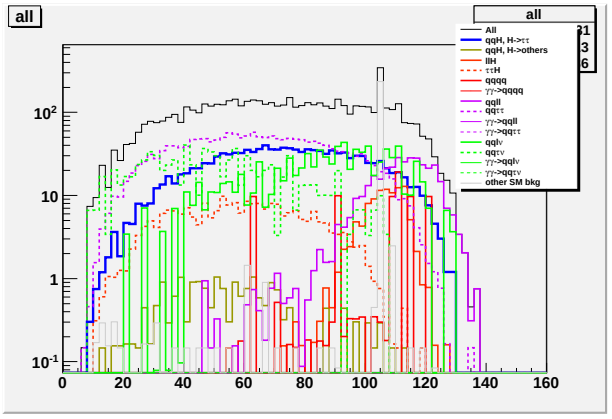

Figure 46: $E_{\tau^+\tau^-} <$ 125 GeV.

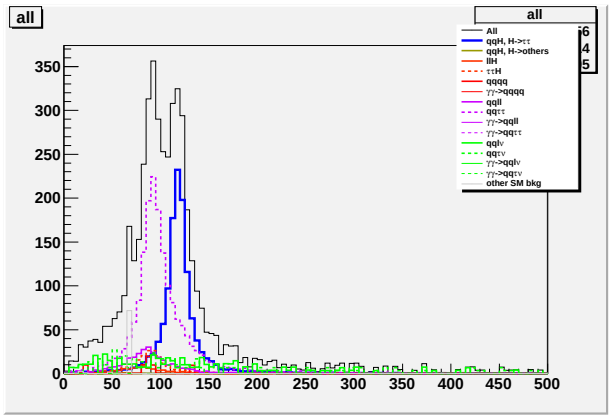

Figure 47: 100 GeV $< M_{\text{colapp}} <$ 170 GeV.

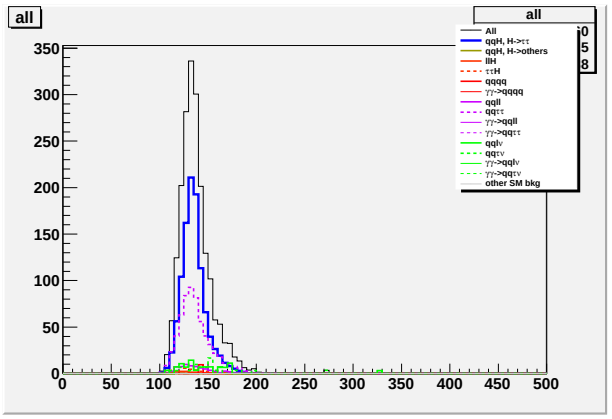

Figure 48: 100 GeV $< E_{\text{colapp}} <$ 280 GeV.

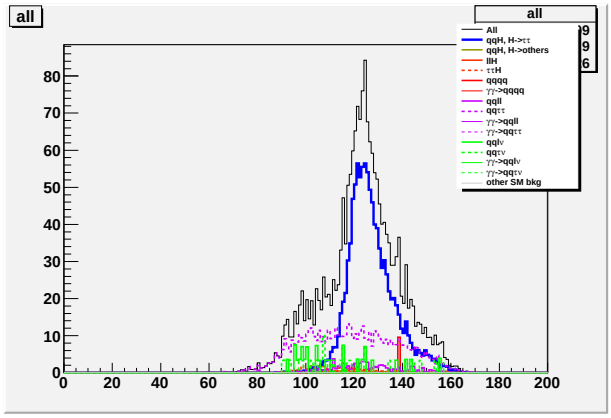

Figure 49: 112 GeV $< M_{\text{recoil}} <$ 160 GeV.

References

[1] The ATLAS Collaboration, "Observation of a new particle in the search for the Standard Model Higgs boson with the ATLAS detector at the LHC", Physics Letters B **716** (2012) 1 - 29

[2] The CMS Collaboration, "Observation of a new boson at a mass of 125 GeV with the CMS experiment at the LHC", Physics Letters B **716** (2012) 30 - 61

[3] P. Mora de Fretias, H. Videau, "Detector simulation with Mokka/Geant4 present and future", LC-TOOL-2003-010 (2003)

[4] `http://geant4.cern.ch/`

[5] S. Jadach, J. H. Kühn, Z. Was, "TAUOLA — a library of Monte Carlo programs to simulate decays of polarized τ leptons", Computer Physics Communications **64** (1991) 275 - 299

[6] The ILD concept group, "International Large Detector — Letter of Intent" (2010)

[7] `http://ilcsoft.desy.de/portal`

[8] T. Sjöstrand, S. Mrenna, P. Skands, "PYTHIA 6.4 physics and manual", Journal of High Energy Phyiscs 0605, 026 (2006)

[9] LHC Higgs Cross Section Working Group, "Handbook of LHC Higgs Cross Sections: 2. Differential Distributions", arXiv:1201.3084v1 [hep-ph]

[10] R. K. Ellis, I. Hinchliffe, M. Soldate, J. J. van der bij, "Higgs decay to $\tau^+\tau^-$ A possible signature of intermediate mass Higgs bosons at high energy hadron colliders", Nuclear Physics B **297** (1988) 221 - 243

[11] S. Catani, Y. L. Dokshitzer, M. Olsson, G. Turnock, B. R. Webber, "New clustering algorithm for multijet cross sections in e^+e^- annihilation", Physics Letters B **269** (1991) 432 - 438

Study of $H \to \mu^+\mu^-$ at $\sqrt{s} = 1$ TeV at the ILC

Constantino Calancha

High Energy Accelerator Research Organization (KEK), Tsukuba, Japan

calancha@post.kek.jp

April 19, 2013

Abstract

The statistical uncertainty of $\sigma(\nu_e\bar{\nu_e}\mathrm{H}) \cdot Br(\mathrm{H} \to \mu^+\mu^-)$ for a 125 GeV/c^2 Standard Model Higgs boson is evaluated, in the context of the 1 TeV ILC [1] e^+e^- linear collider with beam state polarisation (P_{e^-}, P_{e^+})=(-0.8,+0.2), and a total integrated luminosity of 500 fb^{-1}. The study is performed in the ILD [2] detector concept using full simulation. All relevant Standard Model backgrounds are taken into account. The effect of the underlying $\gamma\gamma \to$ hadrons is taken into account by overlaying realistic amounts of $\gamma\gamma \to$ hadrons onto both signal and background events. The cross section times the branching ratio can be measured with a statistical accuracy of 44 ± 3 %.

Contents

1 Introduction

Figure 1: Higgs couplings to SM particles as a function of their masses (left) Higgs branching ratios as a function of the Higgs mass (right).

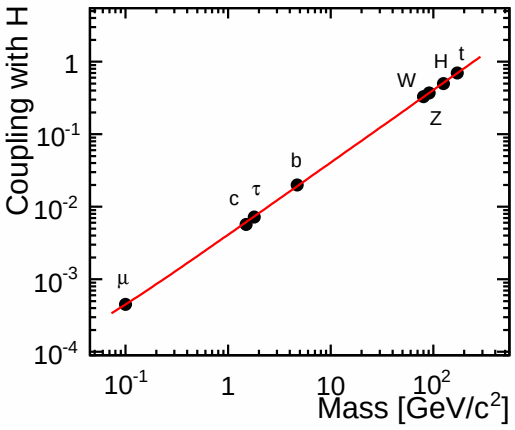

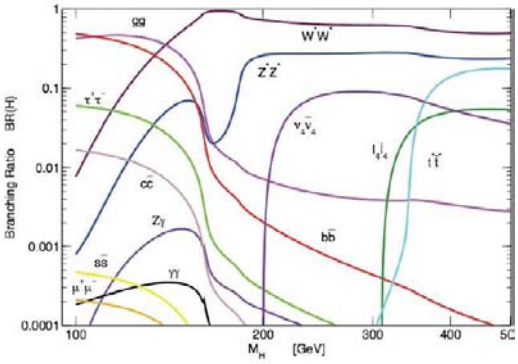

The SM predicts a linear relation between Higgs couplings to SM particles and their masses (Fig. 1). A deviation from this prediction would be a strong indication of new physics. The precise measurement of those couplings is one of the main goals of the ILC physics program.

The recent discovery at ILC of a higgs-like boson with a mass $\sim$ 125 GeV/c^2 makes possible to study many branching ratios of the decay of this boson at the ILC (Fig. 1).

In this note we study $\nu_e\bar{\nu_e}$H, H $\rightarrow \mu^+\mu^-$ at 1 TeV and beam state polarisation (P_{e^-}, P_{e^+})=(-0.8,+0.2), and we determine the expected statistical uncertainty for $\sigma(\nu_e\bar{\nu_e}\mathrm{H}) \cdot Br(\mathrm{H} \rightarrow \mu^+\mu^-)$.

The measurement $\nu_e\bar{\nu_e}$H, H $\rightarrow \mu^+\mu^-$ is quite challenging due to the very low branching ratio Br(H $\rightarrow \mu^+\mu^-$), only 0.02% for a Higgs boson mass of 125 GeV/c^2. After recording 500 fb^{-1} of data with beam polarization state (P_{e^-}, P_{e^+})=(-0.8,+0.2) we expect only 45 $\nu_e\bar{\nu_e}$H, H $\rightarrow \mu^+\mu^-$ events. For the right-handed beam polarisation state (P_{e^-}, P_{e^+})=(+0.8,-0.2) we expect less than 4 events.

2 Software

The event samples used in this analysis were created in the context of the ILD DBD mass production. The event generation is performed using `WHIZARD` [3] v1.95. The fragmentation is taken by `PYTHIA` [4]. The decays of τ leptons are handled by `TAUOLA` [5]. The simulation of the ILD detector is carry out with `GEANT4` [6]. Since the events are generated as head-on collisions in `WHIZARD`, the crossing angle of 7 mrad is taken into account in the simulation step by boosting all particles accordingly. The event reconstruction is perform inside `ILCSOFT` [7] v01-16 framework. The analysis is done using `ROOT` [8] v5.32.00 and the `TMVA` [9] and `RooFit` [10] v3.50 software packages.

3 Event Samples

This section introduces the different samples used in the analysis. Table 1 lists the cross sections and the generated luminosity for all processes. Samples ea_ell, ae_ell, aa_4f and 5f were generated with fast

simulation [11]. All the other samples were fully simulated. In Appendix A it is described the actual final state for every considered process.

Processes	σ [fb]	L[ab^{-1}]
Full Simulation		
hmumu (signal)	0.089	64.8
4f_sznu_l	254.9	0.99996
4f_zzorww_l	190.9	0.99999
4f_sze_l	8534	0.04762
4f_ww_l	184.7	0.99999
2f_z_l	929.6	0.65653
2f_z_h	5270.8	0.02317
2f_z_bhabhag	1580.1	0.02112
4f_ww_h	1812.0	0.02320
4f_ww_sl	2223.5	0.23174
4f_zzorww_h	1510.7	0.02320
4f_zz_h	167.4	0.02320
4f_zz_l	13.3	0.98921
4f_zz_sl	142.38	0.02311
4f_sw_l	1838.5	0.02242
4f_sw_sl	5503.9	0.22426
4f_sze_sl	2464.3	0.02061
4f_sznu_sl	1237.5	0.02320
4f_szorsw_l	950.4	0.02233
6f_ttbar	449	0.75790
Fast Simulation		
ea_ell	105041.2	0.10000
ae_ell	104896.4	0.99999
aa_4f	132.9	1.00000
5f	51.78	1.00001

Table 1: Summary of event generation samples. The quoted cross sections and integrated luminosity are referred to the beam polarisation state: (P_{e^-},P_{e^+})=(-0.8,$+0.2$), at sqrt(s)=1 TeV. The list of SM process with 4 fermions in the final state is exhaustive.

3.1 Signal Sample

The signal events used in this analysis have been created by generating events with a final state of $\nu_e\bar{\nu_e}H$ using `WHIZARD`. The decay of the higgs boson in `PYTHIA` was forced into two muons. The width of a 125 GeV/c^2 Standard Model Higgs is negligible compared with the invariant mass resolution of the detector. The topology of the event comprises two muons and missing energy. Figure 2 shows the Feynman diagrams to $e^+e^- \to \nu_e\bar{\nu_e}$H , H $\to \mu^+\mu^-$ in the ILC. In this analysis the contribution from Higgsstrahlung is negligible compared with WW-fusion.

3.2 Main Backgrounds

The main background comes for those processes with final state $\nu\bar{\nu}\mu^+\mu^-$, where the pair of muons are not from a Higgs decay. The initial state could be e^+e^- or $\gamma\gamma$. The ratio of the production cross

Figure 2: Feynman diagrams for signal: Higgsstrahlung (left) and WW-fusion (right). The WW-fusion is the dominant process at 1 TeV and (P_{e^-}, P_{e^+})=(-0.8,+0.2). In this analysis, the contribution from Higgsstrahlung process is negligible compared with WW-fusion.

sections between these backgrounds and signal exceed 10^3. Table 1 list all the cross sections for those backgrounds.

4 Event Selection

The event selection is done in two steps. First, preselection of the events with two large energy muons in the final state, with invariant mass around to the Higgs mass peak. The final selection cuts are obtained by means an optimization process.

4.1 Preselection

Only events with two reconstructed muons with $E > 15$ GeV are used. The identification of the muons is based on the deposited energy over the calorimeters. Objects not being produced in the primary vertex. are rejected with the requirement $|d_0/\Delta d_0| < 5$.

The missing energy of the event $\not{E}$ is defined as the center-of-mass energy less the total observed energy. A minimum value of $\not{E}$>300 GeV is required to accept the event. The hadronic/semileptonic modes are rejected requiring less than 4 charged PFO's with energy higher than 15 GeV , and less than 3 leptons with $E > 15$ GeV. Table 2 shows the preselection cuts. No isolation requirement is made. The signal efficiency after these preselection requirements is 85 %.

Muons
charged PFO
$E > 15$ GeV
$E_{calE}/(E_{calE} + E_{calH}) < 0.5$
$(E_{calE} + E_{calH})/\lvert\vec{P}\rvert < 0.3$
$\lvert d_0/\Delta d_0\rvert < 5$
Dimuon system
Opposite sign charges
$E_{muon1} + E_{muon2} < 400$ GeV
$\lvert M(\mu^+, \mu^-) - 125\rvert < 30$ GeV/c^2
$\not{E} > 300$ GeV
charged PFO's with $E > 15$ GeV< 4
charged leptons with $E > 15$ GeV< 3

Table 2: Preselection cuts: E_{calE} (E_{calH}) is the deposited energy on the electromagnetic (hadronic) calorimeter by the muon, P is the momentum of the muon and d_0 its impact parameter. The cut on the maximum energy of the dimuon system select one of the process (WW-fusion) in Fig. 2.

4.2 Optimization

A cut based selection is performed using the following variables: $\not\!\!E_T, \not\!\!E$, $\mathrm{P_T}(\mu^+)$+$\mathrm{P_T}(\mu^-)$, $\mathrm{P_T}(\mu^+,\mu^-)$, $cos(\mu^+,\mu^-)$. Optimization of the final cuts is performed using as score function the significance defined by:

$$\frac{S}{\sqrt{S+B}} \tag{1}$$

where S is the number of signal events passing selection on every scan with dimuon invariant mass inside $(124, 126)$ GeV/c^2; B is the number of background events inside sidebands (normalized to the signal window size). The sidebands are defined as: $(115, 120)$ and $(130, 135)$.

- Variables are scanned until we rise a **stable point**.
  - $\mathrm{var}_1 \rightarrow \mathrm{var}_2 \rightarrow \mathrm{var}_{N-1} \rightarrow \mathrm{var}_1$
  - If the var_i best value changes we scan var_1 again.
  - If no variables change in a full cycle ($\mathrm{var}_1 \rightarrow \mathrm{var}_1$): we found a stable point.
- A new variable is added var_N and we scan it.
- New cycle of scans to find a new stable point: $\mathrm{var}_1 \rightarrow \mathrm{var}_2 \rightarrow \mathrm{var}_N \rightarrow \mathrm{var}_1$

The performed scans are included in Appendix C. After the last scan the significance (Eq. 1) reaches ≈ 2.3.

Table 3 summarizes the optimization results. A requirement on the maximum energy deposited on the forward calorimeters is added to supress background contributions as $\gamma e^{\pm} \rightarrow ell\nu\nu$, $\gamma\gamma \rightarrow ll\nu\nu$. Figure 3 shows the dimuon invariant mass distribution before and after optimization.

Table 3: Result of the optimization.

$\not\!\!E_T$> 40 GeV
$\not\!\!E$> 550 GeV
$\mathrm{P_T}(\mu^+)$+$\mathrm{P_T}(\mu^-)$> 130 GeV/c
$cos(\mu^+,\mu^-) > -0.45$
BCal < 70 GeV

5 Branching Ratio Precision

In Section 4.2 it is shown that a statistical significance around $\sigma \approx 2.3$ is reached after the optimization process. This correspond with a statistical precision $\frac{\Delta(\sigma \cdot Br)}{\sigma \cdot Br} = \frac{1}{\sigma} \approx 43$ %; similar value can be obtained from the data after applying the final selection: defining a signal mass window (124, 126) GeV/c^2 the signal (background) contribution inside this window is $S = 14.95$ ($B = 21.96$), thereby we estimate the precision to be $\sqrt{S+B}/S \approx 41$ %.

This value is sensitive to fluctuations in the number of events; signal sample was obtained from high statistics Monte Carlo samples, but the simulated statistics for the background is lower.

Figure 3: Dimuon Invariant Mass after preselection (left) and after optimization (right).

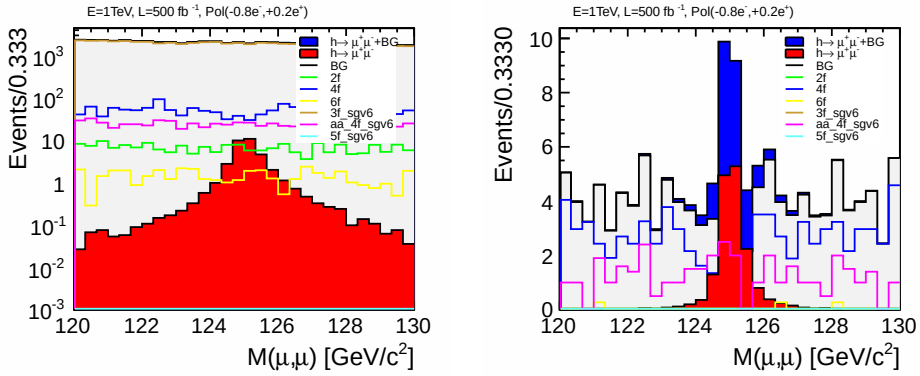

5.1 Pseudoexperiments

The background after optimization is flat (Fig. 3 with a value ≈ 4. A number of 10^5 independent background toy-samples were randomly generated using the background from data as template. For every sample, the value B of events inside (124, 126) GeV/c^2 is extracted and use to fill the distribution $\sqrt{S+B}/S$ [1].

Figure 4 shows the distribution $\sqrt{S+B}/S$ over all these pseudoexperiments with S (B) the number of signal (background) events within the mass window (124, 126) GeV/c^2 . A gaussian fit return the values: mean $= 0.44$, $\sigma = 0.015$.

Figure 4: Distribution $\sqrt{S+B}/S$ over all the pseudoexperiments; S (B) are the signal (background) events passing selection with invariant dimuon mass inside (124, 126) GeV/c^2.

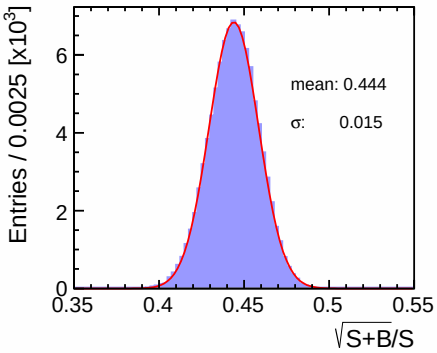

6 Results

In Section 4.2 the statistical significance for $\sigma \cdot Br$ is estimated as $41 - 43$ %. This value is obtained directly from the data samples after the final selection, and it is sensitive to fluctuations in the observed number of events.

[1] The number of signal events, S, is the one observed on the data sample

In Sec. 5 an alternative toy Monte Carlo based approach is followed: many independent background samples are randomly generated from the background shape observed in the data. The number of signal events on the data, S, and the number of background events on every of the toy samples, B, both inside a mass window (124, 126)GeV/c^2 are used to fill the distriution $\sqrt{S+B}/S$ (4). The expected statistical precision for $\sigma \cdot Br$ is estimated as $\pm 2\sigma$ of the peak value of that distribution, thereby, $\frac{\Delta(\sigma \cdot Br)}{\sigma \cdot Br} = 44 \pm 3$ %.

7 Conclusion

The statistical uncertainty for a measurement of the cross section times branching ratio of a light Standard Model Higgs boson, with a mass of 125 GeV/c^2 decaying into two muons has been evaluated. At the ILD, with a center-of-mass energy of 1 TeV , beam polarisation state (P_{e^-}, P_{e^+})=(-0.8,+0.2), and total integrated luminosity of 500 fb^{-1}, $\frac{\Delta(\sigma \cdot Br)}{\sigma \cdot Br} \sim 44 \pm 3$ %.

A Samples Description

This appendix list the final state of the samples used in this analysis.

In the final states of the 6f_ttbar samples:

- e refers to an electron-positron and l other charged lepton.
- v refers to one neutrino.
- x is up-type quark and y is down-type quark (Some channels have one or more final quarks given explicitly).
- ae_ell, ea_ell, aa_4f and 5f samples were generated with fast simulation.
- All other samples were fully simulated.

Full detail about all these samples can be found in [12].

Label	Process
hmumu	$e^-e^+ \to \nu_e\bar{\nu_e}\mathrm{H}, \mathrm{H} \to \mu^+\mu^-$, (signal)
4f_sznu_l	$e^-e^+ \to \nu_e\bar{\nu_e}\, l^+l^-;\quad l = \mu, \tau$
4f_zzorww_l	$e^-e^+ \to \nu_l\bar{\nu_l}\, l^+l^-;\quad l = \mu, \tau$
4f_sze_l	$e^-e^+ \to e^+e^-l^+l^-$, $e^-e^+ \to \nu_i\bar{\nu_i}e^+e^-;\quad i = \mu, \tau;\, l = e, \mu, \tau$
4f_sw_l	$e^-e^+ \to \nu_\tau\tau^+\bar{\nu_e}e^-$
4f_zz_l	$e^-e^+ \to l^-l^-l^+l^+, \nu_i\bar{\nu_i}l^-l^+;\, i, l = \mu, \tau$
4f_ww_l	$e^-e^+ \to \nu_\mu\mu^+\bar{\nu_\tau}\tau^-$
4f_szorsw_l	$e^-e^+ \to \nu_e e^-e^+\bar{\nu_e}$
2f_z_l	$e^-e^+ \to l^+l^-;\quad l = \mu, \tau$
2f_z_h	$e^-e^+ \to q\bar{q};\quad q = u, d, s, c, b$
2f_z_bhabhag	$e^-e^+ \to e^+e^-\gamma$
ww_h	$e^-e^+ \to q_1q_2\bar{q_2}\bar{q_1};\, q_1 = u, c;\, q_2 = d, s$
4f_zz_h	$e^-e^+ \to q_1\bar{q_1}q_2\bar{q_2}, q_1\bar{q_1}q_2\bar{q_3};\, q_1 = u, c; q_2, q_3 = d, b$ $e^-e^+ \to q_1q_1\bar{q_1}\bar{q_1}, q_1q_2\bar{q_1}\bar{q_2}\; q_1 = d, s, b; q_2 = d, s, b$ $e^-e^+ \to q_1q_1\bar{q_1}\bar{q_1}, q_1q_2\bar{q_1}\bar{q_2}\; q_1 = u, c; q_2 = u, c$ $e^-e^+ \to q_1\bar{q_1}q_2\bar{q_2}, q_1\bar{q_1}q_2\bar{q_3};\, q_1 = u; q_2, q_3 = s, b$
4f_ww_sl	$e^-e^+ \to q_1\bar{q_2}l^-\bar{\nu_l};\, q_1 = u, cq_2 = d, b, s; l = \mu, \tau$
4f_zz_sl	$e^-e^+ \to \mu^-\mu^+q_1\bar{q_1}, q_2\bar{q_2}\mu^-\mu^,\nu_l\bar{\nu_l}q_1\bar{q_1},;\, q_1 = u, c; q_2 = d, s, b; l = \mu, \tau$ $e^-e^+ \to \nu_l\bar{\nu_l}q_2\bar{q_2}, q_2\bar{q_2}\tau^-\tau^+;\, q_2 = d, s, b; l = \mu, \tau$
4f_sw_sl	$e^-e^+ \to q_1\bar{q2}e^-\nu_e;\, q_1 = u, c;\, q_2 = d, s, b$
4f_sznu_sl	$e^-e^+ \to \nu_e\bar{\nu_e}q_1\bar{q_1}, \nu_e\bar{\nu_e}q_1\bar{q_2};\, q_1, q_2 = b, s, c, d, u(Q(q_1) = Q(q_2))$
4f_sze_sl	$e^-e^+ \to {}^-e_1^q\bar{q_1}, q_1\bar{q_1}e^-e^;\, q_1 = u, c$
6f_ttbar	yyveev yyvelv yyveyx yyvlev yyvllv yyvlyx yyxyev yyxylv yyuyyu yyuyyc yycyyu yycyyc
ea_ell	$e^-\gamma \to e^+\, l^+l^-$, $l = \mu, \tau$
ae_ell	$\gamma e^+ \to e^+\, l^+l^-$, $l = \mu, \tau$
aa_4f	$\gamma\gamma \to \nu_e\bar{\nu_e}\, l^+l^-;\quad l = \mu, \tau$
5f	$e^+l^+l^-\nu_i\bar{\nu_i};\, l = \mu, \tau; i = e, \mu, \tau$ $e^+l_1^+l_2^-\nu_i\bar{\nu_i};\, l_1, l_2 = \mu, \tau; i = e, \mu, \tau$

B Event Distributions

This appendix contains the event distributions after preselection.

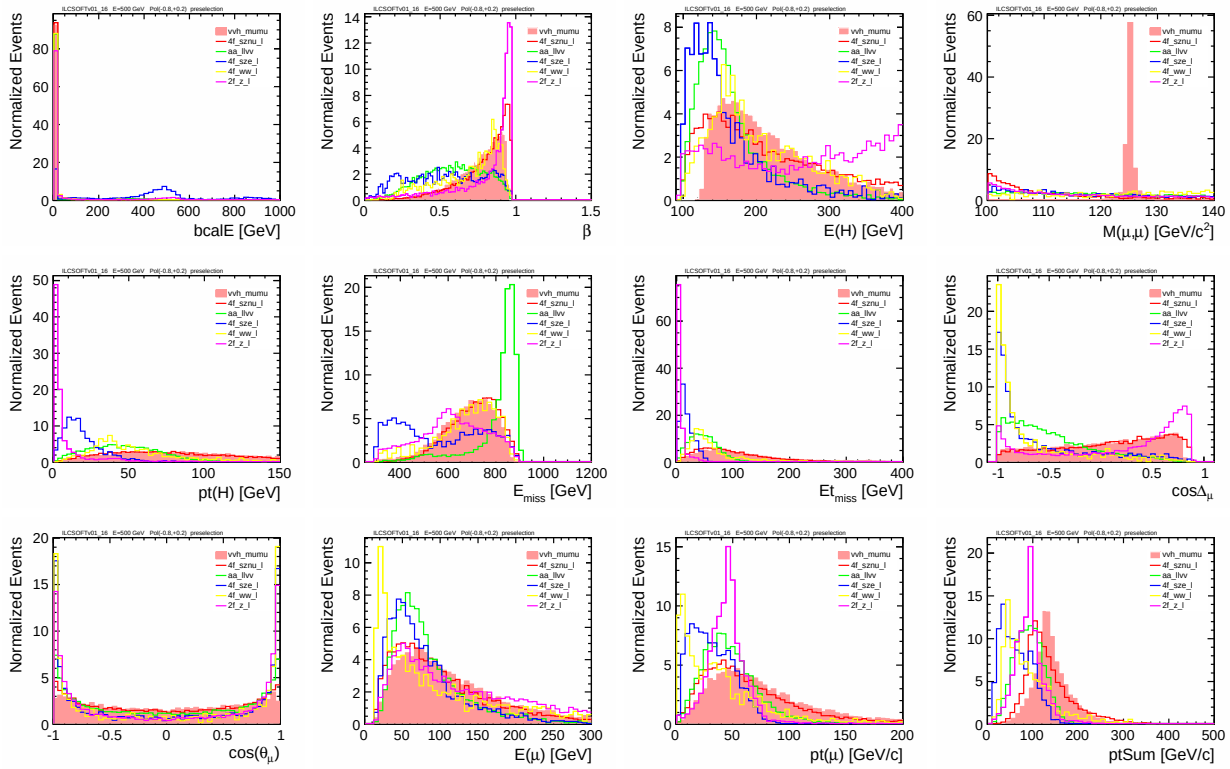

C Optimization Scans

This appendix contains the steps in the optimization process.

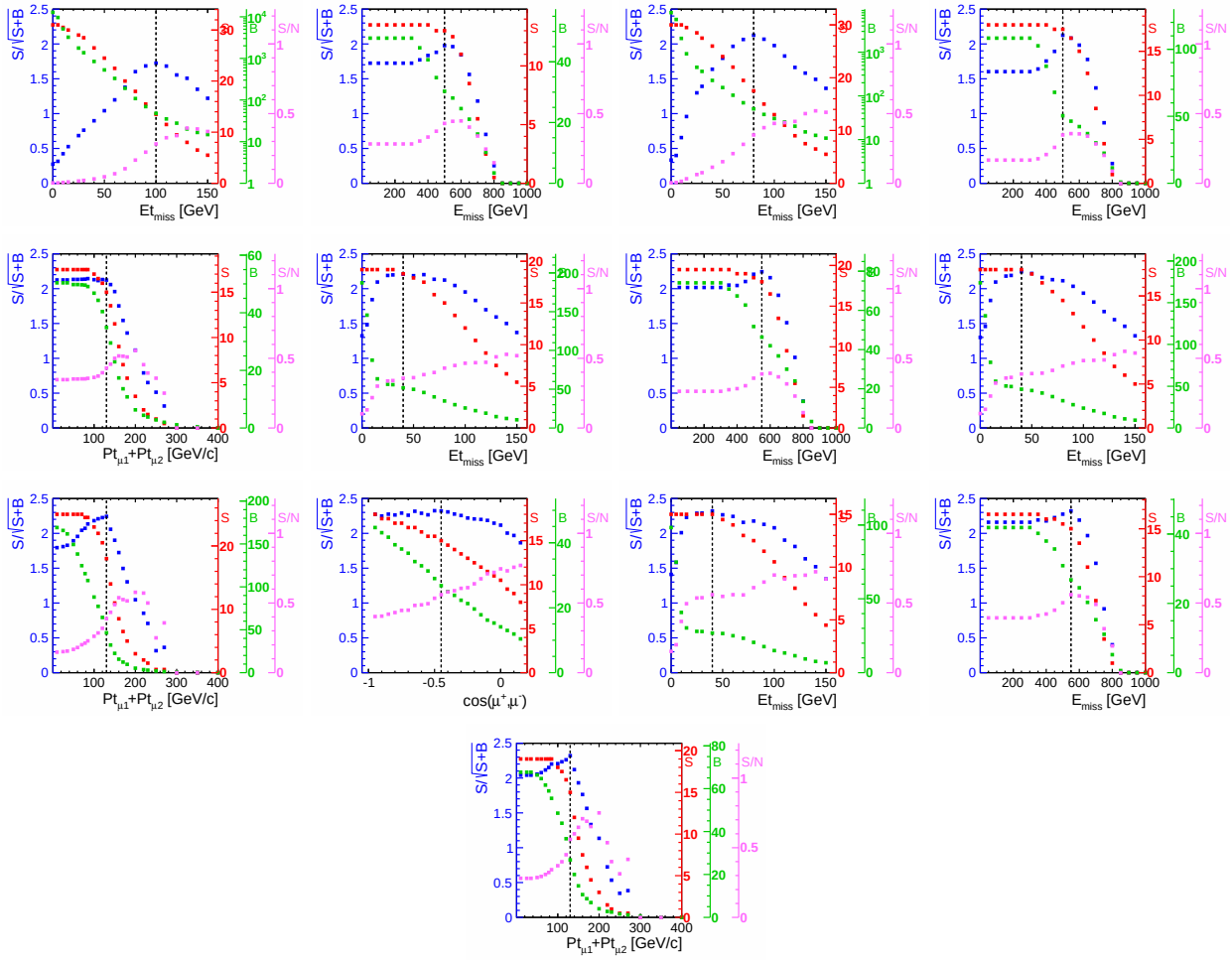

D Event Distributions After Optimization

This appendix contains the event distributions after optimization.

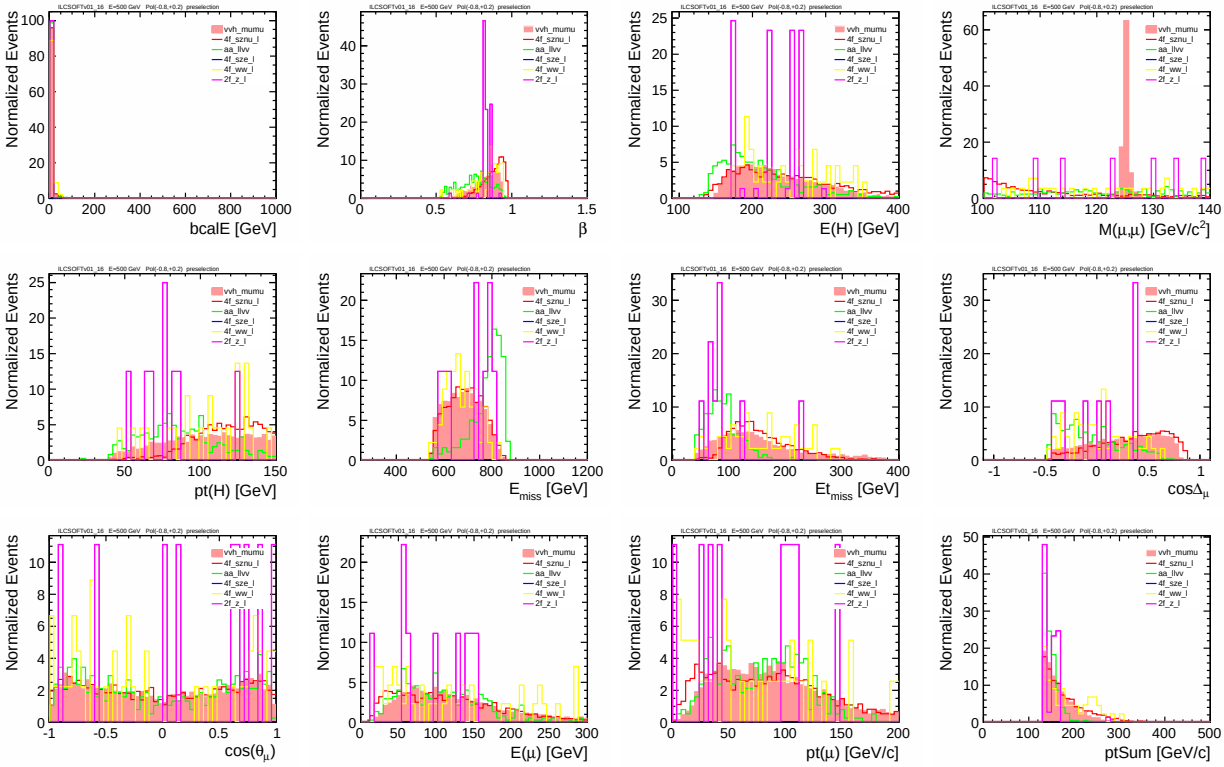

E Cut Flow Table

This appendix contains the analysis cut table. The quoted number of events referes to the **Monte Carlo statistics** (no applied weights); it includes all the beam polarisation states contribuing to the current process. The efficiency for every process can not be obtained just as the ratio of two columns. In order to obtain the efficiency it is necessary separate all the pure polarisation states taking in account their different cross sections. Thereby, the efficiency is defined as:

$$\frac{N_{obs}}{N_{exp}}$$

with N_{obs} (N_{exp}) the total number of observed (expected) events under the experimental conditions, that is, $L = 500$ fb^{-1}and beam state polarisation (P_{e^-}, P_{e^+})=(-0.8,+0.2). The efficiency is included in the last column.

Sample/Cut	generated	preselection	missEt	missE	ptSum	cosD	bcalE	effi
vvh_mumu	19800	10839	9553	8290	5948	5122	4943	.318356
4f_sznu_l	477413	11004	9163	8335	4171	3795	3734	.039122
4f_sze_l	1611426	2309	152	7	1	0	0	0
2f_z_h	338147	5	0	0	0	0	0	0
2f_z_l	2106528	9946	241	132	28	9	9	.000003
4f_sw_l	87453	11	10	7	1	1	1	.000002
4f_sw_sl	2611402	6	3	3	0	0	0	0
4f_ww_h	78039	5	0	0	0	0	0	0
4f_ww_l	343337	1048	680	540	134	46	45	.000632
4f_ww_sl	957247	970	410	40	3	1	1	.000001
4f_zz_h	9671	1	0	0	0	0	0	0
4f_zz_l	37386	352	169	112	42	37	33	.000007
4f_zzorww_h	65524	4	0	0	0	0	0	0
4f_zzorww_l	360269	2685	1776	1499	703	285	253	.001985
4f_zz_sl	8316	16	1	0	0	0	0	0
yycyyc	329537	2	1	0	0	0	0	0
yycyyu	137616	3	0	0	0	0	0	0
yyuyyc	138426	3	1	0	0	0	0	0
yyuyyu	139987	1	0	0	0	0	0	0
yyvelv	42873	30	22	7	1	0	0	0
yyveyx	140251	2	2	0	0	0	0	0
yyvlev	42869	4	4	1	0	0	0	0
yyvllv	53867	664	569	193	69	27	26	.001111
yyvlyx	193651	292	220	6	1	1	1	.000042
yyxyev	170823	3	2	0	0	0	0	0
yyxylv	193929	272	214	12	2	0	0	0
ae_ell	10489608.00	67767	3797	134	5	4	2	0
ea_ell	10504152.00	68295	3929	140	4	1	1	.000015
aa_4f	132939	7531	4513	4213	762	410	357	.000751
ae_ellvv	10356.60	450	289	197	37	25	11	0
ea_ellvv	15526.80	466	299	208	41	28	16	.001544

References

[1] ILC Project, A. Djouadi et al., eds., "International Linear Collider Reference Design Report Volume 2: Physics at the ILC." 2007. arXiv:0709.1893 [hep-ph]. ILC-REPORT-2007-001.

[2] "The International Large Detector: Letter of Intent." arXiv:1006.3396 [hep-ex].

[3] W. Kilian, T. Ohl, and J. Reuter. "WHIZARD: Simulating multi-particle processes at LHC and ILC." 2007. arXiv:0708.4233v1 .

[4] T. Sjostrand, S. Mrenna, and P. Z. Skands. "PYTHIA 6.4 Physics and Manual." *JHEP*, vol. 05 p. 026, 2006. hep-ph/0603175.

[5] Z. Was. "TAUOLA the library for tau lepton decay, and KKMC/KORALB/KORALZ/... status report." *Nucl. Phys. Proc. Suppl.*, vol. 98 pp. 96102, 2001. hep-ph/0011305.

[6] S. Agostinelli et al. "Geant4 A Simulation Toolkit." *Nucl. Instrum. Methods Phys.* Res., Sect. A, vol. 506(3) pp. 250303, 2003.

[7] http://ilcsoft.desy.de/portal/.

[8] R. Brun and F. Rademakers. "ROOT – an object oriented data analysis framework." *Nucl. Instrum. Methods Phys.* Res., Sect. A, vol. 389(1-2) pp. 8186, 1997.

[9] A. Hocker, et al. "TMVA – Toolkit for multivariate data analysis." 2009. arXiv:physics/0703039.

[10] Verkerke and D. P. Kirkby. "The RooFit toolkit for data modeling." 2003. arXiv:physics/0306116.

[11] M. Berggren, SGV 2.31 - A fast and simple program for simulating high energy physics experiments at colliding beam detectors. http://berggren.home.cern.ch/berggren/sgv.html

[12] http://ilcsoft.desy.de/dbd/generated/

Higgs branching ratio study for DBD detector benchmarking in ILD

Hiroaki Ono[1,*]

[1]*Nippon Dental University School of Life Dentistry at Niigata*

Precise measurement of Higgs boson branching ratios (BRs) is one of the key issues for the International Linear Collider (ILC) project to reveal a particles mass generation mechanism via Higgs and particles mass coupling relation. Even though the Higgs boson accurate measurement will be conducted at the center-of-mass (CM) energy of 250 GeV to adapt the 125 GeV of the mass of Higgs-like particle observed at the Large Hadron Collider (LHC) experiments [1, 2], ILC will also keep an extendability of CM energy up to 1 TeV to explore the new particles. In order to demonstrate the detector capability even at the 1 TeV, Higgs BRs measurement is also assigned as one of the detector benchmarking process for the Detailed Baseline Design (DBD) study. In this study, measurement accuracies of the product of the cross section and branching ratio into; two jet final state of $h \to b\bar{b}$, $c\bar{c}$, and gluons; four jet final state of $h \to WW^* \to 4j$, are evaluated with a full detector simulation adopting the International Large Detector (ILD) [3].

Keywords: ILC, Higgs boson, Branching ratio

I. INTRODUCTION

Higgs boson branching ratio measurement at the CM energy of 1 TeV in ILC project is one of the detector performance benchmarking processes listed in Detailed Baseline Design document (DBD) to demonstrate the detectors performance capability at higher energy.

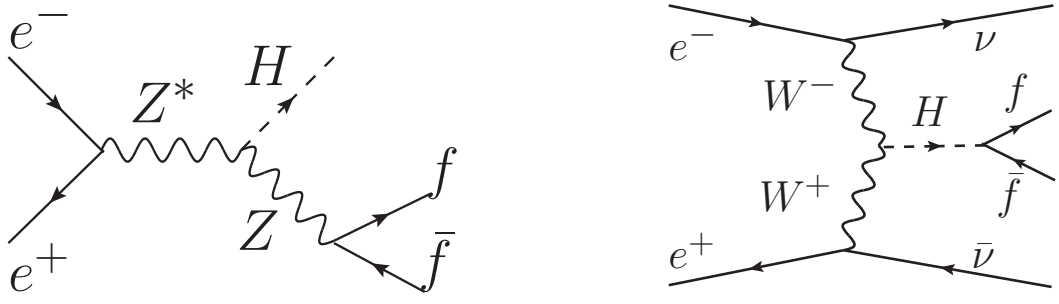

(a) (b)

FIG. 1: Higgs production process via (a) Higgs-strahlung ($e^+e^- \to Zh$) and (b) WW-fusion ($e^+e^- \to \nu_e\bar{\nu_e}h$)

*Electronic address: ono@ngt.ndu.ac.jp

At the CM energy below 500 GeV, Higgs boson mainly produced via Higgs-strahlung process: $e^+e^- \to Zh$ (Fig. 1 (a)) assuming a Higgs mass of 125 GeV and largest Higgs production cross section is obtained around the Zh production threshold of 250 GeV, as shown in Fig. 2. On the other hand, at the CM energy above 500 GeV, Higgs boson is mainly produced via WW-fusion process: $e^+e^- \to \nu_e\bar{\nu}_e h$ (Fig. 1 (b)) and much larger production cross section is obtained around the CM energy of 1 TeV than 250 GeV as shown in Fig. 2 (a) with assuming the $P(e^-,\ e^+) = P(-0.8,\ +0.2)$ left-handed beam polarization. Higgs production cross section assuming the right-handed beam polarization of $P(+0.8,\ -0.2)$ is also shown in Fig. 2 (b) and $\nu_e\bar{\nu}_e h$ production via WW-fusion process is suppressed at $\sqrt{s} = 1$ TeV.

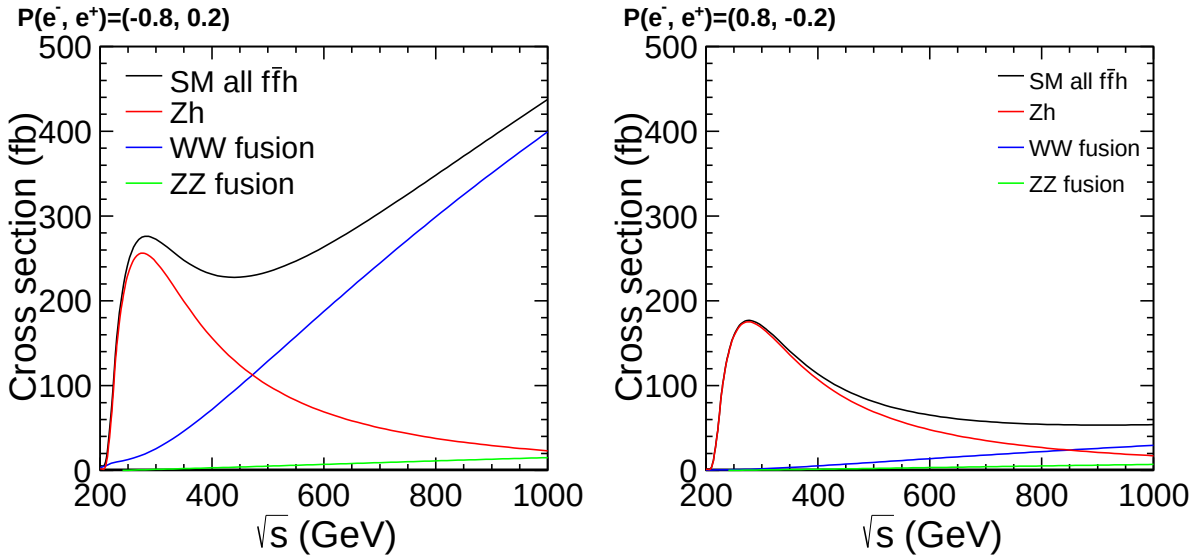

(a) (b)

FIG. 2: Higgs production cross sections as a function of CM energies at the Higgs mass of 125 GeV with (a) $P(e^-, e^+) = P(-0.8,\ +0.2)$ left-handed and (b) $P(+0.8,\ -0.2)$ right-handed beam polarizations.

In DBD benchmarking study, Standard Model (SM) Higgs BRs [4] are used to generate Higgs signal samples and Higgs BRs at different Higgs masses are shown in Fig. 3. Taking into account of the observation of Higgs-like particle in LHC experiments [1, 2], Higgs mass is selected as 125 GeV. From the Fig. 3, Higgs BRs measurement at the Higgs mass around 125 GeV is very suitable for accessing to the most of Higgs decay channels into both Fermions and Bosons. Higgs BRs at the Higgs mass of 125 GeV are summarized in Table I and Higgs mainly decays into $b\bar{b}$.

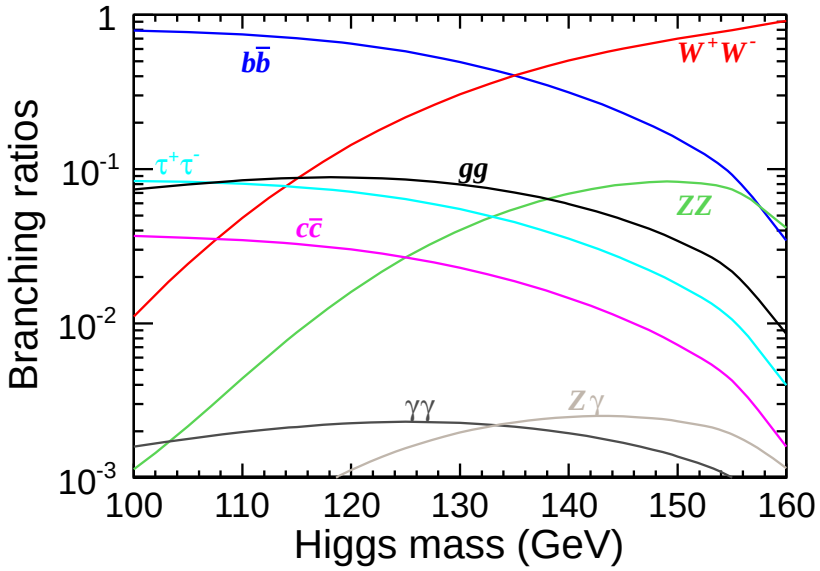

FIG. 3: SM Higgs BRs as a function of Higgs mass referred from [4].

TABLE I: Higgs BRs for each particle at the Higgs mass of 125 GeV.

Higgs decay channels	$b\bar{b}$	$c\bar{c}$	gg	WW*	$\mu^+\mu^-$	$\tau^+\tau^-$	ZZ*	$\gamma\gamma$	$Z\gamma$
Higgs BRs	57.8%	2.7%	8.6%	21.6%	0.02%	6.4%	2.7%	0.23%	0.16%

II. SIMULATION AND RECONSTRUCTION TOOLS

A. ILD standard samples for DBD

In the detector benchmarking study for ILD DBD, standard Higgs signals ($f\bar{f}h$) selecting its mass of 125 GeV and SM background samples were centrally generated employing `whizard 1.95` [5]. All the generated standard signal and background samples are summarized in Table II.

From the Table II, Higgs is mainly produced via WW-fusion process thus large missing energy and transverse momentum is in final state forming multi-jets. Taking into account of this final state, $e\nu W$ and $\nu\nu Z$, WW/ZZ final state from $e^+e^- \to 4f$ channels are supposed to be major background, which makes mass peak around Z and closed to the Higgs mass peak. $e\gamma \to \nu qq$ from $e\gamma \to 3f$ channel also considered as major background, since electrons or photons escapes to the beam pipe, invisible particles contribute as missing energy. Two photon backgrounds of $\gamma\gamma \to \nu\nu qq$ are also considered as similar final state of signal channel.

Simulation and reconstruction were performed employing latest `ilcsoft v01-16-p03` [6]. Gen-

TABLE II: Production cross sections and expected number of events of Higgs and supposed SM backgrounds in this study assuming the integrated luminosity of 500 fb^{-1} for each beam polarization $P(e^-, e^+) = P(\mp 0.8, \pm 0.2)$.

	Higgs signals (M_h = 125 GeV, $\sqrt{s}$ = 1 TeV)			
Processes	$\sigma(-0.8, +0.2)$ (fb)	$\sigma(+0.8, -0.2)$ (fb)	N$(-0.8, +0.2)$	N$(+0.8, -0.2)$
$\nu\bar{\nu}h$	404	33	202,022	16,549
$q\bar{q}h$	18	12	8,885	6,058
$\ell\ell h$	25	16	12,501	8,089
$f\bar{f}h$	447	61	223,408	30,697

Processes	SM backgrounds ($\sqrt{s}$ = 1 TeV)			
$e^+e^- \to 2f$	7,780	5,399	3.9×10^6	2.7×10^6
$e^+e^- \to 4f$	27,028	13,060	13.5×10^6	6.5×10^6
$e^+e^- \to 6f$	693	239	0.4×10^6	0.1×10^6
$e\gamma \to 3f$	460,783	398,016	230.4×10^6	199.0×10^6
$e\gamma \to 5f$	1,370	872	0.8×10^6	0.4×10^6
$\gamma\gamma \to 4f$	3,137	3,137	$1,6 \times 10^6$	1.6×10^6

erated signals were passed through the detector simulation in `Mokka` [7] employing the latest ILD detector model of `ILD_o1_v05`. Simulated hits were digitized and reconstructed in the `MarlinReco` [8].

III. SGV fast simulation

Due to the time limitation of the full detector simulation and reconstruction, several background samples are separately simulated using SGV fast simulator [9], which can reproduce the Mokka detector simulation well. Higgs signal and $e^+e^- \to 2f,\ 4f,\ 6f$ channels are fully simulated and reconstructed by full simulation but other $e\gamma \to 3f,\ 5f$, and $\gamma\gamma \to 4f$ are simulated with SGV fast simulator. In this study, ILD standard generated and reconstructed samples are used. At the analysis stage, each sample is scaled to be the integrated luminosity of 500 fb^{-1} or 1 ab^{-1} and generated 100% polarized samples are mixed with appropriate factors to obtain the expected $P(e^-,\ e^+) = P(\mp 0.8,\ \pm 0.2)$ polarized beam condition.

A. Beam related $\gamma\gamma \to$ hadron background

At the CM energy of 1 TeV, beam induced backgrounds are not negligible even in the lepton collider and 4.1 events of $\gamma\gamma \to$ hadron backgrounds are estimated per one bunch crossing. For each simulated sample, $\gamma\gamma \to$ hadron backgrounds are overlaid on the simulated hits. But note that current reconstructed samples using SGV are not overlaid $\gamma\gamma$ backgrounds, but same k_t algorithm is applied at the reconstruction stage. To treat these beam related backgrounds, k_t jet clustering algorithm implemented in `FastJet` [10] package is employed, which is commonly used for the hadron collider experiment to treat the beam related backgrounds.

In exclusive k_t jet algorithm, beam induced particles are combined as beam jet ($J_{\rm beam}$) and not used as clustered jets [11]. After applying the k_t jet clustering, beam related PFOs mainly

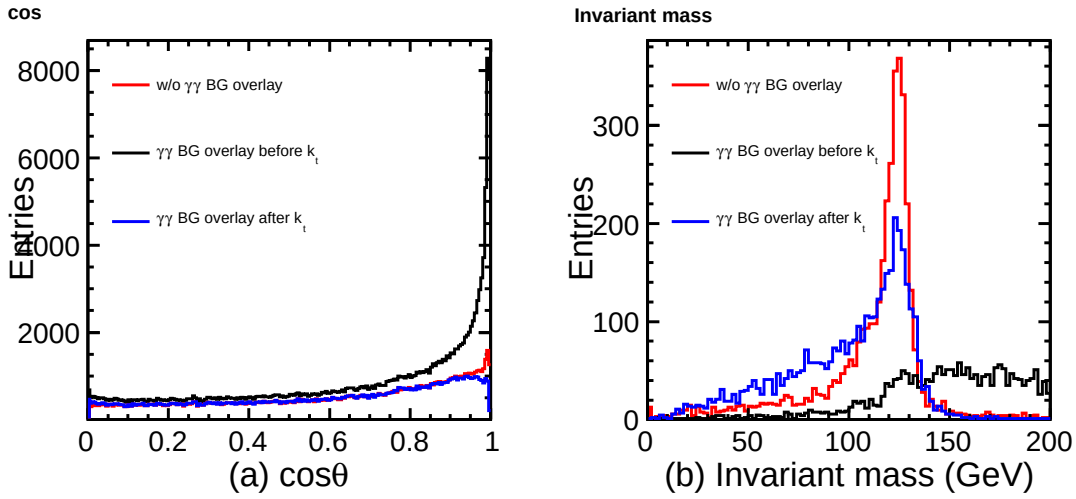

FIG. 4: $\gamma\gamma \to$ hadron background removal employing k_t jet algorithm on (a) $\cos\theta$ of PFOs and (b) invariant mass distribution in $\nu\bar{\nu}$h channel with or without background overlay.

distributed at the forward region are well subtracted as shown in Fig. 4 (a) and exceeded visible particles are suppressed shown in Fig 4 (b).

In k_t jet algorithm, following distance between particle i and j are calculated:

$$d_{ij} = \min(E_{ti}^2, E_{tj}^2) \cdot \frac{\Delta R_{ij}^2}{R^2} \tag{1}$$

where $\Delta R_{ij}^2 = (y_i - y_j)^2 + (\phi_i - \phi_j)^2$ and E_{ti}, y_{ij}, and ϕ_{ij} are a transverse momentum, rapidity, and azimuthal angle of $i-th$ particle and R is a jet-radius parameter. If d_{ij} is closed to the beam axis d_{ibeam}, these particles are merged as beam jet and these particles are treated as not related to any jets and removed. After removing $\gamma\gamma \to$ hadron backgrounds using k_t algorithm, flavor tagging

is performed for all the clustered particles employing `LCFIPlus` [12] implemented in `MarlinReco` package, which was coded in C++ and replaced from the previous `LCFIVertex` [13] implemented in FORTRAN. Neuralnet output for b and c quarks; Btag, Ctag, and their combination of BCtag (=Ctag/(Btag+Ctag)) from `LCFIPlus`, are used as input of flavor templates.

$$\mathrm{x-likeness} = \frac{\mathrm{x_1 x_2}}{\mathrm{x_1 x_2} + (1-\mathrm{x_1})(1-\mathrm{x_2})} \ (\mathrm{x = b,\ c,\ bc}), \tag{2}$$

where $\mathrm{x}_{1/2}$ is a neuralnet output of Btag, Ctag, and BCtag from LCFIPlus.

IV. $\mathrm{h} \to \mathrm{b\bar{b}},\ \mathrm{c\bar{c}},\ \mathrm{gg}$ CHANNEL ANALYSIS

A. Reconstruction and background reduction at $\sqrt{\mathrm{s}} = 1$ TeV

For the $\mathrm{h} \to \mathrm{b\bar{b}}$, $\mathrm{c\bar{c}}$, and gg channel analysis at the CM energy of 1 TeV, $\gamma\gamma \to$ hadrons background should be considered. At first forced two jet clustering is applied employing exclusive k_t algorithm selecting $R = 1.1$.

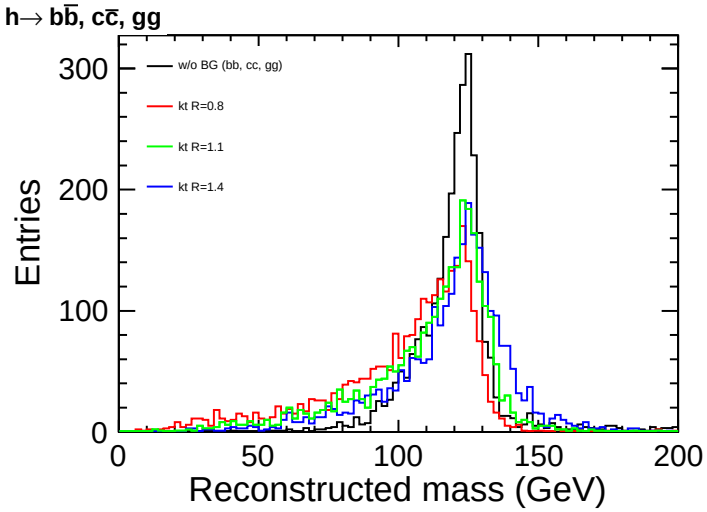

FIG. 5: Reconstructed Higgs mass distribution employing k_t jet clustering algorithm with different R parameters for $\mathrm{h} \to \mathrm{b\bar{b}},\ \mathrm{c\bar{c}},\ \mathrm{gg}$ selected by MC information.

After applying k_t jet clustering, `LCFIPlus` flavor tagging is applied for the particles clustered into jets and reclustered with jet clustering algorithm implemented in the `LCFIPlus` based on the Durham jet clustering algorithm [14]. After the reconstruction procedure, event selection and background reduction is performed for each cut condition, summarized on the Table III.

TABLE III: Cut flow summary of $h \to b\bar{b}$, $c\bar{c}$, gg channel analysis.

1. Visible energy on beam calorimeter	$E_{BCAL} < 50$ GeV
2. Thrust value	Thrust < 0.95
3. Visible energy	$100 < E_{vis} < 400$ GeV
4. Transverse visible momentum	$P_T > 50$ GeV
5. Number of charged particle flow object	$N_{ChdPFO} > 15$
6. Azimuthal angle of Higgs flight direction	$\lvert\cos\theta_h\rvert < 0.95$
7. Reconstructed dijet mass	$110 < M_{jj} < 150$ GeV

In order to identify the electrons or photons going into beam pipe direction from $e\gamma$ or $\gamma\gamma$ process, energy on the beam calorimeter (E_{BCAL}) is used to eliminate the two photon backgrounds event. Further reduction of huge $e\gamma$ processes is efficiently obtained by cut on the thrust variable defined as:

$$\text{Thrust } T = \max_{\vec{n}} \frac{\sum_i |\vec{p_i} \cdot \vec{n}|}{\sum_i |\vec{p_i}|},$$

where $\vec{p_i}$ is a momentum of i-th particle and $\vec{n}$ is an unit vector of the thrust axis which maximize the thrust value T.

Since $\nu\bar{\nu}$h final state has large missing energy and transverse momentum, cuts on the visible energy (E_{vis}) and visible transverse momentum (P_T) are applied to suppress fully hadronic decay and low P_T channels. Cuts on the number of charged particle flow objects (N_{ChdPFO}) and azimuthal angle of the flight direction of reconstructed Higgs ($\cos\theta_h$) are required to suppress the leptonic decay channels or particles going into forward region. Finally Higgs signals are selected with its mass range between 110 to 150 GeV. All the cut variables and cut conditions are shown in Fig. 6.

After passing all the selections, selection efficiencies are obtained as 35.0% ($h \to b\bar{b}$), 37.3% ($h \to c\bar{c}$), and 35.9% ($h \to gg$), respectively. An example of reconstructed Higgs mass distribution requiring additional b-likeness cut ($b - likeness > 0.6$) to select $h \to b\bar{b}$ is shown in Fig. 7. According to the Fig. 7, most of backgrounds are significantly eliminated by b-tagging.

In the DBD detector benchmarking study, both left- and right-handed $P(\mp 0.8, \pm 0.2)$ polarized beam runs are expected accumulating the integrated luminosity of same 500fb^{-1} with each polarization. From the Fig. 2 (b), even though main signal production process is significantly reduced, but WW-fusion production process is still achieved the largest cross section at 1 TeV with respect to the $P(+0.8, -0.2)$ beam polarization. Hence same cut conditions are adopted even for right-handed polarization to select WW-fusion production process. Background reduction on right-handed polarization are summarized in Table V.

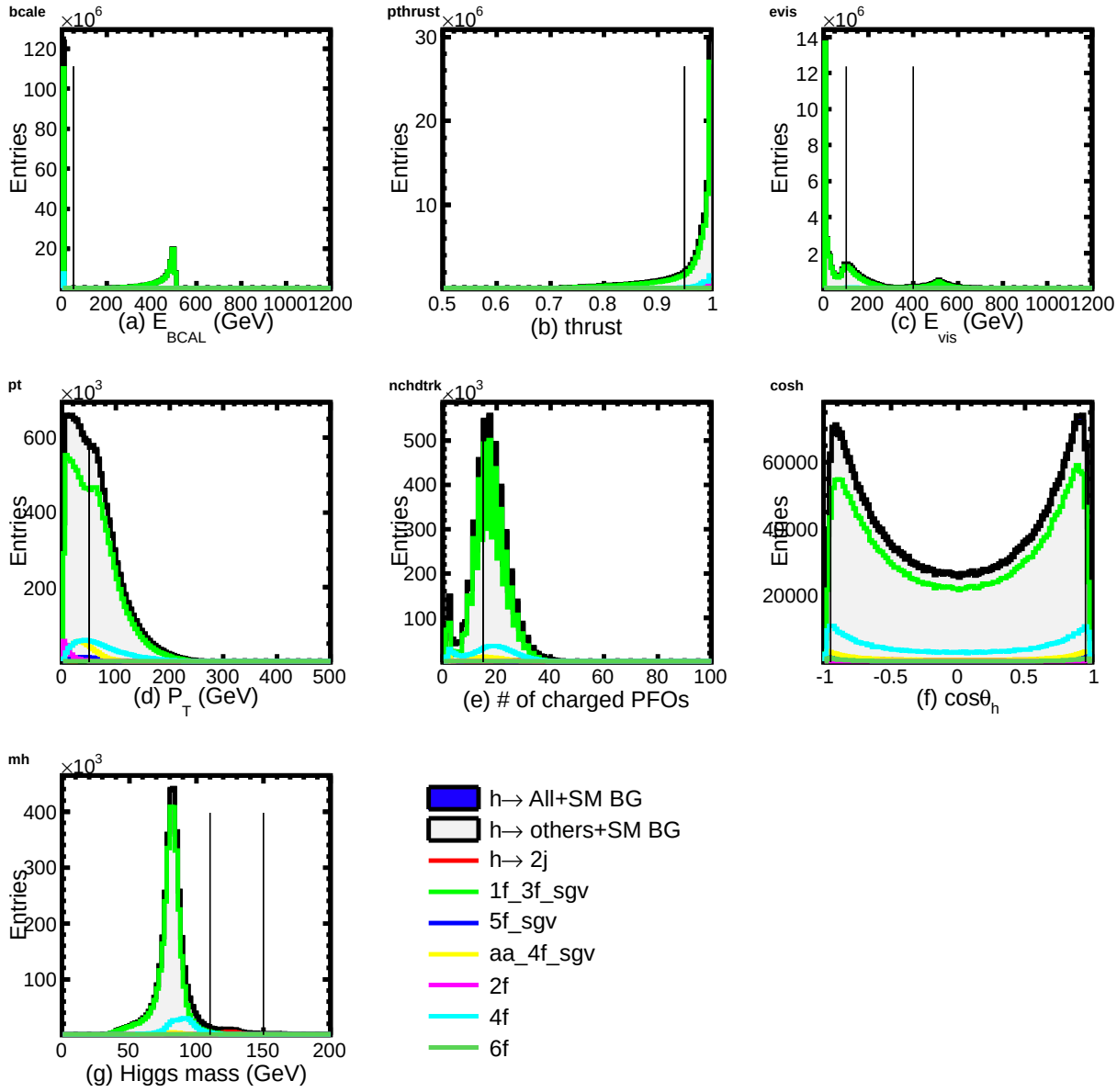

FIG. 6: Cut variables for h → 2j channel reconstruction with integrated luminosity of 500 fb^{-1} regarding P(−0.8, +0.2) left-handed beam polarization.

B. Template fitting and accuracies of σBR

In order to evaluate the σBR with separating h → $b\bar{b}$, $c\bar{c}$, and gg, we apply the flavor template fitting to employ the flavor-likeness template calculated as Eq. 2.

After the all above selections, signal flavor templates of h → $b\bar{b}$, $c\bar{c}$, and gg and background template of the all other Higgs decay channels and SM background are prepared. In order to

TABLE IV: Summary table of cut flow for $h \to b\bar{b}$, $c\bar{c}$, and gg channel at $\sqrt{s} = 1$ TeV with $\mathcal{L} = 500$ fb^{-1} regarding $P(e^-,\ e^+) = P(-0.8,\ +0.2)$ polarization. Note that 3f, 5f, $\gamma\gamma \to 4f$ channels contributions were simulated and estimated using SGV fast simulation sample.

	Signals			Higgs other decays			
Cut flow	$h \to b\bar{b}$	$h \to c\bar{c}$	$h \to gg$	$h \to WW^*$	$h \to ZZ^*$	$h \to \tau\tau$	$h \to s\bar{s}$
No cut	128,700	6,058	19,045	48,320	5,979	14,291	90
1. E_{BCAL}	125,021	5,875	18,514	46,958	5,809	13,896	88
2. Thrust	104,305	4,910	15,506	35,780	4,569	10,248	80
3. E_{vis}	96,807	4,572	14,179	26,199	3,303	6,208	73
4. P_T	74,849	3,577	11,296	20,859	2,544	4,193	63
5. N_{ChdPFO}	70,005	3,152	11,133	16,402	2,074	113	50
6. $\lvert\cos\theta_h\rvert$	65,273	2,913	10,421	15,835	1,981	109	48
7. M_{jj}	44,988	2,258	6,845	4,419	685	32	41
Efficiency	35.0%	37.3%	35.9%	9.1%	11.5%	0.2%	45.7%

	SM backgrounds					
Cuts	3f	5f	$\gamma\gamma \to 4f$	2f	4f	6f
No cut	223,626,000	615,361	1,538,560	3,890,180	13,514,000	346,419
1. E_{BCAL}	110,066,000	498,059	1,374,030	3,354,840	8,473,960	318,340
2. Thrust	39,901,400	338,787	971,486	622,544	2,600,550	205,792
3. E_{vis}	10,449,800	203,570	662,748	208,035	1,233,480	64,422
4. P_T	5,595,070	102,081	225,666	13,986	782,962	48,951
5. N_{ChdPFO}	3,268,180	47,640	106,017	6,120	475,624	37,700
6. $\lvert\cos\theta_h\rvert$	3,175,530	38,739	94,914	4,076	441,836	33,997
7. M_{jj}	44,725	7,106	18,486	219	27,172	6,139
Efficiency	2.0×10^{-4}	1.2×10^{-2}	1.2×10^{-2}	5.6×10^{-5}	2.0×10^{-3}	1.8×10^{-2}

estimate the measurement accuracy of $\sigma BR(h \to s)$ ($s = b\bar{b},\ c\bar{c},\ gg$),

$$\sigma BR(s) = r_s \times \sigma BR^{SM}(s)\ (s = b\bar{b},\ c\bar{c},\ gg,\ bkg), \tag{3}$$

where $\sigma BR(s)$ and $\sigma BR^{SM}(s)$ are observed and expected products of cross section and branching ratio and r_s is a fluctuation from the SM prediction. From the Eq. 3, the measurement accuracy of $\sigma BR(s)$ is estimated as

$$\frac{\Delta\sigma BR(h \to s)}{\sigma BR} = \frac{\Delta r_s}{r_s}. \tag{4}$$

Relative uncertainties of the r_s are estimated with the binned log-likelihood fitting for flavor

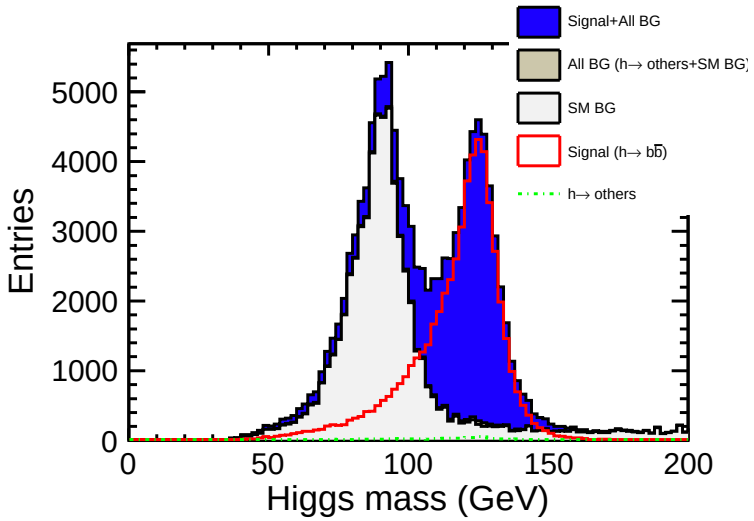

FIG. 7: Example of the reconstructed Higgs mass distribution at $\sqrt{s} = 1$ TeV in $h \to b\bar{b}$ channel assuming the b-likeness cuts ($b-likeness > 0.6$).

templates. Assuming the Poisson statistics, probability of entry in each bin is determined as;

$$P_{ijk} = \frac{\mu^n e^{-\mu}}{n!}, \tag{5}$$

where $n \equiv N_{ijk}^{data}$ is a expected number of data entries in (i, j, k) bin, and μ represents the sum of each template sample entries at (i, j, k) bin, which is defined as $N_{ijk}^{template}$:

$$N_{ijk}^{template} = \sum_{s=bb,\ cc,\ gg} r_s \cdot N_{ijk}^{s} + N_{ijk}^{bkg}, \tag{6}$$

where N_{ijk}^{s} is a number of entries in each template bin predicted in SM and N_{ijk}^{bkg} is a sum of entries from $h \to$ others and SM backgrounds in (i, j, k) bin. Two dimensional images of the three dimensional b−, c−, and bc− flavor-likeness template samples for $h \to b\bar{b}$, $c\bar{c}$, gg, others, and SM backgrounds are shown in Fig. 8.

The uncertainty of the r_s is evaluated by the 5,000 times of Toy-MC with log-likelihood fitting by fluctuating the Data samples assuming the Poisson statistics in each bin. After applying template fitting, accuracies of σBR are extracted from the Gaussian fitting for parameter r_s.

Fitted results and extracted accuracies of σBRs assuming the integrated luminosity of $\mathcal{L} = 500\ fb^{-1}$ with both beam polarization $P(e^-,\ e^+) = P(\mp 0.8,\ \pm 0.2)$ are summarized on the Table VI.

Concerning the precision measurement of the Higgs boson σBRs, left-handed beam polarization $P(-0.8,\ \ +0.2)$ with accumulating the integrated luminosity of $\mathcal{L} = 1\ ab^{-1}$ is also evaluated on the same table. Note that these results are only considered the statistical uncertainty of σBR.

TABLE V: Summary table of background reduction for $h \to b\bar{b}$, $c\bar{c}$, and gg at $\sqrt{s} = 1$ TeV with $\mathcal{L} = 500\ fb^{-1}$ and $P(e^-,\ e^+) = P(+0.8,\ -0.2)$ right-handed beam polarization. Note that 3f, 5f, $\gamma\gamma \to 4f$ channels contributions were simulated and estimated using SGV fast simulation sample.

	Signal			Other Higgs decays			
Cut flow	$h \to b\bar{b}$	$h \to c\bar{c}$	$h \to gg$	$h \to WW^*$	$h \to ZZ^*$	$h \to \tau\tau$	$h \to s\bar{s}$
No cut	17,768	812	2,566	6,592	830	1,992	10
1. E_{BCAL}	17,054	783	2,463	6,331	794	1,917	9
2. Thrust	10,999	512	1,628	3,743	457	1,068	7
3. E_{vis}	8,049	366	1,152	2,230	282	567	6
4. P_T	6,045	284	898	1,722	211	377	5
5. N_{ChdPFO}	5,608	248	882	1,328	171	24	4
6. $\lvert\cos\theta_h\rvert$	5,171	224	815	1,262	157	21	4
7. M_{jj}	3,542	172	537	354	56	4	3
Efficiency	19.9%	21.2%	20.9%	5.4%	6.7%	0.2%	29.5%

	SM backgrounds					
Cut flow	3f	5f	$\gamma\gamma \to 4f$	2f	4f	6f
No cut	205,529,000	415,380	1,538,560	2,699,560	6,530,160	119,252
1. E_{BCAL}	92,815,300	310,618	1,374,030	2,288,410	2,174,560	103,473
2. Thrust	28,610,000	206,465	971,486	401,722	606,529	67,684
3. E_{vis}	4,870,840	131,761	662,748	135,701	252,878	17,727
4. P_T	1,947,590	60,325	225,666	8,963	130,966	12,774
5. N_{ChdPFO}	1,095,980	28,418	106,017	2,634	74,999	10,265
6. $\lvert\cos\theta_h\rvert$	1,060,520	23,195	94,914	1,497	69,081	9,228
7. M_{jj}	15,749	4,417	18,486	144	3,493	1,575
Efficiency	7.7×10^{-5}	1.1×10^{-2}	1.2×10^{-2}	5.3×10^{-5}	5.3×10^{-4}	1.3×10^{-2}

V. $h \to WW^*$ CHANNEL ANALYSIS

In the $h \to WW^*$ analysis, high energetic neutrinos are generated via the production process of $\nu\bar{\nu}h$, therefore $h \to WW^*$ fully hadronic decay channel ($h \to WW^* \to q\bar{q}q\bar{q}$) is analyzed with reconstructing four jet final state.

In order to suppress the $\gamma\gamma \to$ hadron backgrounds, exclusive four jet clustering with k_t algorithm is applied for selecting $R = 0.9$. Owing to this algorithm, beam related backgrounds are well removed, then LCFIPlus flavor tagging is applied for all the reconstructed particles and re-clustered as four jets forcibly by Durham [14] base jet clustering in the LCFIPlus package.

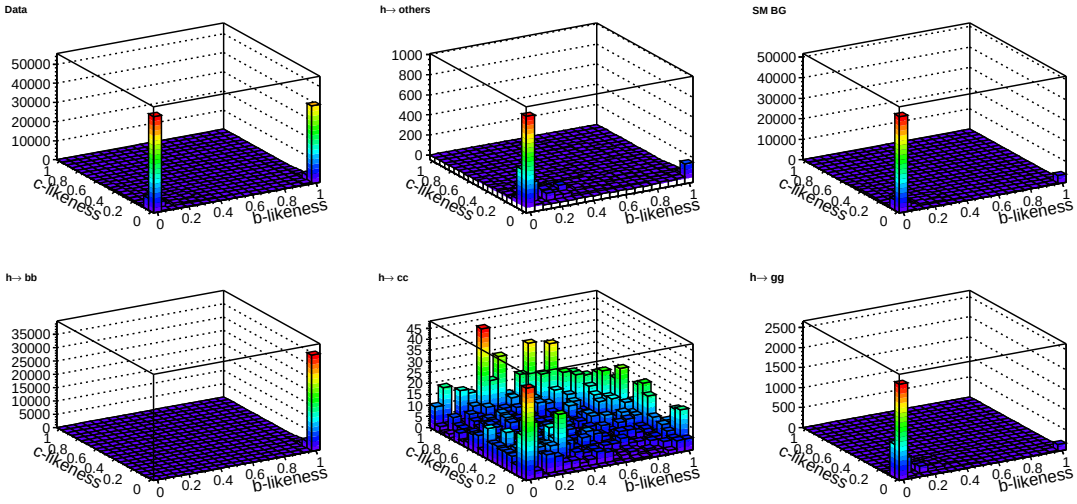

FIG. 8: 2D image of the 3D flavor template samples for Data, $h \to b\bar{b}$, $c\bar{c}$, gg, others, and SM BGs.

TABLE VI: Estimated measurement accuracies of σBR for $h \to b\bar{b}$, $c\bar{c}$, and gg channels at $\sqrt{s} = 1$ TeV with respect to the $\mathcal{L} = 500$ fb^{-1} for both P(e^-, e^+) = (∓ 0.8, ± 0.2) beam polarizations or accumulating $\mathcal{L} = 1$ ab^{-1} regarding P(-0.8, $+0.2$) left-handed polarization. Here these results are taken only statistical uncertainties into account.

Integrated luminosity	500 fb^{-1}	500 fb^{-1}	1 ab^{-1}
Beam polarization P(e^-, e^+)	P(-0.8, $+0.2$)	P($+0.8$, -0.2)	P(-0.8, $+0.2$)
r_{bb}	1.000±0.005	0.999±0.021	1.000±0.004
r_{cc}	1.002±0.057	1.034±0.380	1.001±0.039
r_{gg}	0.998±0.039	1.025±0.263	0.998±0.028
$\Delta\sigma$BR/σBR($h \to b\bar{b}$)	0.54%	2.1%	0.39%
$\Delta\sigma$BR/σBR($h \to c\bar{c}$)	5.7%	36.8%	3.9%
$\Delta\sigma$BR/σBR($h \to gg$)	3.9%	25.7%	2.8%

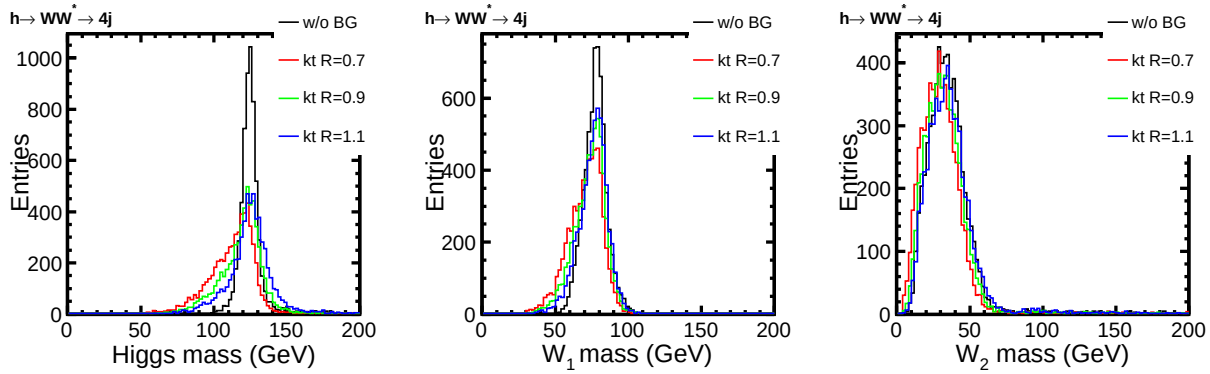

FIG. 9: Four jet reconstruction employing k_t algorithm with different R parameters.

At the Higgs mass of 125 GeV, one W should be off-shell and only one W has mass close to the W mass (M_W). The best jet pair combination is selected as closest dijet mass as M_W, which has minimum mass difference of $|M_{jj} - M_W|$. Selected W candidate is defined as W_1 and remaining dijet is described as W_2, where they are mostly contributed from on-shell and off-shell W, respectively. After the jet clustering and pairing, following cuts are applied to suppress SM backgrounds and other Higgs decay channel contributions.

TABLE VII: Cut flow summary of $h \to WW^*$ channel analysis.

1.	Visible energy on beam calorimeter	$E_{BCAL} < 50$ GeV
2.	Thrust	Thrust < 0.95
3.	Visible energy	$100 < E_{vis} < 400$ GeV
4.	Visible transverse momentum	$P_T > 50$ GeV
5.	Total number of charged particle flow object	$N_{ChargedPFO} > 25$
6.	Azimuthal angle of each jet	$\lvert\cos\theta_j\rvert < 0.90$
7.	Y_{34} value	$-\log_{10}(Y_{34}) < 3.0$
8.	Y_{23} value	$-\log_{10}(Y_{23}) < 2.2$
9.	Sum of B-tagging output for four jets	$Btag_{4j} < 0.8$
10.	W_1 mass (Closest to M_W)	$60 < M_{W_1} < 95$ GeV
11.	W_2 mass (Remaining dijet mass)	$15 < M_{W_2} < 60$ GeV
12.	Higgs mass	$110 < M_h < 140$ GeV

First requiring energetic jets final state to suppress semi-leptonic decay channels in 2f and 4f (WW, ZZ) requiring large visible energy and transverse momentum. In addition, cut on N_{PFO} and N_j are required to suppress the leptonic and semileptonic decay channel from $WW \to \ell\nu qq$. Cuts on the threshold value of jet clustering y value used in the Durham jet algorithm from i to j=i+1 jets ($-\log_{10}(Y_{ij})$) are applied to reduce non-four jets like events. In order to suppress the other Higgs decay channels contribution, mostly comes from the $h \to b\bar{b}$ by largest fraction of the Higgs decay; sum of Btag output for four jets is required ($Btag_{4j} < 0.8$). After applying b-tagging cut, remaining contribution from other Higgs decay channel is mainly coming from $h \to gg$.

Reconstructed Higgs mass distribution regarding $h \to WW^*$ hadronic decay channel is shown in Fig. 11. P(+0.8, − 0.2) right-handed beam polarization running with the same integrated luminosity of 500 fb^{-1} is also estimated. According to the right-handed electron beam polarization, production process via WW − fusion contributed by the t-channel diagram is suppressed, hence both main signal production channel $\nu_e\bar{\nu}_e h$ and WW background productions are reduced.

Therefore, same cut flow is applied as left-handed polarization case which optimized for WW-

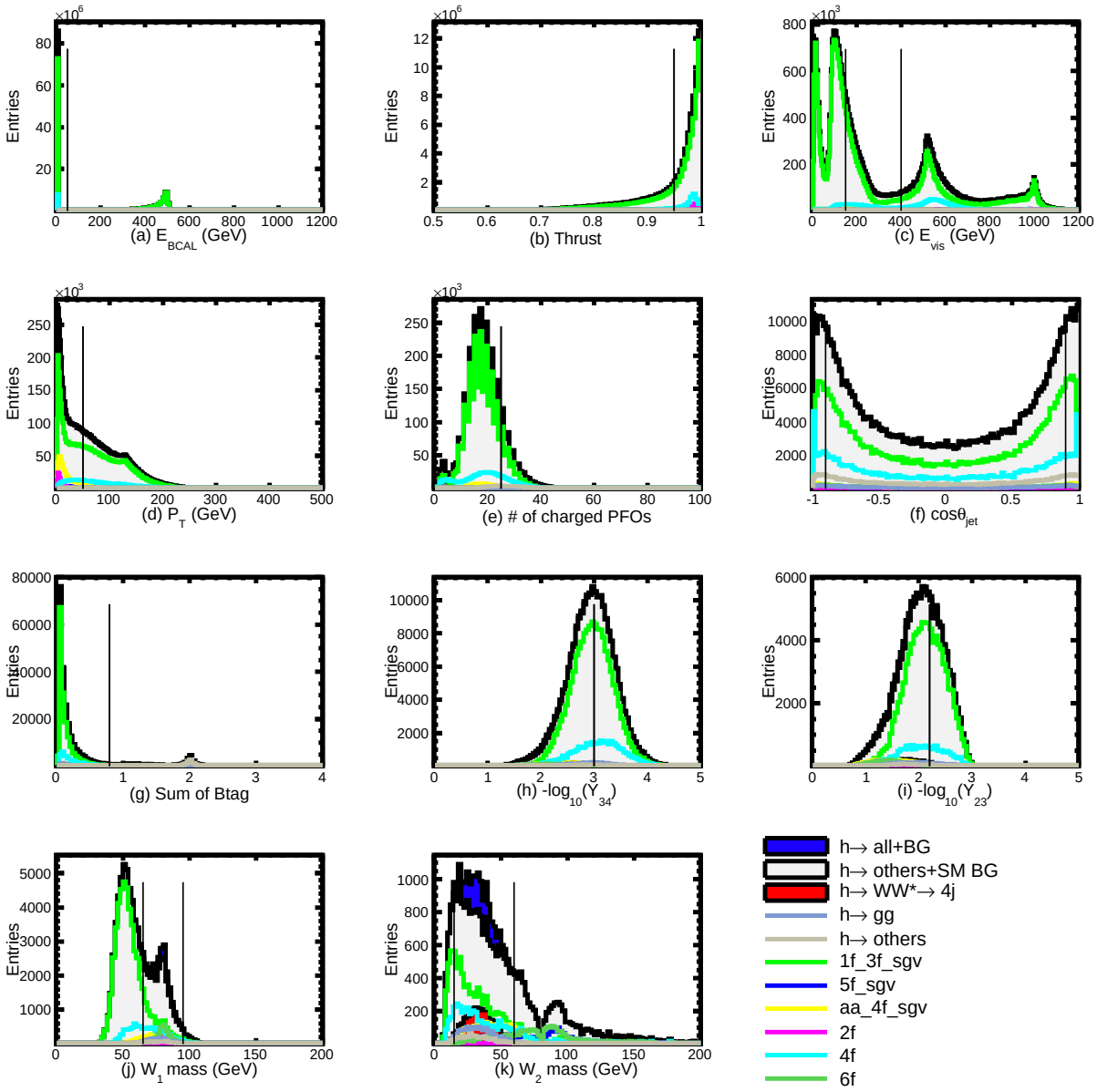

FIG. 10: Cut variables of h → WW* analysis.

fusion process. Backgrounds reductions are summarized on the Table VIII and IX.

After passing all the selections, signal significance $S/\sqrt{(S+B)}$, where S is a number of selected signal samples and B is a total number of background samples; is obtained from the final selected samples as 27.9 with P$(-0.8,\ 0.2)$ left-handed and 4.2 with P$(+0.8,\ -0.2)$ right-handed beam polarizations assuming the same integrated luminosity of $\mathcal{L} = 500$ fb^{-1}.

As a result, $\Delta\sigma$BR$/\sigma$BR(h → WW*) is estimated as 3.6% with P$(-0.8,\ +0.2)$ and 23.7% with P$(+0.8,\ -0.2)$ polarizations. Assuming further statistics of 1 ab^{-1} only running with P$(-0.8,\ +0.2)$ left-handed polarization, measurement accuracy is expected to be improved as 2.5%. Note that

TABLE VIII: Summary table of background reduction on $h \to WW^* \to 4j$ channel assuming $\mathcal{L} = 500$ fb^{-1} with respect to the P(-0.8, $+0.2$) left-handed beam polarization at $\sqrt{s} = 1$ TeV. Note that 3f, 5f, $\gamma\gamma \to 4$f channels contributions were simulated and estimated using SGV fast simulation sample.

	Signal	Other Higgs decays					
Cut flow	$h \to WW^* \to 4j$	$h \to b\bar{b}$	$h \to c\bar{c}$	$h \to gg$	$h \to ZZ^*$	$h \to \tau\tau$	$h \to s\bar{s}$
No cut	21,976	128,700	6,058	19,045	5,979	14,291	90
1. E_{BCAL}	21,348	124,986	5,873	18,514	5,797	13,747	88
2. Thrust	19,256	109,860	5,188	16,530	5,006	11,601	84
3. E_{vis}	14,534	82,950	4,108	12,709	2,924	4,828	66
4. P_T	12,185	67,792	3,375	10,607	2,341	3,388	61
5. N_{ChdPFO}	8,992	38,071	1,534	9,115	1,350	32	24
6. $\lvert\cos\theta_j\rvert$	5,330	20,555	868	5,325	782	10	15
7. $Btag_{4j}$	5,027	651	769	4,958	501	6	15
8. $-\log Y_{34}$	4,363	304	289	2,916	420	5	6
9. $-\log Y_{23}$	3,792	215	203	2,034	348	3	4
10. M_{W1}	3,177	162	167	1,684	280	2	3
11. M_{W2}	3,025	140	145	1,539	257	2	3
12. M_h	2,732	118	124	1,366	231	1	3
Efficiency	12.4%	0.1%	2.0%	7.2%	3.9%	0.0%	3.1%

	SM backgrounds					
Cut flow	3f	5f	$\gamma\gamma \to 4f$	2f	4f	6f
No cut	223,628,000	615,361	1,538,560	3,890,180	13,514,000	346,419
1. E_{BCAL}	72,750,600	483,560	1,284,930	3,347,830	8,442,530	317,394
2. Thrust	23,633,100	408,482	1,102,330	771,237	2,929,920	260,408
3. E_{vis}	4,967,370	105,205	606,486	133,143	803,488	30,640
4. P_T	2,750,240	38,794	95,691	6,925	524,360	22,308
5. N_{ChdPFO}	289,052	7,034	11,092	171	112,904	12,726
6. $\lvert\cos\theta_j\rvert$	170,938	3,393	5,782	60	48,634	7,736
7. $Btag_{4j}$	168,176	3,227	5,641	25	35,396	3,946
8. $-\log Y_{34}$	89,374	2,882	4,746	13	15,194	3,395
9. $-\log Y_{23}$	51,723	2,716	4,395	13	9,464	3,249
10. M_{W1}	8,879	2,397	3,400	13	4,889	3,005
11. M_{W2}	6,064	792	2,369	0	3,350	783
12. M_h	2,568	164	850	0	1,206	113
Efficiency	1.1×10^{-5}	2.7×10^{-4}	5.5×10^{-4}	0.0	8.9×10^{-5}	3.2×10^{-4}

TABLE IX: Summary table of background reduction in $h \to WW^* \to 4j$ channel assuming $\mathcal{L} = 500$ fb^{-1} with respect to the P(+0.8, −0.2) right-handed beam polarization at $\sqrt{s} = 1$ TeV. Note that 3f, 5f, $\gamma\gamma \to 4f$ channels contributions were simulated and estimated using SGV fast simulation sample.

	Signal	Other Higgs decays					
Cut values	$h \to WW^* \to 4j$	$h \to b\bar{b}$	$h \to c\bar{c}$	$h \to gg$	$h \to ZZ^*$	$h \to \tau\tau$	$h \to ss$
No cut	2,972	17,768	812	2,566	830	1,992	10
1. E_{BCAL}	2,870	17,048	782	2,463	794	1,906	9
2. Thrust	2,055	12,071	559	1,824	527	1,259	7
3. E_{vis}	1,126	6,456	315	981	242	430	5
4. P_T	928	5,218	255	811	191	302	5
5. N_{ChdPFO}	683	2,921	116	698	109	7	2
6. $\lvert\cos\theta_j\rvert$	405	1,589	67	411	64	3	1
7. $Btag_{4j}$	381	48	58	382	39	3	1
8. $-\log Y_{34}$	327	22	21	221	32	2	0
9. $-\log Y_{23}$	284	16	15	155	27	1	0
10. M_{W_1}	237	12	12	128	22	1	0
11. M_{W_2}	212	10	10	107	19	1	0
12. M_h	193	8	9	95	17	0	0
Efficiency	6.5%	0.0%	1.1%	3.7%	2.1%	0.0%	0.0%

	SM backgrounds					
Cut values	3f	5f	$\gamma\gamma \to 4f$	2f	4f	6f
No cut	205,530,000	415,380	1,538,560	2,699,560	6,530,160	119,252
1. E_{BCAL}	60,587,000	301,833	1,284,930	2,282,960	2,155,180	103,093
2. Thrust	15,111,000	249,963	1,102,330	486,424	626,178	82,263
3. E_{vis}	2,317,670	69,903	606,486	87,755	143,697	6,761
4. P_T	935,773	21,219	95,691	5,672	74,944	4,289
5. N_{ChdPFO}	96,284	3,251	11,092	117	13,979	2,712
6. $\lvert\cos\theta_j\rvert$	56,987	1,454	5,782	28	4,744	1,691
7. $Btag_{4j}$	56,091	1,387	5,641	25	3,606	491
8. $-\log Y_{34}$	29,965	1,245	4,746	13	1,641	440
9. $-\log Y_{23}$	17,261	1,171	4,395	13	1,033	421
10. M_{W_1}	3,057	1,006	3,400	13	531	390
11. M_{W_2}	1,801	269	1,796	0	320	62
12. M_h	766	79	769	0	143	12
Efficiency	3.7×10^{-6}	1.9×10^{-4}	5.0×10^{-4}	0.0	2.2×10^{-5}	1.0×10^{-4}

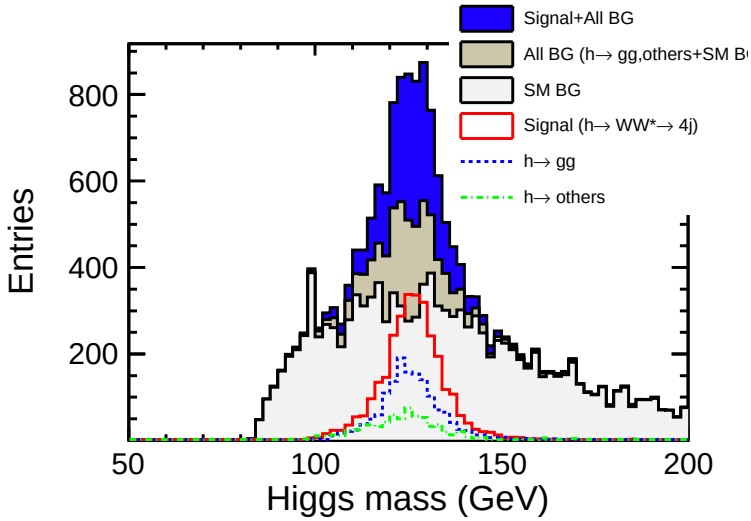

FIG. 11: Reconstructed Higgs mass distribution for h → WW* hadronic decay channel at $\sqrt{s} = 1$ TeV with respect to the $\mathcal{L} = 500$ fb^{-1} with P$(-0.8, +0.2)$ beam polarization.

TABLE X: Measurement accuracies of σBR in h → WW* → 4j channel with respect to the $\mathcal{L} = 500$ fb^{-1} for both P$(\mp 0.8, \pm 0.2)$ beam polarizations or accumulating $\mathcal{L} = 1$ ab^{-1} regarding P$(-0.8, +0.2)$ left-handed polarization.

Integrated luminosity	500 fb^{-1}	500 fb^{-1}	1 ab^{-1}
Beam polarization P(e$^-$, e$^+$)	P$(-0.8, +0.2)$	P$(+0.8, -0.2)$	P$(-0.8, +0.2)$
Signal significance $(S/\sqrt{S+B})$	27.9	4.2	39.7
$\Delta\sigma$BR/σBR(h → WW* → 4j)	3.6%	23.7%	2.5%

current cut based analysis still remains h → gg and ZZ contribution after the all cuts but not taken into account for the systematic uncertainty of σBR(h → WW*). Further improvement is needed to reduce the uncertainty from other Higgs decay channels.

VI. CONCLUSION

Measurement accuracies of the σBR for the Higgs decay channels of h → b$\bar{\text{b}}$, c$\bar{\text{c}}$, gg, and WW* → 4j are analyzed at the CM energy of 1 TeV. All results are summarized on Table XI assuming the $\mathcal{L} = 500$ fb^{-1} and 1 ab^{-1} regarding both P$(\mp 0.8, \pm 0.2)$ beam polarizations. Owing to the good background separation by B-tagging, h → b$\bar{\text{b}}$ channel can also achieve good situation even with right-handed polarization, but that is degraded for other channel case significantly, which is mainly caused by $e\gamma \to \nu qq$ or $\gamma\gamma \to qqqq$. h → cc, gg, WW* are affected by this background except for the h → bb. $\gamma\gamma \to qqqq$ contribution is relatively increased with the right-handed beam

polarization case. Note that all the results are only considered statistical uncertainty of σBR and systematic uncertainty from other decays and backgrounds should be also taken into account in further study.

TABLE XI: Summary table of the measurement accuracies of σBR at $\sqrt{s} = 1$ TeV assuming $\mathcal{L} = 500$ fb^{-1} with $P(\mp 0.8, \ \pm 0.2)$ both polarizations or 1 ab^{-1} only accumulating P$(-0.8, \ +0.2)$ left-handed beam polarization. Results are only considered statistical uncertainty.

Integrated luminosity	500 fb^{-1}		1 ab^{-1}
Beam polarization P(e^-, e^+)	P$(-0.8, \ +0.2)$	P$(+0.8, -0.2)$	P$(-0.8, \ +0.2)$
$\Delta\sigma$BR/σBR($h \to b\bar{b}$)	0.54%	2.1%	0.39%
$\Delta\sigma$BR/σBR($h \to c\bar{c}$)	5.7%	36.8%	3.9%
$\Delta\sigma$BR/σBR($h \to gg$)	3.9%	25.7%	2.8%
$\Delta\sigma$BR/σBR($h \to WW^* \to 4j$)	3.6%	23.7%	2.5%

Acknowledgments

We would like to acknowledge the members who join the ILD Analysis and Software meeting [16] for useful discussion of this work and to ILD software task group members who maintain the analysis tools and MC samples for DBD detector benchmarking study. Especially, Mikael Berggren, Jenny List, and Akiya Miyamoto for useful discussion and suggestion for this analysis, Frank Gaede and Jan Engels for production and manage large amount of simulation/reconstruction samples.

VII. BIBLIOGRAPHY

[1] The ATLAS Collaboration, Phys. Lett. B 710, 49 (2012).

[2] The CMS Collaboration, Phys. Lett. B 710, 26 (2012).

[3] T. Abe et al. [ILD Concept Group - Linear Collider Collaboration], "The International Large Detector: Letter of Intent", KEK Report 2009-6.

[4] LHC Higgs Cross Section Working Group, arXiv:1101.0593v3 [hep-ph] (2011).

[5] W. Kilian *et al.*, arXiv:0708.4233 [hep-ph]
M. Moretti *et al.*, arXiv: 0102.195-rev [hep-ph].

[6] http://ilcsoft.desy.de/portal/.

[7] P. Mora de Freitas and H. Videau, LC-TOOL-2003-010, Prepared for LCWS 2002,. Jeju Island, Korea, 26-30 Aug 2002.

[8] O. Wendt and F. Gaede and T. Krämer, arXiv:physics/0702171v1 [physics.ins-det].

[9] M. Berggren, arXiv:1203.0217v1 [physics.ins-det] (2012).

[10] Matteo Cacciari, Gavin P. Salam, Gregory Soyez, arXiv:1111.6097v1 [hep-ph] (2011).

[11] Detailed Baseline Design document ILD section, http://ific.uv.es/ fuster/DBD-Chapters/Chapter4 ILD.pdf

[12] https://confluence.slac.stanford.edu/display/ilc/LCFIPlus.

[13] Nuclear Instruments and Methods in Physics Research Section A, Volume 610, Issue 2, p. 573-589.

[14] S. Catani *et al.*, Phys. Lett. B 269, 432-438 (1991)

[15] http://www-jlc.kek.jp/subg/physics/ilcphys/

[16] http://ilcagenda-beta.linearcollider.org/categoryDisplay.py?categId=131

[17] T. Sjöstrand, S. Mrenna and P. Skands, JHEyP05 (2006) 026.

Appendix

Appendix A: Higgs BR study at 500 GeV

1. Reconstruction and background reduction at 500 GeV

At the CM energy of 500 GeV, large amount of reconstructed signal and SM background samples are available for which were produced the study of ILD Letter of Intent (LOI), even though these samples were generated employing the Higgs mass of 120 GeV in `whizard-1.40`. Higgs BRs are calculated by `Pythia` [17] instead of used in DBD analysis, where the BRs for $h \to b\bar{b}$, $c\bar{c}$, and gg are $BR(h \to b\bar{b}) = 65.7\%$, $BR(h \to c\bar{c}) = 3.6\%$, and $BR(h \to gg) = 5.5\%$, respectively. These generated samples are also simulated with previous `ILD_00` detector model in Mokka. For the flavor tagging, `LCFIVertex` package [13] was used. In the $h \to b\bar{b}$, $c\bar{c}$, and gg reconstruction, `Durham` jet clustering [14] was applied and forcibly clustered as two jet. Note that at the $\sqrt{s} = 500$ GeV, $\gamma\gamma$ beam induced background contribution is relatively smaller than 1 TeV, thus $\gamma\gamma \to$ hadron backgrounds were not overlaid to the samples.

In order to select the $\nu_e\bar{\nu}_e h$ WW-fusion process, at first cut on missing mass is applied to suppress Zh process. Cuts on P_T, P_Z, P_{max}, and N_{chd} are required to suppress semi-leptonic decay channels. Finally Higgs signal is selected with the cut on reconstructed Higgs mass region.

TABLE XII: Cut flow for $\sqrt{s} = 500$ GeV analysis

1. Missing mass	$M_{miss} > 220$ GeV
2. Transverse visible momentum	$P_T > 20$ GeV
3. Longitudinal visible momentum	$\|P_Z\| < 150$ GeV
4. Maximum momentum PFO	$P_{max} < 50$ GeV
5. Number of charged tracks	$N_{chd} > 10$
6. Reconstructed Higgs mass	$100 < M_h < 130$ GeV

TABLE XIII: Background reduction summary at $\sqrt{s} = 500$ GeV with $\mathcal{L} = 500$ fb^{-1} regarding P$(-0.8,\ +0.3)$ beam polarization. $\nu\nu\ell\ell$ and $\ell\ell\ell\ell$ processes are completely suppressed.

Cuts	$h \to bb$	$h \to c\bar{c}$	$h \to gg$	$h \to$ all	$\nu\bar{\nu}q\bar{q}$	$\nu\ell q\bar{q}$	$\ell\ell qq$	qqqq	ZWW	ZZZ
Gen	59,921	3,336	5,053	90,029	367,779	5,042,400	682,517	4,288,940	513,824	2,681
1	51,619	2,811	4,185	78,712	239,835	192,350	3,739	114,929	28,140	1,068
2	47,889	2,629	4,017	72,087	213,867	155,999	1,230	43,028	26,009	927
3	46,431	2,552	3,895	69,132	197,487	134,599	1,136	42,930	25,679	910
4	43,604	2,308	3,711	61,308	175,734	58,380	613	15,006	16,581	777
5	43,307	2,280	3,711	57,126	166,037	56,281	610	14,976	15,894	699
6	35,054	2,040	3,711	45,473	15,405	16,657	90	663	4,372	226
Efficiency	55.6%	46.0%	64.5%	41.2%	1.7×10^{-2}	2.2×10^{-3}	1.5×10^{-4}	1.7×10^{-4}	7.1×10^{-3}	7.4×10^{-2}

2. Measurement accuracies of σBR at the $\sqrt{s} = 500$ GeV

After applying all above cuts, flavor templates on $h \to b\bar{b}$, $c\bar{c}$, and gg are prepared using the Neuralnet-output for b, c, bc flavor from `LCFIVertex`. 5,000 times of Toy-MC is applied and extracted the accuracies of σBR. Fitted results by template fitting Toy-MC are shown in Fig. 12 and summarized on the Table XIV.

FIG. 12: Fitted r_s distribution for $h \to b\bar{b}$, $c\bar{c}$, and gg at $\sqrt{s} = 500$ GeV with assuming the $\mathcal{L} = 500$ fb^{-1} and P$(-0.8,\ +0.3)$ left-handed beam polarization.

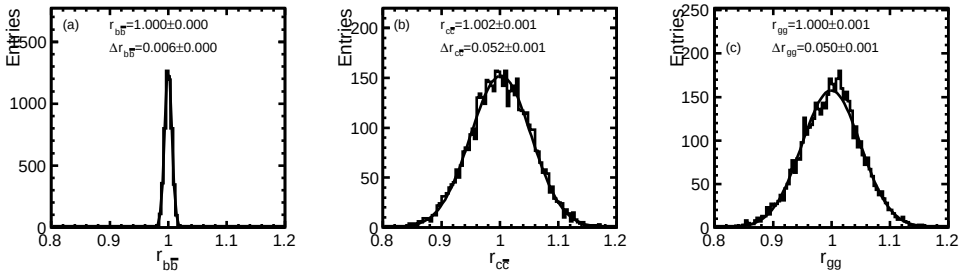

TABLE XIV: Reduction summary for h $\to$ $b\bar{b}$, $c\bar{c}$, gg channels at $\sqrt{s}$ = 500 GeV assuming $\mathcal{L}$ = 500 fb^{-1} and P(-0.8, $+0.3$) beam polarization at the Higgs mass of 120 GeV.

Integrated luminosity	500 fb^{-1}
Beam polarization P(e^-, e^+)	P(-0.8, $+0.3$)
r_{bb}	1.000 $\pm$ 0.006
r_{cc}	1.002 $\pm$ 0.052
r_{gg}	1.000 $\pm$ 0.050
$\Delta\sigma BR/\sigma BR(h \to b\bar{b})$	0.6%
$\Delta\sigma BR/\sigma BR(h \to c\bar{c})$	5.2%
$\Delta\sigma BR/\sigma BR(h \to gg)$	5.0%

Study of Higgs self-coupling at the ILC based on the full detector simulation at $\sqrt{s} = 500$ GeV and $\sqrt{s} = 1$ TeV

Junping Tian

High Energy Accelerator Research Organization (KEK), Tsukuba, Japan

(Dated: January 30, 2013)

In this analysis we investigated the feasibilities of the measurement of Higgs self-coupling at the International Linear Collider (ILC) during its two phases of operation with centre-of-mass energy of 500 GeV and 1 TeV. Three combinations of the decay modes of double Higgs strahlung process $e^+e^- \to ZHH$, where $Z \to l^+l^-$, $Z \to \nu\bar{\nu}$ and $Z \to q\bar{q}$ accompanying with both Higgs decay into $b\bar{b}$, were analyzed together at 500 GeV. The decay mode of WW fusion process $e^+e^- \to \nu\bar{\nu}HH$, where both Higgs decay into $b\bar{b}$ was analyzed at 1 TeV. Both the signal and background event samples are generated by a full detector simulation based on the International Large Detector (ILD). At 500 GeV, assuming an integrated luminosity of 2 ab^{-1} and the Higgs mass of 120 GeV, an excess of the $e^+e^- \to ZHH$ events with a statistical significance of 5.0σ is expected to be observed in case of the polarized electron and positron beams, $P(e^-, e^+) = (-0.8, +0.3)$. The cross section of $e^+e^- \to ZHH$ can be measured to the precision of 27%, corresponding to the precision of 44% on the Higgs trilinear self-coupling. At 1 TeV, in case of $P(e^-, e^+) = (-0.8, +0.2)$, we can expect the precision of self-coupling to be 18%.

Contents

I. INTRODUCTION

The Higgs sector is the piece of Standard Model which is responsible for the spontaneous breaking of electroweak symmetry and offers the source of mass generation for both the gauge bosons and fermions; the expected Higgs boson is the last particle of the Standard Model to be found by experiment. Once a Higgs-like boson is discovered, we need to verify that it is indeed the Higgs boson that condenses in the vacuum and gives masses to all the standard model particles. Higgs self-coupling is just the force that makes the Higgs boson condense in the vacuum, therefore probe of this coupling is one of the most decisive tests of the Higgs sector.

In the Standard Model, after the electroweak symmetry breaking, the Higgs potential, given as

$$V(H) = \lambda v^2 H^2 + \lambda v H^3 + \frac{1}{4}\lambda H^4, \tag{1}$$

where H is the physical Higgs field, $v \approx 246$ GeV is the vacuum expectation value of the neutral component of Higgs field and λ is the Higgs self-coupling, is uniquely determined by the Higgs self-coupling. There are three terms in this potential, the first is the Higgs mass term, with the mass $M_H = \sqrt{2\lambda v^2}$; the second term is a trilinear Higgs self interaction, with the trilinear self-coupling $\lambda_{HHH} = 6\lambda v$; the third term is a quartic Higgs self interaction, with the quartic Higgs self-coupling $\lambda_{HHHH} = 6\lambda$. Considering that all the interactions discovered up to now are gauge interactions, the second and third terms predict non-gauge interactions, which would be a completely new type of interaction. To fully verify the shape of Higgs potential, we need to measure these three terms respectively. The mass term is possible to first be measured at the Tevatron and the LHC and then precisely determined at the ILC. The quartic Higgs self-coupling turns out to be very difficult to be measured at the Tevatron, LHC and the ILC due to the very small cross section of three Higgs bosons production (less than 0.001 fb). Therefore, it becomes crucial to investigate the feasibilities of measuring the trilinear Higgs self-coupling.

On the other hand, alternatively to the Higgs Sector in the standard model, which is the simplest way spontaneously breaking the electroweak symmetry, there are several extended Higgs theories. To reveal these new physics models, the Higgs self-coupling is one of the most important discriminative quantities. One of the latest articles [1] gives a clear conclusion from the theoretical calculation in those extended theories that the Higgs self-coupling measurement is quite useful to explore new physics. In addition, studies of the Higgs self-coupling in the framework of the Minimal Supersymmetric extension of the Standard Model (MSSM) or the general Two Higgs Doublet Model (THDM), where typically there are five Higgs bosons instead of one, can be found in these references [1–4], showing that the Higgs self-coupling can significantly deviate from the standard model value, at the level of order 100% in some scenarios. The Higgs self-coupling can also be a common signature of the Higgs sector with the strong first order electroweak phase transition [5–10], which is required for a successful scenario of electroweak baryogenesis [11–13]. The new physics model with the sequential fourth generation fermions also predict large one loop contributions to the Higgs self-coupling [14]. Therefore, the precision measurement of trilinear Higgs self-coupling could directly reveal the nature of the extended Higgs sector.

II. MEASURING THE HIGGS SELF-COUPLING AT THE ILC

The measurement of trilinear Higgs self-coupling can be carried out at the ILC through two leading processes: double Higgs-strahlung process $e^+e^- \to ZHH$ [15–17] and WW fusion process $e^+e^- \to \nu\bar{\nu}HH$ [18, 19]. Figure 1 shows the cross sections of these two processes as a function of the center of mass energy. The double Higgs-strahlung process is expected to be dominant at around the center of mass energy of 500 GeV and to be taken over by the WW

fusion process at higher energy at around 1 TeV. Their tree-level Feynman diagrams are respectively shown in Figure 2 and Figure 3. However, in both cases, there exist the irreducible Feynman diagrams which have the same final-state particles but don't concern the Higgs self-coupling. The interferences between the interested Higgs self-coupling related diagrams and these irreducible diagrams make the measurement of the Higgs self-coupling more complicated. As a result of the interferences, the cross sections (σ) of $e^+e^- \to ZHH$ and $e^+e^- \to \nu\bar{\nu}HH$, as a function of the Higgs self-coupling (λ), can be formulated as $\sigma = a\lambda^2 + b\lambda + c$, where constant a comes from the contribution of Higgs self-coupling diagram, c comes from the contribution of the irreducible diagrams and b comes from the contribution of the interference between them. For a particular value of the Higgs mass of $M_H = 120$ GeV, Figure 4 shows these functions, by which we can infer the Higgs self-coupling from the cross sections of the two processes. And at the value of the standard model, the precision of the Higgs self-coupling ($\frac{\delta\lambda}{\lambda}$) is determined to be 1.8 times of the precision of the cross section of $e^+e^- \to ZHH$ ($\frac{\delta\sigma}{\sigma}$) at 500 GeV,

$$\frac{\delta\lambda}{\lambda} = 1.8\frac{\delta\sigma}{\sigma}. \tag{2}$$

In case of $e^+e^- \to \nu\bar{\nu}HH$ at 1 TeV, the factor will be 0.85,

$$\frac{\delta\lambda}{\lambda} = 0.85\frac{\delta\sigma}{\sigma}. \tag{3}$$

Here we see the complication caused by the interference, without which the factor will always be 0.5. A new weighting method developed recently [20] shows we can enhance the coupling sensitivity, as a result of which the above factors can be improved correspondingly to 1.66 and 0.76

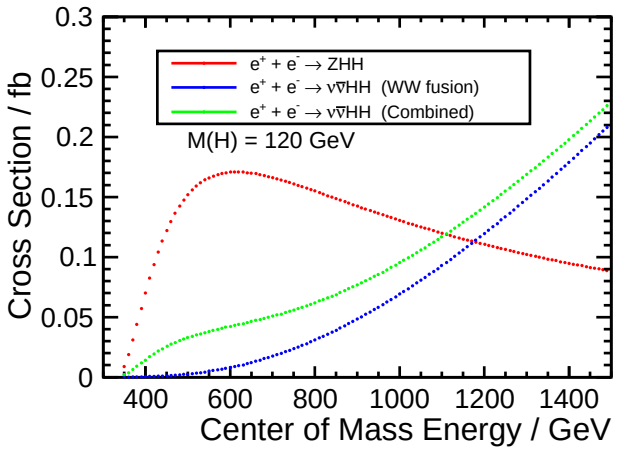

FIG. 1: The separate and combined production cross sections for the ZHH and $\nu\bar{\nu}$HH processes as a function of the center of mass energy assuming the Higgs mass of 120 GeV. The red line is for the ZHH process, the blue line is for the $\nu\bar{\nu}$HH fusion process and the green line is for the combined result.

III. SIMULATION FRAMEWORK

[This Part is to be added later, which nevertheless is common for all the DBD benchmark analyses. In this analysis the $\gamma\gamma$ to low p_t hadrons background has not been overlaid.]

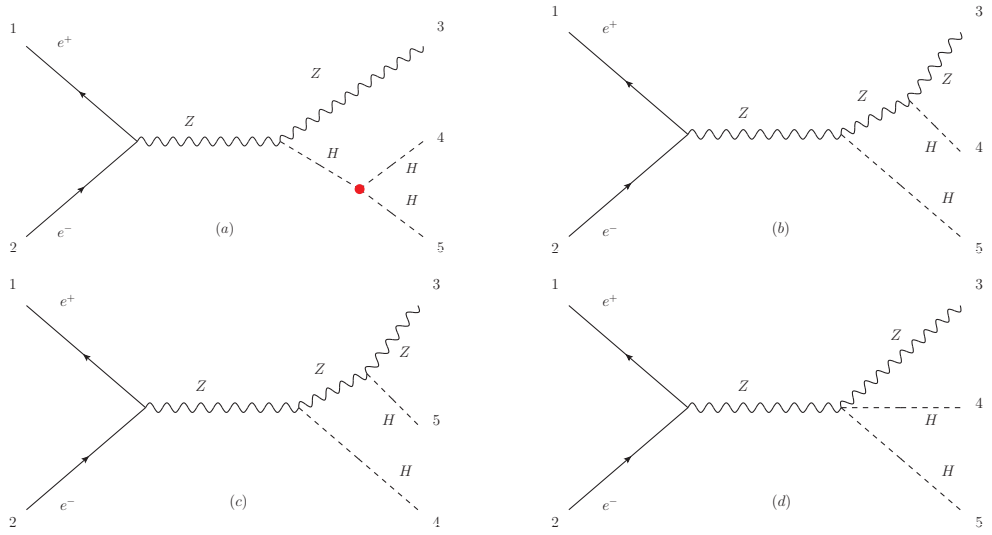

FIG. 2: Feynman diagrams for the double Higgs strahlung process $e^+e^- \to ZHH$. (a): involving trilinear Higgs self-coupling; (b), (c), (d): the irreducible diagrams.

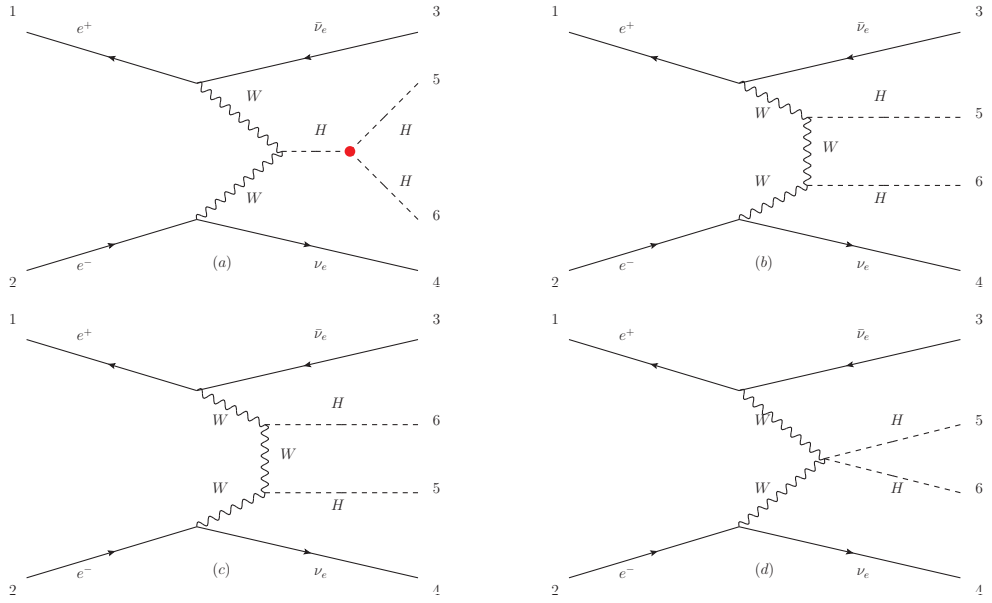

FIG. 3: Feynman diagrams for the WW fusion process $e^+e^- \to \nu\bar{\nu}HH$. (a): involving trilinear Higgs self-coupling; (b), (c), (d): the irreducible diagrams.

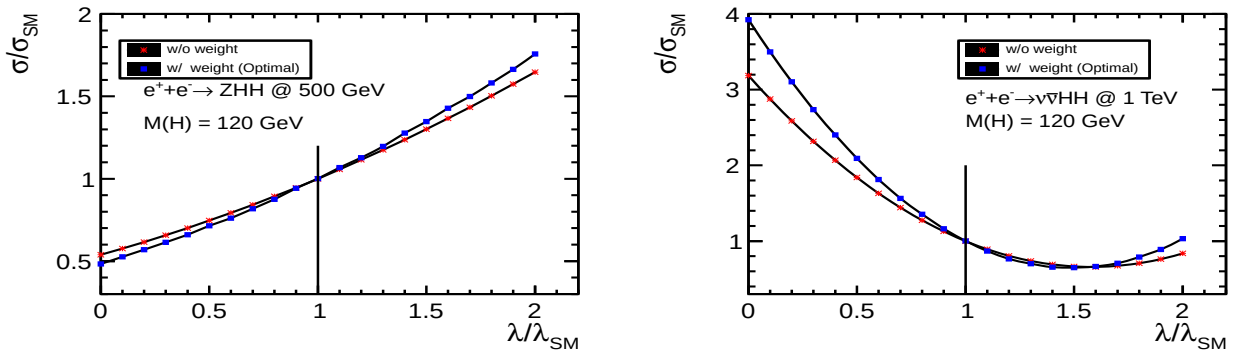

FIG. 4: The evaluation of cross section as a function of the Higgs self-coupling. left: for $e^+e^- \to ZHH$ at 500 GeV; right: for $e^+e^- \to \nu\bar{\nu}HH$ at 1 TeV. The λ_{HHH} stands for the Higgs trilinear self-coupling and $\lambda_{HHH}(SM)$ stands for the standard model value, which is indicated by the vertical line. The red ones are without weighting method and the blue ones are with weighting method.

A. Accelerator and Detector

B. Event Generator

C. Simulation and Reconstruction

IV. ANALYSES OF $e^+e^- \to ZHH$ AT 500 GEV

A. Analysis of the mode $ZHH \to l^+l^-HH \to l^+l^-b\bar{b}b\bar{b}$ at 500 GeV

1. *Pre-selction*

In this search mode, the final state of a candidate signal event contains two isolated charged leptons and four b quarks segmenting into four jets. For the pre-selection, we first require there are two isolated oppositely charged leptons and then force all the particles other than the two selected leptons to four jets and pair the four jets to two Higgs boson candidates.

a. Isolated Lepton Selection Isolated electrons and muons are identified from all of the PFOs. Each PFO contains the information from different sub-detectors, such as energies deposited in the ECAL and HCAL. An electron deposits almost all the energy in ECAL while a muon deposits very small fraction of its energy in both ECAL and HCAL. Other charged particles, being mainly hadrons, deposit most of their energy in HCAL. These pieces of information are used for electron and muon identification. The following two quantities are checked for each PFO. One is the $\frac{E(\text{ecal})}{E(\text{total})}$ ratio, the other is the $\frac{E(\text{total})}{P}$ ratio, where $E(\text{total}) = E(\text{ecal}) + E(\text{hcal})$, $E(\text{ecal})$ and $E(\text{hcal})$ are the energies deposited in ECAL and HCAL and P is the momentum. Some constraints are added to the vertex position which can reduce the selection of the leptons from B-hadrons.

- For electron identification, two samples of PFOs from the process $e^+ + e^- \to e^+e^-HH$ are investigated by using MC truth information. One is the real prompt charged electrons, and the other is all the charged PFOs other than the two prompt charged leptons. Figure 5 shows the distributions of the above two quantities for these two samples, where the red histogram is for the prompt electrons and the blue is for non-prompt charged PFOs. Since the red and blue distributions are very different it is straightforward to add requirements on these two quantities

$$e: \begin{cases} \frac{E(\text{ecal})}{E(\text{total})} > 0.9 \\ 0.8 < \frac{E(\text{total})}{P} < 1.2 \end{cases} \tag{4}$$

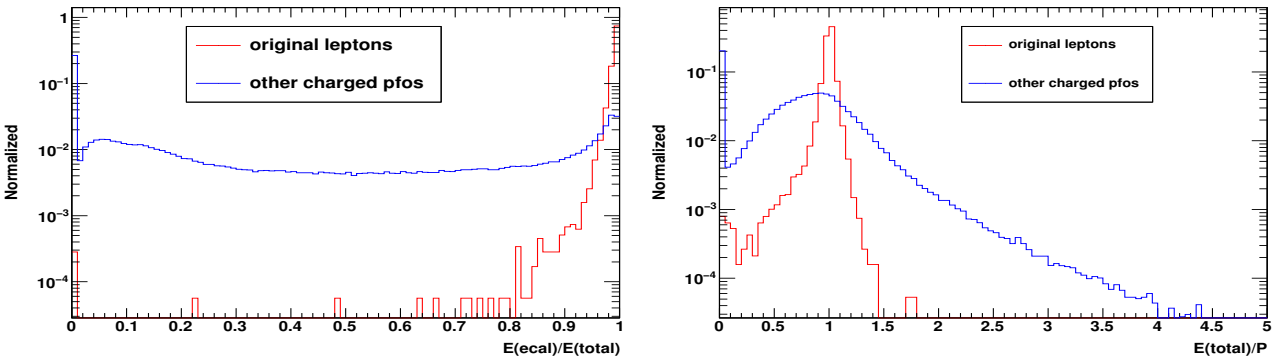

FIG. 5: The distribution of $\frac{E(\text{ecal})}{E(\text{total})}$ (left) and $\frac{E(\text{total})}{P}$ (right) for PFOs in sample $e^+ + e^- \to e^+e^-HH$. The red histogram is for prompt electrons and the blue one is for other charged non-original PFOs.

After these requirements, the mis-identified electrons are mainly from: (i) charged pions, which become neutral pions through charge exchange interaction with the nuclei inside ECAL, decaying into photons which deposit almost all of their energies in ECAL; (ii) electrons from weak decays of b or c quarks, such as $b \to cW^- \to ce^-\bar{\nu}_e$; (iii) electrons from a Higgs boson decaying into WW^* followed by a semi-leptonic W decay. Type (i) and (ii) mis-identified PFOs usually have smaller momenta and more PFOs around them due to parton showering and fragmentation than the prompt electrons. It is hence possible to further reduce the mis-identification by using the cone energy. For each PFO, define a cone with angle θ, around the momentum of that PFO as shown in Figure 6, and sum up the energies of the other PFOs which are inside this cone. This energy sum is called the cone energy. If only the charged PFOs are considered, then the sum is called the charged cone energy. The effect of bremsstrahlung tends to give the prompt electrons a sizable cone energy. This makes the charged cone energy more discriminative to separate the prompt electrons from the other PFOs. Figure 7 shows a scatter plot of charged cone energy versus momentum of the PFOs from these two samples, where the red points denote prompt electrons and the blue points denote the remaining mis-identified non-prompt charged PFOs. By using Fisher classification, we decided to impose

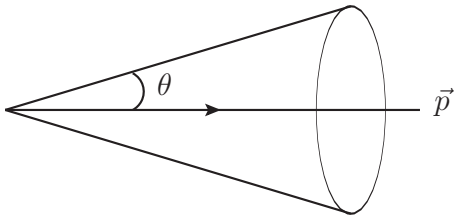

FIG. 6: Schematic view of a cone around a particle with momentum $\vec{p}$. The cone angle is θ.

$$P - 0.25E_{\text{cone}} > 12.6 \text{ GeV} \tag{5}$$

- For muon identification, the strategy is very similar to the electron identification, plus that we require the energy deposited in Yoke to be larger than 1.2 GeV. Samples for prompt muons and the other charged PFOs are from the $e^+ + e^- \to \mu^+\mu^-HH$ process. The distributions of $\frac{E(\text{ecal})}{E(\text{total})}$ and $\frac{E(\text{total})}{P}$ are shown in Figure 8. The requirements to these two quantities are

$$\mu: \begin{cases} \frac{E(\text{ecal})}{E(\text{total})} < 0.5 \\ \frac{E(\text{total})}{P} < 0.3 \end{cases} \tag{6}$$

In this case, the mis-identified muons are mainly from: (i) charge pions which have small momentum and do not reach HCAL, thereby having small energy deposits in ECAL and HCAL; (ii) and (iii) are similar to the electron case, namely from weak decays of b, c quarks and from Higgs decaying into WW^*. Also, the charged cone energy and momentum can be used to further reduce the mis-identification. A scatter plot of the charged

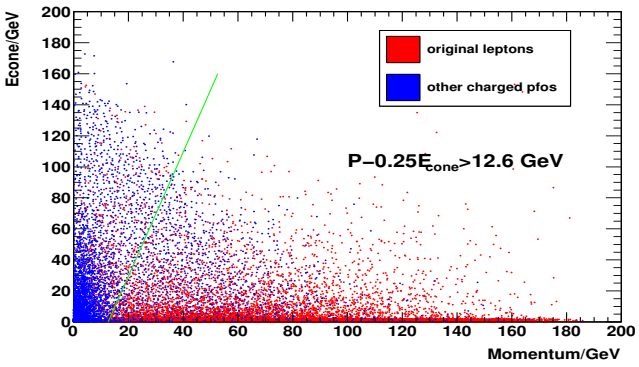

FIG. 7: Scatter plot of charged cone energy versus momentum for PFOs in sample $e^+ + e^- \to e^+e^-HH$. Red points denote original electrons and blue ones denote other charged PFOs.

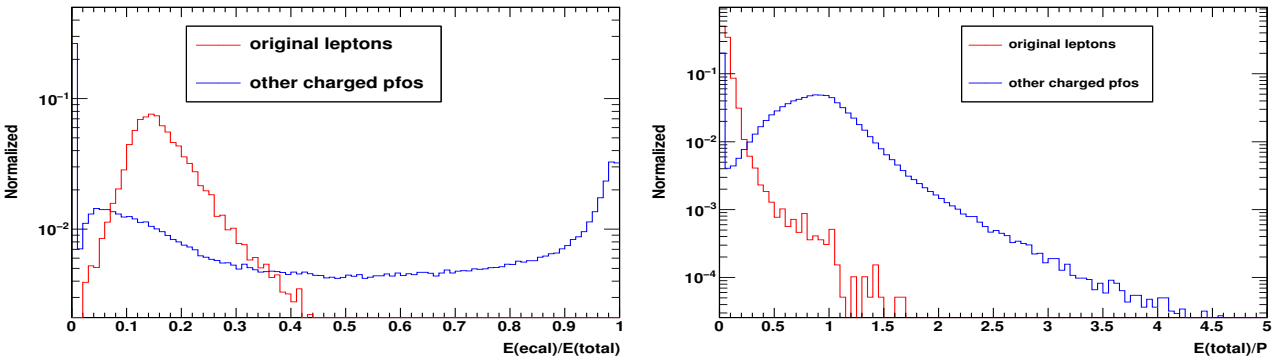

FIG. 8: The distribution of $\frac{E(\text{ecal})}{E(\text{total})}$ (left) and $\frac{E(\text{total})}{P}$ (right) for PFOs in the $e^+ + e^- \to \mu^+\mu^-HH$ sample. The red histogram is for prompt muons and the blue one is for the other charged PFOs.

cone energy versus momentum for the samples of prompt muons and the other non-prompt PFOs are shown in Figure 9. We require

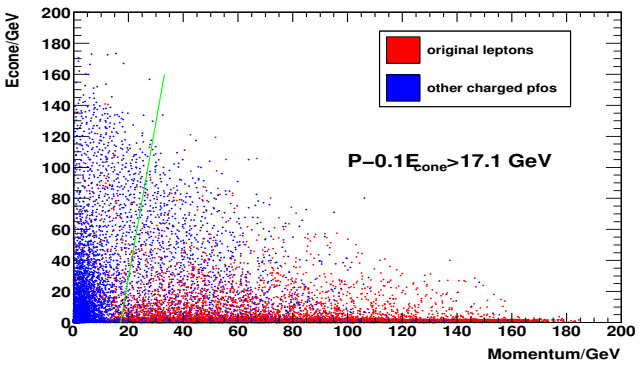

FIG. 9: Scatter plot of charged cone energy versus momentum for PFOs in the $e^+ + e^- \to \mu^+\mu^-HH$ sample. Red points denote prompt muons and blue ones denote the other charged PFOs.

$$P - 0.1E_{\text{cone}} > 17.1 \text{ GeV}. \tag{7}$$

The angle of the cone in Figure 6 is expected to affect the performance of charged lepton selection. To minimize the mis-identification, the value of the cone angle θ is scanned from $\cos\theta = 0.8$ to $\cos\theta = 1$. At each value, while fixing the efficiency for the prompt lepton identification to 98%, we looked at the efficiency of the other charged

PFOs being identified. The result is shown in Figure 10. The optimized cone angle $\cos\theta = 0.98$ giving the minimal mis-identification efficiency is adopted.

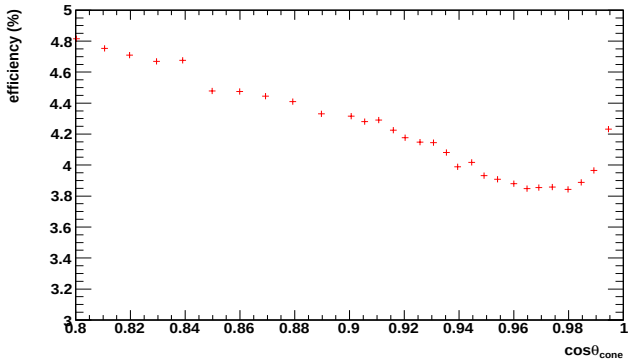

FIG. 10: Optimization of cone angle using PFOs in the $e^+ + e^- \to e^+e^-HH$ sample.

For each event, at least two oppositely charged PFOs are required to be both identified as electron or muon. If there are more than two PFOs identified, we look at all the pairs which have opposite charge. The pair of which the invariant mass is the nearest to the mass of Z, $M(Z) = 91.18$ GeV, is selected as the two prompt charged leptons, effectively suppressing type (iii) mis-identification. As a loose requirement, the invariant mass of the two selected charged leptons $M(l^+l^-)$ should satisfy

$$|M(l^+l^-) - M(Z)| < 40 \text{ GeV}. \tag{8}$$

The distribution of $M(l^+l^-)$ for the signal events after the above selection is shown in Figure 11, where the bremsstrahlung and FSR effects are recovered by using algorithms in ZFinder.

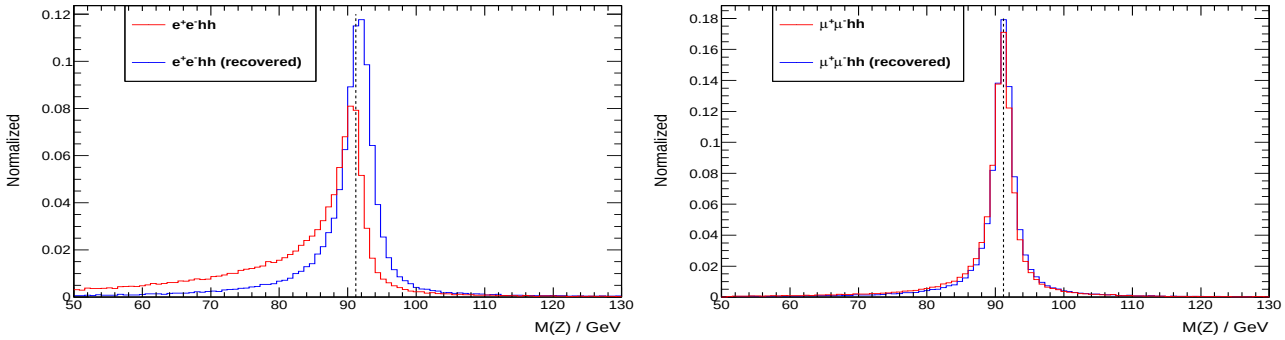

FIG. 11: Invariant mass of the two selected charged leptons. Left one is for the electron mode of the signal $e^+ + e^- \to e^+e^-HH$ process; Right one is for the muon mode of the signal $e^+ + e^- \to \mu^+\mu^-HH$ process.

b. Jet Clustering and Jet Pairing After the two charged leptons are selected, all the other PFOs are forced to four jets by using the Durham jet algorithm. Then the four jets j_1, j_2, j_3 and j_4 are combined to two pairs, each of which contains two jets. Among all the possible combinations, the one which minimizes the χ^2 is selected. The χ^2 is defined by

$$\chi^2 = \frac{(M(j_1,j_2) - M(H))^2}{\sigma_H^2} + \frac{(M(j_3,j_4) - M(H))^2}{\sigma_H^2} \tag{9}$$

where $M(j_1,j_2)$ is the invariant mass of jets j_1 and j_2, $M(H)$ is the nominal Higgs mass, and σ_H is the Higgs mass resolution, which doesn't affect the combination here. The two jets pairs are reconstructed as two Higgs bosons. The order of the two Higgs bosons are determined by the order of jets output from the jet clustering algorithm. Usually a jet output earlier has a relatively larger momentum. While pairing, $M(j_1,j_2)$ and $M(j_3,j_4)$ are required to satisfy loose cuts:

$$|M(j_1,j_2) - M(H)| < 80 \text{ GeV}, \quad |M(j_3,j_4) - M(H)| < 80 \text{ GeV}. \tag{10}$$

The remaining signal and background events can be grouped into four: first one, called full hadronic background, such as *bbcsdu*, *bbuddu*, *bbcssc* and *bbbb*, without leptons in the parton level final states; second one, called jets-poor background, such as *llbb*, only two partons with two leptons in the parton level final states; third one, called semi-leptonic background, such as $l\nu bbqq$, with one charged lepton, one missing neutrino and four partons in the parton level final states; the last one, called the most signal-like background, such *llbbbb* and *llbb*H, with two charged leptons and four partons in the parton level final states. Since the event topologies and the amounts of contamination from these four groups are very different, it is not very efficient if we use only one multivariate classification for the whole backgrounds. Actually it is almost impossible to find any global minimum if we put together the backgrounds with very different topologies and very different weights, considering the limited MC statistics. Instead of one multivariate classification, the strategy adopted is to use a separate multivariate classification to suppress the backgrounds in each group.

a. Full Hadronic Backgrounds The full hadronic backgrounds, which mainly come from $e^+ + e^- \to t\bar{t}$, WWZ and ZZ, are significantly suppressed by the pre-selection mainly due to the requirement of two charged leptons. Even though, the number of remaining events is still much larger than that of the signal. For these backgrounds, the selected charged leptons must have come from the hadronization and decay, as a result of which the momenta of the charged leptons should relatively be smaller and the cone energy relatively larger. A natural strategy to further suppress them is to apply tighter cuts on the cone energy and momenta of the two selected charged leptons. Figure 12 shows the scatter plot of the total cone energy ($E_{\rm cone}12$) versus the total charged cone energy ($E_{\rm cone}$Charge12) of the two leptons, and the distribution of the total momentum ($p{\rm Lep}_1 + p{\rm Lep}_2$). Tighter requirements are imposed to further suppress the full hadronic backgrounds, which is denoted as Cut1:

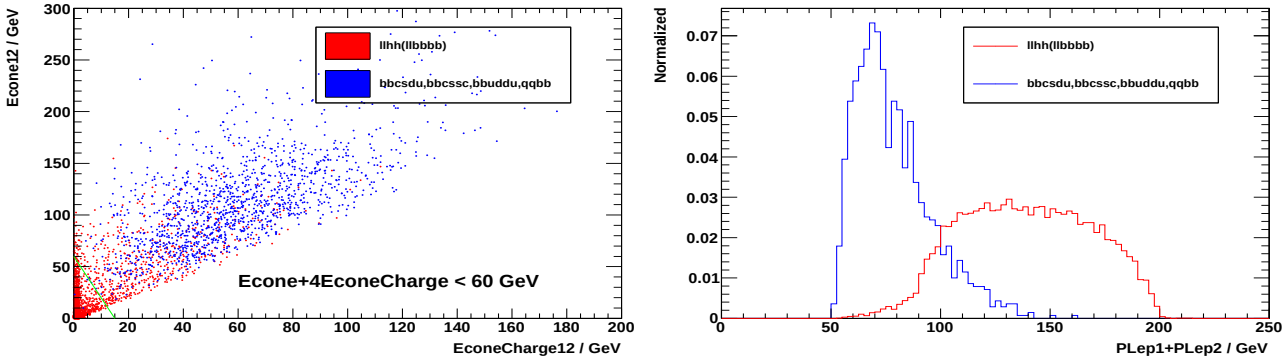

FIG. 12: The scatter plot of $E_{\rm cone}12$ versus $E_{\rm cone}$Charge12(left) and the distribution of $p{\rm Lep}_1 + p{\rm Lep}_2$ (right). Red denotes signal and blue denotes full hadronic backgrounds.

$$\text{Cut1}: \begin{cases} E_{\rm cone}12 + 4E_{\rm cone}{\rm Charge12} < 60 \text{ GeV} \\ p{\rm Lep}_1 + p{\rm Lep}_2 > 80 \text{ GeV} \end{cases} \tag{11}$$

After these tighter requirements, the full hadronic backgrounds are almost completely eliminated.

b. Jets-Poor Backgrounds The jets poor backgrounds *llbb* and *llcc*, which mainly come from ZZ, ZZ^*, $b\bar{b}Z$ and l^+l^-Z, are the dominant backgrounds after the pre-selection. Though there are only two partons in their parton level final states, due to the gluon to qq and the imperfection of the jet clustering algorithm, they can be clustered to four jets and some of them survived the mass constraints in Eqn. 10. To suppress these backgrounds while keeping as many signal events as possible, one of the multivariate data analysis methods, neural-net is used. The following discriminative quantities are included for the neural-net training:

- Y value, which is given by the jet clustering algorithm. Because there are only two partons for these jets poor backgrounds, their Y values are relatively smaller than that of the signal events. Among all the Y values, $Y_{4\to3}$ and $Y_{3\to2}$ turned out to be the most discriminative. The distributions of $Y_{4\to3}$ and $Y_{3\to2}$ are shown in Figure 13, respectively denoted by "yminus"and "yplus2".

- Thrust, which is derived from the quantity

$$p = \frac{\sum_i |\vec{p}_i \cdot \vec{n}|}{\sum_i |\vec{p}_i|} \tag{12}$$

where $\vec{p}_i$ is the momentum of a PFO, $\vec{n}$ is any possible unit vector $|\vec{n}| = 1$ and the summation is over all the PFOs in each event. The thrust is defined to be the maximum of p, and the corresponding $\vec{n}$ is called the axis of the event. The thrust value reflects the anisotropy of an event, indicating if there is any special direction favored by this event. Because these jets poor backgrounds are mainly from two-body t-channel processes, most of the PFOs in each event are very forward or backward. Their thrust is much closer to 1 than that of the signal, which is from a three-body process. The axis of these backgrounds is much closer to the beam direction than that of the signal. The distributions of the thrust value and the polar angle of the thrust axis are shown in Figure 13, respectively denoted by "pthrust" and "cosaxis".

- Reconstructed Z mass. Some of these backgrounds are from ZZ, Zγ, or $\gamma\gamma$ fusion processes and from s-channel processes, where two charged leptons in the final states are not from a Z decay. In this case, the reconstructed Z mass does not peak at the nominal Z mass, as indicated by the flat part in the distribution of the reconstructed Z mass in Figure 13, denoted by "mz".

- The total number of PFOs. For this background, the total number of PFOs is much smaller than that of the signal, because there are only two partons. The distribution of this quantity is shown in Figure 14, denoted by "npfos".

- The smallest number of PFOs in a jet. For the same reason, the smallest number of PFOs in a jet is much smaller than that of the signal. The distribution of this quantity is shown in Figure 14, denoted by "npfomin".

- The largest jet momentum when reconstructed as two jets. If we force the PFOs other than the two selected charged leptons to two jets, the momenta of these jets for the background will be relatively larger than signal. The Distribution of this quantity is shown in Figure 14, denoted by "pjmaxjets2".

- The largest angle between the reconstructed Z and the other two jets. Some of these backgrounds come from $e^+ + e^- \to b\bar{b}Z$, where Z is radiated from one of the two b partons. In this case, the Z is very close to one of the two b jets. The distribution of this quantity is shown in Figure 13, denoted by "cosjzmax2".

These quantities are used as input variables by the MLP method in the TMVA package [21]. A neural-net is trained for the signal and the *llbb* background. For the neural-net training, additional statistically independent signal e^+e^-HH, $\mu^+\mu^-HH$ and background *llbb* samples are used. The weights for different processes are normalized to the corresponding cross sections. The statistics of the training samples are higher than 2 ab^{-1} for both the signal and the background. The neural-net outputs and cut efficiencies for the signal and the background are shown in Figure 15. The *llbb* background is well separated by the neural-net output (MLP$_{llbb}$). A cut, MLP$_{llbb} > 0.56$, is imposed to suppress the *llbb* background, denoted by MLP1. Though the neural-net is trained for the *llbb* background, another jets-poor background *llcc* is also significantly suppressed by this cut.

c. Semi-leptonic Backgrounds The semi-leptonic backgrounds such as $e^-\bar{\nu}b\bar{b}c\bar{s}$, $e^-\bar{\nu}b\bar{b}u\bar{d}$, and their corresponding muon or tau modes, together with their conjugate modes, are mainly from $t\bar{t}$ and W^+W^-Z. After the pre-selection, they are the second dominant backgrounds, being hundreds times more than the signal events. Unlike the jets-poor backgrounds, these semi-leptonic backgrounds have four quarks, but only one prompt charged leptons. We trained another neural-net to suppress these backgrounds by using the following quantities:

- Visible energy and missing P_t. Because there's one prompt neutrino in the backgrounds, the visible energy is smaller and the missing P_t is larger for the backgrounds than for the signal. The distributions of these two quantities are shown in Figure 16, respectively, denoted by "evis" and "mpt".

- Cone energy and momentum of the lower momentum selected charged lepton. Because there's only one prompt charged lepton in the backgrounds, the other selected charged lepton must have originated from hadronization and decay, which has larger charged cone energy and smaller momentum. The distributions of these two quantities are shown in Figure 16, respectively, denoted by "econec2" and "plmin".

- Reconstructed Z mass. The invariant mass of the two selected charged leptons should be very different for the backgrounds, as indicated in Figure 17, denoted by "mz".

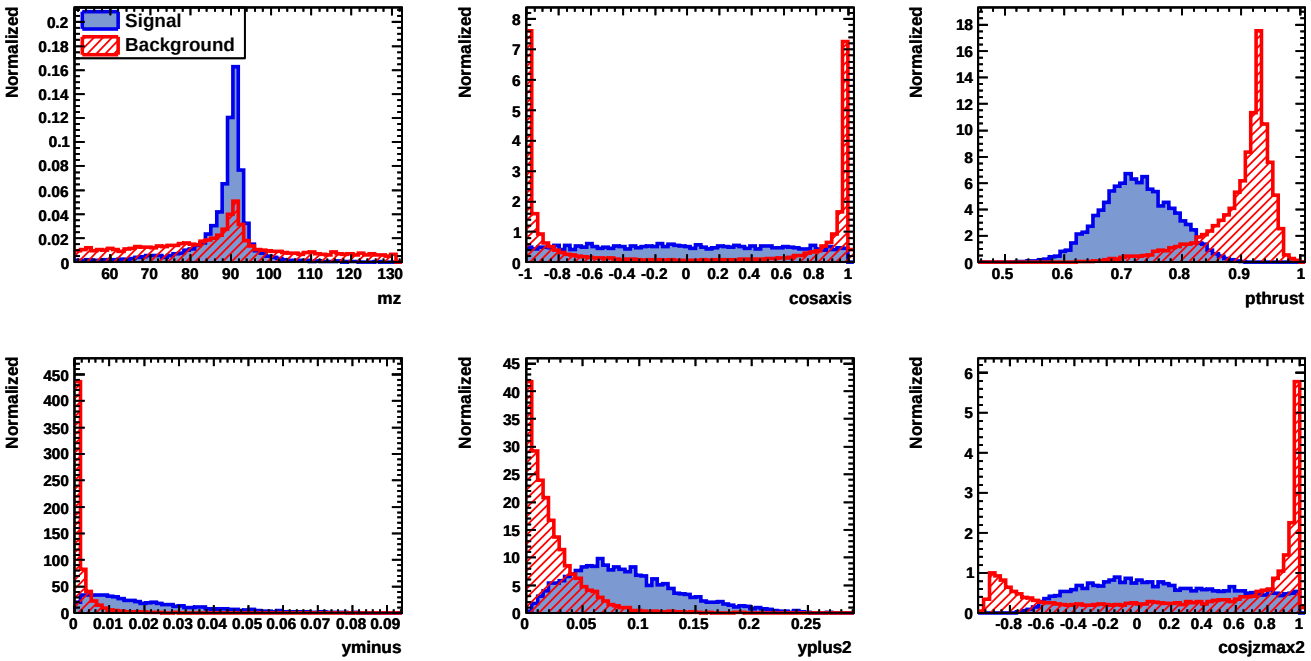

FIG. 13: Discriminative quantities for the signal (blue) and the jets-poor backgrounds *llbb* (red). The variable names are explained in the text.

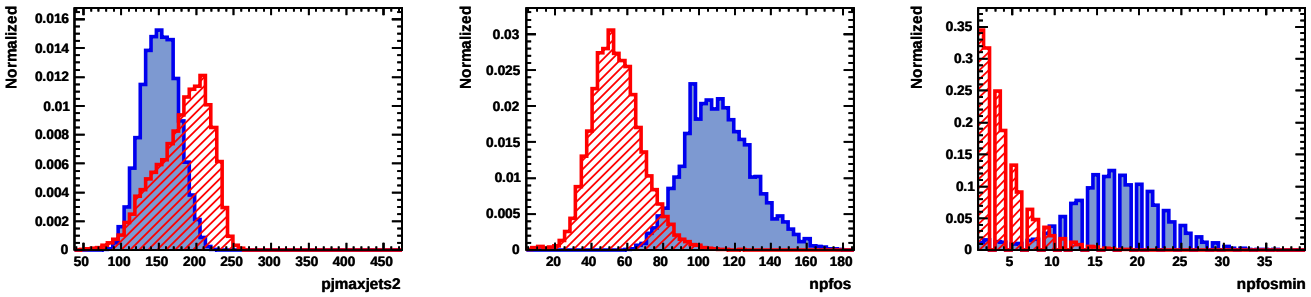

FIG. 14: Discriminative quantities for the signal (blue) and the jets-poor backgrounds *llbb* (red). The variable names are explained in the text.

- The total number of PFOs. During parton showering, a b quark usually results in more particles than light quarks. So the total number of PFOs for the backgrounds is smaller than that of the signal. This information is independent of the b tagging algorithm. The distribution of this quantity is shown in Figure 17, denoted by "npfos".
- Reconstructed W mass. The four jets are ordered from the largest b-likeness to the smallest. The backgrounds contain two b quark jets and two light quark jets. The two light quarks are from a W decay. The invariant mass of the 3rd and 4th jets are reconstructed as the W mass. The distribution of this quantity is shown in Figure 16, denoted by "massb34".
- Angle between two b jets. A large fraction of these backgrounds come from $t\bar{t}$, where the angle between two prompt b jets is relatively large. The angle between 1st and 2nd jets are reconstructed as the angle between the two prompt b jets. The distribution of this quantity is shown in Figure 16, denoted by "cosbmax".

Statistically independent $llHH$ signal sample and the $lvbbqq$ background samples are used for the neural-net training. The statistics are higher than 2 ab^{-1} for both the signal and the background. The neural-net outputs and cut efficiencies for signal and background are shown in Figure 18. The $lvbbqq$ background can well be separated by the

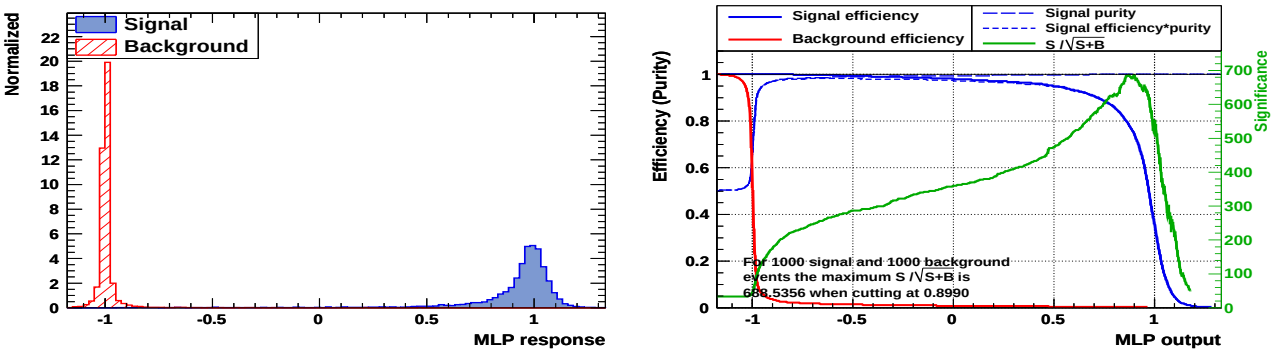

FIG. 15: (left): The neural-net output for the signal versus the *llbb* background, where the blue histogram is for the signal and the red one is for *llbb*. (right): The cut efficiencies for the signal and background at different cut values on neural-net output, where the solid blue curve is for the signal and the red one is for *llbb*.

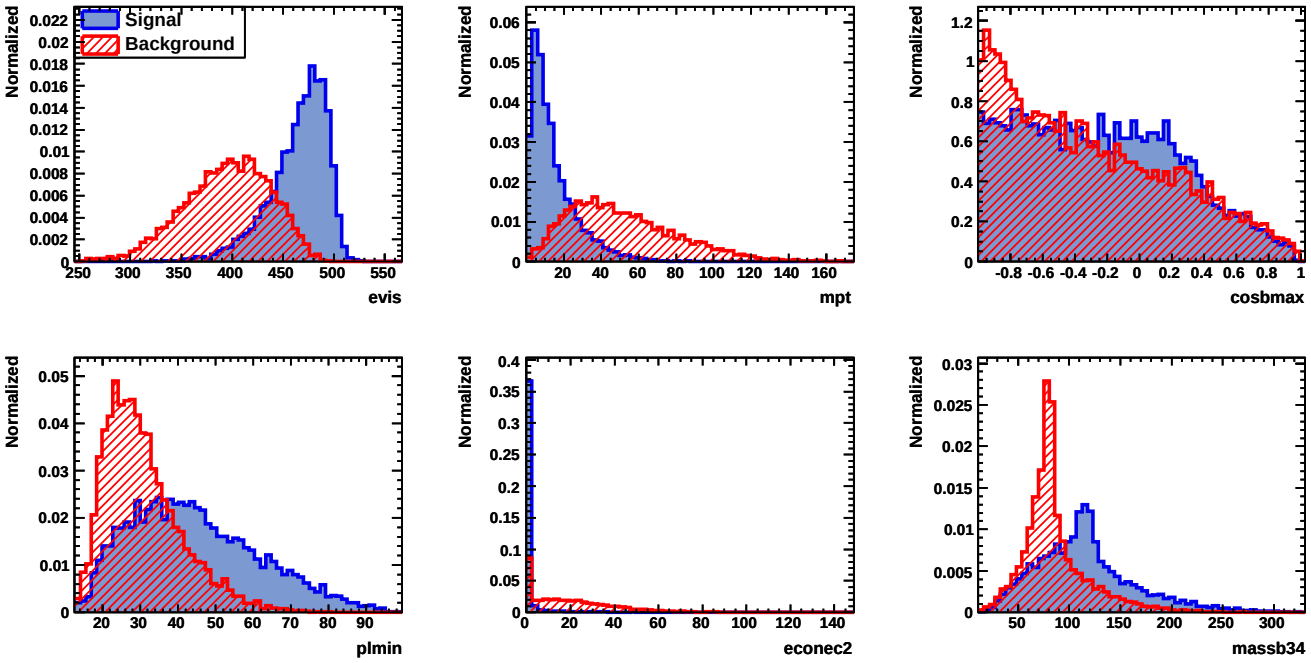

FIG. 16: Discriminative quantities for the signal (blue) and the semi-leptonic backgrounds *lvbbqq* (red). The variable names are explained in the text.

neural-net output (MLP_{lvbbqq}). A cut, $\mathrm{MLP}_{lvbbqq} > 0.81$, is applied to suppress the *lvbbqq* background, denoted by MLP2.

d. Backgrounds with Same Final States These backgrounds including *llbbbb* and *llbbH* mainly come from ZZZ and ZZH. Though their cross sections are not as large as the previous backgrounds, they have the same parton level final states as the signal, and, consequently, are more difficult to suppress. The quantities used in the previous neural-nets are of little use, requiring quantities related to the invariant mass and angular distributions to suppress them. For this purpose yet another neural-net is trained using the following quantities:

- Reconstructed Higgs mass. The two Higgs bosons masses should be the most discriminative to separate these backgrounds. The distributions of these two quantities are shown in Figure 20, respectively, denoted by "mh1" and "mh2".
- Reconstructed Z, H and Z, Z masses. In order to take maximal use of the mass information, in addition to

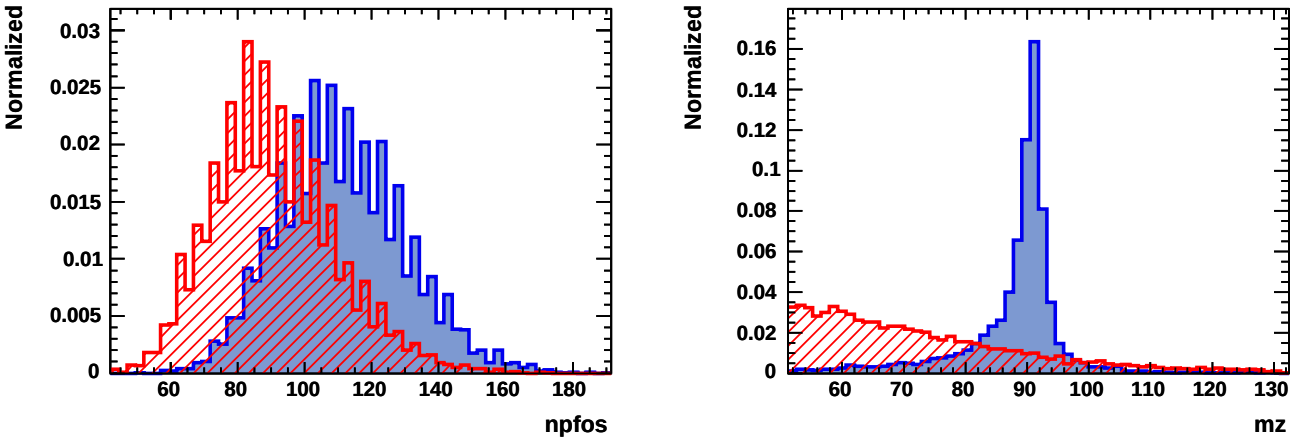

FIG. 17: Discriminative quantities for the signal (blue) and the semi-leptonic backgrounds *lvbbqq* (red). The variable names are explained in the text.

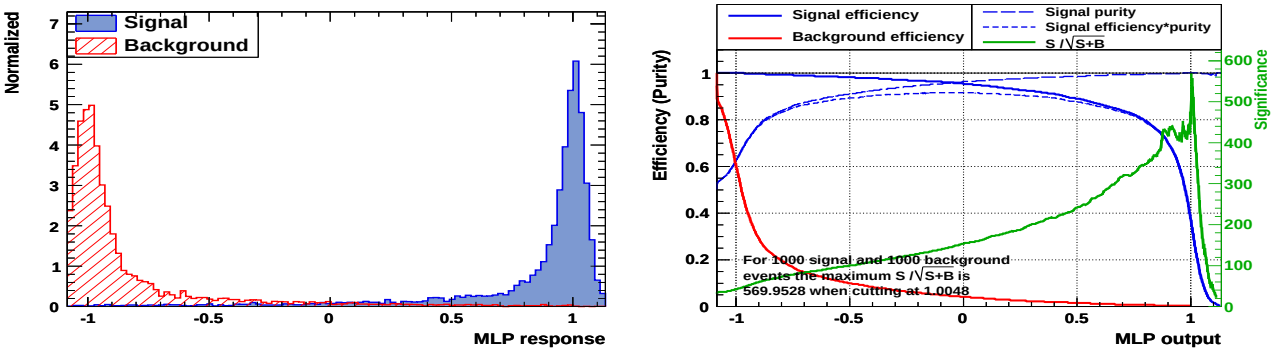

FIG. 18: (left): The neural-net output for the signal versus the *lvbbqq* background, where the blue histogram is for the signal and the red one is for *lvbbqq*. (right): The cut efficiencies of the signal and background at different cut values of the neural-net output, where the solid blue curve is for the signal and the red one is for *lvbbqq* background.

the two Higgs boson masses reconstructed as from the signal process, the four jets are also paired as from the l^+l^-ZH and l^+l^-ZZ processes. The reconstructed Z and Higgs masses in the case of l^+l^-ZH pairing, though correlated with the two Higgs masses in the case of l^+l^-HH pairing, can offer some additional discriminative power to suppress the *llbbH* background. The distributions of these reconstructed Z and Higgs masses are shown in Figure 20, respectively, denoted by "mzzh" and "mhzh". Similarly, the reconstructed two Z masses in the case of l^+l^-ZZ pairing are useful to suppress the *llbbbb* background, distributions of which are shown in Figure 20, respectively, denoted by "mz1zz" and "mz2zz".

- t-channel characteristics. The processes $e^+ + e^- \to ZZZ$ and $e^+ + e^- \to ZZH$ are dominated by diagrams stem from the t-channel process $e^+ + e^- \to ZZ$, with one more Z boson strahlung from the electron line or one more Higgs strahlung from a Z, as shown in Figure 19. This feature makes the two Z bosons emitted from the electron line move very fast and very forward. To effectively use this information, each event is re-reconstructed as from ZZZ or ZZH, and the boson candidate with the largest momentum among the three is identified for the both hypotheses. The largest momentum and its polar angle reflect the t-channel characteristics, distributions of which are shown in Figure 21, respectively, denoted by "p1zzz" and "cos1zzz"in case of ZZZ, "p1zzh" and "cos1zzh"in case of ZZH.

For the neural-net training, statistically independent *llHH* signal samples and the *llbbbb* and *llbbH* background samples are used, with each sample having statistics higher than 2 ab^{-1}. The neural-net outputs and cut efficiencies for the signal and backgrounds are shown in Figure 22. The *llbbbb* and *llbbH* backgrounds are not as well separated as

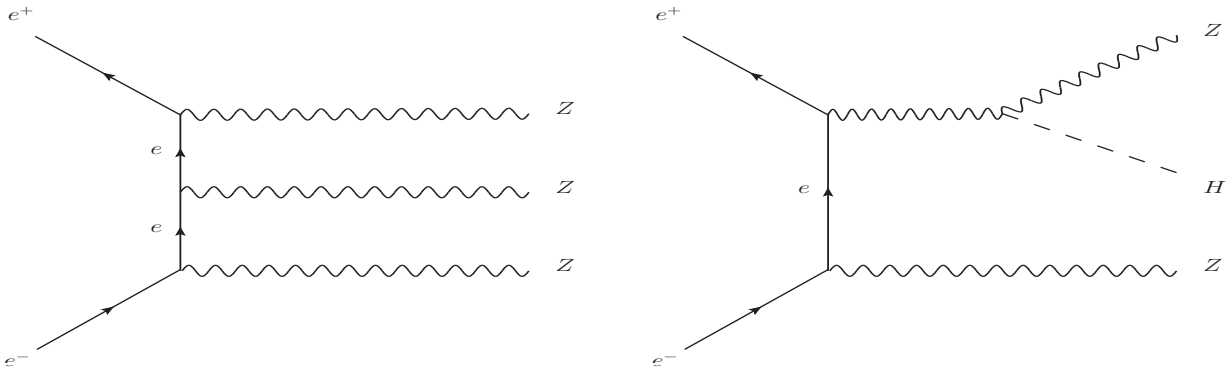

FIG. 19: Typical Feynman diagrams for $e^+ + e^- \to ZZZ$ (left) and $e^+ + e^- \to ZZH$(right).

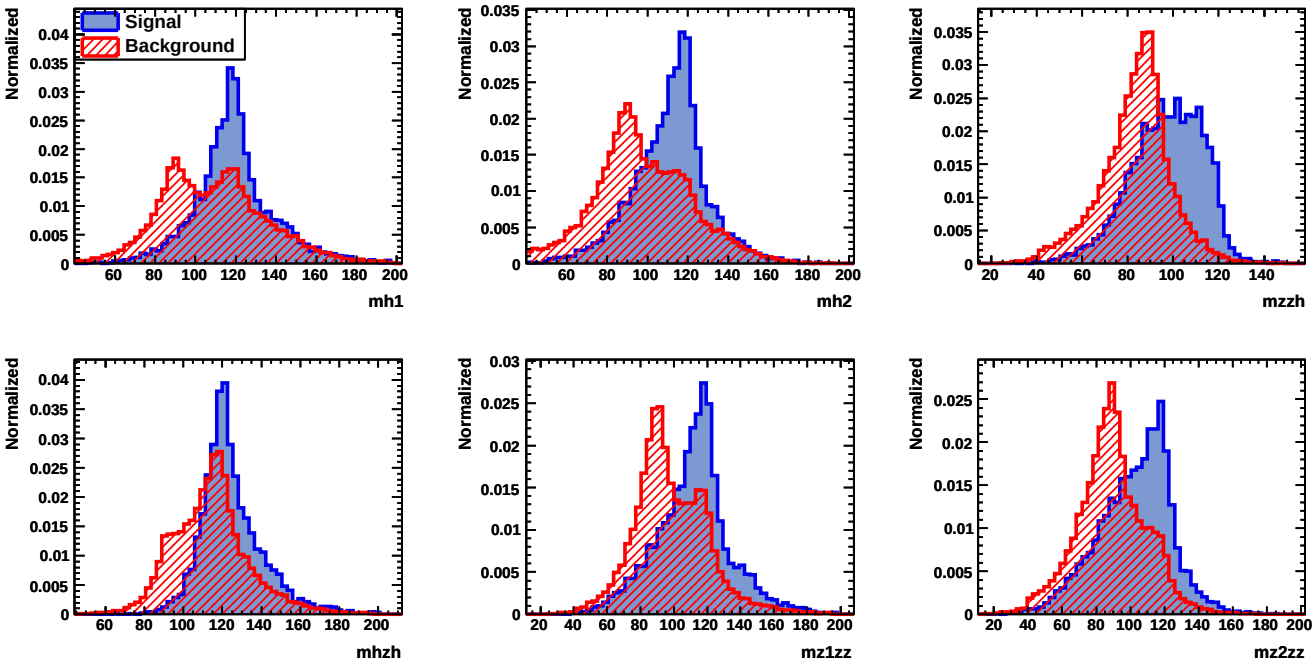

FIG. 20: The discriminative quantities for the signal (blue) and the same final states backgrounds *llbbbb*, *llbbH* (red). The variable names are explained in the text.

the previous two backgrounds. A requirement to the neural-net output $\mathrm{MLP}_{llbbbb} > -0.5$ is imposed to suppress the same final states background, denoted by MLP3. Because the two Higgs masses are the most discriminative quantities in this neural-net, this cut is also effective to suppress all the other backgrounds.

e. B tagging Though the jets-poor backgrounds and the semi-leptonic backgrounds are significantly suppressed by the neural-net, the number of remaining background events is still much larger than that of the signal. On the other hand, so far we have only considered the backgrounds which contain at least two b quarks in the parton level final states. Information of flavour tagging can be used to eliminate the backgrounds with less than two b quarks, and further suppress the jets-poor and the semi-leptonic backgrounds.

For each jet, three outputs (b-likeness, c-likeness and bc-likeness) are calculated. The signal mode is supposed to have four b jets. The b-likeness of the four jets are investigated. To make the difference between the signal and the background more significant, the four jets are ordered by the b-likeness from the largest to the smallest. The distributions of the four b-likeness values are shown in Figure 23, denoted by Bmax1, Bmax2, Bmax3 and Bmax4, where Bmax1 > Bmax2 > Bmax3 > Bmax4. One can see that Bmax1 is usually large and Bmax4 is usually small for both the signal and the backgrounds. Bmax3 turn out to have the most discriminative power. The following cut on

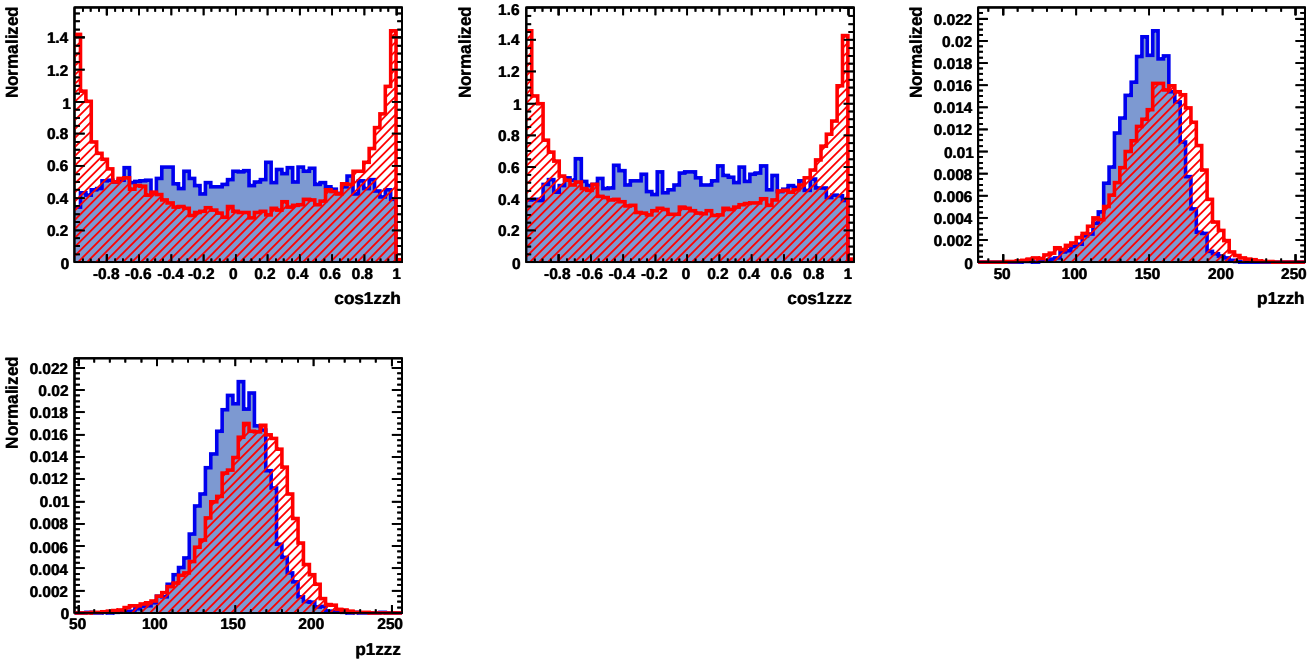

FIG. 21: The discriminative quantities for the signal (blue) and the same final states backgrounds *llbbbb*, *llbbH* (red). The variable names are explained in the text.

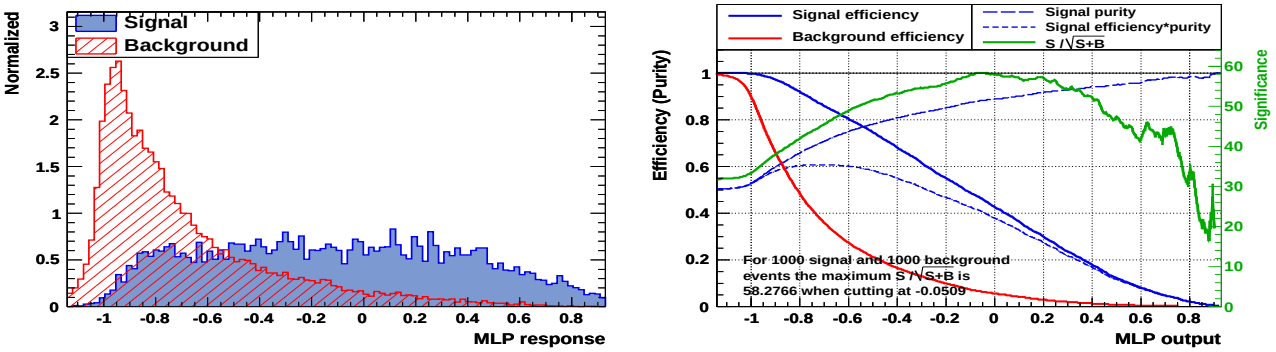

FIG. 22: (left): The neural-net outputs for the signal and the *llbbbb*, *llbbH* backgrounds, where the blue histogram is for the signal and the red one is for *llbbbb* and *llbbH*. (right): The cut efficiencies for the signal and the background at different cut values on the neural-net output, where the solid blue curve is for the signal and the red one is for *llbbbb*, *llbbH*.

Bmax3, denoted by B tagging, is applied to suppress the backgrounds:

$$\text{Bmax3} > 0.19. \tag{13}$$

3. Results

The number of the signal and background events remained after the final selection are shown in the reduction table I and II, where all the events are separated into two categories, electron-type and muon-type. The finally cuts in these two categories are summarized as following:

- For electron-type category, the final cuts are

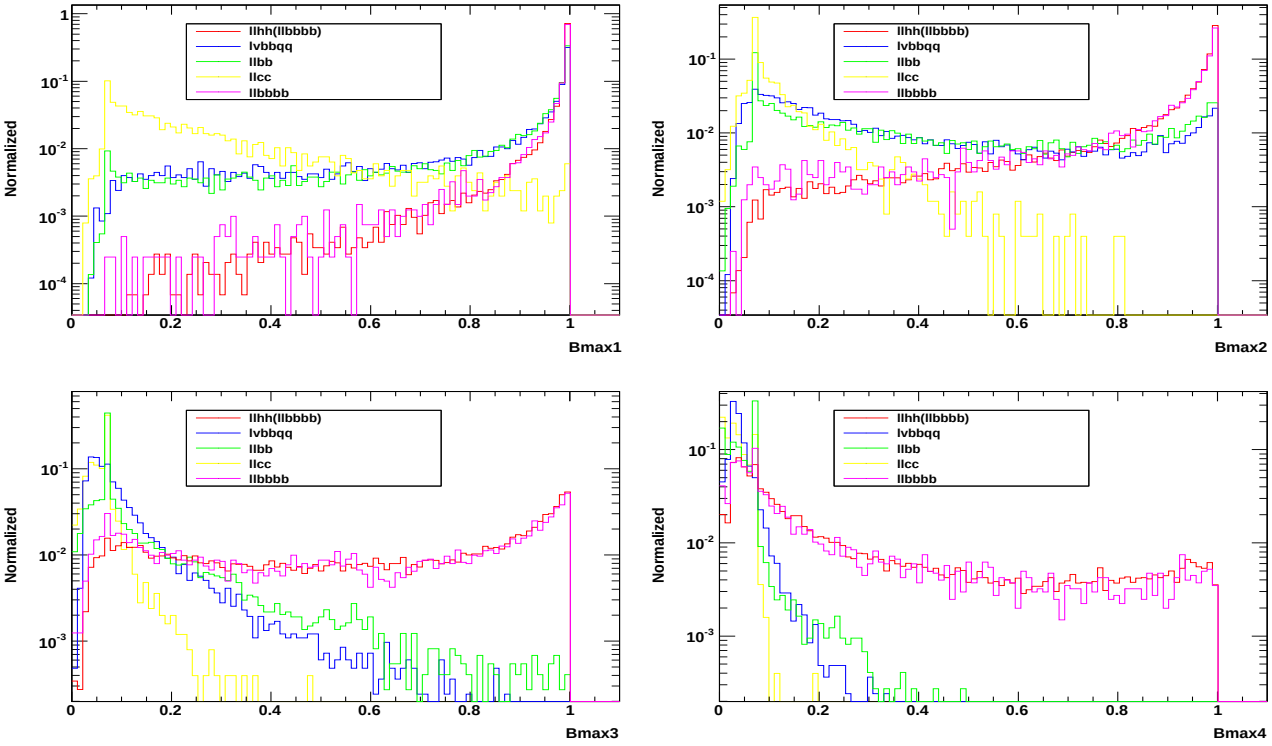

FIG. 23: Distributions of the four b-likeness values, top left for Bmax1, top right for Bmax2, bottom left for Bmax3 and bottom right for Bmax4. Red histograms are for the signal, blue ones for the semi-leptonic background $lvbbqq$, the green and the yellow ones for the jets-poor backgrounds $llbb$ and $llcc$, and pink ones for the same final states background $llbbbb$.

1. Cut1: $E_{\rm cone}12 + 4E_{\rm cone}{\rm Charge}12 < 60$ GeV and $|M(ll) - M(Z)| < 32$ GeV.
2. Cut2: ${\rm MLP}_{llbb} > 0.56$.
3. Cut3: ${\rm MLP}_{lvbbqq} > 0.81$.
4. Cut4: $Bmax3 > 0.19$.
5. Cut5: ${\rm MLP}_{llbbbb} > 0.5$.

- For muon-type category, the final cuts are

1. Cut1: $E_{\rm cone}12 + 4E_{\rm cone}{\rm Charge}12 < 60$ GeV, $p{\rm Lep}_1 + p{\rm Lep}_2 > 80$ GeV and $|M(ll) - M(Z)| < 27$ GeV.
2. Cut2: ${\rm MLP}_{llbb} > 0.53$.
3. Cut3: ${\rm MLP}_{lvbbqq} > 0.2$.
4. Cut4: $Bmax3 > 0.16$.
5. Cut5: ${\rm MLP}_{llbbbb} > 0.52$.

4. Summary of the llHH mode

In the search mode $e^+e^- \to l^+l^-HH$, assuming a Higgs mass of 120 GeV and an integrated luminosity of 2 ab^{-1} with the beam polarization $P(e^-, e^+) = (-0.8, +0.3)$, category a) it is expected to observe 3.7 signal events with 4.3 backgrounds events, corresponding to a ZHH excess significance of 1.5σ and a ZHH cross section measurement significance of 1.1σ; category b) it is expected to observe 4.5 signal events with 6.0 backgrounds events, corresponding to a ZHH excess significance of 1.5σ and a ZHH cross section measurement significance of 1.2σ. [the definition of excess significance and measurement significance can be found in the appendix.]

TABLE I: The reduction table for the signal and backgrounds after the final selection for the electron-type category of $llHH$ mode, together with the number of expected events and generated events. The cuts names are explained in text.

Process	expected	generated	pre-selection	electron-type	Cut1	Cut2	Cut3	Cut4	Cut5
$llHH$	46.5	3.88×10^5	26.5	13.1	12.3	10.1	8.6	4.64	3.73
$eebb$	2.84×10^5	4.18×10^6	3950	3950	2762	75.4	57.8	3.88	0.81
$\mu\mu bb$	4.96×10^4	1.00×10^6	1944	0.74	0.10	0	0	0	0
$e\nu bbqq$	2.48×10^5	1.51×10^6	2437	2437	928	675	25.7	1.93	0.46
$\mu\nu bbqq$	2.46×10^5	1.48×10^6	239	24.5	0.52	0.36	0	0	0
$\tau\nu bbqq$	2.46×10^5	1.35×10^6	156	148	38.6	30.3	1.50	0.25	0
$bbqqqq$	6.24×10^5	3.90×10^6	107	106	3.93	3.93	1.04	0.16	0.16
$bbbb$	4.02×10^4	1.02×10^6	5.84	5.76	0.10	0	0	0	0
$llbbbb$	69.5	1.06×10^5	15.0	7.42	6.69	5.44	4.68	4.18	0.97
$llqqh$	157	6.30×10^4	138	68.1	65.0	51.1	46.9	9.92	1.93
BG	1.74×10^6	1.46×10^7	8992	6748	3806	842	138	20.3	4.32

TABLE II: The reduction table for the signal and backgrounds after the final selection for the muon-type category of $llHH$ mode, together with the number of expected events and generated events. The cuts names are explained in text.

Process	expected	generated	pre-selection	electron-type	Cut1	Cut2	Cut3	Cut4	Cut5
$llHH$	46.5	3.88×10^5	26.5	13.3	13.0	10.6	10.4	5.76	4.47
$eebb$	2.84×10^5	4.18×10^6	3950	0	0	0	0	0	0
$\mu\mu bb$	4.96×10^4	1.00×10^6	1944	1943	1750	73.3	72.8	7.28	2.33
$e\nu bbqq$	2.48×10^5	1.51×10^6	2437	0	0	0	0	0	0
$\mu\nu bbqq$	2.46×10^5	1.48×10^6	239	215	95.7	65.7	33.3	2.78	0
$\tau\nu bbqq$	2.46×10^5	1.35×10^6	156	7.76	2.62	1.82	0.8	0	0
$bbqqqq$	6.24×10^5	3.90×10^6	107	1.09	0	0	0	0	0
$bbbb$	4.02×10^4	1.02×10^6	5.84	0.08	0	0	0	0	0
$llbbbb$	69.5	1.06×10^5	15.0	7.57	7.10	5.92	5.90	5.38	1.29
$llqqh$	157	6.30×10^4	138	69.7	68.4	54.3	54.0	12.8	2.36
BG	1.74×10^6	1.46×10^7	8992	2244	1924	201	167	28.2	5.97

B. Analysis of $e^+ + e^- \to \nu\bar{\nu}HH \to \nu\bar{\nu}b\bar{b}b\bar{b}$ at 500 GeV

In this search mode, the final state of a candidate signal event contains two missing neutrinos and four b quarks fragmenting into four jets. The three types of neutrinos ν_e, ν_μ and ν_τ are considered together. The analysis strategy is quite similar with the lepton pair mode. For pre-selection, we reject the isolated lepton and cluster the events to four jets and pair them by minimizing the χ^2 of two Higgs masses, loose mass cut and b-tagging cut are added. In the final selection, first we use missing energy and missing pt to suppress the full hadronic background. Then we train three neural-nets to suppress the dominant $bbbb$, $l\nu bbqq$ and $\nu\nu bbbb$ backgrounds. And eventually tight b-tagging is added. The reduction table of this searching mode is shown in Table III and the all the final cuts are summarized as following:

- Pre-selection: $|M(bb) - M(H)| < 80$ and $Bmax3 > 0.2$
- Final-selection:
  1. Cut1: $Evis - 0.83MissPt < 360$ GeV, $MissMass > 60$ GeV.
  2. Cut2: $NpfosMin >= 8$, 92 GeV $< M(H_1) <$ 136 GeV, 94 GeV $< M(H_2) <$ 130 GeV, $M(HH) >$ 200 GeV.
  3. Cut3: $\text{MLP}_{bbbb} > 0.83$.
  4. Cut4: $\text{MLP}_{l\nu bbqq} > 0.56$.
  5. Cut5: $\text{MLP}_{\nu\nu bbbb} > 0.61$.
  6. Cut6: $Bmax3 + Bmax4 > 1.14$.

TABLE III: The reduction table for the signal and backgrounds after the final selection for $\nu\nu HH$ mode, together with the number of expected events and generated events. The cuts names are explained in text.

Process	expected	generated	pre-selection	Cut1	Cut2	Cut3	Cut4	Cut5	Cut6
$\nu\nu HH$	103	7.06×10^5	45.0	43.6	26.0	22.7	20.6	17.1	8.47
$\nu\nu bb$	2.73×10^5	4.79×10^5	861	758	9.17	4.25	4.25	3.02	0
$e\nu bbqq$	2.48×10^5	1.51×10^6	3884	2126	504	451	72.6	54.9	0
$\mu\nu bbqq$	2.46×10^5	1.48×10^6	1637	951	22.3	195	72.8	52.1	0
$\tau\nu bbqq$	2.46×10^5	1.59×10^6	37440	24728	2591	3890	959	724	2.07
$bbqqqq$	6.24×10^5	3.88×10^6	58457	1212	178	71.5	38.6	37.2	0
$bbbb$	4.02×10^4	7.06×10^5	30826	3684	350	13.2	9.82	7.87	2.99
$\nu\nu bbbb$	97.1	8.22×10^4	82.1	80.5	10.1	6.90	5.66	2.03	0.87
$\nu\nu qqh$	469	7.41×10^4	82.1	79.0	21.5	17.5	13.0	5.86	1.93
BG			1.33×10^5	33619	5887	4650	1176	887	7.86

1. *Summary of the $\nu\nu HH$ mode*

In the $e^+ + e^- \to \nu\bar{\nu}HH$ search mode, assuming the Higgs mass of 120 GeV, the integrated luminosity of 2 ab^{-1}, and the beam polarization $P(e^-, e^+) = (-0.8, +0.3)$, it is expected to observe 8.5 signal and 7.9 backgrounds events, corresponding to a ZHH excess significance of 2.5σ and a ZHH cross section measurement significance of 2.1σ.

C. Analysis of $e^+ + e^- \to q\bar{q}HH \to q\bar{q}b\bar{b}b\bar{b}$ at 500 GeV

In this search mode, the final state of a candidate signal event contains four of six b quarks each fragmenting into a b jet. In the pre-selction, we require no isolated lepton and cluster the particles to six jets, which are then paired to form two Higgs bosons and one Z boson. The third larges b-likeness of the four jets from two Higgs is required to be larger than 0.16 in the pre-selection. In the final selection, all the events are separated into two categories according to the flavor tagging of the two jets from Z decay, which are correspondingly bbHH dominant and light qqHH dominant. The sum of b-likeness of the two jets from Z decay is used to achieve the separation. The dominant background in this analysis are $bbbb$ from $ZZ(bbZ)$, full hadronic $bbqqqq$ from $t\bar{t}$, $qqbbbb$ from ZZZ and ZZH, each of which is suppressed with a neural-net. The reduction table of this searching mode is shown in Table IV and V, and the all the final cuts are summarized as following:

- $bbHH$ dominant category
  1. Cut1: sum of b-likeness of the two jets from Z > 0.54.
  2. Cut2: $MissPt < 60$ GeV, $Npfos < 245$, 30 GeV $< M(Z) <$ 139 GeV, 73 GeV $< M(H_1) <$ 170 GeV, 73 GeV $< M(H_2) <$ 148 GeV.
  3. Cut3: MLP$_{bbbb} > 0.47$.
  4. Cut4: MLP$_{bbqqqq} > 0.33$.
  5. Cut5: MLP$_{qqbbbb} > 0.16$.
  6. Cut6: $Bmax3 + Bmax4 > 1.17$.
- light $qqHH$ dominant
  1. Cut1: sum of b-likeness of the two jets from Z < 0.54.
  2. Cut2: $MissPt < 60$ GeV, $Npfos < 245$, 60 GeV $< M(Z) <$ 131 GeV, 97 GeV $< M(H_1) <$ 133 GeV, 84 GeV $< M(H_2) <$ 136 GeV.
  3. Cut3: MLP$_{bbbb} > 0.48$.
  4. Cut4: MLP$_{bbqqqq} > 0.51$.
  5. Cut5: MLP$_{qqbbbb} > 0.09$.
  6. Cut6: $Bmax3 > 0.85$, $Bmax3 + Bmax4 > 1.21$.

TABLE IV: The reduction table for the signal and backgrounds after the final selection for $bbHH$ dominant category, together with the number of expected events and generated events. The cuts names are explained in text.

Process	expected	generated	pre-selection	Cut1	Cut2	Cut3	Cut4	Cut5	Cut6
$qqHH$	310	3.73×10^5	111	26.9	25.1	23.0	22.4	21.1	13.6
$l\nu bbqq$	7.40×10^5	3.56×10^6	17240	363	103	18.7	15.9	12.8	0.03
$bbuddu$	1.56×10^5	8.87×10^5	565	11.4	11.3	10.0	7.65	6.92	0.55
$bbcsdu$	3.12×10^5	1.26×10^6	6109	89.0	78.4	67.6	51.2	45.1	1.01
$bbcssc$	1.56×10^5	1.17×10^6	12456	263	246	212	147	129	3.69
$bbbb$	4.02×10^4	7.19×10^5	22889	2319	733	16.5	15.0	11.8	5.25
$qqbbbb$	140	1.23×10^5	82.9	13.9	12.7	9.80	9.19	5.78	3.03
$qqqqh$	818	5.98×10^4	154	27.5	25.4	22.5	21.6	18.5	10.9
ttz	2.20×10^3	8.49×10^4	172	17.2	13.6	12.5	12.3	11.4	2.88
$ttbb$	2.11×10^3	8.25×10^4	450	47.8	29.9	26.0	24.5	22.6	3.40
BG			60119	3152	1253	395	304	264	30.7

TABLE V: The reduction table for the signal and backgrounds after the final selection for light $qqHH$ dominant category, together with the number of expected events and generated events. The cuts names are explained in text.

Process	expected	generated	pre-selection	Cut1	Cut2	Cut3	Cut4	Cut5	Cut6
$qqHH$	310	3.73×10^5	111	84.0	36.9	34.2	31.0	30.8	18.8
$l\nu bbqq$	7.40×10^5	3.56×10^6	17240	16877	408	147	74.0	73.2	1.07
$bbuddu$	1.56×10^5	8.87×10^5	565	554	102	96.7	48.4	47.9	5.93
$bbcsdu$	3.12×10^5	1.26×10^6	6109	6020	1200	1094	501	492	15.7
$bbcssc$	1.56×10^5	1.17×10^6	12456	12193	2308	2111	848	829	16.0
$bbbb$	4.02×10^4	7.19×10^5	22889	20570	273	22.0	18.1	17.2	10.0
$qqbbbb$	140	1.23×10^5	82.9	68.9	11.1	9.49	7.92	6.95	4.07
$qqqqh$	818	5.98×10^4	154	126	37.8	34.0	30.5	29.9	16.1
ttz	2.20×10^3	8.49×10^4	172	155	30.3	29.4	25.7	25.5	7.74
$ttbb$	2.11×10^3	8.25×10^4	450	402	62.4	59.3	49.0	48.6	14.0
BG			60119	56967	4433	3603	1603	1570	90.6

1. *Summary of the qqHH mode*

In this $e^+ + e^- \to q\bar{q}HH$ search mode, assuming the Higgs mass of 120 GeV and the integrated luminosity of 2 ab^{-1}, with the beam polarization $P(e^-, e^+) = (-0.8, +0.3)$, in $bbHH$ dominant category, it is expected to observe 13.6 signal events with 30.7 backgrounds events, corresponding to a ZHH excess significance of 2.2σ and a ZHH cross section measurement significance of 2.0σ; in light $qqHH$ dominant category, it is expected to observe 18.8 signal events with 90.6 backgrounds events, corresponding to a ZHH excess significance of 1.9σ and a ZHH cross section measurement significance of 1.8σ. .

V. COMBINED RESULT OF $e^+e^- \to ZHH$ AT 500 GEV

The results of the three searching modes of $e^+e^- \to ZHH$ are shown in Table VI for the beam polarization $P(e^-, e^+) = (-0.8, +0.3)$, which is favored benefiting with higher cross section. The ZHH excess significance (i) and the measurement significance (ii) are also shown there. Notice that there are two independent parts in the $q\bar{q}HH$ mode. In this section, we will combine these results and try to answer the following two crucial questions:

- Can we observe the ZHH events? How much is the combined ZHH excess significance?
- Can we observe the trilinear Higgs self-interaction? How precisely can we measure the trilinear Higgs self-coupling?

TABLE VI: The numbers of the remaining signal and background events in each search mode of the $e^+e^- \to ZHH$ analysis based on the full detector simulation at 500 GeV, with the beam polarization $P(e^-, e^+) = (-0.8, +0.3)$. The last two columns are ZHH excess significance (i) and cross section measurement significance (ii). The $qqHH$ mode and $llHH$ mode are both separated into two categories: (a) $bbHH$ dominant, (b) light $qqHH$ dominant, (c) electron-type $llHH$, (d) muon-type $llHH$.

Search Mode	Signal	Background	Significance (i)	Significance (ii)
$qqHH$ (a)	13.6	30.7	2.2σ	2.0σ
$qqHH$ (b)	18.8	90.6	1.9σ	1.8σ
$\nu\nu HH$	8.5	7.9	2.5σ	2.1σ
$llHH$ (c)	3.7	4.3	1.5σ	1.1σ
$llHH$ (d)	4.5	6.0	1.5σ	1.2σ

A. Statistical independence of the three modes

Before deriving the combined result, it is necessary to check the statistical independence of the three modes.

- Due to the very different visible energy requirement in the $\nu\nu HH$ mode and the other two modes, events selected for the $\nu\nu HH$ mode will not satisfy the selection criteria for the other two modes. Thus the $\nu\nu HH$ mode is statistically independent of the $llHH$ and $qqHH$ modes.
- Due to the very energetic isolated lepton requirement for the $llHH$ mode, all fully hadronic events will not be selected, so that the $llHH$ mode is statistically independent of the $qqHH$ mode.

Thus we conclude that all the three modes are statistically independent.

B. Combined ZHH excess significance

A hypothesis test is used to calculate the combined ZHH excess significance. Define the null hypothesis:

$$\mathrm{H}_0: \quad \text{there is only background (B).} \tag{14}$$

and the alternative hypothesis:

$$\mathrm{H}_1: \quad \text{there are ZHH signal and background (S+B).} \tag{15}$$

Then define the test variable

$$\chi^2 \equiv -2\ln\frac{L_{s+b}}{L_b} \tag{16}$$

where the likelihood L_{s+b} is defined as

$$L_{s+b} = \prod_i \frac{e^{-(s_i+b_i)}(s_i+b_i)^{n_i}}{n_i!} \tag{17}$$

and the L_b is defined as

$$L_b = \prod_i \frac{e^{-b_i} b_i^{n_i}}{n_i!}. \tag{18}$$

The s_i and b_i are the expected numbers of remaining signal and background events in mode i (search modes $i = 1, .., 4$). The n_i is the total number of observed events in mode i, which is a Poisson random variable, with mean value $s_i + b_i$ under hypothesis H_1, and with mean value b_i under hypothesis H_0.

Figure 24 shows the distributions of the χ^2 test variable under hypothesis H_0, denoted by blue line, and under hypothesis H_1, denoted by red line, produced using a Toy Monte-Carlo. The black line shows the observed value of the test χ^2. The significance of the observed value under no signal hypothesis is obtained to be $s\sigma = 5.0\sigma$, meaning that a statistical significance of 5.0σ is expected to observe the excess of ZHH events.

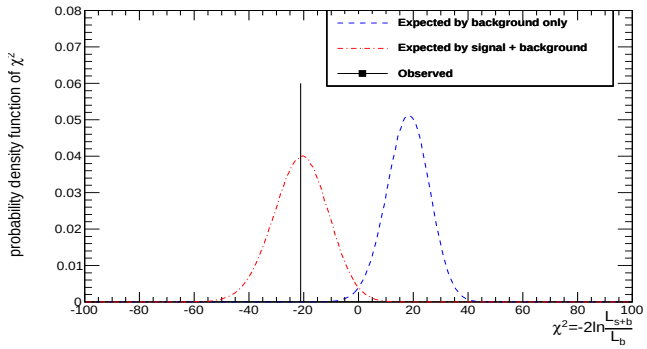

FIG. 24: The distribution of the test χ^2 under the background only hypothesis (blue) and the signal + background hypothesis (red). The black vertical line denotes the observed value of the test χ^2 variable.

C. Extracting the Cross Section of ZHH

The precision of the Higgs self-coupling is determined by the precision of the ZHH cross section, as introduced in Eqn 2. The cross section measurement can be carried out by parameter estimation through Maximum Likelihood. Define the combined likelihood

$$L_{s+b} = \prod_i \frac{e^{-(s_i+b_i)}(s_i+b_i)^{n_i}}{n_i!}, \tag{19}$$

where b_i is the expected number of background events, which is known from MC simulations; n_i is the number of observed events, which is known from the measurement; s_i is related to the cross section σ_{ZHH}, which is the unique parameter. The relation between s_i and σ_{ZHH} is

$$s_i = (\sigma_{ZHH} + \sigma_i) \cdot \text{Lumi} \cdot \text{Br}_i \cdot \text{Eff}_i \tag{20}$$

where Lumi is the integrated luminosity; Br_i is the branch ratio of mode i; Eff_i is the selection efficiency of mode i; σ_i is the fusion contribution for mode i, which is negligible at 500 GeV. The Likelihood hence contains only one parameter σ_{ZHH}. The minimization of $\chi^2 = -2\ln\frac{L}{L_{max}}$ is shown in Figure 25. The result is

$$\sigma_{ZHH} \cdot \text{Lumi} = 443^{+122}_{-115}. \tag{21}$$

For the integrated luminosity of 2 ab^{-1}, we then have

$$\sigma_{ZHH} = 0.22 \pm 0.06 \text{ fb}. \tag{22}$$

The precision of the cross section is 26.7%. Recalling the sensitivity of Higgs self-coupling to the cross section in Figure 4 (left), the Higgs self-coupling can be measured to the precision of 48% in case of without weighting. If we use the weighting method, the precision on Higgs self-coupling would be further improved to 44%.

VI. ANALYSIS OF $e^+e^- \to \nu\bar{\nu}HH$ AT 1 TEV

In this searching mode, the strategy is quite similar as that in $\nu\nu HH$ at 500 GeV. The dominant background here are from the semi-leptonic decay of $t\bar{t}$ and $\nu\nu ZH$ from WW fusion process, which are suppressed by two neural-nets. The pre-selection and final selection are summarized as following and the reduction table is shown in Table VII.

- Pre-selection:
  - no isolated lepton.
  - cluster all pros to 4 jets, each at least with 7 pfos and the third largest b-likeness to be larger than 0.2.

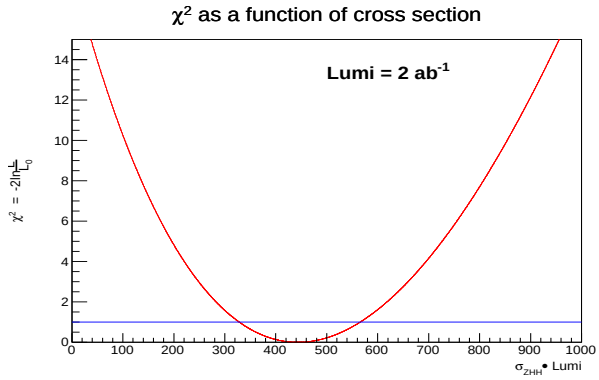

FIG. 25: The χ^2 as a function of $\sigma_{ZHH} \cdot \text{Lumi}$.

– visible energy less than 900 GeV, missing p_t large than 5 GeV, and missing mass larger than 0.

- Final-selection:

  1. Cut1: $Evis < 700 + 5MissPt$ GeV.
  2. Cut2: $\text{MLP}_{l\nu bbqq} > 0.84$.
  3. Cut3: $\text{MLP}_{\nu\nu bbbb} > 0.36$.
  4. Cut4: $Bmax3 + Bmax4 > 0.71$.

TABLE VII: The reduction table for the signal and backgrounds after the final selection for $\nu\nu HH$ at 1 TeV mode, together with the number of expected events and generated events. The cuts names are explained in text.

Process	expected	generated	pre-selection	Cut1	Cut2	Cut3	Cut4
$\nu\nu HH\ (fusion)$	272	1.05×10^5	127	107	77.2	47.6	35.7
$\nu\nu HH\ (ZHH)$	74.0	2.85×10^5	32.7	19.7	6.68	4.88	3.88
$yyxye\nu$	1.50×10^5	6.21×10^5	812	424	44.4	11.0	0.73
$yyxyl\nu$	2.57×10^5	1.17×10^6	13457	4975	202	84.5	4.86
$yyxyyx$	3.74×10^5	1.64×10^6	18951	4422	38.5	26.7	1.83
$\nu\nu bbbb$	650	2.87×10^5	553	505	146	6.21	4.62
$\nu\nu ccbb$	1070	1.76×10^5	269	242	63.3	2.69	0.19
$\nu\nu qqh$	3125	7.56×10^4	522	467	257	30.6	17.6
BG	7.86×10^5		34597	11054	758	167	33.7

1. *Summary of the $\nu\nu HH$ at 1 TeV*

In this $e^+ + e^- \to \nu\bar{\nu}HH$ searching mode, assuming the Higgs mass of 120 GeV and the integrated luminosity of 2 ab^{-1}, with the beam polarization $P(e^-, e^+) = (-0.8, +0.2)$, it is expected to observe 35.7 signal events with 33.7 backgrounds events, expecting the measurement significance of 4.3σ. The cross section of $\nu\nu HH$ from fusion can be measured to the precision of 23%, corresponding to the precision of 20% on the Higg self-coupling according to the sensitivity in Figure 4 (right). And with the weighting method, the precision on Higgs self-coupling would be further improved to 18%. Another important information from this analysis is that the double Higgs production excess with a statistical significance of 7.2σ is expected to be observed.

VII. SUMMARY

Acknowledgments

We would like to thanks all the members of the ILC physics subgroup for useful discussions. This study is supported in part by KEK, Center of High Energy Physics, Tsinghua University and the JSPS Core University Program.

[1] E. Asakawa, D. Harada, S. Kanemura, Y. Okada, and K. Tsumura, Phys.Rev. **D82**, 115002 (2010), 1009.4670.
[2] S. Kanemura, S. Kiyoura, Y. Okada, E. Senaha, and C. Yuan, Phys.Lett. **B558**, 157 (2003), hep-ph/0211308.
[3] S. Kanemura, Y. Okada, E. Senaha, and C.-P. Yuan, Phys.Rev. **D70**, 115002 (2004), hep-ph/0408364.
[4] A. Djouadi, W. Kilian, M. Muhlleitner, and P. M. Zerwas, Eur. Phys. J. **C10**, 27 (1999), hep-ph/9903229.
[5] C. Grojean, G. Servant, and J. D. Wells, Phys.Rev. **D71**, 036001 (2005), hep-ph/0407019.
[6] S. Kanemura, Y. Okada, and E. Senaha, Phys.Lett. **B606**, 361 (2005), hep-ph/0411354.
[7] S. Ham and S. Oh, (2005), hep-ph/0502116.
[8] M. Aoki, S. Kanemura, and O. Seto, Phys.Rev.Lett. **102**, 051805 (2009), 0807.0361.
[9] M. Aoki, S. Kanemura, and O. Seto, Phys.Rev. **D80**, 033007 (2009), 0904.3829.
[10] A. Noble and M. Perelstein, Phys.Rev. **D78**, 063518 (2008), 0711.3018.
[11] A. G. Cohen, D. Kaplan, and A. Nelson, Ann.Rev.Nucl.Part.Sci. **43**, 27 (1993), hep-ph/9302210.
[12] M. Quiros, Helv.Phys.Acta **67**, 451 (1994).
[13] V. Rubakov and M. Shaposhnikov, Usp.Fiz.Nauk **166**, 493 (1996), hep-ph/9603208.
[14] G. D. Kribs, T. Plehn, M. Spannowsky, and T. M. Tait, Phys.Rev. **D76**, 075016 (2007), 0706.3718.
[15] G. Gounaris, D. Schildknecht, and F. Renard, Phys.Lett. **B83**, 191 (1979).
[16] A. Djouadi, H. Haber, and P. Zerwas, Phys.Lett. **B375**, 203 (1996), hep-ph/9602234.
[17] V. Ilyin, A. Pukhov, Y. Kurihara, Y. Shimizu, and T. Kaneko, Phys.Rev. **D54**, 6717 (1996), hep-ph/9506326.
[18] V. D. Barger and T. Han, Mod.Phys.Lett. **A5**, 667 (1990).
[19] F. Boudjema and E. Chopin, Z.Phys. **C73**, 85 (1996), hep-ph/9507396.
[20] J. Tian, (2012), Presentation for LCWS12.
[21] P. Speckmayer, A. Hocker, J. Stelzer, and H. Voss, J.Phys.Conf.Ser. **219**, 032057 (2010).

(i) excess significance. Assuming there's only background, the p value is defined as the probability of observing events equal to or more than the number of the expected events, $N_S + N_B$:

$$p = \int_{N_S+N_B}^{\infty} f(x; N_B)\mathrm{d}x \tag{A1}$$

where $f(x; N_B)$ is the probability density function for the number of observed events when only the background exists, with the expected number N_B. Here, the number of observed events is a Poisson random variable $f(n; N_B) = \frac{e^{-N_B} N_B^n}{n!}$, the p value is calculated as

$$p = \sum_{n=N_S+N_B}^{\infty} f(n; N_B) \tag{A2}$$

corresponding to the significance:

$$1 - p = \int_{-\infty}^{s\sigma} N(x; 0, 1)\mathrm{d}x \tag{A3}$$

where $N(x; 0, 1)$ is the normal gaussian probability density function. The significance $s\sigma$ is defined as the excess significance. In the large statistics limit where if $f(x)$ becomes gaussian, this definition leads to the familiar significance formula $\frac{N_S}{\sqrt{N_B}}$.

(ii) measurement significance. Assuming both signal and background exist, the p value is defined as the probability of observing events equal to or less than the expected number of background events:

$$p = \int_{-\infty}^{N_B} f(x; N_B + N_S)\mathrm{d}x. \tag{A4}$$

This definition of significance is called "measurement significance". In the large statistics limit where if $f(x)$ becomes gaussian, this definition leads to the familiar significance formula $\frac{N_S}{\sqrt{N_S+N_B}}$.

MZ-TH/12-33
TTK-12-34

Determination of the CP parity of Higgs bosons in their τ decay channels at the ILC

Stefan Berge[*1], **Werner Bernreuther**[†2] **and Hubert Spiesberger**[*3]

[*] PRISMA Cluster of Excellence, Institut für Physik (WA THEP),
Johannes Gutenberg-Universität, 55099 Mainz, Germany
[†] Institut für Theoretische Physik, RWTH Aachen University, 52056 Aachen, Germany

Abstract

We investigate a method for determining the *CP* nature of a neutral Higgs boson or spin-zero resonance Φ at a future linear e^+e^- collider (ILC) in its $\Phi \to \tau^-\tau^+$ decay channel. Our procedure is applicable if the production vertex of the Higgs boson can be measured. This will be the case, for example, for the Higgs-strahlung process $e^+e^- \to Z+\Phi$. We show that the method is feasible for both the leptonic and the hadronic 1-prong tau decay modes, $\tau^\pm \to l^\pm + \nu_\tau + \nu_l$, $\tau^\pm \to a_1^\pm, \rho^\pm, \pi^\pm \to \pi^\pm + X$.

PACS numbers: 11.30.Er, 12.60.Fr, 14.80.Bn, 14.80.Cp
Keywords: Linear collider physics, Higgs bosons, tau leptons, parity, CP violation

[1] berge@uni-mainz.de
[2] breuther@physik.rwth-aachen.de
[3] spiesber@uni-mainz.de

I. INTRODUCTION

Recently, the ATLAS and CMS experiments reported the discovery of a neutral boson of mass ~ 126 GeV at the LHC [1, 2]. The experimental findings disfavor the option of a spin $J = 1$ resonance. The experimental results [1, 2] are compatible with the hypothesis of identifying this resonance with the Standard Model (SM) Higgs boson; however, much more detailed investigations will be necessary to establish this conjecture. The investigations of the properties of this resonance will probably be possible at the LHC to a large extent.

A high-energy linear e^+e^- collider would be an ideal machine to investigate the properties of this resonance, i.e., its couplings, decay modes, spin, and *CP* parity, in great detail (and, of course, also of other, not too heavy resonances of similar type if they exist). As it is likely that the ATLAS and CMS resonance is a spin-zero (Higgs) boson, one may revert, for assessing the prospects of exploring this particle at a future linear collider, to the many existing phenomenological investigations, within the SM and many of its extensions, of Higgs-boson production and decay in e^+e^- collisions. As to the prospects of exploring the spin and *CP* properties of a Higgs boson, there have been a number of proposals and studies, including [3–28] that are relevant for Higgs-boson production and decay at a linear collider.

In this workshop contribution we apply a method [26, 27] for the determination of the CP properties of a neutral spin-zero (Higgs) boson Φ in its $\tau^+\tau^-$ decays to the production of Φ at a future e^+e^- linear collider (ILC). For definiteness, we consider $e^+e^- \to Z\Phi$, but the analysis outlined below is applicable to any other Φ production mode. In our analysis all major 1-prong τ decays are taken into account. We demonstrate that the CP properties of Φ can be determined with our method in an unambiguous way.

II. CROSS SECTION AND OBSERVABLES

Here we consider the production of a neutral Higgs boson Φ or, more general, of a spin-zero resonance of arbitrary *CP* nature by the Higgs-strahlung process in high energy e^+e^- collisions:

$$e^+e^- \to Z + \Phi\,. \tag{1}$$

For definiteness, we use $m_\Phi = 126$ GeV in the following. The following remark is in order here. As is well known, for a pure pseudoscalar boson $\Phi = A$, the AZZ vertex must be loop-induced[4]. We assume here, for the sake of choosing a definite Φ production mode, that (1) applies also to the production of a pure pseudoscalar.

For Z boson decays into an electron or a muon pair, the precise reconstruction of the production vertex and of the 4-momentum of the Z boson will be possible. As to Φ, we consider

[4] The strength of the loop-induced AZZ vertex was investigated for a number of SM extensions in [29].

here the decay mode into tau pairs, with subsequent 1-prong $\tau^{\pm}$ decays:

$$\Phi \to \tau^- \tau^+ \to a^- a^+ + X\,, \tag{2}$$

where $a^{\pm} = \{e^{\pm}, \mu^{\pm}, \pi^{\pm}\}$ and X denotes neutrinos and, possibly, neutral pions. We assume that the tau-decay mode of the Φ has a reasonably large branching fraction, which is the case in the Standard Model and in many of its extensions. The interaction of a Higgs boson Φ of arbitrary *CP* nature ($J^{PC} = 0^{++}$, $J^{PC} = 0^{-+}$, or *CP* mixture) to τ leptons is described by the general Yukawa Lagrangian

$$\mathscr{L}_Y = -(\sqrt{2}G_F)^{1/2} m_\tau \left(a_\tau \overline{\tau}\tau + b_\tau \overline{\tau} i\gamma_5 \tau\right)\Phi\,, \tag{3}$$

where G_F denotes the Fermi constant and a_τ, b_τ are the reduced τ Yukawa coupling constants. In the following we take into account in (2) the main 1-prong τ decay channels

$$\begin{aligned}
\tau &\to l + \nu_l + \nu_\tau\,,\\
\tau &\to a_1 + \nu_\tau \to \pi + 2\pi^0 + \nu_\tau\,,\\
\tau &\to \rho + \nu_\tau \to \pi + \pi^0 + \nu_\tau\,,\\
\tau &\to \pi + \nu_\tau\,.
\end{aligned} \tag{4}$$

Our method that will be applied in the following does not require the knowledge of the τ rest frame. Therefore we can include also the leptonic τ decays in our analysis for which the presence of two, respectively four neutrinos would preclude the reconstruction of the $\tau^{\pm}$ rest frames. We do not consider here τ decays into 3 prongs, for instance $\tau \to a_1 \to 3$ charged pions, because in this case the reconstruction of the τ four-momentum should always be possible. This would considerably facilitate the measurement of the tau spin correlations that will be discussed below. (A corresponding analysis for Φ production at the LHC was made in [25].) As an aside, we remark that it will be helpful, but not essential for future experimental analyses if the different hadronic τ-decays can be experimentally distinguished.

Our method to determine the *CP* properties of a spin-zero boson was first developed for the case of Φ production in pp collisions at the Large Hadron Collider in [26] and was then applied to an analysis that included the combination of all 1-prong τ decay channels in [27]. The method is based on the fact that the *CP* quantum number of a neutral spin-zero resonance Φ can be determined in a definite way through its $\tau^-\tau^+$ mode by measuring the two τ spin correlations $S = \mathbf{s}_{\tau^-} \cdot \mathbf{s}_{\tau^+}$ and $S_{CP} = \hat{\mathbf{k}}_\tau \cdot (\mathbf{s}_{\tau^-} \times \mathbf{s}_{\tau^+})$, where $\hat{\mathbf{k}}_\tau = \mathbf{k}_\tau/|\mathbf{k}_\tau|$ is the normalized τ^- momentum vector in the zero-momentum frame (ZMF) of the $\tau^-\tau^+$-pair [5, 16]. For a scalar Φ, the expectation value of S is $\langle S\rangle = 1/4$, whereas for a pseudoscalar, $\langle S\rangle = -3/4$. The *CP*-odd and *T*-odd spin correlation S_{CP} probes whether or not Φ is a mixed *CP* state. If Φ is a *CP* mixture, i.e., if the neutral Higgs sector violates *CP* (that is, $a_\tau b_\tau \neq 0$ in (3)), then a non-zero expectation value of S_{CP} is generated already at tree level [5] and can be as large as 0.5.

The spin of the τ can not be measured directly; however it induces, in the spectrum of polarized tau decay $\tau^\pm \to a^\pm$, a correlation with the direction of flight of the charged particle $a^\pm$:

$$\frac{1}{\Gamma(\tau^\mp \to a^\mp + X)} \frac{\mathrm{d}\Gamma(\tau^\mp(\hat{\mathbf{s}}^\mp) \to a^\mp(q^\mp) + X)}{dE_{a^\mp} d\Omega_{a^\mp}/(4\pi)} = n(E_{a^\mp}) \left(1 \pm b(E_{a^\mp})\, \hat{\mathbf{s}}^\mp \cdot \hat{\mathbf{q}}^\mp\right). \quad (5)$$

Here, $\hat{\mathbf{s}}^\mp$ denote the normalized spin vectors of the $\tau^\mp$ and $\hat{\mathbf{q}}^\mp$ the direction of flight of $a^\mp$ in the respective τ rest frame. The function $b(E_a)$ encodes the τ-spin analyzing power of particle a. The correlation of the τ-spins, $\hat{\mathbf{s}}^+ \cdot \hat{\mathbf{s}}^-$, leads to a nontrivial distribution of the opening angle $\angle(\hat{\mathbf{q}}^+, \hat{\mathbf{q}}^-)$, whereas the *CP*-odd observable $\hat{\mathbf{k}} \cdot (\hat{\mathbf{s}}^+ \times \hat{\mathbf{s}}^-)$ induces the triple correlation $\hat{\mathbf{k}} \cdot (\hat{\mathbf{q}}^+ \times \hat{\mathbf{q}}^-)$. The strength of these correlations depends, for a given strength of the reduced Yukawa couplings a_τ, b_τ, on the product $b(E_{a'^-})b(E_{a^+})$, while $n(E_{a'^-})n(E_{a^+})$ is responsible for the rate of $\tau^+\tau^-$ decay into $a^+a'^-$ final states.

In order to use these observables in an experimental analysis, one has to be able to reconstruct the $\tau^\pm$ and $a^\pm$ momenta in the $\tau^\pm$ and Φ rest frames. This is, in general, not possible for the leptonic τ-decay channel and very difficult in the case of hadronic τ decays, because at a linear collider beamstrahlung effects can shift the initial center of mass energy by a large amount. In [26] it was shown that one can, nevertheless, construct experimentally accessible observables that have a high sensitivity to the *CP* quantum numbers of the Φ. The crucial point is to employ the zero-momentum frame of the $a^+a'^-$ pair. The distribution of the angle

$$\varphi^* = \arccos(\hat{\mathbf{n}}_\perp^{*+} \cdot \hat{\mathbf{n}}_\perp^{*-}) \quad (6)$$

discriminates between $CP = \pm 1$ states. Here $\hat{\mathbf{n}}_\perp^{*\pm}$ are normalized impact parameter vectors defined in the zero-momentum frame of the $a^+a'^-$ pair. These vectors can be reconstructed [26] from the impact parameter vectors $\hat{\mathbf{n}}_\mp$ measured in the laboratory frame by boosting the 4-vectors $n_\mp^\mu = (0, \hat{\mathbf{n}}_\mp)$ into the a'^-a^+ ZMF and decomposing the spatial part of the resulting 4-vectors into their components parallel and perpendicular to the respective $\pi^\mp$ or $l^\mp$ momentum. We emphasize that φ^* defined in Eq. (6) is not the true angle between the τ decay planes, but nevertheless, it carries enough information to discriminate between *CP*-even and *CP*-odd Higgs bosons. The role of the *CP*-odd and *T*-odd triple correlation introduced above is taken over by the triple correlation $\mathcal{O}_{CP}^* = \hat{\mathbf{p}}_-^* \cdot (\hat{\mathbf{n}}_\perp^{*+} \times \hat{\mathbf{n}}_\perp^{*-})$ between the impact parameter vectors just defined and the normalized a'^- momentum in the a'^-a^+ ZMF, which is denoted by $\hat{\mathbf{p}}_-^*$. Equivalently, one can determine the distribution of the angle [26]

$$\psi_{CP}^* = \arccos(\hat{\mathbf{p}}_-^* \cdot (\hat{\mathbf{n}}_\perp^{*+} \times \hat{\mathbf{n}}_\perp^{*-})). \quad (7)$$

Before presenting results we would like to point out the difference of our method as compared to a previous analysis of how to determine the *CP* parity of a Higgs boson in its $\tau^+\tau^-$ decays at a linear collider. Refs. [20–22] analyzed the hadronic 1-prong decay $\tau \to \rho\nu$. The observable used by these authors, namely the acoplanarity angle of the ρ^+ and ρ^- decay planes, requires the reconstruction of the $\rho^+\rho^-$ ZMF, i.e., the measurement of the $\pi^\pm$ and the π^0

momenta, and the reconstruction of approximate $\tau^{\pm}$ rest frames. As emphasized above, our method is applicable to all 1-prong τ decays, in particular $\tau \to l$.

III. RESULTS

For predicting the distributions of the observables φ^* and ψ^*_{CP}, for a specific Φ-decay mode (2), in terms of the unknown reduced Yukawa couplings a_τ, b_τ, one needs to know the spectral function $n(E_a)$ and in particular $b(E_a)$, which determines, as mentioned, the tau-spin analyzing power of particle $a^{\pm} = l^{\pm}, \pi^{\pm}$ and therefore the shapes of the φ^* and ψ^*_{CP} distributions. For the purpose of our analysis, the major 1-prong τ decays (4) can be considered to be experimentally well established Standard Model physics, and the respective spectral functions are known within the SM to sufficient accuracy, cf. [25, 27] and references therein.
At a linear e^+e^- collider, a Higgs boson Φ produced by the Higgs-strahlung process (1) will have on average a much larger transverse momentum as compared to Φ production at the LHC by its major production mode $gg \to \Phi$. This calls for a study – independent of the LHC analyses [26, 27] – of the question how the *CP* properties of a (pseudo)scalar boson are reflected in the distributions of φ^* and ψ^*_{CP}. In addition, for future experimental analyses, differences between LHC and ILC can be expected from the fact that the ILC detectors will be able to measure the τ decay products at transverse momenta as small as about 10 GeV.
As outlined above, our method is based on the reconstruction of the normalized spatial impact parameters of the τ-decay products with respect to the production vertex of the Higgs boson. In the Higgs-strahlung process $e^+e^- \to \Phi + Z$ at the ILC the normalized impact parameters can be reconstructed for events where the Z boson decays into electron or muon pairs, $Z \to e^+e^-, \mu^+\mu^-$ and for $\Phi \to \tau\tau$ decays with sufficiently long τ-decay lengths. Here, we use this process to study the φ^* and ψ^*_{CP} distributions. We apply the following acceptance cuts appropriate for the ILC:

$$\begin{aligned} p_T^{l,\pi} &\geq 10\,\mathrm{GeV}\,, \\ 15^\circ &< \theta_{l,\pi} < 165^\circ\,. \end{aligned}$$

Let us first consider the decays $\tau^-\tau^+ \to l^-l'^+4\nu$, where $l, l' = e, \mu$. The functions $n(E_l)$ and $b(E_l)$, where E_l is the energy of l in the τ rest frame, are shown in Fig. 1a. The function $b(E_l)$, which determines the correlation of the τ spin with the momentum of l, changes sign at $E_l = m_\tau/4$. For a Higgs boson with specified *CP* parity (and specified reduced Yukawa couplings), the sign of the product $b(E_l)b(E_{l'})$ determines the functional form of the φ^* distribution and in particular the sign of the associated asymmetry

$$A_{\varphi^*} = \frac{N(\varphi^* > \pi/2) - N(\varphi^* < \pi/2)}{N(\varphi^* > \pi/2) + N(\varphi^* < \pi/2)}\,. \tag{8}$$

As an illustration we apply the cut $E_l > m_\tau/4$ in the τ rest frames to allow only for contributions with $b(E_l) < 0$. The resulting normalized φ^* distributions are shown as black dotted

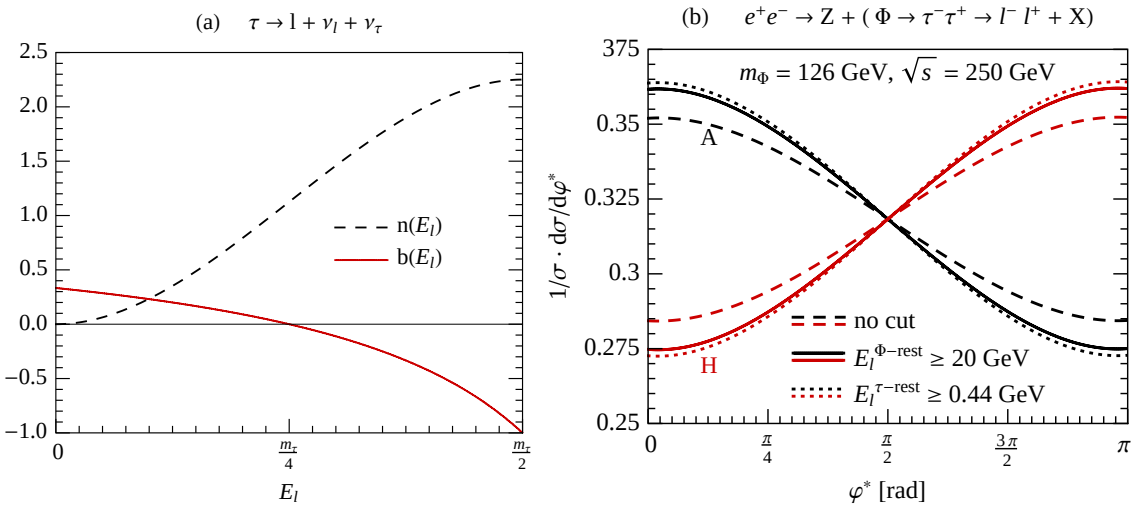

Figure 1: (a) The spectral functions $n(E_l)$ and $b(E_l)$, Eq. (5), for the leptonic τ decays. The function $n(E_l)$ is given in units of GeV^{-1}. (b) Normalized φ^* distribution for a $l^+l'^-$ final state for a Higgs boson with mass of 126 GeV produced at $\sqrt{s} = 250$ GeV. Scalar $\phi = H$, pseudoscalar $\phi = A$. The dashed lines show the distribution if no cuts are applied, the solid lines refer to the case where a cut $E_l^{\Phi-\text{rest}} \geq 20$ GeV was applied on both lepton energies in the Higgs rest frame. The dotted lines show the results for the ideal cut $E_l^{\tau-\text{rest}} \geq m_\tau/4$.

lines in Fig. 1b. For a *CP*-odd boson it has its maximum at $\varphi^* = 0$ and its minimum at $\varphi^* = \pi$, while for a *CP*-even boson (red dotted line) the distribution is flipped, $\varphi^* \leftrightarrow \pi - \varphi^*$. If one applies instead, either for τ^+ or τ^- decay (but not for both), the cut $E_l < m_\tau/4$ which leads to $b(E_l) > 0$, the behavior of the H and A distributions with increasing φ^* will be interchanged. The magnitude of the resulting asymmetry (8) becomes smaller because the maximum of $|b(E_l)|$ is smaller for $E_l < m_\tau/4$ than the maximum of $|b(E_l)|$ for $E_l > m_\tau/4$. In addition, with the cut $E_l < m_\tau/4$ the total decay rate is smaller than for $E_l > m_\tau/4$. This would make a measurement more difficult. Without a cut on the lepton energy, the asymmetry of the normalized φ^*-distributions is reduced, but remains non-zero because the averaging over the different signs of $b(E_l)$ is weighted by the spectral function $n(E_l)$ displayed in Fig. 1a. The result is shown in Fig. 1b (dashed lines, black for a pseudoscalar, red for a scalar boson).
Obviously, it would be an advantage if one could apply a cut on E_l to separate the contributions that involve different signs of $b(E_l)$. However, this would require to reconstruct the full τ 4-momentum in order to perform the necessary boost into the τ rest frame. On the other hand, the energy of the lepton l in the Higgs rest frame, E_l^Φ, is correlated with the energy E_l in the τ rest frame and a cut on the former can enrich the event sample with events in the desired range of the latter. The Higgs rest frame can, in fact, be reconstructed for the production process $e^+e^- \to \Phi + Z$, because the Z-boson 4-momentum is known for $Z \to e, \mu$ decays, provided that initial state radiation is negligible or can be corrected for. This should be the case at least for the TESLA design [30]. In Fig. 1b we show the resulting φ^* distributions

with a cut $E_l^{\Phi} \geq 20$ GeV applied to both leptons from $\tau^{\pm}$ decay. The solid black line (solid red line) shows the distribution for a *CP*-odd (*CP*-even) Higgs boson. The sensitivity of the distributions to the *CP* parity of Φ is clearly enhanced compared to the case where no cut is applied (dashed lines). These distributions are only slightly less sensitive than those with the ideal cut $E_l^{\tau-\text{rest}} > m_\tau/4$ (dotted lines).

In the 2-body decay $\tau \to \pi + \nu_\tau$, the π is monochromatic in the τ rest frame. (Its τ-spin analyzing power is maximal.) A cut on the energy of the charged prong, i.e., of the charged pion, is very important for the hadronic 1-prong decays $\tau^{\pm} \to \rho^{\pm}\nu \to \pi^{\pm} + \pi^0\nu$ and $\tau^{\pm} \to a_1^{\pm}\nu \to \pi^{\pm} + 2\pi^0\nu$. For example, for the decay $\rho^{\pm} \to \pi^{\pm} + \pi^0$, the function $b(E_\pi)$ changes sign within the range of E_π (see, e.g., Fig. 4a in [27]) and the φ^* distributions for both a scalar and a pseudoscalar boson turn out to be flat if no cut was applied. The same is true for the $\tau \to a_1$ decay mode. As in the case of $\tau \to l$, a cut on the energy of the charged pion in the Higgs-boson rest frame such that $b(E_\pi)$ is either positive or negative for the selected events significantly enhances the discriminating power of the φ^* distribution. Provided that the event rate is large enough, a value for $E_{\pi,\text{cut}}^{\Phi}$ may be chosen such as to optimize the separation of events with positive and negative $b(E_\pi)$, and both sets of events could be used to determine the *CP* nature of Φ.

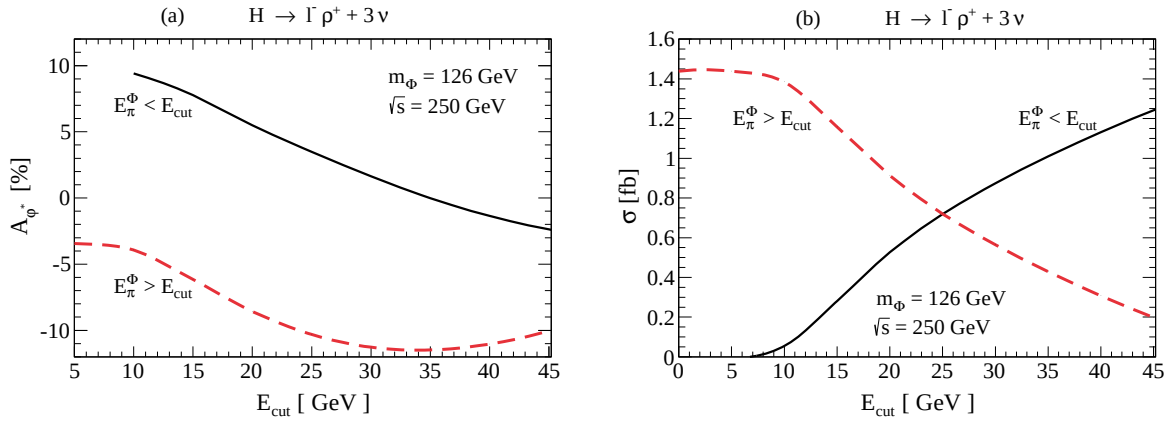

Figure 2: Influence of a cut on the energy of the charged pion in $l + \rho$ final states for a scalar boson $\phi = H$ with a mass of 126 GeV produced at $\sqrt{s} = 250$ GeV: (a) on the φ^* asymmetry, (b) on the cross section. The black full lines correspond to applying the cut $E_\pi^{\Phi} < E_{\pi,\text{cut}}^{\Phi}$, while the red dashed lines are for $E_\pi^{\Phi} > E_{\pi,\text{cut}}^{\Phi}$.

We illustrate this in Fig. 2 for the decay $\Phi \to l^-\rho^+ + 3\nu$ of a scalar boson. The effect can be quantified by calculating the associated asymmetry (8). The dashed red line in Fig. 2a shows the asymmetry for events with $E_\pi^{\Phi} > E_{\pi,\text{cut}}^{\Phi}$. The value $E_{\pi,\text{cut}}^{\Phi} = 0$, not shown in the figure, corresponds to the case without cut. In this case the asymmetry is rather small; applying a cut, the asymmetry increases to almost -12% for $E_{\pi,\text{cut}}^{\Phi} = 35$ GeV. However, increasing $E_{\pi,\text{cut}}^{\Phi}$ will decrease the cross section as shown in Fig. 2b. (The cross section was computed for the Standard Model Higgs boson.) Without any cut the cross section is about 1.5 fb; it

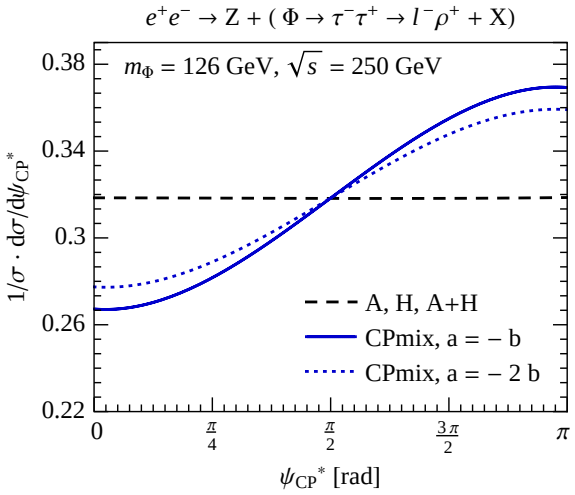

Figure 3: Normalized ψ^*_{CP} distribution for $l\rho$ final states for different types of Higgs bosons with mass of 126 GeV produced at $\sqrt{s} = 250$ GeV. A minimum cut on the π^+ energy of 25 GeV in the Higgs rest frame was applied.

decreases to 0.2 fb for the cut $E^{\Phi}_{\pi,\mathrm{cut}} = 45$ GeV.
On the other hand, the complementary region $E^{\Phi}_{\pi} < E^{\Phi}_{\pi,\mathrm{cut}}$ leads to a positive asymmetry A_{φ^*} for cut values $\lesssim 35$ GeV due to the fact that $b(E_\pi)$ has changed sign. For small values of E_π, one finds $A_{\varphi^*} \sim +9\%$, but the cross section is tiny, about 0.05 fb. The asymmetry decreases to almost -2% for $E^{\Phi}_{\pi,\mathrm{cut}} = 45$ GeV. It is clear that a judicious choice of this cut, taking into account experimental conditions and the available luminosity, is required to reach an optimal discrimination between a *CP*-even and *CP*-odd boson.
The φ^* distribution is well suited to distinguish between *CP*-even and *CP*-odd states. However, if the Higgs boson is a *CP*-mixture, or if there would exist two (almost) mass-degenerate bosons that escape experimental resolution, one of which has *CP* parity $+1$ and the other one -1, the φ^* distribution would be flat, assuming the cross sections are of comparable magnitude. The distribution with respect to the angle ψ^*_{CP} defined in Eq. (7) would be appropriate to resolve these scenarios. A typical result is shown in Fig. 3 which applies to the decay chain $\Phi \to \tau^+\tau^- \to l^-\pi^+ + 3\nu$ via hadronic $\tau \to \rho$ decay. The solid blue line shows the normalized ψ^* distribution of a maximally *CP*-mixed boson ($|a_\tau| = |b_\tau| > 0$) and we have chosen $a_\tau = -b_\tau$. For the scenario of mass degenerate bosons with opposite *CP* parities the ψ^*_{CP} distribution is shown by the horizontal dashed black line. The dotted blue line corresponds to the case of a non-maximal mixture with reduced Yukawa couplings $a_\tau = -2b_\tau$. If a_τ and b_τ have the same sign, the distribution is flipped, $\psi^*_{CP} \leftrightarrow \pi - \psi^*_{CP}$. The resulting asymmetry of the ψ^*_{CP} distribution will clearly be observable, provided the event rates are large enough.
We have also performed a Monte Carlo study to estimate the uncertainty of the measurement of the impact parameters. We applied a simple Gaussian smearing with $\sigma_{\mathrm{impact}} = 25^\circ$ [21] on the direction of the normalized impact parameter vectors. We found that the φ^* and ψ^*_{CP} distributions are only mildly affected by such an uncertainty.

IV. CONCLUSIONS

Using the method of [26, 27] we have shown that the CP nature of a neutral Higgs boson Φ produced at a future linear e^+e^- collider can be determined in a definite way in the $\Phi \to \tau^+\tau^-$ decay channel with subsequent 1-prong τ decays. We have considered the production of Φ with mass $m_\Phi = 126$ GeV by the Higgs-strahlung process, but our method can also be applied to Higgs bosons with other masses and to any other Φ production mode. Our approach does not require the knowledge of the τ rest frames; therefore, all 1-prong τ decays, including $\tau \to l$ can be used. The joint measurement of the distributions and associated asymmetries of the angles φ^* and ψ^*_{CP} allows to discriminate between a number of scenarios, some of which were discussed above. For a statistically significant determination of the *CP* parity of Φ, only very few 1-prong events are required. We will elaborate on this and on other related issues in future work [31].

Acknowledgments

The work of S. B. is supported by the Initiative and Networking Fund of the Helmholtz Association, contract HA-101 ('Physics at the Terascale') and by the Research Center 'Elementary Forces and Mathematical Foundations' of the Johannes-Gutenberg-Universität Mainz. The work of W. B. is supported by BMBF.

[1] G. Aad *et al.* [The ATLAS Collaboration], "Observation of a new particle in the search for the Standard Model Higgs boson with the ATLAS detector at the LHC," arXiv:1207.7214 [hep-ex].

[2] S. Chatrchyan *et al.* [The CMS Collaboration], "Observation of a new boson at a mass of 125 GeV with the CMS experiment at the LHC," arXiv:1207.7235 [hep-ex].

[3] J. R. Dell'Aquila and C. A. Nelson, Phys. Rev. D **33** (1986) 93.

[4] J. R. Dell'Aquila and C. A. Nelson, Nucl. Phys. B **320** (1989) 61.

[5] W. Bernreuther and A. Brandenburg, Phys. Lett. B **314** (1993) 104.

[6] A. Soni and R. M. Xu, Phys. Rev. D **48** (1993) 5259 [hep-ph/9301225].

[7] V. D. Barger, K. Cheung, A. Djouadi, B. A. Kniehl and P. M. Zerwas, Phys. Rev. D **49** (1994) 79 [hep-ph/9306270].

[8] K. Hagiwara and M. L. Stong, Z. Phys. C **62** (1994) 99 [hep-ph/9309248].

[9] T. Arens, U. D. J. Gieseler and L. M. Sehgal, Phys. Lett. B **339** (1994) 127 [hep-ph/9408316].

[10] A. Skjold and P. Osland, Phys. Lett. B **329** (1994) 305 [hep-ph/9402358].

[11] T. Arens and L. M. Sehgal, Z. Phys. C **66** (1995) 89 [hep-ph/9409396].

[12] A. Skjold and P. Osland, Nucl. Phys. B **453** (1995) 3 [hep-ph/9502283].

[13] S. Bar-Shalom, D. Atwood, G. Eilam, R. R. Mendel and A. Soni, Phys. Rev. D **53** (1996) 1162

[hep-ph/9508314].

[14] B. Grzadkowski and J. F. Gunion, Phys. Lett. B **350** (1995) 218 [hep-ph/9501339].

[15] J. F. Gunion, B. Grzadkowski and X. -G. He, Phys. Rev. Lett. **77** (1996) 5172 [hep-ph/9605326].

[16] W. Bernreuther, A. Brandenburg and M. Flesch, Phys. Rev. D **56** (1997) 90 [hep-ph/9701347].

[17] S. Bar-Shalom, D. Atwood and A. Soni, Phys. Lett. B **419** (1998) 340 [hep-ph/9707284].

[18] B. Grzadkowski, J. F. Gunion and J. Kalinowski, Phys. Rev. D **60** (1999) 075011 [hep-ph/9902308].

[19] S. Y. Choi, D. J. Miller, M. M. Muhlleitner and P. M. Zerwas, Phys. Lett. B **553** (2003) 61 [hep-ph/0210077].

[20] G. R. Bower, T. Pierzchala, Z. Was and M. Worek, Phys. Lett. B **543** (2002) 227 [hep-ph/0204292].

[21] K. Desch, Z. Was and M. Worek, Eur. Phys. J. C **29** (2003) 491 [hep-ph/0302046].

[22] K. Desch, A. Imhof, Z. Was and M. Worek, Phys. Lett. B **579** (2004) 157 [hep-ph/0307331].

[23] E. Accomando *et al.*, hep-ph/0608079.

[24] P. S. Bhupal Dev, A. Djouadi, R. M. Godbole, M. M. Muhlleitner and S. D. Rindani, Phys. Rev. Lett. **100** (2008) 051801 [arXiv:0707.2878 [hep-ph]].

[25] S. Berge, W. Bernreuther and J. Ziethe, Phys. Rev. Lett. **100** (2008) 171605 [arXiv:0801.2297 [hep-ph]].

[26] S. Berge and W. Bernreuther, Phys. Lett. B **671** (2009) 470 [arXiv:0812.1910 [hep-ph]].

[27] S. Berge, W. Bernreuther, B. Niepelt and H. Spiesberger, Phys. Rev. D **84** (2011) 116003 [arXiv:1108.0670 [hep-ph]].

[28] R. M. Godbole, C. Hangst, M. Muhlleitner, S. D. Rindani and P. Sharma, Eur. Phys. J. C **71** (2011) 1681 [arXiv:1103.5404 [hep-ph]].

[29] W. Bernreuther, P. Gonzalez and M. Wiebusch, Eur. Phys. J. C **69** (2010) 31 [arXiv:1003.5585 [hep-ph]].

[30] R. Brinkmann, (ed.), K. Flottmann, (ed.), J. Rossbach, (ed.), P. Schmueser, (ed.), N. Walker, (ed.) and H. Weise, (ed.), "TESLA: The superconducting electron positron linear collider with an integrated X-ray laser laboratory. Technical design report. Pt. 2: The accelerator," DESY-01-011.

[31] S. Berge, W. Bernreuther, and H. Spiesberger, in preparation.

Light Higgs Studies for the CLIC CDR

Christian Grefe[1], *Tomas Lastovicka*[2], *Jan Strube*[1]

[1]CERN, 1211 Geneve 23, Switzerland
[2]Institute of Physics, Academy of Sciences, 182 21 Prague 8, Czech Republic

DOI: will be assigned

The Higgs boson is the most anticipated discovery at the LHC, which can only partially explore its true nature. Thus one of the most compelling arguments to build a future linear collider is to investigate properties of the Higgs boson, especially to test the predicted linear dependence of the branching ratios on the mass of the final state. At a 3 TeV CLIC machine the Higgs boson production cross section is relatively large and allows for a precision measurement of the Higgs branching ratio to pairs of b and c quarks, and even to muons. The cross section times branching ratio of the decays $H \to b\bar{b}$, $H \to c\bar{c}$ and $H \to \mu^+\mu^-$ can be measured with a statistical uncertainty of approximately 0.22%, 3.2% and 15%, respectively.

The electroweak symmetry breaking mechanism, called Higgs mechanism, predicts a fundamental spin-0 particle, whose existence currently is being investigated at the LHC. The answer to the question about its existence is expected in 2013. The Standard Model predicted linear dependence of the branching ratios on the mass of the final state could be altered by non-Standard Model couplings. The LHC can deliver only very limited measurements of the Higgs sector, but a detailed exploration is crucial for a deep understanding of its nature.

The compact linear collider (CLIC) is a proposed e^+e^- collider with a maximum centre-of-mass energy $\sqrt{s} = 3\,\text{TeV}$, based on a two-beam acceleration scheme [1]. In the following we present the analysis of the measurement of the branching ratios $H \to b\bar{b}$, $H \to c\bar{c}$ [2] and $H \to \mu^+\mu^-$ [3] at such a machine. The studies are based on fully simulated and reconstructed samples in the CLIC_SiD [4] detector concept and take into account the relevant background processes as well as the main beam-related background.

1 The CLIC_SiD detector concept

The CLIC_SiD detector, used in the full simulation of samples, is based on the SiD detector concept [5] developed for the ILC project. It is designed for particle flow calorimetry using highly granular calorimeters and has been adapted [4] to the specific requirements at CLIC.

A superconducting solenoid with an inner radius of 2.9 m provides a central magnetic field of 5 T. The calorimeters are placed inside of the coil and consist of a 30 layer tungsten-silicon electromagnetic calorimeter with $3.5 \times 3.5\,\text{mm}^2$ segmentation, followed by a tungsten-scintillator hadronic calorimeter with 75 layers in the barrel region and a steel-scintillator hadronic calorimeter with 60 layers in the endcaps. The read-out cell size in the hadronic calorimeters is $30 \times 30\,\text{mm}^2$. The iron return yoke outside of the coil is instrumented with 9 double RPC layers with $30 \times 30\,\text{mm}^2$ read-out cells for muon identification.

The silicon-only tracking system consists of 5 $20 \times 20\,\mu\text{m}^2$ pixel layers followed by 5 strip layers with a pitch of 25 µm, a read-out pitch of 50 µm and a length of 92 mm in the barrel region. The tracking system in the endcap consists of 5 strip disks with similar pitch and a stereo angle of 12°, complemented by 7 pixelated disks of $20 \times 20\,\mu\text{m}^2$ in the vertex and far-forward region at lower radii.

2 Analysis framework and data samples

The physical processes are generated with the Whizard [6, 7] event generator, with fragmentation and hadronization done by Pythia [8]. The full simulation and reconstruction is performed in the software

Process	σ [fb]	N_{events}	Short label
$e^+e^- \to \mathrm{H}\nu_e\bar{\nu}_e$; $\mathrm{H} \to \mu^+\mu^-$	0.120	21000	$\mathrm{H} \to \mu^+\mu^-$
$e^+e^- \to \mathrm{H}\nu_e\bar{\nu}_e$; $\mathrm{H} \to b\bar{b}$	285	45000	$\mathrm{H} \to b\bar{b}$
$e^+e^- \to \mathrm{H}\nu_e\bar{\nu}_e$; $\mathrm{H} \to c\bar{c}$	15	130000	$\mathrm{H} \to c\bar{c}$
$e^+e^- \to \mu^+\mu^-\nu\bar{\nu}$	132*	5000000	$\mu^+\mu^-\nu\bar{\nu}$
$e^+e^- \to \mu^+\mu^- e^+e^-$	346*	1350000	$\mu^+\mu^- e^+e^-$
$e^+e^- \to \mu^+\mu^-$	12*	10000	$\mu^+\mu^-$
$e^+e^- \to \tau^+\tau^-$	250*	100000	$\tau^+\tau^-$
$e^+e^- \to \tau^+\tau^-\nu\bar{\nu}$	125*	100000	$\tau^+\tau^-\nu\bar{\nu}$
$e^+e^- \to q\bar{q}$	3100	96000	qq
$e^+e^- \to q\bar{q}\nu\bar{\nu}$	1300	170000	$qq\nu\nu$
$e^+e^- \to q\bar{q}e^+e^-$	3300	90000	qqe^+e^-
$e^+e^- \to q\bar{q}e\bar{\nu_e}$	5300	91000	$qqe\nu$
$\gamma\gamma \to \mu^+\mu^-$ (generator level only)	20000*	1000000	$\gamma\gamma \to \mu^+\mu^-$

Table 1: List of processes considered for this analysis with their respective cross section σ and the number of simulated events N_{events}. The cross section takes into account the CLIC luminosity spectrum and initial state radiation. Cross sections marked with * include a cut on the invariant mass of the muon pair at generator level to lie between 100 and 140 GeV.

framework of the CLIC_SiD detector concept.

The event simulation is performed using SLIC [9], a wrapper for GEANT4 [10], while the reconstruction is done by lcsim and PandoraPFA packages. We assume a total accumulated luminosty of $2\,\mathrm{ab}^{-1}$, corresponding to 4 years of data taking at the nominal machine parameters. Table 1 lists the physics processes that were taken into account in the analyses, together with their cross sections and the number of simulated events.

The dominant Higgs boson production channel at 3 TeV is the WW fusion channel $e^+e^- \to H\nu\bar{\nu}$ with a cross section of $\sigma_{H\nu\bar{\nu}} = 420\,\mathrm{fb}$. The main background for all channels is the Z boson production via WW fusion, which has similar kinematics as the signal processes.

Beamstrahlung effects on the luminosity spectrum as well as initial and final state radiation are taken into account. For the default configuration of a 3 TeV CLIC [1], 3.2 $\gamma\gamma \to$ hadrons events per bunch crossing are expected on average. With a spacing of 0.5 ns between bunches, these necessarily pile up in the subdetectors, for which we assume integration times of 10 ns, except for the barrel hadronic calorimeter, which has an integration time of 100 ns. To approximate the CLIC beam structure and background conditions, the equivalent of 60 bunch crossing of $\gamma\gamma \to$ hadrons events were mixed with every simulated event. In the $\mathrm{H} \to \mu^+\mu^-$ analysis, only the signal sample was mixed with events from $\gamma\gamma \to$ hadrons background.

For the processes involving jets in the final state, fragmentation products of the hadronic systems are forced to two jets using the exclusive k_t algorithm of the FastJet package [11], where the parameter R is set to 0.7. The LCFI vertexing package [12] is used to identify jets according to their quark content as b, c and light quarks and computes the corresponding jet flavour tag values.

The event classification in $\mathrm{H} \to b\bar{b}$ and $\mathrm{H} \to c\bar{c}$ analyses is based on the open source Fast Artificial Neural Network (FANN) package [13]. FANN was modified to account for event weights during the neural network training. The event classification in the $\mathrm{H} \to \mu^+\mu^-$ analysis is done using the boosted decision tree (BDT) classifier implemented in the TMVA package [14].

3 Measurement of $\mathrm{H} \to b\bar{b}$ and $\mathrm{H} \to c\bar{c}$

The measurement of the $\mathrm{H} \to b\bar{b}$ and $\mathrm{H} \to c\bar{c}$ decays requires resolution of secondary vertices from the primary vertex and is thus an important benchmark of the vertex tracking detector design.

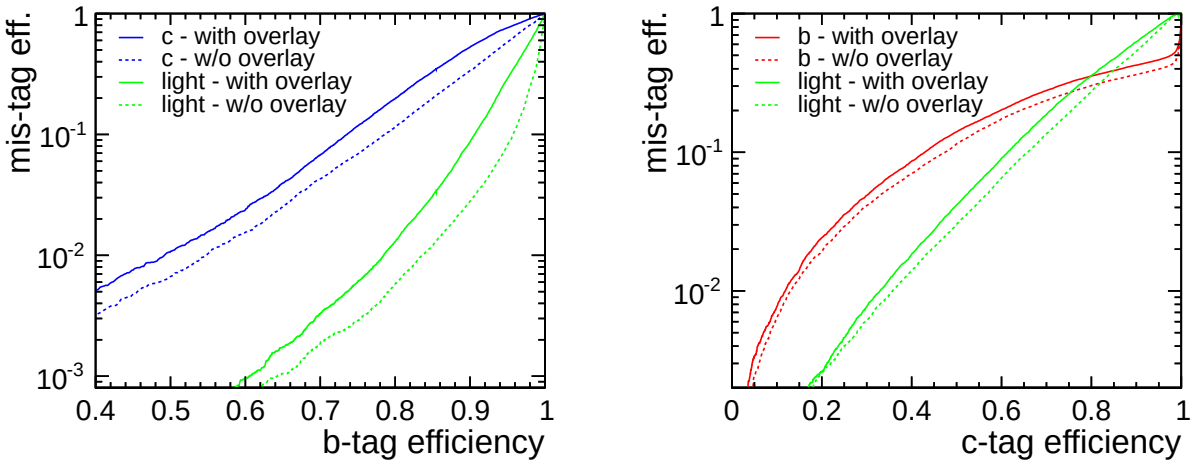

Figure 1: In the left plot, the mis-tag rate in the CLIC_SiD detector for charm (blue) and light (green) jets as a function of the b-tag efficiency is shown. The right plot shows the mis-tag rate for bottom (red) and light (green) jets as a function of the c-tag efficiency. The mean p_{T} of the jets is 70 GeV while the mean energy is $\sim 130\,GeV$.

3.1 Jet flavour tagging

The flavour identification package developed by the LCFI [12] collaboration consists of a topological vertex finder ZVTOP, which reconstructs secondary interactions, and a multivariate classifier which combines several jet-related variables to tag bottom, charm, and light quark jets. Displaced vertices are the most significant characteristic of b quark decays. A combination of several vertex-related variables, complemented by additional track-related variables, form an input for the tagging classifier. A detailed description of the variables and the procedure are given in [12].

The probability to tag a jet with a false flavour, the so called mis-tag rate, is used to assess the performance of the flavour tagging package. Figure 1 (left) shows the mis-tag rate for c-jets (blue line) and light jets (green line) as b-jets versus the b-tag efficiency, while Figure 1 (right) shows the mis-tag rate for b-jets (red line) and light jets (green line) as c-jets versus the c-tag efficiency. The presence of $\gamma\gamma$ backgrounds is found to reduce the flavour tagging performance, although the effect is not dramatic. The degradation of the flavour tag performance, shown in Figure 1, has two sources: the flavour tag degradation itself plus a degradation of the jet quality due to a more difficult jet finding. For instance, at the b-tag efficiency of 70% the mis-tag rate for c-jets (light jets) drops from 4.3% (0.19%) w/o overlay to 6.8% (0.33%) with overlay.

3.2 Results

The basic event selection requires two jets in each event. Apart from this selection, no further cuts are explicitly imposed and a number of relevant variables is given to a neural net for the subsequent multivariate analysis. The invariant mass of the jet pair is the major discriminant between decays of Higgs and of Z bosons. It is used in a event classification neural network, together with the output of the b-flavor tagging network and the following variables:

- The maximum of the absolute values of jet pseudorapidities.
- The sum of the remaining LCFI jet flavour tag values, i.e. c(udsb), c(b)-tags and b(uds)-tag[1].
- $R_{\eta\phi}$, the distance of jets in the $\eta - \phi$ plane.

[1]The notion indicates which flavour is tagged against which set of other flavours. For instance, c(b) is the c-flavour tagged against the b-flavour only, while remaining (uds) flavours are not used during the neural net training.

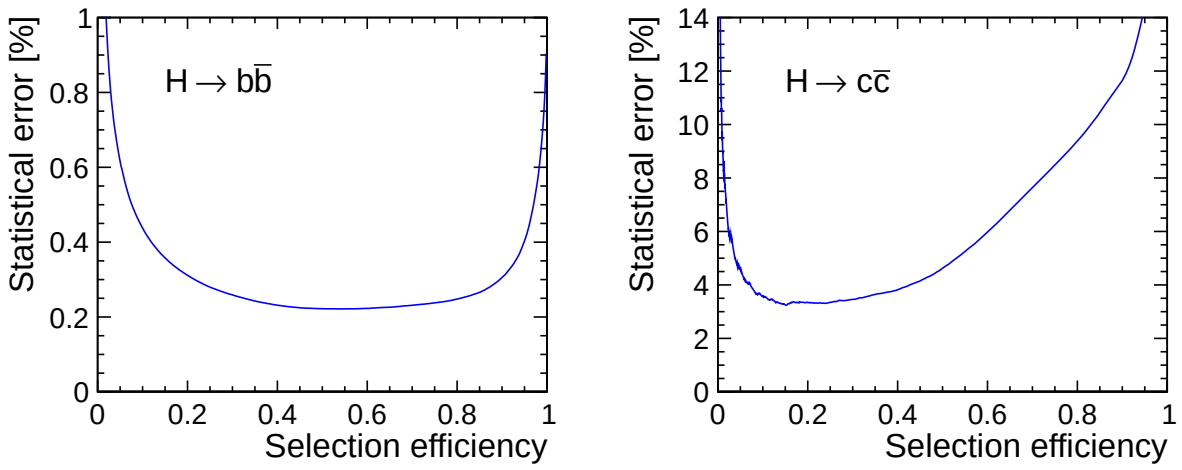

Figure 2: Statistical uncertainty of the measurement of cross section times branching ratio versus selection efficiency of the neural network. The neural network was trained to identify H $\to b\bar{b}$ decays from di-jet backgrounds including H $\to c\bar{c}$ (left). The neural network was trained on H $\to c\bar{c}$ as signal and di-jets backgrounds including H $\to b\bar{b}$ (right).

- The sum of jet energies.
- The total number of leptons in an event.
- The total number of photons in an event.
- Acoplanarity of jets.

Two neural nets were trained to separate either the H $\to b\bar{b}$ or the H $\to c\bar{c}$ signals from background samples accounting for event weights. Thus the amount of the information about the signal, compared to the background, was proportional to its natural contribution. Such a solution delivers optimal results. It is more appropriate than, for instance, choosing the same number of signal and background events with no weights, or, training according to arbitrary sizes of the generated samples.

The neural network selection efficiency versus the statistical uncertainty on the measurement is shown in Figure 2 for the two neural networks that were trained on H $\to b\bar{b}$ and H $\to c\bar{c}$ as signal, respectively. The optimal selection is at the local minimum of the curve, at a selection efficiency of 55% for H $\to b\bar{b}$ with a sample purity of 65%, and a selection efficiency of 15% for H $\to c\bar{c}$ corresponding to a sample purity of 24%. These values reflect the fact that b-jets can be distinguished from c-jets with high purity, while incompletely reconstructed b-jets and light jets make up a large fraction of the background to c-jet selection. Using the output of the reconstruction algorithms in neural networks leads to the minimal statistical uncertainty on the measurement at the eventual cost of an increased dependence on systematic effects. We assume that with sufficient experience at the running machine, the systematic variations are well enough understood so that the systematic uncertainties are comparable to the statistical uncertainties of the H $\to c\bar{c}$ channel and dominate in the H $\to b\bar{b}$ channel.

The resulting statistical H $\to b\bar{b}$ cross section uncertainty amounts to 0.22 % while preserving meaningful values of both the sample purity (65.4 %) and of the signal selection efficiency (54.6 %). The H $\to c\bar{c}$ channel is more difficult to separate from the background and the statistical cross section uncertainty is 3.24 % with a signal selection efficiency of 15.2%.

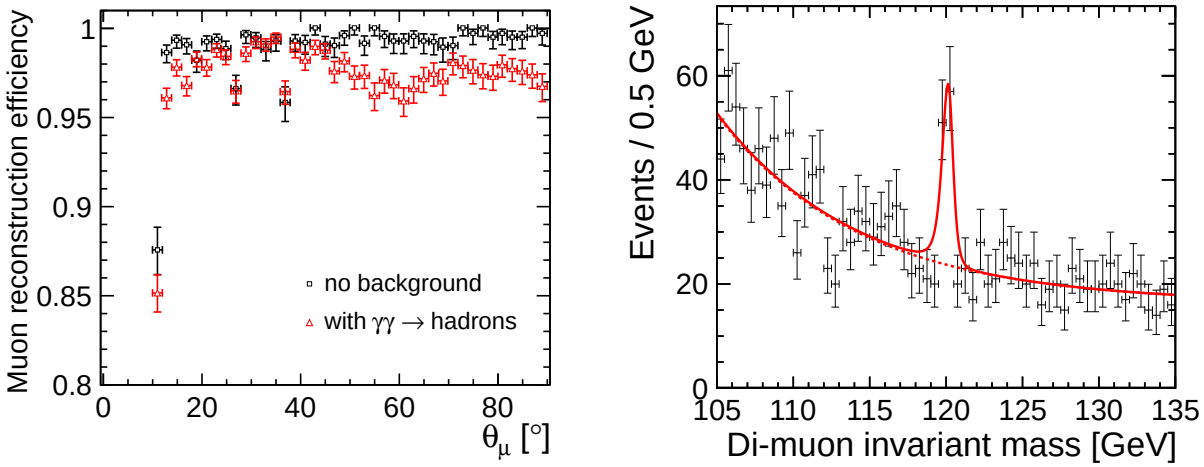

Figure 3: Muon reconstruction efficiency for the signal sample with and without $\gamma\gamma \to$ hadrons pile-up.

4 Measurement of $\mathbf{H} \to \mu^+\mu^-$

The measurement of the rare decay $H \to \mu^+\mu^-$ requires high luminosity operation and sets stringent limits on the momentum resolution of the tracking detectors. The branching ratio of the decay of a Standard Model Higgs boson to a pair of muons is important as the lower end of the accessible decays and defines the endpoint of the test of the predicted linear dependence of the branching ratios to the mass of the final state particles.

The events are selected by requiring two reconstructed muons, each with a transverse momentum of at least 5 GeV. In this note, the most energetic muon is referred to as μ_1 and the second most energetic muon is referred to as μ_2. In addition, the invariant mass of the two muons $M(\mu^+\mu^-)$ is required to lie between 105 GeV and 135 GeV.

The muon reconstruction efficiency is shown in Figure 3 (left). The beam induced background from $\gamma\gamma \to$ hadrons leads to a small deterioration of the muon reconstruction efficiency. The average muon reconstruction efficiency for polar angles greater than 10° is 98.4% with this background compared to 99.6% without. The total reconstruction efficiency of the signal sample, requiring two reconstructed muons with an invariant mass between 105 GeV and 135 GeV is 72% in the presence of background.

The event classification is done using boosted decision tree classifier implemented in TMVA [14]. The BDT is trained to separate the $\mu^+\mu^-\nu\bar{\nu}$ signal events from the $\mu^+\mu^- e^+e^-$ background. The $\mu^+\mu^-$, $\tau^+\tau^-$ and $\tau^+\tau^-\nu\bar{\nu}$ samples are not used in the training of the BDT, but are effectively removed by the classifier nevertheless.

The variables used for the event selection by the BDT are:

- The visible energy excluding the two reconstructed muons E_{vis}.
- The scalar sum of the transverse momenta of the two muons $p_{\text{T}}(\mu_1) + p_{\text{T}}(\mu_2)$.
- The helicity angle $\cos\theta^*(\mu^+\mu^-) = \frac{\vec{p}'(\mu_1)\cdot\vec{p}(\mu^+\mu^-)}{|\vec{p}'(\mu_1)|\cdot|\vec{p}(\mu^+\mu^-)|}$, where $\vec{p}'$ is the momentum in the rest frame of the di-muon system. Since the two muons are back-to-back in the rest frame of the di-muon system there is no additional information to be gained from calculating a similar angle for μ_2.
- The relativistic velocity of the di-muon system $\beta(\mu^+\mu^-)$, where $\beta = \frac{v}{c}$.
- The transverse momentum of the di-muon system $p_{\text{T}}(\mu^+\mu^-)$.
- The polar angle of the di-muon system $\theta(\mu^+\mu^-)$.

The major discriminant is the visible energy whenever there is an electron within the detector acceptance. Otherwise the background can be rejected by the transverse momentum of the di-muon system or the sum

of the two individual transverse momenta. Figure 3 (right) shows the Higgs peak in the invariant mass distribution after the event selection.

The dominant background from $e^+e^- \to e^+e^-\mu^+\mu^-$ events, is effectively reduced by forward electron tagging. While the forward calorimeters were not part of the full detector simulation, assuming a tagging efficiency of 95% down to an angle of 40 mrad for electrons of several hundred GeV to over one TeV is a conservative estimate, even in the presence of $\gamma\gamma \to$ hadrons background. It is found that Bhabha events prevent further rejection of this background at lower angles. The results quoted are based on a ad-hoc rejection of 95% of the electrons in the Luminosity Calorimeter.

4.1 Invariant mass fit

The distribution of the invariant mass in the $H \to \mu^+\mu^-$ sample has a tail towards lower masses because of final state radiation. The shape can be described best by two half Gaussian distributions with an exponential tail. Together with the mean value this results in five free parameters in the fitted function, which can be written as

$$f(x) = n \begin{cases} e^{\frac{-(x-m_0)^2}{2\sigma_L^2+\alpha_L(x-m_0)^2}} & , x \le m_0 \\ e^{\frac{-(x-m_0)^2}{2\sigma_R^2+\alpha_R(x-m_0)^2}} & , x > m_0 \end{cases} ,$$

where m_0 is the mean of both Gaussian distributions, σ_L and σ_R are the widths, and α_L and α_R are the tail parameters of the left and the right Gaussian distribution, respectively; n is a normalization parameter. The background is well described by an exponential parameterization, obtained from a background-only sample.

The number of signal events is obtained from a maximum likelihood fit to the sample containing signal plus background after the event selection.

The average muon momentum resolution of the fully simulated sample is $4 \times 10^5\,\mathrm{GeV}^{-1}$ corresponding to a statistical uncertainty of 23% without the forward electron tagging. If the background from $e^+e^- \to \mu^+\mu^-$ can be reduced using tagging of electrons down to an angle of 40 mrad with an efficiency of 95%, the cross section times branching ratio can be measured to a precision of 15%.

5 Summary

The sensitivity to the decay branching ratios of a neutral 120 GeV Standard Model Higgs boson to bottom and charm quarks and to muons has been studied at the CLIC centre-of-mass energy of $\sqrt{s} = 3\,\mathrm{TeV}$ and integrated luminosity of $2\,\mathrm{ab}^{-1}$. The analysis is based on full simulation and realistic event reconstruction in the CLIC_SiD detector. We have demonstrated the feasibility of such measurements and estimated their statistical uncertainty.

For the measurement of Higgs decays to quarks, 0.22% and 3.2% statistical uncertainty can be achieved for the decays $H \to b\bar{b}$ and $H \to c\bar{c}$, respectively. This includes the effect of background from $\gamma\gamma \to$ hadrons on the flavor tagging.

For the rare decay $H \to \mu^+\mu^-$, the cross section times branching ratio can be measured to a precision of 15% if the background from $e^+e^- \to \mu^+\mu^-$ can be reduced using tagging of electrons down to an angle of 40 mrad with an efficiency of 95%. The effect of $\gamma\gamma \to$ hadrons has been taken into account conservatively by only including it in the signal sample and thus reducing its reconstruction efficiency.

From experience of the LEP experiments one can assume that the systematic uncertainties related to detector effects are of the order of 1% or less. For the measurement of $\sigma_{Z^0 \to \mu^+\mu^-}$ at LEP the systematic uncertainty was between 0.1 and 0.4%, depending on the experiment. Thus we expect that the systematic uncertainty of the $H \to \mu^+\mu^-$ analysis will be negligible compared to the statistical uncertainty, the uncertainty of $H \to b\bar{b}$ analysis will be dominated by the systematic and theoretical uncertainties and in the $H \to c\bar{c}$ analysis the uncertainty sources will contribute comparably.

References

[1] The CLIC Accelerator Design, Conceptual Design Report; https://edms.cern.ch/document/1180032/.

[2] T. Lastovicka. Light Higgs boson production and hadronic decays at 3 TeV, 2011. CERN LCD-Note-2011-036 .

[3] C. Grefe. Light Higgs decay into muons in the CLIC_SiD CDR detector, 2011. CERN LCD-Note-2011-035.

[4] C. Grefe and A. Münnich. The CLIC_SiD_CDR geometry for the CDR Monte Carlo mass production, 2011. CERN LCD-Note-2011-009 .

[5] H. Aihara et al. SiD Letter of Intent, 2009. arXiv:0911.0006, SLAC-R-944.

[6] W. Kilian, T. Ohl, and J. Reuter. WHIZARD: Simulating multi-particle processes at LHC and ILC, 2007. arXiv:0708.4233v1 .

[7] M. Moretti, T. Ohl, and J. Reuter. O'Mega: An optimizing matrix element generator, 2001. arXiv:hep-ph/0102195v1.

[8] T. Sjostrand, S. Mrenna, and P. Z. Skands. PYTHIA 6.4 Physics and Manual. *JHEP*, 05:026, 2006. hep-ph/0603175.

[9] Simulator for the Linear Collider (SLIC), http://www.lcsim.org/software/slic/.

[10] J. Allison et al. Geant4 developments and applications. *IEEE Trans. Nucl. Sci.*, 53:270, 2006.

[11] M. Cacciari and G. P. Salam. Dispelling the N^3 myth for the k_t jet-finder. *Phys. Lett.*, B641:57–61, 2006. hep-ph/0512210.

[12] A. Bailey and *et al.* (LCFI Collaboration). LCFIVertex package: Vertexing, flavour tagging and vertex charge reconstruction with an ILC vertex detector. *Nucl. Instrum. Methods Phys. Res. A*, A 610:573–589, 2009.

[13] Fast Artificial Neural Network Library (FANN). http://leenissen.dk/fann/wp/.

[14] A. Höcker, P. Speckmayer, J. Stelzer, J. Therhaag, E. von Toerne, and H. Voss. TMVA - Toolkit for multivariate data analysis, 2009. arXiv:physics/0703039.

LC-TH-2012-002
KA-TP-12-2012
SFB/CPP-12-17

Determination of Higgs-boson couplings (SFitter)

*Michael Rauch**

Institut für Theoretische Physik, Karlsruher Institut für Technologie (KIT), Karlsruhe, Germany

DOI: will be assigned

After the discovery of a Higgs boson, the next step is to measure its properties and test their accordance with the predictions of the Standard Model, in particular the couplings of the Higgs boson. In this talk we discuss what information the LHC will be able to give us over the coming years, and what remains as a task for a future Linear Collider.

Using the well-established SFitter framework, we map measurements onto a weak-scale effective theory with general Higgs boson couplings. Our sophisticated error treatment allows us to take all theory and experimental errors, including arbitrary correlations, fully into account.

1 Introduction

Completing our understanding of the electro-weak symmetry-breaking mechanism is one of the main tasks for present and future particle colliders. In the Standard Model (SM), this is accomplished by introducing a complex $SU(2)$ doublet, the Higgs field, which obtains a vacuum expectation value (vev) [1, 2, 3]. Three of the four degrees of freedom form the longitudinal modes of W and Z bosons, while the remaining one becomes a physical particle, the Higgs boson. Interactions between these gauge bosons and the Higgs field are introduced automatically via the latter's kinetic term, while interactions with fermions are added via Yukawa-type couplings. Replacing the Higgs field by its vev then yields mass terms for the gauge bosons and fermions. Therefore, the couplings of the Higgs boson to the other particles are fixed and proportional to the measured masses and the vev.

The mass of the Higgs boson is the only remaining unknown parameter in the SM. Direct searches by LEP [4], Tevatron [5] and in particular the LHC experiments ATLAS [6] and CMS [7] have excluded large parts of the parameter space, leaving only a small window around 125 GeV. High-mass values, where the experimental sensitivity drops again, are strongly disfavoured by indirect constraints from electro-weak precision data [8, 9]. As mentioned before, the Higgs couplings in the SM are completely determined by the known particle masses. Therefore, we can use these theoretically predicted values and compare them to future measurements of Higgs boson channels [10, 11, 12, 13, 14, 15, 16]. Thereby, we assume that the discrete quantum numbers, like its CP property or spin [17], are identical to the SM expectation. Many models of new physics predict deviations in the Higgs couplings, which can then be measured. Examples include models with an extended Higgs sector, like the two-Higgs doublet structure e.g. in supersymmetry [18], or also Higgs portal models [19], but modifications can also be more elementary as in composite models [20], where the Higgs boson emerges as a pseudo-Goldstone boson of a new strongly-interacting sector.

A correct treatment of all errors is important to obtain correct results. As in the Higgs boson channels rates are measured, these statistical errors are of the Poisson type. Additionally, there are systematic errors, which are correlated, and we implement the full correlation matrix between different measurements. Theory errors are best described as box-shaped [3], using the prescription of the RFit scheme [21]. In the SFitter tool [22] these different types of errors are fully implemented. As output we obtain a fully-dimensional log-likelihood map, which we can then reduce to plotable one- or two-dimensional distributions via both Bayesian (marginalisation) and Frequentist (profile likelihood) techniques. Furthermore, a list of best-fitting points is obtained.

*for the SFitter collaboration

2 Setup of the Calculation

As the underlying model of our study we assume the Standard Model with a generalised Higgs sector, where the Higgs couplings can take arbitrary values. These are parametrised in the following way: Couplings to particles i, which are present at tree-level in the SM, are modified according to

$$g_{iiH} \to g_{iiH}^{\mathrm{SM}}(1 + \Delta_{iiH}) \ . \tag{1}$$

As a global sign flip of all couplings is not observable, we always take g_{WWH} to be positive, *i.e.* $\Delta_{WWH} > -1$. Additionally, there are two important loop-induced couplings present, namely those to gluons and photons. They are altered in the following way:

$$g_{iiH} \to g_{iiH}^{\mathrm{SM}}(1 + \Delta_{iiH}^{\mathrm{SM}} + \Delta_{iiH}) \ . \tag{2}$$

These can receive two types of contributions. First, there are contributions from changing the tree-level couplings, $\Delta_{iiH}^{\mathrm{SM}}$. Second, there can be additional dimension-five contributions Δ_{iiH}. They originate from new particles running in the loop, e.g. the supersymmetric partners in SUSY models. The numerical values of the couplings are obtained from a modified version of HDecay [23]. Also the masses of the Higgs boson and the top and bottom quark are added as free parameters and corresponding measurements constrain them to their experimentally measured value. Additionally, we define Δ_H as a single free parameter that changes all (tree-level) couplings simultaneously.

The total width of the Higgs boson is too small to be measured directly at the LHC. Therefore we have to make one single model assumption about how to treat the total width, which we take as

$$\Gamma_{\mathrm{tot}} = \sum_{\mathrm{obs}} \Gamma_i(g_{iiH}) + \text{generation universality} \ .$$

This means that there are no further contributions from Higgs decays into invisible particles. The assumption about generation universality is important as the Higgs has a significant branching ratio of several percent into unobservable particles (e.g. charm quarks) for which at the LHC there is no possibility to measure them, and neglecting them would introduce a bias. Further details of the setup have been described in Refs. [11, 12]. We will not consider any couplings that can only be measured with very high luminosity or not at all. This includes the only second-generation Yukawa coupling that might be measurable at the LHC, namely those to muons [24, 25], as well as the Higgs self-couplings [26, 27, 28, 29].

3 Results

3.1 Expectations for the LHC at 14 TeV

The measurements that enter our analysis are derived from an ATLAS Monte Carlo study performed for an integrated luminosity of 30 fb^{-1} and assuming a centre-of-mass energy of 14 TeV [11, 30]. We perform a simulation with typically 5000 toy Monte Carlos, where we smear the signal and background expectations according to their corresponding errors, and fit the resulting Higgs couplings.

In Fig. 1 we show the results of our analysis. The different curves denote the 68% CL errors on the Δ_{iiH} parameter for the respective coupling. As input value for the signal strength we assume a SM Higgs boson of the given mass value and note that for reduced couplings the change in the absolute value of the errors is small. On the left-hand side of the figure we present results where additional contributions from dimension-five operators have been neglected. Also shown is the result for the single-parameter modifier Δ_H. On the right-hand side the dimension-five operators are taken into account as well. In both cases the coupling of the Higgs to W bosons can be measured best, between 10 and 20% over the whole mass range. The dimension-five operators thereby reduce the sensitivity to this coupling somewhat. Yukawa couplings to bottom quarks and τ leptons can only be determined with good accuracy for Higgs masses below 140 to 150 GeV, as for larger masses the corresponding branching ratios become too small. The top quark is strongly affected by the dimension-five operators Without these operators the gluon-fusion production processes contribute to the precision of this coupling. Including them, the top-quark coupling needs to be determined by the badly measurable top-quark-associated production modes, and gluon-fusion production then pins down the size of the additional operators relative to the top quark coupling.

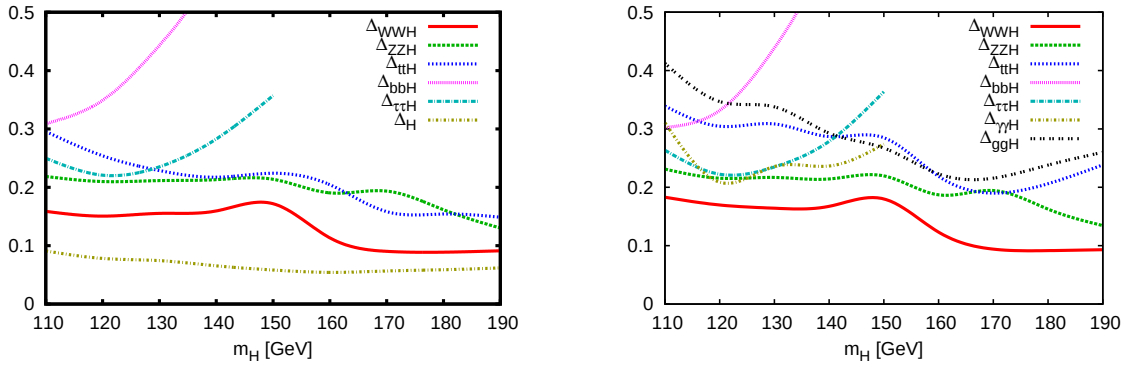

Figure 1: Error on the Higgs-boson couplings as a function of the Higgs mass without *(left)* and including *(right)* additional dimension-five operators. The left-hand plot also includes the result for a single-parameter modification Δ_H. Results are for the LHC at 14 TeV centre-of-mass energy and an integrated luminosity of 30 fb^{-1}, assuming SM Higgs couplings. Figures taken from Ref. [31].

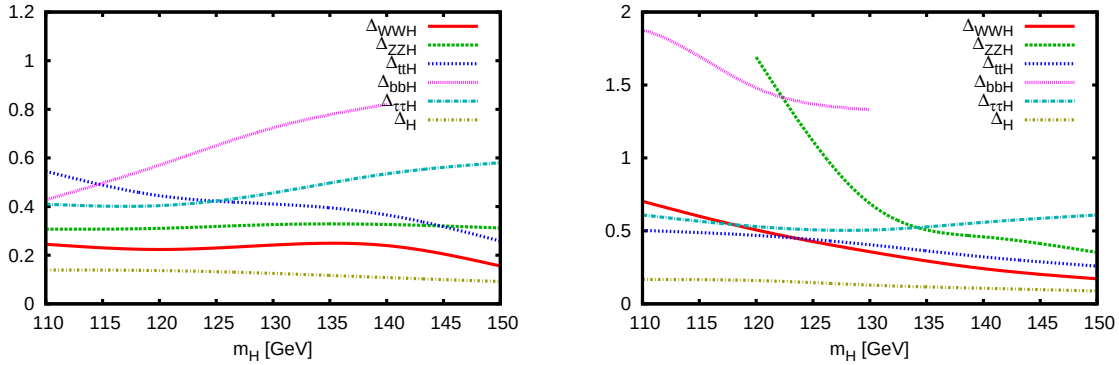

Figure 2: Error on the Higgs-boson couplings as a function of the Higgs mass including *(left)* and without *(right)* the subjet analyses in the Higgsstrahlung production processes with decays into bottom quarks. Results are for the LHC at 7 TeV centre-of-mass energy and an integrated luminosity of 20 fb^{-1}, assuming SM Higgs couplings, obtained by extrapolating the 14-TeV-Monte-Carlo studies.

3.2 Extrapolation to 7 TeV

To get an estimate of what to expect from the LHC in the near future, we have extrapolated these studies to a centre-of-mass energy of 7 TeV. For the backgrounds the inclusive cross sections of the individual contributions were computed with Sherpa [32] and the event rate scaled according to the numbers obtained. For the signal we assume that the signal efficiencies, i.e. the number of signal events remaining after the selection cuts and detector acceptance corrections relative to the original rate, stays unchanged. The cross sections themselves for both centre-of-mass energies are taken from Ref. [3]. As the expected precision on the couplings will be rather low, only the case of vanishing additional dimension-five operators is considered here.

In Fig. 2 we show the corresponding results for an integrated luminosity of 20 fb^{-1}, corresponding to approximately what is expected for the end of 2012[1]. On the left-hand side we include all channels of the 14-TeV analysis. We observe the same principal behaviour as in Fig. 1, but with a significant increase in the expected errors. Nevertheless, with this amount of data a determination of Δ_H with a precision of

[1]The increased centre-of-mass energy of 8 TeV for the 2012 run can be approximated by a corresponding increase in the integrated luminosity.

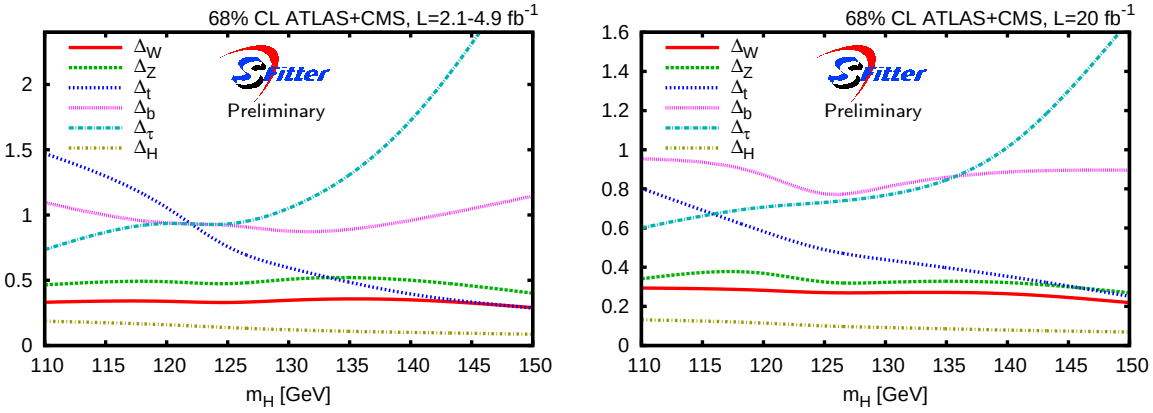

Figure 3: Precision of tree-level Higgs-boson couplings as well as single-parameter modifier as a function of the Higgs mass using current LHC searches as input. Results are presented for the luminosities used in the analyses *(left)* and extrapolated to 20 fb^{-1} *(right)*. Figure from Ref. [15].

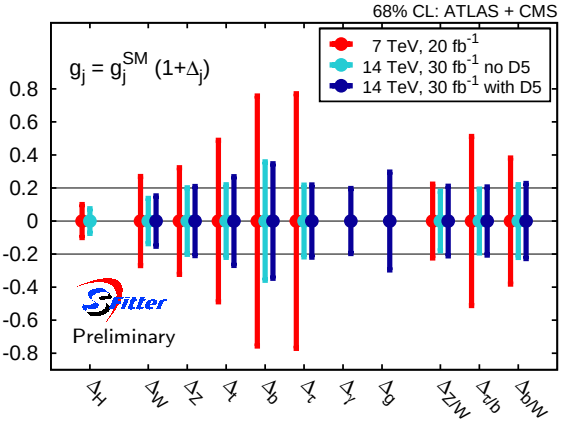

Figure 4: Overview of LHC expectations in different scenarios for energy and integrated luminosity for a SM Higgs boson with mass of 125 GeV. Figure from Ref. [15].

14% is already possible for a Higgs boson mass of 125 GeV. On the right-hand side the channels making use of subjet techniques [33] are removed. These consist of Higgs bosons produced in association with a W or Z boson, where the Higgs decays into bottom quarks and the decay products are required to be strongly boosted in order to reduce backgrounds. A significant drop in accuracy can be observed mainly for two couplings. The coupling to Z bosons is now predominantly determined by the decay of the Higgs to four leptons, which suffers from low event numbers for lighter Higgs masses. The bottom-quark Yukawa coupling has to rely on the top-quark-associated production channel with decays into bottom quarks as well as its contribution to gluon-fusion production. The first one suffers from a large combinatorial background, while in the second case the bottom-quark loop is only a small contribution. The badly determined bottom coupling then influences all other couplings via the total width.

3.3 Results and Expectations from Current Measurements

With direct search results available from the LHC, we can update the results of the previous subsection using the actual background expectations and errors as described in the analyses [6, 7]. Thereby we assume as input that there is a SM Higgs boson at the considered mass value and add a SM Higgs signal to the background expectations. These results are depicted in Fig. 3. On the left we show errors on the Higgs couplings using for each measurement the luminosity for which the analysis has been performed. With this

data a precision of 14% on Δ_H is already possible, and the couplings to the weak bosons can also be measured fairly precisely. The error on the top-quark Yukawa coupling is mostly determined by Higgs production via gluon-fusion decaying into a W pair. The sensitivity of this channel drops rapidly below 125 GeV, leading to the observed behaviour of the top-quark coupling. On the right-hand side we present expectations when extrapolating all analyses to an integrated luminosity of 20 fb^{-1}. This extrapolation is done blindly, i.e. the improvement is purely statistical. The precision on the single-parameter modifier now reaches 9% for a Higgs mass around 125 GeV.

In Fig. 4 the different results shown previously are summarised for a hypothetical Higgs boson at 125 GeV assuming SM couplings as a central value. The three values on the right-hand side of the plot show errors on ratios of couplings. While for the Z over W Higgs couplings at 7 TeV only a small improvement over the absolute measurements is achievable, the situation is different for the two other ratios involving the bottom Yukawa coupling. Here correlations are important and therefore the ratio is better determined. At a 14 TeV LHC the situation is different. Using ratios yields no improvement over absolute values in any case.

4 Models of New Physics

In physics models beyond the Standard Model the couplings between the Higgs boson and the gauge bosons and fermions can be modified from the SM theory prediction. In this section we will discuss two such models, a Higgs portal [19] as well as a strongly-interacting light Higgs [20].

4.1 Higgs Portal

In the Higgs portal model, an additional hidden sector is added which is a singlet under the SM gauge groups. A connection to the SM is only possible via a term connecting the Higgs field of the SM Φ_s with that of the hidden sector Φ_h

$$\mathcal{L} \propto \Phi_s^\dagger \Phi_s \Phi_h^\dagger \Phi_h \ .$$

After electro-weak symmetry-breaking both fields obtain a vev. The two physical Higgs bosons of the SM and the hidden sector mix and need to be rotated into mass eigenstates

$$\begin{pmatrix} H_1 \\ H_2 \end{pmatrix} = \begin{pmatrix} \cos\chi & \sin\chi \\ -\sin\chi & \cos\chi \end{pmatrix} \begin{pmatrix} H_s \\ H_h \end{pmatrix} \ . \tag{3}$$

The parameter $\cos\chi$ corresponds to our single-parameter modifier Δ_H defined before. The cross sections and branching ratios then change in the following way from their SM value for H_1

$$\sigma = \cos^2\chi \cdot \sigma^{\mathrm{SM}} \tag{4}$$

$$\Gamma_{\mathrm{vis}} = \cos^2\chi \cdot \Gamma_{\mathrm{vis}}^{\mathrm{SM}} \tag{5}$$

$$\Gamma_{\mathrm{inv}} = \cos^2\chi \cdot \Gamma_{\mathrm{inv}}^{\mathrm{SM}} + \Gamma_{\mathrm{hid}} \ . \tag{6}$$

$\Gamma_{\mathrm{inv}}^{\mathrm{SM}}$ is induced by Higgs decays into four neutrinos, which has a negligible rate for light Higgs bosons. The partial decay width into the hidden sector Γ_{hid} is a free parameter and depends on the structure, i.e. couplings and masses, of the hidden sector particles, being zero if they are all heavy. Corresponding equations hold for H_2 with the replacement $\cos\chi \leftrightarrow \sin\chi$ plus possibly decays $H_2 \to H_1 H_1$ added, if this channel is kinematically allowed.

In Fig. 5 we present the fitted $\cos^2\chi$ as a function of the Higgs mass in a scenario where the Higgs contains no additional decay modes into invisible particles. $\cos^2\chi$ is a free parameter, which is not constrained to its physical range. On the left-hand side the input value of $\cos^2\chi$ is chosen as one, corresponding to the SM scenario. Hence, this curve corresponds to the Δ_H line of Fig. 1. The central value is correctly reproduced by the fit. Errors at the 95% CL range between 25% and 50% with the highest precision obtainable for a mass of 170 GeV. On the right-hand side the same plot is shown but now with an input value of $\cos^2\chi = 0.6$. The central values are shifted down to smaller values, but the absolute size of the errors stays approximately the same. This is due to the fact that most channels have large backgrounds, which are not affected by a

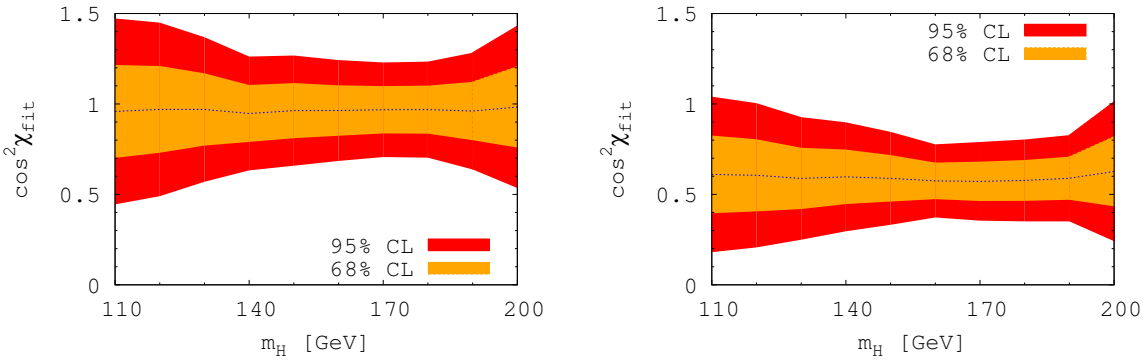

Figure 5: Precision in the Higgs portal model assuming a theory input of $\cos^2\chi = 1$ *(left)*, corresponding to the SM value, and an input value of $\cos^2\chi = 0.6$ *(right)*. Numbers assume LHC data at 14 TeV with an integrated luminosity of 30 fb^{-1} and no invisible decay modes.

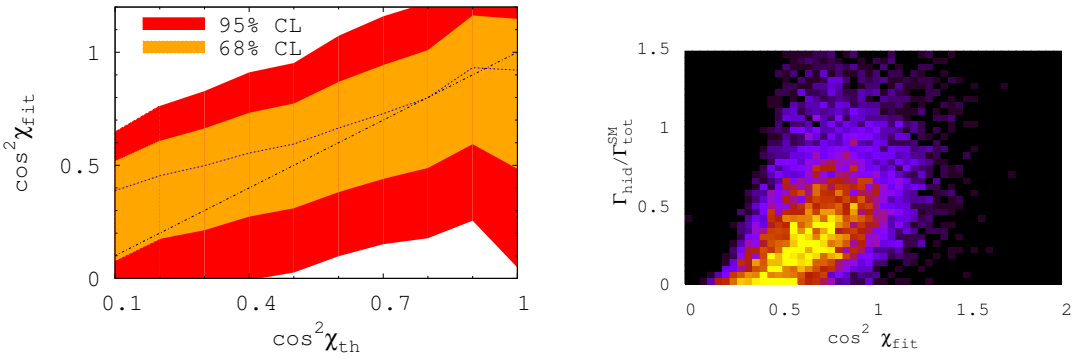

Figure 6: Precision in the Higgs portal model assuming a Higgs mass of 120 GeV and including invisible decays with $\Gamma_{\rm hid} = \sin^2\chi \cdot \Gamma^{\rm SM}_{\rm tot}$. We show the fitted value $\cos^2\chi_{\rm fit}$ over the input value $\cos^2\chi_{\rm th}$ *(left)*, as well as the correlation between $\cos^2\chi_{\rm fit}$ and $\Gamma_{\rm hid}$ for an input value of $\cos^2\chi_{\rm th} = 0.6$ *(right)*. Numbers assume LHC data at 14 TeV with an integrated luminosity of 30 fb^{-1}. The brightness in the correlation plot on the right-hand side denotes the resulting log-likelihood.

reduction in signal cross section. At the chosen luminosity of 30 fb^{-1} these give the dominant effect. Also, the value $\cos^2\chi = 1$ is outside the 95% CL band over almost the whole mass range. Therefore, in this scenario the SM could be excluded at the 95% CL.

Figure 6 shows the fitted over the input $\cos^2\chi$ for a Higgs boson mass of 120 GeV. Now decays into the invisible sector are also included with a partial width of $\sin^2\chi$ times the SM Higgs width. This corresponds for example to the case where the hidden sector is an exact copy of the SM sector. Correspondingly, a measurement of the branching ratio into invisible particles is added [34, 35, 36]. This will be possible only with a rather low precision at the LHC. Therefore, the expected accuracy on $\cos^2\chi$ is much lower than in the previous case, as can be seen on the left-hand side of Fig. 6. Also, at low values of $\cos^2\chi$, we see a deviation of the fitted value, tending to be larger than the input one. This is because only measurements with a positive signal are taken into account. Positive fluctuations are hence always included, while negative ones might get removed. The observation of a Higgs signal therefore favours larger values of the coupling. On the right-hand side of Fig. 6 a correlation plot between the invisible decay width and the fitted $\cos^2\chi$ is depicted for an input value of $\cos^2\chi = 0.6$. A strong correlation between the two variables is visible, which is the origin of the large errors on $\cos^2\chi$ observed before. This correlation is due to the total width of the Higgs boson, where the invisible decay width enters. As the denominator in the branching ratio it enters into all measurements.

4.2 Strongly-interacting Light Higgs

In strongly-interacting light Higgs models [20], the Higgs boson emerges as a pseudo-Goldstone boson of a new, strongly-interacting sector. As a pseudo-Goldstone boson, the Higgs can be much lighter than the other particles of the theory and therefore be in the mass range still allowed by all experimental constraints, while the other ones can be chosen heavy enough to avoid constraints from direct searches. Modifications of the Higgs-boson couplings can be parametrised by $\xi = \left(\frac{v}{f}\right)^2$, where $v = 246$ GeV is the SM Higgs vev and f the Goldstone scale. The limit $f \to \infty$ corresponds to the SM, while $f = v$ are Technicolour models.

There are two important phenomenological implementations. In the first one, called MCHM4, all couplings of the Higgs boson to other particles scale with $\sqrt{1-\xi}$. Therefore, the results of the Higgs portal in the previous subsection can be reused by identifying $\cos^2\chi = 1 - \xi$ and setting invisible decay modes to zero. In the second one, MCHM5, the couplings change differently for vector bosons and fermions

$$g_{VVH} = g^{\mathrm{SM}}_{VVH} \cdot \sqrt{1-\xi}$$
$$g_{f\bar{f}H} = g^{\mathrm{SM}}_{f\bar{f}H} \cdot \frac{1-2\xi}{\sqrt{1-\xi}} \,.$$

The latter one has the interesting feature that the coupling vanishes for $\xi = 0.5$ and flips its sign for values below that. These models also show significant deviations in Higgs pair-production processes [37], which we will not consider further here.

In Fig. 7 we depict the fitted value of ξ over the input one for an integrated luminosity of 30 (left) and 300 fb^{-1} (right) at the 14 TeV LHC. The shaded region around $\xi = 0.5$ denotes the region where the cross sections are so low, that with the given luminosity no evidence of a Higgs boson is yet expected. For the lower luminosity there are always two possible solutions. One corresponds to the correct solution, while the other originates from the ambiguity in the fermion-Higgs coupling. The sign of the coupling is only observable as interference between W-boson and top-quark loop in the effective photon coupling. With the higher luminosity this degeneracy is lifted, as can be seen on the right-hand side of Fig. 7. This is further demonstrated in Fig. 8. Here we show the log-likelihood for 30 fb^{-1} in the two individual channels which contribute most to the parameter determination. Both channels vanish at $\xi = 0.5$ and therefore for this value the log-likelihood is constant independent of the parameter. The left channel is gluon-fusion Higgs production with decays into photons. For each input value two different solutions can be found that cannot be distinguished, as they yield the same rate. On the right-hand side, we show the combination of vector-boson associated production channels with decay into bottom quarks via subjet techniques, which are all governed by the same coupling factors. Here for $\xi \lesssim 0.4$ only a single solution exists, while for larger values additional solutions appear. These do not coincide with the secondary solution of the first channel, however,

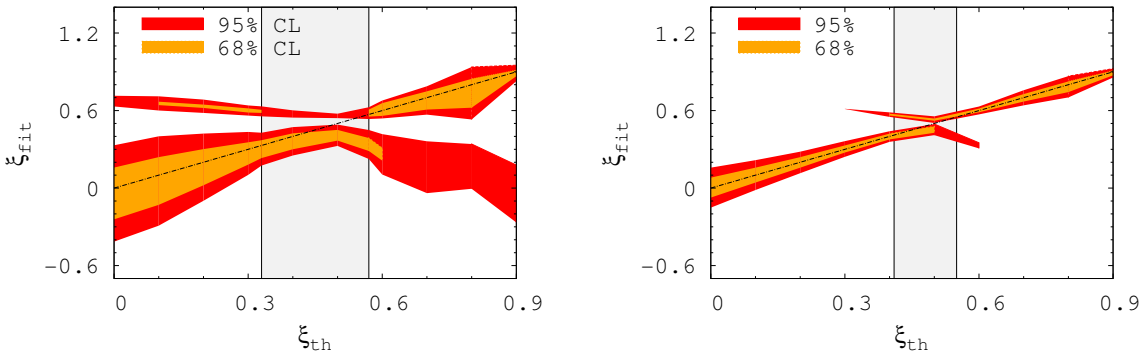

Figure 7: Best-fit values and 68% and 95% CL error bands in the MCHM5 model for the LHC at 14 TeV assuming a Higgs boson mass of 120 GeV as function of the input value $\xi_{\rm th}$. Results are shown for an integrated luminosity of 30 *(left)* and 300 fb^{-1} *(right)*.

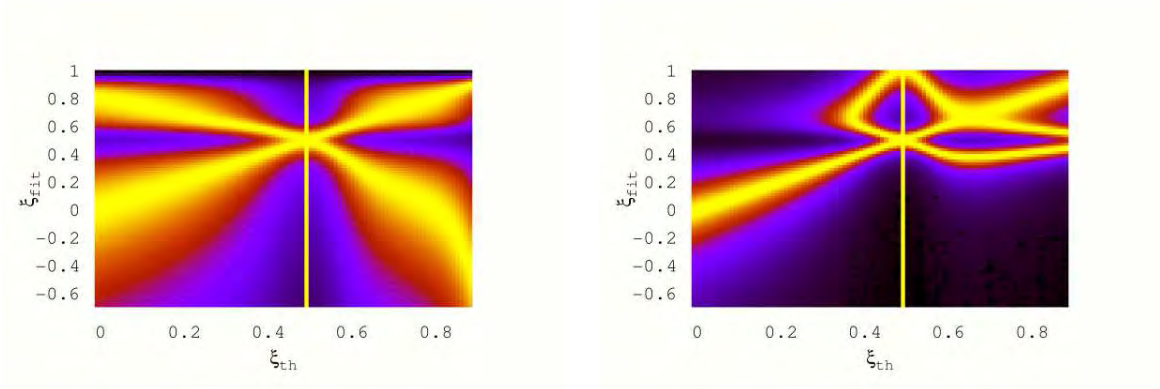

Figure 8: Best-fit distribution for two main channels: gluon-fusion production with decay into photons *(left)* and vector-boson-associated production with decay into bottom quarks *(right)*. Results are shown for a Higgs boson of 120 GeV at the LHC at 14 TeV and an integrated luminosity of 30 fb^{-1}. The brightness denotes the resulting log-likelihood.

so for the nominal values the solution becomes unique. Therefore, the degeneracy is not a true one, but induced by fluctuations due to errors and can be lifted with more data.

5 Conclusions

The determination of the Higgs-boson couplings is an important task to verify our understanding of electroweak symmetry breaking and the Higgs mechanism. We have studied how well we can measure these couplings at the LHC and what remains as a task for a future linear collider. To be independent of any specific new-physics model, we take as a model the Standard Model, where all Higgs couplings are left as free parameters. Using the SFitter framework, all experimental and theory errors, as well as their correlations, can be fully taken into account. For a single parameter modifying all couplings an error of 9% is achievable for a Higgs boson mass of 125 GeV. We have also interpreted our results in terms of new-physics models, namely a Higgs portal and a strongly-interacting light Higgs. For the former, invisible decay modes provide an additional experimental challenge. In the latter case, statistical fluctuations lead to secondary solutions, which also need to be considered.

Acknowledgments

We would like to thank the organisers of the LC-Forum for the friendly atmosphere during the workshop and the possibility to present our results. Support by the Deutsche Forschungsgemeinschaft via the Sonderforschungsbereich/Transregio SFB/TR-9 "Computational Particle Physics" and the Initiative and Networking Fund of the Helmholtz Association, contract HA-101("Physics at the Terascale") is acknowledged.

References

[1] P. W. Higgs, Phys. Lett. **12**, 132 (1964); P. W. Higgs, Phys. Rev. Lett. **13**, 508 (1964); F. Englert and R. Brout, Phys. Rev. Lett. **13**, 321 (1964).

[2] A. Djouadi, Phys. Rept. **457**, 1 (2008) [arXiv:hep-ph/0503172]. V. Büscher and K. Jakobs, Int. J. Mod. Phys. A **20**, 2523 (2005); [arXiv:hep-ph/0504099]. D. Rainwater, arXiv:hep-ph/0702124;

[3] S. Dittmaier *et al.* [LHC Higgs Cross Section Working Group Collaboration], arXiv:1101.0593 [hep-ph]; arXiv:1201.3084 [hep-ph].

[4] [LEP, Tevatron and SLD Collaborations and Working Groups], arXiv:0811.4682 [hep-ex].

[5] [TEVNPH (Tevatron New Phenomina and Higgs Working Group) and CDF and D0 Collaborations], arXiv:1203.3774 [hep-ex].

[6] ATLAS Collaboration, ATLAS-CONF-2012-019.

[7] CMS Collaboration, CMS-PAS-HIG-12-008.

[8] D. Y. .Bardin, P. Christova, M. Jack, L. Kalinovskaya, A. Olchevski, S. Riemann and T. Riemann, Comput. Phys. Commun. **133** (2001) 229 [hep-ph/9908433]; A. B. Arbuzov, M. Awramik, M. Czakon, A. Freitas, M. W. Grunewald, K. Monig, S. Riemann and T. Riemann, Comput. Phys. Commun. **174** (2006) 728 [hep-ph/0507146].

[9] H. Flacher, M. Goebel, J. Haller, A. Hocker, K. Monig, J. Stelzer, Eur. Phys. J. **C60**, 543-583 (2009). [arXiv:0811.0009 [hep-ph]], M. Baak, M. Goebel, J. Haller, A. Hoecker, D. Ludwig, K. Moenig, M. Schott, J. Stelzer, [arXiv:1107.0975 [hep-ph]].

[10] D. Zeppenfeld, R. Kinnunen, A. Nikitenko and E. Richter-Was, Phys. Rev. D **62** (2000) 013009 [hep-ph/0002036]; M. Dührssen, S. Heinemeyer, H. Logan, D. Rainwater, G. Weiglein and D. Zeppenfeld, Phys. Rev. D **70**, 113009 (2004).

[11] R. Lafaye, T. Plehn, M. Rauch, D. Zerwas and M. Duhrssen, JHEP **0908**, 009 (2009) [arXiv:0904.3866 [hep-ph]], M. Rauch [SFitter Collaboration], [arXiv:1005.2843 [hep-ph]].

[12] S. Bock, R. Lafaye, T. Plehn, M. Rauch, D. Zerwas, P. M. Zerwas, Phys. Lett. **B694**, 44-53 (2010). [arXiv:1007.2645 [hep-ph]].

[13] F. Bonnet, M. B. Gavela, T. Ota, W. Winter, [arXiv:1105.5140 [hep-ph]].

[14] D. Carmi, A. Falkowski, E. Kuflik and T. Volansky, arXiv:1202.3144 [hep-ph]; A. Azatov, R. Contino and J. Galloway, arXiv:1202.3415 [hep-ph]; J. R. Espinosa, C. Grojean, M. Muhlleitner and M. Trott, arXiv:1202.3697 [hep-ph]; P. P. Giardino, K. Kannike, M. Raidal and A. Strumia, arXiv:1203.4254 [hep-ph];

[15] M. Rauch, talk at Moriond EW 2012; M. Klute, R. Lafaye, T. Plehn, M. Rauch, D. Zerwas, M. Dührssen, in preparation.

[16] J. A. Aguilar-Saavedra *et al.* [ECFA/DESY LC Physics Working Group Collaboration], hep-ph/0106315; E. Accomando *et al.* [CLIC Physics Working Group Collaboration], hep-ph/0412251; S. Heinemeyer, S. Kanemura, H. Logan, A. Raspereza, T. M. P. Tait, H. Baer, E. L. Berger and A. Birkedal *et al.*, hep-ph/0511332; G. Aarons *et al.* [ILC Collaboration], arXiv:0709.1893 [hep-ph]; W. Lohmann, M. Ohlerich, A. Raspereza and A. Schalicke, eConf C **0705302** (2007) TIG13 [arXiv:0710.2602 [hep-ex]]; and references therein.

[17] J. R. Dell'Aquila and C. A. Nelson, Phys. Rev. D **33**, 93 (1986).; D. J. Miller, 2, S. Y. Choi, B. Eberle, M. M. Muhlleitner and P. M. Zerwas, Phys. Lett. B **505** (2001) 149 [hep-ph/0102023]; T. Plehn, D. Rainwater and D. Zeppenfeld, Phys. Rev. Lett. **88**, 051801 (2002); C. P. Buszello, I. Fleck, P. Marquard and J. J. van der Bij, Eur. Phys. J. C **32**, 209 (2004); V. Hankele, G. Klamke, D. Zeppenfeld and T. Figy, Phys. Rev. D **74**, 095001 (2006); C. Ruwiedel, N. Wermes and M. Schumacher, Eur. Phys. J. C **51**, 385 (2007); K. Hagiwara, Q. Li and K. Mawatari, JHEP **0907** (2009) 101 [arXiv:0905.4314 [hep-ph]]; C. Englert, C. Hackstein and M. Spannowsky, Phys. Rev. D **82** (2010) 114024 [arXiv:1010.0676 [hep-ph]]; R. M. Godbole, C. Hangst, M. Muhlleitner, S. D. Rindani and P. Sharma, Eur. Phys. J. C **71** (2011) 1681 [arXiv:1103.5404 [hep-ph]]; J. Ellis and D. S. Hwang, arXiv:1202.6660 [hep-ph]; C. Englert, M. Spannowsky and M. Takeuchi, arXiv:1203.5788 [hep-ph]; M. Mühlleitner, these proceedings.

[18] for an introduction see e.g. S. P. Martin, arXiv:hep-ph/9709356; I. J. R. Aitchison, arXiv:hep-ph/0505105; J. F. Gunion and H. E. Haber, Phys. Rev. D **67**, 075019 (2003).

[19] T. Binoth and J. J. van der Bij, Z. Phys. C **75**, 17 (1997); A. Hill and J. J. van der Bij, Phys. Rev. D **36** (1987) 3463; R. Schabinger and J. D. Wells, Phys. Rev. D **72**, 093007 (2005); B. Patt, F. Wilczek, [hep-ph/0605188]; C. Englert, T. Plehn, D. Zerwas and P. M. Zerwas, Phys. Lett. B **703** (2011) 298; C. Englert, T. Plehn, M. Rauch, D. Zerwas and P. M. Zerwas, Phys. Lett. B **707** (2012) 512 [arXiv:1112.3007 [hep-ph]]; B. Batell, S. Gori and L. -T. Wang, arXiv:1112.5180 [hep-ph]; A. Djouadi, O. Lebedev, Y. Mambrini and J. Quevillon, Phys. Lett. B **709** (2012) 65 [arXiv:1112.3299 [hep-ph]]; C. Englert, these proceedings.

[20] G. F. Giudice, C. Grojean, A. Pomarol, R. Rattazzi, JHEP **0706**, 045 (2007). [hep-ph/0703164], J. R. Espinosa, C. Grojean and M. Muhlleitner, JHEP **1005**, 065 (2010) arXiv:1003.3251 [hep-ph]; J. R. Espinosa, C. Grojean and M. Muhlleitner, arXiv:1202.1286 [hep-ph].

[21] A. Höcker, H. Lacker, S. Laplace and F. Le Diberder, Eur. Phys. J. C **21**, 225 (2001); J. Charles *et al.* arXiv:hep-ph/0607246.

[22] R. Lafaye, T. Plehn, M. Rauch and D. Zerwas, Eur. Phys. J. C **54**, 617 (2008).

[23] A. Djouadi, J. Kalinowski and M. Spira, Comput. Phys. Commun. **108** (1998) 56 [hep-ph/9704448]; A. Djouadi, M. M. Muhlleitner and M. Spira, Acta Phys. Polon. B **38** (2007) 635 [hep-ph/0609292].

[24] T. Plehn and D. Rainwater, Phys. Lett. B **520**, 108 (2001); K. Cranmer and T. Plehn, Eur. Phys. J. C **51**, 415 (2007); see also T. Han and B. McElrath, Phys. Lett. B **528**, 81 (2002).

[25] S. Su and B. Thomas, arXiv:0812.1798 [hep-ph].

[26] U. Baur, T. Plehn and D. L. Rainwater, Phys. Rev. Lett. **89**, 151801 (2002) and Phys. Rev. D **67**, 033003 (2003); A. Dahlhoff, arXiv:hep-ex/0505022; for a different point of view see also F. Gianotti *et al.*, arXiv:hep-ph/0204087.

[27] V. Barger, T. Han, P. Langacker, B. McElrath and P. Zerwas, Phys. Rev. D **67**, 115001 (2003); C. Grojean, G. Servant and J. D. Wells, Phys. Rev. D **71**, 036001 (2005); S. Kanemura, Y. Okada, E. Senaha and C. P. Yuan, Phys. Rev. D **70**, 115002 (2004).

[28] T. Plehn and M. Rauch, Phys. Rev. D **72**, 053008 (2005); T. Binoth, S. Karg, N. Kauer and R. Rückl, Phys. Rev. D **74**, 113008 (2006).

[29] F. Boudjema and E. Chopin, Z. Phys. C **73** (1996) 85 [hep-ph/9507396]; A. Djouadi, W. Kilian, M. Muhlleitner and P. M. Zerwas, Eur. Phys. J. C **10** (1999) 27 [hep-ph/9903229]; J. Tian, K. Fujii and Y. Gao, arXiv:1008.0921 [hep-ex].

[30] M. Dührssen, ATL-PHYS-2003-030.

[31] M. Rauch, arXiv:1110.1196 [hep-ph].

[32] T. Gleisberg, S. .Hoeche, F. Krauss, M. Schonherr, S. Schumann, F. Siegert and J. Winter, JHEP **0902** (2009) 007 [arXiv:0811.4622 [hep-ph]].

[33] J. M. Butterworth, A. R. Davison, M. Rubin and G. P. Salam, Phys. Rev. Lett. **100**, 242001 (2008), ATLAS Collaboration, ATL-PHYS-PUB-2009-088.

[34] O. J. Éboli and D. Zeppenfeld, Phys. Lett. B **495**, 147 (2000).

[35] G. Aad *et al.* [The ATLAS Collaboration], arXiv:0901.0512 [hep-ex].

[36] G. L. Bayatian *et al.* [CMS Collaboration], J. Phys. G **34**, 995 (2007).

[37] R. Gröber, M. Mühlleitner, JHEP **1106**, 020 (2011) [arXiv:1012.1562 [hep-ph]]; R. Gröber, LC-TH-2012-001.

Higgs boson mass and new physics

Fedor Bezrukov*
Physics Department, University of Connecticut, Storrs, CT 06269-3046, USA
RIKEN-BNL Research Center, Brookhaven National Laboratory, Upton, NY 11973, USA

Mikhail Yu. Kalmykov†
Bernd A. Kniehl‡
II. Institut für Theoretische Physik, Universität Hamburg,
Luruper Chaussee 149, 22761, Hamburg, Germany

Mikhail Shaposhnikov§
Institut de Théorie des Phénomènes Physiques,
École Polytechnique Fédérale de Lausanne, CH-1015 Lausanne, Switzerland

May 15, 2012

Abstract

We discuss the lower Higgs boson mass bounds which come from the absolute stability of the Standard Model (SM) vacuum and from the Higgs inflation, as well as the prediction of the Higgs boson mass coming from asymptotic safety of the SM. We account for the 3-loop renormalization group evolution of the couplings of the Standard Model and for a part of two-loop corrections that involve the QCD coupling α_s to initial conditions for their running. This is one step above the current state of the art procedure ("one-loop matching–two-loop running"). This results in reduction of the *theoretical* uncertainties in the Higgs boson mass bounds and predictions, associated with the Standard Model physics, to $1-2\,\mathrm{GeV}$. We find that with the account of existing experimental uncertainties in the mass of the top quark and α_s (taken at 2σ level) the bound reads $M_H \geq M_{\min}$ (equality corresponds to the asymptotic safety prediction), where $M_{\min} = 129 \pm 6\,\mathrm{GeV}$. We argue that the discovery of the SM Higgs boson in this range would be in agreement with the hypothesis of the absence of new energy scales between the Fermi and Planck scales, whereas the coincidence of M_H with $M_{\min}$ would suggest that the electroweak scale is determined by Planck physics. In order to clarify the

*Email: Fedor.Bezrukov@uconn.edu
†Email: mikhail.kalmykov@desy.de
‡Email: kniehl@desy.de
§Email: Mikhail.Shaposhnikov@epfl.ch

relation between the Fermi and Planck scale a construction of an electron-positron or muon collider with a center of mass energy $\sim 200+200\,\mathrm{GeV}$ (Higgs and t-quark factory) would be needed.

1 Introduction

The mass M_H of the Higgs boson in the Standard Model is an important indicator of the presence of new energy scales in particle physics. It is well known that if $M_{\min}^{\mathrm{stability}} < M_H < M_{\max}^{\mathrm{Landau}}$ then the SM is a consistent effective field theory all the way from the Fermi scale up to the (reduced) Planck scale $M_P = 2.44 \times 10^{18}\,\mathrm{GeV}$. The upper limit comes from the requirement that the Landau pole in the scalar self-coupling[1] must not appear at energies below M_P [1–3]. The lower limit comes from the requirement of the stability of the SM vacuum against tunneling to the states with the Higgs field ϕ exceeding substantially the electroweak value $250\,\mathrm{GeV}$ [4–6] (see Fig. 1).

The estimates of $M_{\max}^{\mathrm{Landau}}$ give a number around $175\,\mathrm{GeV}$ [1–3, 7] which is in the M_H range excluded (at least in the range $129 - 525\,\mathrm{GeV}$) by the searches for the SM Higgs boson at the LHC and Tevatron [8, 9]. In other words, we already know that the SM is a weakly coupled theory up to the Planck scale. Thus, we will focus on the upgrade of existing computations of $M_{\min}^{\mathrm{stability}}$ and on the discussion of the significance of the relation between the Higgs boson (to be discovered yet) mass M_H and $M_{\min}^{\mathrm{stability}}$ for beyond the SM (BSM) physics.

The computation of $M_{\min}^{\mathrm{stability}}$ has been already done in a large number of papers [10–15]. It is divided into two parts. The first one is the determination of the $\overline{\mathrm{MS}}$ parameters from the physical observables and the second one is the renormalization group running of the $\overline{\mathrm{MS}}$ constants from the electroweak to a high energy scale. The most advanced recent works [13, 14] use the so-called "one-loop-matching–two-loop-running" procedure. It can determine the Higgs boson mass bounds with the theoretical accuracy of $2-5\,\mathrm{GeV}$ (see the discussion of uncertainties in [14] and below). Meanwhile, the most important terms in the 3-loop running of the gauge and Higgs coupling constants were computed in [16, 17] (we thank K. Chetyrkin and M. Zoller for sharing these results with us prior to publication). The present work accounts for $O(\alpha\alpha_s)$ corrections in the $\overline{\mathrm{MS}}$-pole matching procedure, which were not known previously. This allows us to decrease the theoretical uncertainties in the Higgs boson mass prediction/bounds, associated with the SM physics down to $1-2\,\mathrm{GeV}$. This is a new result, based on a superior partial "two-loop-matching–three-loop-running" procedure. These findings are described in Section 2.2. We will see that the experimental errors in the mass of the top-quark and in the value of the strong coupling constant are too large to settle up the question of the stability of the electroweak vacuum, even if the LHC will confirm the evidence for the Higgs signal presented by the ATLAS and CMS collaborations [8, 9] in the region $M_H = 124 - 126\,\mathrm{GeV}$.

In Section 3 we will discuss the significance of the relationship between the true Higgs

[1] To be more precise, the scalar self-coupling is infinite in the one-loop approximation only. If higher order terms are included, it may not become infinite, but move away from the region of the weak coupling.

boson mass M_H and $M_{\rm min}^{\rm stability}$ for BSM physics. We will argue that if $M_H = M_{\rm min}^{\rm stability}$ then the electroweak symmetry breaking is likely to be determined by Planck physics and that this would indicate an absence of new energy scales between the Fermi and gravitational scales. We will also address here the significance of $M_{\rm min}^{\rm stability}$ for the SM with gravity included. Of course, this can only be done under certain assumptions. Specifically, we will discuss the non-minimal coupling of the Higgs field to the Ricci scalar (relevant for Higgs-inflation [14, 18, 19]) and the asymptotic safety scenario for the SM [20].

In Section 4 we present our conclusions. We will argue that if only the Higgs boson with the mass around $M_{\rm min}^{\rm stability}$ and nothing else will be found at the LHC, the next step in high energy physics should be the construction a new electron-positron (or muon) collider—the Higgs and t-factory. It will not only be able to investigate in detail the Higgs and top physics, but also elucidate the possible connection of the Fermi and Planck scales.

Appendix A contains a full set of formulas required for the determination of the $\overline{\rm MS}$ coupling constants from the pole masses of the SM particles, including the corrections of the orders of up to $O(\alpha_s^3)$, $O(\alpha)$, and $O(\alpha\alpha_s)$. The computer code for the matching is made publicly available at `http://www.inr.ac.ru/~fedor/SM/`.

2 The stability bound

The stability bound will be found in the "canonical" SM, without any new degrees of freedom or any extra higher dimensional operators added, see Fig. 2.

2.1 The benchmark mass

It will be convenient for computations to introduce yet another parameter, "benchmark mass", which we will call $M_{\rm min}$ (without any superscript). Suppose that all parameters of the SM, except for the Higgs boson mass, are exactly known. Then $M_{\rm min}$, together with the normalisation point μ_0, are found from the solution of two equations:

$$\lambda(\mu_0) = 0, \quad \beta_\lambda(\lambda(\mu_0)) = 0, \tag{1}$$

where β_λ is the β-function governing the renormalisation group (RG) running of λ. Here we define all the couplings of the SM in the $\overline{\rm MS}$ renormalisation scheme which is used de-facto in the most of the higher-loop computations. Clearly, if any other renormalization scheme is used, the equations $\lambda = \beta_\lambda = 0$ will give another benchmark mass, since the definition of all the couplings are scheme dependent.

The procedure of computing $M_{\rm min}$ is very clean and transparent. Take the standard $\overline{\rm MS}$ definition of all coupling constants of the SM, fix all of them at the Fermi scale given the experimentally known parameters such as the mass of the top quark, QCD coupling, etc., and consider the running Higgs self-coupling $\lambda(\mu)$ depending on the standard t'Hooft-Veltman parameter μ. Then, adjust $M_{\rm min}$ in such a way that equations (1) are satisfied at some μ_0.

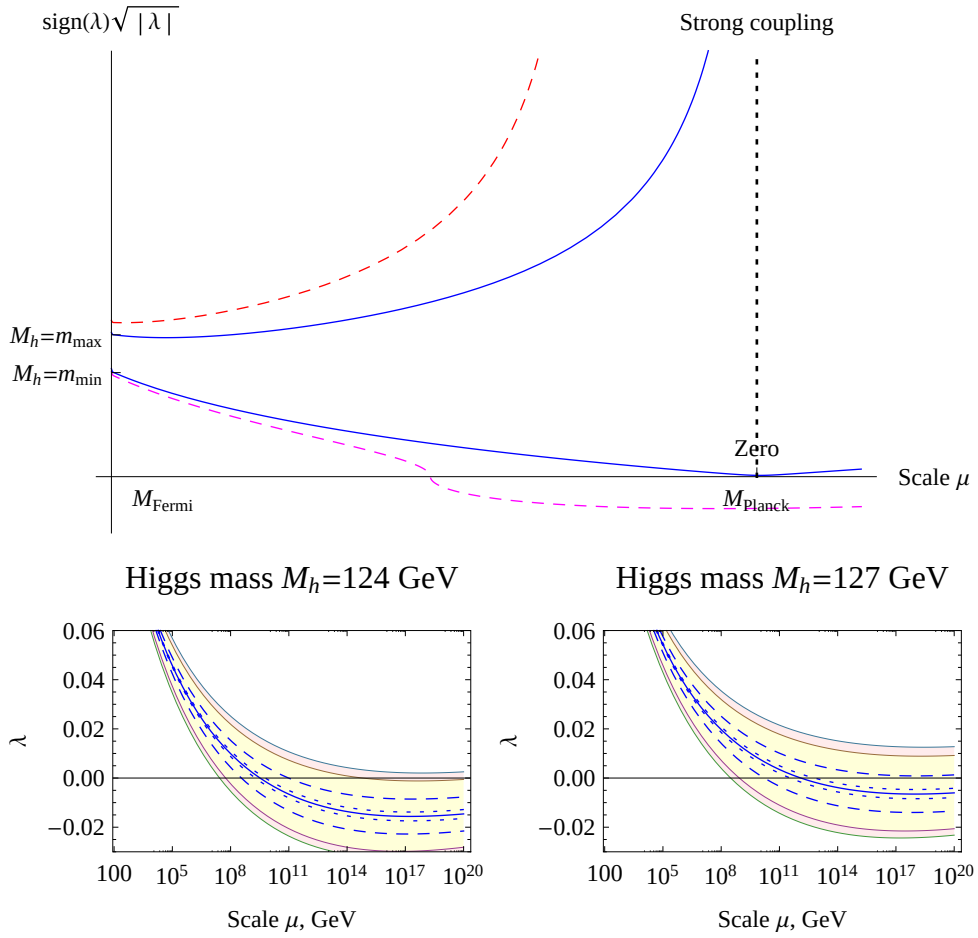

Figure 1: Higgs self-coupling in the SM as a function of the energy scale. The top plot depicts possible behaviors for the whole Higgs boson mass range—Landau pole, stable, or unstable electroweak vacuum. The lower plots show detailed behavior for low Higgs boson masses, with dashed (dotted) line corresponding to the experimental uncertainty in the top mass M_t (strong coupling constant α_s), and the shaded yellow (pink) regions correspond to the total experimental error and theoretical uncertainty, with the latter estimated as 1.2 GeV (2.5 GeV), see section 2 for detailed discussion.

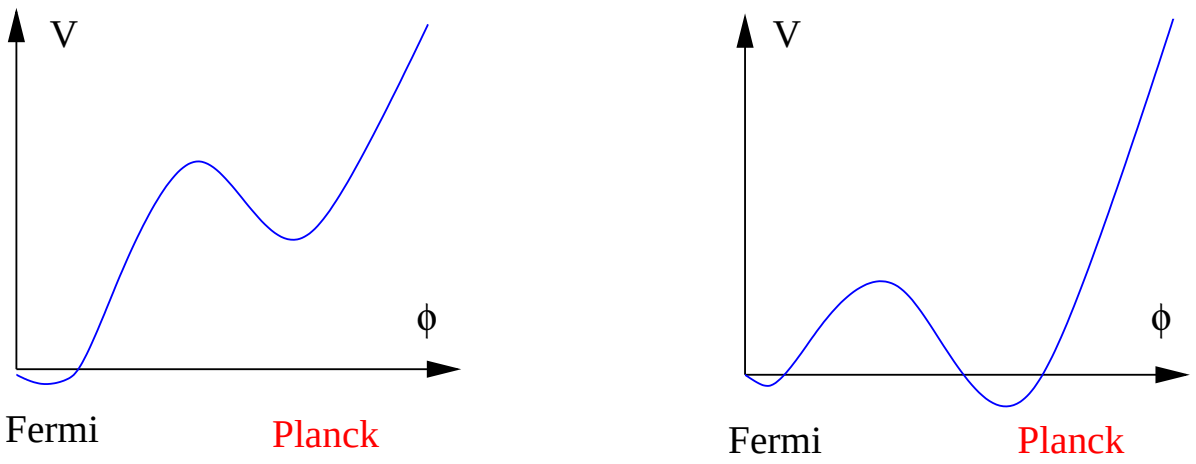

Figure 2: Schematic depiction of the SM effective potential V for the Higgs field for $M_H > M_{\rm min}^{\rm stability}$ (left) and $M_H < M_{\rm min}^{\rm stability}$ (right).

For the stability bound one should find the effective potential $V(\phi)$ and solve the equations

$$V(\phi_{SM}) = V(\phi_1), \quad V'(\phi_{SM}) = V'(\phi_1) = 0, \tag{2}$$

where ϕ_{SM} corresponds to the SM Higgs vacuum, and ϕ_1 correspond to the extra vacuum states at large values of the scalar field. Though the effective potential and the field ϕ are both gauge and scheme dependent, the solution for the Higgs boson mass to these equations is gauge and scheme invariant.

In fact, $M_{\rm min}^{\rm stability}$ is very close to $M_{\rm min}$. Numerically, the difference between them is much smaller, than the current theoretical and experimental precisions for $M_{\rm min}$, see below. The following well known argument explains why this is the case. The RG improved effective potential for large ϕ can be written as [11, 12, 21]

$$V(\phi) \propto \lambda(\phi)\phi^4 \left[1 + O\left(\frac{\alpha}{4\pi}\log(M_i/M_j)\right)\right], \tag{3}$$

where α is here the common name for the SM coupling constants, and M_i are the masses of different particles in the background of the Higgs field. If $O(\alpha)$ corrections are neglected, the equations (2) coincide with (1), meaning that $M_{\rm min} \simeq M_{\rm min}^{\rm stability}$. The numerical evaluation for one loop effective potential gives $\Delta m^{\rm stability} \equiv M_{\rm min}^{\rm stability} - M_{\rm min} \simeq 0.15\,\text{GeV}$, which can be neglected in view of uncertainties discussed below.

Note that in many papers the stability bound is shown as a function of the cutoff scale Λ (the energy scale up to which the SM can be considered as a valid effective field theory). It is required that $V(\phi) > V(\phi_{SM})$ for all $\phi < \Lambda$. This can be reformulated as $\lambda(\mu) > 0$ for all $\mu < \Lambda$ with pretty good accuracy. Interestingly, if $\Lambda = M_P$, this bound is very close to the stability bound following from eq. (2), having nothing to do with the Planck scale (see also below). Note also that the uncertainties in experimental determinations of M_t and α_s together with theoretical uncertainties, described in the next section, lead to significant changes in the scale Λ. Fig. 1 illustrates that for Higgs

boson masses $124 - 127$ GeV this scale may vary from 10^8 GeV up to infinity within currently available precisions.

2.2 Value of $M_{\rm min}$

The state of art computation of $M_{\rm min}$ contained up to now the so called one-loop $\overline{\rm MS}$-pole matching, relating the experimentally measured physical parameters to the parameters of the SM in the $\overline{\rm MS}$ subtraction scheme (to be more precise, the two-loop α_s corrections to the top pole mass–$\overline{\rm MS}$ mass relation has been included [13]). Then the results of the first step are plugged into two-loop RG equations and solved numerically.

Before discussing the upgrade of the one-loop-matching–two-loop-running procedure, we will remind of the results already known and their uncertainties. We will make use of our computations of $M_{\rm min}$ presented in [14].[2] A somewhat later paper [22] contains exactly the same numbers for $M_{\rm min}^{\rm stability}$ (note, however, that the theoretical uncertainties were not discussed in [22]). See also earlier computations in [7, 10–13, 23].

In [14] we found:

$$M_{\rm min} = \left[126.3 + \frac{M_t - 171.2\,{\rm GeV}}{2.1\,{\rm GeV}} \times 4.1 - \frac{\alpha_s - 0.1176}{0.002} \times 1.5\right] {\rm GeV}, \qquad (4)$$

and estimated the theoretical uncertainties as summarized in Table 1 (see also [15]). While repeating this analysis we found some numerical errors which are given at the bottom section of this table (see a detailed discussion below). In total, they shift the value given in eq. (4) up by 0.7 GeV. As for uncertainties, they were estimated as follows. The one-loop matching formulas can be used directly at $\mu = m_t$, or at some other energy scale, e.g. at $\mu = M_Z$, and then the coupling constants at m_t can be derived with the use of RG running. The difference in procedures gives an estimate of two-loop effects in the matching procedure. This is presented by the first two lines in Table 1 (in fact, we underestimated before the uncertainty from λ matching—previously we had here 1.2 GeV and now 1.7 GeV). The next two lines are associated with 3 and 4-loop corrections to the top Yukawa y_t. The 3-loop corrections were computed in [24–26] and the four-loop α_s contribution to the top mass was guessed to be of the order $\delta y_t(m_t)/y_t(m_t) \simeq 0.001$ in [27]. The non-perturbative QCD effects in the top pole mass–$\overline{\rm MS}$ mass matching are expected to be at the same level [28–30]. For 3-loop running we put the typical coefficients in front of the largest couplings α_s and y_t. If these uncertainties are not correlated and can be summed up in squares, the theoretical uncertainty is 2.5 GeV. If they are summed up linearly, then the theoretical error can be as large as ~ 5 GeV.

Now, this computation can be considerably improved. First, in [16] the 3-loop corrections to the running of all gauge couplings has been calculated. Second, in [17] the leading contributions (containing the top Yukawa and α_s) to the running of the top quark Yukawa and the Higgs boson self coupling have been determined. This removes the uncertainty related to 3-loop RG running. In addition, in the present paper, we

[2] The main interest in this paper was the lower bound on the Higgs boson mass in the Higgs-inflation, see below. However, $M_{\rm min}$ has been estimated as well as a by-product of the computation.

Source of uncertainty	Nature of estimate	$\Delta_{\rm theor} M_{\rm min}$, GeV
2-loop matching λ	Sensitivity to μ	1.7
2-loop matching y_t	Sensitivity to μ	0.6
3-loop α_s to y_t	known	1.4
4-loop α_s to y_t	educated guess [27]	0.4
confinement, y_t	educated guess $\sim \Lambda_{QCD}$	0.5
3-loop running $M_W \to M_P$	educated guess	0.8
total uncertainty	sum of squares	2.5
total uncertainty	linear sum	5.4

Corrections to [14]		$\Delta M_{\rm min}$, GeV
Typos in the code used in [14]	error	+0.2
Extra $\delta_{\rm t}^{\rm QED}$ in (A.5) of [13]	error	+0.4
"Exact" formula instead of approximation (2.20) in [31]	clarification	+0.1
Total correction to (7.1) of [14]		+0.7
Total shift to be applied to (7.1) of [14] for comparison		+0.7

Table 1: Theoretical uncertainties and mistakes in the $M_{\rm min}$ evaluation in [14].

determine the two-loop corrections of the order of $O(\alpha\alpha_s)$ to the matching of the pole masses and the top quark Yukawa and Higgs boson self coupling constants. Also, the known [24–26] three loop QCD correction to the top quark mass relation of the order $O(\alpha_s^3)$ can be included (previously it had been used for estimates of uncertainties). All this considerably decreases the theoretical uncertainties in $M_{\rm min}$.

The individual contributions of the various new corrections on top of the previous result are summarized in the Table 2. It is clearly seen that there are two new significant contributions—one is the three-loop pure QCD correction to the top quark mass [24–26], and another is the two loop correction $O(\alpha\alpha_s)$ to the Higgs boson mass, found in the present paper. Together the new contributions sum to the overall shift of the previous prediction [14] by $-0.89\,\text{GeV}$, giving the result

$$M_{\rm min} = \left[128.95 + \frac{M_t - 172.9\,\text{GeV}}{1.1\,\text{GeV}} \times 2.2 - \frac{\alpha_s - 0.1184}{0.0007} \times 0.56\right] \text{GeV}. \qquad (5)$$

The new result (5) is less than 0.2 GeV away from the old one (4) if the same central values for M_t and α_s are inserted. This coincidence is the result of some magic. In the old evaluation several mistakes were present, summarized in Table 1. The largest one was the double counting of $\delta_t^{\rm QED}$ in (A.5) of [13], as compared to the original result [31]. Also, there were minor typos in the computer code for the matching of the Higgs coupling constant, and finally there was a small correction coming from the use of an approximate

Contribution	$\Delta M_{\rm min}$, GeV
Three loop beta functions	-0.23
$\delta y_t \propto O(\alpha_s^3)$	-1.15
$\delta y_t \propto O(\alpha\alpha_s)$	-0.13
$\delta\lambda \propto O(\alpha\alpha_s)$	0.62

Table 2: Contributions to the value of the $M_{\rm min}$.

rather than exact one loop formula for $O(\alpha)$ corrections from [31]. These corrections add 0.7 GeV to the original number in [14]. By chance this almost exactly canceled the -0.89 GeV contribution from the higher loops, Table 2, nearly leading to a coincidence of (5) and (4).

Table 3 summarizes the uncertainties in the new computation. It contains fewer lines. Now we can ignore safely the error from higher order (4-loop) RG corrections for the running up to the Planck scale. The first two lines were derived in the same manner as previously. For the Higgs boson self-coupling we can use the matching formulas (A.42) to get the value of $\lambda(\mu)$ at scale $\mu = M_t$ directly, or to get the value $\lambda(M_Z)$ and then evolve the constants to the scale $\mu = M_t$ with the RG equations. The obtained difference $\delta\lambda(M_t)/\lambda(M_t) \simeq 0.016$ corresponds to the error $\delta m \sim 1.0$ GeV. A similar procedure of comparing evolution between M_t and M_Z using RG equations and direct matching formulas to the order $O(\alpha_s^3, \alpha, \alpha\alpha_s)$ leads for the chang in the top quark Yukawa $\delta y_t/y_t \sim 0.0005$, leading to $\delta M \sim 0.2$ GeV. Note, however, that strictly speaking this test verifies the error of the μ dependent terms in the matching formulas, while the constant ones may lead to larger contributions. We also do not estimate now the contributions of the order $O(\alpha^2)$, where formal order in α may correspond to y_t^4. Thus, this estimate should be better considered as a lower estimate of the error. The 4-loop matching and confinement contributions are the same as before.

As an indication of the dependence on the matching point we present Fig. 3, where the reference Higgs boson mass $M_{\rm min}$ was obtained using the matching formulas at scale μ_0 varying between the Z-boson and top quark masses. One can see that the overall change of the Higgs boson mass is about GeV.

If we assume that these uncertainties are not correlated and symmetric we get a theoretical error in the determination of the critical Higgs boson mass $\delta m_{\rm theor} \simeq 1.2$ GeV. If they are summed up linearly, we get an error of 2.4 GeV. The precision of the theoretical value of $M_{\rm min}$ can be further increased by computing the $O(\alpha^2)$ two-loop corrections to the matching procedure. Numerically, the most important terms are those when α corresponds to y_t^2 and λ.

The result (5) is visualized by Fig. 4. The experimentally allowed regions for the top mass M_t and strong coupling α_s are adopted PDG 2010 edition [32].[3] On top of these

[3]Note however, that the current experimental error estimate is based on averaging over different experimental approaches. In some methods quite a different central values are obtained. See e.g. [33–35] about α_s determination and [36–38] about M_t.

Source of uncertainty	Nature of estimate	$\Delta_{\rm theor} M_{\rm min}$, GeV
3-loop matching λ	Sensitivity to μ	1.0
3-loop matching y_t	Sensitivity to μ	0.2
4-loop α_s to y_t	educated guess [27]	0.4
confinement, y_t	educated guess $\sim \Lambda_{QCD}$	0.5
4-loop running $M_W \to M_P$	educated guess	< 0.2
total uncertainty	sum of squares	1.2
total uncertainty	linear sum	2.3

Table 3: Theoretical uncertainties in the present $M_{\rm min}$ evaluation.

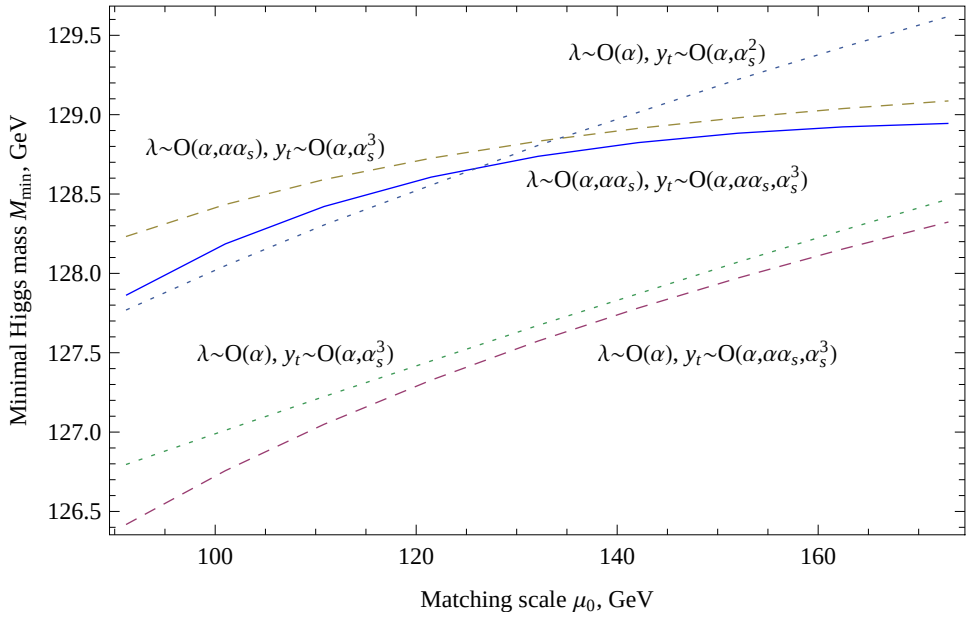

Figure 3: The dependence of the reference Higgs boson mass $M_{\rm min}$ on the matching scale μ_0 (the $\overline{\rm MS}$ constants are obtained by matching formulas at scale μ_0 and then used for the solution of the equations (1)). The solid line corresponds to the full matching formulas $\lambda \sim O(\alpha, \alpha\alpha_s)$, $y_t \sim O(\alpha_s^3, \alpha, \alpha\alpha_s)$; the dashed and dotted lines correspond to using matching formulas of lower order. Here $M_t = 172.9\,{\rm GeV}$ and $\alpha_s = 0.1184$.

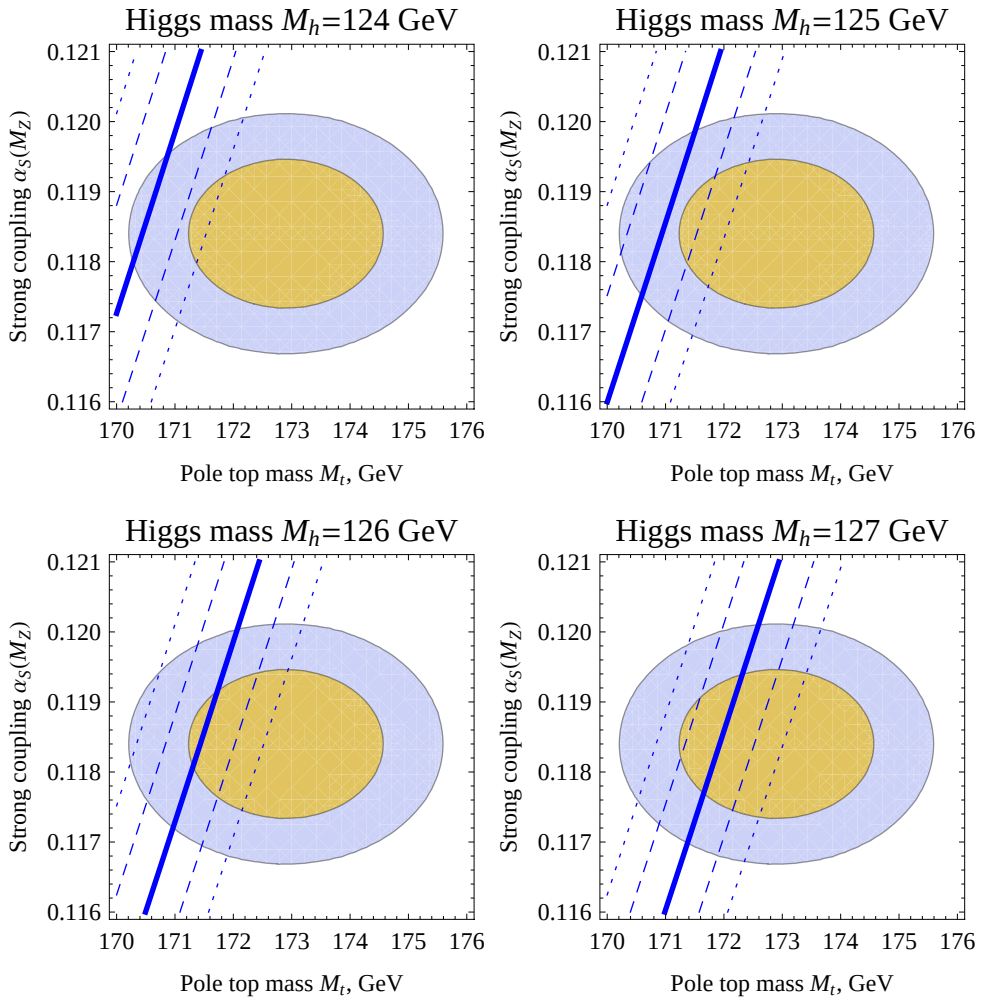

Figure 4: The values of the strong coupling constant α_s and top mass M_t corresponding to several minimal Higgs boson mass $M_{\min}$. The 68% and 95% experimentally allowed regions for α_s and M_t are given by shaded areas. The dashed (dotted) lines correspond to 1.2 GeV (2.45 GeV) uncertainty in the $M_{\min}$ theoretical determination.

allowed regions the bands corresponding to the reference values of the Higgs boson mass $M_{\rm min}$ being equal to $124, 125, 126, 127\,\text{GeV}$ are shown, with the dashed and dotted lines corresponding to quadratically or linearly added estimates of theoretical uncertainties.

One can see that the accuracy of theoretical computations and of the experimental measurements of the top and the Higgs boson masses does not allow yet to conclude with confidence whether the discovery of the Higgs boson with the mass $124 - 127\,\text{GeV}$ would indicate stability or metastability of the SM vacuum. All these reference values of Higgs masses are compatible within 2σ with current observations.

3 $M_{\rm min}$ and BSM physics

Our definition of the "benchmark" Higgs boson mass consists of the solution of the two equations (1) and gives, in addition to $M_{\rm min}$, the value of the scale μ_0 at which the scalar self-coupling and its β-function vanish simultaneously. The central value for μ_0 is $2.9 \times 10^{18}\,\text{GeV}$ and is quite stable if m_t and α_s are varied in their confidence intervals (see Fig. 5). One can see that there is a remarkable coincidence between μ_0 and the (reduced) Planck scale $M_P = 2.44 \times 10^{18}\,\text{GeV}$. The physics input in the computation of μ_0 includes the parameters of the SM only, while the result gives the gravity scale. A possible explanation may be related to the asymptotic safety of the SM, see [20] and below.[4] It remains to be seen if this is just the random play of the numbers or a profound indication that the electroweak symmetry breaking is related to Planck physics. If real, this coincidence indicates that there should be no new energy scales between the Planck and Fermi scales, as they would remove this coincidence unless some conspiracy is taking place.

We will discuss below two possible minimal embeddings of the SM to the theory of gravity and discuss the significance of $M_{\rm min}$ in them.

3.1 Asymptotic safety

The asymptotic safety of the SM [20], associated with the asymptotic safety of gravity [41], is strongly related to the value of the Higgs boson mass. Though General Relativity is non-renormalizable by perturbative methods, it may exist as a field theory non-perturbatively, exhibiting a non-trivial ultraviolet fixed point (for a review see [42]). If true, all other coupling of the SM (including the Higgs self-interaction) should exhibit an asymptotically safe behaviors with the gravity contribution to the renormalisation group running included.

The prediction of the Higgs boson mass from the requirement of asymptotic safety of the SM is found as follows [20]. Consider the SM running of the coupling constants and add to the β-functions extra terms coming from gravity, deriving their structure from

[4] Yet another one is the "multiple point principle" of [39, 40], requiring the degeneracy between the SM vacuum and an extra one appearing at the Planck scale.

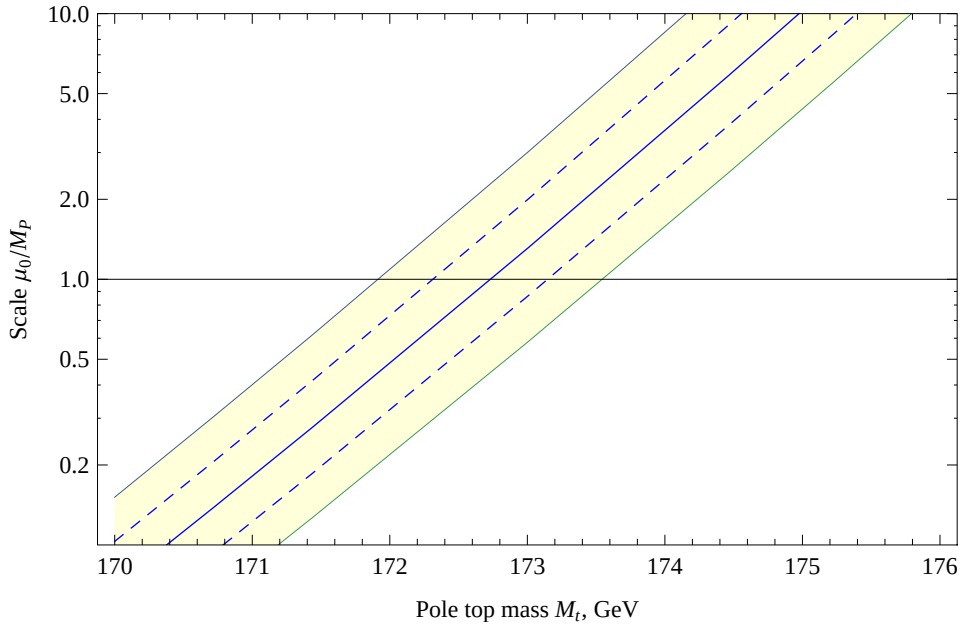

Figure 5: The scale μ_0 (solution of (1)) depending on the top mass M_t. The dashed lines correspond to 1σ uncertainty in the α_s. The yellow shaded region corresponds to adding the α_s experimental error and the theoretical uncertainty in the matching of the top Yukawa y_t and top pole mass.

dimensional analysis:

$$\beta_h^{\rm grav} = \frac{a_h}{8\pi}\frac{\mu^2}{M_P^2(\mu)}h, \tag{6}$$

where a_1, a_2, a_3, a_y, and a_λ are some constants (anomalous dimensions) corresponding to the gauge couplings of the SM g, g', g_s, the top Yukawa coupling y_t, and the Higgs self-coupling λ. In addition,

$$M_P^2(\mu) \simeq M_P^2 + 2\xi_0\mu^2 \tag{7}$$

is the running Planck mass with $\xi_0 \approx 0.024$ following from numerical solutions of functional RG equations [43–45]. Now, require that the solution for all coupling constants is finite for all μ and that λ is always positive. The SM can only be asymptotically safe if a_1, a_2, a_3, a_y are all negative, leading to asymptotically safe behavior of the gauge and Yukawa couplings. For $a_\lambda < 0$ we are getting the interval of admissible Higgs boson masses, $M_{\rm min}^{\rm safety} < M_H < M_{\rm max}^{\rm safety}$. However, if $a_\lambda > 0$, as follows from computations of [44, 45], only one value of the Higgs boson mass $M_H = M_{\rm min}^{\rm safety}$ leads to asymptotically safe behavior of λ. As is explained in [20], this behavior is only possible provided $\lambda(M_P) \approx 0$ and $\beta_\lambda(\lambda(M_P)) \approx 0$. And, due to miraculous coincidence of μ_0 and M_P, the difference $\Delta m^{\rm safety} \equiv M_{\rm min}^{\rm safety} - M_{\rm min}$ is extremely small, of the order 0.1 GeV. The evolution of the Higgs self-coupling for the case of $a_h < 0$ is shown in Fig. 6, and for the case $a_h > 0$ in Fig. 7.

In fact, in the discussion of the asymptotic safety of the SM one can consider a more general situation, replacing the Planck mass in eq. (7) by some cutoff scale $\Lambda = \kappa M_P$.

Figure 6: Schematic depiction of the behavior of the scalar self-coupling if $a_h < 0$ for $M_{\rm min}^{\rm safety} < M_H < M_{\rm max}^{\rm safety}$ (left) and $M_H < M_{\rm min}^{\rm safety}$ (right). In both cases gravity leads to asymptotically free behavior of the scalar self-coupling. Negative λ lead to instability and thus excluded.

Indeed, if the Higgs field has non-minimal coupling with gravity (see below), the behavior of the SM coupling may start to change at energies smaller than M_P by a factor $1/\xi$, leading to an expectation for the range of κ as $1/\xi \lesssim \kappa \lesssim 1$. Still, the difference between $M_{\rm min}$ and $M_{\rm min}^{\rm safety}$ remains small even for $\kappa \sim 10^{-4}$, where $M_{\rm min}^{\rm safety} \simeq 128.4\,{\rm GeV}$, making the prediction $M_H \simeq M_{\rm min}$ sufficiently stable against specific details of Planck physics within the asymptotic safety scenario.

3.2 $M_{\rm min}$ and cosmology

It is important to note that if the mass of the Higgs boson is smaller than the stability bound $M_{\rm min}$, this does not invalidate the SM. Indeed, if the life-time of the metastable SM vacuum exceeds the age of the Universe (this is the case when $M_H > M_{\rm meta}$, with $M_{\rm meta} \simeq 111\,{\rm GeV}$ [13]) then finding a Higgs boson in the mass interval $M_{\rm meta} < M_H < M_{\rm min}$ would simply mean that we live in the metastable state with a very long lifetime. Of course, if the Higgs boson were discovered with a mass below $M_{\rm meta}$, this would prove that there *must be* new physics between the Fermi and Planck scales, stabilizing the SM vacuum state. However, the latest LEP results, confirmed recently by LHC, tell us that in fact $M_H > M_{\rm meta}$, and, therefore, that the presence of a new energy scale is not required, if only the metastability argument is used.

The bound $M_H > M_{\rm meta}$ can be strengthened if thermal cosmological evolution is considered [13]. After inflation the universe should find itself in the vicinity of the SM vacuum and stay there till present. As the probability of the vacuum decay is temperature dependent, the improved Higgs boson mass bound is controlled by the reheating temperature after inflation (or maximal temperature of the Big Bang). The latter is model dependent, leading to the impossibility to get a robust bound much better than $M_{\rm meta}$. For example, in R^2 inflation [46, 47] the reheating temperature is rather low, $T \sim 10^9\,{\rm GeV}$ [47], leading to the lower bound $116\,{\rm GeV}$ [48] on the Higgs boson mass, which exceeds $M_{\rm meta}$ only by $4\,{\rm GeV}$.

However, if no new degrees of freedom besides those already present in the SM are introduced and the Higgs boson plays the role of inflaton, the bound $M_H \gtrsim M_{\rm min}$

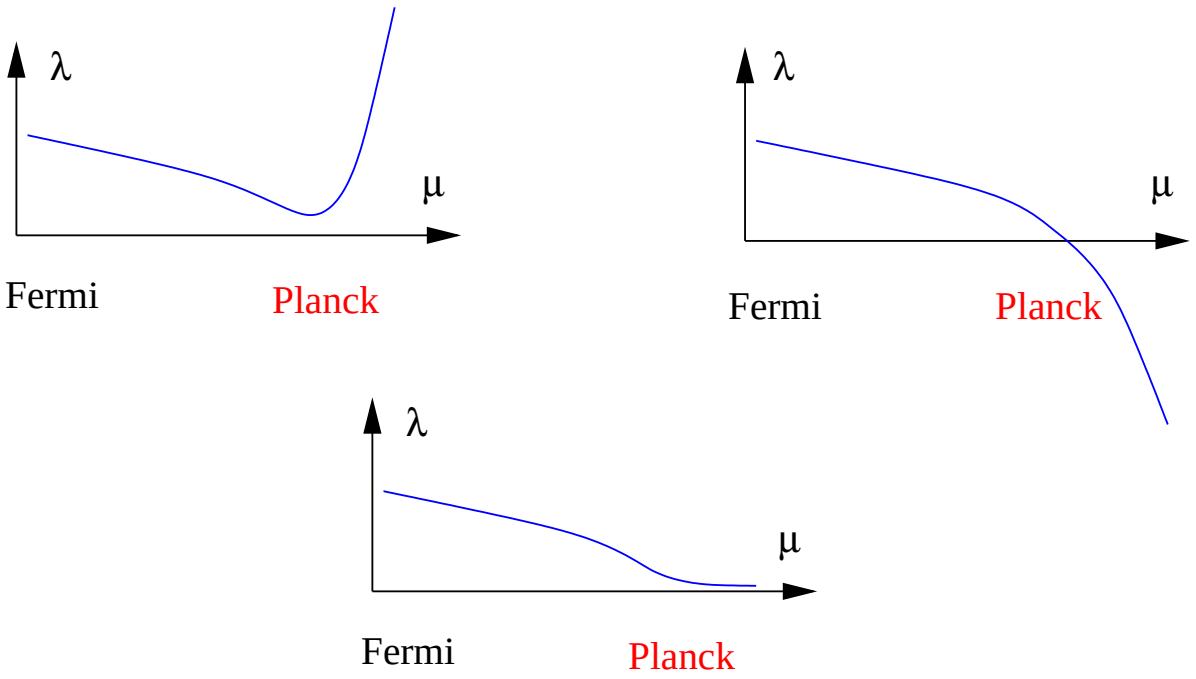

Figure 7: Schematic depiction of the behavior of the scalar self-coupling if $a_h > 0$ for $M_H > M_{\rm min}^{\rm safety}$, leading to Landau-pole behavior (left), $M_H > M_{\rm min}^{\rm safety}$, leading to instability (right) and $M_H = M_{\rm min}^{\rm safety}$, asymptotically safe behavior (middle). Only this choice is admissible.

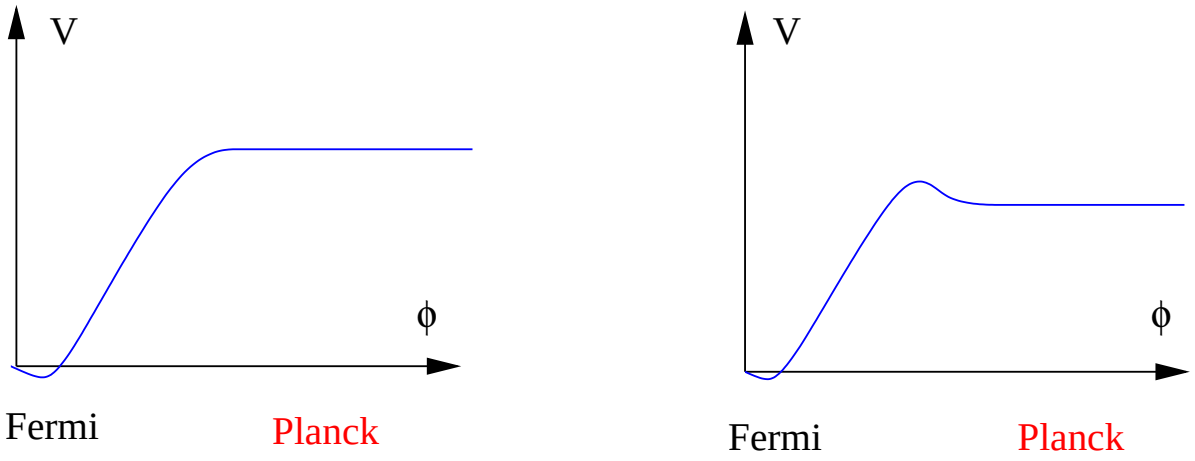

Figure 8: Schematic depiction of the effective potential V for the Higgs field in the Higgs-inflationary theory in the Einstein frame for $M_H > m_{\rm min}^{\rm inflation}$ (left) and $M_H < m_{\rm min}^{\rm inflation}$ (right).

reappears, as is discussed below.

3.3 Higgs inflation

The inclusion of a non-minimal interaction of the Higgs field with gravity, given by the Lagrangian $\xi|\phi|^2 R$, where R is the Ricci scalar, changes drastically the behavior of the Higgs potential in the region of large Higgs fields $\phi > M_{\rm inflation} \simeq M_P/\sqrt{\xi}$ [18]. Basically, the potential becomes flat at $\phi > M_{\rm inflation}$, keeping the value it acquired at $\phi \simeq M_P/\sqrt{\xi}$. This feature leads to a possibility of Higgs-inflation: if the parameter ξ is sufficiently large, $700 < \xi < 10^5$, [14] the Higgs boson of the SM can make the Universe flat, homogeneous and isotropic, and can produce the necessary spectrum of primordial fluctuations. The possibility of the Higgs inflation is also strongly related to the value of the Higgs boson mass: the successful inflation can only occur if $M_{\rm min}^{\rm inflation} < M_H < M_{\rm max}^{\rm inflation}$. The upper limit $M_{\rm max}^{\rm inflation}$ comes from the requirement of the validity of the SM up to the inflation scale $M_{\rm inflation}$. Near $M_{\rm min}^{\rm inflation}$ the behavior of the effective potential in the Einstein frame changes as shown in Fig. 8: if $M_H < M_{\rm min}^{\rm inflation}$ the "bump" in the Higgs potential prevents the system to go to the SM vacuum state. As in the previous case, these bounds can be formulated with the use of the Higgs self-coupling λ. Basically, it must be perturbative and positive for all energy scales below $M_{\rm inflation}$. Though any Higgs boson mass in the interval $M_{\rm min}^{\rm inflation} < M_H < M_{\rm max}^{\rm inflation}$ can lead to successful inflation, the value $M_{\rm min}^{\rm inflation}$ is somewhat special. For the lower part of the admitted interval the value of the non-minimal coupling ξ reaches its minimal value $\xi \simeq 700$, extending the region of applicability of perturbation theory [14, 49, 50].

The computation of the lower bound on the Higgs boson mass from inflation is more complicated. It is described in detail in [14, 19]. Basically, one has to compute the Higgs potential in the chiral electroweak theory associated with large values of the Higgs field and find when the slow-roll inflation in this potential can give the large-scale

perturbations observed by the COBE satellite. The outcome of these computations, however, can be formulated in quite simple terms: for inflationary bound find $M_{\rm min}^{\rm inflation}$ from the condition $\lambda(\mu) > 0$ for all $\mu < M_{\rm inflation}$ [14]. A priori, the inflationary bound could have been very different from $M_{\rm min}$ and thus from $M_{\rm min}^{\rm stability}$. Indeed, both $M_{\rm min}$ and $M_{\rm min}^{\rm stability}$ know *nothing* about the Planck scale and are defined entirely within the SM, whereas the inflationary bound does use M_P. However, the remarkable numerical coincidence, between μ_0 and M_P, makes $M_{\rm min}$ and $M_{\rm min}^{\rm inflation}$ practically the same. The coupling constant λ evolves very slowly near the Planck scale, so that the regions for the Higgs boson mass following from the conditions $\lambda(\mu) > 0$ for $\mu < M_P$ and $\mu < M_{\rm inflation}$ are almost identical. This leads to the result that $\Delta m^{\rm inflation} \equiv M_{\rm min}^{\rm inflation} - M_{\rm min} \simeq -0.1 - 0.2\,{\rm GeV}$. This number is derived within the SM without addition of any higher dimensional operators.

As is explained in [49], adding to the SM higher-dimensional operators with a Higgs-field dependent cutoff modifies the lower bound on the Higgs boson mass in Higgs inflation. If these operators are coming with "natural" power counting coefficients (for exact definition see [49]) the sensitivity of the Higgs boson mass bound to unknown details of ultraviolet physics is rather small $\Delta M_{\rm min}^{\rm inflation} \simeq 0.6\,{\rm GeV}$ [49]. At the same time, it is certainly not excluded that the change of $M_{\rm min}^{\rm inflation}$ can be larger.

4 Conclusions

If the SM Higgs boson will be discovered at LHC in the remaining mass interval $115.5 < M_H < 127\,{\rm GeV}$ not excluded at 95% [8, 9], there is no necessity for a new energy scale between the Fermi and Planck scales. The EW theory remains in a weakly coupled region all the way up to M_P, whereas the SM vacuum state lives longer than the age of the Universe. If the SM Higgs boson mass will be found to *coincide* with $M_{\rm min}$ given by (5), this would put a strong argument in favor of the *absence* of such a scale and indicate that the electroweak symmetry breaking may be associated with the physics at the Planck scale.

The experimental precision in the Higgs boson mass measurements at the LHC can eventually reach 200 MeV and thus be much smaller than the present theoretical ($\sim 1 - 2\,{\rm GeV}$) and experimental ($\sim 5\,{\rm GeV}$, 2σ) uncertainties in determination of $M_{\rm min}$. The largest uncertainty comes from the measurement of the mass of the top quark. It does not look likely that the LHC will substantially reduce the error in the top quark mass determination. Therefore, to clarify the relation between the Fermi and Planck scales a construction of an electron-positron or muon collider with a center-of-mass energy of $\sim 200 + 200\,{\rm GeV}$ (Higgs and t-quark factory) would be needed. This would be decisive for setting up the question about the necessity for a new energy scale besides the two ones already known—the Fermi and the Planck scales. In addition, this will allow to study in detail the properties of the two heaviest particles of the Standard Model, potentially most sensitive to any types on new physics.

Surely, even if the SM is a valid effective field theory all the way up the the Planck scale, it cannot be complete as it contradicts to a number of observations. We would like

to use this opportunity to underline once more that the confirmed observational signals in favor of physics beyond the Standard Model which were not discussed in this paper (neutrino masses and oscillations, dark matter and baryon asymmetry of the Universe) can be associated with new physics *below* the electroweak scale, for reviews see [51, 52] and references therein.[5] The minimal model—νMSM, contains, in addition to the SM particles, three relatively light singlet Majorana fermions. These fermions could be responsible for neutrino masses, dark matter and baryon asymmetry of the Universe. The νMSM predicts that the LHC will continue to confirm the Standard Model and see no deviations from it. At the same time, new experiments at the high-intensity frontier, discussed in [55], may be needed to uncover the new physics below the Fermi scale. In addition, new observations in astrophysics, discussed in [52], may shed light to the nature of Dark Matter. As the running of couplings in the νMSM coincides with that in the SM, all results of the present paper are equally applicable to the νMSM.

Acknowledgements

The work of M.S. has been supported by the Swiss National Science Foundation. The work of M.Yu.K. and B.A.K. was supported in part by the German Federal Ministry for Education and Research BMBF through Grants No. 05 HT6GUA, 05 HT4GUA/4 by the German Research Foundation DFG through the Collaborative Research Centre No. 676 *Particles, Strings and the Early Universe—The Structure of Matter and Space Time,* and by the Helmholtz Association HGF through the Helmholtz Alliance Ha 101 *Physics at the Terascale.* We thank A. Boyarsky, K. Chetyrkin, D. Gorbunov, F. Jegerlehner, G. Passarino, O. Ruchayskiy, and M. Zoller for helpful discussions, collaboration and interest to our work. M.Yu.K is indebted to Fred Jegerlehner for a fruitful long time collaboration on developing and study $\overline{\rm MS}$ scheme beyond one-loop order in framework of quantum field models with spontaneously symmetry breaking, and in particular for collaboration on [56], the results and methods of which were heavily used in the present work.

[5] As for the dark energy, it may be related to a massless dilaton realizing spontaneously broken scale invariance [53, 54].

A $O(\alpha\alpha_s)$ electroweak corrections to the top Yukawa and Higgs self couplings in Standard Model

The evaluation of radiative corrections to the relations between $\overline{\rm MS}$ parameters (coupling constants) and masses of particles includes two steps: evaluation of radiative corrections between the Fermi constant G_F and its $\overline{\rm MS}$ counterpart [57] (see [58–60] for recent reviews) and the evaluation of the radiative corrections between $\overline{\rm MS}$ and pole masses.

The one-loop electroweak corrections $\mathcal{O}(\alpha)$ to the relation between the self-coupling $\lambda(\mu^2)$ and the pole mass of the Higgs boson was obtained in [61] and to the relation between the Yukawa coupling y_t and the pole mass of top quark was found in [31]. The corresponding ingredients for the 2-loop mixed electroweak-QCD corrections were evaluated in [56, 62–66], but has never been assembled. We performed independent (re)calculations of all $O(\alpha)$ and $O(\alpha\alpha_s)$ contributions. In the following we will denote the on-shell masses by capital M and the $\overline{\rm MS}$ masses by lowercase m.

A.1 $O(\alpha\alpha_s)$ corrections to the relation between on-shell and $\overline{\rm MS}$ Fermi constant

The relation between the Fermi coupling constant and the bare parameters is as follows [57]:

$$\frac{G_F}{\sqrt{2}} = \frac{g_0^2}{8m_{W,0}^2}\left\{1+\Delta R_0\right\}, \tag{A.8}$$

where ΔR_0 includes unrenormalized electroweak corrections and $g_0, m_{W,o}^2$ are the SU(2) coupling constant and the bare W boson mass (see for details [58–60]). After performing $\overline{\rm MS}$ renormalization this relation has the following form:

$$\frac{G_F}{\sqrt{2}} = \frac{G_F(\mu^2)}{\sqrt{2}}(1+\Delta_{G_F,\alpha}+\Delta_{G_F,\alpha\alpha_s}+\cdots). \tag{A.9}$$

where on the r.h.s. all masses and coupling constants are taken in the $\overline{\rm MS}$ renormalization scheme. The one-loop coefficient, $\Delta_{G_F,\alpha}$, is known from [57] and for $N_c=3$, $C_F=4/3$ and $m_b=0$ has the following form:

$$\begin{aligned}
\Delta_{G_F,\alpha} = \frac{g^2}{16\pi^2}\Bigg\{ & \frac{m_t^4}{m_W^2 m_H^2}\left(6-6\ln\frac{m_t^2}{\mu^2}\right)+\frac{m_t^2}{m_W^2}\left(-\frac{3}{4}+\frac{3}{2}\ln\frac{m_t^2}{\mu^2}\right)+\frac{m_H^2}{m_W^2}\left(-\frac{7}{8}+\frac{3}{4}\ln\frac{m_H^2}{\mu^2}\right)\\
& +\frac{m_Z^4}{m_H^2 m_W^2}\left(-\frac{1}{2}+\frac{3}{2}\ln\frac{m_Z^2}{\mu^2}\right)+\frac{m_W^2}{m_H^2}\left(-1+3\ln\frac{m_Z^2}{\mu^2}\right)-\frac{m_W^2}{m_H^2-m_W^2}\ln\left(\frac{m_W^2}{m_H^2}\right)\\
& +\frac{m_Z^2}{m_W^2}\left(\frac{5}{8}+\frac{17}{4}\ln\frac{m_W^2}{\mu^2}-5\ln\frac{m_Z^2}{\mu^2}\right)-\frac{3}{4}\ln\frac{m_W^2}{\mu^2}-\frac{3}{4}\ln\frac{m_H^2}{\mu^2}\\
& -\frac{m_Z^2}{m_W^2\sin^2\theta_W}\ln\left(\frac{m_W^2}{m_Z^2}\right)+\frac{5}{4}+\frac{7}{2\sin^2\theta_W}\ln\left(\frac{m_W^2}{m_Z^2}\right)\Bigg\},
\end{aligned} \tag{A.10}$$

Here, $\sin^2\theta_W$ is defined in the $\overline{\rm MS}$ scheme as

$$\sin^2\theta_W \equiv \sin^2\theta_W^{\overline{MS}}(\mu^2) = \frac{g'^2(\mu^2)}{g^2(\mu^2)+g'^2(\mu^2)} = 1 - \frac{m_W^2(\mu^2)}{m_Z^2(\mu^2)}, \tag{A.11}$$

where $g'(\mu^2)$ and $g(\mu^2)$ are the U(1) and SU(2) $\overline{\rm MS}$ gauge coupling constants, respectively. The matching conditions between the $\overline{\rm MS}$ parameter, defined by Eq. (A.11), and its on-shell version, [57], follows from identification

$$\sin^2\theta_W^{OS} = 1 - \frac{M_W^2}{M_Z^2}, \tag{A.12}$$

where M_Z and M_W are the pole masses of the gauge bosons (see detailed discussion in [67–69]). The evaluation of the mixed QCD-EW coefficient, $\Delta_{G_F,\alpha\alpha_s}$, is reduced to the evaluation of the $O(\alpha\alpha_s)$ corrections to the W boson self-energy at zero momenta transfer and may be written in the following way [70–74]:

$$\begin{aligned}\Delta_{G_F,\alpha\alpha_s} &\equiv 2g_R^2 Z_{g,\alpha\alpha_s} - \left[Z_{W,\alpha\alpha_s} - Z_{m_t^2,\alpha_s} m_t^2 \frac{\partial}{\partial m_t^2}\frac{\Pi_{WW,\alpha}(0)}{m_W^2(\mu^2)} - \frac{\Pi_{WW,\alpha\alpha_s}(0)}{m_W^2(\mu^2)}\right] \\ &= C_f N_c \frac{g^2 g_s^2}{(16\pi^2)^2}\frac{m_t^2}{m_W^2}\left[20\frac{m_t^2}{m_H^2} - \frac{13}{8} + \zeta_2 \right. \\ &\qquad \left. + \left(1 - 20\frac{m_t^2}{m_H^2}\right)\ln\left(\frac{m_t^2}{\mu^2}\right) - \left(\frac{3}{2} - 12\frac{m_t^2}{m_H^2}\right)\ln^2\left(\frac{m_t^2}{\mu^2}\right)\right],\end{aligned} \tag{A.13}$$

where for $Z_{g,\alpha\alpha_s}, Z_{g,\alpha\alpha_s}$ and $Z_{W,\alpha\alpha_s}$ we used the results[6] of [69] and n_F is the number of fermion families (n_F is equal to 3 in the SM).

Using the fact, that G_F is RG invariant, i.e. $\mu^2\frac{d}{d\mu^2}G_F = 0$, the μ-dependent terms in Eq. (A.13) can be evaluated explicitly from the one-loop correction and explicit knowledge of anomalous dimension γ_{G_F}. As was shown in [67–69, 75, 76], the anomalous dimension γ_{G_F} can be extracted (i) via the beta-function β_λ of the scalar self-coupling and the anomalous dimension of the mass parameter m^2 (in unbroken phase) or (ii) via the β-function of the SU(2) gauge coupling g and the anomalous dimension of the W

[6] There are typos in Eq. (4.41) of [69]: in all $\overline{\rm MS}$ renormalization constants, $Z_W^{\alpha_s}$ and $Z_Z^{\alpha_s}$, "m_t^2/m_W^2" should be replaced by "m_t^2/m_H^2"

$$\begin{aligned} Z_W^{\alpha_s} &= 1 + \frac{g^2}{(16\pi^2)}\frac{\alpha_s}{4\pi}N_c C_f\left[\frac{1}{\varepsilon}\left(4\frac{m_t^4}{m_H^2 m_W^2} - \frac{5}{4}\frac{m_t^2}{m_W^2} + \frac{1}{2}n_F\right) + \frac{1}{\varepsilon^2}\left(-12\frac{m_t^4}{m_H^2 m_W^2} + \frac{3}{2}\frac{m_t^2}{m_W^2}\right)\right] \\ Z_Z^{\alpha_s} &= 1 + \frac{g^2}{(16\pi^2)}\frac{\alpha_s}{4\pi}N_c C_f\left[\frac{1}{\varepsilon}\left(4\frac{m_t^4}{m_H^2 m_W^2} - \frac{5}{4}\frac{m_t^2}{m_W^2} + \frac{10}{9}n_F\frac{m_W^2}{m_Z^2} + \frac{11}{18}n_F\frac{m_Z^2}{m_W^2} - \frac{11}{9}n_F\right)\right. \\ &\qquad \left. + \frac{1}{\varepsilon^2}\left(-12\frac{m_t^4}{m_H^2 m_W^2} + \frac{3}{2}\frac{m_t^2}{m_W^2}\right)\right], \end{aligned}$$

boson (in broken phase):

$$\gamma_{G_F} \equiv \mu^2 \frac{\partial}{\partial \mu^2} \ln G_F(\mu^2) = \frac{\beta_\lambda}{\lambda} - \gamma_{m^2} = 2\frac{\beta_g}{g} - \gamma_W. \tag{A.14}$$

Eq. (A.9) can be written as

$$\begin{aligned} \frac{G_F}{G_F(\mu^2)} &= 1 - \frac{g^2}{16\pi^2}\left[\gamma_{G_F,\alpha} L - \Delta X^{(1)}_{G_F,\alpha}\right] \\ &\quad + \frac{g^2 g_s^2}{(16\pi)^2}\left[\Delta X^{(2)}_{G_F,\alpha\alpha_s} + C^{(2,2)}_{G_F,\alpha\alpha_s} L^2 - C^{(2,1)}_{G_F,\alpha\alpha_s} L\right], \end{aligned} \tag{A.15}$$

where $L = \ln \frac{\mu^2}{m_t^2}$ and the coefficients $C^{(2,2)}_{G_F,\alpha\alpha_s}$ and $C^{(2,1)}_{G_F,\alpha\alpha_s}$ are defined via the RG equations:

$$2C^{(2,2)}_{G_F,\alpha\alpha_s} = Z_{m_t^2,\alpha_s} \frac{\partial}{\partial m_t^2} \gamma_{G_F,\alpha} = -6C_f \left[\frac{3}{2}\frac{m_t^2}{m_W^2} - 12\frac{m_t^4}{m_W^2 m_H^2}\right]\Bigg|_{N_c=3}, \tag{A.16}$$

$$C^{(2,1)}_{G_F,\alpha\alpha_s} = \gamma_{G_F,\alpha\alpha_s} + Z_{m_t^2,\alpha_s} m_t^2 \frac{\partial}{\partial m_t^2} \Delta X^{(1)}_{G_F,\alpha} + Z_{m_t^2,\alpha_s} \gamma_{G_F,\alpha}, \tag{A.17}$$

with

$$\gamma_{G_F,\alpha\alpha_s} = \left[2\frac{\beta_{g,\alpha\alpha_s}}{g} - 2Z_{W,\alpha\alpha_s}\right] = \frac{1}{2} N_c C_f \left[5\frac{m_t^2}{m_W^2} - 16\frac{m_t^4}{m_W^2 m_H^2}\right]. \tag{A.18}$$

Collecting all terms in Eq. (A.17) we get

$$C^{(2,1)}_{G_F,\alpha\alpha_s}\Big|_{N_c=3, C_f=\frac{4}{3}} = 4\frac{m_t^2}{m_W^2} - 80\frac{m_t^4}{m_W^2 m_H^2}. \tag{A.19}$$

At the end of this section we again point out that the anomalous dimension of the vacuum expectation value $v^2(\mu^2) = 1/(\sqrt{2} G_F(\mu^2))$ within the diagram technique is defined by Eq. (A.14) and it is not equal to the anomalous dimension of the scalar field as in the effective potential approach [77]. Another important property of Eq. (A.14) is the appearance of an inverse power of the coupling constant λ due to the explicit inclusion of the tadpole contribution. As consequence, the limit of zero Higgs mass, $m_H^2 = 0$, does not exist within the perturbative approach. The importance of the inclusion of the tadpole contribution to restore gauge invariance of on-shell counterterms was recognized a long time ago [78] and was explicitly included in the one-loop electroweak corrections to the matching conditions [31, 61]. The RG equations for the mass parameters were discussed in [67–69, 75, 76].

A.2 $O(\alpha\alpha_s)$ corrections to the relation between the $\overline{\rm MS}$ and pole masses of the top quark

The detailed discussion and explicit evaluation[7] have been presented in [66]. For our analysis is enough to write the following symbolic relation between the $\overline{\rm MS}$ and pole masses of the top quark:

$$\frac{m_t(\mu^2)}{M_t} \;=\; 1+\sigma_\alpha+\sigma_{\alpha_s}+\sigma_{\alpha_s^2}+\sigma_{\alpha_s^3}+\sigma_{\alpha\alpha_s}+\cdots\,, \tag{A.20}$$

where σ_α and $\sigma_{\alpha\alpha_s}$ are defined by Eq.(5.54) or Eq.(5.57) of [66].

The pure QCD corrections can be found in [24–26] (only the value of $\sigma_{\alpha_s}(M_t)$ is given there, but the expression for other μ values can be readily reconstructed from the beta functions).

A.3 $O(\alpha\alpha_s)$ corrections to the relation between the $\overline{\rm MS}$ and pole masses of the Higgs boson

At the two-loop level the relation between the pole and $\overline{\rm MS}$ masses is defined as follows:

$$\begin{aligned} s_P &= m_0^2-\Pi_0^{(1)}-\Pi_0^{(2)}-\Pi_0^{(1)}\Pi_0^{(1)\prime}-\left[\sum_j(\delta m^2_{j,0})^{(1)}\frac{\partial}{\partial m^2_{j,0}}+\sum_j(\delta g_{j,0})^{(1)}\frac{\partial}{\partial g_{j,0}}\right]\Pi_0^{(1)} \\ &= m_a^2-\left\{\Pi_a^{(1)}\right\}_{\overline{\rm MS}}-\left\{\Pi_a^{(2)}+\Pi_a^{(1)}\Pi_a^{(1)\prime}\right\}_{\overline{\rm MS}}\,, \end{aligned} \tag{A.21}$$

where the sum runs over all species of particles, $g_j=\alpha$, g_s, $(\delta g_{j,0})^{(1)}$ and $(\delta m^2_{j,0})^{(1)}$ are the one-loop counterterms for the charges and physical masses in the $\overline{\rm MS}$ scheme and after differentiation we put all parameters equal to their on-shell values. The derivatives in Eq. (A.21) correspond to the subtraction of sub-divergences. The genuine two-loop mass counterterm comes from the shift of the m_0^2 term. The relation between the bare and $\overline{\rm MS}$ masses of the Higgs boson has the form

$$\begin{aligned} \left(m_H^B\right)^2 &= \left(m_H^R(\mu^2)\right)^2\left[1+\frac{g^2}{16\pi^2\varepsilon}Z_{H,\alpha}\right. \\ &\left.+\frac{g^4}{(16\pi^2)^2}\left(\frac{1}{\varepsilon}Z^{(2,1)}_{H,\alpha^2}+\frac{1}{\varepsilon^2}Z^{(2,2)}_{H,\alpha^2}\right)+\frac{g_s^2g^2}{(16\pi^2)^2}\left(\frac{1}{\varepsilon}Z^{(2,1)}_{H,\alpha\alpha_s}+\frac{1}{\varepsilon^2}Z^{(2,2)}_{H,\alpha\alpha_s}\right)\right], \end{aligned} \tag{A.22}$$

where g is the SU(2) $\overline{\rm MS}$ renormalized coupling constant.

[7] There is typo in Eq. (4.46) of [66]: the common factor C_f was lost. The correct result is

$$=\frac{\alpha_s}{4\pi}\frac{e^2}{16\pi^2\sin^2\theta_W}C_f\left(\frac{1}{C_f}C^{(2,2)}_{\alpha\alpha_s}\ln^2\frac{m_t^2}{\mu^2}+\frac{1}{C_f}C^{(2,1)}_{\alpha\alpha_s}\ln\frac{m_t^2}{\mu^2}+\text{without modifications}\right).$$

However, all plots, the Eq. (5.57) and the Maple program [79] are correct.

The exact analytical result for the $O(\alpha\alpha_s)$ two-loop quark contribution to the Higgs-boson self-energy was calculated in [65, 72, 72]. The bare two loop mixed QCD-EW contribution (with explicit inclusion of the tadpole) for the quark with mass m_q reads:

$$\begin{aligned}
\Pi^{(2)}_{0,m_H^2,\alpha\alpha_s,q} &= \frac{g^2 g_s^2}{(16\pi^2)^2} N_c C_f \frac{m_q^2}{m_W^2} \Bigg\{ -J_{0qq}(1,1,1;m_H^2)(n-3) \\
&+ J_{0qq}(1,1,2;m_H^2)\left[m_H^2 - 4m_q^2\right] \frac{(n^2-5n+8)}{(n-4)(n-3)} \\
&+ A_0(m_q^2) B_0(m_q^2,m_q^2;m_H^2) \frac{(n-2)}{(n-3)(n-4)} \\
&\quad \times \left[(n^3-8n^2+19n-16) + \frac{m_H^2}{2m_q^2}(n^2-5n+8) \right] \\
&+ \left[B_0(m_q^2,m_q^2;m_H^2)\right]^2 \left[m_H^2 \frac{(n-2)^2}{2(n-4)} - m_q^2 \frac{2(n^2-4n+2)}{(n-4)} \right] \\
&+ \left[A_0(m_q^2)\right]^2 \frac{(n-2)(n^2-5n+8)}{2m_q^2(n-4)(n-3)} + \left[A_0(m_q^2)\right]^2 \frac{3}{2} \frac{(n-1)(n-2)^2}{m_q^2(n-3)} \Bigg\}, \qquad \text{(A.23)}
\end{aligned}$$

where the last terms come from the tadpole, n is the dimension of space-time [80] and

$$\begin{aligned}
J_{0qq}(a,b,c;m^2) &= \int \frac{d^n(k_1 k_2)}{[(k_1+k_2-p)^2]^a [k_1^2+m_q^2]^b [k_2^2+m_q^2]^c}\Bigg|_{p^2=-m^2}, \\
B_0(m_1^2,m_2^2,m^2) &= \int \frac{d^n k_1}{[k_1^2+m_1^2][(k_1-p)^2+m_2^2]}\Bigg|_{p^2=-m^2}, \\
A_0(m^2) &= \int \frac{d^n k_1}{k_1^2+m^2} \equiv \frac{4(m^2)^{\frac{n}{2}-1}}{(n-2)(n-4)}. \qquad \text{(A.24)}
\end{aligned}$$

In accordance with Eq. (A.21), the coefficient $\Delta_{m_H^2,\alpha_s\alpha,q}$ of order $O(\alpha\alpha_s)$ relating the pole and $\overline{\rm MS}$ masses of the Higgs boson, $s_p - m_H^2$, can be written as

$$\begin{aligned}
&\Delta_{m_H^2,\alpha\alpha_s,q} = \qquad \text{(A.25)} \\
&\lim_{\varepsilon\to 0}\left(\frac{g^2 g_s^2}{(16\pi^2)^2} \left[\frac{1}{\varepsilon} Z^{(2,1)}_{H,\alpha\alpha_s,q} + \frac{1}{\varepsilon^2} Z^{(2,2)}_{H,\alpha\alpha_s,q} \right] - \frac{g_s^2}{16\pi^2} \frac{1}{\varepsilon} Z_{m_q^2,\alpha_s} m_q^2 \frac{\partial}{\partial m_q^2} \Pi^{(1)}_{0,H,\alpha} - \Pi^{(2)}_{0,m_H^2,\alpha\alpha_s,q} \right),
\end{aligned}$$

where

$$\frac{\partial}{\partial m_q^2}\Pi^{(1)}_{0,H,\alpha} = \frac{N_c}{m_W^2}\frac{g^2}{16\pi^2}\left\{ B_0(m_q^2,m_q^2,m_H^2)\left[\frac{m_H^2 - 2m_q^2(n+1)}{2}\right] - \frac{(3n-2)}{2} A_0(m_q^2) \right\}. \qquad \text{(A.26)}$$

As result of our calculation we find:

$$Z^{(2,1)}_{H,\alpha\alpha_s,q} = \frac{g^2 g_s^2}{(16\pi^2)^2} N_c C_f \frac{5}{4}\frac{m_q^2}{m_W^2}, \quad Z^{(2,2)}_{H,\alpha\alpha_s,q} = -\frac{g^2 g_s^2}{(16\pi^2)^2} N_c C_f \frac{3}{2}\frac{m_q^2}{m_W^2}. \qquad \text{(A.27)}$$

The contributions of other quarks with non-zero mass are additive. Exploring the ε expansion for the master integral J_{0qq} from [81], we have for t-quark contribution ($q = t$):

$$\Delta_{m_H^2,\alpha_s\alpha} \equiv \Delta_{m_H^2,\alpha_s\alpha,t} = \frac{g_s^2 g^2}{(16\pi^2)^2} N_c C_f \frac{m_t^4}{m_W^2} \left\{ \frac{4(z-2)(z-4)}{z} F(y) - \frac{4(1+y)^3}{y(1-y)} G(y) \right.$$
$$+ \frac{3+20y+16y^2-4y^3-9y^4}{2y(1-y)^2} \ln^2 y + \frac{(1+y)}{(1-y)} \frac{(17+88y+17y^2)}{2y} \ln y$$
$$\left. + \frac{(131+258y+131y^2)}{8y} - 6\zeta_3 \frac{(1+y)^2(1+y^2)}{y(1-y)^2} \right\}$$
$$+ C_{H,\alpha\alpha_s}^{(2,2)} \ln^2\left(\frac{m_t^2}{\mu^2}\right) + C_{H,\alpha\alpha_s}^{(2,1)} \ln\left(\frac{m_t^2}{\mu^2}\right), \tag{A.28}$$

where

$$z = \frac{m_H^2}{m_t^2}, \quad y = \frac{1-\sqrt{\frac{z}{z-4}}}{1+\sqrt{\frac{z}{z-4}}}, \quad z = -\frac{(1-y)^2}{y}, \quad 4m_t^2 - m_H^2 = m_t^2 \frac{(1+y)^2}{y}, \tag{A.29}$$

and we have introduced the two functions $F(y)$ and $G(y)$ (see also [64, 65]) defined as[8]

$$\begin{aligned} F(y) &= 3\left[\mathrm{Li}_3(y) + 2\mathrm{Li}_3(-y)\right] - 2\ln y \left[\mathrm{Li}_2(y) + 2\mathrm{Li}_2(-y)\right] \\ &\quad - \frac{1}{2}\ln^2 y \left[\ln(1-y) + 2\ln(1+y)\right], \\ G(y) &= \left[\mathrm{Li}_2(y) + 2\mathrm{Li}_2(-y)\right] + \ln y \left[\ln(1-y) + 2\ln(1+y)\right], \end{aligned} \tag{A.31}$$

and

$$\ln\left(\frac{m_H^2}{m_t^2}\right) = 2\ln(1-y) - \ln y + i\pi. \tag{A.32}$$

In Eq. (A.28) we explicitly factorized the RG logarithms, $C_{H,\alpha\alpha_s}^{(2,2)}$ and $C_{H,\alpha\alpha_s}^{(2,1)}$, which may be calculated also from the one-loop result and the mass anomalous dimensions (see [75, 76] for the general case). From the parametrization

$$\begin{aligned} M_H^2 &= m_H^2 + \frac{g^2}{16\pi^2}\left[\Delta X_{H,\alpha}^{(1)} - C_{H,\alpha}^{(1)} L\right] + \frac{g^2 g_s^2}{(16\pi^2)^2}\left[\Delta X_{H,\alpha\alpha_s}^{(2)} + C_{H,\alpha\alpha_s}^{(2,2)} L^2 - C_{H,\alpha\alpha_s}^{(2,1)} L\right] \\ &= m_H^2 + \Delta_{m_H^2,\alpha} + \Delta_{m_H^2,\alpha\alpha_s}, \end{aligned} \tag{A.33}$$

[8] We cross checked, that Eq. (A.28) minus tadpole contribution coincides with results of Ref. [64, 72–74] after the following substitutions:

$$r = \frac{z}{4}, \quad 1-r = \frac{(1+y)^2}{4y}, \quad r_+ = 1/\sqrt{y}, \quad r_- = \sqrt{y},$$
$$f = -\frac{1}{2}\ln y, \quad g = \ln(1-y) - 1/2\ln y, \quad h = \ln(1+y) - 1/2\ln y. \tag{A.30}$$

where $L = \ln \frac{\mu^2}{m_t^2}$, and using the fact that pole mass is RG invariant, we have:

$$C^{(1)}_{H,\alpha} = m_H^2 Z_{H,\alpha}, \quad \gamma_{m_t^2,\alpha_s} = Z_{m_t^2,\alpha_s} = -6C_f, \tag{A.34}$$

$$2C^{(2,2)}_{H,\alpha\alpha_s} = Z_{m_t^2,\alpha_s} m_t^2 \frac{\partial}{\partial m_t^2} m_H^2 Z_{H,\alpha} = -3m_H^2 C_f N_c \frac{m_t^2}{m_W^2}, \tag{A.35}$$

$$C^{(2,1)}_{H,\alpha\alpha_s} = m_H^2 \gamma_{H,\alpha\alpha_s} + Z_{m_t^2,\alpha_s} C^{(1)}_{H,\alpha} + Z_{m_t^2,\alpha_s} m_t^2 \frac{\partial}{\partial m_t^2} \Delta X^{(1)}_{H,\alpha}, \tag{A.36}$$

where

$$Z_{H,\alpha} = -\frac{3}{2} - \frac{3}{4}\frac{m_Z^2}{m_W^2} + \frac{3}{4}\frac{m_H^2}{m_W^2} + \sum_{\text{lepton}} \frac{1}{2}\frac{m_l^2}{m_W^2} + N_c \sum_{\text{u}} \frac{1}{2}\frac{m_u^2}{m_W^2} + N_c \sum_{\text{d}} \frac{1}{2}\frac{m_d^2}{m_W^2}. \tag{A.37}$$

In terms of the variable y, defined by Eq. (A.29), the final result reads:

$$C^{(2,1)}_{H,\alpha\alpha_s} = -C_f N_c \frac{m_t^4}{m_W^2} \left[3\frac{(1+y)(1+8y+y^2)}{y(1-y)} \ln y + \frac{(17+38y+17y^2)}{2y} \right]. \tag{A.38}$$

A.4 $O(\alpha\alpha_s)$ corrections to the top Yukawa and Higgs self couplings

The relation between the top Yukawa (Higgs) coupling and the Fermi constant G_F is obtained from Eqs. (A.9), (A.20) and (A.33) as:

$$\frac{y_t^2(\mu^2)}{2\sqrt{2}G_F M_t^2} = \frac{m_t^2(\mu^2)}{M_t^2}\frac{G_F(\mu^2)}{G_F}, \tag{A.39}$$

$$\frac{\lambda(\mu^2)}{\sqrt{2}G_F M_H^2} = \frac{m_H^2(\mu^2)}{M_H^2}\frac{G_F(\mu^2)}{G_F}, \tag{A.40}$$

and the relation between the Higgs coupling constant $\lambda \equiv h_{\text{Sirlin}}$ used in [61] and the parametrization of [66–69] follows from the comparison of the RG functions: $h_{\text{Sirlin}} = \lambda_{\text{Jegerlehner}}(\mu^2)/6$.

The $O(\alpha\alpha_s)$ result for the top-Yukawa coupling reads (see Eq. (21) in [56] and [82])

$$\begin{aligned}
&\sqrt{\frac{y_t^2(\mu^2)}{2\sqrt{2}G_F M_t^2}} - 1 = (1 + \sigma_\alpha + \sigma_{\alpha_s} + \sigma_{\alpha\alpha_s}) \\
&\times \left(1 - \Delta_{G_F,\alpha} - \Delta_{G_F,\alpha\alpha_s} - \sum_f \left[m_f^2 - M_f^2\right]_{\alpha_s} \frac{\partial}{\partial m_f^2} \Delta_{G_F,\alpha} \right)^{\frac{1}{2}} \Bigg|_{m_j^2 = M_J^2 . e^2 = e_{OS}^2} - 1 \\
&= \left(\sigma_\alpha - \frac{1}{2}\Delta_{G_F,\alpha} + \sigma_{\alpha_s} \right) \Bigg|_{m_j^2 = M_J^2 . e^2 = e_{OS}^2} \\
&+ \left(\sigma_{\alpha\alpha_s} - \frac{1}{2}\Delta_{G_F,\alpha\alpha_s} - \frac{1}{2}\sigma_{\alpha_s}\Delta_{G_F,\alpha} - \frac{1}{2}\sum_f \left[m_f^2 - M_f^2\right]_{\alpha_s} \frac{\partial}{\partial m_f^2} \Delta_{G_F,\alpha}(m_t^2) \right) \Bigg|_{m_j^2 = M_J^2 . e^2 = e_{OS}^2}
\end{aligned} \tag{A.41}$$

where σ_X are defined in Eq. (A.20). The $O(\alpha\alpha_s)$ result for the Higgs coupling is

$$\frac{\lambda(\mu^2)}{\sqrt{2}G_F M_H^2} - 1 = + \left(-\Delta_{G_F,\alpha} - \frac{\Delta_{m_H^2,\alpha}}{M_H^2}\right)\Big|_{m_j^2=M_J^2.e^2=e_{OS}^2} \tag{A.42}$$
$$+ \left(-\Delta_{G_F,\alpha\alpha_s} - \frac{\Delta_{m_H^2,\alpha\alpha_s}}{M_H^2} - \left[m_t^2 - M_t^2\right]_{\alpha_s} \frac{\partial}{\partial m_t^2}\left[\Delta_{G_F,\alpha} + \frac{\Delta_{m_H^2,\alpha}}{M_H^2}\right]\right)\Big|_{m_j^2=M_J^2.e^2=e_{OS}^2},$$

where

$$\left[m_t^2 - M_t^2\right]_{\alpha_s} = -2M_t^2 C_f \frac{g_s^2}{16\pi^2}\left(4 - 3\ln\frac{M_t^2}{\mu^2}\right),$$

and the sum runs over all quarks.

For completeness, we present also the explicit expressions for the derivatives (for $N_c = 3$, $C_F = 4/3$ and $m_b = 0$):

$$m_t^2 \frac{\partial}{\partial m_t^2}\Delta_{m_H^2,\alpha} = \frac{g^2}{16\pi^2}\frac{3m_t^4}{m_H^2 m_W^2}\left[\frac{1+4y+y^2}{y} + \frac{(1+y)(1+8y+y^2)}{2y(1-y)}\ln y + \frac{1}{2}\frac{m_H^2}{m_t^2}\ln\left(\frac{m_t^2}{\mu^2}\right)\right], \tag{A.43}$$

$$m_t^2 \frac{\partial}{\partial m_t^2}\Delta_{G_F,\alpha} = \frac{g^2}{16\pi^2}\left\{\frac{m_t^4}{m_W^2 m_H^2}\left(6 - 12\ln\frac{m_t^2}{\mu^2}\right) + \frac{m_t^2}{m_W^2}\left(\frac{3}{4} + \frac{3}{2}\ln\frac{m_t^2}{\mu^2}\right)\right\}. \tag{A.44}$$

Terms of the order $O(\alpha)$, $O(\alpha_s)$ in Eq. (A.41) and Eq. (A.42) correspond to [31] and [61], respectively. Terms of the order $O(\alpha\alpha_s)$ in Eq. (A.41) and Eq. (A.42) are the mixed electroweak-QCD corrections and $\Delta_{G_F,\alpha\alpha_s}$, $\sigma_{\alpha\alpha_s}$, $\Delta_{m_H^2,\alpha\alpha_s}$ are defined by Eq. (A.13), Eq. (A.28), and Eq.(5.54) or Eq.(5.57) of [66].

For completeness we present also the the coefficient $\Delta_{m_H^2,\alpha}$. We divide all corrections into bosonic (diagrams without any fermions) and fermionic (diagrams exhibiting a fermion loop) ones: $\Delta_{m_H^2,\alpha} = \frac{g^2}{16\pi^2} m_H^2 \left(\Delta_{m_H^2,\alpha,\text{boson}} + \Delta_{m_H^2,\alpha,\text{fermion}}\right)$. Using the notations of [67–69] we may write the one-loop corrections in the following form[9]

$$\begin{aligned}
\Delta_{m_H^2,\alpha,\text{boson}} &= \frac{1}{2} - \frac{1}{2}\ln\frac{m_W^2}{\mu^2} - B(m_W^2, m_W^2; m_H^2) \\
&+ \frac{m_H^2}{m_W^2}\left(-\frac{3}{2} + \frac{9}{8}\frac{\pi}{\sqrt{3}} + \frac{3}{8}\ln\frac{m_H^2}{\mu^2} + \frac{1}{4}B(m_W^2, m_W^2; m_H^2) + \frac{1}{8}B(m_Z^2, m_Z^2; m_H^2)\right) \\
&+ \frac{m_Z^2}{m_W^2}\left(\frac{1}{4} - \frac{1}{4}\ln\frac{m_Z^2}{\mu^2} - \frac{1}{2}B(m_Z^2, m_Z; m_H^2)\right) \\
&+ \frac{m_W^2}{m_H^2}\left(3 - 3\ln\frac{m_W^2}{\mu^2} + 3B(m_W^2, m_W; m_H^2)\right) \\
&+ \frac{m_Z^4}{m_W^2 m_H^2}\left(\frac{3}{2} - \frac{3}{2}\ln\frac{M_Z^2}{\mu^2} + \frac{3}{2}B(m_Z^2, m_Z; m_H^2)\right),
\end{aligned} \tag{A.45}$$

[9]For simplicity we assume a diagonal Cabibbo-Kobayashi-Maskawa matrix.

$$\Delta_{m_H^2,\alpha,\text{fermion}} = \frac{1}{2}\frac{m_l^2}{m_W^2}\sum_{lepton}\left[B_0(m_l^2,m_l^2;m_H^2)\left(1-4\frac{m_l^2}{m_H^2}\right)-4\frac{m_l^2}{m_H^2}\left(1-\ln\frac{m_l^2}{\mu^2}\right)\right]$$
$$+ \frac{1}{2}\frac{m_q^2}{m_W^2}N_c\sum_{quark}\left[B_0(m_q^2,m_q^2;m_H^2)\left(1-4\frac{m_q^2}{m_H^2}\right)-4\frac{m_q^2}{m_H^2}\left(1-\ln\frac{m_q^2}{\mu^2}\right)\right], \tag{A.46}$$

where (see Eq. (E.6) in [81])

$$B(m^2,m^2;m_H^2) = \int_0^1 dx\ln\left(\frac{m^2}{\mu^2}x+\frac{m^2}{\mu^2}(1-x)-\frac{m_H^2}{\mu^2}x(1-x)-\mathrm{i}0\right)$$
$$= \ln\frac{m^2}{\mu^2}-2-\frac{1+Y}{1-Y}\ln Y, \tag{A.47}$$

with

$$Y=\frac{1-\sqrt{\frac{r}{r-4}}}{1+\sqrt{\frac{r}{r-4}}},\quad r=\frac{m_H^2}{m^2}.$$

All results are collected in the Maple code of Ref. [79].

B Beta functions

Two loop SM beta functions above the top mass are collected in [13] (see [83–92] for original works). The three loop beta functions can be read off [16, 17].

Below the top mass the one loop beta functions for the gauge couplings were used to evolve the PDG values from M_Z to M_t. For example, for the $\alpha(\mu)$

$$\alpha(\mu)=\frac{\alpha(M_Z)}{1+\frac{11}{6\pi}\alpha(M_Z)\log(\frac{\mu}{m_Z})}. \tag{B.48}$$

The higher loop corrections are not important numerically for the electroweak constants for the small energy range between M_Z and M_t.

For the strong coupling $\alpha_s\equiv g_S^2/(4\pi)$ the RG equation up to order $O({\alpha_s}^3)$ is used

$$\frac{d\alpha_s}{d\log\mu}=-(11-\frac{2}{3}N_f)\frac{{\alpha_s}^2}{2\pi}-(51-\frac{19}{3}N_f)\frac{{\alpha_s}^3}{4\pi^2}-(2857-\frac{5033}{9}N_f+\frac{325}{27}N_f^2)\frac{{\alpha_s}^4}{64\pi^3}, \tag{B.49}$$

and $N_f=5$ is the number of flavors below the top quark. Strictly speaking, the value of $\alpha_s(M_t)$ obtained from this equation should be also shifted to the 6-quark value by

$$\alpha_{S,N_f=6}(M_t)=\alpha_{S,N_f=5}(M_t)-\frac{11}{72\pi^2}\alpha_{S,N_f=5}^3(M_t), \tag{B.50}$$

but this introduces a negligible effect ($<0.1\,\text{GeV}$) for the Higgs mass.

In all the formulas of the Appendix A we use the values of α and α_s at the matching scale μ.

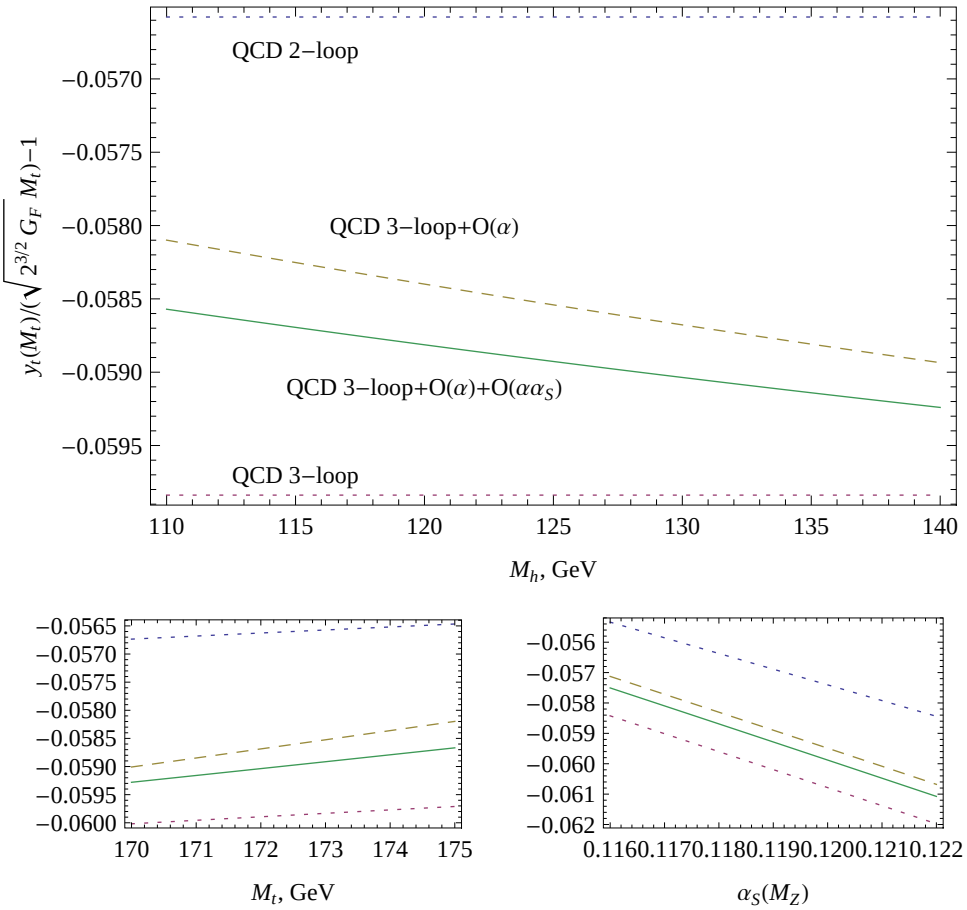

Figure 9: Contributions to the top Yukawa constant from QCD up to 2 loops, up to 3 loops, QCD and 1 loop EW corrections $O(\alpha)$, and QCD with $O(\alpha)+O(\alpha\alpha_s)$ corrections. One parameter is vrying, the two others are chosen from $M_t = 172.9\,\text{GeV}$, $\alpha_s = 0.1184$, $M_h = 125\,\text{GeV}$.

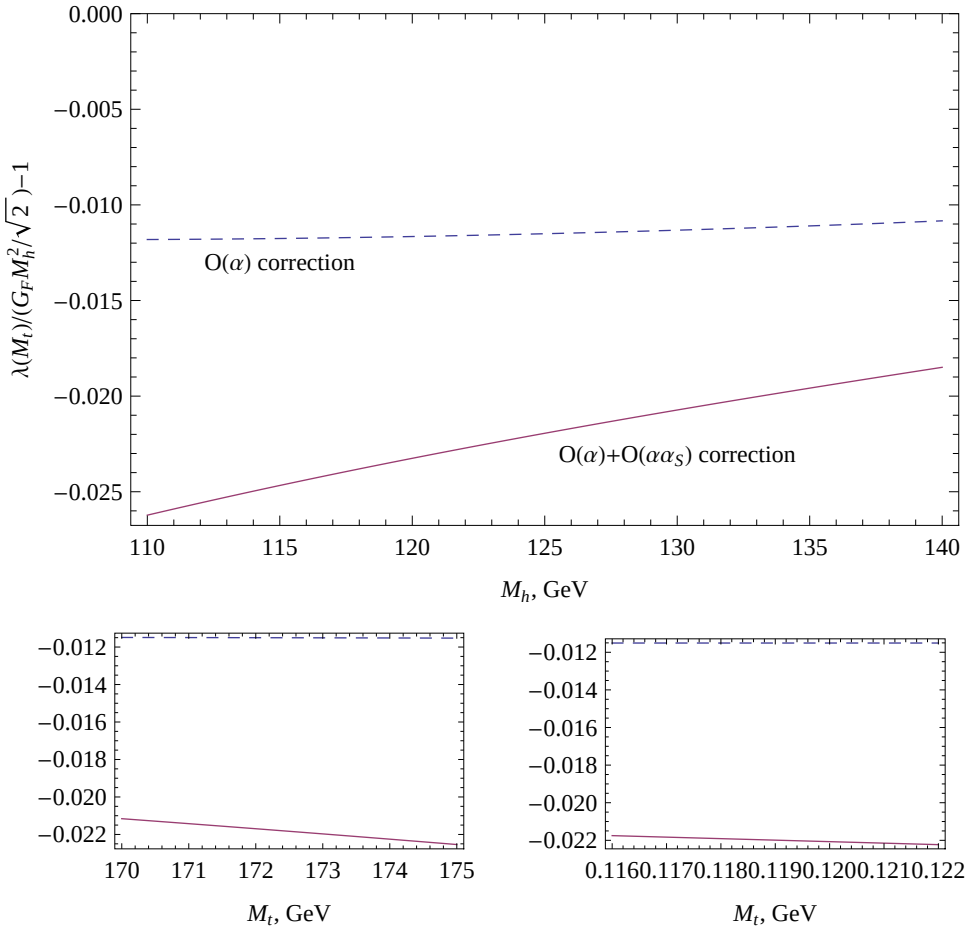

Figure 10: Contributions to the Higgs self coupling constant of the order $O(\alpha)$ and $O(\alpha) + O(\alpha\alpha_s)$. One parameter is vrying, the two others are chosen from $M_t = 172.9\,\text{GeV}$, $\alpha_s = 0.1184$, $M_h = 125\,\text{GeV}$.

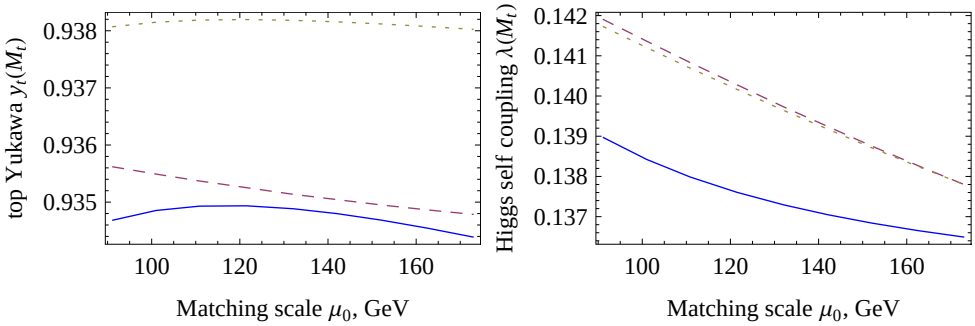

Figure 11: Top Yukawa (left) and Higgs coupling (right) at scale M_t. The constants are extracted by using matching formulas at scale μ and then evolving to the scale M_t by RG equations. Blue solid line corresponds to using full $O(\alpha, \alpha\alpha_s, {\alpha_s}^3)$ matching formulas, dashed line is matching with $O(\alpha, {\alpha_s}^3)$, dotted is matching with $O(\alpha, {\alpha_s}^2)$.

References

[1] L. Maiani, G. Parisi and R. Petronzio, Nucl. Phys. **B136**, 115 (1978).

[2] N. Cabibbo, L. Maiani, G. Parisi and R. Petronzio, Nucl. Phys. **B158**, 295 (1979).

[3] M. Lindner, Zeit. Phys. **C31**, 295 (1986).

[4] N. V. Krasnikov, Yad. Fiz. **28**, 549 (1978).

[5] P. Q. Hung, Phys. Rev. Lett. **42**, 873 (1979).

[6] H. D. Politzer and S. Wolfram, Phys. Lett. **B82**, 242 (1979).

[7] T. Hambye and K. Riesselmann, Phys. Rev. **D55**, 7255 (1997), [hep-ph/9610272].

[8] CMS Collaboration, S. Chatrchyan *et al.*, arXiv:1202.1488 [hep-ex].

[9] ATLAS Collaboration, G. Aad *et al.*, Phys.Lett. **B710**, 49 (2012), [arXiv:1202.1408 [hep-ex]].

[10] G. Altarelli and G. Isidori, Phys. Lett. **B337**, 141 (1994).

[11] J. A. Casas, J. R. Espinosa and M. Quiros, Phys. Lett. **B342**, 171 (1995), [arXiv:hep-ph/9409458].

[12] J. A. Casas, J. R. Espinosa and M. Quiros, Phys. Lett. **B382**, 374 (1996), [arXiv:hep-ph/9603227].

[13] J. R. Espinosa, G. F. Giudice and A. Riotto, JCAP **0805**, 002 (2008), [arXiv:0710.2484 [hep-ph]].

[14] F. Bezrukov and M. Shaposhnikov, JHEP **07**, 089 (2009), [arXiv:0904.1537 [hep-ph]].

[15] M. Holthausen, K. S. Lim and M. Lindner, JHEP **1202**, 037 (2012), [arXiv:1112.2415 [hep-ph]].

[16] L. N. Mihaila, J. Salomon and M. Steinhauser, Phys. Rev. Lett. **108**, 151602 (2012), [arXiv:1201.5868 [hep-ph]].

[17] K. G. Chetyrkin and M. F. Zoller, Three-loop β-functions for top-Yukawa and the Higgs self-interaction in the Standard Model, arXiv submission on the same day.

[18] F. L. Bezrukov and M. Shaposhnikov, Phys. Lett. **B659**, 703 (2008), [arXiv:0710.3755 [hep-th]].

[19] F. L. Bezrukov, A. Magnin and M. Shaposhnikov, Phys. Lett. **B675**, 88 (2009), [arXiv:0812.4950 [hep-ph]].

[20] M. Shaposhnikov and C. Wetterich, Phys. Lett. **B683**, 196 (2010), [arXiv:0912.0208 [hep-th]].

[21] S. R. Coleman and E. Weinberg, Phys. Rev. **D7**, 1888 (1973).

[22] J. Ellis, J. R. Espinosa, G. F. Giudice, A. Hoecker and A. Riotto, Phys. Lett. **B679**, 369 (2009), [arXiv:0906.0954 [hep-ph]].

[23] J. Elias-Miro *et al.*, Phys.Lett. **B709**, 222 (2012), [arXiv:1112.3022 [hep-ph]].

[24] K. G. Chetyrkin and M. Steinhauser, Phys. Rev. Lett. **83**, 4001 (1999), [hep-ph/9907509].

[25] K. G. Chetyrkin and M. Steinhauser, Nucl. Phys. **B573**, 617 (2000), [arXiv:hep-ph/9911434].

[26] K. Melnikov and T. v. Ritbergen, Phys. Lett. **B482**, 99 (2000), [arXiv:hep-ph/9912391].

[27] A. Kataev and V. Kim, PoS **ACAT08**, 004 (2008), [arXiv:0902.1442 [hep-ph]].

[28] M. C. Smith and S. S. Willenbrock, Phys. Rev. Lett. **79**, 3825 (1997), [arXiv:hep-ph/9612329].

[29] A. H. Hoang, A. Jain, I. Scimemi and I. W. Stewart, Phys.Rev.Lett. **101**, 151602 (2008), [arXiv:0803.4214 [hep-ph]].

[30] A. H. Hoang, A. Jain, I. Scimemi and I. W. Stewart, Phys.Rev. **D82**, 011501 (2010), [arXiv:0908.3189 [hep-ph]].

[31] R. Hempfling and B. A. Kniehl, Phys.Rev. **D51**, 1386 (1995), [arXiv:hep-ph/9408313 [hep-ph]].

[32] Particle Data Group, K. Nakamura *et al.*, J.Phys.G **G37**, 075021 (2010).

[33] S. Alekhin, J. Blumlein and S. Moch, arXiv:1202.2281 [hep-ph].

[34] G. Watt, JHEP **1109**, 069 (2011), [arXiv:1106.5788 [hep-ph]], 40 pages, 18 figures. v2: version published in JHEP.

[35] G. Watt, arXiv:1201.1295 [hep-ph].

[36] U. Langenfeld, S. Moch and P. Uwer, Phys.Rev. **D80**, 054009 (2009), [arXiv:0906.5273 [hep-ph]], 22 pages, 10 figures, 5 tables.

[37] Tevatron Electroweak Working Group, for the CDF and D0 Collaborations, arXiv:1107.5255 [hep-ex].

[38] D0 Collaboration, V. M. Abazov *et al.*, Phys.Lett. **B703**, 422 (2011), [arXiv:1104.2887 [hep-ex]].

[39] D. Bennett and H. B. Nielsen, Int.J.Mod.Phys. **A9**, 5155 (1994), [arXiv:hep-ph/9311321 [hep-ph]].

[40] C. Froggatt and H. B. Nielsen, Phys.Lett. **B368**, 96 (1996), [arXiv:hep-ph/9511371 [hep-ph]].

[41] S. Weinberg, in General Relativity: An Einstein centenary survey, edited by S. W.Hawking and W.Israel (Cambridge University Press) , 790 (1979).

[42] M. Niedermaier and M. Reuter, Living Rev.Rel. **9**, 5 (2006).

[43] M. Reuter, Phys.Rev. **D57**, 971 (1998), [arXiv:hep-th/9605030 [hep-th]].

[44] R. Percacci and D. Perini, Phys.Rev. **D68**, 044018 (2003), [arXiv:hep-th/0304222 [hep-th]].

[45] G. Narain and R. Percacci, Class.Quant.Grav. **27**, 075001 (2010), [arXiv:0911.0386 [hep-th]].

[46] A. A. Starobinsky, Phys. Lett. **B91**, 99 (1980).

[47] D. Gorbunov and A. Panin, Phys.Lett. **B700**, 157 (2011), [arXiv:1009.2448 [hep-ph]].

[48] F. Bezrukov and D. Gorbunov, arXiv:1111.4397 [hep-ph].

[49] F. Bezrukov, A. Magnin, M. Shaposhnikov and S. Sibiryakov, JHEP **1101**, 016 (2011), [arXiv:1008.5157 [hep-ph]].

[50] A. Barvinsky, A. Kamenshchik, C. Kiefer, A. Starobinsky and C. Steinwachs, JCAP **0912**, 003 (2009), [arXiv:0904.1698 [hep-ph]].

[51] M. Shaposhnikov, arXiv:0708.3550 [hep-th].

[52] A. Boyarsky, O. Ruchayskiy and M. Shaposhnikov, Ann.Rev.Nucl.Part.Sci. **59**, 191 (2009), [arXiv:0901.0011 [hep-ph]].

[53] M. Shaposhnikov and D. Zenhausern, Phys. Lett. **B671**, 187 (2009), [arXiv:0809.3395 [hep-th]].

[54] M. Shaposhnikov and D. Zenhausern, Phys. Lett. **B671**, 162 (2009), [arXiv:0809.3406 [hep-th]].

[55] D. Gorbunov and M. Shaposhnikov, JHEP **10**, 015 (2007), [arXiv:0705.1729 [hep-ph]].

[56] F. Jegerlehner and M. Kalmykov, Acta Phys.Polon. **B34**, 5335 (2003), [arXiv:hep-ph/0310361 [hep-ph]].

[57] A. Sirlin, Phys.Rev. **D22**, 971 (1980).

[58] W. Marciano and A. Sirlin, Phys.Rev. **D22**, 2695 (1980), [Erratum-ibid. D **31** (1985) 213].

[59] G. Burgers and F. Jegerlehner, Conf.Proc. **C8902201**, 55 (1989).

[60] S. Actis and G. Passarino, Nucl.Phys. **B777**, 100 (2007), [arXiv:hep-ph/0612124 [hep-ph]].

[61] A. Sirlin and R. Zucchini, Nucl.Phys. **B266**, 389 (1986).

[62] T. Chang, K. Gaemers and W. van Neerven, Nucl.Phys. **B202**, 407 (1982).

[63] A. Djouadi, Nuovo Cim. **A100**, 357 (1988).

[64] B. A. Kniehl, Nucl.Phys. **B347**, 86 (1990).

[65] A. Djouadi and P. Gambino, Phys.Rev. **D51**, 218 (1995), [arXiv:hep-ph/9406431 [hep-ph]].

[66] F. Jegerlehner and M. Kalmykov, Nucl.Phys. **B676**, 365 (2004), [arXiv:hep-ph/0308216 [hep-ph]].

[67] F. Jegerlehner, M. Kalmykov and O. Veretin, Nucl.Phys. **B641**, 285 (2002), [arXiv:hep-ph/0105304 [hep-ph]].

[68] F. Jegerlehner, M. Y. Kalmykov and O. Veretin, Nucl.Phys.Proc.Suppl. **116**, 382 (2003), [arXiv:hep-ph/0212003 [hep-ph]].

[69] F. Jegerlehner, M. Y. Kalmykov and O. Veretin, Nucl.Phys. **B658**, 49 (2003), [arXiv:hep-ph/0212319 [hep-ph]].

[70] F. Halzen and B. A. Kniehl, Nucl.Phys. **B353**, 567 (1991).

[71] S. Fanchiotti, B. A. Kniehl and A. Sirlin, Phys.Rev. **D48**, 307 (1993), [arXiv:hep-ph/9212285 [hep-ph]].

[72] B. A. Kniehl and A. Sirlin, Phys.Lett. **B318**, 367 (1993).

[73] B. A. Kniehl, Phys.Rev. **D50**, 3314 (1994), [arXiv:hep-ph/9405299 [hep-ph]].

[74] A. Djouadi and P. Gambino, Phys.Rev. **D49**, 3499 (1994), [arXiv:hep-ph/9309298 [hep-ph]].

[75] F. Jegerlehner, M. Y. Kalmykov and O. Veretin, Nucl.Instrum.Meth. **A502**, 618 (2003).

[76] F. Jegerlehner and M. Y. Kalmykov, Nucl.Instrum.Meth. **A534**, 299 (2004), [arXiv:hep-ph/0404213 [hep-ph]].

[77] H. Arason *et al.*, Phys.Rev. **D46**, 3945 (1992).

[78] J. Fleischer and F. Jegerlehner, Phys.Rev. **D23**, 2001 (1981).

[79] M. Y. Kalmykov, `http://theor.jinr.ru/~kalmykov/pole/pole.html`.

[80] G. 't Hooft and M. Veltman, Nucl.Phys. **B44**, 189 (1972).

[81] A. I. Davydychev and M. Y. Kalmykov, Nucl.Phys. **B699**, 3 (2004), [arXiv:hep-th/0303162 [hep-th]].

[82] B. A. Kniehl, J. H. Piclum and M. Steinhauser, Nucl.Phys. **B695**, 199 (2004), [arXiv:hep-ph/0406254 [hep-ph]].

[83] M. Fischler and J. Oliensis, Phys. Lett. **B119**, 385 (1982).

[84] M. Fischler and J. Oliensis, Phys.Rev. **D28**, 2027 (1983).

[85] C. Ford, D. R. T. Jones, P. W. Stephenson and M. B. Einhorn, Nucl. Phys. **B395**, 17 (1993), [arXiv:hep-lat/9210033].

[86] I. Jack, J. Phys. **A16**, 1083 (1983).

[87] I. Jack and H. Osborn, J. Phys. **A16**, 1101 (1983).

[88] I. Jack, Phys. Lett. **B147**, 405 (1984).

[89] I. Jack and H. Osborn, Nucl. Phys. **B249**, 472 (1985).

[90] M. E. Machacek and M. T. Vaughn, Nucl.Phys. **B222**, 83 (1983).

[91] M. E. Machacek and M. T. Vaughn, Nuclear Physics B **236**, 221 (1984).

[92] M. E. Machacek and M. T. Vaughn, Nuclear Physics B **249**, 70 (1985).

Chapter 5

BSM Higgs Sector

The Higgs Portal from LHC to ILC

Christoph Englert

Institute for Particle Physics Phenomenology, Department of Physics, Durham University, United Kingdom

DOI: will be assigned

Interpretations of searches for the Higgs boson are governed by model-dependent combinations of Higgs production cross sections and Higgs branching ratios. Mixing of the Higgs doublet with a hidden sector captures modifications from the Standard Model Higgs phenomenology in the standard search channels in a representative way, in particular because invisible Higgs decay modes open up. As a consequence, LHC exclusion bounds, which disfavor a heavy Standard Model Higgs can be consistently understood in terms of a standard-hidden mixed Higgs system. Shedding light on the possible existence of such an admixture with a hidden sector and quantifying the resemblance of an eventually discovered scalar resonance with the Standard Model Higgs crucially depends on measurement of invisible decays. This task will already be tackled at LHC, but eventually requires the clean environment of a future linear collider to be ultimately completed.

1 Introduction

Recent measurements at the CERN Large Hadron Collider [1–4] constrain a SM-like Higgs to be lighter than $m_H \lesssim 130$ GeV at 95% confidence level. Moreover, both ATLAS and CMS have observed an excess for Higgs masses around 125 GeV, consistent with each other. These tantalizing hints for a light Higgs boson in the multilepton $H \to 4\ell$ and, more importantly, in the $H \to \gamma\gamma$ channels are in excellent agreement with theoretical expectations, which have been coined by electroweak precision measurements performed during the LEP era [5].

The accumulated statistics of approximately 5 fb^{-1} per experiment, however, is yet too small to draw a conclusive picture about mechanism of electroweak symmetry breaking. Since the assumption of SM-like production and decay explicitly enter the hypothesis tests that lead to the formulation of the LHC exclusion limits, the quantitative resemblance of the observed phenomenology with the SM is, in fact, not entirely transparent. Instead of mere numerical agreement of data with the SM Higgs hypothesis, we can understand the exclusion limits as a measure of how much a more general theory is bound to coincide with the SM in the light of current experimental observations. This exercise naturally yields model-dependent statements, but there is only a limited number of phenomenological patterns of how the Higgs can evade detection [6]. The extension of the Higgs sector by including invisible decay modes and constrain them by measurements is crucial for the re-interpretation of the exclusion bounds is this context. A substantial non-zero branching ratio would signalize a non-standard Higgs sector while being in perfect agreement with a non-observation of the Higgs at the moment.

Constraining invisible branching ratios is a difficult and challenging task at hadron colliders with their busy final states [7]. A statistically significant determination of an invisible Higgs branching ratio requires large statistics (if possible after all) as experimental systematics set the scale of uncertainty. Systematics vastly improves when studying the Higgs sector at a future linear collider. There, $e^+e^- \to HZ$ associated production provides an extremely clean laboratory process to study invisible decays in a model-independent way in recoil analyses [8]. At the LHC, only ratios of branching fractions are accessible in a model-independent fashion, but absolute branching ratio predictions can be formulated in specified models [9]. Hence, performing such an analysis at a future linear collider is going to be of utmost importance to study the Higgs boson in full detail after its discovery at the LHC.

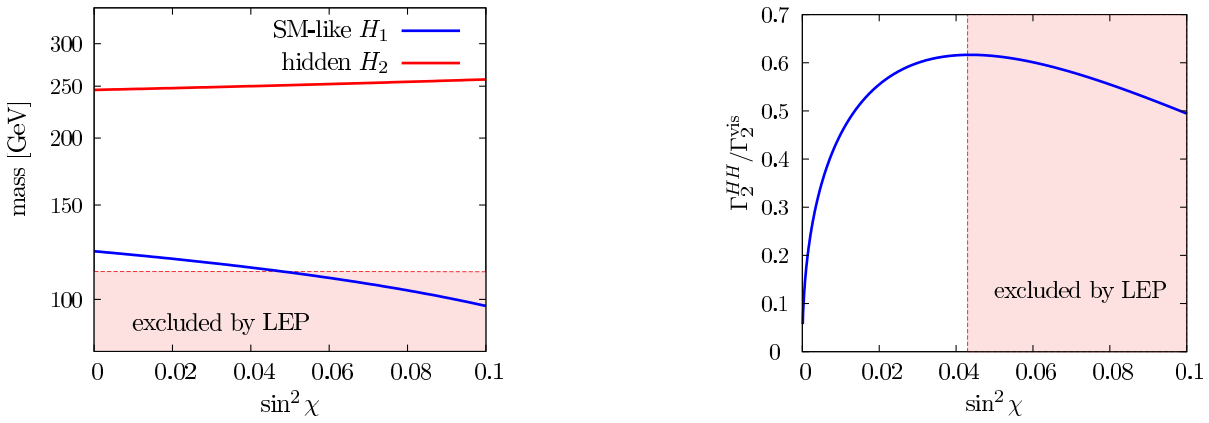

Figure 1: Left: masses of the light SM-like Higgs boson H_1 (blue) and the heavy Higgs boson H_2 (red). We choose the vacuum expectation values $v_h = v_s = 246$ GeV and $\lambda_s = \lambda_h/4 = 1/8$ for illustration purposes. The shaded region displays the LEP bound [5]. Right: cascade decay width Γ_2^{HH} as a function of $\sin^2\chi$ for the same parameters. Again, the region in which H_1 is excluded by LEP is shaded. The figures are taken from Ref. [10].

2 The Higgs portal

We introduce invisible decay channels in an efficient and theoretically consistent way via a particular type of hidden valley [11] interaction in the Higgs sector. The SM Higgs doublet ϕ_s is coupled to a hidden sector scalar field ϕ_h via the gauge-invariant and renormalizable operator $|\phi_s|^2|\phi_h|^2$ so that the potential reads [12]

$$\mathcal{V} = \mu_s^2|\phi_s|^2 + \lambda_s|\phi_s|^4 \;+\; \mu_h^2|\phi_h|^2 + \lambda_h|\phi_h|^4 \;+\; \eta_\chi|\phi_s|^2|\phi_h|^2\,. \tag{1}$$

The mass parameters μ_j can be substituted by v_j after expanding the two Higgs fields about their vacuum expectation values $v_j^2 = (-\mu_j^2 - \eta_\chi v_i^2/2)/\lambda_j$ $(i \neq j = s, h)$. The electroweak gauge boson masses are generated exclusively by the visible fields' vacuum expectation. The so-called Higgs portal interaction operator $\sim \eta$ rotates s, h states into the mass eigenstates

$$\begin{aligned} H_1 &= \cos\chi\, H_s + \sin\chi\, H_h \\ H_2 &= -\sin\chi\, H_s + \cos\chi\, H_h\,, \end{aligned} \tag{2}$$

where $\sin\chi$ is the characteristic mixing angle, which affects the production cross sections $\sigma_{1,2}$ and visible and invisible decay widths $\Gamma_{1,2}^{\rm vis,inv}$ of the two Higgs bosons in an universal fashion [9]

$$\sigma_{1,2} = \cos^2\chi\,\{\sin^2\chi\}\,\sigma_{1,2}^{\rm SM} \tag{3a}$$

and

$$\begin{aligned} \Gamma_1^{\rm vis} &= \cos^2\chi\,\Gamma_1^{\rm SM} \qquad \text{and} \qquad \Gamma_2^{\rm vis} = \sin^2\chi\,\Gamma_2^{\rm SM} \\ \Gamma_1^{\rm inv} &= \sin^2\chi\,\Gamma_1^{\rm hid} \qquad \text{and} \qquad \Gamma_2^{\rm inv} = \cos^2\chi\,\Gamma_2^{\rm hid}\,. \end{aligned} \tag{3b}$$

The index "SM" refers to the values in the SM, and the information on the hidden sector is encoded in the "hid" quantities. If kinematically allowed, *i.e.* for $m_{H_2} \gtrsim 2m_{H_1}$ we can have additional cascade decays (in the following we take H_1 to be the lighter, mostly SM-like state by definition), which, depending on the combinations of the fundamental parameters, can play a significant role [10]. We exemplarily show a Higgs spectrum as a function of $\sin^2\chi$ in Fig. 1. The relations between the suppression factors $\sin^2\chi$, the masses m_{H_1}, m_{H_2} and the fundamental lagrangian parameters of Eq. (1) can be obtained by straightforward calculation and we refer the reader to Refs. [9, 10] for further details.

The model of Eq. (1) is subject to constraints by electroweak precision observables and partial wave unitarity. A guiding principle toward the validity of a model is the comparison of the model's prediction of the Peskin-Takeuchi parameters [13] with measurements performed at LEP [5]. These give rise to the strongest constraints on the Higgs portal model*. This is easy to understand: for larger mixing angles $\sin^2\chi \to 1$ we effectively deal with a heavy Higgs model which is tightly constraint† by the measurements of [5]. At the same time, the isometry Eq. (2) restores unitarity in the high energy limit.

3 Higgs portal lessons from the LHC

Altogether the model predicts the four different phenomenological scenarios of Tab. 1 for standard Higgs resonance searches at typical LHC Higgs discovery luminosities ($\sqrt{s} = 14$ TeV), *cf.* Fig. 2, where we assume $\Gamma^{\rm hid} = \Gamma^{\rm SM}$ for simplicity. Apart from a small window in $\sin^2\chi$, the Higgs portal can be explored in its most symmetric version already at typical SM Higgs discovery luminosities [15].

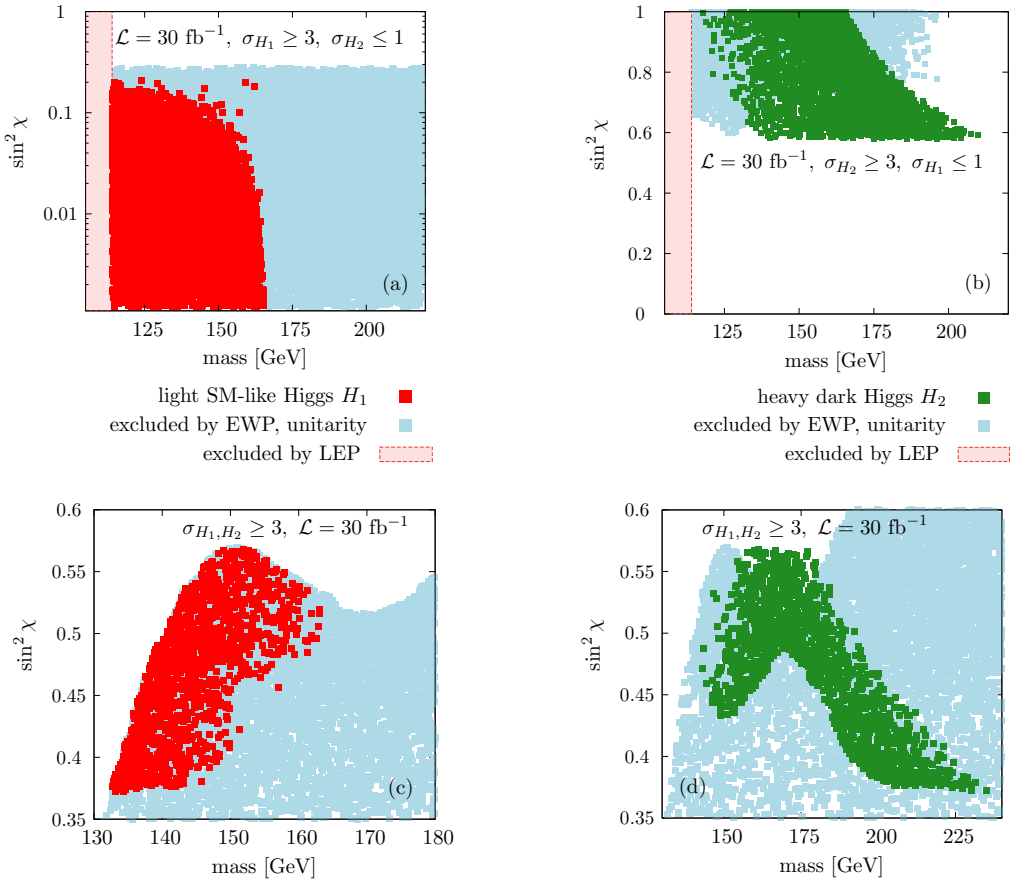

Figure 2: Scan over the Higgs portal model Eq. (1) for parameter ranges $v_h \in (0\text{ GeV}, 246\text{ GeV}], v_s = 246$ GeV, $\lambda_h \in (0, 4\pi]$, $\lambda_s \in (0, 4\pi]$, and $\eta_\chi \in [-4\pi, 4\pi]$. The hidden Higgs decay width is identified with the SM decay width for demonstration purposes, *i.e.* $\Gamma^{\rm hid} \equiv \Gamma^{\rm SM}$. LEP constraints and bounds from S, T, U [5] and unitarity are included. Panel (a) displays the sensitivity for H_1 only, panel (b) for H_2 only, and panels (c) and (d) show where the LHC is sensitive to both H_1 and H_2 at the same time for 30 fb^{-1} at $\sqrt{s} = 14$ TeV. The figures are taken from Ref. [10].

*For a discussion of perturbativity and stability of the potential Eq. (1) see Ref. [14].

†Note that in a realistic scenario we can expect kinetic mixing with a heavy $U(1)$ boson [14], which again loosens the electroweak precision constraints.

LHC sensitivity after 30 fb^{-1} to		
$\sin^2\chi \lesssim 0.2$	only H_1	$(\sigma_{H_1} \geq 3,\ \sigma_{H_2} \leq 1)$
$0.3 \lesssim \sin^2\chi \lesssim 0.4$	neither H_1 nor H_2	$(\sigma_{H_1,H_2} < 3)$
$0.4 \lesssim \sin^2\chi \lesssim 0.6$	both H_1 and H_2	$(\sigma_{H_1,H_2} \geq 3)$
$\sin^2\chi \gtrsim 0.6$	only H_2	$(\sigma_{H_1} \leq 1,\ \sigma_{H_2} \geq 3)$

Table 1: Result of Higgs searches at the LHC ($\sqrt{s} = 14$ TeV) with a luminosity of 30 fb^{-1}, σ refers to the sensitivity in terms of signal/$\sqrt{\text{background}}$.

Relaxing the assumption $\Gamma^{\rm hid} = \Gamma^{\rm SM}$ changes the picture. In fact, there is good reason to also consider the situation $\Gamma^{\rm hid} \gg \Gamma^{\rm SM}$, since the hidden decay width parametrizes our lack of knowledge about the dynamics in the hidden sector, which can be strong. To study the implications for general $\Gamma^{\rm hid}/\Gamma^{\rm SM}$ choices we examine the the 95% confidence level bounds which are formulated by the LHC collaborations with respect to the SM cross section. In the portal model of Eq. (1),(2) these can be expressed as [16]

$$\frac{\sigma[pp \to H_1 \to F]}{\sigma[pp \to H_1 \to F]^{\rm SM}} = \frac{\cos^2\chi}{1 + \tan^2\chi\,[\Gamma_1^{\rm hid}/\Gamma_{\rm tot,1}^{\rm SM}]} \leq \mathcal{R}\,, \tag{4}$$

where $\mathcal{R}$ denotes the observed exclusion limit. An identical quantity can be derived from future constraints on invisible decays [6, 7, 16]:

$$\frac{\sigma[pp \to H_1 \to inv]}{\sigma[pp \to H_1]^{\rm SM}} = \frac{\sin^2\chi\,[\Gamma_1^{\rm hid}/\Gamma_{\rm tot,1}^{\rm SM}]}{1 + \tan^2\chi\,[\Gamma_1^{\rm hid}/\Gamma_{\rm tot,1}^{\rm SM}]} \leq \mathcal{J}\,. \tag{5}$$

In Fig. 3 we exemplarily examine the implications of the current Higgs exclusion bounds for $m_H = 155$ GeV in the $\Gamma_1^{\rm hid}/\Gamma_1^{\rm SM}$-$\cos^2\chi$ plane. For this particular Higgs mass the experiments observe $R = 0.4$ [2–4]. From Fig. 3 we learn that there is a variety portal parameter choices which can accommodate the current phenomenological findings.

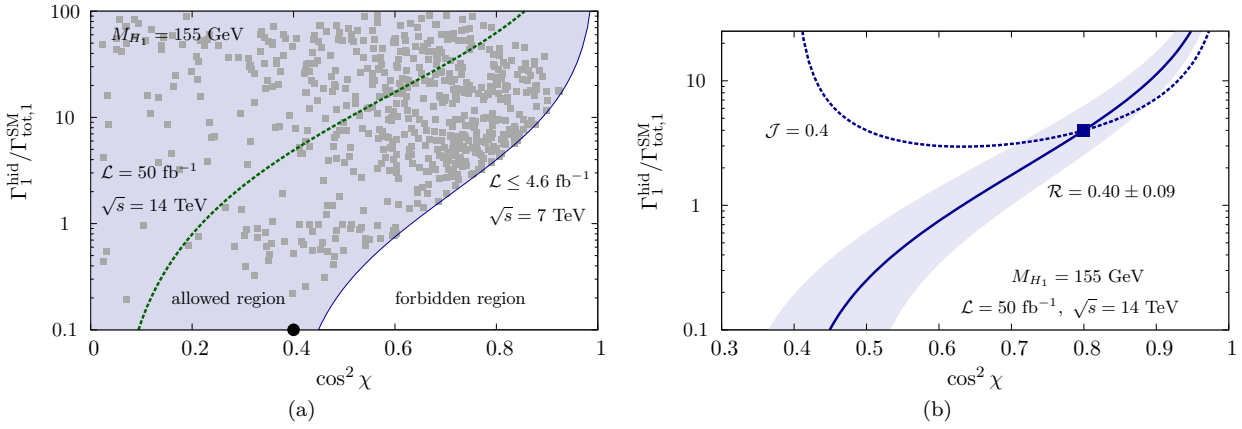

Figure 3: Left: bounds on the mixing and hidden decay width of H_1 for the point $M_{H_1} = 155$ GeV; $\mathcal{R} = 0.4$ in the standard-hidden Higgs scenario, based on current experimental results [2–4]. The regions dappled by small squares are compatible with unitarity and precision measurements. The dot indicates the $\Gamma_1^{\rm hid} \to 0$ limit of the exclusion curve at $\mathcal{R}$. The dotted line indicates the projected search limit for $\mathcal{L} = 50$ fb^{-1}. Right: bounds due to hidden Higgs searches at the LHC for established Higgs masses and cross sections. The figures are taken from Ref. [16].

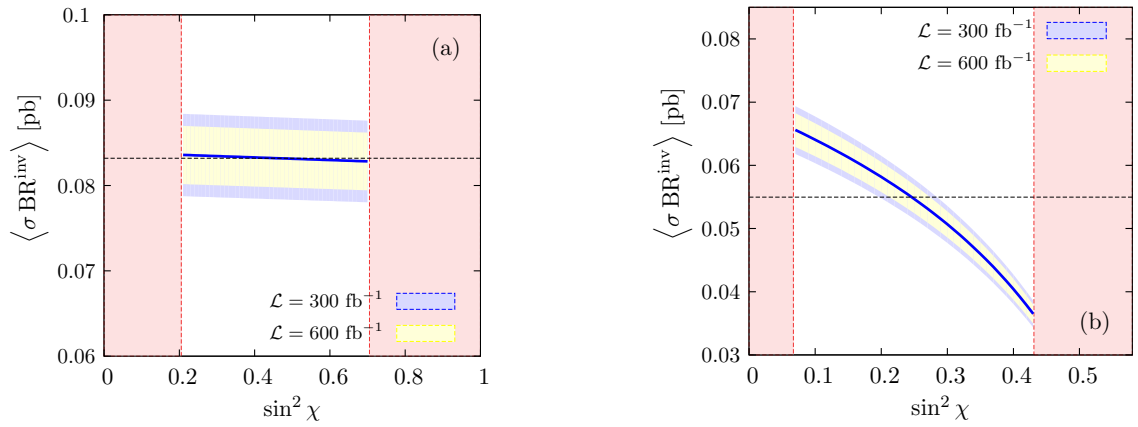

Figure 4: Reconstruction of the mixing angle from a measurement of the superposition of the invisible decays. The shaded area is theoretically not allowed due to positivity of the cross section ratio $\mathcal{R}_i$, uncertainties of these parameters are not considered. (a) is a degenerate mass spectrum $M_{H_1} = 140$ GeV, $M_{H_2} = 160$ GeV, (b) is a mass spectrum $M_{H_1} = 115$ GeV, $M_{H_2} = 300$ GeV, where the mixing can in principle be reconstructed due to Eq. (6) and comments below. Uncertainties follow from statistics only. The figures are taken from Ref. [10].

An additional constraint can be imposed in the same plane by constraining invisible decays at the LHC[‡]. Typically this involves large statistics when the [16] visible cross section of the H_1 state is already measured, *i.e.* the inequality of Eq. (4) becomes an equality within the uncertainty given by statistics and systematics. If $\mathcal{J}$ is yet to be understood as a 95% confidence level exclusion [7], we do not have the enough information to reconstruct the all parameters of Eq. (3).

In fact, when comparing to the SM Higgs potential, the multitude of observables which are potentially accessible in addition to the SM, *i.e.* the Higgs resonance masses and the cascade decay width if present, allow for a *full* reconstruction strategy of the Higgs portal potential Eq. (1). An absolutely crucial input for this analysis is the *measurement* of $\mathcal{J}$. The measurement of $\mathcal{R}$ for both Higgs states will eventually be possible at the LHC for the bulk of the parameter space. The measurement of $\mathcal{J}$ at the LHC, however, is limited by systematics [7] and the fact that we measure a superposition of invisible rates of the two Higgs states (on top of a challenging background) at hadron colliders

$$\langle \sigma \mathrm{BR}^{\mathrm{inv}} \rangle \sim f(\Lambda) - [\cos^2 \chi + \{\sigma_2^{\mathrm{SM}}/\sigma_1^{\mathrm{SM}}\} \sin^2 \chi] \,, \tag{6}$$

where $f(\Lambda)$ depends on the trilinear coupling (if accessible) in the invisible cascade decay $H_2 \to H_1 H_1 \to$ invisible. Even if a measurement turns out to possible, we rely on the separation of the two Higgs states to lift the degeneracy in the invisible decay channel (*cf.* Fig. 4). More concretely, in order to project out the $\cos^2 \chi$ component in Eq. (6) we need $\sigma_2^{\mathrm{SM}}/\sigma_1^{\mathrm{SM}} \ll 1$, *i.e.* $m_{H_2} \gg m_{H_1}$, unless we have a significant trilinear coupling in the resolved cascade decay, which can be used to constrain the mixing parameters.

In total the LHC can not cover the entire parameter space of the Higgs portal model Eq. (1).

4 Higgs Portal spectroscopy at a linear collider

The systematics-plagued determination of invisible branching ratio of the individual resonances can be cured at a linear collider. The clean LC environment allows a precise determination of the Higgs invisible branching ratio over a broad range of Higgs masses (see *e.g.* Ref. [8]). We exemplarily show the improvement due the measurement of $\mathcal{J}_1$ for the $m_{H_1} = 155$ GeV scenario discussed in Fig. 3b of the previous section in Fig. 5a.

[‡]Such an analysis has not been performed by the experiments, but exiting analyses were adopted in Ref. [6,17], demonstrating potentially sufficient sensitivity to $\mathcal{J} \sim 1$ for the combined 2011 data set.

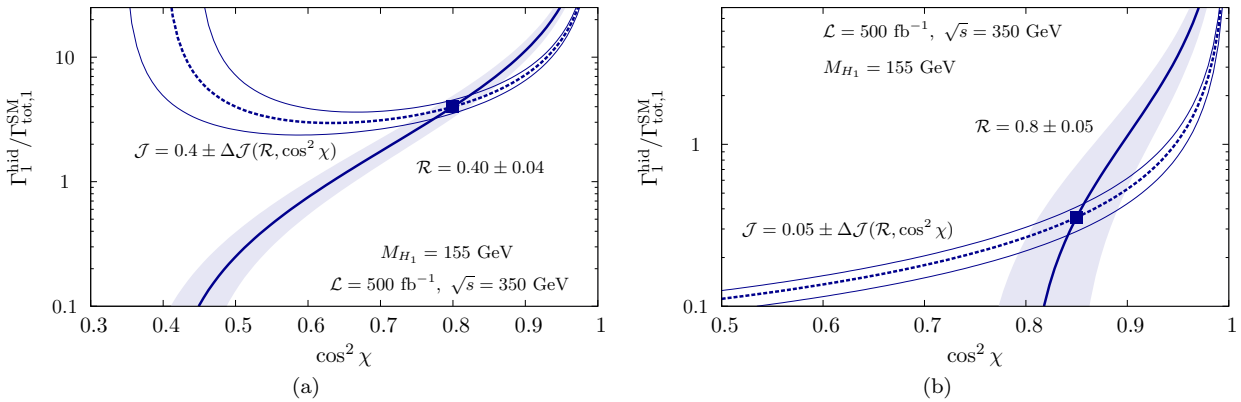

Figure 5: Left: the scenario of Fig 3b at a linear collider ($\sqrt{s} = 500$ GeV, $\mathcal{L} = 500$ fb^{-1}). Right: a Higgs portal scenario with small $\mathcal{J}$. The uncertainties are adopted from Refs. [8, 18], the figure are taken from Ref. [16].

From Fig. 5b it also becomes clear that the linear collider gives a good reconstruction of the Higgs portal for percent level values of $\mathcal{J}$.

Due to the measurement of both $\mathcal{J}_1$ and $\mathcal{R}_1$ we can reconstruct the intersection of both curves, yielding the mixing angle

$$\cos^2\chi = \mathcal{J}_1 + \mathcal{R}_1\,. \tag{7}$$

An independent measurement of $\sin^2\chi = \mathcal{J}_2 + \mathcal{R}_2$ overconstraints the system, giving rise to the sum rule

$$\mathcal{J}_1 + \mathcal{R}_1 + \mathcal{J}_2 + \mathcal{R}_2 = 1\,, \tag{8}$$

which can be used to test the consistency of the portal model Eq. (1) with experimental observations. We stress that this is not possible at the LHC due to Eq. (6).

Coming back to the strategy of approaching the SM with measurements that constrain $\Gamma_1^{\rm inv}/\Gamma_1^{\rm SM}$, it is worthwhile addressing the implications of the measured excess around 125 GeV for the portal model. If this

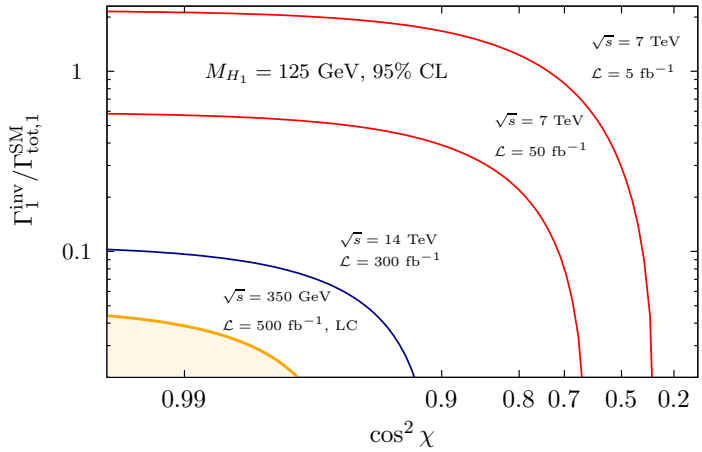

Figure 6: 95% CL contours for a measurement of $\Gamma_1^{\rm hid}/\Gamma_1^{\rm SM}$ at the LHC and a 350 GeV ILC. The LHC uncertainties are computed with SFITTER [19] and the LC uncertainties are again adopted from Refs. [18]; the figure is taken from Ref. [16].

turns out to be the Higgs then a measurement of $\Gamma_1^{\rm inv}/\Gamma_1^{\rm SM}$ give us a measure of the compatibility of the experimental observations with the SM.

Treating $\Gamma_1^{\rm hid}$ as a free parameter, we show 95 % confidence level contours in the $\Gamma_1^{\rm inv}/\Gamma_1^{\rm SM}$-$\cos^2\chi$ plane in Fig. 6. The blue and red lines correspond to measurements at the LHC, while the shaded are gives the prospects at a linear collider. Obviously the current findings at the LHC are not good enough from a statistical point of view to tell us wether or not we observe the SM Higgs. These bounds improve when higher center of mass energy and more integrated luminosity becomes available, but systematic uncertainties saturate the LHC sensitivity at around 300 fb^{-1}.

A future linear collider has the potential to take this LHC legacy to the next level: In Fig. 6 there is only a small region untested for the LC curve. For the chosen set-up of 350 GeV, 500 fb^{-1} the statistical and systematic uncertainties are comparable [8], hence further improvements can be expected by an even larger data sample.

Acknowledgments

References

[1] Atlas collaboration, ATLAS-CONF-2012-019. CMS collaboration, CMS-PAS-HIG-12-008.

[2] ATLAS Collaboration, G. Aad *et al.*, Eur. Phys. J. C **71**, 1728 (2011).

[3] CMS Collaboration, Phys. Lett. B**699** (2011) 25.

[4] ATLAS and CMS collaborations, ATLAS-CONF-2011-157, CMS PAS HIG-11-023.

[5] J. Alcaraz *et al.* [ALEPH Collaboration and DELPHI Collaboration and L3 Collaboration and], arXiv:hep-ex/0612034, [see also `http://lepewwg.web.cern.ch/LEPEWWG/plots/summer2006/`]. J. Erler and P. Langacker *in* K. Nakamura *et al.* [Particle Data Group], J. Phys. G **37** (2010) 075021.

[6] C. Englert, J. Jaeckel, E. Re and M. Spannowsky, Phys. Rev. D **85**, 035008 (2012).

[7] A. De Roeck, J. Ellis, C. Grojean, S. Heinemeyer, K. Jakobs, G. Weiglein, G. Azuelos and S. Dawson *et al.*, Eur. Phys. J. C **66** (2010) 525.

[8] M. Schumacher, LC-PHSM-2003-096.

[9] S. Bock, R. Lafaye, T. Plehn, M. Rauch, D. Zerwas and P. M. Zerwas, Phys. Lett. B **694** (2010) 44.

[10] C. Englert, T. Plehn, D. Zerwas and P. M. Zerwas, Phys. Lett. B **703**, 298 (2011).

[11] M. J. Strassler and K. M. Zurek, Phys. Lett. B **651**, 374 (2007). M. J. Strassler and K. M. Zurek, Phys. Lett. B **661**, 263 (2008).

[12] for early work see *e.g.* T. Binoth and J. J. van der Bij, Z. Phys. C **75**, 17 (1997). R. Schabinger and J. D. Wells, Phys. Rev. D **72**, 093007 (2005). B. Patt and F. Wilczek, arXiv:hep-ph/0605188.

[13] M. E. Peskin and T. Takeuchi, Phys. Rev. Lett. **65** (1990) 964.

[14] M. Bowen, Y. Cui and J. D. Wells, JHEP **0703**, 036 (2007) [hep-ph/0701035].

[15] Atlas collaboration CERN-LHCC-99-14, CERN-LHCC-99-15.

[16] C. Englert, T. Plehn, M. Rauch, D. Zerwas and P. M. Zerwas, Phys. Lett. B **707**, 512 (2012).

[17] O. J. P. Eboli and D. Zeppenfeld, Phys. Lett. B **495** (2000) 147

[18] J. A. Aguilar-Saavedra *et al.* [ECFA/DESY LC Physics Working Group Collaboration], hep-ph/0106315.

[19] R. Lafaye, T. Plehn, M. Rauch, D. Zerwas and M. Dührssen, JHEP **0908**, 009 (2009). M. Rauch, arXiv:1110.1196 [hep-ph].

Higgs boson production at Linear Colliders from a generic 2HDM: the role of triple Higgs self-interactions

David López-Val[1], *Joan Solà*[2]

[1]Institut für Theoretische Physik, Universität Heidelberg
Philosophenweg 16, 67119 Heidelberg, Germany.

[2]High Energy Physics Group, Dept. ECM, and Institut de Ciències del Cosmos
Universitat de Barcelona
Av. Diagonal 647, E-08028 Barcelona, Catalonia, Spain.

DOI: will be assigned

We review selected results for Higgs boson production at Linear Colliders in the framework of the general Two-Higgs Doublet-Model (2HDM). We concentrate on the analysis of i) the pairwise production of neutral Higgs boson pairs (h^0A^0, H^0A^0); and ii) the neutral Higgs boson-strahlung modes (h^0Z^0, H^0Z^0). We identify sizable production rates, in the range of $\sigma \sim \mathcal{O}(10-100)$ fb for $\sqrt{s} = 0.5$ TeV, alongside with large quantum effects ($\delta_r \sim \pm 50\%$), which we can fundamentally track down to the enhancement power of the triple-Higgs self-interactions. This constitutes a telltale signature of the 2HDM, with no counterpart in e.g. the Minimal Supersymmetric Standard Model (MSSM). We compare these results with several complementary double and triple $\mathcal{O}(\alpha_{ew}^3, \alpha_{ew}^4)$ Higgs-boson production mechanisms and spotlight a characteristic phenomenological profile which could eventually be highly distinctive of a non-supersymmetric two-Higgs doublet structure.

1 Introduction

Deciphering the fundamental nature of Electroweak Symmetry Breaking (EWSB) lies at the very frontline of the current theoretical and experimental research in Particle Physics. Even in spite of the tantalizing Higgs boson candidates recently identified by the ATLAS and CMS experiments [1], a long way might yet stand ahead of us until we are able to convincingly close in on such a longstanding conundrum. In particular, were these signatures finally confirmed, a first question to be answered would be whether they can be described within the minimal framework of the Standard Model (SM) or, on the contrary, if they should rather be attributed to an extended EWSB sector [2]. One canonical example of the latter is the general Two-Higgs-Doublet Model (2HDM) [3]. The model is built upon a second scalar $SU_L(2)$ doublet with $Y = +1$ weak hypercharge. This results into a larger Higgs boson spectrum of five physical Higgs fields: neutral CP-even (h^0, H^0), neutral CP-odd (A^0) and charged $H^\pm$. Such a simple, but yet non-minimal extension of the SM Higgs sector has gathered growing attention over the past years [4] and become a cherised setup for model builders and phenomenologists alike. Besides the many novel, and usually highly distinctive features put forward by the model in multifarious domains – from collider to flavor physics or astrophysics –, the 2HDM provides a suitable low-energy description to many UV completions of the the EWSB dynamics.

The model is fully specified once we fix i) the masses of the physical Higgs bosons; ii) the ratio $\tan\beta \equiv \langle H_2^0\rangle/\langle H_1^0\rangle$ of the two Vacuum Expectation Values (VEVs) giving masses to the up- and down-like quarks; iii) the mixing angle α between the two CP-even states; and iv) one remaining Higgs boson self-couplingin the Higgs potential, hereafter dubbed λ_5. We note in passing that the Higgs sector of the MSSM [5] corresponds to a particular realization of the general (unconstrained) 2HDM, for which the invariance under SUSY transformations enforces a number of additional restrictions – most significantly, the Higgs boson self-interactions become tied to the gauge couplings. This situation is remarkably different in the general 2HDM, where the size of these self-interactions is fundamentally unrestricted and it only becomes limited,

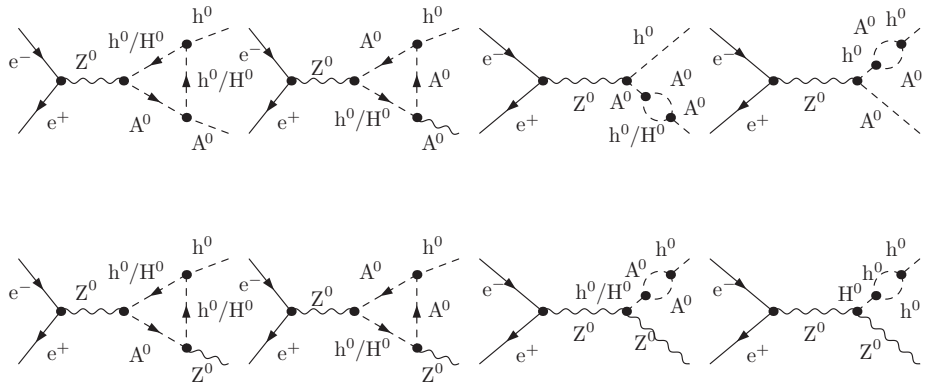

Figure 1: Sample of one-loop Higgs-mediated Feynman diagrams which account for the bulk of the quantum effects to the neutral Higgs pair $e^+e^- \to h^0A^0$ (upper row) and the Higgs-strahlung mechanisms $e^+e^- \to h^0Z^0$ (lower row).

in practice, by the interplay of theoretical consistency conditions (unitarity [6], vacuum stability [7]) and experimental bounds (viz. the excluded Higgs boson mass ranges from the from direct collider searches, and also the constraints derived from electroweak [8] and flavor physics observables [9]). A detailed account of these restrictions and of the model setup can be found in Ref. [10]. For comprehensive analyses of the 2HDM parameter space constraints, see e.g. Refs. [11].

Following the eventual discovery of the Higgs boson(s) at the LHC, it will be crucial to address the precise experimental determination of the corresponding quantum numbers, mass spectrum and couplings to other particles. A linear collider (linac) can play a central role in this enterprise [12]. Dedicated studies have exhaustively scrutinized the phenomenological imprints of the basic 2HDM Higgs boson production modes, such as e.g. i) triple Higgs, $e^+e^- \to 3h$ [13]; ii) inclusive Higgs-pair through EW gauge boson fusion, $e^+e^- \to V^*V^* \to 2h + X$ [14]; iii) exclusive Higgs-pair $e^+e^- \to 2h$ [10, 15]; and iv) Higgs strahlung, or associated production with a weak gauge boson $e^+e^- \to hV$ [16], with $[h \equiv h^0, A^0, H^0, H^\pm]$ and $[V \equiv Z^0, W^\pm]$[1]. As a common highlight, all these studies report on sizable production rates and large quantum effects, arising from the potentially enhanced Higgs self-interactions. Interestingly enough, Higgs boson searches at e^+e^- colliders may also benefit from alternative running modes, particularly from $\gamma\gamma$ scattering. Processes such as $\gamma\gamma$-induced production of single ($\gamma\gamma \to h$) and double ($\gamma\gamma \to 2h$) Higgs bosons have been studied from this viewpoint. These entirely operate at the quantum level, via an effective (loop-induced) Higgs/photon interaction $g_{\gamma\gamma h}$ that we may regard as a direct probe of non-standard (charged) degrees of freedom coupled to the Higgs sector. The aforementioned single Higgs channels have been considered in the framework of the SM [18], the 2HDM [19] and the MSSM [20, 21] and are known to exhibit excellent experimental prospects, not only due to the clean environment inherent to a linac machine, but also owing to the high attainable $\gamma\gamma$ luminosity, and the possibility to tune the γ-beam polarization as a strategy to enlarge the signal-versus-background ratios[2].

2 Numerical analysis

In this contribution we review two particular 2HDM Higgs boson production modes at a linear collider, to wit: i) the pairwise production of neutral Higgs bosons $e^+e^- \to h^0A^0/H^0A^0$; and ii) the associated production of a neutral Higgs and a Z^0 bosons, $e^+e^- \to h^0Z^0/H^0Z^0$ – the so-called Higgs-strahlung mechanism, which we can regard as the 2HDM analog(s) to the Bjorken process in the SM [23]. The motivation herewith is threefold: i) a first focus point is to seek for the most favorable regions across the 2HDM parameter space, for which the Higgs boson production rates become optimal, and to correlate them to alternative multi-Higgs

[1] For related work in the context of MSSM Higgs boson production see e.g. [17].
[2] Analogue studies for the $\gamma\gamma \to hh$ mode are available e.g. in Ref. [22].

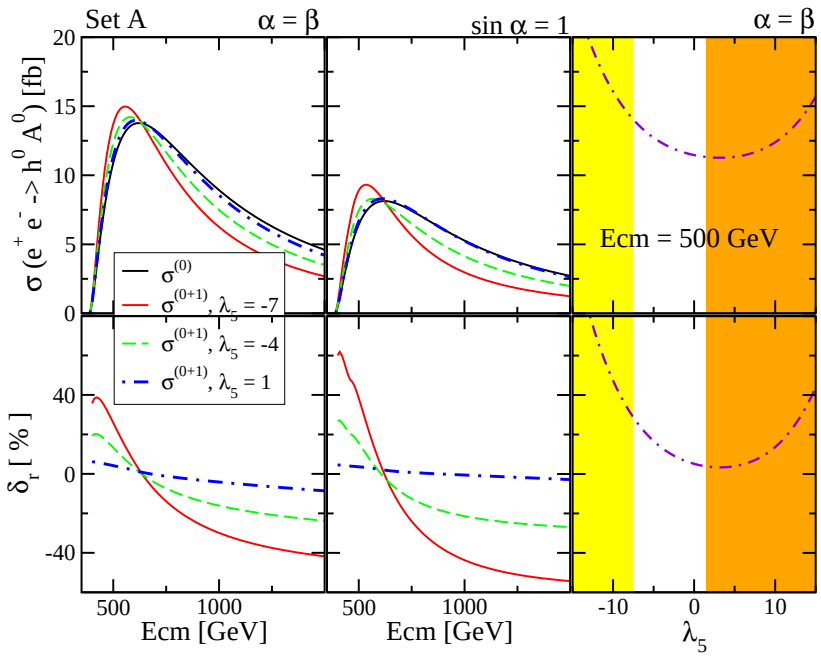

Figure 2: Tree-level and loop-corrected cross section [$\sigma(e^+e^- \to h^0A^0)$] (in fb), alongside with the relative size of the radiative corrections [$\delta_r \equiv [\sigma^{(0+1)} - \sigma^{(0)}]/\sigma^0$] (in %), as a function of $\sqrt{s}$ (left, center) and λ_5 (right). We fix $\tan\beta = 1.2$ (compatible with the lower $\tan\beta$ bound from $B_d^0 - \bar{B}_d^0$ data [9]) and examine the representative choices $\alpha = \beta$ (maximum $g_{h^0A^0Z^0}$ tree-level coupling) and $\alpha = \pi/2$ (fermiophobic limit for h^0 in type-I 2HDM). The influence of the Higgs self-interactions is assessed by dialing the value of the parameter λ_5. The shaded areas on the left (resp. right) are excluded by unitarity (resp. vacuum stability).

production modes; ii) second, we aim at quantifying the importance of the radiative corrections associated to these processes; iii) and third, we shall examine the impact of the Higgs boson self interactions and their potentially enhanced strenght. The leading order production rates merely depend on the Higgs couplings to the Z boson. In other words, they are entirely subdued by the gauge symmetry – and hence they feature no disclosing scenarios between the general 2HDM and e.g. the MSSM. The resulting phenomenological portray, however, may clearly depart once the quantum effects to such couplings are considered. Vertex corrections, in particular, turn out to be sensitive to the triple Higgs self-interactions through the interchange of virtual Higgs bosons which are then linked to the external Higgs boson legs. A sample of such Higgs-mediated one-loop diagrams is displayed in Fig. 1. These effects we can roughly describe by a loop-induced form factor, which spells out how the strength of the bare Higgs-to-gauge boson couplings is modified:

$$g_{hA^0Z^0} \to g_{hA^0Z^0} \left[1 + \frac{|\lambda_{HHH}|^2}{16\pi^2\, s}\, f(M_h^2/s, M_{A^0}^2/s)\right]. \tag{1}$$

Here λ_{HHH} stands for generic triple Higgs self-interaction, and $1/16\pi^2$ for the standard loop integral suppression factor. By $f(M_h^2/s, M_{A^0}^2/s)$ we denote a generic rational function involving the ratios of the different mass scales taking part in the process. The above expression (1) indicates how the Higgs-to-gauge boson couplings, which are entirely anchored by the gauge symmetry at the leading-order, may be strongly promoted at one-loop through the indirect effect of the Higgs boson self-couplings – unlike their MSSM counterparts.

2.1 Calculational setup

Throughout our study we make use of the standard algebraic and numerical packages FeynArts, FormCalc and LoopTools [24]. Updated experimental constraints (from EW precision data, low-energy flavor-

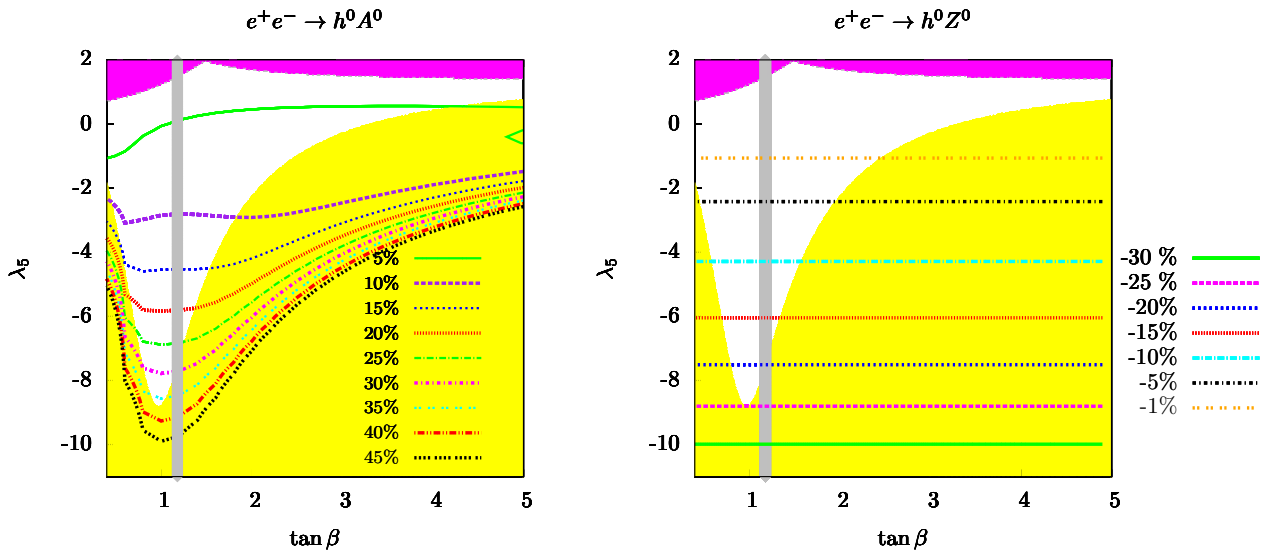

Figure 3: Contour plots for the relative size of the one-loop quantum corrections $\delta_r \equiv [\sigma^{(0+1)} - \sigma^{(0)}]/\sigma^0$ (in %) to the $e^+e^- \to h^0A^0$ (left panel) and $e^+e^- \to h^0Z^0$ (right panel) total rates, as a function of $\tan\beta$ and λ_5. We fix $\alpha = \beta$ (for $e^+e^- \to h^0A^0$) and $\alpha = \beta - \pi/2$ (for $e^+e^- \to h^0Z^0$), in which cases their respective born-level couplings maximize. For the Higgs boson masses we use Set A from Tab. 1. The linac center-of-mass energy is taken to be $\sqrt{s} = 500$ GeV. The shaded areas in the upper (resp. lower) patches of the $\tan\beta - \lambda_5$ plane are excluded by unitarity [6] (resp. vacuum stability [7]) bounds. The vertical grey strip accounts for the lower limit $\tan\beta \simeq 1.18$ stemming from $B_d^0 - \bar{B}_d^0$ data [9].

physics and the Higgs mass regions ruled out by direct collider searches), as well as theoretical consistency conditions (perturbativity, unitarity and vacuum stability) are duly taken into account [6, 7, 9, 11, 25, 26]. For definiteness, we set along two Higgs boson mass benchmark choices A and B, as quoted in Tab. 1:

	M_{h^0} [GeV]	M_{H^0} [GeV]	M_{A^0} [GeV]	$M_{\mathrm{H}^\pm}$ [GeV]
Set A	130	200	260	300
Set B	130	150	200	160

Table 1: Choices of Higgs boson masses employed throughout our calculation.

In order to carry out the complete one-loop computation we are entitled to define suitable UV counterterms, in particular for the renormalization of the Higgs boson masses and wave functions. These we can express in terms of the Higgs 2-point functions at order $\mathcal{O}(\alpha_{ew})$. Conventional on-shell renormalization conditions – see e.g. Ref. [27] – are extended to the 2HDM Higgs sector. In particular, the relations

$$\mathrm{Re}\,\hat{\Sigma}'_{\mathrm{A}^0\mathrm{A}^0}(q^2)\Big]_{q^2=M^2_{\mathrm{A}^0}} = 0; \quad \mathrm{Re}\,\hat{\Sigma}_{\mathrm{A}^0\mathrm{Z}^0}(q^2)\Big]_{q^2=M^2_{\mathrm{A}^0}} = 0,$$

anchor the wave function renormalization of the Higgs doublets, and thereby of all the physical Higgs fields. The remaining Higgs boson masses, as well as the mixing angle α, are determined via on-shell conditions imposed on their respective self-energies (including the $\mathrm{h}^0 - \mathrm{H}^0$ kinetic mixing). The parameter $\tan\beta$ is fixed via Eq. (2) alonside with one additional condition on the Higgs boson tadpoles. An exhaustive account of the renormalization procedure is available in Ref. [10].

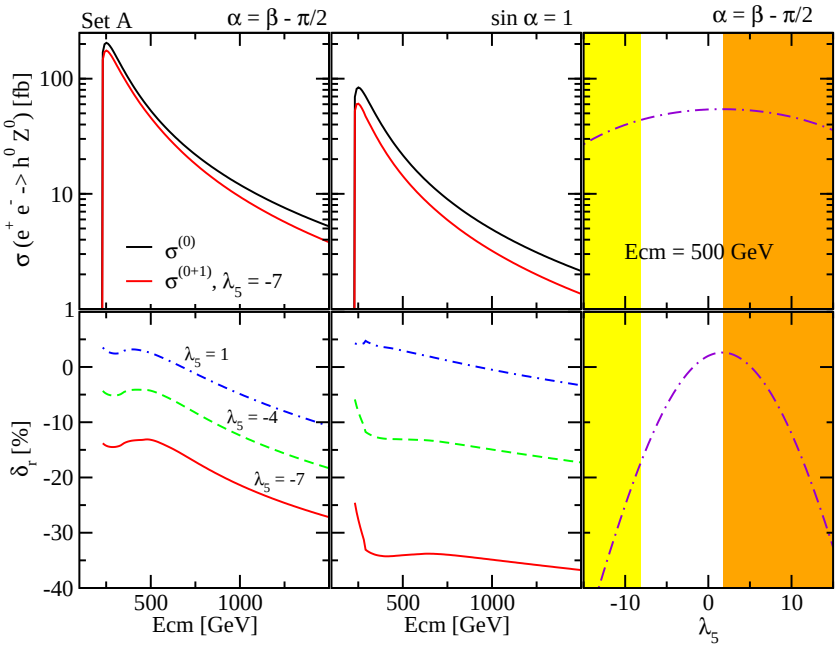

Figure 4: Tree-level and loop-corrected cross section $[\sigma(e^+e^- \to h^0A^0)]$ (in fb) and relative size of the radiative corrections $[\delta_r]$ (in %), as a function of $\sqrt{s}$ (left, center) and λ_5 (right), for an equivalent setup to that of Fig. 2.

2.2 Higgs boson pair production at $\mathcal{O}(\alpha_{ew}^3)$: $e^+e^- \to h^0A^0/H^0A^0$

For definiteness, we focus on the light Higgs mode $[h^0A^0]$ and specialize our results for the Higgs mass spectrum defined by Set A of Tab. 1. We quantify our analysis by means of i) the Born-level, $[\sigma^{(0)}]$, and 1-loop cross sections, $[\sigma^{(0+1)}]$ – in which we include the full set of $\mathcal{O}(\alpha_{ew}^3)$ corrections, and also the leading $\mathcal{O}(\alpha_{ew}^4)$ ones which arise from the squared of the scattering amplitude [10]; ii) the relative size of the 1-loop corrections, via the parameter $\delta_r \equiv [\sigma^{(0+1)} - \sigma^{(0)}]/\sigma^{(0)}$. The upshot of our findings, as summarized in Fig. 2, highlights substantial production rates, which fall roughly in the range of $2 - 15$ fb for $\sqrt{s} = 0.5$ TeV – this is, up to barely $10^3 - 10^4$ events per 500 fb^{-1}; and eventually very large quantum corrections, of the order $|\delta\sigma|/\sigma \sim 20 - 60\,\%$, which can be either positive (for $\sqrt{s} \simeq 0.5$ TeV) or negative ($\sqrt{s} \gtrsim 1$ TeV) and fairly independent on the details of the Higgs mass spectrum, the particular value of the tree-level coupling $[g_{hA^0Z}]$ and the actual type of 2HDM under consideration – namely, whether we specifically target at the type-I or II realizations of the 2HDM. The evolution of $\sigma^{(0+1)}$ and δ_r as a function of $\sqrt{s}$ for different λ_5 values evinces how critically the quantum effects depend on the Higgs self-interaction enhancements. The quadratic dependence on the parameter λ_5, $\sigma \sim (a - b\lambda_5)^2$, as shown in the rightmost panel of Fig. 2, nicely illustrates the dominance of the Higgs mediated one-loop diagrams – these are indeed sensitive to the product of two triple Higgs self-interactions. As a complementary viewpoint, in the left panel of Fig. 3 we display the profile of the radiative corrections δ_r to the total cross-section $[\sigma(h^0A^0)]$ along the $\tan\beta - \lambda_5$ plane, again for Set A of Higgs boson masses, $\alpha = \beta$ and a linac center-of-mass energy of $\sqrt{s} = 0.5\,\text{TeV}$. The choice $\alpha = \beta$ maximizes the tree-level cross section. Unitarity [6] and vacuum stability limits [7] (lower and upper shaded areas, respectively) restrict the largest attainable quantum effects to regions with $\tan\beta \simeq 1$ and $|\lambda_5| \sim 5 - 10$ ($\lambda_5 < 0$). The central grey band depicts the lower limit $\tan\beta \simeq 1.18$ ensuing from $B_d^0 - \bar{B}_d^0$ [9].

2.3 Associated Higgs/Z^0-boson production at $\mathcal{O}(\alpha_{ew}^3)$: $e^+e^- \to h^0Z^0/H^0Z^0$

Again, without loss of generality, we concentrate on the light Higgs mode $[h^0Z^0]$ and arrange the mass spectrum as in Set A of Tab. 1. Our results are shown in Fig.4. In this case we obtain typical cross sections

Process	$\sigma(\sqrt{s} = 0.5\,\text{TeV})$[fb]	$\sigma(\sqrt{s} = 1.0\,\text{TeV})$[fb]	$\sigma(\sqrt{s} = 1.5\,\text{TeV})$[fb]
h^0A^0	26.71 ($\delta_r = 31.32\%$)	4.07	1.27
H^0Z^0	19.09 ($\delta_r = -61.56\%$)	3.73	1.47
$h^0H^0A^0$	0.02	5.03	3.55
$H^0H^+H^-$	0.17	11.93	8.39
$h^0h^0 + X$	1.47	17.36	38.01

Table 2: Compared cross section (in fb) for different associated, pairwise and triple Higgs boson production mechanisms at $\mathcal{O}(\alpha_{ew}^3, \alpha_{ew}^4)$, for $\tan\beta = 1$, $\alpha = \beta$ and $\lambda_5 = -10$. The Higgs boson mass spectrum we fix as in Set B of Tab. 1. The relative size of the one-loop corrections $[\delta_r]$ for the Higgs pair and Higgs strahlung mechanisms is quoted in brackets.

in the range of $\sigma(h^0Z^0) \sim \mathcal{O}(10 - 100)\,\text{fb}$, with very significant (and systematically negative) radiative corrections (up to order $\delta_r \sim -50\%$), reaching their maximum again in the parameter space regions with $\tan\beta \sim \mathcal{O}(1)$ and $|\lambda_5| \sim \mathcal{O}(10)$. Such a characteristic pattern of negative quantum effects we can relate to the dominance of the finite wave function corrections to the external Higgs boson fields – this being the only contribution which retains a quadratic dependence on λ_{HHH} at one loop, as we can also read off the rightmost panel of Fig. 4. The relative size of the quantum effects $[\delta_r]$ and its interplay with the relevant constraints is examined in the right panel of Fig. 3 as we move across the $\tan\beta - \lambda_5$ plane. Set A of Higgs boson masses, a fixed value of $\alpha = \beta - \pi/2$ and a linac center-of-mass energy to $\sqrt{s} = 0.5\,\text{TeV}$ are employed throughout. Worth noticing is that the δ_r isocurves are not responsive to a change of $\tan\beta$. This follows directly from the analytical structure of all the relevant couplings for the particular setup $\alpha = \beta - \pi/2$ [16] – which corresponds to the decoupling (or SM-like) limit of the 2HDM.

3 Discussion and closing remarks

Higgs boson self-interactions constitute a paradigmatic structure of extended Higgs sectors of non-supersymmetric nature. The general (unconstrained) Two-Higgs-Doublet Model is a canonical example of the latter. Here, the triple and quartic Higgs boson self-interactions are not subdued by the gauge symmetry. This entails two major consequences, which are in stark contrast to analogue models, such as e.g. the MSSM: i) the Higgs boson spectrum is fully unconstrained; this is to say, no limitations on the mass splittings between the physical Higgs boson fields must be assumed *a priori*; ii) by the very same token, the Higgs boson self interactions are also fundamentally unrestricted, and hence may accomodate sizable enhancements. Both features are tamed in part by stringent theoretical and phenomenological constraints (unitarity, vacuum stability, electroweak precision and flavor physics) but nevertheless open up a plethora of rich, and highly distinctive, phenomenological possibilities. So much so, the analysis of collider observables which are sensitive to the Higgs self-interactions, either directly or through quantum corrections, may bring forward instrumental handles to disclose non-SUSY vs SUSY multi-doublet Higgs structures.

In this contribution we have concisely revisited two particular examples of Higgs boson production from e^+e^- colliders within the 2HDM context, these are the pairwise production of neutral Higgs bosons (h^0A^0/H^0A^0) and the Higgs-strahlung channels (h^0Z^0/H^0Z^0). We have portrayed their phenomenology at a future linac and have spelled out the features that singularize the 2HDM scenarios with large Higgs boson self-couplings. Our findings can be outlined as follows:

- **Large Higgs boson production rates**, in the ballpark of $\sigma_{2h,hZ} \sim \mathcal{O}(10 - 100)$ fb for $\sqrt{s} = 500$ GeV, and yet of few dozens of fb in the TeV-range center of mass energies – this would correspond to rates of $\mathcal{O}(10^2 - 10^5)$ events for an integrated luminosity of $500\,\text{fb}^{-1}$.
- **Large quantum effects**, which may reach up to $\delta_r \equiv [\sigma^{(0+1)} - \sigma^{(0)}]/\sigma^{(0)} \sim \pm 50\%$, preferably realized within the $\tan\beta \sim \mathcal{O}(1)$ and $|\lambda_5| \sim \mathcal{O}(10)$ domains of the 2HDM parameter space. These may alternatively lead to characteristic enhancements (e.g. for $\sigma(2h)$ at $\sqrt{s} \simeq 500\,\text{GeV}$), or suppressions (for $\sigma(hZ)$ and also for $\sigma(2h)$ at larger $\sqrt{s}$).

- **A generic phenomenological pattern**, in the sense that the above observations barely depend on the very choice of Higgs masses nor the type of Yukawa couplings to fermions, and they hold for broad regions across the $\tan\beta - \sin\alpha$ plane.

Interestingly enough, enhancements of the Higgs boson production rates have also been put forward in the literature for alternative multi-Higgs production processes, such as the $e^+e^- \to hhh$ [13] and $e^+e^- \to VV^* \to hh + X$ [14] channels. In this vein, let us consider the following choice of parameters: $\tan\beta = 1$, $\alpha = \beta$ and $\lambda_5 = -10$, along with Set B of Higgs boson masses from Tab. 1. This particular configuration saturates the unitarity bounds, and thus maximizes the impact of the Higgs boson self-interactions. If we now combine the evaluation of the total production rates for all these different production channels, we come up with the cross-correlated set of predictions displayed in Tab. 2. These results reflect the great complementary of the different multi-Higgs states at different center-of-mass energies. Likewise, the correlation of large negative quantum effects on the Higgs-strahlung channels with the presence of significant positive (for $\sqrt{s} \lesssim 500$ GeV) and negative (for $\sqrt{s} > 600$ GeV) quantum effects on the double Higgs production may eventually constitute an additional hint at a generic (unconstrained) 2HDM dynamics. Notice once more that, in all these cases, the reported pattern of signatures crucially relies on the strenght of the 3H self-couplings. No analogue picture could then be attributed e.g. to the MSSM.

On balance, there is little doubt that a linear collider qualifies as a most cherised tool to carry to completion the Higgs boson research program. Owing to its superbly clean environment, a linac facility should enable accurate measurements of the Higgs boson masses, gauge and Yukawa couplings, as well as of the Higgs boson self-interactions themselves. This means, it could provide us with the firmest possible grip on the fundamental structure of the EWSB sector. In this context, our results underline the possibilities of the Higgs boson self-interactions as a trademark dynamical feature of the generic 2HDM. We prove their capabilities to rubber-stamp significant – and highly distinctive – fingerprints on multi-Higgs production processes, either at the leading order or through quantum corrections, and conclude that these might well constitute a pristine window towards non-standard, non-supersymmetric Higgs sectors.

4 Acknowledgments

DLV wishes to thank the LC2012 local organizing committee and, in particular, Gudrid Moorgat-Pick and Georg Weiglein, for the hospitality extended to him at DESY and also for travel support. JS has been supported in part by MEC and FEDER under project FPA2010-20807, by the Spanish Consolider-Ingenio 2010 program CPAN CSD2007-00042 and by DIUE/CUR Generalitat de Catalunya under project 2009SGR502.

References

[1] ATLAS Collaboration, ATLAS-CONF-2011-157; CMS Collaboration, CMS-PAS-HIG-11-03.

[2] H. Haber, *J. Phys. Conf. Ser.* **G259** (2010) 012017.

[3] J.F. Gunion, H.E. Haber, G.L. Kane, S. Dawson, *The Higgs hunter's guide*, Addison-Wesley, Menlo-Park, 1990; G. C. Branco et al. arXiv:1106.0034 [hep-ph].

[4] M. Moretti, F. Piccinini, R. Pittau, J. Rathsman, JHEP 1011 (097) 2010, M. Aoki et al, Phys. Rev. D **84**, 055028 (2011) [arXiv:1104.3178 [hep-ph]]; S. Chang, J. A. Evans, M. A. Luty, Phys. Rev. D **84** (2011) 095030; S. Kanemura, K. Tsumura, H. Yokoya, arXiv:1111.6089 [hep-ph]; A. Arhrib, C. W. Chiang, D. K. Ghosh, R. Santos, arXiv:1112.5527 [hep-ph]; P. M. Ferreira, R. Santos, M. Sher, J. P. Silva, Phys. Rev. D **85**, 035020 (2012); [arXiv:1201.0019 [hep-ph]]; arXiv:1112.3277 [hep-ph]; G. Burdman, C. Haluch, R. Matheus, arXiv:1112.3961 [hep-ph].

[5] H.P Nilles, *Phys. Rept.* **110** (1984) 1; H.E. Haber, G.L. Kane, *Phys. Rept.* **117** (1985) 75; S. Ferrara, ed., *Supersymmetry*, vol. 1-2 (North Holland, World Scientific, 1987).

[6] S. Kanemura, T. Kubota and E. Takasugi, *Phys. Lett.* **B313** (1993) 155; A. Akeroyd, A.Arhrib, E.-M. Naimi, *Phys. Lett.* **B490** (2000) 119. See also Sect. III of Ref. [10].

[7] M. Sher, *Phys. Rept.* **179** (1989) 273; S. Nie and M. Sher, *Phys. Lett.* **B449** (1999) 89; S. Kanemura, T. Kasai, Y. Okada, *Phys. Lett.* **B471** (1999) 182; P.M. Ferreira, D.R.T. Jones, JHEP 08 (2009) 069.

[8] M. B. Einhorn, D.R.T. Jones, M. J. G. Veltman, *Nucl. Phys.* **B191** (1981) 146.

[9] F. Mahmoudi, *http://superiso.in2p3.fr*; F. Mahmoudi, *Comput. Phys. Commun.* **178** (2008) 745; *Comput. Phys. Commun.* **180** (2009) 1579.

[10] D. López-Val, J. Solà, *Phys. Rev.* **D81** (2010) 033003; *Fortsch. Phys.* **G58** (2010) 660; PoS RADCOR2009, 045 (2010).

[11] A. Wahab El Kaffas, P. Osland, O. M. Greid, *Phys. Rev.* **D76** (2007) 095001; H. Flächer, M. Goebel, J. Haller, A. Höcker, K. Mönig, J. Stelzer, *Eur. Phys. J* **C60** (2009) 543; N. Mahmoudi, O. Stål, *Phys. Rev.* **D81** (2010) 035016; S. R. Juárez, D. Morales, P. Kielanowski, arXiv:1201.1876

[12] *ILC Reference Design Report Volume 2: Physics at the ILC*, arXiv:0709.1893; G. Weiglein *et al.*, *Physics interplay of the LHC and the ILC.*, *Phys. Rept.* **426** (2006) 47, hep-ph/0410364; H. E. Haber, *A framework for precision 2HDM studies at the ILC and CLIC*, arXiv:1203.2631 [hep-ph].

[13] G. Ferrera, J. Guasch, D. López-Val, J. Solà, *Phys. Lett.* **B659** (2008) 297; PoS **RADCOR2007**, 043 (2007), arXiv:0801.3907.

[14] R. N. Hodgkinson, D. López-Val, J. Solà, *Phys. Lett.* **B673** (2009) 47.

[15] A. Arhrib, G. Moultaka, *Nucl. Phys.* **B558** (1999) 3; A. Arhrib, M. Capdequi Peyranère, W. Hollik, G. Moultaka, *Nucl. Phys.* **B581** (2000) 34; J. Guasch, W. Hollik, A. Kraft, *Nucl. Phys.* **B596** (2001) 66.

[16] D. López-Val, J. Solà, N. Bernal, *Phys. Rev.* **D81** (2010) 113005; D. López-Val, J. Solà, PoS **RADCOR2009**, 045 (2010); Fortsch. Phys. 58 (2010) 660.

[17] See e.g. P. Chankowski, S. Pokorski, J. Rosiek, *Nucl. Phys.* **B423** (1994) 437; V. Driesen, W. Hollik, *Zeitsch. f. Physik* **C68** (1995) 485; A. Djouadi, H.E. Haber, P.M. Zerwas, *Phys. Lett.* **B375** (2003) 1996; A. Djouadi, W. Kilian, M. Mühlleitner, P. M. Zerwas, *Eur. Phys. J* **C10** (1999) 27; S. Heinemeyer, W. Hollik, J. Rosiek and G. Weiglein, *Int. J. of Mod. Phys.* **19** (2001) 535; H. E. Logan, S.-f. Su, *Phys. Rev.* **D66** (2003) 035001; E. Coniavitis, A. Ferrari, *Phys. Rev.* **D75** (2007) 015004; O. Brein, T. Hahn, *Eur. Phys. J* **C52** (2007) 397.

[18] D. L. Borden, D. A. Bauer, D. O. Caldwell, Phys. Rev. D **48**, 4018 (1993); P. Niezurawski, A. F. Żarnecki, M. Krawczyk, Acta Phys. Polon. B **34**, 177 (2003)

[19] N. Bernal, D. López-Val, J. Solà, *Phys. Lett.* **B677** (2009) 38.

[20] D. López-Val, J. Solà, *Phys. Lett.* **B702** (2011) 246; J. Solà, D. López-Val, Nuovo Cim. **C34** (2011) 57; D. López-Val, `arXiv:1202.1075`.

[21] B. Grzadkowski, J.F. Gunion, *Phys. Lett.* **B294** (1992) 361; J. F. Gunion, H.E. Haber, *Phys. Rev.* **D48** (1993) 5; S-h. Zhu, C-s. Li, C-s. Gao, *Chin. Phys. Lett.* 15 (1998) 2; M. Mühlleitner, M. Krämer, M. Spira, P. Zerwas, *Phys. Lett.* **B508** (2001) 311; D. M. Asner, J. B. Gronberg, J.F. Gunion, *Phys. Rev.* **D67** (2003) 035009; M. Krawczyk, hep-ph/0307314; P. Niezurawski, A.F. Żarnecki, M. Krawczyk, *Acta Phys. Polon.* **B** 37 (2006) 1187.

[22] see e.g. F. Cornet and W. Hollik, *Phys. Lett.* **B669** (2008) 58; E. Asakawa, D. Harada, S. Kanemura, Y. Okada and K. Tsumura, *Phys. Lett.* **B672** (2009) 354; A. Arhrib, R. Benbrik, C.-H. Chen, R. Santos, *Phys. Rev.* **D80** (2009) 015010; E. Asakawa, D. Harada, S. Kanemura, Y. Okada, K. Tsumura, *Phys. Rev.* **D82** (2010) 115002.

[23] J.D. Bjorken, in: proc. of the 1976 SLAC Summer Institute on Particle Physics, ed. M. Zipf (SLAC Report No. 198, 1976) p. 22; D.R.T. Jones and S.T. Petcov, *Phys. Lett.* **B84** (1979) 440.

[24] T. Hahn, Comput. Phys. Commun. 140, 418 (2001); T. Hahn, C. Schappacher,*Com. Phys. Comm.* **G143** (2002) 54; T. Hahn and M. Pérez-Victoria, *Com. Phys. Comm.* **G118** (1999) 153.

[25] D. Eriksson, J. Rathsman, O. Stål, *Com. Phys. Comm.* **G181** (2010) 189, *http://www.isv.uu.se/thep/MC/2HDMC/*.

[26] P. Bechtle, O. Brein, S. Heinemeyer, G. Weiglein, K. E. Williams, *Com. Phys. Comm.* **G181** (2010) 138; arXiv:1102.1898, *http://www.ippp.dur.ac.uk/HiggsBounds*.

[27] M. Bohm, H. Spiesberger and W. Hollik, *Fortsch. Phys.* **G34** (1986) 87; A. Denner, *Fortsch. Phys.* **G41** (1993) 307.

MSSM Higgs Bosons from Stop and Chargino Decays

S. Heinemeyer[1], F. v.d. Pahlen[1], H. Rzehak[2] and C. Schappacher[3]

1- Instituto de Física de Cantabria (CSIC) 39005 Santander, Spain

2- PH-TH, CERN, CH–1211 Genève 23, Switzerland

3- Institut für Theoretische Physik, Karlsruhe Institute of Technology,
D–76128 Karlsruhe, Germany

The Higgs bosons of the MSSM can be produced from the decay of SUSY particles. We review the evalulation of two decay modes in the MSSM with complex parameters (cMSSM). The first type is the decay of the heavy scalar top quark to a lighter scalar quark and a Higgs boson. The second type is the decay of the heavy chargino to a lighter chargino/neutralino and a Higgs boson. The evaluation is based on a full one-loop calculation including hard QED and QCD radiation. We find sizable contributions to many partial decay widths and branching ratios. They are roughly of $\mathcal{O}(10\%)$ of the tree-level results, but can go up to 30% or higher. These contributions are important for the correct interpretation of scalar top quark decays at a future linear e^+e^- collider.

1 Introduction

One of the most important tasks of current high-energy physics is the search for physics effects beyond the Standard Model (SM), where the Minimal Supersymmetric Standard Model (MSSM) [1] is one of the leading candidates. Supersymmetry (SUSY) predicts two scalar partners for all SM fermions as well as fermionic partners to all SM bosons. Another important task the investigation and identification of the mechanism of electroweak symmetry breaking. The most frequently investigated models are the Higgs mechanism within the SM and within the MSSM. Contrary to the case of the SM, in the MSSM two Higgs doublets are required. This results in five physical Higgs bosons instead of the single Higgs boson in the SM; three neutral Higgs bosons, h_n ($n = 1, 2, 3$), and two charged Higgs bosons, $H^\pm$. In the MSSM with complex parameters (cMSSM) the three neutral Higgs bosons mix [2–4], giving rise to the states h_1, h_2, h_3.

An interesting production channel of Higgs bosons is the decay of the heavy scalar top quark to the lighter scalar top (scalar bottom) quark and a neutral (charged) Higgs boson. Another SUSY particle that can produce a Higgs boson is a chargino, which can decay to a lighter chargino (a lighter neutralino) and a neutral (charged) Higgs boson.

The original heavier SUSY particles can be produced at the LHC, or if kinematically allowed at an e^+e^- collider. At the ILC (or any other future e^+e^- collider such as CLIC) a precision determination of the properties of the observed particles is expected [5, 6]. Thus, if kinematically accessible, Higgs production via scalar top quark or chargino decays could offer important information about the Higgs sector of the MSSM.

In order to yield a sufficient accuracy, one-loop corrections to the various SUSY decay modes have to be considered. For the precise evaluation of the branching ratio at least all two-body decay modes have to be considered and evaluated at the one-loop level. We review the results for the evaluation of these decay widths (and branching ratios) obtained in the MSSM with complex parameters (cMSSM) [7, 8]. We will review the numerical results for

$$\Gamma(\tilde{t}_2 \to \tilde{t}_1 h_n) \qquad (n = 1, 2, 3) \;, \tag{1}$$

$$\Gamma(\tilde{t}_2 \to \tilde{b}_1 H^+) \;, \tag{2}$$

$$\Gamma(\tilde{\chi}_2^- \to \tilde{\chi}_j^0 H^-) \qquad (j = 1, 2, 3) \;, \tag{3}$$

$$\Gamma(\tilde{\chi}_1^- \to \tilde{\chi}_1^0 H^-) \;, \tag{4}$$

where $\tilde{\chi}_k^0$ denotes the neutralinos, $\tilde{\chi}_j^\pm$ the charginos. The total decay width is defined as the sum of the partial decay two-body decay widths, which have *all* be evaluated at the one-loop level.

We also concentrate on the decays of $\tilde{t}_2, \tilde{\chi}_{2,1}^-$ and do not investigate $\tilde{t}_2^\dagger, \tilde{\chi}_{2,1}^+$ decays. In the presence of complex phases this would lead to somewhat different results. Detailed references to existing calculations of these decay widths, branching ratios, as well about the extraction of complex phases can be found in Refs. [7, 8]. Our results will be implemented into the Fortran code `FeynHiggs` [9–12].

2 The complex MSSM and its renormalization

All the relevant two-body decay channels are evalulated at the one-loop level, including hard QED and QCD radiation. This requires the simultaneous renormalization of several sectors of the cMSSM, including the colored sector with top and bottom quarks and their scalar partners as well as the gluon and the gluino, the Higgs and gauge boson sector with all the Higgs bosons as well as the Z and the W boson and the chargino/neutralino sector. Details about our notation and especially about the renormalization of the cMSSM can be found in Refs. [7, 8, 13–16].

An important role play contributions of self-energy type of external (on-shell) particles. While the real part of such a loop does not contribute to the decay width due to the on-shell renormalization, the imaginary part, in product with an imaginary part of a complex coupling (such as A_t or M_1) can give a real contribution to the decay width. These contributions have been taken into account in the analytical and numerical evaluation. The impact of those contributions will be discussed in Sects. 3, 4.

The Feynman diagrams and corresponding amplitudes contributing to the various decays have been obtained with `FeynArts` [17]. The model file, including the MSSM counterterms, is largely based on Ref. [18], however adjusted to match exactly the renormalization prescription described in Ref. [7, 8, 13, 15]. The further evaluation has been performed with `FormCalc` [19]. As regularization scheme for the UV-divergences we have used constrained differential renormalization [20], which has been shown to be equivalent to dimensional reduction [21] at the one-loop level [19]. Thus the employed regularization scheme preserves SUSY [22, 23]. All UV-divergences cancel in the final result.

3 Numerical results for scalar top decays

The numerical examples are shown in two numerical scenarios, S1 and S2, where the parameters are given in Tab. 1. The results shown in this section consist of "tree", which denotes the tree-level value and of "full", which is the partial decay width including *all* one-loop corrections. We only show the results for the decay widths, since size of the loop corrections to the branching ratios are more parameter dependent.

Scen.	$\tan\beta$	$M_{H^\pm}$	$m_{\tilde{t}_2}$	$m_{\tilde{t}_1}$	$m_{\tilde{b}_2}$	μ	A_t	A_b	M_1	M_2	M_3
S1	20	150	650	$0.4\, m_{\tilde{t}_2}$	$0.7\, m_{\tilde{t}_2}$	200	800	400	200	300	350
S2	20	180	1200	$0.6\, m_{\tilde{t}_2}$	$0.8\, m_{\tilde{t}_2}$	300	1800	1600	150	200	400

Table 1: MSSM parameters for the initial numerical investigation; all masses are in GeV.

The production of $\tilde{t}_2$ at the ILC(1000), i.e. with $\sqrt{s} = 1000$ GeV, via $e^+e^- \to \tilde{t}_1^\dagger \tilde{t}_2$ will be possible, with all the decay modes (1), (2) being open. The clean environment of the ILC would permit a detailed study of the scalar top decays. For the parameters in Tab. 1 we find $\sigma(e^+e^- \to \tilde{t}_1^\dagger \tilde{t}_2) \approx 1.4$ fb, i.e. an integrated luminosity of $\sim 1\,\text{ab}^{-1}$ would yield about 1400 $\tilde{t}_2$. The ILC environment would result in an accuracy of the relative branching ratio close to the statistical uncertainty: a BR of 30% could be determined to $\sim 6\%$ for the $m_{\tilde{t}_2}$ values in Tab. 1. Depending on the combination of allowed decay channels a determination of the branching ratios at the few per-cent level might be achievable in the high-luminosity running of the ILC(1000).

We show the results for the various decay widths as a function of φ_{A_t}. The other parameters are chosen according to Tab. 1. Thus, within S1 we have $m_{\tilde{t}_1} + m_{\tilde{t}_2} = 910$ GeV, i.e. the production channel $e^+e^- \to \tilde{t}_1^\dagger \tilde{t}_2$

is open at the ILC(1000). Consequently, the accuracy of the prediction of the various partial decay widths and branching ratios should be at the same level (or better) as the anticipated ILC precision.

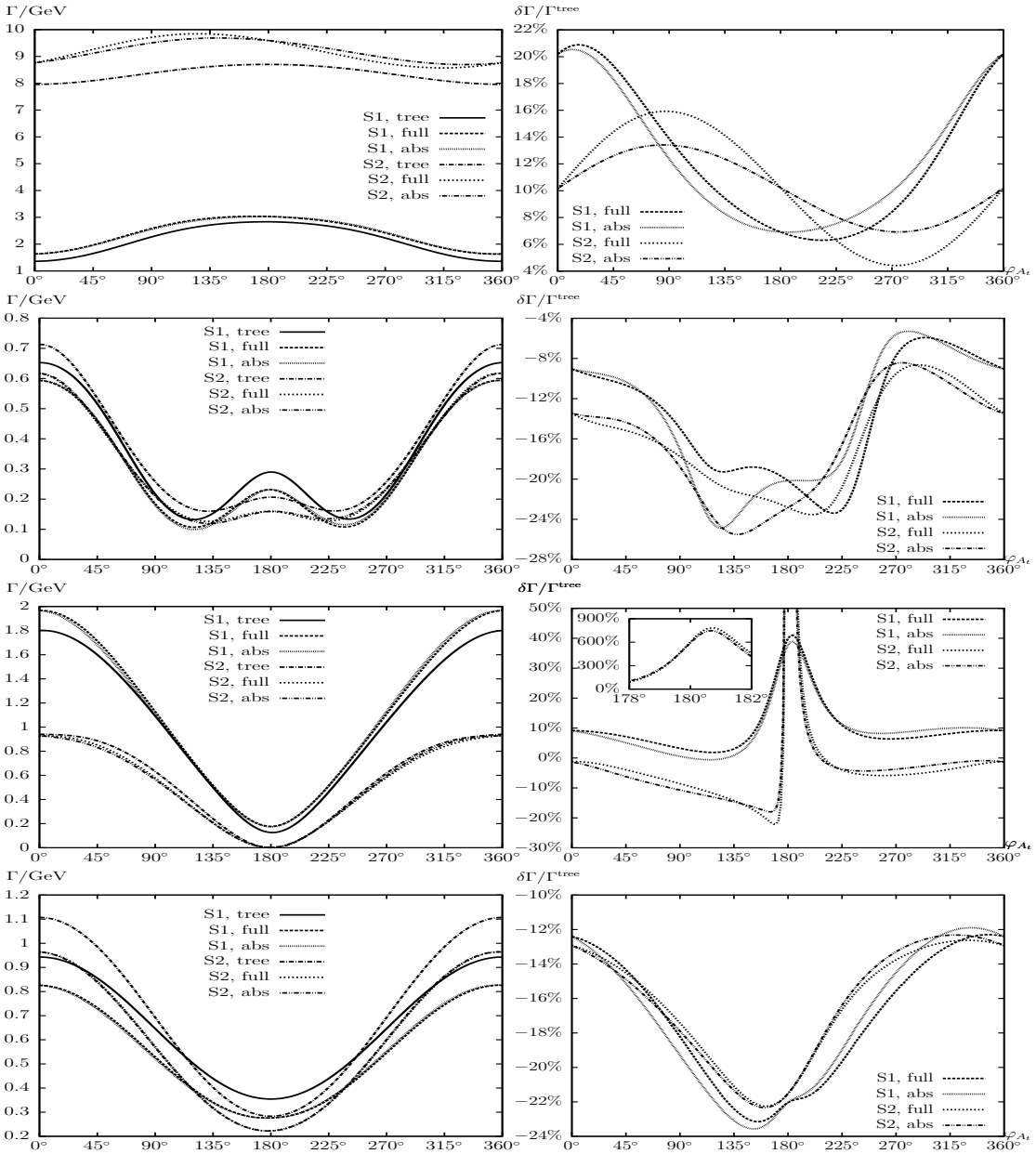

Figure 1: Tree-level ("tree") and full one-loop ("full") corrected partial decay widths are shown with φ_{A_t} varied. Also shown are the full one-loop corrected partial decay widths including absorptive contributions ("abs"). First row: $\Gamma(\tilde{t}_2 \to \tilde{t}_1 h_1)$, second row: $\Gamma(\tilde{t}_2 \to \tilde{t}_1 h_2)$, third row: $\Gamma(\tilde{t}_2 \to \tilde{t}_1 h_3)$, fourth row: $\Gamma(\tilde{t}_2 \to \tilde{b}_1 H^+)$.

In Fig. 1 we show $\Gamma(\tilde{t}_2 \to \tilde{t}_1 h_1)$ (first), $\Gamma(\tilde{t}_2 \to \tilde{t}_1 h_2)$ (second), $\Gamma(\tilde{t}_2 \to \tilde{t}_1 h_3)$ (third) and $\Gamma(\tilde{t}_2 \to \tilde{b}_1 H^+)$ (fourth row) as a function of φ_{A_t} for the parameters in Tab. 1, where the left (right) column displays the (relative one-loop correction to the) decay width. While $\Gamma(\tilde{t}_2 \to \tilde{t}_1 h_1)$ in S2 is of $\mathcal{O}(9$ GeV), the other decay widths shown are of $\mathcal{O}(1$ GeV). The variation with φ_{A_t} can be seen to be very large, of $\mathcal{O}(50\%)$. The size of the one-loop corrections, as shown in the right column are also sizable, of $\mathcal{O}(\pm 20\%)$ and exhibit a

Scen.	$\tan\beta$	$M_{H^\pm}$	$m_{\tilde{\chi}_2^\pm}$	$m_{\tilde{\chi}_1^\pm}$	$M_{\tilde{l}_L}$	$M_{\tilde{l}_R}$	A_l
$\mathcal{S}$	20	160	600	350	300	310	400

Table 2: MSSM parameters for the numerical investigation of chargino decays; all masses are in GeV.

strong variation with φ_{A_t}. The effects of the "absorptive contributions" are clearly visible, especially for $\tilde{t}_2 \to \tilde{t}_1 h_1$. Consequently, the full one-loop corrections must be taken into account in a reliable complex phase determination from scalar top decays.

4 Numerical results for chargino decays

The numerical examples are evaluated using the parameters given in Tab. 2. We assume the scalar quarks heavy such that they do not contribute to the total decay widths of the charginos. We invert the expressions of the chargino masses in order to express the parameters μ and M_2 (which are taken to be real) as a function of $m_{\tilde{\chi}_1^\pm}$ and $m_{\tilde{\chi}_2^\pm}$. This leaves two choices for the hierarchy of μ and M_2:

$$\mathcal{S}_> : \mu > M_2 \quad (\tilde{\chi}_2^\pm \text{ more higgsino-like}) \,, \tag{5}$$

$$\mathcal{S}_< : \mu < M_2 \quad (\tilde{\chi}_2^\pm \text{ more gaugino-like}) \,. \tag{6}$$

The absolute value of M_1 is fixed via the GUT relation (with $|M_2| \equiv M_2$)

$$|M_1| = \frac{5}{3} \tan^2\theta_\mathrm{w} M_2 \approx \frac{1}{2} M_2 \,, \tag{7}$$

leaving φ_{M_1} as a free parameter.

The values of $m_{\tilde{\chi}_{1,2}^\pm}$ allow $\tilde{\chi}_1^\pm \tilde{\chi}_2^\mp$ or $\tilde{\chi}_1^+ \tilde{\chi}_1^-$ at the ILC(1000) via $e^+e^- \to \tilde{\chi}_1^\pm \tilde{\chi}_{1,2}^\mp$ will be possible, with all the subsequent decay modes to a neutralino and a charged Higgs boson, see Eqs. (3), (4). As for the scalar top decays the clean environment of the ILC would permit a detailed study of the chargino decays. For the values in Tab. 2 and unpolarized beams we find, for $\mathcal{S}_>$ ($\mathcal{S}_<$), $\sigma(e^+e^- \to \tilde{\chi}_1^\pm \tilde{\chi}_2^\mp) \approx 4\,(12)$ fb, and $\sigma(e^+e^- \to \tilde{\chi}_1^+ \tilde{\chi}_1^-) \approx 55\,(80)$ fb. Choosing appropriate polarized beams these cross sections can be enhanced by a factor of approximately 2 to 3. An integrated luminosity of $\sim 1\,\mathrm{ab}^{-1}$ would yield about $4 - 12 \times 10^3$ $\tilde{\chi}_1^\pm \tilde{\chi}_2^\mp$ events and about $55 - 80 \times 10^3$ $\tilde{\chi}_1^+ \tilde{\chi}_1^-$ events, with appropriate enhancements in the case of polarized beams. The ILC environment would result in an accuracy of the relative branching ratio close to the statistical uncertainty, see the previous section. Depending on the combination of allowed decay channels a determination of the branching ratios at the per-cent level might be achievable in the high-luminosity running of the ILC(1000).

The results shown in this section consist of "tree", which denotes the tree-level value and of "full", which is the partial decay width including *all* one-loop corrections. Also shown are the full one-loop corrected decay widths omitting the absorptive contributions ("full R"). We only show the results for the decay widths, since size of the loop corrections to the branching ratios are more parameter dependent.

In Fig. 2 we show $\Gamma(\tilde{\chi}_2^- \to \tilde{\chi}_1^0 H^-)$ (first), $\Gamma(\tilde{\chi}_2^- \to \tilde{\chi}_2^0 H^-)$ (second), $\Gamma(\tilde{\chi}_2^- \to \tilde{\chi}_3^0 H^-)$ (third) and $\Gamma(\tilde{\chi}_1^- \to \tilde{\chi}_1^0 H^-)$ (fourth row) as a function of φ_{M_1} for the parameters in Tab. 2, where the left (right) column displays the (relative one-loop correction to the) decay width. The decay widhts are of $\mathcal{O}(0.1$ GeV) in the case of $\tilde{\chi}_2^- \to \tilde{\chi}_1^0 H^-$, about five times larger for $\tilde{\chi}_2^- \to \tilde{\chi}_{2,3}^0 H^-$ and a factor of ten smaller for the light chargino decay. For the heavy chargino decay a strong variation with φ_{M_1} can be observed. The size of the one-loop corrections, as shown in the right column are also sizable in the case of the heavy chargino, between -4% and $+12\%$ and show a non-negligible dependence on φ_{M_1}. Again the effects of the "absorptive contributions" are clearly visible. Also these loop corrections should be taken into account in a reliable complex phase determination in the chargino/neutralino sector.

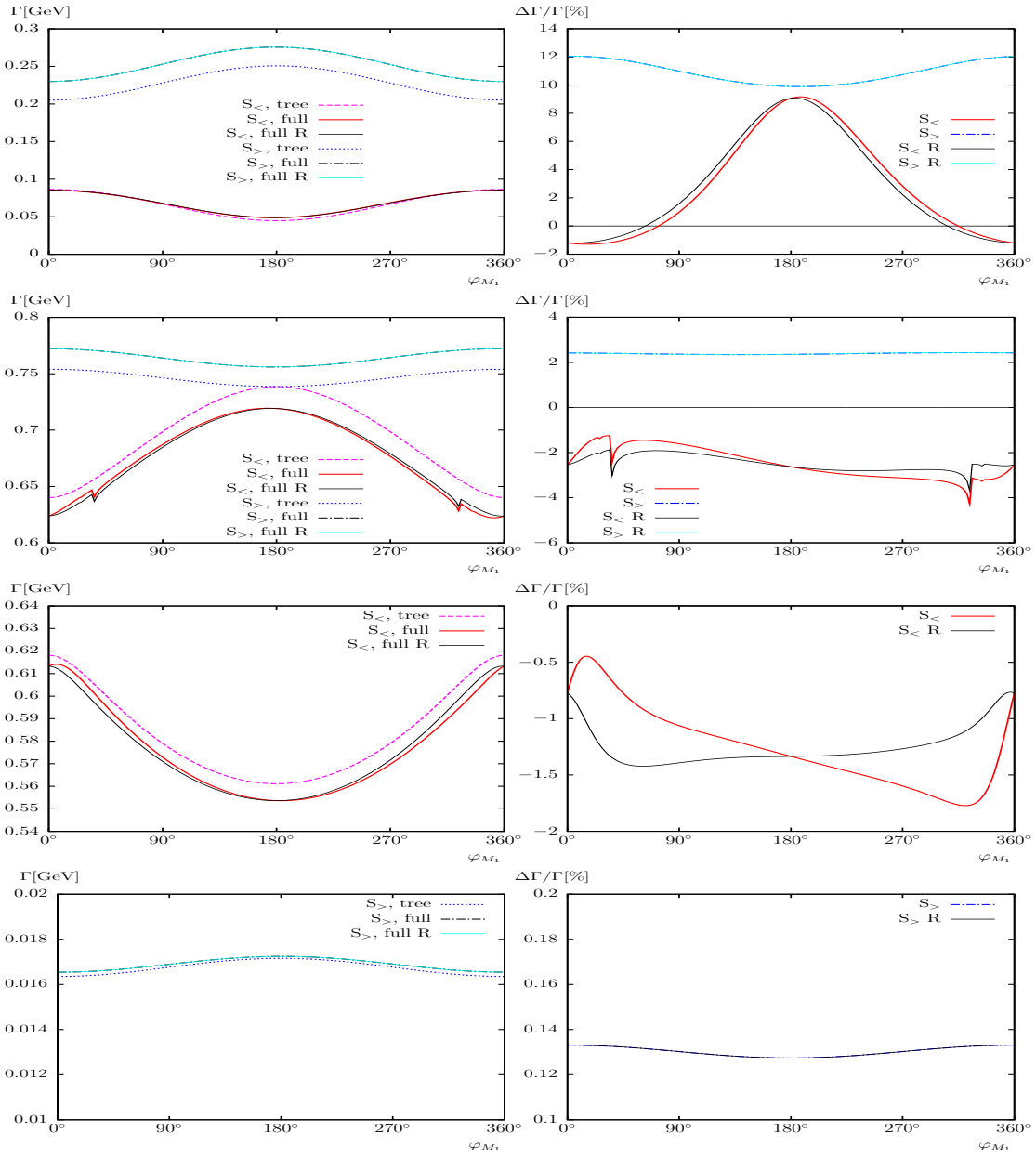

Figure 2: Tree-level ("tree") and full one-loop ("full") corrected decay widths are shown with ϕ_{M_1} varied. Also shown are the full one-loop corrected decay widths omitting the absorptive contributions ("full R"). First row: $\Gamma(\tilde{\chi}_2^- \to \tilde{\chi}_1^0 H^-)$, second row: $\Gamma(\tilde{\chi}_2^- \to \tilde{\chi}_2^0 H^-)$, third row: $\Gamma(\tilde{\chi}_2^- \to \tilde{\chi}_3^0 H^-)$, fourth row: $\Gamma(\tilde{\chi}_1^- \to \tilde{\chi}_1^0 H^-$.

Acknowledgments

The work of S.H. was partially supported by CICYT (grant FPA 2007–66387 and FPA 2010–22163-C02-01). F.v.d.P. was supported by the Spanish MICINN's Consolider-Ingenio 2010 Programme under grant MultiDark CSD2009-00064.

References

[1] H.P. Nilles, *Phys. Rept.* **110** (1984) 1;
H.E. Haber and G.L. Kane, *Phys. Rept.* **117** (1985) 75;
R. Barbieri, *Riv. Nuovo Cim.* **11** (1988) 1.

[2] A. Pilaftsis, *Phys. Rev.* **D 58** (1998) 096010 [arXiv:hep-ph/9803297];
A. Pilaftsis, *Phys. Lett.* **B 435** (1998) 88 [arXiv:hep-ph/9805373].

[3] A. Pilaftsis and C. Wagner, *Nucl. Phys.* **B 553** (1999) 3 [arXiv:hep-ph/9902371].

[4] S. Heinemeyer, *Eur. Phys. J.* **C 22** (2001) 521, hep-ph/0108059.

[5] TESLA Technical Design Report [TESLA Collaboration] Part 3, "Physics at an e^+e^- Linear Collider", arXiv:hep-ph/0106315, see:
`tesla.desy.de/new_pages/TDR_CD/start.html`;
K. Ackermann et al., DESY-PROC-2004-01.

[6] J. Brau et al. [ILC Collaboration], *ILC Reference Design Report Volume 1 - Executive Summary*, arXiv:0712.1950 [physics.acc-ph];
G. Aarons et al. [ILC Collaboration], *International Linear Collider Reference Design Report Volume 2: Physics at the ILC*, arXiv:0709.1893 [hep-ph].

[7] T. Fritzsche, S. Heinemeyer, H. Rzehak and C. Schappacher, *Phys. Rev.* **D 86** (2012) 035014 [arXiv:1111.7289 [hep-ph]].

[8] S. Heinemeyer, F. v.d. Pahlen and C. Schappacher, *Eur. Phys. J.* **C 72** (2012) 1892 [arXiv:1112.0760 [hep-ph]].

[9] S. Heinemeyer, W. Hollik and G. Weiglein, *Comput. Phys. Commun.* **124** (2000) 76 [arXiv:hep-ph/9812320];
T. Hahn, S. Heinemeyer, W. Hollik, H. Rzehak and G. Weiglein, *Comput. Phys. Commun.* **180** (2009) 1426;
see `www.feynhiggs.de` .

[10] S. Heinemeyer, W. Hollik and G. Weiglein, *Eur. Phys. J.* **C 9** (1999) 343 [arXiv:hep-ph/9812472].

[11] G. Degrassi, S. Heinemeyer, W. Hollik, P. Slavich and G. Weiglein, *Eur. Phys. J.* **C 28** (2003) 133 [arXiv:hep-ph/0212020].

[12] M. Frank, T. Hahn, S. Heinemeyer, W. Hollik, R. Rzehak and G. Weiglein, *JHEP* **02** (2007) 047 [arXiv:hep-ph/0611326].

[13] S. Heinemeyer, H. Rzehak and C. Schappacher, *Phys. Rev.* **D 82** (2010) 075010 [arXiv:1007.0689 [hep-ph]]; PoSCHARGED **2010** (2010) 039 [arXiv:1012.4572 [hep-ph]].

[14] A. Bharucha, S. Heinemeyer, F. von der Pahlen and C. Schappacher, *Phys. Rev.* **D 86** (2012) 075023 [arXiv:1208.4106 [hep-ph]].

[15] S. Heinemeyer and C. Schappacher, *Eur. Phys. J.* **C 72** (2012) 1905 [arXiv:1112.2830 [hep-ph]].

[16] S. Heinemeyer and C. Schappacher, *Eur. Phys. J.* **C 72** (2012) 2136 [arXiv:1204.4001 [hep-ph]].

[17] J. Küblbeck, M. Böhm and A. Denner, *Comput. Phys. Commun.* **60** (1990) 165;
T. Hahn, *Comput. Phys. Commun.* **140** (2001) 418 [arXiv:hep-ph/0012260];
T. Hahn and C. Schappacher, *Comput. Phys. Commun.* **143** (2002) 54 [arXiv:hep-ph/0105349].
The program, the user's guide and the MSSM model files are available via
`www.feynarts.de` .

[18] T. Fritzsche, PhD thesis, Cuvillier Verlag, Göttingen 2005, ISBN 3–86537–577–4.

[19] T. Hahn and M. Pérez-Victoria, *Comput. Phys. Commun.* **118** (1999) 153 [arXiv:hep-ph/9807565].

[20] F. del Aguila, A. Culatti, R. Munoz Tapia and M. Perez-Victoria, *Nucl. Phys.* **B 537** (1999) 561 [arXiv:hep-ph/9806451].

[21] W. Siegel, *Phys. Lett.* **B 84** (1979) 193;
D. Capper, D. Jones, and P. van Nieuwenhuizen, *Nucl. Phys.* **B 167** (1980) 479.

[22] D. Stöckinger, *JHEP* **0503** (2005) 076 [arXiv:hep-ph/0503129].

[23] W. Hollik and D. Stöckinger, *Phys. Lett.* **B 634** (2006) 63 [arXiv:hep-ph/0509298].

M_h in the MSSM-seesaw scenario with ILC precision

S. HEINEMEYER[1],M.J. HERRERO[2], S. PEÑARANDA[3,4], A.M. RODRÍGUEZ-SÁNCHEZ[2]

1- Instituto de Física de Cantabria (CSIC-UC), Santander, Spain

2- Departamento de Física Teórica and Instituto de Física Teórica, UAM/CSIC
Universidad Autónoma de Madrid, Cantoblanco, Madrid, Spain

3- Departamento de Física Teórica, Universidad de Zaragoza, Zaragoza, Spain

4- Departament de Física Fonamental, Universitat de Barcelona, Spain

We review the computation of the one-loop radiative corrections from the neutrino/ sneutrino sector to the lightest Higgs boson mass, M_h, within the context of the so-called MSSM-seesaw scenario. This model introduces right handed neutrinos and their supersymmetric partners, the sneutrinos, including Majorana mass terms. We find negative and sizeable corrections to M_h, up to -5 GeV for a large Majorana scale, $10^{13} - 10^{15}$ GeV, and for the lightest neutrino mass in a range $0.1 - 1$ eV. The corrections to M_h are substantially larger than the anticipated ILC precision for large regions of the MSSM-seesaw parameter space.

1 Introduction

The current experimental data on neutrino mass differences and neutrino mixing angles clearly indicate new physics beyond the so far successful Standard Model (SM) of Particle Physics. In particular, neutrino oscillations imply that at least two generations of neutrinos must be massive. Therefore, one needs to extend the SM to incorporate neutrino mass terms.

We have explored [4] the simplest version of a Supersymmetric extension of the SM, the well known Minimal Supersymmetric Standard Model (MSSM), extended by right-handed Majorana neutrinos and where the seesaw mechanism of type I [2] is implemented to generate the small neutrino masses. For simplicity, as a first step, we focus here in the one generation case.

On the other hand, it is well known that heavy Majorana neutrinos, with a Majorana mass scale $m_M \sim 10^{13} - 10^{15}$ GeV, induce large LFV rates [3], due to their potentially large Yukawa couplings to the Higgs sector. For the same reason, radiative corrections to Higgs boson masses due to such heavy Majorana neutrinos could also be relevant. Consequently, our study has been focused on the radiative corrections to the lightest MSSM $\mathcal{CP}$-even h boson mass, M_h, due to the one-loop contributions from the neutrino/sneutrino sector within the MSSM-seesaw framework.

In the following we briefly review the main relevant aspects of the calculation of the mass corrections and the numerical results. Further details can be found in [4], where also an extensive list with references to previous works can be found.

2 The MSSM-seesaw model

The MSSM-seesaw model with one neutrino/sneutrino generation is described in terms of the well known MSSM superpotential plus the new relevant terms given as:

$$W = \epsilon_{ij} \left[Y_\nu \hat{H}_2^i \hat{L}^j \hat{N} - Y_l \hat{H}_1^i \hat{L}^j \hat{R} \right] + \frac{1}{2} \hat{N} m_M \hat{N} , \tag{1}$$

where $\hat{N} = (\tilde{\nu}_R^*, (\nu_R)^c)$ is the additional superfield that contains the right-handed neutrino ν_R and its scalar partner $\tilde{\nu}_R$.

There are also new relevant terms in the soft SUSY breaking potential:

$$V_{\rm soft}^{\tilde{\nu}} = m_{\tilde{L}}^2 \tilde{\nu}_L^* \tilde{\nu}_L + m_{\tilde{R}}^2 \tilde{\nu}_R^* \tilde{\nu}_R + (Y_\nu A_\nu H_2^2 \tilde{\nu}_L \tilde{\nu}_R^* + m_M B_\nu \tilde{\nu}_R \tilde{\nu}_R + \text{h.c.}) \ . \tag{2}$$

After electro-weak (EW) symmetry breaking, the charged lepton and Dirac neutrino masses can be written as

$$m_l \ = \ Y_l \ v_1 \, , \qquad m_D \ = \ Y_\nu \, v_2 \, , \tag{3}$$

where v_i are the vacuum expectation values (VEVs) of the neutral Higgs scalars, with $v_{1(2)} = v \cos(\sin)\beta$ and $v \simeq 174$ GeV.

The 2×2 neutrino mass matrix is given in terms of m_D and m_M by:

$$M^\nu \ = \ \begin{pmatrix} 0 & m_D \\ m_D & m_M \end{pmatrix} . \tag{4}$$

Diagonalization of M^ν leads to two mass eigenstates, which are Majorana fermions with the respective mass eigenvalues given by:

$$m_{\nu,\, N} = \frac{1}{2} \left(m_M \mp \sqrt{m_M^2 + 4 m_D^2} \right) \ . \tag{5}$$

In the seesaw limit, i.e. when $\xi \equiv \frac{m_D}{m_M} \ll 1$, one finds,

$$m_\nu = -m_D \xi + \mathcal{O}(m_D \xi^3) \simeq -\frac{m_D^2}{m_M} \ , \qquad m_N = m_M + \mathcal{O}(m_D \xi) \simeq m_M \ . \tag{6}$$

Regarding the sneutrino sector, the sneutrino mass matrices for the $\mathcal{CP}$-even, $\tilde{M}_+$, and the $\mathcal{CP}$-odd, $\tilde{M}_-$, subsectors are given respectively by

$$\tilde{M}_\pm^2 = \begin{pmatrix} m_{\tilde{L}}^2 + m_D^2 + \frac{1}{2} M_Z^2 \cos 2\beta & m_D (A_\nu - \mu \cot\beta \pm m_M) \\ m_D (A_\nu - \mu \cot\beta \pm m_M) & m_{\tilde{R}}^2 + m_D^2 + m_M^2 \pm 2 B_\nu m_M \end{pmatrix} . \tag{7}$$

The diagonalization of these two matrices, $\tilde{M}_\pm^2$, leads to four sneutrino mass eigenstates. In the seesaw limit, where m_M is much bigger than all the other scales the corresponding sneutrino masses are given by:

$$\begin{aligned} m^2_{\tilde{\nu}_+, \tilde{\nu}_-} &= m_{\tilde{L}}^2 + \frac{1}{2} M_Z^2 \cos 2\beta \mp 2 m_D (A_\nu - \mu \cot\beta - B_\nu) \xi \ , \\ m^2_{\tilde{N}_+, \tilde{N}_-} &= m_M^2 \pm 2 B_\nu m_M + m_{\tilde{R}}^2 + 2 m_D^2 \ . \end{aligned} \tag{8}$$

Finally, in the interaction Lagrangian that is relevant for the present work, there are terms already present in the MSSM: the pure gauge interactions between the left-handed neutrinos and the Z boson, those between the 'left-handed' sneutrinos and the Higgs bosons, and those between the 'left-handed' sneutrinos and the Z bosons. In addition, in this MSSM-seesaw scenario, there are interactions driven by the neutrino Yukawa couplings (or equivalently m_D since $Y_\nu = (g m_D)/(\sqrt{2} M_W \sin\beta)$), as for instance $g_{h \nu_L \nu_R} = -\frac{i g m_D \cos\alpha}{2 M_W \sin\beta}$, and new interactions due to the Majorana nature driven by m_M, which are not present in the case of Dirac fermions, as for instance $g_{h \tilde{\nu}_L \tilde{\nu}_R} = -\frac{i g m_D m_M \cos\alpha}{2 M_W \sin\beta}$. Besides, the Higgs boson sector in the MSSM-seesaw model is as in the MSSM.

3 Calculation

In the Feynman diagrammatic (FD) approach the higher-order corrected $\mathcal{CP}$-even Higgs boson masses in the MSSM, denoted here as M_h and M_H, are derived by finding the poles of the (h, H)-propagator matrix, which is equivalent to solving the following equation [1]:

$$\left[p^2 - m_h^2 + \hat{\Sigma}_{hh}(p^2) \right] \left[p^2 - m_H^2 + \hat{\Sigma}_{HH}(p^2) \right] - \left[\hat{\Sigma}_{hH}(p^2) \right]^2 = 0 \ , \tag{9}$$

where $m_{h,H}$ are the tree level masses. The one loop renormalized self-energies, $\hat{\Sigma}_{\phi\phi}(p^2)$, in (9) can be expressed in terms of the bare self-energies, $\Sigma_{\phi\phi}(p^2)$, the field renormalization constants $\delta Z_{\phi\phi}$ and the mass counter terms δm^2_ϕ, where ϕ stands for h, H. For example, the lightest Higgs boson renormalized self energy reads:

$$\hat{\Sigma}_{hh}(p^2) = \Sigma_{hh}(p^2) + \delta Z_{hh}(p^2 - m_h^2) - \delta m_h^2 \ . \tag{10}$$

Regarding the renormalization prescription, we have used an on-shell renormalization scheme for M_Z, M_W and M_A mass counterterms and T_h, T_H tadpole counterterms. On the other hand, we have used a modified $\overline{\rm DR}$ scheme $\left(\text{m}\overline{\rm DR}\right)$ for the renormalization of the wave function and $\tan\beta$. The $\text{m}\overline{\rm DR}$ scheme is very similar to the well known $\overline{\rm DR}$ scheme but instead of subtracting the usual term proportional to $\Delta = \frac{2}{\epsilon} - \gamma_E + \log(4\pi)$ one subtracts the term proportional to $\Delta_m = \Delta - \log(m_M^2/\mu^2_{\overline{\rm DR}})$, hence, avoiding large logarithms of the large scale m_M. As studied in other works [5], this scheme minimizes higher order corrections when two very different scales are involved in a calculation of radiative corrections.

The full one-loop $\nu/\tilde{\nu}$ corrections to the self-energies, $\hat{\Sigma}^{\nu/\tilde{\nu}}_{hh}$, $\hat{\Sigma}^{\nu/\tilde{\nu}}_{HH}$ and $\hat{\Sigma}^{\nu/\tilde{\nu}}_{hH}$, entering (9) have been evaluated with *FeynArts* and *FormCalc* [6]. The new Feynman rules for the $\nu/\tilde{\nu}$ sector are inserted into a new model file. Since we are interested in exploring the relevance of the new radiative corrections to M_h from the neutrino/sneutrino sector, we will present here our results in terms of the mass difference with respect to the MSSM prediction. Consequently, we define,

$$\Delta m_h^{\text{m}\overline{\rm DR}} := M_h^{\nu/\tilde{\nu}} - M_h, \tag{11}$$

where $M_h^{\nu/\tilde{\nu}}$ denotes the pole for the light Higgs mass including the $\nu/\tilde{\nu}$ corrections (i.e. in the MSSM-seesaw model), and M_h the corresponding pole in the MSSM, i.e without the $\nu/\tilde{\nu}$ corrections. Thus, for a given set of input parameters we first calculate M_h in the MSSM with the help of `FeynHiggs` [7], such that all relevant known higher-order corrections are included. Then we add the new contributions from the neutrino/sneutrino sector and eventually compute $\Delta m_h^{\text{m}\overline{\rm DR}}$.

4 Results

We have obtained the full analytical results for the renormalized Higgs boson self-energies and their expressions in the seesaw limit. In order to understand in simple terms the analytical behavior of our full numerical results we have expanded the renormalized self-energies in powers of the seesaw parameter $\xi = m_D/m_M$:

$$\hat{\Sigma}(p^2) = \left(\hat{\Sigma}(p^2)\right)_{m_D^0} + \left(\hat{\Sigma}(p^2)\right)_{m_D^2} + \left(\hat{\Sigma}(p^2)\right)_{m_D^4} + \dots \ . \tag{12}$$

The zeroth order of this expansion is precisely the pure gauge contribution and it does not depend on m_D or m_M. Therefore, it corresponds to the result in the MSSM. The rest of the terms of the expansion are the Yukawa contribution. The leading term of this Yukawa contribution is the $\mathcal{O}(m_D^2)$ term, because it is the only one not suppressed by the Majorana scale. In fact it goes as $Y_\nu^2 M^2_{\rm EW}$, where $M^2_{\rm EW}$ denotes generically the electroweak scales involved, concretely, p^2, M_Z^2 and M_A^2. In particular, the $\mathcal{O}(p^2 m_D^2)$ terms of the renormalized self-energy, which turn out to be the most relevant leading contributions, separated into the neutrino and sneutrino contributions, read:

$\hat{\Sigma}^{\text{m}\overline{\rm DR}}_{hh}\Big|_{m_D^2 p^2} \sim$ 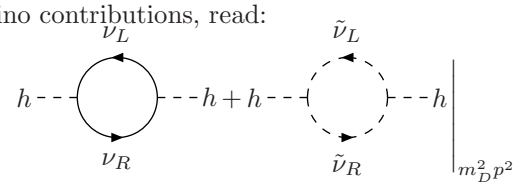

$\Big|_{m_D^2 p^2} \sim \dfrac{g^2 p^2 m_D^2 c_\alpha^2}{64\pi^2 M_W^2 s_\beta^2} + \dfrac{g^2 p^2 m_D^2 c_\alpha^2}{64\pi^2 M_W^2 s_\beta^2}.$ (13)

Notice that the above neutrino contributions come from the Yukawa interaction $g_{h\nu_L\nu_R}$, which is extremely suppressed in the Dirac case but can be large in the Majorana case. The sneutrino contributions come from the new couplings $g_{h\tilde{\nu}_L\tilde{\nu}_R}$, which are not present in the Dirac case. It is also interesting to remark that these terms, being $\sim p^2$, depend on the external momentum. Therefore, at large m_M, to keep just the Yukawa part is a good approximation, but to neglect the momentum dependence or to set the external momentum to zero are certainly not. In consequence, the effective potential method will not provide a realistic result

for the radiative corrections to the Higgs mass. Similarly, obtaining the leading logarithmic terms in a RGE computation, would also miss these finite terms.

The behaviour of the renormalized self-energy with all others parameters entering in the computation have been discussed in [4]. According to our detailed analysis in this paper, the most relevant parameters for our purposes are: m_M (or, equivalently, the heaviest physical Majorana neutrino mass m_N), m_ν and the soft SUSY breaking parameters $m_{\tilde{R}}$ and B_ν. In the literature it is often assumed that m_M has a very large value, $m_M \sim \mathcal{O}(10^{14-15})$ GeV, in order to get $|m_\nu| \sim 0.1$ - 1 eV with large Yukawa couplings $Y_\nu \sim \mathcal{O}(1)$. This is an interesting possibility since it can lead to important phenomenological implications due to the large size of the radiative corrections driven by these large Y_ν. We have explored, however, not only these extreme values but the full range for m_M: $\sim 10^2 - 10^{15}$ GeV.

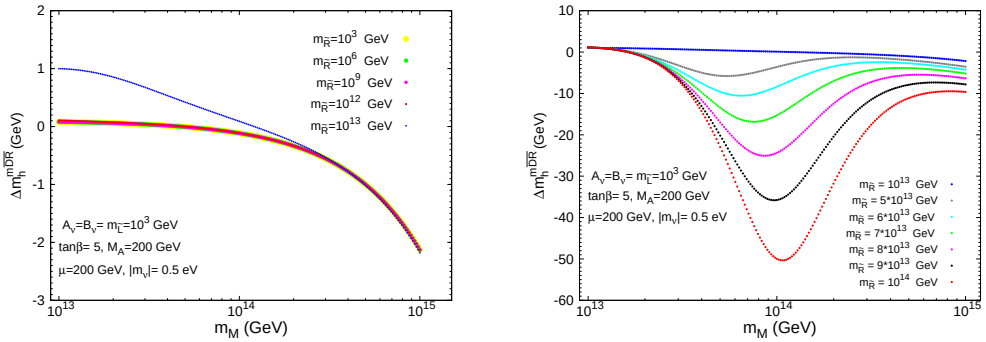

Figure 1: One-loop corrections to M_h from the neutrino/sneutrino sector as a function of m_M for: $m_{\tilde{R}} < 10^{13}$ GeV (left panel) and 10^{13} GeV $< m_{\tilde{R}} < 10^{14}$ GeV (right panel).

Fig. 1 shows the predictions for $\Delta m_h^{\overline{\rm mDR}}$ as a function of m_M, for several input $m_{\tilde{R}}$ values. The Higgs mass corrections are positive and below 0.1 GeV if $m_M \lesssim 5 \times 10^{13}$ GeV and $m_{\tilde{R}} < 10^{12}$ GeV (left panel). For larger Majorana mass values, the corrections get negative and grow up to a few GeV; $\Delta m_h^{\overline{\rm mDR}} = -2.15$ GeV for $m_M = 10^{15}$ GeV. The results in the right plot show that for larger values of the soft mass, $m_{\tilde{R}} \gtrsim 10^{13}$ GeV, the Higgs mass corrections are negative and can be sizeable, a few tens of GeV, reaching their maximum values at $m_{\tilde{R}} \simeq m_M$.

The results of the Higgs mass corrections in terms of the two relevant physical Majorana neutrino masses, light $|m_\nu|$ and heavy m_N, are summarized in the left plot of Fig. 2. For values of $m_N < 3 \times 10^{13}$ GeV and $|m_\nu| < 0.1 - 0.3$ eV the corrections to M_h are positive and smaller than 0.1 GeV. In this region, the gauge contribution dominates. In fact, the wider black contour line with fixed $\Delta m_h^{\overline{\rm mDR}} = 0.09$ coincides with the prediction for the case where just the gauge part in the self-energies have been included. This means that 'the distance' of any other contour-line respect to this one represents the difference in the radiative corrections respect to the MSSM prediction. For larger values of m_N and/or $|m_\nu|$ the Yukawa part dominates, and the radiative corrections become negative and larger in absolute value, up to about -5 GeV in the right upper corner of this figure. These corrections grow in modulus proportionally to m_M and m_ν, due to the fact that the seesaw mechanism impose a relation between the three masses involved, $m_D^2 = |m_\nu| m_N$.

Finally, we present in the right plot of Fig. 2 the contour-lines for fixed $\Delta m_h^{\overline{\rm mDR}}$ in the less conservative case where $m_{\tilde{R}}$ is close to m_M. These are displayed as a function of $|m_\nu|$ and the ratio $m_{\tilde{R}}/m_M$. m_M is fixed to 10^{14} GeV. For the interval studied here, we see again that the radiative corrections can be negative and as large as tens of GeV in the upper right corner of the plot. For instance, $\Delta m_h^{\overline{\rm mDR}} = -30$ GeV for $|m_\nu| = 0.6$ eV and $m_{\tilde{R}}/m_M = 0.7$.

To summarize: for some regions of the MSSM-seesaw parameter space, the corrections to M_h are of the order of several GeV. For all soft SUSY-breaking parameters at the TeV scale we find correction of up to -5 GeV to M_h. These corrections are substantially larger than the anticipated ILC precision of about

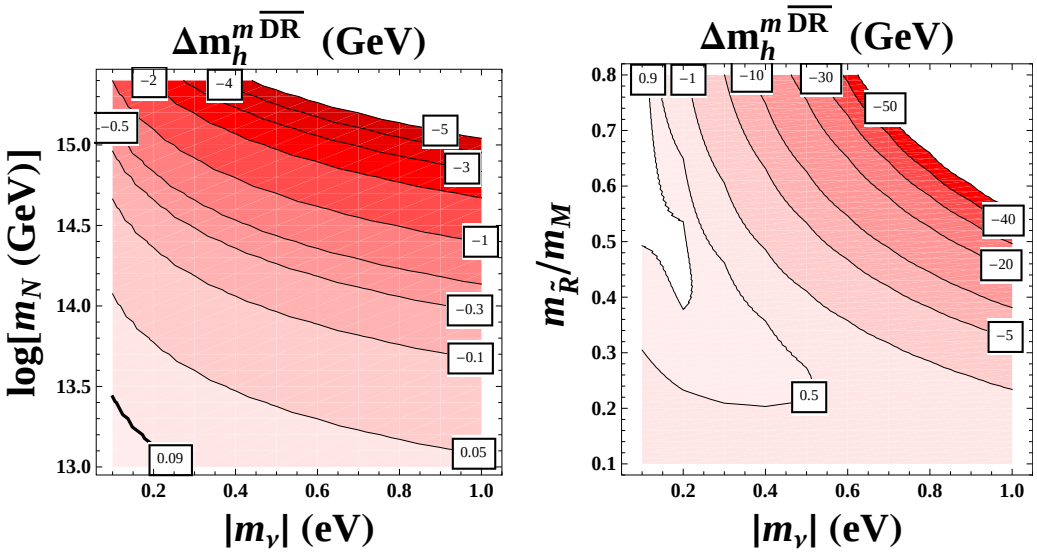

Figure 2: Contour-lines for the Higgs mass corrections from the $\nu/\tilde{\nu}$ sector as a function of: $|m_\nu|$ and m_N (left panel) and the ratio $m_{\tilde{R}}/m_M$ and $|m_\nu|$ (right panel). The other parameters are: $A_\nu = B_\nu = m_{\tilde{L}} = m_{\tilde{R}} = 10^3$ GeV, $\tan\beta = 5, M_A = 200$ GeV, $\mu = 200$ GeV.

50 MeV (and also larger than the anticipated LHC precision of ~ 200 MeV). Consequently, they should be included in any phenomenological analysis of the Higgs sector in the MSSM-seesaw.

References

[1] M. Frank, T. Hahn, S. Heinemeyer, W. Hollik, H. Rzehak and G. Weiglein, *JHEP* **0702** (2007) 047 [arXiv:0611326 [hep-ph]].

[2] P. Minkowski, *Phys. Lett.* **B 67** (1977) 421;

[3] F. Borzumati and A. Masiero, *Phys. Rev. Lett.* **57** (1986) 961;
M. Raidal *et al.*, Eur. Phys. J. C **57**, 13 (2008) [arXiv:0801.1826 [hep-ph]].

[4] S. Heinemeyer, M. J. Herrero, S. Penaranda and A. M. Rodriguez-Sanchez, JHEP **1105** (2011) 063 [arXiv:1007.5512 [hep-ph]].

[5] J. Collins, F. Wilczek and A. Zee, *Phys. Rev.* **D 18** (1978) 242.

[6] J. Küblbeck, M. Böhm and A. Denner, *Comput. Phys. Commun.* **60** (1990) 165;
T. Hahn, *Comput. Phys. Commun.* **140** (2001) 418 [arXiv:hep-ph/0012260];
T. Hahn and C. Schappacher, *Comput. Phys. Commun.* **143** (2002) 54 [arXiv:hep-ph/0105349];
T. Hahn and M. Pérez-Victoria, *Comput. Phys. Commun.* **118** (1999) 153 [arXiv:hep-ph/9807565].

[7] S. Heinemeyer, W. Hollik and G. Weiglein, *Comput. Phys. Commun.* **124** (2000) 76 [arXiv:hep-ph/9812320];
T. Hahn, S. Heinemeyer, W. Hollik, H. Rzehak and G. Weiglein, *Comput. Phys. Commun.* **180** (2009) 1426;
see: `www.feynhiggs.de` .

The Higgs sector of the NMFV MSSM at the ILC

M. Arana-Catania[1], S. Heinemeyer[2], M.J. Herrero[1] and S. Peñaranda[3,4] *†

1- Departamento de Física Teórica and Instituto de Física Teórica, IFT-UAM/CSIC
Universidad Autónoma de Madrid, Cantoblanco, Madrid - Spain

2- Instituto de Física de Cantabria (CSIC-UC), Santander - Spain

3- Departamento de Física Teórica, Universidad de Zaragoza, Spain

4- Departament de Física Fonamental, Universitat de Barcelona, Spain

We calculate the one-loop corrections to the Higgs boson masses within the context of the MSSM with Non-Minimal Flavor Violation in the squark sector. We take into account all the relevant restrictions from BR($B \to X_s\gamma$), BR($B_s \to \mu^+\mu^-$) and ΔM_{B_s}. We find sizable corrections to the lightest Higgs boson mass that are considerably larger than the expected ILC precision for acceptable values of the mixing parameters δ_{ij}^{XY}. We find δ_{ct}^{LR} and δ_{ct}^{RL} specially relevant, mainly at low $\tan\beta$.

1 Introduction

We review the one-loop corrections to the Higgs boson masses in the MSSM with Non-Minimal Flavor Violation (NMFV) [1]. The flavor violation is generated from the hypothesis of general flavor mixing in the squark mass matrices, parameterized by a complete set of δ_{ij}^{XY} ($X, Y = L, R$; $i, j = t, c, u$ or b, s, d). The corrections to the Higgs masses are calculated in terms of these δ_{ij}^{XY} taking into account all relevant restrictions from B-physics data. In particular the present constraints from BR($B \to X_s\gamma$), BR($B_s \to \mu^+\mu^-$) and ΔM_{B_s} are demanded to be fulfilled and our predictions are also compared within NMFV scenarios with the SM predictions. For completeness, we include below the present experimental data [2], and the predictions within the SM [3]:

$$\mathrm{BR}(B \to X_s\gamma)_{\rm exp} = (3.55 \pm 0.26) \times 10^{-4} \quad ; \quad \mathrm{BR}(B \to X_s\gamma)_{\rm SM} = (3.15 \pm 0.23) \times 10^{-4} \tag{1}$$

$$\mathrm{BR}(B_s \to \mu^+\mu^-)_{\rm exp} < 1.1 \times 10^{-8} \ \ (95\%\ \mathrm{CL}); \mathrm{BR}(B_s \to \mu^+\mu^-)_{\rm SM} = (3.6 \pm 0.4) \times 10^{-9} \tag{2}$$

$$\Delta M_{B_s\,\rm exp} = (117.0 \pm 0.8) \times 10^{-10}\ \mathrm{MeV} \quad ; \quad \Delta M_{B_s\,\rm SM} = (117.1^{+17.2}_{-16.4}) \times 10^{-10}\ \mathrm{MeV}\ . \tag{3}$$

Here we focus on the analysis of the Higgs mass corrections that are originated from the flavor mixing between the second and third generations which is the relevant one in B physics and devote special attention to the LR/RL sector. These kind of mixing effects are expected to be sizable, since they enter the off-diagonal A parameters, which appear directly in the coupling of the Higgs bosons to scalar quarks.

In the following we briefly review the main relevant aspects of the calculation and present the numerical results focusing on the light Higgs boson. For further details we address the reader to the full version of our work [1], where also an extensive list with references to related works can be found.

2 SUSY scenarios with Non-Minimal Flavor Violation

The usual procedure to introduce general flavor mixing in the squark sector is to include the non-diagonality in flavor space in the Super-CKM basis. These squark flavor mixings are usually described in terms of a

*Preprint number: IFT-UAM/CSIC-12-10
†Talk given by M. Arana-Catania at LCWS11

set of dimensionless parameters δ_{ij}^{XY} $(X,Y = L,R;\ i,j = t,c,u \text{ or } b,s,d)$, introduced in the SUSY-breaking matrices (after RGE running) at low energy as follows,

$$m^2_{\tilde{U}_L} = \begin{pmatrix} m^2_{\tilde{U}_{L11}} & 0 & 0 \\ 0 & m^2_{\tilde{U}_{L22}} & \delta^{LL}_{23} m_{\tilde{U}_{L22}} m_{\tilde{U}_{L33}} \\ 0 & \delta^{LL}_{23} m_{\tilde{U}_{L22}} m_{\tilde{U}_{L33}} & m^2_{\tilde{U}_{L33}} \end{pmatrix}; m^2_{\tilde{D}_L} = V^\dagger_{\rm CKM} m^2_{\tilde{U}_L} V_{\rm CKM} \tag{4}$$

$$v_2 \mathcal{A}^u = \begin{pmatrix} 0 & 0 & 0 \\ 0 & 0 & \delta^{LR}_{ct} m_{\tilde{U}_{L22}} m_{\tilde{U}_{R33}} \\ 0 & \delta^{RL}_{ct} m_{\tilde{U}_{R22}} m_{\tilde{U}_{L33}} & m_t A_t \end{pmatrix} \tag{5}$$

$$m^2_{\tilde{U}_R} = \begin{pmatrix} m^2_{\tilde{U}_{R11}} & 0 & 0 \\ 0 & m^2_{\tilde{U}_{R22}} & \delta^{RR}_{ct} m_{\tilde{U}_{R22}} m_{\tilde{U}_{R33}} \\ 0 & \delta^{RR}_{ct} m_{\tilde{U}_{R22}} m_{\tilde{U}_{R33}} & m^2_{\tilde{U}_{R33}} \end{pmatrix} \tag{6}$$

and analogously for $v_1 \mathcal{A}^d$ and $m^2_{\tilde{D}_R}$, changing the up-type indexes to the down-type ones in $v_2 \mathcal{A}^u$ and $m^2_{\tilde{U}_R}$, correspondingly. The flavor diagonal entries in these matrices at low energy are found here as usual, namely after RGE running and assuming universality conditions for the soft parameters at the GUT scale (i.e. within constrained models).

In the present study we will restrict ourselves to the case where there is flavor mixing exclusively between the second and third squark generation. These mixings are known to produce the largest flavor violation effects in B meson physics since their size are usually governed by the third generation quark masses. On the other hand, and in order to reduce further the number of independent parameters, we will focus in the following analysis on constrained SUSY scenarios, where the soft mass parameters fulfill universality hypothesis at the gauge unification (GUT) scale. Concretely, we will restrict ourselves here to the so-called Constrained MSSM (CMSSM) which is defined by $m_0, m_{1/2}, A_0, \text{sign}(\mu), \tan\beta$, where A_0 is the universal trilinear coupling, m_0 and $m_{1/2}$ are the universal scalar mass and gaugino mass, respectively, at the GUT scale, sign(μ) is the sign of the μ parameter and $\tan\beta = v_2/v_1$.

For the following numerical estimates we will chose two particular points in the CMSSM that are examples of scenarios with moderate and very heavy sparticles masses, respectively. Firstly, we set the well-known benchmark point SPS2, with $m_0 = 1450$ GeV, $m_{1/2} = 300$ GeV, $A_0 = 0$, sign(μ) > 0, $\tan\beta = 10$. Secondly, we study a peculiar scenario, nowadays favored by LHC recent data, where the SUSY particles are rather heavy, at the TeV scale, but still the Higgs particle is light. We name this scenario as VHeavyS, defined by $m_0 = m_{1/2} = -A_0 = 800$ GeV, sign(μ) > 0, $\tan\beta = 5$ and where $m_h^{\rm MSSM} = 120$GeV. The corresponding analysis for other points in the CMSSM and other scenarios as the Non Universal Higgs Mass case can be found in [1].

3 Results

In this section we review our numerical results for the radiative corrections to the Higgs boson mass m_h from flavor mixing within NMFV-SUSY scenarios. Since all one-loop corrections in the present NMFV scenario are common to the MSSM except for the corrections from squarks, which depend on the δ_{ij}^{XY} values, we will focus just on the results of these corrections as a function of the flavor mixing parameters, and present the differences with respect to the predictions within the MSSM. Correspondingly, we define:

$$\Delta m_h(\delta_{ij}^{XY}) \equiv m_h^{\rm NMFV}(\delta_{ij}^{XY}) - m_h^{\rm MSSM} \tag{7}$$

where $m_h^{\rm NMFV}(\delta_{ij}^{XY})$ and $m_h^{\rm MSSM}$ have been calculated at the one-loop level. It should be noted that $m_h^{\rm NMFV}(\delta_{ij}^{XY} = 0) = m_h^{\rm MSSM}$ and, therefore, by construction, $\Delta m_h(\delta_{ij}^{XY} = 0) = 0$, and Δm_h gives the size of the one-loop NMFV contributions to m_h. The numerical calculation of $m_h^{\rm NMFV}(\delta_{ij}^{XY})$ and $m_h^{\rm MSSM}$ has been done with `FeynHiggs` [4]. The numerical calculations of the rates for the B observables have been done with the FORTRAN subroutine BPHYSICS included in the SuFla code [5], which we have conveniently modified as to include all the relevant contributions within NMFV scenarios (for more details see [1]).

In Fig.1 we show the numerical results for Δm_h as a function of the various δ_{ij}^{XY}. We have also included our predictions for BR($B \to X_s\gamma$), BR($B_s \to \mu^+\mu^-$) and $\Delta M_{B_s}$and their corresponding experimental allowed areas.

In order to conclude on the allowed delta intervals by B physics data, we have assumed that our predictions of the B observables within SUSY-NMFV scenarios have a somewhat larger theoretical error than the SM prediction. Then, by adding linearly the experimental uncertainty (that we take as $3\sigma_{\rm exp}$) and the theoretical uncertainty, a given δ_{ij}^{XY} value is considered by us to be allowed by data if the total predicted ratios lie in the following intervals:

$$2.08 \times 10^{-4} < {\rm BR}(B \to X_s\gamma) < 5.02 \times 10^{-4}, \tag{8}$$

$${\rm BR}(B_s \to \mu^+\mu^-) < 1.22 \times 10^{-8}, \tag{9}$$

$$63 \times 10^{-10} < \Delta M_{B_s}({\rm MeV}) < 168.6 \times 10^{-10}. \tag{10}$$

In table **??** we summarize the total allowed delta intervals by BR($B \to X_s\gamma$), BR($B_s \to \mu^+\mu^-$) and ΔM_{B_s} for SPS2. Notice that for δ_{sb}^{RR} there are two very narrow allowed region close to ± 1, which indeed for SPS2 reduce just to the two single allowed values ± 0.99.

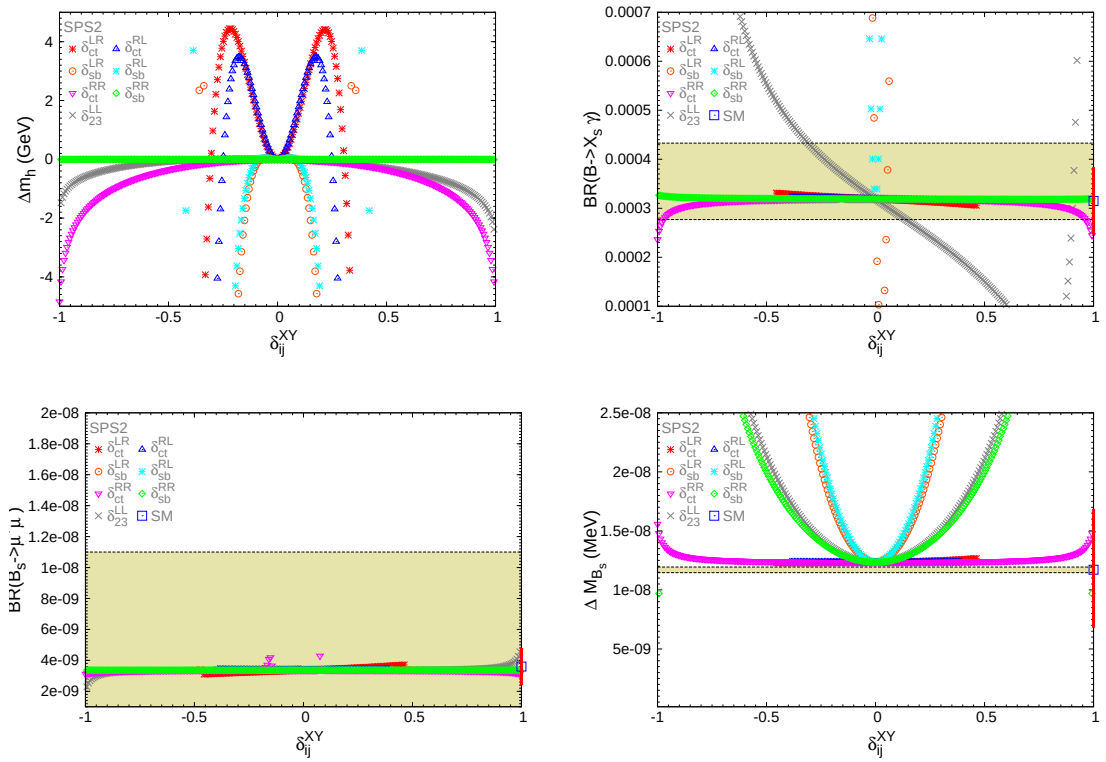

Figure 1: Sensitivity to the NMFV deltas for the SPS2 point for different observables: Δm_h (left upper panel), BR($B \to X_s\gamma$) (right upper panel), BR($B_s \to \mu^+\mu^-$) (left bottom panel), ΔM_{B_s}(right bottom panel). The experimental allowed areas in the plot for B physics observables ($3\sigma_{\rm exp}$ for BR($B \to X_s\gamma$) and ΔM_{B_s}, 95% CL bound for BR($B_s \to \mu^+\mu^-$)) are the horizontal colored bands. The SM prediction for the B physics observables and the theory uncertainty (red bar) is displayed on the right axis, correspondingly.

As we can see in Fig.1, the most restrictive observables are BR($B \to X_s\gamma$) and ΔM_{B_s}, leading to the total allowed delta intervals summarized in table **??**. The main conclusion from this table is that the NMFV deltas in the top-sector can be sizeable $|\delta_{ct}^{XY}|$, larger than $\mathcal{O}(0.1)$ and still compatible with B physics data. In particular δ_{ct}^{RR} is the less constrained parameter. The parameters on the bottom-sector are, in contrast,

SPS2	Total allowed intervals
δ_{23}^{LL}	(-0.37:0.34)
δ_{ct}^{LR}	(-0.46:0.46)
δ_{sb}^{LR}	(-0.0069:0) (0.048:0.055)
δ_{ct}^{RL}	(-0.39:0.39)
δ_{sb}^{RL}	(-0.014:0.014)
δ_{ct}^{RR}	(-1.0:0.99)
δ_{sb}^{RR}	(-0.99) (-0.39:0.39) (0.99)

quite constrained. The most tightly constrained are clearly δ_{sb}^{LR} and δ_{sb}^{RL}. Similar conclusions are found for other CMSSM points studied in [1].

Regarding the size of the mass corrections, Δm_h, we clearly see in this figure that they can be sizable for non-vanishing deltas in the allowed intervals by B physics data. In particular for δ_{ct}^{LR} and δ_{ct}^{RL} they can be positive and up to about 4 GeV or negative and up to tens of GeV. δ_{ct}^{RR} yields negative corrections and up to about 4 GeV.

In order to explore further the size of the Higgs mass corrections, we have computed numerically the size of Δm_h as a function of two non-vanishing deltas and have looked for areas in these two dimensional plots that are allowed by B physics data (see Fig.3 for the color code of the allowed/disallowed areas). The results for VHeavyS are displayed in Fig.2. Contour lines corresponding to mass corrections Δm_h above 60 GeV or below -60 GeV have not been represented.

As we can see, the largest mass corrections Δm_h found, being allowed by B physics data occur in the $(\delta_{23}^{LL}, \delta_{ct}^{LR})$ and $(\delta_{23}^{LL}, \delta_{ct}^{RL})$ planes. This applies also to the other points studied in [1]. They can be as large as -60 GeV for δ_{ct}^{LR} or δ_{ct}^{RL} close to ± 0.3. Again these large corrections from the LR and RL parameters are due to the A-terms. Generically, the plots with largest allowed regions and with largest Higgs mass corrections correspond to scenarios with low $\tan\beta = 5$ and heavy spectra like the VHeavyS point considered here.

There are also important corrections in the allowed areas of the two dimensional plots of $(\delta_{23}^{LL}, \delta_{ct}^{RR})$ for some of the studied points, particularly for SPS5 (and to a lesser extent for SPS2). For the first the corrections can be as large as -50 GeV for δ_{ct}^{RR} close to ± 0.5. In the case of SPS2 they can be up to -2 GeV for this same region.

Regarding the plots involving the down-type squark sector deltas it is clear that the constraints from B physics data are so tighted that the Higgs mass corrections found are very tiny.

4 Conclusions

We have reviewed the analysis of the one-loop corrections to the Higgs boson masses in the MSSM with Non-Minimal Flavor Violation, assuming that the flavor violation is being generated from the hypothesis of general flavor mixing in the squark mass matrices. Here we have focused on the analysis of the light Higgs mass corrections that are originated from the flavor mixing between the second and third generations, and that are compatible with the constraints from BR($B \to X_s\gamma$), BR($B_s \to \mu^+\mu^-$) and ΔM_{B_s} data.

We found large corrections, mainly for the low $\tan\beta$ case, up to several tens of GeV for m_h. These corrections are specially relevant in the case of the light MSSM Higgs boson since they can be negative and up to three orders of magnitude larger than the anticipated ILC precision of 50 MeV [6]. Consequently, these corrections should be taken into account in any Higgs boson analysis in the NMFV MSSM framework. Conversely, in the case of a Higgs boson mass measurement these corrections might be used to set further constraints on δ_{ij}^{XY}. The present work clearly indicates that the flavor mixing parameters δ_{ct}^{LR} and δ_{ct}^{RL} are severely constrained by the present bounds on the lightest Higgs boson mass within the NMFV-MSSM scenarios.

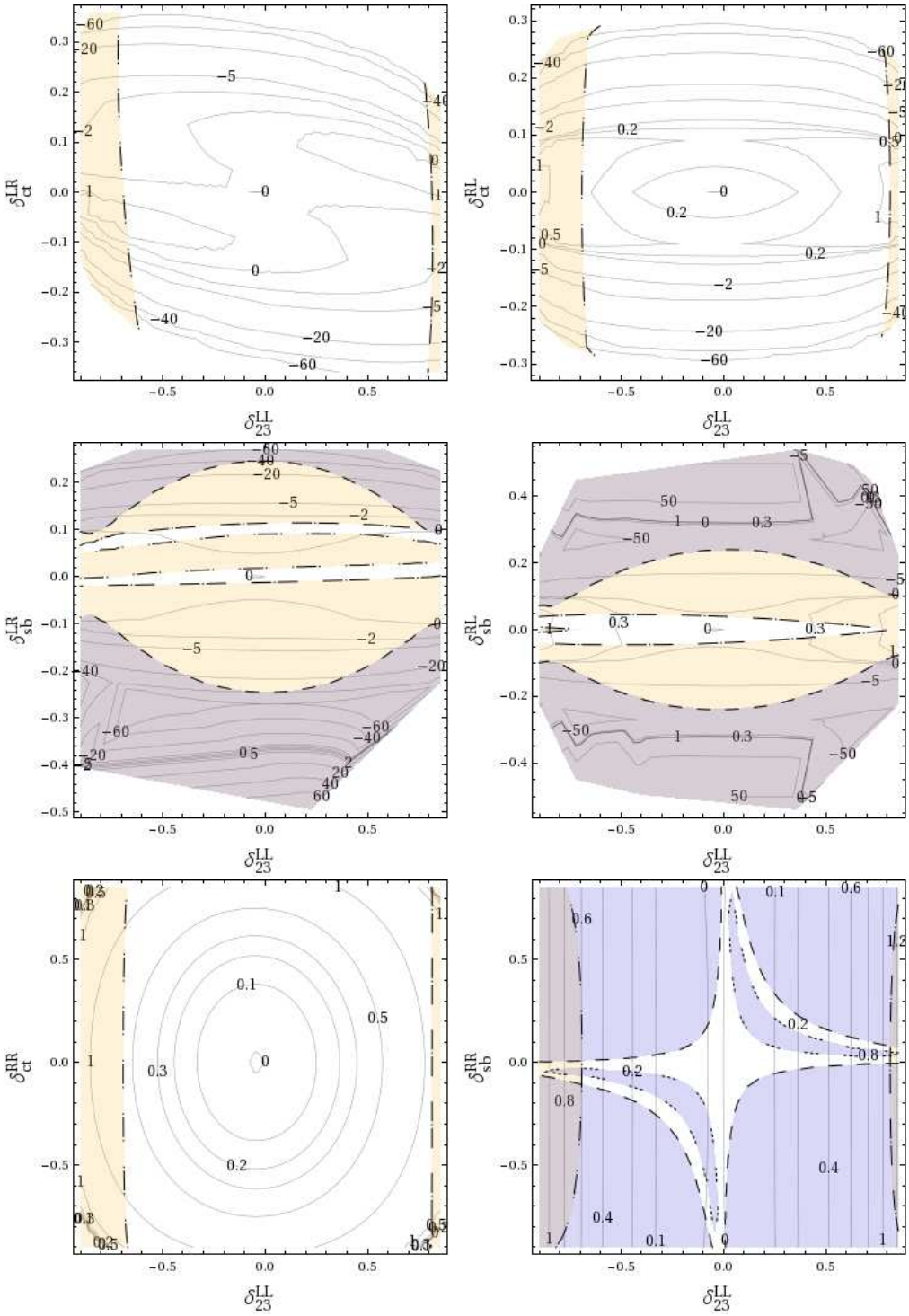

Figure 2: Δm_h (GeV) contour lines from our two deltas analysis for VHeavyS. The color code for the allowed/disallowed areas by B physics data is given in fig.3

Acknowledgments

M. Arana-Catania thanks the organizers of the LCWS11 workshop for the kind invitation to present this talk and for this fruitful and enjoyable meeting at Granada.

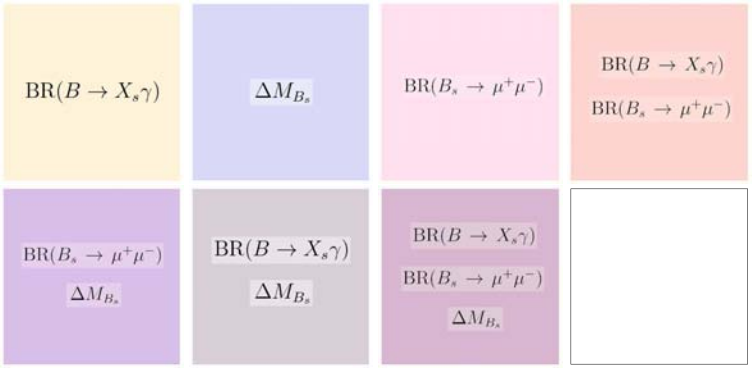

Figure 3: Legend of plots for Fig. 2. Each colored area represents the disallowed region by the specified observable/s inside each box. A white central area represents a region that is allowed by all B physics data

References

[1] M. Arana-Catania, S. Heinemeyer, M. J. Herrero and S. Penaranda, JHEP **1205** (2012) 015 [arXiv:1109.6232 [hep-ph]].

[2] D. Asner *et al.* [Heavy Flavor Averaging Group], `http://www.slac.stanford.edu/xorg/hfag/`, arXiv:1010.1589 [hep-ex].
CMS and LHCb Collaborations, `http://cdsweb.cern.ch/record/1374913/files/BPH-11-019-pas.pdf`.
K. Nakamura *et al.* [Particle Data Group], J. Phys. G **37**, 075021 (2010).

[3] M. Misiak, Acta Phys. Polon. B **40**, 2987 (2009) [arXiv:0911.1651 [hep-ph]].
A. J. Buras, PoS E PS-HEP2009, 024 (2009) [arXiv:0910.1032 [hep-ph]].
A. J. Buras, M. Jamin and P. H. Weisz, Nucl. Phys. B **347**, 491 (1990).
E. Golowich, J. Hewett, S. Pakvasa, A. A. Petrov and G. K. Yeghiyan, Phys. Rev. D **83**, 114017 (2011) [arXiv:1102.0009 [hep-ph]].

[4] S. Heinemeyer, W. Hollik and G. Weiglein, *Comput. Phys. Commun.* **124** (2000) 76 [arXiv:hep-ph/9812320];
T. Hahn, S. Heinemeyer, W. Hollik, H. Rzehak and G. Weiglein, *Comput. Phys. Commun.* **180** (2009) 1426;
see `www.feynhiggs.de` .
S. Heinemeyer, W. Hollik and G. Weiglein, *Eur. Phys. J.* **C 9** (1999) 343 [arXiv:hep-ph/9812472].
G. Degrassi, S. Heinemeyer, W. Hollik, P. Slavich and G. Weiglein, *Eur. Phys. J.* **C 28** (2003) 133 [arXiv:hep-ph/0212020].
M. Frank, T. Hahn, S. Heinemeyer, W. Hollik, H. Rzehak and G. Weiglein, *JHEP* **0702** (2007) 047 [arXiv:hep-ph/0611326].

[5] G. Isidori and P. Paradisi, Phys. Lett. B **639** (2006) 499 [arXiv:hep-ph/0605012]; G. Isidori, F. Mescia, P. Paradisi and D. Temes, Phys. Rev. D **75** (2007) 115019 [arXiv:hep-ph/0703035], and references therein.

[6] J. Aguilar-Saavedra et al., TESLA TDR Part 3: "Physics at an e^+e^- Linear Collider", arXiv:hep-ph/0106315, see: `tesla.desy.de/tdr/`;
K. Ackermann et al., DESY-PROC-2004-01, *prepared for 4th ECFA / DESY Workshop on Physics and Detectors for a 90-GeV to 800-GeV Linear e+ e- Collider, Amsterdam, The Netherlands, 1-4 Apr 2003.*

Higgs-radion interpretation of the LHC Higgs hints

John F. Gunion [1]

[1] *Department of Physics, U.C. Davis, Davis CA 95616, USA*

DOI: will be assigned

Higgs-Radion interpretation of the LHC data?

We explore a Higgs-radion interpretation of the LHC Higgs-like excesses seen by ATLAS and CMS in the current data set.

1 Introduction

The two simplest ways of reconciling the weak energy scale $\mathcal{O}(1$ TeV) and the much higher GUT or reduced Planck mass scale $m_{Pl} \sim \mathcal{O}(10^{18}$ GeV) in a consistent theory are (i) to employ supersymmetry or (ii) to introduce one or more warped extra dimensions. In this contribution, I summarize the results of [1] in which we pursue the 5D version of the latter introduced by Randall and Sundrum (RS) [2], but modified in that all fields other than the Higgs reside in the bulk. Having the gauge and fermion fields in the bulk is needed to adequately suppress flavor changing neutral current (FCNC) operators and to keep corrections to precision electroweak (PEW) observables small [3, 4, 5, 6, 7, 8, 9, 10]. .

By placing the Higgs field on the TeV brane its vev can naturally be order a TeV vs m_{Pl} as a result of the RS metric "warp factor" $\Omega_0 \equiv e^{-m_0 b_0/2}$: $v_0 = \Omega_0 m_{Pl} \lesssim 1$ TeV for $m_0 b_0/2 \sim 35$. (Our notation will basically follow that of [11].) This is a great improvement compared to the original problem of accommodating both the weak and the Planck scale within a single theory.

The quantum excitations of the gravitational metric are the Kaluza-Klein (KK) modes $h^n_{\mu\nu}(x)$ (with mass m_n) and the quantum excitation associated with the distance between the two branes is the radion field $\phi_0(x)$. The vacuum expectation value of the radion field is denoted by Λ_ϕ which is related to the Planck mass by $\Lambda_\phi = \sqrt{6}\Omega_0 m_{Pl}$. To solve the hierarchy problem, Λ_ϕ should be no larger than 10 TeV, with $\Lambda_\phi \sim 1-3$ TeV preferred. In addition to the radion, the model contains a conventional Higgs boson, h_0.

The ratio m_0/m_{Pl} is a particularly crucial parameter that characterizes the 5-dimensional curvature. As discussed shortly, large curvature values $m_0/m_{Pl} \gtrsim 0.5$ are favored for fitting the LHC Higgs excesses and by bounds on FCNC and PEW constraints. In early discussions of the RS model it was argued that $R_5/M_5^2 < 1$ (M_5 being the 5D Planck scale and $R_5 = 20m_0^2$ the size of the 5D curvature) is needed to suppress higher curvature terms in the 5D action, which leads to $m_0/m_{Pl} \lesssim 0.15$ being preferred. However [10] argues that R_5/Λ^2 (with Λ being the energy scale at which the 5D gravity theory becomes strongly coupled, estimated by naive dimensional analysis to be $\Lambda \sim 2\sqrt{3}\pi M_5$) is the appropriate measure, implying that values as large as $m_0/m_{Pl} < \sqrt{3\pi^3/(5\sqrt{5})} \sim 3$ are acceptable.

Let us comment on how it is that propagation of the gauge and matter fields in the bulk can ameliorate the FCNC and PEW problems. In this case, the SM particles are the zero-modes of the 5D fields and the profile of a SM fermion in the extra dimension can be adjusted using a mass parameter. If 1st and 2nd generation fermion profiles peak near the Planck brane then FCNC operators and PEW corrections will be suppressed by scales $\gg$ TeV. Even with this arrangement it is estimated that the masses of the first KK excitations g^1, W^1 and Z^1 must be larger than about 3 TeV (see the summary in [10]). Another more direct bound on the g^1 mass comes from collider experiments. First, there is a universal component to the light quark coupling $q\bar{q}g^1$ that is roughly equal to the SM coupling g times a factor of ζ^{-1}, where $\zeta \sim \sqrt{\frac{1}{2}m_0 b_0} \sim 5-6$. The suppression is due to the fact that the light quarks are localized near the Planck brane whereas the KK gluon is localized near the TeV brane. Even with such suppression, the LHC g^1 production rate due to $u\bar{u}$ and $d\bar{d}$ collisions is large. Further, the $t_R\bar{t}_R g^1$ coupling is large since the t_R profile peaks near the TeV brane – the prediction of [12] is $g_{t_R\bar{t}_R g^1} \sim \zeta g$. As a result, the dominant decay of the

g^1 is to $t\bar{t}$. ATLAS and CMS search for $t\bar{t}$ resonances at high mass. Using $g_{q\bar{q}g^1} \sim g/5$, $q = u, d$, one finds a lower bound of $m_1^g \gtrsim 1.5$ TeV [13] using an update of the analysis of [12]. ([14] gives a weaker bound of $m_1^g > 0.84$ TeV.) .

In terms of Λ_ϕ, we have the following relations:

$$\frac{m_0}{m_{Pl}} = \frac{\sqrt{6}}{x_1^g}\frac{m_1^g}{\Lambda_\phi} \simeq \frac{m_1^g}{\Lambda_\phi}\,, \quad \text{and} \quad \frac{1}{2}m_0 b_0 = -\log\left(\frac{\Lambda_\phi}{\sqrt{6}m_{Pl}}\right) \tag{1}$$

where $x_1^g = 2.45$ is the 1st zero of an appropriate Bessel function. If the model really solves the hierarchy problem then Λ_ϕ cannot be much larger than 1 TeV and certainly $\Lambda_\phi \leq 10$ TeV. If we adopt the CMS limit of $m_1^g > 1.5$ TeV then Eq. (1) implies a lower limit on the 5-dimensional curvature of $m_0/m_{Pl} \gtrsim 0.15$. Thus, a significant lower bound on m_1^g implies that only relatively large values for m_0/m_{Pl} are allowed. As discussed above, m_0/m_{Pl} values up to $\sim 2-3$ are probably consistent with curvature corrections to the RS scenario being small. Still, tension between the lower bound on m_1^g and keeping acceptably small m_0/m_{Pl} could increase to an unacceptable point as the LHC data set increases. We will discuss the phenomenology that applies if the value of Λ_ϕ for any given (m_0/m_{Pl}) is tied to the lower bound of $m_1^g = 1.5$ TeV using Eq. (1). Alterations to the phenomenology using $m_1^g = 3$ TeV, as perhaps preferred by PEW constraints, will also be illustrated.

However, as described in [1], there are alternative approaches in which the tie between m_1^g and Λ_ϕ of Eq. (1) is not present or is very uncertain. In this case, it becomes appropriate to discuss the phenomenology that arises for fixed Λ_ϕ as m_0/m_{Pl} is varied. This will be discussed for $\Lambda_\phi = 1$ TeV and 1.5 TeV.

Since the radion and Higgs fields have the same quantum numbers, it is generically possible to introduce mixing between them. The mixing action [15] has magnitude dictated by a coefficient parameter ξ. The physical mass eigenstates, h and ϕ, are obtained by diagonalizing and canonically normalizing the kinetic (and mass) terms in the Higgs-radion Lagrangian. The diagonalization procedures and results for the h and ϕ using our notation can be found in [11] (see also [15, 16]). The resulting Feynman rules for the h and ϕ were obtained in, for example, [11] (see also [15, 16]) in the case where SM fields do not propagate in the bulk. However, as noted earlier, preventing large FCNC and PEW corrections requires that the gauge and fermion fields propagate in the bulk. The full Feynman rules after mixing for the h and ϕ interactions with gauge bosons and fermions located in the bulk were derived in [17]. These Feynman rules are summarized in our notation in [1]. There are important modifications to the anomaly induced $\gamma\gamma$ and gg couplings as well as to the WW and ZZ couplings

For the fermions, we assume profiles such that there are no corrections to the h_0 and ϕ_0 couplings due to propagation in the bulk. This is a very good approximation for the top quark quark which must be localized near the TeV brane. Also for the bottom quark the approximation is better than 20%, see [17]. Even though the approximation is not necessarily good for light quarks, it is only the heavy quarks that impact the phenomenology of the Higgs-radion system.

In fact, the LHC Higgs-like excesses provide substantial motivation for considering a Higgs-radion RS model. The reasons are as follows. First, the most prominent excesses are in the vicinity of 125 GeV. This is an "awkward" mass for both a SM Higgs boson, in that for this mass the SM cannot be valid all the way up to m_{Pl}, and for supersymmetric models, in that fine-tuning is substantial for the large squark masses needed to achieve such a high mass, especially in the minimal supersymmetric model (MSSM). Further, the LHC excesses at 125 GeV in the $\gamma\gamma$ (and perhaps also the $ZZ \to 4\ell$ channel) appear to be larger than predicted for a SM Higgs boson. If confirmed, this, of course, rules out the SM and is also rather awkward for supersymmetric models with universal or sem-universal GUT scale boundary conditions. In contrast, excesses larger than SM expectations are natural in the context of the Higgs-radion RS model. This is because of the anomalous couplings of the radion to two gluons and to two photons that can, in particular, combine to give values larger than one for the ratios

$$R_h(X) \equiv \frac{\Gamma_h(gg)\mathrm{BR}(h \to X)}{\Gamma_{h_{SM}}(gg)\mathrm{BR}(h_{SM} \to X)}\,, \quad \text{and/or} \quad R_\phi(X) \equiv \frac{\Gamma_\phi(gg)\mathrm{BR}(\phi \to X)}{\Gamma_{h_{SM}}(gg)\mathrm{BR}(h_{SM} \to X)}\,, \tag{2}$$

where numerator and denominator are computed for the same mass, for $X = \gamma\gamma$ and $X = 4\ell$ for the h and ϕ mass eigenstates. (We note that the production of the h and ϕ are dominated by $gg \to h, \phi$ at the LHC.) Finally, the CMS data shows Higgs-like excesses not only at 125 GeV, but also at other masses, most notably at ~ 120 GeV in the 4ℓ channel and at 137 GeV in the $\gamma\gamma$ channel. Obviously, this requires more

than one Higgs-like state. If confirmed, this would rule out the SM. And, supersymmetric model parameter choices with $R(X)$ values larger than one at *two* masses have not yet been found. In the Higgs-radion RS model, it is quite easy to obtain $R(X) > 1$ at two masses and even more Higgs-like excesses can in principle be accommodated by expanding the Higgs sector of the model.

We have concentrated on the situations where either just the ~ 125 GeV excesses survive (with $R(\gamma\gamma) > 1$) or, in addition, there is a 4ℓ excess at ~ 120 GeV or a $\gamma\gamma$ excess at 137 GeV. It is particularly easy to obtain an approximate fit to the $\gamma\gamma$ excess at 125 GeV alone or to the $\gamma\gamma$ excesses at both 125 GeV and 137 GeV since it is most typically the case that $R(\gamma\gamma) > R(4\ell)$ at *both* the physical Higgs and the physical radion masses. However, there is a choice of parameters in the model where Λ_ϕ and m_0/m_{Pl} can be set independently of m_1^g for which at 120 GeV there is an excess in 4ℓ but no excess in $\gamma\gamma$ while at the same time there are both $\gamma\gamma$ and 4ℓ excesses at 125 GeV.

Finally, we note that in the most general model it is necessary to consider KK excitations in the loops responsible for the gg and $\gamma\gamma$ couplings of the unmixed h^0. However, these contributions are only large if the "Y_2" and "Y_1" 5D quark Yukawa couplings are comparable. If $|Y_2| \ll |Y_1|$, a limit in which FCNC problems are minimal, these KK excitation corrections are quite small. (For more details, see [1].) Our results assume that this limit applies.

2 LHC Excesses

Our focus will be on the excesses seen in the $\gamma\gamma$ and 4ℓ final states that have excellent mass resolution. As already noted, in the context of the Higgs-radion model with just a single h_0 at most signals at two different masses can be described. We will consider three cases, labelled as ATLAS, CMSA and CMSB. We quantify the excesses in terms of the best fit value for $R(X) \equiv \sigma(X)/\sigma_{\rm SM}(X)$ for a given final state X. Errors quoted for the excesses are those for $\pm 1\sigma$. The mass locations and excesses in the $\gamma\gamma$ and 4ℓ channels in these three cases are taken from Figs. 8a and 8b of [18] in the ATLAS case and from the appropriate windows of Fig. 14 of [19] in the case of CMSA and CMSB.

Table 1: Three scenarios for LHC excesses in the $\gamma\gamma$ and 4ℓ final states.

	125 GeV (ATLAS) or 124 GeV (CMS)	120 GeV	137 GeV
ATLAS	$R(\gamma\gamma) \sim 2.0^{+0.8}_{-0.8}$ $R(4\ell) \sim 1.5^{+1.5}_{-1.0}$	no excesses	no excesses
CMSA	$R(\gamma\gamma) \sim 1.7^{+0.8}_{-0.7}$ $R(4\ell) \sim 0.5^{+1.1}_{-0.7}$	$R(4l) \sim 2.0^{+1.5}_{-1.0}$ $R(\gamma\gamma) < 0.5$	no excesses
CMSB	$R(\gamma\gamma) \sim 1.7^{+0.8}_{-0.7}$ $R(4\ell) \sim 0.5^{+1.1}_{-0.7}$	no excesses	$R(\gamma\gamma) \sim 1.5^{+0.8}_{-0.8}$ $R(4\ell) < 0.2$

As discussed above, it is appropriate to consider two different kinds of models: one in which Λ_ϕ, m_0/m_{Pl} and m_1^g are tied together as given in Eq. (1) and there is strong lower bound on the masses of the first excitations of the gauge bosons; and one in which there is no such tie and it is appropriate to consider phenomenology for a given fixed Λ_ϕ with varying m_0/m_{Pl}. We consider these two alternatives in turn.

2.1 Lower bound on m_1^g

In this section, we consider a model along the lines of [12] in which FCNC and PEW constraints are satisfied by virtue of the fermionic profiles being peaked fairly close to the Planck brane leading to fairly definitive couplings of the fermions to the excited gauge bosons. As described earlier, a lower bound of $m_1^g \sim 1.5$ TeV can be obtained from LHC data while FCNC and PEW constraints suggest a still higher bound of ~ 3 TeV. We will show some results for both choices as we step through various possible mass locations for the Higgs and radion that are motivated by the LHC excesses in the $\gamma\gamma$ and/or 4ℓ channels. In what follows, each plot will be labelled by the value of m_0/m_{Pl} chosen and the corresponding $m_{Pl}\Omega_0$ value as calculated for the fixed m_1^g using Eq. (1).

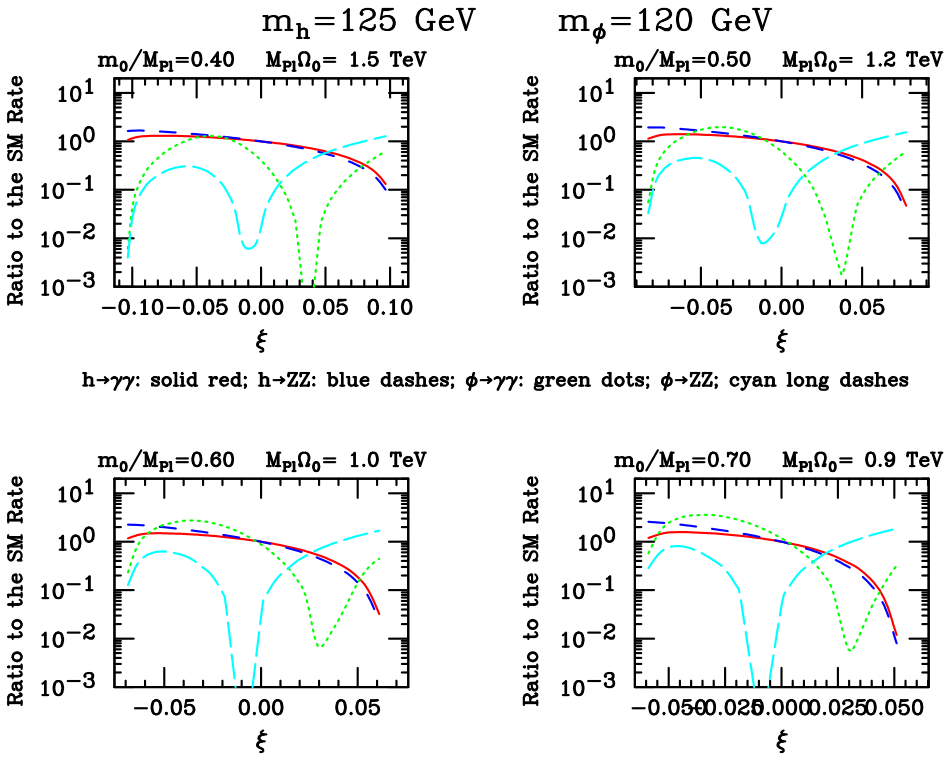

Figure 1: For $m_h = 125$ GeV and $m_\phi = 120$ GeV, we plot $R_h(X)$ and $R_\phi(X)$ for $X = \gamma\gamma$ and $X = ZZ$ (equivalent to $X = 4\ell$) as a function of ξ, assuming $m_1^g = 1.5$ TeV.

2.1.1 Signal at only 125 GeV

In Fig. 1 we illustrate some possibilities for $m_h = 125$ GeV and $m_\phi = 120$ GeV taking $m_1^g = 1.5$ TeV. First, we note that to get an enhanced $\gamma\gamma$ rate at 125 GeV, it is necessary to have $m_0/m_{Pl} \gtrsim 0.4$ and $\xi < 0$. In order to have small $R_\phi(\gamma\gamma)$ and $R_\phi(4\ell)$ at 120 GeV while at the same time $R_h(\gamma\gamma) \gtrsim 1.5$ at 125 GeV, for consistency with the ATLAS scenario, then $m_0/m_{Pl} = 0.4$ and $\xi \sim -0.09$ are good choices. The somewhat larger associated value of $R_h(4\ell)$ is still consistent within errors with the ATLAS observation at 125 GeV. We note that for the reversed assignments of $m_h = 120$ GeV and $m_\phi = 125$ GeV, we cannot find parameter choices that yield a decent description of the ATLAS 125 GeV excesses with $R_h(\gamma\gamma)$ and $R_h(4\ell)$ being sufficiently suppressed at 120 GeV.

2.1.2 Signals at 125 GeV and 120 GeV

Fig. 1 also exemplifies the fact that with $m_1^g = 1.5$ TeV the Higgs-radion model is unable to describe the CMSA scenario. In the regions of ξ for which appropriate signals are present at 125 GeV from the h, then at 120 GeV the 4ℓ and $\gamma\gamma$ rates are either both suppressed or $R_\phi(\gamma\gamma) > R_\phi(4\ell)$. This phenomenon persists at higher m_0/m_{Pl} values as well as higher m_1^g.

2.1.3 Signals at 125 GeV and 137 GeV

Let us next consider the CMSB scenario, *i.e.* neglecting the 4ℓ excess at 120 GeV in the CMS data. In Fig. 2 we see that the choices $m_0/m_{Pl} = 0.5$ and $\xi = 0.12$ give $R_h(\gamma\gamma) \sim 1.3$ and $R_h(4\ell) \sim 1.5$ at 125 GeV and

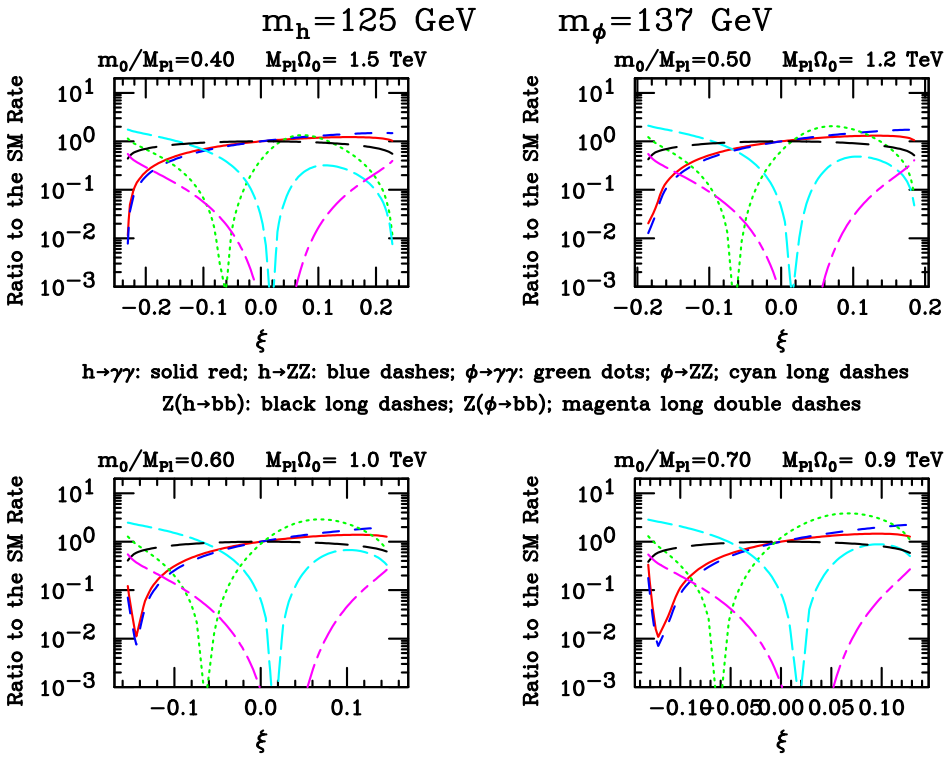

Figure 2: For $m_h = 125$ GeV and $m_\phi = 137$ GeV, we plot $R_h(X)$ and $R_\phi(X)$ for $X = \gamma\gamma$ and $X = ZZ$ (equivalent to $X = 4\ell$) as a function of ξ, assuming $m_1^g = 1.5$ TeV. Also shown are the similarly defined ratios for $Z + h$ production with $h \to b\bar{b}$ and $Z + \phi$ production with $\phi \to b\bar{b}$.

$R_\phi(\gamma\gamma) \sim 1.3$ at 137 GeV, fairly consistent with the CMSB observations. However, $R_\phi(4\ell) \sim 0.5$ at 137 GeV is a bit too large. Also shown in the figure are the rates for $Z, W + h$ with $h \to b\bar{b}$ and $Z, W + \phi$ with $\phi \to b\bar{b}$ relative to their SM counterparts. For the above $m_0/m_{Pl} = 0.5$, $\xi = 0.12$ choices, the $Z, W + h(\to b\bar{b})$ rate at 125 GeV is only slightly below the SM value, whereas the $Z, W + \phi(\to b\bar{b})$ rate is about 10% of the SM level predicted at 137 GeV. The former is consistent with the poorly measured $b\bar{b}$ rate at 124 GeV while confirmation of the latter would require much more integrated luminosity.

We also note that it is not possible to get enhanced $\gamma\gamma$ and 4ℓ h signals at 125 GeV without having visible 137 GeV ϕ signals, *i.e.* the ATLAS scenario of no observable excesses other than those at 125 GeV cannot be realized for $m_\phi = 137$ GeV.

For this case, it is also interesting to consider results for $m_h = 125$ GeV and $m_\phi = 137$ GeV for the higher value of $m_1^g = 3$ TeV. One finds that $R_h(\gamma\gamma)$ and $R_h(4\ell)$ are both $\lesssim 1$ (or less) except for $m_0/m_{Pl} = 0.7$ and large ξ for which $R_\phi(\gamma\gamma) \ll 1$. Thus, a reasonable description of the CMSB scenario requires relatively small m_1^g.

2.1.4 Signals at 125 GeV and high mass

A general question is whether one could explain the ATLAS 125 GeV excesses as being due to the h or ϕ with the other being at high mass. If $m_h = 125$ GeV and $m_\phi > 500$ GeV, one finds that $R_h(\gamma\gamma) \sim R_h(4\ell) \sim 1$ for ξ above some minimum (negative) value, with values substantially below 1 for more negative ξ. In any case, precision electroweak constraints are violated if $|\xi|$ is not quite modest in size since at large $|\xi|$ the

ϕVV ($V = W, Z$) couplings become of SM strength or larger. For more discussion see [20].

If the mass assignments are reversed, $m_\phi = 125$ GeV and $m_h > 500$ GeV, then at the most positive ξ values one can achieve $R_\phi(\gamma\gamma) \sim 2$ and $R_\phi(4\ell) \sim 1$ at 125 GeV for $m_0/m_{Pl} = 0.4$ and 0.5. However, this scenario is even less consistent with precision electroweak constraints since for all ξ the h alone has hVV couplings that are at least SM-like. Much larger Λ_ϕ would be needed to have a hope of achieving PEW consistency [20] and for large Λ_ϕ ATLAS-like >SM signals at $m_h = 125$ GeV would not be achievable. In addition, the $h \to 4\ell$ signal at high mass would be at least as large as predicted for a high-mass SM-like Higgs and therefore quite observable if $m_h \lesssim 500$ GeV, as seemingly inconsistent with ATLAS and CMS data. If $m_h \sim 1$ TeV, then the 4ℓ signal would be beyond current LHC reach but PEW inconsistency would be much worse. Thus, we conclude that for the Higgs-radion model to be of interest, both m_h and m_ϕ should be modest in size.

2.2 Fixed Λ_ϕ

In this section, we consider the second type of model discussed in the introduction in which there is no direct tie between m_1^g, Λ_ϕ and m_0/m_{Pl}. In this case, we feel free to consider the rather low values of Λ_ϕ, $\Lambda_\phi = 1$ TeV and $\Lambda_\phi = 1.5$ TeV, for which the Higgs-radion model can yield LHC rates in the $\gamma\gamma$ and 4ℓ channels that exceed those that are predicted for a SM Higgs. We note that when the gauge bosons propagate in the bulk, the phenomenology does not depend on Λ_ϕ alone — there is strong dependence on m_0/m_{Pl} when m_0/m_{Pl} is small. However, for large $m_0/m_{Pl} \gtrsim 0.5$ the phenomenology is determined almost entirely by Λ_ϕ, but is still not the same as found in the case where all fields are on the TeV brane. Once again, we step through a few possible mass locations for the Higgs and radion that are motivated by the LHC excesses in the $\gamma\gamma$ and/or 4ℓ channels.

2.2.1 Signal only at 125 GeV

As shown in Fig. 3, the choice of $\Lambda_\phi = 1$ TeV with $m_\phi = 125$ GeV and $m_h = 120$ GeV gives a reasonable description of the ATLAS excesses at 125 GeV with no visible signals at 120 GeV in either the $\gamma\gamma$ or 4ℓ channels when one chooses $m_0/m_{Pl} = 1$ and $\xi = -0.016$. In contrast, for $\Lambda_\phi = 1.5$ TeV the 125 GeV predicted excesses are below 1×SM and thus would not provide a good description of the ATLAS data. For the reversed assignments of $m_h = 125$ GeV and $m_\phi = 120$ GeV any choice of parameters that gives a good description of the 125 GeV signals always yields a highly observable $\gamma\gamma$ signal at 120 GeV.

2.2.2 Signals at 125 GeV and 120 GeV

The closest that we can come to fitting this CMSA scenario is to take $m_h = 125$ GeV and $m_\phi = 120$ GeV. One finds that if ξ is at its maximum value and $m_0/m_{Pl} = 1.1$ then the $\gamma\gamma$ and 4ℓ signals at $m_h = 125$ GeV are low, but still within -1σ of the CMS data while at $m_\phi = 120$ GeV one finds $R_\phi(4\ell) \sim 2.5$ while $R_\phi(\gamma\gamma) \sim 0.3$, which values are roughly consistent with the CMSA situation. For the reversed assignments of $m_h = 120$ GeV and $m_\phi = 125$ GeV, Fig 3 illustrates the fact that a satisfactory description of the two CMSA excesses is not possible — for ξ such that appropriate 125 GeV excesses are present, $R_h(\gamma\gamma)$ and $R_h(4\ell)$ at 120 GeV are always small so that the 4ℓ excess at 120 GeV is not explained.

2.2.3 Signals at 125 GeV and 137 GeV

Let us now consider the CMSB scenario. For $\Lambda_\phi = 1$ TeV, one finds $m_h = 125$ GeV and $m_\phi = 137$ GeV with the choices $m_0/m_{Pl} = 0.6$ and $\xi = -0.05$ give $R_h(\gamma\gamma) \sim 2$ and $R_h(4\ell) \sim 1$ at 125 GeV, while $R_\phi(\gamma\gamma) \sim 2$ and $R_\phi(4\ell) \sim 0.4$ at 137 GeV, an ok description of the CMSB excesses. An equally rough description of this same situation is also possible for $\Lambda_\phi = 1$ TeV with $m_0/m_{Pl} = 0.8$ and $\xi = 0.05$.

For $\Lambda_\phi = 1.5$ TeV a somewhat better simultaneous description of these excesses is possible. Fig. 4 shows some results for $m_h = 125$ GeV and $m_\phi = 137$ GeV. For $m_0/m_{Pl} = 0.25$ and $\xi \sim -0.1$ one finds $R_h(\gamma\gamma) \sim 2$ and $R_h(4\ell) \sim 1.5$ at $m_h = 125$ GeV, while $R_\phi(\gamma\gamma) \sim 2$ and $R_\phi(4\ell) \ll 1$ at $m_\phi = 137$ GeV, in pretty good agreement with the CMSB scenario.

If we reverse the configuration to $m_h = 137$ GeV and $m_\phi = 125$ GeV, the only parameter choices that come close to describing the two excess are $\Lambda_\phi = 1$ TeV with $m_0/m_{Pl} = 0.8$ and $\xi \sim 0.05$ for which one finds that the $m_\phi = 125$ GeV $\gamma\gamma$ and 4ℓ signals and the $m_h = 137$ GeV $\gamma\gamma$ signal are all at the level of

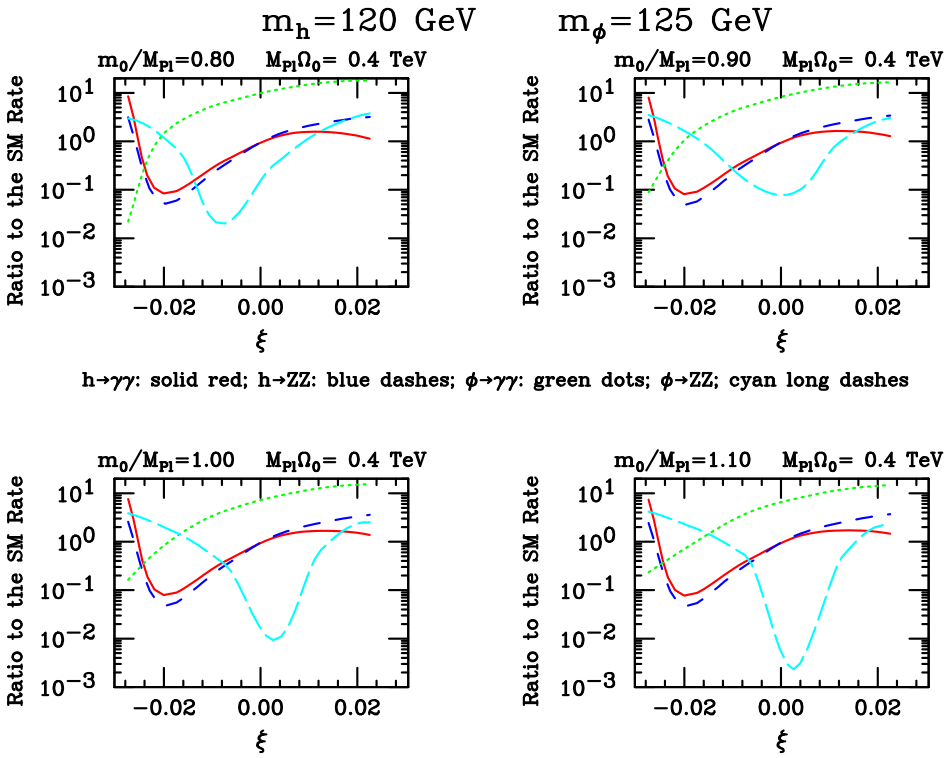

Figure 3: For $m_h = 120$ GeV and $m_\phi = 125$ GeV, we plot $R_h(X)$ and $R_\phi(X)$ for $X = \gamma\gamma$ and $X = ZZ$ (equivalent to $X = 4\ell$) as a function of ξ taking Λ_ϕ fixed at 1 TeV.

$\sim 1.4\times$SM. However, the $m_h = 137$ GeV 4ℓ signal is at the level of $\sim 0.6\times$ SM which is 4σ away from the CMS central value at this mass. For these mass assignments, the higher $\Lambda_\phi = 1.5$ TeV value does not provide any parameter choices that come close to describing the CMS excesses — the $m_\phi = 125$ GeV signals are never both sufficiently large *at the same time* to fit the observed signals.

2.2.4 Signals at 125 GeV and higher mass

We choose not to show any specific plots for this situation. For $\Lambda_\phi = 1$ TeV or 1.5 TeV, it is possible to choose one of either the h or ϕ to have a mass of 125 GeV and find m_0/m_{Pl} and ξ values that result in a decent description of the 125 GeV ATLAS excesses. However, these scenarios always are such as to imply a large inconsistency with PEW constraints and, if the higher mass is chosen below 500 GeV, a highly observable 4ℓ signal that would be inconsistent with ATLAS and CMS observations in that region of mass.

2.2.5 SM Higgs at 125 GeV and Signal at 137 GeV

It is still quite conceivable that, after accumulating more data, the $\gamma\gamma$ and 4ℓ excesses at ~ 125 GeV will converge to those appropriate for a SM Higgs boson. Such a situation would correspond to taking $\xi = 0$ in the Higgs-radion model. In this case, one can ask whether or not there could be a radion at some nearby mass and what its experimental signature would be. To exemplify, let us suppose that the signal at 137 GeV of the CMSB scenario survives. In Fig. 5 we plot $R_\phi(X)$ for $X = \gamma\gamma$ and $X = 4\ell$ as a function of Λ_ϕ for a selection of m_0/m_{Pl} values, taking $\xi = 0$. We also display ratios to the SM for WW fusion production of the ϕ, with

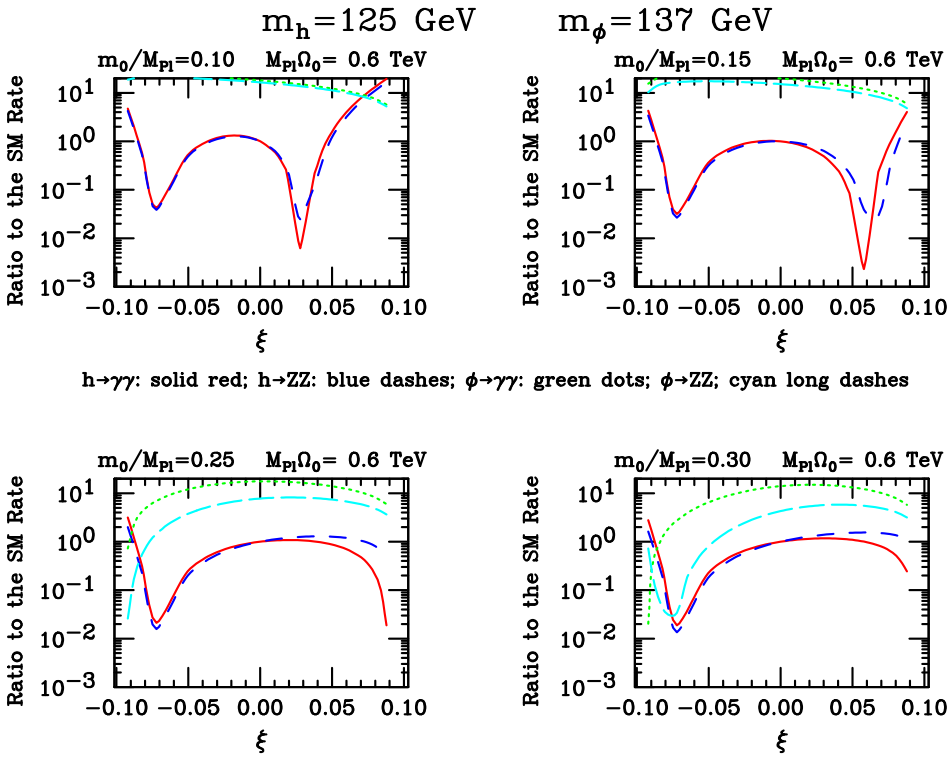

Figure 4: For $m_h = 125$ GeV and $m_\phi = 137$ GeV, we plot $R_h(X)$ and $R_\phi(X)$ for $X = \gamma\gamma$ and $X = ZZ$ (equivalent to $X = 4\ell$) as a function of ξ taking Λ_ϕ fixed at 1.5 TeV.

$\phi \to \gamma\gamma$, 4ℓ and $b\bar{b}$, as well as associated $Z\phi$ production with $\phi \to b\bar{b}$. One observes that a nice description of the $R(\gamma\gamma) \sim 2$ excess at 137 GeV is possible, for example, for $m_0/m_{Pl} = 0.3$ at $\Lambda_\phi \sim 2.8$ TeV with the 4ℓ signal (and all other signals) being very suppressed. As also apparent, other choices of m_0/m_{Pl} and Λ_ϕ will also yield $R_\phi(\gamma\gamma) \sim 2$ with varying levels of 4ℓ and $b\bar{b}$ signals. (However, to suppress $R_\phi(4\ell)$ below 0.2 while achieving $R_\phi(\gamma\gamma) \sim 2$ requires $m_0/m_{Pl} \geq 0.3$.) We also note that for $\xi = 0$ the $Z, W + \phi(\to b\bar{b})$ is greatly suppressed relative to its SM counterpart due to the very suppressed $ZZ\phi$ coupllng.

Plots for the case of a SM Higgs at 125 GeV and $m_\phi = 120$ GeV look very similar and, in particular, it is not possible to find parameters for which the 4ℓ signal substantially exceeds the $\gamma\gamma$ signal — the reverse always applies, as one anticipates from the enhanced anomalous $\gamma\gamma$ coupling of the (unmixed) ϕ.

3 Summary and Conclusions

The Randall Sundrum model solution to the hierarchy problem yields interesting phenomenology for the Higgs-radion sector, especially when Higgs-radion mixing is allowed for, and can be made consistent with FCNC and PEW constraints if fermions and gauge bosons propagate in the 5th dimension. At the moment, there are interesting hints at the LHC of narrow excesses above SM backgrounds in the $\gamma\gamma$ and $ZZ \to 4\ell$ channels, as well as a broad excess in the $WW \to \ell\nu\ell\nu$ channel. ATLAS sees excesses in the $\gamma\gamma$ and 4ℓ channels at a mass of ~ 125 GeV of order 2×SM and 1.5×SM respectively. CMS sees a $\gamma\gamma$ excess of order 1.5× SM at ~ 124 GeV and constrains the 4ℓ channel at this mass to be less than $\sim 1.5\times$SM. Additional excesses at 120 GeV (in the 4ℓ channel) and at 137 GeV (in the $\gamma\gamma$ channel) are present in the CMS data.

Here, we summarized two models with Higgs-radion mixing within the Randall Sundrum model context.

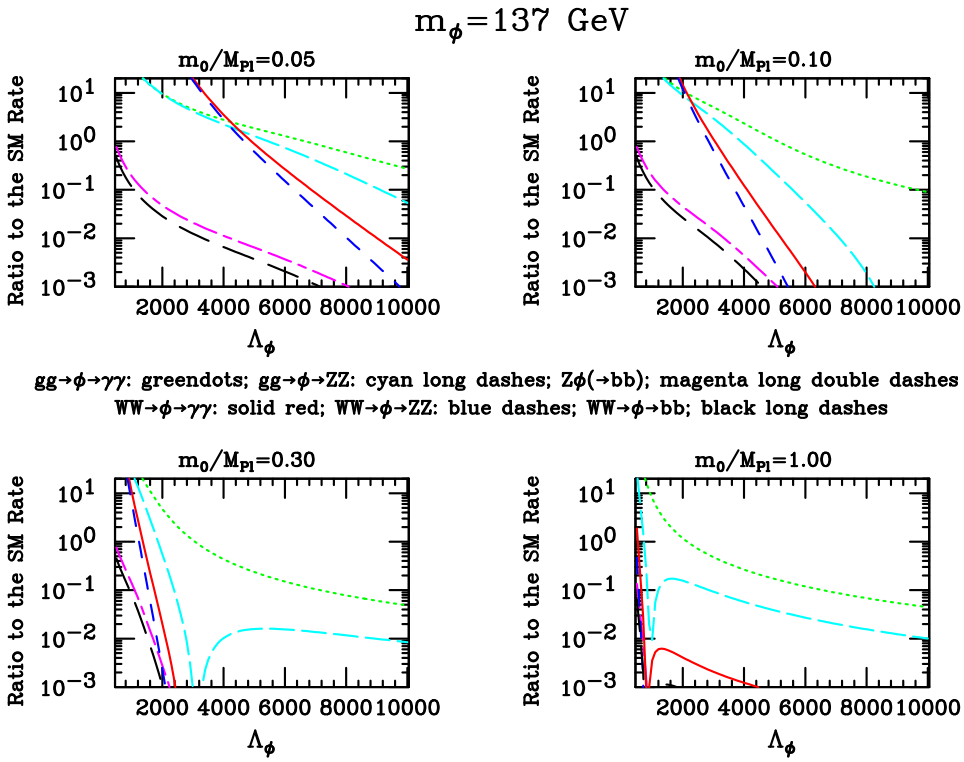

Figure 5: For $m_\phi = 137$ GeV, we plot $R_\phi(X)$ for $X = \gamma\gamma$ and $X = ZZ$ (equivalent to $X = 4\ell$) as functions of Λ_ϕ taking $\xi = 0$. We also plot ratios to the SM for $Z \to Z\phi$ with $\phi \to b\bar{b}$ and for $WW \to \phi \to X$ for $X = \gamma\gamma$, ZZ and $b\bar{b}$.

In the first model, the light fermion profiles are taken to be peaked near the Planck brane in order to avoid corrections to FCNC and PEW constraints that are too large. In this case, there is a lower bound on the mass of the 1st excited gluon state of order $m_1^g \geq 1.5$ TeV and it is necessary to correlate Λ_ϕ (the radion field vacuum expectation value) with the curvature ratio m_0/m_{Pl} and the m_1^g lower bound appropriately. In the second model considered there is no strong tie between the above parameters and it is most appropriate to consider fixed Λ_ϕ values while varying m_0/m_{Pl} — we studied the phenomenologically interesting choices of $\Lambda_\phi = 1$ TeV and 1.5 TeV.

Since the single Higgs plus radion model can describe at most two Higgs-like excesses, we considered three scenarios labelled as: ATLAS, with $\gamma\gamma$ and 4ℓ excesses at 125 GeV larger than SM and no other significant excesses; CMSA, with $\gamma\gamma$ and 4ℓ excesses at 124 GeV (the $\gamma\gamma$ excess being above SM level) and a 4ℓ excess at 120 GeV; and, CMSB, with a $\gamma\gamma$ and 4ℓ excesses at 124 GeV along with a $\gamma\gamma$ excess at 137 GeV larger than would have been predicted for $m_{h_{SM}} = 137$ GeV. In both the fixed m_1^g and the fixed Λ_ϕ model possibilities, the signal levels of the ATLAS and CMSB scenarios could be nicely described. Only for the 2nd model class could a (marginally) satisfactory description of the CMSA case be found. In general, successful fitting of the ATLAS and CMSB excesses required a modest value for the radion vacuum expectation value, typically $\Lambda_\phi \lesssim 2$ TeV, and mostly $m_0/m_{Pl} \gtrsim 0.5$, a range that the most recent discussion suggests is still consistent with higher curvature corrections to the RS scenario being small.

We also considered expectations for the radion signal in the case where the Higgs signal was assumed to ultimately converge to precisely that for a SM Higgs of mass 125 GeV. This situation would arise if the there is no Higgs-radion mixing. We found that interesting excesses at the radion mass would be present for low enough Λ_ϕ, namely $\Lambda_\phi \lesssim 3$ TeV, but would always be characterized by a $\gamma\gamma$ signal that substantially exceeds the 4ℓ signal (as appropriate for the CMS excesses at 137 GeV but in definite contradiction with the CMS excesses at 120 GeV).

Acknowledgments

Thanks go to Kaustubh Agashe, Felix Brummer, Csaba Csaki, Gero Von Gersdorff, Tom Rizzo and John Terning for illuminating discussions on radion physics. JFG thanks his collaborators on this project, Bohdan Grzadkowski and Manuel Toharia. JFG is supported by US DOE grant DE-FG03-91ER40674.

References

[1] B. Grzadkowski, J. F. Gunion, and M. Toharia, arXiv:1202.5017 [hep-ph].

[2] L. Randall and R. Sundrum, Phys. Rev. Lett. **83** (1999) 3370 [arXiv:hep-ph/9905221];

[3] H. Davoudiasl, J. L. Hewett and T. G. Rizzo, Phys. Lett. B **473**, 43 (2000) [hep-ph/9911262].

[4] A. Pomarol, Phys. Lett. B **486**, 153 (2000) [hep-ph/9911294].

[5] T. Gherghetta, A. Pomarol, Nucl. Phys. **B586**, 141-162 (2000). [hep-ph/0003129].

[6] H. Davoudiasl, J. L. Hewett, T. G. Rizzo, Phys. Rev. **D63**, 075004 (2001). [hep-ph/0006041].

[7] C. Csaki, J. Erlich and J. Terning, Phys. Rev. D **66**, 064021 (2002) [hep-ph/0203034].

[8] J. L. Hewett, F. J. Petriello and T. G. Rizzo, JHEP **0209**, 030 (2002) [hep-ph/0203091].

[9] K. Agashe, A. Delgado, M. J. May and R. Sundrum, JHEP **0308**, 050 (2003) [hep-ph/0308036].

[10] K. Agashe, H. Davoudiasl, G. Perez and A. Soni, Phys. Rev. D **76**, 036006 (2007) [hep-ph/0701186].

[11] D. Dominici, B. Grzadkowski, J. F. Gunion and M. Toharia, Nucl. Phys. B **671**, 243 (2003) [arXiv:hep-ph/0206192]; Acta Phys. Polon. B **33**, 2507 (2002) [arXiv:hep-ph/0206197].

[12] K. Agashe, A. Belyaev, T. Krupovnickas, G. Perez and J. Virzi, Phys. Rev. D **77**, 015003 (2008) [hep-ph/0612015].

[13] S. Rappoccio [CMS Collaboration], arXiv:1110.1055 [hep-ex].

[14] The ATLAS Collaboration, ATLAS-CONF-2011-123.

[15] G. F. Giudice, R. Rattazzi and J. D. Wells, Nucl. Phys. B **595**, 250 (2001) [arXiv:hep-ph/0002178].

[16] J. L. Hewett and T. G. Rizzo, JHEP **0308**, 028 (2003) [hep-ph/0202155].

[17] C. Csaki, J. Hubisz, S. J. Lee, Phys. Rev. **D76**, 125015 (2007). [arXiv:0705.3844 [hep-ph]].

[18] ATLAS Collaboration, http://cdsweb.cern.ch/record/1406358ATLAS-CONF-2011-163.

[19] CMS Collaboration, http://cdsweb.cern.ch/record/1406347/CMS-PAS-HIG-11-032.

[20] J. F. Gunion, M. Toharia and J. D. Wells, Phys. Lett. B **585**, 295 (2004) [hep-ph/0311219].

Higgs Pair Production in Composite Higgs Models at the ILC

Ramona Gröber, Margarete Mühlleitner

Institute for Theoretical Physics, Karlsruhe Institute of Technology, 76128 Karlsruhe, Germany

DOI: will be assigned

In order to establish the Higgs mechanism experimentally, also the Higgs potential must be reconstructed. This requires the measurement of the Higgs self-couplings. The trilinear Higgs self-coupling is accessible in Higgs pair production. In this contribution we investigate the prospects of measuring the trilinear Higgs self-coupling at the ILC in composite Higgs models. In these models the Higgs boson arises as a pseudo-Nambu Goldstone boson from a strongly-interacting sector. We focus on two particular composite Higgs models in which the couplings of the Higgs boson to the Standard Model (SM) particles are modified by a parameter ξ which describes the degree of compositeness. We will investigate various final states of Higgs pair production through double Higgs-strahlung and W boson fusion.

1 Introduction

After the discovery of a Higgs-like particle of mass around 125 GeV by the ATLAS and CMS experiments at the LHC [1, 2] its properties have to be investigated in order to clarify the question if it is really the particle responsible for the creation of particle masses through the Higgs mechanism [3]. Thus its couplings to the other SM particles have to be measured and its spin and CP properties must be determined. In the final step the Higgs self-couplings are to be determined. This allows to reconstruct the Higgs potential and test if it really has the typical minimax form inducing a non-vanishing vacuum expectation value as necessary ingredient for the Higgs mechanism. The Higgs self-couplings are accessible in multi-Higgs production processes. The trilinear Higgs coupling can be extracted from Higgs pair production, the quartic Higgs coupling from triple Higgs production. At the LHC this is a very difficult task due to large QCD backgrounds and small production cross sections [4, 5]. At an e^+e^- linear collider on the other hand the signatures are cleaner so that a measurement of the Higgs properties is possible with a higher precision. As for the quartic Higgs self-coupling, however, several studies [6–9] have shown that its measurement is impossible at ILC/CLIC and a high-energy LHC.

Another important question is if the thus established Higgs particle is the one of the SM or of extensions beyond the SM. Although the SM has been tested to very high accuracy there are several reasons to consider physics beyond the SM. One of them is the hierarchy problem, *i.e.* the question how the Higgs boson mass can be kept at the order of the electroweak symmetry breaking (EWSB) scale in the context of large scales up to which the SM is assumed to be valid. These would induce large radiative corrections and hence a large degree of fine-tuning in order to ensure a Higgs boson mass around 125 GeV. A solution to this problem is for example given by composite Higgs models where the Higgs boson is a bound state from a strongly-interacting sector [10]. The Higgs boson arises as a pseudo Nambu-Goldstone boson from an enlarged global symmetry [11]. This symmetry is explicitly broken by the couplings of the SM particles to the strongly-interacting sector. The Higgs potential is created by loops of SM fermions and gauge bosons and the Higgs mass remains naturally light.

In the following we will first give an introduction to the model, briefly discuss Higgs pair production at the LHC and then investigate the prospects of measuring the trilinear Higgs self-coupling at an e^+e^- linear collider in double Higgs-strahlung and W boson fusion into Higgs pairs.

2 Composite Higgs Models

In composite Higgs models a light Higgs boson arises as a pseudo Nambu-Goldstone boson from a strongly-interacting sector [11]. This leads to modified Higgs couplings compared to the SM. An effective low-energy description of a Strongly Interacting Light Higgs boson (SILH) has been given in [10]. The corresponding Lagrangian arises as first term of the expansion in $\xi = (v/f)^2$ where $v \approx 246$ GeV is the EWSB scale and f is scale of the strong dynamics. It can be used in the vicinity of the SM limit given by $\xi \to 0$. In order to reach larger values of ξ as *e.g.* the technicolor limit, $\xi \to 1$, a resummation of the series in ξ is required. This is provided by explicit models built in five-dimensional warped space. In the Minimal Composite Higgs Models (MCHM) of Refs. [12,13] the global symmetry $SO(5)\times U(1)$ is broken down at the scale f to $SO(4)\times U(1)$ on the infrared brane and to the SM $SU(2)_L \times U(1)_Y$ on the ultraviolet brane. In these models the modifications of the Higgs couplings can be described by one single parameter, given by ξ. The modification factor of the Higgs coupling to fermions depends on the representations of the bulk symmetry into which the fermions are embedded. In the model of Ref. [12], called MCHM_4, the fermions are in the spinorial representation of $SO(5)$, in the model MCHM_5 of Ref. [13] they are in the fundamental representation. The Higgs potential is generated by loops of the SM gauge bosons and fermions. The Higgs self-couplings therefore also depend on the representation of the fermions. The composite Higgs couplings with respect to the corresponding SM Higgs boson couplings are shown in Table 1 for MCHM_4 and MCHM_5, respectively. Note in particular, that in MCHM_5 for $\xi = 0.5$ the Higgs coupling to fermions and the trilinear Higgs self-interaction vanish.

	HVV	$HHVV$	Hff	HHH	$HHHH$
MCHM_4	$\sqrt{1-\xi}$	$1-2\xi$	$\sqrt{1-\xi}$	$\sqrt{1-\xi}$	$(1-\frac{7}{3}\xi)$
MCHM_5	$\sqrt{1-\xi}$	$1-2\xi$	$\frac{1-2\xi}{\sqrt{1-\xi}}$	$\frac{1-2\xi}{\sqrt{1-\xi}}$	$\frac{1-\frac{28}{3}(1-\xi)\xi}{1-\xi}$

Table 1: Modification factors of the composite Higgs couplings in MCHM_4 and in MCHM_5, with respect to the SM Higgs boson couplings to vector bosons (HVV and $HHVV$), to fermions ($Hf\bar{f}$) and to the SM Higgs self-couplings (HHH and $HHHH$).

The parameter space of composite Higgs models is constrained by electroweak precision tests and the LHC Higgs search results. Electroweak precision tests prefer low values of ξ [14]. If a partial cancellation of 50% with contributions from new states is allowed ξ should be $\lesssim 0.45$ [15,16]. The current Higgs results allow only for small deviations from the SM [17].

3 Higgs Pair Production at the LHC

At the LHC the dominant Higgs pair production process is given by gluon fusion [18]. The generic Feynman diagrams which contribute to this process are shown in Fig. 1. As can be inferred from the figure, in composite Higgs models a new coupling between two Higgs bosons and two fermions is possible which leads to additional diagrams contributing to gluon fusion into Higgs pairs [19,20]. It grows linearly with ξ and is explicitly given by

$$\begin{aligned} \text{MCHM}_4: &\qquad g_{HHff} = \frac{m_f}{v^2}\xi \\ \text{MCHM}_5: &\qquad g_{HHff} = \frac{m_f}{v^2} 4\,\xi\,. \end{aligned} \tag{1}$$

As expected it vanishes in the SM limit $\xi \to 0$. The coupling is suppressed by an extra power of v compared to the coupling of one Higgs boson to two fermions, but the corresponding diagram in the gluon fusion process Fig. 1 is not suppressed by an extra propagator, so that for large values of ξ it can have sizeable effects on Higgs pair production through gluon fusion. Thus the cross section increases with rising ξ mainly due to the diagram with the new coupling [19]. Since the dominating background processes do not depend on ξ, the signal to background ratio in composite Higgs models becomes larger. On the other hand the sensitivity of the cross section to the trilinear Higgs self-coupling is further diluted by this diagram not involving λ_{HHH}. Furthermore, in MCHM_5, where the self-coupling vanishes at $\xi = 0.5$, the sensitivity vanishes near these ξ

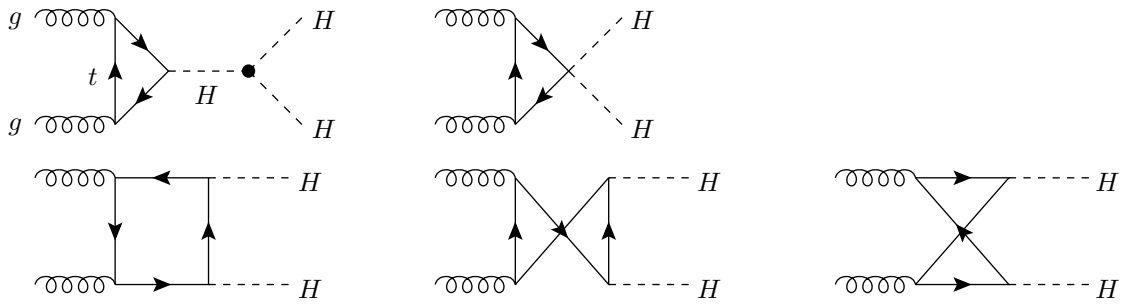

Figure 1: Generic Feynman diagrams contributing to the process $gg \to HH$.

values. In [4, 21] it was found that for $M_H = 125$ GeV the prospects of measuring the trilinear Higgs self-coupling in the $b\bar{b}\gamma\gamma$ and $b\bar{b}\tau\bar{\tau}$ final state are encouraging for the SM. But for a definite answer a dedicated model-dependent analysis taking into account background and detector effects has to be performed.[1]

In composite Higgs models also the top quark can be a composite object through its mixture with heavy fermions of the strong sector. If the additional new top partners have masses below the cut-off scale of the theory they will play a role in the heavy quark loops of the gluon fusion process. As was shown in Refs. [23] the cross section in single Higgs production does not depend on the spectrum of the top partners. This is not the case, however, for Higgs pair production [24]. In order to unambiguously extract the Higgs self-coupling from the gluon fusion process into Higgs pairs, therefore also the couplings and masses of the new resonances have to be known. If they are not too heavy they are accessible in direct production.[2] Otherwise, other processes such as double Higgs-strahlung off W/Z bosons [26] or vector boson fusion [27, 28], where heavy top partners do not play a role, may be exploited to extract the trilinear Higgs self-coupling λ_{HHH}. Their cross sections are, however, much smaller than the one of the gluon fusion process.

4 Higgs Pair Production at the ILC

The clean environment of an e^+e^- linear collider together with high luminosities and a high degree of polarisation of the electron/positron beams offers more promising prospects to extract the trilinear Higgs self-coupling. The most important processes for Higgs pair production are double Higgs-strahlung off Z bosons [26, 29, 30] at low energies and W boson fusion [27, 30, 31] at higher energies [6]. The Z boson fusion process to Higgs pairs is suppressed by an order of magnitude as the electron-Z couplings are small.

In the following Higgs pair production through double Higgs-strahlung and W boson fusion and the prospects of extracting the trilinear Higgs coupling will be discussed in more detail.

4.1 Higgs-Strahlung off Z Bosons

The generic Feynman diagrams contributing to the double Higgs-strahlung off Z bosons are depicted in Fig. 2. In Fig. 3 we show the cross section for this process as a function of ξ for MCHM$_4$ and MCHM$_5$ and for two different c.m. energies, $\sqrt{s} = 500$ GeV and 1 TeV. Here and in the following the Higgs boson mass is set to $M_H = 125$ GeV. The numerical calculation of the cross sections has been performed by using MADGRAPH/MADEVENT [32], where the model files for the composite Higgs models have been implemented. The results have been checked independently by an own FORTRAN routine.

As can be inferred from the figure, the cross sections for small values of ξ decrease with rising ξ. The reason is the reduction with ξ of the involved Higgs couplings. For $\xi = 0.5$ the $HHZZ$ coupling vanishes, and in MCHM$_5$ in addition the trilinear Higgs self-coupling becomes zero. Above $\xi = 0.5$ the $HHZZ$ coupling

[1] In Ref. [22] it was shown that ξ can be extracted with an accuracy of $\mathcal{O}(20\%)$.

[2] Note, that the lightest top partner cannot be too heavy to accommodate a Higgs mass of $M_H = 125$ GeV [25].

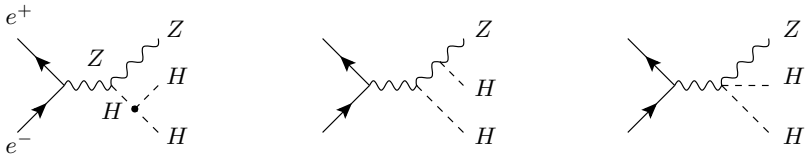

Figure 2: Generic Feynman diagrams contributing to Higgs pair production via Higgs-strahlung off Z bosons.

changes sign and increases again in absolute value. In MCHM$_5$ also the trilinear Higgs self-coupling becomes larger with ξ. In both models hence the cross sections increase for large values of ξ, and depending on the c.m. energies they develop minima around $\xi \approx 0.45 - 0.65$.

The energy behaviour of the process can be understood as follows. The SM cross section decreases with rising c.m. energy, but this is not the case for the composite Higgs models. Because of the modified couplings, for $\xi \gtrsim 0.5$ the cross sections increase with the energy to reach a constant value at very high energies. The reason is the change in the sign of the $HHZZ$ coupling at $\xi = 0.5$ leading to a constructive interference for $\xi \gtrsim 0.5$ between the diagrams containing the $HHZZ$ coupling and the diagram with the Z boson in the s-channel. The diagram including the trilinear Higgs self-coupling becomes less important with increasing energy since it is suppressed by an extra Higgs boson propagator compared to the other diagrams, so that for large energies the sensitivity to the Higgs self-coupling is suppressed.

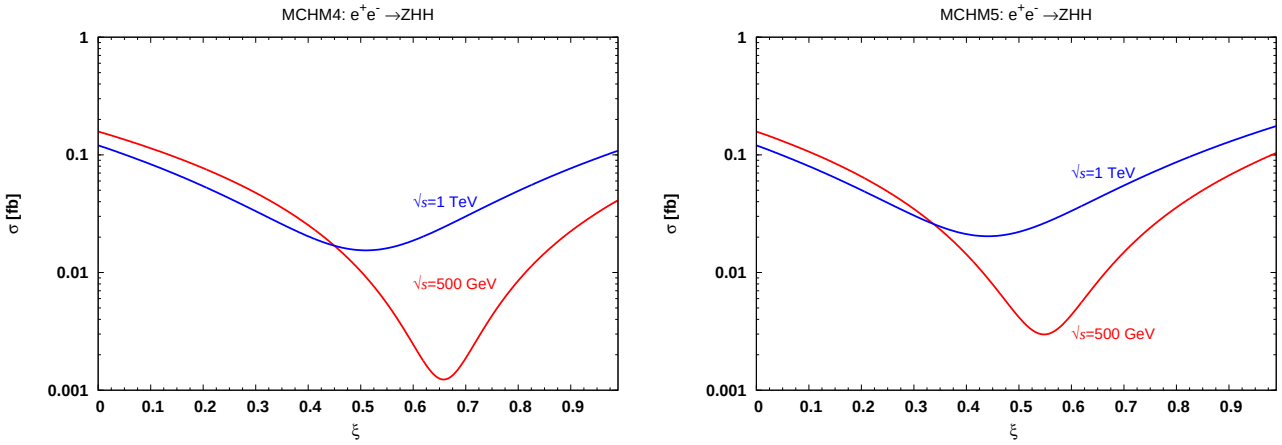

Figure 3: The cross section of Higgs pair production via Higgs-strahlung ZHH as a function of ξ for the MCHM$_4$ (left) and the MCHM$_5$ (right) and for two c.m. energies, $\sqrt{s} = 500$ GeV (red) and 1 TeV (blue).

In order to study the sensitivity of the double Higgs-strahlung process to the trilinear Higgs self-coupling we vary λ_{HHH} in terms of the Higgs self-coupling of the corresponding model, hence

$$\lambda_{HHH} \to \kappa \lambda_{HHH} \; . \tag{2}$$

This allows an estimate of how accurately the Higgs pair production process needs to be measured in order to achieve a certain precision on λ_{HHH} within the model under consideration. It does not represent, however, a test of models beyond the actually investigated theory. In Fig. 4 we show for the SM ($\xi = 0$) and for MCHM$_5$ for three representative values of ξ ($\xi = 0.2, 0.5, 0, 8$) the respective normalised ZHH cross section as a function of the modification factor κ for two c.m. energies, $\sqrt{s} = 500$ GeV and 1 TeV. The normalisation is with respect to the ZHH cross section at $\kappa = 1$ of the respective model (SM and MCHM$_5$ at $\xi = 0.2, 0.5, 0.8$). The figure confirms that the cross section is more sensitive to λ_{HHH} for lower collider energies. For $\xi = 0.5$ there is no sensitivity to a change in the trilinear Higgs self-coupling at all, as $\lambda_{HHH} = 0$ in the MCHM$_5$ for $\xi = 0.5$. The figures 4 also show that there might be ambiguities in the measurement of the trilinear Higgs self-coupling, as *e.g.* for $\xi = 0.2$ in the MCHM$_5$ for $\kappa = 1$ and $\kappa \approx -1.7$ the cross sections

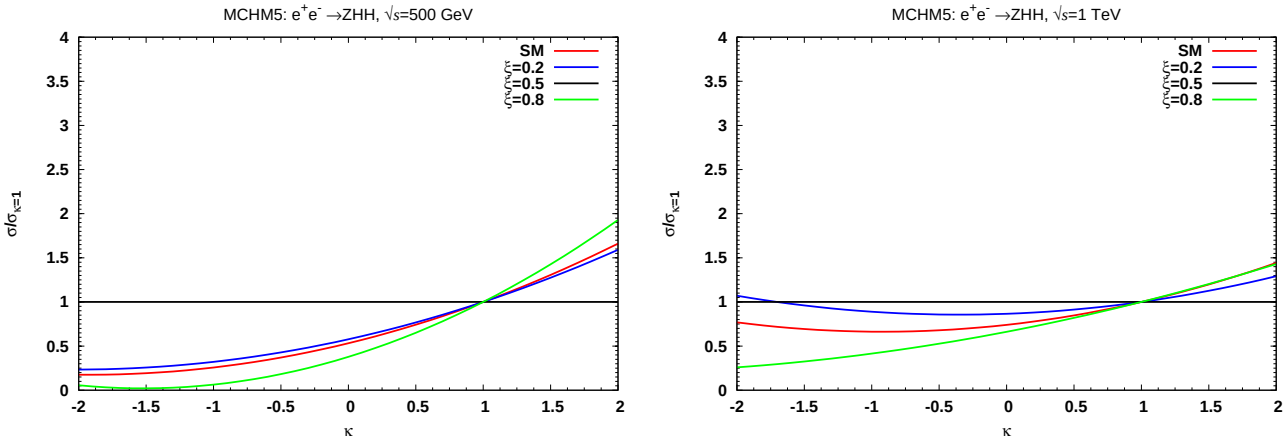

Figure 4: The ZHH cross section in the SM (red) and the MCHM$_5$ for $\xi = 0.2$ (blue), $\xi = 0.5$ (black) and $\xi = 0.8$ (green) divided by the cross section of the corresponding model at κ=1 for $\sqrt{s} = 500$ GeV(left) and $\sqrt{s} = 1$ TeV (right).

at $\sqrt{s} = 1$ TeV have the same value. Such ambiguities can be resolved by investigating other pair production processes like W boson fusion or by measurements of the cross section at different collider energies.

In order to study the experimental sensitivities to the trilinear Higgs self-coupling the decays of the Higgs bosons must be included. In the narrow-width-approximation this can be done by multiplying the production cross section with the respective branching ratios.[3] For the MCHM$_{4,5}$ the branching ratios can be found in Ref. [15] or be calculated with the Fortran program `eHDECAY` [33]. In the MCHM$_4$ the branching ratios do not change compared to the SM since the Higgs couplings are all modified by the same factor. For $M_H = 125$ GeV the Higgs boson decays dominantly into b-quarks followed by the decay into W bosons. In the MCHM$_5$ the branching ratios depend on ξ. For a 125 GeV Higgs boson and small ξ values, again the decays into $b\bar{b}$ dominate. But for $\xi = 0.5$ the fermion coupling vanishes and therefore the branching ratios into fermions and gluons vanish as well, so that in the region around $\xi = 0.5$ the decays into W^+W^- dominate. Above $\xi = 0.5$ with increasing ξ the Higgs coupling to gauge bosons decreases while the coupling to fermions increases, so that for $\xi \gtrsim 0.65$ the decays into $b\bar{b}$ dominate and the decays into W^+W^- become less important.

In order to investigate the question if the double Higgs-strahlung process is sensitive to a change in the trilinear Higgs self-coupling we have constructed sensitivity areas in the $\xi - \kappa$ plane. These sensitivity areas give an idea of how accurately the pair production cross section has to be measured in order to extract the Higgs self-coupling with a certain precision. For the construction of the areas we place ourselves in a particular model (MCHM$_4$ or MCHM$_5$ and a fixed value of ξ) and vary within this model the trilinear Higgs self-coupling in terms of the corresponding coupling of this model by applying a modification factor κ. We then determine the regions where the number of signal events deviates by more than $1, 2, 3, 5\,\sigma$ from the number of signal events at $\kappa = 1$, hence where in the specific model under investigation,

$$S_\kappa < S_{\kappa=1} - a\sqrt{S_{\kappa=1}} \quad \text{or} \quad S_\kappa > S_{\kappa=1} + a\sqrt{S_{\kappa=1}} \quad \text{with} \quad a = 1, 2, 3, 5\,. \tag{3}$$

In Fig. 5 we show these sensitivity areas for MCHM$_4$ in the $b\bar{b}b\bar{b}$ final state at $\sqrt{s} = 500$ GeV and an integrated luminosity of 500 fb^{-1} (left) and 1000 fb^{-1} (right). The darkest (lightest) region corresponds to the 5 (1) σ region. As can be inferred from Fig. 5 the trilinear Higgs self-coupling cannot be measured very precisely in double Higgs-strahlung in the $4b$ final state. In the SM, corresponding to $\xi = 0$, only a variation in the sign can be measured at $3\,\sigma$ or whether the trilinear Higgs self-coupling changes by at least a factor of

[3] The narrow-width-approximation can be applied here as for a 125 GeV SM Higgs boson the total width is $\sim 4 \times 10^{-3}$ GeV, and the total widths of MCHM$_4$ and MCHM$_5$ for the same Higgs boson mass and the three investigated ξ values are in the vicinity of or below the SM total width [15].

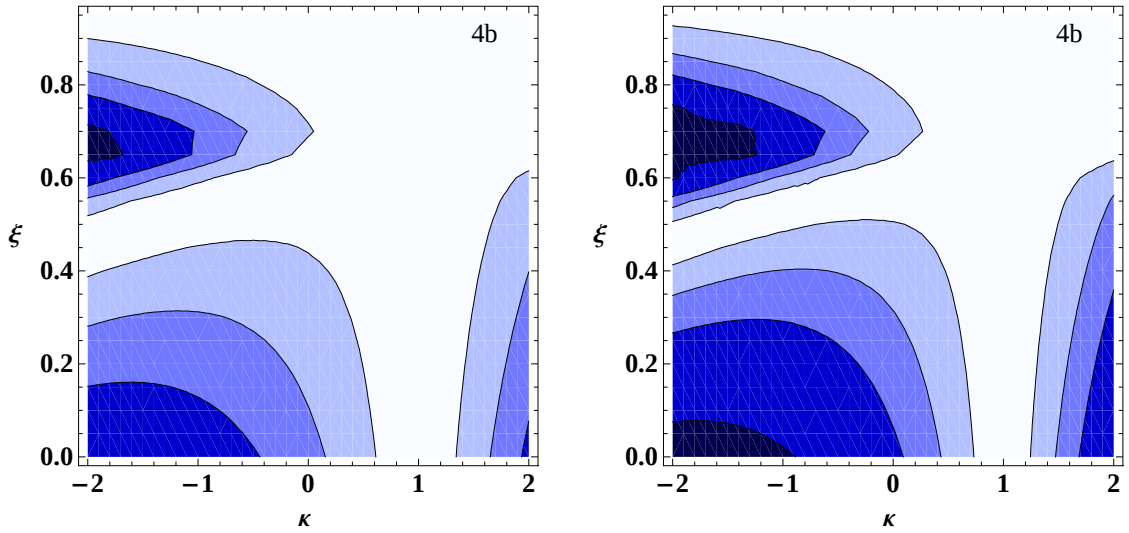

Figure 5: Sensitivity areas in the $\xi - \kappa$ plane of the double Higgs-strahlung process to a change in the trilinear Higgs self-coupling by a multiplicative factor κ in terms of the MCHM$_4$ trilinear Higgs self-coupling for a certain value of ξ in the final state $b\bar{b}b\bar{b}$ at $\sqrt{s} = 500$ GeV and $\int \mathcal{L} = 500\text{fb}^{-1}$ (left) and $\int \mathcal{L} = 1000\text{fb}^{-1}$ (right). The regions correspond from dark blue to light blue to 5, 3, 2, 1 σ, see the text for explanation.

2. For low non-vanishing values of ξ the situation becomes even worse. For larger luminosities the prospects are somewhat better. Note, however, that although in the region around $\xi = 0.7$ we have $5\,\sigma$ regions, the number of signal events is very low here with only $2 - 3$ events for $\int \mathcal{L} = 500\text{fb}^{-1}$. Increasing the energy worsens the prospects due to reduced cross sections.

The corresponding sensitivity plots for MCHM$_5$ can be found in Fig. 6. Here again the trilinear Higgs self-coupling cannot be measured with high accuracy. Around $\xi = 0.5$ there is no sensitivity at all since here the trilinear Higgs self-coupling vanishes. For very large values of ξ there is some sensitivity in the $b\bar{b}b\bar{b}$ final state due to the enhanced branching ratio into b-quarks for large values of ξ where the coupling of the Higgs boson to the vector bosons becomes small. Again the prospects of measuring the trilinear Higgs self-coupling increase significantly with higher luminosity.

So far no background processes or detector effects have been taken into account. For a realistic study, which is beyond the scope of this contribution, they are necessary. We can, however, give an estimate what the prospects of such an analysis are. The dominating background processes do not involve Higgs bosons, so that they do not change in the composite Higgs models compared to the SM. Previous studies found that in the SM the trilinear Higgs self-coupling can be measured with an accuracy of $\sim 10 - 20\%$ for high luminosities at ILC/CLIC [6, 34–37].[4] As, however, the ZHH signal processes in the MCHMs are reduced compared to the SM, a measurement of the trilinear Higgs self-coupling will not be possible with the same accuracy as in the SM. Note also that the number of signal events even without applying any cuts is very small (~ 24 for $\kappa = 1$ and $\xi = 0$ at $\sqrt{s} = 500$ GeV for $\int \mathcal{L} = 500\text{fb}^{-1}$ in the $b\bar{b}b\bar{b}$ final state).

4.2 Vector boson fusion

In the following we discuss vector boson fusion via W bosons into a Higgs boson pair. The generic diagrams contributing to this process are depicted in Fig. 7. The Z boson fusion process is an order of magnitude smaller in the SM. This slightly changes in the composite Higgs models, but not as much as to dominate over W boson fusion.

In Fig. 8 the Higgs pair production cross sections via W boson fusion are shown as a function of ξ for the MCHM$_4$ (left) and MCHM$_5$ (right) at $\sqrt{s} = 500$ GeV and 1 TeV. The cross section increases with ξ

[4] For the sensitivities on Higgs self-couplings in the context of genuine dimension-six operators, see [38].

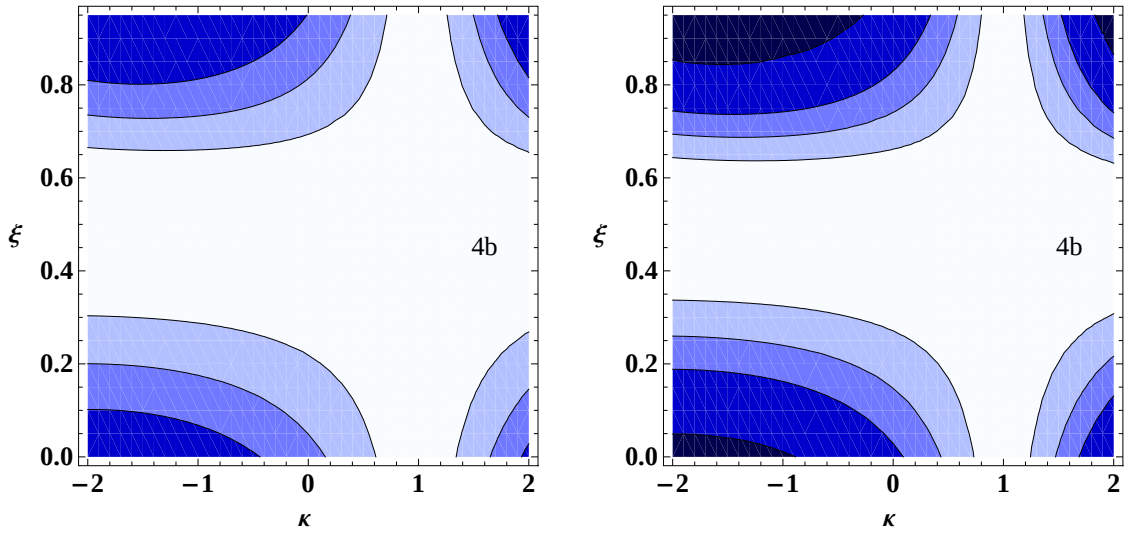

Figure 6: Same as Fig. 5 but in the MCHM$_5$.

because the interference behaviour between the Feynman diagrams changes. In the SM the diagrams with the $WWHH$ coupling and the diagram with the t/u-channel exchange of a W boson interfere destructively whereas in the composite Higgs models for low ξ the destructive interference term becomes smaller. For $\xi = 0.5$ the $HHWW$ coupling and the HHH coupling change sign and they interfere constructively with the other diagrams. In the SM the cross section for double Higgs-strahlung slightly exceeds the W boson fusion cross section. As W boson fusion increases with ξ, in the composite Higgs models already for low values of ξ the W boson fusion process becomes more important than double Higgs-strahlung at $\sqrt{s} = 1$ TeV.

The W boson fusion cross section in composite Higgs models shows an interesting and characteristic energy behaviour of the strongly-interacting Higgs scenario [10,39]. Due to the modified Higgs couplings the amplitude of longitudinal W boson fusion becomes

$$\mathcal{M}_{LL} = G_F \frac{s}{\sqrt{2}} \left\{ (1+\beta_W^2) \left[(1-2\xi) + \frac{A \cdot \lambda_{HHH}^{SM}}{(s-M_H^2)/M_Z^2} \right] + \frac{1-\xi}{\beta_W \beta_H} \left[\frac{(1-\beta_W^4) + (\beta_W - \beta_H \cos\theta)^2}{\cos\theta - x_W} - \frac{(1-\beta_W^4) + (\beta_W + \beta_H \cos\theta)^2}{\cos\theta + x_W} \right] \right\}$$

$$\text{with} \qquad \beta_{W/H} = \sqrt{1 - \frac{4\,M_{W/H}^2}{s}} \qquad \text{and} \qquad x_W = \frac{1 - \frac{2\,M_H^2}{s}}{\beta_W \beta_H} \,. \tag{4}$$

The Higgs production angle in the WW c.m. frame is denoted by θ. The contribution of the diagram with the trilinear Higgs self-coupling $\lambda_{HHH}^{SM} = \frac{3\,M_H^2}{M_Z^2}$ is modified by a factor of $A = 1-\xi$ in MCHM$_4$ and by a factor of $A = 1-2\xi$ in MCHM$_5$. For high energies the amplitude becomes

$$\mathcal{M} \overset{s\to\infty}{\longrightarrow} -\sqrt{2} G_F s\, \xi \tag{5}$$

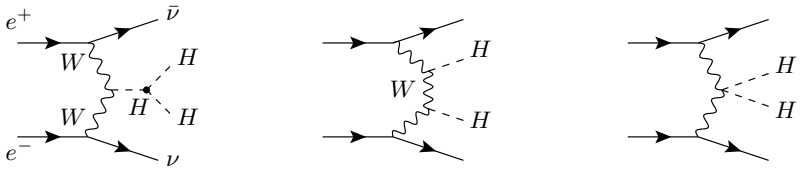

Figure 7: Generic Feynman diagrams contributing to Higgs pair production via W boson fusion.

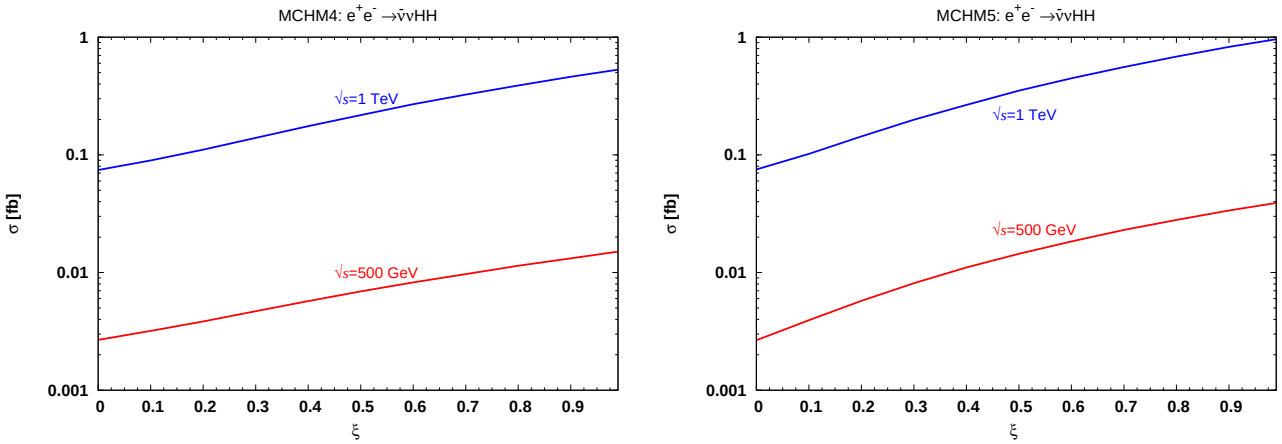

Figure 8: The cross sections of Higgs pair production via W boson fusion as a function of the ξ for the MCHM$_4$ (left) and the MCHM$_5$ (right) at $\sqrt{s} = 500$ GeV (red) and 1 TeV (blue).

and hence increases with the c.m. energy. In Fig. 9 the Higgs pair production cross section via W boson fusion is shown as a function of the c.m. energy in the MCHM$_5$ for $\xi = 0.2, 0.5, 0.8$ and for comparison also in the SM. Indeed, the cross section increases for non-vanishing values of ξ with the c.m. energy, an increase

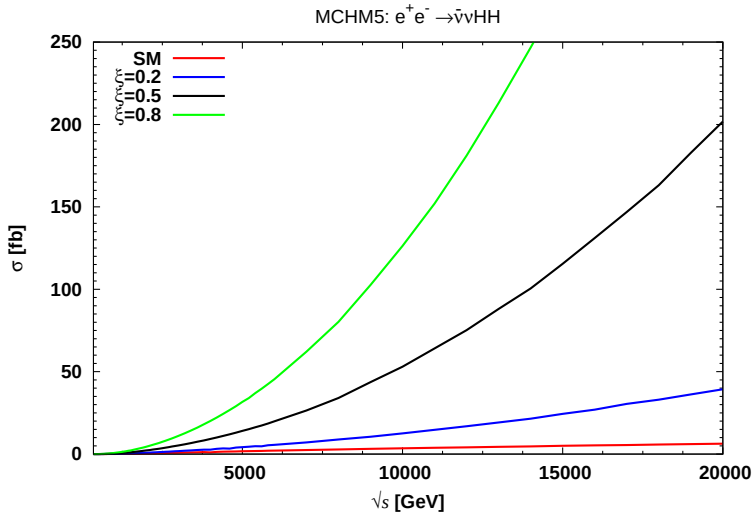

Figure 9: The W boson fusion cross section as a function of the c.m. energy $\sqrt{s}$ in the MCHM$_5$ for $\xi = 0.2$ (blue), 0.5 (black) and $\xi = 0.8$ (green) and compared to the SM (red).

which becomes more and more important with larger ξ values. At the same time the contribution of the diagram involving the trilinear Higgs self-coupling becomes negligible.[5] The energy behaviour results from the Higgs boson not fully unitarising this process any more due to its modified couplings with respect to the SM. Since the couplings depart smoothly from the SM case the breakdown of partial wave unitarity is delayed to higher energies. From the viewpoint of an effective theory, partial wave unitarity can be restored above the cut-off by new resonances of the strongly-interacting sector [40].

[5]Therefore, we did not show Fig. 9 for the MCHM$_4$ since the two models differ for this process only in the trilinear Higgs self-coupling. At high energies, when the contribution from the trilinear Higgs self-coupling is negligible, the two models show no difference.

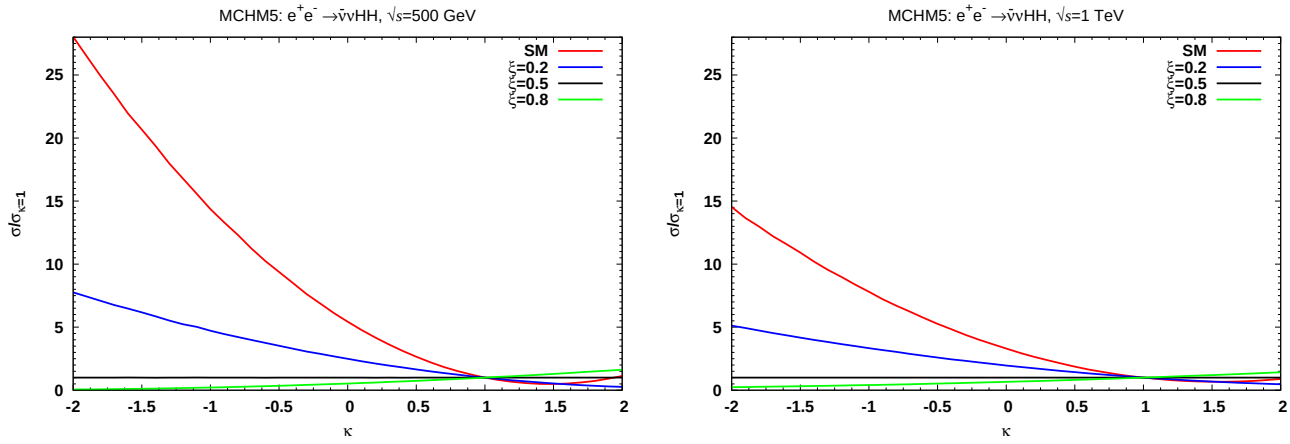

Figure 10: The W boson fusion cross sections in MCHM$_5$ as a function of κ normalised to the cross section at κ=1 for $\xi = 0.2$ (blue), $\xi = 0.5$ (black) and $\xi = 0.8$ (green) and in the SM (red) for a collider energy of $\sqrt{s} = 500$ GeV(left) and $\sqrt{s} = 1$ TeV (right).

In Fig. 10 the sensitivity of Higgs pair production through W boson fusion to the trilinear Higgs self-couplings is investigated by plotting the normalised cross section as function of κ, which is the modification factor applied to λ_{HHH} in terms of the Higgs self-coupling of the respective model. The cross section is normalised to its value where the trilinear Higgs self-coupling takes the value of λ_{HHH} predicted in the model under investigation, *i.e.* for $\kappa = 1$. The variation is shown for $\sqrt{s} = 500$ GeV (left) and 1 TeV (right). As can be inferred from the figure, the cross sections show are stronger variation with λ at lower c.m. energies. This is because the diagram involving the trilinear Higgs self-coupling is suppressed by an extra propagator compared to the other diagrams. Nevertheless, the trilinear Higgs self-coupling can be measured with a higher accuracy at 1 TeV due to the larger number of signal events. The comparison with the double Higgs-strahlung process shows that the sensitivity in W boson fusion to λ_{HHH} is higher.

In Fig. 11 the sensitivity areas in the $\xi - \kappa$ plane are shown for the MCHM$_4$ in the $4b$ final state. Again the dark blue region is the $5\,\sigma$ region, *i.e.* the region where the number of signal events for the modified coupling in terms of the coupling predicted by the model deviates by more than $5\,\sigma$ from the number of signal events where the coupling takes the value predicted by the model. The c.m. energy has been set equal to 1 TeV as it is large enough to produce a sufficient number of signal events but small enough not to spoil the sensitivity to λ_{HHH}. For the integrated luminosity we took $\int \mathcal{L} = 500\,\text{fb}^{-1}$. Furthermore, in Fig. 11 (right) we assumed polarised $e^{\pm}$ beams which gives an additional factor of 4 for the cross section if the beams are perfectly polarised.[6] In practice, a polarisation of the e^-−beam of 80-90% is possible, for the e^+−beam of $\sim$ 60% [41]. The factor of 4 from polarised beams is equivalent to a factor of 4 in the luminosity. The figure shows, that the sensitivity to the trilinear Higgs self-coupling becomes smaller with rising ξ. In other words, the cross section has to be measured with higher precision in order to achieve a certain precision on λ_{HHH}. The reason is that with rising ξ the coupling λ_{HHH} becomes smaller as it is modified by a factor $\sqrt{1-\xi}$ compared to the SM. However, the prospects of measuring the trilinear Higgs self-coupling in W boson fusion look much better than in double Higgs-strahlung. For very low values of ξ this is only due to the higher sensitivity of the W boson fusion compared to the Higgs-strahlung process. For moderate values of ξ also the cross section is larger than for double Higgs-strahlung. The region of poor sensitivity at $\kappa \approx 2$ for values of ξ close to 0 is due to an ambiguity in the cross section. The value $\kappa \approx 2$ leads to the same cross section as $\kappa = 1$.

The sensitivity areas for the MCHM$_5$ in the $\xi - \kappa$ plane can be found in Fig. 12. They are shown for ideally polarised beams for two different final states, $b\bar{b}b\bar{b}$ and $W^+W^-W^+W^-$. Since for $\xi = 0.5$ the fermionic couplings in the MCHM$_5$ are zero, the branching ratio $H \to b\bar{b}$ is zero. Also the sensitivity to the

[6]Note that the double Higgs-strahlung cross section is enhanced by a factor of 2 for 100% polarised $e^{\pm}$ beams.

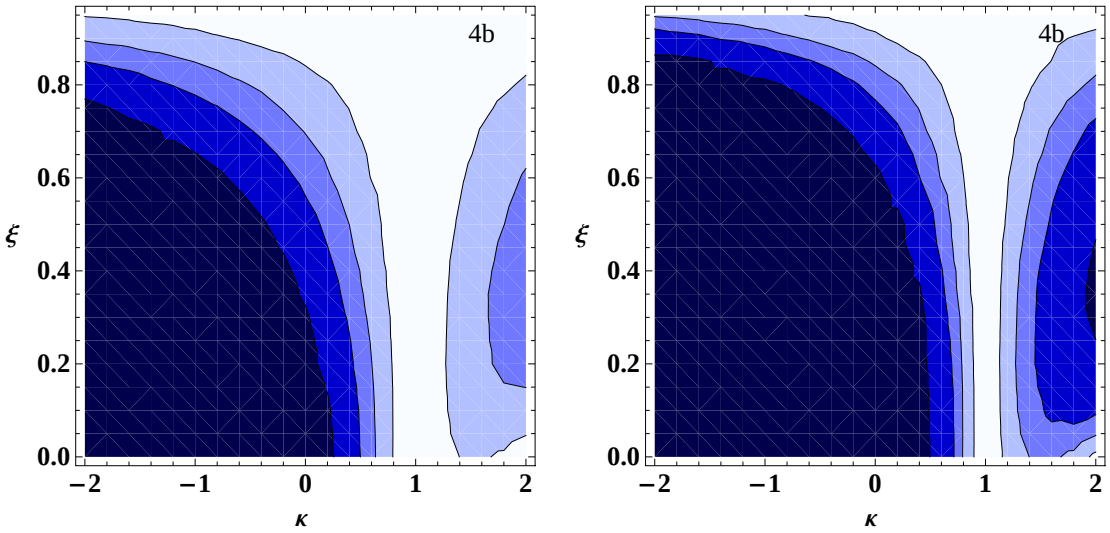

Figure 11: Sensitivity areas in the $\xi - \kappa$ plane of W boson fusion into Higgs pairs to a change in the trilinear Higgs self-coupling by a multiplicative factor κ in terms of the MCHM$_4$ trilinear Higgs self-coupling for a certain value of ξ in the final state $b\bar{b}b\bar{b}$ at $\sqrt{s} = 500$ GeV and $\int \mathcal{L} = 500\text{fb}^{-1}$ and unpolarised beams (left). In the right figure $\int \mathcal{L} = 2000\,\text{fb}^{-1}$ or equivalently we have ideally polarised $e^{\pm}$ beams at $\int \mathcal{L} = 500\text{fb}^{-1}$. The regions correspond from dark blue to light blue to 5, 3, 2, 1 σ, see the text for explanation.

trilinear Higgs self-coupling vanishes for $\xi = 0.5$ because the coupling becomes zero at this ξ value. The $4W$ final state shows some sensitivity to the coupling in the vicinity of $\xi \approx 0.5$, contrary to the $4b$ final state, where the branching ratio of the decay $H \to b\bar{b}$ is still too small. On the other hand, the branching ratio into W^+W^- diminishes for large ξ values since the HWW coupling scales with $\sqrt{1-\xi}$, and also for small ξ values the decays into $H \to b\bar{b}$ dominate leading to a better sensitivity on λ_{HHH}.

Taking into account detector properties and background processes, for the SM it was found that the trilinear Higgs self-coupling can measured with a precision of $\sim 10\%$ in the SM [35–37]. In composite Higgs models the cross section increases and in large areas of the parameter space the cross section is sensitive to the trilinear Higgs self-coupling. As the dominant background processes do not change compared to the SM, for large regions in the parameter space a determination of the trilinear Higgs self-coupling with the same accuracy or even better may therefore be expected in the MCHM$_4$ and MCHM$_5$.

5 Conclusions

The measurement of the Higgs self-couplings is an important but very difficult task in the program of the experimental verification of the Higgs mechanism. We studied the prospects of measuring a non-vanishing trilinear Higgs self-coupling in the context of minimal composite Higgs models. At the LHC this is very difficult in particular for a light Higgs boson with mass of 125 GeV where the decay into $b\bar{b}$ dominates, which faces large QCD backgrounds.

The ILC offers a cleaner environment, high luminosities and a high degree of polarisation of the $e^{\pm}$ beams. We showed that in double Higgs-strahlung off Z bosons the cross sections in the MCHMs become smaller compared to the SM. Therefore, the measurement of the trilinear Higgs self-coupling in this channel is more difficult than in the SM case. For W boson fusion into Higgs pairs, however, the cross section is larger in the MCHMs than in the SM. It has been shown that this process is sensitive to a non-vanishing trilinear Higgs self-coupling in large regions of the parameter space. Due to the expected number of signal events the precision with which the trilinear Higgs self-coupling can be measured should therefore be as good as or even better than in the SM. The cross section of W boson fusion increases with rising c.m. energy. However, this does not lead to better prospects of measuring the trilinear Higgs self-coupling, since the diagram containing

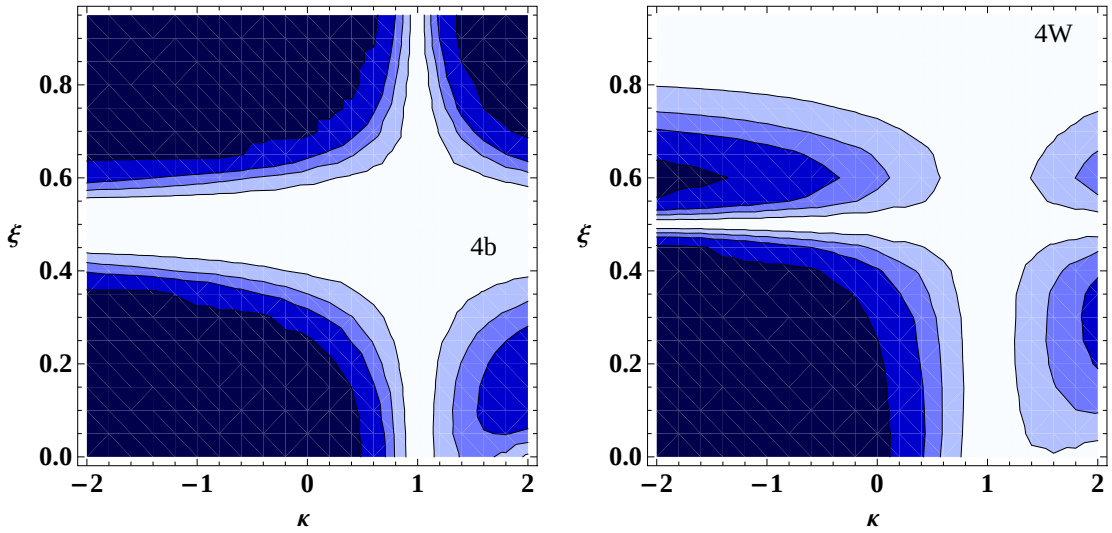

Figure 12: Sensitivity areas in the $\xi - \kappa$ plane of W boson fusion into Higgs pairs to a change in the trilinear Higgs self-coupling by a multiplicative factor κ in terms of the MCHM_5 trilinear Higgs self-coupling for a certain value of ξ in the final state $b\bar{b}b\bar{b}$ (left) and $W^+W^-W^+W^-$ (right) at $\sqrt{s} = 1$ TeV and ideally polarised $e^\pm$ beams at $\int \mathcal{L} = 500$ fb^{-1}. The regions correspond from dark blue to light blue to 5, 3, 2, 1 σ, see the text for explanation.

the trilinear Higgs self-coupling is suppressed by an extra propagator compared to the other diagrams so that the sensitivity to λ_{HHH} becomes more diluted at higher c.m. energies. Altogether, W boson fusion is more sensitive to the trilinear Higgs self-coupling than Higgs-strahlung.

6 Acknowledgments

R.G. would like to thank the organizers for a very nice workshop and the possibility to give a talk. This research was supported in part by the Deutsche Forschungsgemeinschaft via the Sonderforschungsbereich/Transregio SFB/TR-9 Computational Particle Physics.

References

[1] G. Aad *et al.* [ATLAS Collaboration], Phys. Lett. B **716** (2012) 1 [arXiv:1207.7214 [hep-ex]].

[2] S. Chatrchyan *et al.* [CMS Collaboration], Phys. Lett. B **716** (2012) 30 [arXiv:1207.7235 [hep-ex]].

[3] P.W. Higgs, Phys. Lett. **12** (1964) 132; and Phys. Rev. **145** (1966) 1156; F. Englert and R. Brout, Phys. Rev. Lett. **13** (1964) 321; G.S. Guralnik, C.R. Hagen and T.W. Kibble, Phys. Rev. Lett. **13** (1964) 585.

[4] J. Baglio, A. Djouadi, R. Grober, M. M. Muhlleitner, J. Quevillon and M. Spira, arXiv:1212.5581 [hep-ph].

[5] A. Djouadi, W. Kilian, M. Muhlleitner and P. M. Zerwas, Eur. Phys. J. C **10** (1999) 45 [hep-ph/9904287].

[6] A. Djouadi, W. Kilian, M. Muhlleitner and P. M. Zerwas, Eur. Phys. J. C **10** (1999) 27 [hep-ph/9903229].

[7] M. M. Muhlleitner, hep-ph/0008127.

[8] E. Accomando *et al.* [CLIC Physics Working Group Collaboration], hep-ph/0412251.

[9] G. Cynolter, E. Lendvai and G. Pocsik, Acta Phys. Polon. B **31** (2000) 1749 [hep-ph/0003008]; T. Plehn and M. Rauch, Phys. Rev. D **72** (2005) 053008 [hep-ph/0507321]; T. Binoth, S. Karg, N. Kauer and R. Rückl, Phys. Rev. D **74** (2006) 113008.

[10] G. F. Giudice, C. Grojean, A. Pomarol and R. Rattazzi, JHEP **0706** (2007) 045 [hep-ph/0703164].

[11] D. B. Kaplan and H. Georgi, Phys. Lett. B **136** (1984) 183; S. Dimopoulos and J. Preskill, Nucl. Phys. B **199**, 206 (1982); T. Banks, Nucl. Phys. B **243**, 125 (1984); D. B. Kaplan, H. Georgi and S. Dimopoulos, Phys. Lett. B **136**, 187 (1984); H. Georgi, D. B. Kaplan and P. Galison, Phys. Lett. B **143**, 152 (1984); H. Georgi and D. B. Kaplan, Phys. Lett. B **145**, 216 (1984); M. J. Dugan, H. Georgi and D. B. Kaplan, Nucl. Phys. B **254**, 299 (1985).

[12] K. Agashe, R. Contino and A. Pomarol, Nucl. Phys. B **719** (2005) 165 [hep-ph/0412089].

[13] R. Contino, L. Da Rold and A. Pomarol, Phys. Rev. D **75** (2007) 055014 [hep-ph/0612048].

[14] G. Altarelli and R. Barbieri, Phys. Lett. B **253** (1991) 161; R. Barbieri, B. Bellazzini, V. S. Rychkov and A. Varagnolo, Phys. Rev. D **76** (2007) 115008 [arXiv:0706.0432 [hep-ph]].

[15] J. R. Espinosa, C. Grojean and M. Muhlleitner, JHEP **1005** (2010) 065 [arXiv:1003.3251 [hep-ph]].

[16] J. R. Espinosa, C. Grojean and M. Muhlleitner, arXiv:1202.1286 [hep-ph].

[17] See *e.g.*, J. R. Espinosa, C. Grojean, M. Muhlleitner and M. Trott, JHEP **1212** (2012) 045 [arXiv:1207.1717 [hep-ph]]; A. Azatov, R. Contino and J. Galloway, JHEP **1204** (2012) 127 [arXiv:1202.3415 [hep-ph]].

[18] O. J. P. Eboli, G. C. Marques, S. F. Novaes and A. A. Natale, Phys. Lett. B **197** (1987) 269; E. W. N. Glover and J. J. van der Bij, Nucl. Phys. B **309** (1988) 282; D. A. Dicus, C. Kao and S. S. D. Willenbrock, Phys. Lett. B **203** (1988) 457; T. Plehn, M. Spira and P. M. Zerwas, Nucl. Phys. B **479** (1996) 46 [Erratum-ibid. B **531** (1998) 655] [hep-ph/9603205].

[19] R. Grober and M. Muhlleitner, JHEP **1106** (2011) 020 [arXiv:1012.1562 [hep-ph]]; R. Grober and M. Muhlleitner, PoS CORFU **2011** (2011) 021.

[20] R. Contino, M. Ghezzi, M. Moretti, G. Panico, F. Piccinini and A. Wulzer, JHEP **1208** (2012) 154 [arXiv:1205.5444 [hep-ph]].

[21] U. Baur, T. Plehn and D. L. Rainwater, Phys. Rev. D **69** (2004) 053004 [hep-ph/0310056]; M. J. Dolan, C. Englert and M. Spannowsky, JHEP **1210** (2012) 112 [arXiv:1206.5001 [hep-ph]].

[22] S. Bock, R. Lafaye, T. Plehn, M. Rauch, D. Zerwas and P. M. Zerwas, Phys. Lett. B **694** (2010) 44 [arXiv:1007.2645 [hep-ph]].

[23] A. Falkowski, Phys. Rev. D **77** (2008) 055018 [arXiv:0711.0828 [hep-ph]]; I. Low and A. Vichi, Phys. Rev. D **84** (2011) 045019 [arXiv:1010.2753 [hep-ph]]; A. Azatov and J. Galloway, Phys. Rev. D 85 **055013** (2012) [arXiv:1110.5646 [hep-ph]].

[24] M. Gillioz, R. Grober, C. Grojean, M. Muhlleitner and E. Salvioni, JHEP **1210** (2012) 004 [arXiv:1206.7120 [hep-ph]]; S. Dawson, E. Furlan and I. Lewis, Phys. Rev. D **87** (2013) 014007 [arXiv:1210.6663 [hep-ph]].

[25] O. Matsedonskyi, G. Panico and A. Wulzer, arXiv:1204.6333 [hep-ph]; M. Redi and A. Tesi, JHEP **1210** (2012) 166 [arXiv:1205.0232 [hep-ph]]; D. Marzocca, M. Serone and J. Shu, JHEP **1208** (2012) 013 [arXiv:1205.0770 [hep-ph]]; A. Pomarol and F. Riva, JHEP **1208** (2012) 135 [arXiv:1205.6434 [hep-ph]].

[26] V. Barger, T. Han and R.J.N. Phillips, Phys. Rev. **D38** (1988) 2766.

[27] A. Dobrovolskaya and V. Novikov, Z. Phys. **C52** (1991) 427; D.A. Dicus, K.J. Kallianpur and S.S.D. Willenbrock, Phys. Lett. **B200** (1988) 187; A. Abbasabadi, W.W. Repko, D.A. Dicus and R. Vega, Phys. Rev. **D38** (1988) 2770; Phys. Lett. **B213** (1988) 386.

[28] K.J. Kallianpur, Phys. Lett. **B215** (1988) 392;

[29] G. Gounaris, D. Schildknecht and F. Renard, Phys. Lett. **B83** (1979) 191 and (**E**) **89B** (1980) 437.

[30] V.A. Ilyin, A.E. Pukhov, Y. Kurihara, Y. Shimizu and T. Kaneko, Phys. Rev. **D54** (1996) 6717.

[31] F. Boudjema and E. Chopin, Z. Phys. **C73** (1996) 85; V. Barger and T. Han, Mod. Phys. Lett. **A5** (1990) 667;

[32] J. Alwall, P. Demin, S. de Visscher, R. Frederix, M. Herquet, F. Maltoni, T. Plehn and D. L. Rainwater *et al.*, JHEP **0709** (2007) 028 [arXiv:0706.2334 [hep-ph]].

[33] R. Contino, M. Ghezzi, C. Grojean, M. Muhlleitner and M. Spira, arXiv:1303.3876 [hep-ph].

[34] C. Castanier, P. Gay, P. Lutz and J. Orloff, In *2nd ECFA/DESY Study 1998-2001* 1362-1372 [hep-ex/0101028];
J. Tian, K. Fujii and Y. Gao, arXiv:1008.0921 [hep-ex].

[35] M. Battaglia, E. Boos and W. -M. Yao, eConf C **010630** (2001) E3016 [hep-ph/0111276]; Y. Yasui, S. Kanemura, S. Kiyoura, K. Odagiri, Y. Okada, E. Senaha and S. Yamashita, hep-ph/0211047.

[36] U. Baur, Phys. Rev. D **80** (2009) 013012 [arXiv:0906.0028 [hep-ph]].

[37] A. Thamm, PoS CORFU **2011** (2011) 035.

[38] V. Barger, T. Han, P. Langacker, B. McElrath and P. Zerwas, Phys. Rev. D **67** (2003) 115001 [hep-ph/0301097].

[39] R. Contino, C. Grojean, M. Moretti, F. Piccinini and R. Rattazzi, JHEP **1005** (2010) 089 [arXiv:1002.1011 [hep-ph]].

[40] R. Contino, D. Marzocca, D. Pappadopulo and R. Rattazzi, JHEP **1110** (2011) 081 [arXiv:1109.1570 [hep-ph]]; B. Bellazzini, C. Csaki, J. Hubisz, J. Serra and J. Terning, JHEP **1211** (2012) 003 [arXiv:1205.4032 [hep-ph]].

[41] G. Moortgat-Pick *et al.*, Phys. Rept. **460** (2008) 131 [hep-ph/0507011]; T. Abe *et al.* [ILD Concept Group - Linear Collider Collaboration], arXiv:1006.3396 [hep-ex].

Chapter 6

Supersymmetry

Implications of the 125 GeV Higgs for Supersymmetry

Sabine Kraml

Laboratoire de Physique Subatomique et de Cosmologie, UJF Grenoble 1,
CNRS/IN2P3, INPG, 53 Avenue des Martyrs, F-38026 Grenoble, France

The current LHC Higgs results may be used as a guide for where to look for SUSY. This contribution discusses implications of the 125 GeV Higgs boson for the MSSM and NMSSM. Using boundary conditions at the GUT scale, gluinos and light-flavor squarks turn out to be heavy, in accordance with the current SUSY search limits, while stops can still be light, below 1 TeV. The observed Higgs signal is much easier accommodated in the NMSSM than in the MSSM. Particularly interesting are NMSSM scenarios with large λ and small $\tan\beta$: they are characterized by light stops and light higgsinos, and offer the intriguing possibilities of, e.g., observing a second light Higgs boson with lower mass, or two (quasi-)degenerate Higgs bosons near 125 GeV.

1 Introduction

The recent discovery [1, 2] of a new particle with mass around 125 GeV and properties consistent with a Standard Model (SM) Higgs boson is a first triumph for the LHC physics program. However, while this discovery completes our picture of the SM, it still leaves many fundamental questions open. One of the most pressing issues is that the SM does not explain the value of the electroweak (EW) scale itself: Why is the Higgs boson so light when it is predicted to be driven to the scale of Grand Unified Theories ($M_{\rm GUT}$), or even the Planck scale, by radiative corrections? Either new physics appears at the EW scale, or the Higgs mass-squared is fine tuned at the 10^{-32} level.

New particles that couple to the Higgs can however also modify the Higgs couplings, and thus the production and decay rates in various channels. So on the one hand we expect physics beyond the SM (BSM) to explain the Higgs mass, on the other hand the measured mass and signal strengths provide significant constraints on concrete BSM realizations, see *e.g.* [3, 4]. Moreover, while the SM provides a reasonably good fit to to the current data, based on the results published in 2012, some new physics contributions to the effective Higgs couplings to gluons and photons are preferred, as shown in Fig. 1.[1]

The arguably best motivated extension of the SM is weak-scale supersymmetry (SUSY), introducing a new symmetry between fermions and bosons. SUSY solves the hierarchy problem provided SUSY particles exist

[1] Based on the experimental results available at the end of 2012.

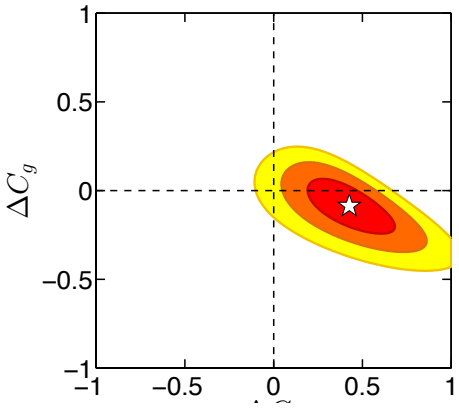

Figure 1: Global fit of additional loop contributions ΔC_g and ΔC_γ from new particles to the Higgs couplings to gluons and photons, assuming SM values for the couplings to W, Z and SM fermions. The fit includes all available Higgs signal strengths from ATLAS, CMS and the Tevatron experiments. The red, orange and yellow ellipses show the 68%, 95% and 99.7% CL regions, respectively. The white star marks the best-fit point $\Delta C_g = -0.086$, $\Delta C_\gamma = 0.426$. From [4].

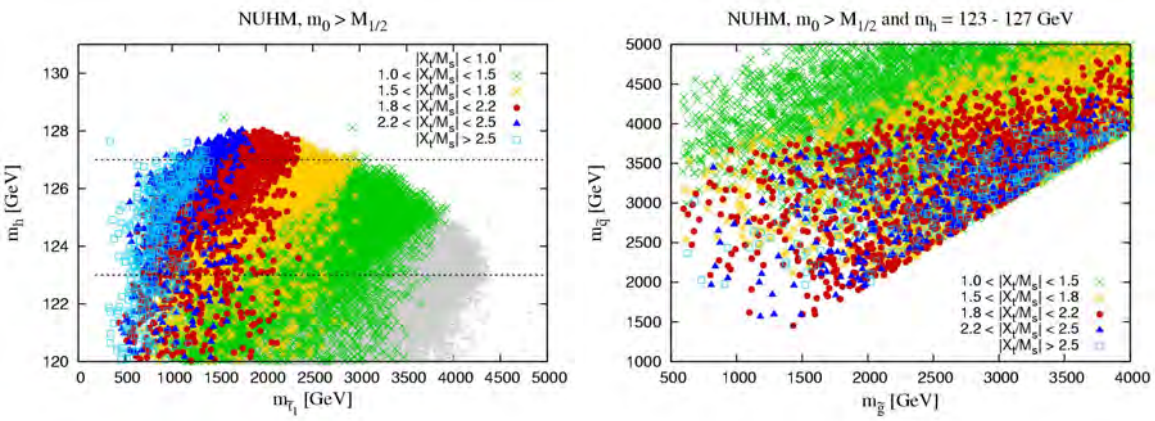

Figure 2: Left: dependence of m_h on $m_{\tilde{t}_1}$ in the NUHM model, with the amount of stop mixing indicated by a color code. Right: projection of the points with $m_h = 123$–127 GeV in the squark versus gluino mass plane. From [6].

at or around the TeV energy scale. The (Next-to-) Minimal Supersymmetric Standard Model, (N)MSSM, moreover predicts a light, often SM-like, Higgs boson with mass below ≈ 135 (140) GeV. This has always been regarded as an intriguing feature, and even more so with the actual observation of a Higgs-like state at 125 GeV. So far, however, SUSY searches at ATLAS and CMS show no signal whatsoever, and the mass limits in particular for squarks and gluinos have been pushed well into the TeV range [7, 8].

So the Higgs has been found — but where is supersymmetry? In fact, the SUSY particles relevant for the Higgs sector and the hierarchy problem, stops and higgsinos, are much less constrained than light-flavor squarks and gluinos. "Natural" SUSY still lives on. In this talk I therefore discuss some implications of the LHC Higgs results for supersymmetric models.

2 Minimal Supersymmetric Standard Model

In the MSSM, $m_h^2 = m_Z^2 \cos^2 2\beta$ at tree level, where $\tan\beta = v_u/v_d$, $v = \sqrt{v_u^2 + v_d^2} = 174$ GeV. This quickly saturates to $m_h^2 \lesssim m_Z^2$ for $\tan\beta \gtrsim 5$. To further lift m_h^2 from $m_Z^2 = (91\text{ GeV})^2$ to around $(125\text{ GeV})^2$, radiative corrections nearly as large as the tree-level value are required. The leading one-loop correction comes from the top–stop sector and is given by [5]

$$\Delta m_h^2 = \frac{3}{4\pi^2}\frac{m_t^4}{v^2}\left(\log\frac{M_S^2}{m_t^2} + \frac{X_t^2}{M_S^2}\left(1 - \frac{X_t^2}{12\,M_S^2}\right)\right). \tag{1}$$

Here m_t is the running top-quark mass at the scale m_t, $M_S^2 = m_{\tilde{t}_1} m_{\tilde{t}_2}$ with $m_{\tilde{t}_{1,2}}$ the stop masses, and X_t is the stop mixing parameter, $X_t = A_t - \mu\cot\beta$, at the scale M_S. The contribution from the logarithmic term in Eq. (1) can be increased by simply raising M_S, but naturalness demands that the SUSY scale should be not too far above the EW scale. The X_t contribution is maximized at $|X_t/M_S| \simeq \sqrt{6} = 2.45$; this is called the maximal-mixing scenario.

As a consequence, $m_h \simeq 125$ GeV requires either (unnaturally) heavy stops, or maximal mixing. This is illustrated in Fig. 2 for a semi-constrained version of the MSSM with universal gaugino mass $M_{1/2}$, scalar mass m_0 and trilinear coupling A_0 all defined at $M_{\rm GUT}$, but non-universal Higgs mass parameters (NUHM model). As can be seen, a 125 GeV Higgs together with stops in the 0.5–1 TeV mass range indeed requires maximal mixing, *i.e.* very large $|A_t|$ (left plot). At the same time, gluinos and 1st/2nd generation squarks turn out to be heavy, with masses above 1–2 TeV (right plot), thus automatically avoiding the current LHC

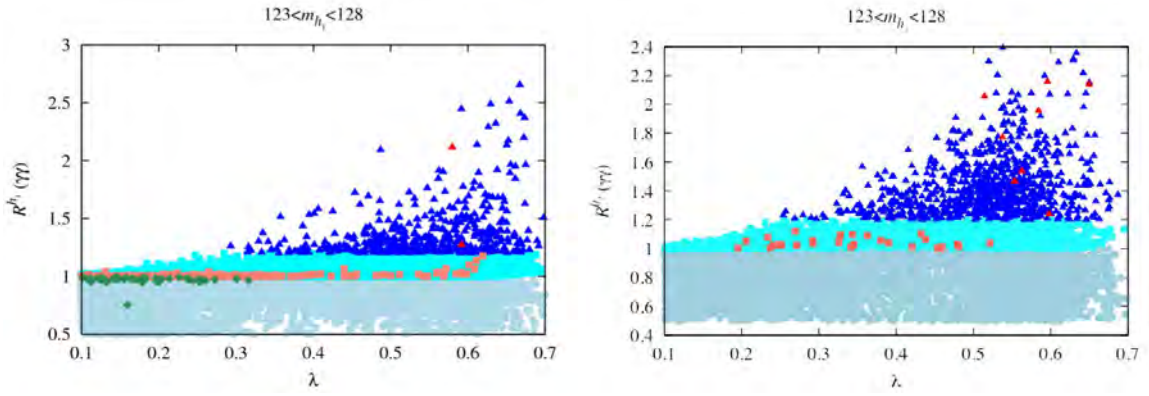

Figure 3: Signal strength (relative to SM) in the $h_i \to \gamma\gamma$ channel as function of λ from a scan over the semi-constrained NMSSM, on the left for the h_1 lying in the $123-128$ GeV mass range, on the right for the h_2 lying in the $123-128$ GeV range. See text for color code.

3 Next-to-Minimal Supersymmetric Standard Model

The NMSSM differs from the MSSM by to the presence of the gauge singlet superfield $\hat{S}$ [9]. In the simplest Z_3 invariant realization of the NMSSM, the Higgs mass term $\mu \hat{H}_u \hat{H}_d$ in the superpotential $W_{\rm MSSM}$ of the MSSM is replaced by the coupling λ of $\hat{S}$ to $\hat{H}_u$ and $\hat{H}_d$ and a self-coupling κS^3. The superpotential $W_{\rm NMSSM}$ is given by:

$$W_{\rm NMSSM} = \lambda \hat{S} \hat{H}_u \cdot \hat{H}_d + \frac{\kappa}{3} \hat{S}^3 + \dots \ , \tag{2}$$

where hatted letters denote superfields, and the dots denote the MSSM-like Yukawa couplings of $\hat{H}_u$ and $\hat{H}_d$ to the quark and lepton superfields. Once the real scalar component of $\hat{S}$ develops a vev $\langle S \rangle$, the first term in $W_{\rm NMSSM}$ generates an effective μ-term, $\mu_{\rm eff} = \lambda \langle S \rangle$.

As compared to two independent parameters in the Higgs sector of the MSSM at tree level, often chosen as $\tan\beta$ and M_A, the Higgs sector is now described by

$$\lambda \ , \ \kappa \ , \ A_\lambda \ , \ A_\kappa, \ \tan\beta \ = v_u/v_d \ , \ \mu_{\rm eff} \ . \tag{3}$$

The neutral Higgs sector of this model consists of three CP-even (h_1, h_2, h_3) and two CP-odd (a_1, a_2) states. The CP-even mass eigenstates are superpositions of the neutral CP-even components of H_u, H_d, S:

$$\begin{aligned} h_1 &= \mathcal{S}_{1,d} \, H_d + \mathcal{S}_{1,u} \, H_u + \mathcal{S}_{1,s} \, S \ , \\ h_2 &= \mathcal{S}_{2,d} \, H_d + \mathcal{S}_{2,u} \, H_u + \mathcal{S}_{2,s} \, S \ , \\ h_3 &= \mathcal{S}_{3,d} \, H_d + \mathcal{S}_{3,u} \, H_u + \mathcal{S}_{3,s} \, S \ , \end{aligned} \tag{4}$$

with the couplings to gauge bosons and fermions determined by the 3×3 mixing matrix $\mathcal{S}$, *e.g.* $g_{h_i VV}/g_{H_{\rm SM}VV} = \cos\beta \, \mathcal{S}_{i,d} + \sin\beta \, \mathcal{S}_{i,u}$.

An interesting feature is that the coupling $\lambda S \hat{H}_u \hat{H}_d$ in the superpotential leads to an extra tree-level contribution to the SM-like Higgs mass $m_h^2 = m_Z^2 \cos^2 2\beta + \lambda v^2 \sin^2 2\beta + \Delta m_h^2$. It is thus much easier to obtain $m_h \simeq 125$ GeV in constrained versions of the NMSSM then in their MSSM equivalents [10]. Moreover, as pointed out by Ellwanger [11, 12], for large λ (and small $\tan\beta$) doublet–singlet mixing can reduce the hbb coupling, thus enhancing the di-photon signal at the LHC. This works in fact for both, the lightest and the second-lightest scalar, h_1 and h_2, and either of them could be the observed state at 125 GeV [12, 10, 13].

For illustration, Fig. 3 shows the result of a scan of the "semi-constrained" NMSSM with universal m_0, $M_{1/2}$ and A_0 at the GUT scale, but the NMSSM-specific parameters of Eq. (3) treated as free parameters at the EW scale. The scan was performed with `NMSSMTools` [14]; all points have a neutralino as the lightest

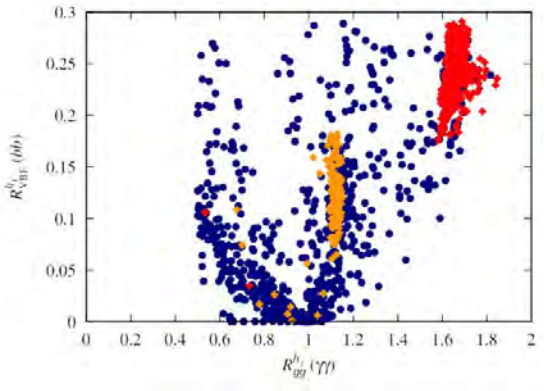

Figure 4: Signal strengths (relative to SM) $R^{h_1}_{\rm VBF}(b\bar{b})$ versus $R^{h_2}_{gg}(\gamma\gamma)$ for $m_{h_1} \in [96, 100]$ GeV and $m_{h_2} \in [123, 128]$ GeV in the semi-constrained NMSSM. Blue points have $\Omega h^2 < 0.094$ while red and orange points have $\Omega h^2 \in [0.094, 0.136]$. From [15].

ΔM_d, BR($B_s \to \mu^+\mu^-$), BR($B^+ \to \tau^+\nu_\tau$) and BR($B \to X_s\mu^+\mu^-$) at 2σ. The light, medium and dark blue points have $\Omega h^2 \leq 0.136$ and obey the bounds on the spin-independent LSP–proton scattering cross section from XENON100. Light and medium red points have $0.094 \leq \Omega h^2 \leq 0.136$ and of course also pass the XENON100 bounds. (The shades of blue and red just help indicate the level of enhancement or suppression of the $\gamma\gamma$ signal.) The green points have $\Omega h^2 \leq 0.136$ and in addition explain Δa_μ within 2σ.

4 Two Higgs bosons at 98 and 125 GeV

If the h_2 of the NMSSM is responsible for the signal at 125 GeV, a particularly interesting question [15] is whether one could simultaneously explain the LHC signal and the small ($\sim 2\sigma$) LEP excess in $e^+e^- \to Zb\overline{b}$ in the vicinity of $M_{b\bar{b}} \sim 98$ GeV. We recall that the LEP excess is clearly inconsistent with a SM-like Higgs boson at this mass, being only about $10 - 20\%$ of the rate predicted for the $H_{\rm SM}$. Consistency with such a result for the h_1 is natural if the h_1 couples at a reduced level to ZZ, which, in turn, is automatic if the h_2 has substantial ZZ coupling, as required by the observed LHC signals.

As above, we perform a scan over the semi-constrained NMSSM. We compute the ratio of the gg or VBF induced Higgs cross section times the Higgs branching ratio to a given final state X, relative to the corresponding value for the SM Higgs boson, as[2]

$$R^{h_i}_{gg}(X) \equiv \frac{\Gamma(h_i \to gg)\ {\rm BR}(h_i \to X)}{\Gamma(H_{\rm SM} \to gg)\ {\rm BR}(H_{\rm SM} \to X)}, \quad R^{h_i}_{\rm VBF}(X) \equiv \frac{\Gamma(h_i \to WW)\ {\rm BR}(h_i \to X)}{\Gamma(H_{\rm SM} \to WW)\ {\rm BR}(H_{\rm SM} \to X)}, \tag{5}$$

where h_i is the i^{th} NMSSM scalar Higgs, and $H_{\rm SM}$ is the SM Higgs boson, taking $m_{H_{\rm SM}} = m_{h_i}$.

To describe the LEP and LHC data the h_1 and h_2 must have $m_{h_1} \sim 98$ GeV and $m_{h_2} \sim 125$ GeV, respectively, with the h_1 being largely singlet and the h_2 being primarily doublet (mainly H_u for the scenarios we consider). Figure 4 shows $R^{h_1}_{\rm VBF}(b\bar{b})$ versus $R^{h_2}_{gg}(\gamma\gamma)$ for the scan points that pass LEP, B-physics and dark matter constraits as above and have in addition $m_{h_1} \in [96, 100]$ GeV and $m_{h_2} \in [123, 128]$ GeV. (These ranges take into account a 2–3 GeV theoretical error in the computation of the Higgs masses.) The points with $0.1 \leq R^{h_1}_{\rm VBF}(b\bar{b}) \leq 0.25$ would provide the best fit to the LEP excess. As can be seen, a large portion of these points have $R^{h_2}_{gg}(\gamma\gamma) > 1$ as preferred by LHC data.

In the following we thus require $m_{h_1} \in [96, 100]$ GeV with $0.1 \leq R^{h_1}_{\rm VBF}(b\bar{b}) \leq 0.25$, and $m_{h_2} \in [123, 128]$ GeV with $R^{h_2}_{gg}(\gamma\gamma) > 1$. We refer to this as the "$98 + 125$ GeV Higgs scenario". Points with $\Omega h^2 < 0.094$ are represented by blue circles and points with $\Omega h^2 \in [0.094, 0.136]$ (the "WMAP window") are represented by red/orange diamonds.

Two distinct WMAP-window regions appear. The red region has $R^{h_2}_{gg}(\gamma\gamma) \sim 1.6$ and corresponds $\mu_{\rm eff} \sim 120$ GeV and $\tan\beta \sim 2$; as can be seen in Fig. 5, it features a partly light spectrum with $m_{\widetilde{\chi}^0_1} \sim 70 - 80$ GeV, $m_{\widetilde{\chi}^\pm_1} \sim 105 - 110$ GeV and $m_{\tilde{t}_1} \sim 0.2 - 1$ TeV, while $m_{\tilde{g}} \gtrsim 1$ TeV and $m_{\tilde{q}} \gtrsim 2$ TeV. Again, LHC SUSY limits are automatically avoided by the Higgs-sector requirements. Moreover, the other Higgses are light,

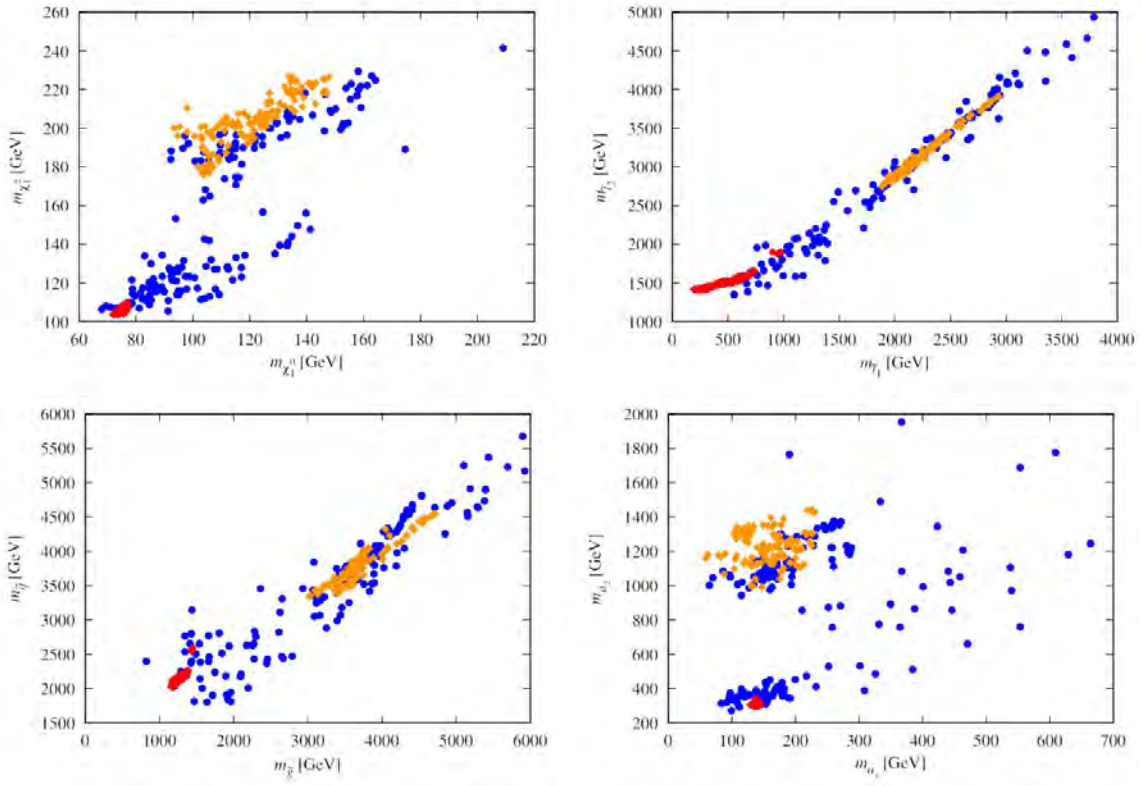

Figure 5: Expectations for sparticle and Higgs masses in the $98+125$ GeV Higgs scenario. Blue points have $\Omega h^2 < 0.094$ while red and orange points have $\Omega h^2 \in [0.094, 0.136]$. From [15].

too, $m_{a_2} \sim 150$ GeV and $m_{h_3} \simeq m_{H^\pm} \simeq m_{a_2} \sim 300-400$ GeV. The orange region is quite different. It appears at $\mu_{\rm eff} \sim 200$ GeV and $\tan\beta \sim 5-8$ and has $R^{h_2}_{gg}(\gamma\gamma) \sim 1.1$. The overall mass scale is much heavier: $m_{\widetilde{\chi}^0_1} \sim 90-150$ GeV and $m_{\tilde{t}_1} > 1.8$ TeV, see Fig. 5. Squarks and gluinos lie in the $3-5$ TeV mass range, above the reach of the 14 TeV LHC. The heavy Higgses also have masses above 1 TeV, only the a_1 is still light with $m_{a_1} \lesssim 250$ GeV.

The LSP decomposition and its expected spin-independent scattering cross section off protons are shown in Fig. 6. The prospects to test the $98+125$ GeV Higgs scenario at the LHC and a future ILC are discussed in detail in [15]. Obviously the ILC would be the ideal machine to explore the light charginos and neutralinos present in this scenario, and to precisely measure their properties.

An e^+e^- collider would also be the ideal machine to produce the additional Higgs states. Production cross sections for the various Higgs final states are shown in Fig. 7 for three illustrative scenarios specified in Table 1 taken from our NMSSM scans. The first plot is for a WMAP-window scenario with $m_{\widetilde{\chi}^0_1} \sim 76$ GeV and light Higgs bosons. The third plot is for the point in region B with smallest m_{h_3}, for which $m_{a_2}, m_{h_3}, m_{H^\pm}$ are all around 1 TeV. The second plot is for a sample scenario with Higgs masses that are intermediate, as only possible if Ωh^2 lies below the WMAP window. With an integrated luminosity of 1000 fb^{-1}, substantial event rates for many Z+Higgs and Higgs pair final states are predicted. In the e^+e^- collider case, it would be easy to isolate signals in many final states. For example, in the case of Higgs pairs, final states such as $(t\overline{t})(t\overline{t})$, $(\widetilde{\chi}^0_1\widetilde{\chi}^0_1)(t\overline{t})$ and so forth could be readily identified above background. Observation of the $(\widetilde{\chi}^0_1\widetilde{\chi}^0_1)(\widetilde{\chi}^0_1\widetilde{\chi}^0_1)$ final states would require a photon tag and would thus suffer from a reduced cross section. Associated Z+Higgs, with Higgs decaying to $t\overline{t}$ or $\widetilde{\chi}^0_1\widetilde{\chi}^0_1$ would be even more readily observed.

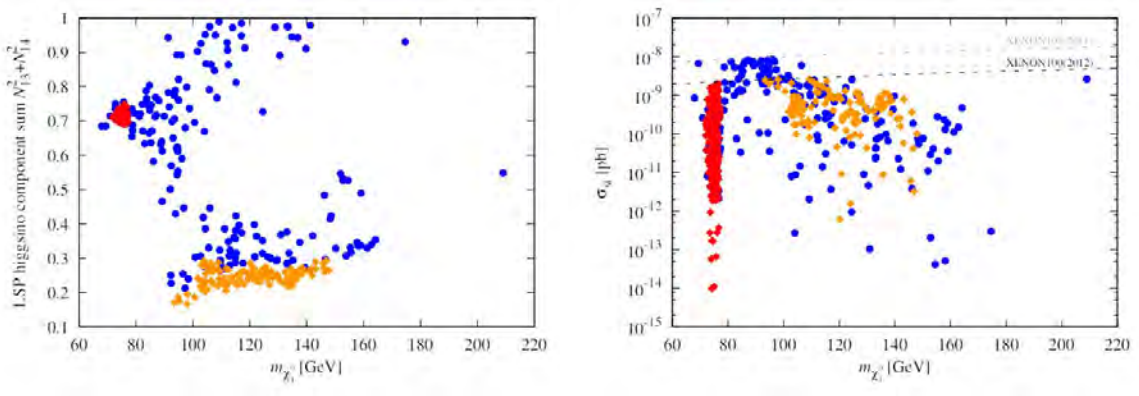

Figure 6: LSP higgsino component (left) and spin-independent scattering cross section (right) as function of the LSP mass for the $98 + 125$ GeV Higgs scenarios. From [15].

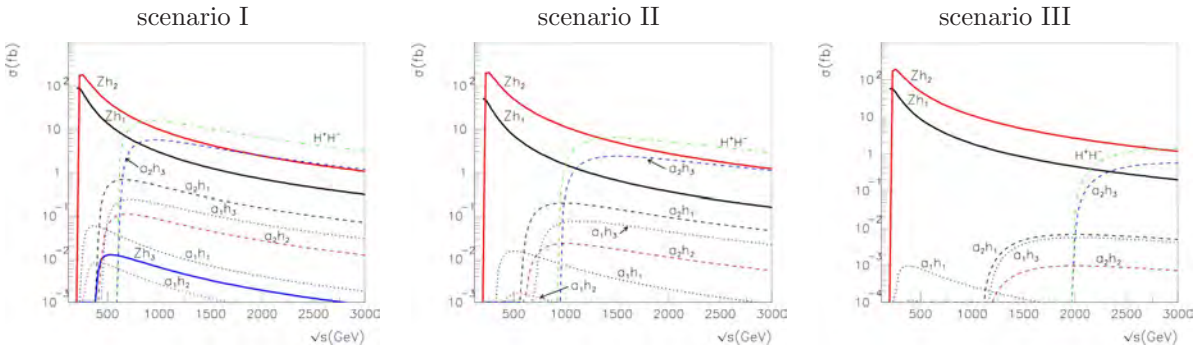

Figure 7: Cross sections for Higgs production at an e^+e^- collider, as functions of the center-of-mass energy $\sqrt{s}$, for three illustrative mass spectra as tabulated in Table 1. From [15].

Table 1: Higgs masses and LSP mass in GeV for the two scenarios for which we plot e^+e^- cross sections in Fig. 7. Also given are Ωh^2, the singlino and Higgsino percentages and $R_{gg}^{h_2}(\gamma\gamma)$. Scenarios I) and III) have Ωh^2 in the WMAP window, with I) being typical of the low-$m_{\widetilde{\chi}_1^0}$ scenarios and III) being that with smallest m_{h_3} in the large-$m_{\widetilde{\chi}_1^0}$ group of points in the WMAP window. Scenario II) is chosen to have m_{a_2} and m_{h_3} intermediate between those for scenario I) and III), a region for which Ωh^2 is substantially below 0.1.

Scenario	m_{h_1}	m_{h_2}	m_{h_3}	m_{a_1}	m_{a_2}	$m_{H^\pm}$	$m_{\widetilde{\chi}_1^0}$	Ωh^2	LSP singlino	LSP Higgsino	$R_{gg}^{h_2}(\gamma\gamma)$
I	99	124	311	140	302	295	76	0.099	18%	75%	1.62
II	97	124	481	217	473	466	92	0.026	20%	74 %	1.53
III	99	126	993	147	991	989	115	0.099	75%	25%	1.14

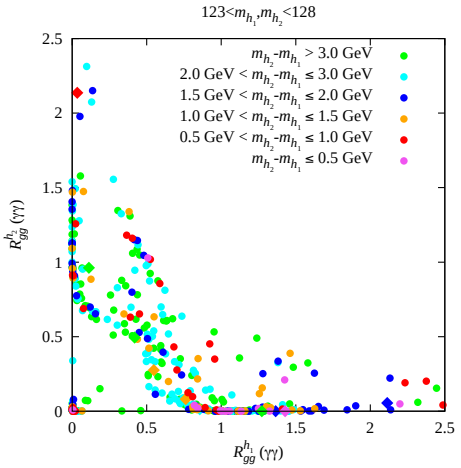

Figure 8: Correlation of $gg \to (h_1, h_2) \to \gamma\gamma$ signal strengths when both h_1 and h_2 lie in the 123–128 GeV mass range. Circular points have $\Omega h^2 < 0.094$, while diamond points have $0.094 \leq \Omega h^2 \leq 0.136$. Points are color coded according to $m_{h_2} - m_{h_1}$ as indicated on the figure. From [16].

5 Degenerate case: two Higgses hiding in the 125 GeV signal?

As mentioned, enhanced rates in the $\gamma\gamma$ channel arise in the NMSSM with large λ when the h_1 and h_2 are sufficiently close in mass that one Higgs, h_i, "steals" (through mixing) some of the $b\bar{b}$ width of the other Higgs, h_j. The state with the enhanced $\gamma\gamma$ signal and mass near 125 GeV can be either the h_1 or the h_2. It is however also possible that h_1 and h_2 both lie in the 123–128 GeV mass window [16]. In this case, a second mechanism for large $\gamma\gamma$ rates emerges — namely both h_1 and h_2 contribute significantly and their summed rate is enhanced even though their individual rates are more or less at, or even somewhat below, the SM level.

Figure 8 shows the correlation of $gg \to (h_1, h_2) \to \gamma\gamma$ signal strengths in the semi-constrained NMSSM when both h_1 and h_2 lie in the 123–128 GeV mass range. We see that often one Higgs dominates the signal, but it is also possible that both have $R_{gg}^{h_i}(\gamma\gamma) \gtrsim 0.5$ thus giving a combined signal larger than 1.

To go a step further, we take the net signal in given production and decay channels Y and X to simply be $R_Y^h(X) = R_Y^{h_1}(X) + R_Y^{h_2}(X)$, and we define the resulting "effective" Higgs mass as

$$m_h^Y(X) \equiv \frac{R_Y^{h_1}(X) m_{h_1} + R_Y^{h_2}(X) m_{h_2}}{R_Y^{h_1}(X) + R_Y^{h_2}(X)} \,. \tag{6}$$

Of course, the extent to which it is appropriate to combine the rates from the h_1 and h_2 depends upon the degree of degeneracy and the experimental resolution. It should be noted that the widths of the h_1 and h_2 are of the same order of magnitude as the width of a 125 GeV SM Higgs boson, *i.e.* they are very much smaller than this resolution.

In Fig. 9, we display in the left-hand plot the strong correlation between $R_{gg}^h(\gamma\gamma)$ and $R_{gg}^h(VV)$, $V = W, Z$. Note that if $R_{gg}^h(\gamma\gamma) \sim 1.5$, as suggested by current experimental results, then in this scenario $R_{gg}^h(VV) \geq 1.2$. In the right-hand plot, we show $R_{gg}^h(\gamma\gamma)$ versus the mass of the lighter pseudoscalar a_1. It is interesting to note that for the bulk of the points with (quasi-)degenerate $h_{1,2}$ also the other Higgs states tend to be light, with $m_{a_1} \lesssim 300$ GeV and $m_{a_2} \simeq m_{h_3} \simeq m_{H^\pm} \lesssim 500$ GeV.

The scenario again prefers small $\mu_{\rm eff}$ of order 100–200 GeV, which is very favorable in point of view of fine tuning, in particular if stops are also light. Indeed a good fraction of our points with degenerate h_1, h_2 and $R(\gamma\gamma) > 1$ features light stops with $m_{\tilde{t}_1} \in [300, 700]$ GeV and $M_{\rm SUSY} = \sqrt{m_{\tilde{t}_1} m_{\tilde{t}_2}} \lesssim 1$ TeV. Because of the small $\mu_{\rm eff}$, the LSP is dominantly a light higgsino. A relic density of $\Omega h^2 \simeq 0.1$ can be achieved for LSP masses just below 80 GeV, see Fig. 10. The LSP is 70–80% higgsino in this case, with order 20% singlino admixture. The ILC would again be the ideal machine to explore this scenario.

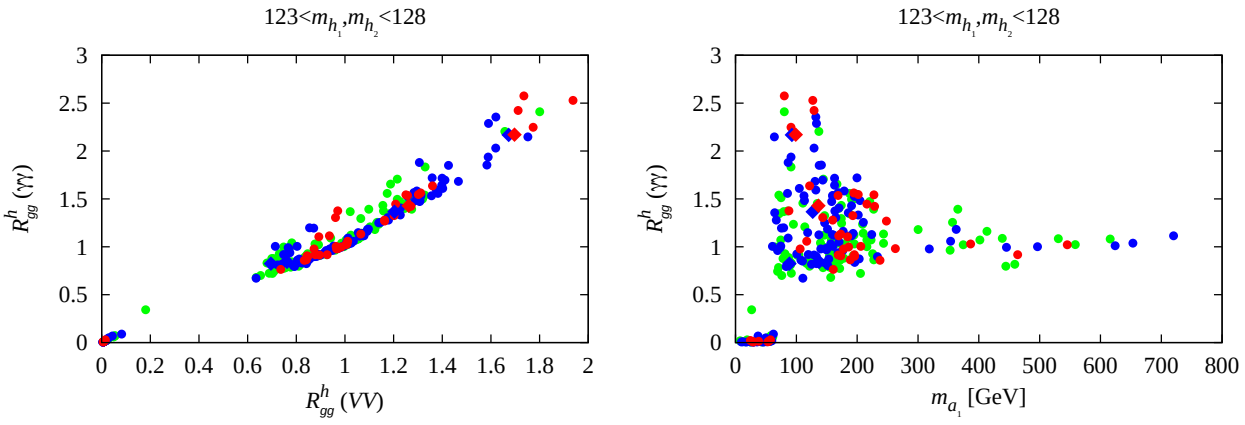

Figure 9: Correlation between the gg induced $\gamma\gamma$ and VV signal strengths (left) and $R^h_{gg}(\gamma\gamma)$ versus the mass of a_1 (right) for NMSSM points with quasi-degenerate h_1 and h_2 in the 123–128 GeV mass window. The green, blue and red points have $\Delta m = m_{h_2} - m_{h_1} = 2$–$3$ GeV, $\Delta m = 1$–2 GeV and $\Delta m \leq 1$ GeV, respectively. From [16].

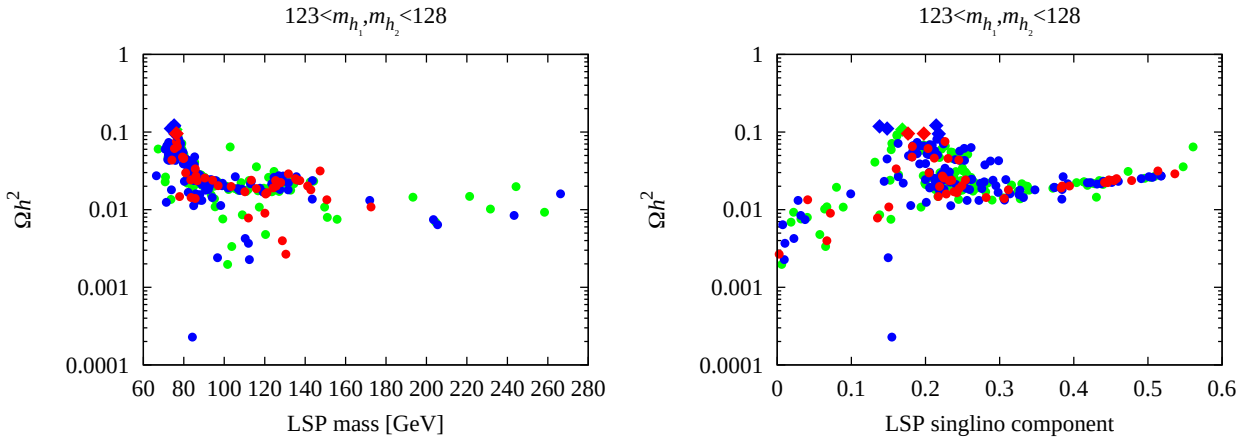

Figure 10: Relic density Ωh^2 versus LSP mass (left) and versus LSP singlino component (right) for NMSSM points with quasi-degenerate h_1 and h_2 in the 123–128 GeV mass window. The green, blue and red points have $\Delta m = m_{h_2} - m_{h_1} = 2$–$3$ GeV, $\Delta m = 1$–2 GeV and $\Delta m \leq 1$ GeV, respectively. From [16].

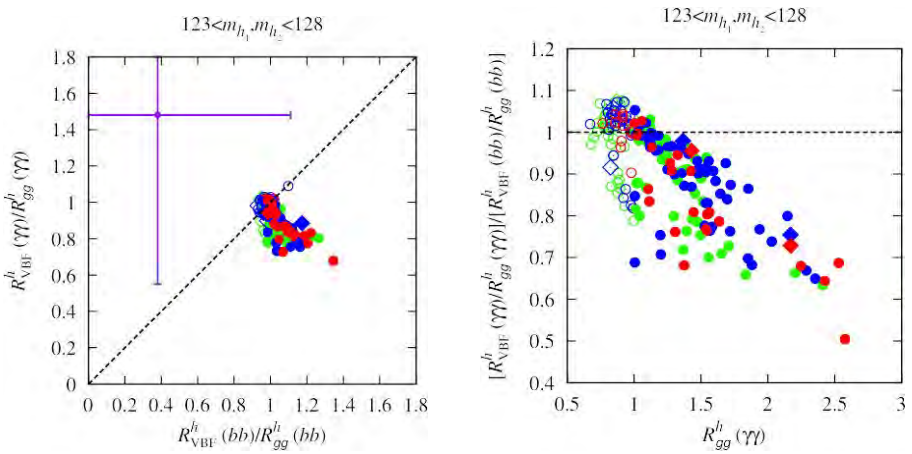

Figure 11: Illustration of the double ratio I) of Eq. (7) for degenerate h_1 and h_2 in the 123–128 GeV mass range in the semi-constrained NMSSM. The green, blue and red points have $\Delta m = m_{h_2} - m_{h_1} = 2$–3 GeV, $\Delta m = 1$–2 GeV and $\Delta m \leq 1$ GeV, respectively. From [17].

6 Diagnosing degenerate Higgs bosons

Two or more degenerate Higgs bosons will in general have different relative production rates in the VBF and gg fusion channels for one or more final states. In [17] we thus proposed double ratios of signal strengths as a useful diagnostic tool to reveal the existence of one ore more quasi-degenerate (but non-interfering in the small width approximation) Higgs states. For models with Higgs doublets+singlets, the relevant double ratios are:

$$\text{I):}\ \frac{R^h_{\rm VBF}(\gamma\gamma)/R^h_{gg}(\gamma\gamma)}{R^h_{\rm VBF}(b\bar{b})/R^h_{gg}(b\bar{b})},\quad \text{II):}\ \frac{R^h_{\rm VBF}(\gamma\gamma)/R^h_{gg}(\gamma\gamma)}{R^h_{\rm VBF}(WW)/R^h_{gg}(WW)},\quad \text{III):}\ \frac{R^h_{\rm VBF}(WW)/R^h_{gg}(WW)}{R^h_{\rm VBF}(b\bar{b})/R^h_{gg}(b\bar{b})}, \tag{7}$$

each of which should be unity if only a single Higgs boson is present but are generally expected to deviate from 1 if two (or more) Higgs bosons are contributing to the net Higgs signals. Values obtained in the semi-constrained NMSSM are shown in Fig. 11.

7 Conclusions

In summary, the observation of the 125 GeV Higgs boson at the LHC has important implications for supersymmetric models. In particular, in the MSSM and NMSSM scenarios discussed here, gluinos and squarks of the first two generations tend to be heavy, in agreement with the non-observation of SUSY signals at the LHC, while stops and EW-inos can be light. Within NMSSM, there exists the intriguing possibility of additional Higgs states in the vicinity of, or degenerate with, the state at 125 GeV. This offers extremely interesting possibilities for precision Higgs physics a the ILC. Neutralinos and charginos are also expected to be light in these scenarios; the lightest states are typically higgsino-like and thus difficult to observe at the LHC. An e^+e^- collider would be the ideal machine to resolve such scenarios.

Acknowledgements

I wish to thank Genevieve Belanger, Felix Brümmer, Beranger Dumont, Ulrich Ellwanger, John F. Gunion, Suchita Kulkarni and Yun Jiang for fruitful and rewarding collaborations, and Gudrid Moortgat-Pick for pushing me to write this contribution. The work presented here was supported in part by IN2P3 under

References

[1] G. Aad *et al.* [ATLAS Collaboration], "Observation of a new particle in the search for the Standard Model Higgs boson with the ATLAS detector at the LHC," Phys. Lett. B **716** (2012) 1 [arXiv:1207.7214 [hep-ex]].

[2] S. Chatrchyan *et al.* [CMS Collaboration], "Observation of a new boson at a mass of 125 GeV with the CMS experiment at the LHC," Phys. Lett. B **716** (2012) 30 [arXiv:1207.7235 [hep-ex]].

[3] G. Cacciapaglia, A. Deandrea, G. D. La Rochelle and J. -B. Flament, "Higgs couplings beyond the Standard Model," JHEP **1303** (2013) 029 [arXiv:1210.8120 [hep-ph]].

[4] G. Belanger, B. Dumont, U. Ellwanger, J. F. Gunion and S. Kraml, "Higgs Couplings at the End of 2012," JHEP **1302** (2013) 053 [arXiv:1212.5244 [hep-ph]].

[5] A. Djouadi, "The Anatomy of electro-weak symmetry breaking. II. The Higgs bosons in the minimal supersymmetric model," Phys. Rept. **459** (2008) 1 [hep-ph/0503173].

[6] F. Brummer, S. Kraml and S. Kulkarni, "Anatomy of maximal stop mixing in the MSSM," JHEP **1208** (2012) 089 [arXiv:1204.5977 [hep-ph]].

[7] `https://twiki.cern.ch/twiki/bin/view/AtlasPublic/SupersymmetryPublicResults`.

[8] `https://twiki.cern.ch/twiki/bin/view/CMSPublic/PhysicsResultsSUS`.

[9] For a review, see *e.g.* U. Ellwanger, C. Hugonie and A. M. Teixeira, "The Next-to-Minimal Supersymmetric Standard Model," Phys. Rept. **496** (2010) 1 [arXiv:0910.1785 [hep-ph]].

[10] J. F. Gunion, Y. Jiang and S. Kraml, "The Constrained NMSSM and Higgs near 125 GeV," Phys. Lett. B **710** (2012) 454 [arXiv:1201.0982 [hep-ph]].

[11] U. Ellwanger, "Enhanced di-photon Higgs signal in the Next-to-Minimal Supersymmetric Standard Model," Phys. Lett. B **698** (2011) 293 [arXiv:1012.1201 [hep-ph]].

[12] U. Ellwanger, "A Higgs boson near 125 GeV with enhanced di-photon signal in the NMSSM," JHEP **1203** (2012) 044 [arXiv:1112.3548 [hep-ph]].

[13] U. Ellwanger and C. Hugonie, "Higgs bosons near 125 GeV in the NMSSM with constraints at the GUT scale," Adv. High Energy Phys. **2012** (2012) 625389 [arXiv:1203.5048 [hep-ph]].

[14] `http://www.th.u-psud.fr/NMHDECAY/nmssmtools.html`.

[15] G. Belanger, U. Ellwanger, J. F. Gunion, Y. Jiang, S. Kraml and J. H. Schwarz, "Higgs Bosons at 98 and 125 GeV at LEP and the LHC," JHEP **1301** (2013) 069 [arXiv:1210.1976 [hep-ph]].

[16] J. F. Gunion, Y. Jiang and S. Kraml, "Could two NMSSM Higgs bosons be present near 125 GeV?," Phys. Rev. D **86** (2012) 071702 [arXiv:1207.1545 [hep-ph]].

[17] J. F. Gunion, Y. Jiang and S. Kraml, "Diagnosing Degenerate Higgs Bosons at 125 GeV," Phys. Rev. Lett. **110** (2013) 051801 [arXiv:1208.1817 [hep-ph]].

Post LHC7 SUSY benchmark points for ILC physics

Howard Baer[1], *Jenny List*[2]

[1]University of Oklahoma, Norman, OK 73019, USA
[2]DESY, Notkestraße 85, 22607 Hamburg, Germany

LC-REP-2012-063

May 30, 2012

We re-evaluate prospects for supersymmetry at the proposed International Linear e^+e^- Collider (ILC) in light of the first year of serious data taking at LHC with $\sqrt{s} = 7$ TeV and ~ 5 fb^{-1} of pp collisions (LHC7). Strong new limits from LHC SUSY searches, along with a hint of a Higgs boson signal around $m_h \sim 125$ GeV, suggest a paradigm shift from previously popular models to ones with new and compelling signatures. We present a variety of new ILC benchmark models, including: natural SUSY, hidden SUSY, NUHM2 with low m_A, non-universal gaugino mass (NUGM) model, pMSSM, Kallosh-Linde model, Brümmer-Buchmüller model, normal scalar mass hierarchy (NMH) plus one surviving case from mSUGRA/CMSSM in the far focus point region. While all these models at present elude the latest LHC limits, they do offer intriguing case study possibilities for ILC operating at $\sqrt{s} \sim 0.25 - 1$ TeV, and present a view of some of the diverse SUSY phenomena which might be expected at both LHC and ILC in the post LHC7 era.

1 Introduction

1.1 Motivation

Supersymmetry (SUSY) is a quantum spacetime symmetry which predicts a correspondence between bosonic and fermionic fields [1, 2, 3, 4]. Supersymmetry is particularly appealing for theories of particle physics in that it reduces scalar field quadratic divergences to merely logarithmic. This fact allows for an elegant solution to the notorious gauge hierarchy problem, rendering the weak scale stable against quantum corrections and allowing for stable extrapolations of the Standard Model (SM) into the far ultraviolet ($E \gg M_{weak}$) regime [5, 6]. Thus, SUSY provides an avenue for connecting the Standard Model to ideas of grand unification (GUTs) and/or string theory, and provides a route to unification with gravity via local SUSY, or supergravity theories [7, 8, 9].

While models of weak scale supersymmetry are theoretically compelling, we note here that a variety of indirect evidence from experiment has emerged which provides support for the idea of weak scale SUSY:

- *Gauge coupling unification:* The values of the three SM gauge couplings, measured at energy scale $Q \simeq M_Z$ at the CERN LEP collider, when extrapolated to high energy scales via renormalization group (RG) running in the Minimal Supersymmetric Standard Model (MSSM) [10], very nearly meet at a point around $Q \simeq 2 \times 10^{16}$ GeV [11, 12, 13]. Unification of gauge couplings is predicted by many grand unified theories (GUTs) and string theories. Gauge coupling unification is violated by numerous standard deviations under SM RG running.

- *Precision electroweak measurements:* Fits of precision electroweak observables (EWPO) to SUSY model predictions find accord provided there exists a rather heavy SUSY particle mass spectrum [14]. Meanwhile, models such as minimal technicolor are highly stressed if not ruled out by EWPO.

- *Top quark mass and electroweak symmetry breaking:* The electroweak scalar potential is highly constrained in SUSY theories compared to the SM, and it is not immediately clear if electroweak symmetry

can be properly broken, yielding the required vector boson and fermion masses while leaving the photon massless. In top-down theories, the soft breaking Higgs mass $m_{H_u}^2$ is driven to negative values by the large top quark Yukawa coupling, triggering an appropriate breakdown of EW symmetry, provided that the top quark mass $m_t \sim 150 - 200$ GeV [15]. The latest measurements find $m_t = 173.2 \pm 0.9$ GeV [16].

- *Higgs mass:* In the SM, the physical Higgs scalar mass $m_{H_{SM}} > 115$ GeV due to LEP2 and LHC searches, and it is lighter than ~ 800 GeV [17] from unitarity constraints [18]. In the MSSM, typically $m_A \gg m_h$ so that h is SM-like. In this case, $m_h > 115$ GeV as in the SM case, but also $m_h \lesssim 135$ GeV due to its more constrained mass calculation including radiative corrections [19]. The latest data from the CERN LHC and Fermilab Tevatron is consistent with 115 GeV $< m_h <$ 127 GeV with a $(2-3)\sigma$ evidence for $m_h \simeq 125$ GeV [108, 109, 110], squarely in the narrow SUSY window of consistency.

- *Dark matter:* While none of the SM particles have the right properties to constitute cold dark matter in the universe, SUSY theories offer several candidates [20]. These include the neutralino (a WIMP candidate), the gravitino or a singlet sneutrino. In SUSY theories where the strong CP problem is solved via the Peccei-Quinn mechanism, there is the added possibility of mixed 1. axion-neutralino [21, 22, 23], 2. axion-axino [24, 25, 26] or 3. axion-gravitino cold dark matter.

- *Baryogenesis:* The measured baryon to photon ratio $\eta \sim 10^{-10}$ is not possible to explain in the SM. In SUSY theories, three prominent possibilities include 1. electroweak baryogenesis (now nearly excluded by limits on $m_{\tilde{t}_1}$ and m_h [27]), 2. thermal and non-thermal leptogenesis [28], and 3. Affleck-Dine baryo- or leptogenesis [29, 30].

1.2 Some problems for SUSY models

While the above laundry list is certainly compelling for the existence of weak scale SUSY in nature, we are faced with the fact that at present there is no evidence for direct superparticle production at high energy colliders, especially at the CERN Large Hadron Collider (LHC). The ATLAS and CMS experiments have accumulated ~ 5 fb^{-1} of integrated luminosity from pp collisions at $\sqrt{s} = 7$ TeV in 2011 (LHC7), and they anticipate collecting ~ 15 fb^{-1} at $\sqrt{s} = 8$ TeV in 2012 (LHC8). Recent analyses by the CMS experiment [120] using 4.4 fb^{-1} of data have now excluded $m_{\tilde{g}} \lesssim 1400$ GeV in the mSUGRA (also known as CMSSM) model, for the case of $m_{\tilde{q}} \simeq m_{\tilde{g}}$, while values of $m_{\tilde{g}} \lesssim 800$ GeV are excluded in the case where $m_{\tilde{q}} \gg m_{\tilde{g}}$. Indeed, fits of the mSUGRA model as recently as 2010 [31] to a variety of observables including EWPO, $(g-2)_\mu$, B-meson decay branching fractions and neutralino cold dark matter density predicted SUSY to lie exactly in this excluded range. In addition, if the light SUSY Higgs boson turns out to have $m_h \simeq 125$ GeV, then the minimal versions of gauge-mediated and anomaly-mediated SUSY breaking models will likely be ruled out [32], since it is difficult to obtain such large values of m_h in these models unless the sparticle mass spectra exist with a lightest MSSM particle with mass greater than about 5 TeV [33].

While the above results may seem disconcerting, at the same time they were not unanticipated by many theorists. Whereas SUSY theories solve a host of problems as mentioned above, they also bring with them considerable phenomenological baggage [35]. Some of these SUSY problems include the following:

- The SUSY flavor problem [36]: In SUSY models based on gravity-mediation, it is generally expected that large flavor-violating terms will occur in the Lagrangian [37], giving rise to large contributions to the kaon mass difference, and flavor violating decays such as $b \to s\gamma$ or $\mu \to e\gamma$. Solutions to the SUSY flavor problem include 1. degeneracy of matter scalar masses, in which case a SUSY GIM mechanism suppresses flavor violation [38], 2. alignment of squark and quark mass matrices [39], or 3. decoupling mainly of first/second generation scalars ($m_{\tilde{q},\tilde{\ell}} \gtrsim 5 - 50$ TeV) [40, 41, 42].[1] Indeed, the SUSY flavor problem provided strong impetus for the development of GMSB and AMSB models, where universality of scalars with the same quantum numbers is automatically expected.

- The SUSY CP problem: In this case, it is expected in gravity mediation that CP-violating phases in the soft SUSY breaking terms and perhaps μ parameter will give rise to large electron and neutron (and

[1] Some degree of alignment or degeneracy would still be needed for the lower portion of this mass range.

other) electric dipole moments (EDMs). Solutions include dialing the CP-violating phases to zero, or decoupling. Models such as GMSB and AMSB are again not expected to have complex, CP-violating soft terms.

- Proton decay in SUSY GUT theories: In SUSY GUT theories, the proton is expected to decay to $K^+\bar{\nu}$ via colored Higgsino $\tilde{h}$ exchange. The lifetime is expected to occur at levels below experimental limits [43]. Since $\tau_p \sim m_p^5/m_{\tilde{h}}^2 m_{\tilde{q}}^2$, large squark masses can again suppress proton decay.

- The gravitino problem [44]: In models of gravity-mediation, the superhiggs mechanism generates SUSY breaking by giving the gravitino a mass $m_{3/2}$. The gravitino mass sets the scale for the visible sector soft breaking terms, and so one expects sparticle masses of order $m_{3/2}$. However, thermal production of gravitinos in the early universe can lead to either 1. an overproduction of dark matter (here, the gravitinos would decay to the stable LSP, or even be the LSP), or 2. late-time decays of gravitinos at time scales $\gtrsim 1$ s after the Big Bang would lead to dissolution of the light nuclei built up during Big Bang nucleosynthesis (BBN). Solutions to the gravitino problem include 1. a rather low re-heat temperature $T_R \lesssim 10^5$ GeV after inflation so that thermal gravitino production is suppressed [45] (but such low T_R values conflict with some baryogenesis mechanisms such as leptogenesis, which seems to require $T_R \gtrsim 10^9$ GeV), 2. a rather light gravitino with $m_{3/2} \ll 1$ GeV, which enhances the goldstino coupling, or 3. a rather heavy gravitino $m_{3/2} \gtrsim 5$ TeV, which lowers the gravitino lifetime so that $\tau_{3/2} \lesssim 1$ sec, and gravitinos decay before BBN [46].

While some proposed solutions solve individual problems listed above (*e.g.* alignment for the SUSY flavor problem, low T_R for the gravitino problem, small phases for the SUSY CP problem), there is one solution– *decoupling of first/second generation matter scalars*– which goes a long way to solving all four.[2] But what of fine-tuning constraints in SUSY models, which seemingly require sparticle masses near the weak scale [47]?

1.3 Fine-tuning in supersymmetric models

The connection between the SUSY breaking scale and the magnitude of the weak scale can be understood most directly by minimization of the scalar potential in the MSSM to determine the magnitude of the electroweak vacuum expectation values. The scalar potential gains contributions from three sectors:

$$V_{SUSY} = V_F + V_D + V_{soft}, \tag{1}$$

and with 50 field "directions" in the MSSM, the scalar potential is rather daunting. Under rather mild conditions, charge and color breaking minima can be avoided, so that instead we just minimize in the neutral/non-colored scalar field directions. A well-defined local minimum can be found where the vacuum expectation values of the real parts of the neutral Higgs fields are given by $\langle h_u^0 \rangle \equiv v_u$ and $\langle h_d^0 \rangle \equiv v_d$ with $\tan\beta \equiv v_u/v_d$. The Z boson acquires a mass $M_Z^2 = \frac{g^2+g'^2}{2}\left(v_u^2 + v_d^2\right)$. Including radiative corrections, the scalar potential minimization condition is then written as

$$\frac{1}{2}M_Z^2 = \frac{(m_{H_d}^2 + \Sigma_d) - (m_{H_u}^2 + \Sigma_u)\tan^2\beta}{(\tan^2\beta - 1)} - \mu^2 \ . \tag{2}$$

Here, Σ_u and Σ_d arise from radiative corrections [48], and are given in the 1-loop approximation to the Higgs effective potential by

$$\Sigma_{u,d} = \frac{1}{v_{u,d}}\frac{\partial \Delta V}{\partial H_{u,d}},$$

where ΔV is the one-loop correction to the tree-level potential, and the derivatives are evaluated at the physical vacuum.

It is then reasonable to say that the theory yields a natural value of M_Z if the individual terms on the right hand side of Eq. (2) are comparable in magnitude so that the observed value of M_Z is obtained without

[2] In gravity mediation, it is expected that the gravitino mass $m_{3/2}$ sets the mass scale for the heaviest of the scalars; in this case, multi-TeV scalar masses would proceed from a multi-TeV gravitino mass.

resorting to large cancellations. Indeed this is why $|\mu|$ has been suggested as a measure of naturalness [49], with theories where $\mu^2 \lesssim M_Z^2$ being the "most natural". This relationship must be accepted with some latitude, since values of $\mu^2 \lesssim (100\ \text{GeV})^2$ are phenomenologically excluded. Here, we will adopt $|\mu| < \Lambda_{NS}$, where $\Lambda_{NS} \sim M_Z$, but might be as high as ~ 200 GeV. Of course, there is nothing special about the magnitude of μ, so that the same considerations apply equally to all the terms in Eq'n 2, including those involving the radiative corrections. Naturalness thus requires that each *individual* term in (2) be $\lesssim \Lambda_{NS}$.

The largest contributions to $\Sigma_{u,d}$ in Eq. (2) arise from superpotential Yukawa interactions of third generation squarks involving the top quark Yukawa coupling. The order of magnitude of these contributions is given by

$$\Sigma_u \sim \frac{3f_t^2}{16\pi^2} \times m_{\tilde{t}_i}^2 \left(\ln(m_{\tilde{t}_i^2}/Q^2) - 1 \right) ,$$

and so grows quadratically with the top squark masses. Clearly, the top squark (and by $SU(2)$ gauge symmetry, also $\tilde{b}_L$) masses must then be bounded from above by the naturalness conditions. In Ref. [50], it has been shown that requiring $\Sigma_u \lesssim \frac{1}{2} M_Z^2$ leads to $m_{\tilde{t}_i} \lesssim 500$ GeV. Scaling this up to allow μ values up to 150-200 GeV leads to a corresponding bound $m_{\tilde{t}_i} \lesssim 1 - 1.5$ TeV. In other words, from this perspective, models with $\mu \lesssim 200$ GeV and top squarks at the TeV scale or below are preferred by naturalness. It is also worth remarking that since

$$m_A^2 \simeq 2\mu^2 + m_{H_u}^2 + m_{H_d}^2 + \Sigma_u + \Sigma_d \ , \tag{3}$$

for moderate to large values of $\tan\beta$, the heavier Higgs scalars can naturally be at the several-TeV scale because of the appearance of $\tan^2\beta - 1$ in the denominator of Eq. (2). Notice, however, that the bound of Λ_{NS}^2 on each term in Eq. (2) translates to an upper bound $m_A \lesssim \Lambda_{NS} \tan\beta$.

There will also be corresponding constraints on other sparticles such as electro-weak charginos and neutralinos that directly couple to the Higgs sector, but since these couplings are smaller than f_t and there are no color factors, the constraints will be correspondingly weaker. Sparticles such as first and second generation squarks and sleptons that have no direct/significant couplings to the Higgs sector are constrained only via two-loop effects and can easily be in the 10-50 TeV range. An important exception would be the gluino, since radiative corrections to the top squark mass are proportional to $m_{\tilde{g}}$ [51]. Using $\delta m_{\tilde{q}}^2 \sim \frac{2g_s^2}{3\pi^2} m_{\tilde{g}}^2 \times log$ and setting logs to be order unity, we expect that $m_{\tilde{g}} \lesssim 3 m_{\tilde{q}}$. For top squarks to remain in the ~ 1.5 TeV range, the gluino must be lighter than 3-4 TeV. In models with electroweak gaugino mass unification, electroweak-inos would then automatically not destroy naturalness.

To summarize, naturalness considerations suggest that SUSY models should give rise to a mass spectrum characterized by

- $|\mu| \lesssim \Lambda_{NS} \sim 200$ GeV,
- third generation squarks $m_{\tilde{t}_{L,R}},\ m_{\tilde{b}_L} \lesssim 1.5$ TeV,
- $m_{\tilde{g}} \lesssim 3 - 4$ TeV and SSB electroweak-ino masses smaller than 1-2 TeV
- $m_{\tilde{q}_{1,2}},\ m_{\tilde{\ell}_{1,2}} \sim 10 - 50$ TeV.

The latter weak constraint on first/second generation matter scalars allows for a decoupling solution to the SUSY flavor, CP, p-decay and (indirectly) gravitino problems. SUSY models with the above generic spectra have been dubbed "natural SUSY" [52].[3] This spectra is closely related to *effective SUSY*[41], but with the additional requirement that $|\mu| \lesssim 150 - 200$ GeV which would likely give rise to a higgsino-like lightest neutralino $\tilde{\chi}_1^0$. In contrast, models such as mSUGRA with rather heavy top squarks are expected to be highly fine-tuned, even when μ is small as in the hyperbolic branch/focus point (HB/FP) region.

The remainder of this report is geared towards presenting a new set of supersymmetry benchmark models suitable for ILC investigations, while maintaining consistency with the latest indirect and direct constraints on supersymmetric models, especially taking into account what has been learned from recent LHC searches. In Sec. 2, we briefly summarize current indirect constraints on SUSY models, and also discuss the current status of SUSY dark matter. In Sec. 3, we present a summary of the most recent results from LHC searches for

[3]For earlier related work, see Ref's [53, 54, 55, 56, 57, 75].

SUSY and Higgs bosons. In Sec. 4, we present a variety of new post LHC7 benchmark points for ILC studies. These new benchmarks reflect a movement away from previous studies within the mSUGRA/CMSSM model. Some models have been selected due to their theoretical motivation (*e.g.* natural SUSY and its relatives), while others have been selected for their diversity of phenomenology which may be expected at ILC. In Sec. 5, we present a brief summary and outlook for physics prospects at the ILC.

2 Indirect constraints on SUSY models

In this section, we review briefly indirect constraints on SUSY models from muon $g-2$ measurements, rare B-decay branching fractions along with an updated discussion of the role of dark matter in SUSY models.

2.1 $(g-2)_\mu$ status

The magnetic moment of the muon $a_\mu \equiv \frac{(g-2)_\mu}{2}$ was measured by the Muon $g-2$ Collaboration [68] and has been found to give a 3.6σ discrepancy with SM calculations based on e^+e^- data [69]: $\Delta a_\mu = a_\mu^{meas} - a_\mu^{SM}[e^+e^-] = (28.7 \pm 8.0) \times 10^{-10}$. When τ-decay data are used to estimate the hadronic vacuum polarization contribution rather than low energy e^+e^- annihilation data, the discrepancy reduces to 2.4σ , correnspondingto $\Delta a_\mu = a_\mu^{meas} - a_\mu^{SM}[\tau] = (19.5 \pm 8.3) \times 10^{-10}$.

The SUSY contribution to the muon magnetic moment is[70] $\Delta a_\mu^{SUSY} \sim \frac{m_\mu^2 \mu M_i \tan\beta}{m_{SUSY}^4}$ where $i = 1, 2$ stands for electroweak gaugino masses and m_{SUSY} is the characteristic sparticle mass circulating in the muon-muon-photon vertex correction: here, $m_{\tilde{\mu}_{L,R}}$, $m_{\tilde{\nu}_\mu}$, $m_{\tilde{\chi}_i^+}$ and $m_{\tilde{\chi}_j^0}$. Attempts to explain the muon $g-2$ anomaly using supersymmetry usually invoke sparticle mass spectra with relatively light smuons and/or large $\tan\beta$ (see *e.g.* Ref. [71]). Some SUSY models where $m_{\tilde{\mu}_{L,R}}$ is correlated with squark masses (such as mSUGRA) are now highly stressed to explain the $(g-2)_\mu$ anomaly. In addition, since naturalness favors a low value of $|\mu|$, tension again arises between a large contribution to Δa_μ^{SUSY} and naturalness conditions. These tensions motivate scenarios with non-universal scalar masses. Of the benchmark scenarios discussed in the following, some feature light smuons which raise $(g-2)_\mu$ to its experimental value, while others are compatible with the Standard Model prediction.

2.2 $b \to s\gamma$

The combination of several measurements of the $b \to s\gamma$ branching fraction finds that $BF(b \to s\gamma) = (3.55 \pm 0.26) \times 10^{-4}$ [72]. This is somewhat higher than the SM prediction [73] of $BF^{SM}(b \to s\gamma) = (3.15 \pm 0.23) \times 10^{-4}$. SUSY contributions to the $b \to s\gamma$ decay rate come mainly from chargino-top-squark loops and loops containing charged Higgs bosons, and so are large when these particles are light and when $\tan\beta$ is large [74].

2.3 $B_s \to \mu^+\mu^-$

The decay $B_s \to \mu^+\mu^-$ occurs in the SM at a calculated branching ratio value of $(3.2 \pm 0.2) \times 10^{-9}$. The CMS experiment [65] has provided an upper limit on this branching fraction of $BF(B_s \to \mu^+\mu^-) < 1.9 \times 10^{-8}$ at 95% CL. The CDF experiment [66] claims a signal in this channel at $BF(B_s \to \mu^+\mu^-) = (1.8 \pm 1.0) \times 10^{-8}$ at 95% CL, which is in some discord with the CMS result. Finally, the LHCb experiment has reported a strong new bound of $BF(B_s \to \mu^+\mu^-) < 4.5 \times 10^{-9}$[67]. In supersymmetric models, this flavor-changing decay occurs through pseudoscalar Higgs A exchange [61, 62], and the contribution to the branching fraction from SUSY is proportional to $\frac{\tan^6\beta}{m_A^4}$.

2.4 $B_u \to \tau^+\nu_\tau$

The branching fraction for $B_u \to \tau^+\nu_\tau$ decay is calculated [63] in the SM to be $BF(B_u \to \tau^+\nu_\tau) = (1.10 \pm 0.29) \times 10^{-4}$. This is to be compared to the value from the Heavy Flavor Averaging group [64], which finds a measured value of $BF(B_u \to \tau^+\nu_\tau) = (1.41 \pm 0.43) \times 10^{-4}$, in agreement with the SM prediction, but

leaving room for additional contributions. The main contribution from SUSY comes from tree-level charged Higgs exchange, and is large at large $\tan\beta$ and low m_{H^+}.

2.5 Dark matter

During the past several decades, a very compelling and simple scenario has emerged to explain the presence of dark matter in the universe with an abundance roughly five times that of baryonic matter. The WIMP miracle scenario posits that weakly interacting massive particles would be in thermal equilibrium with the cosmic plasma at very high temperatures $T \gtrsim m_{WIMP}$. As the universe expands and cools, the WIMP particles would freeze out of thermal equilibrium, locking in a relic abundance that depends inversely on the thermally-averaged WIMP (co)-annihilation cross section [76]. The WIMP "miracle" occurs in that a weak strength annihilation cross section gives roughly the measured relic abundance provided the WIMP mass is of the order of the weak scale [77]. The lightest neutralino of SUSY models has been touted as a protypical WIMP candidate [78, 79, 80].

While the WIMP miracle scenario is both simple and engaging, it is now clear that it suffers from several problems in the case of SUSY theories. The first of these is that in general SUSY theories where the lightest neutralino plays the role of a thermally produced WIMP, the calculated relic abundance $\Omega_\chi h^2$ is in fact typically two-to-four orders of magnitude larger than the measured abundance $\Omega_{CDM}^{meas} h^2 \sim 0.11$ in the case of a bino-like neutralino, and one-to-two orders of magnitude lower than measurements in the case of wino- or higgsino-like neutralinos [81]. In fact, rather strong co-annihilation, resonance annihilation or mixed bino-higgsino or mixed wino-bino annihilation is needed to obtain the measured dark matter abundance. Each of these scenarios typically requires considerable large fine-tuning of parameters to gain the measured dark matter abundance [82]. The case where neutralinos naturally give the measured CDM abundance is when one has a bino-like neutralino annihilating via slepton exchange with slepton masses in the 50-70 GeV range: such mass values were long ago ruled out by slepton searches at LEP2.

The second problem with the SUSY WIMP miracle scenario is that it neglects the gravitino, which is an essential component of theories based on supergravity. Gravitinos can be produced thermally at high rates at high re-heat temperatures T_R after inflation. If $m_{\tilde{G}} > m_{LSP}$, then gravitino decays into a stable LSP can overproduce dark matter for $T_R \gtrsim 10^{10}$ GeV. Even at much lower $T_R \sim 10^5 - 10^{10}$ GeV, thermal production of gravitinos followed by late decays (since gravitino decays are suppressed by the Planck scale) tend to dissociate light nuclei produced in the early universe, thus destroying the successful picture of Big Bang nucleosynthesis [46].

The third problem is that the SUSY WIMP scenario neglects at least two very compelling new physics effects that would have a strong influence on dark matter production in the early universe.

- The first of these is that string theory seems to require the presence of at least one light ($\sim 10 - 100$ TeV) moduli field [83]. The moduli can be produced at large rates in the early universe and decay at times $\sim 10^{-1} - 10^5$ sec after the Big Bang. Depending on their branching fractions, they could either feed additional LSPs into the cosmic plasma [84], or decay mainly to SM particles, thus diluting all relics present at the time of decay [85].

- The second neglected effect is the strong CP problem, which is deeply routed in QCD phenomenology [86]. After more than three decades, the most compelling solution to the strong CP problem is the hypothesis of a Peccei-Quinn axial symmetry whose breaking gives rise to axion particles with mass $\sim 10^{-6} - 10^{-9}$ eV [87]. The axions can be produced non-thermally via coherent oscillations [88, 89, 90], and also would constitute a portion of the dark matter. In SUSY theories, the axions are accompanied by R-odd spin-$\frac{1}{2}$ axinos $\tilde{a}$ and R-even spin-0 saxions s [91]. Thermal production of axinos and non-thermal production of saxions can either feed more dark matter particles into the cosmic plasma, or inject additional entropy, thus diluting all relics present at the time of decay. Theoretical predictions for the relic abundance of dark matter in these scenarios are available but very model-dependent. In the case of mixed axion-neutralino dark matter, it is usually very difficult to lower a standard over-abundance of neutralinos, but it is also very easy to bolster a standard underabundance [23]. This latter case may lead one to consider SUSY models with a standard underabundance of wino-like or higgsino-like neutralinos as perhaps the more compelling possibility for CDM. In the case of mixed

axion-neutralino CDM, it can be very model-dependent whether the axion or the neutralino dominates the DM abundance, and cases where there is a comparable admixture of both are possible.

The upshot for ILC or LHC physics is that one shouldn't take dark matter abundance constraints on SUSY theories too seriously at this point in time.

2.5.1 Status of WIMP dark matter searches

As of spring 2012, a variety of direct and indirect WIMP dark matter detection searches are ongoing. Several experiments – DAMA/Libra, CoGent and Cresst – claim excess signal rates beyond expected backgrounds. These various excesses can be interpreted in terms of a several GeV WIMP particle, although the three results seem at first sight inconsistent with each other. It is also possible that muon or nuclear decay induced neutron backgrounds – which are very difficult to estimate – contribute to the excesses. Numerous theoretical and experimental analyses are ongoing to sort the situation out. A WIMP particle of a few GeV seems hard to accommodate in SUSY theories.

There also exists claims for measured positron excesses in cosmic rays above expected backgrounds by the Pamela collaboration [92] and claims for an electron excess by the Fermi-LAT group [93]. While these claims can be understood in terms of very massive WIMPs of order hundreds of GeV, it is unclear at present whether the positrons arise from exotic astrophysical sources [94] or simply from rare mis-identification of cosmic protons.

A variety of other direct WIMP search experiments have probed deeply into WIMP-model parameter space, with no apparent excesses above SM background. At this time, the best limits come from the Xenon-100 experiment [95], which excludes WIMP-proton scattering cross sections of $\sigma(\chi p) \gtrsim 10^{-8}$ pb at 90%CL for $m_{WIMP} \sim 100$ GeV. The Xenon-100, LUX and CDMS experiments seem poised decisively to probe the expected parameter space of mixed bino-higgsino dark matter [96, 97] (as occurs for instance in focus point SUSY of the mSUGRA model) in the next round of data taking.

2.5.2 Gravitino dark matter

It is possible in SUSY theories that gravitinos are the lightest SUSY particle, and could fill the role of dark matter. In gravity-mediation, the gravitino is expected to have mass of order the weak scale. In this case, late decays of thermally produced neutralinos into gravitinos are often in conflict with BBN constraints. If the gravitinos are much lighter, well below the GeV scale, then their goldstino coupling is enhanced and BBN constraints can be evaded. This scenario tends to occur for instance in gauge-mediated SUSY theories. The simplest GMSB scenarios now appear in conflict with Higgs mass results if indeed LHC is seeing m_h at $\sim$ 125 GeV [32, 33]. We will, however, present an example of a non-minimal GMSB model which is compatible with a Higgs mass of $\sim$ 125 GeV.

3 LHC results

In this section, we present a very brief summary of the status of LHC searches for SUSY Higgs bosons and for SUSY particles as of April 2012.

3.1 Impact of Higgs searches

3.1.1 SM-like Higgs scalar

The ATLAS and CMS experiments reported on search results for a SM-like neutral Higgs scalar H_{SM} in March 2012 based on about 5 fb^{-1} of data at $\sqrt{s} = 7$ TeV [108, 109]. Their analyses exclude a SM-like Higgs boson over the mass range $127 < m_{H_{SM}} < 600$ GeV. Combining this range with a fit of precision electroweak data to SM predictions then allows a SM-like Higgs boson to live in the narrow mass range of 115 GeV $< m_{H_{SM}} <$ 127 GeV. In fact, ATLAS reports an excess of events at 3.5σ level in the $\gamma\gamma$, WW^* and ZZ^* channels which is consistent with $m_{H_{SM}} \sim 126$ GeV. A similar excess is reported by CMS at 3.1σ at $m_{H_{SM}} \sim 124$ GeV, along with an excess of 4ℓ events at $\sim$ 120 GeV. These excesses are also corroborated

by recent reports from CDF and D0 at the Fermilab Tevatron of excess events over the mass range 115-130 GeV [110]. Upcoming data from the 2012 LHC run at $\sqrt{s} = 8$ TeV should validate or exclude a Higgs signal in the 115-127 GeV range.

3.1.2 Non-standard Higgs bosons

Searches by ATLAS and CMS for $H,\ A \to \tau^+\tau^-$ now exclude a large portion of the m_A *vs.* $\tan\beta$ plane [111, 112]. In particular, the region around $\tan\beta \sim 50$, which is favored by Yukawa-unified SUSY GUT theories, now excludes $m_A < 500$ GeV. For $\tan\beta = 10$, the range 120 GeV $< m_A <$ 220 GeV is excluded. ATLAS excludes charged Higgs bosons produced in association with a $t\bar{t}$ pair for masses below about 150 GeV for $\tan\beta \sim 20$ [113].

3.1.3 Impact of Higgs searches on SUSY models

A Higgs mass of $m_h = 125 \pm 3$ GeV lies below the value of $m_h \sim 135$ GeV which is allowed by calculations within the MSSM. However, such a large value of m_h requires large radiative corrections and large mixing in the top squark sector. In models such as mSUGRA, trilinear soft parameters $A_0 \sim \pm 2m_0$ are thus preferred, and values of $A_0 \sim 0$ would be ruled out [114, 115]. In other constrained models such as the minimal versions of GMSB or AMSB, Higgs masses of 125 GeV require even the lightest of sparticles to be in the multi-TeV range [33], as illustrated in Figure 1.

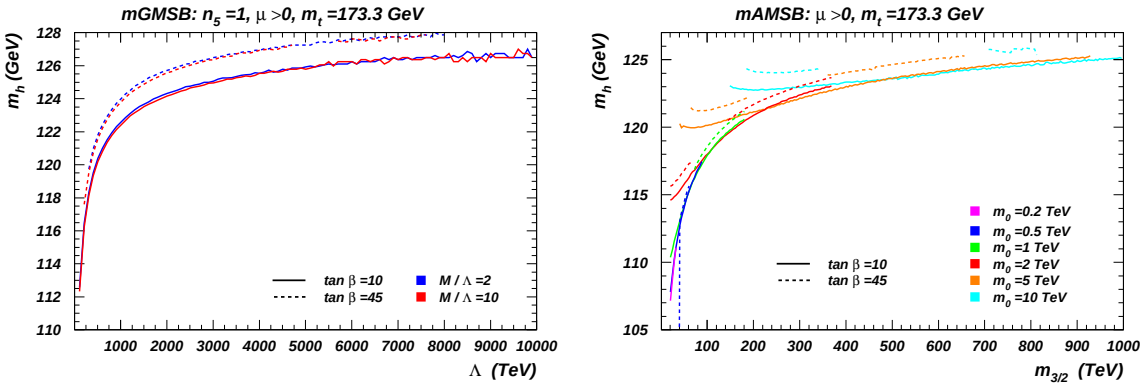

Figure 1: Value of m_h in mGMSB and in mAMSB versus Λ and $m_{3/2}$ from [33].

In the mSUGRA/CMSSM model, requiring a Higgs mass of about 125 GeV pushes the best fit point in m_0 and $m_{\frac{1}{2}}$ space into the multi-TeV range [114] and makes global fits of the model to data increasingly difficult [105]. This has provided motivation for extending the MSSM with gauge singlets [106, 50] or vector-like matter [107] both of which allow for somewhat heavier values of m_h.

3.2 Review of sparticle searches at LHC

3.2.1 Gluinos and first/second generation squarks

The ATLAS and CMS collaborations have searched for multi-jet+$E_T^{\rm miss}$ events arising from gluino and squark pair production in 4.4 fb^{-1} of 2011 data taken at $\sqrt{s} = 7$ TeV [117, 120]. In the limit of very heavy squark masses, they exclude $m_{\tilde{g}} \lesssim 0.8$ TeV, while for $m_{\tilde{q}} \simeq m_{\tilde{g}}$ then $m_{\tilde{g}} \lesssim 1.4$ TeV is excluded. Here, $m_{\tilde{q}}$ refers to a generic first generation squark mass scale, since these are the ones whose production rates depend strongly on valence quark PDFs in the proton.

Both collaborations in addition have searched for gluino and squark cascade decays [121] assuming more specific decay chains leading to signatures involving leptons and photons as well as b-jets [116, 118, 125, 126,

127, 128, 119, 129, 122, 123, 124, 138]. In most cases, the limits on the gluino mass are rather similar to the ones from the multi-jet+$E_T^{\rm miss}$ analyses, with values of $m_{\tilde{g}} \lesssim 0.8 - 1$ TeV being excluded depending on the particular decay chain.

If the gluino decays dominantly into third generation squarks, the gluino mass limits are somewhat weaker, typically in the range of 0.65 to 0.8 TeV, again depending on the exact decay chain [126, 129, 127]. These results are soon expected to be upgraded to include the full 5 fb^{-1} data set.

Some analyses have addressed the situation where there are small mass differences between mother and daughter particles in the decay chain. In one case, ATLAS considered gluino decays via an intermediate chargino [116]. Using a soft-lepton tag, they reach down to $\tilde{g} - \tilde{\chi}_1^0$ mass differences of ~ 100 GeV. In this case, gluino masses are only excluded up to 0.5 TeV.

3.2.2 Sbottom and Stop

A recent ATLAS search for direct bottom squark pair production followed by $\tilde{b}_1 \to b\tilde{\chi}_1^0$ decay ($pp \to \tilde{b}_1\bar{\tilde{b}}_1 \to b\bar{b} + E_T^{\rm miss}$) based on 2 fb^{-1} of data at $\sqrt{s} = 7$ TeV now excludes $m_{\tilde{b}_1} \lesssim 350$ GeV for $m_{\tilde{\chi}_1^0}$ as high as 120 GeV. For larger values of $m_{\tilde{\chi}_1^0}$, the limit vanishes at present [131]. These limits also apply to top squark pair production where $\tilde{t}_1 \to b\tilde{\chi}^+$ decay and the $\tilde{\chi}^+$ decays to soft, nearly invisible particles, as would be expected in natural SUSY. From a search for events with b-jets, same-sign di-leptons and missing energy, CMS puts a limit on the mass of directly produced bottom squarks to be larger than 370 GeV for chargino masses between 100 and 200 GeV and a $\tilde{\chi}_1^0$ mass of $m_{\tilde{\chi}_1^0} = 50$ GeV [129].

In the context of GMSB with the $\tilde{\chi}_1^0$ as higgsino-like NLSP and a gravitino $\tilde{G}$ LSP, ATLAS searched for direct top squark pair production, followed by $\tilde{t}_1 \to b\tilde{\chi}^+$ or, when kinematically allowed, also $t\tilde{\chi}_1^0$. Based on 2 fb^{-1}, they exclude top squark masses up to 330 GeV for NLSP masses around 190 GeV [130]. This limit relies on the GMSB specific decay of the $\tilde{\chi}_1^0$ into $Z\tilde{G}$, especially on two (same flavour, opposite sign) leptons consistent with the Z mass.

3.2.3 Electroweakinos

In models with gaugino mass unification and heavy squarks (such as mSUGRA with large m_0), electroweak gaugino pair production $pp \to \tilde{\chi}_1^\pm\tilde{\chi}_2^0$ is the dominant SUSY particle production cross section at LHC7 for $m_{\tilde{g}} > 0.5$ TeV[157]. If the $\tilde{\chi}_1^\pm$ and $\tilde{\chi}_2^0$ decay leptonically and $\tilde{\chi}_2^0 \to \tilde{\chi}_1^0 Z$ decay is closed, then this reaction leads to the well-known trilepton plus $E_T^{\rm miss}$ final state [132, 133] which may be observable over SM backgrounds. A search by ATLAS using 2.1 fb^{-1} of data [134] has been interpreted in the pMSSM and in a simplified model assuming chargino and neutralino decay to intermediate sleptons, which enhances the leptonic branching fractions. In the simplified model case, $m_{\tilde{\chi}_1^\pm} < 250 - 300$ GeV are ruled out for $m_{\tilde{\chi}_1^0} = 0 - 150$ GeV. In the pMSSM as well as in the simplified model interpretation it is assumed that the lighter set of sleptons, including the third generation, is mass degenerate and fulfils $m_{\tilde{l}} = (m_{\tilde{\chi}_1^\pm} - m_{\tilde{\chi}_1^0})/2$, which maximizes the lepton momenta and thus the acceptance. Thus this analysis does in particular not apply to scenarios with a small $\tilde{\tau}_1$-$\tilde{\chi}_1^0$ mass difference, which are still a viable scenario even for M_2 and μ values depicted as excluded in Fig. 2 of reference [134]. Furthermore, the theoretically more interesting case of chargino and neutralino three-body leptonic decay through W^* and Z^* should be possible with 10-20 fb^{-1} of data, as should the trilepton signal from $pp \to \tilde{\chi}_1^\pm\tilde{\chi}_2^0 \to WZ + E_T^{\rm miss}$ [157].

3.2.4 Electroweakinos with extremely small mass differences

In models such as AMSB where the light chargino $\tilde{\chi}_1^\pm$ and neutralino $\tilde{\chi}_1^0$ are expected to be wino-like, the expected $\tilde{\chi}_1^\pm - \tilde{\chi}_1^0$ mass gap is expected to be $\sim 100 - 200$ MeV. Such a small mass gap implies the $\tilde{\chi}_1^\pm$ will actually fly a short but possibly observable distance before decaying into very soft pion(s). A search by ATLAS using 4.7 fb^{-1} has been made for long lived charginos arising from gluino and squark cascade decays [135]. Thus, the search looks for three high p_T jets plus $E_T^{\rm miss} > 130$ GeV. Within this event class, a search is made for events with hits in the transition radiation tracker (TRT) which ultimately disappear. No signal is seen above expected background levels, leading to limits on $m_{3/2} > 32$ TeV in the mAMSB model. More generally, lifetimes between $\tau_{\tilde{\chi}_1^\pm} \sim 0.2 - 90$ ns are excluded for $m_{\tilde{\chi}_1^\pm} < 90$ GeV at 95% CL.

3.2.5 Heavy stable charged particles

Long-lived quasi-stable charged or colored particles are common in many versions of supersymmetric models. Examples include GMSB models with a $\tilde{\tau}_1$ as NLSP which decays to $\tau + \tilde{G}$, or models such as split SUSY where gluino decays are suppressed by an ultra-heavy squark mass scale. In the latter case, any quasi-stable gluinos which are produced at LHC would be expected to hadronize into a gluino hadron, which could be either charged or neutral.

A search by ATLAS using 2.1 fb^{-1} of data looks for anomalous dE/dx energy loss measurements in the Pixel detector. Since no deviation from expected background levels was found, they were able to exclude the production of gluino hadrons with $m_{\tilde{g}} < 810$ GeV [136].

3.2.6 R-Parity Violation

The ATLAS collaboration has searched for R-parity violating SUSY (for a review, see [137]) in the context of the mSUGRA/CMSSM model in two scenarios.

In the case that $m_0 \sim 0$, the tau-slepton $\tilde{\tau}_1$ is the LSP. To be compatible with cosmological bounds on relic stable charged particles produced in the Big Bang, it is assumed that $\tilde{\tau}_1$ decays to $\tau e^{\mp}(\ell^{\pm}\nu_{\ell})$ where $\ell = e$ or μ via the R-parity coupling λ_{121}. A search for four isolated leptons plus $E_T^{\rm miss}$ in 2 fb^{-1} of data allows them to exclude $m_{1/2} < 800$ GeV at 95% CL for $\tan\beta < 40$ and $m_{\tilde{\tau}_1} > 80$ GeV [143].

Furthermore, ATLAS has published an interpretation of their search for events with one lepton, jets and missing transverse energy in 1 fb^{-1} of data [145] in the context of bilinear R-parity violating SUSY, where the bRPV parameters are determined by fitting them to neutrino oscillation data [146]. For $\tan\beta = 10$, $A_0 = 0$ and $\mu > 0$, they exclude values of m_0 up to 430 GeV for $m_{1/2} = 290$ GeV. For smaller or larger values of $m_{1/2}$ the exclusion in m_0 is weaker; values of $m_{1/2} < 240$ GeV have not been studied at all.

4 Implications for ILC and benchmark points

The results from the previous sections, when summarized, yield the following grand picture:

- **Squarks and gluinos:** Ironically, the strongest LHC limits on sparticle masses apply to the first generation squarks and gluinos, while these are the most remotely connected to the determination of the electroweak scale, and to the weak boson masses. So while $m_{\tilde{g}} \gtrsim 1.4$ TeV for $m_{\tilde{q}} \sim m_{\tilde{g}}$, these limits hardly affect naturalness limits, which prefer $m_{\tilde{g}} \lesssim 3-4$ TeV and basically do not constrain first generation squarks, so that $m_{\tilde{q}}$ values into the tens of TeV regime are certainly allowed.

- **Electroweakinos:** The masses of the electroweakinos – constrained by LEP2 to have $m_{\tilde{\chi}_1} > 103.5$ GeV – are hardly constrained by LHC7 data unless they are connected with 1. a light gluino (via the gaugino mass unification assumption) or first/second generation squarks allowing for strong production or 2. in conjuction with light sleptons appearing in the electroweakino decay right in between the $\tilde{\chi}_1^0$ and $\tilde{\chi}_2^0, \tilde{\chi}_1^{\pm}$ masses. In particular, $m_{\tilde{\chi}_1^0}$, $m_{\tilde{\chi}_2^0}$ and $m_{\tilde{\chi}_1^{\pm}}$ can very well be below 200 GeV as motivated by naturalness. Very likely they have at least a sizable Higgsino component, and thus could very well have small mass splittings. Several of the scenarios proposed below exhibit such a pattern for the light electroweakinos. The heavier electroweakinos are likely not directly observable at the ILC. The proposed benchmarks cover various options in this respect.

- **Sleptons:** The most important indication for light sleptons is still $(g-2)_{\mu}$. They are so far not constrained directly by LHC7 data (but see [147] for projections). If a common matter scalar mass m_0 at the GUT scale is assumed, then the stringent LHC7 bounds on first and second generation squarks imply also rather heavy sleptons. Most of the scenarios below have heavy sleptons and thus do not explain the $(g-2)_{\mu}$ anomaly. If non-universality of matter scalars is assumed, then the slepton masses are completely unconstrained and all sleptons could still lie within reach of the ILC, as illustrated by the $\delta M\tilde{\tau}$ and NMH benchmarks described below: both these scenarios allow for perfect matches to the observed $(g-2)_{\mu}$ value. In natural SUSY – while the first two slepton generations are expected to be heavy – the $\tilde{\tau}_1$ can be quite light due to the limited mass of the top squarks.

- **Third generation squarks:** Direct limits on the third generation squarks from LHC7 are far below those for the first generation, so that especially the top squark could very well be in the regime expected from naturalness and thus accessible at the ILC. Both the natural SUSY benchmark and the $\delta M\tilde{\tau}$ benchmark described in Subsections 4.1 and 4.6 give examples with light $\tilde{t}_1$ and possibly $\tilde{b}_1$ and $\tilde{t}_2$.
- **SUSY Higgses:** The possibly SM-like properties of a 125 GeV Higgs scalar, as hinted at by LHC7 data, suggests that the other SUSY Higgses could be rather heavy, although of course a firm statement in this regard will require not only a Higgs discovery but also precise measurements of the branching ratios. We present in section 4.3 a NUHM2 scenario with light A, H and $H^{\pm}$; also, the $\delta M\tilde{\tau}$ benchmark features heavy Higgses which should be observable at a 1 TeV e^+e^- collider.

Based on these observations, we propose a set of benchmark points which can be used to illustrate the capabilities of ILC with respect to supersymmetry, and for future optimization of both machine and detector design. The suggested points all lie outside the limits imposed by LHC7 searches. Some of these scenarios might be discoverable or excluded by upcoming LHC8 searches, while others will be extremely difficult to detect at LHC even with 3 ab^{-1} of data at $\sqrt{s} = 14$ TeV. The spectra for all benchmarks are available online [144] in the SUSY Les Houches Accord format.

4.1 Natural SUSY

Natural SUSY (NS) models are characterized by [51, 52, 99]:

- a superpotential higgsino mass parameter $\mu < \Lambda_{NS} \sim 200$ GeV,
- a sub-TeV spectrum of third generation squarks $\tilde{t}_1$, $\tilde{t}_2$ and $\tilde{b}_1$,
- an intermediate scale gluino $m_{\tilde{g}} \lesssim 3-4$ TeV with $m_A \lesssim |\mu| \tan\beta$ and
- multi-TeV first/second generation matter scalars $m_{\tilde{q},\tilde{\ell}} \sim 10-50$ TeV.

The last point offers at least a partial decoupling solution to the SUSY flavor and CP problems.

The suggested model parameter space is given by [99]:

$$m_0(1,2),\ m_0(3),\ m_{1/2},\ A_0,\ \tan\beta,\ \mu,\ m_A\ . \tag{4}$$

Here, we adopt a NS benchmark point as calculated using Isasugra 7.82 [100] with parameters $m_0(1,2) = 13.5$ TeV, $m_0(3) = 0.76$ TeV, $m_{1/2} = 1.38$ TeV, $A_0 = -0.167$ TeV, $\tan\beta = 23$ GeV, $\mu = 0.15$ TeV and $m_A = 1.55$ TeV. The resulting mass spectrum is listed in Table 1.

Due to their small mass differences, the higgsino-like light electroweakinos will tend to look like missing transverse energy to the LHC. The next heavier particle is the $\tilde{t}_1$. Since the mass difference $m_{\tilde{t}_1} - m_{\tilde{\chi}_1^0}$ is less than the top mass, the decay $\tilde{t}_1 \to b\tilde{\chi}_1^{\pm}$ dominates, thus making the signature for $\tilde{t}_1$ pair production two acollinear b-jets plus missing transverse energy.

For ILC, the spectrum of higgsino-like $\tilde{\chi}_1^{\pm}$, $\tilde{\chi}_1^0$ and $\tilde{\chi}_2^0$ will be accessible for $\sqrt{s} \gtrsim 320$ GeV via $\tilde{\chi}_1^{\pm}$ and $\tilde{\chi}_2^0\tilde{\chi}_2^0$ pair production and $\tilde{\chi}_1^0\tilde{\chi}_2^0$ mixed production, albeit with a mass gap $m_{\tilde{\chi}_1^{\pm}} - m_{\tilde{\chi}_1^0} \sim m_{\tilde{\chi}_2^0} - m_{\tilde{\chi}_1^0} \sim 7.5$ GeV: thus, visible energy released from decays will be small. Specialized cuts allowing for ILC detection of light higgsinos with small mass gaps have been advocated in Ref's [101] and [102]; there it is also demonstrated that ILC will be able to measure the values of μ and M_2 and show that $|\mu| < M_2$.

In the case of very small mass gaps, a hard ISR photon radiated from the initial state may help to lift the signal out of the substantial background of photon–photon induced processes. The experimental performance of this ISR recoil method has been evaluated recently in full simulation of the ILD detector in context of radiative WIMP / neutralino production [103, 104]. The cross-sections are typically in the few tens of fb region [75] and thus should be detectable in the clean ILC environment. Similar signatures have also been investigated in the context of AMSB for the TESLA TDR [98].

As $\sqrt{s}$ is increased past $600-800$ GeV, then also $\tilde{t}_1\bar{\tilde{t}}_1$, $\tilde{\nu}_\tau\bar{\tilde{\nu}}_\tau$ and $\tilde{\tau}_1\bar{\tilde{\tau}}_1$ become successively accessible. This benchmark model can be converted to a model line by varying the GUT-scale third generation mass parameter $m_0(3)$ or by varying μ. The light higgs mass m_h can be pushed as high as ~ 124 GeV if larger values of $m_0(3)$ and $|A_0|$ are selected [99].

4.2 Hidden SUSY

Models of "hidden SUSY" [75] are motivated by the fact that the magnitude of the superpotential higgsino mass parameter μ itself has been suggested as a measure of fine-tuning [49]. This idea has been used to argue that mSUGRA/CMSSM models in the hyperbolic branch/focus point region are less fine-tuned than generic parameter space regions. Natural SUSY models wherein Λ_{NS} slides into the $\gtrsim 300$ GeV regime but maintain $|\mu| \lesssim 300$ GeV morph into hidden SUSY. Here, we select a model where all mass parameters are large except for the μ parameter, which may lie in the $100-300$ GeV range. The parameter space suggested is that of the 2-parameter non-universal Higgs mass (NUHM2) model:

$$m_0,\ m_{1/2},\ A_0,\ \tan\beta,\ \mu,\ m_A\ . \tag{5}$$

Here, we adopt a benchmark point with parameters $m_0 = 5$ TeV, $m_{1/2} = 0.8$ TeV, $A_0 = -8.3$ TeV, $\tan\beta = 10$ with $\mu = 0.15$ TeV and $m_A = 1$ TeV. The spectrum is given in Table 1.

Hidden SUSY models are very difficult to detect at LHC. In contrast to natural SUSY, the third generation scalars are also beyond 1 TeV. While the higgsino-like light charginos and neutralinos are produced at large rates, the very low energy release from their decays will be hard to detect above background levels, making them all look like missing transverse energy. If the cross-sections are large enough, the decays of the $\tilde{\chi}_3^0 \to \tilde{\chi}_1^\pm W^\pm$, $\tilde{\chi}_{1,2}^0 Z$ or $\tilde{\chi}_{1,2}^0 h$ might provide a source of isolated leptons visible at the LHC if the $\tilde{t}_1$ is too heavy for detection.

The ILC operating at energy $\sqrt{s} \gtrsim 300$ GeV should be able to detect and distinguish $\tilde{\chi}_1^+\tilde{\chi}_1^-$ and $\tilde{\chi}_1^0\tilde{\chi}_2^0$ production as in the natural SUSY case discussed above. The small mass gap, angular distribution and polarization dependence of the signal cross sections may all be used to help establish the higgsino-like nature of the light $\tilde{\chi}_1^\pm$, $\tilde{\chi}_2^0$ and $\tilde{\chi}_1^0$. In addition, the $\tilde{\chi}_3^0$ is accessible in mixed production with the lighter neutralinos already at $\sqrt{s} \gtrsim 500$ GeV.

Phenomenologically similar scenarios – which are even more minimal case in the sense that the $\tilde{\chi}_3^0$ and the $\tilde{t}_1$ are in the multi-TeV regime as well – have been suggested by Brümmer and Buchmüller [140]. We will discuss one example in section 4.8.

4.3 NUHM2 benchmark with light A, H and $H^\pm$

This benchmark point, constructed within the 2-parameter non-universal Higgs model (NUHM2), provides a model with relatively light A, H and $H^\pm$ Higgs bosons while the remaining sparticles are beyond current LHC reach. We adopt parameters $m_0 = 10$ TeV, $m_{1/2} = 0.4$ TeV, $A_0 = -16$ TeV, $\tan\beta = 6$ with $\mu = 5$ TeV and $m_A = 275$ GeV. The values of $m_h = 124.4$ GeV, with $m_H = 277.5$ GeV and $m_{H^+} = 286.0$ GeV are obtained with FeynHiggs [58]. The only colored sparticles accessible to the LHC are the gluinos with $m_{\tilde{g}} = 1.225$ TeV, while most squarks live at around $m_{\tilde{q}} \sim 10$ TeV. The gluino decays are dominated by $\tilde{g} \to \tilde{\chi}_1^0 t\bar{t}$ and $\tilde{g} \to (\tilde{\chi}_1^\pm \to \tilde{\chi}_1^0 W^\pm)tb$, and thus will require dedicated analyses for high multiplicity final states or boosted techniques for identifying W- or t-jets. The signal $pp \to \tilde{\chi}_1\tilde{\chi}_2^0 \to Wh + E_T^{\rm miss} \to \ell\nu_\ell + b\bar{b} + E_T^{\rm miss}$ should ultimately be observable at LHC14 [59]. The Higgs bosons, apart from the light CP-even one, can most probably not be observed at the LHC in this low $\tan\beta$ and m_A region [142].

At the ILC with $\sqrt{s} \sim 0.5$ TeV, we expect $e^+e^- \to Ah,\ ZH$ to occur at observable rates. As $\sqrt{s}$ rises beyond 600 GeV, AH and H^+H^- production becomes accessible while mixed $\tilde{\chi}_1^0\tilde{\chi}_2^0$ pair production, though accessible, is suppressed. At 800 GeV, $\tilde{\chi}_1^\pm$ pairs will be produced in addition. Due to heavy sleptons and the sizable mass gap between $\tilde{\chi}_1^\pm$, $\tilde{\chi}_2^0$ and the $\tilde{\chi}_1^0$, one expects electroweakino decays to real $W^\pm$ and Z bosons, very similar to the "Point 5" benchmark studied in the Letter of Intents of the ILC experiments [158, 159].

4.4 mSUGRA/CMSSM

Large portions of mSUGRA model parameter space are now ruled out by direct searches for gluino and squark production at LHC7. In addition, if one requires $m_h \sim 124-126$ GeV, then even larger portions of parameter space are excluded: $m_{1/2} < 1$ TeV (corresponding to $m_{\tilde{g}} < 2.2$ TeV) for low m_0 and $m_0 < 2.5$ TeV (corresponding to $m_{\tilde{q}} < 2.5$ TeV) for low $m_{1/2}$ [114]. These tight constraints rule out almost all of the co-annihilation and A-funnel annihilation regions [114, 33]. The HB/FP region moves to very large $m_0 > 10$

TeV since now $|A_0|$ must be large to accommodate the rather large value of m_h. Some remaining dark matter allowed parameter space thus remains.

An example is provided by an mSUGRA benchmark point with $m_0 = 15.325$ TeV, $m_{1/2} = 0.845884$ TeV, $A_0 = -10.8126$ TeV and $\tan\beta = 20.197$. The masses are shown in Table 1. At this point, $m_{\tilde{g}} = 2320$ GeV and $m_{\tilde{q}} \sim 15.3$ TeV. However, $\mu \sim 145$ GeV, and so $m_{\tilde{\chi}_1^\pm} = 155.3$ GeV and $m_{\tilde{\chi}_2^0} = 154.8$ GeV and $m_{\tilde{\chi}_1^0} = 141.6$ GeV. Thus, this point – although very fine-tuned in the EW sector (with $m_{\tilde{t}_1} \sim 8.7$ TeV) – would allow $\tilde{\chi}_1^+\tilde{\chi}_1^-$ and $\tilde{\chi}_1^0\tilde{\chi}_2^0$ production at ILC with a $\tilde{\chi}_1^\pm - \tilde{\chi}_1^0$ mass gap of 14 GeV. The $\tilde{\chi}_1^0$ would be of mixed bino-higgsino variety. When increasing $\sqrt{s}$ towards 1 TeV, the heavier neutralinos become accessible in mixed production and $\tilde{\chi}_3^0$ pair production.

Since all scalars are above 10 TeV (apart from the lighter top squark at $m_{\tilde{t}_1} \sim 8$ TeV), the most promising signature for the LHC is gluino production, followed by $\tilde{g} \to \tilde{\chi}_i^0 t\bar{t}$ and $\tilde{g} \to (\tilde{\chi}_j^\pm \to \tilde{\chi}_1^0 W^\pm)tb$ as discussed in case of the NUHM2 benchmark in Section 4.3.

4.5 Model with non-universal gaugino masses (NUGM)

In supergravity, gaugino masses arise from the Lagrangian term (using 4-component spinor notation)

$$\mathcal{L}_F^G = -\frac{1}{4}e^{G/2}\frac{\partial f_{AB}^*}{\partial \hat{h}^{*j}}\Big|_{\hat{h}\to h}\left(G^{-1}\right)_k^j G^k \bar{\lambda}_A \lambda_B \tag{6}$$

where f_{AB} is the holomorphic gauge kinetic function with gauge indices A, B in the adjoint representation, λ_A are four-component gaugino fields and the $\hat{h}_m$ are hidden sector fields needed for breaking of supergravity. If $f_{AB} \sim \delta_{AB}$, then gaugino masses are expected to be universal at the high energy scale where SUSY breaking takes place. However, in general supergravity, f_{AB} need only transform as the symmetric product of two adjoints. In general, gaugino masses need not be universal at any energy scale, giving rise to models with non-universal gaugino masses (NUGM).

For a NUGM benchmark, we select a model with $m_0 = 3$ TeV, $A_0 = -6$ TeV, $\tan\beta = 25$ and $\mu > 0$. We select gaugino masses at the GUT scale as $M_1 = M_2 = 0.25$ TeV with $M_3 = 0.75$ TeV. The spectrum is listed in column 6 of Table 1. With $m_{\tilde{g}} \simeq 1.8$ TeV and $m_{\tilde{q}} \simeq 3$ TeV, the model is clearly beyond current LHC reach for gluinos and squarks. The model should be testable in future LHC searches, not only in with the standard jets plus missing E_t analyses, but also via searches tailored for very high multiplicity final states and using b-jet tagging [34], since the gluino almost exclusively decays via $\tilde{g} \to \tilde{t}_1 t$ followed by $\tilde{t}_1 \to \tilde{\chi}_1^0 t$. In addition, the production channel $pp \to \tilde{\chi}_1^\pm\tilde{\chi}_2^0 \to WZ + E_T^{\rm miss}$ may be testable in the near future [157].

The rather light spectrum of electroweak gauginos with $m_{\tilde{\chi}_1^\pm} \sim 2m_{\tilde{\chi}_1^0} \sim 216$ GeV allows for chargino pair production at ILC followed by $\tilde{\chi}_1^\pm \to \tilde{\chi}_1^0 W$ decay, yielding a $W^+W^- + \not{E}$ signature. The $\tilde{\chi}_1^0\tilde{\chi}_2^0$ and $\tilde{\chi}_2^0\tilde{\chi}_2^0$ production channels tend to be suppressed, but may offer additional search avenues albeit at low rates.

4.6 A pMSSM model with light sleptons

In many constrained SUSY models where slepton and squark masses are correlated at some high energy scale, relatively light sleptons with mass $\sim 100 - 200$ GeV are forbidden. However, if we invoke the greater parameter freedom of the pMSSM, then spectra with light sleptons and heavy squarks can easily be generated. In fact, these models have some degree of motivation in that they naturally reconcile the measured $(g-2)_\mu$ anomaly (which favors light smuons) with the measured $b \to s\gamma$ branching fraction (which favors rather heavy third generation squarks).

In the pMSSM[148, 149], one inputs *weak scale* values of the following parameters: 1. $m_{\tilde{g}}, \mu, m_A, \tan\beta$, 2. m_Q, m_U, m_D, m_L, m_E for each of the three generations, 3. gaugino masses M_1 and M_2 and 4. third generation trilinear A_t, A_b and A_τ. This gives a 19 dimensional parameter space if first and second generation scalar masses are taken as degenerate, else a 24 dimensional parameter space for independent first, second and third generations.[4] As an example, we specify the "$\delta M\tilde{\tau}$" benchmark with the following parameters, all given at a scale of 1 TeV:

[4]Alternatively, the $SU(3)$ gaugino mass M_3 may be substituted for the physical gluino mass as an input.

PMQ	NS	HS	NUHM2	mSUGRA	NUGM
$m_0(1,2)$, $m_0(3)$	13.35, 0.76	5.0	10.0	15.325	3.0
$m_{1/2}$ / M_1, M_2, M_3	1.38	0.7	0.4	0.8459	0.25,0.25,0.75
$\tan\beta$	23	10	6	20.2	25
A_0	-0.167	-8.3	-16.0	-10.81	-6.0
m_h	0.121	0.125	0.124	0.126	0.125
m_A	1.55	1.0	0.275	14.22	3.268
m_H	1.560	1.006	0.277	14.31	3.289
$m_{H^\pm}$	1.563	1.011	0.286	14.31	3.293
μ	0.15	0.15	6.0	0.144	2.36
$m_{\tilde{g}}$	3.27	1.79	1.225	2.32	1.835
$m_{\tilde{\chi}^\pm_{1,2}}$	0.156, 1.18	0.154, 0.611	0.386, 4.9	0.155, 0.756	0.216, 2.37
$m_{\tilde{\chi}^0_{1,2}}$	0.148, 0.156	0.14, 0.158	0.192, 0.384	0.141, 0.155	0.109, 0.215
$m_{\tilde{\chi}^0_{3,4}}$	0.615, 1.18	0.32, 0.621	4.93, 4.93	0.397, 0.780	2.36, 2.36
$m_{\tilde{u}_{L,R}}$	13.58, 13.59	5.12, 5.27	9.92, 10.21	15.31, 15.36	3.30, 3.31
$m_{\tilde{t}_{1,2}}$	0.286, 0.914	1.21, 3.55	4.14, 7.43	8.75, 12.29	1.11, 2.29
$m_{\tilde{d}_{L,R}}$	13.6, 13.6	5.12, 5.09	9.92, 9.89	15.31, 15.37	3.30, 3.31
$m_{\tilde{b}_{1,2}}$	0.795, 1.26	3.58, 5.0	7.45, 9.84	12.26, 14.85	2.30, 2.99
$m_{\tilde{e}_{L,R}}$	13.4, 13.3	5.11, 4.8	10.2, 9.66	15.31, 15.31	3.0, 3.0
$m_{\tilde{\tau}_{1,2}}$	0.43, 0.532	4.73, 5.07	9.61, 10.1	14.68, 14.99	2.6, 2.81
$\Omega^{std}_{\tilde{\chi}^0}h^2$	0.007	0.009	210	0.008	1540
$\langle\sigma v\rangle(v\to 0)$ [cm^3/s]	3.1×10^{-25}	2.8×10^{-25}	5.1×10^{-30}	2.9×10^{-25}	1.5×10^{-32}
$\sigma^{SI}(\tilde{\chi}^0 p)\times 10^9$ [pb]	2.0	11.	0.007	4.0	0.0004
$a_\mu^{SUSY}\times 10^{10}$	0.03	0.09	0.05	0.02	0.45
$BF(b\to s\gamma)\times 10^4$	3.3	3.3	3.48	3.05	2.95
$BF(B_S\to\mu^+\mu^-)\times 10^9$	4.2	3.8	3.9	3.8	3.9
$BF(B_u\to\tau\nu_\tau)\times 10^4$	1.3	1.3	1.3	1.3	1.3

Table 1: Input parameters and mass spectrum and rates for post LHC7 benchmark points $1-5$. All masses and dimensionful parameters are in TeV units. All values have been obtained with Isasugra apart from Higgs masses for the NUHM2 point, which have been taken from FeynHiggs.

- Higgs sector parameters:
  $\tan(\beta) = 10$, $\mu = 200$ GeV, $m_A = 400$ GeV,
- trilinear couplings: $A_t = A_b = A_\tau = -1.8$ TeV,
- gaugino mass parameters:
  $M_3 = 2$ TeV, $M_2 = 225$ GeV, $M_1 = 107$ GeV,
- slepton mass parameters:
  $m_L(1,2,3) = 200$ GeV, $m_E(1,2) = 125$ GeV, $m_E(3) = 103$ GeV,
- squark mass parameters:
  $m_Q(1,2) = m_D(1,2) = m_U(1,2) = 2$ TeV, $m_L(3) = 1.5$ TeV, $m_U(3) = m_D(3) = 400$ GeV.

The resulting sparticle masses, which have been obtained with SPheno [150, 152] with Higgs masses calculated by FeynHiggs [58], along with the neutralino relic density obtained from [60], are listed in Table 2.

With masses around 2 TeV, the gluino and the partners of the light quarks are beyond current LHC limits, especially since the gluino decays dominantly via $\tilde{t}_1 t$ or $\tilde{b}_1 b$. Although light sleptons are present, the current limits on direct electroweakino production [134] do not cover this case due to the small mass difference between the $\tilde{\tau}_1$ and the $\tilde{\chi}^0_1$, which leads to soft τ leptons in the chargino and neutralino decays instead of the searched for high p_t electrons and muons.

All sleptons and electroweakinos are within ILC reach at $\sqrt{s} \lesssim 500$ GeV. In addition, the light top and bottom squarks as well as the heavy Higgs bosons would be accessible at ILC with $\sqrt{s} \sim 1$ TeV.

Due to the large number of production processes open already at $\sqrt{s} \sim 500$ GeV, which often yield long cascades[151], $\delta M\tilde{\tau}$ is actually an experimentally challenging scenario for ILC. Therefore, it is an ideal case study to demonstrate the separation of many closely spaced new matter states with all the tools offered by ILC, including threshold scans and different beam polarization configurations, but also taking into account realistic assumptions on the beam energy spectrum, accelerator backgrounds and detector resolutions.

At a center-of-mass energy of 1 TeV or above, the rather small mass difference of 40 GeV between the light stop and sbottom as well as the separation of the heavy Higgs states will provide additional experimental challenges.

4.7 Kallosh-Linde or G2MSSM benchmark

While minimal anomaly-mediation seems on shaky ground due to its prediction of a light Higgs scalar $m_h \lesssim 120$ GeV, other similar models have emerged as perhaps more compelling. One of these models – by Kallosh and Linde (the KL model [153, 154]) – attempts to stabilize stringy moduli fields via a generalization of the KKLT method [155] utilizing a racetrack superpotential. The moduli in this theory end up superheavy and allow for the chaotic inflationary scenario to emerge in supergravity models. In this class of models, the various scalar fields have a mass of the order of the gravitino mass, with $m_{3/2} \sim 100$ TeV. The gauginos, however, remain below the TeV scale, and adopt the usual AMSB form. Another stringy model by Acharya *et al.* [156] known as G2MSSM also predicts multi-TeV scalars. In the G2MSSM, the gauginos are again light, typically with $M_2 \ll M_1 \sim M_3$ so that again a model with light wino-like $\tilde{\chi}_1$ and $\tilde{\chi}_1^0$ emerges.

To model these cases, we adopt the NUHM2 model, but with non-universal gaugino masses, with parameters chosen as $m_0 = 25$ TeV, $m_{1/2} = 200$ GeV, $A_0 = 0$, $\tan\beta = 10$ with $\mu = m_A = 2$ TeV. We then set GUT scale gaugino masses to the AMSB form given by $M_1 = 1320$ GeV, $M_2 = 200$ GeV and $M_3 = -600$ GeV. The wino-like $\tilde{\chi}_1^0$ state is the lightest MSSM particle with mass $m_{\tilde{\chi}_1^0} = 200.07$ GeV while the wino-like lightest chargino has mass $m_{\tilde{\chi}_1^\pm} = 200.4$ GeV. We also have a bino-like $\tilde{\chi}_2^0$ with $m_{\tilde{\chi}_2^0} = 616.5$ GeV and a gluino with $m_{\tilde{g}} = 1788$ GeV. All matter scalars have mass near the 25 TeV scale, and so decouple. The light Higgs scalar has mass $m_h = 125$ GeV.

In this case, gluino pair production may barely be accessible to LHC14 with of order 10^2 fb^{-1} of data [139]. At ILC, the decay products from chargino decay will be extremely soft. However, the wino-like chargino is then quasi-stable, flying of order centimeters before decay, leaving a highly ionizing track (HIT) which terminates upon decay into very soft decay products. Chargino pair production could be revealed at ILC via initial state radiation of a hard photon, and then identification of one or more HITs, or stubs. In addition, if $\sqrt{s}$ is increased to ~ 1 TeV, then $\tilde{\chi}_1^0\tilde{\chi}_2^0$ production opens up, although rates are expected to be small. In this case, one expects $\tilde{\chi}_2^0 \to W\tilde{\chi}_1^\pm$ or $\tilde{\chi}_1^0 h$ to occur.

4.8 Brümmer-Buchmüller (BB) benchmark

Brümmer and Buchmüller have proposed a model wherein the Fermi scale emerges as a focus point within high scale gauge mediation [140]. The model is inspired by GUT-scale string compactifications which frequently predict a large number of vector-like states in incomplete GUT multiplets which may serve as messenger fields for gauge mediated SUSY breaking which is implemented at or around the GUT scale. By adopting models with large numbers of messenger fields, it is found that the weak scale emerges quite naturally from the scalar potential as a focus point from RG running of the soft terms. The soft SUSY breaking terms receive both gauge-mediated and gravity-mediated contributions. The gauge-mediated contributions are dominant for most soft masses, while the A-terms and μ may be forbidden by symmetry. The superpotential higgsino mass term μ emerges from gravitational interactions and is expected to be of order the gravitino mass $\mu \sim m_{3/2} \sim 150 - 200$ GeV. The spectrum which emerges from the model tends to contain gluino and squark masses in the several TeV range so that the model is compatible with LHC constraints. States accessible to a linear collider would include the higgsino-like light charginos $\tilde{\chi}_1^\pm$ and neutralinos $\tilde{\chi}_{1,2}^0$ similar to the Hidden SUSY model in Subsection 4.2.

For ILC studies, we adopt the benchmark model with messenger indices $(N_1,\ N_2,\ N_3) = (17, 23, 9)$ with $\tan\beta = 52$ and weak scale values of $\mu = 200$ GeV and $m_A = 1120$ GeV, with $A_i \simeq 0$. Then the GUT scale scalar masses are found to be: $m_Q = 1538.5$ GeV, $m_U = 1181.2$ GeV, $m_D = 1033.8$ GeV, $m_L = 1274.7$ GeV and $m_E = 989.5$ GeV. The GUT-scale gaugino masses are given by $M_1 = 4080$ GeV, $M_2 = 4600$ GeV and $M_3 = 1800$ GeV. The spectrum generated from Isasugra is listed in Table 2.

mass	$\delta M\tilde{\tau}$	KL	BB	NMH
m_h	0.124	0.125	0.123	0.125
m_A	0.400	2.0	1.120	5.32
m_H	0.401	2.013	1.127	5.35
$m_{H^\pm}$	0.408	2.014	1.131	5.36
μ	0.2	2.0	0.2	3.0
$m_{\tilde{g}}$	2.0	1.79	3.817	1.496
$m_{\tilde{\chi}^\pm_{1,2}}$	0.155, 0.282	0.2004, 2.05	0.214, 3.76	0.535, 3.0
$m_{\tilde{\chi}^0_{1,2}}$	0.097, 0.162	0.2001, 0.616	0.0.205, 0.208	0.277, 0.533
$m_{\tilde{\chi}^0_{3,4}}$	0.209, 0.282	2.05, 2.05	1.83, 3.78	2.99, 3.0
$m_{\tilde{u}_{L,R}}$	2.03, 2.03	24.8, 25.3	4.55, 3.56	1.237, 1.215
$m_{\tilde{t}_{1,2}}$	0.299, 1.53	16.4, 20.9	2.28, 3.85	1.998, 3.763
$m_{\tilde{d}_{L,R}}$	2.03, 2.03	24.8, 24.8	4.55, 3.41	1.24, 1.167
$m_{\tilde{b}_{1,2}}$	0.338, 1.53	20.8, 24.7	2.54, 3.85	3.789, 4.874
$m_{\tilde{e}_{L,R}}$	0.208, 0.135	25.3, 24.4	3.25, 1.79	0.507, 0.284
$m_{\tilde{\tau}_{1,2}}$	0.104, 0.210	24.3, 25.2	0.69, 3.03	4.65, 4.85
$\Omega^{std}_{\tilde{\chi}^0}h^2$	0.116	0.0025	0.008	0.07
$\langle\sigma v\rangle(v\to 0)\times 10^{-25}$ $[cm^3/s]$	-	19	1.9	0.0005
$\sigma^{SI}(\tilde{\chi}^0 p)\times 10^9$ [pb]	-	0.04	0.24	0.0012
$a_\mu^{SUSY}\times 10^{10}$	33.5	0.0002	0.51	23.4
$BF(b\to s\gamma)\times 10^4$	3.3	3.2	3.2	3.2
$BF(B_S\to\mu^+\mu^-)\times 10^9$	3.9	3.8	4.4	3.9
$BF(B_u\to\tau\nu_\tau)\times 10^4$	1.1	1.3	1.1	1.3

Table 2: Input parameters and mass spectrum and rates for post LHC7 benchmark points $6-9$. All masses and dimensionful parameters are in TeV units. Entries marked "-" have not been calculated. All values are obtained from Isasugra apart from $\delta M\tilde{\tau}$, which have been calculated with SPheno and FeynHiggs (Higgs sector).

4.9 Normal scalar mass hierarchy

Models with a normal scalar mass hierarchy ($m_0(1) \simeq m_0(2) \ll m_0(3)$) [141] are motivated by the attempt to reconcile the $> 3\sigma$ discrepancy in $(g-2)_\mu$ (which requires rather light sub-TeV smuons) with the lack of a large discrepancy in $BF(b\to s\gamma)$, which seems to require third generation squarks beyond the TeV scale. The idea here is to require a high degree of degeneracy amongst first/second generation sfermions in order to suppress the most stringent FCNC processes, while allowing third generation sfermions to be highly split, since FCNC constraints from third generation particles are relatively mild. The *normal mass hierarchy* follows in that first/second generation scalars are assumed much lighter than third generation scalars, at least at the GUT scale. Renormalization group running then lifts first/second generation squark masses to high values such that $m_{\tilde{q}} \sim m_{\tilde{g}}$. However, first/second generation sleptons remain in the several hundred GeV range since they have no strong coupling.

Here, we adopt a NMH benchmark point with separate $\mathbf{5}^*$ and $\mathbf{10}$ scalar masses as might be expected in a $SU(5)$ SUSY GUT model. We adopt the following parameters: $m_5(3) \sim m_{10}(3) = 5$ TeV, $m_{1/2} = 0.63$ TeV, $A_0 = -8.5$ TeV, $\tan\beta = 20$, $\mu > 0$ with $m_L(1,2) = m_D(1,2) \equiv m_5(1,2) = 0.2$ TeV, and $m_Q(1,2) = m_U(1,2) = m_E(1,2) \equiv m_{10}(1,2) = 0.375$ TeV. The spectrum generated using Isasugra 7.82 with

non-universal scalar masses is listed in Table 2, where we find $m_{\tilde{\chi}_1^0} \simeq 277$ GeV, $m_{\tilde{e}_R} \simeq m_{\tilde{\mu}_R} = 284$ GeV, $m_{\tilde{\nu}_{e,\mu L}} \simeq 300$ GeV and $m_{\tilde{e}_L} \simeq m_{\tilde{\mu}_L} = 507$ GeV, as well as $m_h \simeq 125$ GeV. In the colored sector, $m_{\tilde{g}} = 1.5$ TeV with $m_{\tilde{q}} \sim 1.2$ TeV, so the model is compatible with LHC7 constraints, but may be testable at LHC8. The first and second generation squarks decay mainly into $\tilde{\chi}_1^{\pm}$+ jet, followed by $\tilde{\chi}_1^{\pm} \to \tilde{\nu}_l l \to \tilde{\chi}_1^0 \nu_l l$, or alternatively into $\tilde{\chi}_2^0$+ jet, followed by $\tilde{\chi}_2^0 \to \tilde{\nu}_l \nu_l \to \tilde{\chi}_1^0 \nu_l \nu_l$. Thus, squark pair production will give only 2 jets, either accompanied by just missing transverse energy or by 1 or 2 leptons. The gluino decays mostly into first or second generation squarks plus an additional jet. Since the $\tilde{\chi}_2^0$ decays invisibly, the only sign of direct $\tilde{\chi}_1^{\pm}\tilde{\chi}_2^0$ production will be a single lepton from the the $\tilde{\chi}_1^{\pm}$ decay plus missing transverse energy.

The model does indeed reconcile $(g-2)_\mu$ with $BF(b \to s\gamma)$ since $\Delta a_\mu^{SUSY} \sim 23 \times 10^{-10}$ and $BF(b \to s\gamma) = 3.22 \times 10^{-4}$. Also, the thermal neutralino abundance is given as $\Omega_{\tilde{\chi}_1^0} h^2 \simeq 0.07$ due to neutralino-slepton co-annihilation. An ILC with $\sqrt{s} \gtrsim 600$ GeV would be needed to access the $\tilde{e}_R\bar{\tilde{e}}_R$ and $\tilde{\mu}_R\bar{\tilde{\mu}}_R$ pair production. These reactions would give rise to very low energy di-electron and di-muon final states which would be challenging to extract from two-photon backgrounds. However, since it has been demonstrated that mass differences of this size are manageable even in the case of τ leptons from $\tilde{\tau}$ decays [161], it should be feasible also in case of electrons or muons. Since $\tilde{\nu} \to \nu + \tilde{\chi}_1^0$, sneutrinos would decay invisibly, although the reaction $e^+e^- \to \tilde{\nu}_L\bar{\tilde{\nu}}_L\gamma$ may be a possibility. The lack of $\tilde{\tau}^+\tilde{\tau}^-$ pair production might give a hint that nature is described by a NMH model.

5 Conclusions

At first sight, it may appear very disconcerting that after one full year of data taking at LHC7, with ~ 5 fb^{-1} per experiment, no sign of supersymmetry is yet in sight. On the other hand, evidence at the 3σ level seems to be emerging that hints at the presence of a light higgs scalar with mass $m_h \sim 125$ GeV. While m_h can theoretically inhabit a rather large range of values of up to 800 GeV in the Standard Model, the simplest supersymmetric extensions of the SM require it to lie below ~ 135 GeV. A light SUSY Higgs of mass ~ 125 GeV seems to require top squark masses $m_{\tilde{t}_i} \gtrsim 1$ TeV with large mixing: thus, the emerging signal seems more consistent with a super-TeV sparticle mass spectrum than with a sub-TeV spectrum, and indeed the latter seems to be nearly excluded by LHC searches for gluinos and first and second generation squarks (unless there is a highly compressed spectrum, or other anomalies). In addition, a Higgs signal around 125 GeV highly stresses at least the minimal versions of constrained models such as AMSB and GMSB, and may favor gravity-mediated SUSY breaking models which naturally accommodate large mixing in the top squark sector.

While some groups had predicted just prior to LHC running a very light sparticle mass spectrum (based on global fits of SUSY to a variety of data, which may have been overly skewed by the $(g-2)_\mu$ anomaly), the presence of a multi-TeV spectrum of at least first/second generation matter scalars was not unanticipated by many theorists. The basis of this latter statement rests on the fact that a decoupling of first/second generation matter scalars either solves or at least greatly ameliorates: the SUSY flavor problem, the SUSY CP problem, the SUSY GUT proton decay problem and, in the context of gravity mediation where the gravitino mass sets the scale for the most massive SUSY particles, the gravitino problem.

In contrast, examination of electroweak fine-tuning arguments, applied to the radiatively corrected SUSY scalar potential imply that models with 1. low $|\mu| \lesssim \Lambda_{NS} \sim 200$ GeV, 2. third generation squarks with $m_{\tilde{t}_{1,2},\tilde{b}_1} \lesssim 1.5$ TeV and 3. $m_{\tilde{g}} \lesssim 4$ TeV are favored. Since first/second generation matter scalars don't enter the electroweak scalar potential, these sparticles can indeed exist in the 10-50 TeV regime – as required by decoupling – without affecting fine-tuning. The class of models which fulfill these conditions are called *natural SUSY* or NS models. NS models are typically very hard to detect at LHC unless some third generation squarks are very light $\sim 200-600$ GeV, with a large enough decay mass gap to yield sufficient visible energy. The set of light higgsinos $\tilde{\chi}_1^{\pm}$, $\tilde{\chi}_2^0$ and $\tilde{\chi}_1^0$ can be produced at high rates at LHC, but the very tiny visible energy release from higgsino decays makes them exceedingly hard to detect. However, NS at an ILC may well be a boon! An ILC would likely then be a *higgsino factory* in addition to a Higgs factory. The small visible energy release from higgsino-like chargino decays should be visible against backgrounds originating from two-photon initiated processes, especially when an additional hard ISR photon is required. In addition, there is a good chance that some or even most third generation squarks and sleptons may be accessible given

high enough beam energy. As the fine-tuning upper bound Λ_{NS} increases, the NS spectrum blends into Hidden SUSY where the higgsinos are still light, but the third generation is lifted beyond LHC/ILC reach. The HS collider phenomenology is expected to be very similar to that emerging from a non-minimal GMSB model suggested by Brümmer and Buchmüller (BB).

We also present several benchmark models consistent with LHC and other constraints which predict some varied phenomenology. One NUHM2 point with heavy matter scalars and $m_h = 125$ GeV contains A and H Higgs bosons which would also be accessible to ILC. A model with non-universal gaugino masses (NUGM) allows for chargino pair production at ILC followed by $\tilde{\chi}_1^{\pm} \to W\tilde{\chi}_1^0$ decay, leading to $W^+W^- + \not{E}$ events. Also, a rare surviving benchmark from mSUGRA/CMSSM is presented in the far focus point region with $m_h = 125$ GeV, with matter scalars at $m_{\tilde{q},\tilde{\ell}} \sim 15$ TeV, where chargino pairs of the mixed bino-higgsino variety are accessible to an ILC. We also present one benchmark point from the Kallosh-Linde (KL) model. In this case, matter scalars have masses $m_{\tilde{q},\tilde{\ell}} \sim m_{3/2} \sim 25$ TeV, but gaugino masses follow the AMSB pattern, with the $\tilde{\chi}_1^{\pm}$ and $\tilde{\chi}_1^0$ being nearly pure wino, with $m_{\tilde{\chi}_1^{\pm}} - m_{\tilde{\chi}_1^0} \sim 0.33$ GeV mass gap. If the mass gap is small enough, then charginos can fly a measureable distance before decay. It might be possible to detect $e^+e^- \to \tilde{\chi}_1^+\tilde{\chi}_1^-\gamma \to \gamma +$ soft debris including possible highly ionizing tracks which terminate into soft pions. The phenomenology of this model is similar to that expected from G2MSSM of Acharya *et al.* [156]. Finally, we present pMSSM and NMH models with light charginos and sleptons which is in accord with the $(g-2)_\mu$ anomaly, $m_h \sim 124$ GeV and with a standard neutralino relic abundance $\Omega_{\tilde{\chi}_1^0}^{std}h^2 = 0.11$. The ILC-relevant part of the spectrum is very similar to the well-studied SPS1a scenario [160] (or its variant SPS1a').

In summary, results from the LHC7 run in 2011 have resulted so far in no sign of SUSY particles, although impressive new limits on gluino and squark masses have been determined. In addition, much of the expected mass range for a SM-like Higgs boson has been ruled out save for the narrow window of 115 GeV $< M_H <$ 127 GeV. Indeed, within this window, there exists $\sim 3\sigma$ hint for a 125 GeV Higgs signal in several different channels from both Atlas and CMS, and also from CDF/D0 at the Fermilab Tevatron. If the Higgs-hint is verified, this can be regarded as an overall positive for weak scale supersymmetry in that the Higgs would fall squarely within the narrow predicted SUSY window. While the lack of gluino and first generation squark signals at LHC7 may at first be disconcerting, it must be remembered that first generation squarks, and to some degree gluinos, contribute little to naturalness arguments which connect SUSY breaking to the weak scale. Naturalness arguments do favor a value of $\mu \sim M_Z$, with perhaps μ ranging as high as ~ 200 GeV. In this case, a spectrum of light higgsinos is anticipated. Such light higgsinos would be very difficult to detect at LHC, while an ILC with $\sqrt{s} = 0.25 - 1$ TeV would be a *higgsino factory*, in addition to a Higgs factory! Naturalness arguments, and also the muon $g-2$ anomaly, portend a rich assortment of new matter states likely accessible to the ILC, although such states will be difficult for LHC to detect. We hope the benchmark models listed here give some view as to the sort of new SUSY physics which may be expected at ILC in the post LHC7 era.

6 Acknowledgments

We thank Mikael Berggren, Azar Mustafayev, Krzysztof Rolbiecki and Annika Vauth for supporting calculations and valuable discussions, and Benno List and Xerxes Tata for comments on the manuscript.

7 Bibliography

References

[1] J. Wess and B. Zumino, Phys. Lett. B **49**, 52 (1974).

[2] A. Salam and J. A. Strathdee, Phys. Rev. D **11**, 1521 (1975).

[3] A. Salam and J. A. Strathdee, Phys. Lett. B **51**, 353 (1974).

[4] For a review, see *e.g.* H. Baer and X. Tata, Cambridge, UK: Univ. Pr. (2006) 537 p

[5] E. Witten, Nucl. Phys. B **188**, 513 (1981).

[6] R. K. Kaul, Phys. Lett. B **109**, 19 (1982).

[7] S. Ferrara, D. Z. Freedman, P. van Nieuwenhuizen, P. Breitenlohner, F. Gliozzi and J. Scherk, Phys. Rev. D **15**, 1013 (1977).

[8] E. Cremmer, S. Ferrara, L. Girardello and A. Van Proeyen, Nucl. Phys. B **212**, 413 (1983).

[9] For a review, see *e.g.* H. P. Nilles, Phys. Rept. **110**, 1 (1984).

[10] S. Dimopoulos, S. Raby and F. Wilczek, Phys. Rev. D **24**, 1681 (1981).

[11] U. Amaldi, W. de Boer and H. Fürstenau, Phys. Lett. B **260**, 447 (1991).

[12] P. Langacker and M. Luo, Phys. Rev. D **44**, 817 (1991).

[13] J. R. Ellis, S. Kelley and D. V. Nanopoulos, Phys. Lett. B **260**, 131 (1991).

[14] S. Heinemeyer, W. Hollik, D. Stockinger, A. M. Weber and G. Weiglein, JHEP **0608**, 052 (2006) [hep-ph/0604147].

[15] L. E. Ibanez and G. G. Ross, Phys. Lett. B **110**, 215 (1982).

[16] [Tevatron Electroweak Working Group and for the CDF and D0 Collaborations], arXiv:1107.5255 [hep-ex].

[17] L. Reina, hep-ph/0512377.

[18] B. W. Lee, C. Quigg and H. B. Thacker, Phys. Rev. D **16**, 1519 (1977).

[19] For a review, see A. Djouadi, Eur. Phys. J. C **59**, 389 (2009) [arXiv:0810.2439 [hep-ph]].

[20] F. D. Steffen, Eur. Phys. J. C **59**, 557 (2009) [arXiv:0811.3347 [hep-ph]].

[21] K. -Y. Choi, J. E. Kim, H. M. Lee and O. Seto, Phys. Rev. D **77**, 123501 (2008) [arXiv:0801.0491 [hep-ph]].

[22] H. Baer, A. Lessa, S. Rajagopalan and W. Sreethawong, JCAP **1106**, 031 (2011) [arXiv:1103.5413 [hep-ph]].

[23] H. Baer, A. Lessa and W. Sreethawong, JCAP **1201**, 036 (2012) [arXiv:1110.2491 [hep-ph]].

[24] K. Rajagopal, M. S. Turner and F. Wilczek, Nucl. Phys. B **358**, 447 (1991).

[25] L. Covi, H. -B. Kim, J. E. Kim and L. Roszkowski, JHEP **0105**, 033 (2001) [hep-ph/0101009].

[26] H. Baer, A. D. Box and H. Summy, JHEP **0908**, 080 (2009) [arXiv:0906.2595 [hep-ph]].

[27] D. Curtin, P. Jaiswal and P. Meade, arXiv:1203.2932 [hep-ph].

[28] W. Buchmüller, R. D. Peccei and T. Yanagida, Ann. Rev. Nucl. Part. Sci. **55**, 311 (2005) [hep-ph/0502169].

[29] I. Affleck and M. Dine, Nucl. Phys. B **249**, 361 (1985).

[30] M. Dine, L. Randall and S. D. Thomas, Nucl. Phys. B **458**, 291 (1996) [hep-ph/9507453].

[31] O. Buchm"uller *et al.*, Eur. Phys. J. C **71**, 1583 (2011) [arXiv:1011.6118 [hep-ph]].

[32] A. Arbey, M. Battaglia, A. Djouadi, F. Mahmoudi and J. Quevillon, Phys. Lett. B **708**, 162 (2012) [arXiv:1112.3028 [hep-ph]].

[33] H. Baer, V. Barger and A. Mustafayev, arXiv:1202.4038 [hep-ph].

[34] R. H. K. Kadala, P. G. Mercadante, J. K. Mizukoshi and X. Tata, Eur. Phys. J. C **56**, 511 (2008) [arXiv:0803.0001 [hep-ph]].

[35] K. R. Dienes and C. F. Kolda, hep-ph/9712322.

[36] F. Gabbiani, E. Gabrielli, A. Masiero and L. Silvestrini, Nucl. Phys. B **477**, 321 (1996) [hep-ph/9604387].

[37] V. S. Kaplunovsky and J. Louis, Phys. Lett. B **306**, 269 (1993) [hep-th/9303040].

[38] S. Dimopoulos and H. Georgi, Nucl. Phys. B **193**, 150 (1981).

[39] Y. Nir and N. Seiberg, Phys. Lett. B **309**, 337 (1993) [hep-ph/9304307].

[40] M. Dine, A. Kagan and S. Samuel, Phys. Lett. B **243**, 250 (1990).

[41] A. G. Cohen, D. B. Kaplan and A. E. Nelson, Phys. Lett. B **388**, 588 (1996) [hep-ph/9607394].

[42] N. Arkani-Hamed and H. Murayama, Phys. Rev. D **56**, 6733 (1997) [hep-ph/9703259].

[43] H. Murayama and A. Pierce, Phys. Rev. D **65**, 055009 (2002) [hep-ph/0108104].

[44] S. Weinberg, Phys. Rev. Lett. **48**, 1303 (1982).

[45] M. Y. Khlopov and A. D. Linde, Phys. Lett. B **138**, 265 (1984).

[46] M. Kawasaki, K. Kohri, T. Moroi and A. Yotsuyanagi, Phys. Rev. D **78**, 065011 (2008) [arXiv:0804.3745 [hep-ph]].

[47] G. W. Anderson and D. J. Castano, Phys. Rev. D **52**, 1693 (1995) [hep-ph/9412322].

[48] R. L. Arnowitt and P. Nath, Phys. Rev. D **46**, 3981 (1992).

[49] K. L. Chan, U. Chattopadhyay and P. Nath, Phys. Rev. D **58**, 096004 (1998) [hep-ph/9710473].

[50] S. F. King, M. Mühlleitner and R. Nevzorov, Nucl. Phys. B **860**, 207 (2012) [arXiv:1201.2671 [hep-ph]].

[51] C. Brust, A. Katz, S. Lawrence and R. Sundrum, JHEP **1203**, 103 (2012) [arXiv:1110.6670 [hep-ph]].

[52] M. Papucci, J. T. Ruderman and A. Weiler, arXiv:1110.6926 [hep-ph].

[53] S. Dimopoulos and G. F. Giudice, Phys. Lett. B **357**, 573 (1995) [hep-ph/9507282].

[54] R. Kitano and Y. Nomura, Phys. Lett. B **631**, 58 (2005) [hep-ph/0509039].

[55] R. Kitano and Y. Nomura, Phys. Rev. D **73**, 095004 (2006) [hep-ph/0602096].

[56] R. Kitano and Y. Nomura, hep-ph/0606134.

[57] K. Cheung, C. -W. Chiang and J. Song, JHEP **0604**, 047 (2006) [hep-ph/0512192].

[58] M. Frank, T. Hahn, S. Heinemeyer, W. Hollik, H. Rzehak and G. Weiglein, JHEP **0702** (2007) 047 [hep-ph/0611326].
G. Degrassi, S. Heinemeyer, W. Hollik, P. Slavich and G. Weiglein, Eur. Phys. J. C **28** (2003) 133 [hep-ph/0212020].
S. Heinemeyer, W. Hollik and G. Weiglein, Eur. Phys. J. C **9** (1999) 343 [hep-ph/9812472].
S. Heinemeyer, W. Hollik and G. Weiglein, Comput. Phys. Commun. **124** (2000) 76 [hep-ph/9812320].

[59] H. Baer, V. Barger, A. Lessa, W. Sreethawong and X. Tata, Phys. Rev. D **85**, 055022 (2012) [arXiv:1201.2949 [hep-ph]].

[60] G. Belanger, F. Boudjema, A. Pukhov and A. Semenov, Comput. Phys. Commun. **149**, 103 (2002) [hep-ph/0112278].

[61] K. S. Babu and C. F. Kolda, Phys. Rev. Lett. **84**, 228 (2000) [hep-ph/9909476].

[62] J. K. Mizukoshi, X. Tata and Y. Wang, Phys. Rev. D **66**, 115003 (2002) [hep-ph/0208078].

[63] D. Eriksson, F. Mahmoudi and O. Stal, JHEP **0811**, 035 (2008) [arXiv:0808.3551 [hep-ph]].

[64] E. Barberio *et al.* [Heavy Flavor Averaging Group], "Averages of $b-$hadron and $c-$hadron Properties at the End of 2007," arXiv:0808.1297 [hep-ex].

[65] S. Chatrchyan *et al.* [CMS Collaboration], Phys. Rev. Lett. **107** (2011) 191802 [arXiv:1107.5834 [hep-ex]].

[66] T. Aaltonen *et al.* [CDF Collaboration], Phys. Rev. Lett. **107** (2011) 239903 [arXiv:1107.2304 [hep-ex]].

[67] R. Aaij *et al.* [LHCb Collaboration], "Strong constraints on the rare decays $B_s \to \mu^+\mu^-$ and $B^0 \to \mu^+\mu^-$," arXiv:1203.4493 [hep-ex].

[68] G. W. Bennett *et al.* [Muon G-2 Collaboration], Phys. Rev. D **73**, 072003 (2006) [arXiv:hep-ex/0602035].

[69] M. Davier, A. Hoecker, B. Malaescu and Z. Zhang, Eur. Phys. J. C **71**, 1515 (2011) [arXiv:1010.4180 [hep-ph]].

[70] T. Moroi, Phys. Rev. D **53**, 6565 (1996) [Erratum-ibid. D **56**, 4424 (1997)] [hep-ph/9512396].

[71] J. L. Feng and K. T. Matchev, Phys. Rev. Lett. **86**, 3480 (2001) [hep-ph/0102146].

[72] D. Asner *et al.* [Heavy Flavor Averaging Group], "Averages of b-hadron, c-hadron, and τ-lepton Properties," arXiv:1010.1589 [hep-ex].

[73] M. Misiak *et al.*, Phys. Rev. Lett. **98**, 022002 (2007) [hep-ph/0609232].

[74] H. Baer and M. Brhlik, Phys. Rev. D **55**, 3201 (1997) [hep-ph/9610224].

[75] H. Baer, V. Barger and P. Huang, JHEP **1111**, 031 (2011) [arXiv:1107.5581 [hep-ph]].

[76] B. W. Lee and S. Weinberg, Phys. Rev. Lett. **39**, 165 (1977).

[77] E. A. Baltz, M. Battaglia, M. E. Peskin and T. Wizansky, Phys. Rev. D **74**, 103521 (2006) [hep-ph/0602187].

[78] H. Goldberg, Phys. Rev. Lett. **50**, 1419 (1983) [Erratum-ibid. **103**, 099905 (2009)].

[79] J. R. Ellis, J. S. Hagelin, D. V. Nanopoulos, K. A. Olive and M. Srednicki, Nucl. Phys. B **238**, 453 (1984).

[80] For a review, see G. Jungman, M. Kamionkowski and K. Griest, Phys. Rept. **267**, 195 (1996) [hep-ph/9506380].

[81] H. Baer, A. D. Box and H. Summy, JHEP **1010**, 023 (2010) [arXiv:1005.2215 [hep-ph]].

[82] H. Baer and A. D. Box, Eur. Phys. J. C **68**, 523 (2010) [arXiv:0910.0333 [hep-ph]].

[83] B. S. Acharya, G. Kane and E. Kuflik, "String Theories with Moduli Stabilization Imply Non-Thermal Cosmological History, and Particular Dark Matter," arXiv:1006.3272 [hep-ph].

[84] T. Moroi and L. Randall, Nucl. Phys. B **570**, 455 (2000) [hep-ph/9906527].

[85] G. Gelmini, P. Gondolo, A. Soldatenko and C. E. Yaguna, Phys. Rev. D **74**, 083514 (2006) [hep-ph/0605016].

[86] R. D. Peccei, Lect. Notes Phys. **741**, 3 (2008) [hep-ph/0607268].

[87] J. E. Kim and G. Carosi, Rev. Mod. Phys. **82**, 557 (2010) [arXiv:0807.3125 [hep-ph]].

[88] L. F. Abbott and P. Sikivie, Phys. Lett. B **120**, 133 (1983).

[89] J. Preskill, M. B. Wise and F. Wilczek, Phys. Lett. B **120**, 127 (1983).

[90] M. Dine and W. Fischler, Phys. Lett. B **120**, 137 (1983).

[91] H. P. Nilles and S. Raby, Nucl. Phys. B **198**, 102 (1982).

[92] O. Adriani *et al.* [PAMELA Collaboration], Nature **458**, 607 (2009) [arXiv:0810.4995 [astro-ph]].

[93] M. Ackermann *et al.* [Fermi LAT Collaboration], Phys. Rev. D **82**, 092004 (2010) [arXiv:1008.3999 [astro-ph.HE]].

[94] S. Profumo, Central Eur. J. Phys. **10**, 1 (2011) [arXiv:0812.4457 [astro-ph]].

[95] E. Aprile *et al.* [XENON100 Collaboration], Phys. Rev. Lett. **107**, 131302 (2011) [arXiv:1104.2549 [astro-ph.CO]].

[96] H. Baer, A. Mustafayev, E. -K. Park and X. Tata, JCAP **0701**, 017 (2007) [hep-ph/0611387].

[97] J. L. Feng and D. Sanford, JCAP **1105**, 018 (2011) [arXiv:1009.3934 [hep-ph]].

[98] J. A. Aguilar-Saavedra *et al.* [ECFA/DESY LC Physics Working Group], "TESLA: The superconducting electron positron linear collider with an integrated X-ray laser laboratory. Technical Design Report, Part 3: Physics at an e^+e^- linear collider," [hep-ph/0106315].

[99] H. Baer, V. Barger, P. Huang and X. Tata, "Natural Supersymmetry: LHC, dark matter and ILC searches," arXiv:1203.5539 [hep-ph].

[100] F. E. Paige, S. D. Protopopescu, H. Baer and X. Tata, "ISAJET 7.69: A Monte Carlo event generator for pp, anti-p p, and e+e- reactions," [hep-ph/0312045].

[101] H. Baer, A. Belyaev, T. Krupovnickas and X. Tata, JHEP **0402**, 007 (2004) [hep-ph/0311351].

[102] H. Baer, T. Krupovnickas and X. Tata, JHEP **0406**, 061 (2004) [hep-ph/0405058].

[103] C. Bartels, O. Kittel, U. Langenfeld and J. List, "Model-independent WIMP Characterisation using ISR," arXiv:1202.6516 [hep-ex].

[104] C. Bartels, O. Kittel, U. Langenfeld and J. List, "Measurement of radiative neutralino production," arXiv:1202.6324 [hep-ph].

[105] O. Buchmller *et al.*, "Higgs and Supersymmetry," arXiv:1112.3564 [hep-ph].

[106] L. J. Hall, D. Pinner and J. T. Ruderman, JHEP **1204**, 131 (2012) [arXiv:1112.2703 [hep-ph]].

[107] S. P. Martin, Phys. Rev. D **81**, 035004 (2010) [arXiv:0910.2732 [hep-ph]].

[108] S. Chatrchyan *et al.* [CMS Collaboration], "Combined results of searches for the standard model Higgs boson in pp collisions at $\sqrt{s} = 7$ TeV," arXiv:1202.1488 [hep-ex].

[109] ATLAS collaboration, "An update to the combined search for the Standard Model Higgs boson with the ATLAS detector at the LHC using up to 4.9 fb^{-1} of pp collision data at $\sqrt{s} = 7$ TeV," ATLAS-CONF-2012-019.

[110] [TEVNPH (Tevatron New Phenomina and Higgs Working Group) and CDF and D0 Collaborations], "Combined CDF and D0 Search for Standard Model Higgs Boson Production with up to 10.0 fb^{-1} of Data," arXiv:1203.3774 [hep-ex].

[111] S. Chatrchyan *et al.* [CMS Collaboration], "Search for neutral Higgs bosons decaying to tau pairs in pp collisions at $\sqrt{s} = 7$ TeV," arXiv:1202.4083 [hep-ex].

[112] ATLAS collaboration, "Search for charged Higgs bosons decaying via $H^+ \to \tau\nu$ in ttbar events using 4.6 fb^{-1} of pp collision data at $\sqrt{s} = 7$ TeV with the ATLAS detector," ATLAS-CONF-2012-011.

[113] ATLAS collaboration, "Search for neutral MSSM Higgs bosons decaying to $\tau^+\tau^-$ pairs in proton-proton collisions at $\sqrt{s} = 7$ TeV with the ATLAS detector," ATLAS-CONF-2011-132.

[114] H. Baer, V. Barger and A. Mustafayev, Phys. Rev. D **85**, 075010 (2012) [arXiv:1112.3017 [hep-ph]].

[115] S. Heinemeyer, O. Stal and G. Weiglein, Phys. Lett. B **710**, 201 (2012) [arXiv:1112.3026 [hep-ph]].

[116] ATLAS collaboration, "Further search for supersymmetry at $\sqrt{s} = 7$ TeV in final states with jets, missing transverse momentum and one isolated lepton," ATLAS-CONF-2012-041

[117] ATLAS collaboration, "Search for squarks and gluinos with the ATLAS detector using final states with jets and missing transverse momentum and $\mathcal{L} = 4.7$ fb^{-1} of $\sqrt{s} = 7$ TeV proton-proton collision data," ATLAS-CONF-2012-033

[118] ATLAS collaboration, "Hunt for new phenomena using large jet multiplicities and missing transverse momentum with ATLAS in $\mathcal{L} = 4.7$ fb^{-1} of $\sqrt{s} = 7$ TeV proton-proton collisions," ATLAS-CONF-2012-037

[119] CMS collaboration, "Search for Supersymmetry in Events with Photons and Missing Energy," CMS-PAS-SUS-12-001.

[120] CMS collaboration, "Search for supersymmetry with the razor variables at CMS," CMS-PAS-SUS-12-005.

[121] H. Baer, V. D. Barger, D. Karatas and X. Tata, Phys. Rev. D **36**, 96 (1987).

[122] S. Chatrchyan *et al.* [CMS Collaboration], "Search for physics beyond the standard model in events with a Z boson, jets, and missing transverse energy in pp collisions at sqrt(s) = 7 TeV," arXiv:1204.3774 [hep-ex].

[123] S. Chatrchyan *et al.* [CMS Collaboration], "Search for anomalous production of multilepton events in pp collisions at sqrt(s)=7 TeV," arXiv:1204.5341 [hep-ex].

[124] CMS collaboration, "Search for supersymmetry in events with a single lepton, jets, and missing transverse momentum using a neural network," CMS-PAS-SUS-11-026.

[125] G. Aad *et al.* [ATLAS Collaboration], "Search for events with large missing transverse momentum, jets, and at least two tau leptons in 7 TeV proton-proton collision data with the ATLAS detector," arXiv:1203.6580 [hep-ex].

[126] G. Aad *et al.* [ATLAS Collaboration], "Search for supersymmetry in pp collisions at $\sqrt{s} = 7$ TeV in final states with missing transverse momentum and b-jets with the ATLAS detector," arXiv:1203.6193 [hep-ex].

[127] G. Aad *et al.* [ATLAS Collaboration], "Search for gluinos in events with two same-sign leptons, jets and missing transverse momentum with the ATLAS detector in pp collisions at sqrt(s) = 7 TeV," arXiv:1203.5763 [hep-ex].

[128] G. Aad *et al.* [ATLAS Collaboration], "Search for Diphoton Events with Large Missing Transverse Momentum in 1 fb^{-1} of 7 TeV Proton-Proton Collision Data with the ATLAS Detector," arXiv:1111.4116 [hep-ex].

[129] CMS collaboration, "Search for new physics in events with same-sign dileptons, b-tagged jets and missing energy," CMS-PAS-SUS-11-020

[130] ATLAS collaboration, "Search for Scalar Top Quark Pair Production in Natural Gauge Mediated Supersymmetry Models with the ATLAS Detector in pp Collisions at $\sqrt{s} = 7$ TeV," ATLAS-CONF-2012-036

[131] G. Aad *et al.* [ATLAS Collaboration], Phys. Rev. Lett. **108**, 181802 (2012) [arXiv:1112.3832 [hep-ex]].

[132] H. Baer and X. Tata, Phys. Lett. B **155**, 278 (1985).

[133] H. Baer, C. -h. Chen, F. Paige and X. Tata, Phys. Rev. D **50**, 4508 (1994) [hep-ph/9404212].

[134] G. Aad *et al.* [ATLAS Collaboration], "Search for supersymmetry in events with three leptons and missing transverse momentum in sqrt(s) = 7 TeV pp collisions with the ATLAS detector," arXiv:1204.5638 [hep-ex].

[135] ATLAS collaboration, "Search for long-lived charginos in anomaly-mediated supersymmetry-breaking scenarios with the ATLAS detector using $\mathcal{L} = 4.7$ fb^{-1} data of pp collisions at $\sqrt{s} = 7$ TeV," ATLAS-CONF-2012-034

[136] ATLAS collaboration, "Search for charged long-lived heavy particles with the ATLAS Experiment at the LHC," ATLAS-CONF-2012-022

[137] H. K. Dreiner, "An Introduction to explicit R-parity violation," In Kane, G.L. (ed.): "Perspectives on supersymmetry II" 565-583 [hep-ph/9707435].

[138] ATLAS collaboration, "Search for supersymmetry in events with four or more leptons and missing transverse momentum in pp collisions at $\sqrt{s} = 7$ TeV with the ATLAS detector," ATLAS-CONF-2012-001

[139] H. Baer, C. Balazs, A. Belyaev, T. Krupovnickas and X. Tata, JHEP **0306**, 054 (2003) [hep-ph/0304303].

[140] F. Brümmer and W. Buchmüller, "The Fermi scale as a focus point of high-scale gauge mediation," arXiv:1201.4338 [hep-ph].

[141] H. Baer, A. Belyaev, T. Krupovnickas and A. Mustafayev, JHEP **0406**, 044 (2004) [hep-ph/0403214].

[142] ATLAS collaboration, "ATLAS: Detector and physics performance technical design report. Volume 2," CERN-LHCC-99-15, esp. Fig. 19-82, and Fig 2.5.1 of [98]

[143] ATLAS collaboration, "Constraining R-parity violating Minimal Supergravity with $\tilde{\tau}_1$ LSP in a four lepton final state with missing transverse momentum," ATLAS-CONF-2012-035

[144] `http://www-flc.desy.de/ldcoptimization/physics.php`

[145] G. Aad *et al.* [ATLAS Collaboration], Phys. Rev. D **85**, 012006 (2012) [arXiv:1109.6606 [hep-ex]].

[146] W. Porod, M. Hirsch, J. Romao and J. W. F. Valle, Phys. Rev. D **63**, 115004 (2001) [hep-ph/0011248].

[147] H. Baer, C.-H. Chen, F. Paige and X. Tata, Phys. Rev. D **49**, 3283 (1994) [hep-ph/9311248].

[148] H. Baer, F. E. Paige, S. D. Protopopescu and X. Tata, hep-ph/9305342.

[149] A. Djouadi, J. -L. Kneur and G. Moultaka, Comput. Phys. Commun. **176**, 426 (2007) [hep-ph/0211331].

[150] W. Porod, Comput. Phys. Commun. **153**, 275 (2003) [arXiv:hep-ph/0301101].

[151] H. Baer, A. Bartl, D. Karatas, W. Majerotto and X. Tata, Int. J. Mod. Phys. A **4**, 4111 (1989).

[152] W. Porod and F. Staub, "SPheno 3.1: Extensions including flavour, CP-phases and models beyond the MSSM," arXiv:1104.1573 [hep-ph].

[153] R. Kallosh and A. D. Linde, JHEP **0412**, 004 (2004) [hep-th/0411011].

[154] A. Linde, Y. Mambrini and K. A. Olive, Phys. Rev. D **85**, 066005 (2012) [arXiv:1111.1465 [hep-th]].

[155] S. Kachru, R. Kallosh, A. D. Linde and S. P. Trivedi, Phys. Rev. D **68**, 046005 (2003) [hep-th/0301240].

[156] B. S. Acharya, K. Bobkov, G. L. Kane, J. Shao and P. Kumar, Phys. Rev. D **78**, 065038 (2008) [arXiv:0801.0478 [hep-ph]].

[157] H. Baer, V. Barger, S. Kraml, A. Lessa, W. Sreethawong and X. Tata, JHEP **1203**, 092 (2012) [arXiv:1201.5382 [hep-ph]].

[158] T. Abe *et al.* [ILD Concept Group - Linear Collider Collaboration], "The International Large Detector: Letter of Intent," arXiv:1006.3396 [hep-ex].

[159] H. Aihara, (Ed.), P. Burrows, (Ed.), M. Oreglia, (Ed.) *et al.*, "SiD Letter of Intent," arXiv:0911.0006 [physics.ins-det].

[160] B. C. Allanach *et al.*, Eur. Phys. J. C **25**, 113 (2002) [hep-ph/0202233].

[161] P. Bechtle, M. Berggren, J. List, P. Schade and O. Stempel, Phys. Rev. D **82**, 055016 (2010) [arXiv:0908.0876 [hep-ex]].

Long-lived charged sleptons at the ILC/CLIC

Jan Heisig

II. Institute for Theoretical Physics, University of Hamburg, Germany

LC-REP-2012-065

Supersymmetric scenarios with a very weakly interacting lightest superpartner (LSP)—like the gravitino or axino—naturally give rise to a long-lived next-to-LSP (NLSP). If the NLSP is a charged slepton it leaves a very distinct signature in a collider experiment. At the ILC/CLIC it will be possible to capture a significant fraction of the produced charged sleptons and observe their decays. These decays potentially reveal the nature of the LSP and thus provide a unique possibility to measure the properties of a very weakly interacting LSP which otherwise is most likely hidden from any other observation, like direct or indirect dark matter searches. We review the proposals that have been made to measure the LSP properties at the ILC/CLIC and compare its potential to the capability of the LHC.

1 Introduction

In supersymmetric extensions of the standard model (SM) with conserved R-parity the lightest superpartner (LSP) is stable and thus provides a natural dark matter (DM) candidate. The lightest neutralino—being part of the minimal supersymmetric standard model (MSSM)—is the most widely studied candidate. However, in extensions of the MSSM other cosmologically viable DM candidates appear such as the gravitino or the axino.

The spin-3/2 gravitino $\widetilde{G}$ arises in the spectrum of supergravity, i.e., once supersymmetry (SUSY) is promoted from a global to a local symmetry. It is a well motivated DM candidate and can even be regarded as favored since it alleviates the cosmological gravitino problem [1] allowing for a higher reheating temperature as required for thermal leptogenesis [2]. The gravitino acquires a mass through the super Higgs mechanism once SUSY is broken. Its mass depends strongly on the SUSY breaking scheme and can range from the eV scale to scales beyond the TeV scale. Requiring a reheating temperature of $\mathcal{O}(10^9\,\mathrm{GeV})$, masses of around and above $\mathcal{O}(10\,\mathrm{GeV})$ are favored in order not to over-close the universe by the thermally produced gravitino abundance. The very weak coupling of the gravitino causes the next-to-LSP (NLSP) to be long-lived. Thus, in the early universe after the NLSP freeze-out, late NLSP decays taking place during or after big bang nucleosynthesis (BBN) can affect the primordial abundance of light elements. This imposes strong constraints on the couplings and lifetime of the NLSP. Accordingly, a neutralino NLSP is strongly disfavored by BBN constraints from energy injection [3, 4, 5, 6]. The lighter stau $\widetilde{\tau}_1$ is therefore often considered as a natural NLSP candidate.[1] The most severe bound on the stau NLSP lifetime arises from ^{6}Li/H constraints requiring $\tau_{\widetilde{\tau}_1} \lesssim 5\times10^3\,\mathrm{s}$ [8, 9] for a typical stau yield after freeze out. The most conservative bound arises from ^{3}He/D constraint. It excludes lifetimes $\tau_{\widetilde{\tau}_1} \gtrsim 10^6\,\mathrm{s}$ [10]. Conclusively, lifetimes ranging from seconds to a month may be considered as interesting.

The resulting signatures of staus at colliders are charged, muon-like tracks usually leaving the detector—the decay length is large compared to the size of a detector. The tracks of staus can be discriminated against the muon background via high ionization loss and anomalous time-of-flight. The LHC provides a good environment for discovering long-lived staus. Searches for heavy stable charged particles are being performed at ATLAS [11] and CMS [12].

Ionization loss is the main source of energy loss for heavy charged particles when penetrating the detector material. The energy loss increases with decreasing velocity β. Staus that are produced with sufficiently

[1] The basic ideas given in this article are expected to hold with modifications for other charged NLSP candidates or even for very different scenarios. Some of the ideas discussed in this article have initially been brought up in the context of 4th generation lepton searches [7].

small β may lose their kinetic energy completely and stop inside the detector. According to its lifetime, the stau will decay leaving a characteristic signature in the detector which is uncorrelated with the bunch crossing. If it is possible to measure the lifetime, the recoil energy and even the angular distribution of the emitted SM particles in the decay, it is possible to determine the coupling, mass and even the spin of the LSP. This is a unique possibility to test a (stable) gravitino DM scenario which is hopeless to test in direct and indirect DM searches.

Another well motivated DM candidate is the axino $\widetilde{a}$ which appears once the MSSM is extended by the Peccei-Quinn mechanism, in order to solve the strong CP problem. The phenomenology at a collider is virtually identical. The decay of the stau into the axino can give insights into the Peccei-Quinn sector.

We will consider both scenarios here. In section 2 we will describe the decays of the NLSP into the gravitino or axino LSP and explain how to distinguish these cases. In section 3 we will describe the implications from the LHC and its sensitivity to these scenarios. In section 4 we will review some of the experimental ideas that have been brought up in order to realize the investigation of NLSP decays.

2 NLSP decays

In the considered scenarios the dominant decay mode of the staus is the 2-body decay $\widetilde{\tau} \to \widetilde{G}\tau$ or $\widetilde{\tau} \to \widetilde{a}\tau$. For the gravitino LSP the corresponding decay width reads

$$\Gamma(\widetilde{\tau}_1 \to \widetilde{G}\tau) \simeq \frac{m_{\widetilde{\tau}_1}^5}{48\pi\, m_{\widetilde{G}}^2 M_{\rm Pl}^2} \left(1 - \frac{m_{\widetilde{G}}^2}{m_{\widetilde{\tau}_1}^2}\right)^4 , \tag{1}$$

where $M_{\rm Pl}$ is the (reduced) Planck mass. The decay rate is completely determined by the masses $m_{\widetilde{\tau}_1}$ and $m_{\widetilde{G}}$. It is independent of any other SUSY parameter or SM coupling.

For the axino LSP the 2-body decay is loop-induced and contains further SUSY parameters in particular it depends on the stau mixing angle. For a pure right-handed stau the width has been computed in the KSVZ axino model [13],

$$\Gamma(\widetilde{\tau}_1 \to \widetilde{a}\tau) \simeq \frac{9\alpha^4 C_{\rm aYY}^2}{512\pi^5 \cos^8\theta_{\rm W}} \frac{m_{\widetilde{B}}^2}{f_a^2} \frac{(m_{\widetilde{\tau}_1}^2 - m_{\widetilde{a}}^2)^2}{m_{\widetilde{\tau}_1}^3} \xi^2 \log^2\left(\frac{f_a}{m_{\widetilde{\tau}_1}}\right) , \tag{2}$$

where α is the fine structure constant, $\theta_{\rm W}$ is the weak mixing angle, f_a is the Peccei-Quinn scale, $m_{\widetilde{B}}$ is the (pure) bino mass and $C_{\rm aYY}$ and ξ are $\mathcal{O}(1)$ factors expressing the Peccei-Quinn model dependence and loop cut-off uncertainties, respectively.

The typical decay length of the staus is large compared to their traveling range in the detector material. Hence, staus always decay at rest, i.e., we know the center-of-mass frame. Accordingly, if the mass of the stau is known, the LSP mass can be determined from the recoil energy of the τ produced in the 2-body decay, E_τ,

$$m_{\rm LSP} = \sqrt{m_{\widetilde{\tau}_1}^2 + m_\tau^2 - 2 m_{\widetilde{\tau}_1} E_\tau} \, . \tag{3}$$

As pointed out in [14, 15], we can probe the hypothesis of a gravitino LSP by computing the Planck mass from (1) once $m_{\widetilde{\tau}_1}$, $m_{\rm LSP}$ and lifetime $\tau_{\widetilde{\tau}_1} = \Gamma_{\widetilde{\tau}_1}^{-1}$ are known. An agreement with the Planck mass measured in macroscopic experiments would provide a strong evidence for supergravity and the existence of the gravitino. Since the gravitino mass is directly related to the scale of spontaneous SUSY breaking,

$$\langle F \rangle = \sqrt{3} M_{\rm Pl}\, m_{\widetilde{G}} \, , \tag{4}$$

these measurements would provide us with insights in the SUSY breaking sector that are otherwise beyond the reach of any experiment in the near future. For the axino LSP case, from (2) we may be able to estimate the Peccei-Quinn scale and confront it with limits from astrophysical axion studies and axion searches in the laboratory.

A sub-dominant but nevertheless very important decay mode of the stau is the 3-body decay $\widetilde{\tau} \to \widetilde{G}\tau\gamma$ or $\widetilde{\tau} \to \widetilde{a}\tau\gamma$ which has been studied in [14, 13]. As pointed out in these references, from the 3-body decay

branching ratio as well as from the distribution of the angle between the τ and the photon, the spin of the LSP can be determined. More precisely, it has been shown that it is possible to distinguish between the spin-3/2 gravitino and a spin-1/2 axino. The observation of a spin-3/2 LSP would be an important confirmation of supergravity. In particular, for small gravitino masses $m_{\widetilde{G}} \lesssim 0.1\, m_{\widetilde{\tau}_1}$ the determination of $m_{\widetilde{G}}$ requires a very precise measurement of the tau recoil energy at below the percent level. Thus, (3) may only provide an upper limit on the gravitino mass in these cases. In such a situation a much better determination of $m_{\widetilde{G}}$ can be achieved via (1) from the measurement of the stau lifetime once we are convinced that the LSP is indeed a gravitino by the measurement of its spin.

3 Implications from the LHC

Before the stau will be observed at the ILC/CLIC we expect its discovery at the LHC.[2] Therefore, in this section we will briefly review the LHC potential.

Long-lived staus leave a prominent signature in the detectors of the LHC. Combining ionization loss and time-of-flight measurements provide very clean signal regions and, at the same time, high efficiencies. Consequently, the discovery of long-lived staus typically can be claimed on the basis of a very few events and thus is expected to be established in a rather short time period without providing any hints in advance.

The direct production of staus provides a robust lower limit on the stau mass [16]. Null searches for this channel at the 7 TeV, 5 fb^{-1} LHC run [12] can be interpreted in the most conservative limit to exclude stau masses below 216 GeV [17]. Although the LHC provides a very good environment to discover heavy stable charged particles, it is typically difficult to capture a sufficiently large number of staus in the detector in order to be able to study its decays systematically. As shown in [18] especially widely spread spectra (spectra with large mass gaps between the colored sparticles and the stau) provide way too little stopped staus for the desired measurements (see figure 1). For such spectra even a scenario with $m_{\widetilde{\tau}_1}$ just above the above quoted limit provides less than 100 events of staus that are stopped inside a LHC detector for the 14 TeV, 300 fb^{-1} LHC run. Proposals to study stopped staus at the LHC are discussed in [19, 20, 21, 22, 23, 24].

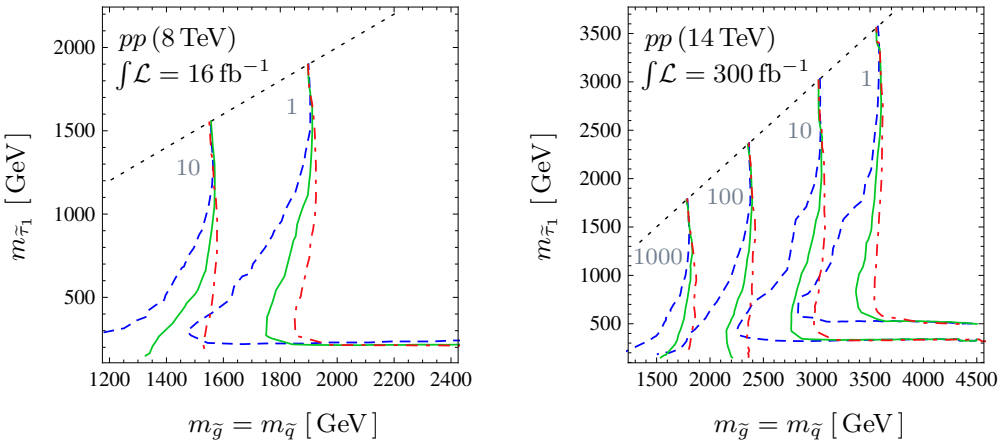

Figure 1: Expected number of events that contain staus that are stopped inside an LHC detector. The results are expressed in a simplified model framework considering direct stau production as well as the production via the decay of strongly produced sparticles. A common squark and gluino mass, $m_{\widetilde{q}} = m_{\widetilde{g}}$, has been chosen. The three different line styles refer to three different mass patterns of intermediate sparticles in the decay chain. Taken from [18].

[2] In the long-lived stau scenario there are very little regions in parameter space that are not accessible with the long-term 14 TeV LHC run but with a mid-term 3 TeV CLIC run.

4 Prospects at the ILC/CLIC

The challenge in the study of stau decays is to trap as many staus as possible in a well defined volume that is sensitive to the observables of the produced SM particles in the decay. An e^+e^--collider provides an appropriate environment for this task. On the one hand the direct production of staus provides a velocity distribution that can be tuned through the center-of-mass energy in order to maximize the number of stopped staus in a given volume. On the other hand it provides a well defined angular distribution. Together with the option of adding extra stopping material in appropriate regions [23] it provides an ideal framework to obtain a large number of observed stau decays.

The stau may be produced directly or in a decay chain following the production of other sparticles. The cross sections for different production processes have different velocity dependencies near threshold. For slepton production via s-channel γ/Z the cross section increases as β^3. For polarized e^+e^- beams the production cross section for selectron pairs via t-channel $\widetilde{\chi}^0$ exchange ($e^+_{\rm L}e^-_{\rm L} \to \widetilde{e}^+_{\rm R}\widetilde{e}^-_{\rm L}$ or $e^+_{\rm R}e^-_{\rm R} \to \widetilde{e}^+_{\rm L}\widetilde{e}^-_{\rm R}$) increases linear in β and thus provides an enhanced number of selectrons close to threshold [25, 26].[3] Hence, if the spectrum features a selectron which is close in mass to the stau, one could greatly benefit from the use of polarized electron beams to increase the number of produced selectrons near threshold and therefore increase the number of stopped staus. For small mass gaps between the selectron and the stau this advantage overcompensates the boost that staus achieve from the decay of the selectron (which would lead to higher stau velocities).

Once a stau pair is produced it will be identified via highly ionizing tracks. Their passage through the detector can be accurately followed. If the stau stops inside the detector the location of the stopped stau is expected to be determinable within a volume of a few cm^3 [29]. The location and time of the stopped stau may be recorded. In general the stau will decay out-of-time with the beam collisions. Hence, the decay can then be triggered by an isolated, out-of-time hadronic or electromagnetic cluster in the hadronic calorimeter (HCAL), a hadronic shower in the iron yoke or by a muon originating in the HCAL or yoke above an appropriate energy threshold ($E > 10\,\text{GeV}$) [29]. Background from cosmic rays may be rejected by a veto against vertices in the outermost detector layers. Background from atmospheric neutrinos is expected to be sufficiently rejected by the required energy threshold and furthermore by the requirement of a matching of the recorded stopping positions [23]. A precise measurement of the stau mass which is required in order to estimate the gravitino mass can be obtained from the reconstruction of the complete event kinematics.

The potential to measure $m_{\widetilde{\tau}_1}$, $m_{\widetilde{G}}$ and $\tau_{\widetilde{\tau}_1}$ at the ILC/CLIC equipped with a general purpose detector [30, 31] has been studied for several benchmark points in [29, 32]. Both studies contain the mSUGRA points GDM ζ ($m_{\widetilde{\tau}_1} = 346\,\text{GeV}$, $m_{\widetilde{G}} = 100\,\text{GeV}$) and GDM η ($m_{\widetilde{\tau}_1} = 327\,\text{GeV}$, $m_{\widetilde{G}} = 20\,\text{GeV}$) [24]. Provided a fixed center-of-mass energy of 800 GeV and a luminosity of $1000\,\text{fb}^{-1}$, $m_{\widetilde{\tau}_1}$ and $\tau_{\widetilde{\tau}_1}$ have been found to be measurable at the level of one per mille and a few per cent, respectively, for both scenarios. The gravitino mass $m_{\widetilde{G}}$ has been found to be measurable at a ten per cent level for GDM ζ and with an uncertainty comparable to its actual value for GDM η [29]. These numbers have been obtained with unpolarized beams. Polarization is expected to enhance the number of stopped staus by a factor of almost three [29] and thus improve these results. The optimization of the beam energy for given stau masses and production processes has been discussed in [32].

Further optimizations can be achieved by placing additional active stopper material [23] around the general purpose detector. Another approach is the installation of water tanks [22] that accumulate stopped staus. The water can then be transported to a quiet environment in order to study the decays. It has also been proposed to collect staus in a storage ring [14]. This could most easily been done if staus where produced preferably in the forward region, i.e., via selectron pair production (see figure 11 in [32]).

The feasibility of studying 3-body decays and distinguishing gravitinos from axinos has been discussed in [13]. The distribution of stau decay events in the two variables θ, the opening angle between the photon and the tau, and $x_\gamma \equiv 2E_\gamma/m_{\widetilde{\tau}_1}$ is shown in figure 2. For the gravitino the events are peaked only in the region of soft and collinear photon emission whereas for the axino a second peak shows up characterized by a back-to-back tau-photo emission and large photon energies. For a total number of 10^4 analyzed stau decays in the scenario considered in [13] it has been found that 110 ± 10 (stat.) and 165 ± 13 (stat.) 3-body decays will be observerd in the gravitno and axino LSP scenario, respectively, 1% and 28% of which are expected

[3] In [27, 28] the possibility of an e^-e^--collider to obtain a $\propto\beta$-behavior near threshold has been discussed.

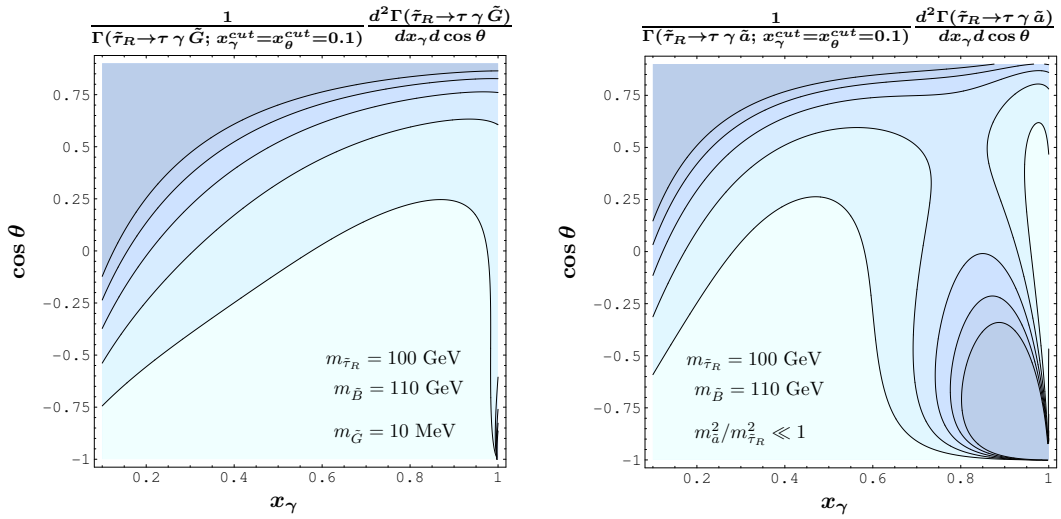

Figure 2: The normalized differential distributions of the visible decay products in the decays $\widetilde{\tau} \to \tau\gamma\widetilde{G}$ for the gravitino LSP scenario (left) and $\widetilde{\tau} \to \tau\gamma\widetilde{a}$ for the axino LSP scenario (right) for $m_{\widetilde{\tau}_1} = 100\,\text{GeV}$, $m_{\widetilde{B}} = 110\,\text{GeV}$, $m_{\widetilde{a}}^2/m_{\widetilde{\tau}_1}^2 \ll 1$, and $m_{\widetilde{G}} = 10\,\text{MeV}$. The contour lines represent the values 0.2, 0.4, 0.6, 0.8, and 1.0, where the darker shading implies a higher number of events. Taken from [13].

to be selected by imposing appropriate cuts in the x_γ-$\cos\theta$-plane. These numbers illustrate that $\mathcal{O}(10^4)$ of analyzed stau decays could be sufficient for a significant distinction of those scenarios.

5 Conclusions

Supersymmetric scenarios with a very weakly interacting LSP are well motivated from cosmology. The very weak coupling naturally gives rise to a long-lived NLSP which is considered to be the lighter stau here. These particles usually pass the detector and can be directly detected. If these particles will be discovered at the LHC, the ILC/CLIC provides the unique environment to study the decays of the stau in detail. Reconstructed 2-body decays will allow for a measurement of the scale of supersymmetry breaking $\langle F \rangle$ (in the case of a gravitino LSP) or the Peccei-Quinn scale (in the case of an axino LSP). From 3-body decays it is even possible to measure the spin of the LSP. For a gravitino LSP this leads to the attractive possibility to test the supergravity paradigm. Additionally, the measurement of the life-time from 2-body decays provides direct access to the gravitational coupling. Hence, two independent unequivocal predictions of supergravity can be probed.

References

[1] J. R. Ellis, D. V. Nanopoulos, and S. Sarkar, "The Cosmology of Decaying Gravitinos", *Nucl. Phys.* **B259** (1985) 175.

[2] M. Bolz, W. Buchmüller, and M. Plümacher, "Baryon asymmetry and dark matter", *Phys. Lett.* **B443** (1998) 209–213, `arXiv:hep-ph/9809381`.

[3] J. L. Feng, S. Su, and F. Takayama, "Supergravity with a gravitino LSP", *Phys. Rev.* **D70** (2004) 075019, `arXiv:hep-ph/0404231 [hep-ph]`.

[4] L. Roszkowski, R. Ruiz de Austri, and K.-Y. Choi, "Gravitino dark matter in the CMSSM and implications for leptogenesis and the LHC", *JHEP* **0508** (2005) 080, `arXiv:hep-ph/0408227 [hep-ph]`.

[5] D. G. Cerdeno, K.-Y. Choi, K. Jedamzik, L. Roszkowski, and R. Ruiz de Austri, "Gravitino dark matter in the CMSSM with improved constraints from BBN", *JCAP* **0606** (2006) 005, arXiv:hep-ph/0509275 [hep-ph].

[6] R. H. Cyburt, J. R. Ellis, B. D. Fields, K. A. Olive, and V. C. Spanos, "Bound-State Effects on Light-Element Abundances in Gravitino Dark Matter Scenarios", *JCAP* **0611** (2006) 014, arXiv:astro-ph/0608562 [astro-ph].

[7] J. Goity, W. Kossler, and M. Sher, "Production, collection and utilization of very longlived heavy charged leptons", *Phys. Rev.* **D48** (1993) 5437–5439, arXiv:hep-ph/9305244 [hep-ph].

[8] M. Pospelov, "Particle physics catalysis of thermal Big Bang Nucleosynthesis", *Phys. Rev. Lett.* **98** (2007) 231301, arXiv:hep-ph/0605215.

[9] J. Pradler and F. D. Steffen, "Implications of catalyzed BBN in the CMSSM with gravitino dark matter", *Phys. Lett.* **B666** (2008) 181–184, arXiv:0710.2213 [hep-ph].

[10] J. Pradler and F. D. Steffen, "CBBN in the CMSSM", *Eur.Phys.J.* **C56** (2008) 287–291, arXiv:0710.4548 [hep-ph].

[11] ATLAS Collaboration, G. Aad *et al.*, "Search for heavy long-lived charged particles with the ATLAS detector in *pp* collisions at $\sqrt{s} = 7$ TeV", *Phys. Lett.* **B703** (2011) 428–446, arXiv:1106.4495 [hep-ex].

[12] CMS Collaboration, S. Chatrchyan *et al.*, "Search for heavy long-lived charged particles in pp collisions at sqrt(s)=7 TeV", arXiv:1205.0272 [hep-ex]. Submitted to Physics Letters B.

[13] A. Brandenburg, L. Covi, K. Hamaguchi, L. Roszkowski, and F. D. Steffen, "Signatures of axinos and gravitinos at colliders", *Phys. Lett.* **B617** (2005) 99–111, arXiv:hep-ph/0501287.

[14] W. Buchmüller, K. Hamaguchi, M. Ratz, and T. Yanagida, "Supergravity at colliders", *Phys. Lett.* **B588** (2004) 90–98, arXiv:hep-ph/0402179.

[15] J. L. Feng, A. Rajaraman, and F. Takayama, "Probing gravitational interactions of elementary particles", *Int. J. Mod. Phys.* **D13** (2004) 2355–2359, arXiv:hep-th/0405248.

[16] J. Heisig and J. Kersten, "Production of long-lived staus in the Drell-Yan process", *Phys. Rev.* **D84** (2011) 115009, arXiv:1106.0764 [hep-ph].

[17] J. Heisig, "Long-lived staus at the LHC", in *Proceedings of the XLVIIth Rencontres de Moriond*. 2012. arXiv:1207.3058 [hep-ph].

[18] J. Heisig and J. Kersten, "Long-lived staus from strong production in a simplified model approach", arXiv:1203.1581 [hep-ph].

[19] K. Hamaguchi, M. M. Nojiri, and A. de Roeck, "Prospects to study a long-lived charged next lightest supersymmetric particle at the LHC", *JHEP* **0703** (2007) 046, arXiv:hep-ph/0612060 [hep-ph].

[20] J. Pinfold and L. Sibley, "Measuring the Lifetime of Trapped Sleptons Using the General Purpose LHC Detectors", *Phys. Rev.* **D83** (2011) 035021, arXiv:1006.3293 [hep-ph].

[21] P. W. Graham, K. Howe, S. Rajendran, and D. Stolarski, "New Measurements with Stopped Particles at the LHC", arXiv:1111.4176 [hep-ph].

[22] J. L. Feng and B. T. Smith, "Slepton trapping at the large hadron and international linear colliders", *Phys. Rev.* **D71** (2005) 015004, arXiv:hep-ph/0409278.

[23] K. Hamaguchi, Y. Kuno, T. Nakaya, and M. M. Nojiri, "A Study of late decaying charged particles at future colliders", *Phys. Rev.* **D70** (2004) 115007, arXiv:hep-ph/0409248.

[24] A. De Roeck, J. R. Ellis, F. Gianotti, F. Moortgat, K. Olive, *et al.*, "Supersymmetric benchmarks with non-universal scalar masses or gravitino dark matter", *Eur. Phys. J.* **C49** (2007) 1041–1066, arXiv:hep-ph/0508198 [hep-ph].

[25] A. Freitas, . Miller, D.J., and P. Zerwas, "Pair production of smuons and selectrons near threshold in e+ e- and e- e- collisions", *Eur. Phys. J.* **C21** (2001) 361–368, arXiv:hep-ph/0106198 [hep-ph].

[26] A. Freitas, A. von Manteuffel, and P. Zerwas, "Slepton production at e+ e- and e- e- linear colliders", *Eur. Phys. J.* **C34** (2004) 487–512, arXiv:hep-ph/0310182 [hep-ph].

[27] J. L. Feng, "Supersymmetry at linear colliders: The Importance of being e- e-", *Int. J. Mod. Phys.* **A13** (1998) 2319–2328, arXiv:hep-ph/9803319 [hep-ph].

[28] J. L. Feng and M. E. Peskin, "Selectron studies at e- e- and e+ e- colliders", *Phys. Rev.* **D64** (2001) 115002, arXiv:hep-ph/0105100 [hep-ph].

[29] H.-U. Martyn, "Detecting metastable staus and gravitinos at the ILC", *Eur. Phys. J.* **C48** (2006) 15–24, arXiv:hep-ph/0605257.

[30] L. Linssen, A. Miyamoto, M. Stanitzki, and H. Weerts, "Physics and Detectors at CLIC: CLIC Conceptual Design Report", arXiv:1202.5940 [physics.ins-det].

[31] ILC Collaboration, E. Brau, James *et al.*, "ILC Reference Design Report: ILC Global Design Effort and World Wide Study", arXiv:0712.1950 [physics.acc-ph].

[32] O. Çakır, İ. T. Çakır, J. R. Ellis, and Z. Kırca, "Study of Metastable Staus at Linear Colliders", arXiv:hep-ph/0703121.

Sneutrino Identification in Lepton Pair Production at ILC with Polarized Beams

A. V. Tsytrinov[1], J. Kalinowski[2], P. Osland[3], A. A. Pankov[1]

[1]The Abdus Salam ICTP Affiliated Centre, Technical University of Gomel, 246746 Gomel, Belarus
[2]Faculty of Physics, University of Warsaw, Hoża 69, 00-681 Warsaw, Poland
[3]Department of Physics and Technology, University of Bergen, Postboks 7803, N-5020 Bergen, Norway

DOI: will be assigned

July 26, 2012

Numerous non-standard dynamics are described by contact-like effective interactions that can manifest themselves in electron-positron collisions only through deviations of the observables (cross sections, asymmetries) from the Standard Model predictions. If such a deviation were observed, it would be important to identify the actual source among the possible non-standard interactions as many different new physics scenarios may lead to very similar experimental signatures. We study the possibility of uniquely identifying the indirect effects of s-channel sneutrino exchange, as predicted by supersymmetric theories with R-parity violation, against other new physics scenarios in high-energy e^+e^- annihilation into lepton pairs at the International Linear Collider. These competitive models are interactions based on gravity in large and in TeV-scale extra dimensions, anomalous gauge couplings, Z' vector bosons and compositeness-inspired four-fermion contact interactions. To evaluate the identification reach on sneutrino exchange, we use as basic observable a double polarization asymmetry, that is particularly suitable to directly test for such s-channel sneutrino exchange effects in the data analysis. The availability of both beams being polarized plays a crucial rôle in identifying the new physics scenario.

1 Introduction

Numerous new physics (NP) scenarios, candidates as solutions of Standard Model (SM) conceptual problems, are characterized by novel interactions mediated by exchanges of very heavy states with mass scales significantly greater than the electroweak scale. In many cases, theoretical considerations as well as current experimental constraints indicate that the new objects may be too heavy to be directly produced even at the highest energies of the CERN Large Hadron Collider (LHC) and at foreseen future colliders, such as the e^+e^- International Linear Collider (ILC). In this situation the new, non-standard, interactions would only be revealed by indirect, virtual, effects manifesting themselves as deviations from the predictions of the SM. In the case of indirect discovery the effects may be subtle since many different NP scenarios may lead to very similar experimental signatures and they may easily be confused in certain regions of the parameter space for each class of models.

At the available energies provided by the accelerators, where we study reactions among the familiar SM particles, effective contact interaction Lagrangians represent a convenient theoretical tool to physically parameterize the effects of the above-mentioned non-standard interactions and, in particular, to test the corresponding virtual high-mass exchanges. There are many very different NP scenarios that predict new particle exchanges which can lead to contact interactions (CI) which may show up below direct production thresholds. These are compositeness [1], a Z' boson from models with an extended gauge sector [2–5], scalar or vector leptoquarks [6], R-parity violating sneutrino ($\tilde{\nu}$) exchange [7, 8], bi-lepton boson exchanges [9], anomalous gauge boson couplings (AGC) [10], virtual Kaluza–Klein (KK) graviton exchange in the context of gravity propagating in large extra dimensions, exchange of KK gauge boson towers or string excitations [11–16], *etc.* Of course, this list is not exhaustive, because other kinds of contact interactions may be at play.

If R-parity is violated it is possible that the exchange of sparticles can contribute significantly to SM processes and may even produce peaks or bumps [7,8] in cross sections if they are kinematically accessible. Below threshold, these new spin-0 exchanges may make their manifestation known via indirect effects on observables (cross sections and asymmetries), including spectacular decays [17]. Here we will address the question of whether the effects of the exchange of scalar (spin-0) sparticles can be differentiated at linear colliders from those associated with the wide class of other contact interactions mentioned above.

For a sneutrino in an R-parity-violating theory, we take the basic couplings to leptons and quarks to be given by

$$\lambda_{ijk} L_i L_j \bar{E}_k + \lambda'_{ijk} L_i Q_j \bar{D}_k. \tag{1}$$

Here, L (Q) are the left-handed lepton (quark) doublet superfields, and $\bar{E}$ ($\bar{D}$) are the corresponding left-handed singlet fields. If just the R-parity violating $\lambda LL\bar{E}$ terms of the superpotential are present it is clear that observables associated with leptonic processes

$$e^+ + e^- \to \mu^+ + \mu^- \quad (\text{or } \tau^- + \tau^+), \tag{2}$$

will be affected by the exchange of $\tilde{\nu}$'s in the t- or s-channels [7,8]. For instance, in the case only one nonzero Yukawa coupling is present, $\tilde{\nu}$'s may contribute to, e.g. $e^+e^- \to \mu^+\mu^-$ via t-channel exchange. In particular, if λ_{121}, λ_{122}, λ_{132}, or λ_{231} are nonzero, the $\mu^+\mu^-$ pair production proceeds via additional t-channel sneutrino exchange mechanism. However, if only the product of Yukawa, e.g. $\lambda_{131}\lambda_{232}$, is nonzero the s-channel $\tilde{\nu}_\tau$ exchange would contribute to the $\mu^+\mu^-$ pair final state. Below we denote by λ the relevant Yukawa coupling from the superpotential (1) omitting the subscripts.

In this note, we discuss the deviations induced by the s-channel sneutrino exchange and contact interactions in electron–positron annihilation into lepton pairs (2) at the planned ILC. In particular, we use as a basic observable a double polarization asymmetry that will unambiguously identify s-channel sneutrino exchange effects in the data, relying on its spin-0 character and by *filtering* out contributions of other NP interactions.[1] The availability of both beams being polarized plays a crucial rôle in identifying that new physics scenario [18]. On the other hand, we note that if only single (electron) beam polarization is available, the left-right asymmetry does not help to unambiguously identify an s-channel sneutrino exchange signature.[2]

The R-parity violating s-channel sneutrino exchange in the process (2) requires a non-zero coupling λ_{131} (λ_{121}). This would necessarily induce non-standard contributions to Bhabha scattering,

$$e^+ + e^- \to e^+ + e^-, \tag{3}$$

which we also study, in order to compare the sensitivities in these channels.

We also compare the capability of the ILC to distinguish effects of s-channel sneutrino exchange in the lepton pair production process from other NP interactions with the corresponding potential of the Drell-Yan process ($l = e, \mu$) [19]

$$p + p \to l^+ + l^- + X \tag{4}$$

at the LHC.

For completeness, we will in Sec. 2 recall a minimum of relevant formulae defining the basic observables used in our analysis. In Sec. 3 we perform the numerical analysis, evaluating discovery and identification reaches on sneutrinos. Finally, Sec. 4 contains some concluding remarks.

2 Observables and NP parametrization

We concentrate on the process $e^+ + e^- \to \mu^+ + \mu^-$. With P^- and P^+ denoting the longitudinal polarizations of the electrons and positrons, respectively, and θ the angle between the incoming electron and the outgoing muon in the c.m. frame, the differential cross section in the presence of contact interactions can be expressed as ($z \equiv \cos\theta$) [20,21]:

$$\frac{\mathrm{d}\sigma^{\mathrm{CI}}}{\mathrm{d}z} = \frac{3}{8}\left[(1+z)^2\sigma_+^{\mathrm{CI}} + (1-z)^2\sigma_-^{\mathrm{CI}}\right]. \tag{5}$$

[1] This approach was earlier exploited for the discrimination against Z' exchange [8].

[2] For the case of single beam polarization, A_{LR} is an analogue of A_{double} defined by Eq. (16).

Model	$\Delta_{\alpha\beta}$
composite fermions [1]	$\pm\dfrac{s}{\alpha_{\rm em}}\dfrac{1}{\Lambda^2_{\alpha\beta}}$
extra gauge boson Z' [2–5]	$g'^{\,e}_{\alpha}\, g'^{\,f}_{\beta}\, \chi_{Z'}$
AGC ($f = \ell$) [10]	$\Delta_{\rm LL} = s\left(\dfrac{\tilde{f}_{DW}}{2s^2_W} + \dfrac{2\tilde{f}_{DB}}{c^2_W}\right)$, $\dfrac{\Delta_{\rm RR}}{2} = \Delta_{\rm LR} = \Delta_{\rm RL} = s\dfrac{4\tilde{f}_{DB}}{c^2_W}$
TeV-scale extra dim. [15, 16]	$-(Q_e Q_f + g^e_\alpha\, g^f_\beta)\,\dfrac{\pi^2\, s}{3\, M^2_G}$
ADD model [11, 13]	$\Delta_{\rm LL} = \Delta_{\rm RR} = f_G\,(1-2\,z)$, $\Delta_{\rm LR} = \Delta_{\rm RL} = -f_G\,(1+2\,z)$
R-parity violating SUSY [7, 8] ($\tilde{\nu}$ exchange in t-channel)	$\Delta_{\rm LL} = \Delta_{\rm RR} = 0$, $\Delta_{\rm LR} = \Delta_{\rm RL} = \dfrac{1}{2}\, C^t_{\tilde{\nu}}\, \chi^t_{\tilde{\nu}}$

Table 1: Parametrization of the $\Delta_{\alpha\beta}$ functions in different NP models ($\alpha, \beta = {\rm L}, {\rm R}$). For the explanation of notation see text.

In terms of the helicity cross sections $\sigma^{\rm CI}_{\alpha\beta}$ (with $\alpha, \beta = {\rm L}, {\rm R}$), directly related to the individual CI couplings $\Delta_{\alpha\beta}$ (see Eq. (10)):

$$\begin{aligned}
\sigma^{\rm CI}_{+} &= \frac{1}{4}\left[(1-P^-)(1+P^+)\,\sigma^{\rm CI}_{\rm LL} + (1+P^-)(1-P^+)\,\sigma^{\rm CI}_{\rm RR}\right] \\
&= \frac{D}{4}\left[(1-P_{\rm eff})\,\sigma^{\rm CI}_{\rm LL} + (1+P_{\rm eff})\,\sigma^{\rm CI}_{\rm RR}\right], \qquad (6) \\
\sigma^{\rm CI}_{-} &= \frac{1}{4}\left[(1-P^-)(1+P^+)\,\sigma^{\rm CI}_{\rm LR} + (1+P^-)(1-P^+)\,\sigma^{\rm CI}_{\rm RL}\right] \\
&= \frac{D}{4}\left[(1-P_{\rm eff})\,\sigma^{\rm CI}_{\rm LR} + (1+P_{\rm eff})\,\sigma^{\rm CI}_{\rm RL}\right], \qquad (7)
\end{aligned}$$

where the first (second) subscript refers to the chirality of the electron (muon) current. Furthermore,

$$P_{\rm eff} = \frac{P^- - P^+}{1 - P^- P^+} \qquad (8)$$

is the effective polarization, $|P_{\rm eff}| \leq 1$, and $D = 1 - P^- P^+$. For unpolarized positrons $P_{\rm eff} \to P^-$ and $D \to 1$, but with $P^+ \neq 0$, $|P_{\rm eff}|$ can be larger than $|P^-|$. Moreover, in Eqs. (6) and (7):

$$\sigma^{\rm CI}_{\alpha\beta} = \sigma_{\rm pt} |\mathcal{M}^{\rm CI}_{\alpha\beta}|^2, \qquad (9)$$

where $\sigma_{\rm pt} \equiv \sigma(e^+e^- \to \gamma^* \to \mu^+\mu^-) = (4\pi\alpha^2_{\rm em})/(3s)$. The helicity amplitudes $\mathcal{M}^{\rm CI}_{\alpha\beta}$ can be written as

$$\mathcal{M}^{\rm CI}_{\alpha\beta} = \mathcal{M}^{\rm SM}_{\alpha\beta} + \Delta_{\alpha\beta} = Q_e Q_\mu + g^e_\alpha\, g^\mu_\beta\, \chi_Z + \Delta_{\alpha\beta}, \qquad (10)$$

where

$$\chi_Z = \frac{s}{s - M^2_Z + i M_Z \Gamma_Z} \qquad (11)$$

represents the Z propagator, $g^l_{\rm L} = (I^l_{3L} - Q_l s^2_W)/s_W c_W$ and $g^l_{\rm R} = -Q_l s^2_W / s_W c_W$ are the SM left- and right-handed lepton ($l = e, \mu$) couplings of the Z with $s^2_W = 1 - c^2_W \equiv \sin^2\theta_W$ and Q_l the leptonic electric charge. The $\Delta_{\alpha\beta}$ functions represent the contact interaction contributions coming from TeV-scale physics.

The structure of the differential cross section (5) is particularly interesting in that it is equally valid for a wide variety of NP models listed in Table 1. Note that only graviton and t-channel sneutrino exchanges induce a modified angular dependence to the differential cross section via the z-dependence of $\Delta_{\alpha\beta}$.

In Table 1 $\Lambda_{\alpha\beta}$ denote compositeness scales; $\chi_{Z'}$ and $\chi^t_{\tilde{\nu}}$ parametrize the Z' and sneutrino propagators defined analogously to Eq. (11), with superscript t referring to the t-channel, e.g., $\chi^t_{\tilde{\nu}} = s/(t - M^2_{\tilde{\nu}})$, where $M_{\tilde{\nu}}$ is the sneutrino mass. For the t-channel $\tilde{\nu}$ sneutrino exchange $C^t_{\tilde{\nu}} = \lambda^2/4\pi\alpha_{\rm em}$ with λ being the relevant

Yukawa coupling. ${g'_\alpha}^f$ parametrizes the Z' couplings to the f current of chirality α. Furthermore, $\tilde{f}_{DW}$ and $\tilde{f}_{DB}$ are related to f_{DW} and f_{DB} of ref. [10] by $\tilde{f} = f/m_t^2$ (f_{DW} and f_{DB} parametrize new-physics effects associated with the SU(2) and hypercharge currents, respectively); M_C is the compactification scale; $f_G = \pm s^2/(4\pi\alpha_{\rm em} M_H^4)$ parametrizes the strength associated with massive graviton exchange with M_H the cut-off scale in the KK graviton tower sum.

The doubly polarized total cross section can be obtained from Eq. (5) after integration over z within the interval $-1 \le z \le 1$. In the limit of s, t small compared to the CI mass scales, the result takes the form

$$\sigma^{\rm CI} = \sigma_+^{\rm CI} + \sigma_-^{\rm CI} = \frac{1}{4}\left[(1-P^-)(1+P^+)\,(\sigma_{\rm LL}^{\rm CI} + \sigma_{\rm LR}^{\rm CI}) + (1+P^-)(1-P^+)\,(\sigma_{\rm RR}^{\rm CI} + \sigma_{\rm RL}^{\rm CI})\right]. \tag{12}$$

It is clear that the formula in the SM has the same form where one should replace the superscript CI $\to$ SM in Eq. (12).

Since the $\tilde{\nu}$ exchanged in the s-channel does not interfere with the s-channel SM γ and Z exchanges, the differential cross section with both electron and positron beams polarized can be written as [8, 22]

$$\frac{{\rm d}\sigma^{\tilde{\nu}}}{{\rm d}z} = \frac{3}{8}\left[(1+z)^2\sigma_+^{\rm SM} + (1-z)^2\sigma_-^{\rm SM} + 2\,\frac{1+P^-P^+}{2}\,(\sigma_{\rm RL}^{\tilde{\nu}} + \sigma_{\rm LR}^{\tilde{\nu}})\right]. \tag{13}$$

Here, $\sigma_{\rm RL}^{\tilde{\nu}} (= \sigma_{\rm LR}^{\tilde{\nu}}) = \sigma_{\rm pt}\,|\mathcal{M}_{\rm RL}^{\tilde{\nu}}|^2$, $\mathcal{M}_{\rm RL}^{\tilde{\nu}} = \mathcal{M}_{\rm LR}^{\tilde{\nu}} = \frac{1}{2}\,C_{\tilde{\nu}}^s \chi_{\tilde{\nu}}^s$, and $C_{\tilde{\nu}}^s$ and $\chi_{\tilde{\nu}}^s$ denote the product of the R-parity violating couplings and the propagator of the exchanged sneutrino. For the s-channel $\tilde{\nu}_\tau$ sneutrino exchange they read

$$C_{\tilde{\nu}}^s\,\chi_{\tilde{\nu}}^s = \frac{\lambda_{131}\lambda_{232}}{4\pi\alpha_{\rm em}}\,\frac{s}{s - M_{\tilde{\nu}_\tau}^2 + iM_{\tilde{\nu}_\tau}\Gamma_{\tilde{\nu}_\tau}} \tag{14}$$

Below we will use the abbreviation $\lambda^2 = \lambda_{131}\lambda_{232}$.

As seen from Eq. (13) the polarized differential cross section picks up a z-independent term in addition to the SM part. The corresponding total cross section can be written as

$$\begin{aligned}\sigma^{\tilde{\nu}} &= \frac{1}{4}\,(1-P^-)(1+P^+)\,(\sigma_{\rm LL}^{\rm SM} + \sigma_{\rm LR}^{\rm SM}) + \frac{1}{4}\,(1+P^-)(1-P^+)\,(\sigma_{\rm RR}^{\rm SM} + \sigma_{\rm RL}^{\rm SM}) \\ &+ \frac{3}{2}\,\frac{1+P^-P^+}{2}\,(\sigma_{\rm RL}^{\tilde{\nu}} + \sigma_{\rm LR}^{\tilde{\nu}}).\end{aligned} \tag{15}$$

It is possible to uniquely identify the effect of the s-channel sneutrino exchange exploiting the double beam polarization asymmetry defined as [8, 22]

$$A_{\rm double} = \frac{\sigma(P_1,-P_2) + \sigma(-P_1,P_2) - \sigma(P_1,P_2) - \sigma(-P_1,-P_2)}{\sigma(P_1,-P_2) + \sigma(-P_1,P_2) + \sigma(P_1,P_2) + \sigma(-P_1,-P_2)}, \tag{16}$$

where $P_1 = |P^-|$, $P_2 = |P^+|$. It can easily be checked for the whole set of contact interactions listed in Table 1, with the exception of the s-channel sneutrino exchange, that from (12) and (16) one finds

$$A_{\rm double}^{\rm SM} = A_{\rm double}^{\rm CI} = P_1 P_2 = 0.48, \tag{17}$$

where the numerical value corresponds to electron and positron degrees of polarization: $P_1 = 0.8$, $P_2 = 0.6$. This is because these contact interactions contribute to the same amplitudes as shown in (10). Eq. (17) demonstrates that $A_{\rm double}^{\rm SM}$ and $A_{\rm double}^{\rm CI}$ are indistinguishable for any values of the contact interaction parameters, $\Delta_{\alpha\beta}$, i.e. $\Delta A_{\rm double} = A_{\rm double}^{\rm CI} - A_{\rm double}^{\rm SM} = 0$.

On the contrary, the $\tilde{\nu}$ exchange in the s-channel will force this observable to a smaller value, $\Delta A_{\rm double} = A_{\rm double}^{\tilde{\nu}} - A_{\rm double}^{\rm SM} \propto -P_1P_2\,|C_{\tilde{\nu}}^s \chi_{\tilde{\nu}}^s|^2 < 0$. The value of $A_{\rm double}$ below P_1P_2 can provide a signature of scalar exchange in the s-channel. All those features in the $A_{\rm double}$ behavior are shown in Fig. 1.

The non-zero value of the λ_{131} coupling implies that the Bhabha scattering process will receive $\tilde{\nu}_\tau$ contributions from both the s- and t-channel exchanges. The differential cross section can be written in this

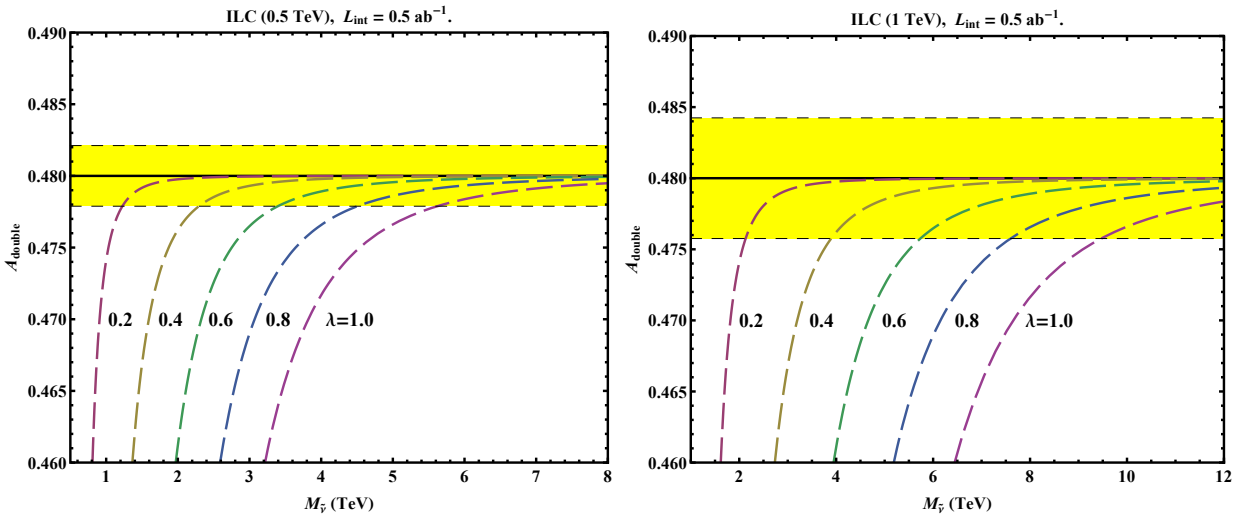

Figure 1: Double beam polarization asymmetry $A^{\tilde{\nu}}_{\rm double}$ as a function of sneutrino mass $M_{\tilde{\nu}}$ for different choices of λ (dashed lines) at the ILC with $\sqrt{s} = 0.5$ TeV (left panel) and $\sqrt{s} = 1.0$ TeV (right panel), $\mathcal{L}_{\rm int} = 0.5$ ab^{-1}. From left to right, λ varies from 0.2 to 1.0 in steps of 0.2. The solid horizontal line corresponds to $A^{\rm SM}_{\rm double} = A^{\rm CI}_{\rm double}$. The yellow bands indicate the expected uncertainty in the SM case.

case as

$$\begin{aligned}\frac{{\rm d}\sigma^{\tilde{\nu}}}{{\rm d}z} = \frac{\pi\alpha_{\rm em}^2}{8s}\big[&(1+z)^2\{(1-P^-)(1+P^+)\,|f^s_{LL}+f^t_{LL}|^2+(1+P^-)(1-P^+)\,|f^s_{RR}+f^t_{RR}|^2\}\\ &+(1-z)^2\{(1-P^-)(1+P^+)\,|f^s_{LR}|^2+(1+P^-)(1-P^+)\,|f^s_{RL}|^2\}\\ &+4\,(1+P^-P^+)\{|f^t_{LR}|^2+|f^t_{RL}|^2\}\big]\end{aligned} \tag{18}$$

where[3]

$$\begin{aligned} f^s_{LL} &= 1+(g^e_L)^2\chi_Z, & f^s_{RR} &= 1+(g^e_R)^2\chi_Z,\\ f^s_{LR} &= 1+g^e_Lg^e_R\chi_Z+\frac{1}{2}C_{\tilde{\nu}}\chi^t_{\tilde{\nu}}, & f^s_{RL} &= 1+g^e_Rg^e_L\chi_Z+\frac{1}{2}C_{\tilde{\nu}}\chi^t_{\tilde{\nu}},\\ f^t_{LL} &= \frac{s}{t}+(g^e_L)^2\chi^t_Z, & f^t_{RR} &= \frac{s}{t}+(g^e_R)^2\chi^t_Z,\\ f^t_{LR} &= \frac{s}{t}+g^e_Lg^e_R\chi^t_Z+\frac{1}{2}C_{\tilde{\nu}}\chi^s_{\tilde{\nu}}, & f^t_{RL} &= \frac{s}{t}+g^e_Rg^e_L\chi^t_Z+\frac{1}{2}C_{\tilde{\nu}}\chi^s_{\tilde{\nu}}, \end{aligned} \tag{19}$$

where $\chi^t_i = s/(t-M_i^2)$ Note that we use the same notation as in Eq. (14) for the reduced sneutrino coupling $C_{\tilde{\nu}}$. However, since now the same lepton generation is present in the initial and final states, consequently in Eq. (19) we have

$$C_{\tilde{\nu}} = \frac{\lambda^2_{131}}{4\pi\alpha_{\rm em}} \tag{20}$$

for both s- and t-channel sneutrino exchanges.

3 Numerical analysis

In the numerical analysis, cross sections are evaluated including initial- and final-state radiation by means of the program ZFITTER [23], together with ZEFIT [24], with $m_{\rm top} = 175$ GeV and $m_H = 125$ GeV. One-loop SM electroweak corrections are accounted for by improved Born amplitudes [25], such that the forms of the

[3]Note that Ref. [7], for example, uses a different convention for the chirality of the final state current.

previous formulae remain the same. Concerning initial-state radiation, a cut on the energy of the emitted photon $\Delta = E_\gamma/E_{\rm beam} = 0.9$ is applied in order to avoid the radiative return to the Z peak and enhance the signal originating from the nonstandard physics contribution [21].

As numerical inputs, we shall assume the identification efficiencies of $\epsilon = 95\%$ for $\mu^+\mu^-$ final states, integrated luminosity of $\mathcal{L}_{\rm int} = 0.5$ ab^{-1} with uncertainty $\delta\mathcal{L}_{\rm int}/\mathcal{L}_{\rm int} = 0.5\%$, and a fiducial experimental angular range $|\cos\theta| \leq 0.99$. Also, regarding electron and positron degrees of polarization, we shall consider the following values: $P^- = \pm 0.8$; $P^+ = \pm 0.6$, with $\delta P^-/P^- = \delta P^+/P^+ = 0.5\%$.

Discovery and identification reaches on the sneutrino mass $M_{\tilde\nu}$ (95% C.L.) plotted in Fig. 2 are obtained from conventional χ^2 analysis. The discovery limit (Disc) is obtained from a combined analysis of the polarized differential cross sections, $d\sigma/dz$, in 10 equal-size z-bins in the range $[-0.99, 0.99]$, with beam polarizations of the same sign, $(P^-, P^+) = (+0.8, +0.6); (-0.8, -0.6)$. This procedure provides the best sensitivity to sneutrino parameters, whereas the identification reach (ID) is derived from $A_{\rm double}$. In the latter case the χ^2 function is constructed as follows: $\chi^2 = (\Delta A_{\rm double}/\delta A_{\rm double})^2$ where $\delta A_{\rm double}$ is the expected experimental uncertainty accounting for both statistical and systematic components.

For comparison, current limits from low-energy data are also shown [26,27]. From Fig. 2 one can see that identification of sneutrino exchange effects in the s-channel with $A_{\rm double}$ is feasible in the region of parameter and mass space far beyond the current limits.

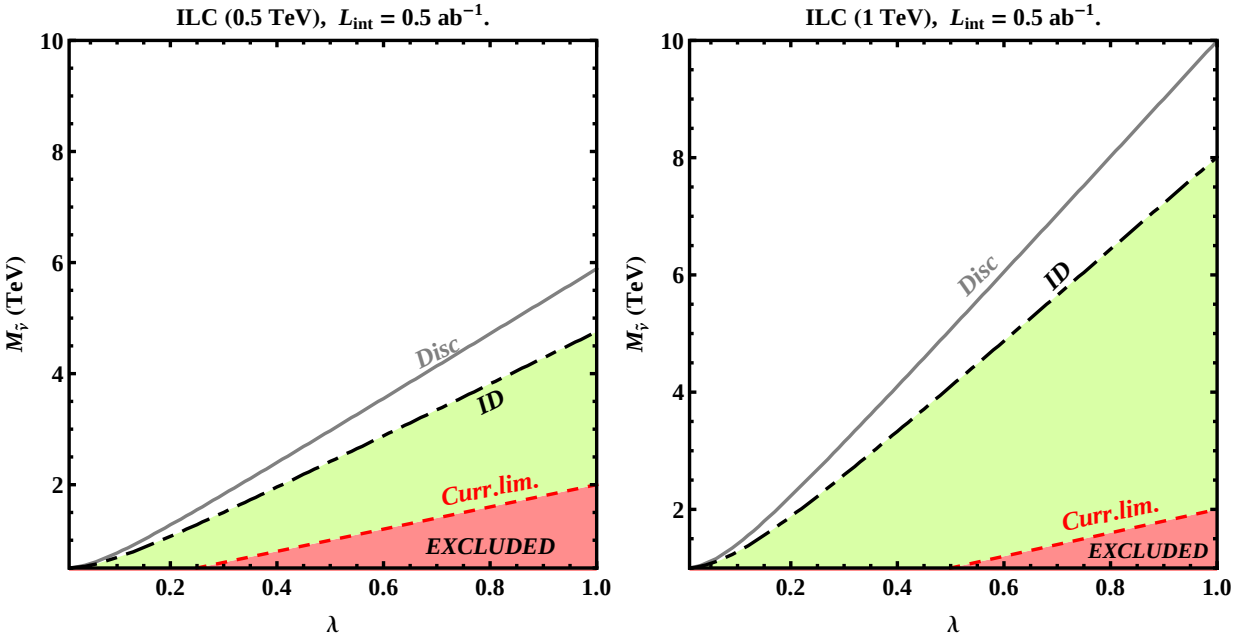

Figure 2: Discovery and identification reaches on sneutrino mass $M_{\tilde\nu}$ (95% C.L.) as a function of λ for the process $e^+e^- \to \mu^+\mu^-$ at the ILC with $\sqrt{s} = 0.5$ TeV (left panel) and $\sqrt{s} = 1.0$ TeV (right panel), $\mathcal{L}_{\rm int} = 0.5$ ab^{-1}. For comparison, current limits from low energy data are also displayed.

As was demonstrated in Ref. [19] the resonant s-channel production of sneutrino $\tilde\nu$ with their subsequent decay into purely leptonic final states via R-parity violating couplings can be observed over a wide range of parameters (couplings and masses) in hadronic collisions (4). This process provides a clean and powerful probe of R-parity violating supersymmetric parameter space and the corresponding LHC search reaches in the parameter plane spanned by the sneutrino mass and the R-parity-violating coupling were obtained there. Specifically, in the dilepton process (4) of interest here, a spin-0 sneutrino can be exchanged through the subprocess $d\bar d \to \tilde\nu \to l^+l^-$ and manifest itself as a peak in the dilepton invariant mass distribution and also with a flat angular distribution. The cross section is proportional to the R-parity violating product $X = (\lambda')^2 B_l$ where B_l is the sneutrino leptonic branching ratio and λ' the relevant sneutrino coupling to the $d\bar d$ quarks. The experimental 95% CL lower limits on $M_{\tilde\nu}$ range from 397 GeV (for $X = 10^{-4}$) to 866

GeV (for $X = 10^{-2}$) [28].

If this signature is observed, the leptonic center-edge integrated asymmetry [29] can be successfully used to distinguish slepton resonances from those associated with new spin-1 Z' gauge bosons and the Randall-Sundrum graviton resonance (spin-2). Once large integrated luminosities of order ~ 100 fb^{-1} are obtained at the LHC, these new scalar resonances should be visible for masses as large as $\sim 1.5 - 5.5$ TeV depending on the specific details of the model (couplings and leptonic branching ratios). Accordingly, the analysis performed in [19] indicates that the identification of the sneutrino against the RS graviton and Z' bosons by center-edge asymmetry is possible at the LHC for $M_{\tilde{\nu}} \leq 4.5$ TeV for X in the range of $10^{-5} < X < 10^{-1}$.

As mentioned above, future e^+e^- colliders operating in the TeV energy range can indirectly probe for new physics effects by exploring contact-interaction-like deviations from the cross sections and asymmetries predicted by the SM. For luminosity expected at ILC, ~ 0.5 ab^{-1}, and with both electron and positron beams polarized, from Fig. 2 we see that this implies that the parameter space region $\lambda/M_{\tilde{\nu}} > 0.17$ (0.10) ($M_{\tilde{\nu}}$ in TeV unit) would certainly be probed at $\sqrt{s} = 0.5$ (1) TeV by such measurements while identification parameter space populates the region 0.21 (0.13) $< \lambda/M_{\tilde{\nu}} <$0.5.

For Bhabha scattering, the angular range $|\cos\theta| < 0.90$ is divided into nine equal-size bins. We combine the cross sections with the following initial electron and positron longitudinal polarizations: $(P^-, P^+) = (|P^-|, -|P^+|)$; $(-|P^-|, |P^+|)$; $(|P^-|, |P^+|)$; $(-|P^-|, -|P^+|)$. The assumed reconstruction efficiencies, that determine the expected statistical uncertainties, are 100% for e^+e^- final pairs. Concerning the $\mathcal{O}(\alpha_{\rm em})$ QED corrections, the (numerically dominant) effects from initial-state radiation for Bhabha scattering are again accounted for by a structure function approach including both hard and soft photon emission [30], and by a flux factor method [31], respectively.

One can parametrize the bounds depicted in Fig. 2 (in the plane ($M_{\tilde{\nu}}$, λ)) approximately as a straight line, $M_{\tilde{\nu}} = k_\mu \lambda$ ($M_{\tilde{\nu}}$ is taken in TeV units), $\lambda = \sqrt{\lambda_{131} \cdot \lambda_{232}}$ and k_μ is the slope of the these lines for the process $e^+e^- \to \mu^+\mu^-$. For instance, for the discovery reach we have $k_\mu \approx 5.9$ (10) for $\sqrt{s} = 0.5$ (1) TeV. In order to convert the bounds shown in Fig. 2 into limits on $M_{\tilde{\nu}}$ vs λ_{131} one should fix λ_{232}. For that purpose one can take the (mass dependent) current limit on that Yukawa coupling λ_{232} represented as $\lambda_{232}/M_{\tilde{\nu}} = 0.5$. From these formulae one finds: $M_{\tilde{\nu}} < (k_\mu^2/2)\,\lambda_{131}$. These areas which can be explored in the muon pair production process are shown in Fig. 3. In contrast to the limits shown in Fig. 2 as curves, limits on $M_{\tilde{\nu}}$ vs λ_{131} for both the discovery and the identification are represented in Fig. 3 as areas constrained by the line for the current limit, $M_{\tilde{\nu}} = 2\lambda_{131}$, and the lines for the upper bounds, $M_{\tilde{\nu}} = (k_\mu^2/2)\,\lambda_{131}$.

In contrast to muon pair production, identification of the sneutrino exchange effects by means of Bhabha scattering is impossible because CI and sneutrino give rise to the same helicity amplitudes as clearly seen from (18) and (19) [32]. Therefore only the discovery reach for the Bhaba process is shown in the figure.

4 Concluding remarks

In this note we have studied how uniquely identify the indirect (propagator) effects of spin-0 sneutrino predicted by supersymmetric theories with R-parity violation, against other new physics scenarios in high energy e^+e^- annihilation into lepton-pairs at the ILC. The competitive models are the interactions based on gravity in large and in TeV-scale extra dimensions, anomalous gauge couplings, extra Z' bosons, and the compositeness-inspired four-fermion contact interactions. All those kinds of new physics can lead to qualitatively similar modifications of SM cross sections, angular distributions and various asymmetries, but they differ in detail. To evaluate the identification reach on the sneutrino exchange signature, we develop a technique based on a double polarization asymmetry formed by polarizing both beams in the initial state, that is particularly suitable to directly test for such s-channel sneutrino exchange effects in the data analysis. We show that the availability of both beams being polarized, plays a crucial rôle in identifying that new physics scenario, as the commonly considered asymmetry, $A_{\rm LR}$, formed when only a single beam is polarized, was shown not to be useful for the purpose of sneutrino identification.

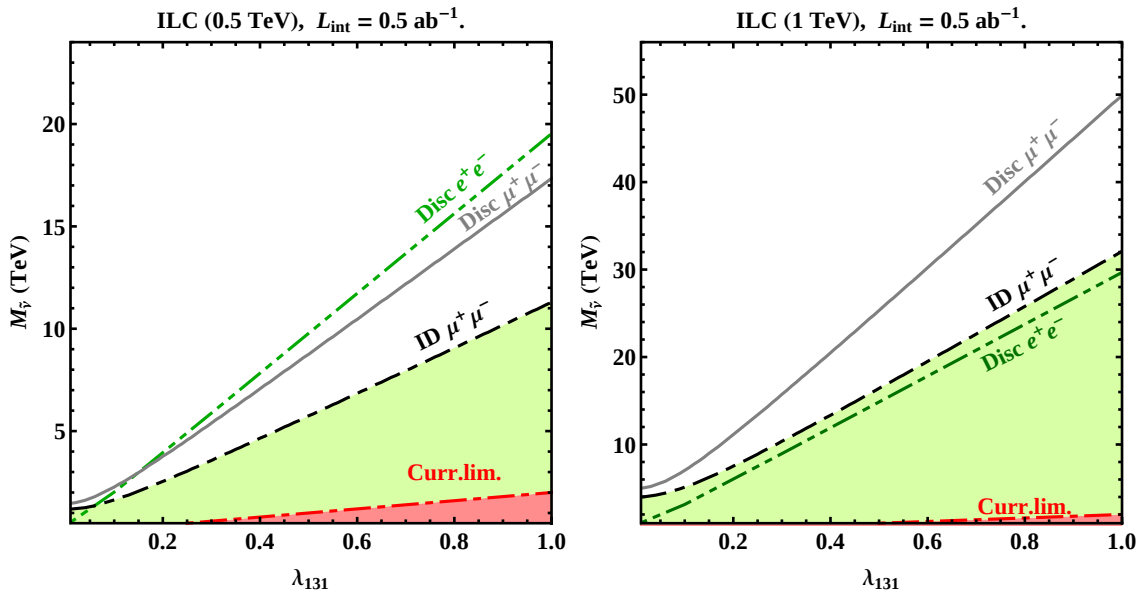

Figure 3: Discovery reach on sneutrino mass (95% C.L.) in Bhabha scattering as a function of λ_{131} at $\sqrt{s} = 0.5$ TeV (left panel) and 1 TeV (right panel), for $\mathcal{L}_{\rm int} = 0.5$ ab^{-1}. For comparison, discovery reach on $M_{\tilde{\nu}}$ in muon pair production is also depicted for $\lambda_{232} = 0.5 \times M_{\tilde{\nu}}/\text{TeV}$.

Acknowledgements

It is a pleasure to thank G. Moortgat-Pick for helpful discussions. This research has been partially supported by the Abdus Salam ICTP (TRIL Programme and Associates Scheme) and the Collaborative Research Center SFB676/1-2006 of the DFG at the Department of Physics, University of Hamburg. JK was partially supported by the Polish Ministry of Science and Higher Education Grant N N202 230337. The work of AVT has been partially supported by the INFN "Fondo Affari Internazionali". The work of PO has been supported by the Research Council of Norway.

References

[1] E. Eichten, K. D. Lane and M. E. Peskin, Phys. Rev. Lett. **50**, 811 (1983);
R. Rückl, Phys. Lett. B **129**, 363 (1983).

[2] P. Langacker, Rev. Mod. Phys. **81**, 1199-1228 (2009). [arXiv:0801.1345 [hep-ph]].

[3] T. G. Rizzo, [hep-ph/0610104].

[4] A. Leike, Phys. Rept. **317**, 143-250 (1999). [hep-ph/9805494].

[5] J. L. Hewett, T. G. Rizzo, Phys. Rept. **183**, 193 (1989).

[6] W. Büchmuller, R. Rückl and D. Wyler, Phys. Lett. B **191**, 442 (1987) [Erratum-ibid. B **448**, 320 (1999)];
G. Altarelli, J. R. Ellis, G. F. Giudice, S. Lola and M. L. Mangano, Nucl. Phys. B **506**, 3 (1997) [hep-ph/9703276];
R. Casalbuoni, S. De Curtis, D. Dominici and R. Gatto, Phys. Lett. B **460**, 135 (1999) [hep-ph/9905568];
V. D. Barger and K. -m. Cheung, Phys. Lett. B **480**, 149 (2000) [hep-ph/0002259].

[7] J. Kalinowski, R. Rückl, H. Spiesberger and P. M. Zerwas, Phys. Lett. B **406**, 314 (1997) [hep-ph/9703436]; Phys. Lett. B **414**, 297 (1997) [hep-ph/9708272].

[8] T. G. Rizzo, Phys. Rev. D **59**, 113004 (1999) [hep-ph/9811440].

[9] For a review, see F. Cuypers and S. Davidson, Eur. Phys. J. C **2**, 503 (1998) [hep-ph/9609487], and references therein.

[10] G. J. Gounaris, D. T. Papadamou and F. M. Renard, Phys. Rev. D **56**, 3970 (1997) [hep-ph/9703281].

[11] N. Arkani-Hamed, S. Dimopoulos and G. R. Dvali, Phys. Lett. B **429**, 263 (1998) [hep-ph/9803315]; Phys. Rev. D **59**, 086004 (1999) [hep-ph/9807344];
L. Randall and R. Sundrum, Phys. Rev. Lett. **83**, 3370 (1999) [hep-ph/9905221];
I. Antoniadis, N. Arkani-Hamed, S. Dimopoulos and G. R. Dvali, Phys. Lett. B **436**, 257 (1998) [hep-ph/9804398].

[12] G. F. Giudice, R. Rattazzi and J. D. Wells, Nucl. Phys. B **544**, 3 (1999) [hep-ph/9811291]; Nucl. Phys. B **630**, 293 (2002) [hep-ph/0112161].

[13] J. L. Hewett, Phys. Rev. Lett. **82**, 4765 (1999) [hep-ph/9811356];
T. Han, J. D. Lykken and R. -J. Zhang, Phys. Rev. D **59**, 105006 (1999) [hep-ph/9811350];
T. G. Rizzo, Phys. Rev. D **64**, 095010 (2001) [hep-ph/0106336];
H. Davoudiasl, J. L. Hewett and T. G. Rizzo, Phys. Rev. Lett. **84**, 2080 (2000) [hep-ph/9909255]; Phys. Rev. D **63**, 075004 (2001) [hep-ph/0006041];
E. A. Mirabelli, M. Perelstein and M. E. Peskin, Phys. Rev. Lett. **82**, 2236 (1999) [hep-ph/9811337];
S. Cullen, M. Perelstein and M. E. Peskin, Phys. Rev. D **62**, 055012 (2000) [hep-ph/0001166].

[14] I. Antoniadis and K. Benakli, Phys. Lett. B **326**, 69 (1994) [arXiv:hep-th/9310151]; I. Antoniadis, K. Benakli and M. Quiros, Phys. Lett. B **331**, 313 (1994) [arXiv:hep-ph/9403290].

[15] G. Pasztor and M. Perelstein, in *Proc. of the APS/DPF/DPB Summer Study on the Future of Particle Physics (Snowmass 2001)* ed. N. Graf, arXiv:hep-ph/0111471.

[16] K.-m. Cheung and G. L. Landsberg, Phys. Rev. D **65**, 076003 (2002) [hep-ph/0110346].

[17] N.-E. Bomark, D. Choudhury, S. Lola and P. Osland, JHEP **1107**, 070 (2011) [arXiv:1105.4022 [hep-ph]].

[18] G. Moortgat-Pick *et al.*, Phys. Rept. **460**, 131 (2008) [arXiv:hep-ph/0507011].

[19] P. Osland, A. A. Pankov, N. Paver and A. V. Tsytrinov, Phys. Rev. D **82**, 115017 (2010) [arXiv:1008.1389 [hep-ph]].

[20] B. Schrempp, F. Schrempp, N. Wermes and D. Zeppenfeld, Nucl. Phys. B **296**, 1 (1988).

[21] A. Djouadi, A. Leike, T. Riemann, D. Schaile and C. Verzegnassi, Z. Phys. C **56**, 289 (1992).

[22] P. Osland, A. A. Pankov and N. Paver, Phys. Rev. D **68**, 015007 (2003) [arXiv:hep-ph/0304123].

[23] D. Y. Bardin, P. Christova, M. Jack, L. Kalinovskaya, A. Olchevski, S. Riemann and T. Riemann, Comput. Phys. Commun. **133**, 229 (2001) [hep-ph/9908433].

[24] S. Riemann, FORTRAN program ZEFIT, Version 4.2.

[25] M. Consoli, W. Hollik and F. Jegerlehner, CERN-TH-5527-89, presented at the *Workshop on Z Physics at LEP*;
G. Altarelli, R. Casalbuoni, D. Dominici, F. Feruglio and R. Gatto, Nucl. Phys. B **342**, 15 (1990).

[26] Y. Kao and T. Takeuchi, arXiv:0910.4980 [hep-ph].

[27] G. Bhattacharyya, H. Pas and D. Pidt, Phys. Rev. D **84**, 113009 (2011) [arXiv:1109.6183 [hep-ph]].

[28] T. Aaltonen *et al.* [CDF Collaboration], Phys. Rev. Lett. **102**, 091805 (2009) [arXiv:0811.0053 [hep-ex]].

[29] E. W. Dvergsnes, P. Osland, A. A. Pankov and N. Paver, Phys. Rev. D **69**, 115001 (2004) [hep-ph/0401199].

[30] For reviews see, e.g., O. Nicrosini and L. Trentadue, in *Radiative Corrections for e^+e^- Collisions*, ed. J. H. Kühn 25 (Springer, Berlin, 1989), p. 25; in *QED Structure Functions, Ann Arbor, MI, 1989*, ed. G. Bonvicini, AIP Conf. Proc. No. 201 (AIP, New York, 1990), p. 12.

[31] For a review see, e.g., W. Beenakker and F. A. Berends: *Proc. of the Workshop on Physics at LEP2*, CERN 96-01, vol. 1, p. 79 and references therein.

[32] A. A. Pankov, N. Paver and A. V. Tsytrinov, Phys. Rev. D **73**, 115005 (2006) [hep-ph/0512131].

DESY 12-207

One-loop effects on MSSM parameter determination via chargino production at the LC

Aoife Bharucha[*,1], Jan Kalinowski[†,2], Gudrid Moortgat-Pick[‡,1,3], Krzysztof Rolbiecki[§,3,4] and Georg Weiglein[¶,3]

[1] *II. Institut für Theoretische Physik, University of Hamburg, Luruper Chaussee 149, D-22761 Hamburg, Germany*

[2] *Faculty of Physics, University of Warsaw, 00681 Warsaw, Poland*

[3] *DESY, Deutsches Elektronen-Synchrotron, Notkestr. 85, D-22607 Hamburg, Germany*

[4] *Instituto de Física Teórica, IFT-UAM/CSIC, 28049 Madrid, Spain.*

Abstract

At a future linear collider very precise measurements, typically with errors of $< 1\%$, are expected to be achievable. Such an accuracy gives sensitivity to the quantum corrections, which therefore must be incorporated in theoretical calculations in order to determine the underlying new physics parameters from prospective linear collider measurements. In the context of the chargino–neutralino sector of the minimal supersymmetric standard model, this involves fitting one-loop predictions to prospective measurements of the cross sections, forward-backward asymmetries and of the accessible chargino and neutralino masses. Taking recent results from LHC SUSY and Higgs searches into account we consider three phenomenological scenarios, each with characteristic features. Our analysis shows how an accurate determination of the desired parameters is possible, providing in addition access to the stop masses and mixing angle.

[*]aoife.bharucha@desy.de
[†]jan.kalinowski@fuw.edu.pl
[‡]gudrid.moortgat-pick@desy.de
[§]krzysztof.rolbiecki@desy.de
[¶]georg.weiglein@desy.de

1 Introduction

A linear collider (LC) [1–5] will be an ideal environment for high precision studies of physics beyond the standard model (BSM). A particularly well-motivated BSM theory is the minimal supersymmetric standard model (MSSM). This provides the lightest neutralino as a candidate to explain the evidence for dark matter in the universe [6, 7]. Further, naturalness arguments (see e.g. ref. [8]) support light higgsino-like charginos and neutralinos, as also predicted by GUT motivated SUSY models [9]. Due to the challenges involved in detecting electroweakinos at the LHC, current bounds coming from the ATLAS and CMS exclude only small regions of parameter space, see e.g. refs. [10,11]. The charginos and neutralinos could therefore be within reach of a first stage linear collider.

One approach to determine the fundamental MSSM parameters is to consider constrained models such as the constrained minimal supersymmetric standard model (CMSSM), and perform a global fit of this reduced set of parameters to all relevant experimental results available, see e.g. ref. [12]. Here on the other hand, in order to precisely determine the nature of the underlying SUSY model, we wish to determine the fundamental parameters in the most model-independent way possible. The determination of the U(1) parameter M_1, the SU(2) parameter M_2, the higgsino parameter μ and $\tan\beta$, the ratio of the vacuum expectation values of the two neutral Higgs doublet fields, at the percent level via chargino and neutralino pair-production has been shown to be possible at LO (see ref. [13] and references therein). Due to the expected high precision of mass and coupling measurements at the LC, as well as the fact that one-loop effects in the MSSM may be sizeable, higher order effects have to be considered. Taking these corrections into account additional MSSM parameters become relevant, such as the masses of the stops and sleptons, which are also so far weakly constrained by the LHC.

In this paper we show how it would be possible to determine the fundamental parameters of the chargino and neutralino sector at the LC, including the complications arising due to higher order effects. Specifically, we calculate the next-to-leading order (NLO) corrections to the cross-section (σ) and forward-backward asymmetry (A_{FB}) for chargino production, and also to the chargino and neutralino masses. A number of next-to-leading order (NLO) calculations of chargino and neutralino pair production at the LC can be found in the literature [14–18]. We perform our calculations in the on-shell (OS) scheme such that, as far as possible, the mass parameters can be interpreted as the physical masses. Recent work on the OS renormalization of the chargino-neutralino sector can be found in refs. [18–24].

By fitting loop corrected predictions to these experimental results we show

that it is possible to extract the fundamental parameters of the MSSM Lagangian. However due to the greater number of parameters, performing the fit is more involved than for the LO analysis. Choosing three potential MSSM scenarios, we assess the impact of the loop corrections and the feasibility of such an extraction in each. We further investigate the impact of obtaining masses of the charginos and neutralinos from threshold scans rather than the continuum (see ref. [1]) on the resulting accuracy of the parameters obtained from the fit.

The paper is organised as follows. In sec. 2 we introduce the process studied and define necessary notation. We then provide details of the calculation of the loop corrections in sec. 3, including details of the renormalization scheme used. In sec. 4 we further discuss the method employed in order to fit to the MSSM parameters, define the scenarios considered, and present our results. Finally in sec. 5 we discuss the implications of the results of the fits.

2 Process studied and tree-level relations

In this paper we study the determination of the fundamental parameters in the chargino–neutralino sector of the MSSM, via chargino production at a LC. The charginos, $\tilde{\chi}^{\pm}$, and neutralinos, $\tilde{\chi}^0$, are the mass eigenstates of the gauginos and higgsinos, as seen from the relevant part of the MSSM Lagrangian [25],

$$\begin{aligned}\mathcal{L}_{\tilde{\chi}} =& \overline{\tilde{\chi}_i^-}(\not{p}\delta_{ij} - P_L(U^* X V^\dagger)_{ij} - P_R(V X^\dagger U^T)_{ij})\tilde{\chi}_j^- \\ &+ \frac{1}{2}\overline{\tilde{\chi}_i^0}(\not{p}\delta_{ij} - P_L(N^* Y N^\dagger)_{ij} - P_R(N Y^\dagger N^T)_{ij})\tilde{\chi}_j^0, \end{aligned} \tag{1}$$

where $P_{L/R} = 1/2(1 \mp \gamma_5)$. The mass matrix for the charginos is given by

$$X = \begin{pmatrix} M_2 & \sqrt{2}M_W s_\beta \\ \sqrt{2}M_W c_\beta & \mu \end{pmatrix}, \tag{2}$$

where $s_\beta/c_\beta \equiv \sin\beta/\cos\beta$, and M_W is the mass of the W boson. This matrix is diagonalised via the bi-unitary transformation $\mathbf{M}_{\tilde{\chi}^+} = U^* X V^\dagger$, where U and V are complex unitary matrices. The mass matrix for the neutralinos in the $(\tilde{B}, \tilde{W}, \tilde{H}_1, \tilde{H}_2)$ basis is given by

$$Y = \begin{pmatrix} M_1 & 0 & -M_Z c_\beta s_W & M_Z s_\beta s_W \\ 0 & M_2 & M_Z c_\beta c_W & -M_Z s_\beta c_W \\ -M_Z c_\beta s_W & M_Z c_\beta c_W & 0 & -\mu \\ M_Z s_\beta s_W & -M_Z s_\beta c_W & -\mu & 0 \end{pmatrix}, \tag{3}$$

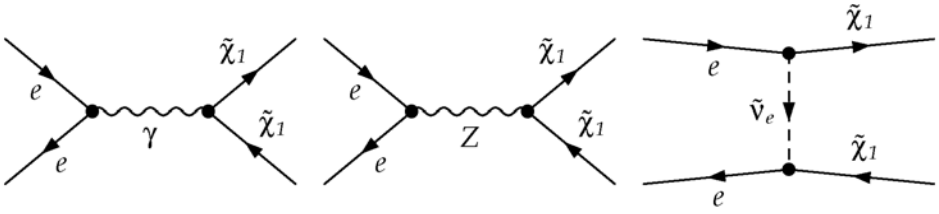

Figure 1: Tree-level diagrams for the production of charginos $\tilde{\chi}_1^+$ and $\tilde{\chi}_1^-$ at the LC.

where $s_W(c_W)$ is the sin(cos) of the weak mixing angle θ_W. Since Y is complex symmetric, its diagonalisation requires only one unitary matrix N, via $\mathbf{M}_{\tilde{\chi}^0} = N^* Y N^\dagger$.

As described in detail in sec. 4, the parameter determination relies on the measurement of the masses of the charginos and neutralinos, the polarised cross-section for the pair production of charginos, $\tilde{\chi}_1^-$,

$$\sigma(e^+e^- \to \tilde{\chi}_1^+ \tilde{\chi}_1^-), \tag{4}$$

and the forward-backward asymmetry defined by,

$$A_{FB} = \frac{\sigma(\cos\theta > 0) - \sigma(\cos\theta < 0)}{\sigma(\cos\theta > 0) + \sigma(\cos\theta < 0)}, \tag{5}$$

for the unpolarised cross-section, where θ is the angle of the momentum of the chargino $\tilde{\chi}_1^-$ with respect to the momentum of the incoming electron e^-.

Neglecting the electron-Higgs couplings, this process occurs at leading order via three diagrams, as seen in fig. 1.

The transition matrix element can be written as [26],

$$\mathcal{M}_{\alpha\beta}(e^+e^- \to \tilde{\chi}_i^+ \tilde{\chi}_j^-) = \frac{e}{s} Q_{\alpha\beta} \left[\bar{v}(e^+)\gamma_\mu P_\alpha u(e^-)\right] \left[\bar{u}(\tilde{\chi}_j^-)\gamma^\mu P_\beta v(\tilde{\chi}_i^+)\right], \tag{6}$$

where $Q_{\alpha\beta}$ denotes the bilinear charges, $\alpha = L, R$ refers to the chirality of the e^+e^- current and $\beta = L, R$ to that of the $\tilde{\chi}_i^+ \tilde{\chi}_j^-$ current. The summation over α and β is implied. The bilinear charges are comprised of the propagators and couplings

$$\begin{aligned}
Q_{LL} &= C^L_{\tilde{\chi}_i^+ \tilde{\chi}_j^- \gamma} - D_Z G_L C^L_{\tilde{\chi}_i^+ \tilde{\chi}_j^- Z}, \\
Q_{RL} &= C^L_{\tilde{\chi}_i^+ \tilde{\chi}_j^- \gamma} - D_Z G_R C^L_{\tilde{\chi}_i^+ \tilde{\chi}_j^- Z}, \\
Q_{LR} &= C^R_{\tilde{\chi}_i^+ \tilde{\chi}_j^- \gamma} + D_Z G_L \left(C^R_{\tilde{\chi}_i^+ \tilde{\chi}_j^- Z}\right)^* + \frac{i}{2\,e} D_{\tilde{\nu}} \left(C^R_{\tilde{\nu}_e e^+ \tilde{\chi}_i^-}\right)^* C^R_{\tilde{\nu}_e e^+ \tilde{\chi}_j^-}, \\
Q_{RR} &= C^R_{\tilde{\chi}_i^+ \tilde{\chi}_j^- \gamma} + D_Z G_R \left(C^R_{\tilde{\chi}_i^+ \tilde{\chi}_j^- Z}\right)^*,
\end{aligned} \tag{7}$$

for which the required MSSM couplings for the $\tilde{\chi}_i^+ \tilde{\chi}_j^- \gamma$, $\tilde{\chi}_i^+ \tilde{\chi}_j^- Z$ and $e\tilde{\nu}_e \tilde{\chi}_i^+$ vertices are given by

$$\begin{aligned}
C^{L/R}_{\tilde{\chi}_i^+ \tilde{\chi}_j^- \gamma} &= ie\delta_{ij}, \\
C^{L}_{\tilde{\chi}_i^+ \tilde{\chi}_j^- Z} &= -\frac{ie}{c_W s_W}\left(s_W^2 \delta_{ij} - U^*_{j1}U_{i1} - \frac{1}{2}U^*_{j2}U_{i2}\right), \\
C^{R}_{\tilde{\chi}_i^+ \tilde{\chi}_j^- Z} &= C^{L}_{\tilde{\chi}_i^+ \tilde{\chi}_j^- Z}(U \to V^*), \\
C^{R}_{\tilde{\nu}_e e^+ \tilde{\chi}_i^-} &= -\frac{ie}{s_W} V_{i1},
\end{aligned} \tag{8}$$

and G_L, G_R, D_Z and $D_{\tilde{\nu}}$ are defined via

$$\begin{aligned}
G_L &= \frac{s_W^2 - \frac{1}{2}}{s_W c_W}, & G_R &= \frac{s_W}{c_W}, \\
D_Z &= \frac{s}{s - M_Z^2}, & D_{\tilde{\nu}} &= \frac{s}{t - m_{\tilde{\nu}}^2}.
\end{aligned} \tag{9}$$

In the equations above, e denotes the electric charge, m_e and M_Z are the masses of the electron and Z boson. D_Z and $D_{\tilde{\nu}}$ refer to the propagators of the Z boson and sneutrino (of mass $m_{\tilde{\nu}}$), in terms of the Mandelstam variables s and t.

One can therefore express the transition matrix element in terms of M_2, μ and $\tan\beta$, in addition to the known SM parameters. However, the expected accuracy of the measurements at the linear collider is such that one-loop corrections become relevant, and we shall see in the following section how the higher order expressions depend on many additional MSSM parameters.

3 NLO contributions and renormalization

We have calculated the full one-loop corrections to the forward-backward asymmetry for process $e^+e^- \to \tilde{\chi}_1^+ \tilde{\chi}_1^-$, within the complex MSSM; the corresponding corrections to the cross section were calculated in ref. [18]. Examples for the contributing self-energy, vertex and box diagrams are shown in fig. 2. As in ref. [18], for the calculation we have used the program `FeynArts` [27–31], which allowed an automated generation of the Feynman diagrams and amplitudes. Together with the packages `FormCalc` [32–34] and `LoopTools` [32] we derived the final matrix elements and loop integrals. We assume a unit CKM matrix. We regularise using dimensional reduction [35–37], which ensures that SUSY is preserved, via the implementation described in refs. [32, 38].

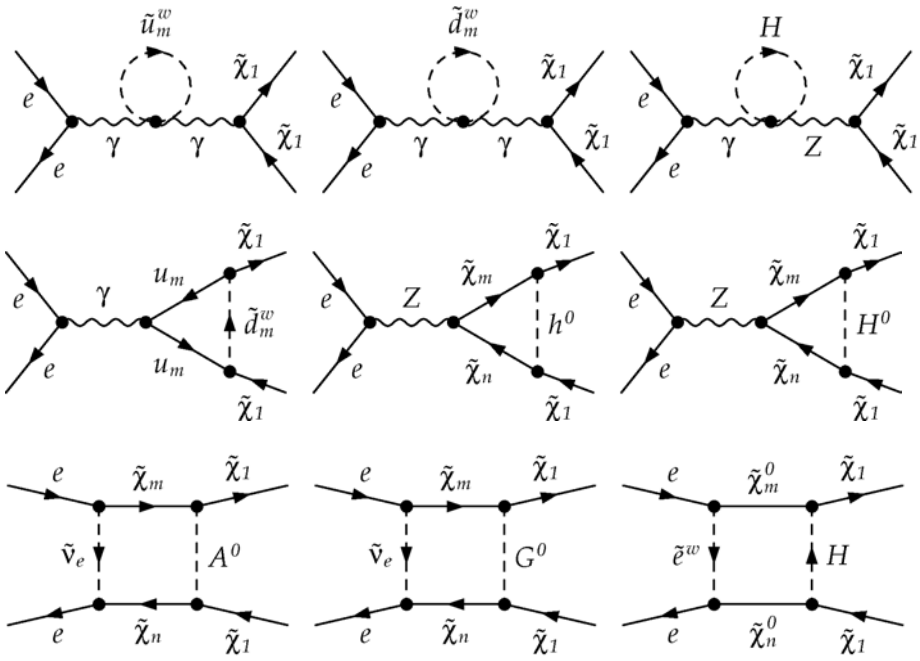

Figure 2: Examples of one-loop self-energy (upper), vertex (middle) and box (lower) diagrams for the production of charginos $\tilde{\chi}_1^+$ and $\tilde{\chi}_1^-$ at the LC.

A number of one-loop calculations in the gaugino-higgsino sector can be found in the literature, mainly in the CP-conserving MSSM [14, 39–46], but some of which apply a renormalization scheme that is also applicable for complex parameters [14, 45]. CP-odd observables have also been calculated at the one-loop level, for instance in refs. [47–49], but no dedicated renormalization scheme was required in these cases as the observables studied were UV-finite. Since we intend to extend the current study to the case of complex parameters, here we follow the approach of refs. [18,20] closely, where a dedicated on-shell renormalization scheme for the chargino and neutralino sector of the MSSM with complex parameters was developed. In the following we will therefore only discuss the parameter renormalization of the chargino and neutralino sector, relevant for the definitions of the parameters at loop level, briefly and for further details about the chargino field renormalization and the renormalization of other sectors we refer the reader to refs. [18,20,21,24].

The mass matrix in the chargino sector, eq. (2), is renormalized via

$$X \to X + \delta X, \tag{10}$$

where δX is defined by

$$\delta X = \begin{pmatrix} \delta M_2 & \sqrt{2}\delta(M_W s_\beta) \\ \sqrt{2}\delta(M_W c_\beta) & \delta\mu \end{pmatrix}, \tag{11}$$

containing the renormalization constants δM_2 and $\delta\mu$, as well as renormalization constants (RCs) from other sectors, δc_β, δs_β (which can be expressed in terms of $\delta \tan\beta$), and δM_W, defined in ref. [18]. The neutralino mass matrix, eq. (3), is similarly renormalized via

$$Y \to Y + \delta Y, \tag{12}$$

where δY is defined analogously to δX in eq. (11) and contains the additional RC δM_1, cf. eq. (3).

Following e.g. ref. [20], δM_1, δM_2 and $\delta\mu$ are determined by choosing three out of the total six physical masses of the charginos and neutralinos to be on-shell, i.e. the tree-level masses, $m_{\tilde{\chi}_i}$, coincide with the one-loop renormalized masses, $M_{\tilde{\chi}_i} = m_{\tilde{\chi}_i} + \Delta m_{\tilde{\chi}_i}$,

$$\begin{aligned} \Delta m_{\tilde{\chi}_i} &\equiv -\frac{m_{\tilde{\chi}_i}}{2}\mathrm{Re}[\hat{\Sigma}^L_{ii}(m^2_{\tilde{\chi}_i}) + \hat{\Sigma}^R_{ii}(m^2_{\tilde{\chi}_i})] - \frac{1}{2}\mathrm{Re}[\hat{\Sigma}^{SL}_{ii}(m^2_{\tilde{\chi}_i}) + \hat{\Sigma}^{SR}_{ii}(m^2_{\tilde{\chi}_i})] \\ &= 0. \end{aligned} \tag{13}$$

We define the coefficients $\Sigma^{L/R}_{ij}(p^2)$ and $\Sigma^{SL/SR}_{ij}(p^2)$ of the self energy via

$$\Sigma_{ij}(p^2) = \not{p} P_L \Sigma^L_{ij}(p^2) + \not{p} P_R \Sigma^R_{ij}(p^2) + P_L \Sigma^{SL}_{ij}(p^2) + P_R \Sigma^{SR}_{ij}(p^2), \tag{14}$$

and define the left and right handed vector and scalar coefficients of the renormalized self-energy analogously via $\hat{\Sigma}^{L/R}_{ij}(p^2)$ and $\hat{\Sigma}^{SL/SR}_{ij}(p^2)$ respectively.

As stated earlier, we consider the parameter renormalization as for the complex MSSM, such that our setup is easily adaptable for future extensions. In ref. [18,21], it was shown that in the CP violating case, the 1-loop corrections to the phases of M_1 and μ, i.e. ϕ_{M_1} and ϕ_μ respectively[1] are UV finite. Therefore we take the approach that these phases can be left unrenormalized. We can then determine the necessary conditions to obtain the absolute values $|M_1|$, $|M_2|$ and $|\mu|$, depending on which three physical masses are chosen to be on-shell. As we have two external charginos, and in order to easily extend our setup to the case of $\tilde{\chi}^+_1\tilde{\chi}^-_2$ production, we assume the NCC scheme with $\tilde{\chi}^0_1$, $\tilde{\chi}^\pm_1$ and $\tilde{\chi}^\pm_2$ on-shell [18, 20–22], such that $i' = 1$ and $i'' = 1$ and 2. Note that in choosing the scheme, it is desirable that the on-shell particles should contain significant bino, wino and higgsino components, in order that the

[1]We adopt the convention that M_2 is real.

M_1, M_2 and μ parameters are accessible [18, 20–22]. For the above choice, these conditions are satisfied for all the scenarios defined in sec. 4, in which the lightest neutralino always has a sizeable bino-like component. The parameters in question of the chargino mass matrix can then be renormalized via expressions given in refs. [18, 21, 24], which we list here for completeness,

$$\begin{aligned}\delta|M_1| = &-\frac{1}{\mathrm{Re}\,(e^{-i\phi_{M_1}}\,N_{i1}^2)F}\\ &\Big((2\mathrm{Re}\,(e^{-i\phi_\mu}N_{i3}N_{i4})\mathrm{Re}\,(U_{j1}V_{j1}) + \mathrm{Re}\,N_{i2}^2\mathrm{Re}\,(e^{-i\phi_\mu}U_{j2}V_{j2}))C_k\\ &+ (\mathrm{Re}\,(U_{j1}V_{j1})\mathrm{Re}\,(e^{-i\phi_\mu}U_{k2}V_{k2}) - \mathrm{Re}\,(e^{-i\phi_\mu}U_{j2}V_{j2})\mathrm{Re}\,(U_{k1}V_{k1}))N_i\\ &- (\mathrm{Re}\,N_{i2}^2\mathrm{Re}\,(e^{-i\phi_\mu}U_{k2}V_{k2}) + 2\mathrm{Re}\,(e^{-i\phi_\mu}N_{i3}N_{i4})\,\mathrm{Re}\,(U_{k1}V_{k1}))C_j\Big), \quad (15)\end{aligned}$$

$$\delta|M_2| = \frac{1}{F}\Big(\mathrm{Re}\,(e^{-i\phi_\mu}U_{j2}V_{j2})C_k - \mathrm{Re}\,(e^{-i\phi_\mu}U_{k2}V_{k2})C_j\Big), \quad (16)$$

$$\delta|\mu| = -\frac{1}{F}\Big(\mathrm{Re}\,(U_{j1}V_{j1})C_k - \mathrm{Re}\,(U_{k1}V_{k1})C_j\Big). \quad (17)$$

F, C_i and N_i are defined by

$$F = 2\big(\mathrm{Re}\,(U_{k1}V_{k1})\mathrm{Re}\,(e^{-i\phi_\mu}U_{j2}V_{j2}) - \mathrm{Re}\,(U_{j1}V_{j1})\,\mathrm{Re}\,(e^{-i\phi_\mu}U_{k2}V_{k2})\big), \quad (18)$$

$$\begin{aligned}C_i = &\,\mathrm{Re}\,\big[m_{\tilde\chi_i^+}[\Sigma^L_{\pm,ii}(m^2_{\tilde\chi_i^+}) + \Sigma^R_{\pm,ii}(m^2_{\tilde\chi_i^+})] + \Sigma^{SL}_{\pm,ii}(m^2_{\tilde\chi_i^+}) + \Sigma^{SR}_{\pm,ii}(m^2_{\tilde\chi_i^+})\big]\\ &- \sum_{\substack{j=1,2\\k=1,2}} 2\delta X_{jk}\mathrm{Re}\,(U_{ij}V_{ik}), \quad (19)\end{aligned}$$

$$\begin{aligned}N_i = &\,\mathrm{Re}\,\big[m_{\tilde\chi_i^0}[\Sigma^L_{0,ii}(m^2_{\tilde\chi_i^0}) + \Sigma^R_{0,ii}(m^2_{\tilde\chi_i^0})] + \Sigma^{SL}_{0,ii}(m^2_{\tilde\chi_i^0}) + \Sigma^{SR}_{0,ii}(m^2_{\tilde\chi_i^0})\big]\\ &- \sum_{\substack{j=1,2\\k=3,4}} 4\delta Y_{jk}\mathrm{Re}\,(N_{ij}N_{ik}), \quad (20)\end{aligned}$$

and the subscripts $\pm$ and 0 identify the coefficients of the chargino and neutralino self-energy respectively.[2]

Finite results for the process of interest at one-loop are obtained by adding the counterterm diagrams shown in fig. 3. Although `FeynArts` generates these diagrams, expressions for the counterterms which renormalize the couplings defined at tree-level in eq. (6), calculated in ref. [18], are required as input, and therefore, again for completeness, we provide expressions for these explicitly. For the $\gamma\tilde\chi_i^+\tilde\chi_j^-$, $Z\tilde\chi_i^+\tilde\chi_j^-$ and $e\tilde\nu_e\tilde\chi_i^+$ vertices, these can be expressed as follows,

$$\delta C^L_{\tilde\chi_i^+\tilde\chi_j^-\gamma} = C^L_{\tilde\chi_i^+\tilde\chi_j^-\gamma}\left(\delta Z_e + \frac{\delta Z_{\gamma\gamma}}{2}\right) + C^L_{\tilde\chi_i^+\tilde\chi_j^- Z}\frac{\delta Z_{Z\gamma}}{2} + \frac{ie}{2}\left(\delta Z^L_{\pm,ij} + \delta\bar Z^L_{\pm,ij}\right),$$

[2]Here N_i should not be confused with the neutralino mass matrix N_{ij}.

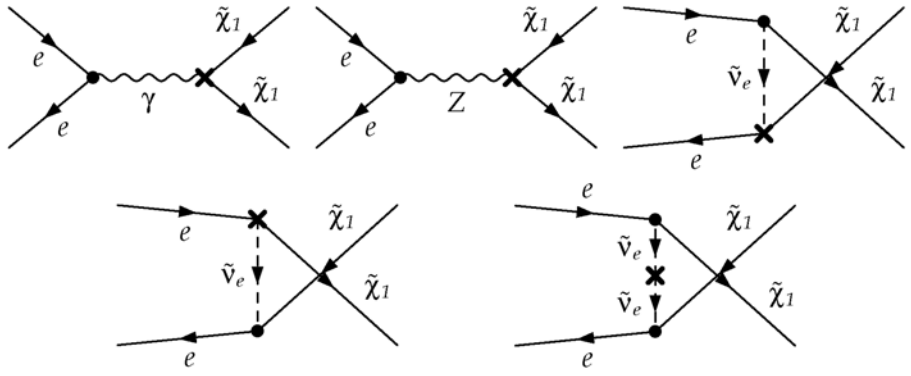

Figure 3: Counterterm diagrams in the MSSM for the production of charginos $\tilde{\chi}_1^+$ and $\tilde{\chi}_1^-$ at the LC.

$$\delta C^L_{\tilde{\chi}_i^+\tilde{\chi}_j^- Z} = C^L_{\tilde{\chi}_i^+\tilde{\chi}_j^- Z}\left(\delta Z_e - \frac{\delta c_W}{c_W} - \frac{\delta s_W}{s_W} + \frac{\delta Z_{ZZ}}{2}\right) + C^L_{\tilde{\chi}_i^+\tilde{\chi}_j^-\gamma}\frac{\delta Z_{\gamma Z}}{2} - 2ie\frac{\delta s_W}{c_W}\delta_{ij} + \frac{1}{2}\sum_{n=1,2}\left(\delta C^L_{\tilde{\chi}_i^+\tilde{\chi}_n^- Z} Z^L_{\pm,nj} + C^L_{\tilde{\chi}_n^+\tilde{\chi}_j^- Z}\delta\bar{Z}^L_{\pm,in}\right), \quad (21)$$

where the analogous right-handed parts are obtained by the replacement $L \to R$, and

$$\delta C^R_{\tilde{\nu}_e e^+\tilde{\chi}_i^-} = C^R_{\tilde{\nu}_e e^+\tilde{\chi}_i^-}\left(\delta Z_e - \frac{\delta s_W}{s_W} + \frac{1}{2}\left(\delta Z_{\tilde{\nu}_e} + \delta Z_e^{L^*}\right)\right) + \frac{1}{2}\left(C^R_{\tilde{\nu}_e e^+\tilde{\chi}_1^-}\delta Z^R_{\pm,1i} + C^R_{\tilde{\nu}_e e^+\tilde{\chi}_2^-}\delta Z^R_{\pm,2i}\right). \quad (22)$$

Note that the renormalization constants of the SM fields, i.e. Z_{VV} $(V = \gamma, Z)$ and δZ_e^L for the vector bosons and electron, and parameters, i.e. δZ_e and $\delta c_W(s_W)$ for the electric charge and cos(sin) of the weak mixing angle respectively, can be found in ref. [18]. The renormalization for the chargino fields is performed in the most general manner, making use of separate RCs for the incoming and outgoing fields, i.e. coefficients $\delta Z^{L/R}_{\pm,ij}$ and $\delta\bar{Z}^{L/R}_{\pm,ij}$ respectively for left and right-handed charginos as given in ref. [18]. Finally, the counterterm for the sneutrino self energy takes the form

$$\delta C_{\bar{\tilde{\nu}}_i\tilde{\nu}_j} = i\delta_{ij}\left(\frac{1}{2}(\delta Z_{\tilde{\nu}_i} + \delta Z^*_{\tilde{\nu}_i})p^2 - \delta m^2_{\tilde{\nu}_i} - \frac{m^2_{\tilde{\nu}_i}}{2}(\delta Z_{\tilde{\nu}_i} + \delta Z^*_{\tilde{\nu}_i})\right), \quad (23)$$

for $\tilde{\nu}_i = \tilde{\nu}_e$, $\tilde{\nu}_\mu$, $\tilde{\nu}_\tau$, where the sneutrino field and mass RCs, $\delta Z^*_{\tilde{\nu}_i}$ and $\delta m_{\tilde{\nu}_i}$, are also defined following ref. [18].

Inital and final state soft radiation must also be included to obtain an infra-red finite result as the incoming and outgoing particles are charged, and this is done as described in detail in ref. [18], using the phase-space slicing method to define the singular soft and collinear contributions in the regions $E < \Delta E$ and $\theta < \Delta\theta$ respectively. In the soft and collinear limit, the results are regularised using electron and photon masses, respectively, and factorised into analytically integrable expressions proportional to the tree-level cross-section $\sigma^{\text{tree}}(e^+e^- \to \tilde{\chi}_1^+\tilde{\chi}_1^-)$. However the result is cut-off dependent (i.e. on ΔE and $\Delta\theta$), and removing this dependence requires a calculation of the cross section for the three body final state, excluding the soft and collinear regions, which we perform using `FeynArts` and `FormCalc`. We further require that soft photon radiation is included in the cross-section obtained from `FormCalc`. Finally we obtain a complete IR finite and cut-off independent result by adding the collinear contribution, which is calculated following the procedure outlined in ref. [14].

4 Fit strategy and numerical results

4.1 Obtaining MSSM parameters from the fit

With the loop corrections calculated as in section 3, we can determine the fundamental parameters of the MSSM at NLO. From now on, we will restrict our study to the case of real parameters. In the chargino and neutralino sectors there are four real parameters, see sec. 2, which we fit to,

$$M_1, \quad M_2, \quad \mu, \quad \tan\beta\,. \tag{24}$$

We additionally fit to the sneutrino mass, as this enters at tree level and will therefore significantly affect cross sections and forward-backward asymmetries. However in those scenarios where the sneutrino would already have been observed at the LC, its mass is assumed to be known. At the loop level, a large number of MSSM parameters will contribute. Depending on the scenario, only limited knowledge about some of these may be available. In particular LHC data may only provide limited information about the parameters of the stop sector, and direct production at the LC might not be possible. However, our analysis also offers good sensitivity to these parameters at the LC, as stops could significantly contribute to chargino/neutralino observables at NLO.

At the LC, masses are expected to be measured with high precision using different methods [1]. In the following we adopt the experimental precision which could be achieved using the threshold scan method, however we also

investigate how the fit precision would change if the masses were obtained from the continuum. In case of the cross sections, the experimental uncertainty is dominated by the statistical uncertainty [50],

$$\frac{\Delta\sigma}{\sigma} = \frac{\sqrt{S+B}}{S}, \tag{25}$$

where S and B are the signal and background contributions, respectively. In addition, we assume that the statistical uncertainties for the cross sections correspond to an integrated luminosity of $\mathcal{L} = 200$ fb^{-1} per polarisation assuming the efficiency of $\epsilon = 15\%$, which includes branching ratios for semileptonic final states and a selection efficiency of 50% [50]. Similarly, for the forward-backward asymmetry we have

$$\delta A_{FB}^{\text{stat}} = \sqrt{\frac{1 - A_{FB}^2}{N}}, \tag{26}$$

and the total number of events $N = N_+ + N_-$ [50].

In order to estimate the theoretical uncertainty on the masses, cross-sections and forward backward asymmetries, we consider the size of possible effects due to neglected higher order corrections as well as unknown MSSM parameters not included in the fit. NNLO corrections are an important source of theoretical uncertainty, however, at present, corrections of this kind are only known for chargino and neutralino masses, for which the leading SUSY-QCD NNLO corrections were calculated in ref. [46]. Based on these results we estimate the uncertainty on the masses due to NNLO corrections to be of the order of 0.5 GeV, i.e. comparable to the expected experimental uncertainty. Note that the masses chosen on-shell are assigned no theoretical uncertainty. We further neglect the currently unknown uncertainties arising due to NNLO corrections to the cross-sections and forward backward asymmetries, assuming that in the future NNLO results for these could be incorporated. However, we do include the additional uncertainty arising due to any unknown MSSM parameters which are not included in the fit, dominated by the contribution from the heavy pseudoscalar Higgs boson mass m_{A^0}. We perform a multi-dimensional χ^2 fit using `Minuit` [51, 52]

$$\chi^2 = \sum_i \left| \frac{\mathcal{O}_i - \bar{\mathcal{O}}_i}{\delta\mathcal{O}_i} \right|^2, \tag{27}$$

where the sum runs over the input observables $\mathcal{O}_i$, depending on the scenario, with their corresponding experimental uncertainties $\delta\mathcal{O}_i$.

4.2 Scenarios studied and motivation

We carry out the fit for three scenarios, S1, S2 and S3, shown in tab. 1, chosen in order to realistically assess the sensitivity to the desired parameters in a number of possible situations. Due to the current status of direct LHC searches [53,54], in all scenarios we require heavy first and second generation squarks and gluinos, while the stop sector is assumed to be relatively light.[3] In S1 and S2 we take the masses of the stops, $m_{\tilde{t}_1}$ and $m_{\tilde{t}_2}$, to be 400 GeV and 800 GeV respectively, and the mixing angle to be $\cos\theta_t = 0$. The sbottom sector can then be obtained by defining $m_{\tilde{b}_1} = 400$ GeV and $\cos\theta_b = 0$. On the other hand in S3, in order to obtain $m_h = 125$ GeV, calculated using `FeynHiggs 2.9.1` [55–58], such that it is compatible with the recent Higgs results from the LHC [59, 60], the stop sector parameters are chosen to be $m_{u_3} = 450$ GeV, $m_{q_3} = 1500$ GeV and $A_t = -1850$ GeV, ensuring large mixing between the stops, such that $\cos\theta_t = 0.148$. The sbottom sector is then obtained by defining $m_{\tilde{b}_1} = 450$ GeV and $\cos\theta_b = 0$. In fig. 4, for each of these scenarios, the mass corrections for neutralinos $\tilde{\chi}^0_2$ and $\tilde{\chi}^0_3$ are seen to be sensitive to the stop mixing angle.

As a result of indirect limits (checked using `micrOmegas 2.4.1` [61,62]), we have chosen mixed gaugino higgsino scenarios favoured by the relic density measurements [63] and relatively high pseudoscalar Higgs masses in light of flavour physics constraints, e.g. the branching ratio of $\mathcal{B}(B_s \to \mu^+\mu^-)$ [64]. We also check that our scenarios agree with the experimental results for branching ratio $\mathcal{B}(b \to s\gamma)$ and the anomalous magnetic moment of the muon $\Delta(g_\mu - 2)/2$. Further, in S2 we study the sensitivity of the fit to large values of M_2, such that the wino-like chargino and neutralino are heavy and decoupled from the bino and higgsino-like particles. Finally, in S1/S2 we consider the case that the sleptons (with the exception of the light stau) and pseudoscalar Higgs bosons are at the TeV scale, and in S3 the case that they are relatively light. Therefore, while S1/S2 are not in keeping with the 125 GeV Higgs boson, they provide illustrative examples of the potential of the LC in scenarios complementary to S3.[4]

[3] Note that in light of current LHC limits, the value M_3=700 GeV in S1 and S2 means that the gluino mass is rather low, however our results are largely independent of this choice as M_3 only enters our calculations via two loop corrections to m_h.

[4] Note that in S1(S2) a Higgs mass of $m_h = 125$ GeV can also be achieved by adopting $\cos\theta_t = -0.4\,(-0.5)$.

Scenario 1/2			
M_1	125	M_2	250/2000
μ	180	M_{A^0}	1000
M_3	700	$\tan\beta$	10
$M_{q_{1,2}}$	1500	$A_{q_{1,2}}$	650
$M_{l/e_{1,2}}$	1500	A_{l_i}	650
M_{l_3}	800	M_{e_3}	400
Scenario 3			
M_1	106	M_2	212
μ	180	M_{A^0}	500
M_3	1500	$\tan\beta$	12
$M_{q_{1,2}}$	1500	$A_{q_{1,2}}$	-1850
M_{l_i}	180	A_{l_i}	-1850
$M_{e_{1,2}}$	125	M_{e_3}	106

Table 1: Parameters for scenarios 1/2 and 3 (S1/S2 and S3), in GeV with the exception of $\tan\beta$. Here $M_{(l/q)_i}$ ($M_{(e/u/d)_i}$) represents the left (right) handed mass parameter for a slepton/squark of generation i respectively (jointly referred to as M_{f_i}), and A_f is the trilinear coupling for a sfermion $\tilde{f}$. See text for stop and sbottom parameter definitions.

4.3 Results for scenario 1

In this scenario, only the charginos and three neutralinos will be accessible at the LC. As input for the fit we therefore use:

- the masses of the charginos ($\tilde{\chi}_1^{\pm}$, $\tilde{\chi}_2^{\pm}$) and three lightest neutralinos ($\tilde{\chi}_1^0$, $\tilde{\chi}_2^0$, $\tilde{\chi}_3^0$)
- the light chargino production cross section $\sigma(\tilde{\chi}_1^+\tilde{\chi}_1^-)$ with polarised beams at $\sqrt{s} = 350$ and 500 GeV
- the forward-backward asymmetry A_{FB} at $\sqrt{s} = 350$ and 500 GeV
- the branching ratio $\mathcal{B}(b \to s\gamma)$ calculated using `micrOmegas 2.4.1` [61, 62].

The input variables, together with errors, namely the assumed experimental precision of the prospective LC measurements as well as the theoretical

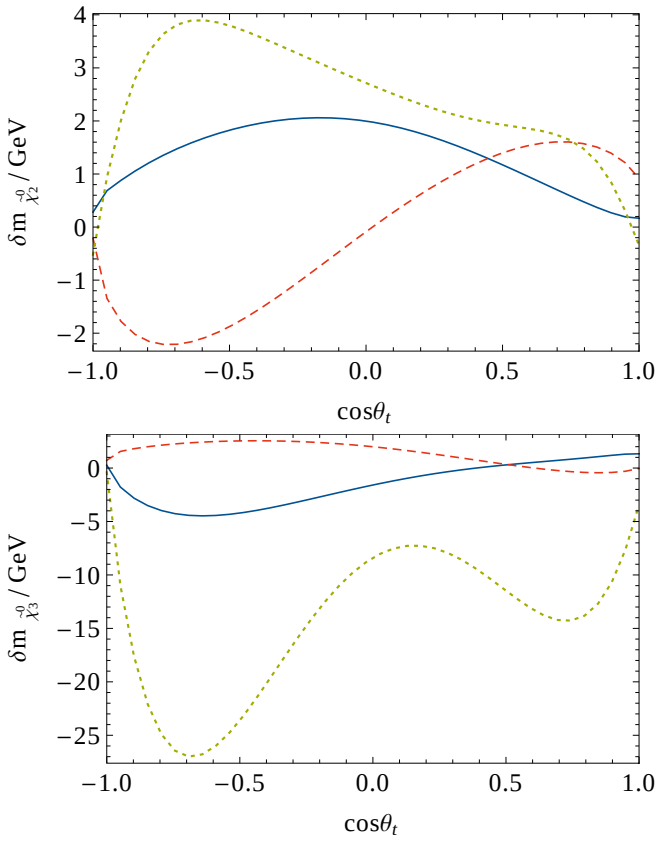

Figure 4: One-loop corrections to the masses of neutralinos $\tilde{\chi}_2^0$ (upper) and $\tilde{\chi}_3^0$ (lower) as a function of the stop mixing angle $\cos\theta_t$, for scenarios S1 (blue), S2 (red, dashed) and S3 (green, dotted).

uncertainties, are listed in tab. 4.3. It is interesting to observe the large NLO corrections to A_{FB}, which even result in a change of sign. Note that $\mathcal{B}(b \to s\gamma)$ is included in order to increase sensitivity to the third generation squark sector, and the estimated experimental precision of $0.3 \cdot 10^{-4}$, taken from ref. [65], is adopted. We found that the impact of the muon anomalous magnetic moment is negligible in this scenario, mainly due to the heavy smuon sector. It should be possible to probe the supersymmetric QCD sector, with sqark masses of ∼1.5 TeV and the gluino mass of ∼ 700 GeV, at the LHC, such that the theoretical uncertainty arising due to these parameters is small in comparison to that due to the unknown M_{A^0}. We therefore include the small dependence on the A^0 mass as an additional source of error, having explicitly checked that the impact of all other parameters is negligible. Note that there are no theoretical errors for masses chosen to be on-shell. Even

Observable	Tree value	Loop corr.	Error exp.	Error th.
$m_{\tilde{\chi}_1^\pm}$	149.6	–	0.1 (0.2)	–
$m_{\tilde{\chi}_2^\pm}$	292.3	–	0.5 (2.0)	–
$m_{\tilde{\chi}_1^0}$	106.9	–	0.2	–
$m_{\tilde{\chi}_2^0}$	164.0	2.0	0.5 (1.0)	0.5
$m_{\tilde{\chi}_3^0}$	188.6	−1.5	0.5 (1.0)	0.5
$\sigma(\tilde{\chi}_1^+\tilde{\chi}_1^-)^{350}_{(-0.8,0.6)}$	2347.5	−291.3	8.7	2.0
$\sigma(\tilde{\chi}_1^+\tilde{\chi}_1^-)^{350}_{(0.8,-0.6)}$	224.4	7.6	2.7	0.5
$\sigma(\tilde{\chi}_1^+\tilde{\chi}_1^-)^{500}_{(-0.8,0.6)}$	1450.6	−24.4	8.7	2.0
$\sigma(\tilde{\chi}_1^+\tilde{\chi}_1^-)^{500}_{(0.8,-0.6)}$	154.8	12.7	2.0	0.5
$A_{FB}^{350}(\%)$	−2.2	6.8	0.8	0.1
$A_{FB}^{500}(\%)$	−2.6	5.3	1.0	0.1

Table 2: Observables (masses in GeV, cross sections in fb) used as input for the fit in S1, tree-level values and loop corrections are specified. Here the superscript on σ and A_{FB} denotes $\sqrt{s}$ in GeV, and the subscript on σ denotes the beam polarisation $(\mathcal{P}(e^-), \mathcal{P}(e^+))$. The central value of the theoretical prediction, $\mathcal{B}(b \to s\gamma) = 3.3 \cdot 10^{-4}$ GeV, calculated using state-of-the-art tools, is also included in the fit. Errors in brackets are for masses obtained from the continuum. See text for details of error estimation.

at one loop, these masses are related to the fundamental parameters via the tree level relations, and are included in the fit.

In S1 we fit 8 MSSM parameters: M_1, M_2, μ, $\tan\beta$, $m_{\tilde{\nu}}$, $\cos\theta_t$, $m_{\tilde{t}_1}$, and $m_{\tilde{t}_2}$. The results of the fit are given in tab. 3. We find that the gaugino and higgsino mass parameters are determined with an accuracy better than 1%, while $\tan\beta$ is determined with an accuracy of 5%. Excellent precision of 2-3% is obtained for the mass of the otherwise unobservable sneutrino. Including NLO effects even allows us to constrain the parameters of the stop sector. Although the precision shown in tab. 3 is rather limited, this could lead to an important hint concerning the masses of the stops, which, if not already seen, might allow for a well-targeted search at the LHC. This could be another example of LC-LHC interplay [66].

Parameter	Threshold fit		Continuum fit	
M_1	125±0.3	(±0.7)	125±0.6	(±1.2)
M_2	250±0.6	(±1.3)	250±1.6	(±3)
μ	180±0.4	(±0.8)	180±0.7	(±1.3)
$\tan\beta$	10±0.5	(±1)	10±1.3	(±2.6)
$m_{\tilde{\nu}}$	1500±24	$(^{+60}_{-40})$	1500±20	(±40)
$\cos\theta_t$	0±0.15	$(^{+0.4}_{-0.3})$	–	
$m_{\tilde{t}_1}$	400^{+180}_{-120}	$(^{\text{at limit}}_{\text{at limit}})$	–	
$m_{\tilde{t}_2}$	800^{+300}_{-170}	$(^{+1000}_{-290})$	800^{+350}_{-220}	$(^{\text{at limit}}_{\text{at limit}})$

Table 3: Fit results (masses in GeV) for S1, for masses obtained from threshold scans (threshold fit) and from the continuum (continuum fit). Numbers in brackets denote 2σ errors.

Finally, in tab. 3 we compare the fit results using masses of the charginos and neutralinos obtained from threshold scans and from the continuum. For the latter, the accuracy at which the parameters can be determined is seen to deteriorate, with errors on the fundamental parameters almost doubling, clearly indicating the need to measure chargino and neutralino masses via threshold scans.

4.4 Results for scenario 2

In this scenario, where the M_2 parameter is set to 2 TeV, only the light chargino and three lightest neutralinos will be accessible at the LC. As input for the fit we therefore use:

- the masses of the lighter chargino ($\tilde{\chi}_1^{\pm}$) and neutralinos ($\tilde{\chi}_1^0, \tilde{\chi}_2^0, \tilde{\chi}_3^0$)
- the light chargino production cross section $\sigma(\tilde{\chi}_1^+\tilde{\chi}_1^-)$ with polarised beams at $\sqrt{s} = 400$ and 500 GeV
- the forward-backward asymmetry A_{FB} at $\sqrt{s} = 400$ and 500 GeV
- the branching ratio $\mathcal{B}(b \to s\gamma)$.

Observable	Tree value	Loop corr.	Error exp.	Error th.
$m_{\tilde{\chi}_1^\pm}$	179.1	–	0.1	–
$m_{\tilde{\chi}_1^0}$	111.1	–	0.2	–
$m_{\tilde{\chi}_2^0}$	183.6	0.07	0.5	0.5
$m_{\tilde{\chi}_3^0}$	194.2	1.9	0.5	0.5
$\sigma(\tilde{\chi}_1^+\tilde{\chi}_1^-)^{400}_{(-0.8,0.6)}$	1214.9	−344.7	6.0	0.1
$\sigma(\tilde{\chi}_1^+\tilde{\chi}_1^-)^{400}_{(0.8,-0.6)}$	250.6	−32.4	2.7	0.1
$\sigma(\tilde{\chi}_1^+\tilde{\chi}_1^-)^{500}_{(-0.8,0.6)}$	1079.2	−194.8	6.0	0.1
$\sigma(\tilde{\chi}_1^+\tilde{\chi}_1^-)^{500}_{(0.8,-0.6)}$	229.6	−8.7	2.7	0.1
$A_{FB}^{400}(\%)$	0.0	3.0	1.0	0.1
$A_{FB}^{500}(\%)$	0.0	5.0	1.0	0.1

Table 4: Observables (masses in GeV, cross sections in fb) used as an input for the fit in S2, as in tab. 4. The central value of the theoretical prediction, $\mathcal{B}(b \to s\gamma) = 3.3 \cdot 10^{-4}$ GeV, calculated using state-of-the-art tools, is also included in the fit. See text for details of error estimation.

As we again find that the muon anomalous magnetic moment has a negligible impact, it is not used in the fit. The input variables, together with errors, namely the assumed experimental precision of the prospective LC measurements as well as the theoretical uncertainties, are listed in tab. 4. While A_{FB} is negligible at LO, the NLO corrections to it are again found to be large.

We again fit 8 MSSM parameters: M_1, M_2, μ, $\tan\beta$, $m_{\tilde{\nu}}$, $\cos\theta_t$, $m_{\tilde{t}_1}$, and $m_{\tilde{t}_2}$. The impact of other parameters, except the heavy Higgs boson mass, can be neglected. The results from the fit are given in tab. 5. The higgsino and bino mass parameters are well constrained in this scenario since bino-like neutralino and all higgsinos are directly accessible. Even though the winos are not directly accessible, the wino mass parameter M_2 can be constrained with 10% accuracy at 1σ level. An accuracy of 20% is achieved for $\tan\beta$, significantly worse than in S1. This can be understood by the fact that the mixing in S2 between chargino states is weak due to M_2 being heavy, and the constraint on $\tan\beta$ is dependent on this mixing. No limits can be derived on the sneutrino mass, due to the Yukawa suppressed coupling of the higgsino-like $\tilde{\chi}_1^\pm$ to the electron and sneutrino. We are however, as shown in tab. 5, still able to derive limits on the stop masses and mixing parameter.

Parameter	Fit result
M_1	$125^{+0.9}_{-0.6}$ $\left(^{+2.1}_{-1.2}\right)$
M_2	2000 ± 200 $\left(^{+600}_{-400}\right)$
μ	180 ± 0.2 $\left(^{+0.5}_{-0.3}\right)$
$\tan\beta$	10 ± 2 $\left(^{+5}_{-4}\right)$
$m_{\tilde{\nu}}$	unconstrained
$\cos\theta_t$	$0^{+0.13}_{-0.09}$ $\left(^{+0.4}_{-0.3}\right)$
$m_{\tilde{t}_1}$	400^{+250}_{-50} $\left(^{+500}_{-80}\right)$
$m_{\tilde{t}_2}$	800^{+300}_{-200} $\left(^{+900}_{-400}\right)$

Table 5: Fit results (in GeV with the exception of $\tan\beta$ and $\cos\theta_t$) for S2, as in tab. 3, where numbers in brackets denote 2σ errors.

4.5 Results for parameters in scenario 3

This final scenario features the richest phenomenology of the studied benchmark scenarios. As input for the fit we therefore use:

- the masses of the charginos ($\tilde{\chi}_1^\pm$, $\tilde{\chi}_2^\pm$) and neutralinos ($\tilde{\chi}_1^0, \tilde{\chi}_2^0, \tilde{\chi}_3^0$)
- the light chargino production cross section $\sigma(\tilde{\chi}_1^+\tilde{\chi}_1^-)$ with polarised beams at $\sqrt{s} = 400$ and 500 GeV
- the forward-backward asymmetry A_{FB} at $\sqrt{s} = 400$ and 500 GeV
- the Higgs boson mass, m_h
- the branching ratio $\mathcal{B}(b \to s\gamma)$
- the anomalous muon magnetic moment

Compared to the previous scenarios, these observables are supplemented by the Higgs boson mass, m_h, calculated using `FeynHiggs 2.9.1` [55–58]. The estimated experimental precision at the LC for m_h, taken from ref. [1], is adopted. We further assume the future theoretical uncertainty on the Higgs boson mass to be 1 GeV [58]. As before, the remaining two observables, the branching ratio $\mathcal{B}(b \to s\gamma)$ and the anomalous muon magnetic moment are calculated using `micrOmegas 2.4.1` [61, 62], and a projected experimental

Observable	Tree value	Loop corr.	Error exp.	Error th.
$m_{\tilde{\chi}_1^\pm}$	139.3	–	0.1	–
$m_{\tilde{\chi}_2^\pm}$	266.2	–	0.5	–
$m_{\tilde{\chi}_1^0}$	92.8	–	0.2	–
$m_{\tilde{\chi}_2^0}$	148.5	2.4	0.5	0.5
$m_{\tilde{\chi}_3^0}$	189.7	−7.3	0.5	0.5
$\sigma(\tilde{\chi}_1^+\tilde{\chi}_1^-)^{400}_{(-0.8,0.6)}$	709.7	−85.1	4.5	–
$\sigma(\tilde{\chi}_1^+\tilde{\chi}_1^-)^{400}_{(0.8,-0.6)}$	129.8	20.0	2.0	–
$\sigma(\tilde{\chi}_1^+\tilde{\chi}_1^-)^{500}_{(-0.8,0.6)}$	560.0	−70.1	4.5	–
$\sigma(\tilde{\chi}_1^+\tilde{\chi}_1^-)^{500}_{(0.8,-0.6)}$	97.1	16.4	2.0	–
$A_{FB}^{400}(\%)$	24.7	−2.8	1.4	0.1
$A_{FB}^{500}(\%)$	39.2	−5.8	1.5	0.1

Table 6: Observables (masses in GeV, cross sections in fb) used as an input for the fit in S3, as in tab. 4.3. The central values of the theoretical predictions $\mathcal{B}(b \to s\gamma) = 2.7 \cdot 10^{-4}$, $\Delta(g_\mu - 2)/2 = 2.4 \cdot 10^{-9}$ and $m_h = 125$ GeV, calculated using state-of-the-art tools, are also included in the fit. See text for details of error estimation.

error on the anomalous muon magnetic moment of $3.4 \cdot 10^{-10}$ is employed [67], which we assume would dominate over the theoretical uncertainty. The input variables, together with errors, namely the assumed experimental precision of the prospective LC measurements and the theoretical uncertainties, are summarised in tab. 6. Because the sneutrino is now directly accessible, we assume that its mass has been measured and it is therefore not included in the fit. On the other hand, due to the stronger dependence of the NLO cross-section and forward-backward asymmetry on M_{A^0}, this is now used as an additional fit prameter. We neglect the remaining theoretical uncertainty on the cross-sections, as it is found to be negligible in comparison to the experimental error.

This means that in scenario 3, we fit to M_1, M_2, μ, $\tan\beta$, $\cos\theta_t$, $m_{\tilde{t}_1}$, $m_{\tilde{t}_2}$ and M_{A^0}. The results of the fit are collected in tab. 7. The parameters of the electroweak gaugino-higgsino sector are determined with high precision.

Parameter	Fit result
M_1	106 ± 0.3 (±0.5)
M_2	212 ± 0.5 (±1.0)
μ	180 ± 0.4 (±0.9)
$\tan\beta$	12 ± 0.3 (±0.7)
$\cos\theta_t$	$0.15^{+0.08}_{-0.06}$ $(^{+0.16}_{-0.09})$
$m_{\tilde{t}_1}$	430^{+200}_{-130} $(^{+300}_{-400})$
$m_{\tilde{t}_2}$	1520^{+200}_{-300} $(^{+300}_{-400})$
m_{A^0}	< 650 (< 1000)

Table 7: Fit results (in GeV with the exception of $\tan\beta$ and $\cos\theta_t$) for S3, including results for the masses of the heavier stop mass ($m_{\tilde{t}_2}$) and the pseudoscalar higgs boson (m_{A^0}).

Due to a significant mixing in the stop sector, and the improvement in the fit quality due to the inclusion of the higgs mass, we find that the fit is now also sensitive to the mass of the heavy stop. The accuracy is better than 20% for this particle even though it is far beyond the reach of the LC and also most likely of the LHC. In addition, in this scenario an upper limit on the mass of the heavy Higgs boson can be placed at 1000 GeV, at the 2σ level. It is the particular sensitivity of the NLO corrections to M_{A^0} which presents this unique opportunity to set such an upper bound.

5 Conclusions

The evidence for the Higgs boson and dark matter, when examined in the context of supersymmetry, suggests the possibility of a light μ and M_1. We have extended previous analyses, which fitted observables for chargino production at the LC to extract fundamental MSSM parameters, by incorporating NLO corrections. The loop corrections are calculated for all observables fitted, namely the polarised cross-sections and forward backward asymmetry for chargino production as well as the $\tilde{\chi}_1^\pm, \tilde{\chi}_2^\pm$ and $\tilde{\chi}_1^0, \tilde{\chi}_2^0, \tilde{\chi}_3^0$ masses, in an on-shell scheme which facilitates the extension to the complex case. We have fitted these observables for three complementary scenarios. We found that

on including NLO corrections, when M_1, M_2 and μ are light they can be determined to percent-level accuracy, and $\tan\beta$ to $< 5\%$. Further we showed that obtaining masses of the charginos and neutralinos from the continuum as opposed to threshold scans would result in the uncertainty on the fundamental parameters almost doubling, reinforcing the importance of threshold scans for mass measurements. As a heavy M_2 is still a viable possibility, we also considered $M_2 = 2000$ GeV, and found that the sensitivity to M_2 is approximately 10%. As the error on $\tan\beta$ is dependent on the degree of mixing in the chargino sector, here it increases to $\sim 20\%$. Note that the inclusion of $\mathcal{B}(b \to s\gamma)$, as well as the use of masses determined via threshold scanning, in the fit was seen to improve the sensitivity to the stop sector. We finally considered a scenario compatible with the latest Higgs results. For this scenario we found that including $\mathcal{B}(b \to s\gamma)$, $\Delta(g_\mu - 2)/2$ and m_h in the fit, along with the significant mixing in the stop sector, helped to obtain an accuracy better than 20% on the mass of the heavy stop, even though this particle is far beyond the reach of the LC and also most likely of the LHC. We also included m_{A^0} in the fit, and found that, due to the particular sensitivity of the NLO corrections to M_{A^0}, it would even be possible to place a 2σ upper bound on this parameter of 1000 GeV. In summary, we have shown that incorporating NLO corrections is required for the precise determination of the fundamental parameters of the chargino and neutralino sector at the LC, and could further provide sensitivity to the parameters describing particles which contribute via loop corrections.

Acknowledgements

The authors gratefully acknowledge support of the DFG through the grant SFB 676, "Particles, Strings, and the Early Universe", as well as the Helmholtz Alliance, "Physics at the Terascale". This work was also partially supported by the Polish National Science Centre under research grant DEC-2011/01/M/ST2/02466 and the MICINN, Spain, under contract FPA2010-17747; Consolider-Ingenio CPAN CSD2007- 00042. KR thanks as well the Comunidad de Madrid through Proyecto HEPHACOS S2009/ESP-1473 and the European Commission under contract PITN-GA-2009-237920.

References

[1] **ECFA/DESY LC Physics Working Group** Collaboration, J. Aguilar-Saavedra et al. `hep-ph/0106315`.

[2] **ACFA Linear Collider Working Group** Collaboration, K. Abe et al. hep-ph/0109166.

[3] **American Linear Collider Working Group** Collaboration, T. Abe et al. hep-ex/0106056.

[4] **ILC** Collaboration, E. Brau, James et al. arXiv:0712.1950.

[5] **ILC** Collaboration, G. Aarons et al. arXiv:0709.1893.

[6] H. Goldberg *Phys.Rev.Lett.* **50** (1983) 1419.

[7] J. R. Ellis, J. Hagelin, D. V. Nanopoulos, K. A. Olive, and M. Srednicki *Nucl.Phys.* **B238** (1984) 453–476.

[8] L. J. Hall, D. Pinner, and J. T. Ruderman *JHEP* **1204** (2012) 131, [arXiv:1112.2703].

[9] F. Brummer and W. Buchmuller *JHEP* **1107** (2011) 010, [arXiv:1105.0802].

[10] **CMS Collaboration** Collaboration, S. Chatrchyan et al. *JHEP* **1211** (2012) 147, [arXiv:1209.6620].

[11] **ATLAS Collaboration** Collaboration, G. Aad et al. *Phys.Lett.* **B718** (2013) 841–859, [arXiv:1208.3144].

[12] P. Bechtle, T. Bringmann, K. Desch, H. Dreiner, M. Hamer, et al. *JHEP* **1206** (2012) 098, [arXiv:1204.4199].

[13] **ILC** Collaboration, H. Baer et al., "International Linear Collider Technical Design Report - Volume 1: Physics at the International Linear Collider." 2012.

[14] W. Oller, H. Eberl, and W. Majerotto *Phys.Rev.* **D71** (2005) 115002, [hep-ph/0504109].

[15] T. Fritzsche and W. Hollik *Nucl.Phys.Proc.Suppl.* **135** (2004) 102–106, [hep-ph/0407095].

[16] W. Kilian, J. Reuter, and T. Robens *Eur.Phys.J.* **C48** (2006) 389–400, [hep-ph/0607127].

[17] T. Robens, J. Kalinowski, K. Rolbiecki, W. Kilian, and J. Reuter *Acta Phys.Polon.* **B39** (2008) 1705–1714, [arXiv:0803.4161].

[18] A. Bharucha, A. Fowler, G. Moortgat-Pick, and G. Weiglein arXiv:1211.3134.

[19] T. Fritzsche. PhD thesis, Universitaet Karlsruhe, 2005.

[20] A. Fowler and G. Weiglein *JHEP* **1001** (2010) 108, [arXiv:0909.5165].

[21] A. Fowler. PhD thesis, Durham University, 2010.

[22] A. Chatterjee, M. Drees, S. Kulkarni, and Q. Xu arXiv:1107.5218.

[23] S. Heinemeyer, F. von der Pahlen, and C. Schappacher *Eur.Phys.J.* **C72** (2012) 1892, [arXiv:1112.0760].

[24] A. Bharucha, S. Heinemeyer, F. von der Pahlen, and C. Schappacher arXiv:1208.4106.

[25] H. E. Haber and G. L. Kane *Phys.Rept.* **117** (1985) 75–263.

[26] S. Choi, A. Djouadi, M. Guchait, J. Kalinowski, H. Song, et al. *Eur.Phys.J.* **C14** (2000) 535–546, [hep-ph/0002033].

[27] J. Kublbeck, M. Bohm, and A. Denner *Comput.Phys.Commun.* **60** (1990) 165–180.

[28] A. Denner, H. Eck, O. Hahn, and J. Kublbeck *Nucl.Phys.* **B387** (1992) 467–484.

[29] J. Kublbeck, H. Eck, and R. Mertig *Nucl.Phys.Proc.Suppl.* **29A** (1992) 204–208.

[30] T. Hahn *Comput.Phys.Commun.* **140** (2001) 418–431, [hep-ph/0012260].

[31] T. Hahn and C. Schappacher *Comput.Phys.Commun.* **143** (2002) 54–68, [hep-ph/0105349].

[32] T. Hahn and M. Perez-Victoria *Comput.Phys.Commun.* **118** (1999) 153–165, [hep-ph/9807565].

[33] T. Hahn *Comput.Phys.Commun.* **178** (2008) 217–221, [hep-ph/0611273].

[34] T. Hahn and M. Rauch *Nucl.Phys.Proc.Suppl.* **157** (2006) 236–240, [hep-ph/0601248].

[35] W. Siegel *Phys.Lett.* **B84** (1979) 193.

[36] W. Siegel *Phys.Lett.* **B94** (1980) 37.

[37] D. Stockinger *JHEP* **0503** (2005) 076, [hep-ph/0503129].

[38] F. del Aguila, A. Culatti, R. Munoz Tapia, and M. Perez-Victoria *Nucl.Phys.* **B537** (1999) 561–585, [hep-ph/9806451].

[39] A. Lahanas, K. Tamvakis, and N. Tracas *Phys.Lett.* **B324** (1994) 387–396, [hep-ph/9312251].

[40] D. Pierce and A. Papadopoulos *Phys.Rev.* **D50** (1994) 565–570, [hep-ph/9312248].

[41] D. Pierce and A. Papadopoulos *Nucl.Phys.* **B430** (1994) 278–294, [hep-ph/9403240].

[42] H. Eberl, M. Kincel, W. Majerotto, and Y. Yamada *Phys.Rev.* **D64** (2001) 115013, [hep-ph/0104109].

[43] T. Fritzsche and W. Hollik *Eur.Phys.J.* **C24** (2002) 619–629, [hep-ph/0203159].

[44] W. Oller, H. Eberl, W. Majerotto, and C. Weber *Eur.Phys.J.* **C29** (2003) 563–572, [hep-ph/0304006].

[45] M. Drees, W. Hollik, and Q. Xu *JHEP* **0702** (2007) 032, [hep-ph/0610267].

[46] R. Schofbeck and H. Eberl *Phys.Lett.* **B649** (2007) 67–72, [hep-ph/0612276].

R. Schofbeck and H. Eberl *Eur.Phys.J.* **C53** (2008) 621–626, [arXiv:0706.0781].

[47] K. Rolbiecki and J. Kalinowski *Phys.Rev.* **D76** (2007) 115006, [arXiv:0709.2994].

[48] H. Eberl, T. Gajdosik, W. Majerotto, and B. Schrausser *Phys.Lett.* **B618** (2005) 171–181, [hep-ph/0502112].

[49] P. Osland and A. Vereshagin *Phys.Rev.* **D76** (2007) 036001, [arXiv:0704.2165].

[50] K. Desch, J. Kalinowski, G. Moortgat-Pick, K. Rolbiecki, and W. Stirling *JHEP* **0612** (2006) 007, [hep-ph/0607104].

[51] F. James and M. Roos *Comput.Phys.Commun.* **10** (1975) 343–367.

[52] F. James *CERN Program Library Long Writeup D506* (1994).

[53] **ATLAS Collaboration** Collaboration, G. Aad et al. arXiv:1208.0949.

[54] **CMS Collaboration** Collaboration, S. Chatrchyan et al. arXiv:1207.1798.

[55] S. Heinemeyer, W. Hollik, and G. Weiglein *Comput.Phys.Commun.* **124** (2000) 76–89, [hep-ph/9812320].

[56] S. Heinemeyer, W. Hollik, and G. Weiglein *Eur.Phys.J.* **C9** (1999) 343–366, [hep-ph/9812472].

[57] G. Degrassi, S. Heinemeyer, W. Hollik, P. Slavich, and G. Weiglein *Eur.Phys.J.* **C28** (2003) 133–143, [hep-ph/0212020].

[58] M. Frank, T. Hahn, S. Heinemeyer, W. Hollik, H. Rzehak, et al. *JHEP* **0702** (2007) 047, [hep-ph/0611326].

[59] **ATLAS Collaboration** Collaboration, G. Aad et al. *Phys.Lett.* **B716** (2012) 1–29, [arXiv:1207.7214].

[60] **CMS Collaboration** Collaboration, S. Chatrchyan et al. *Phys.Lett.* **B716** (2012) 30–61, [arXiv:1207.7235].

[61] G. Belanger, F. Boudjema, A. Pukhov, and A. Semenov *Comput.Phys.Commun.* **176** (2007) 367–382, [hep-ph/0607059].

[62] G. Belanger, F. Boudjema, P. Brun, A. Pukhov, S. Rosier-Lees, et al. *Comput.Phys.Commun.* **182** (2011) 842–856, [arXiv:1004.1092].

[63] **WMAP Collaboration** Collaboration, E. Komatsu et al. *Astrophys.J.Suppl.* **192** (2011) 18, [arXiv:1001.4538].

[64] **LHCb Collaboration** Collaboration, R. Aaij et al. *Phys.Rev.Lett.* **110** (2013) 021801, [arXiv:1211.2674].

[65] **SuperB Collaboration** Collaboration, B. O'Leary et al. arXiv:1008.1541.

[66] **LHC/LC Study Group** Collaboration, G. Weiglein et al. *Phys.Rept.* **426** (2006) 47–358, [hep-ph/0410364].

[67] R. Carey, K. Lynch, J. Miller, B. Roberts, W. Morse, et al.

Measurement of CP Violation in the MSSM Neutralino Sector with the ILD

M. Terwort[1], O. Kittel[2], G. Moortgat-Pick[1,3], K. Rolbiecki[1] and P. Schade[1,4]

1- DESY, Notkestraße 85, D-22607 Hamburg, Germany

2- Departamento de Física Teórica y del Cosmos and CAFPE, Universidad de Granada, E-18071 Granada, Spain

3- University of Hamburg, Luruper Chaussee 149, D-22761 Hamburg, Germany

4- CERN, CH-1211 Geneve 23, Switzerland

Supersymmetric models provide many new complex phases which lead to CP violating effects in collider experiments. As an example, CP-sensitive triple product asymmetries in neutralino production $e^+ e^- \to \tilde{\chi}_i^0 \tilde{\chi}_1^0$ and subsequent leptonic two-body decays $\tilde{\chi}_i^0 \to \tilde{\ell}_R \ell$, $\tilde{\ell}_R \to \tilde{\chi}_1^0 \ell$, for $\ell = e, \mu$, are studied within the Minimal Supersymmetric Standard Model. A full ILD detector simulation has been performed at a center of mass energy of $\sqrt{s} = 500$ GeV, including the relevant Standard Model background processes, a realistic beam energy spectrum, beam backgrounds and a beam polarization of 80% and −60% for the electron and positron beams, respectively. Assuming an integrated luminosity of 500 fb^{-1} collected by the experiment and the performance of the current ILD detector, a relative measurement accuracy of 10% for the CP-sensitive asymmetry can be achieved in the chosen scenario.

1 Introduction

Supersymmetry (SUSY) [1] is among the most favoured and most studied extensions of the Standard Model (SM) and is capable of solving many of its problems. One of its features is that the Minimal Supersymmetric Standard Model (MSSM) provides a number of complex parameters which can serve as sources of CP violation. They are conventionally chosen to be the Higgsino mass parameter, $\mu = |\mu| e^{i\phi_\mu}$, the U(1) and SU(3) gaugino mass parameters, $M_1 = |M_1| e^{i\phi_1}$ and $M_3 = |M_3| e^{i\phi_3}$, respectively, and the trilinear scalar coupling parameters, $A_f = |A_f| e^{i\phi_{A_f}}$, of the third generation sfermions ($f = b, t, \tau$). CP phases can give rise to CP-violating signals in collider experiments [2], which have to be measured to determine or constrain the phases independently of measurements of electric dipole moments (EDM). Although also CP-even observables, such as masses or branching ratios, are sensitive to the CP phases, CP-odd observables are needed for direct evidence of CP violation.

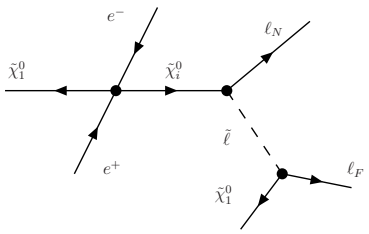

Figure 1: Schematic picture of neutralino production and decay.

In this report neutralino pair production $e^+ e^- \to \tilde{\chi}_i^0 \tilde{\chi}_1^0$, for $i = 2, 3$, and the subsequent leptonic two-body decay of one of the neutralinos $\tilde{\chi}_i^0 \to \tilde{\ell}_R \ell$ followed by $\tilde{\ell}_R \to \tilde{\chi}_1^0 \ell$, for $\ell = e, \mu$, at the ILC is studied [3]. Figure 1 shows a schematic picture of the process. The CP-sensitive spin correlations of the neutralino in its production process allow to probe the phase of the Higgsino mass parameter μ and the gaugino parameter M_1 [4].

A full ILD [5] detector simulation is performed in order to investigate in detail the prospects to measure CP-sensitive observables at the ILC. All relevant SM background is taken into account, simulated with a realistic beam energy spectrum and beam backgrounds [6].

2 CP-odd observables and benchmark scenario

In neutralino production, effects from CP-violating phases can only occur if two different neutralinos are produced. CP asymmetries can then be defined with triple products of particle momenta. Due to the spin correlation the asymmetries show hints for CP phases already at tree level. For the process shown in Fig. 1, a T-odd triple product of the beam and the final lepton momenta can be defined as [3]

$$\mathcal{T} \;=\; (\mathbf{p}_{e^-} \times \mathbf{p}_{\ell^+}) \cdot \mathbf{p}_{\ell^-}. \tag{1}$$

The corresponding asymmetry is

$$\mathcal{A}(\mathcal{T}) \;=\; \frac{\sigma(\mathcal{T} > 0) - \sigma(\mathcal{T} < 0)}{\sigma(\mathcal{T} > 0) + \sigma(\mathcal{T} < 0)}, \tag{2}$$

where σ is the cross section for neutralino production and decay. Its sign depends on the charge of the leptons, which has to be tagged in the experimental analysis.

For the full simulation study a benchmark scenario has been chosen such that the gaugino phase $\phi_1 = 0.2\pi$ corresponds to a maximal CP asymmetry and the Higgsino phase is zero, since it is strongly constrained by EDM bounds. The other parameters in the neutralino sector are $M_2 = 300\,\text{GeV}$, $|M_1| = 150\,\text{GeV}$, $|\mu| = 165\,\text{GeV}$ and $\tan\beta = 10$. This leads to the neutralino masses $m_{\tilde{\chi}^0_1} = 117$ GeV, $m_{\tilde{\chi}^0_2} = 169$ GeV, $m_{\tilde{\chi}^0_3} = 181$ GeV and $m_{\tilde{\chi}^0_4} = 330$ GeV, while the slepton masses are $m_{\tilde{\ell}_R} = 166$ GeV and $m_{\tilde{\ell}_L} = 280$ GeV. The neutralino pair production cross sections are calculated to be $\sigma(e^+e^- \to \tilde{\chi}^0_1\tilde{\chi}^0_2) = 244$ fb and $\sigma(e^+e^- \to \tilde{\chi}^0_1\tilde{\chi}^0_3) = 243$ fb, while the slepton pair production cross sections are $\sigma(e^+e^- \to \tilde{e}^+_R\tilde{e}^-_R) = 304$ fb and $\sigma(e^+e^- \to \tilde{\mu}^+_R\tilde{\mu}^-_R) = 97$ fb. The slepton pair production is the main background, since there are two lightest neutralinos and two opposite-sign electrons or muons in the final state as in the case of the neutralino $\tilde{\chi}^0_1\tilde{\chi}^0_i$ production. Furthermore, beam polarizations of $(P_{e^-}, P_{e^+}) = (0.8, -0.6)$ have been chosen, which enhance slightly the SUSY cross section and the asymmetries, while the background from WW- and chargino-pair production is suppressed. In this scenario the CP asymmetries are $\mathcal{A}(\mathcal{T})_{\tilde{\chi}^0_1\tilde{\chi}^0_2} = -9.2\%$ and $\mathcal{A}(\mathcal{T})_{\tilde{\chi}^0_1\tilde{\chi}^0_3} = 7.7\%$.

3 Detector simulation study and parameter fit

The ILD is a concept under study for a multipurpose particle detector for the ILC. It is designed for an excellent precision in momentum and energy measurement over a large solid angle. A detailed description can be found in [5]. In the simulation all active elements and also cables, cooling systems, support structures and dead regions are taken into account [6]. The radiation hard beam calorimeter is used to suppress background from $\gamma\gamma$ events at low angles. All relevant SM backgrounds and SUSY processes are generated using `Whizard` [7].

initial selection	no significant activity in BCAL
	number of all tracks $N_{\text{tracks}} \leq 7$
lepton selection	$\ell^+\ell^-$ pair with $\ell = e, \mu$
	$\lvert\cos\theta\rvert < 0.99$, min. energy $E > 3$ GeV
	lower energetic ℓ with $E < 18$ GeV, or
	higher energetic ℓ with $E > 38$ GeV
	higher energetic ℓ with $E \in [15, 150]$ GeV
	$\theta_{\text{acop}} > 0.2\pi$, $\theta_{\text{acol}} > 0.2\pi$
final preselection	$\mathbf{p}_{\text{T}}^{\text{miss}} > 20$ GeV
	$E_{\text{vis}} < 150$ GeV
	$m_{\ell\ell} < 55$ GeV

Table 1: Preselection cuts, see Ref. [3] for details.

3.1 Event selection and measured asymmetry

A clean sample of signal events is needed in order to clearly measure the CP-violating effects in neutralino production. Otherwise the asymmetry will be reduced by the CP-even background events. Therefore, preselection cuts as listed in Tab. 1 are applied to reject as much background as possible, while preserving good signal efficiency. Electrons and muons are identified using the *Particle Flow* approach [3]. The cuts exploit the energy and angular distributions of the final state leptons, as well as the high missing transverse momentum $\mathbf{p}_{\text{T}}^{\text{miss}}$ due to the escaping neutralinos. Additional cuts on the total visible energy E_{vis} as well as on the invariant mass $m_{\ell\ell}$ distributions further reduce the background contamination.

Figure 2(a) shows the $\mathbf{p}_{\text{T}}^{\text{miss}}$ distribution of the SM and SUSY background as well as of the signal after the lepton selection. It can be seen that most of the background is removed with the cut $\mathbf{p}_{\text{T}}^{\text{miss}} > 20$ GeV. Figure 2(b) shows the distribution of the invariant di-lepton mass after all cuts except the one on $m_{\ell\ell}$. The signal lepton pair from $\tilde{\chi}_3^0$ ($\tilde{\chi}_2^0$) decays has a sharp endpoint at 51 GeV (22 GeV), which can also be exploited for mass measurements. The invariant mass cut also removes SM backgrounds from ZZ and WW production. The remaining event sample consists of 28039 $\tilde{\chi}_1^0\tilde{\chi}_2^0 \to \tilde{\chi}_1^0\tilde{\chi}_1^0\ell\ell$ ($\ell \neq \tau$) events, 45966 $\tilde{\chi}_1^0\tilde{\chi}_3^0 \to \tilde{\chi}_1^0\tilde{\chi}_1^0\ell\ell$ ($\ell \neq \tau$) events and 34223 $\tilde{\ell}\tilde{\ell} \to \tilde{\chi}_1^0\tilde{\chi}_1^0\ell\ell$ ($\ell \neq \tau$) events. All other SM and SUSY background processes sum up to about 6000 events.

In order to distinguish the $\tilde{\chi}_1^0\tilde{\chi}_2^0$ events from the $\tilde{\chi}_1^0\tilde{\chi}_3^0$ events, and to further clean the event sample, a kinematic selection procedure is applied, as described in [3]. A number of kinematic constraints derived from the final state momenta are used to classify events as signal or background. An event is selected only if it is classified exclusively as signal-like. Four event classes are considered: $\tilde{\chi}_1^0\tilde{\chi}_2^0$, $\tilde{\chi}_1^0\tilde{\chi}_3^0$, $\tilde{\ell}_R^+\tilde{\ell}_R^-$ and W^+W^-. Table 2 shows the number of events that are classified exclusively as one of the four event classes. It can be observed that the large contamination of the event sample by $\tilde{\ell}_R^+\tilde{\ell}_R^-$ events can be drastically reduced.

The CP asymmetry can now be calculated from Eq. (2) to be $\mathcal{A}(\mathcal{T})_{\tilde{\chi}_1^0\tilde{\chi}_2^0} = -11.3\% \pm 0.7\%$ and $\mathcal{A}(\mathcal{T})_{\tilde{\chi}_1^0\tilde{\chi}_3^0} = +10.9\% \pm 0.7\%$. The absolute values are slightly higher than the ones

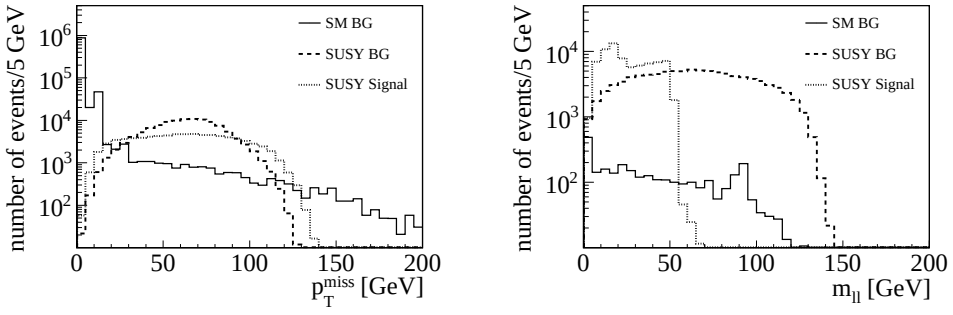

(a) (b)

Figure 2: (a) Missing transverse momentum $\mathbf{p}_{\mathrm{T}}^{\mathrm{miss}}$ distribution of SM background, SUSY background and SUSY signal after the lepton selection. (b) Invariant mass $m_{\ell\ell}$ distribution of the lepton pair after all preselection cuts except the cut on $m_{\ell\ell}$. The events are simulated for $\mathcal{L} = 500$ fb^{-1}, beam polarization $(P_{e^-}, P_{e^+}) = (0.8, -0.6)$ at $\sqrt{s} = 500$ GeV, and MSSM parameters as in the benchmark scenario discussed in Sec. 2.

class	only $\tilde{\chi}_1^0\tilde{\chi}_2^0$	only $\tilde{\chi}_1^0\tilde{\chi}_3^0$	only $\tilde{\ell}_R^+\tilde{\ell}_R^-$	only W^+W^-
$\tilde{\chi}_1^0\tilde{\chi}_2^0 \to \tilde{\chi}_1^0\tilde{\chi}_1^0\ell\ell$ $(\ell \neq \tau)$	18343	615	51	855
$\tilde{\chi}_1^0\tilde{\chi}_3^0 \to \tilde{\chi}_1^0\tilde{\chi}_1^0\ell\ell$ $(\ell \neq \tau)$	290	20132	372	635
all SUSY background	1153	3055	5626	951
all SM background	87	256	44	81

Table 2: Number of preselected events, that fulfill the requirements of the kinematic selection procedure, for $\mathcal{L} = 500$ fb^{-1}.

calculated in the benchmark scenario, since the asymmetry depends non-trivially on the cut values. This has been studied in [3] and can be taken into account in a parameter fit.

3.2 Fit of the parameters in the neutralino sector

In the final step of the analysis, the accuracy to determine the parameters in the neutralino sector of the MSSM is estimated. These are the six free parameters of the neutralino mass matrix $|M_1|$, M_2, $|\mu|$, $\tan\beta$, ϕ_1 and ϕ_μ. As input for the fit a number of CP-even observables is used together with the measured asymmetries (see Ref. [3] for details): $m_{\tilde{\chi}_1^0} = 117.3 \pm 0.2$ GeV, $m_{\tilde{\chi}_2^0} = 168.5 \pm 0.5$ GeV, $m_{\tilde{\chi}_3^0} = 180.8 \pm 0.5$ GeV, $\sigma(\tilde{\chi}_1^0\tilde{\chi}_2^0) \times \mathrm{BR}(\tilde{\chi}_2^0 \to \tilde{\ell}_R\ell) = 130.9 \pm 1.4$ fb, $\sigma(\tilde{\chi}_1^0\tilde{\chi}_3^0) \times \mathrm{BR}(\tilde{\chi}_3^0 \to \tilde{\ell}_R\ell) = 155.7 \pm 1.6$ fb, $\sigma(\tilde{\chi}_2^0\tilde{\chi}_2^0) \times \mathrm{BR}(\tilde{\chi}_2^0 \to \tilde{\ell}_R\ell)^2 = 4.8 \pm 0.3$ fb, $\sigma(\tilde{\chi}_3^0\tilde{\chi}_3^0) \times \mathrm{BR}(\tilde{\chi}_3^0 \to \tilde{\ell}_R\ell)^2 = 26.3 \pm 0.7$ fb and $\sigma(\tilde{\chi}_2^0\tilde{\chi}_3^0) \times \mathrm{BR}(\tilde{\chi}_2^0 \to \tilde{\ell}_R\ell) \times \mathrm{BR}(\tilde{\chi}_3^0 \to \tilde{\ell}_R\ell) = 28.9 \pm 0.7$ fb. The fitted values of the parameters of the neutralino mass matrix are listed in Tab. 3. It is remarkable that the moduli of the phases ϕ_1, ϕ_μ can also be determined with high precision, using the CP-even observables alone. However, only an inclusion of CP-odd asymmetries in the fit allows to resolve the sign ambiguities of the

$\lvert M_1\rvert$	M_2	$\lvert\mu\rvert$	$\tan\beta$	ϕ_1	ϕ_μ
150.0 ± 0.7 GeV	300 ± 5 GeV	165.0 ± 0.3 GeV	10.0 ± 1.6	0.63 ± 0.05	0.0 ± 0.2

Table 3: Results of the parameter fit.

phases. Without the CP-odd asymmetries in the fit there is a twofold ambiguity, $\phi_1 = \pm 0.6$, and even fourfold if $\phi_\mu \neq 0$. Thus, the triple product asymmetries are not only a direct test of CP violation, but are also essential to determine the correct values of the phases.

4 Summary and conclusions

The first full detector simulation study to measure SUSY CP phases at the ILC has been presented. Triple products of the final state lepton momenta in neutralino decays have been used as CP-odd observables. Realistic collider conditions have been simulated and all relevant SM backgrounds have been taken into account. A detailed cut flow analysis has been performed, including the development of a kinematic selection procedure that was used to obtain a very clean signal sample and to distinguish events from different neutralino decays. In the chosen benchmark scenario the asymmetry could be measured with a relative precision of 10% with $500\,\mathrm{fb}^{-1}$ of data. Finally, the parameters of the neutralino mixing matrix have been fitted to CP-even and CP-odd observables and the complex phases could be determined with a precision of about 10%.

Acknowledgments

We would like to thank Steve Aplin, Mikael Berggren, Jan Engels, Frank Gaede, Nina Herder, Jenny List, and Mark Thomson for very useful discussions and help with the detector simulations.

References

[1] H. E. Haber and G. L. Kane, Phys. Rept. 117 (1985) 75-263; H. P. Nilles, Phys. Rept. 110 (1984) 1-162.

[2] S. Kraml, *CP violation in SUSY*, arXiv:0710.5117.

[3] O. Kittel et al., *Measurement of CP asymmetries in neutralino production at the ILC*, arXiv:1108.3220.

[4] A. Bartl et al., *CP asymmetries in neutralino production in e^+e^- collisions*, Phys. Rev. D69 (2004) 035007, arXiv:hep-ph/0308141.

[5] ILD Concept Group, *The International Large Detector: Letter of Intent*, arXiv:1006.3396.

[6] P. Bechtle et al., *Prospects for the study of the $\tilde{\tau}$-system in SPS1a' at the ILC*, Phys. Rev. D82 (2010) 055016, arXiv:0908.0876.

[7] W. Kilian et al., *WHIZARD: Simulating Multi-Particle Processes at LHC and ILC*, Eur. Phys. J. C71 (2011) 1742, arXiv:0708.4233.

CP Violating Effects in Stop Decay

Kian Salimkhani[1], *Jamie Tattersall*[1], *Gudrid Moortgat-Pick*[2,3]

[1]Bethe Center for Theoretical Physics & Physikalisches Institut, Universität Bonn, D-53115 Bonn, Germany
[2]DESY, D-22607 Hamburg, Germany
[3]Universität Hamburg, D-22761 Hamburg, Germany

LC-REP-2012-067

We study the discovery potential of new CP violating phases in a $\tilde{t}_1$ cascade decay via $\tilde{\chi}_2^0$ at a future linear electron-positron collider of 1 TeV center-of-mass energy. As observables we discuss triple product asymmetries. We find that assuming successful momentum reconstruction a maximal asymmetry can be observed with at least 1000 fb^{-1} collected data.

1 Introduction

Although the Standard Model very successfully describes the elementary particles and their interactions apart from gravity, the model not only fails to give a description of all matter in the universe, but furthermore cannot illuminate thoroughly why matter exists at all. To answer this question we know that a proper understanding of CP-violation is crucial [1]. Unfortunately, the single CP violating phase in the CKM matrix of the Standard Model that has been determined by B-meson experiments [2] is not sufficient [1]. Thus, we need additional sources of CP-violation to describe the observed baryon asymmetry in the universe.

Such new CP violating phases are introduced in the MSSM. Given that they can change masses [3], total cross sections [4] and branching ratios [5], there are in principle various ways to detect them at colliders. However, these all are CP-even observables. This means that one cannot be sure about their definite CP violating nature, because particle and antiparticle both exhibit the same dependence. This is especially problematic in a model that has as many free parameters as the MSSM. A potential way to fake a CP violating effect on the stop mass, for example, is to arrange the soft breaking scalar quark masses with non-universal values. Additionally, potentially large loop corrections can complicate CP-violation studies by also changing these observables. Therefore one would like to work with CP-odd observables, which cannot be mimicked by other parameters of the theory and thus are a definite signature of CP-violation. However, the problem with many of these observables, like rate asymmetries of branching ratios [6], rate asymmetries of cross sections [7] or angular distributions [8], is that they are actually loop effects. Thus, obvious problems arise concerning the measurability, since one does not expect large signals from loop effects. Fortunately the CPT-theorem connects CP- and T-violation. Combined with additional assumptions one can then construct so-called $\mathrm{T_N}$-odd observables that are useful to examine tree-level CP-violation at colliders [9, 10]. If re-scattering effects are absent, a non-vanishing expectation value of a $\mathrm{T_N}$-odd observable indicates CP-violation. Therefore we must also probe the charge conjugated process to exclude the possibility of re-scattering. For further information we recommend [11] which review CP-violation in the context of supersymmetry.

2 Studying CP-Violation in Stop Decay

2.1 Formalism and Chosen Scenario

We study the discovery potential of new CP violating phases in the following two-body cascade decay of the stop at a future linear electron-positron collider of 1 TeV center-of-mass energy,

$$\tilde{t}_1 \to \tilde{\chi}_2^0 + t\,, \qquad t \to W^+ + b\,, \qquad \tilde{\chi}_2^0 \to \tilde{l}_{\mathrm{R}}^{\pm} + l_1^{\mp}\,, \qquad \tilde{l}_{\mathrm{R}}^{\pm} \to \tilde{\chi}_1^0 + l_2^{\pm}\,.$$

The stop and neutralino sector contain three phases, namely a phase of the trilinear top quark coupling, ϕ_{A_t}, a phase of the higgsino mass parameter, ϕ_μ, and conventionally a phase of the first gaugino mass, ϕ_{M_1}. However, the latter two (especially ϕ_μ) are heavily constrained by experiment [12]. Therefore we do not consider them and focus on ϕ_{A_t} in this study.

Since we want to test the capability of a future linear collider, we use a "light" scenario without strict unification of gaugino and scalar masses. The relevant masses and branching ratios are presented in Tab. 1.

As CP-odd observables we use asymmetries of triple products of final state or reconstructed momenta,

$$\mathcal{A}_T = \frac{N_{\mathcal{T}+} - N_{\mathcal{T}-}}{N_{\mathcal{T}+} + N_{\mathcal{T}-}} = \frac{\int \text{sign}\,\{\mathcal{T}\}\,|T|^2 \text{dlips}}{\int |T|^2 \text{dlips}} \ ,$$

$m_{\tilde{t}}$	$m_{\tilde{\chi}_1^0}$	$m_{\tilde{\chi}_2^0}$	$m_{\tilde{l}_R^\pm}$	$\text{BR}_{\tilde{t}_1}$	$\text{BR}\tilde{\chi}_2^0$
344	84.5	124.5	96	11.99 %	11.53 %

Table 1: Masses in GeV and branching ratios for the chosen scenario with all CP violating phases set to zero.

where $N_{\mathcal{T}\pm}$ denote the numbers of events with positive or negative triple product, respectively, T the amplitude of the process of interest and dlips the Lorentz invariant phase space. In our case the above decay chain provides two triple products originating from the covariant product in the spin-spin-dependent part of the amplitude, namely

$$\mathcal{T}_{l_1}^{\mp} = \left(\vec{p}_{l_1^\mp} \ \cdot \ [\vec{p}_W \times \vec{p}_t]\right) \ , \qquad \mathcal{T}_{ll} = (\vec{p}_b \ \cdot \ [\vec{p}_{l^+} \times \vec{p}_{l^-}]) \ .$$

To reveal CP-violation we then measure the corresponding triple product asymmetries, $\mathcal{A}_{l_1}$ and $\mathcal{A}_{ll}$. However, in order to make a definite statement on CP-violation, we need to combine the measurements of both charge-conjugated processes. Since the asymmetry changes sign under charge conjugation, this forces us to claim knowledge of the stop charge for both triple products. Not knowing the charge of the stop would result in a cancellation of the asymmetry. Fortunately, the $\tilde{t}_1$-charge can be established by requiring that the antiparticle decays via a single lepton. Thus, overall we observe a tri-lepton final state [10]. But in demanding this we loose statistical significance, since we reduce the total number of events due to requiring specific decays. To optimise the situation and gain a factor of two one therefore should not fix the charge determination to the antiparticle decay, but allow charge determination from the particle as well. Here we would use the antiparticle decay to form the triple product.

Furthermore, we need to identify the leptons from the neutralino and slepton decay for the triple product, $\mathcal{T}_{l_1}^{\mp}$. This is due to the fact that the correlation for the far lepton is much weaker than for the near lepton. Hence, the use of the far lepton results in a smaller triple product, which dilutes the asymmetry. The identification of the leptons can be done by the momentum reconstruction technique presented in [10]. Note, however, that we have to know the masses of all particles of the decay chain for this.

Nevertheless, momentum reconstruction is very important apart from lepton identification, because unlike the covariant product the mentioned triple products are not Lorentz invariant. The asymmetry, $\mathcal{A}_{l_1}$, for example, is maximal in the neutralino or stop rest frame and is diluted for any boost.

In contrast to $\mathcal{T}_{l_1}^{\mp}$, we do not need to identify the leptons for $\mathcal{T}_{ll}$, but only to measure the lepton charges. Thus, if a distinction between near and far lepton is not possible for some reason, this triple product provides an alternative. However, an inertial frame in which $\mathcal{T}_{ll}$ is completely equivalent to the covariant product does not exist. This is the case, because the covariant product contains a $\tilde{\chi}_1^0$-dependent contribution. Consequently, although $\mathcal{T}_{ll}$ is valuable when momentum reconstruction is not possible, it will lead to a smaller asymmetry than $\mathcal{T}_{l_1}^{\mp}$ (assuming full momentum reconstruction). This can also be understood physically, since the second lepton is not directly correlated to the spin of the intermediate neutralino. Hence, the triple products are smaller.

2.2 Numerical Results

To obtain a maximal asymmetry, we evaluate $\mathcal{A}_{l_1}$ in the reconstructed $\tilde{\chi}_2^0$ rest frame and $\mathcal{A}_{ll}$ in the reconstructed W rest frame (see Fig. 1). The shape of the curves immediately illustrates that $\mathcal{A}_{l_1}$ and $\mathcal{A}_{ll}$ are CP-odd. The triple product, $\mathcal{T}_{l_1}$, evokes the larger asymmetry, because $\mathcal{T}_{ll}$ does not represent the complete covariant product in any inertial frame. Both asymmetries are maximal for $\phi_{A_t} \approx 1.2\pi$, with $\mathcal{A}_{ll} \approx 9.3$ % and $\mathcal{A}_{l_1} \approx 15.5$ %.

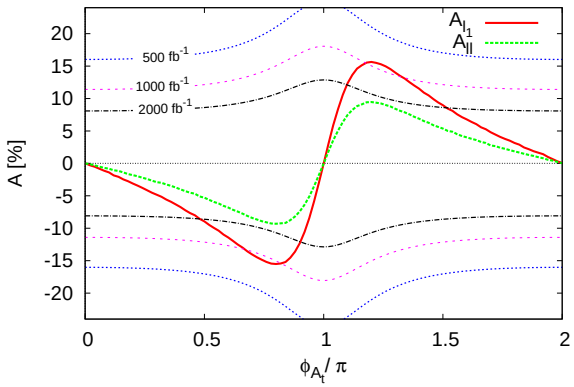

Figure 1: The asymmetries, $\mathcal{A}_{l_1}$ and $\mathcal{A}_{ll}$, along with the lines showing the asymmetry required for a 3σ observation at a given integrated luminosity of 500 fb^{-1}, 1000 fb^{-1} and 2000 fb^{-1} at $\sqrt{s} = 1$ TeV in the case of momentum reconstruction. $\mathcal{A}_{l_1}$ is evaluated in the $\tilde{\chi}_2^0$ and $\mathcal{A}_{ll}$ in the W rest frame.

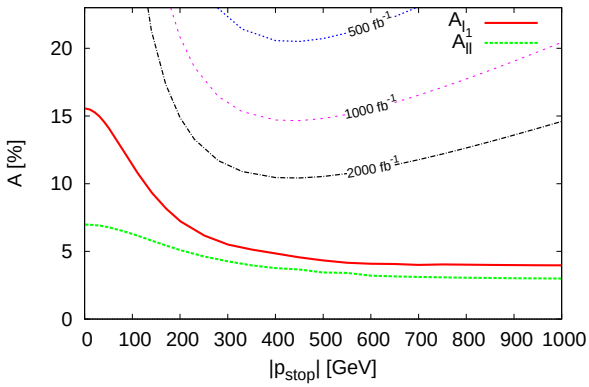

Figure 2: Both triple product asymmetries, $\mathcal{A}_{l_1}$ and $\mathcal{A}_{ll}$, for $\phi_{A_t} = 1.2\pi$ in the laboratory frame as functions of the absolute value of stop three-momentum and 3σ-limits for integrated luminosities of 500 fb^{-1}, 1000 fb^{-1} and 2000 fb^{-1}.

Furthermore, Fig. 1 contains the 3σ-limits for integrated luminosities of 500 fb^{-1}, 1000 fb^{-1} and 2000 fb^{-1}. Assuming successful momentum reconstruction we see that for 2000 fb^{-1} collected data one would be able to observe a triple product asymmetry in the region of a maximal CP violating angle, $1.1\pi < \phi_{A_t} < 1.5\pi$. With 1000 fb^{-1} the asymmetry can still be exposed close to the maximum ($1.18\pi < \phi_{A_t} < 1.33\pi$), whereas 500 fb^{-1} is not sufficient to reveal CP-violation via triple product asymmetries here. In particular $\mathcal{A}_{ll}$ needs more data.

If we are not able to reconstruct the $\tilde{\chi}_1^0$-momentum and are forced to use the diluted asymmetries in the laboratory frame directly, both asymmetries attain too small magnitudes to be detected at a 3σ-level with the expected luminosity. At the maximum of $\phi_{A_t} \approx 1.2\pi$ the asymmetries are determined to be $\mathcal{A}_{ll} \approx 3.9$ % and $\mathcal{A}_{l_1} \approx 5.0$ %. Note that the dilution due to energy dependence of $\mathcal{A}_{ll}$ is less significant than for $\mathcal{A}_{l_1}$, which is diluted by approximately 70 %. Notice further that we have not included the dilution from misidentified leptons in $\mathcal{A}_{l_1}$ yet. We will come back to both points in a moment.

Looking at Fig. 1 again, we notice that the bands which indicate the limit of measurability for a certain luminosity are not constant, but vary with ϕ_{A_t}. The reason for this is that the stop mass - and hence the production cross section - as well as the branching ratio, BR($\tilde{t}_1 \to \tilde{\chi}_2^0 t$), depend on the trilinear coupling phase, ϕ_{A_t}. As the stop mass increases as $\phi_{A_t} \to \pi$ from 344 GeV to 354 GeV, the production cross section, $\sigma(e^+e^- \to \tilde{t}_1\tilde{t}_1^*)$, decreases from 12.3 fb to 11.2 fb. At the same time, the stop branching ratio, BR($\tilde{t}_1 \to \tilde{\chi}_2^0 t$), drops from 11.99 % to 5.16 %, since due to the increasing stop mass and changing mixing angle another decay channel, namely $\tilde{t}_1 \to \tilde{\chi}_2^+ b$, becomes prominent. This affects the total cross section which in turn influences the significance of our observable. The total number of events one can expect for a certain luminosity is calculated using our result for the production cross section and the `Herwig++`-results for the branching ratios at tree-level [13]. We draw attention to the fact that the depletion of the branching ratio is much more severe.

We already mentioned that the reconstruction of all momenta in the decay chain is important for a measurement of the triple product asymmetries, because these quantities are not Lorentz invariant. To demonstrate this we compute both asymmetries at their maximum, $\phi_{A_t} = 1.2\pi$, as functions of the stop three-momentum in the laboratory frame, as is presented in Fig. 2.

We read off that both asymmetries are maximal in the stop rest frame and are depleted for increasing stop three-momentum. This can be understood recalling the geometrical picture of triple products. Concerning the relative orientation of $\vec{p}_{l_1}$ to the three-momenta, $\vec{p}_W$ and $\vec{p}_t$, that establish the plane in our triple product, we note that the triple product and therefore the angle between $\vec{p}_{l_1}$ and the plane is maximal in the rest

frame of the neutralino. Performing a boost on the system results in a smaller angle as all momenta are boosted forward in the same direction. Thus, as all vectors lie close together, it is more likely that the lepton can accidentially flip orientation with respect to the reference plane and hence change the sign of the triple product. Since this inversion is a random function of the boost and not connected to CP-violation, the asymmetry is depleted.

Although both asymmetries exhibit a manifest energy dependence, the triple product asymmetry, $\mathcal{A}_{l_1}$, is significantly more diluted than the asymmetry, $\mathcal{A}_{ll}$. This can be explained by the fact that the far lepton included in this triple product originates from the slepton which always experiences a boost, even if the stop is at rest. Therefore a boost of the stop will result in a proportionally less boosted slepton and far lepton, because the stop momentum is shared over the whole decay chain.

From the additionally plotted 3σ-limits we can extract a strong energy dependence of the level of measurability. This traces back to the severe energy dependence of the production process. Note that for an absolute value for the stop three-momentum of around 400 GeV we obtain the best measurability. This corresponds to a center-of-mass energy of roughly 1 TeV for our 344 GeV stop.

Recall that $\mathcal{A}_{l_1}$ requires lepton identification via momentum reconstruction. Thus, another dilution can be caused by the wrong assignment of near and far leptons for the triple product, $\mathcal{T}_{l_1}^{\mp}$. Although the second lepton is correlated via the slepton decay to the neutralino, which determines the momentum of the near lepton, the correlation is much weaker. Consequently the triple product is smaller. The corresponding depletion of our observable can be quantified to around 60 %. However, if we are not able to reconstruct momenta, we are forced to evaluate the triple product in the laboratory frame. As specified above, this already accounts for a dilution by approximately 70 %. Thus without momentum reconstruction, the asymmetry, $\mathcal{A}_{l_1}$, is reduced to roughly 2 % at the maximum and therefore not feasible for our study.

3 Conclusions

We observed that for the chosen scenario the CP violating phase, ϕ_{A_t}, of the trilinear top coupling accounted for a maximal triple product asymmetry of approximately 15.5 %. Under the assumption of successful momentum reconstruction this asymmetry could be measured for 2000 fb^{-1} collected data in the region of a maximal CP violating angle, $1.10\pi < \phi_{A_t} < 1.5\pi$. With an integrated luminosity of 1000 fb^{-1} the asymmetry could still be exposed close to the maximum ($1.18\pi < \phi_{A_t} < 1.33\pi$).

As a conclusion we emphasise that a future linear collider is essential for a precise measurement of the parameters of supersymmetry. However, for the particular scenario studied, it turned out to be challenging to reveal CP-violation with a reasonable amount of data. Nevertheless, other decay chains, *e. g.* via charginos, may result in a higher cross section and hence a better statistical significance.

References

[1] A.D. Sakharov, Zh. Eksp. Teor. Fiz. Pis'ma **5** 32-35 (1967).

[2] B. Aubert *et al.* (BELLE Collab.), Phys. Rev. Lett. **86** 2509 (2001); Phys. Rev. Lett. **86** 2515 (2001).

[3] A. Pilaftsis, Phys. Lett. **B435** 88-100 (1998);
D.A. Demir, Phys. Rev. **D60** 055006 (1999);
A. Pilaftsis, C.E.M. Wagner, Nucl. Phys. **B553** 3-42 (1999);
S.Y. Choi, M. Drees and J.S. Lee, Phys. Lett. **B481** 57-66 (2000);
J.L. Kneur and G. Moultaka, Phys. Rev. **D59** 015005 (1999).

[4] S.Y. Choi *et al.*, Eur. Phys. J. **C14** 535-546 (2000);
J.L. Kneur and G. Moultaka, Phys. Rev. **D61** 095003 (2000).

[5] A. Bartl, S. Hesselbach, K. Hidaka, T. Kernreiter and W. Porod, Phys. Rev. **D70** 035003 (2004);
K. Rolbiecki, J. Tattersall and G. Moortgat-Pick, Eur. Phys. J. **C71** 1517 (2011).

[6] H. Eberl, T. Gajdosik, W. Majerotto and B. Schrausser, Phys. Lett. **B618** 171-181 (2005);
E. Christova, H. Eberl, W. Majerotto and S. Kraml, Nucl. Phys. **B639** 263-280 (2002); JHEP **12** 021 (2002);
M. Frank and I. Turan, Phys. Rev. **D76** 016001 (2007); Phys. Rev. **D76** 076008 (2007).

[7] E. Christova, H. Eberl, E. Ginina and W. Majerotto, Phys. Rev. **D79** 096005 (2009).

[8] E. Christova, H. Eberl, E. Ginina and W. Majerotto, JHEP **02** 075 (2007).

[9] A. Bartl, E. Christova, K. Hohenwarter-Sodek and T. Kernreiter, Phys. Rev. **D70** 095007 (2004);
J. Ellis, F. Moortgat, G. Moortgat-Pick, J.M. Smillie and J. Tattersall, Eur. Phys. J. **C60** 633-651 (2009);
H. Dreiner, O. Kittel, S. Kulkarni and A. Marold, Phys. Rev. **D83** 095012 (2011).

[10] G. Moortgat-Pick, K. Rolbiecki and J. Tattersall, Phys. Rev. **D83** 115012 (2011).

[11] S. Kraml, arXiv:hep-ph/0710.5117 (2007);
S. Hesselbach, arXiv:hep-ph/0709.2679 (2007).

[12] C.A. Baker *et al.*, Phys. Rev. Lett. **97** 131801 (2006);
B.C. Regan, E.D. Commins, C.J. Schmidt and D. DeMille, Phys. Rev. Lett. **88** 071805 (2002);
W.C. Griffith *et al.*, Phys. Rev. Lett. **102** 101601 (2009);
Y. Li, S. Profumo and M. Ramsey-Musolf, JHEP **1008** 062 (2010). S. Abel, S. Khalil and O. Lebedev, Nucl. Phys. **B606** 151-182 (2001);
M. Pospelov and A. Ritz, Annals Phys. **318** 119-169 (2005);
T. Falk and K.A. Olive, Phys. Lett. **B375** 196-202 (1996); Phys. Lett. **B439** 71-80 (1998);
T. Ibrahim and P. Nath, Phys. Rev. **D58** 111301 (1998); Phys. Rev. **D61** 093004 (2000).

[13] M. Bahr *et al.*, arXiv:hep-ph/0803.0883v3;
S. Gieseke *et al.*, arXiv:hep-ph/1102.1672.

Neutralinos from Chargino Decays in the Complex MSSM

S. Heinemeyer[1], F. v. d. Pahlen[1] and C. Schappacher[2] *

1-Instituto de Física de Cantabria (CSIC-UC)
E–39005 Santander, Spain

2-Institut für Theoretische Physik, Karlsruhe Institute of Technology,
D–76128 Karlsruhe, Germany

We review the evaluation of two-body decay modes of charginos in the Minimal Supersymmetric Standard Model with complex parameters (cMSSM). Assuming heavy scalar quarks we take into account all decay channels involving charginos, neutralinos, (scalar) leptons, Higgs bosons and SM gauge bosons. The evaluation of the decay widths is based on a full one-loop calculation including hard and soft QED radiation. Here we focus on the decays involving the Lightest Supersymmetric Particle (LSP), i.e. the lightest neutralino, or a heavier neutralino and a W boson. The higher-order corrections of the chargino decay widths can easily reach a level of $\pm 10\%$, translating into corrections of similar size in the respective branching ratios. These corrections are important for the correct interpretation of LSP and heavier neutralino production at the LHC and at a future linear e^+e^- collider.

1 Introduction

The search for physics effects beyond the Standard Model (SM), both at present and future colliders, constitutes one of the priorities of current high energy physics, where the Minimal Supersymmetric Standard Model (MSSM) [1] is one of the leading candidates. A related important task is investigating the production and measurement of the properties of Cold Dark Matter (CDM). The MSSM offers a natural candidate of CDM, the Lightest Supersymmetric Particle (LSP), i.e. the lightest neutralino, $\tilde{\chi}_1^0$ [2]. Having a stable LSP also ensures that any produced supersymmetric particle will lead to cascades with neutralinos in the final state, motivating experimental and phenomenological analyses of these decay chains. While discoveries of supresymmetric particles will possibly be made by the LHC, a precise determination of their properties is expected at the ILC [3–5] (or any other future e^+e^- collider such as CLIC).

Charginos, $\tilde{\chi}_i^\pm$, $(i = 1, 2)$, and neutralinos, $\tilde{\chi}_j^0$, $(j = 1, 2, 3, 4)$, are, respectively, the charged and neutral supersymmetric partners of the Higgs and gauge bosons. Therefore masses and couplings of charginos and neutralinos depend on common parameters, and an analysis of chargino decays provides direct and indirect information on the neutralino sector.

In order to yield a sufficient accuracy, one-loop corrections to the various chargino decay modes have to be considered. A precise calculation of the branching ratio (BR) at the one-loop level requires the calculation of all decay modes at this level of precision. Here we review the results for the evaluation of these decay modes (and BRs) obtained in the MSSM with complex parameters (cMSSM) [6] (original results for the tree-level decays were presented in [7]). We show results for

$$\Gamma(\tilde{\chi}_2^\pm \to \tilde{\chi}_j^0 W^\pm), \quad j = 1, 2, 3 \; . \tag{1}$$

The total decay width is defined as the sum of all the partial two-body decay widths, *all* evaluated at the one-loop level. Detailed references to existing calculations of these decay widths, branching ratios, as well as about the extraction of complex phases can be found in Ref. [6]. Our results will be implemented into the Fortran code `FeynHiggs` [8–11].

*KA-TP-05-2012

2 Renormalization of the cMSSM

All the relevant two-body decay channels have been evaluated at the one-loop level, including hard QED radiation. This requires the simultaneous renormalization of several sectors of the cMSSM: the gauge and Higgs sector, the chargino/neutralino sector, and the lepton and slepton sector. The on-shell renormalization conditions for the chargino/neutralino sector are fixed requiring that the masses of the two charginos and of the lightest neutralino are not renormalized. An analysis of various renormalization schemes for the chargino/neutralino sector was recently published in Ref. [12]. Further details about our notation and about the renormalization of the cMSSM can be found in Refs. [6, 13, 14].

In order to highlight the important role of the absorptive contributions in the presence of complex couplings, we also evaluated for comparison the decay widths neglecting the imaginary parts of self-energy type corrections to external (on-shell) particles. These imaginary contributions, in product with an imaginary part of a complex coupling (such as M_1 in our case), can give an additional real contribution to the decay width. This contribution is odd under charge conjugation and leads to a difference in the decay widths for the chargino and its antiparticle. The resulting CP-asymmetry, however, is one-loop suppressed (and will not be analyzed here).

The diagrams and corresponding amplitudes have been obtained with `FeynArts` [15]. The model file, including the MSSM counter terms, is based largely on Ref. [16] and is discussed in more detail in Ref. [13]. The further evaluation has been performed with `FormCalc` (and `LoopTools`) [17]. As regularization scheme for the UV-divergences we have used constrained differential renormalization [18], which has been shown to be equivalent to dimensional reduction [19] at the one-loop level [17]. Thus the employed regularization preserves SUSY [20, 21]. All UV-divergences cancel in the final result. (Also the IR-divergences cancel in the one-loop result as required.)

3 Numerical results

The numerical examples shown below have been evaluated using the parameters given in Tab. 1. We assume that the scalar quarks are heavy such that they do not contribute to the total decay widths of the charginos. We invert the expressions of the chargino masses in order to express the parameters μ and M_2 (which are chosen real) as a function of $m_{\tilde{\chi}_1^\pm}$ and $m_{\tilde{\chi}_2^\pm}$. This leaves two choices for the hierarchy of μ and M_2:

$$\mathcal{S}_> : \mu > M_2 \quad (\tilde{\chi}_2^\pm \text{ more higgsino-like}) \,, \tag{2}$$

$$\mathcal{S}_< : \mu < M_2 \quad (\tilde{\chi}_2^\pm \text{ more gaugino-like}) \,. \tag{3}$$

Scen.	$\tan\beta$	$M_{H^\pm}$	$m_{\tilde{\chi}_2^\pm}$	$m_{\tilde{\chi}_1^\pm}$	$M_{\tilde{l}_L}$	$M_{\tilde{l}_R}$	A_l
$\mathcal{S}$	20	160	600	350	300	310	400

Table 1: MSSM parameters for the initial numerical investigation; all masses are in GeV.

The absolute value of M_1 is fixed via the GUT relation (with $|M_2| \equiv M_2$),

$$|M_1| = \frac{5}{3} \tan^2\theta_\mathrm{w} M_2 \approx \frac{1}{2} M_2 \,. \tag{4}$$

leaving φ_{M_1} as a free parameter.

The values of $m_{\tilde{\chi}_{1,2}^\pm}$ allow copious production of the charginos in SUSY cascades at the LHC. Furthermore, the production of $\tilde{\chi}_1^\pm \tilde{\chi}_2^\mp$ or $\tilde{\chi}_1^+ \tilde{\chi}_1^-$ at the ILC(1000), i.e. the ILC with $\sqrt{s} = 1000$ GeV, via $e^+e^- \to \tilde{\chi}_1^\pm \tilde{\chi}_{1,2}^\mp$ will be possible, with all the subsequent decay modes to a neutralino and a W boson being open. The clean environment of the ILC would permit a detailed study of the chargino decays [4, 5]. For the values in Tab. 1 and unpolarized beams we find, for $\mathcal{S}_>$ ($\mathcal{S}_<$), $\sigma(e^+e^- \to \tilde{\chi}_1^\pm \tilde{\chi}_2^\mp) \approx 4\,(12)$ fb, and $\sigma(e^+e^- \to$

$\tilde{\chi}_1^+\tilde{\chi}_1^-) \approx 55\,(80)$ fb. Choosing appropriate polarized beams these cross sections can be enhanced by a factor of approximately 2 to 3. An integrated luminosity of $\sim 1\,\text{ab}^{-1}$ would yield about $4 - 12 \times 10^3$ $\tilde{\chi}_1^\pm\tilde{\chi}_2^\mp$ events and about $55 - 80 \times 10^3$ $\tilde{\chi}_1^+\tilde{\chi}_1^-$ events, with appropriate enhancements in the case of polarized beams.

The ILC environment would result in an accuracy of the relative branching ratio close to the statistical uncertainty: assuming an integrated luminosity of $1\,\text{ab}^{-1}$ a BR of 10% could be determined to $\sim 2\%$ for the $m_{\tilde{\chi}_i^\pm}$ values of Tab. 1.

The results shown here consist of "tree", which denotes the tree-level value and of "full", which is the decay width including *all* one-loop corrections. Also shown in Fig. 1, is the result leaving out the contributions from absorptive parts of the one-loop self-energy corrections as discussed in the previous section, labeled as "full R". Not shown here are the BRs and their relative corrections, since they are more parameter dependent.

In Figure 1 we show $\Gamma(\tilde{\chi}_2^- \to \tilde{\chi}_1^0 W^-)$ (top), $\Gamma(\tilde{\chi}_2^- \to \tilde{\chi}_2^0 W^-)$ (middle), and $\Gamma(\tilde{\chi}_2^- \to \tilde{\chi}_3^0 W^-)$ (bottom row) as a function of of φ_{M_1}, for the parameters of Tab. 1. The left (right) columns display the (relative one-loop correction to the) decay width.

We observe a strong dependence on φ_{M_1} in scenario $\mathcal{S}_<$, in which the three lightest neutralinos are highly mixed states. The effect of the absorptive contributions, both from the imaginary parts of the self energies (see as the difference between the "full" and "full R" curves), as well as from the imaginary parts of the vertex corrections, turn out to be of a few percent. On the contrary, in scenario $\mathcal{S}_>$, where only $\tilde{\chi}_2^- \to \tilde{\chi}_{1,2}^0 W^-$ is kinematically allowed, the mixing of the neutralinos is small, and consequently the dependence on φ_{M_1} turns out to be much smaller. The size of the one-loop corrections, reach $\mathcal{O}(10\%)$ for $\mathcal{S}_<$ and show an important dependence on φ_{M_1}. For $\mathcal{S}_>$ the corrections are of the order of a few percent with a negligible φ_{M_1} dependence.

Figure 2 shows $\Gamma(\tilde{\chi}_2^- \to \tilde{\chi}_1^0 W^-)$ (top) and $\Gamma(\tilde{\chi}_2^- \to \tilde{\chi}_{2,3}^0 W^-)$ (bottom row) as a function of $m_{\tilde{\chi}_2^\pm}$, keeping all other parameters as in Tab. 1. As in the previous figure, the left (right) column shows (the relative size of the corrections of) the decay widths. The vertical lines indicate where $m_{\tilde{\chi}_1^\pm} + m_{\tilde{\chi}_2^\pm} = 1000$ GeV, i.e. the maximum reach of the ILC(1000). Coincidentally, around this value of $m_{\tilde{\chi}_2^\pm}$ we observe a level crossing of the second and third neutralino in $\mathcal{S}_<$, which points out at the large neutralino mixing for these paramters.

The decay widths show a strong dependence on $m_{\tilde{\chi}_2^\pm}$ which is mainly due to the changing chargino-neutralino couplings, as well as the change in the phase space. For $\mathcal{S}_<$ the decay width into the lightest neutralino almost vanishes at one point, resulting in large relative corrections. The relative one-loop corrections are mostly of $\mathcal{O}(10\%)$. The dips in the one-loop corrections are due to thresholds in the vertex corrections. It should be noted that a calculation very close to threshold requires the inclusion of additional (non-relativistic) contributions, which is far beyond the scope of this analysis.

The decay width into $\tilde{\chi}_2^0$ reaches ~ 2 GeV at $m_{\tilde{\chi}_2^\pm} = 1$ TeV, while for the decay into $\tilde{\chi}_3^0$ it reaches ~ 1 GeV in the region of maximal neutralino mixing. The relative one-loop corrections are of $\mathcal{O}(5 - 10\%)$.

Summarizing, we reviewed the evaluation of two-body decay modes of charginos in the cMSSM, and show numerical results for the decay of the heavier chargino into neutralinos. The relative size of the one-loop corrections is found to be significant and should be taken into account in a reliable determination of the chargino/neutralino sector parameters. This also applies in particular to the effects of the imaginary parts of the self-energies of the external particles.

Acknowledgments

The work of S.H. was partially supported by CICYT (grant FPA 2007–66387 and FPA 2010–22163-C02-01). F.v.d.P. was supported by the Spanish MICINN's Consolider-Ingenio 2010 Programme under grant MultiDark CSD2009-00064.

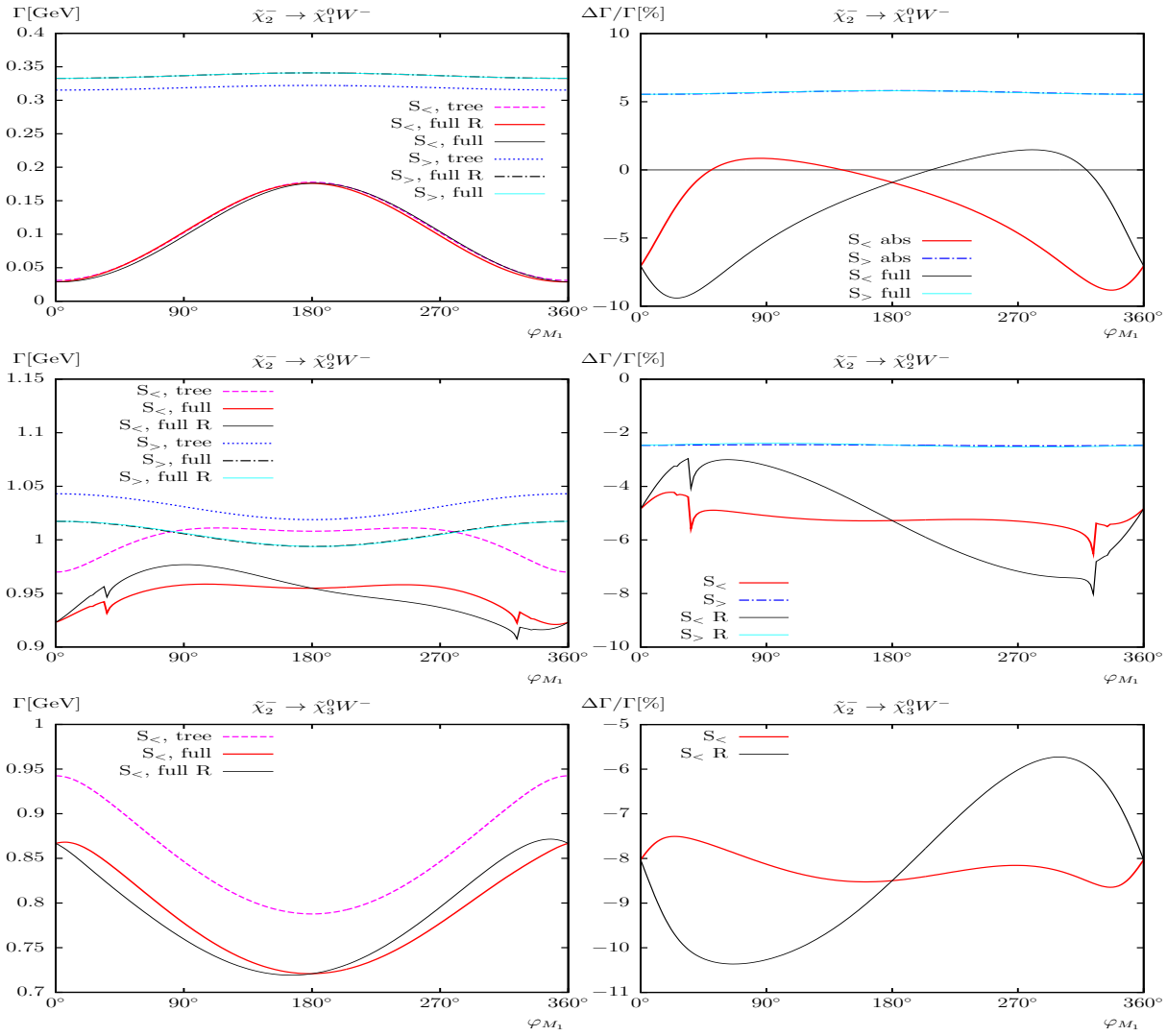

Figure 1: $\Gamma(\tilde{\chi}_2^- \to \tilde{\chi}_j^0 W^-)$, $j = 1, 2, 3$. Tree-level ("tree") and full one-loop ("full") corrected decay widths are shown with the parameters chosen according to $\mathcal{S}$ (see Tab. 1), with ϕ_{M_1} varied. Also shown are the full one-loop corrected decay widths omitting the absorptive contributions ("full R"). The left (right) plots show (the relative size of the corrections of) the decay width.

References

[1] H.P. Nilles, *Phys. Rept.* **110** (1984) 1;
H.E. Haber and G.L. Kane, *Phys. Rept.* **117** (1985) 75;
R. Barbieri, *Riv. Nuovo Cim.* **11** (1988) 1.

[2] H. Goldberg, *Phys. Rev. Lett.* **50** (1983) 1419;
J. Ellis, J. Hagelin, D. Nanopoulos, K. Olive and M. Srednicki, *Nucl. Phys.* **B 238** (1984) 453.

[3] TESLA Technical Design Report [TESLA Collaboration] Part 3, "Physics at an e^+e^- Linear Collider", arXiv:hep-ph/0106315, see:
`tesla.desy.de/new_pages/TDR_CD/start.html`;
K. Ackermann et al., DESY-PROC-2004-01.

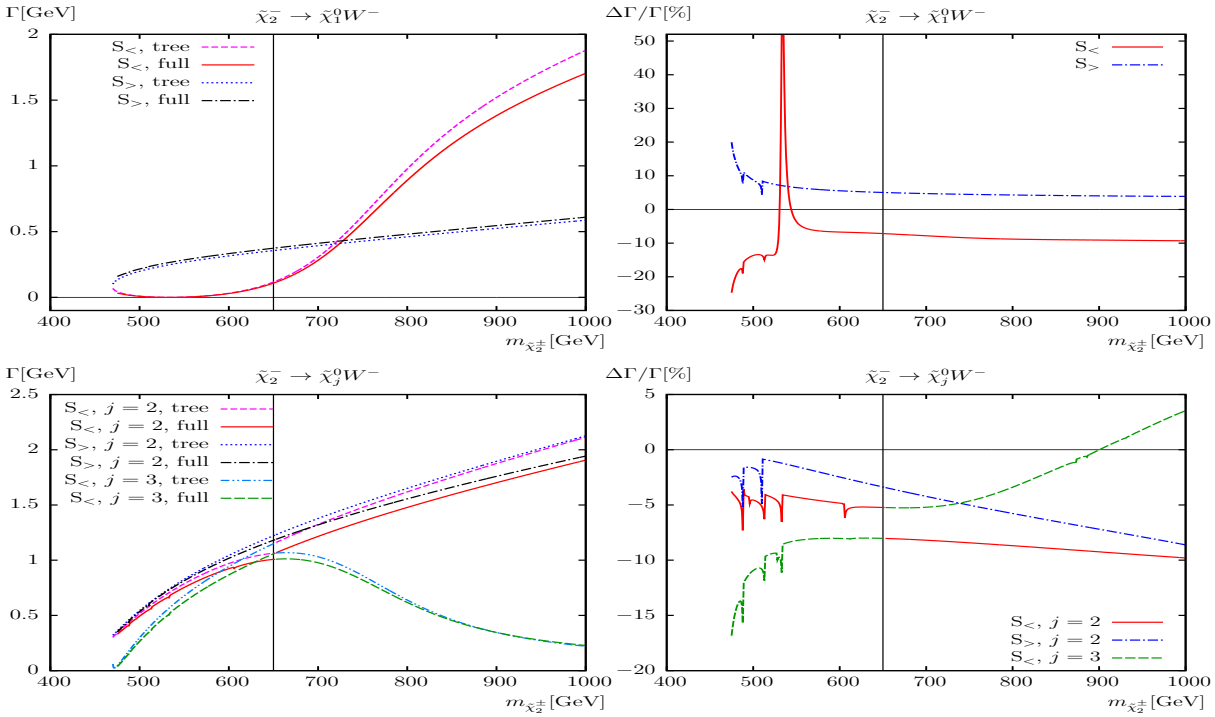

Figure 2: $\Gamma(\tilde{\chi}_2^- \to \tilde{\chi}_j^0 W^-)$, $j = 1, 2, 3$. Tree-level ("tree") and full one-loop ("full") corrected decay widths are shown with the parameters chosen according to $\mathcal{S}$ (see Tab. 1), with $m_{\tilde{\chi}_2^\pm}$ varied. The left (right) plots show the decay width (the relative size of the corrections).

[4] J. Brau et al. [ILC Collaboration], *ILC Reference Design Report Volume 1 - Executive Summary*, arXiv:0712.1950 [physics.acc-ph];
G. Aarons et al. [ILC Collaboration], *International Linear Collider Reference Design Report Volume 2: Physics at the ILC*, arXiv:0709.1893 [hep-ph];
E. Accomando et al. [CLIC Physics Working Group Collaboration], arXiv:hep-ph/0412251.

[5] G. Weiglein et al. [LHC/ILC Study Group], *Phys. Rept.* **426** (2006) 47 [arXiv:hep-ph/0410364];
A. De Roeck et al., *Eur. Phys. J.* **C 66** (2010) 525 [arXiv:0909.3240 [hep-ph]];
A. De Roeck, J. Ellis, S. Heinemeyer, CERN Cour. **49N10** (2009) 27.

[6] S. Heinemeyer, F. von der Pahlen and C. Schappacher, *Eur. Phys. J.* **C 72** (2012) 1892 [arXiv:1112.0760 [hep-ph]].

[7] J. Gunion, H. Haber, R. Barnett, M. Drees, D. Karatas, X. Tata and H. Baer, *Int. J. Mod. Phys.* **A 2** (1987) 1145;
H. Baer, A. Bartl, D. Karatas, W. Majerotto and X. Tata, *Int. J. Mod. Phys.* **A 4** (1989) 4111.

[8] S. Heinemeyer, W. Hollik and G. Weiglein, *Comput. Phys. Commun.* **124** (2000) 76 [arXiv:hep-ph/9812320];
T. Hahn, S. Heinemeyer, W. Hollik, H. Rzehak and G. Weiglein, *Comput. Phys. Commun.* **180** (2009) 1426;
see `www.feynhiggs.de` .

[9] S. Heinemeyer, W. Hollik and G. Weiglein, *Eur. Phys. J.* **C 9** (1999) 343 [arXiv:hep-ph/9812472].

[10] G. Degrassi, S. Heinemeyer, W. Hollik, P. Slavich and G. Weiglein, *Eur. Phys. J.* **C 28** (2003) 133 [arXiv:hep-ph/0212020].

[11] M. Frank, T. Hahn, S. Heinemeyer, W. Hollik, R. Rzehak and G. Weiglein, *JHEP* **02** (2007) 047 [arXiv:hep-ph/0611326].

[12] A. Chatterjee, M. Drees, S. Kulkarni, Q. Xu, *Phys. Rev.* **D 85** (2012) 075013 [arXiv:1107.5218 [hep-ph]].

[13] T. Fritzsche, S. Heinemeyer, H. Rzehak and C. Schappacher, *Phys. Rev.* **D 86** (2012) 035014 [arXiv:1111.7289 [hep-ph]].

[14] S. Heinemeyer, H. Rzehak and C. Schappacher, *Phys. Rev.* **D 82** (2010) 075010 [arXiv:1007.0689 [hep-ph]];
PoSCHARGED **2010** (2010) 039 [arXiv:1012.4572 [hep-ph]].

[15] J. Küblbeck, M. Böhm and A. Denner, *Comput. Phys. Commun.* **60** (1990) 165;
T. Hahn, *Comput. Phys. Commun.* **140** (2001) 418 [arXiv:hep-ph/0012260];
T. Hahn and C. Schappacher, *Comput. Phys. Commun.* **143** (2002) 54 [arXiv:hep-ph/0105349].
The program, the user's guide and the MSSM model files are available via
`www.feynarts.de` .

[16] T. Fritzsche, PhD thesis, Cuvillier Verlag, Göttingen 2005, ISBN 3–86537–577–4.

[17] T. Hahn and M. Pérez-Victoria, *Comput. Phys. Commun.* **118** (1999) 153 [arXiv:hep-ph/9807565].

[18] F. del Aguila, A. Culatti, R. Muñoz Tapia and M. Pérez-Victoria, *Nucl. Phys.* **B 537** (1999) 561 [arXiv:hep-ph/9806451].

[19] W. Siegel, *Phys. Lett.* **B 84** (1979) 193;
D. Capper, D. Jones, and P. van Nieuwenhuizen, *Nucl. Phys.* **B 167** (1980) 479.

[20] D. Stöckinger, *JHEP* **0503** (2005) 076 [arXiv:hep-ph/0503129].

[21] W. Hollik and D. Stöckinger, *Phys. Lett.* **B 634** (2006) 63 [arXiv:hep-ph/0509298].

Full simulation study of very light gravitino at the ILC

Ryo Katayama,[1] Takuaki Mori,[1] Keisuke Fujii,[2] Shigeki Matsumoto,[3]
Taikan Suehara,[4] Tomohiko Tanabe,[4] and Satoru Yamashita[4]

[1] *Department of Physics, The University of Tokyo, Tokyo 113-0033, Japan*
[2] *High Energy Accelerator Research Organization (KEK), Tsukuba 305-0801, Japan*
[3] *Kavli Institute for the Physics and Mathematics of the Universe, Kashiwa 277-8583, Japan*
[4] *International Center for Elementary Particle Physics, The University of Tokyo, Tokyo 113-0033, Japan*

We explore the capability of the International Linear Collider (ILC) to measure the mass of a stable gravitino whose mass is in the $\mathcal{O}$(1–10) eV range using full simulation of the ILD detector model. Such gravitino masses typically arise in low-scale gauge mediation scenarios of the supersymmetry breaking. The next-to-lightest supersymmetric particle is chosen to be the stau. Through the measurement of the stau mass and lifetime, the gravitino mass can be determined. We work with the benchmark point of stau mass of $m_{\tilde{\tau}} = 120\,\mathrm{GeV}$ and stau lifetime of $c\tau_{\tilde{\tau}} = 100\,\mu\mathrm{m}$. The $e^+e^- \to \tilde{\tau}^+\tilde{\tau}^-$ reaction is identified using the one-prong decay of the tau lepton. The main background processes are identified to be $e^+e^- \to VV \to l^+l^-\nu\overline{\nu}$ where $V = W^\pm$ or Z^0, $e^+e^- \to \tau^+\tau^-$, $\gamma\gamma$, $e\gamma$, and Bhabha scattering events. The precision of the stau mass is estimated to be $\Delta m/m = 0.6\%$ from the threshold scan at $\sqrt{s} = 250\,\mathrm{GeV}$ with an integrated luminosity of $100\,\mathrm{fb}^{-1}$, while with the detection of kinematic edge of the tau decay products at $\sqrt{s} = 500\,\mathrm{GeV}$ assuming an integrated luminosity of $500\,\mathrm{fb}^{-1}$ offers a precision of $\Delta m/m = 1.4\%$. The precision of the stau lifetime at $500\,\mathrm{fb}^{-1}$ is estimated to be $\Delta\tau/\tau = 1.4\%$, corresponding to the precision of the gravitino mass of 2% when combining with the threshold scan, or 4% when combining with the kinematic edge fit.

I. INTRODUCTION

Among many new theories beyond the standard model, supersymmetry (SUSY) is a promising candidate in that it can naturally solve the hierarchy problem by canceling the quadratic divergences in the radiative corrections to the Higgs mass parameter with the introduction of supersymmetric particles whose couplings are determined by gauge principles. Moreover, grand unification could be achieved by imposing SUSY. New sources of CP violation and flavor-changing neutral current may arise due to the presence of additional SUSY particles, known as the SUSY flavor problem, many SUSY models incorporate explicit mechanisms to suppress such effects. The gauge-mediated SUSY breaking (GMSB) scenarios [2] naturally solve the SUSY flavor problem by generating SUSY breaking soft mass terms at the messenger scale below the grand unification scale.

In GMSB scenarios with R-parity conservation, the gravitino appears as the lightest supersymmetric particle (LSP). Taking into account the cosmological data, the gravitino mass can be classified into two regions [3, 4]: the so-called low-scale region corresponds to the gravitino mass of around $m_{3/2} \approx 1$–$10\,\mathrm{eV}$, while the high-scale region corresponds to $m_{3/2} \approx 10^6$–$10^9\,\mathrm{eV}$. The low-scale region is not constrained by considerations of the reheating temperature, which makes thermal leptogenesis viable. This is in contrast to the high-scale region which requires low reheating temperatures. The high-scale region is expected to be eventually covered by LHC data, while the low-scale region will remain largely unexplored.

Precision measurements of the gravitino mass, such as those at the International Linear Collider (ILC), can help constrain the SUSY breaking scale. In this study, we estimate the sensitivity of the ILC to a very light gravitino mass in the GMSB scenario, assuming that the next lightest supersymmetric particle (NLSP) is the stau. We study the stau pair production process $e^+e^- \to \tilde{\tau}^+\tilde{\tau}^-$ with the subsequent stau decay $\tilde{\tau} \to \tau\tilde{G}$, whose diagram is shown in Fig. 1. The stau lifetime $\tau_{\tilde{\tau}}$ can be expressed

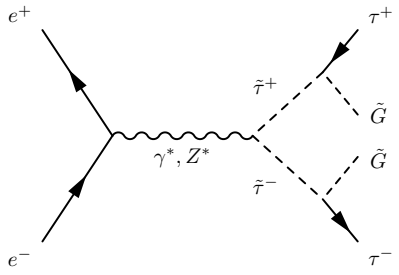

FIG. 1. Feynman diagram for the $e^+e^- \to \tilde{\tau}^+\tilde{\tau}^-$ reaction including the stau decay $\tilde{\tau} \to \tau\tilde{G}$.

in terms of the stau mass $m_{\tilde{\tau}}$ and the gravitino mass $m_{3/2}$ as follows [5]:

$$\tau_{\tilde{\tau}} = 48\,\pi\,{M_{\mathrm{Pl}}}^2\,{m_{3/2}}^2/{m_{\tilde{\tau}}}^5 \tag{1}$$

where M_{Pl} is the Planck scale. In this study, we adopt the following benchmark point: stau mass of $m_{\tilde{\tau}} = 120\,\mathrm{GeV}$, and stau lifetime of $100\,\mu\mathrm{m}$. This corresponds to a gravitino mass of 3.7 eV. Since the observed particles will be the decay products of the tau, which itself decays from the stau, the challenge imposed on the detector is to discriminate the tau decay products whose displacement from the primary interaction point is slightly enhanced by the flight of the stau. In this study, only the one-prong decay of the tau is considered. Thus our primary observ-

able in the lifetime measurement will be the impact parameter of the tau decay products. Our analysis strategy is summarized as follows. First, we determine the precision of the stau mass from the cross section scan near the stau pair production threshold around $\sqrt{s} \approx 250\,\text{GeV}$. Then we perform the analysis at $\sqrt{s} = 500\,\text{GeV}$ for an alternative determination of the stau mass precision through the use of kinematic edges, as well as the stau lifetime measurement from the impact parameter distribution. Finally, we propagate the estimated precision into the gravitino mass via Eq. (1).

The paper is organized as follows. In Sec. II, the signal and background processes are described, along with the simulation framework. We describe the stau mass measurement through the cross section scan in Sec. III and the stau mass measurement from kinematic edges and the lifetime measurement in Sec. IV. We summarize the precision estimates in Sec. V.

II. SIGNAL AND BACKGROUND PROCESSES

The signal process is stau pair production $e^+e^- \to \tilde{\tau}^+\tilde{\tau}^- \to \tau^+\tau^-\tilde{G}\tilde{G}$. The left-handed stau is assumed to be heavy. Thus the production is dominated by the right-handed stau. In this study, the tau lepton is reconstructed in the one-prong mode, which corresponds to 85% of its decay. We take advantage of the beam polarizations at the ILC by choosing the right-handed electron and left-handed positron configuration ($P_{e^-} = +0.8$ and $P_{e^+} = -0.3$) in order to reduce background contributions from SM processes. The following processes are identified as possible background sources:

- $e^+e^- \to \tau^+\tau^-$
- $e^+e^- \to VV \to l^+l^-\nu\overline{\nu}$, where $V = W^\pm$ or Z^0
- $e^+e^- \to e^+e^-$ (Bhabha scattering)
- $e\gamma, \gamma\gamma \to l^+l^-X$, $q\overline{q}$

The $e^+e^- \to \tau^+\tau^-$ background can be reduced by requiring that the tau pair is back-to-back. The $e^+e^- \to VV \to l^+l^-\nu\overline{\nu}$ processes can be a source of background if the final state contains tau leptons. In particular, the former is an irreducible background because of its event topology is similar to that of the signal. While the beam-related backgrounds $\gamma\gamma \to l^+l^-$, $q\overline{q}$ and Bhabha scattering reactions have different event topologies, their background contribution is nevertheless investigated because their cross sections are large. The cross sections at $\sqrt{s} = 250\,\text{GeV}$ and $500\,\text{GeV}$ for the signal and background processes are summarized in Tab. I.

Signal events are generated using PHYSSIM [6], which calculates the scattering amplitude using HELAS [7]. properly taking into account the angular distributions of the decay products. Background samples are generated using WHIZARD [9]. The decay of the tau lepton is handled by TAUOLA [11]. The final state particles are passed as input to PYTHIA [10]. The effects of initial state radiation and beamstrahlung are included in the event generation.

TABLE I. Cross sections $\sigma_{\sqrt{s}}$ for signal and background processes for $\sqrt{s} = 250\,\text{GeV}$ and $500\,\text{GeV}$. The beam polarizations are taken to be $(\text{P}_{e^-}, \text{P}_{e^+}) = (+80\%, -30\%)$.

Process	σ_{100} (fb)	σ_{500} (fb)
$e^+e^- \to \tilde{\tau}^+\tilde{\tau}^-$ ($m_{\tilde{\tau}} = 120\,\text{GeV}$)	11.3	270.4
$e^+e^- \to \tau^+\tau^-$	10454.8	1591.2
$e^+e^- \to VV \to l^+l^-\nu\overline{\nu}$	4386.0	3341.6
$e^+e^- \to e^+e^-$ (Bhabha scattering)	1.73×10^7	1.74×10^7
$e\gamma, \gamma\gamma \to l^+l^-X$, $q\overline{q}$ (includes preselection)	3.58×10^7	5.64×10^6

The detector response is simulated using Mokka, which is based on GEANT4 [12]. The detector model `ILD_00` is used; it consists of a beam pipe, vertex and silicon tracking detectors and a time projection chamber for charged-particle tracking, and highly granular electromagnetic calorimeter (ECAL) and hadronic calorimeter (HCAL) which are placed within a superconducting solenoid which provides a magnetic field of 3.5 T, and a muon detector and tail catcher. In addition, several calorimeter components are placed in the forward regions to provide lepton identification down to very low polar angles.

III. STAU MASS MEASUREMENT VIA THRESHOLD SCAN

To evaluate the precision of the stau mass measurement, the technique of the threshold scan is used. We have chosen to perform measurements at three center-of-mass energies: $\sqrt{s} = 250$, 256, and 261 GeV. The assumed integrated luminosity is $100\,\text{fb}^{-1}$ at each point, making it a total of $300\,\text{fb}^{-1}$. The cross sections are shown in Fig. 2. These samples are also fully simulated and reconstructed. The background samples are simulated and reconstructed at $\sqrt{s} = 250$ GeV; their contributions are assumed to not vary up to $\sqrt{s} = 261$ GeV.

The following event selection is applied to reduce the background contributions. The visible energy in the event is required to be between 25 GeV and 140 GeV. This suppresses the Bhabha scattering and $\gamma\gamma$ backgrounds. The number of charged tracks exceeding a transverse momentum of 5 GeV is required to be exactly two. The track pair is required to have opposite charges. The selected tracks are required to have a polar angle of $|\cos\theta| < 0.82$. This suppresses Bhabha scattering in the t-channel process. The difference in the azimuthal angles of the selected tracks is used to impose the requirement of $\cos(\phi_2 - \phi_1) > -0.90$ to reduce the $e^+e^- \to \tau^+\tau^-$ process, in which the tau pair is produced in the back-to-back configuration. Tracks are required to have a large transverse impact parameter significance $|d_0/\sigma(d_0)| > 4.0$ to enrich the sample with tau decay

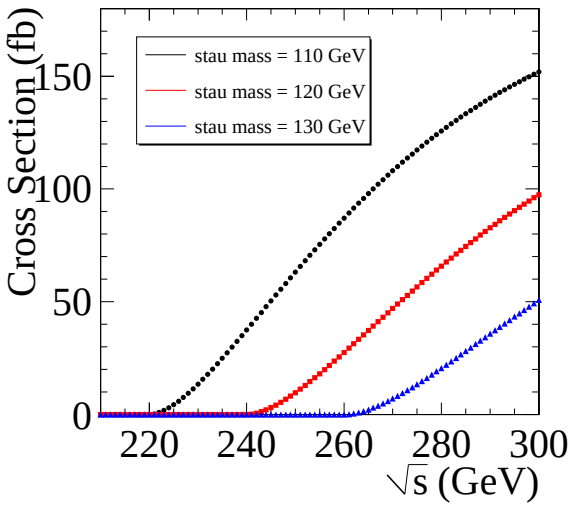

FIG. 2. Cross sections for $e^+e^- \to \tilde{\tau}^+\tilde{\tau}^-$ with polarized beams $(P_{e^-}, P_{e^+}) = (80\%, -30\%)$ for different stau mass.

events. In addition, the missing mass is required to be $M_{\rm miss} > 122\,{\rm GeV}$, and the polar angle of the missing momentum direction $|\cos\theta_{\rm miss}| < 0.82$. Lepton identification based on calorimeter energy deposition is applied to reject track pairs which are identified as ee or $\mu\mu$, which suppresses additional SM background. The estimated yields for the event selection are summarized in Tab. II.

Based on the resulting precision of the cross sections, a study of toy Monte-Carlo (MC) experiments is performed to estimate the precision of mass determination. The cross sections of the signal with varying stau mass ($m_{\tilde{\tau}} = 115, 118, 120, 122, 125\,{\rm GeV}$) are computed at the three center-of-mass energies, to compare against the toy MC experiments. For each toy MC experiment, the signal and background yields are obtained using Poisson statistics. The χ^2 is computed for each center-of-mass-energy by taking the difference between the measured cross section and the theoretical value, for each stau mass value, divided by the uncertainty of the measured cross section, then squaring it:

$$\chi^2{}_i = \left(\frac{\sigma_i^{\rm exp} - \sigma_i^{\rm th}}{\Delta\sigma_i^{\rm exp}}\right)^2, \quad i = 250,\ 256,\ 261\,{\rm GeV} \qquad (2)$$

The χ^2 values as a function of the stau mass are then fit to a parabolic curve to extract the minimum value corresponding to the stau mass estimate. The toy MC is repeated 10,000 times; the resulting stau mass distribution is fit to a Gaussian curve as shown in Fig. 3 to extract the stau mass precision of 0.7 GeV (0.6%).

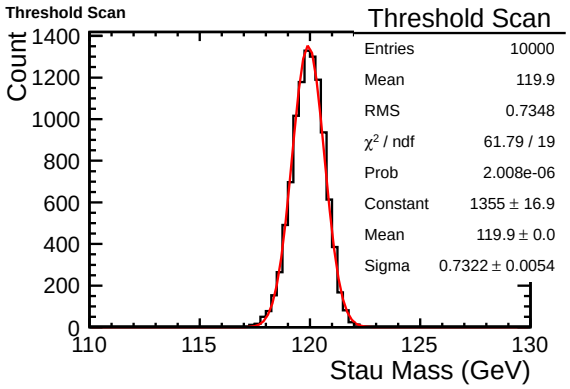

FIG. 3. Result of toy MC for the threshold scan.

IV. STAU MEASUREMENTS AT 500 GEV

The strategy to measure the stau lifetime is through the impact parameter distribution of the tau decay products. We choose $\sqrt{s} = 500\,{\rm GeV}$ as the center-of-mass energy for this analysis, as the boost of the stau helps in determining its lifetime. An alternative way to obtain the stau mass through the detection of the kinematic edges of the stau decay products is also presented. While the precision obtained from this method is not expected to exceed that from the cross section scan, the kinematic edge method does not require additional data taking and thus offers a complementary way to determine the mass. The assumed integrated luminosity is $500\,{\rm fb}^{-1}$. The event selection follows similarly to the threshold scan analysis.

A. Common event selection

We describe the event selection procedures which pertain to both the kinematic edge analysis and the lifetime analysis. The visible energy in the event is required to be greater than 50 GeV to suppress $\gamma\gamma$ backgrounds. The number of reconstructed tracks is required to be two, with opposite charges, each having transverse momentum greater than 5 GeV, to further suppress $\gamma\gamma$ backgrounds. The polar angle of each track is required to be $|\cos\theta| < 0.8$ to reduce the Bhabha scattering events. The difference in the azimuthal angles is required to be $\cos(\phi_2 - \phi_1) > -0.93$ to suppress the tau pair events. In order to discriminate the signal events from SM backgrounds, the following requirement based on the visible energy and the 3-dimensional angle $\theta_{\rm 3D}$ between the two tracks is imposed: $\theta_{\rm 3D}/E_{\rm vis} > 3^\circ/450\,{\rm GeV}$. The estimated yields of the event selection are summarized in Tab. III, assuming an integrated luminosity of $500\,{\rm fb}^{-1}$ and beam polarizations $(P_{e^-}, P_{e^+}) = (+0.8, -0.3)$.

TABLE II. Estimated yields in the threshold scan analysis at $\sqrt{s} = 250\,\text{GeV}$, normalized to an integrated luminosity of 250 fb^{-1} with beam polarizations $(P_{e^-}, P_{e^+}) = (+0.8, -0.3)$.

	$\tilde{\tau}^+\tilde{\tau}^-$ ($m_{\tilde{\tau}} = 250\,\text{GeV}$)	$\tilde{\tau}^+\tilde{\tau}^-$ ($m_{\tilde{\tau}} = 256\,\text{GeV}$)	$\tilde{\tau}^+\tilde{\tau}^-$ ($m_{\tilde{\tau}} = 261\,\text{GeV}$)	$\tau^+\tau^-$	$\gamma\gamma$, $e\gamma$, e^+e^-	$VV \to l^+l^-\nu\overline{\nu}$
1. No cut	970	2.00×10^3	2.94×10^3	8.04×10^5	–	3.72×10^4
2. Preselection	–	–	–	–	1.13×10^8	–
3. Number of tracks = 2	310	645	922	8.44×10^3	3.63×10^5	9.87×10^3
4. Strong preselection	238	505	731	3.84×10^3	1.23×10^4	6.87×10^3
5. $E_{\text{vis}} < 140\,\text{GeV}$	238	503	726	1.02×10^3	7.22×10^4	5.53×10^3
6. $\lvert\cos\theta_{\text{mis}}\rvert < 0.82$	227	482	694	580	1.03×10^3	5.06×10^3
7. $M_{\text{mis}} > 122.4\,\text{GeV}$	208	436	629	165	755	2.91×10^3
8. Lepton identification	178	387	548	138	358	1.80×10^3
9. $\lvert d_0/\sigma(d_0)\rvert > 4.0$ for each track	122	270	383	70.4	5.3	163

TABLE III. Estimated yields in the 500 GeV analysis, normalized to an integrated luminosity of 500 fb^{-1} with beam polarizations $(P_{e^-}, P_{e^+}) = (+0.8, -0.3)$.

	$\tilde{\tau}^+\tilde{\tau}^-$	$\tau^+\tau^-$	$\gamma\gamma$, $e\gamma$, e^+e^-	$VV \to l^+l^-\nu\overline{\nu}$
1. No cut	6.81×10^4	6.34×10^5	–	2.08×10^5
2. Preselection	–	–	4.74×10^7	–
3. Number of tracks = 2	4.57×10^4	3.08×10^5	2.19×10^7	9.67×10^4
4. $p_T > 5\,\text{GeV}$ for each track	3.36×10^4	2.28×10^5	7.49×10^6	8.30×10^4
5. $E_{\text{vis}} > 50\,\text{GeV}$	3.05×10^4	2.25×10^5	4.06×10^6	8.25×10^4
6. $\lvert\cos\theta\rvert < 0.8$ for each track	2.50×10^4	1.21×10^5	2.92×10^6	1.96×10^4
7. $\cos(\phi_2 - \phi_1) > -0.93$	1.49×10^4	9.15×10^3	2.71×10^6	1.07×10^4
8. $\theta_{3\text{D}}/E_{\text{vis}} > 3.0^\circ/\,450\,\text{GeV}$	1.46×10^4	1.06×10^3	9.21×10^5	7.44×10^3
Selections 1–8 are common to both analyses at 500 GeV.				
9. $\lvert\cos\theta_{\text{mis}}\rvert < 0.9$	1.44×10^4	779	3.25×10^3	7.11×10^3
10. Lepton identification (loose)	1.20×10^4	560	129	1.65×10^3
Selections 1–10 are used for the lifetime measurement.				
A. $\lvert d_0/\sigma(d_0)\rvert > 1.0$ for each track	1.38×10^4	753	8.25×10^4	1.07×10^3
B. $\lvert\Delta E_{\text{jet}}\rvert > 100\,\text{GeV}$	2.31×10^3	570	5.95×10^4	301
C. Lepton identification (loose)	2.14×10^3	404	1.13×10^4	132
D. $180 < E_{\text{trk}} < 250\,\text{GeV}$	201	0.0	0.0	85.6
E. Lepton identification (tight)	186	0.6	0.0	0.3
Selections 1–8 and A–E are used for the mass determination via kinematic edges.				
Selections D and E are applied to individual tracks.				

B. Stau lifetime determination

Additional selections are imposed for the analysis of the stau lifetime. The angle of the missing momentum is required to be $\lvert\cos\theta_{\text{miss}}\rvert < 0.9$ for the suppression of $\gamma\gamma$ and Bhabha scattering events. The energy depositions in the ECAL and HCAL are used to identify leptons; the event configuration with ee or $\mu\mu$ are rejected to further reduce SM backgrounds. The estimated yields of the event selection are summarized in Tab. III.

We investigate the stau lifetime determination method which takes exploits the dependence the transverse impact parameter distribution on the stau lifetime. The transverse impact parameter distribution after the event selection is shown in Fig. 4 for a stau mass of 120 GeV and lifetime of $c\tau = 100\,\mu\text{m}$. High statistics signal samples with various stau lifetime are generated and simulated for the purpose of template fits. The template samples are chosen to have lifetimes of $c\tau = (90, 95, 100, 105, 110)\,\mu\text{m}$. The expected backgrounds are included, as shown in Fig. 4, for the case of $c\tau = 100\,\mu\text{m}$. We perform toy MC experiments, each experiment consisting of distributions based on the $c\tau = 100\,\mu\text{m}$ sample with Poisson statistics folded in, according to the number of events expected for an integrated luminosity of $500\,\text{fb}^{-1}$. The resulting events are put into a histogram of $N = 200$ bins, which are then compared against the template samples, to compute the χ^2 quantity, defined as

$$\chi^2 = \sum_{i=1}^{N} \left(\frac{n_i^{\text{exp}} - n_i^{\text{templ}}}{\Delta n_i^{\text{exp}}} \right)^2 \tag{3}$$

where N is the number of bins, and n_i^{exp} (n_i^{exp}) is the number of events in the i-th bin for the experiment (tem-

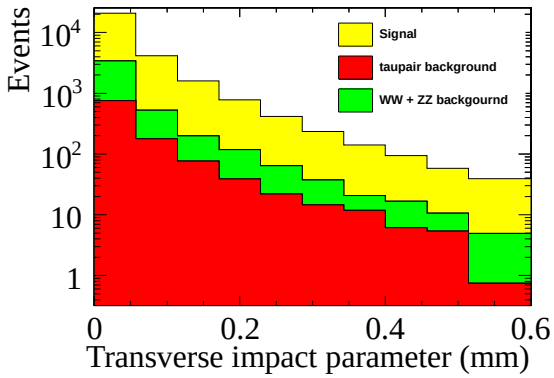

FIG. 4. The transverse impact parameter distributions for signal and background processes after the event selection. Each events contains two tracks, each of which carries a weight of 0.5.

plate) sample. The χ^2 is computed for the five template samples corresponding to the five different stau lifetime. The χ^2 points are fit to a parabolic curve, whose minimum is used as the estimate of the stau lifetime for this experiment. The toy MC experiments are performed 10,000 times. We extract the expected precision for stau lifetime from the resulting distribution of the χ^2 minima. As a result, it is 1.4% for an integrated luminosity of $500\,\mathrm{fb}^{-1}$ and beam polarizations of $(P_{e^-}, P_{e^+}) = (+0.8, -0.3)$.

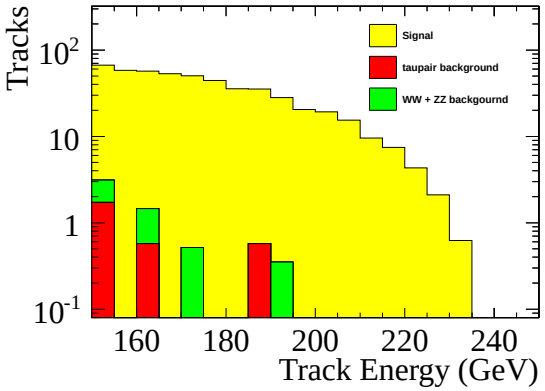

FIG. 5. Track energy distributions for signal and background processes after the event selection.

C. Stau mass determination via kinematic edges

The event selection is reoptimized for the stau mass measurement through kinematic edges. Starting with the common sample as described in Sec. IV A, additional requirements are imposed as follows. The requirement on the transverse impact parameter significance $|d_0/\sigma(d_0)| > 1.0$ is used to suppress discrimination of signal and background events. A tight lepton identification is applied. The fit region in the track energy is restricted to be in the range of $150 < E_{\mathrm{trk}} < 250\,\mathrm{GeV}$. Furthermore, the energy of the track and the surrounding neutral clusters as identified by jet finders with the number of jets $N_{\mathrm{jet}} = 2$ is used to discriminate the heavy mass of stau from lighter SM particles by placing a requirement on the difference in the energy such that $|\Delta E_{\mathrm{jet}}| > 100\,\mathrm{GeV}$. The estimated yields are summarized in Tab. III.

The mass distribution is modeled via the following function

$$f(x) = \alpha(\beta - x)\exp(-\gamma x)\,\theta(\beta - x) \qquad (4)$$

where α, β, and γ are fit parameters constrained to be positive, and $\theta(x)$ is the Heaviside step function to ensure positivity along the mass distribution. The value of β is used to extract the edge position. Again, toy MC experiments are performed to estimate the precision of the stau mass determination. The result is $\Delta m/m = \Delta\beta/\beta = 1.4\%$ for an integrated luminosity of $500\,\mathrm{fb}^{-1}$ and beam polarizations of $(P_{e^-}, P_{e^+}) = (+0.8, -0.3)$. This result however depends on the stau lifetime having $100 = \mu$m as we have applied the requirement on the transverse impact parameter.

V. CONCLUSIONS

In this study, we have looked at the low-scale GMSB scenario with R-parity conservation and the stau as the NLSP, working with the stau mass of 120 GeV and lifetime of $c\tau = 100\,\mu$m as a benchmark point. Throughout this study, the beam polarizations are assumed to be $(\mathrm{P_{e^-}}, \mathrm{P_{e^+}}) = (+80\%, -30\%)$. The precision of stau mass was evaluated for one-prong tau decays at two different energies: $\sqrt{s} = 250$ and 500 GeV. In the former case, the mass is determined through the scan of cross section near the threshold; its precision is found to be 0.6% with an integrated luminosity of $250\,\mathrm{fb}^{-1}$. In the latter case, the kinematic edge of the decay products is used; the precision is found to be 1.4% with an integrated luminosity of $500\,\mathrm{fb}^{-1}$. The precision of the stau lifetime determined from the impact parameter distribution at $\sqrt{s} = 500\,\mathrm{GeV}$ is found to be 1.4% with an integrated luminosity of $500\,\mathrm{fb}^{-1}$. This translates to the precision of the gravitino mass of 1.7 (3.6)% when combining the lifetime determination with the mass from the threshold scan (kinematic edge). These numbers take into account only the statistical uncertainty. The determination of the stau lifetime using three-prong decays of the tau lepton should be attempted in future studies.

VI. ACKNOWLEDGMENTS

The authors would like to thank T. Moroi, and the members of the ILC Physics Working Group for valu-

able discussions. This work was supported in part by the Grant-in-Aid for Specially Promoted Research No. 23000002 by the Japan Society for Promotion of Science.

[1] K. A. Intriligator and N. Seiberg, Class. Quant. Grav. 24, S741 (2007).
[2] M. Dine and A. E. Nelson, Phys. Rev. D 48, 1277 (1993); M. Dine, A. E. Nelson and Y. Shirman, Phys. Rev. D 51, 1362 (1995); M. Dine, A. E. Nelson, Y. Nir and Y. Shirman, Phys. Rev. D 53, 2658 (1996).
[3] T. Moroi, hep-ph/9503210.
[4] S. Shirai, M. Yamazaki and K. Yonekura, JHEP **1006**, 056 (2010) [arXiv:1003.3155 [hep-ph]].
[5] S. Matsumoto and T. Moroi, Phys. Lett. B **701**, 422 (2011) [arXiv:1104.3624 [hep-ph]].
[6] http://www-jlc.kek.jp/subg/offl/physsim/.
[7] H. Murayama, I. Watanabe, and K. Hagiwara, , KEK Report No. 91-11 (1992).
[8] S. Kawabata, Comput. Phys. Commun., 41, 127 (1986).
[9] W. Kilian, T. Ohl and J. Reuter, Eur. Phys. J. C **71**, 1742 (2011) [arXiv:0708.4233 [hep-ph]].
[10] T. Sjostrand, L. Lonnblad, S. Mrenna and P. Z. Skands, hep-ph/0308153.
[11] S. Jadach, Z. Ws, R. Decker, JH. Kuehn, Comp. Phys. Comm. 76 361 (1993).
[12] S. Agostinelli et al. [GEANT4 Collaboration], "GEANT4: A simulation toolkit," Nucl.Instrum. Meth. A 506 (2003) 250.
[13] J.-C. Brient and H. Videau, (2002), arXiv:hep-ex/0202004.

Precision study of the minimal $B-L$ model using the SUSY-Toolbox

Ben O'Leary[1], Thorsten Ohl[1], Werner Porod[1], Christian Speckner[2], Florian Staub[1,3]
[1]Institut für Theoretische Physik und Astrophysik, Universität Würzburg, 97074 Würzburg, Germany
[2]Albert-Ludwigs-Universität Freiburg, Physikalisches Institut, 79104 Freiburg, Germany
[3]Physikalisches Institut der Universität Bonn, 53115 Bonn, Germany

DOI: will be assigned

We discuss a CMSSM variant of the minimal, supersymmetric $B-L$ extension of the minimal supersymmetric standard model. This model provides many new, phenomenological aspects because it extends not only the gauge, but also the Higgs, the neutralino, the neutrino and the sneutrino sector. We demonstrate how the SUSY-Toolbox can be used to perform a comprehensive study of this model with a precision needed for a linear collider. This includes a calculation of the mass spectrum based on two-loop RGEs and a complete one-loop renormalization using SPheno and the possibility performing exhaustive collider studies due to a full-fledged implementation in well-tested Monte-Carlo tools like WHIZARD or CalcHep. In addition, checks of Higgs and dark matter constraints can be applied using HiggsBounds and MicrOmegas. This tool-chain is based on the easy implementation of new models in the SARAH.

1 Introduction

Models with an additional $U(1)_{B-L}$ gauge symmetry at the TeV scale have recently received considerable attention: they can explain neutrino data, they might help to understand the origin of R-parity and its possible spontaneous violation in supersymmetric models [1, 2, 3] as well as the mechanism of leptogenesis [4, 5] and they provide a rich phenomenology by introducing new states in the Higgs, the neutralino and the neutrino/sneutrino sector. This has already observable consequences at the LHC [6, 7, 8, 9], which will be most likely much more pronounced at a linear collider (LC).
An extended gauge sector containing $U(1)_Y \times U(1)_{B-L}$ can be embedded in an $E_8 \times E_8$ heterotic string theory [10]. We include in our study [11] a detailed analysis of impact of kinetic mixing what has been neglected so far in literature [3, 12]. It is well known that in models with several $U(1)$ gauge groups, kinetic mixing terms

$$-\chi_{ab}\hat{F}^{a,\mu\nu}\hat{F}^{b}_{\mu\nu}, \quad a \neq b \tag{1}$$

between the field strength tensors are allowed by gauge and Lorentz invariance [13], see *e.g.* [14]. Even if these terms are absent at tree level at a particular scale, they might be generated by RGE effects [15, 16]. To perform our studies we have used the environment provided by the SUSY-Toolbox [17]. The SUSY-Toolbox includes scripts to download, to configure and to install the public codes CalcHep [18, 19], HiggsBounds [20, 21], MicrOmegas [22], SARAH [23, 24, 25], SPheno [26, 27], SSP and WHIZARD [28, 29]. In addition, it gives the possibility for a one-step implementation of new SUSY models in all packages based on the implementation in SARAH.We discuss the implementation of the model presented in [1, 3] in SARAH and present results of our detailed analysis concerning the mass spectrum using SPheno [11]. In particular we will demonstrate that gauge kinetic mixing effects are particularly important in the Higgs and neutralino sectors. These effects do not only change the masses of these particles but have quite some impact of their nature, *e.g.* they induce tree-level mixing which would be absent if these effects were to be neglected. Therefore, it should be no longer neglected in the analysis of this and similar models, especially with regard to the precision necessary for a LC.
We will show that new light Higgs states are possible without being in conflict with current data while having

Superfield	Spin 0	Spin $\frac{1}{2}$	Generations	$(U(1)_Y \otimes SU(2)_L \otimes SU(3)_C \otimes U(1)_{B-L})$
$\hat{Q}$	$\tilde{Q}$	Q	3	$(\frac{1}{6}, \mathbf{2}, \mathbf{3}, \frac{1}{6})$
$\hat{D}$	$\tilde{d}^c$	d^c	3	$(\frac{1}{3}, \mathbf{1}, \overline{\mathbf{3}}, -\frac{1}{6})$
$\hat{U}$	$\tilde{u}^c$	u^c	3	$(-\frac{2}{3}, \mathbf{1}, \overline{\mathbf{3}}, -\frac{1}{6})$
$\hat{L}$	$\tilde{L}$	L	3	$(-\frac{1}{2}, \mathbf{2}, \mathbf{1}, -\frac{1}{2})$
$\hat{E}$	$\tilde{e}^c$	e^c	3	$(1, \mathbf{1}, \mathbf{1}, \frac{1}{2})$
$\hat{\nu}$	$\tilde{\nu}^c$	ν^c	3	$(0, \mathbf{1}, \mathbf{1}, \frac{1}{2})$
$\hat{H}_d$	H_d	$\tilde{H}_d$	1	$(-\frac{1}{2}, \mathbf{2}, \mathbf{1}, 0)$
$\hat{H}_u$	H_u	$\tilde{H}_u$	1	$(\frac{1}{2}, \mathbf{2}, \mathbf{1}, 0)$
$\hat{\eta}$	η	$\tilde{\eta}$	1	$(0, \mathbf{1}, \mathbf{1}, -1)$
$\hat{\bar{\eta}}$	$\bar{\eta}$	$\tilde{\bar{\eta}}$	1	$(0, \mathbf{1}, \mathbf{1}, 1)$

Table 1: Chiral superfields and their quantum numbers.

matter aspects using `MicrOmegas`: we show that in our model the nature of lightest supersymmetric particle (LSP) can be quite different in comparison to the minimal supersymmetric standard model (MSSM). We identify regions where it is either mainly a $SU(2)_L$-doublet Higgsino, a $U(1)_{B-L}$-gaugino which we dub the BLino, or a fermionic partner of the $U(1)_{B-L}$-breaking scalar which we dub the bileptino. It turns out that the BLino and the bileptino can have the correct abundance for being valid dark matter candidates [30].

2 The Model

2.1 Particle content and superpotential

The model under consideration, called $B-L$SSM in the following, extends the MSSM matter content by three generations of right-handed neutrino superfields. Moreover, below the GUT scale the usual MSSM Higgs doublets are present as well as two fields η and $\bar{\eta}$ responsible for the breaking of the $U(1)_{B-L}$. Furthermore, η is responsible for generating a Majorana mass term for the right-handed neutrinos and thus we call this field a bilepton. We summarize the quantum numbers of the chiral superfields with respect to $U(1)_Y \times SU(2)_L \times SU(3)_C \times U(1)_{B-L}$ in Table 1.

The superpotential is given by

$$W = Y_u^{ij}\,\hat{U}_i\,\hat{Q}_j\,\hat{H}_u - Y_d^{ij}\,\hat{D}_i\,\hat{Q}_j\,\hat{H}_d - Y_e^{ij}\,\hat{E}_i\,\hat{L}_j\,\hat{H}_d + \mu\,\hat{H}_u\,\hat{H}_d + Y_\nu^{ij}\,\hat{L}_i\,\hat{H}_u\,\hat{\nu}_j - \mu'\,\hat{\eta}\,\hat{\bar{\eta}} + Y_x^{ij}\,\hat{\nu}_i\,\hat{\eta}\,\hat{\nu}_j \tag{2}$$

and we have the additional soft SUSY-breaking terms:

$$\begin{aligned} L_{SB} =& L_{MSSM} - \lambda_{\tilde{B}}\lambda_{\tilde{B}'}M_{BB'} - \frac{1}{2}\lambda_{\tilde{B}'}\lambda_{\tilde{B}'}M_{B'} - m_\eta^2|\eta|^2 - m_{\bar{\eta}}^2|\bar{\eta}|^2 - m_{\nu,ij}^2(\tilde{\nu}_i^c)^*\tilde{\nu}_j^c \\ & - \eta\bar{\eta}B_{\mu'} + T_\nu^{ij}H_u\tilde{\nu}_i^c\tilde{L}_j + T_x^{ij}\eta\tilde{\nu}_i^c\tilde{\nu}_j^c \end{aligned} \tag{3}$$

i, j are generation indices. The extended gauge group breaks to $SU(3)_C \otimes U(1)_{em}$ as the Higgs fields and bileptons receive vacuum expectation values (VEVs):

$$H_d^0 = \frac{1}{\sqrt{2}}\left(\sigma_d + v_d + i\phi_d\right), \qquad H_u^0 = \frac{1}{\sqrt{2}}\left(\sigma_u + v_u + i\phi_u\right) \tag{4}$$

$$\eta = \frac{1}{\sqrt{2}}\left(\sigma_\eta + v_\eta + i\phi_\eta\right), \qquad \bar{\eta} = \frac{1}{\sqrt{2}}\left(\sigma_{\bar{\eta}} + v_{\bar{\eta}} + i\phi_{\bar{\eta}}\right) \tag{5}$$

We define $\tan\beta' = \frac{v_\eta}{v_{\bar{\eta}}}$ in analogy to the ratio of the MSSM VEVs ($\tan\beta = \frac{v_u}{v_d}$).

2.2 Gauge kinetic mixing

As already mentioned in the introduction, the presence of two Abelian gauge groups in combination with

one Abelian gauge group: the gauge kinetic mixing. This can be seen most easily by inspecting the matrix of the anomalous dimension, which at one loop is given by $\gamma_{ab} = \frac{1}{16\pi^2}\mathrm{Tr}Q_aQ_b$, where the indices a and b run over all $U(1)$ groups and the trace runs over all fields charged under the corresponding $U(1)$ group. For our model we obtain

$$\gamma = \frac{1}{16\pi^2} N \begin{pmatrix} 11 & 4 \\ 4 & 6 \end{pmatrix} N. \tag{6}$$

and we see that there are sizable off-diagonal elements. N contains the GUT normalization of the two Abelian gauge groups. We will take as in ref. [3] $\sqrt{\frac{3}{5}}$ for $U(1)_Y$ and $\sqrt{\frac{3}{2}}$ for $U(1)_{B-L}$, i.e. $N = \mathrm{diag}(\sqrt{\frac{3}{5}}, \sqrt{\frac{3}{2}})$. In practice it turns out that it is easier to work with non-canonical covariant derivatives instead of off-diagonal field-strength tensors such as in Eq. (1). However, both approaches are equivalent [31]. Hence in the following, we consider covariant derivatives of the form

$$D_\mu = \partial_\mu - iQ_\phi^T G A \tag{7}$$

where Q_ϕ is a vector containing the charges of the field ϕ with respect to the two Abelian gauge groups, G is the gauge coupling matrix

$$G = \begin{pmatrix} g_{YY} & g_{YB} \\ g_{BY} & g_{BB} \end{pmatrix} \tag{8}$$

and A contains the gauge bosons $A = (A_\mu^Y, A_\mu^B)^T$.

As long as the two Abelian gauge groups are unbroken, we have still the freedom to perform a change of basis. This freedom can be used to choose a basis such that electroweak precision data can be accommodated in an easy way. A convenient choice is the basis where $g_{BY} = 0$. Therefore we choose the following basis at the electroweak scale [32]:

$$g'_{YY} = \frac{g_{YY}g_{BB} - g_{YB}g_{BY}}{\sqrt{g_{BB}^2 + g_{BY}^2}} = g_1\,, \qquad g'_{BB} = \sqrt{g_{BB}^2 + g_{BY}^2} = g_{BL} \tag{9}$$

$$g'_{YB} = \frac{g_{YB}g_{BB} + g_{BY}g_{YY}}{\sqrt{g_{BB}^2 + g_{BY}^2}} = \tilde{g}\,, \qquad g'_{BY} = 0 \tag{10}$$

Immediate consequences of this kinetic mixing are: (i) it induces mixing at tree level between the H_u, H_d and η, $\bar{\eta}$; (ii) additional D-terms contribute to the mass matrices of the squarks and sleptons; (iii) off-diagonal soft-SUSY breaking terms for the gauginos are induced via RGE evolution [31, 33] with important consequences for the neutralino sector, even if at some fixed scale $M_{ab} = 0$ for $a \neq b$.

2.3 Tadpole equations

We solve the minimum conditions at tree-level with respect to μ, B_μ, μ' and $B_{\mu'}$ as these parameters do not enter any of the RGEs of the other parameters. Using $x^2 = v_\eta^2 + v_{\bar{\eta}}^2$ and $v^2 = v_d^2 + v_u^2$ we find an approximate relation between M'_Z and μ'

$$M_{Z'}^2 \simeq -2|\mu'|^2 + \frac{4(m_{\bar{\eta}}^2 - m_\eta^2 \tan^2\beta') - v^2\tilde{g}g_{BL}\cos\beta(1+\tan\beta')}{2(\tan^2\beta' - 1)} \tag{11}$$

A closer inspection of the system shows that either $m_{\bar{\eta}}^2$ or m_η^2 has to become negative to break $U(1)_{B-L}$. Because of the structure of the RGEs [11], $m_{\bar{\eta}}$ will always be positive whereas m_η^2 can become negative for sufficient large Y_x and T_x. In addition, we expect that large values of m_0 and A_0 will be preferred, implying heavy sfermions. Moreover, $\tan\beta'$ has to be small and of $O(1)$ in order to get a small denominator in the second term of Eq. 11.

For the numerical results we include one-loop corrections to the tadpole equations as well as for all masses. This is done by using the $\overline{\mathrm{DR}}$ scheme and extending the MSSM results given in ref. [34] in a similar

2.4 Gauge boson mixing

Due to the presence of the kinetic mixing terms, the B' boson mixes at tree level with the B and W^3 bosons. Requiring the conditions of Eqs. (9)-(10) means that the corresponding mass matrix reads, in the basis (B, W^3, B'),

$$\begin{pmatrix} \frac{1}{4}g_1^2v^2 & -\frac{1}{4}g_1g_2v^2 & \frac{1}{4}g_1\tilde{g}v^2 \\ -\frac{1}{4}g_1g_2v^2 & \frac{1}{4}g_2^2v^2 & -\frac{1}{4}\tilde{g}g_2v^2 \\ \frac{1}{4}g_1\tilde{g}v^2 & -\frac{1}{4}\tilde{g}g_2v^2 & (g_{BL}^2x^2+\frac{1}{4}\tilde{g}^2v^2) \end{pmatrix} \tag{12}$$

In the limit $\tilde{g} \to 0$ both sectors decouple and the upper 2×2 block is just the standard mass matrix of the neutral gauge bosons in EWSB. This mass matrix can be diagonalized by a unitary mixing matrix to get the physical mass eigenstates γ, Z and Z'. Expanding the eigenvalues in powers of v^2/x^2, we find up to first order:

$$M_Z = \frac{1}{4}\left(g_1^2+g_2^2\right)v^2\,, \qquad M_{Z'} = g_{BL}^2x^2 + \frac{1}{4}\tilde{g}^2v^2 \tag{13}$$

All parameters so far as well as in the following mass matrices are understood as running parameters at a given renormalization scale Q.

2.5 The Higgs sector

In this section we present the tree-level formulas for the Higgs sector and we briefly discuss the main steps to include the one-loop corrections. The one-loop formulas and further details will be presented elsewhere [36].

2.5.1 Pseudo scalar Higgs bosons

It turns out that in this sector there is no mixing between the $SU(2)$ doublets and the bileptons at tree level and we obtain in the basis $(\phi_d, \phi_u, \phi_\eta, \phi_{\bar{\eta}})$:

$$m_{A,T}^2 = \begin{pmatrix} B_\mu \tan\beta & B_\mu & 0 & 0 \\ B_\mu & B_\mu \cot\beta & 0 & 0 \\ 0 & 0 & B_{\mu'}\tan\beta' & B_{\mu'} \\ 0 & 0 & B_{\mu'} & B_{\mu'}\cot\beta' \end{pmatrix}. \tag{14}$$

Obviously, both sectors decouple at tree level. One obtains two physical states A^0 and A_η^0 with masses

$$m_{A^0}^2 = \frac{2B_\mu}{\sin 2\beta}\,, \qquad m_{A_\eta^0}^2 = \frac{2B_{\mu'}}{\sin 2\beta'}\,. \tag{15}$$

2.5.2 Scalar Higgs bosons

In the scalar sector the gauge kinetic terms do induce a mixing between the $SU(2)$ doublet Higgs fields and the bileptons. The mass matrix reads at tree level in the basis $(\sigma_d, \sigma_u, \sigma_\eta, \sigma_{\bar{\eta}})$:

$$m_{h,T}^2 = \begin{pmatrix} m_{A^0}^2 s_\beta^2 + \bar{g}^2 v_u^2 & -m_{A^0}^2 c_\beta s_\beta - \bar{g}^2 v_d v_u & \frac{\tilde{g}g_{BL}}{2}v_d v_\eta & -\frac{\tilde{g}g_{BL}}{2}v_d v_{\bar{\eta}} \\ -m_{A^0}^2 c_\beta s_\beta - \bar{g}^2 v_d v_u & m_{A^0}^2 c_\beta^2 + \bar{g}^2 v_d^2 & -\frac{\tilde{g}g_{BL}}{2}v_u v_\eta & \frac{\tilde{g}g_{BL}}{2}v_u v_{\bar{\eta}} \\ \frac{\tilde{g}g_{BL}}{2}v_d v_\eta & -\frac{\tilde{g}g_{BL}}{2}v_u v_\eta & m_{A_\eta^0}^2 c_{\beta'}^2 + g_{BL}^2 v_\eta^2 & -m_{A_\eta^0}^2 c_{\beta'}s_{\beta'} - g_{BL}^2 v_\eta v_{\bar{\eta}} \\ -\frac{\tilde{g}g_{BL}}{2}v_d v_{\bar{\eta}} & \frac{\tilde{g}g_{BL}}{2}v_u v_{\bar{\eta}} & -m_{A_\eta^0}^2 c_{\beta'}s_{\beta'} - g_{BL}^2 v_\eta v_{\bar{\eta}} & m_{A_\eta^0}^2 s_{\beta'}^2 + g_{BL}^2 v_{\bar{\eta}}^2 \end{pmatrix} \tag{16}$$

where we have defined $\bar{g}^2 = \frac{1}{4}(g_1^2+g_2^2+\tilde{g}^2)$, $c_x = \cos(x)$ and $s_x = \sin(x)$ $(x = \beta, \beta')$. The one-loop corrections are included by calculating the real part of the poles of the corresponding propagator matrices [34, 36]

where

$$m^2_{h,1L}(p^2) = m^{2,h}_T - \Pi_{hh}(p^2). \tag{18}$$

Equation (17) has to be solved for each eigenvalue $p^2 = m_i^2$ which can be achieved in an iterative procedure, see [35].

2.6 Neutralinos

In the neutralino sector we find that the gauge kinetic effects lead to a mixing between the usual MSSM neutralinos with the additional states, similar to the mixing in the CP-even Higgs sector. The mass matrix reads in the basis $\left(\lambda_{\tilde{B}}, \tilde{W}^0, \tilde{H}^0_d, \tilde{H}^0_u, \lambda_{\tilde{B}'}, \tilde{\eta}, \tilde{\bar{\eta}}\right)$

$$m_{\tilde{\chi}^0} = \begin{pmatrix} M_1 & 0 & -\frac{1}{2}g_1 v_d & \frac{1}{2}g_1 v_u & \frac{1}{2}M_{BB'} & 0 & 0 \\ 0 & M_2 & \frac{1}{2}g_2 v_d & -\frac{1}{2}g_2 v_u & 0 & 0 & 0 \\ -\frac{1}{2}g_1 v_d & \frac{1}{2}g_2 v_d & 0 & -\mu & -\frac{1}{2}\tilde{g} v_d & 0 & 0 \\ \frac{1}{2}g_1 v_u & -\frac{1}{2}g_2 v_u & -\mu & 0 & \frac{1}{2}\tilde{g} v_u & 0 & 0 \\ \frac{1}{2}M_{BB'} & 0 & -\frac{1}{2}\tilde{g} v_d & \frac{1}{2}\tilde{g} v_u & M_B & -g_{BL} v_\eta & g_{BL} v_{\bar{\eta}} \\ 0 & 0 & 0 & 0 & -g_{BL} v_\eta & 0 & -\mu' \\ 0 & 0 & 0 & 0 & g_{BL} v_{\bar{\eta}} & -\mu' & 0 \end{pmatrix} \tag{19}$$

In this model, for the chosen boundary conditions, the lightest supersymmetric particle (LSP), and therefore the dark matter candidate, is in general the lightest neutralino. The reason is that m_0 must be very heavy in order to solve the tadpole equations, and therefore all sfermions are heavier than the lightest neutralino. However, under special conditions also a CP even or odd sneutrinos can be the lightest SUSY particle. A neutralino LSP is in general a mixture of all seven gauge eigenstates. However, normally the character is dominated by only one or two constituents. In that context, we can distinguish the following extreme cases: (i) $M_1 \ll M_2, \mu, M_B, \mu'$: Bino-like LSP, (ii) $M_2 \ll M_1, \mu, M_B, \mu'$: Wino-like LSP, (iii) $\mu \ll M_1, M_2, M_B, \mu'$: Higgsino-like LSP, (iv) $M_B \ll M_1, M_2, \mu, \mu'$: BLino-like LSP, (v) $\mu' \ll M_1, M_2, \mu, M_B$: Bileptino-like LSP. Although the gauge kinetic effects do lead to sizable effects in the spectrum, they are not large enough to lead to a large mixing between the usual MSSM-like states and the new ones. Therefore, we find that the LSP is either mainly a MSSM-like state or mainly an admixture between the BLino and the bileptinos.

2.7 Sfermions and charginos

We don't consider here the the chargino and sfermion sector. Interested readers are referred to [11].

2.8 Boundary conditions at the GUT scale

We will study in the following a scenario motivated by minimal supergravity (mSUGRA). This means that we assume a GUT unification of all soft-breaking scalar masses as well as a unification of all gaugino mass parameters

$$m_0^2 = m^2_{H_d} = m^2_{H_u} = m^2_\eta = m^2_{\bar{\eta}} \tag{20}$$

$$m_0^2 \delta_{ij} = m^2_D \delta_{ij} = m^2_U \delta_{ij} = m^2_Q \delta_{ij} = m^2_E \delta_{ij} = m^2_L \delta_{ij} = m^2_\nu \delta_{ij} \tag{21}$$

$$M_{1/2} = M_1 = M_2 = M_3 = M_{\tilde{B}'} \tag{22}$$

Also, for the trilinear soft-breaking coupling, the ordinary mSUGRA conditions are assumed

$$T_i = A_0 Y_i, \qquad i = e, d, u, x, \nu\ . \tag{23}$$

We do not fix the parameters μ, B_μ, μ' and $B_{\mu'}$ at the GUT scale but determine them from the tadpole equations. In addition, we consider the mass of the Z' and $\tan\beta'$ as inputs and use the following set of free parameters

Y_ν is constrained by neutrino data and must therefore be very small in comparison to the other couplings. Y_x can always be taken diagonal and thus effectively we have 9 free parameters and two signs. If not mentioned otherwise, we will always take positive signs for μ and μ'. Finally, we assume that there are no off-diagonal gauge couplings or gaugino mass parameters present at the GUT scale

$$g_{BY} = g_{YB} = 0 \qquad M_{BB'} = 0 \tag{25}$$

3 Results obtained using the SUSY toolbox

In this section we discuss the implementation of the $B-L$SSM in the `SUSY-Toolbox` presented in [17]. The `SUSY-Toolbox` scripts can be downloaded from

`http://projects.hepforge.org/sarah/Toolbox.html`

After the installation of all packages via `configure` and `make`, each model implemented in `SARAH` can be added to the other tools due to

```
> ./butler MODEL
```

3.1 Implementation of the $B-L$SSM in SARAH

`SARAH` is a package for `Mathematica` version 5.2 or higher and has been designed to handle every $N = 1$ SUSY theory with an arbitrary direct product of $SU(n)$ and/or $U(1)$ factors as gauge group. The chiral superfields can transform under arbitrary, irreducible representations with regard to this gauge group, and all possible renormalizable superpotential terms are supported. There are no restrictions on either the number of gauge group factors, the number of chiral superfields or the number of superpotential terms. Furthermore, any number of symmetry breakings or field rotations is allowed.
The implementation of new models in `SARAH` is straightforward. The fastest and easiest way is usually to start with the model files for the MSSM and apply the changes necessary for the new mode. For instance, to create a new gauge group according to $U(1)_{B-L}$, only one line has to be added to the array `Gauge`

```
Gauge[[1]]={B,   U[1], hypercharge, g1,False};
Gauge[[2]]={WB, SU[2], left,        g2,True};
Gauge[[3]]={G,  SU[3], color,       g3,False};
Gauge[[4]]={Bp,  U[1], BminusL,     g1p, False};
```

and afterwards the corresponding quantum numbers for all MSSM fields and the new $B-L$ fields are defined:

```
Fields[[1]] = {{uL,  dL},  3, q,   1/6, 2, 3, 1/6};
...
Fields[[9]]  = {et, 1, eta, 0, 1, 1, -1};
Fields[[10]] = {etb, 1, etabar,  0, 1, 1, 1};
```

First, the root of the names is given, at second position the number of generations is defined and the third entry is the name of the entire superfield. The remaining entries are the transformation properties with respect to the different gauge groups. Using these definitions, the superpotential Eq. 2 can be defined as

```
SuperPotential = { {{1, Yu},{u,q,Hu}}, {{-1,Yd},{d,q,Hd}}, {{-1,Ye},{e,l,Hd}},
  {{1,\[Mu]},{Hu,Hd}}, {{1,Yv},{l,Hu,vR}}, {{-1,MuP},{eta,etabar}}, {{1,Yn},{vR,eta,vR}}  };
```

In addition, the definition of gauge symmetry breaking, the gauge fixing terms, the mixing in the gauge and matter sector have to be adjusted. Also, these changes are intuitive to understand and the entire model file is given in the appendix of [11]. Furthermore, the model files are already part of the public version of `SARAH` and can be used out of the box.
Using this model file `SARAH` calculates analytically all mass matrices, vertices as well as the two-loop Renormalization Group Equations (RGEs) and one-loop corrections to self-energies and tadpoles. The calculation of the loop corrections is performed in $\overline{\text{DR}}$ scheme and 't Hooft gauge. This information can after-

OMEGA/WHIZARD, or to create modules for SPheno or just to write a LaTeX file containing all information in a readable form.

3.2 Spectrum calculation with SPheno

We start the calculation of the mass spectrum using SPheno. SPheno [26, 27] is a F95 program designed for the precise calculation of the masses of supersymmetric particles. SPheno provides fast numerically routines for the evaluation of the RGEs, calculating the phase space of 2- and 3-body decays as well as Passarino Veltman integrals and much more. Since these routines are model independent, they can be used for all SUSY models implemented in SARAH. As mentioned above SARAH calculates all analytical expressions needed for a complete analysis of the model. This information is exported to Fortran code in a way suitable for inclusion in SPheno. This generates a fully functional version of SPheno for the new model without any need to change the source code by hand. The SPheno version generated by SARAH calculates the complete mass spectrum using 2-loop RGEs and 1-loop corrections to the masses, including the full momentum dependence of all loop integrals. In addition, for MSSM-like Higgs sectors, the known two loop corrections to the Higgs masses and tadpoles can be included. All calculations are performed with the most general flavor structure and allow for the inclusion of CP phases and fully support kinetic mixing. To show the importance of the

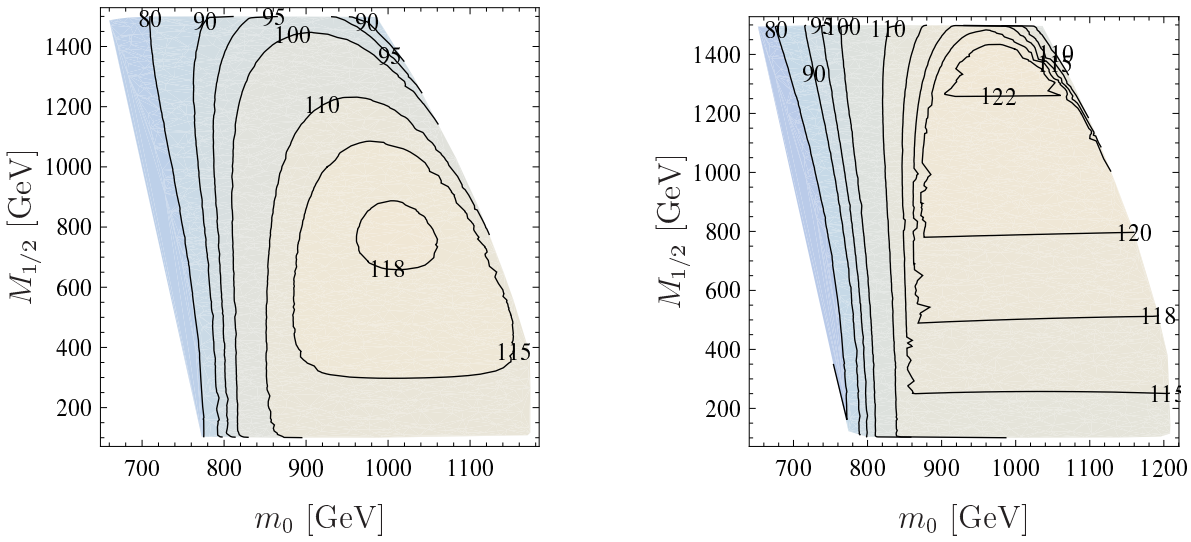

Figure 1: Mass of the lightest Higgs. The other parameters have been $\tan(\beta) = 10$, $A_0 = -1000$ GeV, $\tan(\beta') = 1.07$, $M_{Z'} = 3000$ GeV, $Y_x^{ii} = 0.41$. Left: with kinetic mixing, right: without kinetic mixing.

kinetic mixing we give in Fig. 1 a comparison between the mass and bilepton fraction of the lightest with and without kinetic mixing. It can be seen that the masses are only slightly shifted while, of course, there is a huge difference of several orders in the bilepton fraction between both cases. While the bilepton contribution for MSSM-like scalars in the case without kinetic mixing is solely based on the mixing at one-loop level, the off-diagonal gauge couplings introduce already a tree-level mixing. Close to the border of the allowed regions in the $(m_0, M_{1/2})$-plane shown in Fig. 1, the lightest Higgs particles become bilepton-like. This can not only be observed for a variation of m_0 and $M_{1/2}$ but also by adjusting $\tan\beta'$, as shown in Fig. 2 where we have fixed $m_0 = 1000$ GeV and $M_{1/2} = 500$ GeV. As can be seen in Fig. 2, the mass of the MSSM-like Higgs boson gets pushed to larger values for very light bilepton scalars. Such a behavior has already been observed in the literature when considering models with extended gauge symmetries [40, 41, 42, 43, 44, 45]. If the very light bileptons are consistent with all experimental data will be discussed in sec. 3.3. We turn now to the neutralino sector. Similarly to the CMSSM, the lightest neutralino is often bino-like and the main difference is, in this case, that the relation between the parameters at different scales gets changed due

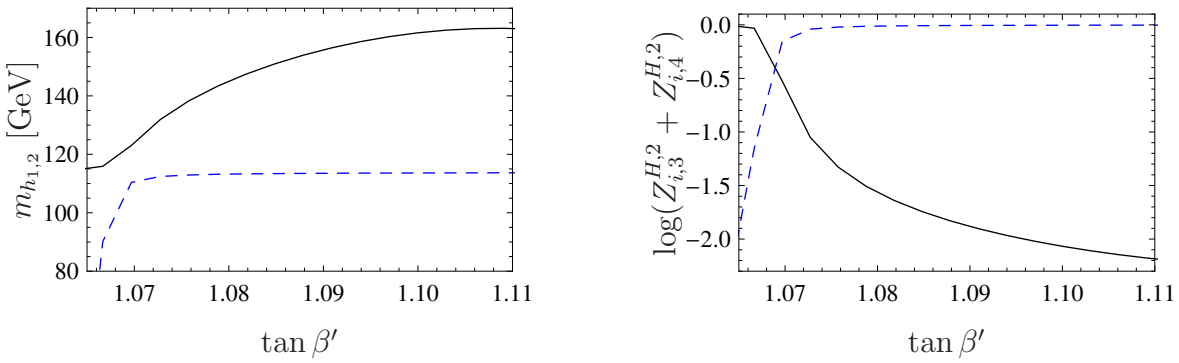

Figure 2: a) masses of two lightest scalars. b) doublet (green) and bilepton (blue) fraction of lightest Higgs as function of $\tan\beta'$. The other input parameters are $m_0 = 1$ TeV, $M_{1/2} = 500$ GeV, $\tan(\beta) = 20$, $A_0 = -1$ TeV, $M_{Z'} = 2750$ GeV, $Y_x^{ii} = 0.43$.

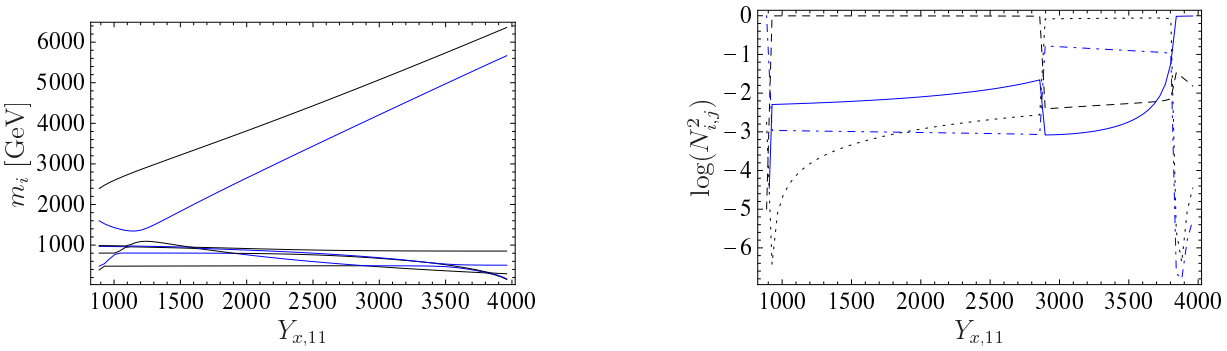

Figure 3: a) μ' as function of m_0. b) masses of all neutralinos. c) content of the lightest neutralino: gaugino fraction (red), Higgsino fraction (green), BLino fraction (blue) and bileptino fraction (black). The input parameters were $M_{1/2} = 1000$ GeV, $\tan\beta = 40, A_0 = 1500$ GeV, $\tan\beta' = 1.20, M_{Z'} = 2$ TeV.

always smaller than M_1, because, at one-loop level and without kinetic mixing, the relation

$$\frac{M_{1/2}}{g_{GUT}^2} = \frac{M_1}{g_Y^2} = \frac{M_{B'}}{g_{BL}^2} \tag{26}$$

would hold and g_{BL} is always smaller than g_Y if unification at the GUT scale is assumed, as can be seen in Eq. (6). However, usually there is a large mixing between the BLino with the bileptinos, leading to heavy states. However, there are regions where this mixing is small and the BLino becomes the LSP. In particular this happens if $\mu' \gg g_{BL}x \simeq M_{Z'}$ which happens either for large $|Y_x|$ or large m_0, as this increases the difference $m_{\tilde{\eta}}^2 - m_\eta^2$. As an example we show in Fig. 3 that μ' grows with increasing m_0 leading to a larger mass splitting between the bileptino-like neutralinos and the others. For very large values of μ', the bilepton fields are nearly decoupled and the nature of the LSP becomes BLino-like. Finally, we note that also a bileptino-like LSP can be obtained in this model. The necessary condition, $|\mu'|$ being smaller than $|\mu|$ and all gaugino mass parameters, can be obtained if the difference between m_η^2 and $m_{\tilde{\eta}}^2$ becomes small. This can be accommodated by adjusting the entries of Y_x. As an example, we show in Fig. 4 the masses of all neutralinos as well as the composition of the lightest neutralino as function of $Y_{x,11}$ while keeping all other values fixed. Already a 10 per-cent decrease leads to a nearly a pure bileptino LSP and its mass depends

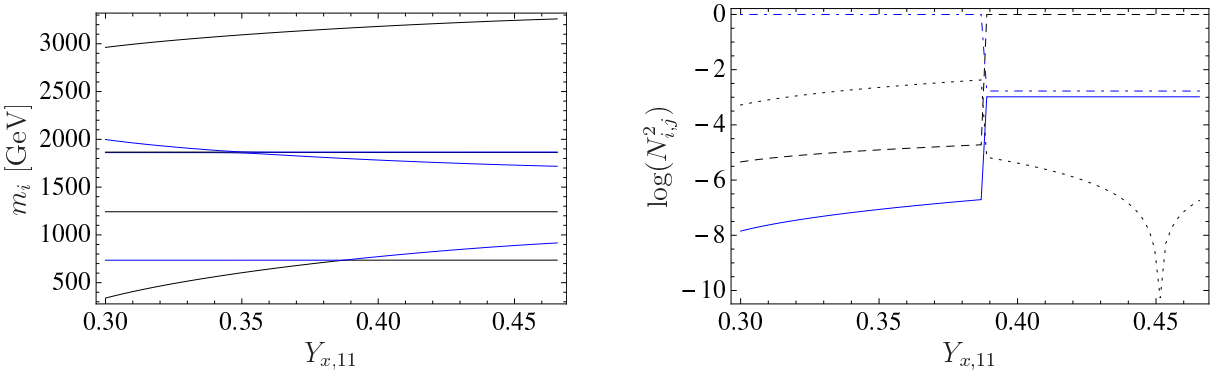

Figure 4: LSP with large bileptino fraction: a) mass of neutralinos, b) neutralino content. The color code on the right hand side is as follows: gaugino fraction (red), Higgsino fraction (green), BLino fraction (blue), bileptino fraction (black). The other parameters have been $m_0 = 1$ TeV, $M_{1/2} = 1.5$ TeV $\tan(\beta) = 20$, $A_0 = -1.5$ TeV, $\tan(\beta') = 1.15$, $M_{Z'} = 2.5$ TeV, $Y_x^{22} = Y_x^{33} = 0.40$

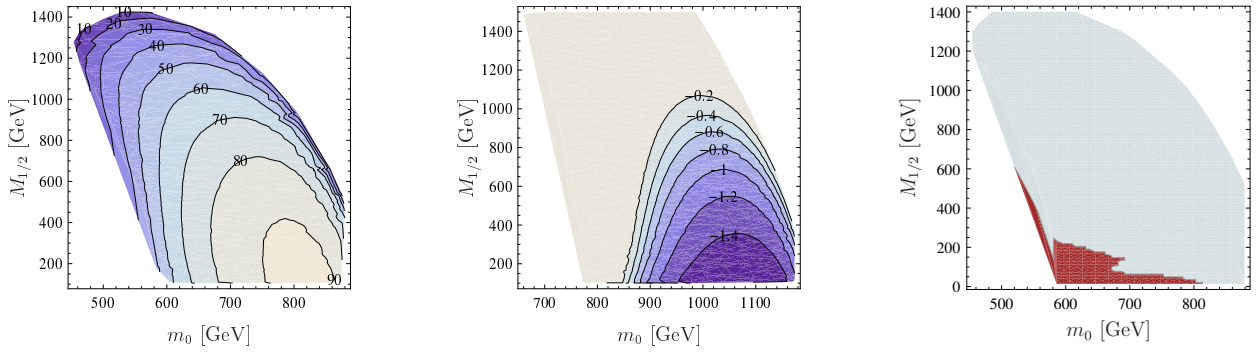

Figure 5: Mass of the two lightest Higgs fields (first row) as well as the logarithm of the bilepton fraction (left plot in second row) in the $(m_0, M_{1/2})$-plane. The right plot in the second row shows the saturation of the tightest bound (which is all cases $e^+e^- \to Zh_1, h_1 \to b\bar{b}$) as calculated by `HiggsBounds`: the blue area is allowed, the red one excluded by Higgs searches: The most sensitive channels are $e^+e^- \to Zh_2, h_2 \to b\bar{b}$, $pp \to A^0 \to \tau\bar{\tau}$ and $pp \to h_2 \to W^+W^-$. The other parameters are those of Fig. 2 and we used $\tan(\beta') = 1.075$.

3.3 Checking Higgs constraints with `HiggsBounds`

As show in Fig. 2 very light bilepton states can be present. Hence, existing constraints on Higgs masses coming from collider experiments have to be checked carefully. This can be done with `HiggsBounds`. `HiggsBounds` [20, 21] is a tool to test the neutral and charged Higgs sectors against the current exclusion bounds from the Higgs searches at the LEP, Tevatron and LHC experiments. The required input consists of the masses, width and branching ratios of the Higgs fields. In addition, it is either possible to provide full information about production cross sections in e^+e^- and pp collisions, or to work with a set of effective couplings. Although `HiggsBounds` supports the LesHouches interface, this functionality is restricted so far to at most 5 neutral Higgs fields, and therefore, we don't use it. Instead, `SPheno` modules generated by `SARAH` can create all necessary input files needed for a run of `HiggsBounds` with effective couplings (option `whichinput=effC`). We checked that very light bilepton-like Higgs scalars are not ruled out by experimental data using `HiggsBounds 3.6.1beta`. However, the mixing between the bilepton and the MSSM-like Higgs is rather small and thus the branching ratio $h_2 \to h_1 h_1$ is at most a few per-cent. Therefore, the main decay

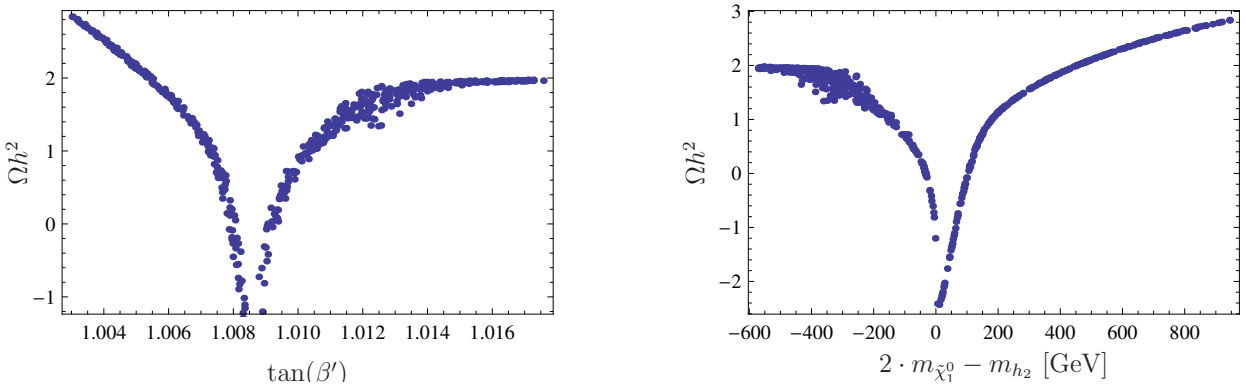

Figure 6: Left: $\log(\Omega h^2)$ as a function of $\tan(\beta')$. Right: mass difference between the LSP and twice the light bilepton scalar. The other parameters have been $m_0 \sim 2.8$ TeV, $M_{1/2} \sim 650$ GeV, $\tan\beta \sim 7$, $A_0 \sim -2.8$ TeV, $M_{Z'} \sim 3.2$ TeV, $Y_x^{ii} \sim 0.42$.

$\tan(\beta') = 1.075$ and vary m_0 and $M_{1/2}$. We see that there is a sizable region where the lightest Higgs, being essentially a bilepton, has a mass of less than half of the second lightest, which is mainly like the MSSM h^0. Even though the bilepton has only a small admixture of the doublet Higgs bosons, it is large enough to determine its main decay properties, which are mainly SM-like with respect to its decay into SM fermions.

3.4 Calculating dark matter relic density with `MicrOmegas`

It has been shown in sec. 3.2 that there are new possibilities for LSP coming from the $B-L$-sector. The question arises if a BLino- or a Bileptino-like neutralino can have the correct relic density for being the dark matter in the universe. To test this, we have used `MicrOmegas` . `MicrOmegas` [22] is a well known tool for the calculation of the relic density of a dark matter candidate. As `MicrOmegas` uses `CalcHep` for the calculation of (co-)annihilation cross sections, the `CalcHep` output of `SARAH` is sufficient to calculate the relic density for new models. As the SLHA+ import functionality of `CalcHep` [46] can also be used with `MicrOmegas`, it is sufficient to simply copy the spectrum file written by `SPheno` to the directory of `MicrOmegas` and start the calculation. It turns out that it is indeed possible to have valid BLino and Bileptino dark matter candidate [30]. For instance, we give in Fig. 6 the relic density as function of $\tan(\beta')$. Since the main annihilation comes from a resonance with the lightest bilepton scalar, there is a strong dependence on $\tan(\beta')$: not only the mass of the bilepton is sensitive to $\tan(\beta')$, but also the BLino-Bileptino mixing depends on it. For sufficient annihilation, not only $m_{\tilde{\chi}_1^0} = \frac{1}{2} m_{h_2}$ is needed but also some admixture of the bileptino to the BLino. Similarly, also the bileptino can annihilate via a bilepton resonance.

3.5 Collider studies with `WHIZARD`

Finally, it is of course very interesting to study the impact on the new states and the kinetic mixing effects on the phenomenology on a linear collider. Therefore, the next step in our study of the $B-L$MSSM will be to perform collider studies using `WHIZARD`. `WHIZARD` [29] is a fast tree-level Monte Carlo generator for parton level events. A particular strength of the code is the efficient generation of unweighted events for high multiplicity final states (simulations with 8 final state particles have been performed successfully) using exact matrix elements. This makes it particularly useful for the study of supersymmetric models which generically feature complicated multiparticle final states arising from long decay chains. The interface between `SARAH` and `WHIZARD` shares significant parts of its code with the interface between `FeynRules` [47], with a thin layer on top to interface with `SARAH`. In order to communicate the numerical values of the parameters calculated by `SPheno` to `WHIZARD`, each `SPheno` version generated by `SARAH` is capable of writing out a separate file

Acknowledgments

CS has been supported by the Deutsche Forschungsgemeinschaft through the Research Training Group GRK 1102 *Physics of Hadron Accelerators*. BOL, WP and TP have been supported by the German Ministry of Education and Research (BMBF) under contract no. 05H09WWEF.

4 Bibliography

*** ***

References

[1] S. Khalil and A. Masiero. Radiative B-L symmetry breaking in supersymmetric models. *Phys. Lett.*, B665:374–377, 2008.

[2] Vernon Barger, Pavel Fileviez Perez, and Sogee Spinner. Minimal gauged $U(1)_{B-L}$ model with spontaneous R-parity violation. *Phys. Rev. Lett.*, 102:181802, 2009.

[3] Pavel Fileviez Perez and Sogee Spinner. The Fate of R-Parity. *Phys. Rev.*, D83:035004, 2011.

[4] Juho Pelto, Iiro Vilja, and Heidi Virtanen. Leptogenesis in B-L gauged SUSY with MSSM Higgs sector. *Phys. Rev.*, D83:055001, 2011.

[5] K. S. Babu, Yanzhi Meng, and Zurab Tavartkiladze. New Ways to Leptogenesis with Gauged B-L Symmetry. *Phys. Lett.*, B681:37–43, 2009.

[6] W. Emam and S. Khalil. Higgs and Z' Phenomenology in B-L extension of the Standard Model at LHC. *Eur. Phys. J.*, C55:625–633, 2007.

[7] Lorenzo Basso, Alexander Belyaev, Stefano Moretti, and Claire H. Shepherd-Themistocleous. Phenomenology of the minimal B-L extension of the Standard model: Z' and neutrinos. *Phys. Rev.*, D80:055030, 2009.

[8] Lorenzo Basso, Stefano Moretti, and Giovanni Marco Pruna. Phenomenology of the minimal $B - L$ extension of the Standard Model: the Higgs sector. *Phys. Rev.*, D83:055014, 2011.

[9] Lorenzo Basso, Stefano Moretti, and Giovanni Marco Pruna. The Higgs sector of the minimal B-L model at future Linear Colliders. *Eur. Phys. J.*, C71:1724, 2011.

[10] Michael Ambroso and Burt A. Ovrut. The B-L/Electroweak Hierarchy in Smooth Heterotic Compactifications. *Int. J. Mod. Phys.*, A25:2631–2677, 2010.

[11] Ben O'Leary, Werner Porod, and Florian Staub. Mass spectrum of the minimal SUSY B-L model. 2011.

[12] Michael Ambroso and Burt Ovrut. The B-L/Electroweak Hierarchy in Heterotic String and M- Theory. *JHEP*, 10:011, 2009.

[13] Bob Holdom. Two U(1)'s and Epsilon Charge Shifts. *Phys. Lett.*, B166:196, 1986.

[14] K. S. Babu, Christopher F. Kolda, and John March-Russell. Implications of generalized Z Z' mixing. *Phys. Rev.*, D57:6788–6792, 1998.

[15] F. del Aguila, G.D. Coughlan, and M. Quiros. GAUGE COUPLING RENORMALIZATION WITH SEVERAL U(1) FACTORS. *Nucl.Phys.*, B307:633, 1988.

[16] F. del Aguila, J.A. Gonzalez, and M. Quiros. RENORMALIZATION GROUP ANALYSIS OF EXTENDED ELECTROWEAK MODELS FROM THE HETEROTIC STRING. *Nucl.Phys.*, B307:571, 1988.

[17] Florian Staub, Thorsten Ohl, Werner Porod, and Christian Speckner. A tool box for implementing supersymmetric models. 2011.

[18] E.E. Boos, M.N. Dubinin, V.A. Ilyin, A.E. Pukhov, and V.I. Savrin. CompHEP: Specialized package for automatic calculations of elementary particle decays and collisions. 1994.

[19] A. Pukhov. CalcHEP 2.3: MSSM, structure functions, event generation, batchs, and generation of matrix elements for other packages. 2004.

[20] Philip Bechtle, Oliver Brein, Sven Heinemeyer, Georg Weiglein, and Karina E. Williams. HiggsBounds: Confronting Arbitrary Higgs Sectors with Exclusion Bounds from LEP and the Tevatron. *Comput. Phys. Commun.*, 181:138–167, 2010.

[21] Philip Bechtle, Oliver Brein, Sven Heinemeyer, Georg Weiglein, and Karina E. Williams. HiggsBounds 2.0.0: Confronting Neutral and Charged Higgs Sector Predictions with Exclusion Bounds from LEP and the Tevatron. *Comput. Phys. Commun.*, 182:2605–2631, 2011.

[22] G. Belanger, F. Boudjema, A. Pukhov, and A. Semenov. micrOMEGAs2.0: A program to calculate the relic density of dark matter in a generic model. *Comput. Phys. Commun.*, 176:367–382, 2007.

[24] Florian Staub. From Superpotential to Model Files for FeynArts and CalcHep/CompHep. *Comput.Phys.Commun.*, 181:1077–1086, 2010.

[25] Florian Staub. Automatic Calculation of supersymmetric Renormalization Group Equations and Self Energies. *Comput.Phys.Commun.*, 182:808–833, 2011.

[26] Werner Porod. SPheno, a program for calculating supersymmetric spectra, SUSY particle decays and SUSY particle production at e+ e- colliders. *Comput. Phys. Commun.*, 153:275–315, 2003.

[27] W. Porod and F. Staub. SPheno 3.1: extensions including flavour, CP-phases and models beyond the MSSM. 2011.

[28] Mauro Moretti, Thorsten Ohl, and Jurgen Reuter. O'Mega: An Optimizing matrix element generator. 2001.

[29] Wolfgang Kilian, Thorsten Ohl, and Jurgen Reuter. WHIZARD: Simulating Multi-Particle Processes at LHC and ILC. *Eur. Phys. J.*, C71:1742, 2011.

[30] Lorenzo Basso, Ben O'Leary, Werner Porod, and Florian Staub. Work in preperation.

[31] Renato M. Fonseca, Michal Malinsky, Werner Porod, and Florian Staub. Running soft parameters in SUSY models with multiple U(1) gauge factors. *Nucl. Phys.*, B854:28–53, 2012.

[32] Piotr H. Chankowski, Stefan Pokorski, and Jakub Wagner. Z' and the Appelquist-Carrazzone decoupling. *Eur. Phys. J.*, C47:187–205, 2006.

[33] Felix Braam and Juergen Reuter. A Simplified Scheme for GUT-inspired Theories with Multiple Abelian Factors. 2011.

[34] Damien M. Pierce, Jonathan A. Bagger, Konstantin T. Matchev, and Ren-jie Zhang. Precision corrections in the minimal supersymmetric standard model. *Nucl. Phys.*, B491:3–67, 1997.

[35] Florian Staub, Werner Porod, and Bjorn Herrmann. The electroweak sector of the NMSSM at the one-loop level. *JHEP*, 10:040, 2010.

[36] Ben O'Leary, Manuel Krauss, Werner Porod, and Florian Staub. Work in preperation.

[37] Thomas Hahn. Generating Feynman diagrams and amplitudes with FeynArts 3. *Comput.Phys.Commun.*, 140:418–431, 2001.

[38] T. Hahn and M. Perez-Victoria. Automatized one loop calculations in four-dimensions and D-dimensions. *Comput.Phys.Commun.*, 118:153–165, 1999.

[39] Johan Alwall, Michel Herquet, Fabio Maltoni, Olivier Mattelaer, and Tim Stelzer. MadGraph 5 : Going Beyond. *JHEP*, 1106:128, 2011.

[40] Howard E. Haber and Marc Sher. HIGGS MASS BOUND IN E(6) BASED SUPERSYMMETRIC THEORIES. *Phys.Rev.*, D35:2206, 1987.

[41] Manuel Drees. COMMENT ON 'HIGGS BOSON MASS BOUND IN E(6) BASED SUPERSYMMETRIC THEORIES.'. *Phys.Rev.*, D35:2910–2913, 1987.

[42] Mirjam Cvetic, Durmus A. Demir, J.R. Espinosa, L.L. Everett, and P. Langacker. Electroweak breaking and the mu problem in supergravity models with an additional U(1). *Phys.Rev.*, D56:2861, 1997.

[43] Yue Zhang, Haipeng An, Xiang-dong Ji, and Rabindra N. Mohapatra. Light Higgs Mass Bound in SUSY Left-Right Models. *Phys.Rev.*, D78:011302, 2008.

[44] Ernest Ma. Exceeding the MSSM Higgs Mass Bound in a Special Class of U(1) Gauge Models. *Phys.Lett.*, B705:320–323, 2011.

[45] Martin Hirsch, Michal Malinsky, Werner Porod, Laslo Reichert, and Florian Staub. Hefty MSSM-like light Higgs in extended gauge models. 2011.

[46] G. Belanger, Neil D. Christensen, A. Pukhov, and A. Semenov. SLHAplus: a library for implementing extensions of the standard model. *Comput.Phys.Commun.*, 182:763–774, 2011.

[47] Neil D. Christensen and Claude Duhr. FeynRules - Feynman rules made easy. *Comput. Phys. Commun.*, 180:1614–1641, 2009.

*** ***

WHIZARD @ LCFORUM 2012: A Status Report

Jürgen Reuter[1]

[1]DESY, Notketraße 85, 22607 Hamburg, Germany

DOI: will be assigned

This is a status report of the WHIZARD Monte Carlo multi-purpose event generator given at the LCFORUM 2012 at DESY. In case you use the program, please do cite the official reference(s), [1, 2]. I review here the development of the WHIZARD generator version 2 with a special emphasis on linear collider physics.

1 Introduction

The multi-purpose Monte Carlo event generator WHIZARD was developed as a tool for linear collider physics during the late 1990s [3]. Some of the first studies with exclusive four, six and eight fermion final states for linear collider physics have been done with WHIZARD [4, 5, 6, 7]. The first public version, 1.00, of WHIZARD has been released in December 2000. It was written in `Fortran90/95` and used from its beginnings the VAMP package [8] for a multi-channel adaptive Monte Carlo integration. The major improvement was an algorithm to model the phase space channels for a process under consideration and to provide the corresponding phase space mappings to flatten out the divergencies of the integrand for an optimized importance sampling. In the 1.xx (now called legacy) versions of WHIZARD, matrix elements from early version of MadGraph [9] and CompHep [10] as well as from the at that time newly developed Optimized Matrix Element Generator O'Mega [2] could be used. Parton shower and hadronization could be simulated via an interface to PYTHIA [11].

During the years 2001-2005/06, many technical and physics features have been added on demand of either theoretical or experimental users of the program or the authors itself. Support for several event file formats have been added. For a realistic simulation of linear lepton colliders, the ability to use structured beams have become crucial, specifically for experimental feasibility studies and detector development. Along these lines, initial state radiation (ISR) following the approach of Ref. [28], k_T distribution of the radiating initial beams as well as explicit photons from ISR in the final state events. Beamstrahlung, i.e. the modifications of the beam spectra due to classical electromagnetic interactions of the lepton beams, as well as photon beam options via Compton backscattering off laser photons could be simulated by attaching the CIRCE1 and CIRCE2 generators [12] to the main WHIZARD program. The main core in version 1.xx connects the different parts of the program via glueing shell scripts that steer the compilation of different processes as well as the integration, event generation and the built-in graphical analysis of WHIZARD.

WHIZARD has been extensively used for linear collider physics, e.g for the development of the TESLA Technical Design Report [13, 14, 15]. The big SLAC event samples for the Standard Model backgrounds have been generated with WHIZARD. Though here WHIZARD has been used as a generator for SM backgrounds one of the main focuses of the tool has always been the realm of beyond the Standard Model (BSM) physics. Many of these developments have already been present in the legacy branch WHIZARD 1.xx, but I will summarize them together with the overview of the new features in WHIZARD 2.

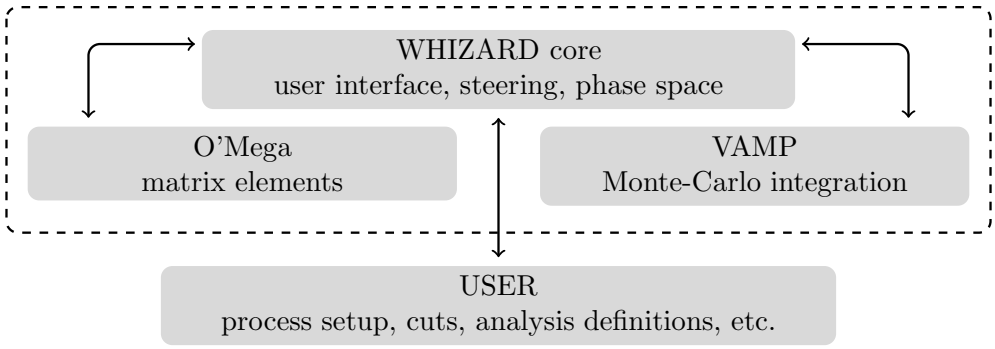

Figure 1: Structure of the WHIZARD program.

2 WHIZARD 2: (New) Technical and Physics Features

2.1 Structure and technical features

WHIZARD has been basically rewritten since 2007. One of the main motivations was the inclusion of several features like event-dependent scales, running couplings, parton showering, handling of a large number of BSM models which are necessary for the purpose of simulating signals and backgrounds at the Large Hadron Collider (LHC). But it was also a question of maintenance of the code, documentation, easening release productions, bug fixes, and treating regressions that made a complete rewriting of the code necessary. Since roughly the same time WHIZARD is located at the HepForge web page, [16], where also the revision control system of the project has been moved to. With the start of the first release candidates of WHIZARD 2 late in 2009 the line of development for the legacy branch, 1.xx, stopped with revision 1.94. Until then, only bug fixes and documentation issues are tackled, and the latest release, 1.97, appeared with a completed manual documenting the final status and usage of WHIZARD 1.9x. For the new release branch, the version system has changed to the triple number system, i.e. (main release).(major version).(minor version). The first release was in April 2010 for the MC4BSM workshop in Copenhagen, the actual release at the moment is 2.0.7 from March 2012.

WHIZARD 2 now is a well-structured program containing the exclusive optimized matrix element generator O'Mega [2, 17], the multi-channel adaptive integration package VAMP [8], the two programs CIRCE1 and CIRCE2 [12] for ISR, beamstrahlung and photon collider physics, as well as tools for graphical data analysis. The basic structure of the program is shown in Fig. 1. The rewriting of the code (in total more than 60,000 lines of new code) was a major undertaking. The code has been completely streamlined, in the sense that now there are only programming languages used, Fortran2003 and OCaml (for the matrix element generator O'Mega). All system calls to binaries are done from the Fortran code itself, so that all shell and Perl scripts have been abandoned. A huge standardization of modern programming tools was the usage of the *autotools*, i.e. *automake/autoconf/libtool* setup which leads to a much easier control of distributions and easier maintenance (e.g. regressions etc.). To further control the line of development, the revision control system (subversion) at the HepForge page is used, together with the trac system for bug, feature request and enhancement tickets for the project management of the software. A cruise control system is used which checks new submissions to the software repository for compatibility for different compiler suites and operating systems and runs a very large class of compatibility tests, sanity and regression checks. A very clean modularization has been achieved using the object-oriented features in Fortran2003. WHIZARD 2 now works as a shared library, which makes a core re-compilation unnecessary whenever one physics process had been changed. New processes can be dynamically included, while the old static option is still available, e.g. for the use in batch systems and on the Grid. The matrix elements which for LHC multi-leg processes can become rather lengthy are automatically split up in subroutines which makes compilation by over-eager compiler optimizers much faster. WHIZARD can also be run as a shell (WHISH) now, though this is still in an experimental status. For using parallelization and multiple threads, an OpenMP parallelization for the helicity amplitudes has been set up, while an MPI parallelization of the multi-channel integration will be

```
cuts = any 5 degree < Theta < 175 degree
         [select if abs (Eta) < eta_cut [lepton]]
cuts = any E > 2 * mW [extract index 2
                         [sort by Pt [lepton]]]
```

Figure 2: Example for a SINDARIN scripting language expression for cuts.

released soon.

The program can be downloaded from the HepForge page, unpacked and then the standard steps should be taken to compile and install it: *configure*, *make*, and *make install*. For the configuration, it might be necessary to specify paths or flags for external programs to be linked in, like e.g. LHAPDF, StdHEP, HepMC. Before the last *make install* step, an optional *make check* is recommended to ascertain that everything runs correctly on the current system. WHIZARD 2 is intended to be installed centrally, e.g. in *usr/local* but can also be installed locally without administrator rights. Each user can then work in his own home or work directory.

2.2 Physics and Performance features

In this section I summarize the main physics features of WHIZARD with a special emphasis both on the new developments in WHIZARD 2 as well as on the ILC-relevant features. First of all, there was an improvement on the already quite performant phase space setup of WHIZARD, where due to a symmetrized phase space forest construction a further performance gain could be achieved. The new modular structure of WHIZARD 2 made it possible to easily include event-dependent scales like they are used in parton density functions (PDFs) as well as running coupling constants like α_s. A very powerful invention was the new steering syntax of the program, Scripting INtegration, Data Analysis, Results display and INterfaces, or short SINDARIN. This is similar to a scripting language, and allows to easily define arbitrary (algebraic) expressions for cuts, scales etc. as well as to denote all the commands necessary to generate matrix elements, compile them, integrate them, generate events and set up an analysis. Fig. 2 shows an example for a cut definition in SINDARIN: the first line selects any lepton with polar angle 5 degrees away from the beam axis under the condition that its absolute rapidity is below some predefined cut variable. The second line selects any second-hardest lepton in p_T if its energy exceeds twice the W mass. Analysis expressions and histograms can be defined in the same way.

WHIZARD 2 uses process libraries, which allows the usage of processes from different BSM models in parallel. As not the multi-leg matrix elements, but the high-dimensional phase space integration is the major bottleneck for going to higher and higher multiplicities, factorizing amplitudes into production and subsequent decays is (in a well-defined approximation) not to bad an idea. WHIZARD 2 realizes this for the event generation and hence distributions where the user can specify whether he wants no spin correlations, only classical spin correlations (i.e. the diagonal of the spin density matrix) or full spin correlations. An example for squark pair production where one of the two squarks decays via a slepton into jet, lepton and the lightest neutralino is shown in Fig. 3. One is able to define containers of particles for decays and can therefore handle inclusive processes and decays. With respect to WHIZARD 1.xx, the algorithms for the flavor sums of initial and final state particles have been greatly improved. A more elaborate elimination of redundancies from summation over internal and external combinations of flavours (particularly quarks in jets, especially for LHC physics) will be available soon and is expected to further improve both code size and speed. For the analysis, the graphical package GAMELAN based on LaTeX and MetaPost has been also improved. Again on the technical side, the algorithm using MD5 check sums has been revisited, such that is now possible to reuse every bit and piece of the steps: the code, the object files, the phase space setup file, the integration grids and the already generated events, whenever those things are still compatible with the setup in the input file. Other new features, that will be discussed in more detail below, are the interface [18] to the program FeynRules [19] which allows to include a new BSM model just by specifying its Lagrangian, and the initial and final state parton shower of WHIZARD [20] together with an MLM matching procedure between hard matrix elements and the parton shower.

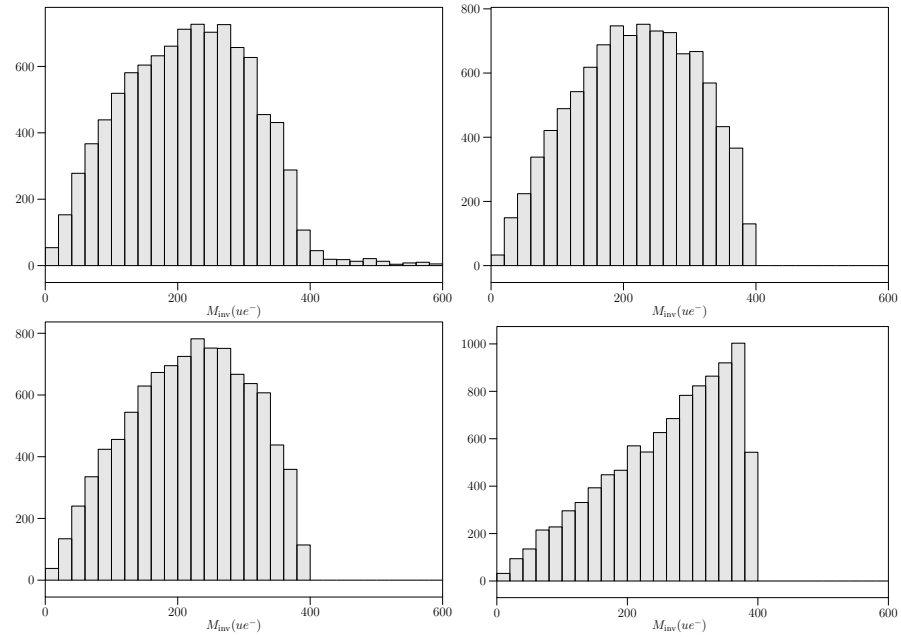

Figure 3: Factorization of processes in distributions: the jet-lepton invariant mass is shown for squark pair production at the LHC, where one of the squarks subsequently decays into a jet, a lepton and the lightest neutralino. Upper left: full matrix element, upper right factorized with full spin correlations, lower row: factorized with classical (left) and no spin correlations (right), respectively.

2.3 Fields, Beams, Interactions, Models in WHIZARD

In the discussion of the implemented physics content in WHIZARD (2), we first start with the hard matrix elements, particle types, interaction types, Lorentz structures etc. The possible particle types in WHIZARD contain scalars, spin 1/2 fermions (both Dirac and Majorana) together with fermion-number violating vertices following the rules in [21, 22], spin 1 particles (both massless and massive, in unitarity and Feynman gauge as well as in principle for arbitrary R_ξ gauges), spin 3/2 particles (only as Majorana particles in their incarnation as gravitinos), as well as spin 2 particles (massless and massive). Particles could be dynamic (i.e. propagating particles) or pure insertions. The latter can e.g. be used as spurion fields in operator insertions. There are also unphysical particles for testing purposes inside Ward- and Slavnoy-Taylor identities (see e.g. [23, 24]). Note that for all the particle types there are routines that add up to a large test suite, testing (especially numerically) equations of motion, transversality, irreducibility of the on-shell fields as well as e.g. Majorana proerties of different vertices.

For the vertices, there is a huge list of Lorentz structures that are supported by WHIZARD ranging from purely scalar couplings over scalar-vector couplings (incl. dimension 5 operators), pure vector couplings, fermionic couplings to scalars, to vectors, to tensors as well as dimension 5 and 6 operators that appear e.g. in the context of supersymmetric Ward identities), as well as gravitino couplings of dimensions 5 and 6. Completely general Lorentz structures that will allow an automatic generation of a library with the corresponding Fortran routines is under construction, and will presumably be ready by the end of the year.

Color flows in WHIZARD are generated in the color flow formalism [25, 26]. While in the legacy version WHIZARD 1.9x this was done in a rather slow approach with the help of a PERL script, in WHIZARD 2 this was performed directly inside the core of O'Mega and finally even more refined as a colorizing of the Directed Acyclical Graph (DAG) as a representation of the colored amplitude [17]. Though in principle every $SU(N)$ gauge group is supported, we focus here on standard $SU(3)$ for QCD. At the moment, the fundamental and anti-fundamental representations are supported, the adjoint representation, which already covers all standard particles in the SM, SUSY and extra-dimensional models. In preparation are generalized color structures including color sextets and decuplets as well as baryon-number violating vertices as in $\epsilon_{ijk}\phi_i\phi_j\phi_k$.

```
beams = p, p => lhapdf { $lhapdf_file = "cteq5l.LHgrid" }
beams = p, p => pdf_builtin {$pdf_builtin_set = "mstw2008nlo"}
beams = e1, E1 => circe1 => isr
beams = A, A => circe2 { $circe2_file = "teslagg_500.circe" }
beams = e1, E1
     => beam_events { $beam_events_file = "uniform_spread_2.5%.dat" }
beams = e1, E1 => user_strfun ("escan"), none
```

Figure 4: Structured beams in WHIZARD 2 as they appear in SINDARIN commands.

These color structures are foreseen to be made public in late 2012.

Concerning structured beams, the complete setup for beam structure relevant for lepton colliders from WHIZARD 1 have been taken over in or re-implemented for WHIZARD 2, while the support for structured beams for hadron colliders has been much enlarged and modernized. Examples for structured beams as SINDARIN commands are shown in Fig. 4 [1]. For lepton colliders, initial state radiation (ISR) is implemented according to the calculations presented in [28, 29] which contains the resummed results for soft-collinear photon from [30, 31] together with the explicit calculation of hard-collinear photons up to third order in perturbation theory. WHIZARD can also generate explicity the p_T distribution of the photons in the event as well as of the electron beam remnants from the ISR recoil.

Polarized beams are supported, where it is possible to specify arbitrary polarization states (not only linear or circular polarization modes) by using an explicit spin density matrix as input. Beamstrahlung, i.e. the deformation of the beam spectrum due to macrosopic (classical) electromagnetic interactions can be simulated via the CIRCE module [12], while photon collider spectra from Compton back scattering are contained in the CIRCE2 generator within the WHIZARD package. External beam spectra which are basically long lists of energy ratio (or explicit energy) values can be read in, or user-defined code can be included, compiled and linked in the dynamic setup of WHIZARD 2 at runtime. What is at the moment not (yet) implemented is electromagnetic final state radiation (FSR) using a Yennie-Frautschi-Suura approach [32].

Concerning hadronic beam environments, the support for PDFLIB inside CERNLIB for PDFs has been abandoned in WHIZARD 2. Like WHIZARD 1, WHIZARD 2 now exclusively contains an interface to the LHAPDF external library [33] supporting in principle all (modern) PDF sets, including photon PDF and pion PDFs. To be independent from installing LHAPDF and linking it into WHIZARD, the most prominent and recent PDF sets have been directly included into WHIZARD together with the routines for the running strong coupling from the PDF collaborations. Hadronization as well as hadronic events can be simulated through PYTHIA [11] which ships with the main WHIZARD distribution. Of course, it also possible to write out parton level events into some event file, read them in into a different hadronization program and then read the hadronic event file back into WHIZARD for an analysis.

2.4 Parton Shower

Parton showering can be done as in WHIZARD 1 with an external program that is either linked to WHIZARD or via the pipe over an external event file that is to be converted from partonic to hadron level. In WHIZARD 2, the latest Fortran version of PYTHIA [11] is included in the distribution tarball, so parton showering via PYTHIA (like hadronzation and hadronic decays) can be directly steered from the SINDARIN input file. In WHIZARD 2, there are now two homebrew parton showers, one along the lines of the PYTHIA parton shower as k_T-ordered shower including angular ordering, the other one an analytic parton shower. The details of this latter shower are described in full detail in [20] (also cf. references therein). Concerning the original analytic final state parton shower [34], several improvements have been made, like a running scale of the strong coupling constant and color coherence by imposing angular ordering. A comparison to experimental results from the LEP collaborations have been made, cf. Fig. 5. The main new feature, however, is the analytic initial state shower, which is the main part of [20]. There, an automatic MLM-type matching procedure [35] has been implemented to smoothly connect high-p_T tails of jet distributions e.g. in

[1] For a complete overview of SINDARIN commands, cf. the WHIZARD manual [27].

MODEL TYPE	with CKM matrix	trivial CKM
QED with e, μ, τ, γ	–	QED
QCD with d, u, s, c, b, t, g	–	QCD
Standard Model	SM_CKM	SM
SM with anomalous gauge couplings	SM_ac_CKM	SM_ac
SM with anomalous top couplings	SMtop_CKM	SMtop
SM with K matrix	—	SM_KM
MSSM	MSSM_CKM	MSSM
MSSM with gravitinos	—	MSSM_Grav
NMSSM	NMSSM_CKM	NMSSM
extended SUSY models	—	PSSSM
Littlest Higgs	—	Littlest
Littlest Higgs with ungauged $U(1)$	—	Littlest_Eta
Littlest Higgs with T parity	—	Littlest_Tpar
Simplest Little Higgs (anomaly-free)	—	Simplest
Simplest Little Higgs (universal)	—	Simplest_univ
3-site model	—	Threeshl
UED	—	UED
SUSY Xdim. (inoff.)	—	SED
SM with Z'	—	Zprime
SM with gravitino and photino	—	GravTest
Augmentable SM template	—	Template

Table 1: List of implemented BSM models in WHIZARD.

Drell-Yan processes with the low-p_T regime. As this is a workshop on linear collider, I do not go into the details of the initial state shower, which has been compared to Tevatron and LHC data in [20], here.

2.5 Models and BSM physics

Coming back to hard matrix elements, many BSM models have been implemented in WHIZARD and used for LHC and ILC simulations, and most of them have been validated with the help of the FeynRules interface of WHIZARD. Among these are, first of all, SUSY models [36, 37] have been implemented, the MSSM together with implementations of non-minimal models like the NMSSM [38] or extended SUSY models [39, 40, 41]. Already in WHIZARD 1 existed an interface to other codes following the SUSY Les Houches Accord (SLHA 1/2) [42, 43, 44]. Also some pioneering work on the combination of SUSY NLO matrix elements with the electromagnetic showers have been done [46, 45]. A second focus lay on Little Higgs models (with and without T-parity), again with several studies for linear collider physics [47, 48]. On the more exotic side, models based on noncommutative spacetime have been studied with WHIZARD [49, 50, 51]. One of the original motivations was the study on a strongly interacting sector of electroweak symmetry breaking, which has been pursued in WHIZARD 2 both along the lines of anomalous couplings [52] as well as in terms of new resonances in the electroweak sector [53]. For the unitarization of these channels, a method had to be found to distinguish in the framework of the DAGs of the matrix element generation s- from t-/u-like channels.

Table 1 gives a list of all the models that are implemented. For implementing a new model, it is highly recommended that this is done via the WHIZARD-FeynRules interface [18].

2.6 NLO development in WHIZARD

There has been some work on the inclusion of (virtual) NLO corrections into WHIZARD mentioned in the previous paragraph in the context of SUSY studies at the ILC. The goal of the more recent developments is to have a setup for NLO calculations and simulations within WHIZARD for both LHC and ILC physics that is as

automated as possible. NLO calculations nowadays are mostly based on some sort of subtraction formalism, that groups the soft-collinear divergences into specific parts of the calculations to make them finite and performable for a phase-space integration. The most widely used is the Catani-Seymour dipole subtraction formalism [54, 55]. A first proof-of-principle implementation of the integrated and unintegrated dipoles have been done in [56, 57]. An automated generation of the CS dipoles is in construction at the moment, but already gives correct results for QED processes. Along with the dipoles comes an implementation of using several instances of the process setup within the phase space integration, which is necessary for the unintegrated dipoles in order to take care of the squeezed kinematics in the phase space integration of the subtraction terms. The implementation will be made public several steps (together with a BLHA interface [58]) several steps from summer until the end of this year.

3 Summary and Outlook

WHIZARD 2 is a completely newly structured update of an already versatile multi-purpose Monte Carlo event generator that has been released with many new technical and physics features in April 2010. Many further improvements and features have been added in the past two years. Though the main motivation for the restructuring of the code was to deal with the complexities of LHC physics, linear collider physics has always been a major field of application for WHIZARD. Quite recently, all relevant features regarding ILC/CLIC physics from WHIZARD 1 have been reimplemented in WHIZARD 2, and many improvements on the phase space setup, color, parton shower, BSM models, speed and performance, maintenance and usability have been made. Continuos effort will go specifically into the direction of multi-leg amplitudes, NLO development and more BSM coverage to be ready for the high-energy phase of LHC and a possible future linear collider.

4 Acknowledgments

JRR thanks the WHIZARD team, F. Bach, H.-W. Boschmann, W. Kilian, T. Ohl, S. Schmidt, C. Speckner, M. Trudewind, D. Wiesler, and T. Wirtz as well as F. Braam for the joint effort to make this project successful.

This project has been partially supported by the Helmholtz Alliance "Physics at the Terascale", the German ministry BMBF, the ministry MWK of the German state Baden-Württemberg, the German Research Association DFG, as well as the Scottish Universities Physics Alliance (SUPA). JRR wants to thank the institutes at Carleton University, Ottawa, the Institute of Physics in Freiburg as well as the School of Physics and Astronomy in Edinburgh as well as the Aspen Center of Physics for their hospitality, as part of this project has been realized there.

References

[1] W. Kilian, T. Ohl and J. Reuter, Eur. Phys. J. C **71**, 1742 (2011) [arXiv:0708.4233 [hep-ph]].

[2] M. Moretti, T. Ohl and J. Reuter, In *2nd ECFA/DESY Study 1998-2001* 1981-2009 [hep-ph/0102195].

[3] W. Kilian, In *2nd ECFA/DESY Study 1998-2001* 1924-1980

[4] W. Kilian, "WHIZARD: Complete simulations for electroweak multi-particle processes"

[5] W. Kilian, "$e^-e^+ \to 6$, 8 fermions with WHIZARD"

[6] E. Boos, H. J. He, W. Kilian, A. Pukhov, C. P. Yuan and P. M. Zerwas, Phys. Rev. D **57**, 1553 (1998) [hep-ph/9708310].

[7] E. Boos, H. J. He, W. Kilian, A. Pukhov, C. P. Yuan and P. M. Zerwas, Phys. Rev. D **61**, 077901 (2000) [hep-ph/9908409].

[8] T. Ohl, Comput. Phys. Commun. **120**, 13 (1999) [hep-ph/9806432].

[9] T. Stelzer and W. F. Long, Comput. Phys. Commun. **81**, 357 (1994) [hep-ph/9401258].

[10] E. E. Boos, M. N. Dubinin, V. A. Ilyin, A. E. Pukhov and V. I. Savrin, hep-ph/9503280.

[11] T. Sjostrand, L. Lonnblad and S. Mrenna, hep-ph/0108264.

[12] T. Ohl, Comput. Phys. Commun. **101**, 269 (1997) [hep-ph/9607454].

[13] F. Richard, (ed.), J. R. Schneider, (ed.), D. Trines, (ed.) and A. Wagner, (ed.), hep-ph/0106314.

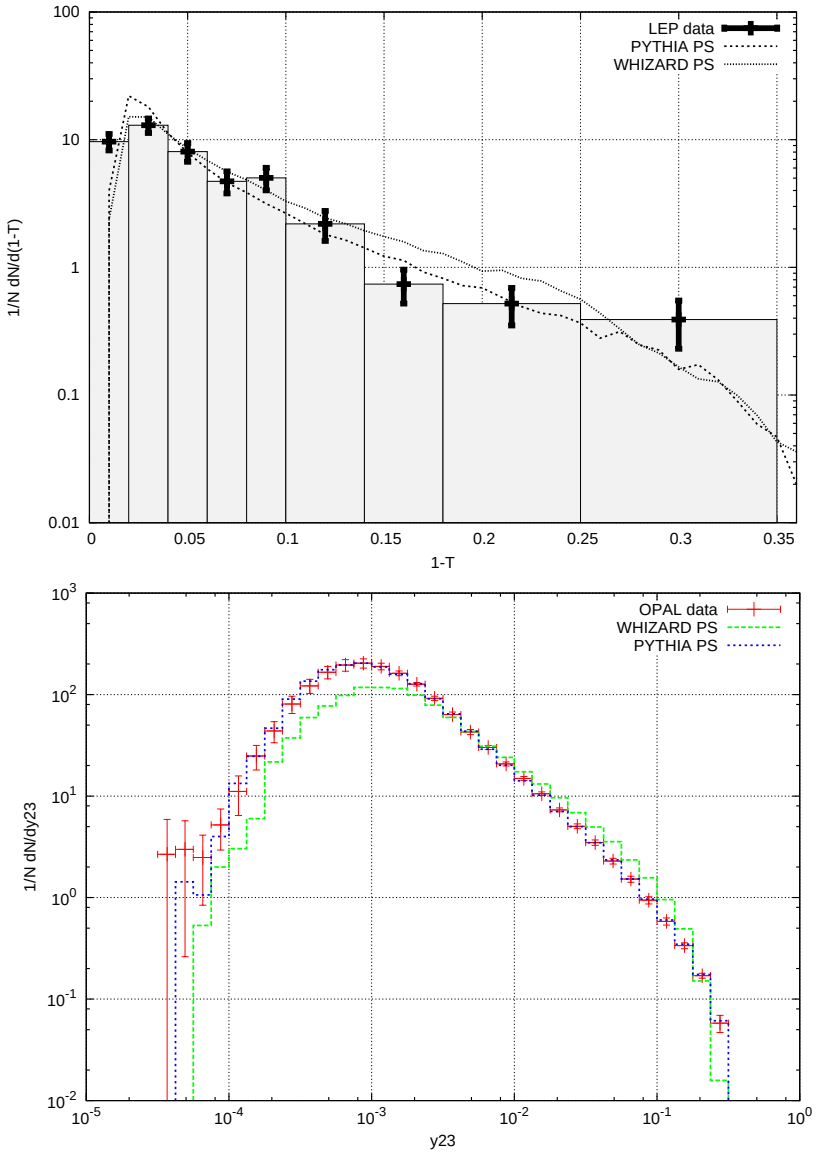

Figure 5: Validation of the analytic final state shower in WHIZARD: On top the thrust distribution in $e^+e^- \to$ jets, where the grey histograms with error bars are the data, the dashed line is PYTHIA, the dotted WHIZARD, on the bottom the Y_{23} parameter which shows the value of the jet definition parameter at which a two-jet event starts to be resolved as a three-jet event (in red [error bars] OPAL data, the green curve shows WHIZARD, while the blue one os PYTHIA). For more details cf. [20].

[14] J. A. Aguilar-Saavedra *et al.* [ECFA/DESY LC Physics Working Group Collaboration], hep-ph/0106315.

[15] T. Behnke, (ed.), S. Bertolucci, (ed.), R. D. Heuer, (ed.) and R. Settles, (ed.), DESY-01-011.

[16] `http://projects.hepforge.org/whizard`

[17] W. Kilian, T. Ohl, J. Reuter, *O'Mega: An Otimizing Matrix Element Generator. II: Amplitudes with Color Flow and without fermion number conservation*, DESY 11-131.

[18] N. D. Christensen, C. Duhr, B. Fuks, J. Reuter and C. Speckner, EPJ **C** (in print), arXiv:1010.3251 [hep-ph].

[19] N. D. Christensen and C. Duhr, Comput. Phys. Commun. **180**, 1614 (2009) [arXiv:0806.4194 [hep-ph]].

[20] W. Kilian, J. Reuter, S. Schmidt and D. Wiesler, JHEP **1204**, 013 (2012) [arXiv:1112.1039 [hep-ph]].

[21] A. Denner, H. Eck, O. Hahn and J. Kublbeck, Phys. Lett. B **291**, 278 (1992).

[22] A. Denner, H. Eck, O. Hahn and J. Kublbeck, Nucl. Phys. B **387**, 467 (1992).

[23] J. Reuter, hep-th/0212154.

[24] T. Ohl and J. Reuter, Eur. Phys. J. C **30**, 525 (2003) [hep-th/0212224].

[25] F. Maltoni, K. Paul, T. Stelzer and S. Willenbrock, Phys. Rev. D **67**, 014026 (2003) [hep-ph/0209271].

[26] W. Kilian, T. Ohl, J. Reuter, C. Speckner, *QCD in the color flow representation*, DESY 11-215.

[27] `http://whizard.hepforge.org/manual`

[28] M. Skrzypek and S. Jadach, Z. Phys. C **49**, 577 (1991).

[29] S. Jadach, M. Skrzypek and B. F. L. Ward, Phys. Lett. B **257**, 173 (1991).

[30] V. N. Gribov and L. N. Lipatov, Sov. J. Nucl. Phys. **15**, 675 (1972) [Yad. Fiz. **15**, 1218 (1972)].

[31] E. A. Kuraev and V. S. Fadin, Sov. J. Nucl. Phys. **41**, 466 (1985) [Yad. Fiz. **41**, 733 (1985)].

[32] D. R. Yennie, S. C. Frautschi and H. Suura, Annals Phys. **13**, 379 (1961).

[33] M. R. Whalley, D. Bourilkov and R. C. Group, hep-ph/0508110.

[34] C. W. Bauer, F. J. Tackmann and J. Thaler, JHEP **0812**, 010 (2008) [arXiv:0801.4026 [hep-ph]].

[35] M. Mangano, Talk given at *ME/MC Tuning WG Meeting*, Fermilab, Batavia, U.S.A., 15 November 2002.

[36] K. Hagiwara, W. Kilian, F. Krauss, T. Ohl, T. Plehn, D. Rainwater, J. Reuter and S. Schumann, Phys. Rev. D **73**, 055005 (2006) [hep-ph/0512260].

[37] J. Kalinowski, W. Kilian, J. Reuter, T. Robens and K. Rolbiecki, JHEP **0810**, 090 (2008) [arXiv:0809.3997 [hep-ph]].

[38] J. Reuter and F. Braam, AIP Conf. Proc. **1200**, 470 (2010) [arXiv:0909.3059 [hep-ph]].

[39] W. Kilian and J. Reuter, Phys. Lett. B **642**, 81 (2006) [hep-ph/0606277].

[40] F. Braam, A. Knochel and J. Reuter, JHEP **1006**, 013 (2010) [arXiv:1001.4074 [hep-ph]].

[41] J. Reuter and D. Wiesler, Phys. Rev. D **84**, 015012 (2011) [arXiv:1010.4215 [hep-ph]].

[42] P. Z. Skands, B. C. Allanach, H. Baer, C. Balazs, G. Belanger, F. Boudjema, A. Djouadi and R. Godbole *et al.*, JHEP **0407**, 036 (2004) [hep-ph/0311123].

[43] B. C. Allanach, C. Balazs, G. Belanger, M. Bernhardt, F. Boudjema, D. Choudhury, K. Desch and U. Ellwanger *et al.*, Comput. Phys. Commun. **180**, 8 (2009) [arXiv:0801.0045 [hep-ph]].

[44] J. A. Aguilar-Saavedra, A. Ali, B. C. Allanach, R. L. Arnowitt, H. A. Baer, J. A. Bagger, C. Balazs and V. D. Barger *et al.*, Eur. Phys. J. C **46**, 43 (2006) [hep-ph/0511344].

[45] W. Kilian, J. Reuter and T. Robens, Eur. Phys. J. C **48**, 389 (2006) [hep-ph/0607127].

[46] T. Robens, J. Kalinowski, K. Rolbiecki, W. Kilian and J. Reuter, Acta Phys. Polon. B **39**, 1705 (2008) [arXiv:0803.4161 [hep-ph]].

[47] W. Kilian, D. Rainwater and J. Reuter, Phys. Rev. D **71**, 015008 (2005) [hep-ph/0411213].

[48] W. Kilian, D. Rainwater and J. Reuter, Phys. Rev. D **74**, 095003 (2006) [Erratum-ibid. D **74**, 099905 (2006)] [hep-ph/0609119].

[49] T. Ohl and J. Reuter, Phys. Rev. D **70**, 076007 (2004) [hep-ph/0406098].

[50] A. Alboteanu, T. Ohl and R. Ruckl, Phys. Rev. D **74**, 096004 (2006) [hep-ph/0608155].

[51] T. Ohl and C. Speckner, Phys. Rev. D **82**, 116011 (2010) [arXiv:1008.4710 [hep-ph]].

[52] M. Beyer, W. Kilian, P. Krstonosic, K. Monig, J. Reuter, E. Schmidt and H. Schroder, Eur. Phys. J. C **48**, 353 (2006) [hep-ph/0604048].

[53] A. Alboteanu, W. Kilian and J. Reuter, JHEP **0811**, 010 (2008) [arXiv:0806.4145 [hep-ph]].

[54] S. Catani and M. H. Seymour, Nucl. Phys. B **485**, 291 (1997) [Erratum-ibid. B **510**, 503 (1998)] [hep-ph/9605323].

[55] S. Catani, S. Dittmaier, M. H. Seymour and Z. Trocsanyi, Nucl. Phys. B **627**, 189 (2002) [hep-ph/0201036].

[56] T. Binoth, N. Greiner, A. Guffanti, J. Reuter, J. -P. .Guillet and T. Reiter, Phys. Lett. B **685**, 293 (2010) [arXiv:0910.4379 [hep-ph]].

[57] N. Greiner, A. Guffanti, T. Reiter and J. Reuter, Phys. Rev. Lett. **107**, 102002 (2011) [arXiv:1105.3624 [hep-ph]].

[58] T. Binoth, F. Boudjema, G. Dissertori, A. Lazopoulos, A. Denner, S. Dittmaier, R. Frederix and N. Greiner *et al.*, Comput. Phys. Commun. **181**, 1612 (2010) [arXiv:1001.1307 [hep-ph]].

Chapter 7

Alternative Physics Scenarios

DESY 12-016
CERN-PH-TH/2012-077

Discriminating Z' from anomalous trilinear gauge coupling signatures in $e^+e^- \to W^+W^-$ at ILC with polarized beams

V. V. Andreev,[a,*] G. Moortgat-Pick,[b,†] P. Osland,[c,d,‡] A. A. Pankov[e,§] N. Paver[f,¶]

[a] *The F. Scorina Gomel State University, 246019 Gomel, Belarus*

[b] *DESY FLC, Notkestrasse 85, Hamburg 22607, Germany*

[c] *Department of Physics and Technology,*

University of Bergen, Postboks 7803, N-5020 Bergen, Norway

[d] *CERN, CH-1211 Genève 23, Switzerland*

[e] *The Abdus Salam ICTP Affiliated Centre,*

Technical University of Gomel, 246746 Gomel, Belarus

[f] *University of Trieste and INFN-Trieste Section, 34100 Trieste, Italy*

* quarks@gsu.by
† gudrid.moortgat-pick@desy.de
‡ per.osland@ift.uib.no
§ pankov@ictp.it
¶ nello.paver@ts.infn.it

Abstract

New heavy neutral gauge bosons Z' are predicted by many models of physics beyond the Standard Model. It is quite possible that Z's are heavy enough to lie beyond the discovery reach of the CERN Large Hadron Collider LHC, in which case only indirect signatures of Z' exchanges may emerge at future colliders, through deviations of the measured cross sections from the Standard Model predictions. We discuss in this context the foreseeable sensitivity to Z's of $W^{\pm}$-pair production cross sections at the e^+e^- International Linear Collider (ILC), especially as regards the potential of distinguishing observable effects of the Z' from analogous ones due to competitor models with anomalous trilinear gauge couplings (AGC) that can lead to the same or similar new physics experimental signatures at the ILC. The sensitivity of the ILC for probing the Z-Z' mixing and its capability to distinguish these two new physics scenarios is substantially enhanced when the polarization of the initial beams and the produced $W^{\pm}$ bosons are considered. A model independent analysis of the Z' effects in the process $e^+e^- \to W^+W^-$ allows to differentiate the full class of vector Z' models from those with anomalous trilinear gauge couplings, with one notable exception: the sequential SM (SSM)-like models can in this process not be distinguished from anomalous gauge couplings. Results of model dependent analysis of a specific Z' are expressed in terms of discovery and identification reaches on the Z-Z' mixing angle and the Z' mass.

PACS numbers: 12.60.-i, 12.60.Cn, 14.70.Fm, 29.20.Ej

I. INTRODUCTION

The $W^{\pm}$ boson pair production process

$$e^+ + e^- \to W^+ + W^- \tag{1}$$

is a crucial one for studying the electroweak gauge symmetry in e^+e^- annihilation. Properties of the weak gauge bosons are closely related to electroweak symmetry breaking and the structure of the gauge sector in general. Thus, detailed examination of (1) at the ILC will both test this sector of the standard model (SM) with the highest accuracy and throw light on New Physics (NP) that may appear beyond the SM.

In the SM, for zero electron mass, the process (1) is described by the amplitudes mediated by photon and Z boson exchange in the s-channel and by neutrino exchange in the t-channel. Therefore, this reaction is particularly sensitive to both the leptonic vertices and the trilinear couplings to W^+W^- of the SM Z and of any new heavy neutral boson that can be exchanged in the s-channel. A popular example in this regard, is represented by the Z's envisaged by electroweak scenarios based on spontaneously broken 'extended' gauge symmetries, with masses much larger than M_Z and coupling constants different from the SM. The variety of the proposed Z' models is broad. Therefore, rather than attempting an exhaustive analysis, we shall here focus on the phenomenological effects in reaction (1) of the so-called $Z'_{\rm SSM}$, Z'_{E_6} and $Z'_{\rm LR}$ models. Actually, in some sense, we may consider these Z' models as representative of this New Physics (NP) sector [1–8].

The direct manifestation of Z's would be the observation of peaks in cross sections at very high energy colliders, this would be possible only for $M_{Z'}$ lying within the kinematical reach of the machine and sufficient luminosity. Indeed, current lower limits on $M_{Z'}$ are obtained from direct searches of Z's in Drell-Yan dilepton pair production at the CERN LHC: from the analysis of the 7 TeV data, the observed bounds at 95% C. L. range approximately in the interval $1.8 - 2.3$ TeV, depending on the particular Z' model being tested [9, 10]. For too high masses, Z' exchanges can manifest themselves indirectly, *via* deviations of cross sections, and in general of the reaction observables, from the SM predictions. Clearly, this kind of searches requires great precision and therefore will be favoured by extremely high collider luminosity, such as will be available at the ILC. Indirect lower bounds on Z' masses from the high precision LEP data at the Z lie in the range $\sim 0.4 - 1.8$ TeV, depending on the model considered [7, 8].

Indirect effects may be quite subtle, as far as the identification of the source of an observed deviation is concerned, because *a priori* different NP scenarios may lead to the same or similar experimental signatures. Clearly, then, the discrimination of one NP model (in our case the Z') from other possible ones needs an appropriate strategy for analyzing the data.[1]

In this paper, we study the indirect effects evidencing the mentioned extra Z' gauge bosons in $W^{\pm}$ pair production (1) at the next generation e^+e^- International Linear Collider (ILC), with a center of mass energy $\sqrt{s} = 0.5{-}1$ TeV and typical time-integrated luminosities of $\mathcal{L}_{\rm int} \sim 0.5 - 1$ ab^{-1} [12, 13]. At the foreseen, really high luminosity this process should be quite sensitive to the indirect NP effects at a collider with $M_Z \ll \sqrt{s} \ll M_{Z'}$ [14–19], the deviations of cross sections from the SM predictions being expected to increase with $\sqrt{s}$ due to the violation of the SM gauge cancellation among the different contributions.

Along the lines of the previous discussion, apart from estimating the foreseeable sensitivity of process (1) to the considered Z' models, we will consider the problem of establishing the potential of ILC of distinguishing the Z' effects, once observed, from the ones due to NP competitor models that can lead to analogous physical signatures in the cross section. For the latter, we will choose the models with Anomalous Gauge Couplings (AGC), and compare them with the hypothesis of Z' exchanges. In the AGC models, there is no new gauge boson exchange, but the $WW\gamma$, WWZ couplings are modified with respect to the SM values, this violates the SM gauge cancellation too and leads to deviations of the process cross sections. AGC couplings are described *via* a sum of effective interactions, ordered by dimensionality, and we shall restrict our analysis to the dimension-six terms which conserve C and P [20, 21].

The baseline configuration of the ILC envisages a very high electron beam polarization (larger than 80%) that is measurable with high precision. Also positron beam polarization, around 30%, might be initially obtainable, and this polarization could be raised to about 60% or higher in the ultimate upgrade of the machine. As is well-known, the polarization option represents an asset in order to enhance the discovery reaches and identification sensitivities on NP models of any kind [22, 23]. This is the case, in particular, of Z' exchanges and AGC interactions in process (1), an obvious example being the suppression of the ν-exchange channel by using right-handed electrons. Additional ILC diagnostic ability in Z's and AGC

[1] Actually, this should be necessary also in the case of direct discovery, because different NP models may in principle produce the same peaks at the same mass so that, for example, for model identification some angular analyses must be applied, see [11] and references therein.

would be provided by measures of polarized W^+ and W^- in combination with initial beam polarizations.

The paper is organized as follows. In Section II, we briefly review the models involving additional Z' bosons and emphasize the role of Z-Z' mixing in the process (1). In Section III we give the parametrization of Z' and AGC effects, as well as formulae for helicity amplitudes and cross sections of the process under consideration. Section IV contains, for illustrative purposes, some plots of the unpolarized and polarized cross sections showing the effect of Z' and of Z-Z' mixing. In Section V we present the approach, which allows to obtain the discovery reach on Z' parameters (actually, on the deviations of the transition amplitudes from the SM) and the obtained numerical results. Section VI includes the results of both model dependent and model independent analyses of the possibilities to differentiate Z' effects from similar ones caused by AGC. Finally we conclude in Section VII.

II. Z' MODELS AND Z-Z' MIXING

The Z' models that will be considered in our analysis are the following [1, 2, 4, 6]:

(i) The four possible $U(1)$ Z' scenarios originating from the spontaneous breaking of the exceptional group E_6. In this case, two extra, heavy neutral gauge bosons appear as consequence of the symmetry breaking and, generally, only the lightest is assumed to be within reach of the collider. It is defined, in terms of a new mixing angle β, by the linear combination

$$Z' = Z'_\chi \cos\beta + Z'_\psi \sin\beta. \tag{2}$$

Specific choices of β: $\beta = 0$; $\beta = \pi/2$; $\beta = -\arctan\sqrt{5/3}$ and $\beta = \arctan\sqrt{3/5}$, corresponding to different E_6 breaking patterns, define the popular scenarios Z'_χ, Z'_ψ, Z'_η and Z'_I, respectively.

(ii) The left-right models, originating from the breaking down of an $SO(10)$ grand-unification symmetry, and where the corresponding $Z'_{\rm LR}$ couple to a linear combination of right-handed and $B-L$ neutral currents (B and L being baryon and lepton numbers, respectively):

$$J^\mu_{\rm LR} = \alpha_{\rm LR} J^\mu_{3R} - \frac{1}{2\alpha_{\rm LR}} J^\mu_{B-L} \quad \text{with} \quad \alpha_{\rm LR} = \sqrt{\frac{c_W^2}{s_W^2}\,\kappa^2 - 1}. \tag{3}$$

Here, $s_W = \sin\theta_W$, $c_W = \sqrt{1 - s_W^2}$, additional parameters are the ratio $\kappa = g_{\rm R}/g_{\rm L}$ of the $SU(2)_{\rm L,R}$ gauge couplings and $\alpha_{\rm LR}$, restricted to the range $\sqrt{2/3} \lesssim \alpha_{\rm LR} \lesssim 1.52$. The upper bound corresponds to the so-called LR-symmetric $Z'_{\rm LRS}$ model with $g_{\rm R} = g_{\rm L}$, while the lower bound is found to coincide with the Z'_χ model introduced above. We will consider the former one, $Z'_{\rm LRS}$, throughout the paper.

(iii) The $Z'_{\rm ALR}$ predicted by the so-called 'alternative' left-right scenario. For the LR model we need not introduce additional fermions to cancel anomalies. However, in the E_6 case a variant of this model (called the Alternative LR model) can be constructed by altering the embeddings of the SM and introducing exotic fermions into the ordinary 10 and 5 representations.

(iv) The so-called sequential $Z'_{\rm SSM}$, where the couplings to fermions are the same as those of the SM Z.

Detailed descriptions of these models, as well as the specific references, can be found, e. g., in Refs. [1, 2, 4, 6].

In the extended gauge theories predicting the existence of an extra neutral Z' gauge boson, the mass-squared matrix of the Z and Z' can have non-diagonal entries δM^2, which are related to the vacuum expectation values of the fields of an extended Higgs sector [4]:

$$M^2_{ZZ'} = \begin{pmatrix} M_Z^2 & \delta M^2 \\ \delta M^2 & M_{Z'}^2 \end{pmatrix} . \tag{4}$$

Here, Z and Z' denote the weak gauge boson eigenstates of $SU(2)_L \times U(1)_Y$ and of the extra $U(1)'$, respectively. The mass eigenstates, Z_1 and Z_2, diagonalizing the matrix (4), are then obtained by the rotation of the fields Z and Z' by a mixing angle ϕ:

$$Z_1 = Z\cos\phi + Z'\sin\phi \, , \tag{5}$$

$$Z_2 = -Z\sin\phi + Z'\cos\phi \, . \tag{6}$$

Here, the mixing angle ϕ is expressed in terms of masses as:

$$\tan^2\phi = \frac{M_Z^2 - M_1^2}{M_2^2 - M_Z^2} \simeq \frac{2M_Z\Delta M}{M_2^2} \, , \tag{7}$$

where $\Delta M = M_Z - M_1 > 0$, M_Z is the mass of the Z_1-boson in the absence of mixing, i.e., for $\phi = 0$. Once we assume the mass M_1 to be determined experimentally, the mixing

depends on two free parameters, which we identify as ϕ and M_2. We shall here consider the configuration $M_1 \ll \sqrt{s} \ll M_2$.

The mixing angle ϕ will play an important role in our analysis. In general, such mixing effects reflect the underlying gauge symmetry and/or the Higgs sector of the model. To a good approximation, for $M_1 \ll M_2$, in specific "minimal-Higgs models" [24],

$$\phi \simeq -s_{\rm W}^2 \, \frac{\sum_i \langle \Phi_i \rangle^2 I_{3L}^i Q_i'}{\sum_i \langle \Phi_i \rangle^2 (I_{3L}^i)^2} = \mathcal{C} \, \frac{M_1^2}{M_2^2}. \tag{8}$$

Here $\langle \Phi_i \rangle$ are the Higgs vacuum expectation values spontaneously breaking the symmetry, and Q_i' are their charges with respect to the additional $U(1)'$. In addition, in these models the same Higgs multiplets are responsible for both generation of mass M_1 and for the strength of the Z-Z' mixing [1]. Thus $\mathcal{C}$ is a model-dependent constant. For example, in the case of E_6 superstring-inspired models $\mathcal{C}$ can be expressed as [24]

$$\mathcal{C} = 4 s_{\rm W} \left(A - \frac{\sigma - 1}{\sigma + 1} B \right), \tag{9}$$

where σ is the ratio of vacuum expectation values squared, and the constants A and B are determined by the mixing angle β: $A = \cos\beta / 2\sqrt{6}$, $B = \sqrt{10}/12 \sin\beta$.

An important property of the models under consideration is that the gauge eigenstate Z' does not couple to the W^+W^- pair since it is neutral under $SU(2)_L$. Therefore the process (1), and the searched-for deviations of the cross sections from the SM, are sensitive to a Z' only in the case of a non-zero Z-Z' mixing. The mixing angle is rather highly constrained, to an upper limit of a few $\times 10^{-3}$, mainly from LEP measurements at the Z [7, 8]. The high statistics on W-pair production expected at the ILC might in principle allow to probe such small mixing angles effectively.

From (5) and (6), one obtains the vector and axial-vector couplings of the Z_1 and Z_2 bosons to fermions:

$$v_{1f} = v_f \cos\phi + v_f' \sin\phi \, , \quad a_{1f} = a_f \cos\phi + a_f' \sin\phi \, , \tag{10}$$

$$v_{2f} = -v_f \sin\phi + v_f' \cos\phi \, , \quad a_{2f} = -a_f \sin\phi + a_f' \cos\phi, \tag{11}$$

with $(v_f, a_f) = (g_L^f \pm g_R^f)/2$, and (v_f', a_f') similarly defined in terms of the Z' couplings. The fermonic Z' couplings can be found in [1, 2, 4, 6].

Analogously, one obtains according to the remarks above:

$$g_{WWZ_1} = \cos\phi \; g_{WWZ} \, , \tag{12}$$

$$g_{WWZ_2} = -\sin\phi \; g_{WWZ} \, , \tag{13}$$

where $g_{WWZ} = \cot\theta_W$.

III. PARAMETERIZATIONS OF Z'-BOSON AND AGC EFFECTS

A. Z' boson

The starting point of our analysis will be the amplitude for the process (1). In the Born approximation, this can be written as a sum of a t-channel and an s-channel component. In the SM case, the latter will be schematically written as follows:

$$\mathcal{M}_s^{(\lambda)} = \left(-\frac{1}{s} + \frac{\cot\theta_W (v - 2\lambda a)}{s - M_Z^2} \right) \times \mathcal{G}^{(\lambda)}(s, \theta), \tag{14}$$

where s and θ are the total c.m. squared energy and W^- production angle. Omitting the fermion subscripts, electron vector and axial-vector couplings in the SM are denoted as $v = (T_{3,e} - 2Q_e\, s_W^2)/2 s_W c_W$ and $a = T_{3,e}/2 s_W c_W$, respectively, with $T_{3,e} = -1/2$, and λ denoting the electron helicity ($\lambda = \pm 1/2$ for right/left-handed electrons). Finally, $\mathcal{G}^{(\lambda)}(s, \theta)$ is a kinematical coefficient, depending also on the $W^\pm$ helicities. The explicit form can be found in the literature [20, 21] or derived from the entries of Table V, which also shows the form of the t-channel neutrino exchange.

In the extended gauge models the process (1) is described by the set of diagrams displayed in Fig. 1. The amplitude with the extra Z' depicted in Fig. 1 will be written as:

$$\mathcal{M}_s^{(\lambda)} = \left(-\frac{1}{s} + \frac{g_{WWZ_1}(v_1 - 2\lambda a_1)}{s - M_1^2} + \frac{g_{WWZ_2}(v_2 - 2\lambda a_2)}{s - M_2^2} \right) \times \mathcal{G}^{(\lambda)}(s, \theta). \tag{15}$$

The contribution of the new heavy neutral gauge boson Z_2 to the amplitude of process (1) is represented by the fourth diagram in Fig. 1. In addition, there are indirect contributions to the Z_1-mediated diagram, represented by modifications of the electron and three-boson vertices induced by the Z-Z' mixing.

It is convenient to rewrite Eq. (15) in the following form [17]:[2]

$$\mathcal{M}_s^{(\lambda)} = \left(-\frac{g_{WW\gamma}}{s} + \frac{g_{WWZ}(v - 2\lambda a)}{s - M_Z^2} \right) \times \mathcal{G}^{(\lambda)}(s, \theta), \tag{16}$$

where the 'effective' gauge boson couplings $g_{WW\gamma}$ and g_{WWZ} are defined as:

$$g_{WW\gamma} = 1 + \Delta_\gamma = 1 + \Delta_\gamma(Z_1) + \Delta_\gamma(Z_2), \tag{17}$$

[2] Note that $M_Z = M_1 + \Delta M$, where M_1 refers to the mass eigenstate.

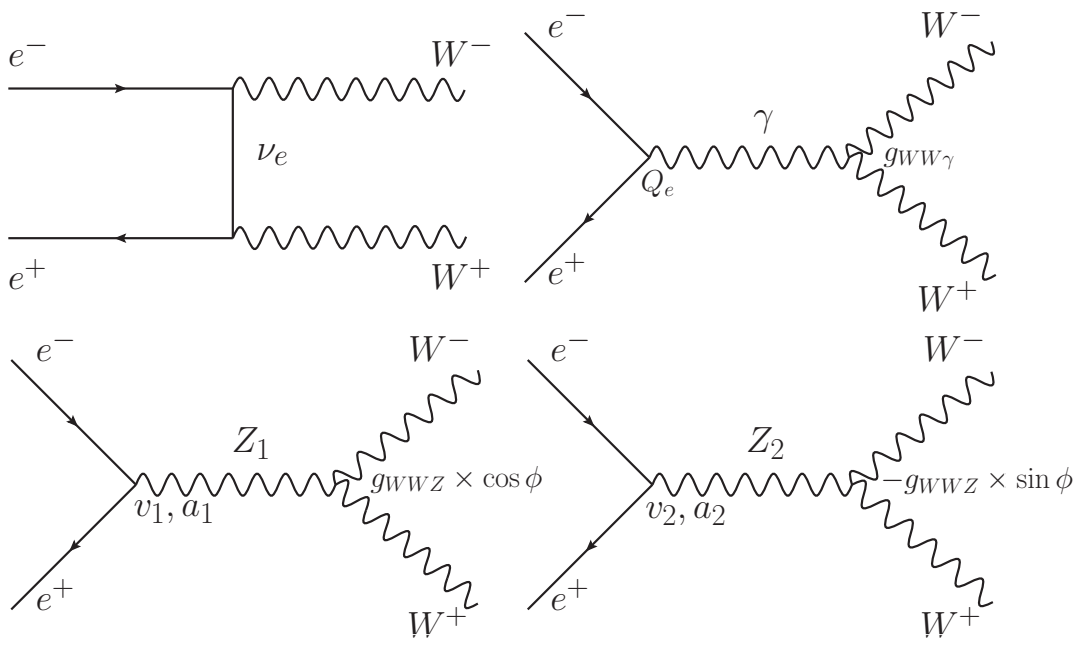

FIG. 1: Feynman diagrams for the process $e^-e^+ \to W^-W^+$ in the Born approximation

$$g_{WWZ} = \cot\theta_W + \Delta_Z = \cot\theta_W + \Delta_Z(Z_1) + \Delta_Z(Z_2), \tag{18}$$

with

$$\Delta_\gamma(Z_1) = v\,\cot\theta_W \left(\frac{\Delta a}{a} - \frac{\Delta v}{v}\right)(1+\Delta\chi)\,\chi; \quad \Delta_\gamma(Z_2) = v\,g_{WWZ_2}\left(\frac{a_2}{a} - \frac{v_2}{v}\right)\chi_2, \tag{19}$$

$$\Delta_Z(Z_1) = \Delta g_{WWZ} + \cot\theta_W \left(\frac{\Delta a}{a} + \Delta\chi\right); \qquad \Delta_Z(Z_2) = g_{WWZ_2}\,\frac{a_2}{a}\,\frac{\chi_2}{\chi}. \tag{20}$$

In Eqs. (19) and (20) we have introduced the deviations of the fermionic and trilinear bosonic couplings $\Delta v = v_1 - v$, $\Delta a = a_1 - a$ and $\Delta g_{WWZ} = g_{WWZ_1} - \cot\theta_W$, and the neutral vector boson propagators (neglecting their widths):

$$\chi(s) = \frac{s}{s - M_Z^2}; \qquad \chi_2(s) = \frac{s}{s - M_2^2}; \qquad \Delta\chi(s) \simeq -\frac{2M_Z\Delta M}{s - M_Z^2}, \tag{21}$$

where $\Delta M = M_Z - M_1$ is the Z-Z_1 mass shift. Because W pair production is studied sufficiently far away from the Z_1 peak, we can neglect the Z and $Z_{1,2}$ widths in (15) and (16).

It should be stressed that, not referring to specific models, the parametrization (16)-(18) is both general and useful for phenomenological purposes, in particular to compare different sources of nonstandard effects contributing finite deviations (19) and (20) to the SM predictions. Note that Δ_γ vanishes as $s \to 0$, consistent with gauge invariance.

We know from current measurements [7] that $\Delta M < 100$ MeV. This allows the approximation $\Delta\chi(s) \ll 1$. One can rewrite (19) and (20) in a simplified form taking into account the approximation above as well as the couplings to first order in ϕ as:

$$(v_1,\, a_1) \simeq (v + v'\,\phi,\, a + a'\,\phi) \Rightarrow (\Delta v,\, \Delta a) \simeq (v'\,\phi,\, a'\,\phi), \tag{22}$$

$$(v_2,\, a_2) \simeq (-v\,\phi + v',\, -a\,\phi + a'), \tag{23}$$

and

$$g_{WWZ_1} \simeq g_{WWZ}; \qquad g_{WWZ_2} \simeq -g_{WWZ}\,\phi. \tag{24}$$

In the case of extended models considered here, e.g. E_6, v' and a' are explicitly parametrized in terms of the angle β which characterizes the direction of the Z'-related extra $U(1)'$ generator in the E_6 group space, and reflects the pattern of symmetry breaking to $SU(2)_L \times U(1)_Y$ [1, 2, 4, 6]:

$$v' = \frac{\cos\beta}{c_W\sqrt{6}}; \qquad a' = \frac{1}{2c_W\sqrt{6}}\left(\cos\beta + \sqrt{\frac{5}{3}}\sin\beta\right). \tag{25}$$

Substituting Eqs. (22)–(24) into (19) and (20), one finds the general form of Δ_γ and Δ_Z:

$$\Delta_\gamma = \phi \cdot v\,\cot\theta_W\,\left(\frac{a'}{a} - \frac{v'}{v}\right)\left(1 - \frac{\chi_2}{\chi}\right)\chi, \tag{26}$$

$$\Delta_Z = \phi \cdot \cot\theta_W\,\frac{a'}{a}\left(1 - \frac{\chi_2}{\chi}\right). \tag{27}$$

Both these quantities have the *same* dependence on ϕ and M_2, via the product $\phi(1-\chi_2/\chi)$. Thus, ϕ and M_2 can not be separately determined from a measurement of Δ_γ and Δ_Z, only this composite function can be determined. We also note that for an SSM-type model, the first parenthesis in Eq. (26) vanishes, resulting in $\Delta_\gamma = 0$. Thus, these models can not be distinguished from the AGC models, introduced in the next section. Further, the terms proportional to χ_2 in Eqs. (26) and (27) dominate in the case $\sqrt{s} \approx M_2$ but will be very small in the case $\sqrt{s} \ll M_2$.

B. Anomalous Gauge Couplings

As pointed out in the Introduction, a model with an extra Z' would produce virtual manifestations in the final W^+W^- channel at the ILC that in principle could mimic those of a model with AGC, hence of completely different origin. This is due to the fact that, as

shown above, the effects of the extra Z' can be reabsorbed into a redefinition of the WWV couplings ($V = \gamma,\ Z$). Therefore, the identification of such an effect, if observed at the ILC, becomes a very important problem [25].

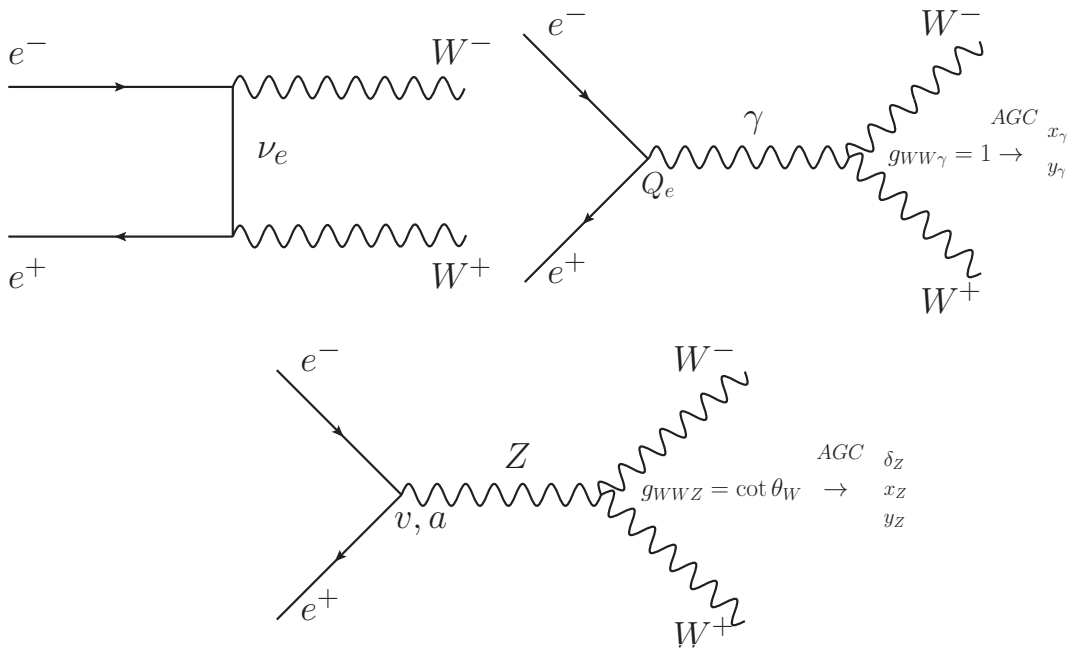

FIG. 2: Feynman diagrams for the process $e^+e^- \to W^+W^-$ in the Standard Model and with anomalous trilinear gauge couplings (AGC).

Using the notations of, e.g., Ref. [20, 21], the relevant trilinear WWV interaction up to operators of dimension-6, which conserves $U(1)_{\rm e.m.}$, C and P, can be written as ($e = \sqrt{4\pi\alpha_{em}}$):

$$\begin{aligned}
\mathcal{L}_{\rm eff} \;=\; & -ie\left[A_\mu\left(W^{-\mu\nu}W^+_\nu - W^{+\mu\nu}W^-_\nu\right) + F_{\mu\nu}W^{+\mu}W^{-\nu}\right] \\
& -\; ie\,(\cot\theta_W + \delta_Z)\left[Z_\mu\left(W^{-\mu\nu}W^+_\nu - W^{+\mu\nu}W^-_\nu\right) + Z_{\mu\nu}W^{+\mu}W^{-\nu}\right] \\
& -\; ie\,x_\gamma\,F_{\mu\nu}W^{+\mu}W^{-\nu} - ie\,x_Z\,Z_{\mu\nu}W^{+\mu}W^{-\nu} \\
& +\; ie\,\frac{y_\gamma}{M_W^2}\,F^{\nu\lambda}W^-_{\lambda\mu}W^{+\mu}_{\ \ \nu} + ie\,\frac{y_Z}{M_W^2}\,Z^{\nu\lambda}W^-_{\lambda\mu}W^{+\mu}_{\ \ \nu}\,,
\end{aligned} \tag{28}$$

where $W^\pm_{\mu\nu} = \partial_\mu W^\pm_\nu - \partial_\nu W^\pm_\mu$ and $Z_{\mu\nu} = \partial_\mu Z_\nu - \partial_\nu Z_\mu$. In the SM at the tree-level, the anomalous couplings in (28) vanish: $\delta_Z = x_\gamma = x_Z = y_\gamma = y_Z = 0$.

The anomalous gauge couplings are here parametrized in terms of five real independent parameters. This number can be reduced by imposing additional constraints, like local

$SU(2)_L \times U(1)_Y$ symmetry, in which case the number would be reduced to three (see for example Tables 2 and 1 of [26] and [27], respectively).

Current limits reported by the Particle Data Group [28], that show the sensitivity to the AGCs attained so far, are roughly of the order of 0.04 for δ_Z, 0.05 for x_γ, 0.02 for y_γ, 0.11 for x_Z and 0.12 for y_Z. As will be shown in the next sections, at the ILC in the energy and luminosity configuration considered here, sensitivities to deviations from the SM, hence of indirect New Physics signatures, down to the order of 10^{-3} will be reached. This would compare with the expected order of magnitude of the theoretical uncertainty on the SM cross sections after accounting for higher-order corrections to the Born amplitudes of Figs. 1 and 2, formally of order $\alpha_{\rm em}$ [29, 30], but that for distributions can reach the size of 10%, depending on $\sqrt{s}$ [31, 32].

C. Helicity amplitudes and cross sections

The general expression for the cross section of process (1) with longitudinally polarized electron and positron beams described by the set of diagrams presented in Fig. 2 can be expressed as

$$\frac{d\sigma}{d\cos\theta} = \frac{1}{4}\left[(1+P_L)\left(1-\bar{P}_L\right)\frac{d\sigma^+}{d\cos\theta} + (1-P_L)\left(1+\bar{P}_L\right)\frac{d\sigma^-}{d\cos\theta}\right], \tag{29}$$

where P_L and $\bar{P}_L$ are the actual degrees of electron and positron longitudinal polarization, respectively, and $\sigma^\pm$ are the cross sections for purely right-handed ($\lambda = 1/2$) and left-handed ($\lambda = -1/2$) electrons. From Eq. (29), the cross section for polarized (unpolarized) electrons and unpolarized positrons corresponds to $P_L \neq 0$ and $\bar{P}_L = 0$ ($P_L = \bar{P}_L = 0$).

The polarized cross sections can generally be written as follows:

$$\frac{d\sigma^\pm}{d\cos\theta} = \frac{|\mathbf{p}|}{16\pi s\sqrt{s}}\sum_{\tau,\tau'}|F_{\lambda\tau\tau'}(s,\cos\theta)|^2. \tag{30}$$

Here, the helicities of the W^- and W^+ are denoted by $\tau, \tau' = \pm 1, 0$. Corresponding to the interaction (28), the helicity amplitudes $F_{\lambda\tau\tau'}(s,\cos\theta)$ have the structure shown in Table V [20, 21] in Appendix A. In Table V, $\beta_W = \sqrt{1-4M_W^2/s} = 2p/\sqrt{s}$, with $p = |\boldsymbol{p}|$ the c.m. momentum of the W^-. Furthermore, s and t are the Mandelstam variables, and θ the c.m. scattering angle, with $t = M_W^2 - s(1-\beta\cos\theta)/2$. For comparison, we also show in Appendix A the corresponding helicity amplitudes for the case of a Z'.

We define the differential cross sections for correlated spins of the produced W^- and W^+,

$$\frac{d\sigma(W_L^+W_L^-)}{d\cos\theta}, \qquad \frac{d\sigma(W_T^+W_T^-)}{d\cos\theta}, \qquad \frac{d\sigma(W_T^+W_L^- + W_L^+W_T^-)}{d\cos\theta}, \tag{31}$$

which correspond to the production of two longitudinally ($\tau = \tau' = 0$), two transversely ($\tau = \pm\tau'$; $\tau, \tau' = \pm 1$) and one longitudinally plus one transversely ($\tau = 0$, $\tau' = \pm 1$ etc.) polarized vector bosons, respectively.

IV. Z' ILLUSTRATIONS

For illustrative purposes, the energy behavior of the total unpolarized cross section for the process $e^+e^- \to W^+W^-$ is shown in Fig. 3 (top panel) for the SM (extrapolated to 2 TeV) as well as for the case of an additional Z'_χ originated from E_6 at mixing angle $\phi = \pm\, 1.6 \cdot 10^{-3}$ and $M_{Z'} = 2$ TeV. In the lower panel we show the corresponding cross section for right-handed electrons ($P_L = 1$). The deviation of the cross sections from the SM prediction caused by the Z' boson at the planned ILC energy of $\sqrt{s} = 0.5$ TeV is most pronounced for the latter (polarized) case while the cross section is lower than that for unpolarized beams. The main reason for this is the removal of the neutrino exchange in the t-channel. Such a removal is indispensable for evidencing the Z'-exchange effect through Z–Z' mixing in the process (1). The complete removal of the neutrino exchange contribution depends of course on having pure electron polarization. In both cases experimental constraints on the W^- scattering angle ($|\cos\theta| \leq 0.98$) were imposed.

The effects of the Z' boson shown in Fig. 3 were parametrized by the mass $M_{Z'}$ and the Z-Z' mixing angle ϕ while those behaviors and their relative deviations shown in Fig. 4, are parametrized by the effective parameters $(\Delta_\gamma, \Delta_Z)$, defined in Eqs. (26) and (27) for the same values of ϕ and $M_{Z'}$. Rather steep energy behavior of relative deviations of the cross sections can be appreciated from Fig. 4.

As was mentioned in the Introduction, the process (1) is sensitive to a Z' in the case of non-zero Z-Z' mixing. The individual (interference) contributions to the cross section of process (1) rise proportional to s. In the SM, the sum over all contributions to the total cross section results in its proper energy dependence that scales like $\log s/s$ in the limit when $2M_W \ll \sqrt{s} \ll M_2$ due to a delicate gauge cancellation. In the case of a non-zero Z-Z' mixing, the couplings of the Z_1 differ from those of the SM predictions for Z. Then,

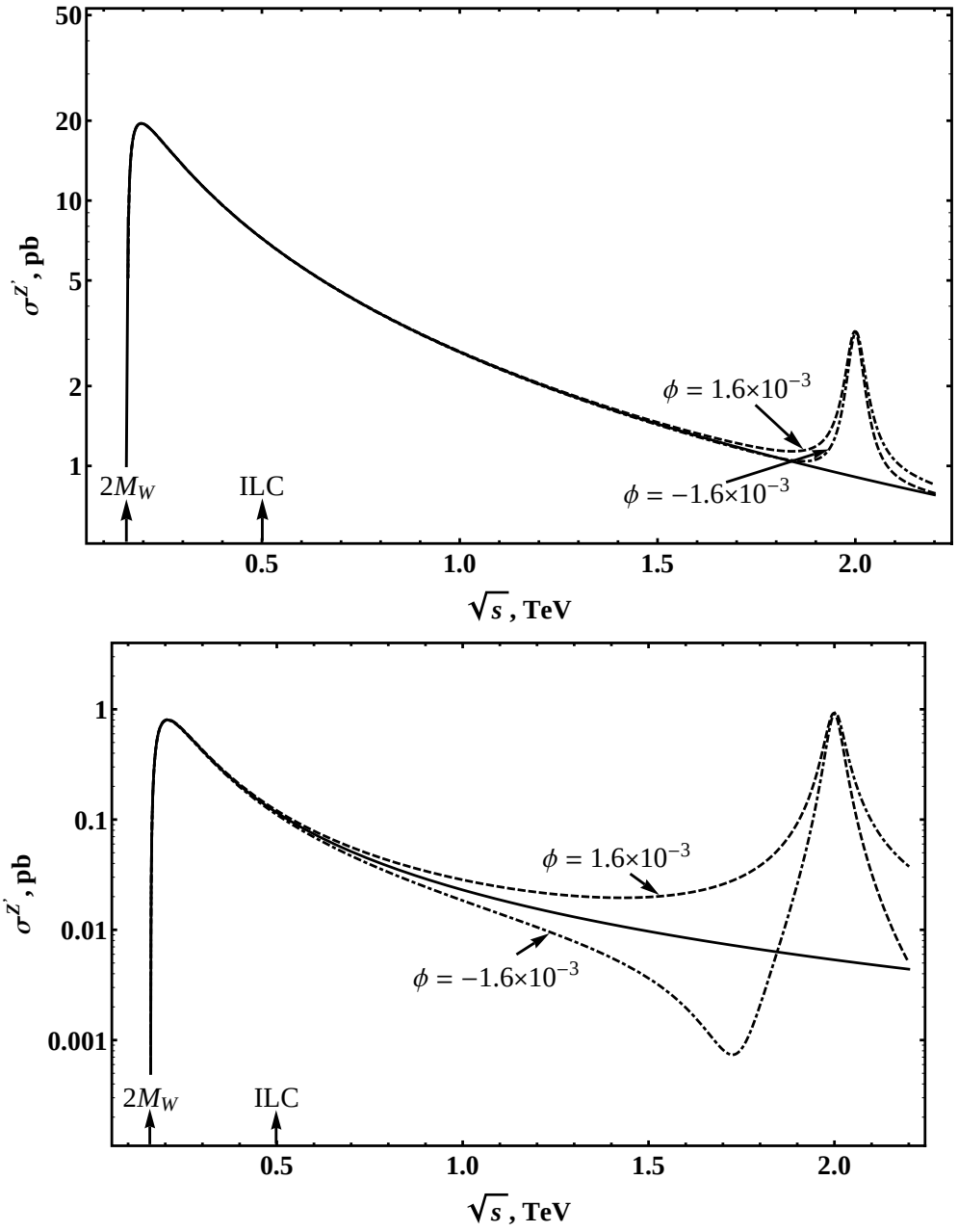

FIG. 3: Top panel: Unpolarized total cross section for the process $e^+e^- \to W^+W^-$ for Z'_χ from E_6. Bottom panel: Polarized total cross section. Solid lines correspond to the SM case. Dashed (dash-dotted) lines correspond to a Z' model with $\phi = 1.6 \cdot 10^{-3}$ ($\phi = -1.6 \cdot 10^{-3}$), $\Gamma_2 = 0.025 \times M_2$ and $M_2 = 2$ TeV.

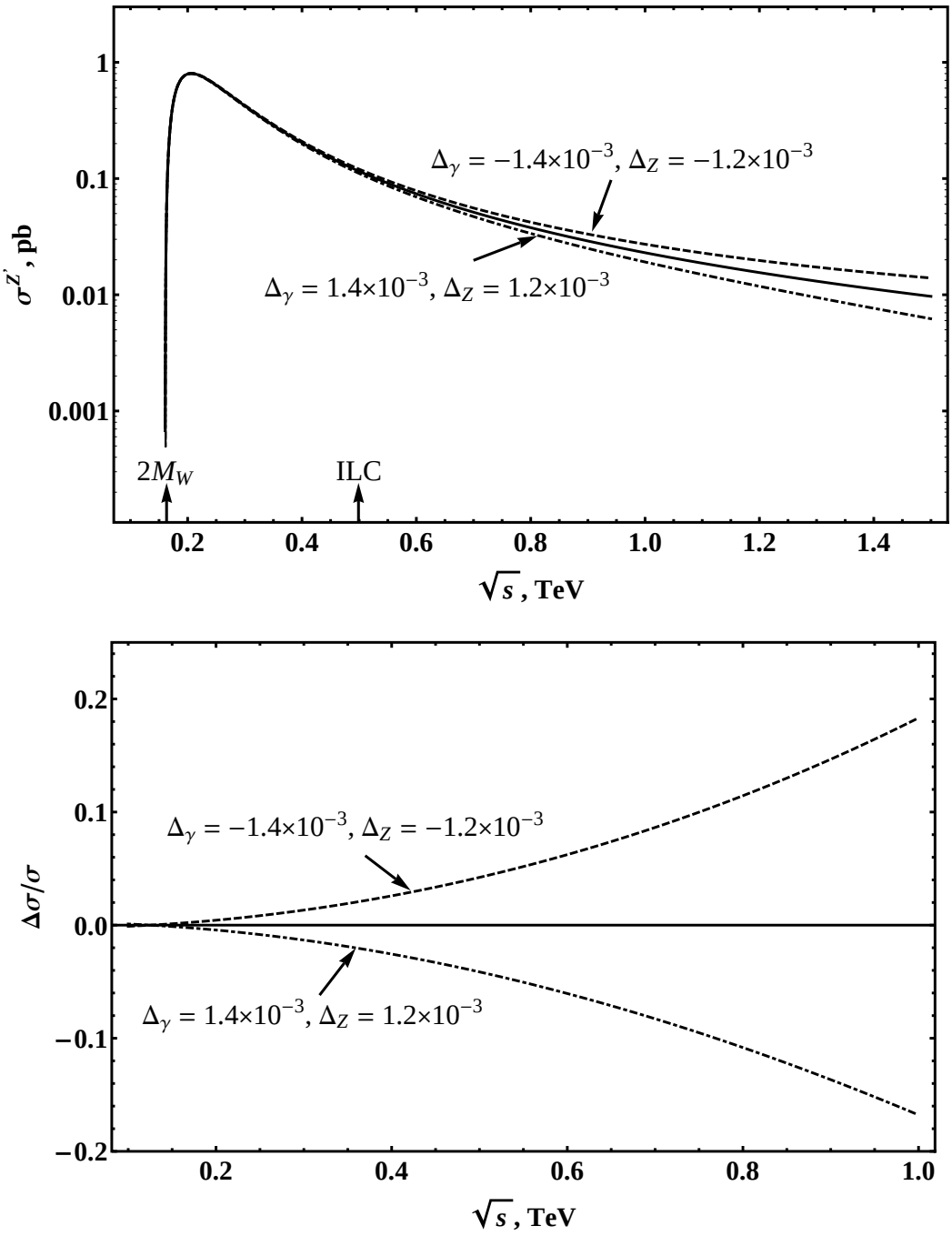

FIG. 4: Top panel: Polarized total cross section for the process $e^+e^- \to W^+W^-$ as a function of $\sqrt{s}$ with perfectly polarized electrons ($P_L = 1$) and unpolarized final states. Solid line corresponds to the SM. Contribution to the cross section caused by Z' is determined by different sets of parameters $(\Delta_\gamma, \Delta_Z) = (1.4 \cdot 10^{-3}, 1.2 \cdot 10^{-3})$ and $(-1.4 \cdot 10^{-3}, -1.2 \cdot 10^{-3})$. Bottom panel: Relative deviation of the polarized total cross section from the SM prediction, $\Delta\sigma/\sigma = (\sigma^{Z'} - \sigma^{SM})/\sigma^{SM}$.

the gauge cancellation occurring in the SM is destroyed, leading to an enhancement of new physics effects at high energies, though well below M_2. Unitarity is restored only at energies $\sqrt{s} \gg M_2$ independently of details of the extended gauge group.

V. DISCOVERY REACH ON Z' PARAMETERS

The sensitivity of the polarized differential cross sections to Δ_γ and Δ_Z is assessed numerically by dividing the angular range $|\cos\theta| \leq 0.98$ into 10 equal bins, and defining a χ^2 function in terms of the expected number of events $N(i)$ in each bin for a given combination of beam polarizations:

$$\chi^2 = \chi^2(\sqrt{s}, \Delta_\gamma, \Delta_Z) = \sum_{\{P_L, \bar{P}_L\}} \sum_{i}^{\text{bins}} \left[\frac{N_{\text{SM}+Z'}(i) - N_{\text{SM}}(i)}{\delta N_{\text{SM}}(i)} \right]^2 , \tag{32}$$

where $N(i) = \mathcal{L}_{\text{int}}\, \sigma_i\, \varepsilon_W$ with $\mathcal{L}_{\text{int}}$ the time-integrated luminosity. Furthermore,

$$\sigma_i = \sigma(z_i, z_{i+1}) = \int_{z_i}^{z_{i+1}} \left(\frac{d\sigma}{dz} \right) dz, \tag{33}$$

where $z = \cos\theta$ and polarization indices have been suppressed. Also, ε_W is the efficiency for W^+W^- reconstruction, for which we take the channel of lepton pairs ($e\nu + \mu\nu$) plus two hadronic jets, giving $\varepsilon_W \simeq 0.3$ basically from the relevant branching ratios. The procedure outlined above is followed to evaluate both $N_{\text{SM}}(i)$ and $N_{\text{SM}+Z'}(i)$.

The uncertainty on the number of events $\delta N_{\text{SM}}(i)$ combines both statistical and systematic errors where the statistical component is determined by $\delta N_{\text{SM}}^{\text{stat}}(i) = \sqrt{N_{\text{SM}}(i)}$. Concerning systematic uncertainties, an important source is represented by the uncertainty on beam polarizations, for which we assume $\delta P_L/P_L = \delta \bar{P}_L/\bar{P}_L = 0.5\%$ with the "standard" envisaged values $|P_L| = 0.8$ and $|\bar{P}_L| = 0.5$ [12, 13, 22]. As for the time-integrated luminosity, for simplicity we assume it to be equally distributed between the different polarization configurations. Another source of systematic uncertainty originates from the efficiency of reconstruction of $W^\pm$ pairs which we assume to be $\delta\varepsilon_W/\varepsilon_W = 0.5\%$. Also, in our numerical analysis to evaluate the sensitivity of the differential distribution to model parameters we include initial-state QED corrections to on-shell $W^\pm$ pair production in the flux function approach [33, 34] that assures a good approximation within the expected accuracy of the data.

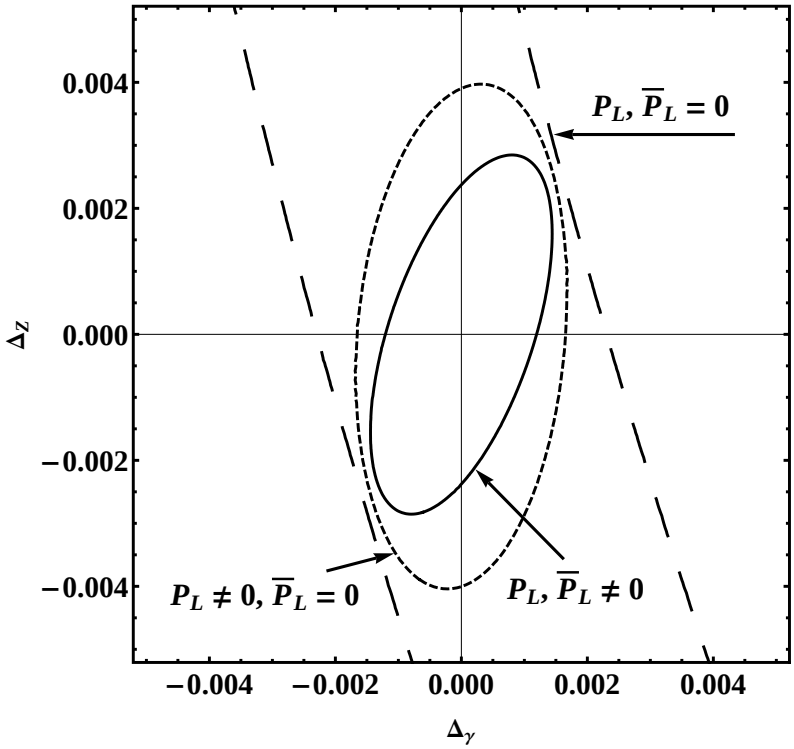

FIG. 5: Discovery reach (see Eq. (34)) at 95% CL on the Z' parameters Δ_γ, Δ_Z obtained from polarized differential cross sections at different sets of polarization: $P_L = \pm 0.8,\ \bar{P}_L = \mp 0.5$ (solid line), $P_L = \pm 0.8,\ \bar{P}_L = 0$ (short-dashed line), unpolarized beams $P_L = 0,\ \bar{P}_L = 0$ (long-dashed line), $\sqrt{s} = 0.5$ TeV and $\mathcal{L}_{\rm int} = 500$ fb^{-1}.

As a criterion to derive the constraints on the coupling constants in the case where no deviations from the SM were observed within the foreseeable uncertainties on the measurable cross sections, we impose that

$$\chi^2 \leq \chi^2_{\rm min} + \chi^2_{\rm CL}, \tag{34}$$

where $\chi^2_{\rm CL}$ is a number that specifies the chosen confidence level, $\chi^2_{\rm min}$ is the minimal value of the χ^2 function. With two independent parameters in Eqs. (17) and (18), the 95% CL is obtained by choosing $\chi^2_{\rm CL} = 5.99$.

From the numerical procedure outlined above, we obtain the allowed regions in Δ_γ and Δ_Z determined from the differential polarized cross sections with different sets of polarization (as well as from the unpolarized process (1)) depicted in Fig. 5, where $\mathcal{L}_{\rm int} = 500$ fb^{-1} has been taken [12, 13, 22]. According to the condition (34), the values of Δ_γ and Δ_Z for which Z's can be discovered at the ILC is represented by the region external to the ellipse. The same is true for the AGC model except that, having assumed no renormalization of the

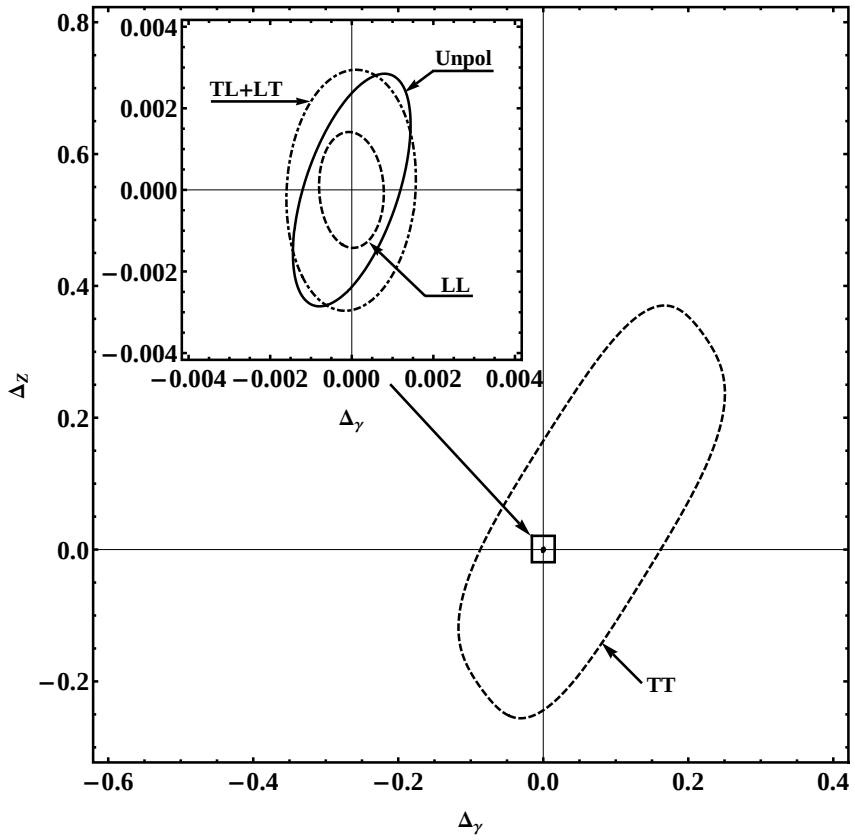

FIG. 6: Discovery reach on the Z' parameters Δ_γ, Δ_Z from the cross section with polarized beams $P_L = \pm 0.8,\ \bar{P}_L = \mp 0.5$ and different sets of $W^\pm$ polarizations. Here, $\sqrt{s} = 0.5$ TeV and $\mathcal{L}_{\rm int} = 500$ fb^{-1}.

residue of the photon pole exchange ($\delta_\gamma = 0$), in this case Δ_γ will be proportional to s times the coefficients x_γ or y_γ of Eq. (28), and Δ_Z to a combination of the coefficients δ_Z, x_Z and y_Z (see Table V). The role of initial beam polarization is seen to be essential in order to set meaningful finite bounds on the parameters.

Analogous to Fig. 5, the discovery reach on the parameters Δ_γ, Δ_Z from the cross section with polarized beams $P_L = \pm 0.8,\ \bar{P}_L = \mp 0.5$ and different sets of $W^\pm$ polarizations is depicted in Fig. 6 which demonstrates that $d\sigma(W_L^+ W_L^-)/dz$ is most sensitive to the parameters Δ_γ, Δ_Z while $d\sigma(W_T^+ W_T^-)/dz$ has the lowest sensitivity to those parameters. The reason for the lower sensitivity in the TT case is that for $s \gg M_Z^2$, the NP contributions to these amplitudes only interfere with a sub-dominant part of the SM amplitude [26].

As regards the NP scenarios of interest here, one may remark that constraints on Δ_γ and Δ_Z of Eqs. (17) and (18) (for the example of Z's), are model-independent in the sense that

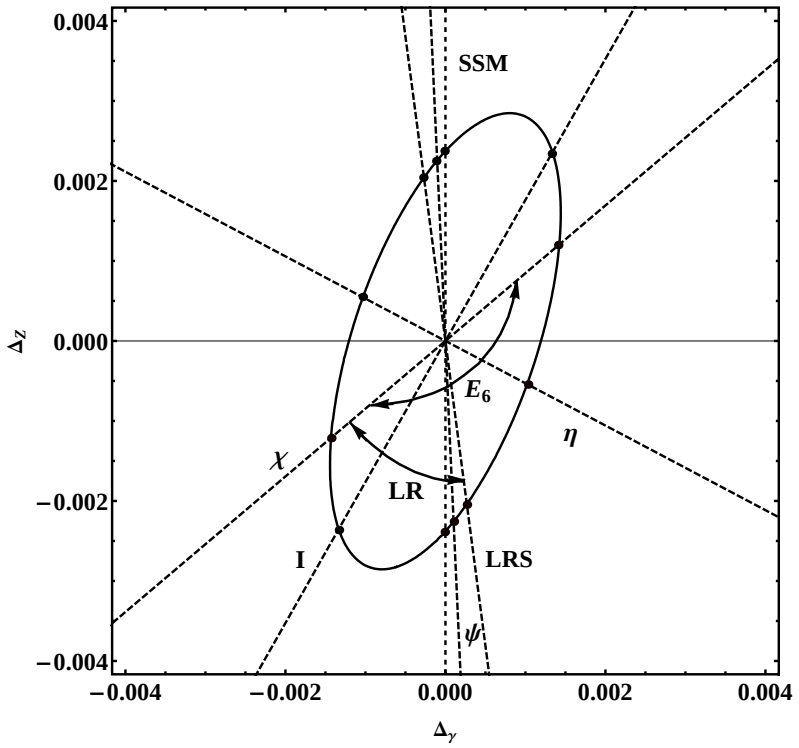

FIG. 7: Discovery reach (95% C.L.) on Z' parameters $(\Delta_\gamma, \Delta_Z)$ obtained from differential polarized cross sections with $(P_L = \pm 0.8,\ \bar{P}_L = \mp 0.5)$. Dashed straight lines correspond to specific extended gauge models (χ, ψ, η, I and LRS) according to Eq. (35). The segments of the ellipse correspond to the whole classes of E_6 and LR-models, respectively. Here, $\sqrt{s} = 0.5$ TeV and $\mathcal{L}_{\rm int} = 500$ fb^{-1}.

they constrain the whole class of Z' models considered. They may turn into constraints on the parameters of specific Z' models by replacing expressions (19) and (20). Specializing to those models, one can notice the important linear relation characterizing the deviations from the SM:

$$\Delta_Z = \Delta_\gamma \cdot \frac{1}{v\chi} \frac{(a'/a)}{(a'/a) - (v'/v)}, \tag{35}$$

where v and a refer to vector and axial-vector couplings. This relation is rather unique, and depends neither on ϕ nor on M_2, only on ratios of the electron couplings with the Z and Z' bosons.

In Fig. 7 we depict, as an illustration, the cases corresponding to the models denoted χ, ψ, η and I originated from E_6 as well as the LR symmetric model (LRS). The model independent bound on Δ_γ and Δ_Z can be converted into limits on the Z-Z' mixing angle ϕ and mass M_2 for any specific Z' model. These model dependent constraints will be presented

in the next section along with identification reaches. For fixed ϕ and M_2, every model is represented by a point in the (Δ_γ, Δ_Z) parameter plane. The discovery regions in the Δ_γ–Δ_Z plot at the ILC are represented by the straight segments lying outside the ellipse. If one varies the mixing angle ϕ, the point representative of the specific Z' model moves along the corresponding line. The intercept of the lines with the elliptic contour, once translated to ϕ and M_2, determine the constraint on these two parameters relevant to Z-Z' mixing for the individual models.

Also, one can determine the region in the $(\Delta_\gamma, \Delta_Z)$ plane relevant to constraining the full class of E_6 (and LR) Z' models obtained by varying the parameters $\cos\beta$ and $\alpha_{\rm LR}$ of Eqs. (2) and (3) within their full allowed ranges. The corresponding discovery region at the ILC for that class of models is the one delimited by the arcs of ellipse indicated in Fig. 7.

VI. IDENTIFICATION OF Z' VS AGC

A. Model independent analysis

We will here discuss how one can differentiate various Z' models from similar effects caused by anomalous gauge couplings, following the procedure employed in Refs. [23, 35]. The philosophy is as follows: A particular Z' model will be considered identified, if the measured values of Δ_γ and Δ_Z are statistically different from values corresponding to other Z' models (for a discussion, see Ref. [23]), and also different from ranges of $(\Delta_\gamma, \Delta_Z)$ that can be populated by AGC models. Clearly, at least one of these parameters must exceed some minimal value.

Let us assume the data to be consistent with one of the Z' models and call it the "true" model. It has some non-zero values of the parameters Δ_γ, Δ_Z. We want to assess the level at which this "true" model is distinguishable from the AGC models, that can compete with it as sources of the assumed deviations of the cross section from the SM and we call them "tested" models, for any values of the corresponding AGC parameters. We assume for simplicity that all AGC parameters are zero, except the one whose values are probed.

We start by considering as a "tested" AGC model that with a value of x_γ to be scanned over. To that purpose, we can define a "distance" between the chosen "true" model and the

"tested" AGC model(s) by means of a χ^2 function analogous to Eq. (32) as

$$\chi^2 = \sum_{\{P_L,\,\bar{P}_L\}} \sum_{i}^{\text{bins}} \left[\frac{N_{Z'}(i) - N_{\text{AGC}}(i)}{\delta N_{Z'}(i)} \right]^2 , \tag{36}$$

with $\delta N_{Z'}(i)$ defined in the same way as $\delta N_{\text{SM}}(i)$ but, in this case, the statistical uncertainty refers to the Z' model and therefore depends on the relevant, particular, values of Δ_γ and Δ_Z.

On the basis of such χ^2 we can study whether these "tested" models can be excluded or not to a given confidence level (which we assume to be 95%), once the considered Z' model (defined in terms of Δ_γ, Δ_Z) has been assumed as "true". In our explicit example, we want to determine the range in x_γ for which there is "confusion" of deviations from the SM cross sections between the selected "true" Z' model and the AGC one, by imposing the condition, similar to Eq. (34). Then we scan all values of Δ_γ, Δ_Z allowed by the Z' models down to their discovery reach, and determine by iteration in this procedure the general confusion region between the class of Z' models considered here and the AGC model with $x_\gamma \neq 0$.

Besides the dependence on the c.m. energy $\sqrt{s}$, the χ^2 function defined above can be considered a function of three independent variables, Δ_γ and Δ_Z from the Z' model, and, in our starting example, the parameter x_γ of the AGC scenario. The contours of the confusion regions, at given $\sqrt{s}$, are thus defined by the region *inside* of which (in the Δ_γ-Δ_Z space)

$$\chi^2(\Delta_\gamma, \Delta_Z, x_\gamma) = \chi^2_{\text{min}} + \chi^2_{\text{CL}}, \tag{37}$$

for any value of x_γ compatible with experimental limits.

In Fig. 8 we show the region of confusion in the Z' parameter plane $(\Delta_\gamma, \Delta_Z)$, outside of which the Z' model can be identified at the 95% C.L. against the AGC model for any value of the parameter x_γ. It is obtained from the polarized cross section with $P_L = \pm 0.8$ and $\bar{P}_L = \mp 0.5$ using the algorithm outlined above. Also, note that the inner dash-dotted ellipse in Fig. 8 delimits the discovery reach on Z' parameters.

The graphical representation of the region of confusion presented in Fig. 8 is straightforward. Equation (37) defines a three-dimensional surface enclosing a volume in the $(\Delta_\gamma, \Delta_Z, x_\gamma)$ parameter space in which there can be discovery as well as confusion between Z' and (in this case) the x_γ-AGC model. The planar surface delimited by the solid ellipse is determined by the projection of such three-dimensional surface, hence of the corresponding

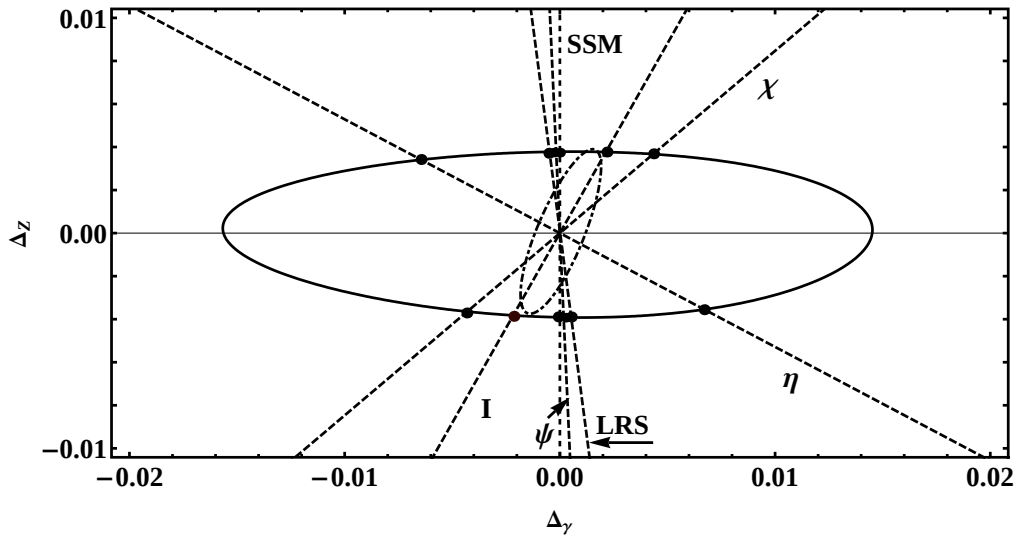

FIG. 8: The outer ellipse (solid) shows the confusion region (95% C.L., see Eq. (37)) in the parameter plane $(\Delta_\gamma, \Delta_Z)$, outside of which a generic Z' model can be identified against an AGC model with non-vanishing parameter x_γ. Polarized cross section with $P_L = \pm 0.8$ and $\bar{P}_L = \mp 0.5$ are assumed. The dashed inner ellipse reproduces the discovery reach on the Z' of Fig. 7, corresponding to $x_\gamma = 0$ in Eq. (37), where the AGC model coincides with the SM. The dashed straight lines correspond to specific extended gauge models (χ, ψ, η, I and LRS). Here, $\sqrt{s} = 0.5$ TeV and $\mathcal{L}_{\rm int} = 500$ fb^{-1}.

confusion region, onto the plane $(\Delta_\gamma, \Delta_Z)$. Any determination of Δ_γ and Δ_Z in the planar domain exterior to the ellipse would allow both Z' discovery and identification against the x_γ-AGC model. Similar to the case of discovery, also in the case of Z' identification the bounds on Δ_γ and Δ_Z could be translated into limits on the Z-Z' mixing angle ϕ and mass M_2 for any specific Z' model.

The procedure outlined above can be repeated for all other types of models with AGC parameters (δ_Z, x_Z, y_γ, y_Z), and consequently one can evaluate the corresponding "confusion regions" in the $(\Delta_\gamma, \Delta_Z)$ parameter plane. The results of this kind of analysis are represented in Fig. 9 displaying the overlap of the confusion regions (95% C.L.) in the parameter plane $(\Delta_\gamma, \Delta_Z)$ for a generic Z' vector model and AGC models with parameters varying one at a time.

The resulting confusion area (obtained from the overlap of all confusion regions) turns out to be open in the vertical direction, i.e., along the Δ_Z axis. The reason is that the Z' model defined by a particular parameter set where $(\Delta_\gamma = 0, \Delta_Z)$ is indistinguishable from

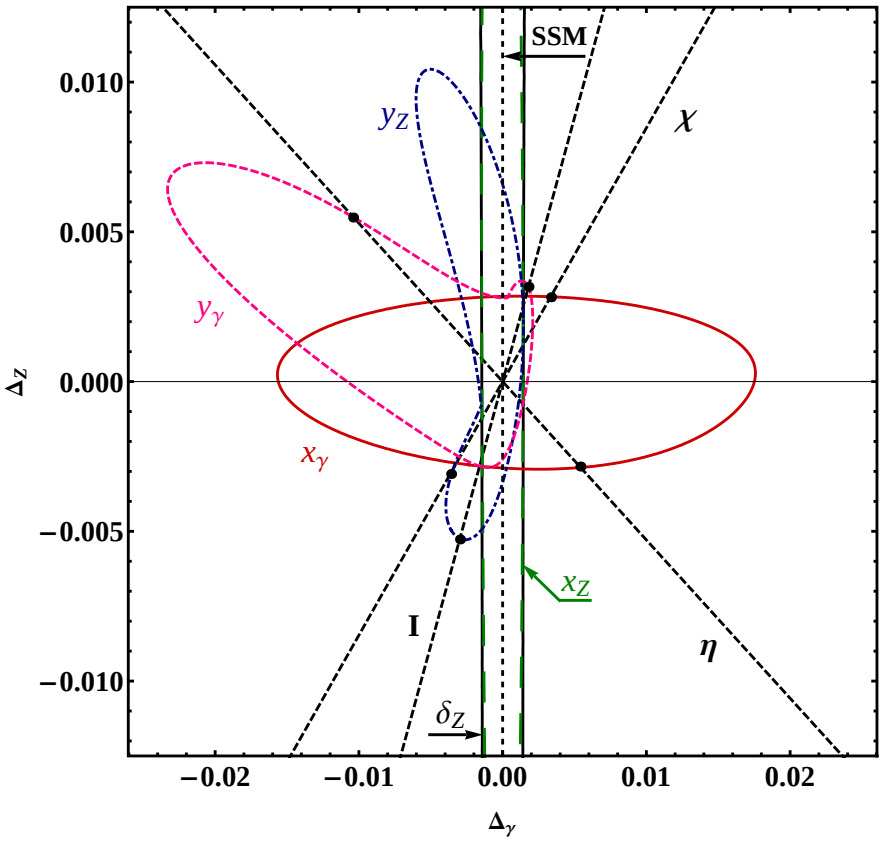

FIG. 9: The closed contours indicate regions of $(\Delta_\gamma, \Delta_Z)$ that can be populated by variations of an AGC parameter, such as for example x_γ. They are thus confusion regions (95%C.L.) in the parameter plane $(\Delta_\gamma, \Delta_Z)$ for a generic Z' model and AGC models with parameters taking non-vanishing values, one at a time: x_γ, x_Z, y_γ, y_Z and δ_Z. Polarized cross sections with $P_L = \pm 0.8$ and $\bar{P}_L = \mp 0.5$ have been exploited. Dashed straight lines correspond to specific Z' models (χ, ψ, η, I and LRS). Here, $\sqrt{s} = 0.5$ TeV and $\mathcal{L}_{\rm int} = 500$ fb^{-1}.

those originating from AGC with the same $\delta_Z = \Delta_Z$. Moreover, from a comparison of the confusion region depicted in Fig. 9 with the corresponding discovery reach presented in Fig. 7 one can conclude that all Z' models might be discovered in the process (1) with polarized beams. However, they may not all be *identified*, the reason being that the confusion region shown in Fig. 9 is not closed, in contrast to the reach shown in Fig. 7.

An example relevant to the current discussion can be found in the SSM model. In fact, from Eq. (35) one can conclude that the signature space of the SSM model in the $(\Delta_\gamma, \Delta_Z)$ parameter plane extends along Δ_Z. It implies that the SSM might be discovered in the process (1) but not separated from AGC models characterized by the parameter Δ_Z. More

generally, those models where the Z'-electron couplings satisfy the equation $v'/a' = v/a$ that, as follows from Eq. (26), lead to $\Delta_\gamma = 0$ can not be distinguished from the AGC case in the $W^\pm$ pair production process. However, all other Z' models (apart from the considered exceptional case) described by the pair of parameters $(\Delta_\gamma, \Delta_Z)$ that are located outside of the confusion area shown in Fig. 9 can be identified. Notice that the above constraint on the electron couplings is fulfilled for an E_6 model at $\beta = 87^\circ$ and for an LRS model with $\alpha_{LR} = 1.36$.

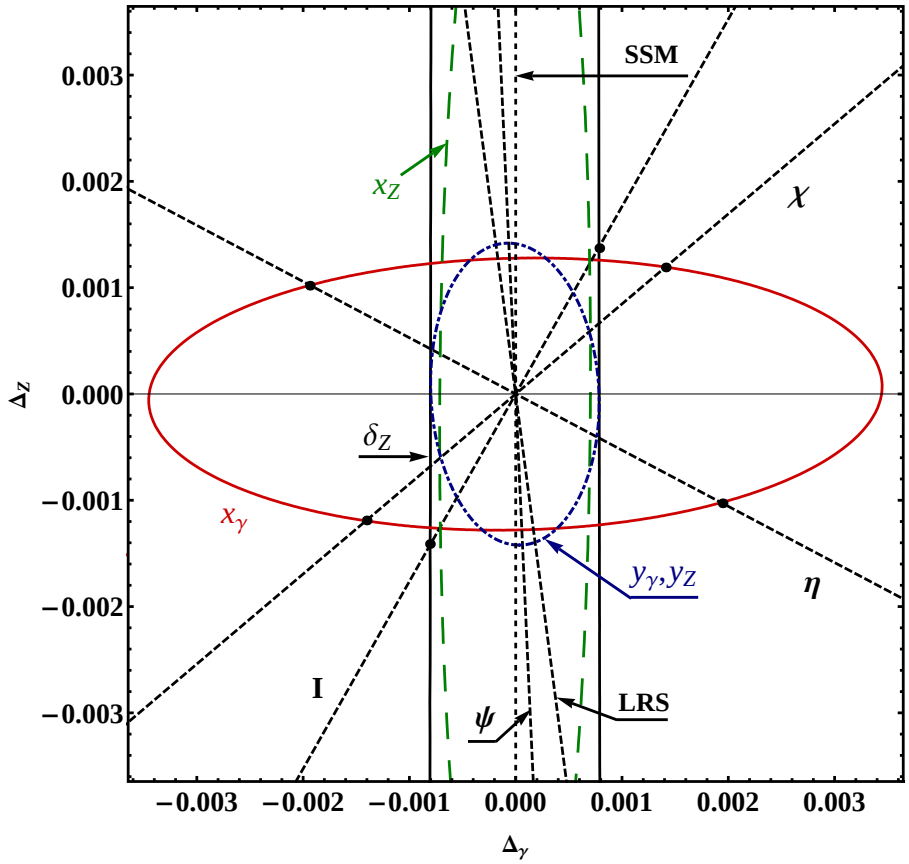

FIG. 10: Same as in Fig. 9 but obtained from combined analysis of the process (1) with polarized initial beams and polarized $W^\pm$ final states. The x_Z contour closes at $\Delta_Z \simeq \pm 0.006$.

The results of a further potential extension of the present analysis are presented in Fig. 10 where the feasibility of measuring polarized $W^\pm$ states in the process (1) is assumed. This assumption is based on the experience gained at LEP2 on measurements of W polarisation [36]. The relevant theoretical framework for measurement of $W^\pm$ polarisation was described in [20, 21]. The method exploited for the measurement of W polarisation is based on the spin density matrix elements that allow to obtain the differential cross sections for polarised

W bosons. Information on spin density matrix elements as functions of the W^- production angle with respect to the electron beam direction was extracted from the decay angles of the charged lepton in the W^- (W^+) rest frame.

B. Model dependent analysis

As mentioned above, the ranges of Δ_γ and Δ_Z allowed to the specific models in Figs. 9 and 10 can be translated into discovery and identification reaches on the mixing angle ϕ and the heavier gauge boson mass M_2, using Eqs. (26)–(27). The resulting allowed regions, discovery and identification (at the 95% CL) in the (ϕ, M_2) plane is limited in this case by the thick dashed and solid lines, respectively, in Figs. 11– 12 for some specific E_6 models. These limits are obtained from the polarized differential distributions of W with collider energy $\sqrt{s} = 0.5$ TeV and integrated luminosity $\mathcal{L}_{\rm int} = 500$ fb^{-1}. Also, an indicative typical lower bound on M_2 from direct searches at the LHC with $\sqrt{s} = 7$ TeV [9, 10] is reported in these figures as horizontal straight lines. The vertical arrows then indicate the range of available Z' mass values according to LHC limits.

TABLE I: Discovery and identification reach on the Z-Z' mixing angle ϕ for Z' models with $M_2 = 2$ TeV obtained from the polarized differential cross section with ($P_L = \pm 0.8$, $\bar{P}_L = \mp 0.5$) and unpolarized final states for the case $\sqrt{s} = 0.5$ TeV and $\mathcal{L}_{\rm int} = 500$ fb^{-1}. The corresponding limits for polarized Ws are given in parenthesis.

Z' model	χ	ψ	η	I	LRS	SSM
$\phi^{\rm DIS}, 10^{-3}$	$\pm 1.5(0.8)$	$\pm 2.3(1.4)$	$\pm 1.6(1.3)$	$\pm 2.0(0.8)$	$\pm 1.4(1.0)$	$\pm 1.2(0.7)$
$\phi^{\rm ID}, 10^{-3}$	$\pm 3.8(1.5)$	$\pm 36.8(18.5)$	$\pm 17.4(3.2)$	$\pm 4.3(1.2)$	$\pm 8.1(4.2)$	–

Figures 11 and 12 show that the process $e^+e^- \to W^+W^-$ at 0.5 TeV has a potential sensitivity to the mixing angle ϕ of the order of 10^{-4}–10^{-3} or even less, depending on the mass M_2. This sensitivity would increse for the c.m. energy $\sqrt{s}$ approaching M_2 because the contribution of the Z_2 exchange diagram in Fig. 1 would be enhanced. However, Z' bosons relevant to the extended models under study with mass below $\sim 2.0 - 2.3$ TeV are already excluded by LHC data, and the ILC c.m. energies considered here are therefore

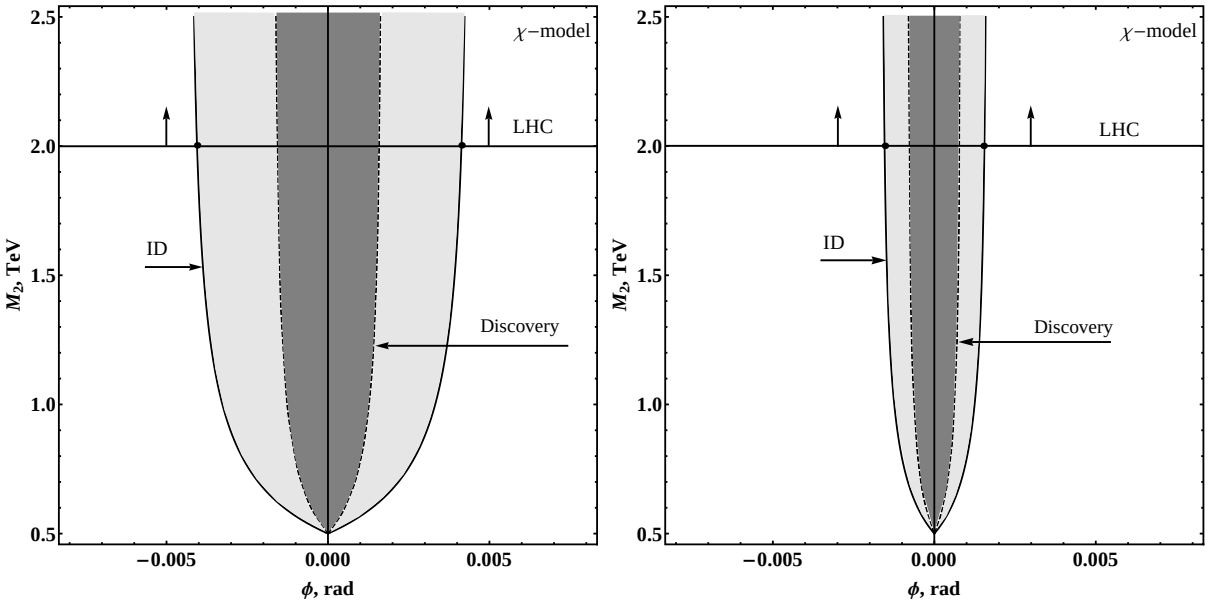

FIG. 11: Left: Discovery (dashed line) and identification (solid line) reach for the χ model in the (ϕ, M_2) plane obtained from polarized initial e^+ and e^- beams with $(P_L = \pm 0.8,\ \bar{P}_L = \mp 0.5)$ and unpolarized final $W^\pm$ states. Right: The same with polarized final $W^\pm$ states. Here, $\sqrt{s} = 0.5$ TeV and $\mathcal{L}_{\rm int} = 500$ fb^{-1}. The horizontal line with vertical arrows, here and in the next figures, approximately indicates the range of M_2 currently allowed by LHC.

quite far from the admissible M_2. Conversely, for masses M_2 much larger than $\sqrt{s}$ such that the Z_2 exchange contribution $|\chi_2/\chi|$ is much less than unity, the limiting contour is mostly determined by the modification (10) of the Z couplings to electrons. The discovery and identification reaches on ϕ at $M_2 = 2$ TeV are summarized in Table I.

For the ILC with higher energy and luminosity, $\sqrt{s} = 1$ TeV and $\mathcal{L}_{\rm int} = 1$ ab^{-1}, one expects further improvement of the discovery and identification reach on the Z-Z' mixing angle and M_2 (see Figures 13, 14 and Table II).

TABLE II: Same as in Table I but for ILC with $\sqrt{s} = 1$ TeV and $\mathcal{L}_{\rm int} = 1$ ab^{-1}.

Z' model	χ	ψ	η	I	LRS	SSM
$\phi^{\rm DIS}, 10^{-4}$	$\pm 3.8(1.8)$	$\pm 5.8(3.4)$	$\pm 4.6(3.2)$	$\pm 4.4(1.9)$	$\pm 3.7(2.4)$	$\pm 3.1(1.7)$
$\phi^{\rm ID}, 10^{-4}$	$\pm 9.0(4.2)$	$\pm 94(45)$	$\pm 24(9.5)$	$\pm 6.1(2.8)$	$\pm 18(10)$	–

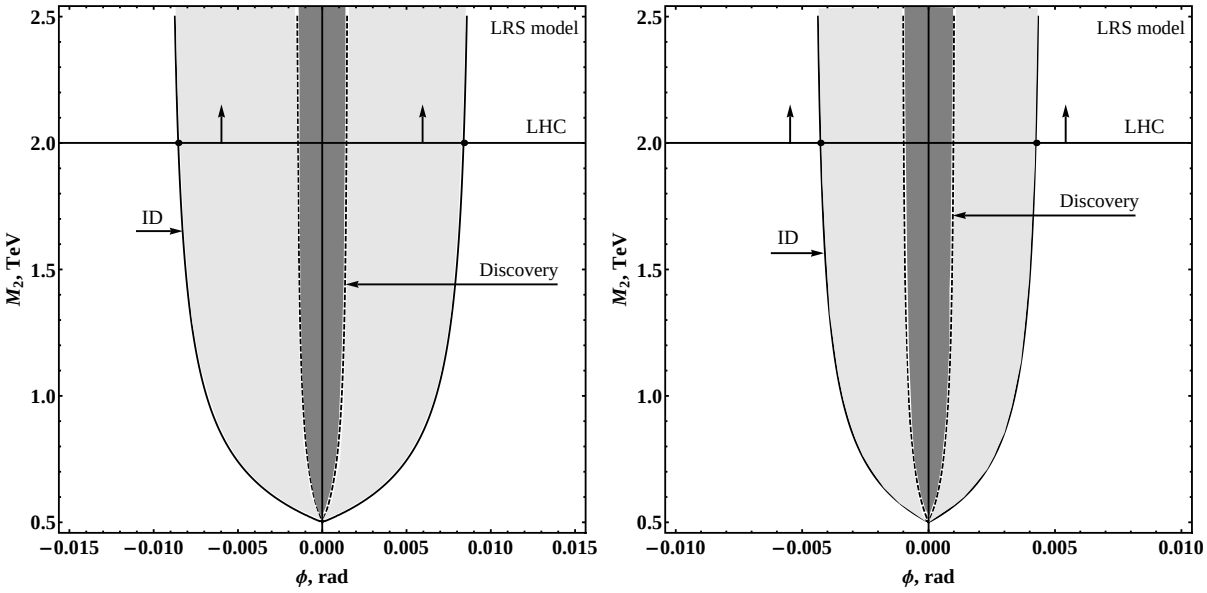

FIG. 12: Same as in Fig.11 but for the LRS model.

As already mentioned, the horizontal lines in Figs. 11–14 denote the current LHC lower limits on M_2, therefore only the upper parts, as indicated by the vertical arrows, will be available for discovery and identification of a Z' *via* indirect manifestations at the ILC with the considered values for the c.m. energy of 0.5 and 1 TeV. Since those limits are so much higher than $\sqrt{s}$, the corrections from finite Z' widths, assumed in the range $\Gamma_{Z'} = (0.01-0.10)M_{Z'}$ [1], are found to be numerically negligible in the "working" regions indicated in those figures by the horizontal lines and vertical arrows. Tables I and II demonstrate that ILC (0.5 TeV) and ILC (1 TeV) allow to improve current bounds on Z–Z' mixing for most of the Z' models, and also differentiating Z' from AGC is feasible.

C. Low-energy option

Currently, physics at the ILC in a low-energy option is extensively studied and discussed, as it in this mode might act as a "Higgs factory". The results for discovery and identification reach on Z-Z' mixing and mass M_2 obtained from the ILC with $\sqrt{s} = 0.25$ TeV and 0.35 TeV are summarized in Tables III and IV.

The comparison of these constraints with those obtained from electroweak precision data derived mostly from on-Z-resonance experiments at LEP1 and SLC [7] shows that the ILC (0.25 TeV) and ILC (0.35 TeV) allow to obtain bounds on Z-Z' mixing at the same

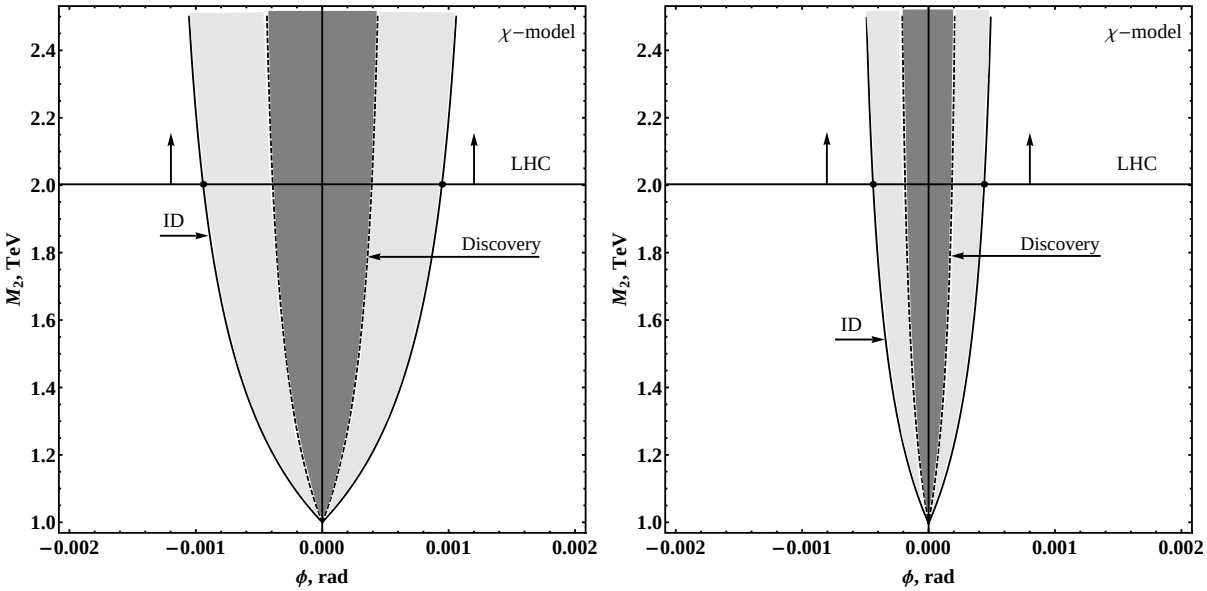

FIG. 13: Left: Discovery (dashed line) and identification (solid line) reach for the χ model in the (ϕ, M_2) plane obtained from polarized initial e^+ and e^- beams with $(P_L = \pm 0.8,\ \bar{P}_L = \mp 0.5)$ and unpolarized final $W^\pm$ states. Right: The same with polarized final $W^\pm$ states. Here, $\sqrt{s} = 1$ TeV and $\mathcal{L}_{\rm int} = 1$ ab^{-1}.

TABLE III: Same as in Table I but for the ILC with $\sqrt{s} = 0.25$ TeV and $\mathcal{L}_{\rm int} = 100$ fb^{-1}.

Z' model	χ	ψ	η	I	LRS	SSM
$\phi^{\rm DIS}, 10^{-3}$	$\pm 5.1(3.8)$	$\pm 8.4(7.0)$	$\pm 6.8(6.7)$	$\pm 5.7(3.9)$	$\pm 5.4(4.9)$	$\pm 4.4(3.6)$
$\phi^{\rm ID}, 10^{-3}$	$\pm 14(6.8)$	$\pm 109(86)$	$\pm 29(14)$	$\pm 7.8(5.9)$	$\pm 45(21)$	–

level as those of current experimental limits, thereby providing complementary bounds on Z's.

Increasing the luminosity at fixed energy, asymptotically allows for an increase of the sensitivity $\propto 1/\sqrt{\mathcal{L}_{\rm int}}$. In the example shown in Table IV, this behavior is not quite reached, due to the impact of systematic uncertainties.

VII. CONCLUDING REMARKS

We have discussed the foreseeable sensitivity to Z's in $W^\pm$-pair production cross sections at the ILC, especially as regards the potential of distinguishing observable effects of a Z' from

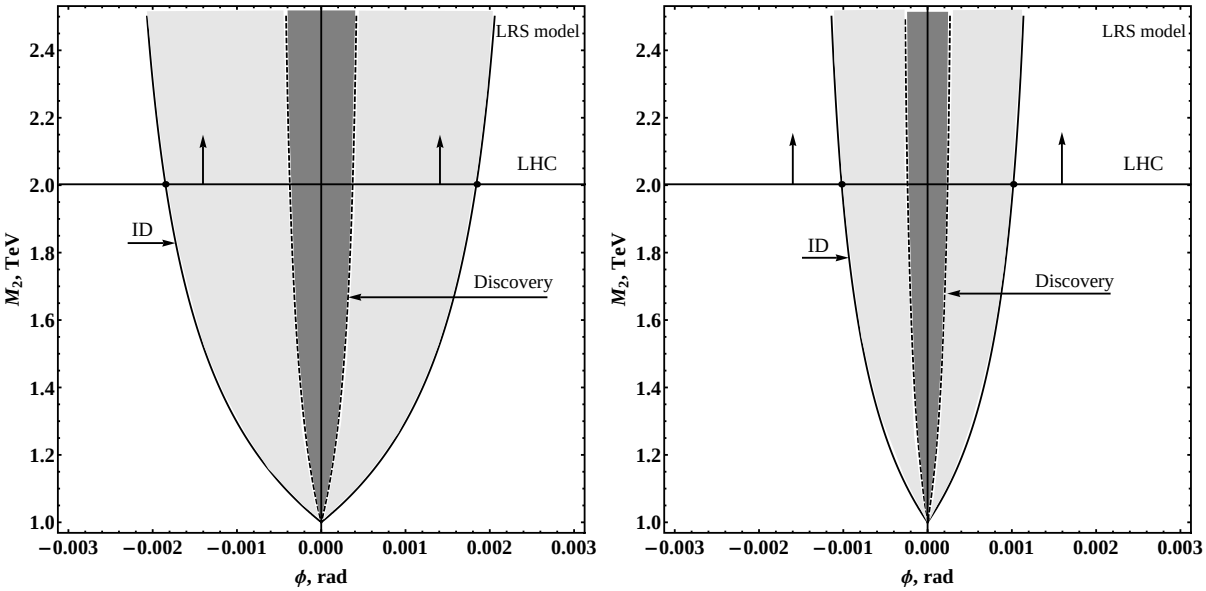

FIG. 14: Same as in Fig.13 but for the LRS model.

TABLE IV: Same as in Table III but for the ILC with $\sqrt{s} = 0.35$ TeV, and two values of integrated luminosity.

Z' model		χ	ψ	η	I	LRS	SSM
100 fb^{-1}	$\phi^{\rm DIS}, 10^{-3}$	$\pm 3.7(2.4)$	$\pm 6.0(4.5)$	$\pm 4.9(4.3)$	$\pm 4.1(2.5)$	$\pm 3.9(3.1)$	$\pm 3.2(2.3)$
	$\phi^{\rm ID}, 10^{-3}$	$\pm 8.4(4.6)$	$\pm 77(61)$	$\pm 27(9.4)$	$\pm 13.5(3.8)$	$\pm 19(14)$	–
500 fb^{-1}	$\phi^{\rm DIS}, 10^{-3}$	$\pm 2.3(1.3)$	$\pm 3.4(2.3)$	$\pm 2.5(2.1)$	$\pm 3.1(1.4)$	$\pm 2.1(1.6)$	$\pm 1.8(1.2)$
	$\phi^{\rm ID}, 10^{-3}$	$\pm 5.9(2.4)$	$\pm 54(30)$	$\pm 15(4.7)$	$\pm 4.0(1.9)$	$\pm 16(6.8)$	–

analogous ones due to competitor models with Anomalous Gauge Couplings that can lead to the same or similar new physics experimental signatures. The discovery and identification reaches on E_6 and LRS models have been determined in the parameter plane spanned by the Z-Z' mixing angle ϕ, and Z' mass, M_2.

We have shown that the sensitivity of the ILC for probing the Z-Z' mixing and its capability to distinguish these two new physics scenarios is substantially enhanced when the polarization of the initial beams (and also, possibly, the produced $W^{\pm}$ bosons) are considered.

Acknowledgements

It is a pleasure to thank S. Dittmaier for valuable comments on the importance of the radiative corrections. This research has been partially supported by the Abdus Salam ICTP under the TRIL and STEP Programmes and the Belarusian Republican Foundation for Fundamental Research. The work of AAP has been partially supported by the SFB 676 Programme of the Department of Physics, University of Hamburg. The work of PO has been supported by the Research Council of Norway.

Appendix A. Helicity amplitudes

In this appendix, we collect the helicity amplitudes for the different initial (e^+e^-) and final-state (W^+W^-) polarizations. In Table V we quote the amplitudes for the case of Anomalous Gauge Couplings [20, 21], whereas in Table VI we give the corresponding results for the case of a Z'.

Note that the quantity δ_Z appearing in Table V is different from, but plays a role similar to that of Δ_Z entering in the parametrization of Z' effects. Furthermore, in analogy with the Δ_γ which enters the description of Z' effects, one could imagine a factor $(1+\delta_\gamma)$ multiplying the photon-exchange amplitudes in Table V. Such a term could be induced by dimension-8 operators, but δ_γ would have to vanish as $s \to 0$, due to gauge invariance.

TABLE V: Helicity amplitudes for $e^+e^- \to W^+W^-$ in the presence of AGC [20, 21]. To obtain the amplitude $F_{\lambda\tau\tau'}(s, \cos\theta)$ for definite helicity $\lambda = \pm 1/2$ and definite spin orientations $\tau(W^-)$ and $\tau'(W^+)$ of the $W^\pm$, the elements in the corresponding column have to be multiplied by the common factor on top of the column. Subsequently, the elements in a specific column have to be multiplied by the corresponding elements in the first column and the sum over all elements is to be taken. In the last column, the amplitude for the case of $\tau = \pm 1$, $\tau' = 0$ is obtained by replacing τ' by $-\tau$ in the elements of this last column.

$e^+_{-\lambda}e^-_\lambda \to W^+_L W^-_L$	$\tau = \tau' = 0$ $-\frac{e^2 s\lambda}{2}\sin\theta$	
$\frac{2\lambda-1}{4\,t\,s_W^2}$	$\frac{s}{2M_W^2}[\cos\theta - \beta_W(1+\frac{2M_W^2}{s})]$	
$-\frac{2}{s} + \frac{2(\cot\theta_W+\delta_Z)}{s-M_Z^2}(v-2a\lambda)$	$-\beta_W(1+\frac{s}{2M_W^2})$	
$-\frac{x_\gamma}{s} + \frac{x_Z}{s-M_Z^2}(v-2a\lambda)$	$-\beta_W\frac{s}{M_W^2}$	
$e^+_{-\lambda}e^-_\lambda \to W^+_T W^-_T$	$\tau = \tau' = \pm 1$ $-\frac{e^2 s\lambda}{2}\sin\theta$	$\tau = -\tau' = \pm 1$ $-\frac{e^2 s\lambda}{2}\sin\theta$
$\frac{2\lambda-1}{4\,t\,s_W^2}$	$\cos\theta - \beta_W$	$-\cos\theta - 2\tau\lambda$
$-\frac{2}{s} + \frac{2(\cot\theta_W+\delta_Z)}{s-M_Z^2}(v-2a\lambda)$	$-\beta_W$	0
$-\frac{y_\gamma}{s} + \frac{y_Z}{s-M_Z^2}(v-2a\lambda)$	$-\beta_W\frac{s}{M_W^2}$	0
$e^+_{-\lambda}e^-_\lambda \to W^+_T W^-_L$	$\tau = 0,\ \tau' = \pm 1$ $-\frac{e^2 s\lambda}{2\sqrt{2}}(\tau'\cos\theta - 2\lambda)$	$\tau = \pm 1,\ \tau' = 0$ $\frac{e^2 s\lambda}{2\sqrt{2}}(\tau\cos\theta + 2\lambda)$
$\frac{2\lambda-1}{4\,t\,s_W^2}$	$\frac{\sqrt{s}}{2M_W}[\cos\theta(1+\beta_W^2) - 2\beta_W]$ $-\frac{2M_W}{\sqrt{s}}\frac{\tau'\sin^2\theta}{\tau'\cos\theta - 2\lambda}$	$\frac{\sqrt{s}}{2M_W}[\cos\theta(1+\beta_W^2) - 2\beta_W]$ $-\frac{2M_W}{\sqrt{s}}\frac{\tau\sin^2\theta}{\tau\cos\theta + 2\lambda}$
$-\frac{2}{s} + \frac{2(\cot\theta_W+\delta_Z)}{s-M_Z^2}(v-2a\lambda)$	$-\beta_W\frac{\sqrt{s}}{M_W}$	$-\beta_W\frac{\sqrt{s}}{M_W}$
$-\frac{x_\gamma+y_\gamma}{s} + \frac{x_Z+y_Z}{s-M_Z^2}(v-2a\lambda)$	$-\beta_W\frac{\sqrt{s}}{M_W}$	$-\beta_W\frac{\sqrt{s}}{M_W}$

TABLE VI: Helicity amplitudes for $e^+e^- \to \gamma, Z_1, Z_2 \to W^+W^-$.

$e^+_{-\lambda}e^-_{\lambda} \to W^+_L W^-_L$	$\tau = \tau' = 0$ $-\frac{e^2 s\lambda}{2}\sin\theta$	
$\frac{2\lambda-1}{4\,t\,s_W^2}$	$\frac{s}{2M_W^2}[\cos\theta - \beta_W(1+\frac{2M_W^2}{s})]$	
$-\frac{2}{s} + \frac{2\,g_{WWZ_1}}{s-M_1^2+iM_1\Gamma_1}(v_1 - 2a_1\lambda)$ $+\frac{2\,g_{WWZ_2}}{s-M_2^2+iM_2\Gamma_2}(v_2 - 2a_2\lambda)$ $\approx -\frac{2(1+\Delta_\gamma)}{s} + \frac{2(\cot\theta_W+\Delta_Z)}{s-M_Z^2}(v-2a\lambda)$	$-\beta_W(1+\frac{s}{2M_W^2})$	

$e^+_{-\lambda}e^-_{\lambda} \to W^+_T W^-_T$	$\tau = \tau' = \pm 1$ $-\frac{e^2 s\lambda}{2}\sin\theta$	$\tau = -\tau' = \pm 1$ $-\frac{e^2 s\lambda}{2}\sin\theta$
$\frac{2\lambda-1}{4\,t\,s_W^2}$	$\cos\theta - \beta_W$	$-\cos\theta - 2\tau\lambda$
$-\frac{2}{s} + \frac{2\,g_{WWZ_1}}{s-M_1^2+iM_1\Gamma_1}(v_1 - 2a_1\lambda)$ $+\frac{2\,g_{WWZ_2}}{s-M_2^2+iM_2\Gamma_2}(v_2 - 2a_2\lambda)$ $\approx -\frac{2(1+\Delta_\gamma)}{s} + \frac{2(\cot\theta_W+\Delta_Z)}{s-M_Z^2}(v-2a\lambda)$	$-\beta_W$	0

$e^+_{-\lambda}e^-_{\lambda} \to W^+_T W^-_L$	$\tau = 0,\ \tau' = \pm 1$ $-\frac{e^2 s\lambda}{2\sqrt{2}}(\tau'\cos\theta - 2\lambda)$	$\tau = \pm 1,\ \tau' = 0$ $\frac{e^2 s\lambda}{2\sqrt{2}}(\tau\cos\theta + 2\lambda)$
$\frac{2\lambda-1}{4\,t\,s_W^2}$	$\frac{\sqrt{s}}{2M_W}[\cos\theta(1+\beta_W^2) - 2\beta_W]$ $-\frac{2M_W}{\sqrt{s}}\frac{\tau'\sin^2\theta}{\tau'\cos\theta - 2\lambda}$	$\frac{\sqrt{s}}{2M_W}[\cos\theta(1+\beta_W^2) - 2\beta_W]$ $-\frac{2M_W}{\sqrt{s}}\frac{\tau\sin^2\theta}{\tau\cos\theta + 2\lambda}$
$-\frac{2}{s} + \frac{2\,g_{WWZ_1}}{s-M_1^2+iM_1\Gamma_1}(v_1 - 2a_1\lambda)$ $+\frac{2\,g_{WWZ_2}}{s-M_2^2+iM_2\Gamma_2}(v_2 - 2a_2\lambda)$ $\approx -\frac{2(1+\Delta_\gamma)}{s} + \frac{2(\cot\theta_W+\Delta_Z)}{s-M_Z^2}(v-2a\lambda)$	$-\beta_W\frac{\sqrt{s}}{M_W}$	$-\beta_W\frac{\sqrt{s}}{M_W}$

[1] P. Langacker, Rev. Mod. Phys. **81**, 1199-1228 (2009) [arXiv:0801.1345 [hep-ph]].

[2] T. G. Rizzo, [hep-ph/0610104].

[3] A. Leike and S. Riemann, Z. Phys. C **75**, 341 (1997) [hep-ph/9607306].

[4] A. Leike, Phys. Rept. **317**, 143-250 (1999) [hep-ph/9805494].

[5] S. Riemann, eConf C **050318**, 0303 (2005) [hep-ph/0508136].

[6] J. L. Hewett, T. G. Rizzo, Phys. Rept. **183**, 193 (1989).

[7] J. Erler, P. Langacker, S. Munir, E. Rojas, JHEP **0908**, 017 (2009) [arXiv:0906.2435 [hep-ph]].

[8] P. Langacker, [arXiv:0911.4294 [hep-ph]].

[9] S. Chatrchyan *et al.* [CMS Collaboration], Phys. Lett. **B714**, 158-179 (2012) [arXiv:1206.1849 [hep-ex]].

[10] ATLAS Collaboration, Note ATLAS-CONF-2012-007 (March 2012).

[11] P. Osland, A. A. Pankov, A. V. Tsytrinov, N. Paver, Phys. Rev. **D79**, 115021 (2009) [arXiv:0904.4857 [hep-ph]].

[12] J. Brau *et al.* [ILC Collaboration], "ILC Reference Design Report Volume 1 - Executive Summary," arXiv:0712.1950 [physics.acc-ph].

[13] G. Aarons *et al.* [ILC Collaboration], "International Linear Collider Reference Design Report Volume 2: PHYSICS AT THE ILC," arXiv:0709.1893 [hep-ph].

[14] A. A. Pankov, N. Paver, Phys. Lett. **B272**, 425-430 (1991).

[15] A. A. Pankov, N. Paver, Phys. Rev. **D48**, 63-77 (1993).

[16] A. A. Pankov, N. Paver, Phys. Lett. **B324**, 224-230 (1994).

[17] A. A. Pankov, N. Paver, C. Verzegnassi, Int. J. Mod. Phys. **A13**, 1629-1650 (1998) [hep-ph/9701359].

[18] D. -W. Jung, K. Y. Lee, H. S. Song, C. Yu, J. Korean Phys. Soc. **36**, 258-264 (2000) [hep-ph/9905353].

[19] B. Ananthanarayan, M. Patra, P. Poulose, JHEP **1102**, 043 (2011) [arXiv:1012.3566 [hep-ph]].

[20] G. Gounaris, J. L. Kneur, J. Layssac, G. Moultaka, F. M. Renard and D. Schildknecht, Proceedings of the Workshop e^+e^- *Collisions at 500 GeV: the Physics Potential*, Ed. P.M. Zerwas (1992), DESY 92-123B, p.735.

[21] G. Gounaris, J. Layssac, G. Moultaka, F. M. Renard, Int. J. Mod. Phys. **A8**, 3285-3320 (1993).

[22] G. Moortgat-Pick, T. Abe, G. Alexander, B. Ananthanarayan, A. A. Babich, V. Bharadwaj, D. Barber, A. Bartl *et al.*, Phys. Rept. **460**, 131-243 (2008) [hep-ph/0507011].

[23] P. Osland, A. A. Pankov, A. V. Tsytrinov, Eur. Phys. J. **C67**, 191-204 (2010) [arXiv:0912.2806 [hep-ph]].

[24] P. Langacker and M. -x. Luo, Phys. Rev. D **45**, 278 (1992).

[25] K. Hagiwara, R. D. Peccei, D. Zeppenfeld and K. Hikasa, Nucl. Phys. B **282**, 253 (1987)

[26] M. S. Bilenky, J. L. Kneur, F. M. Renard and D. Schildknecht, Nucl. Phys. B **409**, 22 (1993).

[27] M. S. Bilenky, J. L. Kneur, F. M. Renard and D. Schildknecht, Nucl. Phys. B **419**, 240 (1994) [hep-ph/9312202].

[28] K. Nakamura *et al.* [Particle Data Group Collaboration], J. Phys. G **37**, 075021 (2010).

[29] J. Fleischer, K. Kolodziej and F. Jegerlehner, Phys. Rev. D **47**, 830 (1993).

[30] W. Beenakker and A. Denner, Int. J. Mod. Phys. A **9**, 4837 (1994).

[31] A. Denner, S. Dittmaier, M. Roth and L. H. Wieders, Phys. Lett. B **612**, 223 (2005) [Erratum-ibid. B **704**, 667 (2011)] [hep-ph/0502063].

[32] A. Denner, S. Dittmaier, M. Roth and L. H. Wieders, Nucl. Phys. B **724**, 247 (2005) [Erratum-ibid. B **854**, 504 (2012)] [hep-ph/0505042].

[33] W. Beenakker, F. A. Berends and T. Sack, Nucl. Phys. B **367**, 287 (1991).

[34] W. Beenakker, K. Kolodziej and T. Sack, Phys. Lett. B **258**, 469 (1991).

[35] A. A. Pankov, N. Paver and A. V. Tsytrinov, Phys. Rev. D **73**, 115005 (2006) [arXiv:hep-ph/0512131].

[36] G. Abbiendi *et al.*, [OPAL collaboration], Phys. Lett. **B585**, 223 (2004);
P. Achard *et al.*, [L3 collaboration], Phys. Lett. **B557**, 147 (2003);
J. Abdallah *et al.*, [DELPHI Collaboration], Eur. Phys. J. C **54**, 345 (2008) [arXiv:0801.1235 [hep-ex]];
J.P. Couchman, A measurement of the triple gauge boson couplings and W boson polarisation in W-pair production at LEP2, Ph.D. thesis, University College London, 2000.

Unique heavy lepton signature at e^+e^- linear collider with polarized beams

G. Moortgat-Pick,[a,b,*] P. Osland,[c†] A. A. Pankov[d,‡] A. V. Tsytrinov[d,§]

[a] *II. Inst. of Theor. Physics, University of Hamburg, Luruper Chaussee 149, 22761 Hamburg, Germany*

[b] *DESY, Notkestrasse 85, 22607 Hamburg, Germany*

[c] *Department of Physics and Technology, University of Bergen, Postboks 7803, N-5020 Bergen, Norway*

[d] *The Abdus Salam ICTP Affiliated Centre, Technical University of Gomel, 246746 Gomel, Belarus*

Abstract

We explore the effects of neutrino and electron mixing with exotic heavy leptons in the process $e^+e^- \to W^+W^-$ within E_6 models. We examine the possibility of uniquely distinguishing and identifying such effects of heavy neutral lepton exchange from Z-Z' mixing within the same class of models and also from analogous ones due to competitor models with anomalous trilinear gauge couplings (AGC) that can lead to very similar experimental signatures at the e^+e^- International Linear Collider (ILC) for $\sqrt{s} = 350$, 500 GeV and 1 TeV. Such clear identification of the model is possible by using a certain double polarization asymmetry. The availability of both beams being polarized plays a crucial role in identifying such exotic-lepton admixture. In addition, the sensitivity of the ILC for probing exotic-lepton admixture is substantially enhanced when the polarization of the produced $W^\pm$ bosons is considered.

PACS numbers: 12.60.-i, 12.60.Cn, 14.70.Fm, 29.20.Ej

* gudrid.moortgat-pick@desy.de
† per.osland@ift.uib.no
‡ pankov@ictp.it
§ tsytrin@rambler.ru

I. INTRODUCTION

Detailed examination of the process

$$e^+ + e^- \to W^+ + W^- \tag{1}$$

at the ILC is a crucial one for studying the electroweak gauge symmetry, in particular, electroweak symmetry breaking and the structure of the gauge sector in general, and allows to observe a manifestation of New Physics (NP) that may appear beyond the Standard Model (SM). In the SM, the process (1) is described by the amplitudes mediated by photon and Z boson exchange in the s-channel and by neutrino exchange in the t-channel. This reaction is quite sensitive to both the leptonic vertices and the trilinear couplings to W^+W^- of the SM Z and of any new heavy neutral boson or a new heavy lepton that can be exchanged in the s-channel or t-channel, respectively. A popular example in this regard, is represented by E_6 models [1–6]. In particular, an effective $SU(2)_L \times U(1)_Y \times U(1)_{Y'}$ model, which originates from the breaking of the exceptional group E_6, leads to extra gauge bosons. Indeed, in the breaking of this group down to the SM symmetry, two additional neutral gauge bosons could appear and the lightest Z' is defined as

$$Z' = Z'_\chi \cos\beta + Z'_\psi \sin\beta \tag{2}$$

and can be parametrized in terms of the hypercharges of the two groups $U(1)_\psi$ and $U(1)_\chi$ which are involved in the breaking of the E_6 group into a low-energy group of rank 6:

$$\begin{aligned} E_6 &\to SO(10) \times U(1)_\psi \to SU(5) \times U(1)_\chi \times U(1)_\psi \\ &\to SU(3)_c \times SU(2)_L \times U(1)_Y \times U(1)_\psi \times U(1)_\chi. \end{aligned} \tag{3}$$

For a sufficiently large vacuum expectation value of the Higgs field an effective rank-5 model, which leads to the decomposition (see, for example Ref. [7]) $SU(3)_c \times SU(2)_L \times U(1)_Y \times U(1)_{Y'}$ can be deduced from the rank-6 model (see below) so that one of the new gauge bosons decouples from low energy phenomenology. The remaining (lighter) new gauge bosons Z' is in general a mixture of Z_ψ and Z_χ and is assumed to lead to measurable effects at the collider, and an angle β specifies the orientation of the $U(1)'$ generator in the E_6 group space, where the values $\beta = 0$ and $\beta = \pi/2$ would correspond, respectively, to pure Z'_χ and Z'_ψ bosons, while the value $\beta = -\arctan\sqrt{5/3}$ would correspond to a Z'_η boson originating from the direct breaking of E_6 to a rank-5 group in superstring inspired models.

Another characteristic of extended models, apart from the Z', is the existence of new matter, new heavy leptons and quarks. In E_6 models the fermion sector is enlarged, since the matter multiplets are in larger representations (the $\underline{27}$ fundamental representation), that contains, in particular, a vector doublet of leptons. From the phenomenological point of view it is convenient to classify the fermions present in E_6 in terms of their transformation properties under $SU(2)$. We denote the particles with unconventional isospin assignments (right-handed doublets) as exotic fermions. We here consider two heavy left- and right-handed $SU(2)$ exotic lepton doublets [8, 9]

$$\begin{pmatrix} N \\ E^- \end{pmatrix}_L , \quad \begin{pmatrix} N \\ E^- \end{pmatrix}_R , \tag{4}$$

and one Z' boson, with masses larger than M_Z and coupling constants that may be different from those of the SM. These leptons are called *vector leptons* because both the left- and right- handed components transform identically under $SU(2)$. We also assume that the new, "exotic" fermions only mix with the standard ones within the same family (the electron and its neutrino being the ones relevant to process (1)), which assures the absence of tree-level generation-changing neutral currents [10].

Current lower limits on $M_{Z'}$ obtained from dilepton pair production at the LHC with $\sqrt{s} = 8$ TeV and $\mathcal{L}_{\rm int} \approx 20$ fb^{-1} [11, 12] range in the interval $\sim 2.6 - 2.9$ TeV, depending on the particular Z' model being tested. Already these masses are too high for a Z' to be directly seen at the ILC. However, even at such high masses, Z' exchanges can manifest themselves indirectly *via* deviations of cross sections, and in general of the reaction observables, from the SM predictions.

In this paper, we study the indirect effects induced by heavy lepton exchange in $W^\pm$ pair production (1) at the ILC, with a center of mass energy $\sqrt{s} = 0.5 - 1$ TeV and time-integrated luminosity of $\mathcal{L}_{\rm int} = 0.5 - 1$ ab^{-1}. We also present results for a lower energy run at $\sqrt{s} = 350$ GeV. For early papers on these effects, see Refs. [13–15]. We allow for effects due to extra Z' gauge boson exchange. Indirect effects may be quite subtle, both when it comes to distinguishing an effect from the SM, and also as far as the identification of the source of an observed deviation is concerned, because *a priori* different NP scenarios may lead to the same or similar experimental signatures. Clearly, then, the discrimination of one NP model (in our case the E_6) from other possible ones needs an appropriate strategy for analyzing the data.

Recently, the problem of distinguishing the Z' effects, once observed in process (1), from the anomalous gauge couplings, has been studied in [16]. In the AGC models, there is no new gauge boson exchange, but the $WW\gamma$, WWZ couplings are modified with respect to the SM values, this violates the SM gauge cancellation too and leads to deviations of the cross sections. We consider the CP-conserving set of such couplings, often referred to as κ_γ, κ_Z, λ_γ, λ_Z and δ_Z [17, 18]. An alternative effective-field-theory approach to these effects was recently presented [19].

In this note, we extend the analysis of Ref. [16], considering the possibility of uniquely identifying the effects of heavy neutral lepton exchange from Z-Z' mixing within the same class of E_6 models. This is relevant, since in this class of models lepton mixing and Z-Z' mixing can be simultaneously present. We also distinguish them from analogous ones due to competitor models with anomalous trilinear gauge couplings in the process (1) by exploiting a double polarization asymmetry that will unambiguously identify the heavy exotic-lepton mixing effects[1] and is only accessible with the availability of both beams being polarized [21].

While the high precision observables determined at LEP severely constrain the electroweak sector [22], they leave room for effects at the energies that are discussed here.

The paper is organized as follows. In Section II, we briefly review the E_6 models involving additional Z' bosons and new heavy charged and neutral leptons and emphasize the role of the heavy neutral lepton and boson mixings in the process (1). Then, in Sect. III we review the structure of the polarized cross section. In Sect. IV we determine the discovery reach on the NWe coupling constants, and in Sect. V we determine the identification reach, i.e., down to what coupling strength such a heavy neutral lepton can be distinguished from other new-physics effects. Then, in Sect. VI we comment on the 350 GeV option, before concluding in Sect. VII.

---

[1] This approach was recently exploited for uniquely identifying the indirect effects of s-channel sneutrino exchange against other new physics scenarios described by contact-like effective interactions in high-energy e^+e^- annihilation into lepton pairs [20].

II. LEPTON AND $Z - Z'$ MIXING

A. Weak basis

To describe the formalism for mixing among exotic and ordinary leptons, we start from the leptonic $SU(2) \times U(1) \times U(1)'$ interaction:[2]

$$-\mathcal{L} = e\,\left(\tilde{J}^{\mu}_{\rm em}A_{\mu} + \tilde{J}^{\mu}_{Z}Z_{\mu} + \tilde{J}^{\mu}_{Z'}Z'_{\mu}\right) + \frac{g}{\sqrt{2}}\left(\tilde{J}^{\mu}_{W}W_{\mu} + {\rm h.c.}\right), \tag{5}$$

where, in the weak-eigenstate basis, and with $V = \gamma,\ Z,\ Z'$, the currents in Eq. (5) can be written as:

$$\tilde{J}^{\mu}_{V} = \sum_{a} \bar{\varepsilon}^{0}_{a}\gamma^{\mu}Q^{\varepsilon^{0}}_{a}\varepsilon^{0}_{a}, \qquad \tilde{J}^{\mu}_{W} = \sum_{a} \bar{\eta}^{0}_{a}\gamma^{\mu}G^{\eta^{0}}_{a}\varepsilon^{0}_{a}, \tag{6}$$

where the coupling matrices $Q^{\varepsilon^0}_a$ and $G^{\eta^0}_a$ of the neutral and charged currents are defined by Eqs. (8) and (11) below. The superscript "0″ labels the weak-eigenstate basis. Furthermore, in Eq. (5) we adopt the following notations: $e = \sqrt{4\pi\alpha_{\rm em}}$, $g = e/s_W$, $s_W = \sin\theta_W$. In Eq. (6), we have introduced, with $a = (L,\ R)$ the left- and right-handed helicities, the charged and neutral leptons by means of the notation:

$$\varepsilon^{0}_{a} = \begin{pmatrix} e^{0}_{a} \\ E^{0}_{a} \end{pmatrix}, \qquad \eta^{0}_{a} = \begin{pmatrix} \nu^{0}_{a} \\ N^{0}_{a} \end{pmatrix}, \tag{7}$$

where e and ν are the ordinary SM electron and neutrino, and E and N are the exotic charged and neutral heavy leptons, which we assume to be doublets under electroweak $SU(2)$. Furthermore, the neutral current couplings are represented by the matrices $Q^{\varepsilon^0}_a = Q^{\varepsilon^0}_{{\rm em},a};\ g^{\varepsilon^0}_a;\ g'^{\varepsilon^0}_a$, with:

$$Q^{\varepsilon^0}_{{\rm em},a} = \begin{pmatrix} -1 & 0 \\ 0 & -1 \end{pmatrix}, \qquad g^{\varepsilon^0}_{a} = \begin{pmatrix} g^{e^0}_a & 0 \\ 0 & g^{E^0}_a \end{pmatrix}, \qquad g'^{\varepsilon^0}_{a} = \begin{pmatrix} g'^{e^0}_a & 0 \\ 0 & g'^{E^0}_a \end{pmatrix}, \tag{8}$$

for the γ, Z and Z', respectively, where ($\varepsilon^0 = e^0,\ E^0$)

$$g^{\varepsilon^0}_{a} = (T^{\varepsilon^0}_{3a} - Q^{\varepsilon^0}_{{\rm em},a}s^2_W)g_Z, \tag{9}$$

and $T^{\varepsilon^0}_{3a}$ is the third isospin component. Furthermore, $g_Z = 1/s_W c_W$, with $c_W = \cos\theta_W$.

[2] The needed fermion mixing formalism has been introduced also, e.g., in [15].

For the Z' couplings to fermions in E_6 models, we follow the notation of [15]:

$$g_L'^{e^0} = (3A + B)g_{Z'}, \qquad g_R'^{e^0} = (A - B)g_{Z'},$$
$$g_L'^{E^0} = (-2A - 2B)g_{Z'}, \quad g_R'^{E^0} = (-2A + 2B)g_{Z'}, \tag{10}$$

where $g_{Z'} = 1/c_W$, $A = \cos\beta/(2\sqrt{6})$, $B = \sqrt{10}\sin\beta/12$.

The charged current couplings read:

$$G_a^{\eta^0} = \begin{pmatrix} G_a^{\nu^0} & 0 \\ 0 & G_a^{N^0} \end{pmatrix} \tag{11}$$

with $G_L^{\nu^0} = 1$, $G_R^{\nu^0} = 0$, $G_a^{N^0} = -2\,T_{3a}^E$.

B. Fermion mass basis

We introduce mass eigenstates in the same notation as (7):

$$\varepsilon_a = \begin{pmatrix} e_a \\ E_a \end{pmatrix}, \qquad \eta_a = \begin{pmatrix} \nu_a \\ N_a \end{pmatrix}. \tag{12}$$

These states are related to the weak eigenstates (7) by the following transformations:

$$\varepsilon_a = U(\psi_{1a})\varepsilon_a^0; \qquad \eta_a = U(\psi_{2a})\eta_a^0, \tag{13}$$

where the unitary mixing matrices $U(\psi_{1a})$ and $U(\psi_{2a})$ diagonalize, respectively, the charged and neutral fermion mass matrices. $U(\psi_{1a})$ and $U(\psi_{2a})$ can be written as:

$$U(\psi_{1a}) = \begin{pmatrix} \cos\psi_{1a} & \sin\psi_{1a} \\ -\sin\psi_{1a} & \cos\psi_{1a} \end{pmatrix} \equiv \begin{pmatrix} c_{1a} & s_{1a} \\ -s_{1a} & c_{1a} \end{pmatrix}, \tag{14}$$

$$U(\psi_{2a}) = \begin{pmatrix} \cos\psi_{2a} & \sin\psi_{2a} \\ -\sin\psi_{2a} & \cos\psi_{2a} \end{pmatrix} \equiv \begin{pmatrix} c_{2a} & s_{2a} \\ -s_{2a} & c_{2a} \end{pmatrix}. \tag{15}$$

Present limits on s_{1a}^2 and s_{2a}^2 are in general less than 1-2% [9, 23, 24] and $m_N > 100$ GeV [10]. In the fermion-mass-eigenstate basis one can rewrite the interaction Lagrangian (5) as:

$$-\mathcal{L} = e\,\left(J_{\rm em}^\mu A_\mu + J_Z^\mu Z_\mu + J_{Z'}^\mu Z'_\mu\right) + \frac{g}{\sqrt{2}}\left(J_W^\mu W_\mu + \text{h.c.}\right), \tag{16}$$

where

$$J_V^\mu = \sum_a \bar{\varepsilon}_a \gamma^\mu Q_a^\varepsilon \varepsilon_a, \qquad J_W^\mu = \sum_a \bar{\eta}_a \gamma^\mu G_a^\eta \varepsilon_a. \tag{17}$$

Since the gauge fields of Eq. (16) are the same as those of (5), we must have

$$Q_a^{\varepsilon} = U(\psi_{1a})\, Q_a^{\varepsilon^0}\, U^{-1}(\psi_{1a}), \qquad G_a^{\eta} = U(\psi_{2a})\, G_a^{\eta^0}\, U^{-1}(\psi_{1a}), \tag{18}$$

and $Q_a^{\varepsilon} = Q_{em,a}^{\varepsilon}$, g_a^{ε}, $g_a'^{\varepsilon}$, with

$$g_a^{\varepsilon} = \begin{pmatrix} g_a^e & g_a^{eE} \\ g_a^{eE} & g_a^E \end{pmatrix}, \qquad g_a'^{\varepsilon} = \begin{pmatrix} g_a'^e & g_a'^{eE} \\ g_a'^{eE} & g_a'^E \end{pmatrix}, \qquad G_a^{\eta} = \begin{pmatrix} G_a^{\nu} & G_a^{\nu E} \\ G_a^{Ne} & G_a^N \end{pmatrix}. \tag{19}$$

It is clear that the electromagnetic current remains diagonal under the rotation (18), and therefore is not affected by lepton mixing.

In the weak charged currents of Eq. (17) the exotic-lepton mixings modify not only the left-handed currents but also induce an admixture with the right-handed currents. The off-diagonal term in J_W^{μ} of Eqs. (17)–(19) induces NWe couplings which allow an additional t-channel exotic-lepton-exchange contribution for the process (1) (see Fig. 1). Parametrization of the mixing-modified νWe and the mixing-induced NWe couplings are summarized in Eqs. (21) and (22), respectively.

From (18) and (19) one can obtain expressions for the lepton coupling constants:

$$g_a^e = g_a^{e^0} c_{1a}^2 + g_a^{E^0} s_{1a}^2, \qquad g_a'^e = g_a'^{e^0} c_{1a}^2 + g_a'^{E^0} s_{1a}^2; \tag{20}$$

$$G_L^{\nu} = c_{1L}c_{2L} - 2\, T_{3L}^E\, s_{1L}\, s_{2L}, \qquad G_R^{\nu} = -2\, T_{3R}^E\, s_{1R}s_{2R}; \tag{21}$$

$$G_L^{Ne} = -s_{2L}c_{1L} - 2\, T_{3L}^E c_{2L}\, s_{1L}, \qquad G_R^{Ne} = -2\, T_{3R}^E\, c_{2R}s_{1R}. \tag{22}$$

C. Z-Z' mixing

Concerning Z-Z' mixing, it can be parametrized as

$$\begin{pmatrix} Z_1 \\ Z_2 \end{pmatrix} = \begin{pmatrix} \cos\phi & \sin\phi \\ -\sin\phi & \cos\phi \end{pmatrix} \begin{pmatrix} Z \\ Z' \end{pmatrix}, \tag{23}$$

where Z, Z' are weak eigenstates, Z_1, Z_2 are mass eigenstates and ϕ is the Z-Z' mixing angle. Finally, taking Eq. (23) into account, the lepton neutral current couplings to Z_1 and Z_2 are, respectively [15]:

$$g_{1a}^e = g_a^e \cos\phi + g_a'^e \sin\phi\,; \qquad g_{2a}^e = -g_a^e \sin\phi + g_a'^e \cos\phi. \tag{24}$$

Current limits are of the order $\phi = (2-5)\times 10^{-3}$ [10].

III. POLARIZED CROSS SECTION

In the Born approximation the process (1) is described by the set of five diagrams shown in Fig. 1 and corresponding to mass-eigenstate exchanges (i.e. γ, ν, N, Z_1 and Z_2), with couplings given by Eqs. (20)-(22) and (24).

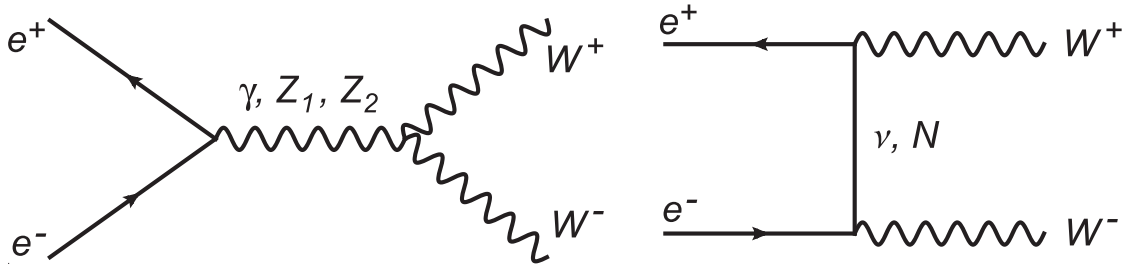

FIG. 1: Feynman diagrams.

The polarized cross section for the process (1) can be written as [15]

$$\frac{d\sigma\left(P_L^-,\,P_L^+\right)}{d\cos\theta} = \frac{1}{4}\left[\left(1+P_L^-\right)\left(1-P_L^+\right)\frac{d\sigma^{RL}}{d\cos\theta} + \left(1-P_L^-\right)\left(1+P_L^+\right)\frac{d\sigma^{LR}}{d\cos\theta}\right.$$
$$\left. + \left(1+P_L^-\right)\left(1+P_L^+\right)\frac{d\sigma^{RR}}{d\cos\theta} + \left(1-P_L^-\right)\left(1-P_L^+\right)\frac{d\sigma^{LL}}{d\cos\theta}\right], \qquad (25)$$

where P_L^- (P_L^+) are degrees of longitudinal polarization of e^- (e^+), θ the scattering angle of the W^- with respect to the e^- direction. The superscript "RL" refers to a right-handed electron and a left-handed positron, and similarly for the other terms. The relevant polarized differential cross sections for $e_a^- e_b^+ \to W_\alpha^- W_\beta^+$ contained in Eq. (25) can be expressed as [15, 25]

$$\frac{d\sigma_{\alpha\beta}^{ab}}{d\cos\theta} = C\sum_{k=0}^{k=2} F_k^{ab}\,\mathcal{O}_{k\,\alpha\beta}, \qquad (26)$$

where $C = \pi\alpha_{e.m.}^2\beta_W/2s$, $\beta_W = (1-4M_W^2/s)^{1/2}$ the W velocity in the CM frame, and the helicities of the initial e^-e^+ and final W^-W^+ states are labeled as $ab = (RL,\, LR,\, LL,\, RR)$ and $\alpha\beta = (LL,\, TT,\, TL)$, respectively. The $\mathcal{O}_k$ are functions of the kinematical variables dependent on energy $\sqrt{s}$, the scattering angle θ and the W mass, M_W, which characterize the various possibilities for the final W^+W^- polarizations (TT, LL, $TL + LT$ or the sum over all W^+W^- polarization states for unpolarized W's).

The F_k are combinations of lepton and trilinear gauge boson couplings, g_{WWZ_1} and g_{WWZ_2}, including lepton and Z-Z' mixing as well as propagators of the intermediate states.

For instance, for the LR case one finds

$$
\begin{aligned}
F_0^{LR} &= \frac{1}{16 s_W^4}\left[\left(G_L^{\nu}\right)^2 + r_N\left(G_L^{Ne}\right)^2\right]^2, \\
F_1^{LR} &= 2\left[1 - g_{WWZ_1} g_{1L}^e \chi_1 - g_{WWZ_2} g_{2L}^e \chi_2\right]^2, \\
F_2^{LR} &= -\frac{1}{2 s_W^2}\left[\left(G_L^{\nu}\right)^2 + r_N\left(G_L^{Ne}\right)^2\right]\left[1 - g_{WWZ_1} g_{1L}^e \chi_1 - g_{WWZ_2} g_{2L}^e \chi_2\right],
\end{aligned}
\tag{27}
$$

where the χ_j ($j = 1, 2$) are the Z_1 and Z_2 propagators, i.e. $\chi_j = s/(s - M_j^2 + i M_j \Gamma_j)$, $r_N = t/(t - m_N^2)$, with $t = M_W^2 - s/2 + s\cos\theta\beta_W/2$, and m_N is the neutral heavy lepton mass. Also, in Eq. (27), $g_{WWZ_1} = g_{WWZ}\cos\phi$ and $g_{WWZ_2} = -g_{WWZ}\sin\phi$ where $g_{WWZ} = \cot\theta_W$. Note that Eq. (27) is obtained in the approximation where the imaginary parts of the Z_1 and Z_2 boson propagators are neglected, which is fully appropriate far away from the poles. (Accounting for this effect would require the replacements $\chi_j \to \mathrm{Re}\,\chi_j$ and $\chi_j^2 \to |\chi_j|^2$ on the right-hand side of Eq. (27).)

Since the gauge eigenstate Z' is neutral under $SU(2)_L$ and does not couple to the W^+W^- pair, the process (1) is sensitive to a Z' only in the case of a non-zero Z-Z' mixing. Moreover, as one can easily see from the formulae above, the s-channel Z_2 and the t-channel N exchange amplitudes arise only in the case of non-vanishing mixing angles. In this case, the expression for the SM cross section [25] can be obtained from (25) in the limit of vanishing mixing angles.

The first term F_0^{LR} describes the contributions to the cross section caused by neutrino ν and heavy neutral lepton N exchanges in the t-channel while the second one, F_1^{LR}, is responsible for s-channel exchange of the photon γ and the gauge bosons Z_1 and Z_2. The interference between s- and t-channel amplitudes is contained in the term F_2^{LR}. The RL case is simply obtained from Eq. (27) by exchanging $L \to R$.

For the LL and RR cases there is only N-exchange contribution,

$$
F_0^{LL} = F_0^{RR} = \frac{1}{16 s_W^4} r_N^2 \left(G_L^{Ne} G_R^{Ne}\right)^2. \tag{28}
$$

Concerning the $\mathcal{O}_{k\,\alpha\beta}$ multiplying the expression in Eq. (28) (see Eq. (26)) their explicit expressions for polarized and unpolarized final states W^+W^- can be found in, e.g. [15].

IV. DISCOVERY REACH ON HEAVY LEPTON COUPLINGS

We take "discovery" of new physics to mean exclusion of the Standard Model at a given confidence level. In the following, this will be the 95% C.L.

A. No Z-Z' mixing

Let us start the analysis with a case where there is only lepton mixing and no Z-Z' mixing, i.e., $\phi = 0$. Since the mixing angles are bounded by s_i^2 at most of order 10^{-2}, we can expect that retaining only the terms of order s_1^2, s_2^2 and $s_1 s_2$ in the cross section (25) should be an adequate approximation. To do that we expand the couplings of Eqs. (20)-(22) taking Eq. (9) into account. We find for E_6 models, where $T_{3L}^E = T_{3R}^E = -1/2$:

$$\begin{aligned} G_L^{Ne} &= s_{1L} - s_{2L}, & G_R^{Ne} &= s_{1R} \\ g_L^e &= g_L^{e^0}, & g_R^e &= g_R^{e^0} - \frac{1}{2}(G_R^{Ne})^2 g_Z, \\ G_L^\nu &= G_L^{\nu^0} - \tfrac{1}{2}(G_L^{Ne})^2, & G_R^\nu &= s_{1R}\, s_{2R}. \end{aligned} \tag{29}$$

From Eqs. (27)-(29) one can see that in the adopted approximation the cross section (25) allows to constrain basically the pair of heavy lepton couplings squared, $((G_L^{Ne})^2, (G_R^{Ne})^2)$, it is not possible to constrain s_{2R}^2, which represents mixing in the right-handed neutral-lepton sector.

The sensitivity of the polarized differential cross section (25) to the couplings G_L^{Ne} and G_R^{Ne} is evaluated numerically by dividing the angular range $|\cos\theta| \leq 0.98$ into 10 equal bins, and defining a χ^2 function in terms of the expected number of events $N(i)$ in each bin for a given combination of beam polarizations [16]:

$$\chi^2 = \sum_{\{P_L^-, P_L^+\}} \sum_{i}^{\text{bins}} \left[\frac{N_{\text{SM+NP}}(i) - N_{\text{SM}}(i)}{\delta N_{\text{SM}}(i)} \right]^2, \tag{30}$$

where $N(i) = \mathcal{L}_{\text{int}}\, \sigma_i\, \varepsilon_W$ with $\mathcal{L}_{\text{int}}$ the time-integrated luminosity. Furthermore,

$$\sigma_i = \sigma(z_i, z_{i+1}) = \int_{z_i}^{z_{i+1}} \left(\frac{d\sigma}{dz} \right) dz, \tag{31}$$

where $z = \cos\theta$ and polarization indices have been suppressed. Also, ε_W is the efficiency for W^+W^- reconstruction, for which we take the channel of lepton pairs $(e\nu + \mu\nu)$ plus two hadronic jets, giving $\varepsilon_W \simeq 0.3$ basically from the relevant branching ratios. The procedure outlined above is followed to evaluate both $N_{\text{SM}}(i)$ and $N_{\text{SM+NP}}(i)$.

The uncertainty on the number of events $\delta N_{\text{SM}}(i)$ combines both statistical and systematic errors where the statistical component is determined by $\delta N_{\text{SM}}^{\text{stat}}(i) = \sqrt{N_{\text{SM}}(i)}$. Concerning systematic uncertainties, an important source is represented by the uncertainty on

beam polarizations, for which we assume $\delta P_L^-/P_L^- = \delta P_L^+/P_L^+ = 0.5\%$ with the "standard" envisaged values $|P_L^-| = 0.8$ and $|P_L^+| = 0.6$ [21]. As for the time-integrated luminosity, for simplicity we assume it to be equally distributed between the different polarization configurations. Another source of systematic uncertainty originates from the efficiency of reconstruction of $W^\pm$ pairs which we assume to be $\delta\varepsilon_W/\varepsilon_W = 0.5\%$. Also, in our numerical analysis to evaluate the sensitivity of the differential distribution to model parameters we include initial-state QED corrections to on-shell $W^\pm$ pair production in the flux function approach [26–30] that assures a good approximation within the expected accuracy of the data.

As a criterion to derive constraints on the coupling constants in the case where no deviations from the SM were observed within the foreseeable uncertainties on the measurable cross sections, we impose that

$$\chi^2 \leq \chi^2_{\rm min} + \chi^2_{\rm CL}, \tag{32}$$

where $\chi^2_{\rm CL}$ is a number that specifies the chosen confidence level, and $\chi^2_{\rm min}$ is the minimal value of the χ^2 function.

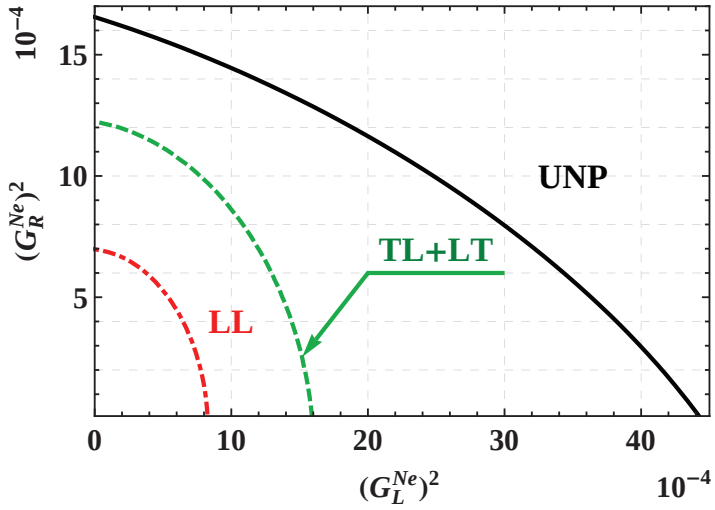

FIG. 2: Discovery reach (95% C.L.) on the heavy neutral lepton couplings $(G_L^{Ne})^2$ and $(G_R^{Ne})^2$ obtained from differential polarized cross sections with $(P_L^- = \pm 0.8,\ P_L^+ = \mp 0.6)$ and different sets of $W^\pm$ polarizations. Here, $\sqrt{s} = 0.5$ TeV, $\mathcal{L}_{\rm int} = 0.5$ ab^{-1} and $m_N = 0.3$ TeV.

From the numerical procedure outlined above, we obtain the allowed regions in $(G_L^{Ne})^2$ and $(G_R^{Ne})^2$ determined from the differential polarized cross sections with different sets of

polarization (as well as from the unpolarized process (1)) depicted in Fig. 2, where $\mathcal{L}_{\rm int} = 500$ fb^{-1} has been taken [21].

The results of a further potential extension of the present analysis are also shown in Fig. 2 where the feasibility of measuring polarized $W^{\pm}$ states in the process (1) is assumed. This assumption is based on the experience gained at LEP2 on measurements of W polarisation [31]. The method exploited for the measurement of W polarisation is based on the spin density matrix elements that allow to obtain the differential cross sections for polarised W bosons. Information on spin density matrix elements as functions of the W^- production angle with respect to the electron beam direction was extracted from the decay angles of the charged lepton in the W^- (W^+) rest frame. The relevant theoretical framework for measurement of $W^{\pm}$ polarisation was described in [18, 25].

In Fig. 2, we consider different cases of polarized Ws, with W_L and W_T referring to longitudinally and transversely polarized Ws, respectively. As shown in the figure, $d\sigma(W_L^+W_L^-)/dz$ is most sensitive to the parameters $(G_L^{Ne})^2$ and $(G_R^{Ne})^2$ while $d\sigma(W_T^+W_T^-)/dz$ has the lowest sensitivity to those parameters. The bounds on heavy lepton couplings obtained from $d\sigma(W_T^+W_T^-)/dz$ are not presented here as they are outside of the range shown in Fig. 2. The role of W polarization is seen to be essential in order to set meaningful finite bounds on the NWe couplings.

The obtained bounds are reminiscent of arcs of circles in the $(G_L^{Ne})^2$-$(G_R^{Ne})^2$ plane. This reflects the fact that the deviations in the LR and RL cross sections are approximately the same for the right-handed and left-handed couplings (recall that $T_{3L}^E = T_{3R}^E$) and thus approximately behave as $(G_L^{Ne})^4 + (G_R^{Ne})^4$.

In this Fig. 2, we considered a fairly low mass, $m_N = 0.3$ TeV. As one can see from Fig. 3 the constraints on heavy lepton couplings become more severe for larger values of m_N. The point is that the deviation of the cross section induced by the lepton mixing, from the SM prediction can be expressed, e.g., for the LR case, as

$$\Delta\sigma_{LR} \equiv \sigma_{\rm NP} - \sigma_{\rm SM} \propto (G_L^{Ne})^2\,(1 - r_N), \tag{33}$$

where we have used Eqs. (27) and (29). This structure $(1 - r_N)$ arises from negative interference between a mixing contribution to ν exchange and the N-exchange contribution. It reflects the decreasing impact of the heavy neutrino exchange contribution to $\Delta\sigma_{LR}$, since at large values of m_N the last term will be small. This leads to a better sensitivity on the

mixing angles with increasing m_N. The analogous dependence also holds for $\Delta\sigma_{RL}$ case.

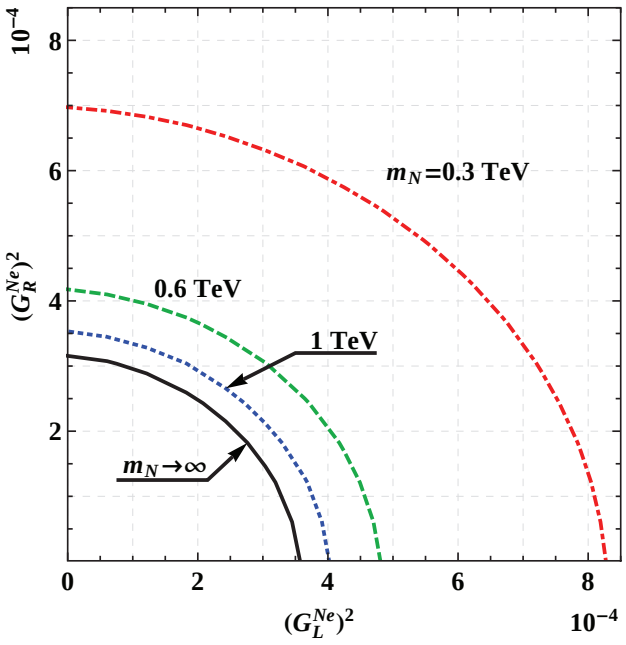

FIG. 3: Same as in Fig. 2 but obtained from the differential polarized cross sections $d\sigma(W_L^+W_L^-)/dz$ only, with ($P_L^- = \pm 0.8$, $P_L^+ = \mp 0.6$) and different values of the lepton mass $m_N = 0.3$ TeV, 0.6 TeV, 1 TeV and $m_N \to \infty$. Here, $\sqrt{s} = 0.5$ TeV and $\mathcal{L}_{\rm int} = 0.5$ ab^{-1}.

B. Including Z-Z' mixing

Now we turn to the generic case where both lepton mixing and Z-Z' mixing occur, so that the leptonic coupling constants are as in Eq. (24) and the Z_1, Z_2 couplings to $W^\pm$ are as in Eq. (27). In this case, in order to evaluate the influence of the Z-Z' mixing on the allowed discovery region on the heavy lepton coupling plane ($(G_L^{Ne})^2$, $(G_R^{Ne})^2$) one should vary the mixing angle ϕ within its current constraints which depend on the specific Z' model [32], namely $-0.0018 < \phi < 0.0009$ for the ψ model and $-0.0016 < \phi < 0.0006$ for the χ model. Within a specific Z' model and with fixed m_N, the χ^2 function basically depends on three parameters: ϕ, G_L^{Ne} and G_R^{Ne}. In this case, Eq. (32) describes a tree-dimensional surface. Its projection on the ($(G_L^{Ne})^2$, $(G_R^{Ne})^2$) plane demonstrates the interplay between leptonic and Z-Z' mixings. Fig. 4 shows, as a typical example, the results of this analysis for the χ-model (left panel) and the ψ-model (right panel), respectively, with fixed $m_N = 0.3$ TeV. As one can see, the shapes of the allowed regions for the coupling constants G_L^{Ne} and G_R^{Ne}

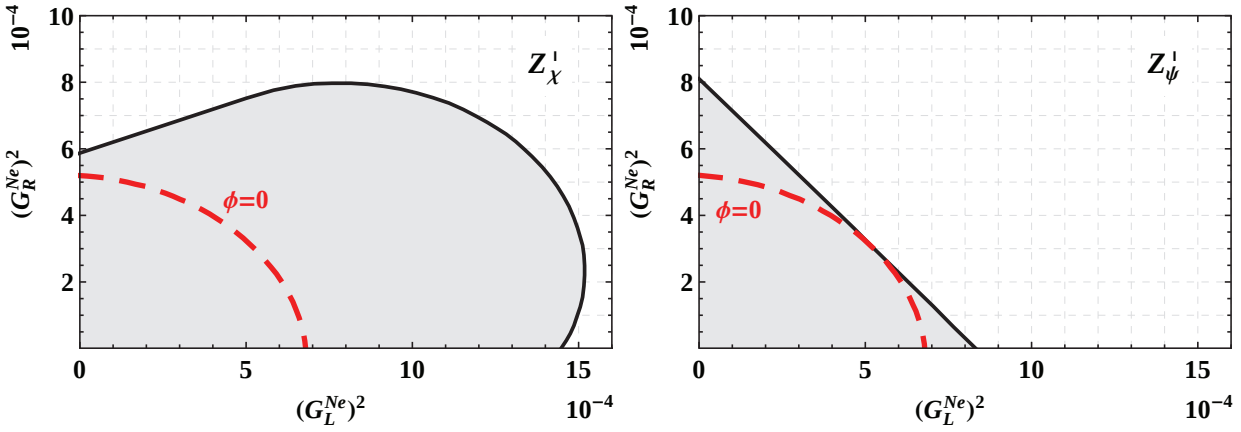

FIG. 4: Discovery reach at 95% CL on the heavy neutral lepton coupling plane $((G_L^{Ne})^2, (G_R^{Ne})^2)$ at $m_N = 0.3$ TeV in the case where both lepton mixing and Z-Z' mixing are simultaneously allowed for the Z'_χ model (left panel) and the Z'_ψ model (right panel), obtained from combined analysis of polarized differential cross sections $d\sigma(W_L^+W_L^-)/dz$ at different sets of polarization, $P_L^- = \pm 0.8$, $P_L^+ = \mp 0.6$, at the ILC with $\sqrt{s} = 0.5$ TeV and $\mathcal{L}_{\rm int} = 1$ ab^{-1}. The dashed curves labelled "$\phi = 0$" refer to the case of no Z-Z' mixing.

are quite dependent on the Z' model and different for these two cases. From the explicit calculation it turns out that this is due to the different relative signs between the lepton and Z-Z' mixing contributions to the deviations of the cross section $\Delta\sigma$.

Concerning Fig. 4 and the corresponding analysis for the χ and ψ models, we should note that the bounds on the lepton couplings $(G_L^{Ne})^2$ and $(G_R^{Ne})^2$ are somewhat looser than in the case $\phi = 0$ discussed above (roughly, by a factor as large as two), but still numerically competitive with the current situation. Also, we can remark that the cross sections for longitudinal W^+W^- production provide by themselves the most stringent constraints for this model.

Finally, one should note that although the discovery reach on the lepton couplings $(G_L^{Ne})^2$ and $(G_R^{Ne})^2$ obtained from polarized differential cross sections is quite dependent on the Z' model, this is not the case for the identification reach as the double beam polarization asymmetry $A^N_{\rm double}$ is basically independent of the Z-Z' boson mixing.

V. IDENTIFICATION OF HEAVY LEPTON EFFECTS WITH $A_{\rm double}$

By "identification" we shall here mean *exclusion* of a certain set of competitive models, including the SM, to a certain confidence level. For this purpose, the double beam polarization asymmetry, defined as [20, 33, 34]

$$A_{\rm double} = \frac{\sigma(P_1,-P_2)+\sigma(-P_1,P_2)-\sigma(P_1,P_2)-\sigma(-P_1,-P_2)}{\sigma(P_1,-P_2)+\sigma(-P_1,P_2)+\sigma(P_1,P_2)+\sigma(-P_1,-P_2)}, \tag{34}$$

is very useful. Here $P_1 = |P_L^-|$, $P_2 = |P_L^+|$, and $\sigma(\pm P_1, \pm P_2)$ denotes the polarized integrated cross section determined within the allowed range of the W^- scattering angle (or $\cos\theta$). From Eqs. (25) and (34) one finds for the $A_{\rm double}$ of the process (1)

$$A_{\rm double} = P_1 P_2 \frac{(\sigma^{RL}+\sigma^{LR})-(\sigma^{RR}+\sigma^{LL})}{(\sigma^{RL}+\sigma^{LR})+(\sigma^{RR}+\sigma^{LL})}. \tag{35}$$

We note that this asymmetry is only available if both initial beams are polarized.

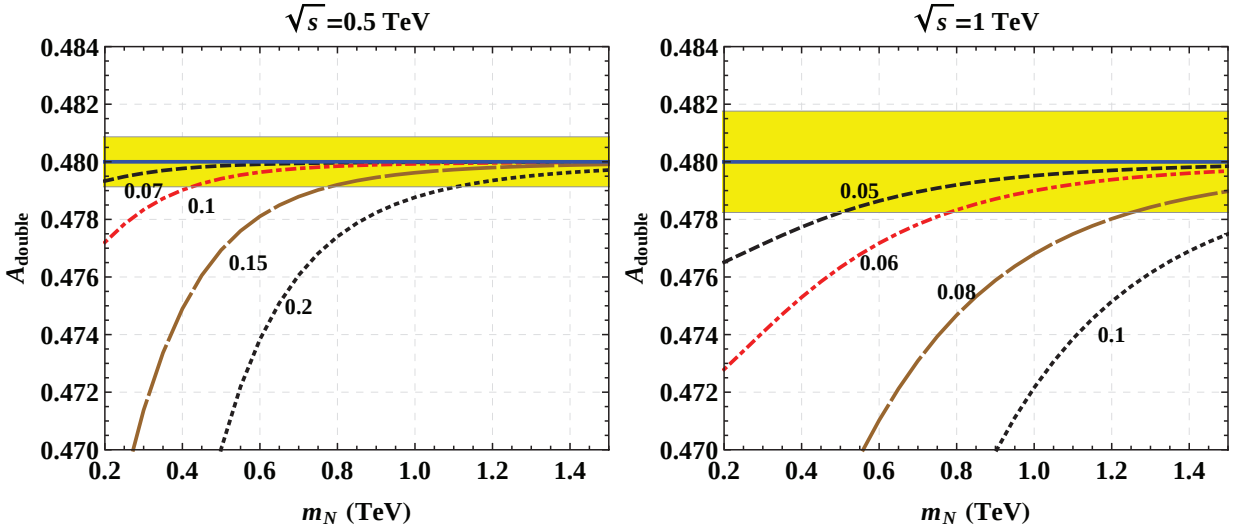

FIG. 5: Double beam polarization asymmetry $A_{\rm double}$ for the production of unpolarized $W^\pm$ as a function of neutral heavy lepton mass m_N for different choices of couplings $\sqrt{G_L^{Ne}G_R^{Ne}}$ (attached to the lines) at the ILC with $\sqrt{s} = 0.5$ TeV (left panel) and $\sqrt{s} = 1.0$ TeV (right panel), $\mathcal{L}_{\rm int} = 1$ ab^{-1}. The solid horizontal line corresponds to $A_{\rm double}^{\rm SM} = A_{\rm double}^{\rm Z'} = A_{\rm double}^{\rm AGC}$. The error bands indicate the expected uncertainty in the SM case at the 1-σ level.

It is important to also note that the SM gives rise only to σ^{LR} and σ^{RL} such that the structure of the integrated cross section has the form

$$\sigma_{\rm SM} = \frac{1}{4}\left[\left(1+P_L^-\right)\left(1-P_L^+\right)\,\sigma_{\rm SM}^{RL} + \left(1-P_L^-\right)\left(1+P_L^+\right)\,\sigma_{\rm SM}^{LR}\right]. \tag{36}$$

This is also the case for anomalous gauge couplings (AGC) [25], and Z'-boson exchange (including Z-Z' mixing and Z_2 exchange) [16]. The corresponding expressions for those cross sections can be obtained from (36) by replacing the specification SM $\to$ AGC and Z', respectively. Accordingly, the double beam polarization asymmetry has a common form for all those cases:

$$A_{\rm double}^{\rm SM} = A_{\rm double}^{\rm AGC} = A_{\rm double}^{\rm Z'} = P_1 P_2 = 0.48, \tag{37}$$

where the numerical value corresponds to the product of the electron and positron degrees of polarization: $P_1 = 0.8$, $P_2 = 0.6$. Eq. (37) demonstrates that $A_{\rm double}^{\rm SM}$, $A_{\rm double}^{\rm AGC}$ and $A_{\rm double}^{\rm Z'}$ are indistinguishable for any values of NP parameters, AGC or Z' mass and strength of Z-Z' mixing, i.e. $\Delta A_{\rm double} = A_{\rm double}^{\rm AGC} - A_{\rm double}^{\rm SM} = A_{\rm double}^{\rm Z'} - A_{\rm double}^{\rm SM} = 0$.

On the contrary, the heavy neutral lepton N-exchange in the t-channel will induce non-vanishing contributions to σ^{LL} and σ^{RR}, and thus force $A_{\rm double}$ to a smaller value, $\Delta A_{\rm double} = A_{\rm double}^{N} - A_{\rm double}^{\rm SM} \propto -P_1 P_2\, r_N^2\, \left(G_L^{Ne} G_R^{Ne}\right)^2 < 0$ irrespectively of the simultaneous lepton and Z-Z' mixing contributions to σ^{RL} and σ^{LR}. A value of $A_{\rm double}$ below $P_1 P_2$ can provide a signature of heavy neutral lepton N-exchange in the process (1). All those features in the $A_{\rm double}$ behavior are shown in Fig. 5, where we consider unpolarized Ws.

The identification reach (ID) on the plane of heavy lepton coupling $((G_L^{Ne})^2$, $(G_R^{Ne})^2)$ (at 95% C.L.) for various lepton masses m_N plotted in Fig. 6 is obtained from conventional χ^2 analysis with $A_{\rm double}$. In that case the χ^2 function is constructed as $\chi^2 = (\Delta A_{\rm double}/\delta A_{\rm double})^2$ where $\delta A_{\rm double}$ is the expected experimental uncertainty accounting for both statistical and systematic components. Note that discovery is possible in the green and yellow regions, whereas identification is only possible in the green region. The hyperbola-like limit of the identification reach is due to the appearance of a product of the squared couplings $(G_L^{Ne})^2$ and $(G_R^{Ne})^2$ in the deviation from the SM cross section, given by Eq. (28).

It should be stressed that the identification reach is independent of the Z' model assumed, whereas the discovery reach is not. In fact, in the lower left corner of these figures, we show how the discovery reach gets modified if we allow for Z-Z' mixing within the Z'_χ model (cf. Fig. 4).

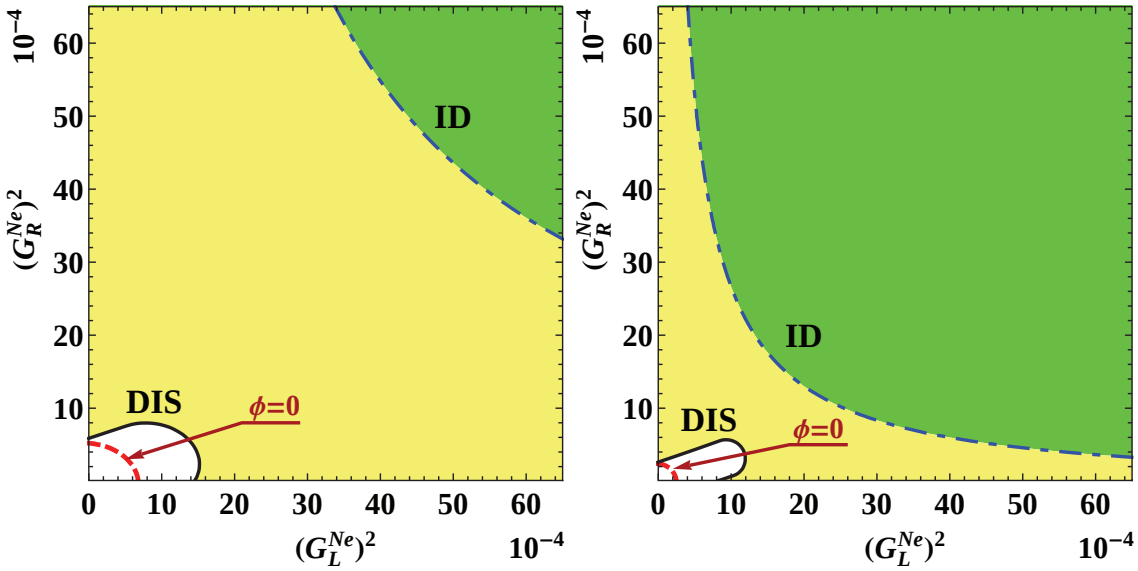

FIG. 6: Left panel: discovery (DIS) and identification (ID) reaches at 95% CL on the heavy neutral lepton coupling plane $((G_L^{Ne})^2, (G_R^{Ne})^2)$, obtained from a combined analysis of polarized differential cross sections $d\sigma(W_L^+W_L^-)/dz$ at different sets of polarization, $P_L^- = \pm 0.8$, $P_L^+ = \mp 0.6$, and exploiting the double polarization asymmetry. Furthermore, $m_N = 0.3$ TeV, $\sqrt{s} = 0.5$ TeV and $\mathcal{L}_{\rm int} = 1$ ab^{-1}. Right panel: similar, with $\sqrt{s} = 1.0$ TeV and for $m_N = 0.6$ TeV. The dashed curves labelled "$\phi = 0$" refer to the case of no Z-Z' mixing, whereas the outer contour labelled "DIS" refer to the minimum discovery reach in the presence of mixing.

VI. DISCOVERY AND IDENTIFICATION REACH AT $\sqrt{s} = 350$ GEV

In view of the possibility of a staged ILC construction, we would like to comment on the possibility of obtaining bounds on heavy neutral leptons at 350 GeV. As illustrated in Fig. 7, polarized beams would already at this low energy allow to place a limit on possible NWe couplings, in particular at low masses m_N. In this figure we explore masses beyond the corresponding kinematical reach. Even at this rather low energy there is already sensitivity to discover heavy lepton couplings in the range of $G^2 \sim 10^{-3}$ for low masses and up to $G^2 \sim 5 \times 10^{-4}$ for heavy masses m_N and with an assumed integrated luminosity of 500 fb^{-1}. It is seen that one can identify heavy-lepton-mixing effects for masses up to $m_N \sim 400$ GeV.

Discovery is seen to become more sensitive at higher masses, since the effect is approximately proportional to $1 - r_N$, whereas for identification the sensitivity is governed by r_N, and thus becomes less efficient at higher masses. For higher beam energy, both sensitivities

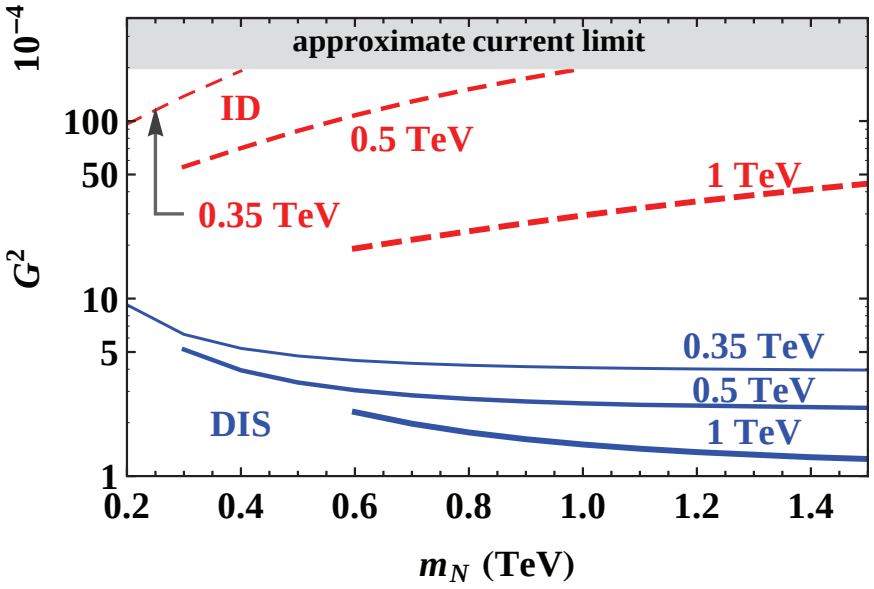

FIG. 7: Discovery (DIS) and identification (ID) reach on $G^2 \equiv (G_L^{Ne})^2 = (G_R^{Ne})^2$. The low-energy case (350 GeV) is compared with the nominal energy cases of 500 GeV and 1 TeV, all at an assumed integrated luminosity of 500 fb^{-1}. The approximate current limit on these couplings is indicated as a grey band.

improve.

VII. CONCLUDING REMARKS

In this note we have studied the process $e^+e^- \to W^+W^-$ and seen how to uniquely identify the indirect (propagator and exotic-lepton mixing) effects of a heavy neutral lepton exchange in the t-channel. Discovery of new physics, meaning exclusion of the Standard Model, does not depend on having both initial beams polarized, but the sensitivity is improved with beam polarization. Such "discovery" could be due to the existence of a Z', anomalous gauge couplings, or the effect of a heavy neutral lepton. The potential of the ILC to discover heavy lepton effects depends on the possible presence of a Z' contribution, and is vastly improved if one is able to determine the polarization of the produced Ws.

Identification of such new physics effect as being due to a heavy neutral lepton exchange, as opposed to a Z' or AGC can be achieved via the determination of a double polarization asymmetry. This identification of heavy-lepton admixture is independent of the strength of any Z-Z' mixing, as well as the Z' model, but requires having both initial beams polarized.

Acknowledgements

This research has been partially supported by the Abdus Salam ICTP under the TRIL and Associates Scheme and the Belarusian Republican Foundation for Fundamental Research. The work of AAP has been partially supported by the Collaborative Research Center SFB676/1-2006 of the DFG at the Department of Physics, University of Hamburg. The work of PO has been supported by the Research Council of Norway.

---

[1] P. Langacker, Rev. Mod. Phys. **81**, 1199-1228 (2009) [arXiv:0801.1345 [hep-ph]].

[2] T. G. Rizzo, [hep-ph/0610104].

[3] A. Leike and S. Riemann, Z. Phys. C **75**, 341 (1997) [hep-ph/9607306].

[4] A. Leike, Phys. Rept. **317**, 143-250 (1999) [hep-ph/9805494].

[5] S. Riemann, eConf C **050318**, 0303 (2005) [hep-ph/0508136].

[6] J. L. Hewett, T. G. Rizzo, Phys. Rept. **183**, 193 (1989).

[7] S. Hesselbach, F. Franke and H. Fraas, Eur. Phys. J. C **23** (2002) 149 [hep-ph/0107080].

[8] P. H. Frampton, P. Q. Hung and M. Sher, Phys. Rept. **330** (2000) 263 [hep-ph/9903387].

[9] P. Langacker and D. London, Phys. Rev. D **38** (1988) 886.

[10] J. Beringer *et al.* [Particle Data Group Collaboration], Phys. Rev. D **86** (2012) 010001.

[11] ATLAS Collaboration, *"Search for high-mass dilepton resonances with 5 fb^{-1} of pp collisions at $\sqrt{s} = 7$ TeV with the ATLAS experiment"*, ATLAS-CONF-2012-007; ATLAS-CONF-2012-129;

[12] S. Chatrchyan *et al.* [CMS Collaboration], Phys. Lett. B **714**, 158 (2012) [arXiv:1206.1849 [hep-ex]]; S. Chatrchyan *et al.* [CMS Collaboration], Phys. Lett. B **2**, 3 (2013) [arXiv:1212.6175 [hep-ex]]; S. Chatrchyan *et al.* [CMS Collaboration], EXO-12-061.

[13] S. Singh, A. K. Nagawat and N. K. Sharma, Mod. Phys. Lett. A **5**, 1717 (1990).

[14] A. K. Nagawat, S. Singh and N. K. Sharma, Phys. Rev. D **42**, 2984 (1990).

[15] A. A. Babich, A. A. Pankov and N. Paver, Phys. Lett. B **299** (1993) 351; B **346** (1995) 303.

[16] V. V. Andreev, G. Moortgat-Pick, P. Osland, A. A. Pankov and N. Paver, Eur. Phys. J. C **72** (2012) 2147 [arXiv:1205.0866 [hep-ph]].

[17] K. Hagiwara, R. D. Peccei, D. Zeppenfeld and K. Hikasa, Nucl. Phys. B **282**, 253 (1987).

[18] G. Gounaris, J. L. Kneur, J. Layssac, G. Moultaka, F. M. Renard and D. Schildknecht, Proceedings of the Workshop e^+e^-*Collisions at 500 GeV: the Physics Potential*, Ed. P.M. Zerwas (1992), DESY 92-123B, p.735.

[19] G. Buchalla, O. Cata, R. Rahn and M. Schlaffer, arXiv:1302.6481 [hep-ph].

[20] A. V. Tsytrinov, J. Kalinowski, P. Osland and A. A. Pankov, Phys. Lett. B **718** (2012) 94 [arXiv:1207.6234 [hep-ph]].

[21] G. Moortgat-Pick, T. Abe, G. Alexander, B. Ananthanarayan, A. A. Babich, V. Bharadwaj, D. Barber, A. Bartl *et al.*, Phys. Rept. **460**, 131-243 (2008) [hep-ph/0507011].

[22] J. Alcaraz *et al.* [ALEPH and DELPHI and L3 and OPAL and LEP Electroweak Working Group Collaborations], arXiv:0712.0929 [hep-ex].

[23] E. Nardi, E. Roulet and D. Tommasini, Phys. Rev. D **46**, 3040 (1992).

[24] E. Nardi, E. Roulet and D. Tommasini, Phys. Lett. B **327**, 319 (1994) [hep-ph/9402224].

[25] G. Gounaris, J. Layssac, G. Moultaka and F. M. Renard, Int. J. Mod. Phys. A **8** (1993) 3285.

[26] W. Beenakker, F. A. Berends and T. Sack, Nucl. Phys. B **367**, 287 (1991).

[27] W. Beenakker, K. Kolodziej and T. Sack, Phys. Lett. B **258**, 469 (1991).

[28] W. Beenakker and A. Denner, Int. J. Mod. Phys. A **9**, 4837 (1994).

[29] A. Denner, S. Dittmaier, M. Roth and L. H. Wieders, Phys. Lett. B **612**, 223 (2005) [Erratum-ibid. B **704**, 667 (2011)] [hep-ph/0502063].

[30] A. Denner, S. Dittmaier, M. Roth and L. H. Wieders, Nucl. Phys. B **724**, 247 (2005) [Erratum-ibid. B **854**, 504 (2012)] [hep-ph/0505042].

[31] G. Abbiendi *et al.*, [OPAL collaboration], Phys. Lett. **B585**, 223 (2004);
P. Achard *et al.*, [L3 collaboration], Phys. Lett. **B557**, 147 (2003);
J. Abdallah *et al.*, [DELPHI Collaboration], Eur. Phys. J. C **54**, 345 (2008) [arXiv:0801.1235 [hep-ex]];
J.P. Couchman, A measurement of the triple gauge boson couplings and W boson polarisation in W-pair production at LEP2, Ph.D. thesis, University College London, 2000.

[32] J. Erler, arXiv:0909.5309 [hep-ph].

[33] T. G. Rizzo, Phys. Rev. D **59** (1999) 113004 [arXiv:hep-ph/9811440].

[34] P. Osland, A. A. Pankov and N. Paver, Phys. Rev. D **68**, 015007 (2003) [arXiv:hep-ph/0304123].

Chapter 8

Specific Detector and Machine Design Issues

Study of the anti-DID magnetic Fields' Effects on the Beam-induced Pair Backgrounds in ILD

Eduard Avetisyan[1]

[1]DESY, Notketraße 85, 22607 Hamburg, Germany

DOI: will be assigned

The main goal of the study is the update of the hit rates in ILD detectors to account for the changes in the detector geometry and beam characteristics from the time of the LOI [1], to be included into DBD [2]. Both 500GeV and 1TeV options are considered. The comparison of the hits rates with the most up-to-date setup of ILD (o1_v05) with those reported in [1, 3] revealed a dramatic increase (factor $\sim$ 20) of the hit rates in the VTX and other detectors. A detailed study has shown that these are mainly caused by particles backscattering from the BCal area, instead of being guided to the beam exit by the anti-DID field version X03. It has been found that the previous version of the anti-DID, *fieldX02*, despite being slightly unphysical in large radii in the region of the TPC, directs the pair background more accurately into the beam exits, producing significantly less backscatter hits, and hence should be used in the estimate of the hit density in the ILD.

1 Introduction

High energies and luminosities that are mandatory requirements for next-generation electron-positron colliders come at the price of the so-called *beamstrahlung* [4] – an intense production of charged electron-positron pairs resulting from bremsstrahlung of initial beam particles pass through the highly focused and boosted EM fields of the oncoming bunches of the colliding beam. While most of these particles are high-energetic and follow the trajectory of the incoming beam and are dumped in the corresponding beam exits, some low-energy particles produce direct hits or showers in the detectors or in the support materials, which then backscatter into the detector. Guided by the solenoid field of the ILD these low-energy particles may curl for a relatively long time and create a large amount of hits in the nearby detectors, possibly saturating these and distorting the physics measurement. Such beam-induced backgrounds can be reduced by applying a special (dipole) magnetic field on top of the usual solenoid field of the detector which would guide those low-energetic background out of the sensitive area. For the ILD with 14mrad crossing angle the minimization of such backgrounds is achieved by applying an anti-DID [5, 6] field. Several studies [7, 8] have been performed in the past with various detector geometries, beam parameters and magnetic field configurations, in order to make sure that the hit loads created by such pair backgrounds in individual detector components are within safe boundaries. This note reports the recent results of the detector occupancies using the most up-to-date (for the moment) version of ILD setup *o1_v05*, included in [2], and compares those with the corresponding values of the previous publication [1].

2 Simulation of the events

For this studies *ee*-pairs generated by the *GuineaPig* [9] package were used for beam energies 500GeV and 1000GeV, beam setup options *TDR_ws* and *B1b_ws*, respectively. In comparison with the previous study for [1] where the *nominal* and *low-power* options were considered, the number of bunches is reduced (by factor 2 in 500GeV case, and by 10% for 1TeV), but the bunches are compressed in z-direction, and *travelling focus* technique is used to increase the luminosities[10]. The output of this generator is stored in ascii files, with a single bunch-crossing in each, containing 50-400k particles. As this number of particles is way too large

to be digested by the *Mokka*[11] simulation package as a single event, these input are split into chunks of semi-arbitrary size and processed separately, then joined together to calculate occupancies or overlay with physics events, based on luminosity.

The pair background files have been processed with Mokka, initially using the o1_v05 detector geometry with the default settings and ILC softare v01-14-p00. Further studies have been made using the v01-16-01 version of the ILC software, which didn't reveal any differences in the hit rates obtained with the v01-14-p00 version with identical detector setups.

In the simulation, the Mokka options */Mokka/init/TPCLowPtStepLimit true* and */Mokka/init/TPCCut 0 keV* were used. The default value of 10mm for TPC step length has been used (*TPC_max_step_length = 10* in Mokka).

3 Calculation of the hit rates

For the sake of consistency the procedure of the hit rate calculation has been kept as close as possible to that used in the LOI. The initial GuineaPig pair background files have been simulated using the corresponding detector geometry model, then processed through a simple Marlin [12] processor looping through all collections and counting the hits in the detectors. One exception was the TPC, where the raw number of hits produced in simulation doesn't reflect the actual detector occupancy due to certain arbitrariness in the choice of the assignment of the spacepoints by Mokka. Hence it was decided to have the TPC hits digitized by the corresponding standard processor (*TPCDigiProcessor*) in Marlin and only then count the hits. Since the previous study made for the LOI [1, 8] lacked the *TPCLowPt* collection where the relevant particles creating the largest amount of hits are stored, the hit rates quoted in both old and new documents are not suitable for direct comparison.

3.1 Error calculation

The errors on the hit rates are calculated by merely extracting the RMS from a certain number of bunch crossings analyzed (between 100 and 300, depending on the setup). While the statistical accuracy of the extraction was sufficient for most of the detectors, in some rare cases the low-energetic back-scattered particles created an enormous amount (e.g. an order of magnitude higher than usual) of hits in some detectors by curling around the solenoid field lines. Hence the uncertainty on the hit rates remained high despite the abundance of statistics generated.

4 Differences in setups of LOI and DBD

For the LOI studies the hit rates were extracted using the *v01-06-fw* version of the ILC software, with Mokka version *06-07-patch02* and the geometry model *ILD_00fw*. The current study uses *v16-01* of the ILC software, Mokka version *08-00-03* and the geometry model *ILD_o1_v05*. While there were plenty of changes within the two geometry models, the main focus of this study was on the BCal geometry and the anti-DID field map. The BCal was changed from model version BCal08 (with circular holes for incoming and outgoing beams) back to BCal01 (with a keyhole shape filled with graphite to reduce the soft backscattering). Similarly, the anti-DID field version *fieldX02* used for the LOI studies was shown [13] to have slightly unphysical field lines at high radii (roughly at TPC level), and has been replaced by *fieldX03* which has more natural shape of the field lines, while being slighly larger in magnitude.

Figure 1: Different BCal models used

5 Background rates with the default settings of o1_v05

The comparison of the hit rates using the default setting of the ILD_o1_v05 geometry (e.g. BCal08+fieldX03) with the older ones revealed significantly higher (roughly factor 20!) counts in the vertex detector as well as

different angular distribution of the hits, as can be seen on Fig. 2(*figure need to be reproduced to correct the labelling*). The hits in the new study are clearly asymmetric, hitting mostly one side of the vertex detector.

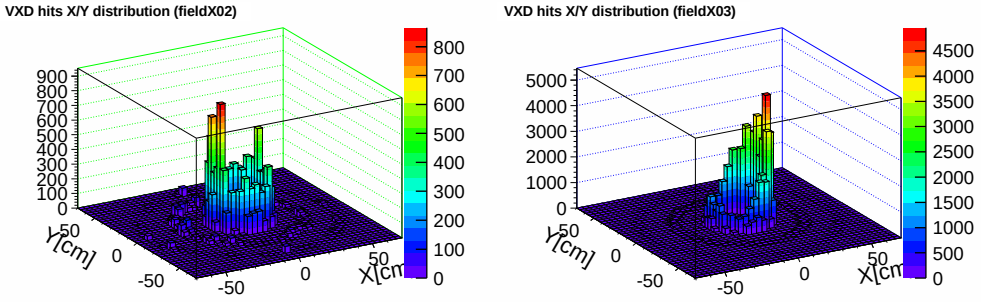

Figure 2: Left: LOI, Right: DBD. The pair background hit distributions in VXD X/Y plane.

The study of the origin of the particles (*MCParticle* collection) revealed that the majority of the extra hits in the new geometry arise from the area close to BCal and further downstream beampipes (see Fig. 3 *need to redo the figure to correct the labels*).

To study the cause of the increased background rates additional simulations were made using combinations of old and new BCal geometries (BCal08 and BCal01) and magnetic field versions (fieldX02, fieldX03 or SField01). Each simulation for 1TeV case was made using 100 bunch crossings.

Already the first results proved that the difference in the BCal geometry didn't cause any serious differences in the hit rates, but rather the changed anti-DID field. A comparison of the field strengths has revealed that fieldX03 has slightly larger magnitude than fieldX02, as can be seen on Figure 4. This results in a stronger than necessary kick sideways for a large amount of low-energetic pair particles that hit the tungsten and graphite in the BCal and therefore cause backscatter hits. In fact, the increase in the background rates have been observed in [13] already, but not directly attributed to the changed field.

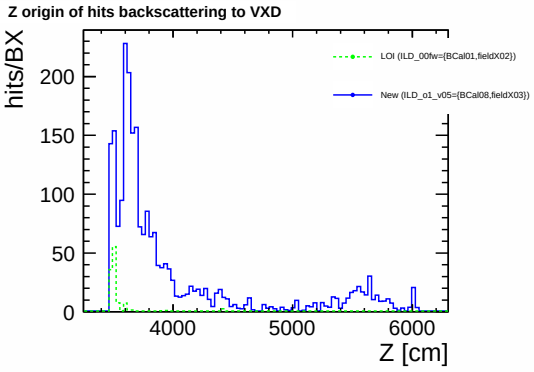

Figure 3: The z-origin of MCParticles creating hits in the vertex detector.

6 Background hits with fieldX02

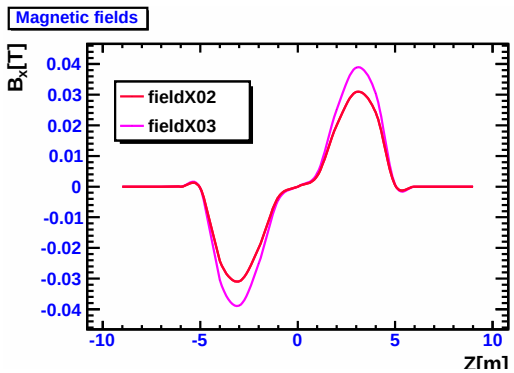

As the geometry of the BCal has been shown to play no significant role in the surplus of the background hits it has been decided to use the simulation with the default BCal geometry for ILD_o1_v05 and only "downgrade" the anti-DID field to fieldX02, as used in LOI studies. The resulting hit rates are presented in Table 2. In comparison with the values obtained for the LOI (see Table 1) the hit rates in the vertex detectors have increased slightly due to the modified beam parameters (shorter bunches, higher luminosity per bunch etc.). Similarly, the increase of the hit rates in the ECal and HCal also gets contribution

Subdetector	Units	Layer	Nom-500	Low-P-500	Nom-1000
VTX-DL	hits/cm^2/BX	1	3.214±0.601	7.065±0.818	7.124±1.162
		2	1.988±0.464	4.314±0.604	4.516±0.780
		3	0.144±0.080	0.332±0.107	0.340±0.152
		4	0.118±0.074	0.255±0.095	0.248±0.101
		5	0.027±0.026	0.055±0.037	0.046±0.036
		6	0.024±0.022	0.046±0.030	0.049±0.044
SIT	hits/cm^2/BX	1	0.017±0.001	0.031±0.007	0.032±0.012
		2	0.004±0.003	0.016±0.005	0.008±0.002
FTD	hits/cm^2/BX	1	0.013±0.005	0.031±0.007	0.019±0.006
		2	0.008±0.003	0.023±0.007	0.013±0.005
		3	0.002±0.001	0.005±0.002	0.003±0.001
		4	0.002±0.001	0.007±0.002	0.004±0.001
		5	0.001±0.001	0.006±0.002	0.002±0.001
		6	0.001±0.001	0.005±0.002	0.002±0.001
		7	0.001±0.001	0.007±0.002	0.001±0.001
SET	hits/BX	1	5.642±2.480	57.507±10.686	13.022±7.338
		2	5.978±2.360	59.775±8.479	13.711±7.606
TPC	hits/BX	-	408±292	3621±709	803±356
ECAL	hits/BX	-	155±50	1176±105	274±76
HCAL	hits/BX	-	8419±649	24222±744	19905±650

Table 1: (LOI) Pair induced backgrounds in the subdetectors for nominal (500 GeV and 1 TeV) and Low-P (500 GeV) beam parameters. The numbers for the ECAL and the HCAL are summed over barrel and endcaps. For the vertex detecor, the double-layer option has been chosen for this simulation, the numbers for the single-layer option differ. The errors represent the RMS of the hit distributions of the simulation of $\approx$ 100 bunch crossings (BX).

from more complete description of the cabling and holding structures of the detectors. As mentioned in 4, the numbers obtained for the TPC use somewhat different counting scheme, hence a direct comparison isn't fully valid here. While the hit rates in FTD increased significantly w.r.t. the values of the previous study (still remaining in the safe boundaries), the SET and SIT register only very few hits per bunch train in the current setup, a feature isn't yet studied thoroughly.

7 Summary

The active ongoing development of both the accelerator and the detector components requires also a regular monitoring of the pair backgrounds as one of the largest contributions in some of the detector occupancies, and a corresponding adjustment of the protective magnetic fields. The current study has shown that the current version of the anti-DID fieldX03 overcorrects the trajectories of the low-energetic pair particles causing subsequent backscattering which could potentially distort the physics measurement. Using an earlier version of the fieldX02 allows a reasonable estimate of the pair backgrounds, despite some minor deficits of that field at higher radii. In comparison with the earlier results, there is a slight increase of the backgrounds in the vertex detector, caused by the modifications in the beam parameters and more complete description of the detector holding structures and cabling in GEANT. It is obvious that the elimination of these unphysical features of the anti-DID field shall be performed while keeping the background levels at acceptable levels.

Data file locations Guinea-Pig generated files for beam energies of 500GeV and 1TeV are located (on GRID) in directories */grid/ilc/prod/ilc/mc-dbd/generated/500-TDR_ws/eepairs* and */grid/ilc/prod/ilc/mc-dbd/generated/1000-B1b_ws/eepairs* , respectively, with one full bunch train in each.

The simulated LCIO files for standard geometry setup can be found on GRID in */grid/ilc/prod/ilc/mc-dbd/ild/sim/500-TDR_ws/eepairs/ILD_o1_v05/v01-14-01-p00* and */grid/ilc/prod/ilc/mc-dbd/ild/sim/1000-B1b_ws/eepairs/ILD_o1_v05/v01-14-p00* for 500 and 1000 GeV beam energies, respectively.

Sub-detector	Units	Layer	TDR_ws 500 GeV	B1b_ws 1000 GeV
VTX-DL	hits/cm^2/BX	1	6.320 ± 1.763	11.774 ± 0.992
		2	4.009 ± 1.176	7.479 ± 0.747
		3	0.250 ± 0.109	0.431 ± 0.128
		4	0.212 ± 0.094	0.360 ± 0.108
		5	0.048 ± 0.031	0.091 ± 0.044
		6	0.041 ± 0.026	0.082 ± 0.042
SIT	hits/cm^2/BX	1	0.0009 ± 0.0013	0.0016 ± 0.0016
		2	0.0002 ± 0.0003	0.0004 ± 0.0005
FTD	hits/cm^2/BX	1	0.072 ± 0.024	0.145 ± 0.024
		2	0.046 ± 0.017	0.102 ± 0.016
		3	0.025 ± 0.009	0.070 ± 0.009
		4	0.016 ± 0.005	0.046 ± 0.007
		5	0.011 ± 0.004	0.034 ± 0.005
		6	0.007 ± 0.004	0.024 ± 0.006
		7	0.006 ± 0.003	0.022 ± 0.006
SET	hits/BX	1	0.196 ± 0.924	0.588 ± 2.406
		2	0.239 ± 1.036	0.670 ± 2.616
TPC	hits/BX	-	216 ± 302	465 ± 356
ECAL	hits/BX	-	444 ± 118	1487 ± 166
HCAL	hits/BX	-	18049 ± 729	54507 ± 923

Table 2: (DBD) Pair induced backgrounds in the subdetectors for nominal 500 GeV and 1 TeV collision energy beam parameters. The numbers for the ECAL and the HCAL are summed over barrel and endcaps. For the vertex detecor, the double-layer option has been chosen for this simulation. The TPC hits are the digitised hits that would be written to the data acquisition system. The errors represent the RMS of the hit number fluctuations of ≈ 100 bunch crossing (BX) simulations.

The simulated LCIO files for ILD_o1_v05 with fieldX02 for 1TeV can be found on NAF(HH) in subdirectories of */scratch/hh/dust/naf/ilc/user/dich/projects/beam/mokka/* . The simulated files for 500GeV case with the anti-DID fieldX02 can be found on GRID in */grid/ilc/prod/ilc/mc-dbd/ild/sim/500-TDR_ws/eepairs/ILD_o1_v05/v01-14-01-p00_fieldX02* directory.

A Acknowledgments

I'm thankful to Jenny List, Katarzyna Wichmann, Frank Gäde, Karsten Büßer and Akiya Miyamoto for useful discussions, assistence and clarifications.

B Bibliography

References

[1] Toshinori Abe et al. The International Large Detector: Letter of Intent. 2010.

[2] ILD Concept Group. Detailed Baseline Design Report. 2013.

[3] A. Besson et al. Estimation of the background on the vertex detector of ILD from beamstrahlung . 2009.

[4] G.A. Moortgat-Pick, S. Hesselbach, I.R. Bailey, G.A. Moortgat-Pick, B.J.A. Shepherd, et al. Depolarization and Beam-beam Effects at the Linear Collider. *Conf.Proc.*, C0806233:MOPP024, 2008.

[5] Brett Parker and Andrei Seryi. Compensation of the effects of detector solenoid on the vertical beam orbit in NLC. *Phys.Rev.ST Accel.Beams*, 8:041001, 2005.

[6] Andrei Seryi, Takashi Maruyama, and Brett Parker. IR Optimization, DID and anti-DID. 2006.

[7] Adrian Vogel. Beam-induced backgrounds in detectors at the ILC. 2008.

[8] Katarzyna Klimek. Private communication.

[9] D. Schulte. Beam-beam simulations with GUINEA-PIG. 1999.

[10] N. Walker and Benno List. Ilc parameters. *http://ilc-edmsdirect.desy.de/ilc-edmsdirect/item.jsp?edmsid=D00000000925325*.

[11] Ties Behnke and Frank Gaede. Software for the International Linear Collider: Simulation and reconstruction frameworks. *Pramana*, 69:1089–1092, 2007.

[12] F. Gaede. Marlin and LCCD: Software tools for the ILC. *Nucl.Instrum.Meth.*, A559:177–180, 2006.

[13] Akiya Miyamoto. A study of pair backgrounds. 2012.

"Banana Shape" Bunches and the Luminosity for the ILC*

L.I. Malysheva†, O.S. Adeyemi, V. Kovalenko, G.A. Moortgat-Pick, A. Ushakov, Hamburg University, Hamburg, Germany
K. Buesser, A.F. Hartin, N.J. Walker, DESY, Hamburg, Germany
S. Riemann, F. Staufenbiel, DESY, Zeuthen, Germany

April 17, 2013

Abstract

The success of the linear collider depends upon the luminosity achieved at the interaction region. The nominal luminosity of 2x10^{34} [cm^{-2} s^{-1}] for the current ILC design can be significantly reduced by various reasons such as beam-beam effects at the interaction point, misalignment of the beams or the distortion in the bunch shape due to short-range wakefields. The latter, so-called "banana" effect, can also lead to a significant (10%-15%) luminosity loss even for perfectly aligned bunches. The results discussed in this paper suggest that previously this effect was underestimated for the ILC parameter sets.

1 Introduction

The luminosity is the measure of the interaction probability of the colliding beams. The high luminosity at the interaction point is a key issue for the future linear collider program. It can be written as

$$L = \frac{n_b N^2 f_{rep}}{4\pi\sigma_x\sigma_y} \times H_D \tag{1}$$

where n_b is the number of bunches per train, N is the number of particles per bunch and f_{rep} is the repetition rate of bunch trains. The transverse sizes $\sigma_{x,y}$ of the bunch are determined by the so-called Twiss parameters $\beta_{x,y}$ of the accelerator lattice and the emittance of the beam ϵ as $\sigma_{x,y} = \sqrt{\beta_{x,y}\epsilon}$. The parameter H_D is the pinch enhancement factor, which describes the increase in luminosity due to the extra focusing of the bunch by the field of the opposite bunch. The

*Work supported by the German Federal Ministry of education and research, Joint Research project R&D Accelerator "Spin Management", contract N 05H10CUE
†larisa.malysheva@desy.de

number of particles per bunch N cannot be increased beyond some limits as the dense bunch population can lead to various bunch-bunch instabilities.Thus for the nominal luminosity of the ILC of order of 10^{34} [cm^{-2} s^{-1}] very small transverse beam sizes (nanometers) and a beam power of order of 10 MW are required. The production of a beam with the required small transverse characteristics is a challenge. In addition, if the vertical bunch size σ_y[1] is small at the interaction point (IP) so does the vertical beta function β_y but then the beam divergence grows as $\sqrt{\epsilon/\beta_y}$. However, if β_y is smaller then the bunch length σ_z this hourglass effect will reduce the luminosity. It had been demonstrated in reference [1] that the use of the special focusing regime, so-called "travelling focus" [2], might overcome the hourglass effect by arranging the tail and the head of the bunches to be focused at proportionally displaced longitudinal position. In principle the use of this scheme could provide additional 30% of luminosity.

Finally the nominal luminosity calculated for an "ideal" case can be significantly reduced in the presence of the orbital/angular misalignments of the beam. The examples of such sensitivity for some parameter sets of the International Linear Collider can be found in reference [3] where the influence of orbital and angular beam-beam offsets were investigated. This paper is an update of reference [3] and evaluates the influence of misalignments and bunch shape distortions for different ILC parameter sets including that of the 'travelling focus'.

2 Luminosity loss due to orbital or angular offset for the ILC.

2.1 The new parameter sets for the ILC.

Since the publication of the Reference Design Report (RDR) [4] important changes have been suggested in order to reduce the cost of the ILC. In Table 1 the comparison of these new parameter sets [5] with the former RDR parameter set is given. Three new sets, i.e. "SB2009", "Low Charge" and "New Low Charge" are based on the reduction of the cost of the machine via the reduction of the charge per bunch train which leads to a smaller spatial extent of the machine and lower power supply. It should be noticed that the production of short bunches will require a two stage bunch compressor while the SB2009 design for the ILC has a one stage bunch compressor.

The "SB2009" is based on the application of the so-called "travelling focus" regime [1]. The alternative "Low Charge" (LC) and "New Low Charge" (J. Gao) parameter sets based on the reduction of the number of particles per bunch and on the reduction of the bunch length, could also provide the luminosity of 2×10^{34} [cm^{-2} s^{-1}]. In Table 1 the nominal luminosity values were calculated with the guineapig++ simulation code [6] which is C++ version of GUINEA-PIG [7].

[1]The use of the flat beams with $\sigma_x \ll \sigma_y$ are typical for the linear collider. Thus the example is given for vertical beam size σ_y and vertical beta function β_y.

Table 1: The ILC parameter sets

	RDR	SB2009	Low Charge	New Low Charge
$N_{particles}$	2x10^{10}	2x10^{10}	1x10^{10}	1x10^{10}
$N_{bunches}$	2625	1320	5640	2625
β_x/β_y $[mm]$	20/0.4	11/0.2	12/0.2	8/0.166
$\gamma\epsilon_x$ $[\mu m]$	10	10	10	10
$\gamma\epsilon_y$ $[\mu m]$	40	36	30	10
$\sigma_x[nm]$	639	474	495	404
$\sigma_y[nm]$	5.7	3.8	3.5	2.0
$\sigma_z[\mu m]$	300	300	150	166
D_y	19.0	38.4	10.0	24.0
Lumi.$\times 10^{34}[cm^{-2}s^{-1}]$	1.97	1.96	1.96	2.12

2.2 Study of the effects of orbital and angular offsets on luminosity.

The nominal luminosity for the ILC should be delivered even in the case of the new parameter sets for reduced beam power. The beam power is directly proportional to the centre-of-mass energy E_{CM} as

$$P_{beam} = E_{CM} n_b N f_{rep} \tag{2}$$

It follows from Eq. 1 and Eq. 2 that the luminosity is directly proportional to the beam power.

The luminosity is very sensitive to orbital and angular offsets of the interacting bunches. This effect was studied for all three new parameter sets and compared with the former RDR parameter set. The value of luminosity for the different orbital (Fig.1a) and angular (Fig.1b) offsets was normalised with respect to the nominal luminosity and plotted as function of the relative vertical orbital offset $\Delta y/\sigma_y$ or as a function of the relative vertical bunch divergence α_y/θ_y where $\theta_y = \sqrt{(\epsilon_y/\beta_y)}$.

It was found that the Low Charge (LC) parameter set is less sensitive to the orbital bunch displacement at the interaction point, while the values for the New Low Charge (J. Gao) set are very close to those of the RDR parameter set. As expected, the travelling focus (SB2009) regime has proved to be more sensitive to the orbital offsets compared to the other sets of parameters. The same parameter sets were used for the luminosity calculations in the presence of angular offsets. For the travelling focus regime the relative luminosity loss could be of order of 60%, while the Low Charge (LC) option gives a relatively small loss of luminosity $\approx 12\%$. It can be explained by the fact that for the LC set the disruption parameter Dy is nearly 4 times smaller than the Dy parameter for the travelling focus regime. The behavior of the New Low Charge (J. Gao) regime is again close to the RDR parameter set.

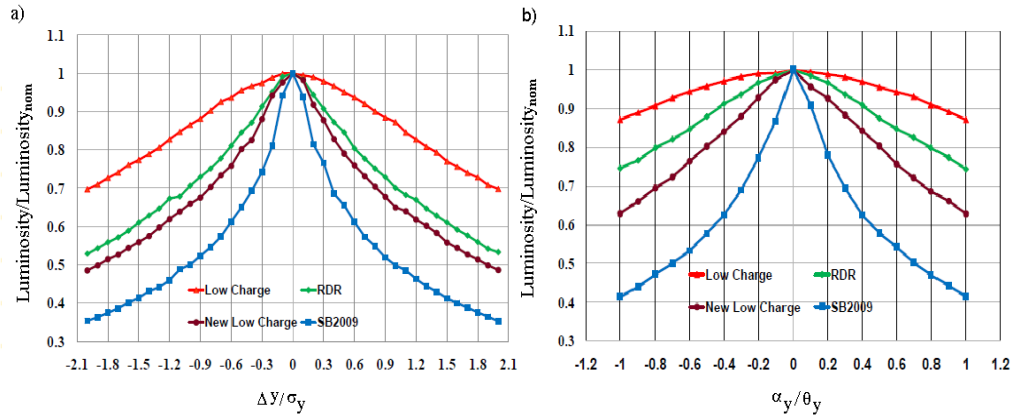

Figure 1: The ILC 500 GeV centre-of-mass energy parameter sets. Scans of effects of orbital a) and angular b) offsets on the normalized luminosity.

3 "Banana shape" bunches and the luminosity for the ILC.

3.1 "Banana shape " bunches.

In the presence of short range wakefields the originally gaussian bunches are distorted. This effect is often referred as "banana shape " bunches. Despite the relatively small change in the beam emittance the impact on the luminosity can be significant. For the TESLA lattice the effect of "banana shape" bunches was previously studied in [8] and for an emittance growth $\approx 6\%$ the relative luminosity loss is 30% even without any orbital or angular offsets was reported. This effect can be compensated by a very sophisticated feed-back system. A similar behavior can be confirmed explicitly by the orbital offset scans for the new parameter sets of the ILC and "banana shape" bunches.

In Figure 1 the sensitivity of the Gaussian beams to various orbital and angular offsets is demonstrated for 4 different parameter sets for the ILC. In all four cases the maximum luminosity is achieved at zero orbital and angular offset and the presence of any of such offsets can reduce the luminosity dramatically. In addition, for the Gaussian beam the maximum luminosity value corresponds to the minimum value of beam-beam vertical kick angle. Nevertheless this property does not hold for the distorted bunches. For the non-gaussian beams the maximum luminosity may occur at the non-zero value of orbital (or angular) offset. It is demonstrated in Fig.2 where the maximum attainable luminosity for "banana shaped" bunches of the SB2009 parameter set is achieved at $0.5\Delta y/\sigma_y$ fractional orbital offset and -16 $[\mu rad]$ vertical beam-beam kick angle. Finally, the non-Gaussian shape of bunches can significantly reduce the maximum attainable luminosity even in the absence of orbital offsets. In Fig.3

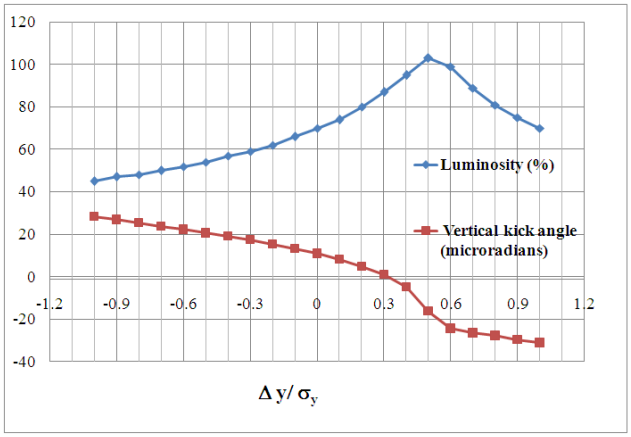

Figure 2: The SB2009 parameter set. Blue: The normalised luminosity for a non-Gaussian ("banana shaped" bunch with 1% vertical emittance growth as a function of the orbital offset. Red: The corresponding vertical kick angle to achieve the luminosity given in the blue curve.

the normalized luminosity is given as function of the vertical beam-beam kick angle for Gaussian and non-Gaussian "banana" beams for the SB2009 parameter set where the combination of two bunches with similar linear orbital tilt (+O/+O) results in $\approx 11\%$ of luminosity loss.

3.2 The emittance growth. Linearised model.

For the relativistic beam the square of the RMS emittance ϵ is given by the determinant of the covariance (σ) matrix as

$$\epsilon^2 = det\,\sigma = \langle y^2\rangle\langle y'^{\,2}\rangle - \langle yy'\rangle^2 \tag{3}$$

In the presence of additional orbital(Δy) and/or the angular ($\Delta y'$) kicks the beam vertical phase-space is changed according to

$$\begin{aligned} y &= y + \Delta y \\ y' &= y' + \Delta y' \end{aligned} \tag{4}$$

and the new perturbed emittance ϵ_{per} can be found as function of the beam Twiss parameters α, β,γ, the unperturbed emittance ϵ_0 and the kicks amplitudes Δy, $\Delta y'$. The relative emittance growth is given by

$$\frac{\Delta\epsilon}{\epsilon_0} = \frac{\epsilon_{per} - \epsilon_0}{\epsilon_0} \tag{5}$$

For the uncorrelated kicks and the small emittance growth $\Delta\epsilon/\epsilon_0 \ll 1$ the formula can be derived explicitly as in [9] (see also the Appendix). For example

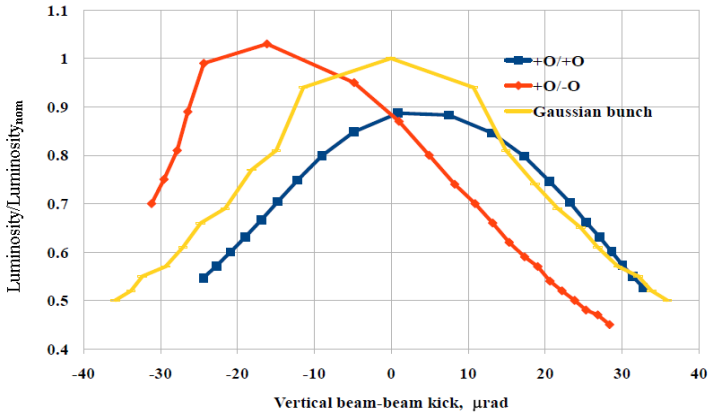

Figure 3: The SB2009 parameter set. The normalized luminosity as a function of vertical kick angle for Gaussian and banana shape bunches with 1% vertical emittance growth.

if only the angular kick $\Delta y'$ is present the relative emittance growth scales quadratically with the RMS angular kick

$$\frac{\Delta\epsilon}{\epsilon_0} = \frac{\beta_0}{2\epsilon_0}\langle\Delta y'^2\rangle \tag{6}$$

To study the the impact of "banana" shape on the luminosity the originally Gaussian bunch should be tracked through the linac and the Beam Delivery System (BDS) to the Interaction Point. In [10] it was done by using the orbit tracking codes such as PLACET and MatMerlin. Nevertheless for the quick estimation the distortion of the bunch shape can be introduced by applying the linear (y-z) tilt correlation to the gaussian bunch by "hand". Using the linearised version of spacial and angular kicks in form

$$y = y + k_1 z \qquad or \qquad y' = y' + k_2 z \tag{7}$$

and the assumptions that the kicks are uncorrelated, a bunch with the required emittance growth can be generated. The values of the coefficients k_1, k_2 for 1% of the relative emittance growth and different ILC parameter sets are given in Table 2. The details of derivation are presented in Appendix A1.

Table 2: The coefficients for the linearized model assuming 1% emittance growth

	RDR	SB2009	Low Charge	New Low Charge
$\lvert k_1\rvert$	2.6958x10^{-6}	1.7831x10^{-6}	3.3017x10^{-6}	1.5693x10^{10}
$\lvert k_2\rvert$ $[m^{-1}]$	6.7396x10^{-3}	8.9157 x10^{-3}	1.6509x10^{-2}	9.4535x10^{-3}

According to the results reported in [3], where 6% emittance growth was assumed, the relative loss of luminosity was found to be small and a scheme

of compensation via subsequent angular scans was suggested. For the current ILC setting the emittance growth due to the "banana" effect is expected approximately 1% or 2%. Nevertheless the new guineapig++ simulations using

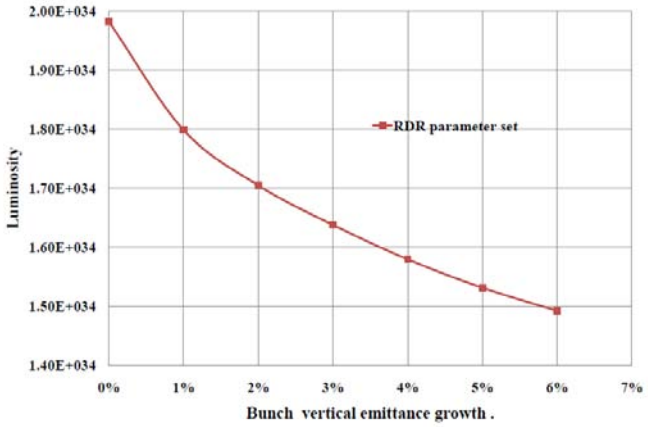

Figure 4: The loss of the nominal luminosity due to emittance growth for perfectly aligned bunches.

the linearised model of emittance growth suggest that for 1% of the emittance growth the luminosity loss can be as significant as 10% -15% even in the case of perfectly aligned bunches. In Fig.4 the luminosity for the RDR parameter set in the absence of any orbital or angular distortion is plotted as a function of the vertical emittance growth. It should be noted that the calculations in [3] coresond in fact to only 0.4% of emittance growth (and not 6%). This explains why the luminosity loss due to "banana" shape bunches was underestimated previously.

3.3 Luminosity scans for the banana shape bunches for the ILC

In Table 2 the absolute values of the coefficients k_1 and k_2 are given. In principle the electron and positron bunches can be tilted in both ways, thus there are 16 possible combinations of orbital($\pm$ O) and angular($\pm$ a) tilted for two interacting bunches.

In Fig.5a the results of orbital offset scans are given for 6 combinations of the orbital (y, z) and angular (y', z) correlations leading to 1% emittance growth for RDR parameters. The relative luminosity loss is plotted versus the normalized vertical orbital offsets. Surprisingly, the scheme of compensation suggested in [3] still works. The nominal luminosity value can be restored via subsequent angular scan as it seen in Fig.5b.

The results of orbital/angular scans for the travelling focus regime SB2009 are presented in Fig.6a/6b respectively. The polarisation loss due to "banana"

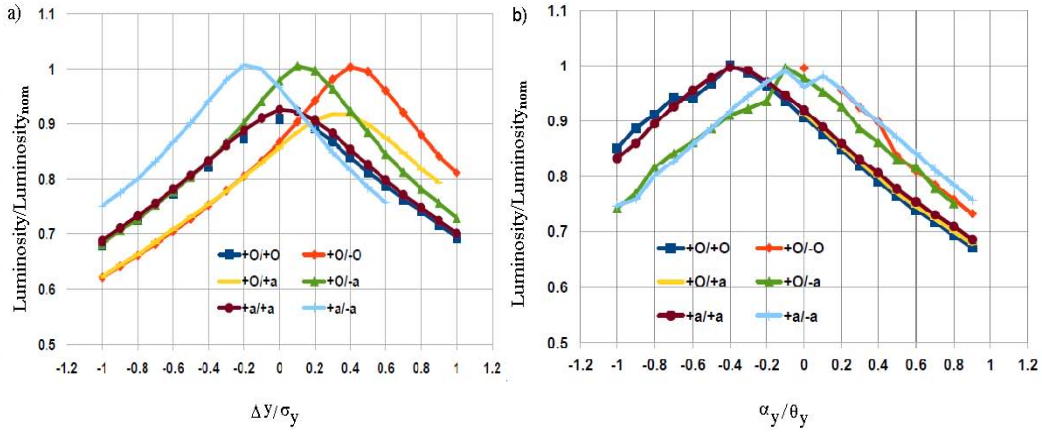

Figure 5: The RDR parameter set scans for different combinations of orbital (O) and angular (a) correlations leading to 1% of emittance growth.

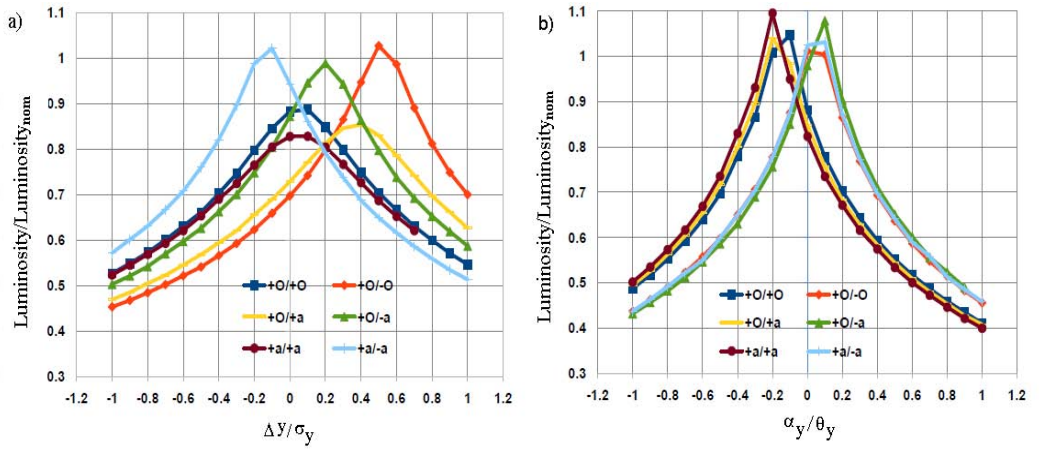

Figure 6: The SB2009 parameter set scans for different combinations of orbital (O) and angular (a) correlations leading to 1% of emittance growth.

shape bunches is even larger, but again can be compensated by angular scan. In Fig.7 the results for the Low Charge parameter set are given. Similar results were obtained for J.Gao set.

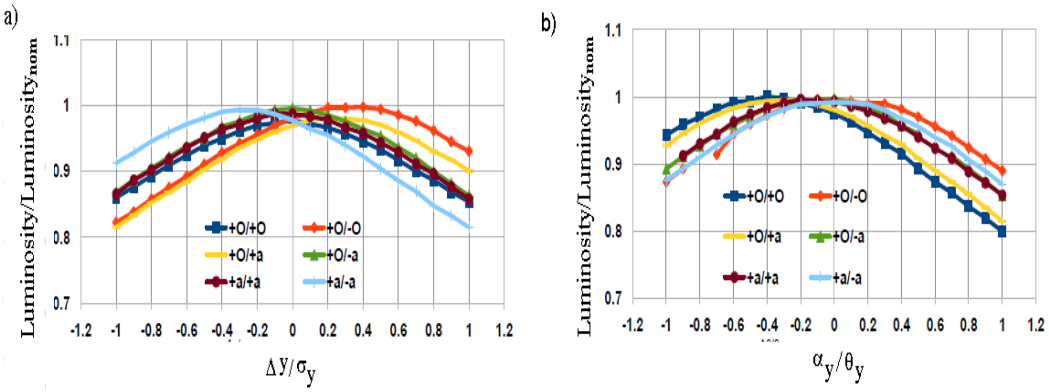

Figure 7: The Low Charge parameter set scans for different combinations of orbital (O) and angular (a) correlations leading to 1% of emittance growth.

4 CONCLUSIONS

The study of the new parameter sets confirms that the travelling focus regime is very promising but also very sensitive to the bunch-bunch orbital and angular offsets and requires elaborated feed-back system to deliver the required luminosity. It was also found that the "banana" effect may have significant impact on the luminosity. The results of guineapig++ simulations using a linear model make clear that more investigation should be done. An even more realistic representation of "banana" bunches will be obtained by using a simulation package such as Merlin [10], which can model the wakefields in the linac. Using such generated "banana" shape bunches, the luminosity and relative luminosity loss can be calculated by guineapig++.

5 ACKNOWLEDGMENT

The authors are grateful to all members of DESY Spin Management group for fruitful discussions and suggestions.

A The derivation of the coefficients for linearized model of emittance growth

Let's evaluate the relative emittance growth $\Delta\epsilon/\epsilon_0$ using the linearised version of orbital kicks in form

$$y = y + k_1 z \tag{8}$$

If the kicks are uncorrelated (i.e. $\langle y\, k_1 z\rangle = \langle y'\, k_1 z\rangle = 0$) the new perturbed emittance can be written as

$$\begin{aligned}\sigma &= \begin{pmatrix} \langle (y+k_1 z)^2\rangle & \langle (y+k_1 z)\, y'\rangle \\ \langle (y+k_1 z)\, y'\rangle & \langle y'^2\rangle \end{pmatrix} = \begin{pmatrix} \langle y^2\rangle + k_1^2\sigma_z^2 & \langle y\, y'\rangle \\ \langle y\, y'\rangle & \langle y'^2\rangle \end{pmatrix} \\ &= \begin{pmatrix} \epsilon_0\beta_0 + k_1^2\sigma_z^2 & -\alpha_0\,\epsilon_0 \\ -\alpha_0\,\epsilon_0 & \gamma_0\,\epsilon_0 \end{pmatrix} \end{aligned} \tag{9}$$

where the expressions for $\langle y^2\rangle = \epsilon_0\beta_0$, $\langle y'^2\rangle = \gamma_0\,\epsilon_0$ and $\langle y\, y'\rangle = -\alpha_0\,\epsilon_0$ has been used.
The perturbed emittance $\epsilon_{per}^2 = \det\sigma$, then from Eq. 9 follows that

$$\epsilon_{per}^2 = \epsilon_0^2 + \frac{k_1^2\,\sigma_z^2\,\epsilon_0}{\beta_0} \tag{10}$$

and

$$\frac{\epsilon_{per}}{\epsilon_0} = \sqrt{1 + \frac{k_1^2\,\sigma_z^2}{\beta_0\,\epsilon_0}} \approx 1 + \frac{k_1^2\,\sigma_z^2}{2\beta_0\,\epsilon_0} \tag{11}$$

The relative emittance growth is normally given in the percents and for small emittance growth

$$\frac{\Delta\epsilon}{\epsilon_0} = \frac{\epsilon_{per}-\epsilon_0}{\epsilon_0} = \frac{\epsilon_{per}}{\epsilon_0} - 1 = \frac{k_1^2\,\sigma_z^2}{2\beta_0\,\epsilon_0} \tag{12}$$

The values of $|k_1|$ could be found from Eq. 12 as

$$|k_1| = \sqrt{\frac{\Delta\epsilon}{\epsilon_0}\,\frac{2\epsilon_0\beta_0}{\sigma_z^2}} \tag{13}$$

In the similar way the expression can be obtained for the angular offset $\Delta y' = k_2 z$:

$$|k_2| = \sqrt{\frac{\Delta\epsilon}{\epsilon_0}\,\frac{2\epsilon_0}{\beta_0\sigma_z^2}} \tag{14}$$

The equations Eq. 13 and Eq. 14 allow to get the coefficients for different values of β_0 and σ_z and the required relative emittance growth, $\frac{\Delta\epsilon}{\epsilon_0}$.

References

[1] A. Seryi, Power saving optimization for linear collider interaction region parameters. SLAC-PUB-13767.

[2] V. Balakin, Travelling focus, LC-91, 1991. http://www.JACoW.org.

[3] I.-A. Melzer-Pellmann, Study of beam-beam effects with offset and angle scans, EUROTeV-Report-2007-021.

[4] ILC-Report-2007-001(2007); http://www.linearcollider.org/about/Publication/Reference-Design-Report.

[5] J. Gao, New low charge parameters for ILC, GDE Baseline Assessment Workshop (BAW-2), 2011

[6] G. Le Meur et al., Description of guineapig++, the C++ upgraded version of GUINEA-PIG beam-beam simulation program, EUROTeV-Report-2008-067

[7] D. Schulte, PhD thesis, University of Hamburg,1996, TESLA-97-08

[8] D. Schulte, Update on banana simulation, Nanobeams Workshop 2002

[9] P.Emma, Emittance growth mechanisms in linac based free-electron lasers, 32 Free Electron Laser Conference. http://fel2010.maxlab.lu.se/Programme/presentations/

[10] G.White, N. Walker, Multi-bunch simulations of the ILC for the luminosity performance studies, PAC'2005, Knoxville

[11] http://www.desy.de/ merlin/

Simulations of the ILC positron source with 120 GeV electron drive beam

A. Ushakov[1], *V. Kovalenko*[1], *G. Moortgat-Pick*[1,2], *S. Riemann*[2], *F. Staufenbiel*[2]

[1]II. Institute for Theoretical Physics, University of Hamburg, Germany
[2]DESY, Germany

DOI: will be assigned

The International Linear Collider (ILC) baseline design includes an undulator-based positron source. The accelerated electron beam will be used for the positron generation before it goes to the collision point. For the whole ILC energy range the source has to generate 1.5 positrons per electron. However, the efficiency of positron production goes down with decreasing electron drive beam energy. This effect can be compensated to some extend by the choice of undulator parameters and an optimized capture section. This simulation study considers, for the range of electron beam energies down to low values of 120 GeV, the feasibility of achieving the required positron yield. In particular, the optimum parameters for the undulator and capture section of the source at 120 GeV electron beam are presented.

1 INRODUCTION

The baseline design of the International Linear Collider (ILC) is focused on center-of-mass energies of 500 GeV and 350 GeV; operation at low energies and upgrade to energy of 1 TeV is foreseen. The undulator based positron source placed at the end of the main electron accelerator uses the main electron beam for the positron generation. The discovery of a Higgs boson with 126 GeV mass at the Large Hadron Collider suggests a staged approach in building the ILC. Starting with a Higgs factory at a center-of-mass energy of 250 GeV as first phase of the ILC project requires a proper working of the positron source. However, the efficiency of the undulator-based source goes down rapidly at lower drive beam energies. Therefore, in this work, the positron yield and polarization have been calculated for a 120 GeV electron beam and different settings of the undulator and positron capture system.

2 POSITRON GENERATION

The positrons are produced in a thin metal target by multi-MeV photons generated by the electron main linac beam in an helical undulator. The generated positrons are focused first in a flux concentrator (FC) and after that they are captured and accelerated in RF cavities. At energies 125 MeV the positrons are separated from the electrons and photons. The positron beam is accelerated further to 5 GeV and injected into the damping ring (DR).

To simulate the positron production and capture, the Geant4-based code named PPS-Sim has been used [1]. The simplified models of all source parts up to 125 MeV point have been implemented in PPS-Sim. The DR acceptance is emulated at 125 MeV as a series of cuts: the sum of x and y normalized emittances $\epsilon_{nx} + \epsilon_{ny} < 0.07$ rad m; the energy spread is less ± 37.5 MeV; the longitudinal bunch size Δz is less 34 mm. According to the ILC requirements [2], the source should have 50% safety margin. That means the source has to deliver to the DR 1.5 positrons per electron going through the undulator.

Due to relatively low conversion efficiency of photons into e^+e^- pairs (below one percent at low drive beam energy), the undulator has to be long enough. ILC design reserves a space for 231 meters of active undulator (magnet) length. The total length of the undulator lattice is about 320 meters. The space between the end of the undulator and the target is 412 meters. The period of undulator is 11.5 mm and the highest K value is 0.92. The prototype of undulator module has been developed and tested at Daresbury [3].

The efficiency of e^+ generation in Ti6Al4V target of different thicknesses is shown in Fig. 1 for a 120 GeV electron beam and an undulator K value of 0.92. The positron yield after the target, normalized per electron going through the undulator, is shown in Fig. 1 by the blue curve. The yield reaches a maximum value of 5.6 e^+/e^- at the target thickness of 14 mm. This thickness is equal to 0.4 radiation length. Though the yield after the target is much higher than 1.5, the quality of positron beam (high divergence angles and big emittance) results in significant positron losses on the way to the DR. The green curve in Fig. 1 shows the yield after the target that fits into the DR emittance acceptance.

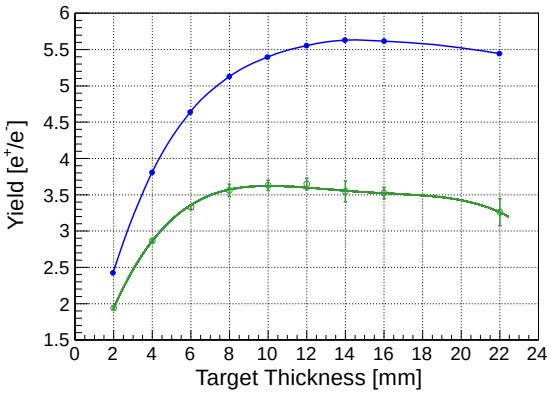

Figure 1: Yield after target without any cuts (blue curve) and with DR emittance acceptance cut (green curve) versus thickness of target. $E_{e^-} = 120\,\text{GeV}$, 231 m undulator with $K = 0.92$ and 11.5 mm period.

Figure 2 shows the yield at 125 MeV point with all DR acceptance parameters (emittance, energy spread and longitudinal bunch size Δz) taken into account . To see impact of Δz cut on the yield, two different Δz cuts (34 mm and 9.6 mm) were applied. The tighter 9.6 mm cut was selected due to historical reasons. Some of our previous simulations were done with a bunch length cut that is equivalent to the electric field phase of ± 7.5 degree at 1.3 GHz.

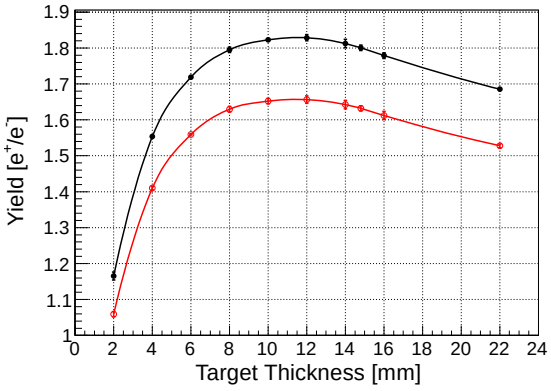

Figure 2: Yield at 125 MeV vs target thickness for 34 mm bunch length cut (black curve) and 9.6 mm (red curve).

The comparison of the yield values in Fig. 1 and Fig. 2 indicates that the positron losses between the target and DR is about 70%. The complete optimization of positron capture and transport system is out of scope of this paper but some of the characteristic tendencies will be shown in the next sections.

3 POSITRON CAPTURE

For positron capture after the target, a pulsed flux concentrator (FC) was chosen as a magnetic focusing device of the ILC source. The ideal field inside the FC along the symmetry axis z is described by the following function: $B(z) = B_0/(1 + g\,z)$, where B_0 is the initial (highest) field close to the entry face of the FC and g is the taper parameter.

The variation of g for the fixed fields at start and end of the FC requires adjusting of the FC length. The impact of the taper parameter on the positron yield is relatively small, as shown in Fig. 3 for g values between 0.03 and 0.075 mm^{-1} and a B field changed from 3.2 T to 0.5 T.

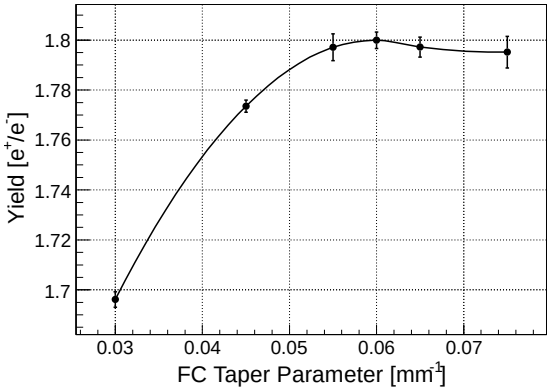

Figure 3: Yield vs taper parameter of flux concentrator.

The yield dependence on the initial field B_0 for $g = 0.06$ mm^{-1} (9 cm length of FC) is shown in Fig. 4. This figure and all other figures below includes simulation results for two bunch length cuts (34 mm shown in black and 9.6 mm shown in red). The current development of the FC in LLNL [4] having a maximal field of 3.2 T will perfectly fit to the source operation at 120 GeV.

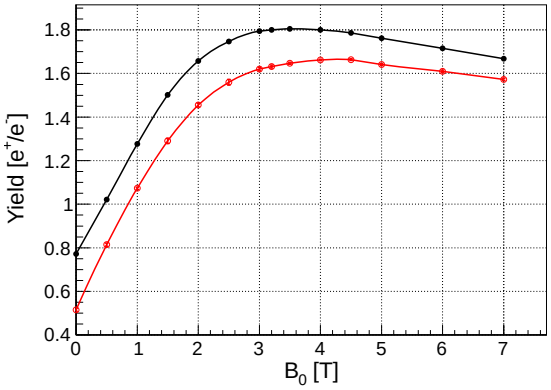

Figure 4: Yield vs initial field of flux concentrator.

The reduction of the electron beam energy increases the photon spot size on the target. For the case of using the full available length of the undulator with highest K (0.92) and 120 GeV e$^-$ beam, the average radius of photons is about 5 mm. Therefore, the proper choice of the aperture size of the FC ($R_{\rm FC}$) becomes important. Figure 5 shows the yield versus different $R_{\rm FC}$. A significant fraction of positrons will be absorbed in the FC with radii less than 8.5 mm. The small aperture reduces the source efficiency and increases the heat load in the FC.

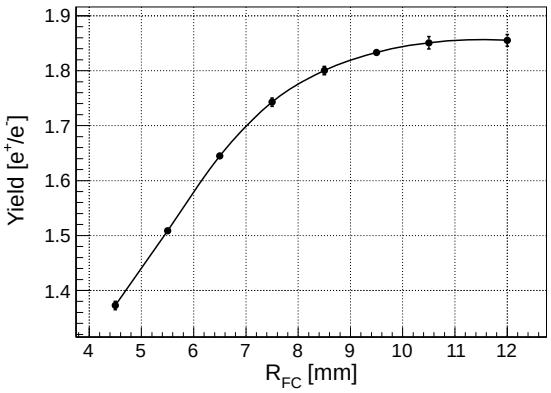

Figure 5: Yield vs initial (entry) aperture radius of FC. $E_{e^-} = 120\,\text{GeV}$, $K = 0.92$, $B_0 = 3.2$ T.

4 POSITRON POLARIZATION

The polarization of a source without photon collimator can be increased by a reduction of the undulator field. For a source with a fixed undulator length, the efficiency of photon generation is smaller in the case of using a lower-field (lower-K) undulators. For example, the reduction of K from 0.92 to 0.76 results in a reduction of the undulator photon yield from 1.95 to 1.39 positrons per electron and meter of undulator. The higher cut-off energy of the first harmonic E_1 (for example, $E_1 = 6.44$ MeV for $K = 0.92$ and $E_1 = 7.54$ MeV for $K = 0.76$) can not compensate the reduction of photon yield. The positron yield dependence on K is in Fig. 6 (left plot) for two different longitudinal bunch length cuts 34 mm (black curve) and 9.6 mm (red curve). The positron polarization is about 31% at 1.5 e^+/e^- yield, see the right plot in Fig. 6.

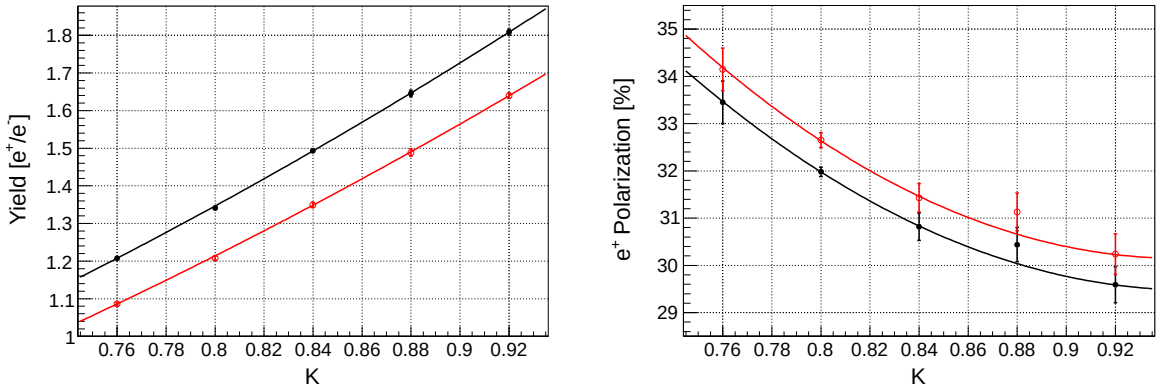

Figure 6: Positron yield (left) and polarization (right) vs undulator K value.

Another more efficient way to increase the polarization of positrons is to apply a photon collimator upstream the target. The e^+ yield and polarization for different aperture radii of collimator R_{col} are shown in Fig. 7. The highest e^+ polarization at 120 GeV is approx. 40% with 3.5 mm radius of the collimator and an undulator K of 0.92. The polarization without collimator is about 30%.

5 SUMMARY

At 120 GeV electron drive beam energy, the positron source based on a 231 m helical undulator with 11.5 mm period and a K value of 0.92 generates 5.6 e^+/e^- in a $0.4X_0$ thick Ti6Al4V target. The choice of a pulsed flux concentrator with 3.2 Tesla peak field on axis and a radius of entry aperture increased to 8.5 mm provides the required 1.5 e^+/e^- at the end of the positron source. The highest polarization without photon

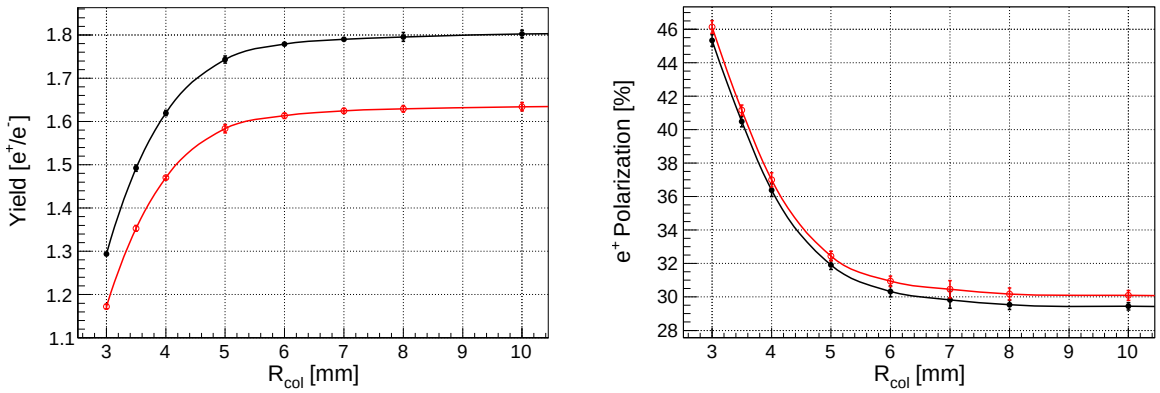

Figure 7: Positron yield (left) and polarization (right) vs aperture radius of photon collimator.

collimator between the undulator and target is 31% at slightly reduced undulator K value of 0.84. To get 40% polarization a photon collimator with 3.5 mm radius is needed.

References

[1] A. Ushakov, S. Riemann, and A. Schälicke, "Positron source simulations using Geant4", IPAC'10, Kyoto, Japan, 23-28 May 2010, THPEC023, p. 4095-4097.

[2] ILC Positron Source Parameters, ILC Document, EDMS D*0943695, `http://ilc-edmsdirect.desy.de/ilc-edmsdirect/item.jsp?edmsid=D00000000943695`

[3] E. Baynham *et al.*, "The development of a superconducting undulator for the ILC positron source", PAC09, 4-8 May 2009, Vancouver, Canada, 1839-1843.

[4] J. Gronberg *et al.*, LCWS 2012, University of Texas at Arlington, USA, 22-26 October 2012, `http://ilcagenda.linearcollider.org/getFile.py/access?contribId=216&sessionId=21&resId=0&materialId=slides&confId=5468`

Positron Source Simulations for ILC 1 TeV Upgrade*

Andriy Ushakov†, Gudrid Moortgat-Pick, *University of Hamburg, Germany*
Sabine Riemann, *DESY, Zeuthen, Germany*
Wanming Liu, Wei Gai, *Argonne National Laboratory, USA*

Abstract

The generation and capture of polarized positrons at a source with a superconducting helical undulator having 4.3 cm period and 500 GeV electron drive beam have been simulated. The positron polarization has been calculated for the different undulator K values (up to $K = 2.5$). Without applying a photon collimator, the maximal polarization of positrons is about 25% for 231 meters active magnet length of undulator with $K = 0.7$. Using an undulator with $K = 2.5$ and a collimator with an aperture radius of 0.9 mm results in increase of positron polarization to 54%. The energy deposition, temperature rise and stress induced by high intense photon beam in the rotated titanium-alloy target have been estimated. The maximal thermal stress in the target is about 224 MPa for the source with photon collimation to achieve a positron polarization of 54%.

1 Introduction

The current design for the future International Linear Collider (ILC) includes a positron source based on a superconducting helical undulator which is placed at the end of main linear accelerator. Due to the helical undulator the generated photons are circularly polarized and created positrons are longitudinally polarized. The degree of polarization is determined by the undulator and electron beam parameters.

A prototype of a helical undulator for the ILC positron source has been developed and tested at Daresbury [1]. According to the ILC requirements [2], the yield of the source should have 50% safety margin in a wide energy range of drive beam energy (between 100 GeV and 250 GeV). That means the positron yield at the injection point into the Dumping Ring (DR) has to be 1.5 positrons per electron going through the undulator. A center-of-mass energy of 1 TeV is considered as upgrade option.

Figure 1 shows the positron yield depending on the electron beam (drive) energy for a source with a fixed undulator length of $L = 231$ m, an undulator period $\lambda = 11.5$ mm and $K = 0.92$. The source with these undulator parameters (RDR undulator) can generate much more positrons than required, therefore, there are two ways to keep the yield at 1.5 e^+/e^-, either to reduce the undulator length by switching-off unnecessary modules (see the right plot in Fig. 1) or to reduce the magnetic field of the undulator.

*Work supported by the German Federal Ministry of Education and Research, Joint Research Project R&D Accelerator "Spin Optimization", contract number 19XL7IC4

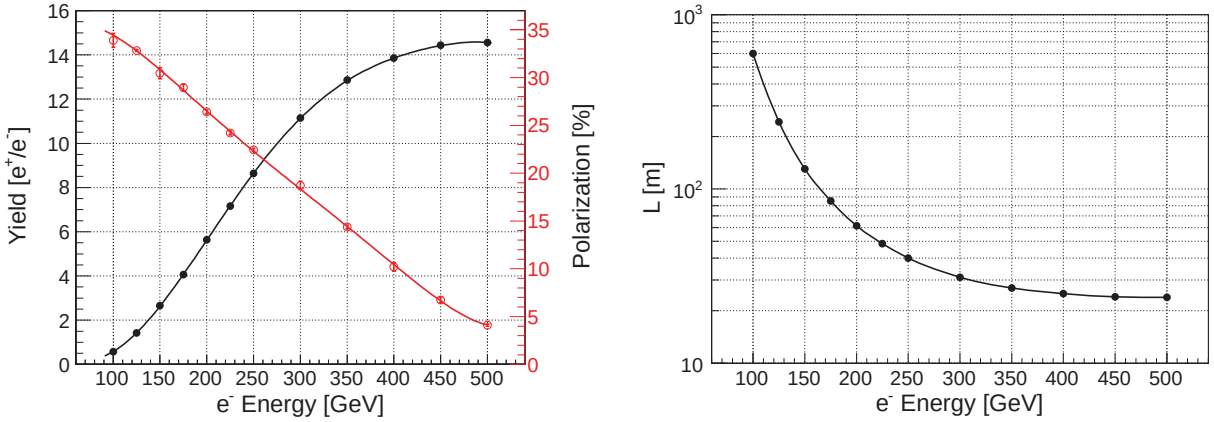

Figure 1: Positron yield and polarization of the positron source with 231 m RDR undulator and 3.2 Tesla peak field of pulsed flux concentrator (left) and undulator length required for a yield of 1.5 e^+/e^- (right).

The source parameters, especially the target thickness and positron capture optics, have been optimized for getting maximal positron yield for a 250 GeV drive beam: the titanium alloy (Ti6Al4V) target has a thickness of 0.4 radiation length; the 12 cm long pulsed flux concentrator has 3.2 Tesla maximal field. These parameters have been kept in all our calculations presented in this report. The simulations have been performed by a Geant4-based tool that was specially developed for Polarized Positron Source Simulations (PPS-Sim) [3]. Figure 2 shows the capture efficiency of the source with RDR undulator. The capture efficiency is the ratio of the number of positrons at the end of the source (the positron beam has to fit DR acceptance) to the number of positrons after the target. The maximum of capture efficiency is about 27% at 250 GeV. For a 500 GeV e^- beam the capture efficiency is falling down to 21%.

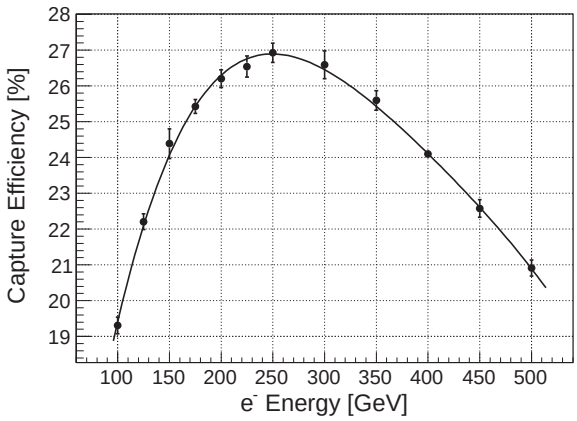

Figure 2: Capture efficiency of the source with RDR undulator and 3.2 Tesla peak field of pulsed flux concentrator.

Figure 1 shows the dependence of polarization on the e^- energy (see the red curve on the left plot). The higher e^- energy results in lower polarization. 5% polarization at 500 GeV is too low to get any advantages for physics of using such low polarized positron beams.

The opening angle of undulator radiation (as well as the radius of photon spot size on

results in four times higher energy deposition density in a stationary target. With lower K values higher polarization can be achieved. However, lowering the undulator B field will additionally reduce the photon spot size. Therefore, for the 1 TeV upgrade of the ILC, another undulator with higher period has been proposed in [4].

In this report, the maximum achievable polarization of a positron source using a 4.3 cm period undulator and configurations with and without photon collimator has been estimated. The energy deposition and thermal stress in the target has been simulated.

2 Yield and Polarization of a Source with 4.3 cm Period Undulator

The e^+ yield and polarization of a source at 500 GeV e^- and with different undulator periods have been estimated earlier (see Ref. [4]). In this report, the dependence on the undulator K value will be analyzed for the selected 4.3 cm undulator period.

In PPS-Sim, the implementation of undulator radiation is based on Kincaid's model [5]. The efficiency of photon generation in the undulator having different K values is shown in Fig. 3 (left plot). The photon yield has been normalized per electron and meter of undulator. The photon energy cut-off of the 1st harmonic and the average photon energy are also shown in Fig. 3 (right plot).

An undulator with higher K value yields lower energy of the fundamental harmonic but larger contribution of higher harmonics. As result the average energy over the whole photon spectrum is growing with increasing field of undulator.

Both tendencies (yield and average energy versus K) indicate that an electron beam passing an undulator with higher K generates a positron beam with higher current.

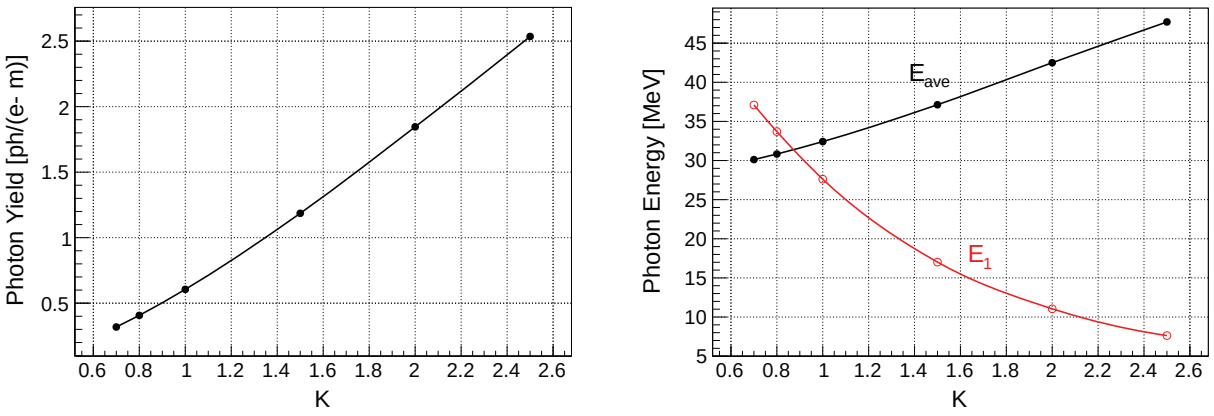

Figure 3: Photon yield (left) and energy of photons (right) vs undulator K-value. E_{ave} is the average photon energy and E_1 is the energy cutoff of the 1^{st} harmonic.

The impact of the undulator field on the e^+ polarization is shown in Fig. 4. In these simulations we suppose that the magnet length of an undulator cryomodule is 11 meters and the drift space between the end of the undulator and the target is 412 meters. If not all modules are necessary upstream modules are switched off.

Table 1 summarizes the required number of active undulator modules and the e^+ yield. Figure 5 shows the average photon beam power of the source. The increase of required

(Fig. 5, right plot) and a higher energy of photons resulting in a higher energy spread of the positron beam. This makes the e^+ capture more difficult.

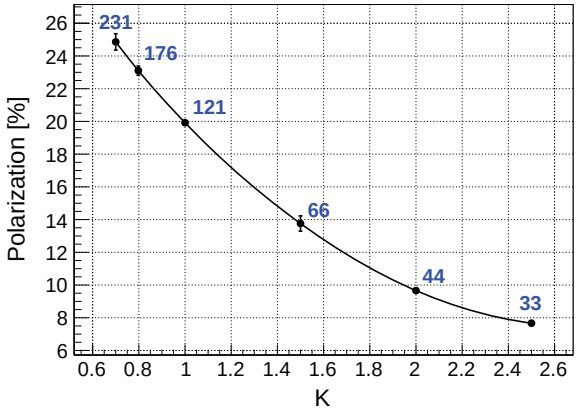

Figure 4: Positron polarization vs K for a source without collimator and with FC having 3.2 T peak field on beam axis. The blue numbers indicate the required undulator length.

Table 1: Required number of active undulator modules and e^+ yield vs K for a source without collimator.

K	# Modules	e^+ Yield [e^+/e^-]
0.7	21	1.564
0.8	16	1.500
1.0	11	1.521
1.5	6	1.586
2.0	4	1.655
2.5	3	1.688

As it could be seen in Fig. 4, the maximal polarization of a source without photon collimator is 25% for 231 meter undulator with $K = 0.7$. One possibility to get the polarization above 25% is a further reduction of the undulator field. In this case the undulator has to be longer then 231 meters. If such elongation of the undulator is not possible or not desired, the capture system must be improved to increase the polarization.

For instance, a flux concentrator with higher field improves both yield and polarization. Figure 6 shows the dependencies of positron yield and polarization on the peak field of a 12 cm long FC with a taper parameter of 0.035 mm^{-1}.

The efficiency of positron generation is growing fast for stronger undulator fields. Figure 4 shows that even for the moderate 3.2 T peak field of FC, the source needs 121 meters undulator with strength $K = 1$; such choice of source parameters results in 20% positron polarization. Only three undulator modules (33 meters of total active undulator length) are needed to get the required intensity of the positron beam at $K = 2.5$. Hence, there is a big reserve in undulator length in case of using a high K undulator. One possible way to increase the polarization is applying photon collimator [6]. The absorption of photons in the collimator and the reduction of the e^+ yield can be compensated by lengthening the undulator.

Figure 7 summarizes the dependence of maximal achievable positron polarization on

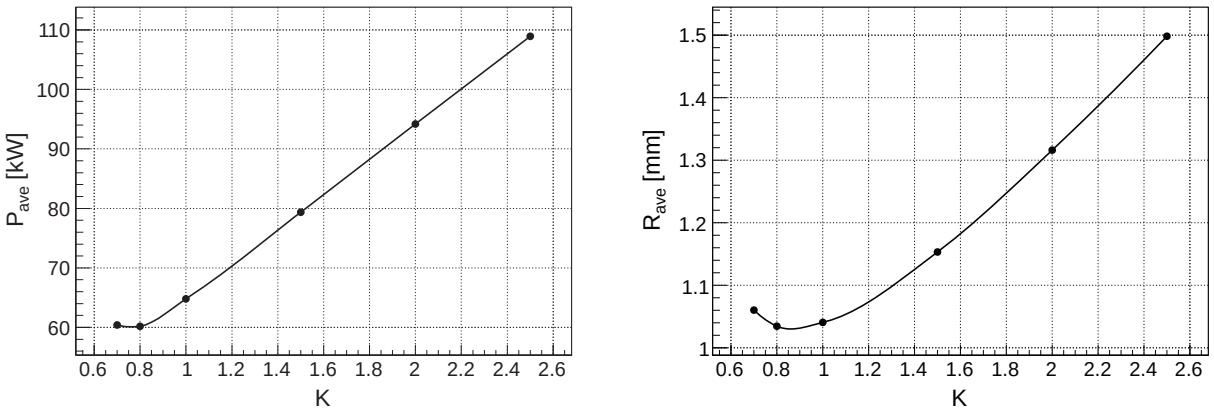

Figure 5: Average power (left) and radius (right) of photon beam on the target.

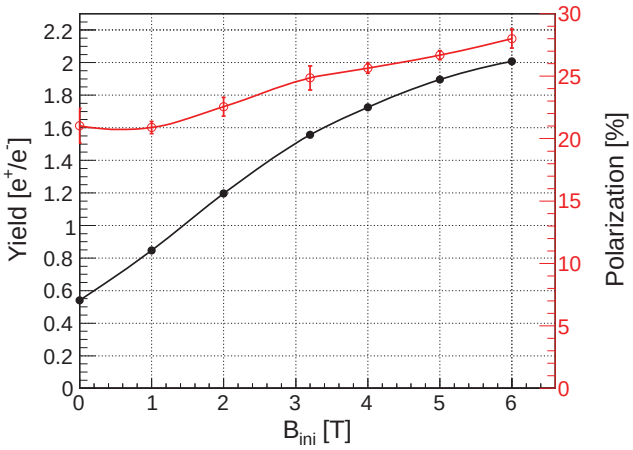

Figure 6: Positron yield and polarization of a source with 231 m undulator and a flux concentrator with different peak fields at the entrance of FC (B_{ini}). FC length is 12 cm, FC taper parameter is 0.035 mm^{-1}.

photon collimators and the required (for 1.5 e^+/e^-) undulator lengths are shown as red and blue numbers respectively. 54% polarization can be reached with a photon collimator having 0.9 mm aperture radius and $K = 2.5$. The source with $K = 1$ requires a lower collimator aperture ($r = 0.7$ mm) and the e^+ polarization is about 41%.

3 Deposited Energy, Temperature Rise and Thermal Stess in Target

To get 54% polarization while keeping the yield at 1.5 e^+/e^- for a source with $K = 2.5$, the undulator length has to be increased from 33 meters (Fig. 4) to 176 meters (Fig. 7). In spite of the major part of photon power will be absorbed in collimator, and the peak energy deposition in the target will be increased significantly. Therefore, the heat load and the thermal stress induced in the target have to be studied thoroughly. First, the energy deposition in the target has been calculated in FLUKA for a single bunch (see left plot in Fig. 8). In this figure, the density of deposited energy is shown as a function of the transverse (to the beam direction) coordinate x. In the second step, the target rotation

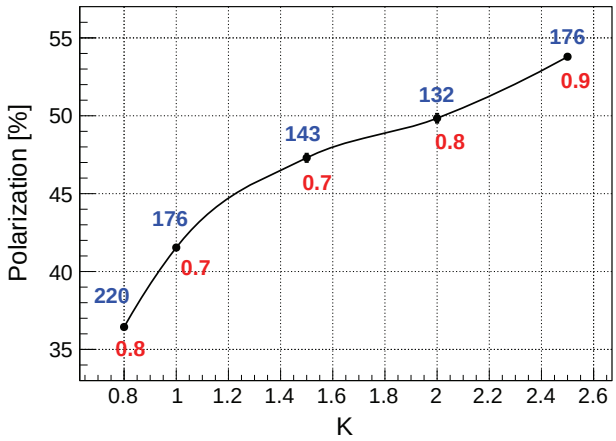

Figure 7: Positron polarization vs K for a source with collimator. The red numbers indicate the aperture radius of collimator and the blue numbers show the required undulator length.

rotation has been simulated by the motion in x-direction only: the distribution shown in Fig. 8 (left) has been shifted in x-direction after every bunch. The right plot in Fig. 8 shows the resulting profile of deposited energy along x-axis for 366 ns bunch separation. The energy density in the moving target saturates after few hundred bunches at the level of about 1.2 GeV per cm^3. The ratio of maxima in right and left plots shown in Fig. 8 defines the "bunch overlapping factor" for the rotated target.

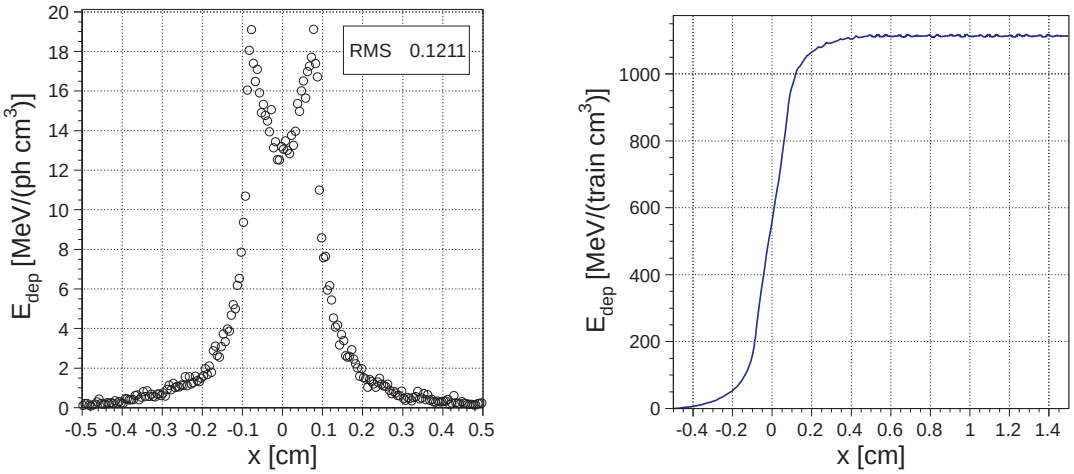

Figure 8: Deposited energy in the target after an one bunch (left) and after one pulse (right). Rotation of the target has been modelled as a motion in x-direction and the speed $v = 100$ m/s. The undulator has a period $\lambda = 4.3$ cm and $K = 2.5$. The collimator has an aperture $R_c = 0.9$ mm.

The three dimensional spatial energy distribution deposited by one bunch scaled by the number of photons per bunch and multiplied by the bunch overlapping factor has been imported in ANSYS [8]. The temperature map after a bunch train is shown in Fig. 9 (left). The maximal rise of temperature after one pulse is about 125°C.

The fast increase of target temperature induces thermal stress. The stress distribution in the target shortly after the bunch train passed (82 ns delay) is shown in Fig. 9 (right).

tensile yield stress, and it is about 44% of the fatigue stress of untouched Ti6Al4V target material (grade 5, annealed) at 10^7 cycles. The material properties of titanium alloy were taken from matweb.com database [9]. Such stress values (without taking into account the stress due to centrifugal forces of rotating wheel and without accumulating/superposition effects of multiple pulses) can be considered as safe. The region with highest stress is located on the beam axis and close to the back side of target.

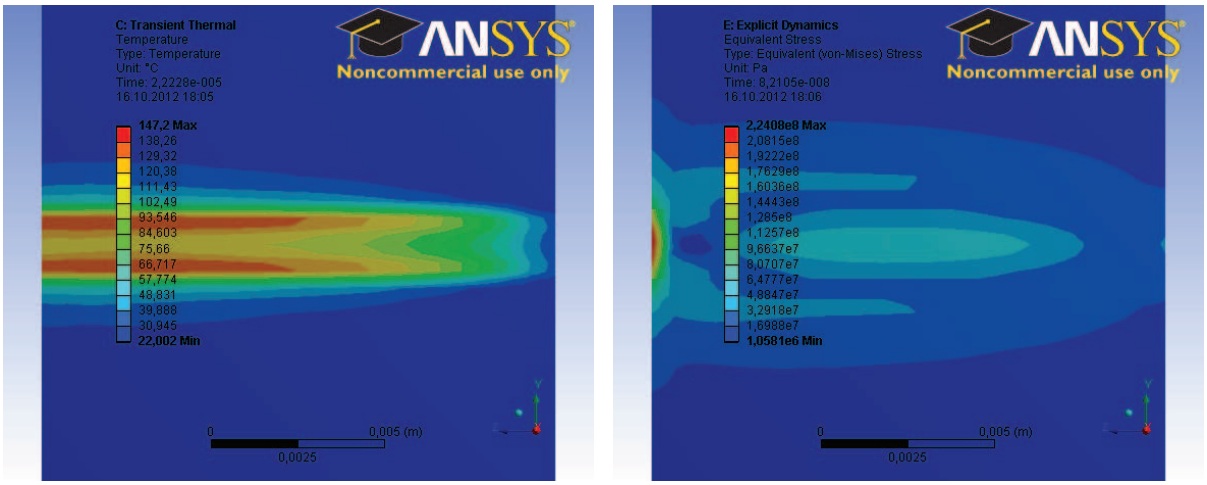

Figure 9: Maximal temperature after first pulse (left) and equivalent von-Mises stress in the rotated target shortly after the pulse has passed the target (right). Undulator period $\lambda = 4.3$ cm, $K = 2.5$; collimator aperture $R_c = 0.9$ mm; target rotation speed $v = 100$ m/s.

4 Summary

The simulations of a positron source with a helical undulator, 4.3 cm period, using a 500 GeV electron beam show that a positron beam with 25% polarization can be generated without photon collimator; only the magnetic field of the undulator has to be reduced ($K = 0.7$). The required undulator length is 231 m. The polarization can be increased up to 54% by applying an undulator with $K = 2.5$ and a collimator with 0.9 mm aperture. However, the energy deposited in target and the induced stress are high. So, the maximal thermal stress in the target is increased up to 224 MPa shortly after the photon pulse left the target. It does not destroy the target. To be sure that the target withstands the heat load and mechanical stress during a long time source operation, the model used in ANSYS simulations has to be extended: the centrifugal forces of rotating wheel has to be added and the accumulating/superposition effects of multiple pulses have to be studied too. In addition, a method has to be found to evaluate the fatigue stress and the consequences for the target and collimator material.

References

[1] E. Baynham *et al.*, "The development of a superconducting undulator for the ILC positron source", in Proceedings of the 23st Particle Accelerator Conference, 4-8

[2] ILC Positron Source Parameters, ILC Document, EDMS D*0943695, http://ilc-edmsdirect.desy.de/ilc-edmsdirect/item.jsp?edmsid=D00000000943695

[3] A. Ushakov, S. Riemann, and A. Schälicke, "Positron Source Simulations Using Geant4", IPAC'10, Kyoto, Japan, May 2010, THPEC023, p. 4095-4097.

[4] Wanming Liu *et al.*, "On the ILC positron source TeV upgrade option", ILC Document, EDMS D*1007715, http://ilc-edmsdirect.desy.de/ilc-edmsdirect/item.jsp?edmsid=D00000001007715

[5] B.M. Kincaid, "A short-period helical wiggler as an improved source of synchrotron radiation", J. Appl. Phys. **48** (1977) 2684-2691.

[6] A. Ushakov *et al.*, "Production of highly polarized positron beams", in Proceedings of the 2nd International Particle Accelerator Conference, San Sebastian, Spain, 4-9 September 2011, 997-999.

[7] A. Fassò *et al.*, "FLUKA: a multi-particle transport code", CERN-2005-10 (2005), INFN/TC-05/11, SLAC-R-773.

[8] *ANSYS*, http://www.ansys.com

[9] Aerospace Specification Metals, Inc., Titanium Ti6Al4V Annealed (Grade 5), http://asm.matweb.com/search/SpecificMaterial.asp?bassnum=MTP641

THE SPIN-ROTATOR WITH A POSSIBILITY OF HELICITY SWITCHING FOR POLARIZED POSITRON AT THE ILC*

L.I. Malysheva†, O.S. Adeyemi, V. Kovalenko, G.A. Moortgat-Pick,
A. Ushakov, Hamburg University, Hamburg, Germany
S. Riemann, F. Staufenbiel, DESY, Zeuthen, Germany
A. Hartin, B. List, N.J. Walker, DESY, Hamburg, Germany

April 18, 2013

Abstract

Polarized beams are essential for revealing a full potential of the ILC [1]. The electron and positron beams produced at the source are longitudinally polarized. The results of spin transport study for the ILC [2] suggest that only the vertical component of spin will survive in the damping ring without polarization loss. In order to manipulate polarized beams and to preserve the degree of polarization during beam transport spin rotators are included in the current ILC lattice. Recent update of parameters for the ILC central region provides extra space for a new design of pre-damping ring spin rotator section which is presented below. It consists of two parallel sections for spin rotation with opposite polarities, i.e. setting the spin parallel or antiparallel to the field in the damping ring. The advantage of this new design is in the possibility of quick and random switching between two helicities for the positrons.

1 INTRODUCTION

Polarized beams play important role on the experiment. For example, for the ILC scenario the effective luminosity can be increased by approximately 50% in the case of both beams polarized [1]. Furthermore a suitable combinations of polarized electron and positron beams suppress significantly unwanted background processes and enhance signal rates. While the electron polarization can be switched at the source by switching the polarity of the laser beam, the polarization of the positron beam depends on helicity of the undulator and cannot

*Work supported by the German Federal Ministry of education and research, Joint Research project R&D Accelerator "Spin Management", contract N 05H10CUE

†larisa.malysheva@desy.de

be switched at the source. Some dedicated helicity flipper for positron beam is required. The "traditional design" version of spin rotator, based on dipole and solenoidal fields, are well established. For the basic theory see the Appendix where these two "classical design" are explained in more details. A few spin rotator designs suggested previously for the ILC can be found in [3, 4]. The disadvantage of all these design is that they cannot provide a fast helicity reversal in the time scale desirable for the ILC, i.e. from train to train. The concept of the spin flipper combined with fast switching between 2 polarities was considered in "general" in [5], but no detailed lattice design was produced. For the RDR parameter set spin flipper design was investigated in [6]. It is based on single pre-damping ring spin rotator followed by a combination of two post-damping ring rotators. In theory, by clever manipulation of latter, any direction of polarization at the IP can be achieved. Nevertheless the manipulation of post-damping ring beams is complicated as the emittance preservation constraints should be fulfilled. The TDR changes in the layout of the Central Region of the ILC design allows spin rotation with quick switch between two helicities be done before DR. Fig. 2 gives a possible configuration of the pre-damping ring spin rotator with two parallel beam lines for the spin rotator similar to the one presented in [5].

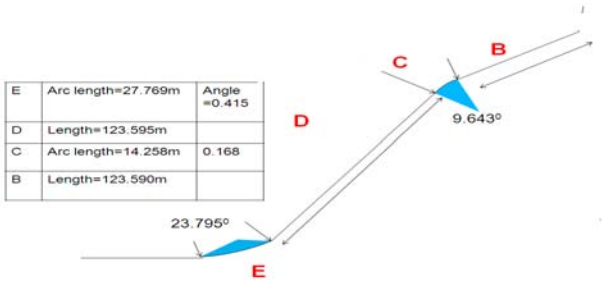

Figure 1: Schematic layout of new PLTR section

2 THE SPIN FLIPPER-ROTATOR FOR THE ILC

2.1 The ILC Pre-damping Rind Spin Rotator Requirements and Constraints

Following the recent update of parameters for the ILC central region the possibility of fast helicity switching for the positron beam was considered and a some extra space in PLTR (the Positron Linac To Damping Ring) was allocated to it. The schematic layout of the new PLTR is given in Fig. 1. In section E the spin rotation from longitudinal to the horizontal direction is done by means of horizontally bending dipoles with the total orbital rotation angle

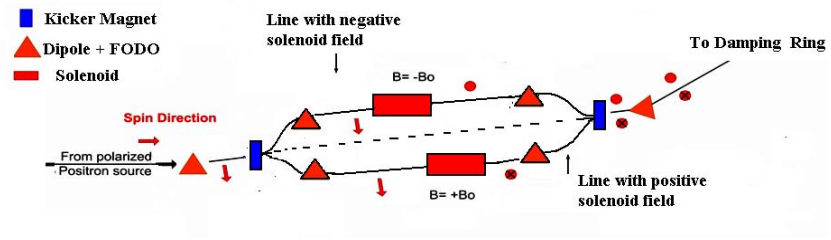

Figure 2: The schematic layout of positron transport to Damping Ring with a two parallel lines spin rotator section.

of $23.795^0 = 3 \times 7.929^0$ which corresponds to the 3π spin rotation around the bending dipole field direction for 5 GeV. The energy compression in section D matches the beam energy spread to the DR acceptance. Previously spin was rotated in section D by solenoid spin rotator from transverse to the vertical direction. The length of new section D was increased from 37.9m to 123.595m. This particular change allows to insert also a splitter for the fast spin flip. Section C and B don't affect the spin direction, as it is already parallel/antiparallel to the field direction of horizontal bending magnets in arc C and in DR.

Fig. 2 gives a possible configuration of the pre-damping ring spin rotator with two parallel beam lines for the spin rotator similar to the one presented in [5]. The new spin rotator section consists of two parallel spin rotation lines with a solenoidal field of opposite polarity placed symmetrically with respect to design orbit. Each branch consists of a first order achromat FODO dogleg section, a solenoid section and another dogleg to recombine the line back to the design orbit. The achromat design assures that no dispersion suppressors will be required. The pre-damping ring position of the spin- rotator makes the emittance preservation constrains less severe. Thus, the simple solenoid rotator design, similar to the one used in [6] was applied.

2.2 Symmetric Design

The spin-rotator design is based on the concept of branch splitter/merger used for the post-damping ring positron lines [7] with some modifications: only horizontal bends are used, the length of the splitter section is shortened to approximately 26 m in order to fit the available space, 2m of two horizontal branches separation was taken. The shortening of the section is achieved by using stronger bending magnets as the emittance preservation requirements for the pre-damping ring section are less challenging.

The section consists of the first irregular FODO-like cell with pulsed kicker and a combined function defocusing/bending magnet, followed by 4 regular FODO cells with 120^0 phase advance forming together an achromat dogleg, a solenoid matching section and a 8.32 m long solenoid with an integrated field of 26.18 $[T \cdot m]$. In the solenoid $\beta_x = \beta_y$ and are reaching the minimum in the

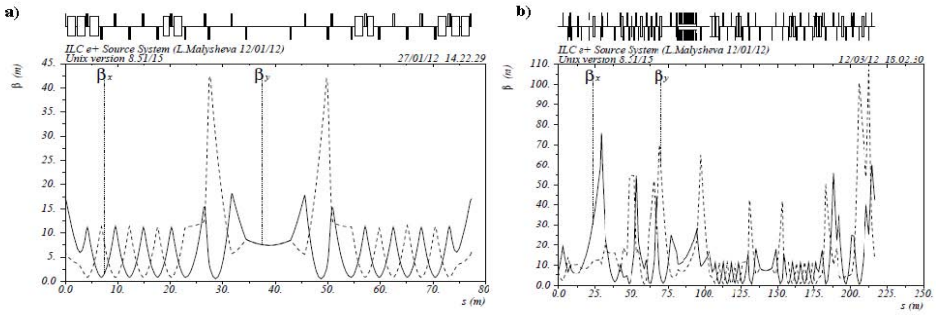

Figure 3: a) Spin rotator branch matched by MAD8. b) Complete PLTR section including one of spin rotator branch matched by MAD8.

middle of the solenoid. The rest of the section is a mirror image of the first part with respect to the middle of solenoid. The second branch of the lattice is obtained by switching the sign of the kick in the pulsed kicker and the bending angles in the following dogleg. The section was optimized by MAD8 package [8] to meet the constraints on the length. Then this spin-rotator part of section D was matched to the PLTR lattice developed by W. Liu [9] thus including two extra matching sections. In Fig. 3 the results of the optics is given for one branch of such spin rotator.

Similar results were obtained for the 5m long super-conducting solenoid with a field of 5.24 $[T \cdot m]$. These matching results were cross-checked by ELEGANT [10] code. Spin tracking with BMAD [11] were done by Kovalenko [12].

2.3 Asymmetric Design

In order to save some transverse space the original design was adjusted in such a way that two solenoid sections in the opposite branches are placed with $\approx 6-11$ m shift, thus leading to a smaller value of horizontal offset for each branch. The horizontal offset of 0.54m was used instead of 1m. The latter could be done

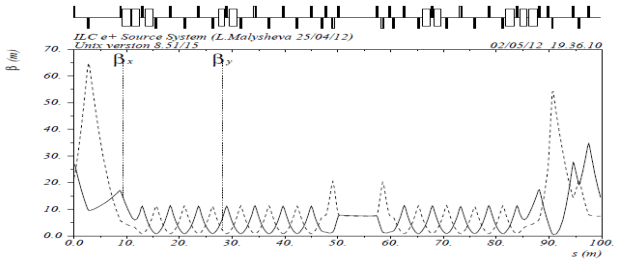

Figure 4: Asymmetric section for one of spin rotator branch matched by MAD8.

adding one or two extra FODO cells before the solenoid section, keeping the lattice unchanged after the solenoid for one branch and adding extra FODO cells after the solenoid section for another branch. As it leads to increase of the length of the whole spin rotator section, some rematching was necessary in order to fit the length of section D (123.595m) and the total PLTR length. In Fig. 4 the design of the new spin rotation section with super-conducting solenoid is given.

3 CONCLUSIONS

The suggested spin rotator design confirms that the fast helicity switching for the positron beam is possible. The train to train polarity selection for electron and positron beams at the IP can be achieved. In particular:

- The suggested optic design for the fast helicity reversal spin rotator section satisfies to the PLTR section requirements.
- An asymmetric design for the solenoid position shifted in two parallel line of spin rotator is produced.
- The optic design is cross-checked with different accelerator design codes
- Depolarization effects in a new lattice are estimated by BMAD [10] and no significant depolarization connected with beam optics is discovered.

4 ACKNOWLEDGMENT

The authors are grateful to the all members of the Spin-management group for the fruitful discussions. We are also would like to thank Dr. W. Liu for close collaboration, practical advices and for providing the matching parameters of the PLTR lattice. L.I. Malysheva also thanks Mr. J. Jones and Dr. P. Williams from ASTeC (Daresbury) for help and advices concerning ELEGANT running.

A Appendix: Basic Theory

A spin rotator is a device which manipulates polarized beams. Various designs for spin rotators and some examples can be found in [3, 4]. The use of spin rotators allows to preserve the degree of polarization during beam transport as well as selecting the desired direction of polarization at the interaction point (IP). According to the design, spin rotators can be divided in two classes which are illustrated in Fig. 5:

The first is based on spin rotation in dipole fields orthogonal to the direction of motion. The precession of spin is around the field direction and proportional to the orbit deflection angle θ_{orbit} as $\theta_{spin} = a\,\gamma\,\theta_{orbit}$, where γ is the Lorentz factor and $a = 0.00115965$ is an anomalous gyromagnetic ratio of

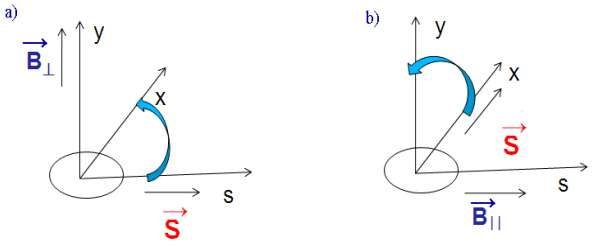

Figure 5: Spin rotation in horizontally bending dipole (a) and solenoidal (b) fields.

a positron/electron. For example, for positrons at 5 GeV the orbital angle of 7.929^0 produce a spin rotation of 90^0. Starting from longitudinal polarization a set of interleaving vertical and horizontal bends can be used for producing the vertical spin direction. The second type is a solenoid based spin rotators where the spin is precessing around the longitudinal direction by the angle θ_{spin} which is proportional to the solenoidal field B_z and its length L_{sol} as

$$\theta_{spin} \approx \frac{B_z \quad L_{sol}}{B\rho} \tag{1}$$

where $B\rho$ is the magnetic rigidity. For a 5 GeV positron beam a solenoid with field integral of 26.18 T m is required. This type of spin rotators has a potential of destroying the vertical beam emittance via orbit coupling in solenoid, thus the specially designed so-called Emma rotators [3] with compensating quadrupoles should be used.

References

[1] G.Moortgat-Pick et al., Phys.Report.460:131-243,(2008) www.ippp.dur.ac.uk/gudrid/power/.

[2] L.I. Malysheva and D.P. Barber. Depolarisation in the damping rings of the ILC.Proceedings of International Linear Collider Workshop LCWS2007, Hamburg, Germany, June 2007.

[3] P.Emma, A spin rotator system for the NLC, SLAC NLC-Note-07,1994.

[4] P.Schmidt, A spin rotator for the ILC,EUROTev-Report-2005-024-01.

[5] K.Moffeit et al., Spin rotation schemes at the ILC for two interaction regions and positron polarisation with both helicities, SLAC-TN-05-045,2005.

[6] F.Zhou et al.,Start-to-end beam optics development and multiparticle tracking for the ILC undulator based positron source, SLAC-PUB-12239, Jan.2007.

[7] N. Solyak, RTML General Layout and Parameters.; ILC Source/RTML/BDS+MDI Baseline Technical Review, DESY, October 2011

[8] `http://mad.web.cern.ch/mad/`

[9] W.Liu, Private conversation.

[10] M. Borland. elegant: A Flexible SDDS-Comliant Code for Accelerator Simulation, Proceedings of the 6^{th} International Computational Accelerator Physics Conference, ICAP2000, September 2000

[11] www.lepp.cornell.edu/ dcs/bmad

[12] V.Kovalenko et al, Spin Tracking Simulation of a Future International Linear collider, Procceding of the 3rd International Particle Accelerator Conference, New Orlean, 1807 .

A Transverse Polarimeter for a Linear Collider of 250 GeV $e^{\pm}$ Beam Energy

Itai Ben Mordechai[1] **and Gideon Alexander**[2]

School of Physics and Astronomy
Raymond and Beverly Sackler Faculty of Exact Sciences
Tel-Aviv University, 69978 Tel-Aviv, Israel

Abstract

The setup and features of a transverse polarimeter based on Compton scattering is described for a 250 GeV electron (positron) beam and its performance is investigated via a Monte Carlo data sample. The position of the Compton backward scattered electrons are registered by a Silicon pixel detector situated some 38 meters away from the $e\gamma$ collision position. Specifically it is shown that, for the planned International Linear Collider beam parameters at 250 GeV, a measurement of the transverse polarization reaches a statistical precision of $\leq 0.5\%$ within a very short time. The over all systematic error is estimated to be $\sim 0.2\%$.

July 30, 2012

[1]Email: *itaibm@gmail.com*
[2]Email: *gideong@post.tau.ac.il*

1 Introduction

In planning future high energy e^+e^- linear colliders, like the International Linear Collider (ILC) and the Compact Linear Collider (CLIC), the benefit of the implementation of a longitudinal polarized $e^{\pm}$ beams has been stressed in many studies [1]. Although even if only the electron beam is longitudinal polarized the collider physics capabilities is increased, as has been demonstrated with the SLC, the situation where both beams are polarized allows additional physics problems to be investigated.

More recently the benefit from the investigation of e^+e^- interactions with transversed polarized beams has also been emphasized [2]. Unlike the case of the longitudinal polarization in the transverse polarization case both the electron and the positron beams have to be polarized in order to benefit from it. To utilize the transverse polarized colliding beams it is necessary to have measuring devices that can measure the transverse polarization values, near or at the e^+e^- interaction point ($IP_{e^+e^-}$), down to a level of 0.5% or even better.

At low electron beam energies transverse polarization measurement devices, denoted by Transverse Polarimeters (TPOL), have been designed constructed and operated successfully [3]. In the present work we study the feasibility to design and construct a transverse polarimeter at high beam energy of 250 GeV, envisaged for the ILC, having a precision of $\leq 0.5\%$ via the Compton scattering of a polarized laser light off the $e^{\pm}$ beams.

2 The Compton scattering

For the basic formulae of the Compton scattering of a laser beam on an electron beam we have followed closely reference [3]. In the electron center of mass (CM) system (see Fig. 1) the differential Compton scattering is given by

$$\frac{d\sigma}{d\Omega}(S,P) = \Sigma_0 + S_1\Sigma_1 + S_3[P_y\Sigma_{2y} + P_z\Sigma_{2z}] \tag{1}$$

where

$$\begin{aligned}
\Sigma_0 &= C[(1+\cos^2\theta) + (k_i - k_f)(1-\cos\theta)] \\
\Sigma_1 &= C\cos(2\phi)\sin^2\theta) \\
\Sigma_{2y} &= -Ck_f\sin\phi\sin\theta(1-\cos\theta) \\
\Sigma_{2z} &= -C(1-\cos\theta)(k_f+k_i)\cos\theta
\end{aligned}$$

Here $P = (P_x, P_y, P_z)$ is the polarization of the initial electron in Cartesian coordinates. S_1 is the linear polarization component of the photon and S_3 is the circular component of the photon. The initial and final photon momenta k_i and k_f are defined in the electron CM system and $C = 0.5r_0^2k_f^2/k_i^2$ where r_0 is the classical radius of the electron. The angles θ and ϕ

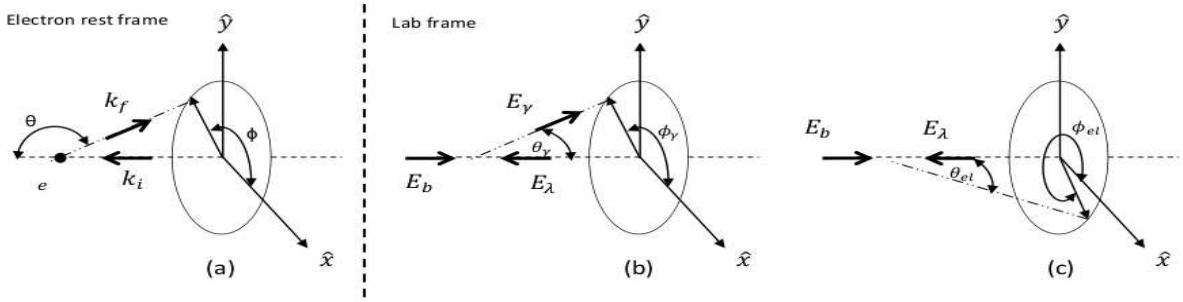

Figure 1: Geometry and coordinate system of the Compton scattering, showing in (a) the incoming electron rest frame and in (b) in the laboratory system both for the back scattering angles of the photon. In (c) the process is shown in the laboratory system for the scattered electron.

are the polar and azimuthal angles of the backward scattered photon in the electron CM system. To transform these formulae to the laboratory system one has the relations

$$\cos\theta = \frac{E_{beam} - E_\gamma(1 + 1/k_i)}{E_{beam} - E_\gamma} \quad \text{and} \quad \mathrm{E}_\gamma = \mathrm{E}_{\mathrm{beam}} + \mathrm{E}_\lambda - \mathrm{E}_\mathrm{e} \tag{2}$$

where the energies are defined in the laboratory system and E_e is the energy of the scattered electron. The electron scattered angle in the laboratory system is given by

$$\theta_e^{lab} = \frac{Y}{1-Y}\frac{m_e}{E_{beam}}\sqrt{\frac{2k_i}{Y} - (2k_i + 1)} \tag{3}$$

where $Y = 1 - E_e/E_{beam}$. The method for the determination of the electron transverse polarization involves the measurement of the y distribution of the scattered electrons on the detector surface which is placed perpendicular to the beam direction. In term of the scattered polar and azimuthal angles y is equal to

$$y = D\sin\phi\tan\theta_e^{lab} \quad \overset{\theta_e^{lab} \ll 1}{\longrightarrow} D\sin\phi\theta_e^{lab} \tag{4}$$

where D is the distance between the Compton interaction point and the detector surface. In practice one considers $< y >$, the average value of the measured y positions.

3 Transverse Polarimetry for the ILC

In our study we consider the case where the laser beam has no linear component and the electron beam has no longitudinal polarization component. In this case the differential Compton scattering expression given by Eq. 1 reduces to

$$\frac{d\sigma}{d\Omega}(S,P) = \Sigma_0 + S_3 P_y \Sigma_{2y} \tag{5}$$

where the relevant parameters of the ILC are: $S_1 = 0$, $S_3 = \pm 1$, $P_z = 0$, $E_{beam} = 250$ GeV and $D = 37.95$ m [8]. For the polarimeter we have taken a green laser of 2.33 eV. For a given E_γ

value the average y is given by;

$$\langle y \rangle \;=\; \frac{\int \frac{d^2\sigma}{dE_e d\phi} y d\phi}{\int \frac{d^2\sigma}{dE_e d\phi} d\phi} \tag{6}$$

The distribution of $\langle y \rangle$ as a function of E_e for $P_T = 1.0$ and $S_3 = +1$ is shown in Fig. 2.

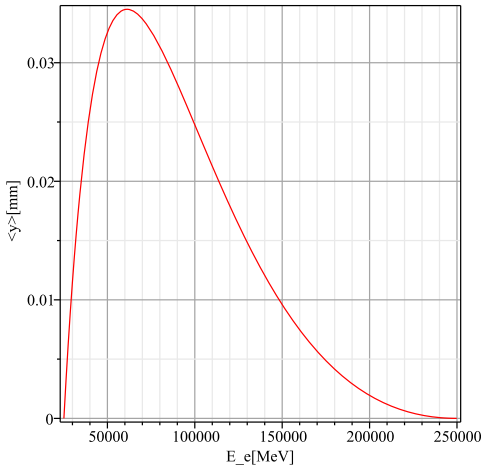

Figure 2: The $\langle y \rangle$ distribution as function of the scattered electron energy for the ILC setup with $P_T = 100\%$, $S_3 = +1$, $\lambda = 2.33$ eV and $D = 37.95$ m.

In order not to be dependent on the exact y position of the $IP_{\gamma e}$ it is a safer way to determine the polarization via the measurement of the difference in $\langle y \rangle$ between the left and right helicity states of the laser ($S = \pm 1$), i.e.

$$\frac{\langle y \rangle_{\;S_3=+1} - \langle y \rangle_{\;S_3=-1}}{2} = P_T \Pi(E_e) \tag{7}$$

where P_T is the transverse polarization level and $\Pi(E_e)$, the Analyzing Power (AP) of the polarimeter, is its value for a 100% polarization. In this way one assures that the measured effect is indeed due to a vertical electron polarization and is not due to an instrumental deficiency.

4 The γe Luminosity

4.1 Luminosity for a continuous laser

The luminosity $\mathcal{L}$ of a continuous laser colliding with a round pulsed electron beam, that is $\sigma_x = \sigma_y = \sigma$, can be expressed [4] as:

$$\mathcal{L} \;=\; \frac{1+\cos\theta_0}{\sqrt{2\pi}} \frac{I_e}{e} \frac{W_L \lambda}{hc^2} \frac{1}{\sqrt{\sigma_e^2 + \sigma_\gamma^2}} \frac{1}{\sin\theta_0}, \tag{8}$$

where θ_0 is the crossing angle of the two beams, I_e is the mean electron current, W_L is the power of the laser, λ is the wavelength of the laser and σ_e and σ_γ are the rms beam sizes. As

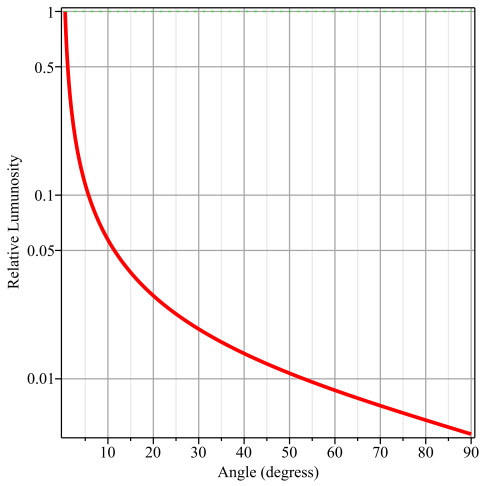

Figure 3: The relative $e\gamma$ luminosity as a function of the crossing angle θ_0 of the incident electron and laser beams.

expected, the luminosity will decrease substantially when the angle between the laser and the beam will approach 90^o (see in Fig. 3) so that a continuous laser beam perpendicular to the electron beam will result in an undesired very low luminosity[3]. For a small crossing angle θ_0 one has:

$$\mathcal{L} \;=\; 8.36\ 10^{24} cm^{-2} s^{-1}\ \frac{\lambda}{\sqrt{\sigma_e^2+\sigma_\gamma^2}} \frac{I_e W_L}{\theta_0}\ . \tag{9}$$

According to Ref. [5] at the ILC where $\sigma_e \ll \sigma_\gamma$, and with the following parameters settings:
$\theta_0 = 0.01$ rad,
$\lambda = 532$ nm $= 2.33$ eV,
$\sigma_\gamma = 50\ \mu$m,
$W_L = 0.5$ W,
$I_e = 9\ \mu$A,
one obtains a luminosity of

$$\mathcal{L}(\gamma e) \;=\; 1.75 \times 10^{29}\ cm^{-2} s^{-1}\ . \tag{10}$$

4.2 The luminosity value with a pulsed laser

For a pulsed laser the γe luminosity is given by [6]:

$$\mathcal{L} \;=\; f_b N_e N_\gamma g \tag{11}$$

where f_b is the number of bunch crossing per second, N_e the number of electrons per bunch, N_γ the number of photons per laser pulse and g is a geometrical factor which takes in account the spatial overlap of the two beams. For a small crossing angle θ_0 one has:

$$g^{-1} \;=\; 2\pi\sqrt{\sigma_{xe}^2+\sigma_{x\gamma}^2}\sqrt{(\sigma_{ye}^2+\sigma_{y\gamma}^2)cos^2(\theta_0/2)+(\sigma_{ze}^2+\sigma_{z\gamma}^2)sin^2(\theta_0/2)}\ . \tag{12}$$

[3]Note that $\theta_0 = 0^o$ means here that the laser and the beam directions are exactly opposite.

If the transverse dimensions of the electron beam are small in comparison to the laser focus i.e., $\sigma_{xe} \ll \sigma_{x\gamma}$ and $\sigma_{ye} \ll \sigma_{y\gamma}$ (which certainly is valid at the $IP_{\gamma e}$ region), one obtains for g^{-1} :

$$g^{-1} \;=\; 2\pi\sigma_{x\gamma}\sigma_{y\gamma}\sqrt{1+(0.5\theta_0\sigma_{z\gamma}/\sigma_{y\gamma})^2} \tag{13}$$

and for the luminosity:

$$\mathcal{L} \;=\; \frac{f_b N_e N_\gamma}{2\pi\sigma_{x\gamma}\sigma_{y\gamma}\sqrt{1+(0.5\theta_0\sigma_{z\gamma}/\sigma_{y\gamma})^2}} \;=\; \frac{\mathcal{L}_{max}}{\sqrt{1+(0.5\theta_0\sigma_{z\gamma}/\sigma_{y\gamma})^2}} \tag{14}$$

where $\mathcal{L}_{max}$ is the maximum luminosity reached at very small θ_0 angle for a given transverse size $\sigma_{x\gamma}\sigma_{y\gamma}$, namely:

$$\mathcal{L}_{max} \;=\; \frac{f_b N_e N_\gamma}{2\pi\sigma_{x\gamma}\sigma_{y\gamma}}\;. \tag{15}$$

Note that this last formula is very similar to the expression given for the luminosity of e^+e^- colliding beams. In the ILC, the dimensions of the electron bunches at $IP_{e^+e^-}$ are smaller than that of the laser. The number of bunches per second is $f_b = 14100$ and each bunch consists of $N_e = 2\times10^{10}$ electrons. From this follows that the $e\gamma$ luminosity at the $IP_{\gamma e}$ is

$$\mathcal{L}_{max}(IP_{\gamma e}) \;=\; 4.49\times\frac{N_\gamma}{\sigma_{x\gamma}\sigma_{y\gamma}}\;10^{13} cm^{-2}s^{-1} \tag{16}$$

where N_γ is the number of laser photons per pulse and the laser is fired in synchronization with the same pulse repetition rate as the accelerator. For a round laser focus with $\sigma_{x\gamma} = \sigma_{y\gamma} = 50\mu m$ one obtains:

$$\mathcal{L}_{max}(IP_{\gamma e}) \;=\; 1.12\times\frac{j_\gamma[\mu J]}{\epsilon_\gamma[eV]}10^{31} cm^{-2}s^{-1} \tag{17}$$

where j_γ and ϵ_γ are the laser current and energy. The Compton $e\gamma$ luminosity at the ILC operating at 0.25 TeV beam energy for three pulsed laser configurations are shown in Table 1.

Table 1: Compton $e\gamma$ luminosity before the $IP_{e^+e^-}$ of the ILC operating at 0.25 TeV beam energy with a round pulsed laser of $\sigma_{x\gamma} = \sigma_{y\gamma} = 50\mu m$. A full synchronization between the beam bunches and the laser repetition is assumed.

ϵ_γ (eV)	λ (nm)	$< W_L >$ (Watt)	j_γ (μJ)	$\mathcal{L}_{max}$ (10^{31}cm$^{-2}s^{-1}$)
1.165	1064	1	71	68.3
2.33	532	0.5	35	16.8
4.66	266	0.2	14	3.4

5 The polarimeter setup

A sketch of the Compton scattering collision setup is shown in Fig. 4. The 250 GeV electron beam is moving in the $+z$ direction reaching the first two $B_1(-y)$ and $B_2(+y)$ magnets which steer the beam to a parallel straight trajectory. In position 2 the laser beam collides with the electron beam. The unperturbed beam is then restored to its original trajectory by the set of the $B_2(+y)$ and $B_1(-y)$ magnets all of which have a strength of 0.097 T. The scattered electrons which suffered a loss of energy will be separated in the x direction according to their energy values to reach the detector at a distance of 37.95 m.

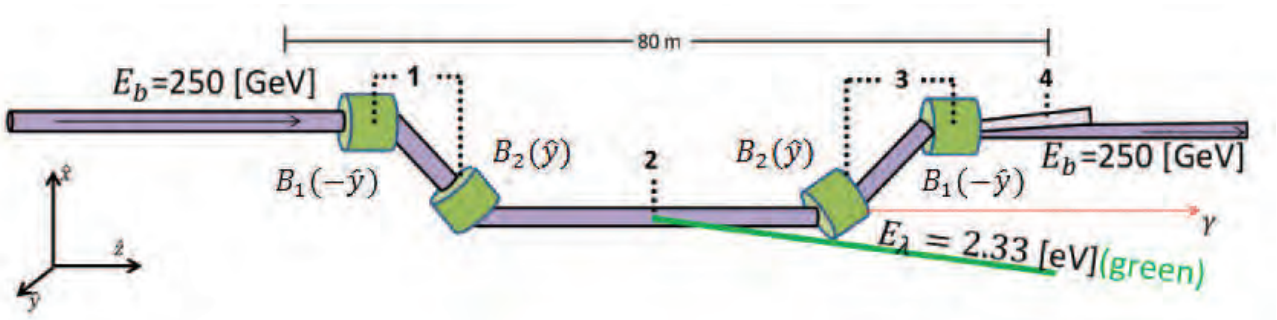

Figure 4: The setup scheme of the laser collision with the 250 GeV electron beam which moves in the z direction. The magnets are steering the beam to a parallel trajectory for the laser collision point and back to their original direction. The scattered electrons are deviated from the bean direction toward a detector 37.95 m away.

5.1 The energy spectrometer

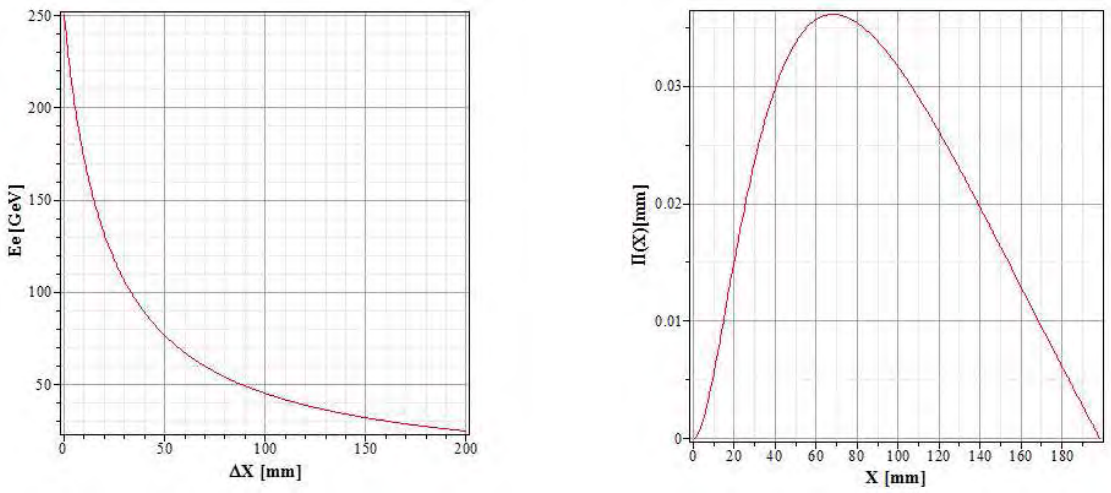

Figure 5: Left: The scattered electron energy as a function of the x shift from the non-scattered beam. Right: The transverse polarization analyzing power $\Pi(x)$ as a function of the x shift.

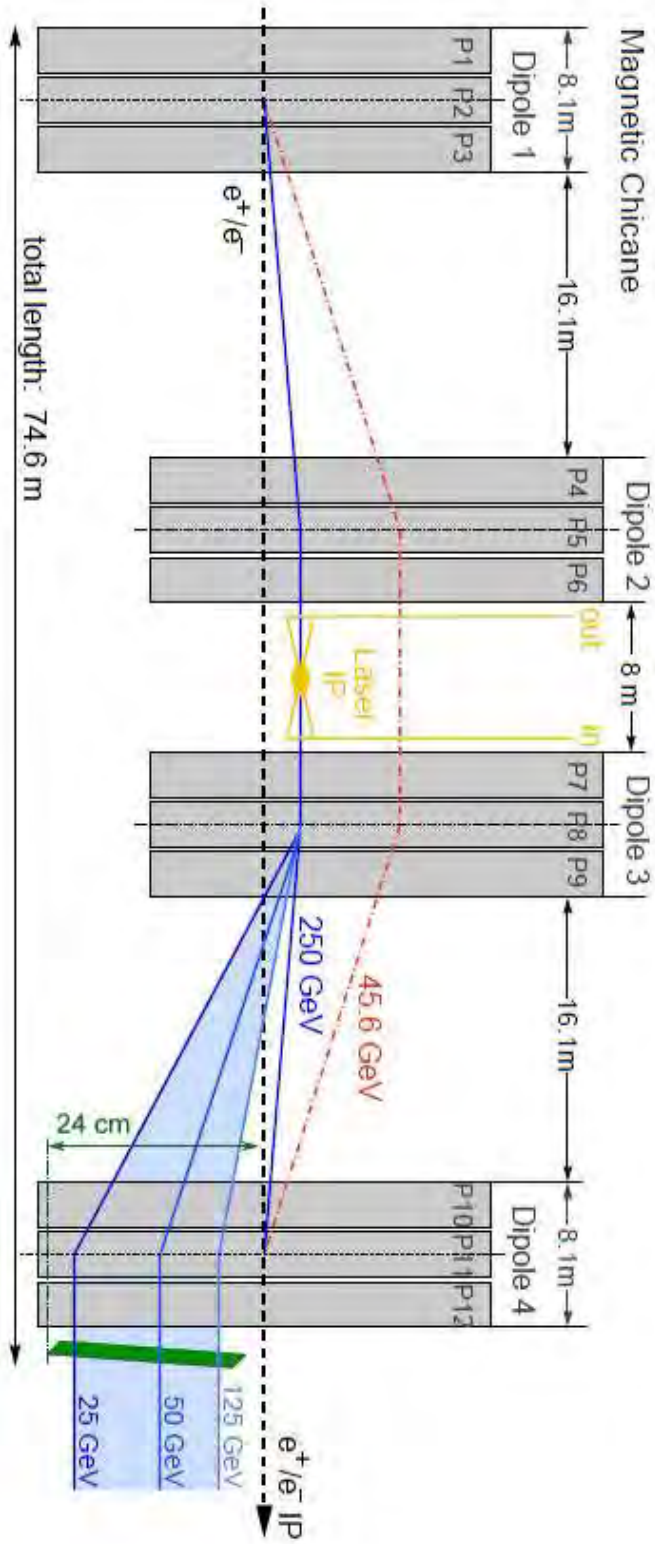

Figure 6: The general scheme of the envisaged ILC of the four magnets chicane for the Compton polarimetry taken from Ref. [8]. The shifted electron beam shown by the solid line is colliding with the laser beam and then restored to its original trajectory (dashed line). The scattered electrons are separated according to their energy values. The 45.6 GeV beam (dot dashed line) is planned to be used for calibration purposes.

The relation between x and the energy of the scattered electrons is shown in Fig. 5(left) was determined from a Monte Carlo (MC) program [7] using the actual general scheme of the envisaged ILC four magnets chicane [8] as shown in Fig. 6. A fit to the distribution shown in Fig. 5(left) yields

$$E_e = \frac{10^6}{4 + 18.04 \cdot x[mm]} \text{ MeV} . \tag{18}$$

By replacing the energy dependence in Eq. 7 by its dependence on x according to Eq. 18 one obtains the dependence of AP on x. As can be seen from in Fig. 5(right), the AP changes considerably with x and reaches its maximum value around 70 mm from the main beam direction.

5.2 The detector

For the detection of the scattered electrons we consider only a position measurement using a Silicon pixel detector placed at a distance of 37.95 m from the Compton $IP_{\gamma e}$. The active dimension of the detector is 2×200 mm^2. The size of the pixels cell taken is 50 × 400 μm^2 similar to the one used in the ATLAS detector [9]. This scheme yields an approximate two dimensional resolution of 14.4× 115.5 $m\mu^2$ [10] with a data read-out rate of 160 Mb/sec.

For the simulation and analysis of the polarization measurement we have used a Monte Carlo program which generates the Compton scattering and simulates the polarimeter setup [7].

6 The polarization measurement

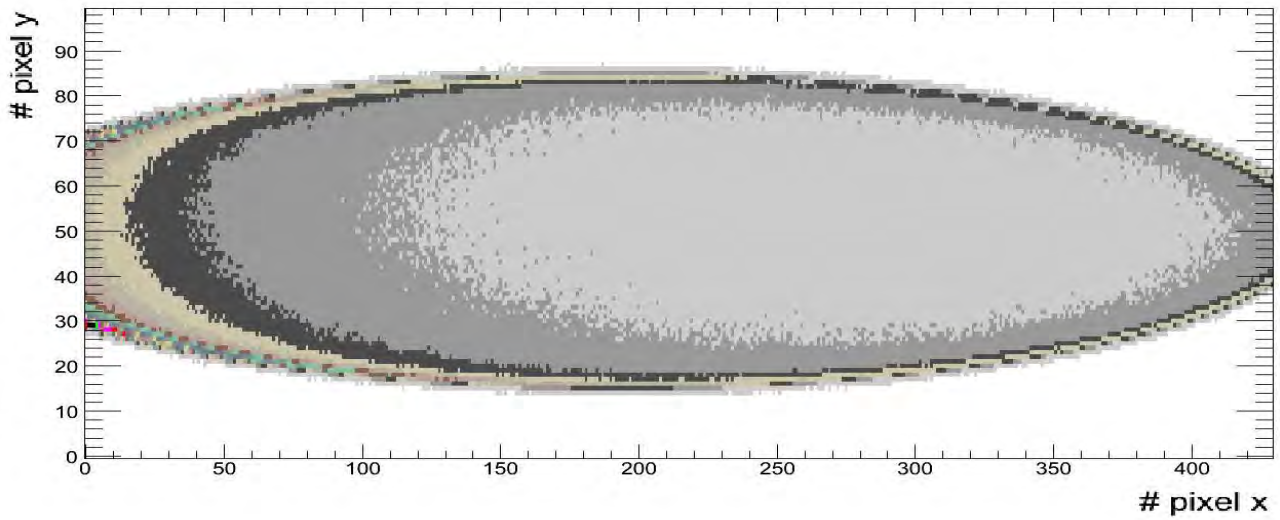

Figure 7: A MC ILC simulated pixel detector image, in arbitrary units, after it was hit for 1 sec by the Compton scattered electrons for $S_3 = +1$ and $P_T = 0.9$.

6.1 The measurement method

For the measurement of the polarization we have used the scattered electron detector hits in the left and right ($S_3 = +1$ and $S_3 = -1$) helicity positions of the laser. A 1 second typical hit distribution of the detector is shown in Fig. 7 for $S_3 = +1$ and $P_T = 0.9$. After the readout of the pixel detector's x and y positions of the hits we calculate the average $\langle y \rangle$ as a function of x sampled in 2 mm steps for the two laser helicity states. In Fig, 8(left) the y distribution for $S_3 = +1$ is shown in the range of 36 $mm \leq x \leq 38$ mm where a clear asymmetry due to the transverse polarization is seen.

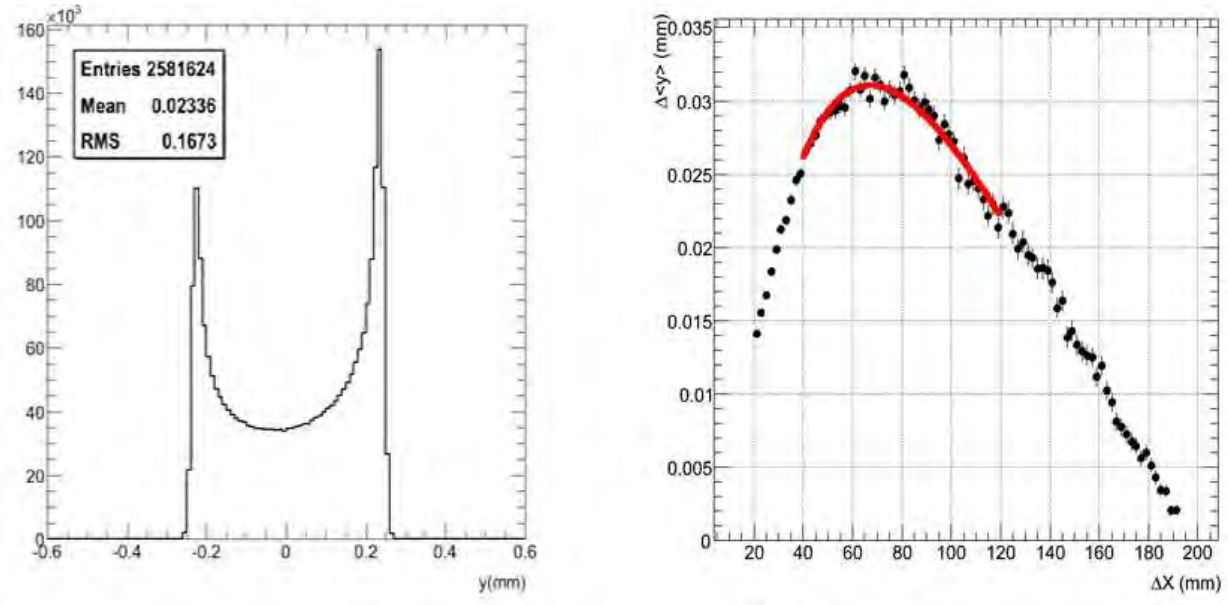

Figure 8: Monte Carlo data simulation. Left: The distribution of y within the x range of 36 to 38 mm from the electron beam direction for the $S_3 = +1$ helicity and $P_T = 0.9$. A clear asymmetry due to the transverse polarization is seen. Right: The dependence of $P_T\Pi(x)$ on x reevaluated in steps of 2 mm obtained from 1 sec run. The solid line is the results of a fit of Eq. 19 to the Monte Carlo data.

We next calculate the quantity $(\langle y \rangle_L - \langle y \rangle_R)/2$ as a function of x. The results for 1 sec run (14100 bunches) are shown in Fig. 8(right) where the small fluctuations of the MC data points are due to the finite beam dimension and the pixel detector resolution. Next we fit P_T from the MC data in a given x range around its maximum value according to Eq. 19

$$\Delta y(x) = \left.\frac{\langle y \rangle_L - \langle y \rangle_R}{2}\right|_X = P_T \Pi(x) \tag{19}$$

where $\Pi(x)$ is the analyzing power. The result of the fit, shown by the solid line in Fig. 8(right), yielded $P_T = 0.899 \pm 0.003$, with χ^2/dof =1.39, which agrees very well with the MC input value of $P_T = 0.9$.

6.2 The statistical error

We have evaluated the statistical error on the transverse polarizations measurements from our Monte Carlo data sample assuming a zero detector dead time. Obviously this error is related to the number of scattered electrons recorded by the detector. This is shown in Fig. 9 where the error dependence on the measurement time can be expressed by $\Delta P_T/P_T = 0.29 \times t^{-0.53}$ %. As expected, already for a very short measurement time, the statistical error can be neglected in comparison with the systematic errors which are discussed in the following section.

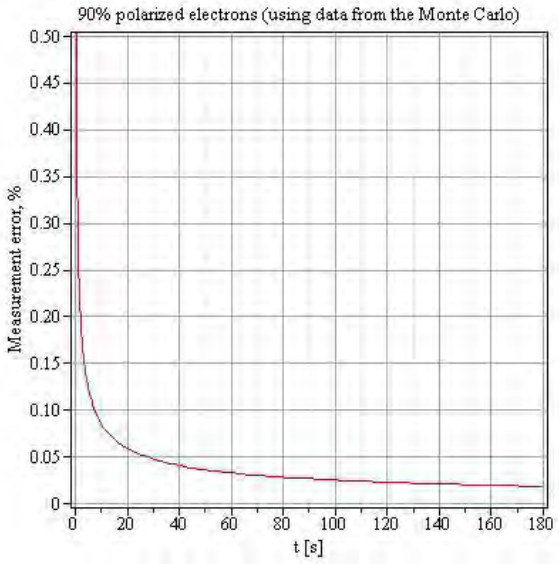

Figure 9: The measurement statistical error on a $P_T = 0.9$ level as a function of the measuring time derived from the Monte Carlo data sample assuming zero detector dead time.

6.3 The systematic errors

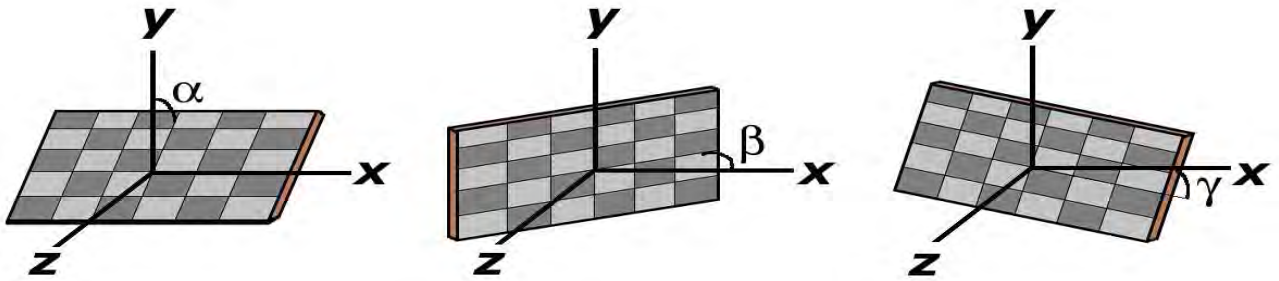

Figure 10: The deviation of the Silicon pixel detector orientation which is set to be perpendicular to the non-scattered electron beam that moves in the z direction.

A substantial contribution to the systematic error of the polarization measurement is coming from possible y displacement of the IP_{e^-} and or the pixel detector. Due to the fact that the

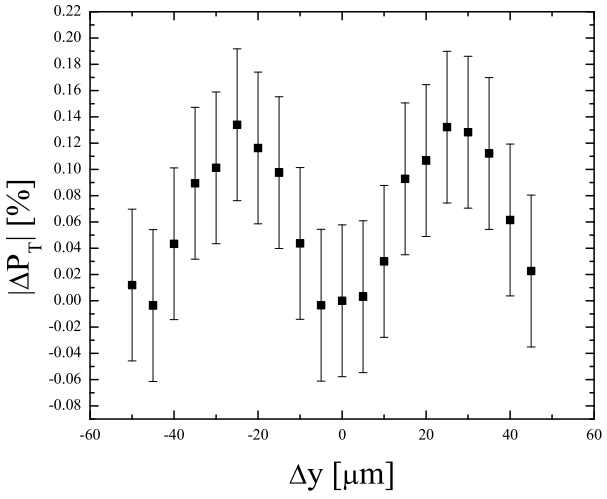

Figure 11: The ΔP_T dependence on Δy calculated for $P_T = 0.9$ via a MC program. The statistical errors correspond to a measurement time of 1 minute with the ILC and polarimeter setup as described in the text.

dimension of the pixels are finite, in our setup of 50 μm in the y direction, one does not achieve a complete Δy compensation via Eq. 7. From our MC simulation we obtain a quasi-sinusoidal dependence of ΔP_T on Δy which is shown in Fig. 11. As expected a maximum compensation of the Δy displacement is reached when its value is $n \times 50$ μm where $|n|$ is equal to zero or an integer. At the same time the systematic error on $|P_T|$ does not exceed the value of $\sim 0.13\%$. This systematic error and other ones have been estimated by changing individually various parameters of the planned ILC and its polarimeter setup according to their uncertainties estimated in Ref. [5]. These are listed in Table 2. The first three parameters of the table concern the displacements of the $IP_{\gamma e}$ or the pixel detector positions. The next three parameters are associated with detector orientation with respect to the beam position as defined in Fig. 10. The next two parameters are related to the magnetic field of the spectrometer. The following pair of parameters are connected to the beam tremor and the last two parameters are related to the beam energy uncertainty. As seen from the table, the over all systematic error added in quadrature amounts to 0.20 % . Additional sources of systematic error like those related to the radiation background from the collider and the polarimeter structure will have to be evaluated after their detailed design and construction.

Acknowledgments

We would like to thank S. Riemann and many of her colleagues in the Linear Collider groups of DESY/Zeuthen and DESY/Hamburg for their many useful comments and suggestions. Our thanks are in particular due to J. List for allowing us to make use of her Monte Carlo

Table 2: A list of the collider and polarimeter setup parameters that are expected to contribute to the systematic errors of the transverse polarization measurement. From the assessed systematic uncertainties of these parameters the corresponding systematic errors were obtained from a MC program simulating the ILC polarimeter features with a beam polarization value of $P_T = 0.9$.

Source of the systematic error	Δ	$\lvert\Delta P_T\rvert$ %
Δy axis displacement	≥ 25 μm	0.13
Δx axis displacement	0.1 mm	0.007
Δz axis displacement	1 cm	0.08
$\Delta\alpha$ deviation of the detector	0.1^0	0.002
$\Delta\beta$ deviation of the detector	0.1^0	0.004
$\Delta\gamma$ deviation of the detector	0.1^0	0.1
Spectrometer ΔB_1	0.0001 T	0.02
Spectrometer ΔB_2	0.0001 T	0.005
y axis beam position tremor	5 μm	0.01
x axis beam position tremor	5 μm	0.03
Beam energy tremor	0.22 GeV	0.03
ΔE_{beam} beam energy	0.22 GeV	0.052
$\sqrt{\sum_i \Delta P_i^2}$	0.20%	

program and her help in its adaptation to out transverse polarimeter setup.

References

[1] See e.g. G. Moortgat-Pick et al., Phys. Rept. 460 (2008) 131.

[2] See e.g. T.G. Rizzo, SLAC-PUB-14280, *arXiv:1011.2185*; K. Desch, LC-PHSM-2003-002; F. Franco-Sollova, LC-PHSM-2004-011.

[3] See e.g. D.P. Barber et al., Nucl. Inst. and Method. A329 (1993) 79 for more details.

[4] G. Bardin, et al., *Compton polarimeter studies for TESLA*, DESY print, TESLA 97-03.

[5] J. Brau (Ed), *et al.,* ILC collaboration, arXiv:0712.1950 [physics.acc-ph].

[6] T. Suzuki, *General formulae of luminosity for various types of colliding beam machines*, KEK-76-3 (1976), *http://ccdb4fs.kek.jp/cgi-bin/img_index?197624003* .

[7] C. Bartels et al., Nucl. Inst. Meth. A623 (2010) 570.

[8] S. Boogert et al., JINST 4 (2009) P10015.

[9] ATLAS pixel collaboration, Technical Design Report, (CERN/LHCC, 98-13), 2007.

[10] L. Rossi et al., *Pixel detectors: from fundamentals to applications* Springer Verlag, 2006.

List of Authors